



# ANSYS Mechanical APDL Technology Demonstration Guide

---



ANSYS, Inc.  
Southpointe  
2600 ANSYS Drive  
Canonsburg, PA 15317  
ansysinfo@ansys.com  
<http://www.ansys.com>

Release 17.0  
January 2016

ANSYS, Inc. is  
certified to ISO  
9001:2008.

---

(T) 724-746-3304

(F) 724-514-9494

---

## Copyright and Trademark Information

© 2015 SAS IP, Inc. All rights reserved. Unauthorized use, distribution or duplication is prohibited.

ANSYS, ANSYS Workbench, Ansoft, AUTODYN, EKM, Engineering Knowledge Manager, CFX, FLUENT, HFSS, AIM and any and all ANSYS, Inc. brand, product, service and feature names, logos and slogans are registered trademarks or trademarks of ANSYS, Inc. or its subsidiaries in the United States or other countries. ICEM CFD is a trademark used by ANSYS, Inc. under license. CFX is a trademark of Sony Corporation in Japan. All other brand, product, service and feature names or trademarks are the property of their respective owners.

### Disclaimer Notice

THIS ANSYS SOFTWARE PRODUCT AND PROGRAM DOCUMENTATION INCLUDE TRADE SECRETS AND ARE CONFIDENTIAL AND PROPRIETARY PRODUCTS OF ANSYS, INC., ITS SUBSIDIARIES, OR LICENSORS. The software products and documentation are furnished by ANSYS, Inc., its subsidiaries, or affiliates under a software license agreement that contains provisions concerning non-disclosure, copying, length and nature of use, compliance with exporting laws, warranties, disclaimers, limitations of liability, and remedies, and other provisions. The software products and documentation may be used, disclosed, transferred, or copied only in accordance with the terms and conditions of that software license agreement.

ANSYS, Inc. is certified to ISO 9001:2008.

### U.S. Government Rights

For U.S. Government users, except as specifically granted by the ANSYS, Inc. software license agreement, the use, duplication, or disclosure by the United States Government is subject to restrictions stated in the ANSYS, Inc. software license agreement and FAR 12.212 (for non-DOD licenses).

### Third-Party Software

See the [legal information](#) in the product help files for the complete Legal Notice for ANSYS proprietary software and third-party software. If you are unable to access the Legal Notice, Contact ANSYS, Inc.

Published in the U.S.A.

---

---

---

---

# Table of Contents

What You Need to Know .....	xxxv
<b>1. Brake Squeal Analysis</b> .....	1
1.1. Introduction .....	1
1.2. Problem Description .....	2
1.3. Modeling .....	2
1.3.1. Understanding the Advantages of Contact Element Technology .....	2
1.3.2. Modeling Contact Pairs .....	3
1.3.3. Generating Internal Sliding Motion .....	3
1.3.4. Meshing the Brake Disc-Pad Model .....	4
1.4. Material Properties .....	4
1.5. Boundary Conditions and Loading .....	4
1.6. Analysis and Solution Controls .....	5
1.6.1. Linear Non-prestressed Modal Analysis .....	5
1.6.2. Partial Nonlinear Perturbed Modal Analysis .....	6
1.6.3. Full Nonlinear Perturbed Modal Analysis .....	7
1.7. Results and Discussion .....	8
1.7.1. Determining the Modal Behavior of Individual Components .....	11
1.7.2. Parametric Study with Increasing Friction Coefficient .....	11
1.8. Recommendations .....	12
1.9. References .....	13
1.10. Input Files .....	13
<b>2. Nonlinear Analysis of a 2-D Hyperelastic Seal Using Rezoning</b> .....	15
2.1. Introduction .....	15
2.2. Problem Description .....	16
2.2.1. Understanding Requirements and Physical Behaviors .....	16
2.2.2. Using Rezoning to Repair Mesh Distortions .....	17
2.2.2.1. Horizontal vs. Vertical Rezoning .....	18
2.2.2.2. Understanding the Rezoning Process .....	18
2.2.2.3. Understanding the Remeshing Phase of the Rezoning Operation .....	18
2.3. Modeling .....	19
2.3.1. Specific Modeling Details .....	19
2.3.1.1. The Rezoning Process .....	20
2.4. Material Properties .....	21
2.5. Boundary Conditions and Loading .....	21
2.6. Analysis and Solution Controls .....	21
2.6.1. Common Solution Controls .....	22
2.6.2. Solution Controls for Each Load Step .....	22
2.6.3. Rezoning Considerations .....	22
2.6.3.1. Step 1. Select the Optimal Substep for Rezoning .....	22
2.6.3.2. Step 2. Select a Region and Remesh .....	24
2.6.3.2.1. Selecting Elements for Splitting .....	24
2.6.3.2.2. Methods for Remeshing Using Element Splitting .....	24
2.6.3.2.3. Using Nesting to Control Split Element Size .....	25
2.6.3.3. Step 3. Map Quantities from Old to New Mesh and Rebalance Residuals .....	25
2.6.3.4. Step 4. Perform the Multiframe Restart .....	26
2.7. Results and Discussion .....	26
2.8. Recommendations .....	40
2.9. References .....	42
2.10. Input Files .....	42
<b>3. Fluid-Pressure-Penetration Analysis of a Sealing System</b> .....	43

3.1. Introduction .....	43
3.2. Problem Description .....	44
3.3. Modeling .....	45
3.4. Material Properties .....	47
3.5. Boundary Conditions and Loading .....	49
3.6. Analysis and Solution Controls .....	50
3.7. Results and Discussion .....	51
3.8. Recommendations .....	58
3.9. Acknowledgments .....	58
3.10. Input Files .....	59
<b>4. Ring-Gear Forging Simulation with Rezone</b> .....	<b>61</b>
4.1. Introduction .....	61
4.2. Problem Description .....	62
4.3. Modeling .....	62
4.3.1. Contact .....	63
4.4. Material Properties .....	63
4.5. Boundary Conditions and Loading .....	64
4.6. Analysis and Solution Controls .....	64
4.6.1. Solution Parameters and Analysis .....	64
4.6.2. Rezone Techniques Applied to Ring-Gear Forging .....	64
4.6.2.1. Step 1: Select the Substep to Initiate Rezone .....	65
4.6.2.1.1. First Rezone .....	65
4.6.2.1.2. Second Rezone .....	66
4.6.2.2. Step 2: Select a Region to Remesh .....	67
4.6.2.3. Step 3: Apply a New Mesh .....	67
4.6.2.4. Map Variables and Balance Residuals .....	69
4.6.2.5. Perform a Multiframe Restart .....	71
4.7. Results and Discussion .....	72
4.8. Recommendations .....	76
4.9. References .....	77
4.10. Input Files .....	77
<b>5. Delamination of a Stiffened Composite Panel Under a Compressive Load</b> .....	<b>79</b>
5.1. Introduction .....	79
5.2. Problem Description .....	80
5.3. Modeling .....	80
5.4. Material Properties and Section Definitions .....	82
5.5. Boundary Conditions and Loading .....	85
5.6. Analysis and Solution Controls .....	86
5.7. Results and Discussion .....	86
5.8. Recommendations .....	88
5.9. Input Files .....	89
<b>6. Thermal-Stress Analysis of a Cooled Turbine Blade</b> .....	<b>91</b>
6.1. Introduction .....	91
6.2. Problem Description .....	92
6.3. Modeling .....	93
6.4. Material Properties .....	94
6.5. Boundary Conditions and Loading .....	95
6.6. Analysis and Solution Controls .....	95
6.7. Results and Discussion .....	96
6.8. Recommendations .....	101
6.9. References .....	102
6.10. Input Files .....	102

<b>7. Nonlinear Transient Analysis of a Camshaft Assembly</b> .....	103
7.1. Introduction .....	103
7.1.1. Differences Between General Axisymmetric and Harmonic Axisymmetric Elements .....	103
7.1.2. Where to Find More Information .....	104
7.2. Problem Description .....	104
7.3. Modeling .....	104
7.3.1. Camshaft Modeling .....	104
7.3.1.1. General Axisymmetric Element Model .....	105
7.3.1.2. Full 3-D Model .....	106
7.3.2. Contact Modeling .....	106
7.4. Material Properties .....	108
7.5. Boundary Conditions and Loading .....	108
7.6. Analysis and Solution Controls .....	109
7.7. Results and Discussion .....	110
7.7.1. Results Comparison: General Axisymmetric Model and Full 3-D Model .....	111
7.8. Recommendations .....	113
7.9. Input Files .....	113
<b>8. Nuclear Piping System Under Seismic Loading</b> .....	115
8.1. Introduction .....	115
8.2. Problem Description .....	115
8.3. Modeling .....	116
8.3.1. Global Nuclear Piping System Model .....	116
8.3.2. Local Elbow Model Meshed with ELBOW290 Elements .....	118
8.3.3. Local Elbow Model Meshed with SHELL281 Elements .....	119
8.4. Material Properties .....	120
8.5. Boundary Conditions and Loading .....	121
8.5.1. Global Nuclear Piping System Model .....	121
8.5.2. Local Elbow Model Meshed with ELBOW290 Elements .....	122
8.5.3. Local Elbow Model Meshed with SHELL281 Elements .....	122
8.6. Analysis and Solution Controls .....	122
8.6.1. Modal Analysis of the Global Piping System Model .....	123
8.6.2. Nonlinear Static Analyses of the Local Elbow Models .....	123
8.7. Results and Discussion .....	123
8.7.1. Global Piping System: Modal Analysis Results .....	123
8.7.2. Local Elbow Models: Nonlinear Static Analysis Results .....	124
8.8. Recommendations .....	125
8.9. References .....	126
8.10. Input Files .....	126
<b>9. Reliability Study of a Composite Overwrapped Pressure Vessel</b> .....	127
9.1. Introduction .....	127
9.2. Problem Description .....	127
9.3. Modeling .....	128
9.4. Material Properties .....	130
9.5. Boundary Conditions and Loading .....	130
9.6. Analysis and Solution Controls .....	131
9.7. Results and Discussion .....	131
9.8. Recommendations .....	136
9.9. References .....	136
9.10. Input Files .....	136
<b>10. Simulation of a Lumbar Motion Segment</b> .....	139
10.1. Introduction .....	139
10.2. Problem Description .....	140

10.3. Modeling .....	140
10.4. Material Properties .....	140
10.5. Boundary Conditions and Loading .....	141
10.6. Analysis and Solution Controls .....	141
10.7. Results and Discussion .....	141
10.8. References .....	144
10.9. Input Files .....	144
<b>11. Rocket Nozzle Extension Simulation: Fabrication .....</b>	<b>147</b>
11.1. Introduction .....	147
11.2. Problem Description .....	147
11.3. Modeling .....	148
11.4. Material Properties .....	150
11.5. Boundary Conditions and Loading .....	151
11.6. Analysis and Solution Controls .....	151
11.7. Results and Discussion .....	152
11.8. Recommendations .....	157
11.9. References .....	157
11.10. Input Files .....	157
<b>12. Dynamic Simulation of a Nuclear Piping System Using RSA Methods .....</b>	<b>159</b>
12.1. Introduction .....	159
12.2. Problem Description .....	160
12.3. Modeling .....	161
12.3.1. BM3 Piping System Modeling .....	161
12.3.2. Elastic Support Modeling .....	161
12.4. Material Properties .....	162
12.5. Boundary Conditions and Loading .....	163
12.6. Analysis and Solution Controls .....	164
12.6.1. Response-Spectrum Analysis Summary .....	164
12.6.2. Full-Transient Analysis Summary .....	164
12.7. Results and Discussion .....	165
12.7.1. Results Comparison of the Time-History and Response-Spectrum Analyses .....	165
12.7.1.1. RSAs A1 and A2 .....	166
12.7.1.2. RSA A3 .....	167
12.7.1.3. RSAs A4 and A5 .....	168
12.7.1.4. RSA A6 .....	169
12.7.1.5. RSA A7 .....	171
12.8. Recommendations .....	172
12.9. References .....	173
12.10. Input Files .....	173
<b>13. Centrifugal Impeller Analysis Using Cyclic Symmetry and Linear Perturbation .....</b>	<b>175</b>
13.1. Introduction .....	175
13.2. Problem Description .....	175
13.3. Modeling .....	177
13.3.1. Impeller Blade Modeling .....	177
13.3.2. Contact Modeling .....	178
13.4. Material Properties .....	179
13.5. Boundary Conditions and Loading .....	179
13.6. Analysis and Solution Controls .....	180
13.6.1. Modal Cyclic Symmetry Analysis .....	180
13.6.2. Linear Prestressed Modal Cyclic Symmetry Analysis with Linear Perturbation .....	181
13.6.3. Nonlinear Prestressed Modal Cyclic Symmetry Analysis with Linear Perturbation .....	182
13.6.4. Full Harmonic Cyclic Symmetry Analysis .....	183



13.6.5. Nonlinear Prestressed Full Harmonic Cyclic Symmetry Analysis with Linear Perturbation .....	183
13.6.6. Nonlinear Prestressed Mode-Superposition Harmonic Cyclic Symmetry Analysis with Linear Perturbation .....	184
13.7. Results and Discussion .....	185
13.7.1. Performance Benefits of Cyclic Symmetry Analysis .....	196
13.7.2. Performance Benefits of the Variational Technology (VT) Solver .....	199
13.8. Recommendations .....	200
13.9. References .....	201
13.10. Input Files .....	201
<b>14. Rotordynamics of a Shaft Assembly Based on a Representative Model of Nelson-Vaugh Rotor .....</b>	<b>203</b>
14.1. Introduction .....	203
14.2. Problem Description .....	204
14.3. Modeling .....	205
14.3.1. 3-D Modeling of Flexible Rotor Component .....	205
14.3.2. Axisymmetric Modeling of the Flexible Rotor Component from 3-D Geometry .....	206
14.3.3. Disk and Bearing Modeling .....	208
14.3.3.1. Disk Modeling .....	209
14.3.3.2. Modeling Bearings .....	211
14.4. Material Properties .....	212
14.5. Boundary Conditions and Loading .....	213
14.6. Analysis and Solution Controls .....	214
14.6.1. Modal Analysis .....	214
14.6.1.1. Modal Analysis without Gyroscopic Effects .....	214
14.6.1.2. Modal Analysis with Gyroscopic Effects .....	215
14.6.2. Campbell Diagram Analysis .....	215
14.6.3. Unbalance Response Analysis .....	216
14.7. Results and Discussion .....	217
14.7.1. Performance Benefits of the 2-D Axisymmetric Model .....	221
14.8. Recommendations .....	222
14.9. References .....	223
14.10. Input Files .....	223
<b>15. Calibrating and Validating a Hyperelastic Constitutive Model .....</b>	<b>225</b>
15.1. Introduction .....	225
15.2. Problem Description .....	225
15.3. Material Properties .....	225
15.3.1. Calibration Experiments .....	226
15.3.2. Validation Experiment .....	227
15.4. Analysis and Solution Controls .....	227
15.4.1. Calibrating Parameters .....	227
15.4.2. Validating Parameters .....	228
15.5. Results and Discussion .....	229
15.5.1. Calibration Results .....	229
15.5.2. Validation Results .....	233
15.6. Recommendations .....	234
15.7. References .....	234
15.8. Input Files .....	234
<b>16. Evaluation of Mixed-Mode Stress Intensity Factors and T-stress for 3-D Surface Flaws .....</b>	<b>235</b>
16.1. Introduction .....	235
16.2. Problem Description .....	236
16.2.1. Rectangular Block with a Semicircular Surface Flaw .....	236
16.2.2. X-Joint Pipe with Warped Surface Flaw .....	237
16.3. Modeling .....	238

16.4. Material Properties .....	242
16.5. Boundary Conditions and Loading .....	242
16.6. Analysis and Solution Controls .....	243
16.7. Results and Discussion .....	243
16.7.1. Rectangular Block with Semicircular Surface Flaw .....	243
16.7.2. X-joint Pipe with Warped Flaw .....	245
16.8. Recommendations .....	247
16.9. References .....	247
16.10. Input Files .....	248
<b>17. Impact of a Metal Bar on a Rigid Wall .....</b>	<b>249</b>
17.1. Introduction .....	249
17.2. Problem Description .....	249
17.3. Modeling .....	250
17.3.1. Impact Scenarios .....	251
17.4. Material Properties .....	251
17.5. Boundary Conditions and Loading .....	252
17.6. Analysis and Solution Controls .....	252
17.6.1. Solution Options for Capturing Simulation Results .....	252
17.6.1.1. Rigid Impact .....	252
17.6.1.2. Elastic Impact .....	253
17.6.1.3. Elastoplastic Impact .....	253
17.7. Results and Discussion .....	253
17.7.1. Rigid Impact Results .....	253
17.7.2. Elastic Impact Results .....	257
17.7.3. Elastoplastic Impact Results .....	260
17.7.4. Performance Summary .....	263
17.8. Recommendations .....	264
17.9. References .....	264
17.10. Input Files .....	264
<b>18. Viscoelastic Analysis of an All-Ceramic Fixed Partial Denture .....</b>	<b>267</b>
18.1. Introduction .....	267
18.2. Problem Description .....	268
18.3. Modeling .....	269
18.3.1. Denture Modeling .....	269
18.3.2. Contact Modeling .....	270
18.4. Material Properties .....	271
18.4.1. Transient Thermal Analysis Material Properties .....	271
18.4.2. Static Structural Analysis Material Properties .....	271
18.5. Boundary Conditions and Loading .....	272
18.5.1. Thermal Analysis BC and Loading .....	273
18.5.2. Structural Analysis BC and Loading .....	273
18.6. Analysis and Solution Controls .....	274
18.6.1. Adjusting the Time Step .....	275
18.7. Results and Discussion .....	275
18.8. Recommendations .....	278
18.9. References .....	279
18.10. Input Files .....	279
<b>19. Transient Dynamic Analysis of a Digger-Arm Assembly .....</b>	<b>281</b>
19.1. Introduction .....	281
19.2. Problem Description .....	282
19.3. Modeling .....	283
19.3.1. Modeling Rigid Parts .....	283

19.3.2. Modeling Joints .....	285
19.3.3. Modeling Flexible Parts .....	289
19.3.4. Modeling Flexible Parts with CMS Superelements .....	289
19.4. Material Properties .....	291
19.5. Boundary Conditions and Loading .....	291
19.6. Analysis and Solution Controls .....	292
19.7. Results and Discussion .....	292
19.8. Recommendations .....	296
19.9. Input Files .....	296
<b>20. Dynamic Simulation of a Printed Circuit Board Assembly Using Modal Analysis Methods .....</b>	<b>299</b>
20.1. Introduction .....	299
20.2. Problem Description .....	300
20.3. Modeling .....	300
20.3.1. Modeling of the PCB Structure .....	300
20.3.2. Contact Modeling .....	300
20.4. Material Properties .....	301
20.5. Boundary Conditions and Loading .....	301
20.6. Analysis and Solution Controls .....	303
20.6.1. Residual Vector Method .....	304
20.6.2. Mode Expansion .....	304
20.7. Results and Discussion .....	304
20.7.1. Computational Efficiency .....	305
20.7.2. Accuracy of Results .....	305
20.8. Recommendations .....	308
20.9. References .....	308
20.10. Input Files .....	308
<b>21. Buckling and Post-Buckling Analysis of a Ring-Stiffened Cylinder Using Nonlinear Stabilization ...</b>	<b>311</b>
21.1. Introduction .....	311
21.2. Problem Description .....	312
21.3. Modeling .....	312
21.4. Material Properties .....	314
21.5. Boundary Conditions and Loading .....	315
21.6. Analysis and Solution Controls .....	315
21.6.1. Performing the Nonlinear Buckling Analysis .....	315
21.6.1.1. Run a Linear (Eigenvalue) Buckling Analysis .....	315
21.6.1.2. Generate Imperfections .....	316
21.6.1.3. Run the Nonlinear Buckling Analysis .....	316
21.6.2. Post-Buckling Analysis .....	317
21.6.3. Applying Nonlinear Stabilization .....	318
21.6.3.1. Damping Method .....	318
21.6.3.2. Energy Method .....	319
21.7. Results and Discussion .....	320
21.7.1. Buckling Behavior Is Expected .....	321
21.7.2. Number of Buckles Decreases .....	325
21.7.3. Buckle Size and Behavior Is Consistent with Reference Results .....	326
21.7.4. Plasticity Affects Buckling Results Insignificantly .....	328
21.8. Recommendations .....	330
21.8.1. Buckling Analysis Guidelines .....	330
21.8.2. Nonlinear Stabilization Guidelines .....	331
21.9. References .....	332
21.10. Input Files .....	332
<b>22. Modal and Harmonic Frequency Analyses of an Automotive Suspension Assembly Using CMS ....</b>	<b>333</b>

22.1. Introduction .....	333
22.2. Problem Description .....	334
22.3. Modeling .....	334
22.4. Material Properties .....	335
22.5. Boundary Conditions and Loading .....	335
22.6. Analysis and Solution Controls .....	337
22.6.1. Substructure .....	337
22.6.2. Component Mode Synthesis .....	340
22.6.3. Modal Analysis .....	342
22.6.4. Harmonic Analysis .....	342
22.7. Results and Discussion .....	344
22.7.1. Modal Analysis Comparison of Accuracy and Efficiency .....	344
22.7.2. Full Harmonic Analysis Comparison of Accuracy and Efficiency .....	345
22.7.3. Analysis of Peak Response .....	346
22.8. Recommendations .....	348
22.9. References .....	348
22.10. Input Files .....	349
<b>23. Modal Analysis of a Wind Turbine Blade Using Beam Elements .....</b>	<b>351</b>
23.1. Introduction .....	351
23.2. Problem Description .....	352
23.3. Modeling .....	353
23.3.1. Wind Turbine Blade: BEAM188 Models .....	353
23.3.2. Wind Turbine Blade: SHELL281 Reference Model .....	355
23.4. Material Properties .....	356
23.5. Boundary Conditions and Loading .....	356
23.5.1. BEAM188 Blade Model Boundary Conditions .....	356
23.5.2. SHELL281 Blade Model Boundary Conditions .....	357
23.6. Analysis and Solution Controls .....	358
23.7. Results and Discussion .....	358
23.8. Recommendations .....	361
23.9. Input Files .....	361
<b>24. Hydrostatic Fluid Analysis of an Inflating and Rolling Tire .....</b>	<b>363</b>
24.1. Introduction .....	363
24.2. Problem Description .....	363
24.3. Modeling .....	364
24.3.1. Model the Tire as a Solid .....	365
24.3.2. Model the Air Inside of the Tire .....	365
24.3.3. Model the Tire Reinforcing .....	367
24.3.4. Model the Tire Rim .....	368
24.3.5. Model Tire Contact with the Road Surface .....	369
24.4. Material Properties .....	370
24.5. Boundary Conditions and Loading .....	371
24.5.1. BCs and Loading in Load Step 1 .....	371
24.5.2. BCs and Loading in Load Step 2 .....	371
24.5.3. BCs and Loading in Load Step 3 .....	371
24.5.4. BCs and Loading in Load Step 4 .....	371
24.5.5. BCs and Loading in Load Step 5 .....	371
24.6. Analysis and Solution Controls .....	372
24.7. Results and Discussion .....	372
24.7.1. Expected Results .....	372
24.7.2. Simulation Result Using Hydrostatic Fluid Element HSFLD242 .....	372
24.7.3. Time-History Response .....	373

24.7.4. Tire Deformation Simulation .....	374
24.8. Recommendations .....	374
24.9. Input Files .....	375
<b>25. Cardiovascular Stent Simulation .....</b>	<b>377</b>
25.1. Introduction .....	377
25.2. Problem Description .....	378
25.3. Modeling .....	378
25.3.1. Stent Modeling .....	379
25.3.2. Artery and Plaque Modeling .....	379
25.3.3. Stent-Plaque Contact Modeling .....	380
25.4. Material Properties .....	381
25.5. Boundary Conditions and Loading .....	381
25.5.1. Artery Boundary Conditions .....	381
25.5.2. Stent Boundary Conditions .....	382
25.5.3. Plaque Wall Loading .....	382
25.6. Analysis and Solution Controls .....	383
25.7. Results and Discussion .....	384
25.8. Recommendations .....	387
25.9. References .....	388
25.10. Input Files .....	388
<b>26. Nonlinear Analysis of a Rubber Boot Seal .....</b>	<b>389</b>
26.1. Introduction .....	389
26.2. Problem Description .....	390
26.3. Modeling .....	390
26.3.1. Model the Rubber Boot Seal .....	391
26.3.2. Model the Contact Pairs .....	391
26.3.2.1. Rigid-flexible Contact Pair between Rigid Shaft and Rubber Boot .....	391
26.3.2.2. Self Contact Pairs at Inner and Outer Surfaces of Rubber Boot .....	392
26.4. Material Properties .....	393
26.5. Boundary Conditions and Loading .....	393
26.6. Analysis and Solution Controls .....	395
26.7. Results and Discussion .....	396
26.8. Recommendations .....	400
26.9. Input Files .....	400
<b>27. Hot-Rolling Structural Steel Analysis with 3-D Rezoneing .....</b>	<b>401</b>
27.1. Introduction .....	401
27.1.1. Description of the Hot-Rolling Process .....	401
27.1.2. Hot-Rolling Process Simulation .....	402
27.2. Problem Description .....	402
27.3. Modeling .....	404
27.3.1. Modeling the Block .....	405
27.3.2. Modeling the Rollers .....	405
27.3.3. Contact Modeling .....	406
27.3.3.1. Contact Pair Between Block and Top Roller .....	406
27.3.3.2. Contact Between Block and Side Roller .....	407
27.4. Material Properties .....	408
27.5. Boundary Conditions and Loading .....	408
27.5.1. Load Step 1: Establish Contact with Rollers .....	409
27.5.2. Load Step 2: Hot-Rolling .....	410
27.6. Analysis and Solution Controls .....	410
27.6.1. Rezoneing Initiated at the 30th Substep .....	411
27.6.2. Distorted Mesh Replaced by an Imported New Mesh .....	412

27.6.3. Solution Items Mapped from Original Mesh to New Mesh .....	413
27.6.4. Analysis Resumes Using the New Mesh .....	413
27.7. Results and Discussion .....	414
27.7.1. Deformation Animations .....	418
27.8. Recommendations .....	419
27.9. Input Files .....	420
<b>28. Friction Stir Welding (FSW) Simulation .....</b>	<b>421</b>
28.1. Introduction .....	421
28.2. Problem Description .....	422
28.3. Modeling .....	423
28.3.1. Workpiece and Tool Modeling .....	423
28.3.2. Contact Modeling .....	424
28.3.2.1. Contact Pair Between the Plates .....	424
28.3.2.2. Contact Pair Between Tool and Workpiece .....	425
28.3.2.3. Rigid Surface Constraint .....	426
28.4. Material Properties .....	427
28.5. Boundary Conditions and Loading .....	428
28.5.1. Thermal Boundary Conditions .....	428
28.5.2. Mechanical Boundary Conditions .....	429
28.5.3. Loading .....	429
28.6. Analysis and Solution Controls .....	430
28.7. Results and Discussion .....	431
28.7.1. Deformation and Stresses .....	432
28.7.2. Temperature Results .....	434
28.7.3. Welding Results .....	438
28.7.4. Heat Generation .....	439
28.8. Recommendations .....	442
28.9. References .....	442
28.10. Input Files .....	443
<b>29. Rocket Nozzle Extension Simulation: Operation .....</b>	<b>445</b>
29.1. Introduction .....	445
29.2. Problem Description .....	447
29.3. Modeling .....	447
29.4. Material Properties .....	450
29.5. Boundary Conditions and Loading .....	451
29.6. Analysis and Solution Controls .....	452
29.7. Results and Discussion .....	452
29.8. Recommendations .....	458
29.9. Input Files .....	459
<b>30. Acoustic Analysis of a Small Speaker System .....</b>	<b>461</b>
30.1. Introduction .....	461
30.2. Problem Description .....	462
30.3. Modeling .....	463
30.4. Material Properties .....	464
30.5. Boundary Conditions and Loading .....	464
30.5.1. Structural Loads and Boundary Conditions .....	464
30.5.2. Acoustic Loads and Boundary Conditions .....	464
30.6. Analysis and Solution Controls .....	465
30.7. Results and Discussion .....	465
30.7.1. Structural-Only Modes .....	465
30.7.2. Plotting Sound Pressure Levels .....	465
30.7.3. Plotting Velocities .....	470

30.7.4. Plotting Far-Field Results .....	471
30.8. Recommendations .....	473
30.8.1. Harmonic Sweep and Mesh Generation .....	473
30.8.2. GPU Accelerator .....	473
30.9. Input Files .....	473
<b>31. Fitting Parameters for a Chaboche Kinematic Hardening Model .....</b>	<b>475</b>
31.1. Introduction .....	475
31.2. Modeling .....	475
31.2.1. Chaboche Nonlinear Kinematic Hardening Model .....	476
31.2.2. Determining Material Parameters .....	477
31.3. Results and Discussion .....	479
31.3.1. Uniaxial Strain-Controlled Experiment .....	479
31.3.1.1. Curve Fitting .....	479
31.3.1.2. Simulation .....	480
31.3.2. Uniaxial Stress-Controlled Experiment .....	482
31.3.2.1. Curve Fitting .....	482
31.3.2.2. Simulation .....	483
31.3.3. Fitting to Multiple Data Sets .....	484
31.3.4. Fitting the Ratcheting Strain .....	485
31.4. Recommendations .....	486
31.5. References .....	487
31.6. Input Files .....	487
<b>32. Anterior Cruciate Ligament (ACL) Simulation .....</b>	<b>489</b>
32.1. Introduction .....	489
32.2. Problem Description .....	490
32.3. Modeling .....	491
32.4. Material Properties .....	491
32.5. Boundary Conditions and Loading .....	493
32.6. Analysis and Solution Controls .....	493
32.7. Results and Discussion .....	493
32.7.1. Uniaxial Loading .....	493
32.7.2. Knee Flexion .....	497
32.8. Recommendations .....	498
32.9. References .....	498
32.10. Input Files .....	499
<b>33. Analysis of a Piezoelectric Flextensional Transducer in Water .....</b>	<b>501</b>
33.1. Introduction .....	501
33.2. Problem Description .....	502
33.3. Modeling .....	504
33.3.1. 2-D Transducer Model .....	504
33.3.2. 3-D Transducer Model .....	505
33.4. Material Properties .....	506
33.5. Boundary Conditions and Loading .....	507
33.5.1. Structural Boundary Conditions .....	507
33.5.2. Acoustic Boundary Conditions and Flags .....	507
33.5.2.1. 2-D Acoustic Wave-Absorption Condition .....	507
33.5.2.2. 3-D Acoustic Wave-Absorption Condition .....	507
33.5.3. Piezoelectric Boundary Conditions .....	508
33.6. Analysis and Solution Controls .....	508
33.7. Results and Discussion .....	508
33.8. Recommendations .....	511
33.9. References .....	511

33.10. Input Files .....	512
<b>34. Dynamic Simulation of a Nuclear Island .....</b>	<b>513</b>
34.1. Introduction .....	513
34.2. Problem Description .....	514
34.3. Modeling .....	517
34.4. Material Properties .....	518
34.5. Boundary Conditions and Loading .....	519
34.5.1. Loading .....	519
34.6. Analysis and Solution Controls .....	521
34.6.1. Step 1: Modal Analysis .....	521
34.6.2. Step 2: PSD Analysis .....	522
34.6.3. Step 3: Response PSD (RPSD) Calculation .....	523
34.7. Results and Discussion .....	523
34.7.1. Performance Evaluation .....	529
34.8. Recommendations .....	532
34.9. References .....	533
34.10. Input Files .....	533
<b>35. Elastoplastic Creep Analysis of Lead-Free Solder Bumps .....</b>	<b>535</b>
35.1. Introduction .....	535
35.2. Problem Description .....	537
35.3. Modeling .....	538
35.3.1. Flip Chip Modeling .....	538
35.3.2. Contact Modeling .....	539
35.4. Material Properties .....	540
35.5. Boundary Conditions and Loading .....	543
35.5.1. Thermal Analysis .....	543
35.5.2. Structural Analysis .....	544
35.6. Analysis and Solution Controls .....	544
35.7. Results and Discussion .....	544
35.8. Recommendations .....	550
35.9. References .....	551
35.10. Input Files .....	551
<b>36. VCCT-Based Crack-Growth Simulation of a Composite Laminated T-Joint .....</b>	<b>553</b>
36.1. Introduction .....	553
36.2. Problem Description .....	554
36.3. Modeling .....	556
36.4. Material Properties .....	558
36.5. Boundary Conditions and Loading .....	560
36.6. Analysis and Solution Controls .....	560
36.6.1. Energy Release-Rate Calculation Setup .....	561
36.6.2. Crack-Growth Calculation Setup .....	561
36.6.3. Input for Defining Energy-Release Rate and Crack Growth .....	561
36.7. Results and Discussion .....	562
36.7.1. Comparison to the Debonding Capability .....	565
36.8. Recommendations .....	568
36.9. References .....	569
36.10. Input Files .....	569
<b>37. Bolt Thread Simulation .....</b>	<b>571</b>
37.1. Introduction .....	571
37.2. Problem Description .....	572
37.3. Modeling .....	573
37.3.1. Model the Bolt with Cover Plate and Base Plate .....	574



37.3.1.1. Model the True Threaded Bolt with Cover Plate and Base Plate .....	574
37.3.1.2. Model the Simplified Bolt with Cover Plate and Base Plate .....	576
37.3.2. Model the Pretension Section .....	578
37.3.3. Model the Contact Pairs .....	578
37.3.3.1. Contact in the Thread Region .....	579
37.3.3.1.1. Contact in the Thread Region for the True Thread Simulation Method .....	579
37.3.3.1.2. Contact in the Thread Region for Bolt Section Simulation Method .....	579
37.3.3.1.3. Contact in the Thread Region for the MPC Simulation Method .....	581
37.3.3.2. Contact Between the Bolt Head and the Cover Plate .....	581
37.3.3.3. Contact Between the Cover Plate and the Base Plate .....	581
37.4. Material Properties .....	582
37.5. Boundary Conditions and Loading .....	583
37.6. Analysis and Solution Controls .....	583
37.7. Results and Discussion .....	583
37.7.1. Results for 2-D Models .....	584
37.7.2. Results for 3-D Models .....	586
37.7.3. Comparison of Computation Time .....	589
37.8. Recommendations .....	590
37.9. Input Files .....	590
<b>38. Large-Deformation Neo-Hookean Analysis (via UserMat Subroutine) .....</b>	<b>591</b>
38.1. Introduction .....	591
38.2. Problem Description .....	591
38.3. Modeling .....	592
38.3.1. Neo-Hookean Model .....	592
38.3.1.1. Stress .....	593
38.3.1.2. Tangent Stiffness .....	593
38.3.2. Co-rotational Frame .....	594
38.3.2.1. Polar Decomposition .....	594
38.3.2.2. Stress .....	595
38.3.2.3. Tangent Stiffness .....	595
38.3.3. Voigt Notation .....	595
38.3.3.1. Stress .....	596
38.3.3.2. Tangent Stiffness .....	597
38.3.3.3. Change of Basis .....	598
38.4. Material Properties .....	599
38.5. Boundary Conditions and Loading .....	599
38.6. Analysis and Solution Controls .....	599
38.7. Results and Discussion .....	600
38.8. Recommendations .....	601
38.9. References .....	601
38.10. Input Files .....	601
<b>39. Wire Bonding Ultrasonic Transducer .....</b>	<b>603</b>
39.1. Introduction .....	603
39.2. Problem Description .....	603
39.3. Modeling .....	605
39.4. Material Properties .....	607
39.5. Boundary Conditions and Loading .....	608
39.5.1. Structural Boundary Condition .....	608
39.5.2. Voltage Coupling and Boundary Condition .....	608
39.6. Analysis and Solution Controls .....	608
39.6.1. Prestressed Modal Analysis with Linear Perturbation Method .....	609
39.6.2. Prestressed Full Harmonic Response Analysis .....	609

39.7. Results and Discussion .....	609
39.7.1. Results from Prestressed Modal Analysis with Linear Perturbation Method .....	609
39.7.2. Results from Prestressed Full Harmonic Response Analysis .....	612
39.8. Recommendations .....	614
39.9. References .....	614
39.10. Input Files .....	614
<b>40. Shape Memory Alloy (SMA) with Thermal Effect .....</b>	<b>617</b>
40.1. Introduction .....	617
40.2. SMA Phase Transformation Theory .....	617
40.3. SMA Thermal Effect Simulations .....	618
40.3.1. Simulation of a Spinal Spacer Implant .....	619
40.3.1.1. Problem Description .....	619
40.3.1.2. Modeling .....	620
40.3.1.3. Material Properties .....	620
40.3.1.4. Boundary Conditions and Loading .....	621
40.3.1.5. Analysis and Solution Controls .....	621
40.3.1.6. Results and Discussion .....	621
40.3.2. Simulation of a Spring Actuator .....	624
40.3.2.1. Problem Description .....	624
40.3.2.2. Modeling .....	624
40.3.2.3. Material Properties .....	625
40.3.2.4. Boundary Conditions and Loading .....	625
40.3.2.5. Analysis and Solution Controls .....	626
40.3.2.6. Results and Discussion .....	626
40.4. Recommendations .....	629
40.5. References .....	629
40.6. Input Files .....	630
<b>41. Acoustic Analysis of a Viscothermal Resonator .....</b>	<b>631</b>
41.1. Introduction .....	631
41.2. Problem Description .....	632
41.3. Modeling .....	634
41.4. Material Properties .....	634
41.5. Boundary Conditions and Loading .....	635
41.6. Analysis and Solution Controls .....	636
41.7. Results and Discussion .....	636
41.8. Recommendations .....	638
41.9. References .....	638
41.10. Input Files .....	638
<b>42. Wire Crimping Modeled with General Contact .....</b>	<b>639</b>
42.1. Introduction .....	639
42.2. Problem Description .....	639
42.3. Modeling .....	640
42.3.1. Model the Grip and Wire .....	640
42.3.2. Model the Rigid Punch and Base Support .....	641
42.3.3. Model the Contact Using the General Contact Method .....	642
42.4. Material Properties .....	644
42.5. Boundary Conditions and Loading .....	644
42.6. Analysis and Solution Controls .....	645
42.7. Results and Discussion .....	645
42.8. Recommendations .....	648
42.9. Input Files .....	648
<b>43. Contact Surface Wear Simulation .....</b>	<b>649</b>

43.1. Introduction .....	649
43.2. Problem Description .....	649
43.3. Modeling .....	650
43.3.1. Defining the Wear Model .....	651
43.3.1.1. Wear on One Contact Surface (Asymmetric Contact) .....	651
43.3.1.2. Wear on Both Contact Surfaces (Symmetric Contact) .....	652
43.3.1.3. User-Defined Wear ( <code>userwear</code> Subroutine) .....	653
43.3.2. Improving Mesh Quality During the Solution .....	653
43.4. Material Properties .....	654
43.5. Boundary Conditions and Loading .....	654
43.6. Analysis and Solution Controls .....	654
43.7. Results and Discussion .....	655
43.7.1. Effect of Wear on Contact Pressure .....	655
43.7.2. Effect of Wear on Stress and Element Quality .....	657
43.7.3. Evolution of Wear with Time .....	661
43.8. Recommendations .....	662
43.9. Input Files .....	662
<b>44. C*-integral Evaluation for 3-D Surface Flaws .....</b>	<b>665</b>
44.1. Introduction .....	665
44.2. Problem Description .....	665
44.2.1. Rectangular Block with a Semicircular Surface Flaw .....	666
44.2.2. X-Joint Pipe with Warped Surface Flaw .....	667
44.3. Modeling .....	668
44.4. Material Model and Material Properties .....	673
44.5. Boundary Conditions and Loading .....	674
44.6. Analysis and Solution Controls .....	674
44.6.1. Nonlinear Static Analysis .....	674
44.6.2. C*-integral Calculation ( <b>CINT</b> ) .....	675
44.7. Results and Discussion .....	675
44.7.1. Rectangular Block with Semicircular Surface Flaw .....	675
44.7.2. X-joint Pipe with Warped Flaw .....	678
44.8. Recommendations .....	682
44.9. References .....	682
44.10. Input Files .....	683
<b>45. Forced Response Analysis of a Mistuned Bladed Disk .....</b>	<b>685</b>
45.1. Introduction .....	685
45.2. Problem Description .....	686
45.3. CFD Modeling .....	688
45.3.1. Problem Description and Setup .....	688
45.3.2. Solution Monitor Plots and Convergence Pattern .....	690
45.3.3. Unsteady Pressure Results .....	691
45.4. Structural Modeling .....	691
45.4.1. Rotor 67 Fan Blade Modeling .....	691
45.4.2. Contact Modeling .....	692
45.5. Structural Material Properties .....	693
45.6. Boundary Conditions and Loading .....	694
45.7. Analysis and Solution Controls .....	699
45.7.1. Nonlinear Prestressed Mode-Superposition Harmonic Cyclic Symmetry Analysis with Linear Perturbation - Tuned Response .....	699
45.7.2. Nonlinear Prestressed Mode-Superposition Harmonic Cyclic Symmetry Analysis with Linear Perturbation - Mistuned Response .....	701
45.8. Results and Discussion .....	703

45.9. Recommendations .....	711
45.10. References .....	712
45.11. Input Files .....	712
Index .....	715

---

# List of Figures

1.1. Brake Disc-Pad Assembly .....	2
1.2. Contact Pair Definition .....	3
1.3. Meshed Brake Disc-Pad Assembly .....	4
1.4. Boundary Conditions (Displacement Constraints and Pressure Loading) .....	5
1.5. Mode Shape for Unstable Mode (Mode 21) Obtained from the Linear Non-prestressed Modal Solution ....	9
1.6. Mode Shape for Unstable Mode (Mode 22) Obtained from the Linear Non-prestressed Modal Solution ...	10
1.7. Effect of Friction Coefficient on Unstable Modes .....	12
2.1. Schematic of a Static Elastomeric Seal Assembly .....	16
2.2. Schematic of Finite-Element Static Elastomeric Seal Assembly with Dimensions .....	16
2.3. Progression of Seal Deformation .....	17
2.4. Deformed Mesh Plot of Seal After Third Load Step Without Rezoning .....	23
2.5. Deformation Profile at Load Step 1 -- Substep 20 (First Rezoning) .....	27
2.6. Deformation Profile at Load Step 1 -- Substep 50 (Second Rezoning) .....	28
2.7. Deformation Profile at Load Step 2 -- Substep 10 (Third Rezoning) .....	29
2.8. Final Mesh (After Third Load Step) .....	31
2.9. Contact Pressure-Distribution Trends .....	32
2.10. Seal Hydrostatic Pressures .....	35
2.11. Seal $\sigma_{YY}$ Profile .....	36
2.12. Seal $\sigma_{YY}$ Plot Animation .....	38
2.13. Extrusion $\sigma_{YY}$ Profile .....	39
2.14. Extrusion $\sigma_{XY}$ Profile .....	40
2.15. Mesh Gradation Created with Nested Element Splitting During Vertical Rezoning .....	41
3.1. 3-D View of Sealing System .....	44
3.2. Sealing System and Finite Element Model .....	45
3.3. Sealing System Contact Pairs .....	47
3.4. Material Model Test Data .....	48
3.5. Sealing System with Applied Fluid Pressure to Contact Pairs .....	50
3.6. Sealing System Contact Pressure Following Housing Compression (First Load Step) .....	51
3.7. Sealing System fluid Penetration Pressure Distributions (During Second Load Step) .....	52
3.8. Animation of Fluid Penetration Pressure Distribution .....	54
3.9. Sealing System Contact Pressure Distributions (During Second Load Step) .....	54
3.10. Animation of Contact Pressure Distribution .....	56
3.11. Sealing System Von Mises Stress Contour (After Second Load Step) .....	57
3.12. Sealing System Equivalent Plastic Strain Contour (After Second Load Step) .....	57
3.13. Sealing System Total Strain Energy and Stabilization Energy Time History .....	58
4.1. Original Finite Element Model with Boundary Conditions and Loading .....	63
4.2. Effective Plastic Strain and Deformed Mesh at Time of First Rezoning .....	66
4.3. Effective Plastic Strains and Deformed Mesh at Time of Second Rezoning .....	67
4.4. New Mesh Read in During the First Rezoning .....	68
4.5. New Mesh Read in During the Second Rezoning .....	69
4.6. Effective Plastic Strain Distribution After First Mapping .....	70
4.7. Effective Plastic Strain After Second Mapping .....	71
4.8. Effective Strain Distribution and Deformed Shape at the Final Stage (Complete Die Fill) .....	73
4.9. Final Stage Animation .....	74
4.10. Von Mises Stress Distribution at the Final Stage .....	75
4.11. Half Expanded Plot of Von Mises Stress at the Final Stage of Ring-Gear Forging .....	76
5.1. Geometry .....	80
5.2. Symmetry Section .....	80
5.3. Meshed Geometry .....	81
5.4. Two Contact Pair Definitions (Initial Crack and CZM Area) .....	81

5.5. Contact Elements .....	82
5.6. Target Elements .....	82
5.7. Boundary Conditions .....	85
5.8. Time History Plot of Strain and Stabilization Energies .....	86
5.9. Global Deformed Shape (Last Substep) .....	87
5.10. Equivalent Stress (Last Substep) .....	87
5.11. Contact Status at Final Substep .....	88
5.12. Contact Status for the Initial Bonded Contact Region .....	88
6.1. Turbine Blade Cooling Passages .....	92
6.2. Turbine Blade Cooling Passages .....	93
6.3. Solid Region Mesh .....	94
6.4. Solid Region Temperature Distribution .....	96
6.5. Fluid Temperatures .....	97
6.6. Solid Surface Temperatures .....	98
6.7. Fluid Temperature Along Path of Hole Number 1 .....	99
6.8. Solid Temperature Along Path of Hole Number 1 .....	99
6.9. Von Mises Stresses for Solid Region .....	100
6.10. Von Mises Stress Along Path of Hole Number 1 .....	101
7.1. Full 3-D Geometry of a Camshaft Assembly .....	104
7.2. Simplified Geometry of a Camshaft Assembly .....	105
7.3. Meshed Camshaft Model Prior to Generating the 3-D Mesh .....	105
7.4. Meshed Camshaft Model After Generating the 3-D Mesh .....	106
7.5. Bonded Contact Pairs .....	107
7.6. Revolute Joints and Surface-to-Surface Contact Pair .....	108
7.7. USUM Plots of Camshaft Assembly During Analysis .....	110
7.8. Maximum and Minimum Principal Stress Plots .....	111
7.9. Comparison of USUM Plots: General Axisymmetric Model and Full 3-D Model .....	112
8.1. Large-Scale Nuclear Piping System .....	116
8.2. Entire Nuclear Piping System Line Diagram .....	117
8.3. Entire Nuclear Piping System Meshed with Pipe and Elbow Elements .....	117
8.4. Elbow Model Line Diagram .....	118
8.5. Elbow Model Meshed with ELBOW290 Elements .....	119
8.6. Midsurface Geometry of Elbow (SHELL281 Model) .....	119
8.7. Elbow Model Meshed with SHELL281 Elements .....	120
8.8. Boundary Conditions of Entire Nuclear Piping System .....	122
8.9. USUM Plot Comparison: Local ELBOW290 and SHELL281 Models .....	124
8.10. Von Mises Stress Comparison: Local ELBOW290 and SHELL281 Models .....	124
8.11. Von Mises Strain Comparison: Local ELBOW290 and SHELL281 Models .....	125
9.1. COPV Geometry .....	128
9.2. COPV Mesh .....	129
9.3. COPV Boundary Conditions .....	131
9.4. COPV Total Displacement .....	132
9.5. COPV Thickness Strain .....	132
9.6. Layer with Maximum Failure Criteria in Matrix and Fibers .....	133
9.7. Type of Maximum Failure Criteria in Matrix and Fibers .....	133
9.8. Value of Maximum Failure Criterion in Matrix and Fibers .....	134
9.9. Radial Strain Against the Axial Location .....	134
9.10. Equivalent Stresses at Critical Layer in Matrix and Fibers .....	135
9.11. COPV Membrane Stress in the Element X Coordinate Direction .....	135
9.12. COPV Bending Stress in the Element X Coordinate Direction .....	136
10.1. Vertebral Body Components .....	139
10.2. Finite Element Model of a Human Lumbar Motion Segment .....	140

10.3. IVD Deformation .....	141
10.4. IVD von Mises Stresses .....	142
10.5. Lumbar Motion Segment Animation of Vertical Displacement Increasing with Time .....	142
10.6. Displacements of Vertebral Body Over Time .....	143
10.7. Lumbar Motion Segment Creep Response .....	143
10.8. IVD Pore-Pressure Dissipation .....	144
11.1. Nozzle Extension Geometry .....	148
11.2. Nozzle Extension 1° Base Sector Geometry .....	148
11.3. Ring Element Plot .....	149
11.4. Expanded Solid Representation of the Shell Mesh .....	149
11.5. Nozzle Wall and Ring Connection <i>with</i> Shell Offsets .....	150
11.6. Nozzle Wall and Ring Connection <i>without</i> Shell Offsets .....	150
11.7. Nozzle Model Boundary Conditions .....	151
11.8. Nozzle Radial (X) Stress .....	152
11.9. Nozzle Hoop (Y) Stress .....	152
11.10. Nozzle Axial (Z) Stress .....	153
11.11. Nozzle Radial Stresses (Bottom and Top Sections) .....	154
11.12. Nozzle Hoop Stresses (Bottom and Top Sections) .....	155
11.13. Nozzle Axial Stresses (Bottom and Top Sections) .....	156
12.1. Full Model of the BM3 Nuclear Piping System .....	160
12.2. BM3 Model Meshed with PIPE289 and ELBOW290 Elements .....	161
12.3. Elastic Supports Meshed with COMBIN14 Elements .....	162
12.4. Input-Acceleration Response Spectra (1% X Direction) .....	163
12.5. Input-Acceleration Time History (X Direction) .....	163
13.1. Sector Model of Centrifugal Impeller Blade .....	176
13.2. Full Model of Centrifugal Impeller Blade .....	176
13.3. Element Plot of the Cyclic-Sector Model .....	177
13.4. Low-Edge Component of Sector Model of Centrifugal Impeller Blade .....	177
13.5. High-Edge Component of Sector Model of Centrifugal Impeller Blade .....	178
13.6. Bonded Contact Pair Between the Shroud and Impeller .....	178
13.7. Static Fluid Pressure Load on Hub Wall, Main Blade, and Splitter .....	179
13.8. Total Deformation Pattern at Frequency of 2920 Hz .....	186
13.9. Total Deformation Pattern at Frequency of 4210 Hz .....	187
13.10. Nodal Solution Plots with Respect to the Frequency of Excitation .....	188
13.11. Total Deformation Pattern at Frequency of 2920 Hz .....	190
13.12. Total Deformation Pattern at Frequency of 4210 Hz .....	191
13.13. Nodal Solution Plots with Respect to the Frequency of Excitation .....	192
13.14. Total Deformation Pattern at Frequency of 2920 Hz .....	193
13.15. Total Deformation Pattern at Frequency of 4210 Hz .....	194
13.16. Nodal Solution Plots with Respect to the Frequency of Excitation .....	195
13.17. Comparison of CPU Time Between the Cyclic Sector Model and the Full Model for Various Analyses ...	198
13.18. Comparison of CPU Time Between the VT Solver and the Sparse Solver for Harmonic Analysis on the Cyclic Sector Model .....	200
14.1. 3-D Geometry of Nelson-Vaugh Rotor .....	204
14.2. 2-D Axisymmetric Geometry of Nelson-Vaugh Rotor .....	205
14.3. 3-D Model Meshed with SOLID187 Elements .....	205
14.4. 3-D Geometry .....	206
14.5. 2-D Axisymmetric Geometry Extracted from 3-D Geometry .....	206
14.6. 2-D Axisymmetric Geometry Meshed with SOLID272 Elements .....	207
14.7. 2-D Axisymmetric Model with Fourier Nodal Planes .....	208
14.8. 3-D View of SOLID272 Mesh .....	208
14.9. Rigid Disk Modeled Using MASS21 Element (3-D Solid Model) .....	209

14.10. Disk Modeled Using MASS21 Element (2-D Axisymmetric Model) .....	210
14.11. Bearings Modeled with COMBI214 Elements (3-D solid model) .....	211
14.12. Bonded Contact Pairs at Bearing Locations (3-D Solid Model) .....	212
14.13. Bearings Modeled with COMBI214 Elements (2-D Axisymmetric Model) .....	212
14.14. Boundary Conditions (3-D Solid Model) .....	213
14.15. Campbell Diagram .....	217
14.16. Unbalance Response .....	219
14.17. Orbits Plot of 2-D Axisymmetric Model .....	221
14.18. CPU Time of 2-D Axisymmetric and 3-D Solid Models (Unbalance Response Analysis) .....	222
15.1. Hyperelastic Test Suite: Test Specimens .....	226
15.2. Hyperelastic Test Suite: Experimental Data .....	226
15.3. Tension-Torsion Test Specimen .....	227
15.4. Tension-Torsion Experimental Data .....	227
15.5. Tension-Torsion Test Specimen Mesh .....	228
15.6. Comparison of the Data and Fits Over the Entire Range of Data .....	230
15.7. Parameters Fit to Experimental Data to About 100 Percent Strain .....	231
15.8. Comparison of the Data and Fits Showing Predictions Outside the Range of Fitted Data .....	232
15.9. Strain-Energy Density Contours of the Tension-Torsion Test .....	233
15.10. Comparison of Tension-Torsion Experiment to the Five-Parameter Mooney-Rivlin Model .....	233
16.1. Rectangular Block Geometry with Semicircular Surface Flaw .....	236
16.2. Semicircular Crack and Torus Along the Crack Front .....	237
16.3. X-Joint Pipe Full Model with Warped Surface Flaw at Welded Joint .....	237
16.4. Semi-elliptical Surface Crack Dimensions .....	238
16.5. Two-plane Symmetry of X-joint Pipe with Warped Surface Flaw Geometry .....	238
16.6. Rectangular Block Model with Boundary Conditions and Loading Applied .....	239
16.7. Sweep Mesh with SOLID186 Around Crack Front .....	239
16.8. Two-plane Symmetry of X-joint Pipe with Warped Surface Flaw at Welded Joint .....	240
16.9. X-joint Pipe with Warped Surface Flaw at Welded Joint in Thickness Direction. ....	240
16.10. Sweep Mesh with SOLID186 Around the Crack Front .....	241
16.11. Crack Tip Nodal Component: Rectangular Block Model .....	242
16.12. Crack Tip Nodal Component: X-joint Pipe Model .....	242
16.13. USUM Results (Rectangular Block) .....	243
16.14. Von Mises Stress Plot (Rectangular Block) .....	244
16.15. Normalized KI Results .....	244
16.16. Normalized T-Stress Results: Semicircular Surface Flaw .....	245
16.17. USUM Results (X-joint Pipe) .....	245
16.18. Von Mises Stress Plot (X-joint Pipe) .....	246
16.19. Normalized SIF Results: Comparison with Chong Rhee[4] .....	246
16.20. Normalized T-Stress Results: X-Joint Pipe with Warped Flaw .....	247
17.1. Geometry and FE Model of a Metal Bar Impacting a Rigid Wall .....	250
17.2. Rigid Impact: Newmark Method with No Damping .....	255
17.3. Rigid Impact: Newmark Method with Damping .....	256
17.4. Rigid Impact: HHT Method with Damping .....	257
17.5. Elastic Impact: Newmark Method with No Damping .....	258
17.6. Elastic Impact: Newmark Method with Damping .....	259
17.7. Elastic Impact: HHT Method with Damping .....	260
17.8. Elastoplastic Impact: Newmark Method with No Damping .....	261
17.9. Elastoplastic Impact: Newmark Method with Damping .....	262
17.10. Elastoplastic Impact: HHT Method with Damping .....	262
17.11. Animation: Elastoplastic Impact Using the HHT Method with Damping .....	263
18.1. FPD Viscoelastic (Glass) Veneer Geometry .....	268
18.2. FPD Ceramic Core Geometry (Inside the Veneer) .....	269



18.3. FPD Veneer and Core Mesh (SOLID87) .....	270
18.4. Contact Between Veneer and Core (CONTA174 and TARGE170) .....	270
18.5. FPD Boundary Conditions: Thermal Analysis .....	273
18.6. FPD Boundary Conditions: Structural Analysis .....	274
18.7. Temperature Distribution in Veneer and Core at 60 Seconds .....	275
18.8. Temperature Distribution in Veneer and Core at 300 Seconds .....	276
18.9. Temperature Distribution in Veneer and Core at 600 Seconds .....	276
18.10. Von Mises Stress in Veneer and Core at 60 Seconds .....	276
18.11. Von Mises Stress in Veneer and Core at 300 Seconds .....	277
18.12. Von Mises Stress in Veneer and Core at 600 Seconds .....	277
18.13. Residual Principal Stress Distribution in Veneer and Core 600 Seconds .....	278
18.14. Reference Results: Residual Principal Stress Distribution in Veneer and Core .....	278
19.1. Dagger-Arm Assembly .....	282
19.2. Rigid Modeling of the Connecting Rod .....	283
19.3. Rigid Representation of the Digger-Arm Assembly .....	285
19.4. Connections Between Piston, Cylinder, and Arms .....	287
19.5. Connecting Rods Modeled with SOLID185 Elements .....	289
19.6. Relative Displacement Specifications for Cylinders and Pistons .....	291
19.7. Digger-Arm Assembly Animation .....	293
19.8. Relative Rotation at Cylindrical Joint (Ground-to-Frame) .....	293
19.9. Relative Rotation at General Joint Along Local Z Axis (Bucket-Frame) .....	293
19.10. USUM Plots of Connecting Rods .....	294
19.11. Equivalent Stress Plots of Connecting Rods .....	295
20.1. Full 3-D Geometry of a PCB assembly .....	300
20.2. Bonded Contact Pairs Between IC Packages and Circuit Boards .....	301
20.3. PCB Boundary Conditions .....	302
20.4. PSD Base Excitation Values .....	303
20.5. Solution Times With and Without <b>MXPAND</b> .....	305
20.6. Mode Shape of the Residual Vector .....	306
20.7. Improved Accuracy of RPSD Values with Residual Vectors for 50 Modes .....	308
21.1. Geometry and Finite-Element Model .....	313
21.2. Inside View of a 45-Degree Sector .....	314
21.3. Stiffening Ring Detail with Dimensions .....	314
21.4. Monitor File of Initial Run .....	317
21.5. Time-History Plot of Stiffness Energy (SENE) and Stabilization Energy (STEN) .....	320
21.6. Load Factor and Mode Shape for the First Eigenvalue .....	321
21.7. Applied Pressure and Axial Shortening .....	322
21.8. Applied Pressure vs. Radial Displacement .....	323
21.9. Total Deformation at the Time of Buckling Initiation .....	324
21.10. Total Deformation at Zero Slope on the Load-Deformation Curve .....	325
21.11. Total Deformation at the End of the Post-Buckling Analysis .....	327
21.12. Another Total Deformation View .....	328
21.13. Von Mises Stress Distribution at Buckling Initiation .....	329
21.14. Von Mises Stress Distribution at the End of the Analysis .....	330
22.1. 3-D Suspension Model .....	334
22.2. Meshed Suspension Model .....	335
22.3. Suspension Assembly with Boundary Conditions and Displacement Loading .....	336
22.4. Superelements of the Suspension Assembly .....	337
22.5. Interface Master Nodes Between the Superelements of the Suspension Assembly .....	338
22.6. Master Nodes Defined at Fixed Bolts .....	338
22.7. Master Nodes Defined at Points of Application of Harmonic Displacement .....	339
22.8. Superelement of the Suspension Model After the Use Pass .....	341

22.9. Non-Master Nodes for Response Calculation in the Expansion Pass .....	343
22.10. Nodal Responses Due to Harmonic Displacement Excitation at the Bottom of the Wheels .....	347
22.11. Mode Shapes at the Undamped Natural Frequency of 187.22 Hz .....	347
22.12. Mode Shapes at the Undamped Natural Frequency of 223.63 Hz .....	348
22.13. Mode Shapes at the Undamped Natural Frequency of 237.48 Hz .....	348
23.1. Wind Turbine Blade Geometry and Structural Components .....	352
23.2. Representative Blade Cross-Section Areas at Various Locations .....	353
23.3. Line Diagram of Wind Turbine Blade Model .....	354
23.4. BEAM188 Blade Model with Fine Mesh and Linear Interpolation .....	355
23.5. BEAM188 Blade Model with Coarse Mesh and Cubic Interpolation .....	355
23.6. SHELL281 Reference Blade Model .....	356
23.7. Boundary Conditions on the BEAM188 Blade Model .....	357
23.8. Boundary Conditions on the Reference SHELL281 Blade Model .....	357
23.9. Comparison of Mode Shapes Predicted by BEAM188 and SHELL281 Models .....	359
23.10. Averaged Bending-Stress Distribution (Corresponding to Third Mode Shape at Location $x = 15\text{m}$ ) .....	360
23.11. Nonaveraged Bending-Stress Distribution (Corresponding to Third Mode Shape at Location $x = 15\text{m}$ ) .....	360
24.1. 3-D Model of an Inflated Tire and a Road Surface .....	364
24.2. 3-D Tire Model Using a Solid Element .....	365
24.3. Hydrostatic Fluid Element with Positive Volume .....	365
24.4. Hydrostatic Fluid Element with Negative Volume .....	366
24.5. Tire Reinforcing: Road Contact Area .....	367
24.6. Tire Reinforcing: Side Wall .....	367
24.7. Tire Reinforcing: Sectional View .....	368
24.8. Rim Model with Tire .....	369
24.9. Model of Tire Contact with Road Surface .....	370
24.10. Fluid Pressure Variation .....	373
24.11. Fluid Volume Variation .....	373
24.12. Fluid Density Variation .....	374
24.13. Fluid Mass Variation .....	374
24.14. Tire Deformation (All Load Steps) .....	374
25.1. Effect of Stent Placement in Increasing Blood Flow .....	377
25.2. Cross-sectional View of Unloaded Artery and Stent .....	378
25.3. Stent Model 3-D Expanded Solid Display .....	379
25.4. Simplified Atherosclerotic Artery Model .....	380
25.5. Standard Line-to-Surface Contact Between Stent and Inner Plaque Wall .....	381
25.6. Artery Boundary Conditions .....	382
25.7. Stent Boundary Conditions .....	382
25.8. Uniform Pressure Loading on the Inner Plaque Wall (a) and Load History (b) .....	383
25.9. Cross-Sectional View of Artery and Stent After Balloon Angioplasty (Load Step 1) .....	384
25.10. Arterial Wall Deformation During Balloon Angioplasty (a) and After Stent Placement (b) .....	385
25.11. Arterial Wall Displacement and Tissue Prolapse Results .....	385
25.12. Arterial Wall von Mises Stress Results .....	386
25.13. Stent Retraction Resulting from Arterial Compression .....	387
26.1. 3-D Model of Rubber Boot Seal and Rigid Shaft .....	390
26.2. Half Symmetry Model of the 3-D Rubber Boot Seal .....	391
26.3. Rigid-Flexible Contact Pair .....	392
26.4. Self Contact Pairs .....	393
26.5. Boundary Conditions at a Symmetry Plane .....	394
26.6. Boundary Conditions at the Bottom of the Rubber Boot (in the Axial Direction) .....	394
26.7. Boundary Conditions at the Bottom of the Rubber Boot (in the Radial Direction) .....	395

26.8. Comparison of Cumulative Iterations for Different Contact Detection Methods .....	396
26.9. Displacement Vector Sum at the Maximum Shaft Angle .....	397
26.10. Von Mises Stress at the Maximum Shaft Angle .....	398
26.11. Total Strain at First Contact between Outer Plaits of Rubber Boot .....	398
26.12. Total Strain at Second Contact between Inner Plaits of Rubber Boot .....	399
26.13. Total Strain at Third Contact between Inner Plaits of Rubber Boot and Shaft .....	399
26.14. Animated Results .....	400
27.1. Hot-Rolling Model .....	403
27.2. Symmetric Hot-Rolling Model .....	404
27.3. Hot-Rolling Quarter Model Geometry .....	405
27.4. Meshed Model with Dimensions .....	405
27.5. Contact Between Block and Top Roller .....	406
27.6. Contact Between Block and Side Roller .....	407
27.7. Symmetric Boundary Conditions on the Block .....	409
27.8. Loadings .....	409
27.9. Deformation in First Load Step, 40th Substep .....	411
27.10. Deformed Mesh of the Block at 30th Substep of First Load Step .....	412
27.11. Original Deformed Mesh and Imported New Mesh .....	412
27.12. Comparison of Contact Pressure Results Before and After Rezonig .....	413
27.13. USUM Plots: Initial Run at Last Converged Substep .....	414
27.14. USUM Plots: After Building Up the Rolling Process .....	415
27.15. USUM Plots: End of Analysis (After Second Load Step) .....	415
27.16. USUM Plot of Full Model after Symmetry Expansion .....	416
27.17. Variation of the Moment (Mx) of the Top Roller .....	416
27.18. Variation of the Reaction Forces of the Top Roller .....	417
27.19. Equivalent Plastic Strain Plot in the Full Expanded Model .....	417
27.20. Deformation (USUM) in the Initial Run .....	418
27.21. Deformation (USUM) After Rezonig .....	418
27.22. Deformation (USUM) After Rezonig in the Expanded Model .....	419
28.1. 3-D Model of Workpiece and Tool .....	423
28.2. 3-D Meshed Model of Workpiece and Tool .....	424
28.3. Contact Pair Between Plates .....	424
28.4. Contact Pair Between Tool and Workpiece .....	425
28.5. Rigid Surface Constrained .....	426
28.6. Thermal Boundary Conditions .....	428
28.7. Mechanical Boundary Conditions .....	429
28.8. Friction Stir Welding Animation .....	432
28.9. Deflection at Workpiece After Load Step 1 .....	432
28.10. von Mises Stress After Load Step 1 .....	433
28.11. Temperature After Load Step 1 .....	433
28.12. Frictional Stress After Load Step 1 .....	434
28.13. Frictional Stress After Load Step 2 .....	434
28.14. Temperature After Load Step 2 .....	435
28.15. Temperature After Load Step 3 .....	435
28.16. Maximum Temperature (on Workpiece Beneath the Tool) Variation with Time .....	436
28.17. Temperature Distribution on the Top Surface of Workpiece at Various Locations .....	436
28.18. Various Locations on the Workpiece .....	437
28.19. Temperature Distribution in Thickness Direction at Location 1 .....	437
28.20. Temperature Variation with Time on Various Joint Locations .....	438
28.21. Contact Status at Interface with Bonding Temperature 1000 °C .....	438
28.22. Contact Status at Interface with Bonding Temperature 900 °C .....	439
28.23. Total Frictional Heat Rate Variation with Time .....	439

28.24. Total Plastic Heat Rate Variation with Time .....	441
29.1. Element Coordinate System .....	446
29.2. 3-D Solid Element Model .....	446
29.3. Thermal-Structural Analysis .....	447
29.4. Nozzle Extension Geometry .....	448
29.5. Nozzle Extension 1° Base Sector Geometry .....	448
29.6. Ring Element Plot .....	449
29.7. Expanded Layer Representation of the Solid Mesh .....	449
29.8. Thermal Boundary Conditions .....	451
29.9. Structural Boundary Conditions .....	452
29.10. Layered Temperature Results .....	453
29.11. Layered TF Results .....	453
29.12. Layered Temperature Gradient Results .....	454
29.13. Layer 3 Temperature Results .....	455
29.14. homogeneous Thermal - homogeneous Structural Results .....	456
29.15. homogeneous Thermal - Layered Structural Results .....	456
29.16. Layered Thermal - homogeneous Structural Results .....	457
29.17. Layered Thermal - Layered Structural Results .....	457
29.18. Layer 1 Equivalent Stresses .....	458
29.19. Single Element Coordinate System .....	459
29.20. Multiple Element Coordinate Systems .....	459
30.1. 3-D Model of the Speaker Assembly .....	462
30.2. Acoustic Fluid Elements .....	463
30.3. Modal Analysis at 807 Hz .....	465
30.4. Displacement Frequency Response Plot .....	466
30.5. SPL at 50 mm .....	467
30.6. SPL at 800 Hz .....	468
30.7. SPL at 860 Hz .....	469
30.8. Velocity Magnitude Contour Plot .....	471
30.9. SPL Polar Plot at 800 Hz .....	472
31.1. Stable Hysteresis Strain-Controlled Data .....	477
31.2. Plot Comparing Curve-Fitting Tool Results .....	479
31.3. Loading History for Strain-Controlled Experiment .....	480
31.4. Schematic for Single-Element Uniaxial Test .....	481
31.5. Plot Comparing Strain-Controlled Experimental Data with Simulation Data .....	482
31.6. Plot Comparing Stress-Controlled Experimental Data with Simulation Data .....	483
31.7. Plot Comparing Stabilized Hysteresis Data to Fit of Multiple Data Sets .....	484
31.8. Plot Comparing Stress Data to Fit of Multiple Data Sets .....	485
31.9. Plot Comparing Ratcheting Strain Data to Prediction from Fitted Chaboche Model .....	486
32.1. Human Knee Components .....	490
32.2. Finite Element Model of an ACL .....	491
32.3. Von Mises Stress (Anisotropic Visco-Hyperelastic and Neo-Hookean Viscoelastic) .....	494
32.4. ACL Stress-Strain Plot .....	495
32.5. Stress-Strain at Differing Strain Rates .....	496
32.6. Stress Relaxation .....	496
32.7. Von Mises Stresses Under 45° Knee Flexion .....	497
32.8. Von Mises Stresses Under 11.25° Knee Rotation .....	498
33.1. Class IV Flextensional Underwater Acoustic Transducer Shell .....	502
33.2. Flextensional Transducer Components .....	503
33.3. Transducer Surrounded by Water .....	504
33.4. 2-D Transducer Model Mesh .....	505
33.5. 3-D Transducer Model Mesh .....	506

33.6. SPL Plot of Full Transducer Model .....	508
33.7. SPL Plot Along an Arc 1 m from Center .....	509
33.8. 2-D SPL Plot .....	510
33.9. 3-D SPL Plot .....	510
33.10. Overlaid 2-D and 3-D Plots .....	511
34.1. NPP Structure Footprint .....	515
34.2. Ground Motion Response Spectrum (5%) .....	516
34.3. NPP Structures FEM (Mesh Size Adapted to 50 Hz Cutoff Frequency) .....	518
34.4. Ground Motion Power Spectral Density (Acceleration PSD) .....	519
34.5. EPRI-TR 1014101 -- Plane Wave Coherency Model for Horizontal Direction .....	520
34.6. Constant Modal Density Checking .....	522
34.7. 1- $\sigma$ Absolute Acceleration Values on NPP .....	524
34.8. Keypoints Location for Estimation of PSD Reduction .....	527
34.9. PSD Reduction Due to Incoherency and Wave-Passage Effects .....	528
34.10. Comparison of Wall Time Spent on Solution .....	530
34.11. Comparison of Wall Time for RPSD Calculation (POST26 Postprocessing Time) .....	531
34.12. Comparison of Wall Time of Solution for Various Numbers of Cores .....	532
35.1. Creep Stages .....	536
35.2. Distribution of Solder Bumps in Full Flip Chip Model and Size of Solder Bump .....	537
35.3. 1/8 Symmetry of Flip Chip Pack .....	538
35.4. Flip Chip Mesh with SOLID90 for Thermal and SOLID186 for Structural Analysis .....	539
35.5. Contact Between Solder, Chip, Underfill, and Substrate .....	539
35.6. Creep Experimental Data [4-6] at Different Temperatures Used for Curve Fitting .....	541
35.7. Temperature Cycle History .....	543
35.8. Temperature Distribution in Flip Chip at 3150 Seconds and 3750 Seconds .....	545
35.9. USUM Results from Creep Curve Fitting Constants and Reference Constants at the End of 12th Load Step (3150 Seconds) .....	546
35.10. USUM Results from Creep Curve Fitting Constants and Reference Constants at the End of 14th Load Step (3750 Seconds) .....	546
35.11. Node Used for Plotting Post Process Results .....	547
35.12. Time History Post Process Results of Equivalent Stress: Comparison with Wen-Ren Jong [3] .....	547
35.13. Von Mises Creep Strain at Node Number 4112 .....	548
35.14. Von Mises Elastic Strain at Node Number 4112 .....	548
35.15. Von Mises Plastic Strain at Node Number 4112 .....	549
35.16. Von Mises Creep Strain Animation of Solder with Time-History Results at Node Number 4112 .....	549
35.17. Figure 17: Von Mises Stress Animation of Solder with Time-History Results at Node Number 4112 .....	550
36.1. T-Joint .....	554
36.2. T-Joint Layup Configuration .....	555
36.3. T-Joint with Initial Cracks .....	556
36.4. T-Joint Dimensions (a) and Cracks with Crack Tip IDs (b) .....	557
36.5. T-Joint Finite Element Model with Initial Cracks and Crack Paths .....	558
36.6. T-Joint Model Boundary Conditions and Loading .....	560
36.7. Distribution of Y-Component of Stresses .....	562
36.8. Y-Force vs. Y-Displacement .....	563
36.9. Animation: T-Joint Panel Delamination .....	564
36.10. Crack Growth .....	565
36.11. Distribution of Y-Component Stresses: VCCT Model .....	566
36.12. Distribution of Y-Component Stresses: CZM Models .....	567
36.13. T-Joint Y-Force vs. Y-Displacement: VCCT and CZM Models .....	568
37.1. 3-D Half Model of a Bolted Joint .....	572
37.2. 2-D Axisymmetric Problem Setup for (a) True Thread, (b) Bolt Section, (c) MPC Bonded Method .....	573
37.3. 3-D Model of a Threaded M120 Bolt .....	574

37.4. 3-D Half Model of a Threaded Bolt Joint with Mesh Details .....	575
37.5. 2-D Axisymmetric Model of a True Threaded Bolt Joint with Mesh Details .....	575
37.6. Simplified 3-D Model of an M120 Bolt .....	576
37.7. 2-D Axisymmetric Model of a Simplified Bolt Joint with Mesh Details .....	577
37.8. 3-D Half Model of a Simplified Bolt Joint with Mesh Details .....	577
37.9. Pretension Section in the Bolt Model at $y = 260$ mm .....	578
37.10. Contact and Target Surfaces at the Bolt Thread and the Base Plate Thread .....	579
37.11. Contact and Target Surfaces at the Bolt Surface and Base Plate .....	580
37.12. Contact and Target Surfaces at the Bolt Head and Cover Plate .....	581
37.13. Contact and Target Surfaces at the Cover Plate and Base Plate .....	582
37.14. Boundary Conditions and Loading on the 3-D Model .....	583
37.15. UY Displacement in the 2-D Axisymmetric Model for all Three Methods .....	584
37.16. von Mises Stress in the 2-D Axisymmetric Model for all Three Methods .....	585
37.17. Linearized Stress in the Bolt Shank Along a Path at $y = 280$ for all Three Methods. ....	586
37.18. Contact Status in the Thread Region for all Three Methods .....	587
37.19. UY Displacement in the 3-D Half Model for all Three Methods .....	587
37.20. von Mises Stress in the 3-D Half Model for all Three Methods .....	588
37.21. von Mises Stress in the Bolt for all Three Methods .....	588
37.22. von Mises Stress in the Bolt Shank at Section $y = 280$ for all Three Methods .....	589
38.1. Stress-vs.-Strain Plot .....	601
39.1. Ultrasonic Transducer Model .....	604
39.2. Approximate Location for Positioning the Holder .....	605
39.3. Meshed Ultrasonic Transducer Model .....	606
39.4. Top and Bottom Plate Connection .....	607
39.5. First Longitudinal Mode of Interest (16) at 26.6 kHz .....	610
39.6. Second Longitudinal Mode of Interest (30) at 58.9 kHz .....	611
39.7. Third Longitudinal Mode of Interest (39) at 87.3 kHz .....	612
39.8. Electrical Impedance .....	613
39.9. Tip Displacement .....	613
40.1. Spinal Spacer Implant .....	619
40.2. Loading and Recovery of a Spinal Spacer Implant .....	620
40.3. Spinal Spacer 1/4 Model .....	620
40.4. Displacements of Central Node A of the Spinal Spacer .....	622
40.5. Spinal Spacer Deformation and Stress .....	623
40.6. Motion of a Vertical Helical Spring .....	624
40.7. Finite Element Models of a Spring Actuator .....	625
40.8. Temperature and Force Load Steps .....	626
40.9. Spring Actuator Deformation at Step 1 .....	627
40.10. Spring Actuator Deformation at Step 2 .....	627
40.11. Spring Actuator Deformation at Step 3 .....	628
40.12. Displacement History: Bottom of a Spring Actuator with Temperature .....	629
41.1. 3-D Model of a Resonator Panel .....	632
41.2. 3-D Model of a Quarter-Wave Tubes Resonator .....	632
41.3. Resonator Cross-Section .....	633
41.4. 3-D Mesh of Resonator Panel .....	634
41.5. Absorption Coefficient of the Resonator: BLI Model .....	636
41.6. Absorption Coefficient of the Resonator: LRF Model .....	637
41.7. BLI and LRF Results Comparison .....	637
42.1. 3-D Crimp Joint Model .....	640
42.2. 3-D Meshed Model of Grip with Seven Stranded Wires .....	641
42.3. Rigid Punch and Rigid Base .....	642
42.4. Surface Contact Elements (a) and Edge Contact Elements (b) .....	643

42.5. UY Time Varying Remote Displacement .....	644
42.6. Results at 2.5e-4 Seconds: (a) Displacement, (b) Equivalent Plastic Strain, (c) Contact Status .....	645
42.7. Results at 3.4e-4 Seconds: (a) Displacement, (b) Equivalent Plastic Strain, (c) Contact Status .....	646
42.8. Detailed Views of Deformed Wires .....	647
42.9. Animation of Crimping Process .....	648
43.1. 2D Axisymmetric Model of a Hemispherical Ring Rotating on a flat Ring .....	650
43.2. Contact Pressure Before and After Wear of Hemispherical Ring (Axisymmetric Contact) .....	656
43.3. Contact Pressure Before and After Wear of Both Rings (Symmetric Contact) .....	657
43.4. Stress in the Loading Direction (Y) Before and After Wear of Hemispherical Ring .....	658
43.5. Stress in the Loading Direction (Y) and Element Shapes Before and After Mesh Morphing .....	659
43.6. Animation of Stress in the Loading Direction During Load Step 2 .....	660
43.7. Stress in the Loading Direction (Y) Along the Contact Interface Before and After Wear .....	661
43.8. Time Evolution of Wear in Y Direction at the Initial Point of Contact .....	662
44.1. Rectangular Block Geometry with Semicircular Surface Flaw .....	666
44.2. Semicircular Crack and Torus Along the Crack Front .....	667
44.3. X-Joint Pipe Full Model with Warped Surface Flaw at Welded Joint .....	667
44.4. Semi-elliptical Surface Crack Dimensions .....	668
44.5. Two-plane Symmetry of X-joint Pipe with Warped Surface Flaw Geometry .....	668
44.6. Rectangular Block Model with Boundary Conditions and Loading Applied .....	669
44.7. Sweep Mesh with SOLID186 Around Crack Front .....	669
44.8. Two-plane Symmetry of X-joint Pipe with Warped Surface Flaw at Welded Joint .....	670
44.9. X-joint Pipe with Warped Surface Flaw at Welded Joint in Thickness Direction .....	671
44.10. Sweep Mesh with SOLID186 Around the Crack Front .....	672
44.11. Crack Tip Nodal Component: Rectangular Block Model .....	673
44.12. Crack Tip Nodal Component: X-joint Pipe Model .....	673
44.13. Equivalent Elastic Strain -- Rectangular Block .....	675
44.14. Equivalent Creep Strain -- Rectangular Block .....	676
44.15. Von Mises Stress -- Rectangular Block .....	677
44.16. C*-integral Along the Crack Front -- Rectangular Block .....	678
44.17. Equivalent Elastic Strain -- X-joint Pipe .....	679
44.18. Equivalent Creep Strain -- X-joint Pipe .....	680
44.19. Von Mises Stress -- X-joint Pipe .....	681
44.20. C*-integral Along the Crack Front -- X-Joint Pipe with Warped Flaw .....	682
45.1. Sector Model of the NASA Rotor 67 Fan .....	686
45.2. Full Model of the NASA Rotor 67 Fan .....	687
45.3. One Per Revolution Signal Excitation .....	689
45.4. CFX Model Showing the Domain of the NASA Rotor 67 Fan .....	689
45.5. Solution Convergence Pattern of the NASA Rotor 67 Fan .....	690
45.6. Unsteady Pressure Plots Obtained from TBR Analysis .....	691
45.7. Element Plot of the Cyclic-Sector Model .....	692
45.8. Bonded Contact Pair Between the Disk and the Fan Blade .....	693
45.9. Fixed Support Condition Near Disk .....	694
45.10. Target and Source Geometries of the Rotor Fan Blade .....	697
45.11. Mapped Target Pressure Plots on the Rotor Fan Blade Surface .....	698
45.12. Mistuning in the NASA Rotor 67 Fan Blade .....	701
45.13. (a) Element Component of Fan Blade; (b) Blade Boundary Nodes at the Blade-to-Disk Interface .....	702
45.14. Interference Diagram of NASA Rotor 67 Fan Blade Model .....	704
45.15. Total Deformation Pattern (Real Only) at Frequency of 522.76 Hz .....	705
45.16. Equivalent Stress Pattern (Real Only) at Frequency of 522.76 Hz .....	705
45.17. Equivalent Strain Pattern (Real Only) at Frequency of 522.76 Hz .....	706
45.18. Nodal Solution Plots with Respect to the Frequency of Excitation .....	706
45.19. Directional Deformation at the Blade Tip Along the Z-Direction .....	707

45.20. CYCSPEC Histogram Response Plot at Frequency 522.76 .....	708
45.21. Total Deformation Pattern (Real Only) at Frequency of 534.76 Hz .....	708
45.22. Equivalent Stress Pattern (Real Only) at Frequency of 534.76 Hz .....	709
45.23. Equivalent Strain Pattern (Real Only) at Frequency of 534.76 Hz .....	709
45.24. Nodal Solution Plots with Respect to the Frequency of Excitation .....	710
45.25. Directional Deformation at the Blade Tip Along the Z-Direction .....	710
45.26. CYCSPEC Histogram Response Plot at Frequency 534.76 Hz .....	711



---

## List of Tables

1.1. Solution Output .....	10
12.1. X-Direction Input .....	166
12.2. X-Direction Input (with Missing-Mass Effect) .....	167
12.3. X-Direction Input (with Missing-Mass and Rigid-Response Effects) .....	168
12.4. X-Direction Input Motion .....	169
12.5. X-Direction Input (with Missing-Mass and Rigid-Response Effects) .....	170
12.6. 3-Direction Input (with Missing-Mass and Rigid-Response Effects) .....	171
12.7. 3-Direction Input Motion .....	172
22.1. Comparison of Eigenfrequencies for Full and CMS Models .....	344
22.2. Comparison of CPU and Elapsed Times for Modal Analysis .....	345
22.3. Comparison of Response Amplitudes for Full and CMS Models .....	345
22.4. Comparison of CPU and Elapsed Times for Harmonic Analysis .....	346
26.1. Simulation Statistics for Different Contact Detection Methods .....	397
28.1. Workpiece Material Properties .....	427
28.2. Material Properties of the PCBN Tool .....	427
28.3. Load Steps .....	430
28.4. Solution Settings .....	430
28.5. Locations on Weld Line .....	437
31.1. Initial and Fitted Parameters for the Strain-Controlled Experiment .....	480
31.2. Comparison of Strain-Controlled Experimental Data with Simulated Data .....	481
31.3. Initial and Fitted Parameters for the Stress-Controlled Experiment .....	482
31.4. Initial and Fitted Parameters for Fit to Both Data Sets .....	484
34.1. Coherency Function Coefficients .....	517
34.2. Comparison of Wall Time .....	530
34.3. Comparison of Wall Time for Various Numbers of Cores (R14.5) .....	531
35.1. Implicit Creep Models .....	536
35.2. Generalized Garofalo Creep Constants from Curve Fitting and Reference .....	541
35.3. Flip Chip Material Properties .....	542
35.4. Temperature-Dependent Properties .....	542
37.1. Material Properties of Bolt .....	582
37.2. Material Properties of Cover Plate and Base Plate .....	582
37.3. Simulation Time and Cumulative Iterations for 2-D Models .....	589
37.4. Simulation Time and Cumulative Iterations for 3-D Models .....	589
42.1. Material Properties of Grip and Wire .....	644
45.1. Aliased Engine Order (Excited Harmonic Index) .....	698
45.2. Comparison of Modal Frequencies .....	703
45.3. Comparison of Prestressed Modal Frequencies .....	703



---

# What You Need to Know

---

The purpose of these technical demonstration problems is to encourage you to take advantage of the extraordinarily broad simulation capabilities of ANSYS Mechanical APDL. The real-world problems showcase the features and effectiveness of Mechanical APDL by presenting a series of analyses from a variety of engineering disciplines.

The problems are more substantive and complex than examples found in the standard documentation set. The documentation thoroughly examines the physics involved with each problem and the considerations necessary for translating problems into numerical models. Approximation issues, accuracy considerations, and recommended practices are discussed.

## How Problems Are Presented

Each problem description provides information about the nature and physical characteristics of the problem, specific modeling techniques, material properties, boundary conditions and loading, analysis details and solution controls.

A comprehensive results and discussion section carefully examines analysis results (often comparing them to baseline or known good results using more traditional analysis methods), and illustrates why specific strategies and methods were chosen.

Each problem concludes with valuable hints and recommendations for performing a similar type of analysis. In many cases, references are provided for additional background information. Each example presented can therefore serve as a template for setting up similar types of simulations.

## Your Results May Vary

The analyses described herein were run on a 64-bit Linux system. The results shown for each problem may differ from those that you obtain depending upon the computer hardware and operating system platforms in use at your site.

## Use of ANSYS Mechanical APDL Assumed

The problem descriptions are presented via Mechanical APDL commands, element types, procedures, and material models. It is entirely feasible, however, to use another ANSYS, Inc. application such as ANSYS Mechanical to accomplish similar simulation goals but with a different workflow.

## Obtaining the Input Files

Input files for the technology demonstration problems in this guide are available via the [ANSYS Customer Portal \(Knowledge Resources > Tutorials & Training Materials](#) for the Mechanical APDL application). The files for each problem reside in individual folders named `td-nn` (where *nn* corresponds to a given problem, as documented).

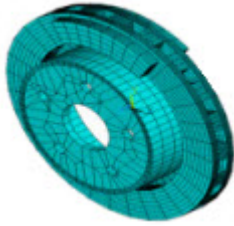
1. Open the `Mechanical-APDL-Technology-Demonstration-Guide-Part1-vnn.zip` file (Files 1 link), or the `Mechanical-APDL-Technology-Demonstration-Guide-Part2-vnn.zip` file (Files 2 link).
2. Unzip or copy (drag and drop) the appropriate `td-nn` folder to any convenient location of your choosing.
3. After starting Mechanical APDL, issue the **File > Change Directory** command to navigate to the `td-nn` folder.

4. Issue the **File > Read Input From** command to read in the .dat file. (Do nothing with any .cdb files, as .dat files call .cdb files as needed.)

### Problem Summary

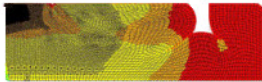
The following analysis demonstration problems are available:

TD-1 Brake Squeal Analysis (p. 1)



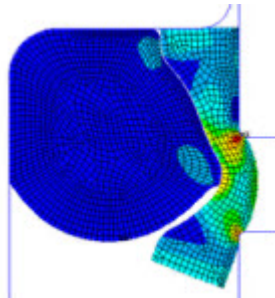
Solves a brake squeal problem. **Three analysis methods (p. 5)** are highlighted: linear non-prestressed modal, partial nonlinear prestressed modal, and full nonlinear prestressed modal. The problem demonstrates sliding frictional contact and uses complex eigensolvers to predict unstable modes.

TD-2 Nonlinear Analysis of a 2-D Hyperelastic Seal Using Rezoning (p. 15)



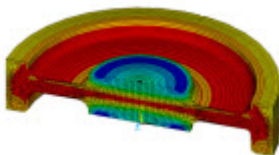
A nonlinear analysis of a 2-D hyperelastic seal assembly using manual **rezoning** with remeshing via the **element-splitting method**. The problem shows how multiple vertical rezoning steps can be used to ensure convergence and completion of an analysis.

TD-3 Fluid-Pressure-Penetration Analysis of a Sealing System (p. 43)



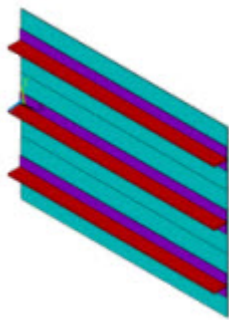
Analyzes fluid-pressure-penetration effects on a sealing system. The use of seals is primarily to prevent the transfer of fluid (liquid, solid, or gas) between two or more regions.

TD-4 Ring-Gear Forging Simulation with Rezoning (p. 61)



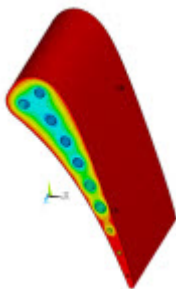
Demonstrates the efficiency and usefulness of **rezoning** in a 2-D simulation of metal-forming processes. Rezoning facilitates the convergence of a nonlinear finite element simulation in which excessive element distortion occurs.

TD-5 Delamination of a Stiffened Composite Panel Under a Compressive Load (p. 79)



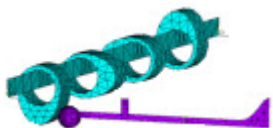
Uses solid-shell element technology to model a layered-composite structure. The problem simulates interface delamination through the debonding capability of contact elements.

TD-6 Thermal Stress Analysis of a Cooled Turbine Blade (p. 91)



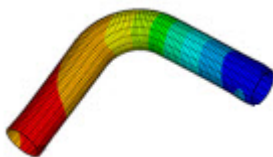
Shows how to easily set up and perform a thermal-stress analysis of a cooled turbine blade. The problem uses surface-effect capabilities to simulate convection loading on solid regions, and one-dimensional fluid-flow capabilities to obtain a highly accurate thermal solution for convection loading.

TD-7 Nonlinear Transient Analysis of a Camshaft Assembly (p. 103)



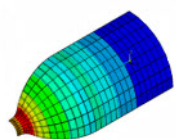
Shows how to easily set up and perform an analysis involving both axisymmetric and nonaxisymmetric components. The problem demonstrates how modeling with [general axisymmetric element technology](#) can reduce computational resources significantly while maintaining the same degree of accuracy as a simulation using a full 3-D model.

TD-8 Nuclear Piping System Under Seismic Loading (p. 115)



Demonstrates the advantages of [elbow element technology](#) over traditional shell and pipe element technology for modeling pipe bends in a typical nuclear piping system.

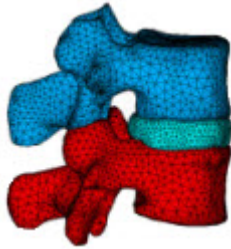
TD-9 Reliability Study of a Composite Overwrapped Pressure Vessel (p. 127)



A reliability study of a composite overwrapped pressure vessel (COPV). The model uses reinforcing fibers in a layered composite. A finite-element simulation of a COPV is performed first to gain insight into its mechanical behaviors, then simulation results are processed using failure analysis to determine the most vulnerable layer. The problem generates linearized stress

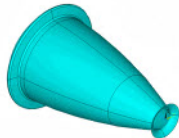
output for pressure-vessel design optimization and code compliance.

TD-10 Simulation of a Lumbar Motion Segment (p. 139)



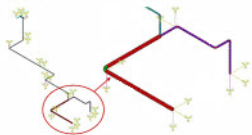
Uses **coupled pore-pressure element** technology to study the creep response of a lumbar motion segment under compression. The simulation reveals the interaction between the solid phase and the fluid phase in soft tissues.

TD-11 Rocket Nozzle Extension Simulation: Fabrication (p. 147)



Simulates thermal stresses during the manufacturing of a rocket nozzle. Uses **current** structural-shell element technology to accurately model the orthotropic thermal expansion in curved-shell structures. Section offsets are applied when connecting shell-to-shell or to shell-to-other element types.

TD-12 Dynamic Simulation of a Nuclear Piping System Using RSA Methods (p. 159)



A problem that accounts for the **missing-mass** effect and **rigid-response** effects in a spectrum analysis, and how including those effects improves results accuracy as compared to full-transient analysis results. The problem uses a piping system model from an actual nuclear power plant.

TD-13 Centrifugal Impeller Analysis Using Cyclic Symmetry and Linear Perturbation (p. 175)



A centrifugal impeller blade analysis using **cyclic modeling methods** and **linear-perturbation** solution approaches. The problem includes a modal analysis, a full harmonic analysis, a prestressed modal analysis using linear perturbation, and a prestressed full harmonic analysis using linear perturbation.

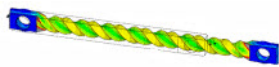
TD-14 Rotordynamics of a Shaft Assembly Based Representative Model of Nelson-Vaugh Rotor (p. 203)

A **rotordynamic analysis** of a rotating structure. A 2-D axisymmetric geometry is extracted from a 3-D solid model of the rotating structure. Modal, Campbell



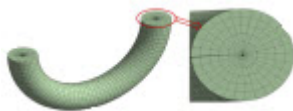
diagram, and unbalance response analyses are performed for the 2-D and 3-D models. Results for the 2-D axisymmetric model are compared to the full 3-D solid model results.

TD-15 **Calibrating and Validating a Hyperelastic Constitutive Model (p. 225)**



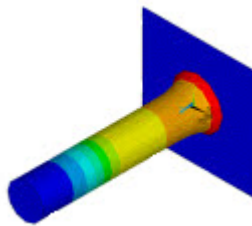
Uses **hyperelastic curve-fitting** to select constitutive model parameters to fit **experimental data**. Several issues influencing the accuracy of the curve fit are discussed. Validation of the resulting constitutive model is demonstrated by comparison with a tension-torsion experiment.

TD-16 **Evaluation of Mixed-Mode Stress Intensity Factors and T-stress for 3-D Surface Flaws (p. 235)**



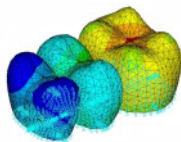
Demonstrates the linear elastic fracture mechanics of 3-D structures. The problem shows how fracture mechanics can be used to evaluate mixed-mode **stress-intensity factors**, **J-integrals**, and **T-stresses**. Analyses of a simple semicircular surface flaw in a rectangular block and a warped flaw along a tubular joint are discussed.

TD-17 **Impact of a Metal Bar on a Rigid Wall (p. 249)**



An impact simulation using a model of a 3-D metal bar hitting a rigid wall. The problem shows the advantages of using impact constraints for modeling contact in a nonlinear transient dynamic analysis. Several combinations of available time-integration methods and contact algorithms are also investigated, using different material models to show how various choices affect the performance and accuracy of the finite-element solution of impact problems.

TD-18 **Viscoelastic Analysis of an All-Ceramic Fixed Partial Denture (FPD) (p. 267)**



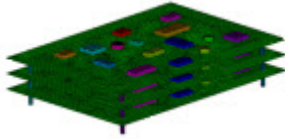
Demonstrates the fictive-temperature model using the Tool-Narayanaswamy (TN) **shift function** to study residual stresses in an all-ceramic fixed partial denture (FPD). A coupled-field solution process, including transient thermal and nonlinear structural analyses, is used in the problem simulation.

TD-19 **Transient Dynamic Analysis of a Digger-Arm Assembly (p. 281)**



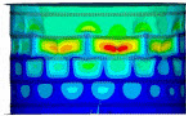
A digger-arm assembly problem demonstrating a **transient dynamic analysis** of a **multibody system**. The problem shows how to model joints and rigid/flexible parts, mitigate overconstraints, and represent flexible parts using **component mode synthesis (CMS)**.

TD-20 [Dynamic Simulation of a Printed Circuit Board Assembly Using Modal Analysis Methods \(p. 299\)](#)



Uses [residual vectors](#) to improve the solution accuracy in modal subspace based analysis methods, such as [modal superposition](#) and [power spectral density \(PSD\)](#) analyses. The problem includes a study of the computational efficiency of the results-expansion procedure used to obtain the full model solution.

TD-21 [Buckling and Post-Buckling Analysis of a Ring-Stiffened Cylinder Using Nonlinear Stabilization \(p. 311\)](#)



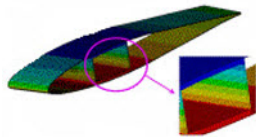
A nonlinear buckling and post-buckling analysis using [nonlinear stabilization](#). The problem uses a stiffened cylinder subjected to uniform external pressure to demonstrate how to find the nonlinear buckling loads, achieve convergence at the post-buckling stage, and interpret the results.

TD-22 [Modal and Harmonic Frequency Analyses of an Automotive Suspension Assembly Using CMS \(p. 333\)](#)



Modal and full harmonic analyses of an automotive suspension assembly exhibiting harmonic displacement excitation at the wheel bottoms. [Component mode synthesis \(CMS\)](#) is used to generate dynamic superelements for use in downstream linear dynamics analyses. Analysis results from the full (non-substructure) and the CMS generated models are compared to highlight the benefits of CMS technology.

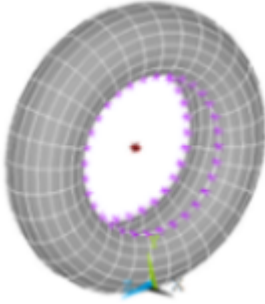
TD-23 [Modal Analysis of a Wind Turbine Blade Using Beam Elements \(p. 351\)](#)



Simulates a wind turbine blade, a slender composite structure, using a [current-technology](#) beam element. A simplified 1-D beam-based model of the typically complex blade geometry is especially useful in the early design stage, when small design variations can lead to partial or even complete reconstruction of a 3-D model, generally an impractical solution given the difficulty of building the model.

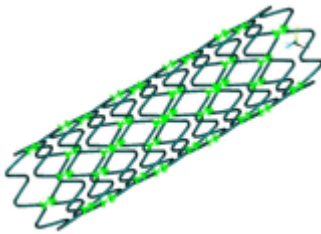


TD-24 Hydrostatic Fluid Analysis of an Inflating and Rolling Tire (p. 363)



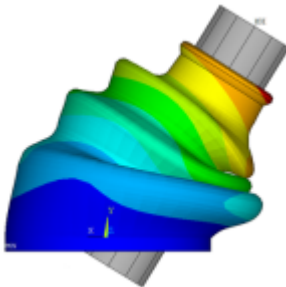
Models a fluid that is fully enclosed within a solid (container). The problem shows how loading and deformation on the container affects the contained fluid pressure, volume, density and mass.

TD-25 Cardiovascular Stent Simulation (p. 377)



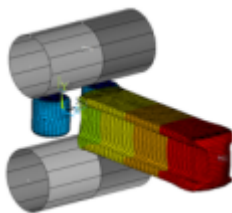
Simulates stent-artery interaction during and after stent placement. The analysis uses advanced modeling techniques including contact, element birth and death, mixed u-P formulation, and nonlinear stabilization

TD-26 Nonlinear Analysis of a Rubber Boot Seal (p. 389)



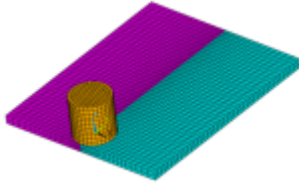
A nonlinear analysis of a rubber boot seal that includes geometric nonlinearities (large strain and large deformation), nonlinear material behavior (incompressible hyperelastic material model), and changing status nonlinearities (contact). The analysis demonstrates the advantages of the surface-projection-based contact contact method.

TD-27 Hot-Rolling Structural Steel Analysis with 3-D Rezoning (p. 401)



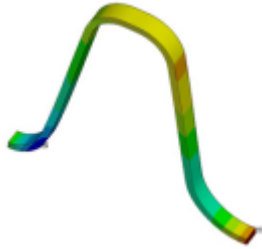
A 3-D large-deformation problem demonstrating the use of rezoning to repair a severely distorted mesh. The example also uses contact technology and symmetric expansion.

**TD-28 Friction Stir Welding (FSW) Simulation (p. 421)**



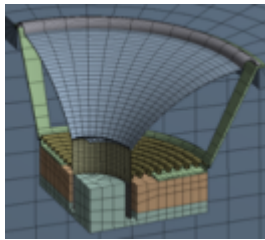
Simulates the friction stir welding (FSW) process. Several characteristics of FSW are presented, including plastic deformation, tool-workpiece surface interaction, and heat generation due to friction and plastic deformation. Thermal and mechanical behaviors are mutually dependent and coupled together during the FSW process. A nonlinear direct coupled-field analysis is performed.

**TD-29 Rocket Nozzle Extension Simulation: Operation (p. 445)**



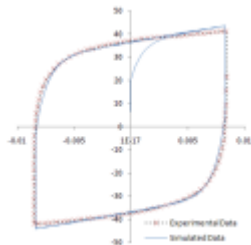
Simulates the thermal stresses induced during the operation of a rocket nozzle. Hot gases flow through the nozzle, subjecting the inside and outside of the nozzle body to convection heat loading. Solid thermal and structural elements accurately simulate the multiphysics of the problem. A loose coupling method is used for the analysis. Because the body material could be homogeneous or a layered composite, the simulation uses a solid element type with both homogeneous and layered material capabilities.

**TD-30 Acoustic Analysis of a Small Speaker System (p. 461)**



Uses acoustic elements coupled with structural elements to analyze the performance of a speaker assembly. Features structural-acoustic coupling using **fluid-structure interaction (FSI)** in 3-D, a symmetric FSI algorithm, perfectly matched layers (PML) to absorb outgoing acoustic waves, postprocessing sound pressure level (SPL) and velocity, far-field postprocessing of acoustic field, and user-defined symmetric expansion options.

**TD-31 Fitting Parameters for a Chaboche Kinematic Hardening Model (p. 475)**



Determines material parameters for a third-order Chaboche kinematic hardening model using the **curve-fitting tool**.

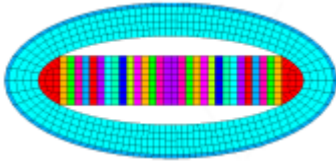
A method is presented to estimate the initial parameters and obtain a least-squares best fit to the data. The fitted parameters are validated by conducting uniaxial simulations using a single element and comparing the results with the experimental data.

**TD-32 Anterior Cruciate Ligament (ACL) Simulation (p. 489)**



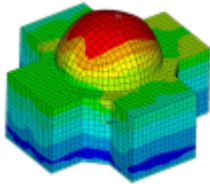
Simulates the response of an anterior cruciate ligament (ACL) of a human knee subjected to tension, flexion, and rotation. The problem uses an **anisotropic hyperelastic** material model with **viscoelasticity**.

TD-33 Analysis of a Piezoelectric Flextensional Transducer in Water (p. 501)



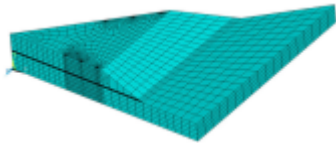
Couples structural, piezoelectric, and acoustic elements to analyze the acoustic response of a flextensional transducer to voltage excitation. The problem highlights fluid-structure interaction (FSI), piezoelectric materials, infinite acoustic elements, the Robin boundary condition, and far-field postprocessing.

TD-34 Dynamic Simulation of a Nuclear Island (p. 513)



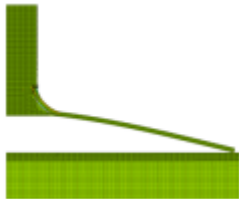
A power spectral density (PSD) analysis of a nuclear island component of a nuclear power plant (NPP). The problem shows the analysis methods available to simulate the response of an NPP to a seismic event, accounting for motion incoherency and wave-passage effects.

TD-35 Elastoplastic Creep Analysis of Lead-Free Solder Bumps (p. 535)



A thermo-mechanical analysis of lead-free solder bumps subjected to cyclic thermal loading. The problem shows how to obtain implicit creep material constants using experimental data, uses creep and plasticity material models to simulate viscoplastic behavior, and determines accumulated creep strain due to thermal loading.

TD-36 VCCT-Based Crack-Growth Simulation of a Composite Laminated T-Joint



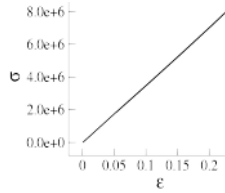
Simulates interfacial crack growth occurring in a laminated T-Joint using the virtual crack closure technique (VCCT). The simulation involves growing an existing crack along a predefined path using interface elements.

TD-37 Bolt Thread Simulation



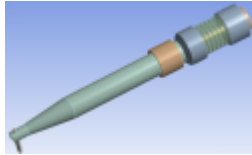
A comparison of three modeling techniques for bolt threading: true threading simulation, the bolt section method, and the multi-point constraint (MPC) method. The comparison shows that the bolt section method offers accurate results while requiring significantly less computational time.

TD-38 **Large-Deformation Neo-Hookean Analysis (with UserMat Subroutine)**



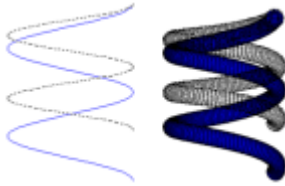
Formulates a 3-D large deformation, hyperelastic material to demonstrate the user material capability in nonlinear geometry analyses. Details are given for stress and material tangent calculations and formulation in a co-rotated frame, as well as conversion of tensor quantities to Voigt notation. The problem also serves as a usage example of the [UserMat](#) subroutine, a user-programmable feature for developing a custom, constitutive model to define the stress-strain behavior of a material.

TD-39 **Wire Bonding Ultrasonic Transducer (p. 603)**



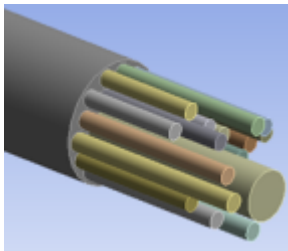
Simulates electrical excitation of an ultrasonic transducer used for wire bonding applications. The model includes piezoelectric material definition as well as prestressed modal and harmonic response analyses.

TD-40 **Shape Memory Alloy (SMA) with Thermal Effect**



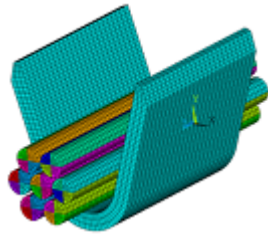
Two shape memory alloy (SMA) simulations: a spinal spacer implant and a spring actuator. A shape memory alloy (SMA) is a material that, after being subjected to mechanical loading/unloading cycles, is able to undergo large deformations without showing residual strains (pseudoelasticity) or that can recover from large deformations via temperature change (shape memory effect). The simulations demonstrate the utility of the [SMA material model](#) using martensite and austenite (nitinol), and the behavior of the SMA with thermal loading.

TD-41 **Acoustic Analysis of a Viscothermal Resonator**



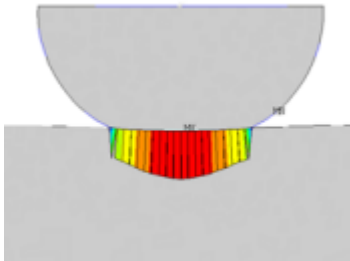
Uses acoustic elements and viscothermal losses comparing the [boundary layer impedance \(BLI\) model](#) and the [low reduced frequency \(LRF\) model](#) to analyze the noise reduction of sound-absorbing trim panels with quarter-wave resonators.

TD-42 Wire Crimping Modeled with General Contact (p. 639)



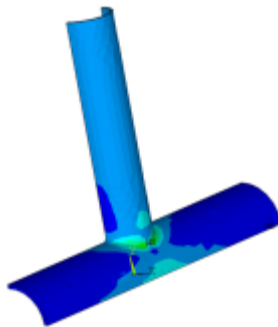
Demonstrates the ease of contact modeling via the [general contact](#) method. This method offers automated contact creation and requires minimal user input. The general contact procedure is especially useful when a large number of contacting surfaces are involved in the model and the geometry makes it difficult to determine contact pairs.

TD-43 Contact Surface Wear Simulation



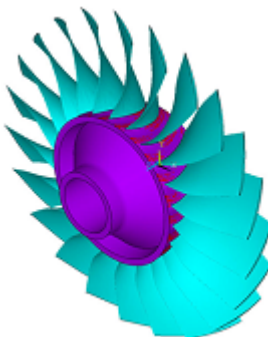
Demonstrates how to model [contact surface wear](#) using the Archard wear model or a user-defined wear model (`userwear` subroutine). The wear model calculates how much and in what direction a contact node is to be moved to simulate wear based on the contact results. In this example the wear occurs at the interface of a hemispherical ring rotating over a flat ring. [Mesh nonlinear adaptivity based on a wear criterion](#) is used to improve the mesh during the wear process.

TD-44 C\*-integral Evaluation for 3-D Surface Flaws



Evaluates the [C\\*-integral](#) for cracks in structural components. Analyses of a simple semicircular surface flaw in a rectangular block and a warped flaw along a tubular joint are presented.

TD-45 Forced Response Analysis of a Mistuned Bladed Disk Using Cyclic Symmetry and Linear Perturbation



Demonstrates the free vibration and forced response analysis of a tuned and mistuned NASA Rotor 67 fan using [cyclic modeling methods](#) and [linear perturbation](#) solution approaches. Includes a modal analysis, a prestressed modal analysis using linear perturbation, and a prestressed mode-superposition harmonic analysis using linear perturbation.



---

# Chapter 1: Brake Squeal Analysis

---

This example problem shows how to solve a brake squeal problem. [Three analysis methods \(p. 5\)](#) are highlighted: linear non-prestressed modal, partial nonlinear perturbed modal, and full nonlinear perturbed modal. The problem demonstrates sliding frictional contact and uses complex eigensolvers to predict unstable modes.

Topics related to this example problem follow:

- 1.1. Introduction
- 1.2. Problem Description
- 1.3. Modeling
- 1.4. Material Properties
- 1.5. Boundary Conditions and Loading
- 1.6. Analysis and Solution Controls
- 1.7. Results and Discussion
- 1.8. Recommendations
- 1.9. References
- 1.10. Input Files

## 1.1. Introduction

Eliminating brake noise is a classic challenge in the automotive industry. Brake discs develop large and sustained friction-induced oscillations, referred to simply as brake squeal.

Two common theories describe brake squeal phenomena:

- *Stick-Slip Theory* -- The self-excited vibration of a brake system occurs when the static friction coefficient is greater than the sliding friction coefficient. Variable friction forces introduce energy into the system which is not properly dissipated during the squealing event, resulting in large vibration.
- *Mode-Coupling Theory* -- When two similar characteristic modes couple with each other, instability is introduced to the braking system. This instability is caused primarily by improperly selected geometric parameters.

Both theories attribute brake squeal to variable friction forces at the disc-pad interface.

Brake noise is generally categorized as follows:

- Low-frequency noise -- An example of a low-frequency noise is the “groaning” noise which occurs in the frequency range between 100 and 1000 Hz. Any noise having a frequency above 1000 Hz is considered a squeal.
- Low frequency squeal -- This squeal is a result of mode coupling occurring between the out-of-plane modes of the rotor and the bending modes of the brake pad.
- High frequency squeal -- This squeal is a result of mode coupling occurring between the in-plane modes of the rotor.

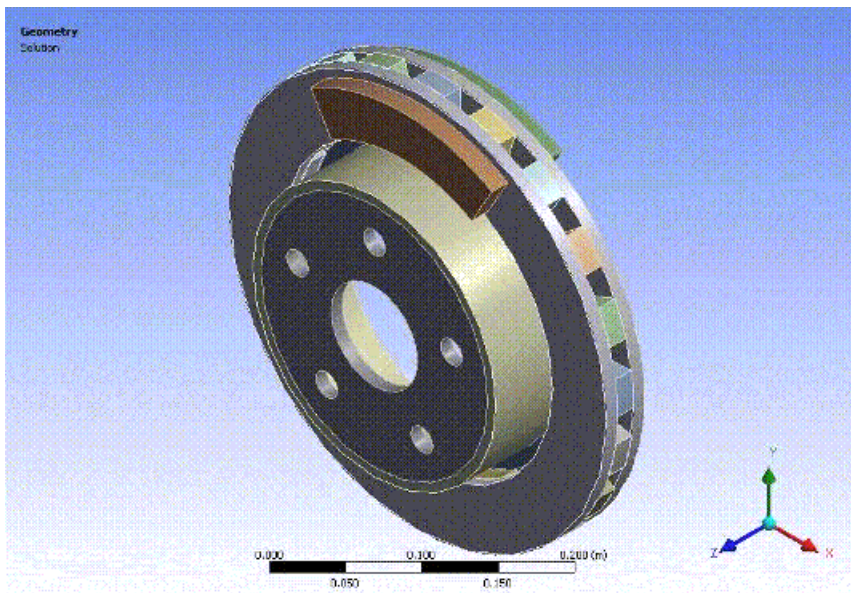
Low- and high-frequency squealing can be determined via complex eigensolvers. The presence of unstable modes suggests that the geometry parameters and material properties of the braking system should be modified.

For more information, see [Brake Squeal \(Prestressed Modal\) Analysis](#) in the *Structural Analysis Guide*.

### 1.2. Problem Description

The following model is a simple brake disc-pad assembly. The disc has a thickness of 10 mm and the brake pads have a thickness of 15 mm. The inner diameter of the disc is 250 mm and outer diameter is of 350 mm. A prestressed modal analysis is performed on this model using various methods to determine the unstable modes. A parametric study is then performed to examine the effect of the friction coefficient on the dynamic stability of the model.

**Figure 1.1: Brake Disc-Pad Assembly**



### 1.3. Modeling

This section describes modeling details for the brake disc-pad assembly. The following topics are available:

- [1.3.1. Understanding the Advantages of Contact Element Technology](#)
- [1.3.2. Modeling Contact Pairs](#)
- [1.3.3. Generating Internal Sliding Motion](#)
- [1.3.4. Meshing the Brake Disc-Pad Model](#)

#### 1.3.1. Understanding the Advantages of Contact Element Technology

Brake squeal problems typically require manual calculations of the unsymmetric terms arising from sources such as frictional sliding, and then inputting the unsymmetric terms using special elements (such as [MATRIX27](#)). It is a tedious process requiring a matched mesh at the disc-pad interface along with assumptions related to the amount of area in contact and sliding.

3-D contact elements (CONTA17x) offer a more efficient alternative by modeling surface-to-surface contact at the pad-disc interface. With contact surface-to-surface contact elements, a matched mesh is unnecessary at the contact/target surface, and there is no need to calculate the unsymmetric terms.



Contact surface-to-surface elements offer many controls for defining contact pairs, such as the type of contact surface, algorithm, contact stiffness, and gap/initial penetration effect.

### 1.3.2. Modeling Contact Pairs

Frictional surface-to-surface contact pairs with a 0.3 coefficient of friction are used to define contact between the brake pads and disc to simulate frictional sliding contact occurring at the pad-disc interface. Bonded surface-to-surface contact pairs are used to define the contact for other components which will be always in contact throughout the braking operation.

The augmented Lagrange algorithm is used for the frictional contact pairs, as the pressure and frictional stresses are augmented during equilibrium iterations in such a way that the penetration is reduced gradually. The augmented Lagrange algorithm also requires fewer computational resources than the standard Lagrange multiplier algorithm, which normally requires additional iterations to stabilize the contact conditions. The augmented Lagrange is well suited for modeling general frictional contact, such as the contact between the brake pad and disc defined in this example.

An internal multipoint constraint (MPC) contact algorithm is used for bonded contact because it ties contact and target surface together efficiently for solid-solid assembly. The MPC algorithm builds equations internally based on the contact kinematics and does not require the degrees of freedom of the contact surface nodes, reducing the wave front size of the equation solver. A contact detection point is made on the Gauss point for frictional contact pairs, and on the nodal point (normal-to-target surface) for MPC bonded contact pairs.

**Figure 1.2: Contact Pair Definition**

Details of "Frictional - Pad-1 To Disc-1"		Details of "Bonded - Solid To Solid"	
<b>Scope</b>		<b>Scope</b>	
Scoping Method	Geometry Selection	Scoping Method	Geometry Selection
Contact	1 Face	Contact	1 Face
Target	1 Face	Target	1 Face
Contact Bodies	Pad-1	Contact Bodies	Solid
Target Bodies	Disc-1	Target Bodies	Solid
<b>Definition</b>		<b>Definition</b>	
Type	Frictional	Type	Bonded
<input type="checkbox"/> Friction Coefficient	0.3	Scope Mode	Manual
Scope Mode	Manual	Behavior	Symmetric
Behavior	Asymmetric	Suppressed	No
Suppressed	No	<b>Advanced</b>	
<b>Advanced</b>		Formulation	MPC
Formulation	Augmented Lagrange	Pinball Region	Radius
Interface Treatment	Adjust to Touch	Pinball Radius	1.e-002 m
Normal Stiffness	Program Controlled		
Update Stiffness	Each Equilibrium Iteration		
Pinball Region	Radius		
Pinball Radius	2.e-003 m		
Time Step Controls	None		

Frictional contact between pad and disc (left) and bonded contact between other braking components (right)

### 1.3.3. Generating Internal Sliding Motion

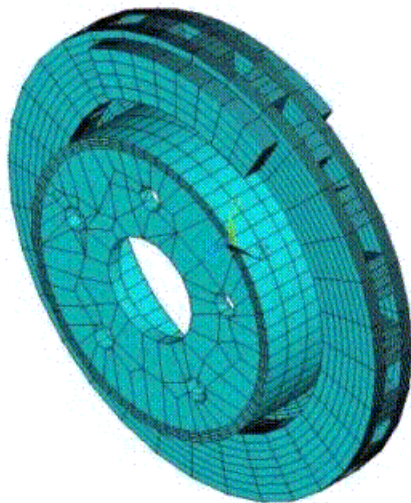
The **CMROTATE** command defines constant rotational velocities on the contact/target nodes to generate internal sliding motion. The specified rotational velocity is used only to determine the sliding direction and has no effect on the final solution. The element component used should include only the contact or the target elements that are on the brake disc/rotor. In this example, the target elements are defined

on the disc surface and the contact elements are defined on the pad surface. The target elements attached to the disc surface are grouped to form a component named E\_ROTOR which is then later specified in the **CMROTATE** command to generate a sliding frictional force.

### 1.3.4. Meshing the Brake Disc-Pad Model

The Sweep method is used to generate a hexahedral dominant mesh of the brake system assembly. Brake discs, pads and all other associated components are meshed with 20-node structural solid **SOLID186** elements with uniform reduced-integration element technology. The edge sizing tool is used to obtain a refined mesh at the pad-disc interface to improve the solution accuracy. For problems with a large unsymmetric coefficient, a finer mesh should be used at the pad-disc interface to accurately predict the unstable modes. **CONTA174** (3-D 8 node surface to surface contact) elements are used to define the contact surface and **TARGE170** (3-D target segment) elements are used to define the target surface. The brake disc-pad assembly is meshed with total of 60351 nodes and 11473 elements.

**Figure 1.3: Meshed Brake Disc-Pad Assembly**



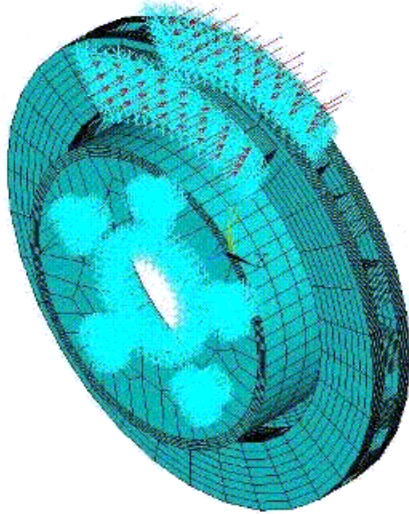
## 1.4. Material Properties

Linear elastic isotropic materials are assigned to all the components of the braking system.

Material Properties	
Young's Modulus (Nm <sup>-2</sup> )	2.0 E+11 Pa
Density	7800 Kg/m <sup>3</sup>
Poisson's Ratio	0.3

## 1.5. Boundary Conditions and Loading

The inner diameter of the cylinder hub and bolt holes is constrained in all directions. Small pressure loading is applied on both ends of the pad to establish contact with the brake disc and to include prestress effects. The displacement on the brake pad surfaces where the pressure loading is applied is constrained in all directions except axial one (along Z).

**Figure 1.4: Boundary Conditions (Displacement Constraints and Pressure Loading)**

## 1.6. Analysis and Solution Controls

The analysis settings and solution controls differ depending upon the method used to solve a brake squeal problem. This section describes three possible methods:

- 1.6.1. Linear Non-prestressed Modal Analysis
- 1.6.2. Partial Nonlinear Perturbed Modal Analysis
- 1.6.3. Full Nonlinear Perturbed Modal Analysis

### 1.6.1. Linear Non-prestressed Modal Analysis

A [linear non-prestressed modal analysis](#) is effective when the stress-stiffening effects are not critical. This method requires less run time than the other two methods, as Newton-Raphson iterations are not required. The contact-stiffness matrix is based on the initial contact status.

Following is the general process for solving a brake squeal problem using this method:

1. Perform a linear partial-element analysis with no prestress effects.
2. Generate the unsymmetric stiffness matrix (**NROPT,UNSYM**).
3. Generate sliding frictional force (**CMROTATE**).
4. Perform a complex modal analysis using the QRDAMP or UNSYM eigensolver.

---

#### Note

When using the QRDAMP solver, you can reuse the symmetric eigensolution from the previous load steps (**QRDOPT**). This is very effective when performing a friction sensitive/parametric analysis, because it saves time by not re-computing the real symmetric modes after the first solve.

---

5. Expand the modes and postprocess the results from `Jobname .RST`.

For this analysis, the UNSYM solver is selected to solve the problem. (Guidelines for selecting the eigensolver for brake squeal problems appear in [Recommendations](#) (p. 12).)

The frequencies obtained from the modal solution have real and imaginary parts due the presence of an unsymmetric stiffness matrix. The imaginary frequency reflects the damped frequency, and the real frequency indicates whether the mode is stable or not. A real eigenfrequency with a positive value indicates an unstable mode.

The following input fragments show the solution steps involved in this method:

### Modal Solution

```

/SOLU
ANTYPE, MODAL      ! Perform modal solve
NROPT, UNSYM      ! To generate non symmetric
CMSEL, S, C1_R    ! Select the target elements of the disc
CMSEL, A, C2_R
CM, E_ROTOR, ELEM ! Form a component named E_ROTOR with the selected target elements
ALLSEL, ALL
CMROTATE, E_ROTOR, , , 2 ! Rotate the selected element along global Z using CMROTATE command

MODEPT, UNSYM, 30 ! Use UNSYM to extract 30 modes
MXPAND, 30        ! Expand 30 modes, do not calculate element results
SOLVE
FINISH

```

## 1.6.2. Partial Nonlinear Perturbed Modal Analysis

A partial nonlinear perturbed modal analysis is used when stress-stiffening has an effect on the final modal solution. The initial contact conditions are established, and a prestressed matrix is generated at the end of the first static solution.

Following is the general process for solving a brake squeal problem using this method:

1. Perform a nonlinear, large-deflection static analysis (**NLGEOM,ON**).

Use the unsymmetric Newton-Raphson method (**NROPT,UNSYM**). Specify the restart control points needed for the linear perturbation analysis (**RESCONTROL**)

Create components for use in the next step.

The static solution with external loading establishes the initial contact condition and generates a prestressed matrix.

2. Restart the previous static solution from the desired load step and substep, and perform the first phase of the perturbation analysis while preserving the `.ldhi`, `.rnnn` and `.rst` files (**ANTYPE,STATIC,RESTART,,,PERTURB**).

Initiate a modal linear perturbation analysis (**PERTURB,MODAL**).

Generate forced frictional sliding contact (**CMROTATE**), specifying the component names created in the previous step.

The contact stiffness matrix is based only on the contact status at the restart point.

Regenerate the element stiffness matrix at the end of the first phase of the linear perturbation solution (**SOLVE,ELFORM**).

- Obtain the linear perturbation modal solution using the QRDAMP or UNSYM eigensolver (**MODOPT**).

---

### Note

When using the QRDAMP solver, you can reuse the symmetric eigensolution from the previous load steps (**QRDOPT**). This is very effective when performing a friction sensitive/parametric analysis, because it saves time by not re-computing the real symmetric modes after the first solve.

---

- Expand the modes and postprocess the results (from the Jobname .RSTP file).

The following input fragments show the solution steps involved with this method:

### Static Solution

```

ANTYPE, STATIC           ! Perform static solve
OUTRES, ALL, ALL         ! Write all element and nodal solution results for each sub steps
NROPT, UNSYM             ! Specify unsymmetric Newton-Raphson option to solve the problem
RESCONTROL, DEFINE, ALL, 1 ! Control restart files
NLGEOM, ON               ! Activate large deflection
AUTOTS, ON               ! Auto time stepping turned on
TIME, 1.0                ! End time = 1.0 sec
CMSEL, S, C1_R           ! Select target elements of the disc
CMSEL, A, C2_R
CM, E_ROTOR, ELEM        ! Form a component named E_ROTOR
SOLVE                    ! Solve with prestress

```

### Perturbed Modal Solution

```

ANTYPE, STATIC, RESTART, , , PERTURB ! Restart from last load step and sub step
PERTURB, MODAL              ! Perform linear perturbation modal solve
CMROT, E_ROTOR, , , 2      ! Rotate the target element to generate sliding frictional contact
SOLVE, ELFORM              ! Regenerate the element stiffness matrix

MODOPT, UNSYM, 30          ! Use UNSYM eigensolver and extract 30 modes
MXPAND, 30                 ! Expand 30 modes
SOLVE                      ! Solve linear perturbation modal solve

```

## 1.6.3. Full Nonlinear Perturbed Modal Analysis

A full nonlinear perturbed modal analysis is the most accurate method for modeling the brake squeal problem. This method uses Newton-Raphson iterations for *both* of the static solutions.

Following is the general process for solving a brake squeal problem using this method:

- Perform a nonlinear, large-deflection static analysis (**NLGEOM,ON**).

Use the unsymmetric Newton-Raphson method (**NROPT,UNSYM**).

Specify the restart control points needed for the linear perturbation analysis (**RESCONTROL**).

- Perform a full second static analysis.

Generate sliding contact (**CMROTATE**) to form an unsymmetric stiffness matrix.

- After obtaining the second static solution, postprocess the contact results.

Determine the status (that is, whether the elements are sliding, and the sliding distance, if any).

- Restart the previous static solution from the desired load step and substep, and perform the first phase of the perturbation analysis while preserving the `.ldhi`, `.rnnn` and `.rst` files (**ANTYPE,STATIC,RESTART,,,PERTURB**).

Initiate a modal linear perturbation analysis (**PERTURB,MODAL**).

Regenerate the element stiffness matrix at the end of the first phase of the linear perturbation solution (**SOLVE,ELFORM**).

- Obtain the linear perturbation modal solution using the QRDAMP or UNSYM eigensolver (**MODOPT**).
- Expand the modes and postprocess the results (from the `Jobname.RSTP` file).

The following input fragments show the solution steps involved with this method:

### First Static Solution

```

ANTYPE, STATIC           ! Perform static solve
OUTRES, ALL, ALL         ! Write all element and nodal solution results for each substep
NROPT, UNSYM             ! Specify unsymmetric Newton-Raphson option to solve the problem
RESCONTROL,DEFINE,ALL,1 ! Control restart files
NLGEOM, ON               ! Activate large deflection
AUTOTS, ON               ! Auto time stepping turned on
TIME, 1.0                ! End time = 1.0 sec
CMSEL, S, C1_R           ! Select the target elements of the disc
CMSEL, A, C2_R
CM, E_ROTOR, ELEM        ! Form a component named E_ROTOR with the selected target elements
ALLSEL, ALL
SOLVE                    ! Solve with prestress loading
    
```

### Second Static Solution

```

CMROTATE, E_ROTOR, , , 2 ! Rotate the selected element along global Z using CMROTATE command
TIME, 2.0                ! End time = 2.0sec
SOLVE                    ! Perform full solve
FINISH
    
```

### Perturbed Modal Solution

```

ANTYPE,STATIC,RESTART,,,PERTURB ! Restart from last load step and sub step
PERTURB,MODAL                   ! Perform linear perturbation modal solve
SOLVE,ELFORM                     ! Regenerate the element stiffness matrix

MODOPT,UNSYM,30                  ! Use UNSYM eigensolver and extract 30 modes
MXPAND,30                        ! Expand 30 modes
SOLVE                            ! Solve linear perturbation modal solve
    
```

## 1.7. Results and Discussion

The unstable mode predictions for the brake disc-pad assembly using all three methods were very close due to the relatively small prestress load. The [linear non-prestressed modal solution \(p. 5\)](#) predicted unstable modes at 6474 Hz, while the other two solution methods predicted unstable modes at 6470 Hz.

The mode shape plots for the unstable modes suggest that the bending mode of the pads and disc have similar characteristics. These bending modes couple due to friction, and produce a squealing noise.

**Figure 1.5: Mode Shape for Unstable Mode (Mode 21) Obtained from the Linear Non-prestressed Modal Solution (p. 5)**

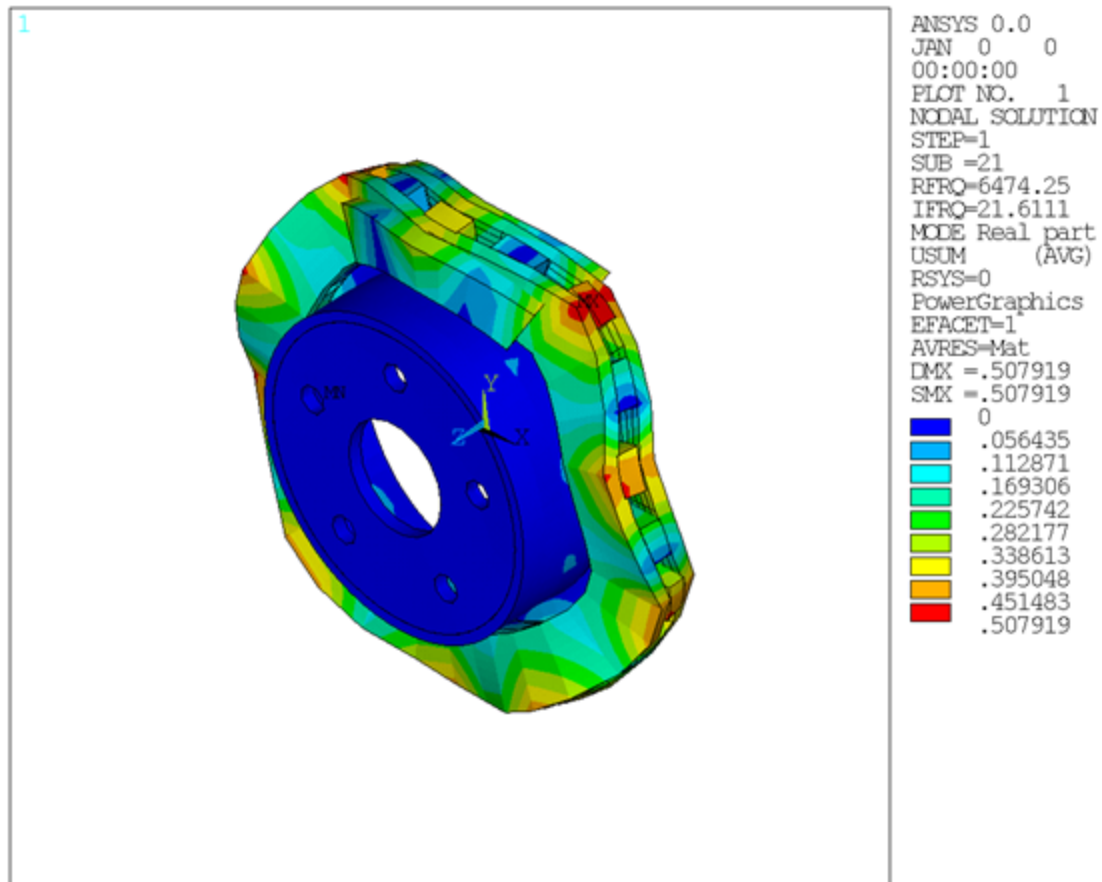


**Figure 1.6: Mode Shape for Unstable Mode (Mode 22) Obtained from the Linear Non-prestressed Modal Solution (p. 5)**

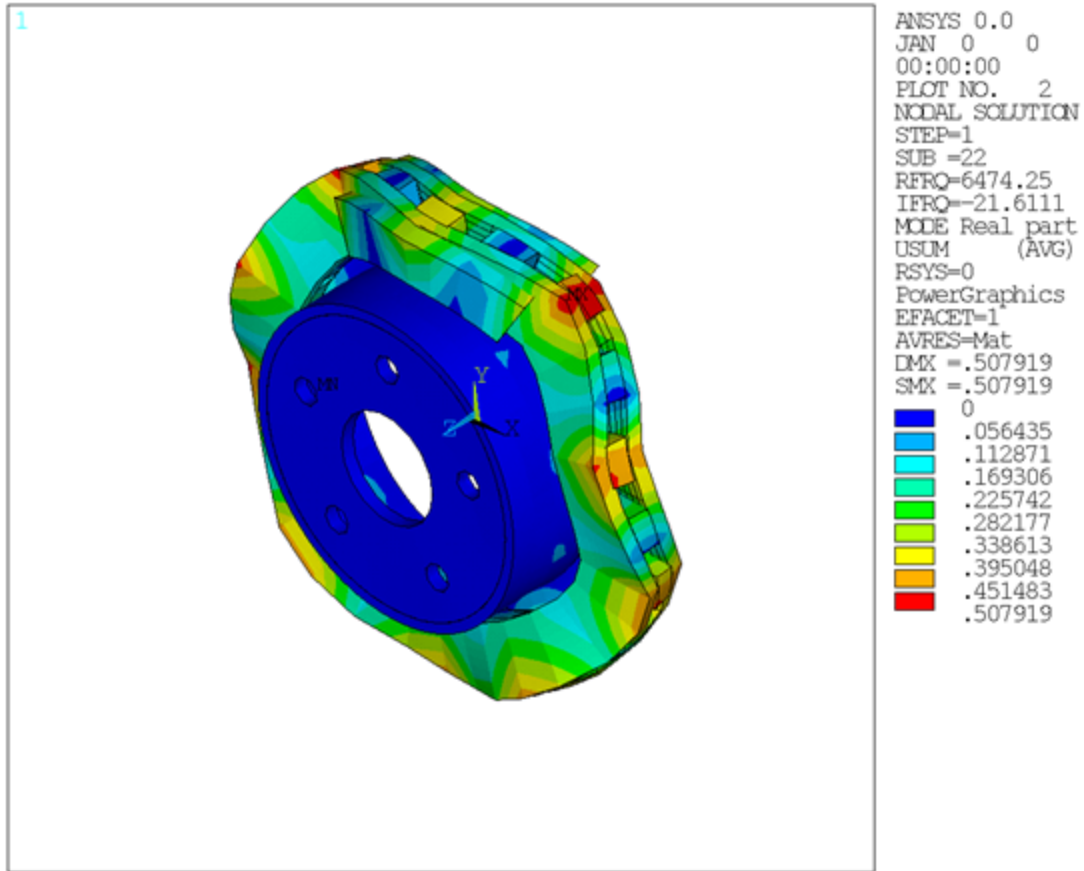


**Table 1.1: Solution Output**

Mode	Linear non-prestressed modal		Partial nonlinear perturbed modal		Full nonlinear perturbed modal	
	Imaginary	Real	Imaginary	Real	Imaginary	Real
1.00	775.91	0.00	775.73	0.00	775.73	0.00
2.00	863.54	0.00	863.45	0.00	863.45	0.00
3.00	1097.18	0.00	1097.03	0.00	1097.03	0.00
4.00	1311.54	0.00	1311.06	0.00	1311.06	0.00
5.00	1328.73	0.00	1328.07	0.00	1328.07	0.00
6.00	1600.95	0.00	1600.66	0.00	1600.66	0.00
7.00	1616.15	0.00	1615.87	0.00	1615.87	0.00
8.00	1910.50	0.00	1910.50	0.00	1910.50	0.00
9.00	2070.73	0.00	2070.44	0.00	2070.44	0.00
10.00	2081.26	0.00	2080.98	0.00	2080.98	0.00
11.00	2676.71	0.00	2675.23	0.00	2675.23	0.00
12.00	2724.05	0.00	2722.61	0.00	2722.61	0.00
13.00	3373.96	0.00	3373.32	0.00	3373.32	0.00



	Linear non-prestressed modal		Partial nonlinear perturbed modal		Full nonlinear perturbed modal	
14.00	4141.64	0.00	4141.45	0.00	4141.45	0.00
15.00	4145.16	0.00	4145.04	0.00	4145.04	0.00
16.00	4433.91	0.00	4431.08	0.00	4431.08	0.00
17.00	4486.50	0.00	4484.00	0.00	4484.00	0.00
18.00	4668.51	0.00	4667.62	0.00	4667.62	0.00
19.00	4767.54	0.00	4766.95	0.00	4766.95	0.00
20.00	5241.61	0.00	5241.38	0.00	5241.38	0.00
21.00	6474.25	21.61	6470.24	21.90	6470.24	21.90
22.00	6474.25	-21.61	6470.24	-21.90	6470.24	-21.90
23.00	6763.36	0.00	6763.19	0.00	6763.19	0.00
24.00	6765.62	0.00	6765.51	0.00	6765.51	0.00
25.00	6920.64	0.00	6919.64	0.00	6919.64	0.00
26.00	6929.25	0.00	6929.19	0.00	6929.19	0.00
27.00	7069.69	0.00	7066.72	0.00	7066.72	0.00
28.00	7243.80	0.00	7242.71	0.00	7242.71	0.00
29.00	8498.41	0.00	8493.08	0.00	8493.08	0.00
30.00	8623.76	0.00	8616.68	0.00	8616.68	0.00

### 1.7.1. Determining the Modal Behavior of Individual Components

It is important to determine the modal behavior of individual components (disc and pads) when predicting brake squeal noise. A modal analysis performed on the free pad and free disc model gives insight into potential coupling modes. The natural frequency and mode shapes of brake pads and disc can also be used to define the type of squeal noise that may occur in a braking system. Bending modes of pads and disc are more significant than twisting modes because they eventually couple to produce squeal noise.

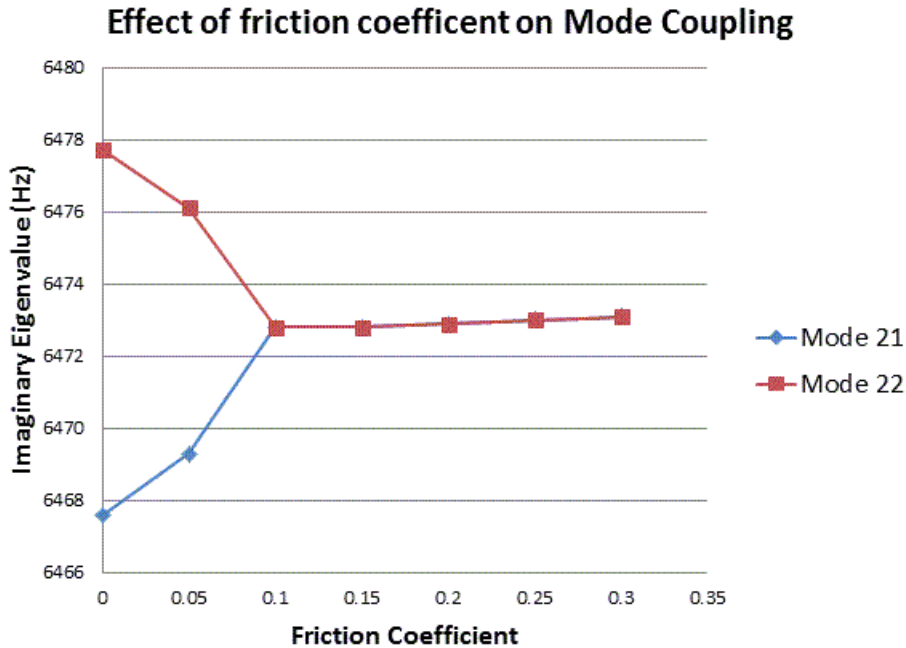
An examination of the results obtained from the modal analysis of a free disc and pad shows that the second bending mode of the pad and ninth bending mode of the disc can couple to create dynamic instability in the system. These pad and disc bending modes can couple to produce an intermediate lock, resulting in a squeal noise at a frequency close to 6470 Hz.

### 1.7.2. Parametric Study with Increasing Friction Coefficient

A parametric study was performed on the brake disc model using a linear non-prestressed modal solution with an increasing coefficient of friction. QRDAMP eigensolver is used to perform the parametric studies by reusing the symmetric real modes (**QRDOPT,ON**) obtained in the first load step.

The following plot suggests that modes with similar characteristics approach each other and couple as the coefficient of friction increases.

**Figure 1.7: Effect of Friction Coefficient on Unstable Modes**



## 1.8. Recommendations

The following table provides guidelines for selecting the optimal analysis method to use for a brake squeal problem:

Analysis Method	Benefits	Costs
Linear non-prestressed modal	Fast run time No convergence issues Good method for performing parametric studies	Accuracy Does not include prestress effects
Partial nonlinear perturbed modal	No convergence issues Includes prestress effects	Accuracy
Full nonlinear perturbed modal	Accurate Includes prestress effects	Longer run time Convergence issues

The following table provides guidelines for selecting the optimal eigensolver (**MODOPT**) for obtaining the brake squeal solution:

Eigensolver	Benefits	Costs
<b>QRDAMP</b>	Fast run time An excellent solver for performing parametric studies	Accuracy, as it approximates the unsymmetric stiffness matrix

Eigensolver	Benefits	Costs
		Not recommended when the number of elements contributing to unsymmetric stiffness matrix exceeds 10 percent of the total number of elements in the model
UNSYM	Accuracy, as it uses the full unsymmetric stiffness matrix to solve the problem	Long run time when many modes are extracted

For further information, see [Brake Squeal Analysis](#) in the *Structural Analysis Guide*.

## 1.9. References

The following references are cited in this example problem:

1. Triches M., Jr, S.N.Y. Gerges, R. Jordon. "Reduction of Squeal Noise from Disc Brake Systems Using Constrained Layer Damping." *Journal of the Brazilian Society of Mechanical Sciences and Engineering*. Volume XXVI: 340–343. July-September 2004.
2. Allgair, R. et al. "Mode Lock-In and Friction Modeling." *Computational Methods in Contact Mechanics IV*. 35-47. WIT Press: Southampton (1999).
3. Schroth, R., N. Hoffmann, R. Swift. *Mechanism of Brake Squeal--From Theory to Experimentally Measured Mode Coupling*. Robert Bosch, Corporate Research and Development, Germany.

## 1.10. Input Files

The following input files were used for this problem:

- `linear_non_prestressed.dat` -- Linear non-prestressed modal solve input file
- `partial_prestressed.dat` -- Partial prestressed modal solve input file
- `full_non_linear.dat` -- Full nonlinear prestressed modal solve input file
- `linear_non_prestressed_par.dat` -- Parametric studies with increasing coefficient of friction
- `disc_pad_model.cdb` -- Common database file used for the linear non-prestressed modal analysis, the partial prestressed modal analysis, and the full nonlinear prestressed modal analysis (called by the `linear_non_prestressed.dat`, `partial_prestressed.dat`, `full_non_linear.dat` and `linear_non_prestressed_par.dat` files, respectively).

The files are available in the `td-1` folder. See [Obtaining the Input Files \(p. xxxv\)](#) for more information.



---

## Chapter 2: Nonlinear Analysis of a 2-D Hyperelastic Seal Using Rezoning

---

This example problem is a nonlinear analysis of a 2-D hyperelastic seal assembly using [rezoning](#) via the [element-splitting method](#). The problem shows how multiple vertical rezoning steps can be used to ensure convergence and completion of an analysis.

Topics related to this example problem follow:

- [2.1. Introduction](#)
- [2.2. Problem Description](#)
- [2.3. Modeling](#)
- [2.4. Material Properties](#)
- [2.5. Boundary Conditions and Loading](#)
- [2.6. Analysis and Solution Controls](#)
- [2.7. Results and Discussion](#)
- [2.8. Recommendations](#)
- [2.9. References](#)
- [2.10. Input Files](#)

### 2.1. Introduction

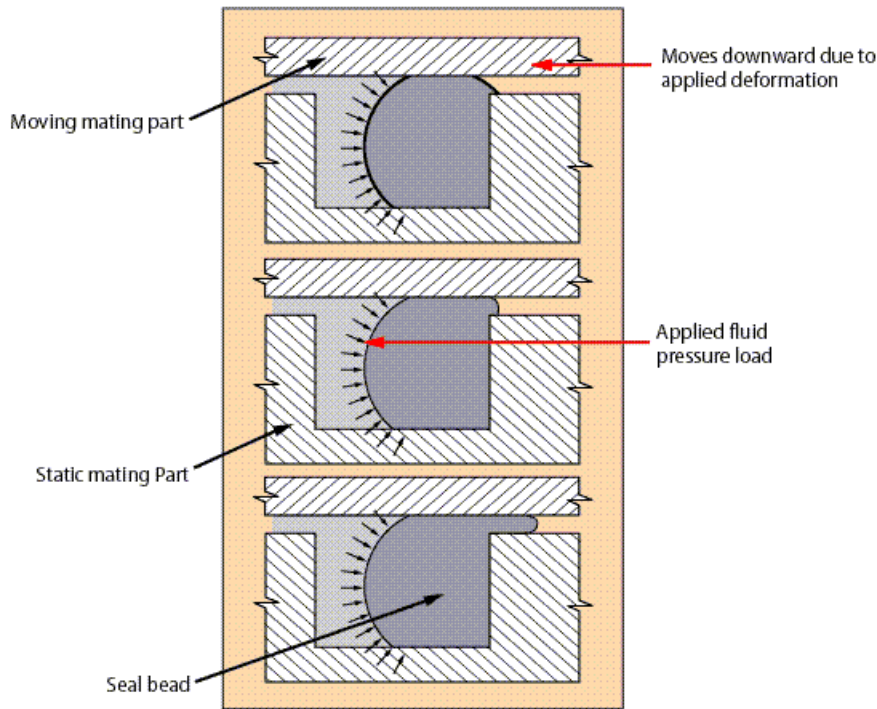
Seals create a mating region between two connecting parts so that the complete assembly can transfer forces and motion without separation. For typical seals, the seal material must:

- Conform to all irregularities of the mating surface and prevent any fluid passage or leakage
- Adapt to the clearance gap changes in the gland in response to loads
- Resist extrusion (caused by shear forces) due to pressure differential between the pressured and nonpressured sides of the seal.

The most common sealing applications are rotating-shaft sealing, elastomeric compressive sealing, and flange sealing. Sealing applications can be classified into two types: static and dynamic sealing. This problem focuses on a static elastomeric sealing application modeled as a 2-D nonlinear finite-element problem.

Static elastomeric seals are characterized by a fixed mating surface, a moving mating surface, and the *bead* (seal material). The bead is typically compressed between the mating surfaces, providing a fluid-tight interface between them, as shown:

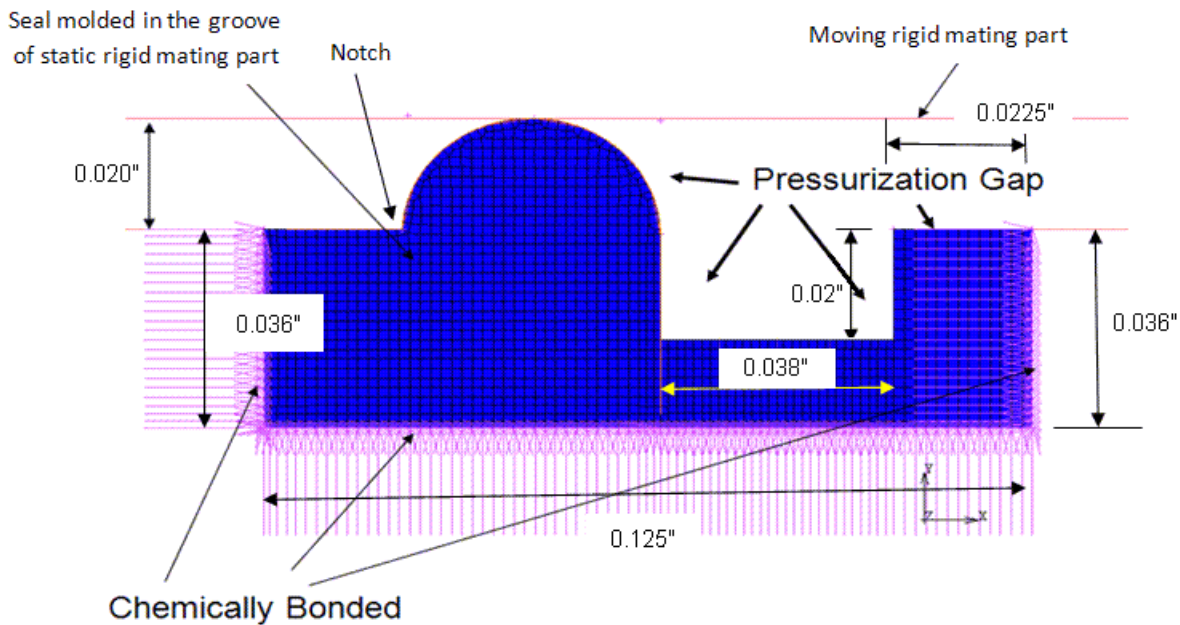
**Figure 2.1: Schematic of a Static Elastomeric Seal Assembly**



## 2.2. Problem Description

The following static elastomeric seal assembly is considered for analysis:

**Figure 2.2: Schematic of Finite-Element Static Elastomeric Seal Assembly with Dimensions**



### 2.2.1. Understanding Requirements and Physical Behaviors

The following requirements and physical behaviors are considered in the finite-element model and solution procedure for this problem:

- **The coefficient of friction (between the bead and the mating surface) is not critical for static seals.**

The coefficient is therefore not modeled here.

- **A fluid pressure of 4000 psi is applied.**

The pressure improves seal integrity, but can also create extrusions of the bead. The extrusions are due to shear stresses (caused by differential axial pressure created by the fluid, as an extrusion gap is provided).

- **As fluid pressure increases, sealing capacity improves but bead extrusion can occur.**

The fluid pressure on the seal surfaces tends to compress the seal axially, forcing the deformed bead further into the gland thus improving contact. As the fluid pressure increases, the seal's internal shear stresses also increase slowly, driving the seal material into the extrusion gap.

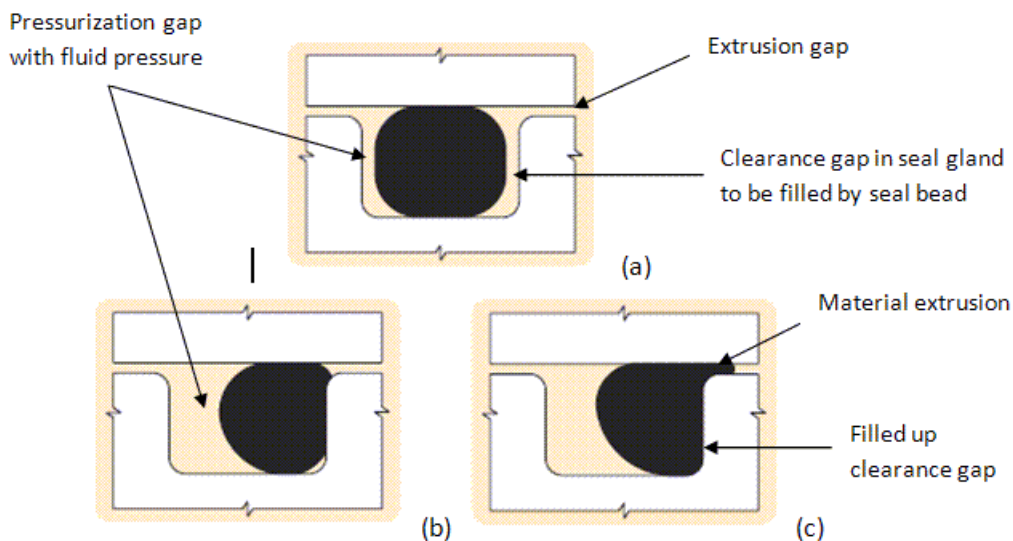
The degree and severity of the extrusion depends on the operating pressures, operating temperatures, geometry of the clearance gap, and seal shape and material.

- **It is of critical importance for the model to predict any bead extrusion.**

This type of extrusion typically causes nibbling damage [1] to the seal, caused by large tensile stresses close to the free surface of the extruded material.

The following figure illustrates the progression of seal deformation, showing the seal gland being filled and the corresponding bead extrusion as fluid pressure is applied:

**Figure 2.3: Progression of Seal Deformation**



### 2.2.2. Using Rezoning to Repair Mesh Distortions

The action of the seal assembly and functional loads on the seal can cause large deformations and strains, in turn causing severe mesh distortions and leading to convergence failure in the nonlinear analysis. In such situations, rezoning can repair the mesh, map results from the old (distorted) mesh to the new mesh, and allow the analysis to continue.

Convergence failure caused by [material or geometric instability](#) cannot be remedied by rezoning.

### **2.2.2.1. Horizontal vs. Vertical Rezoning**

Rezoning can occur on the entire domain or on specific regions within the domain.

If one or more regions are selected for rezoning *at the same time* during the analysis, the process is called *horizontal* rezoning.

If one or more rezoning operations are performed *at different times* during the analysis, the process is called *vertical* rezoning.

### **2.2.2.2. Understanding the Rezoning Process**

Following are the general steps in the [rezoning process](#):

1. Within a given load step, [select the substep](#) at which rezoning should be initiated.
2. Select the region(s) to be rezoned.
3. [Remesh](#) the selected region(s), replacing the old (distorted) mesh with a new mesh.

After remeshing has occurred, boundary conditions and loading from the old mesh are mapped to the new mesh.

4. [Map state variables](#) from the old mesh to the new mesh.

This step establishes equilibrium in the new mesh by [balancing residual forces](#).

5. Continue the analysis with the new mesh via a [restart](#).

### **2.2.2.3. Understanding the Remeshing Phase of the Rezoning Operation**

During the remeshing phase of a rezoning operation, a new mesh is created in the distorted geometry and replaces the old mesh.

Remeshing can occur by reading in a [generated mesh](#) or a [generic third-party mesh](#) (CDB file), or by using [element-splitting refinement](#) of selected regions of the distorted mesh.

In this example, remeshing via the element-splitting method is used because splitting increases the number of degrees of freedom in a given region without changing mesh topology. This remeshing method is especially useful for modeling material flow through confined cavities (the primary physical behavior of hyperelastic seals).

With element splitting, the mesh topology does not change in the interior of the selected regions where elements are simply split evenly. In the transition region between the refined (new mesh) and the old mesh, however, layers of transition of elements are generated, changing the mesh topology in these regions. The transitions can be all quadrilateral or can be composed of degenerate quadrilaterals.

Typically, an all-quadrilateral transition requires more than one element layer to create a compatible mesh between the split and unsplit regions. The degenerate elements can do the same in just one element layer; however, a degenerate element transition is more prone to locking than a quadrilateral element transition zone.



## 2.3. Modeling

This example is modeled as a plane strain problem.

The moving and static mating parts are considered to be rigid. The seal bead is modeled as a hyperelastic material.

The seal is chemically bonded (zero applied displacement) to the static rigid mating part, as shown in [Figure 2.2: Schematic of Finite-Element Static Elastomeric Seal Assembly with Dimensions \(p. 16\)](#).

The pressurization gap is the location for the fluid insertion. The moving rigid mating part moves downward, reducing the 0.02-inch gap to a 0.002-inch gap, at which an extrusion may form.

The notch indicates the region where self-contact in the seal bead is expected to occur.

Three load steps are applied to secure the seal:

1. The top of the seal is compressed first by moving the rigid part downward by 0.018 inches, leaving a small gap of 0.002 inches at the top (TIME = 0 - 1 s). This load step simulates the first phase of the seal assembly where the rigid mating parts come together to form the seal gland which the seal bead must eventually fill.
2. The temperature of the seal is increased from the current room temperature (72° F) to 302° F (TIME = 1 - 2 s).

This load step simulates the thermal loading phase, where the seal is allowed to expand laterally, filling most of the clearance gaps.

3. A uniform pressure of 4000 PSI is applied in the pressurization gap (to all open status contact elements), effectively pressurizing the seal (TIME = 2 - 3 s). This is the pressure exerted by the sealing fluid in the pressurization gap.

This load step simulates the injection of the fluid, which pressurizes the seal laterally. The seal fills all clearance gaps and possibly creates some material extrusion.

The nonlinear sparse solver is used for the solution. A static analysis is required when geometric nonlinearity is present (**NLGEOM,ON**).

### 2.3.1. Specific Modeling Details

The seal bead is modeled by **PLANE182** plane strain (KEYOPT(3) = 2) elements. The elements have full integration with B-Bar formulation (KEYOPT(1) = 0). Mixed u-P formulation (KEYOPT(6) = 1) is specified to counter any chance of volumetric locking (which can occur at high strains).

The contact elements are modeled with **CONTA171** with augmented Lagrangian formulation (KEYOPT(2) = 0). The stiffness updates of the contact elements are done at each iteration, based on the mean stress of the underlying solid element (KEYOPT(10) = 2).

The target elements are modeled with **TARGE169** elements.

The fixed mating part is chemically bonded to the seal bead, as shown in [Figure 2.2: Schematic of Finite-Element Static Elastomeric Seal Assembly with Dimensions \(p. 16\)](#). The bonding is modeled by constraining the displacements on the seal bead in the chemically bonded boundaries (**D**).

The seal bead material is modeled using an **Ogden hyperelastic material**, as shown in this input fragment:

```
TB,HYPE, 1, 1, 2, OGDEN
TBTEMP,0.000000
TBDATA, 1, 2.80000e+00, 7.90000e+00, -1.86000e+02,
TBDATA,4,-1.85000e+00, 1.00000e-05, 0.00000e+00,
```

For more information about the seal bead material, see [Material Properties \(p. 21\)](#).

In [load step 3 \(p. 19\)](#), the fluid-penetration loads are applied as a uniform element pressure in the pressurization gap (shown in [Figure 2.2: Schematic of Finite-Element Static Elastomeric Seal Assembly with Dimensions \(p. 16\)](#)). The fluid-penetration loads are applied via the following command sequences:

- Specific contact elements (on which the fluid penetration loads are to be applied) are selected as follows:

```
esel,s,,2166,2186
esel,a,,2248
esel,a,,2250,2261
esel,a,,2556
```

- The default fluid-penetration starting points are selected as follows:

```
sfe,all,2,pres,,-1
```

The third argument is set to 2 to allow the **SFE** command to specify the starting points for the fluid penetration. The argument -1 specifies that none of the selected element nodes can be considered a starting point for fluid penetration.

- The fluid pressure magnitude is specified as follows:

```
sfe,all,1,pres,,4000
```

The command specifies a pressure magnitude of 4000 PSI on face 1 (the default face for 2-D contact elements) of the selected elements.

- The specific fluid-penetration starting points are specified as follows:

```
sfe,2186,2,pres,,1
sfe,2248,2,pres,,1
sfe,2556,2,pres,,1
```

The input specifies that the nodes of the contact elements 2186, 2248, and 2556 are starting points, as they are initially exposed to the fluid. Also, depending on the contact status (open or closed), the node can either be a fluid penetrating point (for “open” contact) or can no longer be a starting point (if contact closes).

### 2.3.1.1. The Rezoning Process

The manual [rezoning process](#) occurs as follows:

```
/clear,nostart      ! clear environment
/file,base          ! load the database named 'base'
/solu              ! enter solution processor
rezone>manual,2,10  ! start rezoning at load step 2
remesh,start       ! start the remeshing

! select a group of elements which need to be refined by
! splitting

ESEL,S,ELEM,,6169   ! elements 6169,6175,6182 and 6185 are
ESEL,A,ELEM,,6175   ! are selected. They may be contiguous
ESEL,A,ELEM,,6182   ! or isolated from each other
ESEL,A,ELEM,,6185

remesh,split       ! split the selected elements and
                  ! automatically create quad transitions
```

```

remesh,finish      ! automatically generate BC, loads, temp
                  ! etc on new mesh and generate new contact
                  ! or target elements on new mesh as needed

mapsolve,500, pause ! mapping of state variables and
                  ! residual balancing

finish

```

In this case, the load step selected to start rezoning is 2. [Element-splitting refinement](#) is used to increase the number of degrees of freedom in the selected region to enhance flexibility. All-quadrilateral transition elements are generated to connect the new refined mesh to the old unrefined mesh.

After every rezoning, a [multiframe restart](#) is necessary. Issuing a (**RESCONTROL**,DEFINE,ALL,1) command ensures that restart files are written at all substeps, which potentially enables rezoning at any substep. Issuing an (**OUTRES**,ALL,ALL) command ensures that the results file is written at every substep; the results at each substep are viewable from within the GUI to determine where the rezoning needs to be done.

Vertical rezoning is used for this problem. Three nested rezonings occur at:

- Load step 1, substep 20 (TIME = 0.4 s),
- Load step 1, substep 50 (TIME = 0.8996 s), and
- Load step 2, substep 10 (TIME = 1.145 s).

## 2.4. Material Properties

The seal bead material is modeled as a three-parameter [Ogden hyperelastic material](#).

Material properties are provided for one temperature data point. The material properties are assumed not to change with temperature.

For details about this material model's strain-energy function, see [Ogden Hyperelastic Material Constants](#) in the [Material Reference](#).

## 2.5. Boundary Conditions and Loading

Contact pressures developed in the mating surface-bead interface provide seal integrity. From the finite-element modeling perspective, the bead is usually modeled with a hyperelastic material and the mating surfaces are assumed to be rigid.

Loads are generally applied as pressure/displacement on the moving mating surface, as temperature on the seal bead, and sometimes as fluid pressure in the seal cavity. The loads cause progressive deformation, as seen in [Figure 2.1: Schematic of a Static Elastomeric Seal Assembly \(p. 16\)](#).

Although a moving mating part exists, the analysis is considered to be quasi-static; that is, velocity of the moving mating part is very small, constant, and does not change direction.

## 2.6. Analysis and Solution Controls

The following topics concerning the analysis and solution controls for this problem are available:

[2.6.1. Common Solution Controls](#)

[2.6.2. Solution Controls for Each Load Step](#)

[2.6.3. Rezoning Considerations](#)

## 2.6.1. Common Solution Controls

The common solution parameters used in all load steps of the analysis are as follows:

```
antype,static           ! Static / quasi-static analysis type
rescontrol,define,all,1 ! Restart files available at every substep
nlgeom,on              ! Allow large deformation
eqslv,sparse           ! Direct sparse solver
outres,all,all         ! Write out RST files for each substep
```

## 2.6.2. Solution Controls for Each Load Step

For each of the three load steps (p. 19), specific solution controls are added, as follows:

- **Load Step 1:**

```
time,1.0               ! analysis up to 1.0s
nsubst,50,2000,50     ! initial, maximum and minimum number of
                       ! substeps
```

The corresponding time step sizes are 0.02s, 5.0E-04s, and 0.02s, respectively. To ensure solution accuracy, the smallest time step is given.

- **Load Step 2:**

```
time,2.0               ! analysis upto 2.0s
deltim, 0.01, 1.e-05, 0.1 ! initial, minimum and maximum time step
```

- **Load Step 3:**

```
time,3.0               ! analysis upto 3.0s
deltim, 0.001, 1.e-05, 0.01 ! initial, minimum and maximum timestep
```

To minimize the possibility of convergence issues, the initial time step for load step 3 is the smallest. Convergence with fluid penetration loads is more difficult to achieve because, depending on the contact status, loaded contact surfaces may become unloaded and reloaded during solution.

## 2.6.3. Rezoning Considerations

The rezoning process itself has several steps which must be performed for a successful analysis. The most important steps relate to remeshing using the element-splitting method, as follows:

- 2.6.3.1. Step 1. Select the Optimal Substep for Rezoning
- 2.6.3.2. Step 2. Select a Region and Remesh
- 2.6.3.3. Step 3. Map Quantities from Old to New Mesh and Rebalance Residuals
- 2.6.3.4. Step 4. Perform the Multiframe Restart

### 2.6.3.1. Step 1. Select the Optimal Substep for Rezoning

Determining the specific substep at which rezoning should be performed is a nontrivial, problem-dependent task.

Remeshing is usually necessary when the mesh becomes too distorted (when element angles approach 180 degrees). If old elements are too distorted at the rezoning step, however, mapping variables from the old mesh to a new mesh can be difficult. At extreme distortions, it is not possible to map new nodes at the corners of old elements accurately, affecting boundary condition mapping. This concern is critical in element splitting because old nodes are shared in new elements generated by splitting.

Element splitting does not change the mesh topology in the interior of the rezoned domain. The element angles before and after splitting remain the same, and the element aspect ratios remain the same; therefore, a badly shaped element cannot be improved by splitting alone. For best results, element splitting should occur a few substeps *before* the elements angles approach 180 degrees.

Mapping on state variables and residual equilibration can be difficult if the remeshing is done in the presence of very high stress/strain gradients. Remeshing should therefore be attempted at substeps where the gradients are not so high.

In general, the earlier remeshing is done in a load step, the more difficult it becomes for the problem to converge during restart. (It is also difficult to determine the correct rezoning region in the beginning of a loadstep, especially if it is the first loadstep.) Conversely, if remeshing occurs too late, the mapping may not succeed because the base mesh is already too distorted or large stress/strain gradients have developed.

For best results, attempt the first remeshing at a substep (S1) toward the later stages of a load step if that substep is not very close to divergence and where reasonable regions in the problem are clear. If successful, the solution can proceed; otherwise, attempt another remeshing at a different substep (S0) *prior* to S1, which reduces the element sizes by the time the remeshing at S1 can occur. This size reduction smooths out possible gradients and creates less element distortion by the time the solution reaches S1.

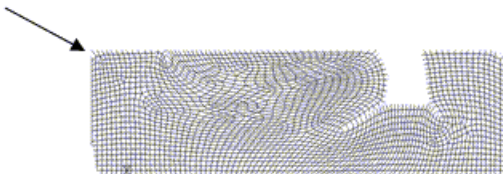
In this problem, the first rezoning is attempted first at load step 1, substep 20 (TIME = 0.4 s), which corresponds to substep S0. The next rezoning is done at load step 1, substep 50 (TIME = 0.8996 s) which corresponds to substep S1. If rezoning at S1 is attempted on its own, convergence does not improve (because at 0.8996 seconds, the seal bead already deforms to a large degree and creates mapping difficulties).

The focus of rezoning should be to perform the minimum number of remeshing steps possible while ensuring that the simulation results and the model mirror the actual physical problem behavior as closely as possible. It is possible that a nonlinear problem may converge without rezoning; however, the results may not be indicative of true physical behavior. For example, this seal problem was run without rezoning, producing the following results:

**Figure 2.4: Deformed Mesh Plot of Seal After Third Load Step Without Rezoning**

```
DISPLACEMENT
STEP=3
SUB =110
TIME=3
DMX =.025885
```

No extrusion detected



Because an extrusion gap is present and the problem is classified as a medium-to-low pressure seal, the extrusion is expected to occur. Without rezoning, a successful convergence in this case fails to provide a physically meaningful solution, as the mesh size is greater than the extrusion gap and therefore extrusion does not occur.

Using rezoning in the third load step (where fluid pressure is applied) causes convergence difficulties during remapping. Large shear-strain gradients develop near the extrusion due to the pressure differential caused by the fluid pressure. It is therefore necessary that remeshing occur *before* the fluid pressure is applied so that mapping does not occur when large strain gradients are present. To enable material flow in the extrusion gap, however, element sizes near the gap should be sufficiently small by the time the third load step is applied.

For this problem, optimal rezoning substeps occur in load steps 1 and 2. The magnitude of deformation in the seal bead is much larger in load step 1 (where the mating parts move) as opposed to load step 2 (a uniform temperature load). Because most of the deformation occurs in load step 1, remeshing is more critical there than in load step 2 (and two vertical rezonings in load step 1 are justified).

Load step 2 is a temperature load which expands the seal axially, thereby filling up most of the clearance gaps. The thermal expansion also contributes to the seal bead material being pushed through the extrusion gap. At least one local rezoning is required (around the extrusion) at load step 2 so that the incipient extrusion behavior can be modeled, and so the third and final rezoning is done in load step 2, substep 10 (TIME = 1.145s).

### 2.6.3.2. Step 2. Select a Region and Remesh

When a substep at which to remesh is identified, select the region(s) to be remeshed. The following remeshing topics are available:

- 2.6.3.2.1. Selecting Elements for Splitting
- 2.6.3.2.2. Methods for Remeshing Using Element Splitting
- 2.6.3.2.3. Using Nesting to Control Split Element Size

#### 2.6.3.2.1. Selecting Elements for Splitting

The element-selection process for splitting can be done in any of the following ways:

- Manually (**ESEL**)
- By generating element-based components (**CM**) which can then be selected (**CMSEL**)
- By graphical picking in the GUI.

Only solid elements are candidates for splitting. Contact and target elements are ignored.

If no elements are selected prior to mesh splitting (**REMESH,SPLIT**), *all* solid elements in the model are split and no transition elements are created.

Existing contact and target elements attached to base solid elements which have been split, and those which have been replaced by smaller transition elements, are automatically deleted.

#### 2.6.3.2.2. Methods for Remeshing Using Element Splitting

Two methods for remeshing using element splitting are available:

- Create all quad transitions between split and unsplit elements:

```
REMESH,SPLIT
```

or

```
REMESH,SPLIT,,,TRAN,QUAD
```

- Create degenerate (triangular) transitions between split and unsplit elements:

```
REMESH,SPLIT,,,TRAN,DEGE
```

An all-quad transition is usually more than a single element layer deep. It is topologically difficult to resolve nodal incompatibilities from the split to the unsplit elements in a single-element layer, especially in an unstructured quad mesh.

Using degenerate transitions between the split and unsplit elements usually resolves nodal incompatibilities in a single element layer. Triangular elements tend to lock, however.

Provided that the transition elements are not too distorted and do not overlay other transition elements, it is preferable to use an all-quad transition for nonlinear problems. The degenerate transition is useful in cases where the quad transitions become too distorted or where the problem is not bending- or compression-dominated. In this problem, an all-quad transition is used to prevent volumetric locking. With nested splitting schemes, it is possible to prevent the all-quad transition regions from intersecting.

### 2.6.3.2.3. Using Nesting to Control Split Element Size

Relative size control of split elements is of prime importance to remeshing by element splitting.

The splitting operation subdivides a quad element into four quad elements, a triangular element into four triangular elements, and a degenerate element into three quadratic elements. After one cycle of splitting a quad base element, therefore, the split elements are 1/4 the area of the base element.

If  $N$  such splittings occur, the final split elements have an area of  $(1/4)^N$  of that of the base element. If multiple horizontal rezonings overlap or multiple vertical rezonings are done on the same region, it becomes increasingly difficult to generate proper transitions due to the increasing size disparity of the split and unsplit elements.

One method for overcoming the size disparity between split and unsplit elements is to design a nesting scheme for splitting during vertical rezoning. The nesting should allow the  $N$ th remeshing region to be sufficiently larger than the  $(N+1)$ th remeshing so that the transitions between the two regions do not overlap.

Using such nesting schemes, it is possible to design mesh grading from coarse to fine, improving solution performance. In this problem, the nesting scheme allows the remeshed regions in the first, second, and third rezonings to be successively reduced while overlapping, thus creating a good gradation of the mesh.

Nesting schemes can also alleviate the effect of large tensile strains on element splitting strategies, where aspect ratios of split elements can be adversely affected.

### 2.6.3.3. Step 3. Map Quantities from Old to New Mesh and Rebalance Residuals

After remeshing (**REMESH,FINI**), corresponding new contact and target elements which respect the topology of the split solid elements are generated automatically for the meshed region. Isolated rigid target elements (as done in the modeling of the moving mating part) cannot be remeshed and persist throughout the life cycle of the analysis.

At this stage, it is necessary to **map** boundary conditions, loads, and temperatures from the old mesh to the new mesh.

The **MAPSOLVE** command maps the state variables from the old mesh to the new mesh and balances the residuals by modifying the displaced state of the new mesh. The presence of large stress or strain gradients in the old mesh may cause nonconvergence of the residuals in the new mesh. View the result plot to determine if the mesh substep can be split depending on the presence of stress/strain gradients.

Convergence problems during mapping can also occur if a very large size difference exists between the elements of the old and new meshes. Regions are allowed to overlap during horizontal splitting operations, so it is possible to generate an arbitrarily small element size if many such regions overlap (given that the new element area after N such overlapped horizontal splitting operations is  $(1/4)^N$  of the old element size). [Nesting \(p. 25\)](#) the remeshed regions can alleviate this problem.

In most cases, convergence difficulties during mapping also indicate convergence difficulties during the analysis restart. It is therefore good practice to remesh a few substeps earlier (if possible) if **MAP-SOLVE** requires a large number of bisections to converge.

#### **The Degree of Element Deformation Affects Mapping**

For contact-element generation and remapping, the program attempts to detect a new node (of a split element) in an old element. Because element splitting retains the nodes of the old element in the new elements, the algorithm often involves detecting a new node at the corner of an old element. Element splitting also retains the element angular values, so for badly skewed elements, it is difficult to map a corner node of a new element to the corresponding parent element. This mapping difficulty can cause the creation of new contact elements to fail, and boundary conditions may not be properly generated for the new mesh.

It is therefore important to perform element splitting *before* the element becomes too badly skewed. The guidelines used to select the [substep \(p. 22\)](#) and [region \(p. 24\)](#) for splitting also apply when considering how base element skewness may affect contact- and boundary-condition generation.

#### **2.6.3.4. Step 4. Perform the Multiframe Restart**

After mapping quantities from the old to the new mesh and rebalancing the residual forces, a multiframe restart (**ANTYPE,,RESTART,,CONTINUE**) resumes the nonlinear solution with the new mesh.

It is possible to readjust the number of substeps at this stage to improve convergence.

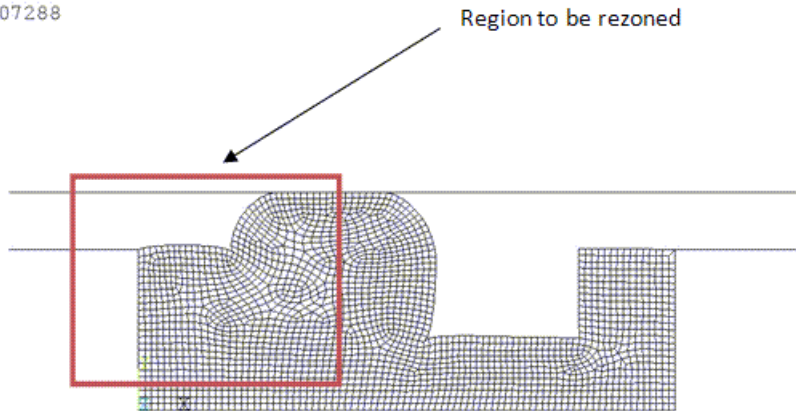
## **2.7. Results and Discussion**

In this problem, element-splitting methodologies are used during rezoning to ensure proper seal assembly behavior, including gland filling and extrusion detection. The following results are obtained at various load steps:



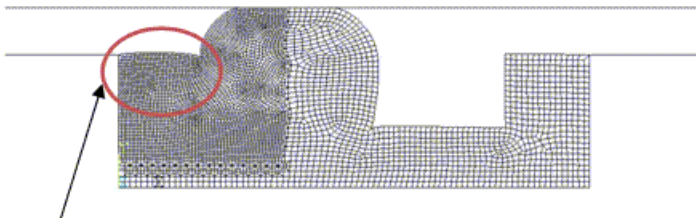
**Figure 2.5: Deformation Profile at Load Step 1 -- Substep 20 (First Rezoning)**

```
DISPLACEMENT
STEP=1
SUB =20
TIME=.4
DMX =.007288
```



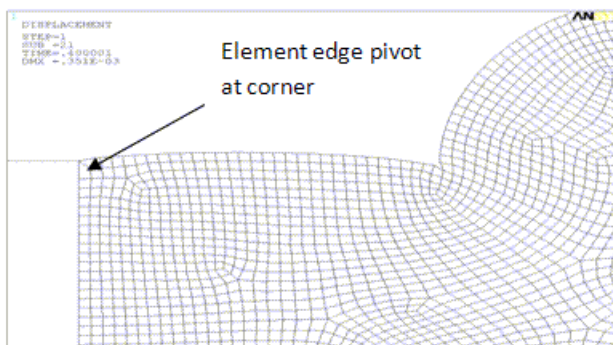
(a) Deformation profile at load step 1, substep 20, time = 0.4 sec, at which the first rezoning occurs

```
DISPLACEMENT
STEP=1
SUB =21
TIME=.400001
DMX =.351E-03
```



See the following  
figure for a zoomed  
view of this region

(b) Selected elements from (a) refined by splitting



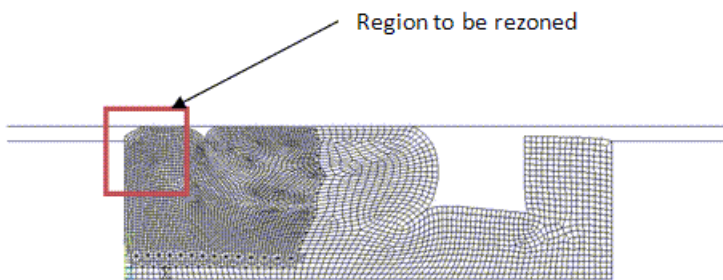
(c) Close-up view of the refined region in (b), showing the element edge pivot at the corner around which the mesh must “rotate”

At the first rezoning, shown by (a) in the figure, the mesh is split around the region where the extrusion is expected to take place. The mesh topology is adjusted so that there is an edge pivot at the corner, around which the material is expected to flow into the extrusion gap (c).

A slightly larger area in (a) is selected for refinement because subsequent rezoning refinements are intended (using nesting). The larger area ensures better self contact in the notch (p. 16) in later stages, as shown:

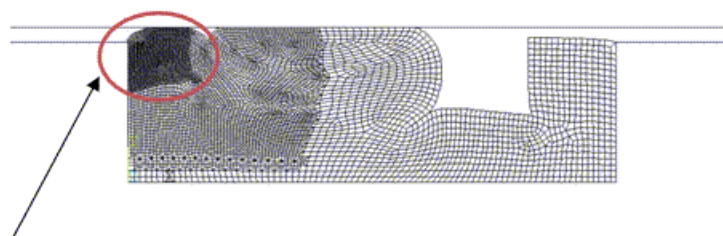
**Figure 2.6: Deformation Profile at Load Step 1 -- Substep 50 (Second Rezoning)**

```
DISPLACEMENT  
STEP=1  
SUB =50  
TIME=.8996  
DMX =.011692
```



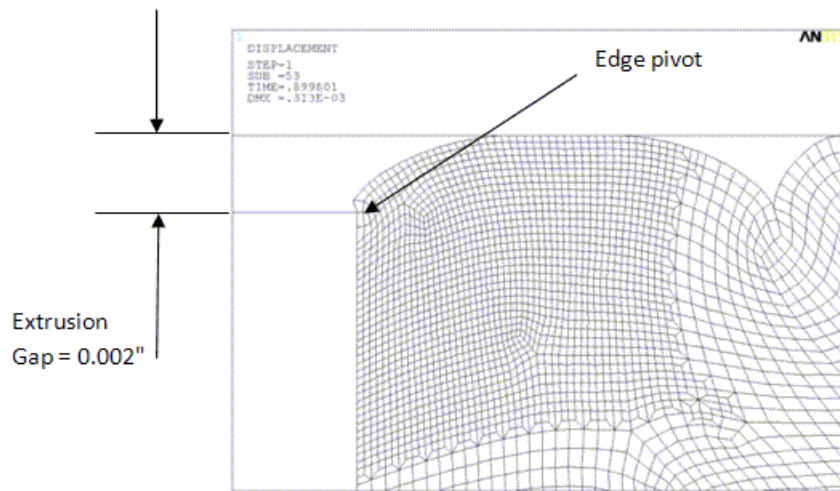
(a) Deformation profile at step 1, substep 50, (time = 0.8996 sec), at which the second rezoning occurs

```
DISPLACEMENT  
STEP=1  
SUB =53  
TIME=.899601  
DMX =.313E-03
```



See the following figure for a zoomed view of this region

(b) Selected elements from (a) refined by splitting



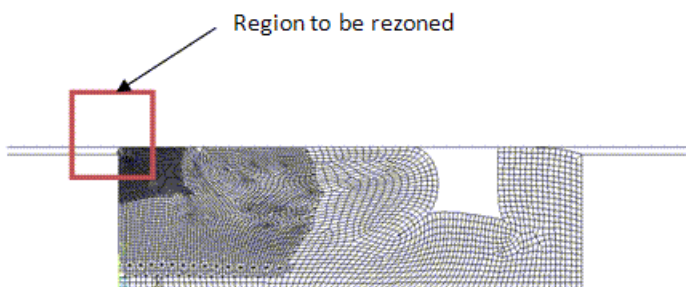
(c) Close-up view of the refined region in (b) showing the start of material flow into the extrusion gap about the pivot

In the absence of the edge pivot at the corner of the extrusion gap (shown by (c) in [Figure 2.5: Deformation Profile at Load Step 1 -- Substep 20 \(First Rezoning\)](#) (p. 27) and [Figure 2.6: Deformation Profile at Load Step 1 -- Substep 50 \(Second Rezoning\)](#) (p. 28) the element at that location would collapse from compression as the seal material begins to flow into the extrusion gap.

The [nested element-splitting scheme](#) (p. 25) gradually increases the number of degrees of freedom in the extrusion region to model the material flow in that region with increasing loads, as shown:

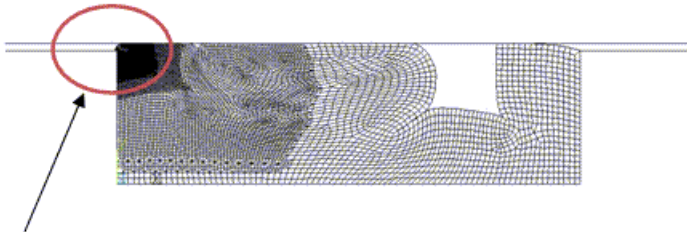
### Figure 2.7: Deformation Profile at Load Step 2 -- Substep 10 (Third Rezoning)

```
DISPLACEMENT
STEP=2
SUB =10
TIME=1.145
DMX =.005812
```



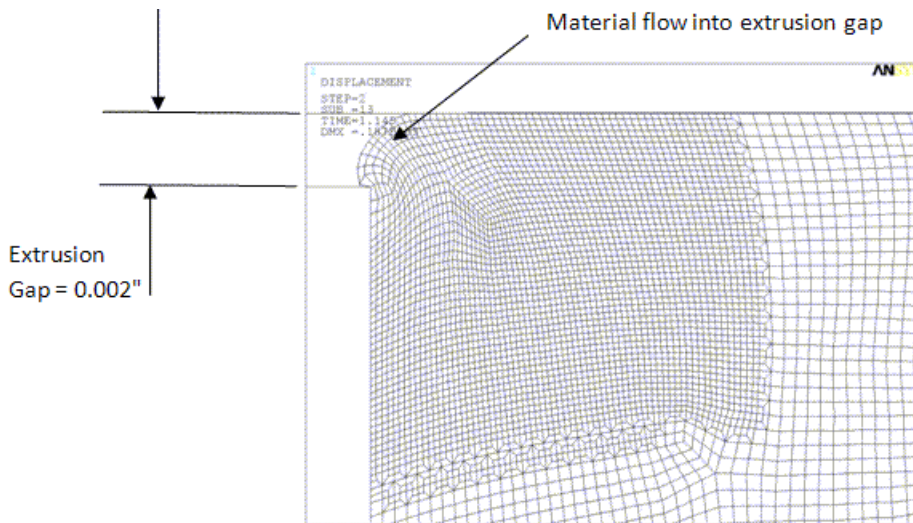
(a) Deformation profile at load step 21, substep 10, time = 1.145 sec, which the third rezoning occurs

```
DISPLACEMENT  
STEP=2  
SUB =13  
TIME=1.145  
DMX =.187E-03
```



See the following figure for a zoomed view of this region

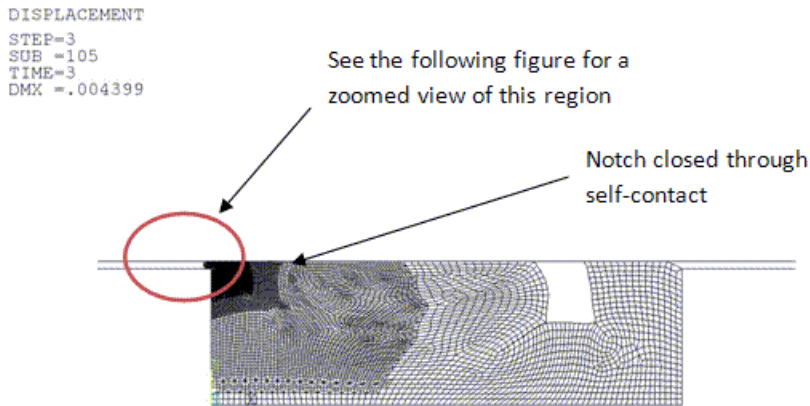
(b) Selected elements from (a) refined by splitting



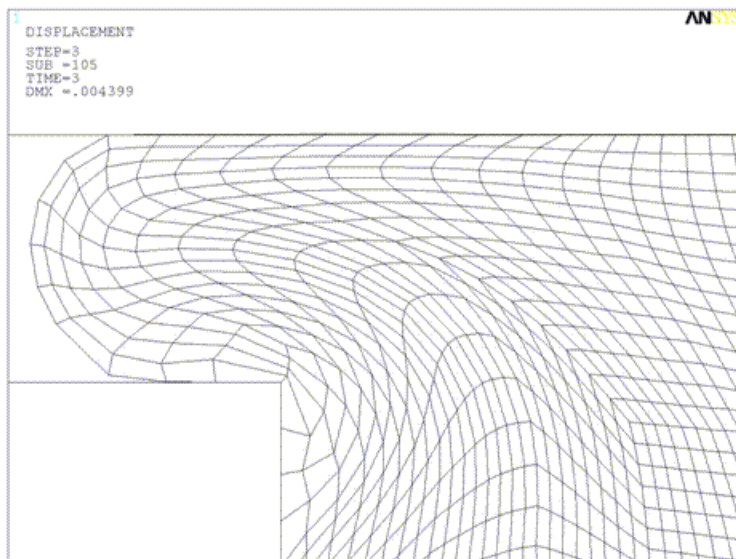
(c) Close-up view of the refined region in (b), showing the material flow into the extrusion gap about the pivot

As shown in (b) and (c), the nested refinement by element splitting can gradually increase the number of degrees of freedom in the region of the extrusion gap and correctly predict the material flow. The nested refinement creates a thin layer of transition elements for each block of split elements and places them far from each other, preventing the formation of badly shaped elements close to this high strain zone (which can lead to premature convergence).

After the three rezoning operations have been performed, the problem converges correctly at the end of the third load step. The following figure shows the final meshes:

**Figure 2.8: Final Mesh (After Third Load Step)**

(a) Final mesh after load step 3, time = 3.0 sec



(b) Close-up view of the refined region in (a), showing the extent of extrusion of the seal bead through the extrusion gap

As shown by (a) and (b), the primary objectives of the seal assembly simulation have been met:

- **The seal bead model is adequate to enable it to establish proper contact and fill the seal gland.**

Subsequent results (shown below) quantify the extent of fluid sealing capacity and the uniformity of the contact pressures.

- **The seal bead model predicts the formation of an extrusion.**

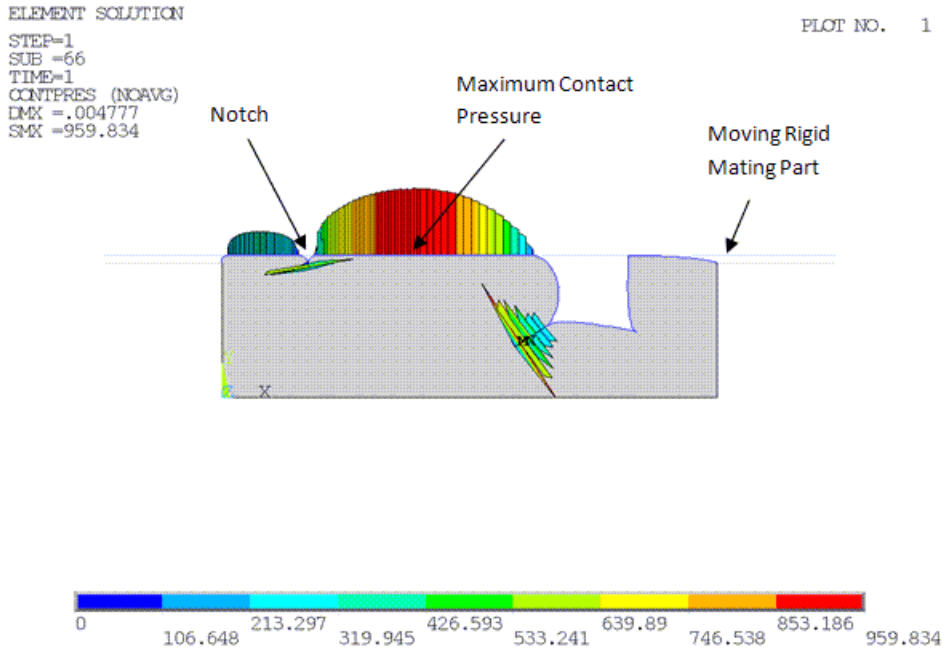
Depending on the seal pressure, the extrusion may or may not damage the material. The addition of extra degrees of freedom (via multiple vertical nested rezonings) allows the material enough flexibility to flow through the extrusion gap.

To determine if the seal assembly analysis predicts the extent of the seal's integrity (that is, the capacity to successfully fill the gland and develop sufficient pressure to prevent fluid leakage), the contact pressure distribution must be evaluated at the three load steps. Because the seal is **molded in the**

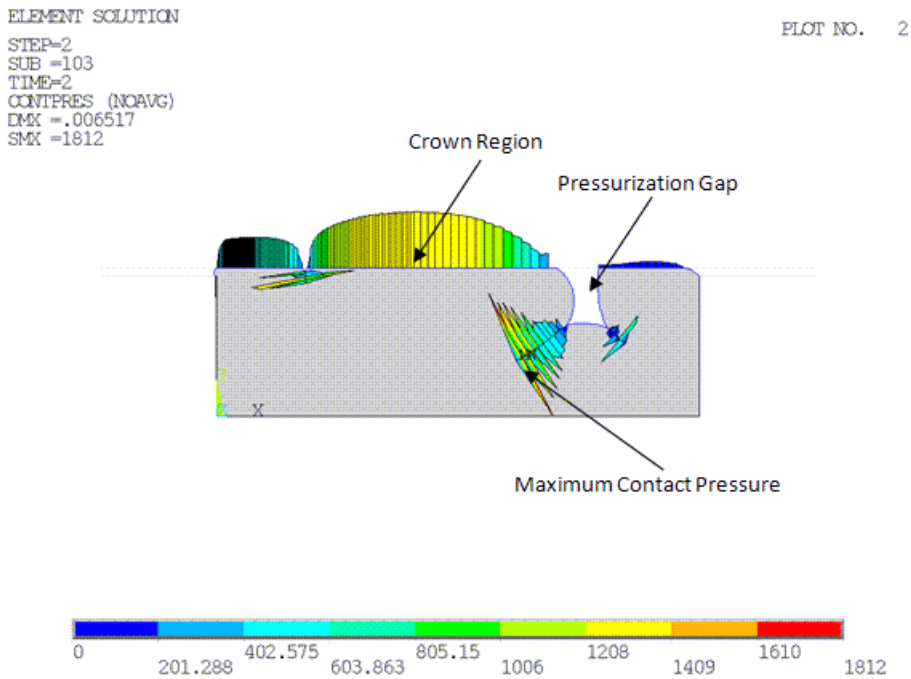
metal groove in the bottom and sides (p. 16), it is necessary to consider only the contact conditions on the top part of the seal.

The following figure shows the contact pressure-distribution trends at the load steps:

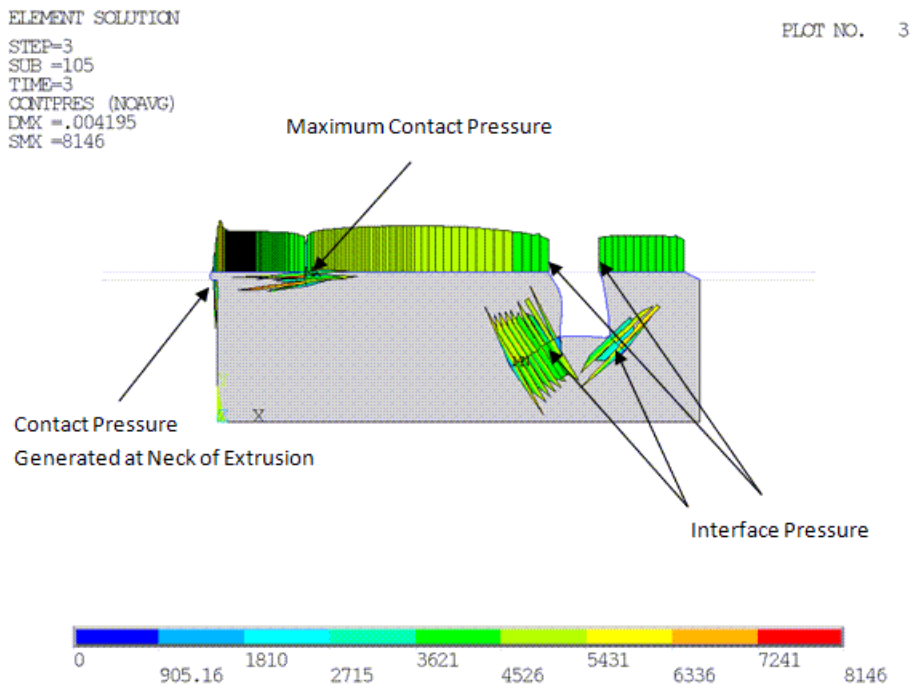
**Figure 2.9: Contact Pressure-Distribution Trends**



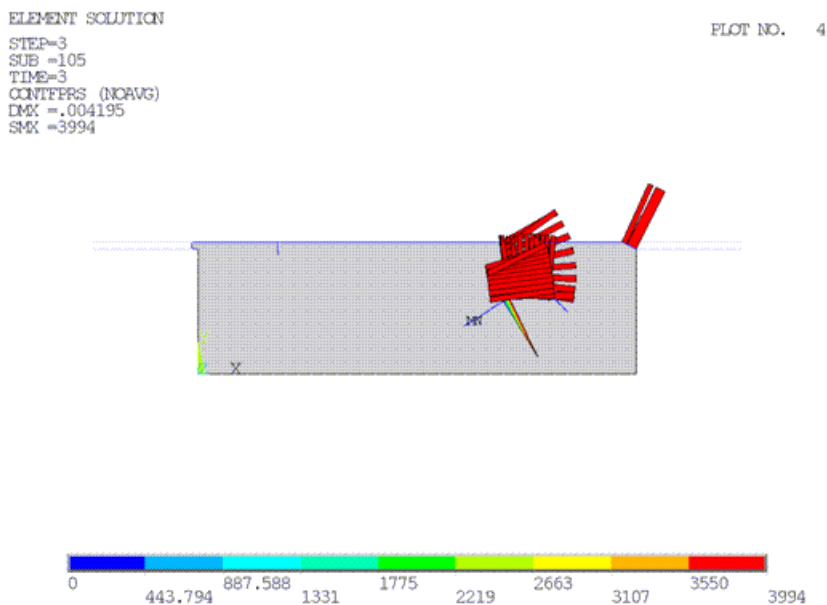
(a) Contact pressure distribution after load step 1



(b) Contact pressure distribution after load step 2



(c) Contact pressure distribution after load step 3



(d) Fluid pressure distribution after load step 3

As shown by (a), at the end of load step 1 (where the moving rigid mating part descends by 0.018 inches), the maximum contact pressure of 960 PSI develops as expected at the region where the maximum geometry change occurs. The incomplete and uneven distribution of the contact pressure indicates that the seal assembly forces are not yet activated. The notch (p. 16) is not completely closed at this stage, providing incomplete sealing capacity.

As shown by (b), at the end of load step 2 (where the seal temperature is raised from 720 F to 3020 F), the maximum contact pressure of 1812 PSI now develops at a self-contact zone bounding the pressur-

ization gap. The reason for this behavior is that load step 2 is a temperature load, where the temperature of the seal bead is raised uniformly by 2300 F. The uniform temperature increase expands the seal into the pressurization gap (and, to a smaller extent, the extrusion gap). As the seal expansion occurs, some pressure releases from the crown region, and contact pressure increases in the self-contact zone, as the material tries to close the pressurization gap.

Compared to load step 1 (shown by a), the contact pressures are better distributed at the rigid flexible interface between the mobile mating part and the seal bead. The notch is closed better than in load step 1, and the self-contact developed in the closed notch is approximately 1400 PSI (about twice that of load step 1). In order to maintain seal integrity in case the rigid mating parts move during operation, it is essential that the self-contact pressures in the notch are high.

Parts (c) and (d) of the figure show the final contact pressure distribution and the corresponding fluid pressure distribution (in the pressurization gap) at the end of the third load step (fluid pressure in the pressurization gap). The action of the applied fluid pressure is to expand the pressurization gap, which in turn creates an axial (along the X axis) pressure on the seal. The axial pressure causes the maximum contact pressure to develop in the notch, thereby creating better seal integrity. The application of fluid pressure also causes a pressure differential, leading to the extrusion. Some contact pressure is created at the neck of the extrusion (which by design should not rupture the seal material). The interface pressure (as shown in (c)) indicates the contact pressure at the interface of the penetrated fluid and the solid material. The interface pressures range from 4300-4500 PSI; the pressures are greater than the applied fluid pressure of 4000 PSI, implying that the seal will not leak under the present set of loads. Downstream of the interface pressure regions, the contact pressure increases, guaranteeing the fluid-sealing capacity.

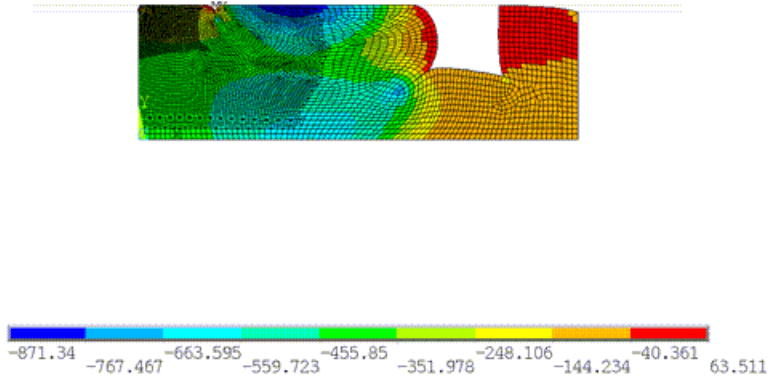
The overall contact pressure profile (at the seal-mating surface boundary) after load step 3 is more uniform than that in load steps 1 or 2 (as shown in (a) and (b)), so the seal integrity is established at this point. Local high-contact pressure peaks can cause surface damage to the seal. The evolution of the contact pressures show that local high-contact pressures have not developed except in the extrusion region.

To ensure seal bead life, the assembly and functional loads on the seal must not create large pressure differentials in the seal bead. Pressure differentials cause large shear stresses which can rupture the material, so be sure to [check the hydrostatic pressure development in the seal \(p. 35\)](#). Unusually high hydrostatic pressures at finite deformation may also indicate volumetric locking in the element.



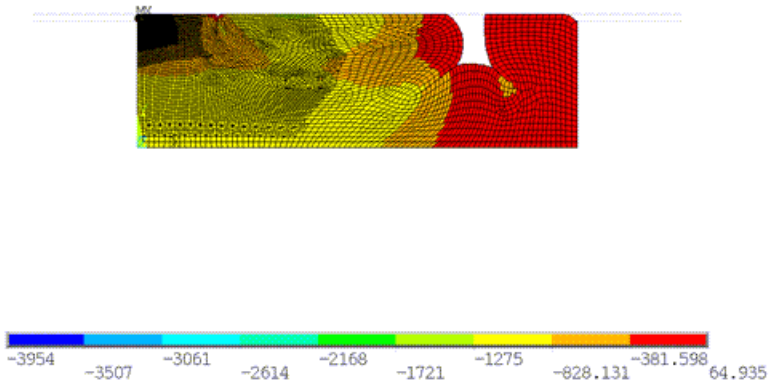
**Figure 2.10: Seal Hydrostatic Pressures**

ELEMENT SOLUTION PLOT NO. 5  
 STEP=1  
 SUB =66  
 TIME=1  
 NLHERE (NCAVG)  
 DMX =.004777  
 SMN =-871.34  
 SMX =63.511



(a) Seal hydrostatic pressure after load step 1

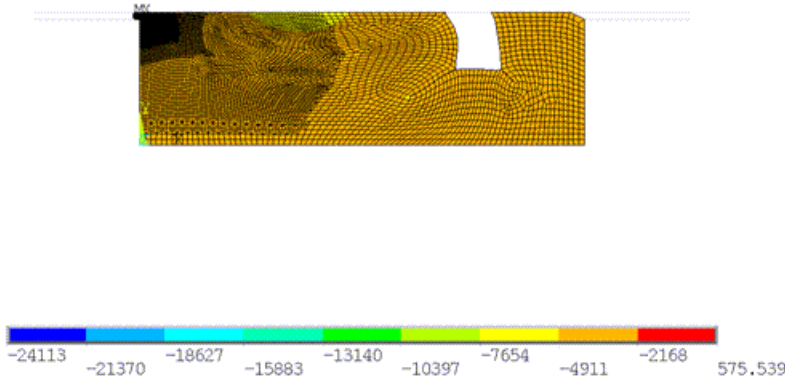
ELEMENT SOLUTION PLOT NO. 7  
 STEP=2  
 SUB =103  
 TIME=2  
 NLHERE (NCAVG)  
 DMX =.006517  
 SMN =-3954  
 SMX =64.935



(b) Seal hydrostatic pressure after load step 2

ELEMENT SOLUTION  
 STEP=3  
 SUB =105  
 TIME=3  
 NLHERE (NOAVG)  
 DMX =.004195  
 SMN =-24113  
 SMX =575.539

PLOT NO. 9

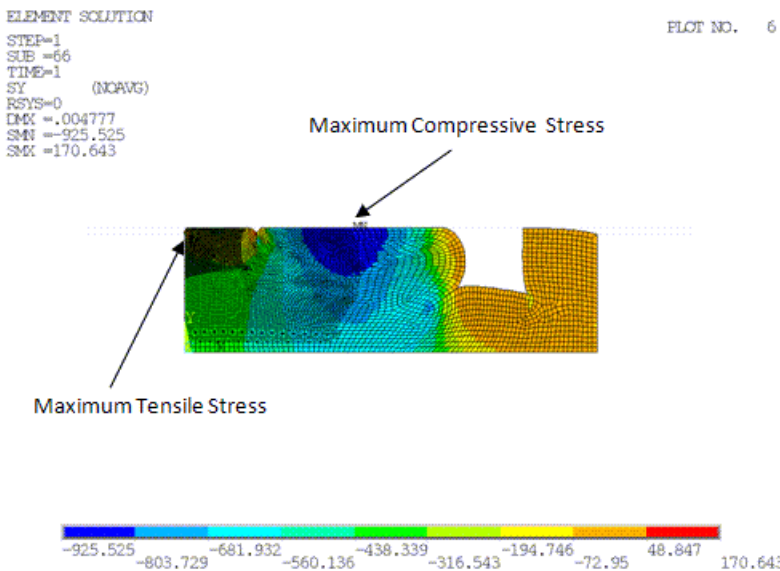


(c) Seal hydrostatic pressure after load step 3

As shown by (a) and (b), pressure differentials exist (especially around the notch and the pressurization gaps), indicating incomplete seal assembly. At the end of load step 3 (c), the addition of fluid pressure causes a nearly uniform pressure in the seal, except for a peak in the vicinity of the extrusion. The peak pressure near the extrusion and the free surface of the seal bead at the extrusion gap actually drives the extrusion and causes shearing strains.

The largest assembly forces in the seal are applied vertically via the rigid mating surfaces. For optimal seal stresses, the  $\sigma_{YY}$  profile inside the seal must be as uniform as possible when all assembly loads have been applied. The following figure shows the  $\sigma_{YY}$  profile of the seal bead under the three load steps, respectively:

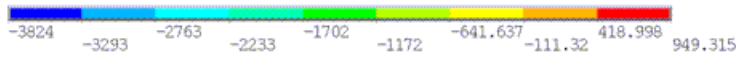
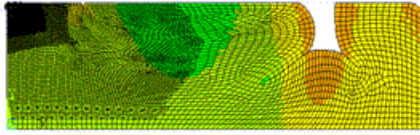
**Figure 2.11: Seal  $\sigma_{YY}$  Profile**



(a)  $\sigma_{YY}$  profile for seal at load step 1

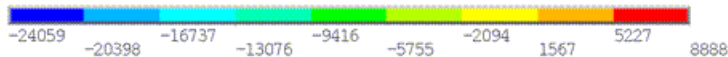
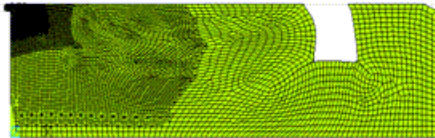
ELEMENT SOLUTION  
 STEP=2  
 SUB =103  
 TIME=2  
 SY (NOAVG)  
 RSYS=0  
 DMX =.006517  
 SMN =-3824  
 SMX =949.315

PLOT NO. 8

(b)  $\sigma_{YY}$  profile for seal at load step 2

ELEMENT SOLUTION  
 STEP=3  
 SUB =105  
 TIME=3  
 SY (NOAVG)  
 RSYS=0  
 DMX =.004195  
 SMN =-24059  
 SMX =8888

PLOT NO. 10

(c)  $\sigma_{YY}$  profile for seal at load step 3

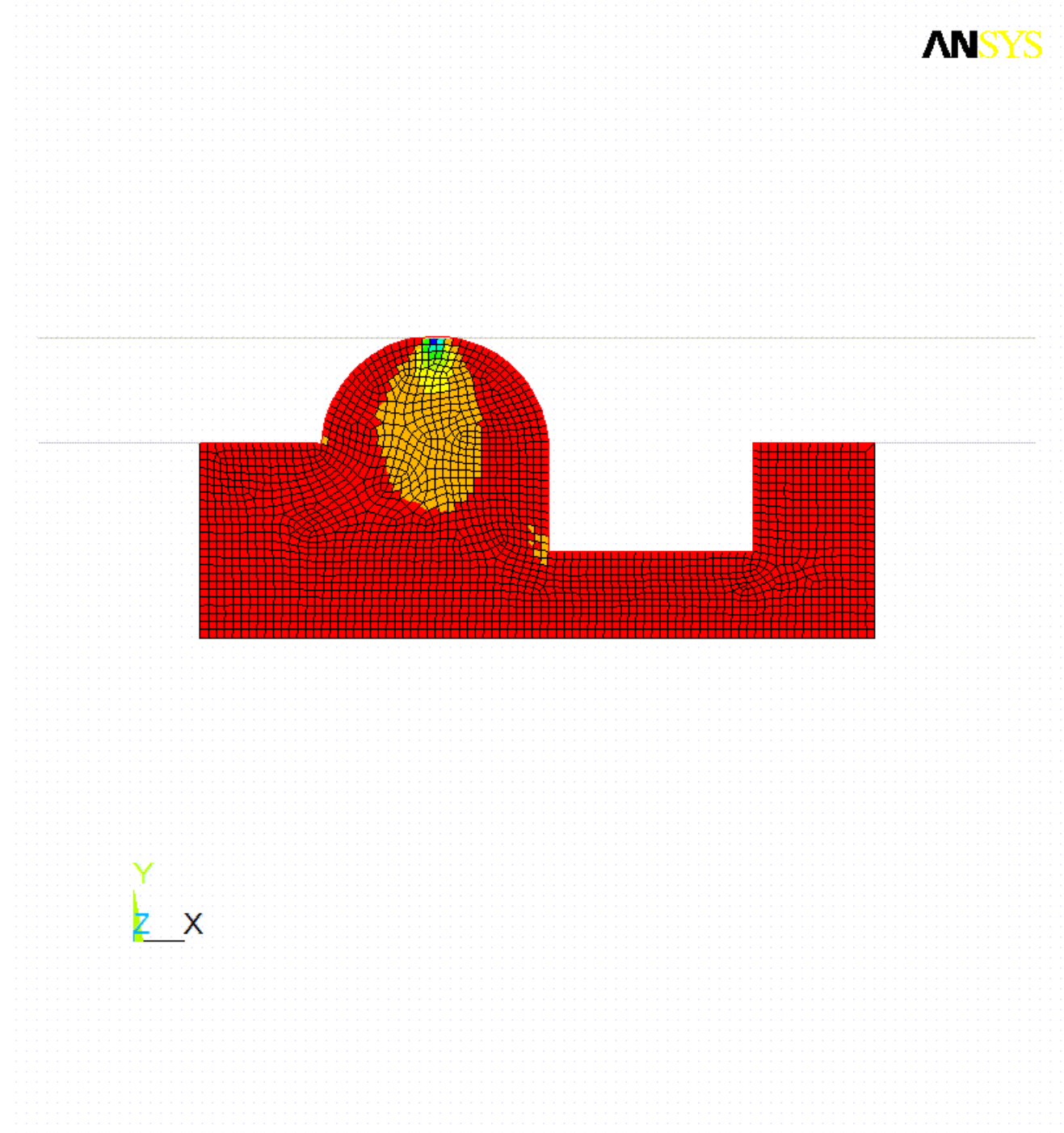
As shown by (a) in the figure, the maximum tensile stress occurs at the extrusion, and the maximum compression occurs at the crown region where maximum geometry change has occurred. The tensile stress occurs because the extrusion gap causes a reentrant corner to be formed at the seal (where stress concentrations may occur).

At the stage shown by (b), the temperature increase tries to expand the seal through the pressurization and the extrusion gaps, thereby moving the maximum compressive stress to a location close to the extrusion.

At (c) in the figure, fluid pressure is applied and the overall stress distribution is nearly uniform, creating near-optimal sealing conditions. Maximum tensile and compressive stresses are localized near the extrusion.

At the end of the third load step, the rigid-flexible contact pressures are near-uniform, preventing fluid leakage. The overall pressure and the  $\sigma_{YY}$  stresses are near-uniform in the seal bead, indicating optimal seal assembly loading.

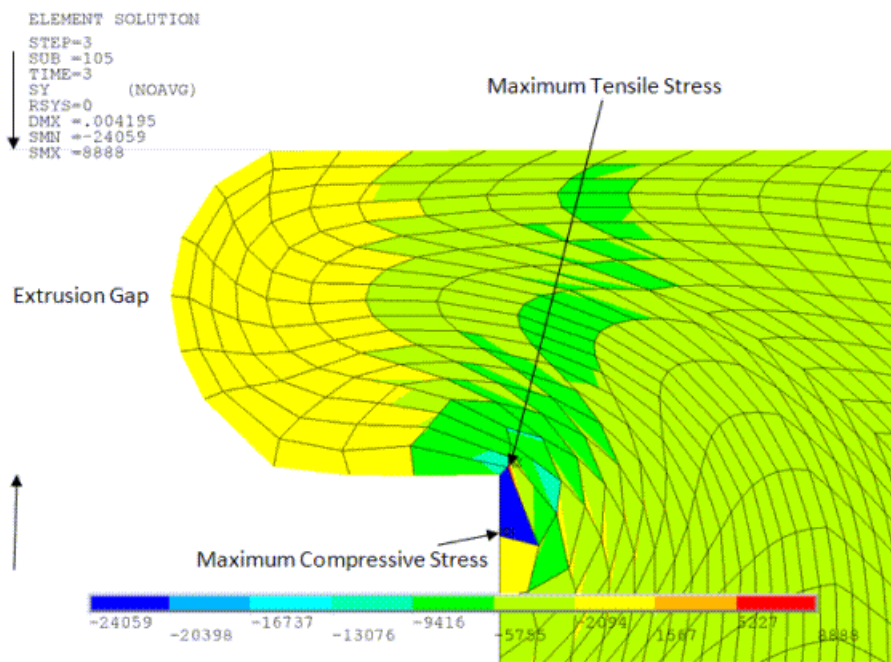
**Figure 2.12: Seal  $\sigma_{YY}$  Plot Animation**



Evidence of shearing-contact pressure spikes due to pressure differentials exists and is localized near the extrusion. This condition has been modeled adequately by the nested step-wise rezoning with element-splitting refinement used in this problem.

The following figure shows the  $\sigma_{YY}$  profile at the extrusion after the third load step:

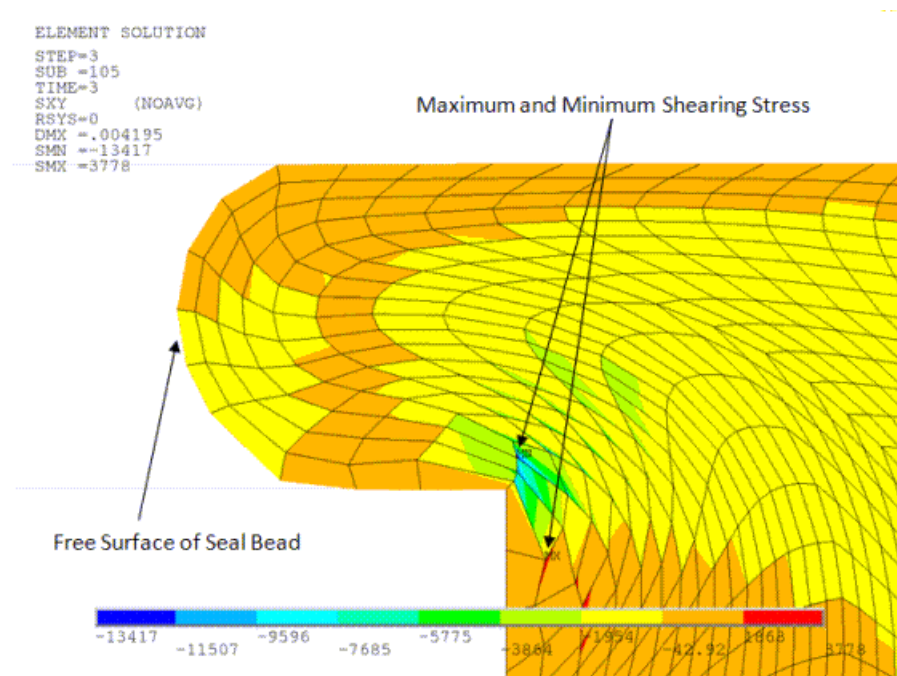
**Figure 2.13: Extrusion  $\sigma_{YY}$  Profile**



The maximum tensile and compressive stress peaks at the end of the third load step are due to the singularity near the reentrant corner. Thus, with reference to (c) in [Figure 2.10: Seal Hydrostatic Pressures](#) (p. 35), the  $\sigma_{YY}$  profile is virtually uniform in the seal bead.

The following figure shows the  $\sigma_{XY}$  profile at the extrusion after the third load step:

**Figure 2.14: Extrusion  $\sigma_{XY}$  Profile**



The maximum and minimum shearing stresses occurring at the location shown are caused by the pressure differential between the free surface of the seal bead and the seal bead itself. The shearing stress occurs as a result of the shearing strain created by the extrusion.

## 2.8. Recommendations

To perform a similar type of analysis, consider the following recommendations:

- **Rezone using element-splitting refinement.**

Rezoning with element splitting is essential for solving this type of problem properly. Extrusion modeling is critical for simulating accurate physical behavior of the seal. A gradual reduction of element size in the vicinity of the extrusion gap is necessary as the material flow into the gap increases over time.

- **Use element edge pivots to facilitate extrusion flow.**

See the edge pivot shown by (c) in [Figure 2.5: Deformation Profile at Load Step 1 -- Substep 20 \(First Rezoning\)](#) (p. 27). The pivot prevents the elements at the reentrant corner from deforming too severely under compression and can, in general, improve convergence. Providing for a pivot in the starting mesh allows it to remain until the end of the analysis, as element splitting does not change mesh topology.

- **Perform rezoning early to minimize convergence issues during mapping.**

Large stress and strain gradients are not easily equilibrated (**MAPSOLVE**) and can cause nonlinear convergence issues. The problem may converge better if rezoning is done early enough when the gradients have a lesser chance of occurring.

Performing rezoning *too* early in the analysis process, however, may be counterproductive as the mesh may not have sufficiently deformed, possibly causing the rezoned mesh itself to deform later

in the analysis. It is also difficult to discern regions likely to benefit from rezoning too early in the analysis.

- **Minimize intersections of transition regions for overlapped meshes.**

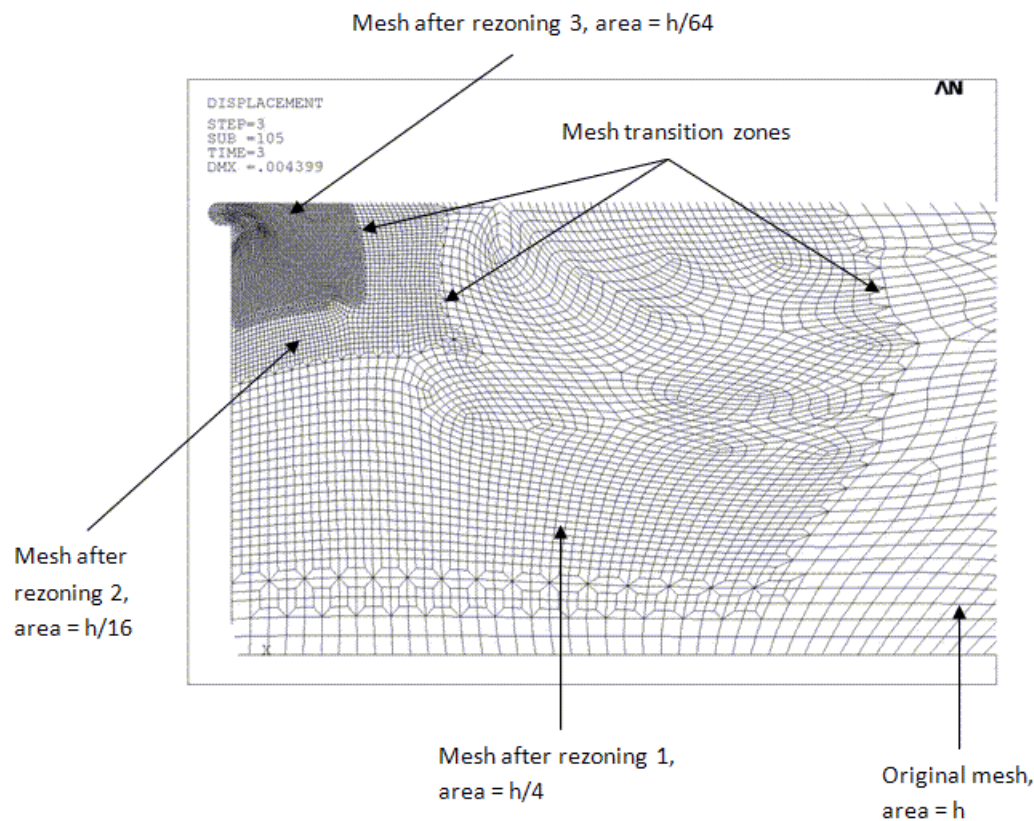
When element-splitting refinement is used for rezoning, ensure that the transition regions of overlapped rezoned meshes do not intersect to a great degree. Excessive intersections can cause badly shaped elements.

- **Use nesting during vertical rezoning.**

If using *vertical* (p. 18) rezoning with element splitting, *nesting the refinements* (p. 25) ensures that transition regions do not overlap, resulting in better element quality. Maintain mesh gradation during the vertical rezoning process to avoid mesh distortion in large strains and to better resolve large stress/strain gradients.

The following figure shows the mesh gradation obtained from nesting the remeshing zones properly:

**Figure 2.15: Mesh Gradation Created with Nested Element Splitting During Vertical Rezoning**



The mesh area reduces from  $h$  to  $h/64$  in three rezoning steps. The nesting scheme ensures that the transition zones do not overlap, and no badly shaped elements occur. Despite the presence of large strains, a remeshing strategy using only element splitting refinement does not create elements with bad aspect ratios, or skew.

#### Rezoning Hints:

- **Remeshing generates contact and target elements automatically.**

Contact elements (rigid-flex contact, self-contact, and flex-flex contact) and target elements (for self-contact and flex-flex contact) for the rezoned solid elements are generated automatically at the end of the remeshing operation (**REMESH,FINISH**).

- **Rezoning around a reentrant corner does not improve convergence.**

Excess rezoning around a reentrant corner does not improve convergence due to the effect of the singularity.

## 2.9. References

The following references are used in this example problem:

1. Muller, H. K., B.S. Nau. *Fluid Sealing Technology, Principles and Applications*. Mechanical engineering: 117. Marcel Dekker. 1998.

ANSYS, Inc. gratefully acknowledges [Parker Hannifin Corporation](#) for providing the initial mesh, material description, loading information, and illustrations for the seal used in this problem.

## 2.10. Input Files

The following files were used in this problem:

- `seal_assembly.dat` -- Parker seal assembly input file.
- `seal_assembly.cdb` -- Common database file for the Parker seal assembly model (called by the `seal_assembly.dat` file).

The files are available in the `td-2` folder. See [Obtaining the Input Files \(p. xxxv\)](#) for more information.



---

## Chapter 3: Fluid-Pressure-Penetration Analysis of a Sealing System

---

This example problem demonstrates a method for examining fluid-pressure-penetration effects on a sealing system. The use of seals is primarily to prevent the transfer of fluid (liquid, solid, or gas) between two or more regions.

The following features and capabilities are highlighted:

- Use of 2-D axisymmetric finite element technology
- Use of 2-D surface-to-surface contact-pair element technology
- Frictional contact
- Fluid-penetration loading
- Ogden hyperelasticity (curve fitting) and multilinear isotropic hardening plasticity
- Nonlinear stabilization

Topics related to this example problem follow:

- 3.1. Introduction
- 3.2. Problem Description
- 3.3. Modeling
- 3.4. Material Properties
- 3.5. Boundary Conditions and Loading
- 3.6. Analysis and Solution Controls
- 3.7. Results and Discussion
- 3.8. Recommendations
- 3.9. Acknowledgments
- 3.10. Input Files

### 3.1. Introduction

The applications of mechanical seals are numerous. The most common sealing systems involve rotating-shaft, elastomer, and flange sealing.

The sealing capability of an elastomeric seal depends upon the contact stresses that develop between the seal and the surfaces with which it comes into contact. Leakage may occur when the pressure differential across the seal exceeds the contact stress.

As a general nonlinear finite element tool, the ANSYS Mechanical APDL program can:

- Predict seal-deformation shapes and stress distributions
- Predict contact stress profiles after installation, in operation, and under various loading conditions
- Account for the effects of fluid pressure penetration between seals and other structural components in the analysis.

All of this information is crucial to understanding how mechanical seal systems are designed, how they operate, and how best to apply them to prevent fluid leakage.

Mechanical APDL's fluid-pressure-penetration capability simulates pressure penetration between contacting surfaces based on the contact status (described in [Applying Fluid Pressure-Penetration Loads](#) in the *Contact Technology Guide*). The fluid penetration pressure load has a path-dependent nature. The penetrating path can propagate and vary, and is determined iteratively.

At the start of each iteration, the program finds all possible starting points which are exposed to the fluid pressure. Among the starting points, the program then finds fluid-penetrating points where the contact status is open or lost, or where the contact pressure is smaller than the user-defined pressure-penetration criterion.

When a contact-detection point has a contact condition of "penetrating," both it and its nearest neighboring nodes are considered to be starting points that are exposed to the fluid pressure.

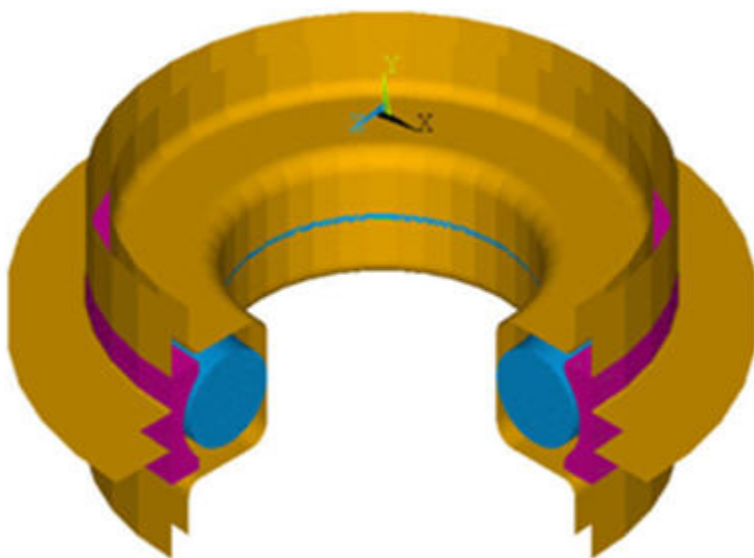
The fluid pressure begins to penetrate into the interface between contact and target surfaces from the starting points. The fluid penetration can be cut off when contact between the surfaces is reestablished or when contact pressure is larger than the fluid-penetration criterion.

### 3.2. Problem Description

An elastomeric o-ring relies on a compressive contact pressure acting on the exterior surface of the o-ring seal to prevent fluid leakage between regions. Successful seal design ensures adequate seal compressive pressure while minimizing the desctructive effects of stress acting on the o-ring as a result of the compression.

The components of the sealing system to be modeled are an elastomer o-ring and a rolled-shape plastic cap. The figure below is a 3-D view of the model with a one-quarter cutout to show the o-ring configuration.

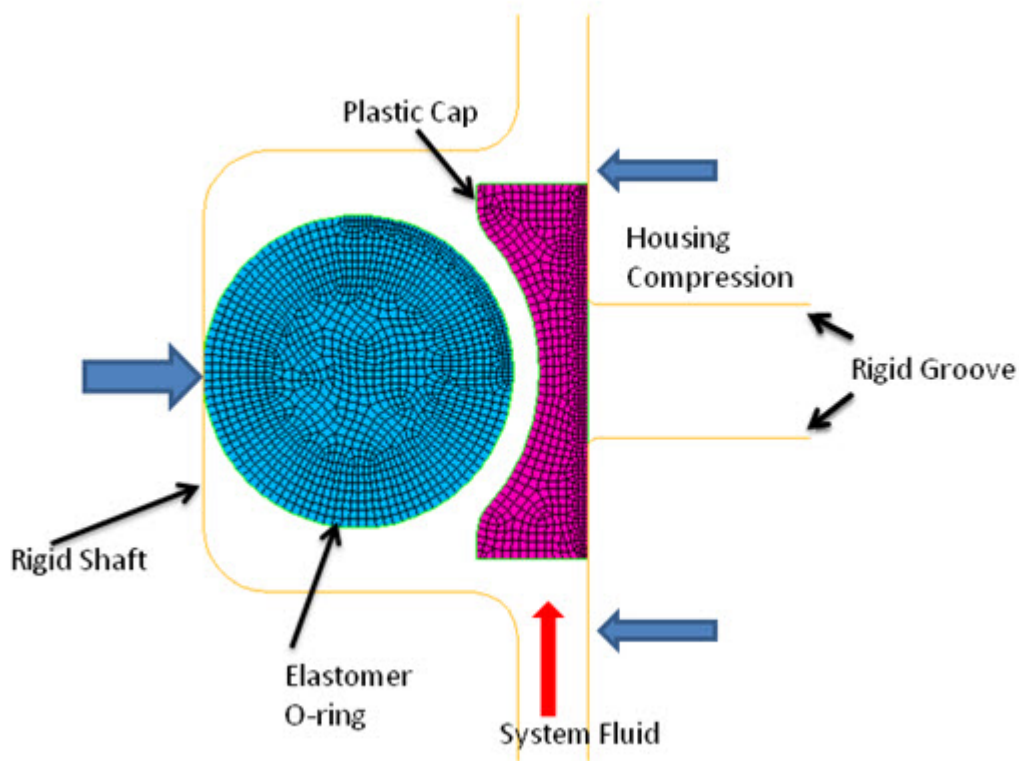
**Figure 3.1: 3-D View of Sealing System**



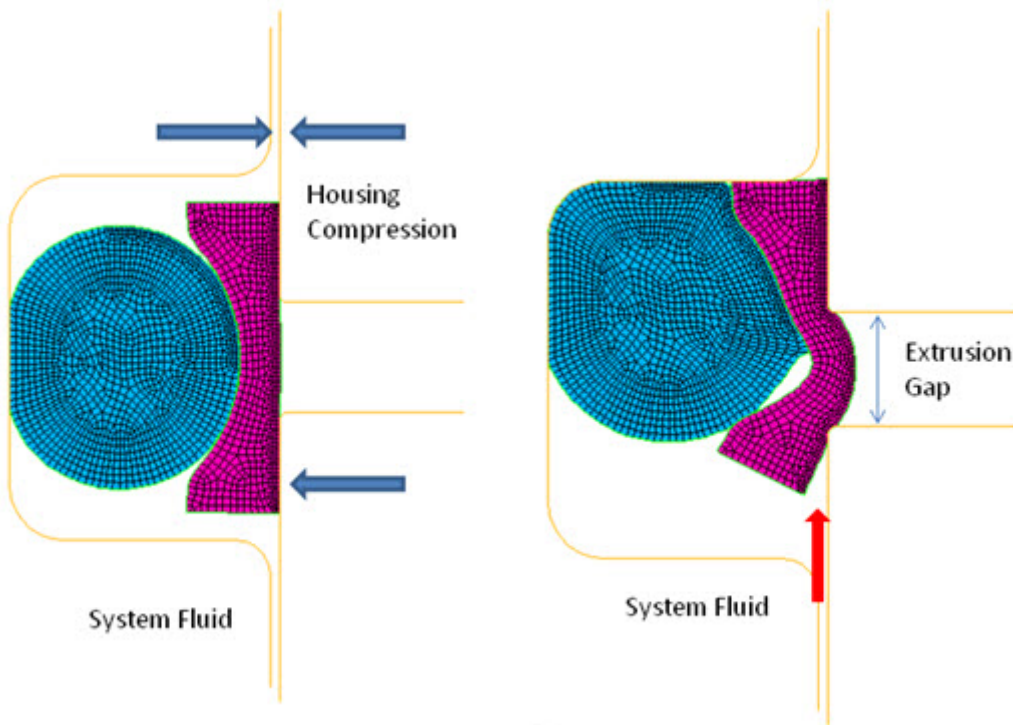
### 3.3. Modeling

Following is an axisymmetric model of the seal components, an elastomer o-ring and a plastic cap. The rigid surface on the right represents the groove, and the left rigid surface represents the shaft.

**Figure 3.2: Sealing System and Finite Element Model**



**(a) Initial Configuration**



**(b) End of Housing Compression**

**(c) End of fluid Penetration Pressure**

The geometric properties of the model are as follows:

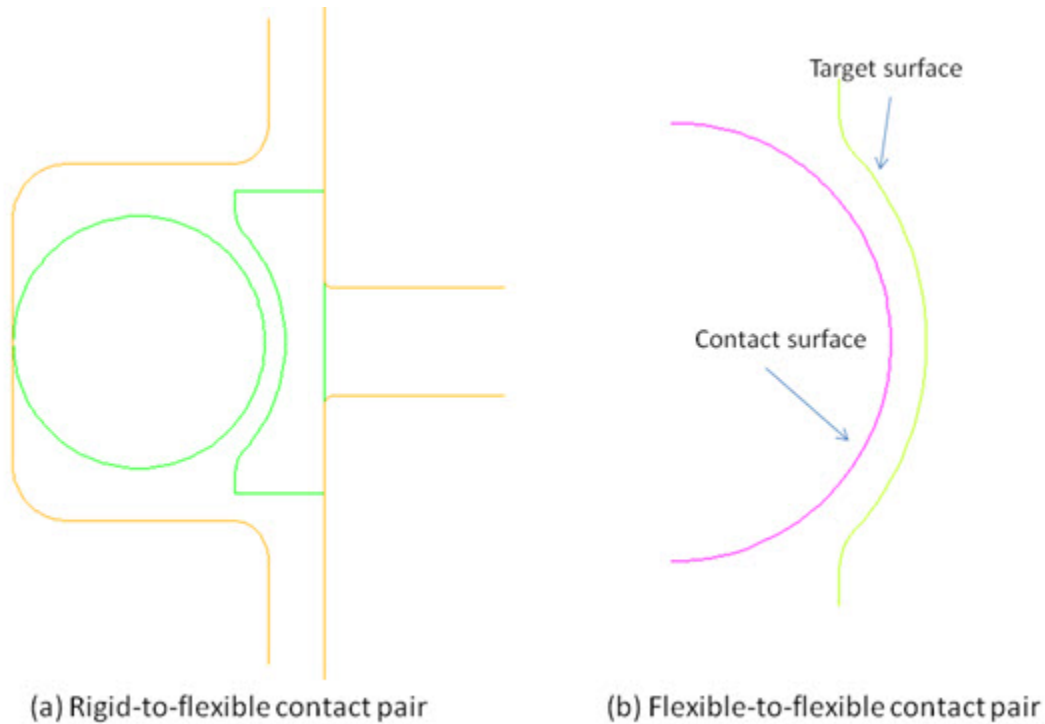
Property	Value
O-ring radius	0.89 mm
Cap width	0.623 mm
Cap height	2.123 mm

The following elements are used in this model:

Element	Description	Key Option (KEYOPT) Setting	Total Number of Elements Used
PLANE182	2-D 4-Node Structural Solid	KEYOPT(3) = 1 (axisymmetric behavior)	2065
CONTA171	2-D 2-Node Surface-To-Surface Contact	KEYOPT(2) = 3 (Lagrange multiplier on contact normal and penalty on tangent)	495
TARGE169	2-D Target Segment	---	290

The o-ring and cap are modeled using [PLANE182](#) elements.

Two contact pairs are defined using [CONTA171](#) and [TARGE169](#) elements. One rigid-to-flexible contact pair models the contact between the entire exterior surface of seals (o-ring and cap) and the rigid surfaces, as shown by (a) in the following figure:

**Figure 3.3: Sealing System Contact Pairs**

Another flexible-to-flexible contact pair models the contact between the o-ring and the cap, as shown by figure (b).

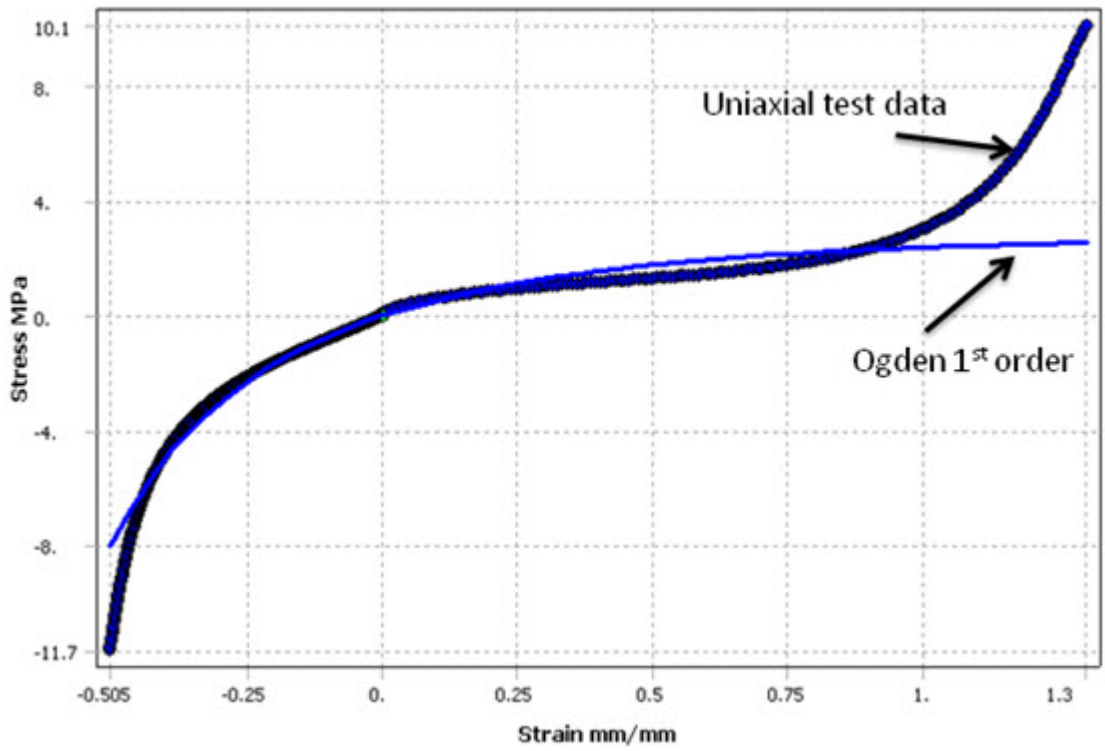
A frictional interaction is defined for the contact pairs and the friction coefficient of 0.1 is applied (via the **MP** command). The contact formulation used is the "Lagrange multiplier on contact-normal and penalty-on-tangent" (KEYOPT(2) = 3 on **CONTA171**).

### 3.4. Material Properties

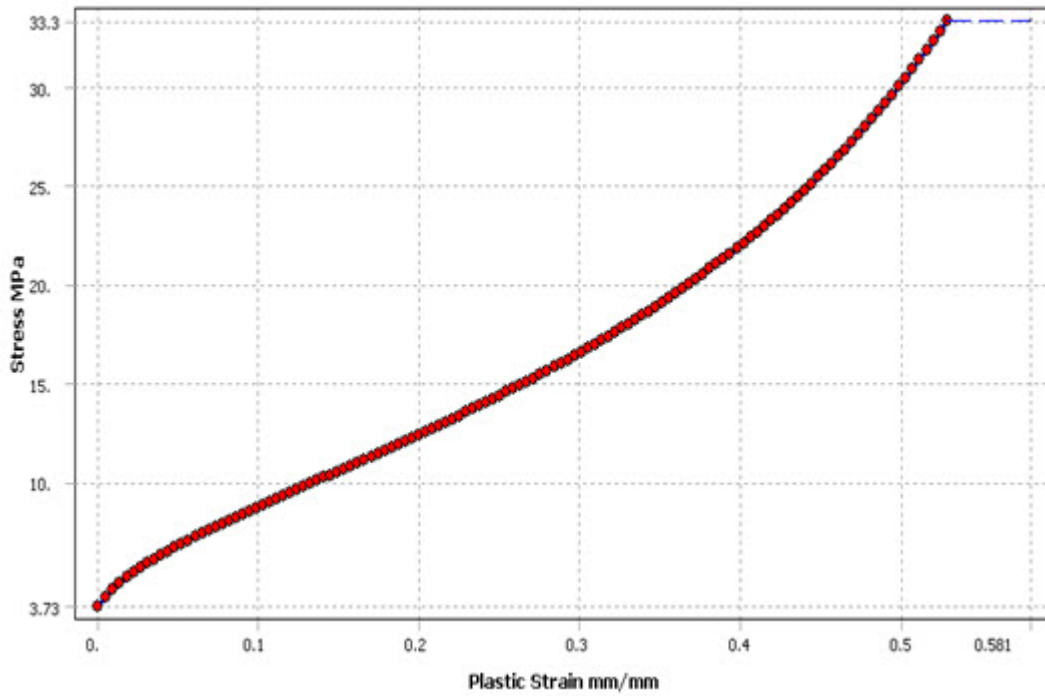
The material of the o-ring is taken to be an incompressible elastomer material modeled by the Ogden first-order hyperelastic form. Three material constants representing an initial shear modulus of 1.99408 MPa are input via the **TB,HYPE,,,OGDEN** command.

In the following figure, part (a) displays the original uniaxial test data and fitted curve with the Ogden first-order hyperelastic form. The plastic cap is modeled by an elastic-plastic material which is softer than the o-ring material. The isotropic hardening stress-strain curve (initialized via the **TB,PLAS,,,MISO** command) is shown in part (b).

Figure 3.4: Material Model Test Data



(a) Uniaxial Test Data and Fitted Curve with Ogden First Order



(b) Isotropic Hardening Strain-Stress Curve

Material Properties		
Coefficient of Friction for Contact Interface	O-Ring [1]	Cap
$\mu = 0.1$	$\mu_1 = 7.5605 \text{ MPa}$ $\alpha_1 = 0.54275$ $d_1 = 1e-4$	$E = 171.47 \text{ MPa}$ $\nu = 0.4$

#### 1. Hyperelastic Ogden material constants

For more information about the Ogden form, see [Ogden Hyperelasticity](#) in the *Material Reference*.

For more information about the multilinear curve, see [Multilinear Isotropic Hardening](#) in the *Material Reference*.

### 3.5. Boundary Conditions and Loading

Two load steps are defined (parts (b) and (c) in [Figure 3.2: Sealing System and Finite Element Model](#) (p. 45)).

Loading is applied as follows:

#### Load Step 1

$$U_x \text{ rigid shaft} = 0.2794 \text{ mm}$$

$$U_x \text{ rigid groove} = -0.05715 \text{ mm}$$

The housing compression is analyzed in the first load step. The rigid shaft surface (left side) moves 0.2794 mm in the x direction and the rigid groove surfaces (right side) move 0.05715 in the negative x direction, simulating the housing assembly.

#### Load Step 2

$$\text{PRES} = 5.171 \text{ MPa}$$

In the second load step, a fluid penetration pressure of 5.171 MPa is applied to the contact pairs (via the **SFE** command with the load key value *LKEY* set to 1), as shown:

```

esel,s,real,,6                ! select rigid-flexible contact pair
esel,r,ename,,171            ! reselect contact elements only
esel,a,real,,8                ! select flexible-flexible contact pair
sfe,all,1,pres,,5.171        ! apply fluid pressure
allsel

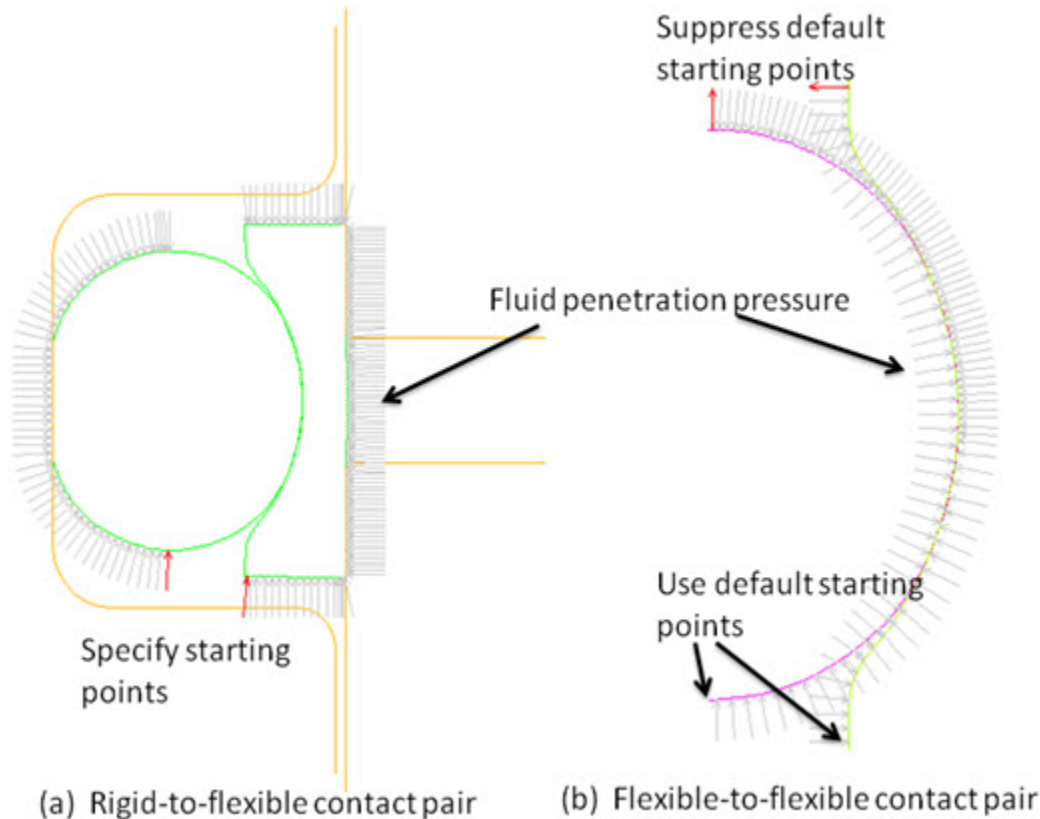
```

The following input prevents fluid penetration loads from being applied multiple times on overlapping contact elements from different pairs:

```

esel,s,real,,8                ! select flexible-flexible contact pair
nsle
esln,s,1
esel,r,real,,6                ! reselect rigid-flexible contact pair
sfedele,all,all,all          ! remove overlapping fluid pressure loads
allsel

```

**Figure 3.5: Sealing System with Applied Fluid Pressure to Contact Pairs**

The fluid-penetration starting points are also specified in order to model the system fluid pressure exposed from the bottom part (the opening between the shaft and the lower part of groove). For the rigid-to-flexible contact pair, no default starting points exist because the contact surfaces are in a closed loop, as shown in (a). To activate the fluid penetration pressure, two contact elements are chosen as starting points initially exposed to the fluid (via the **SFE** command, with the load key value *LKEY* set to 2 and the first starting point status value *VAL1* set to 1), as follows:

```
SFE,3121,2,PRES,,1    ! starting point for o-ring
SFE,3308,2,PRES,,1    ! starting point for cap
```

One starting point is for the contact surface of the o-ring, and the other is for the contact surface of the cap, respectively.

For the flexible-to-flexible contact pair, the ending points of the contact and target surfaces are the default starting points. To force the fluid to penetrate from the bottom only, the two default starting points on the top part of the seals are suppressed (via the **SFE** command, with the load key value *LKEY* set to 2 and the first starting point status value *VAL1* set to -1), as follows:

```
SFE,2529,2,PRES,, -1
SFE,2625,2,PRES,, -1
```

### 3.6. Analysis and Solution Controls

A static analysis (**ANTYPE,STATIC**) is performed for the fluid-penetration simulation.

The gaps (between the o-ring and the shaft, the o-ring and the cap, and the cap and lower part of the groove) are closed after the first load step, so the fluid does not initially penetrate into those contacting



regions. The fluid gradually opens the contact and penetrates into those regions with increasing pressure loading. Since a default value of zero for the pressure penetration criterion (PPCN input via the real constant command **R**) is used, the fluid pressure penetration occurs immediately as soon as the contact is open or lost.

The entire system is very unstable during the second load step. The seals are pushed up due to the fluid pressure. Rigid body motion may occur when the frictional stresses are not large enough to hold the seals vertically. Convergence difficulty due to an unstable problem is usually the result of a large displacement for smaller load increments. To overcome the instability, the nonlinear stabilization capability (**STABILIZE** command) is used in the second load step, as follows:

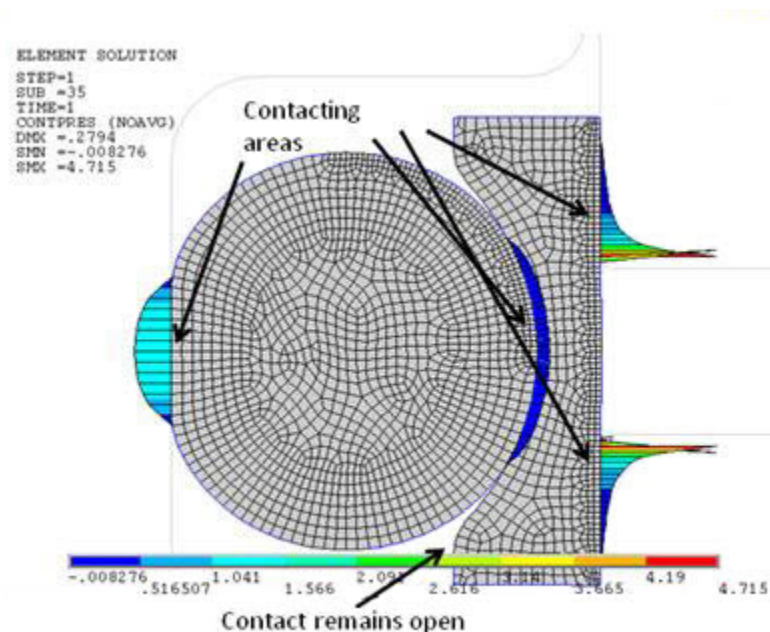
```
STABILIZE, CONSTANT, ENERGY, 0.01, ANYTIME
```

### 3.7. Results and Discussion

The analysis uses an automatic time-stepping scheme, performing approximately 35 substeps in the first load step and approximately 204 substeps in the second load step. (The exact number of substeps is subject to change depending on the hardware platform used to run the analysis.)

The deformed configuration and the contour of the contact pressures on the seals at the end of the first load step are shown in the following figure:

**Figure 3.6: Sealing System Contact Pressure Following Housing Compression (First Load Step)**



Contact occurs in several areas, as follows:

- The middle part of the contact interface between the o-ring and the shaft
- The middle part of the contact interface between the o-ring and the cap
- The top and bottom part of the contact interface between the cap and the groove.

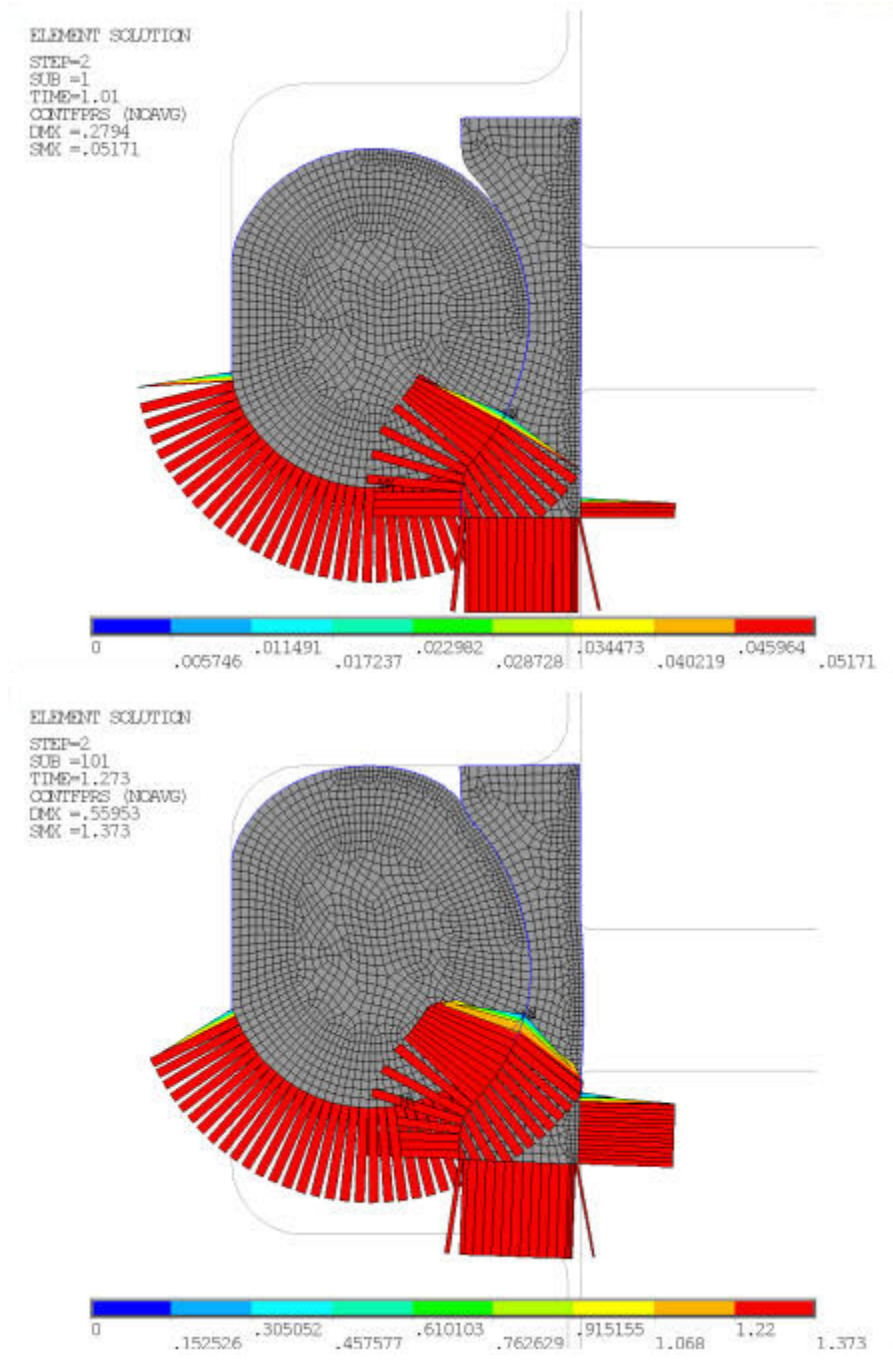
The top and bottom part of contact interfaces between the seals and the shaft remains open.

The fluid penetration pressure loads are applied during the second load step. The fluid pressure is active immediately on elements near the bottom part of contact interfaces where the contact status is open.

The fluid pressure does not spread to the elements around the top part of the seals because gaps have been closed near the middle part of the interfaces.

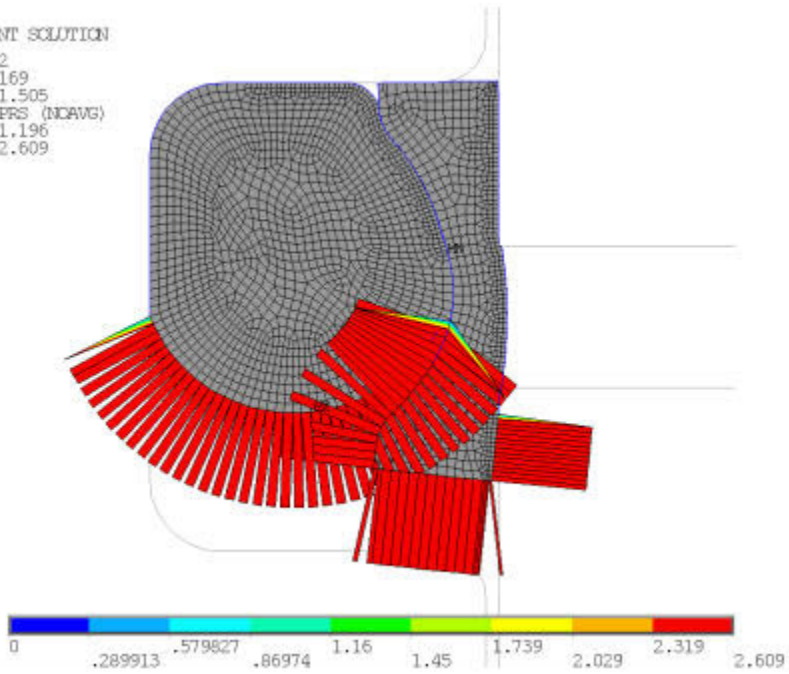
The propagation of the fluid penetration is captured in the following figures showing the deformed shape, the fluid pressure contour, and the contact pressure contour corresponding to different stages of the applied loading. The fluid pressures applied to the surfaces range from 0.052 MPa in the first substep to 5.171 MPa in the last substep.

**Figure 3.7: Sealing System fluid Penetration Pressure Distributions (During Second Load Step)**



## ELEMENT SOLUTION

STEP=2  
SUB =169  
TIME=1.505  
CMINPPS (NCAVG)  
DMX =1.196  
SMX =2.609



## ELEMENT SOLUTION

STEP=2  
SUB =204  
TIME=2  
CMINPPS (NCAVG)  
DMX =1.911  
SMX =5.171

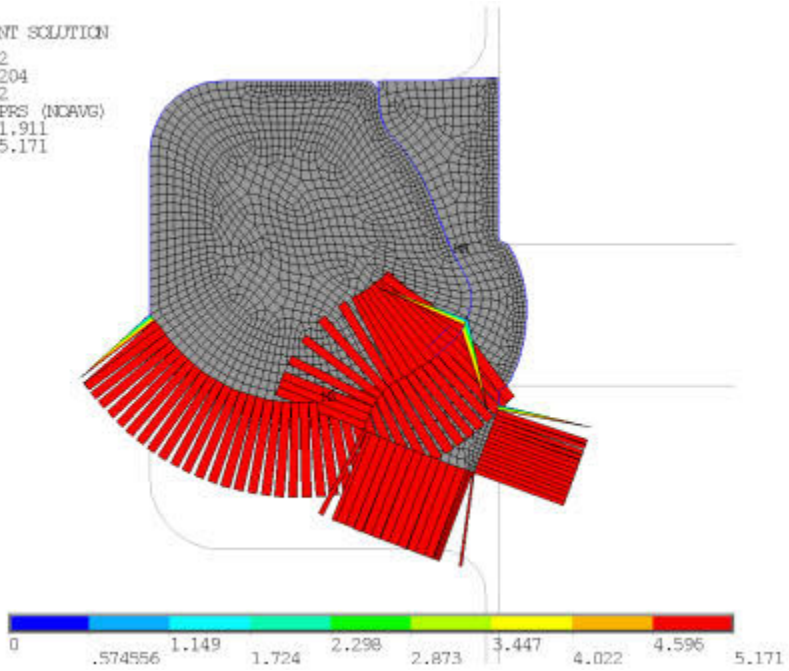


**Figure 3.8: Animation of Fluid Penetration Pressure Distribution**

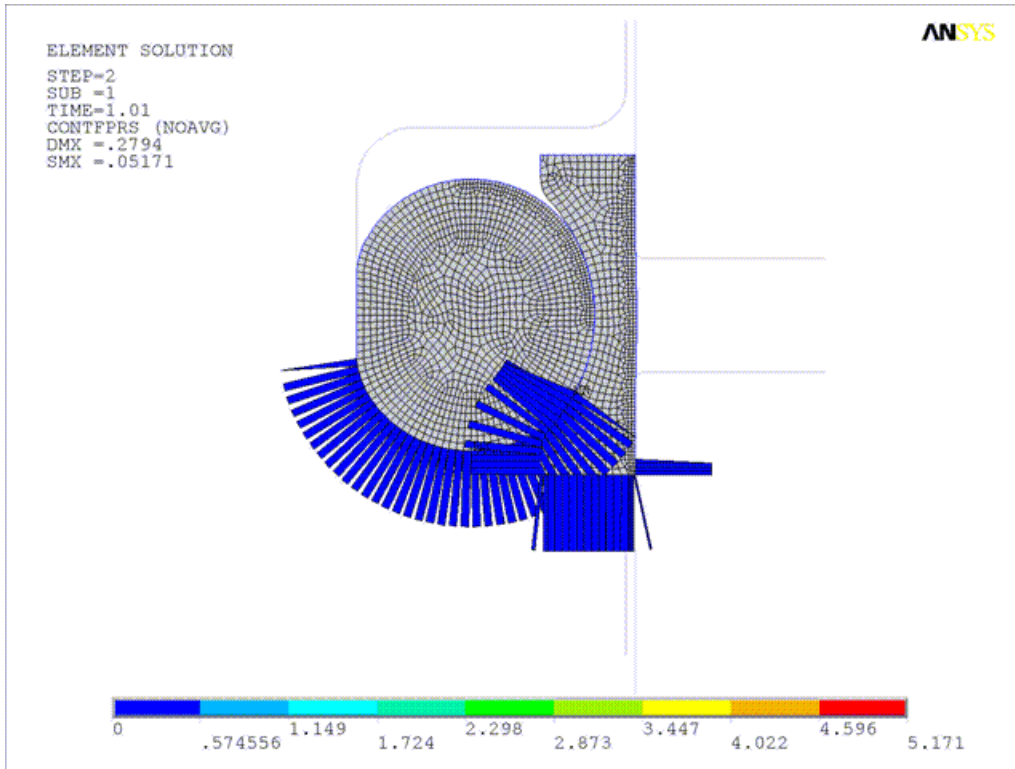
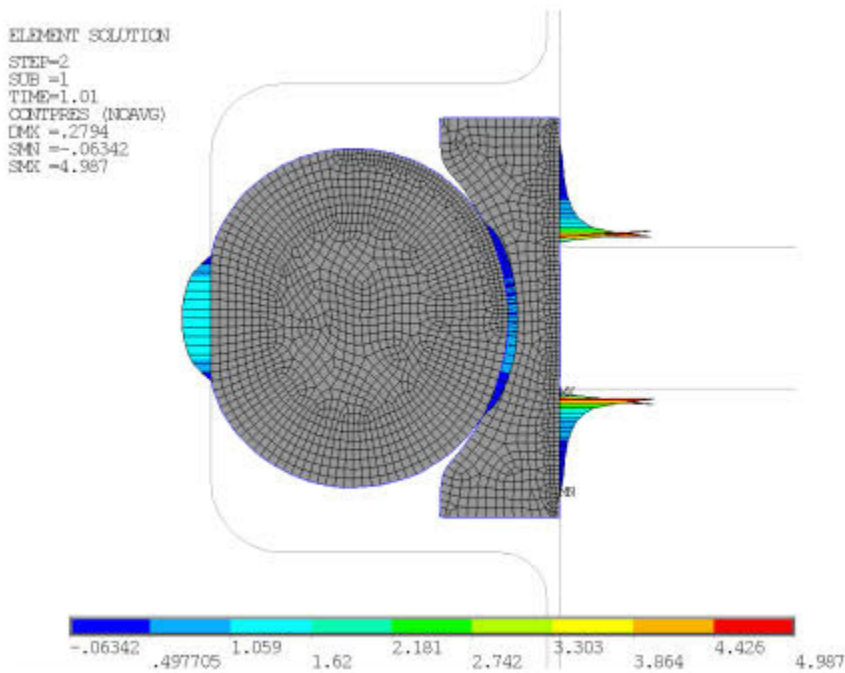
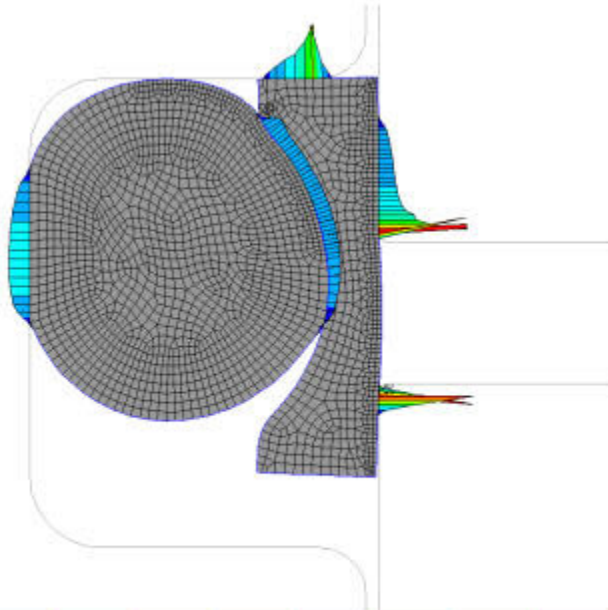


**Figure 3.9: Sealing System Contact Pressure Distributions (During Second Load Step)**



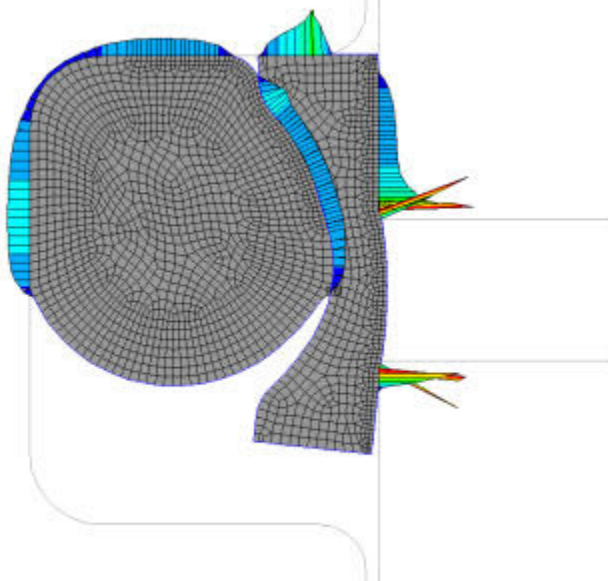
ELEMENT SOLUTION

STEP=2  
 SUB =101  
 TIME=1.273  
 COMPPRES (NCAVG)  
 DMX =-.55953  
 SMN =-.358565  
 SMX =10.684



ELEMENT SOLUTION

STEP=2  
 SUB =169  
 TIME=1.505  
 COMPPRES (NCAVG)  
 DMX =1.196  
 SMN =-.03456  
 SMX =17.199



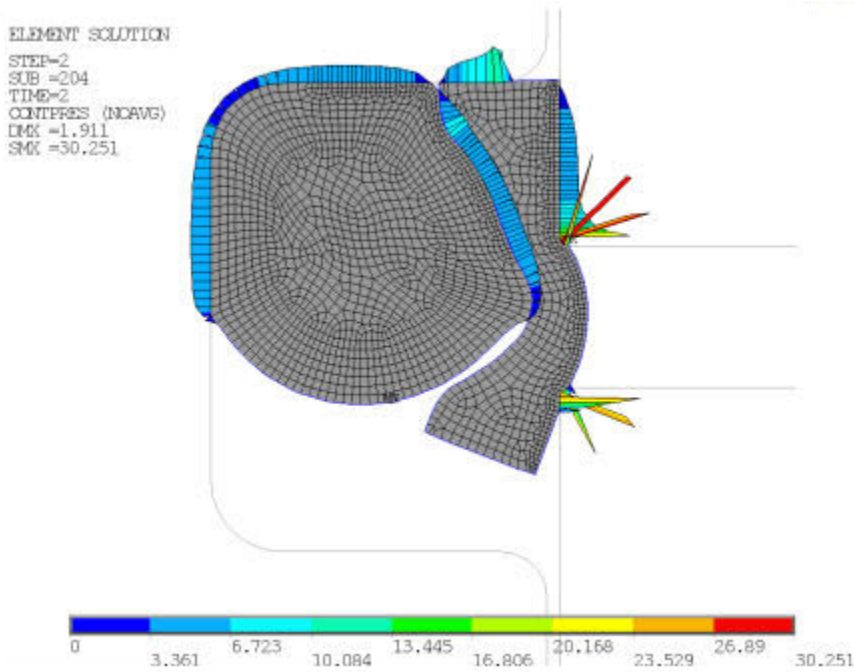
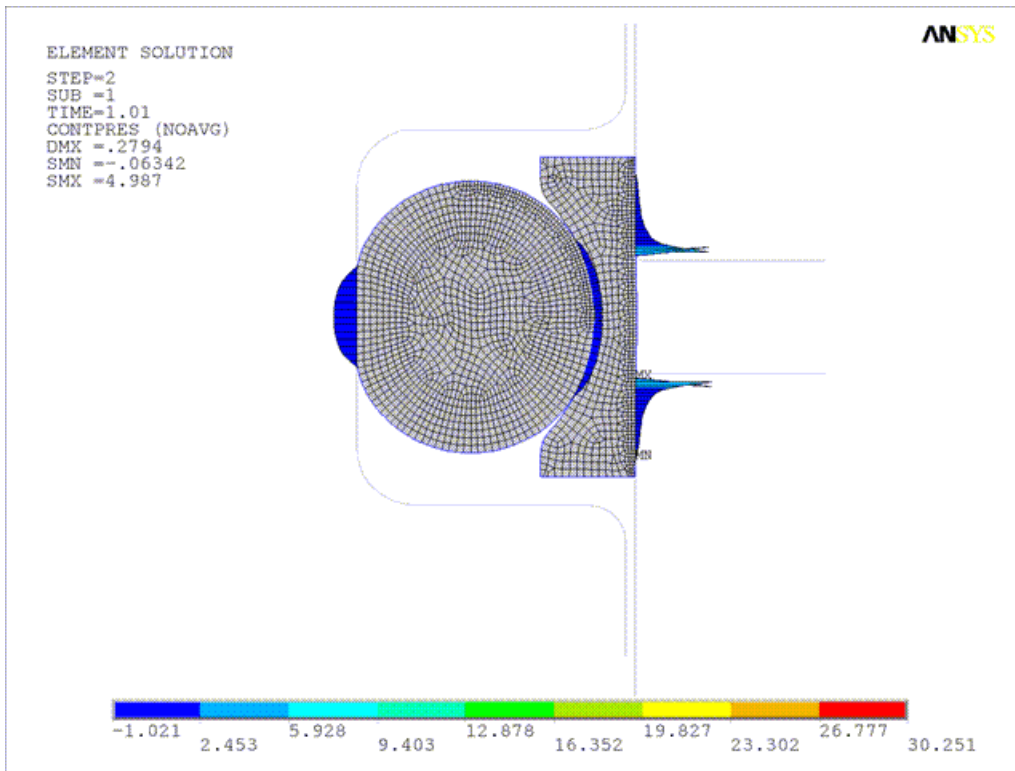
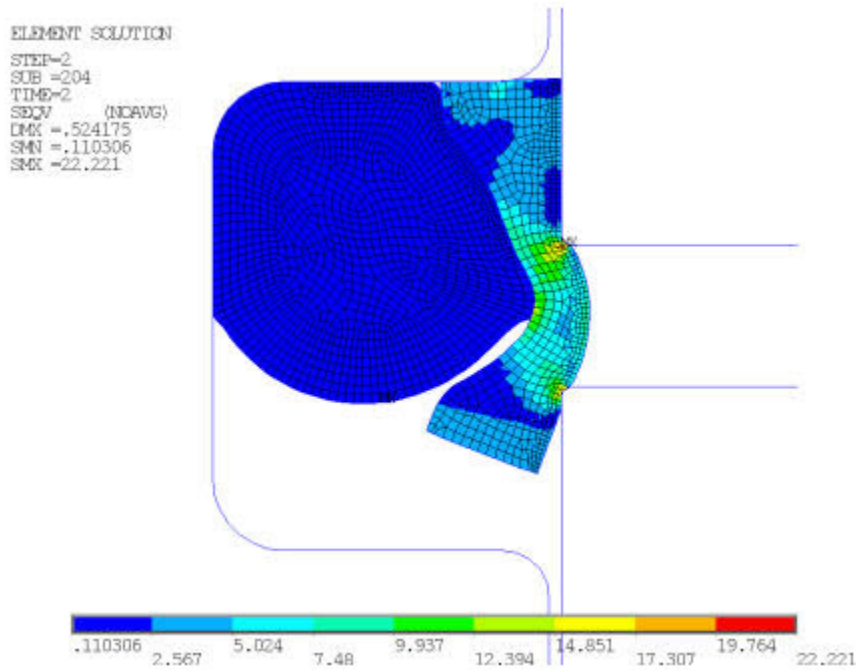
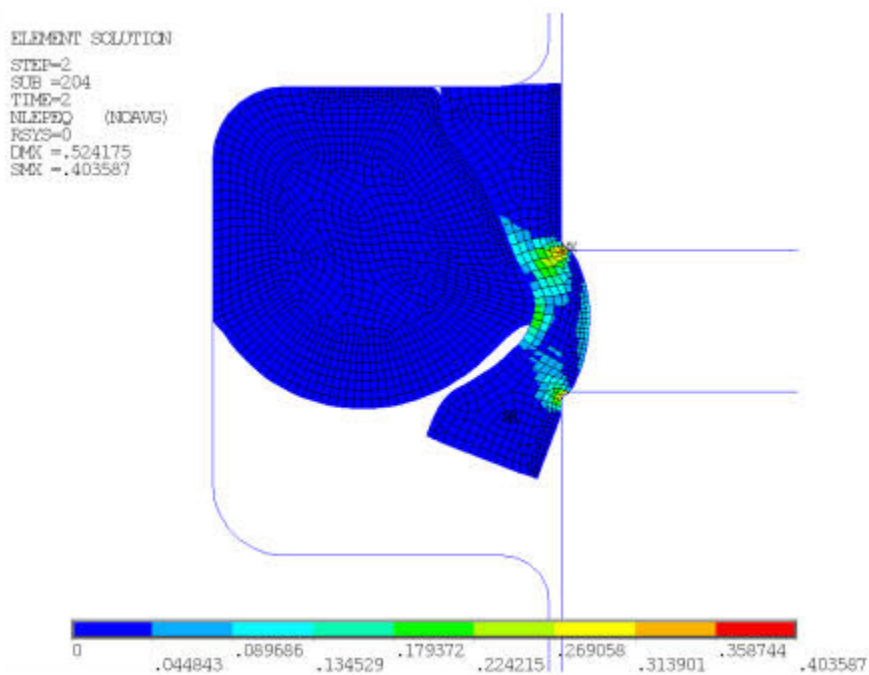


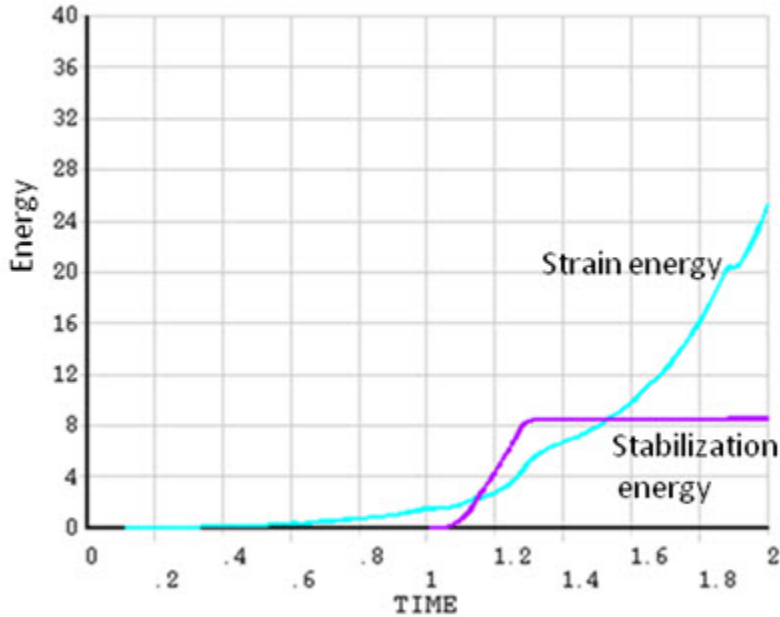
Figure 3.10: Animation of Contact Pressure Distribution



Increasing pressure penetration loads applied in the second load step force the o-ring and cap to be pushed up against the shaft, eventually causing complete contact between the seals and upper part of the shaft. Throughout the loading history, there is no evidence of complete fluid penetration as the contact in certain regions remains closed.

**Figure 3.11: Sealing System Von Mises Stress Contour (After Second Load Step)****Figure 3.12: Sealing System Equivalent Plastic Strain Contour (After Second Load Step)**

The analysis also shows a certain degree of extrusion of the plastic cap through the extrusion gap of the groove near the end of the second load step. Because the plastic cap is softer than the o-ring, deformations and stresses in the cap are higher than those in the o-ring.

**Figure 3.13: Sealing System Total Strain Energy and Stabilization Energy Time History**

In the early stages of loading (TIME < 1.27), slight strain energy is developed and the seals are pushed up almost rigidly. The stabilization energy is developed to prevent rigid body motion; without stabilization, the solution diverges.

In the later stage of the loading (TIME > 1.27), the seals deform as the result of compression and strain energy is developed while the stabilization energy remains constant. Eventually, the stabilization energy is less than the strain energy by a factor of three. The stabilization feature helps to prevent potential rigid body motion and improves the convergence while having little effect on the final results.

### 3.8. Recommendations

To perform a similar type of analysis, consider the following recommendations:

- Fluid pressure penetration is a path-dependent loading. Therefore, you should define the “starting points” with great care. In many cases, you might need to remove invalid default starting points and properly define the physical location of the fluid penetration loading. For more information, see [Specifying Fluid Penetration Starting Points](#) in the *Contact Technology Guide*.
- You should be careful not to apply fluid pressures multiple times when contact pairs overlap. Duplicate fluid penetration loads should be removed as demonstrated in [Boundary Conditions and Loading](#) (p. 49).
- Determining an appropriate stabilization constant (**STABILIZE** command) may require some experimentation. The defined constant should be large enough to prevent rigid body motion, but also ensure that the resulting stabilization energy is much smaller than the strain energy. Trial and error is often required to obtain a suitable value.

### 3.9. Acknowledgments

ANSYS, Inc. gratefully acknowledges [Trelleborg Sealing Solutions](#) for providing the geometry and material properties used in this example.



---

## 3.10. Input Files

The following input files were used in this problem:

- `oring.dat` -- Input file for the o-ring seal static analysis.
- `oring.cdb` -- The common database file for the axisymmetric model of the o-ring (called by `oring.dat`).

The files are available in the `td-3` folder. See [Obtaining the Input Files \(p. xxxv\)](#) for more information.



---

## Chapter 4: Ring-Gear Forging Simulation with Rezoning

---

This example problem demonstrates the efficiency and usefulness of [rezoning](#) in a simulation of metal-forming processes. Rezoning facilitates the convergence of a nonlinear finite element simulation in which excessive element distortion occurs.

Topics related to this example problem follow:

- [4.1. Introduction](#)
- [4.2. Problem Description](#)
- [4.3. Modeling](#)
- [4.4. Material Properties](#)
- [4.5. Boundary Conditions and Loading](#)
- [4.6. Analysis and Solution Controls](#)
- [4.7. Results and Discussion](#)
- [4.8. Recommendations](#)
- [4.9. References](#)
- [4.10. Input Files](#)

### 4.1. Introduction

Finite element analysis plays a significant role in designing and analyzing complex metal-forming processes that improve product quality. Successful simulation of these processes is often complicated due to the nonlinear nature of the problems involved. Causes for nonlinearity in such problems include large-deformation analysis, material plasticity, and the contact needed between the work piece and the dies.

Rezoning is a powerful tool for overcoming convergence difficulties that can arise due to mesh distortion. Through its capabilities, a distorted mesh can be repaired and the simulation can be continued to completion. Rezoning is not intended for cases where the material or structure becomes unstable or where the mesh deformation has become too severe to repair.

If necessary, several regions can be repaired at the same time ([horizontal rezoning](#)), and multiple rezoning operations are allowed on a region at different times during the analysis (vertical rezoning).

#### The rezoning process requires the following general steps:

1. [Select the substep](#) to initiate rezoning.
2. Select the region(s) to be repaired (typically via graphical picking).
3. Generate the [new mesh](#).
4. [Map variables](#) and solve to balance residuals and achieve equilibrium.
5. [Continue the analysis](#) based on the new mesh.

This ring-gear forging example demonstrates the above steps in detail.

## 4.2. Problem Description

A nonlinear large-deformation analysis of a ring-gear forging simulation is performed with two vertical rezonings (multiple rezonings on a region occurring at different times). Both rezonings use a new mesh. (The new mesh is created using any common meshing software application.)

The forging process is simulated using a 2-D axisymmetric model meshed with a 2-D four-node structural solid element (PLANE182). The model represents an elastoplastic cylindrical block (the work piece) sitting in a rigid surface (static die).

The block is deformed by another rigid surface (moving die) that moves at an infinitesimal speed, such that the final shape of the work piece becomes a ring gear with complete die fill, as shown in [Figure 4.1: Original Finite Element Model with Boundary Conditions and Loading](#) (p. 63).

The initial analysis diverges due to excessive mesh distortion when 96 percent of the total loading (TIME = 0.96) is reached. The initial rezoning is applied at TIME = 0.716 (substep 26), and the entire work piece is remeshed.

The analysis continues with the new mesh and converges to completion, but the mesh is severely distorted.

A second rezoning is performed at TIME = 0.9 (substep 45), and the entire work piece is remeshed again to ensure proper die fill and more accurate results at TIME = 1.

The results of effective plastic strains and total strains are compared with results of a similar problem.[1]

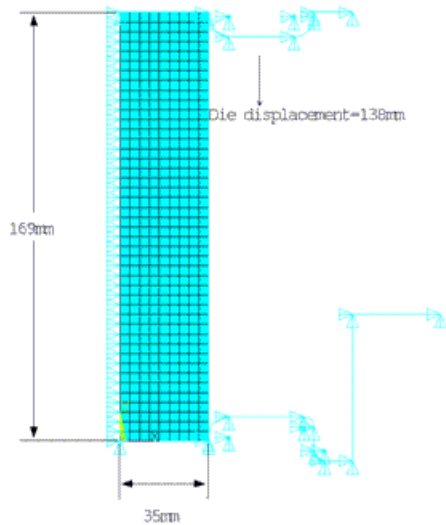
A *single* rezoning at a later stage of the analysis may have been sufficient to solve this problem, but the solution described here was chosen instead so that the problem could also demonstrate how vertical rezoning is performed.

## 4.3. Modeling

The cylindrical block is modeled using 396 plane elements (PLANE182) with axisymmetric behavior (element key option KEYOPT(3) = 1). Options for full integration with the B-bar method (KEYOPT(1) = 0) and mixed u-P formulation (KEYOPT(6) = 1) are also specified.

```
et,1,182
keyopt,1,1,0      ! B-bar method (default)
keyopt,1,3,1      ! Axisymmetric
keyopt,1,6,1      ! Mixed u-P formulation
```

The B-bar method and the mixed u-P formulation prevent the volumetric locking that can be triggered by large plastic deformation. Following is the initial finite element model with loading and boundary conditions applied:

**Figure 4.1: Original Finite Element Model with Boundary Conditions and Loading**

### 4.3.1. Contact

Two rigid-deformable contact pairs without friction are defined using target and contact elements (TARGE169 and CONTA171, respectively) with the Augmented Lagrangian formulation (KEYOPT(2) = 0) activated.

The contact stiffness is updated at each iteration (KEYOPT(10) = 2).

The first contact pair is defined between the top die (moving) and the top and right edges of the work piece. The second contact pair is defined between the bottom die (static) and the bottom and right edges of the work piece.

## 4.4. Material Properties

The work piece is AISI8620 alloy with the following properties:[1]

Young's Modulus:  $E = 200e3$  MPa

Poisson's ratio:  $\nu = 0.3$

The material is approximated as an elastoplastic material with a nonlinear isotropic hardening behavior. The power-hardening law for nonlinear isotropic behavior is represented as:

$$\frac{\sigma_Y}{\sigma_0} = \left( \frac{\sigma_Y}{\sigma_0} + \frac{3G}{\sigma_0} \bar{\epsilon}^p \right)^N \quad (4.1)$$

where:

$\sigma_Y$  = Current yield strength

$\sigma_0$  = Initial yield strength = 385.4 MPa

$G$  = shear modulus

$N$  = power value = 0.13

$\bar{\epsilon}^p$  = Equivalent plastic strain

The power-hardening option is activated via the following input:

```
tb,nliso,1,,power
tbdata,1, 0,n
```

## 4.5. Boundary Conditions and Loading

Symmetry displacement boundary conditions are applied to all nodes on the axis of symmetry.

No boundary conditions are applied to the rigid targets, as they are automatically restrained via the **TARGE169** target element's default behavior (**KEYOPT(2) = 0**).

The top rigid surface is displaced downwards by 138 mm in one load step. The downward displacement compresses the cylindrical block (work piece), and the material flows to fill up the space between the dies.

## 4.6. Analysis and Solution Controls

The following topics concerning analysis details and solution controls for this problem are available:

[4.6.1. Solution Parameters and Analysis](#)

[4.6.2. Rezoning Techniques Applied to Ring-Gear Forging](#)

### 4.6.1. Solution Parameters and Analysis

The solution parameters used in this model are input as follows:

```
nlgeom,on           ! specifies geometric nonlinearity
time,1             ! end time
ncnv,2            ! continues analysis after failure via rezoning and multiframe restart
rescontrol,define,all,1 ! makes restart files available
outres,all,all
nsubst,20,2000,10 !
```

Rezoning requires a static analysis with geometric nonlinearity (**NLGEOM,ON**).

The end time is 1. The initial, minimum, and maximum time step sizes are 20, 2000, and 10, respectively; they are applied with an initial time step size of 0.05 and a minimum time increment of 0.5e-3.

Because the program execution ends if the analysis fails to converge, the analysis is continued after failure by performing rezoning and a multiframe restart. (Without the **NCNV** command, running the full analysis in batch mode would not be possible due to analysis termination after the first divergence.)

All restart files must be available; otherwise, it is impossible to know which substeps to perform to initiate the rezoning. It is also a good idea to save the results; doing so makes it easier to investigate the reason for solution termination and decide which substep to use to activate rezoning. If it is not possible to save results (due to disk space limitations, for example), they can be generated for a specific substep from the restart files (**ANTYPE,,REST,Loadstep,Substep,RSTCREATE**).

### 4.6.2. Rezoning Techniques Applied to Ring-Gear Forging

The general [rezoning process](#) (p. 61) for vertical rezoning, horizontal rezoning, or a combination of both is the same. Following are helpful techniques for applying rezoning specifically to a ring-gear forging problem:

[4.6.2.1. Step 1: Select the Substep to Initiate Rezoning](#)

[4.6.2.2. Step 2: Select a Region to Remesh](#)

[4.6.2.3. Step 3: Apply a New Mesh](#)

[4.6.2.4. Map Variables and Balance Residuals](#)

[4.6.2.5. Perform a Multiframe Restart](#)

### 4.6.2.1. Step 1: Select the Substep to Initiate Rezoning

Selecting the best substep to initiate rezoning is the crucial factor in the rezoning process. No unique selection criteria can be applied universally to all rezoning problems. Various substep-selection techniques can be used for the initial rezoning or subsequent ones.

Generally, the best way to select a substep is by visual inspection of results in the postprocessing module (**/POST1**). It is helpful to use the most important element solutions (**PLESOL**) to create animation files that capture the specific moment when the mesh becomes sufficiently distorted, but not yet severely distorted (that is, when internal angles approach or exceed 180 degrees).

It is good practice to correlate the element solutions plots with corresponding steps in the monitor file (`.montr`) and the convergence pattern in general. To initiate rezoning, select a substep where the current time increment is not close to the specified minimum and where the convergence pattern of the solution has not slowed down significantly (before bisections have started to occur).

In this example, no more than two rezonings are needed because the initial divergence occurs close to the end of analysis (TIME = 0.96). The initial rezoning cannot be performed very close to the end of the last converged substep, because another rezoning is planned before the end of the solution. If the initial rezoning is performed at the beginning of the analysis, large subsequent deformations distort the refined mesh too early in the process, necessitating more vertical rezonings.

#### 4.6.2.1.1. First Rezoning

In this case, substep 26 (TIME = 0.716) is chosen because of the results and monitor file examinations. Although this substep has fewer convergence difficulties than the original solution, experimentation shows that some substeps close to substep 26 may also be good candidates for the first rezoning step.

In the following figure, the element solution of effective plastic strains at this stage shows the deformed mesh, where some of the elements exhibit a very high aspect ratio and internal angles close to 180 degrees:

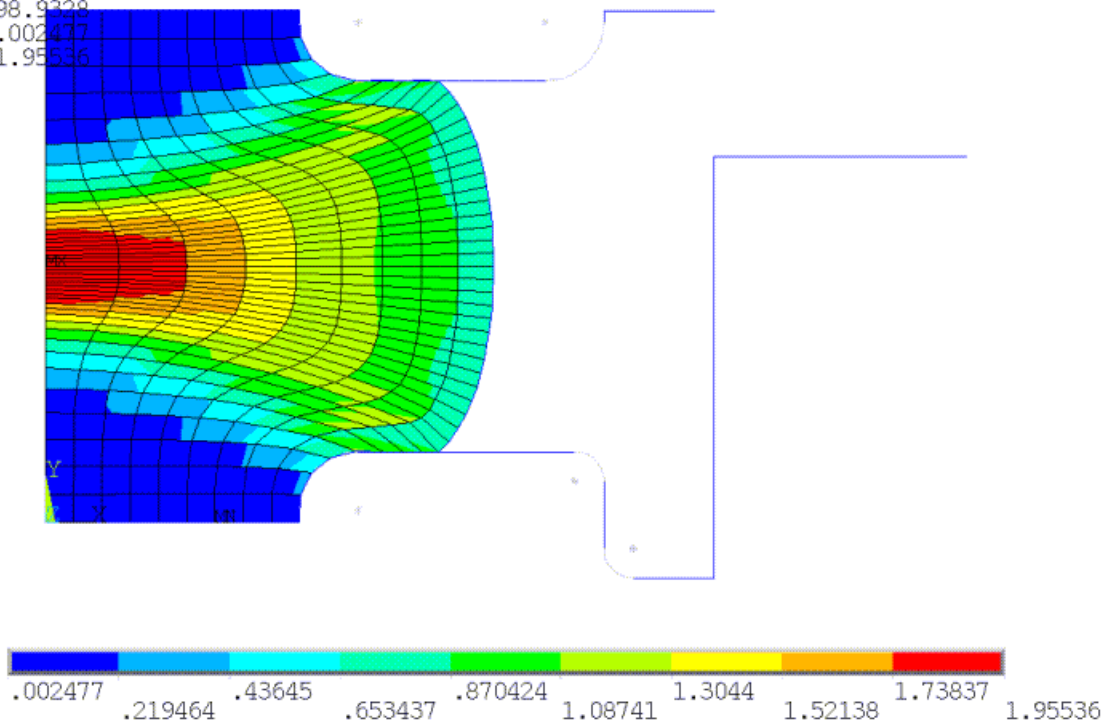
**Figure 4.2: Effective Plastic Strain and Deformed Mesh at Time of First Rezoning**

ELEMENT SOLUTION

```

STEP=1
SUB =26
TIME=.716904
EPPLEQV (NOAVG)
DMX =98.9228
SMN =.002477
SMX =1.95536

```



#### 4.6.2.1.2. Second Rezoning

For the second rezoning, the selection technique changes somewhat because the deformation is more pronounced. The strain gradients are larger, and the mapping of variables is more difficult, than in the first rezoning. It is necessary, therefore, to perform the next rezoning as close as possible to the end time so that after restart, the analysis can continue to completion. Often, this technique involves a few trial-and-error iterations to isolate the optimal substep for rezoning.

Substep 47 (TIME = 0.9138) or thereabouts appears to be best suited for remeshing from the perspective of limited element distortions. The final selection of substep 45 (TIME = 0.9s) as the optimal substep, however, is guided by the convergence from the prior balancing of the residual forces (**MAPSOLVE**).

Element distortions guide the general range of substeps best suited for remeshing. The residual-force balancing determines the precise substep.



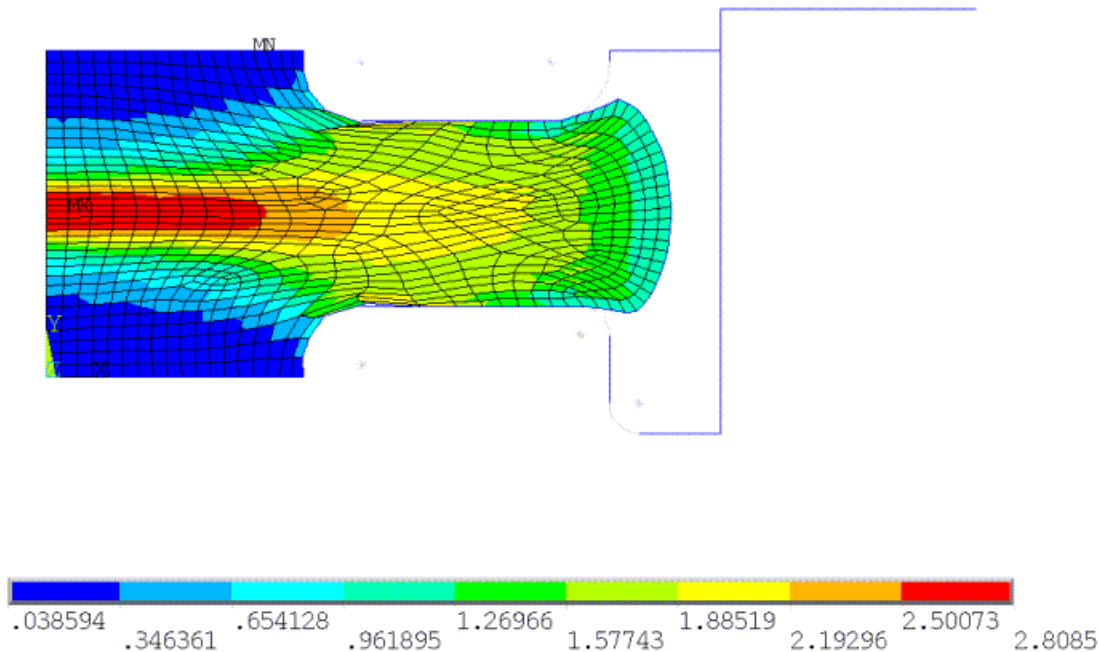
**Figure 4.3: Effective Plastic Strains and Deformed Mesh at Time of Second Rezoning**

ELEMENT SOLUTION

```

STEP=1
SUB =45
TIME=.902924
EPPLEQV (NOAVG)
DMX =31.3637
SMN =.038594
SMX =2.8085

```



#### 4.6.2.2. Step 2: Select a Region to Remesh

After selecting the substep, the region to be remeshed must be selected (typically an easier task than the substep selection process).

Generally, if the model is too large or too complex or if the mesh distortion is localized, horizontal (multiple) remeshing is a better option than remeshing the entire model.

If the model is not large or the mesh distortion is widely spread as in this problem, the entire model can be selected for remeshing.

Horizontal rezoning may be necessary depending on the model size, computational costs, and the degree of accuracy required.

A region selected for remeshing should contain all of the highly distorted elements and, if possible, should be slightly larger than the area containing the distorted elements. The only condition is that all regions must be of the same element type, material type, thickness (for plane stress), and nodal coordinate system (except for boundary nodes).

#### 4.6.2.3. Step 3: Apply a New Mesh

Generating an improved mesh by remeshing is the key to successful rezoning. To improve convergence, the new mesh should have better shape characteristics than the old mesh. To avoid mapping difficulties, the size of the new mesh should not be changed drastically. Retaining the same element size (**ESIZE**)

in the new mesh can work, provided that the new element connections and topology reflect better shape characteristics.

The new mesh can be:

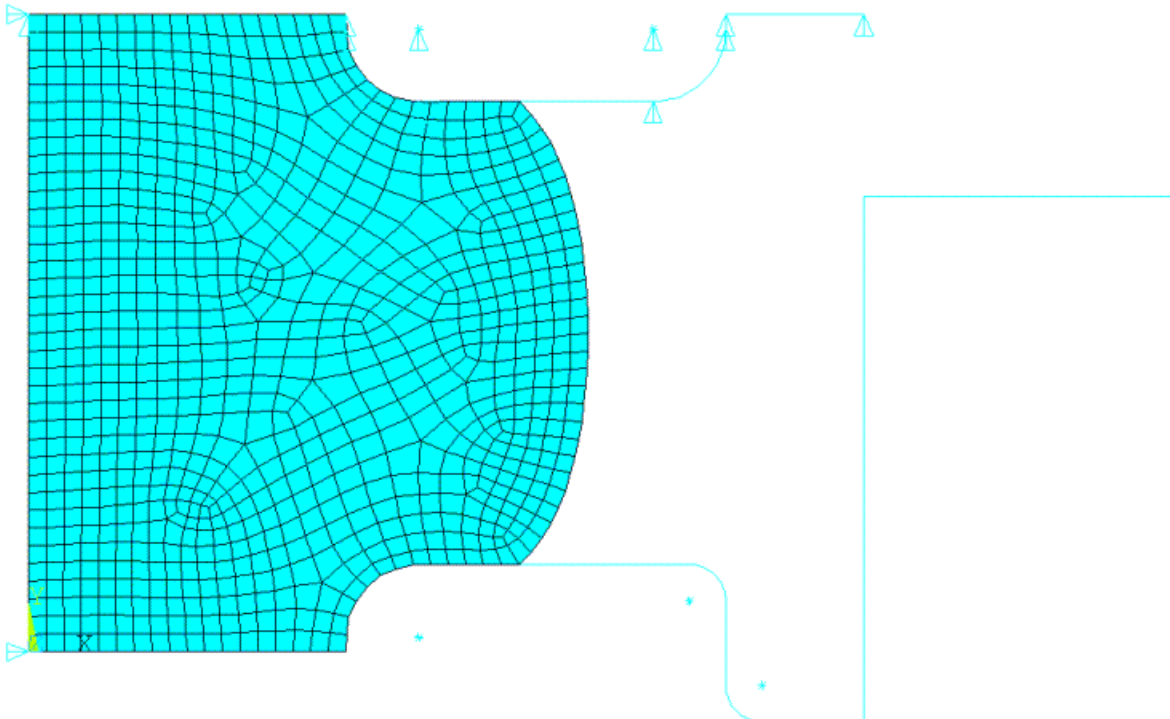
- program-generated (**AREMESH** and **AMESH**),
- read in from a `.cdb` file created by another application (**REMESH,READ**)
- created by splitting existing elements (**REMESH,SPLIT**)

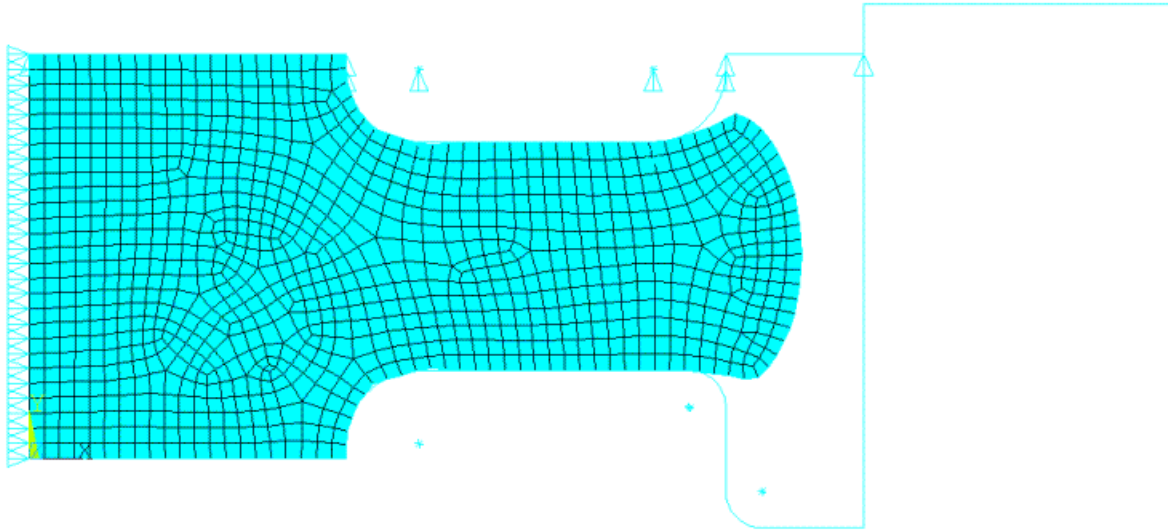
For this problem, a new mesh generated as a `.cdb` file is read in (**REMESH,READ**). The new mesh contains only solid elements, as the contact elements are generated automatically when remeshing is complete (**REMESH,FINISH**).

The rigid target elements remain the same throughout the analysis and cannot be remeshed. While it is possible for the new mesh to contain contact and target information as well, it is faster and more reliable to read in only the remeshed solid elements and allow the contact/target elements to be generated automatically.

The initial element size is approximately 4. The first rezoning decreases it by a factor of two, and the second rezoning uses an element size of 1.7. The new meshes appear in [Figure 4.4: New Mesh Read in During the First Rezoning](#) (p. 68) and [Figure 4.5: New Mesh Read in During the Second Rezoning](#) (p. 69)

**Figure 4.4: New Mesh Read in During the First Rezoning**



**Figure 4.5: New Mesh Read in During the Second Rezoning****Mesh Size Affects Mapping**

The quality of the new mesh, and the mapping operation in general, can be sensitive to mesh size. If the mesh quality is mediocre due to a less-than-optimal element size, mapping difficulties may occur, leading to convergence failure. In such cases, a better mesh using a different element size is necessary.

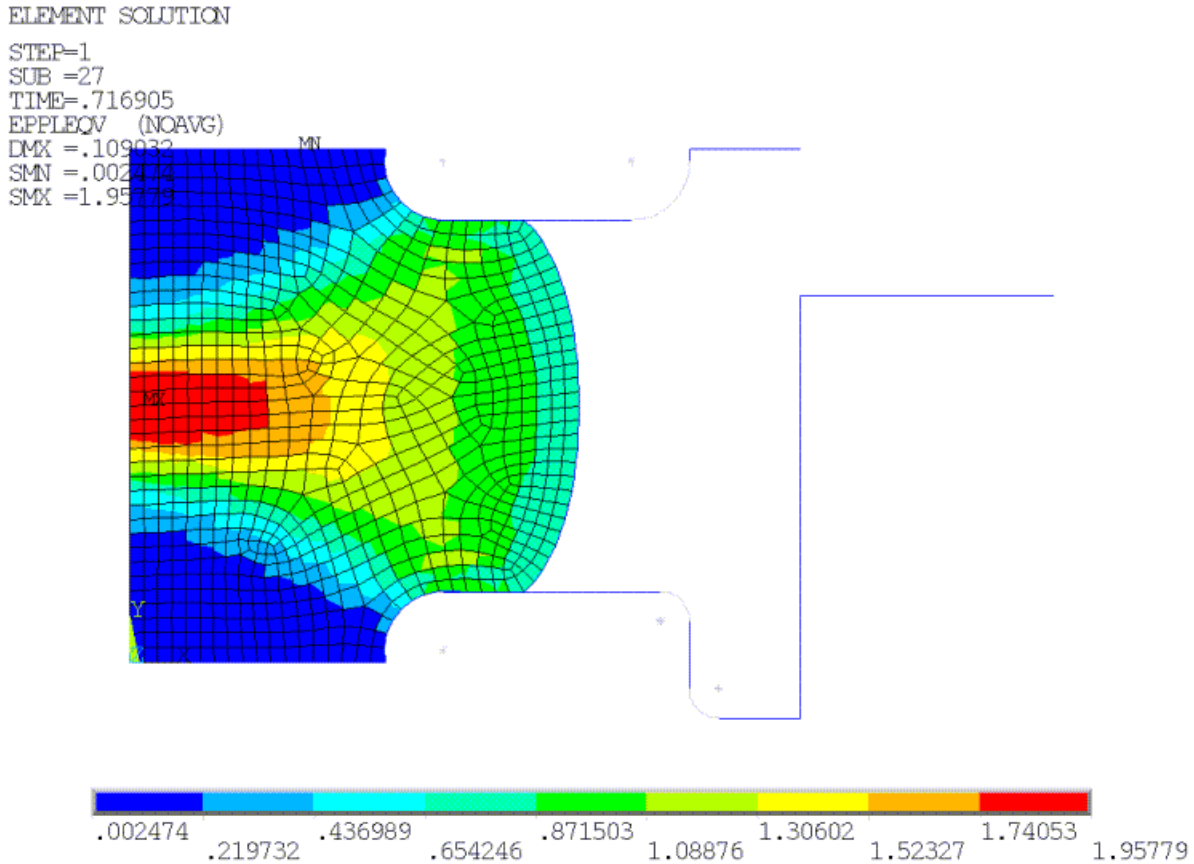
**4.6.2.4. Map Variables and Balance Residuals**

After remeshing, the solution is mapped automatically from the old mesh to the new mesh (**MAPSOLVE**). The mapping operation introduces extra substeps to balance the residual forces and achieve equilibrium.

Although the default is five substeps, it is generally better to use more substeps, especially when contact is included in the problem. This problem uses 500 substeps as the maximum in the case of convergence problems becoming an issue. Using a larger number of substeps does not affect computational efficiency and is recommended for solving nonlinear problems characterized by large strains.

The results of the element solution of effective plastic strains after the first and second mapping are shown in the following two figures. The [results are compared \(p. 72\)](#) with the same plots before mapping (as shown in [Figure 4.2: Effective Plastic Strain and Deformed Mesh at Time of First Rezoning \(p. 66\)](#) and [Figure 4.3: Effective Plastic Strains and Deformed Mesh at Time of Second Rezoning \(p. 67\)](#)).

**Figure 4.6: Effective Plastic Strain Distribution After First Mapping**



If the old mesh is heavily distorted by rezoning, or if the differences in mesh density and topology between the old and new mesh are especially large (specifically in the elements on boundaries), mapping variables may become difficult, possibly resulting in errors or convergence failure.

If mapping leads to a successful convergence despite the distortion, the results may be slightly different than those which existed before mapping. To observe this effect, compare [Figure 4.2: Effective Plastic Strain and Deformed Mesh at Time of First Rezoning](#) (p. 66) to the following figure

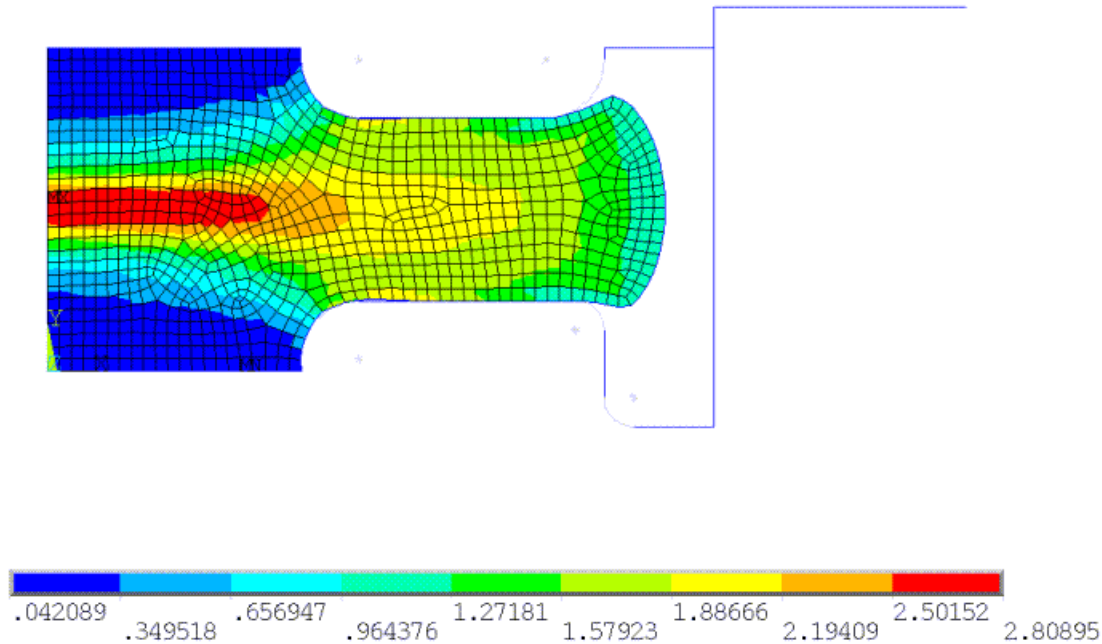
**Figure 4.7: Effective Plastic Strain After Second Mapping**

ELEMENT SOLUTION

```

STEP=1
SUB =46
TIME=.902925
EPPLEQV (NOAVG)
DMX =.220951
SMN =.042089
SMX =2.80895

```



Convergence issues after mapping often indicate that the restarted analysis will also have convergence difficulties; therefore, if mapping uses many substeps to achieve equilibrium, try to rezone from an earlier substep or improve the quality of the new mesh.

#### 4.6.2.5. Perform a Multiframe Restart

After each rezoning, the analysis is continued by performing a standard multiframe restart, provided that all necessary files are available. During restart, the number of substeps can be adjusted to achieve better convergence.

The following input shows the vertical rezoning process as described for this problem:

```

/clear,nostart
/file,ringforging

/solu                                ! First rezoning at substep 26 (time = 0.716)
rezone,manual,1,26
remesh,start
remesh,read,mesh1,cdb                 ! Read in the first mesh with esize = 2
allsel,all
remesh,finish
mapsolve,500,pause
finish
/solu                                ! First multiframe restart
antype,,rest,,continue
solve
finish
/clear,nostart
/file,ringforging

/solu                                ! Second Rezoning at substep 45 (time = 0.9)

```

```
rezone,manual,1,45
remesh,start
remesh,read,mesh2,cdb           ! Read in the second mesh with esize=1.7
allsel,all
remesh,finish
mapsolve,500,pause
finish
/solu                           ! Second multiframe restart
antype, , rest, , , continue
solve
finish
```

### 4.7. Results and Discussion

At the conclusion of the ring-gear forging simulation, the cylindrical block (work piece) completely fills the die gap. The die gap becomes very narrow as deformation progresses and rezoning becomes necessary, as there are not enough elements and nodes in the free surface to completely fill this gap as the work piece material flows.

The effective plastic strain distribution before and after the first rezoning is shown in [Figure 4.2: Effective Plastic Strain and Deformed Mesh at Time of First Rezoning](#) (p. 66) and [Figure 4.6: Effective Plastic Strain Distribution After First Mapping](#) (p. 70), respectively.

The same contours apply before and after the second rezoning, as shown in [Figure 4.3: Effective Plastic Strains and Deformed Mesh at Time of Second Rezoning](#) (p. 67) and [Figure 4.7: Effective Plastic Strain After Second Mapping](#) (p. 71), respectively. The effective plastic strain distribution and the similar contours both indicate that the mapping of data was achieved with accuracy.

Because the mesh changes significantly during the first rezoning, it is expected that results before and after first mapping are different (by about 0.1 percent in this case). The difference is due to the balancing of residuals that are larger when compared to the situation when mesh changes are not significant (as seen in the second rezoning).

Few new elements were added during the second rezoning; therefore the maximum effective strains are identical before and after mapping. The maximum value of effective strain is 3.53, which is close to the reference effective strain value.[1] The contours of effective strains are similar to those of the reference, with a region of very concentrated strains in the middle part where the material flows.

**Figure 4.8: Effective Strain Distribution and Deformed Shape at the Final Stage (Complete Die Fill)**

ELEMENT SOLUTION

STEP=1  
SUB =100  
TIME=1  
EPTOEQV (NOAVG)  
DMX =23.7195  
SMN =.126671  
SMX =3.52222

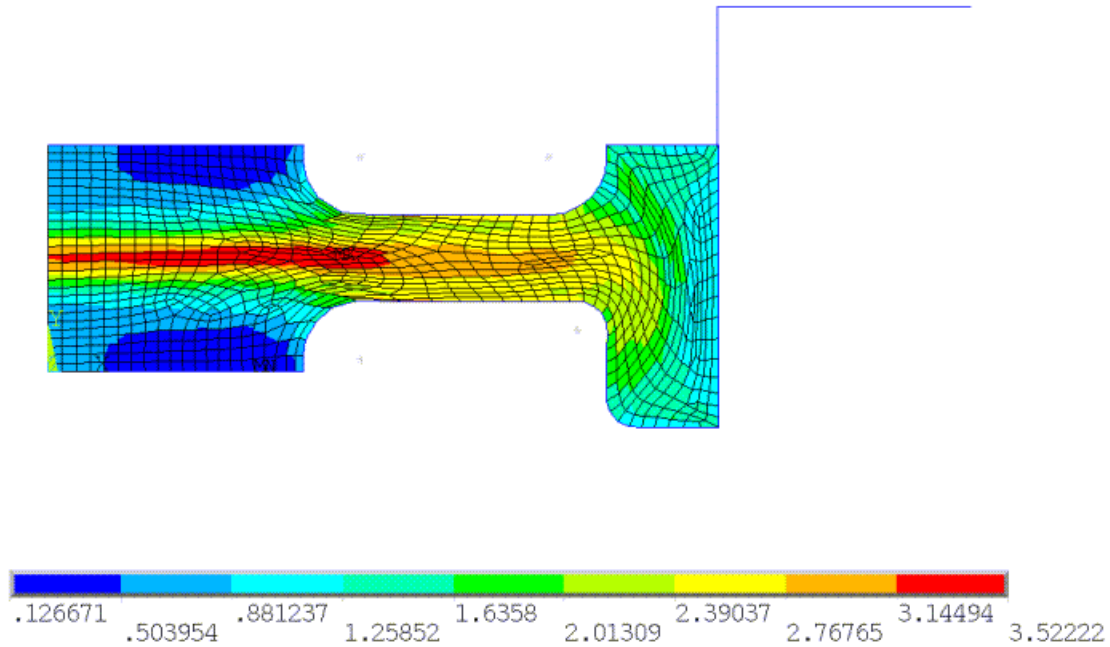
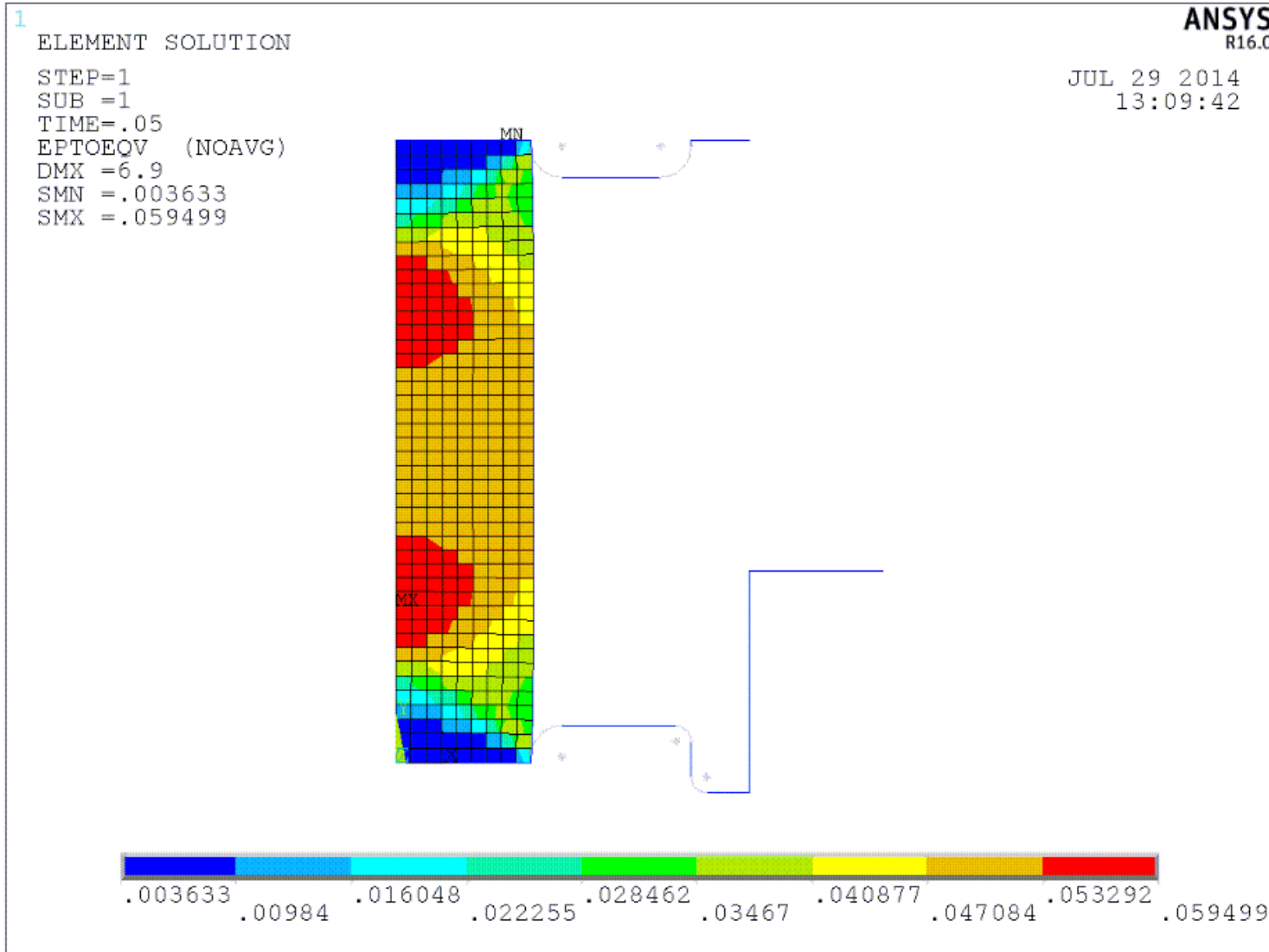


**Figure 4.9: Final Stage Animation**



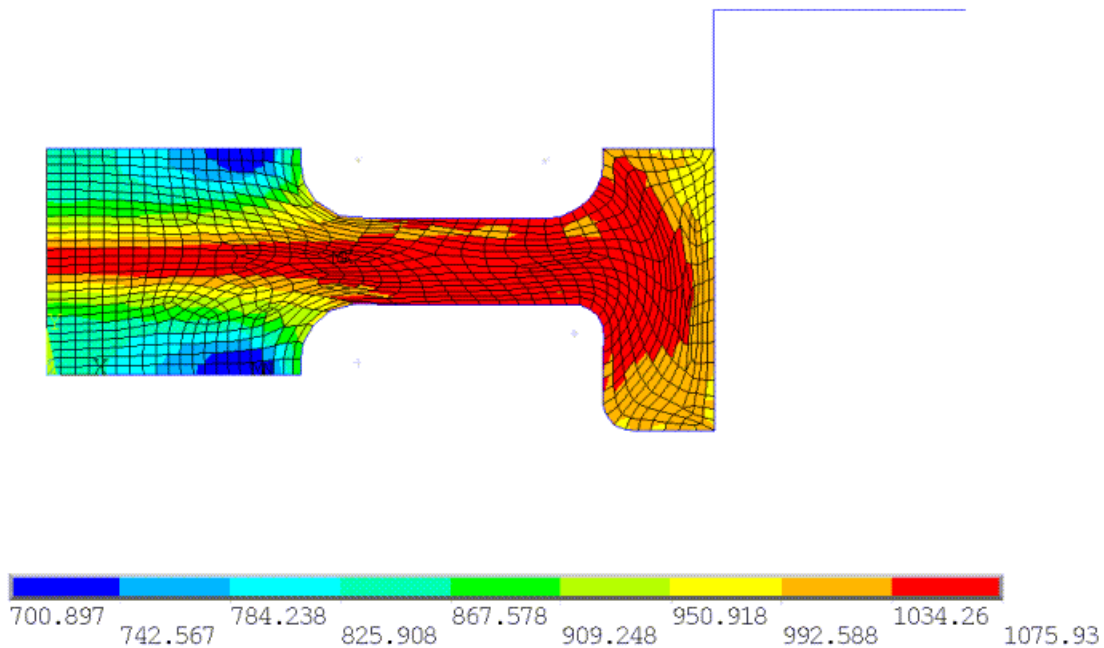
The von Mises stress distribution in the following figure shows that elastic deformation is extremely small compared to plastic deformation:



**Figure 4.10: Von Mises Stress Distribution at the Final Stage**

ELEMENT SOLUTION

```
STEP=1
SUB =100
TIME=1
SEQV (NOAVG)
DMX =23.7195
SMN =700.897
SMX =1075.93
```



The tiny elastic deformation occurs because the minimum stresses are much higher than the initial yield stress of the material.

In this figure, a half 2-D axisymmetric expansion is performed on the von Mises stress, which offers a better visualization of the plastic flow in this process:

**Figure 4.11: Half Expanded Plot of Von Mises Stress at the Final Stage of Ring-Gear Forging**

ELEMENT SOLUTION

STEP=1

SUB =100

TIME=1

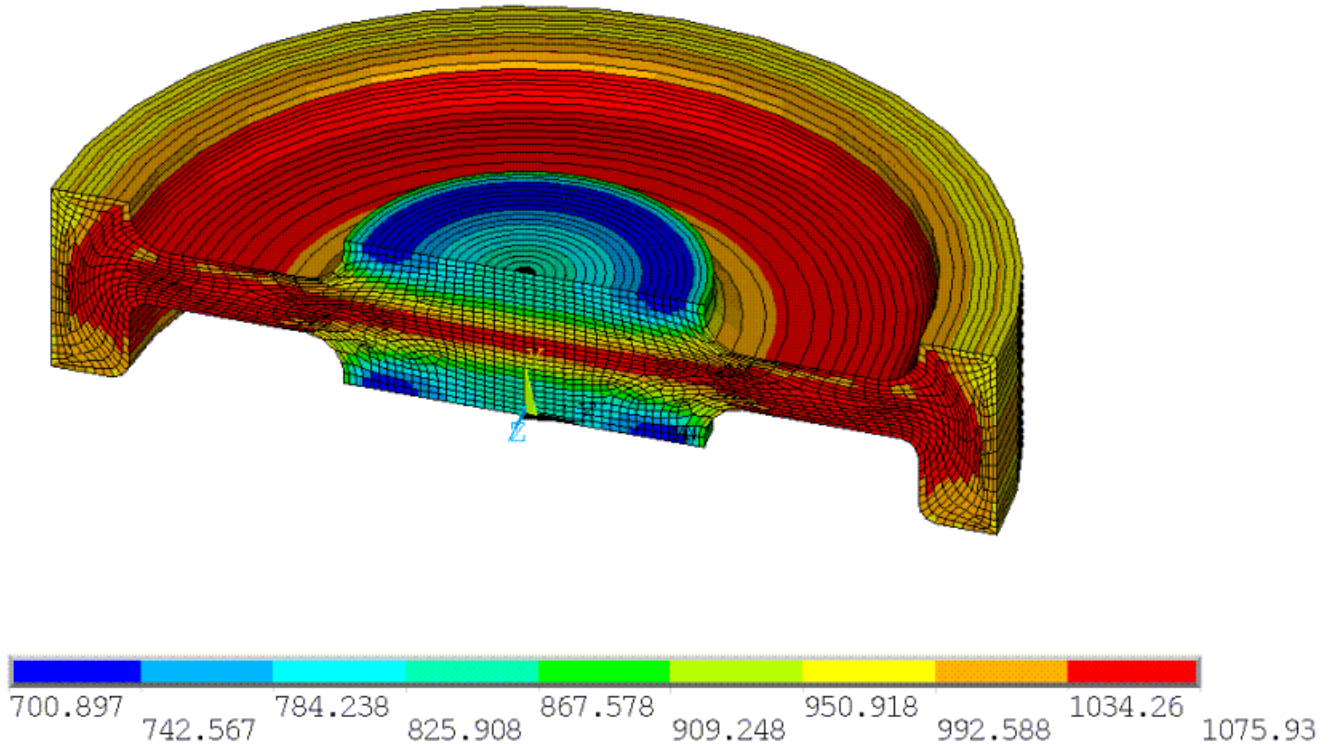
/EXPANDED

SEQV (NOAVG)

DMX =23.7195

SMN =700.897

SMX =1075.93



## 4.8. Recommendations

To perform a similar ring-gear forging simulation using rezoning, consider the following hints and recommendations:

- **Rezoning has limitations.**

Use rezoning only in problems experiencing mesh distortion as a result of large deformation.

- **Select the substep to initiate rezoning carefully.**

Determine the optimal substep after carefully examining the element solution, the deformed mesh (in **/POST1**), and the convergence pattern.

The best substep to rezone is the one where the mesh is distorted (though not too severely distorted) and the time increment is not close to (or at) its minimum.

- **Use an earlier substep or a better mesh if necessary.**

If any of the following situations are encountered, initiate rezoning at an earlier substep or improve the quality of the new mesh:

- Remeshing errors (**REMESH**,FINISH)
- Error, failure, or convergence difficulty during remapping (**MAPSOLVE**)
- Convergence failure in the restarted analysis.
- New mesh shape characteristics are bad due to distortion.

- **Three methods exist for obtaining a new mesh.**

A new mesh can be program-generated (**AREMESH** and **AMESH**), created via mesh splitting (**REMESH,SPLIT**), or read in (**REMESH,READ**).

If an external mesh (.cdb file) created by a third-party meshing application is used, two considerations exist:

- If a partial region is rezoned, the nodal locations on the interior boundaries must be retained by the third-party meshing application when creating the new mesh. The locations are necessary to maintain nodal compatibility between the new and existing meshes.
- If **PLANE183** (quadratic) elements are used in the original mesh, the third-party meshing software should retain the location of midside nodes by generating the new nodes using element-based quadratic interpolation.

- **More than one region can be remeshed at the same time.**

Multiple regions can be remeshed at the same substep via *horizontal rezoning*. Multiple regions where the new mesh is read in (**REMESH,READ**) cannot intersect, though they may touch at a boundary.

Repeated rezonings can be performed at different locations in time via *vertical rezoning*. The only vertical rezoning restriction is that a program-generated mesh (**AREMESH** and **AMESH**) cannot be used *after* obtaining a new mesh either by reading it in (**REMESH,READ**) or by splitting the mesh (**REMESH,SPLIT**). (The restriction is due to the loss of associativity of the mesh and geometry which occurs in cases where the new mesh is read in or created from mesh splitting.)

- **Mesh size affects mapping.**

If the new mesh size is drastically different from that of the old mesh, convergence issues may occur during mapping. It may be necessary to resize the new mesh to more closely match the old one.

- **Specify more substeps if needed.**

A larger maximum number of substeps may need to be specified to handle convergence difficulties during mapping and in the restarted analysis.

## 4.9. References

The following reference was used in this example problem:

1. Kwak, Dae-Young, J.S. Cheon, Y.T. Im. "Remeshing for Metal Forming Simulations - Part I: Two-Dimensional Quadrilateral Remeshing." *International Journal for Numerical Methods in Engineering*. 53.11 (2002): 2463-2500.

## 4.10. Input Files

The following input files were used in this problem:

- ringforging.dat --The input file used in the ring-gear forging problem.

- `ringforging.cdb` -- Common database file containing the initial mesh information (called by `ringforging.dat`).
- `mesh1.cdb` -- Common database file for the new mesh, read in during the first rezoning (called by `ringforging.dat`).
- `mesh2.cdb` -- Common database file for the new mesh, read in during the second rezoning (called by `ringforging.dat`).

The files are available in the `td-4` folder. See [Obtaining the Input Files \(p. xxxv\)](#) for more information.

---

## Chapter 5: Delamination of a Stiffened Composite Panel Under a Compressive Load

---

This example problem demonstrates the use of solid-shell element technology to model a layered-composite structure. The problem simulates interface delamination through the debonding capability of contact elements.

The following features and capabilities are highlighted:

- Use of the [solid-shell element technology](#) to model layered composites
- Bonded contact with a cohesive zone model to simulate delamination (also known as [debonding](#))
- [Shell section definitions](#)
- Use of [constraint equations](#) to model periodic symmetry
- [Nonlinear stabilization](#)

Topics related to this example problem follow:

- [5.1. Introduction](#)
- [5.2. Problem Description](#)
- [5.3. Modeling](#)
- [5.4. Material Properties and Section Definitions](#)
- [5.5. Boundary Conditions and Loading](#)
- [5.6. Analysis and Solution Controls](#)
- [5.7. Results and Discussion](#)
- [5.8. Recommendations](#)
- [5.9. Input Files](#)

### 5.1. Introduction

Stiffened composite panels are ideal for aircraft fuselage construction because of their excellent durability and optimal strength-to-mass ratios. The program provides a variety of element types for modeling layered composite structures. In this example, the eight-node solid-shell element [SOLSH190](#) is chosen for its general applicability to layered structures and its continuum element connectivity that greatly simplifies the modeling process.

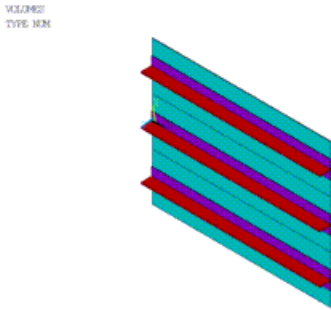
The unique properties of the [SOLSH190](#) element used in this example greatly simplify the modeling of contact between thin parts. For example, when using [SOLSH190](#) instead of shells, you do not have to worry about the section offset, contact surface orientation, or thickness change in large deflection.

The stiffened panel may undergo various local and global failure modes when subjected to a service load. This example focuses primarily on the global buckling of the panel and the progressive failure of the bonding material between different structural components. To simulate this highly nonlinear and unstable phenomenon, the [nonlinear stabilization](#) method and bonded contact with a cohesive zone model are used.

## 5.2. Problem Description

The stiffened panel consists of three components: the skin, the stringer web, and the stringer flange. The construction of stiffeners (stringer web and flange) repeats at a fixed interval, as shown in the figure below. All three components are made of layered composite materials. An in-plane compressive load is gradually applied, causing the panel to buckle and the bond between the skin and the flange to be damaged. The debonding is initialized at an artificial imperfection and allowed to propagate as the load increases.

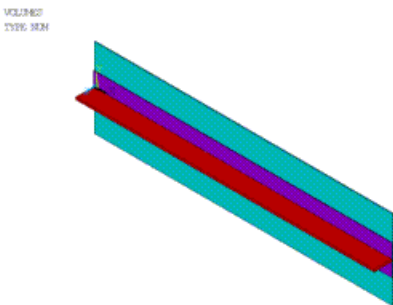
**Figure 5.1: Geometry**



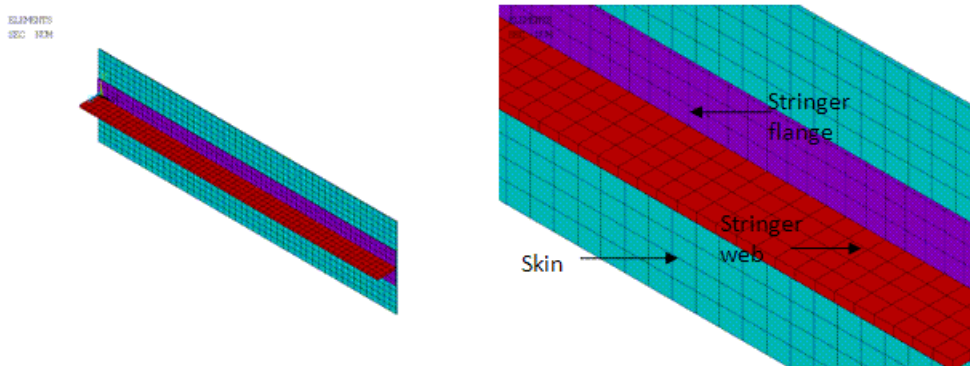
## 5.3. Modeling

Due to the symmetry of the problem, it is possible to model only one representative section of the whole panel. The representative section shown below contains a 600 mm x 160 mm portion of the panel skin and one stiffener assembly.

**Figure 5.2: Symmetry Section**

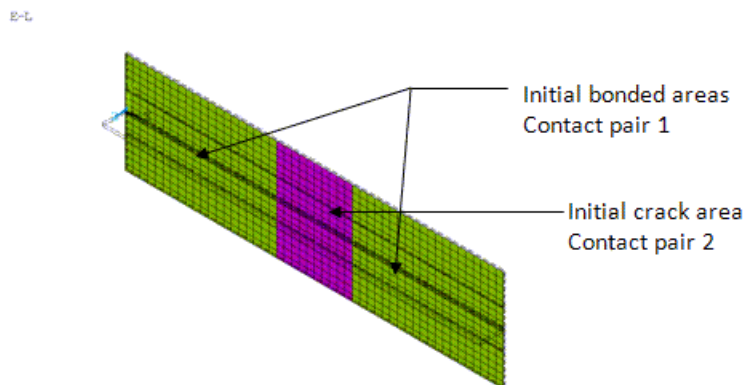


The section is meshed with **SOLSH190** elements, as shown below. Note that the elements on the skin and the flange do not need to match when the interfaces are modeled with contact elements.

**Figure 5.3: Meshed Geometry**

A secure bond is assumed between the web and the flange. This perfect bonding is simulated through the use of common nodes for both components.

The interfaces between the skin and the flange are meshed with [CONTA173](#) and [TARGE170](#) elements. Two distinct contact pairs are established, as shown in [Figure 5.4: Two Contact Pair Definitions \(Initial Crack and CZM Area\)](#) (p. 81). Since debonding is permitted in the entire interfacing area between the skin and flange, `KEYOPT(12) = 6` is set for the [CONTA173](#) elements to allow only an initially bonded contact, and a cohesive zone material (CZM) is assigned to these elements for modeling any subsequent debonding. An area of artificial imperfection is introduced in the skin-flange interface. In this area, the bonding material is completely missing and the standard contact behavior (`KEYOPT(12) = 0`) is assigned to the [CONTA173](#) elements.

**Figure 5.4: Two Contact Pair Definitions (Initial Crack and CZM Area)**

The following two figures show the coordinate systems of the contact and target elements.

**Figure 5.5: Contact Elements**

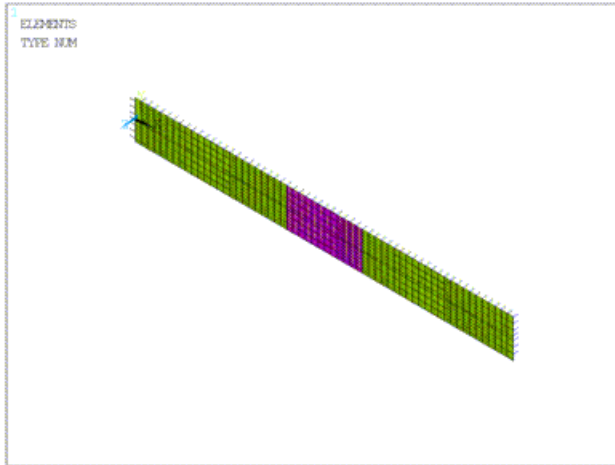
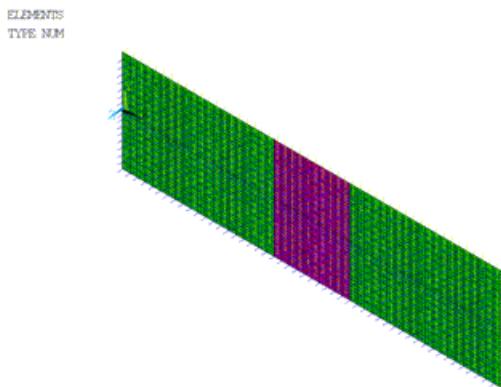


**Figure 5.6: Target Elements**



Please refer to the [Contact Technology Guide](#) for more information on the extensive contact options and modeling procedures.

## 5.4. Material Properties and Section Definitions

### Composite Materials

The properties of the two orthotropic materials used in this problem are summarized in the tables below. They are assumed to be linear elastic and temperature independent. These materials are used to define the layers of the composite materials that make up the skin, stringer flange, and stringer web (refer to the [shell section definitions](#) (p. 83) later in this section).

Linear Elastic Material Number 1	
Young's Modulus in X direction (MPa)	130000
Young's Modulus in Y direction (MPa)	8000
Young's Modulus in Z direction (MPa)	8000



Linear Elastic Material Number 1	
Poisson's Ratio (PRXY, PRYZ, PRXZ)	0.3
Shear Modulus GXY (MPa)	5000
Shear Modulus GYZ (MPa)	2500
Shear Modulus GXZ (MPa)	5000

Linear Elastic Material Number 2	
Young's Modulus in X direction (MPa)	68918
Young's Modulus in Y direction (MPa)	68918
Young's Modulus in Z direction (MPa)	4000
Poisson's Ratio (PRXY, PRYZ, PRXZ)	0.31
Shear Modulus GXY (MPa)	4000
Shear Modulus GYZ (MPa)	3250
Shear Modulus GXZ (MPa)	3250

### Cohesive Zone Model

The properties of the bilinear cohesive zone material model with the CBDE option are summarized in the table below. The **TB** and **TBDATA** commands are used to define this material model. See [Cohesive Zone Material for Contact Elements](#) in the *Material Reference* for details on the definition of cohesive zone models.

Cohesive Zone Model Properties	
Maximum normal contact stress ( $\sigma_{\max}$ )	61
Critical fracture energy for normal separation ( $G_{cn}$ )	0.075
Maximum equivalent tangential contact stress ( $\tau_{\max}$ )	68
Critical fracture energy for tangential slip ( $G_{ct}$ )	0.6
Artificial damping coefficient ( $\eta$ )	5.e-4
Flag for tangential slip under compressive normal contact stress ( $\beta$ )	1

### Shell Section Definitions

Shell sections are used for defining the layup of the composite materials. See the **SECTYPE** and **SECDATA** commands for details on how to define the material, thickness, material orientation, and the number

of integration points of each layer. The following tables summarize the section properties for the skin, the flange, and the web.

<b>Section Properties for Skin</b>			
<b>Layer Thickness</b>	<b>Material</b>	<b>Orientation Angle from local x direction</b>	<b>Integration Points</b>
0.14	1	45	3
0.14	1	-45	3
0.14	1	45	3
0.14	1	-45	3
0.14	1	45	3
0.14	1	-45	3
0.14	1	0	3
0.14	1	0	3
0.14	1	-45	3
0.14	1	45	3
0.14	1	-45	3
0.14	1	45	3
0.14	1	-45	3
0.14	1	45	3

<b>Section Properties for Stringer Flange</b>			
<b>Layer Thickness</b>	<b>Material</b>	<b>Orientation Angle from local x direction</b>	<b>Integration Points</b>
0.36	2	45	3
0.125	1	0	3
0.125	1	0	3
0.36	2	45	3
0.125	1	0	3
0.125	1	0	3
0.36	2	45	3

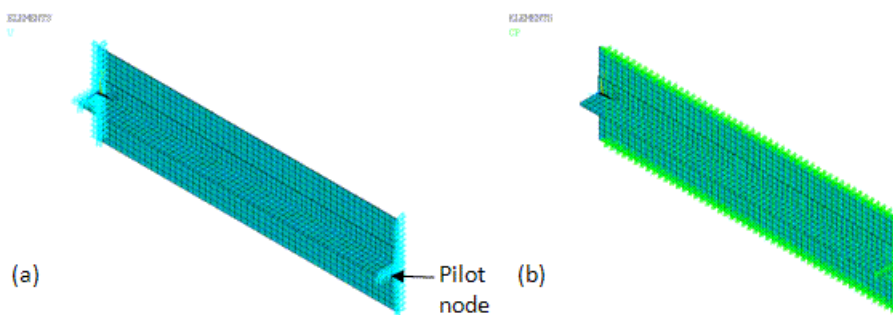
<b>Section Properties for Stringer Web</b>			
<b>Layer Thickness</b>	<b>Material</b>	<b>Orientation Angle from Local x Direction</b>	<b>Integration Points</b>
0.36	2	45	3
0.125	1	0	3
0.125	1	0	3
0.125	1	0	3
0.125	1	0	3
0.36	2	45	3
0.125	1	0	3

Section Properties for Stringer Web			
Layer Thickness	Material	Orientation Angle from Local x Direction	Integration Points
0.125	1	0	3
0.125	1	0	3
0.125	1	0	3
0.36	2	45	3
0.125	1	0	3
0.125	1	0	3
0.125	1	0	3
0.125	1	0	3
0.36	2	45	3
0.125	1	0	3
0.125	1	0	3
0.125	1	0	3
0.125	1	0	3
0.36	2	45	3
0.125	1	0	3
0.125	1	0	3
0.125	1	0	3
0.125	1	0	3
0.36	2	45	3

## 5.5. Boundary Conditions and Loading

One end of the panel is completely constrained, as shown in (a) in the figure below. The other end is assumed rigid and allowed only uniform displacement in the longitudinal (global X) direction. To simulate these conditions, a pilot node is created and the **CP** command is used to couple the X displacement of the pilot node and the X displacement of all other nodes at this end.

**Figure 5.7: Boundary Conditions**



The periodic symmetry requires that any node on one cut boundary of the representative model moves in the same way as the corresponding node at the other cut boundary. The coupling condition (**CP**) is

shown in (b) in the above figure. APDL scripting is adopted for locating coupled nodal pairs. (See [Input Files \(p. 89\)](#) for more details.)

An in-plane compressive force of 76666 N in the negative X direction is applied at the pilot node to induce buckling and debonding.

## 5.6. Analysis and Solution Controls

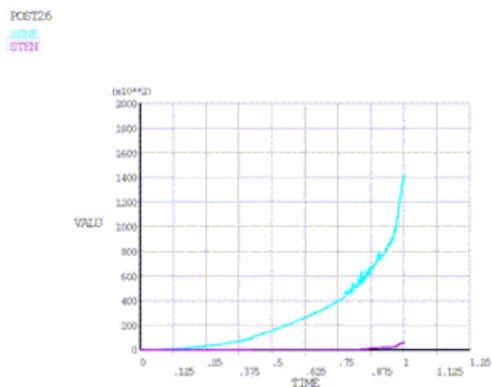
A static analysis is performed. Large deflection effects are included (**NLGEOM**). To achieve a converged solution with this unstable problem, a constant stabilization energy dissipation ratio equal to 0.1 is included (**STABILIZE**).

## 5.7. Results and Discussion

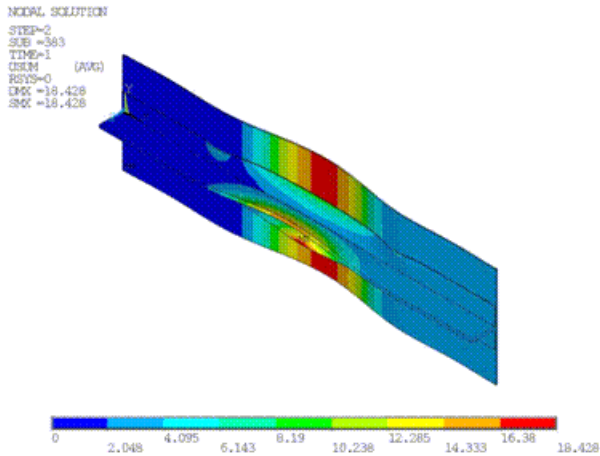
A converged solution is obtained with the help of the [nonlinear stabilization](#) technique.

The energy dissipation ratio is carefully chosen to avoid excessive artificial stabilization energy. As shown in [Figure 5.8: Time History Plot of Strain and Stabilization Energies \(p. 86\)](#), the level of stabilization energy (STEN) is low compared to the total strain energy (SENE) throughout the simulation; therefore, the validity of the simulation results can be guaranteed. The figure also shows that the solution becomes increasingly unstable toward the end of simulation. If you encounter a convergence difficulty, you can increase the energy dissipation ratio to an adequate level; however, validation of the new energy dissipation ratio is required.

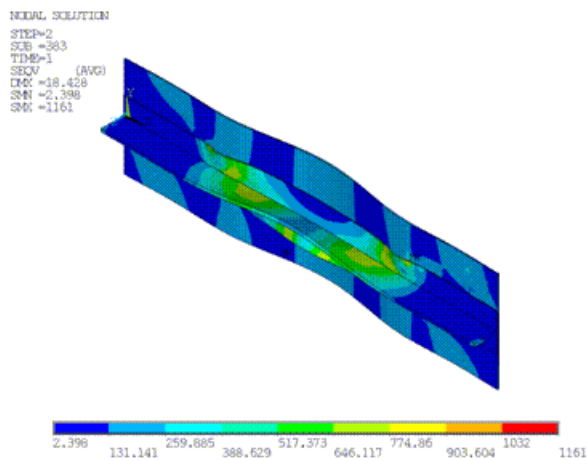
**Figure 5.8: Time History Plot of Strain and Stabilization Energies**



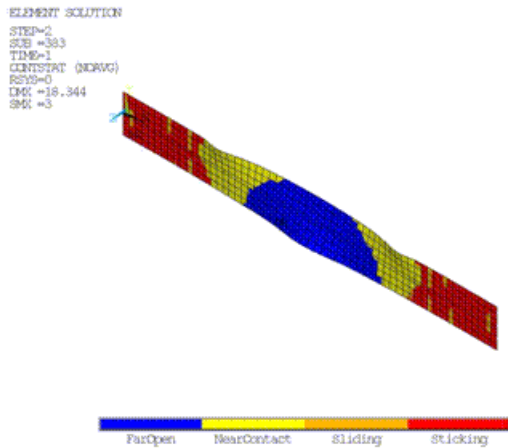
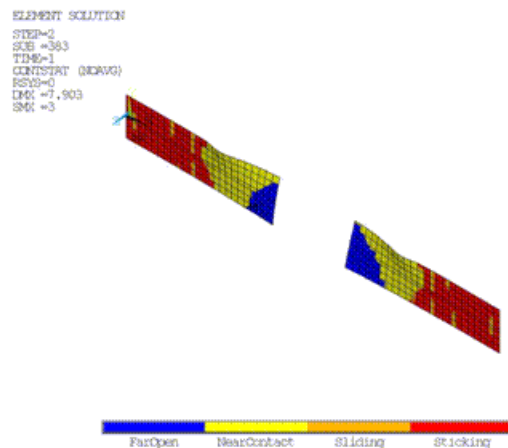
The buckling of the stiffener and the separation of the skin-flange connection are clearly indicated by the final deformed shape, shown below.

**Figure 5.9: Global Deformed Shape (Last Substep)**

This highly nonlinear deformation leads to complex overall stress distributions and a number of significant stress concentrations, as shown below.

**Figure 5.10: Equivalent Stress (Last Substep)**

The following two figures show the final contact status on the skin and the flange. As expected, debonding of the skin-flange interface starts at the edges of the imperfection and propagates further into the bonded areas as the load increases.

**Figure 5.11: Contact Status at Final Substep****Figure 5.12: Contact Status for the Initial Bonded Contact Region**

The figure above shows that the initial sticking status of the large skin-flange interface areas has changed to open or near-contact status at the final converged stage. The structure may undergo catastrophic failure and fail to withstand any further load as debonding progresses. In this case, a transient simulation would be more suitable.

## 5.8. Recommendations

To perform a similar analysis, keep the following recommendations in mind:

- Consider the [SOLSH190](#) element for modeling general layered composite structures, especially where contact, variable thickness, 3-D constitutive relations, and/or thin to thick part transitions are present.
- Choose the proper technology (bonded contact or cohesive zone elements) for simulating interface debonding. In this example, contact with a cohesive zone model simulates the interface debonding. Another option is available for debonding analysis via interface elements ([INTER205](#) in this case). See [Crack Growth Simulation, Interface Delamination, and Fatigue Crack Growth in the Mechanical APDL Fracture Analysis Guide](#); for more information about both methods.
- To ensure a reliable solution, avoid an excessive energy dissipation ratio or mass damping factor in [nonlinear stabilization](#).

---

## 5.9. Input Files

The following files were used in this problem:

- `delamination.dat` -- The input file used in this delamination analysis.
- `delamination.cdb` -- The common database file used in this analysis, called by the `delamination.dat` file.

The files are available in the `td-5` folder. See [Obtaining the Input Files \(p. xxxv\)](#) for more information.





---

## Chapter 6: Thermal-Stress Analysis of a Cooled Turbine Blade

---

This example problem shows how to easily set up and perform a thermal-stress analysis of a cooled turbine blade.

The following features and capabilities are highlighted:

- Use of surface-effect capabilities to simulate convection loading on solid regions.
- Use of one-dimensional fluid flow capabilities to obtain a highly accurate thermal solution for convection loading.

Topics related to this example problem follow:

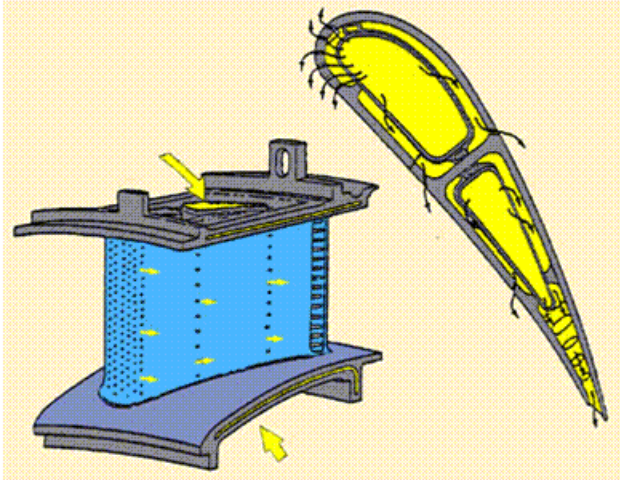
- 6.1. Introduction
- 6.2. Problem Description
- 6.3. Modeling
- 6.4. Material Properties
- 6.5. Boundary Conditions and Loading
- 6.6. Analysis and Solution Controls
- 6.7. Results and Discussion
- 6.8. Recommendations
- 6.9. References
- 6.10. Input Files

### 6.1. Introduction

It is common practice in the turbine industry to cool turbine blades with a fluid flowing through cooling holes. As a result of the thermal gradients setup in the blade, thermal stresses are induced which can lead to failure of the blades.

In a typical thermal-stress analysis, temperatures are calculated and then applied as load conditions for the stress analysis. While it is possible to solve for the temperature using a conjugate heat transfer capability of a computational fluid dynamics (CFD) code, it can significant computational resources. A reduced-order model for CFD, assuming a one-dimensional flow through the holes, can provide a relatively inexpensive solution without much loss in accuracy. Typically, the mass flow rates are known through the cooling holes, and certain empirical correlations are used to estimate the film coefficients for heat transfer from the solid to the fluid.

Because of the proprietary nature of these types of analyses, it was not possible to obtain a realistic model and loading conditions for this analysis from industry sources. A simplified model described in a [NASA report \(p. 102\)](#) is used instead, and an understanding that turbine blade cooling passages and loading conditions are much more complex in realistic models is assumed. For example, the following figure illustrates that the cooling passages in an actual turbine blade (shown in yellow) can join or branch with each other inside the blade, and the coolant is allowed to bleed through the cooling holes and cool the external surface of the blade:

**Figure 6.1: Turbine Blade Cooling Passages**

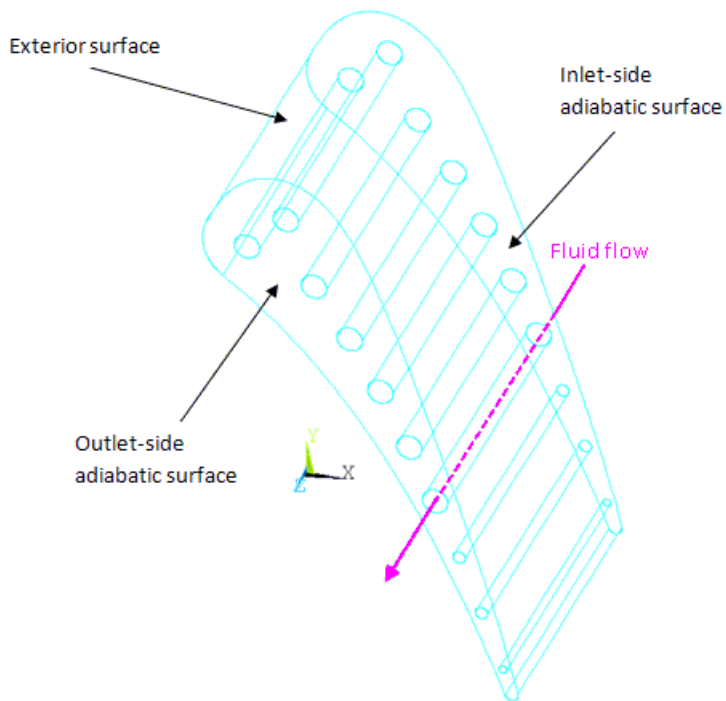
In this problem, however, the cooling holes do not interact with each other and the coolant is confined to the interior of the blade.

For further information, see the following resources:

- [Thermal Analysis Guide](#).
- SURF152 and FLUID116 documentation in the [Element Reference](#).
- SURF152 - 3-D Thermal Surface Effect and FLUID116 - Coupled Thermal-Fluid Pipe in the [Mechanical APDL Theory Reference](#).

## 6.2. Problem Description

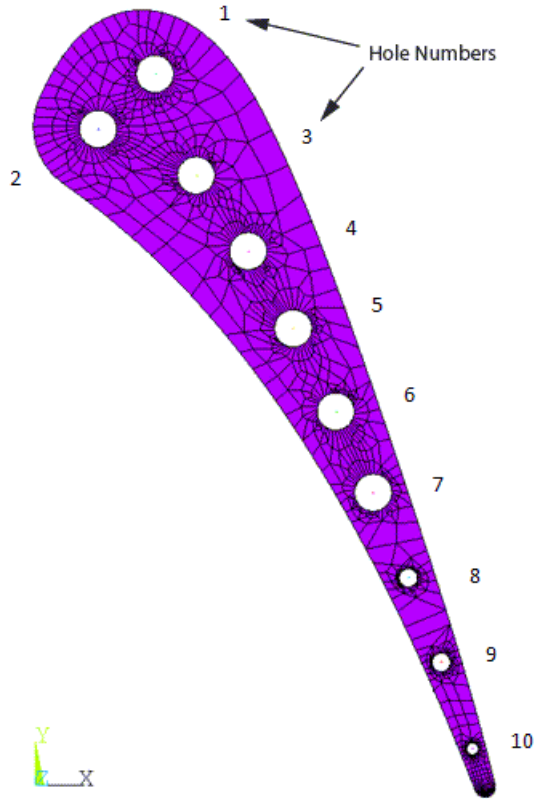
As shown in the following figures, the turbine blade has 10 cooling passages. It is assumed that the external surface is fixed at a constant temperature. The adiabatic surfaces are assumed to be fixed for the stress analysis. The fluid flows through the holes at different rates and cooling occurs primarily via convection. The convection coefficients, inflow temperatures, and mass flow rates are all specified. If the film coefficients are high, the solid loses more heat to the fluid and, accordingly, the fluid temperature rise is higher. If the fluid mass flow rate is higher, the fluid temperature rise is not as high.

**Figure 6.2: Turbine Blade Cooling Passages**

### 6.3. Modeling

The solid and fluid regions of a parasolid model are already meshed, and the model is read into the database (**CDREAD**). The solid region is meshed with **SOLID70** elements, as shown in this figure:

**Figure 6.3: Solid Region Mesh**



The fluid region is meshed with **FLUID116** line elements. The cross-sectional area of each fluid element is set through a real constant. Appropriate components of nodes and elements have also been created in order to facilitate the application of loads. The components can be viewed if necessary (**CMLIST**).

**SURF152** elements are generated on the inside of the holes (**ESURF**); however, these surface-effect elements are not coupled to the fluid elements. The following example input couples the **SURF152** and **FLUID116** elements:

```
keyop,3,5,2           ! Allow 2 extra nodes for SURF152 elements for hole # 1
esel,s,type,,13       ! Select Fluid116 elements corresponding to hole # 1
cm,com116,elem        ! Create a component using the fluid116 elements in each channel
esel,s,type,,3       ! Select SURF152 elements corresponding to hole# 1
cm,com152,elem        ! Create a component using the surf152 elements in each channel
allsel               ! Select all nodes & elements before using MSTOLE
mstole,1,'com152','com116' ! Map component 'com152' to 'com116' using projection method
```

## 6.4. Material Properties

Material properties for the steel blade in MKS units are as follows:

Blade Material Properties	
Thermal Conductivity	43
Young's Modulus	2.00E+11
Poisson's Ratio	0.3
Coefficient of Thermal Expansion	1.08E-5

Fluid properties in MKS units are as follows:

Fluid Material Properties	
Thermal Conductivity	1.00E-16
Specific Heat	2.26E+3

The film coefficients in units of W/(m)<sup>2</sup>(°K) are as follows:

Hole Number	Film Coefficient
1	295.43
2	296.29
3	300.76
4	314.16
5	314.95
6	301.99
7	302.47
8	443.43
9	285.27
10	895.86

## 6.5. Boundary Conditions and Loading

The exterior surface temperature of the solid is maintained at 568° K.

The inflow temperatures and mass flow rates are as follows:

Hole Number	Inflow Temperature (°K)	Mass Flow Rate (kg/sec)
1	348.83	0.228E-01
2	349.32	0.239E-01
3	339.49	0.228E-01
4	342.30	0.243E-01
5	333.99	0.239E-01
6	364.95	0.242E-01
7	343.37	0.232E-01
8	365.41	0.799E-02
9	408.78	0.499E-02
10	453.18	0.253E-02

## 6.6. Analysis and Solution Controls

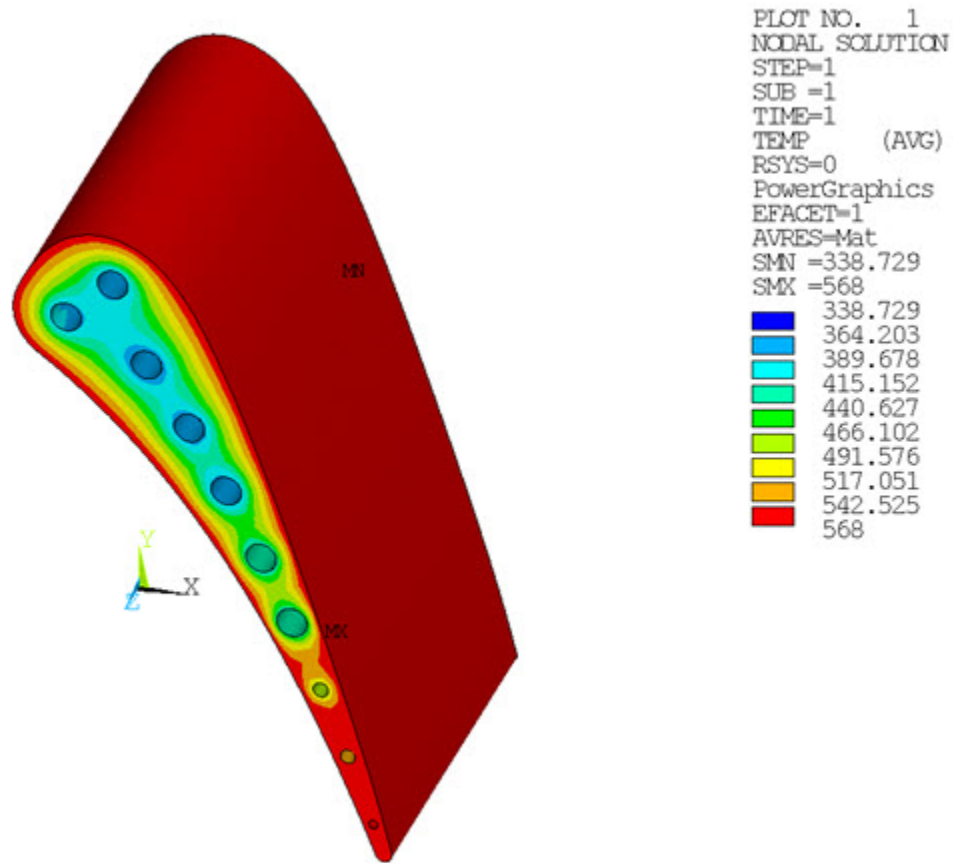
The analysis type is set to static (**ANTYPE,STATIC**) for the thermal analysis .

For the stress analysis, **SOLID70** elements are converted to **SOLID185** elements, and the **SURF152** and **FLUID116** elements are suppressed.

## 6.7. Results and Discussion

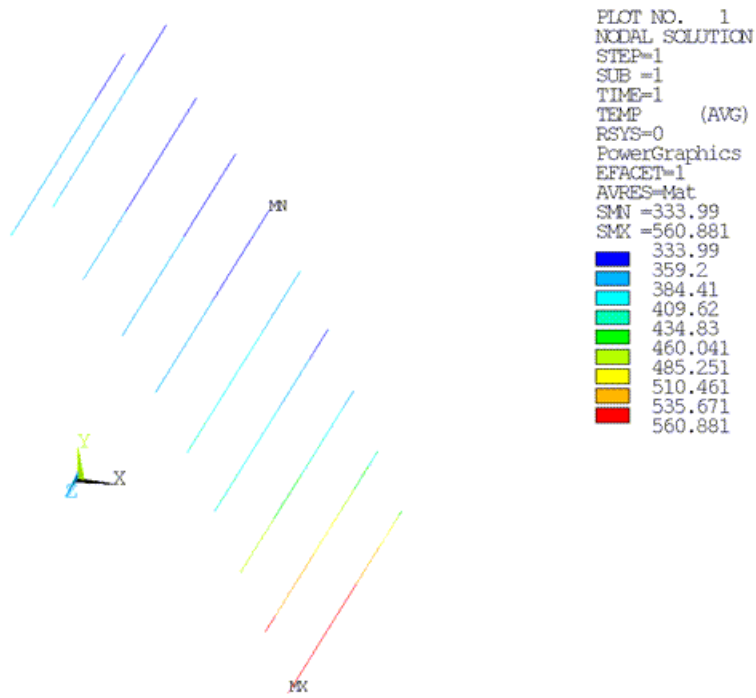
The following figure shows the temperature distribution in the solid region. As expected, the blade is cooler near the holes.

**Figure 6.4: Solid Region Temperature Distribution**

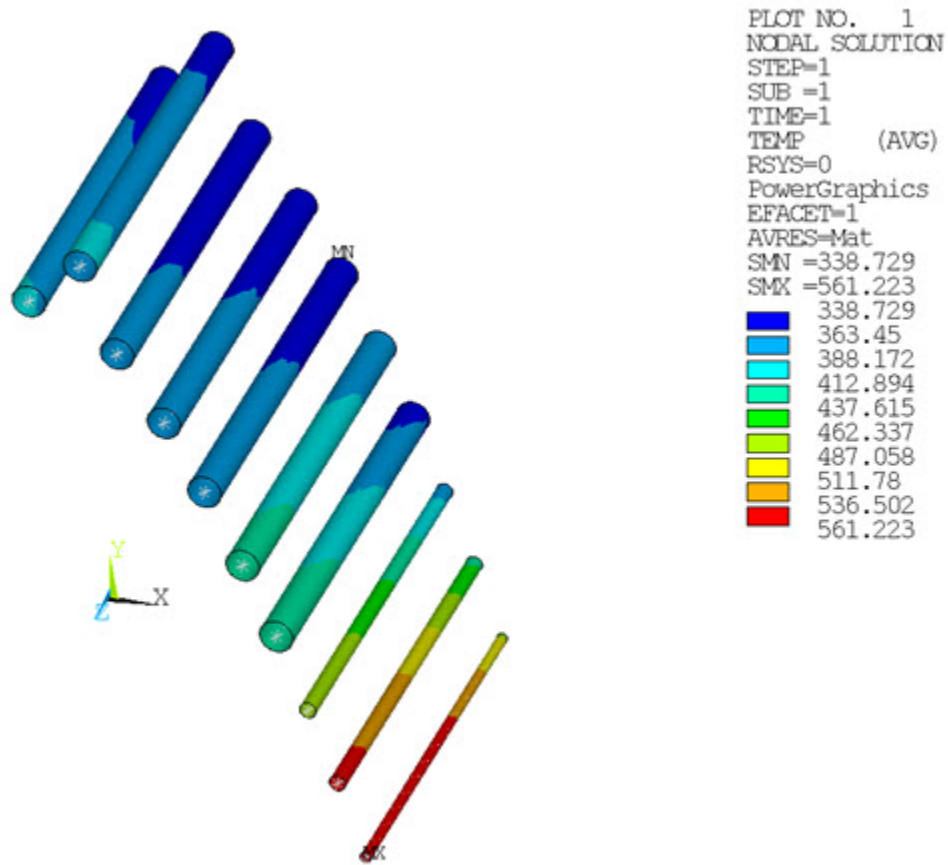


The following two figures show the fluid and solid surface temperatures, respectively. The fluid temperature rises from inlet to outlet. The solid surface temperature shows a similar trend.

Figure 6.5: Fluid Temperatures

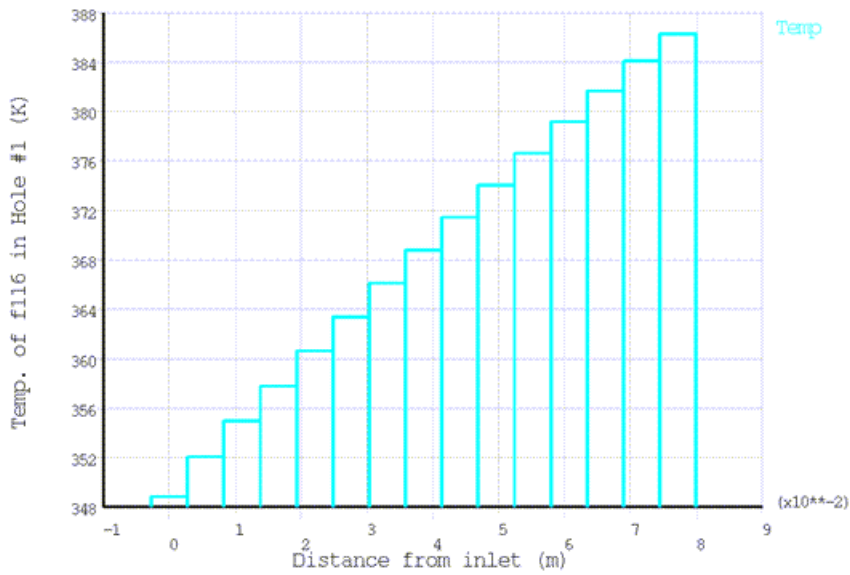
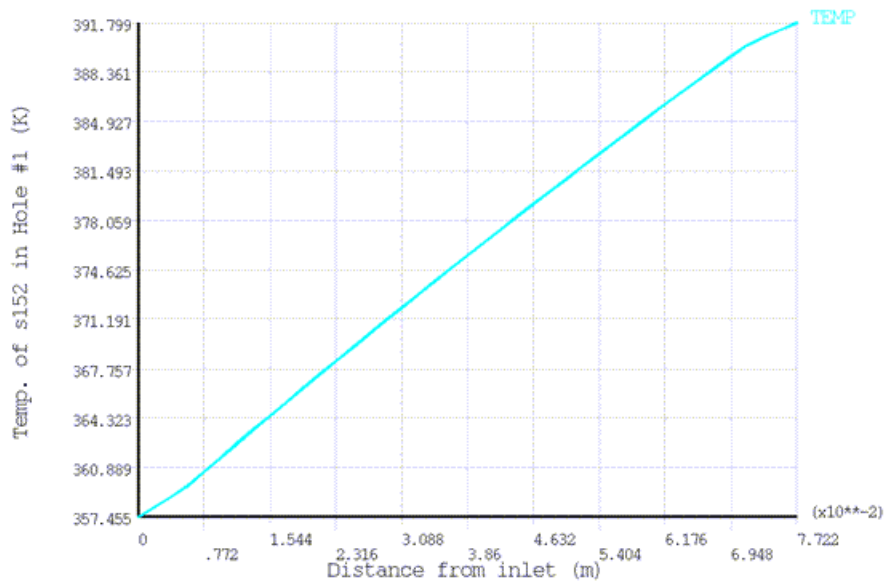


**Figure 6.6: Solid Surface Temperatures**



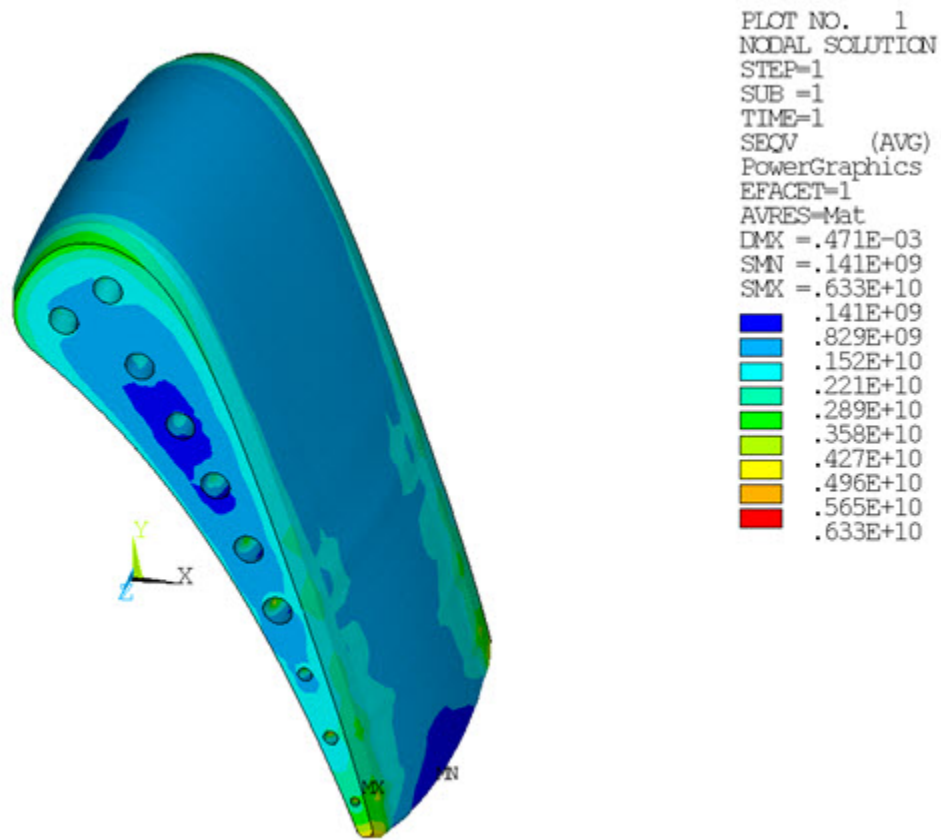
The following two XY plots show the fluid and solid temperatures, respectively, along the fluid path of hole number 1.



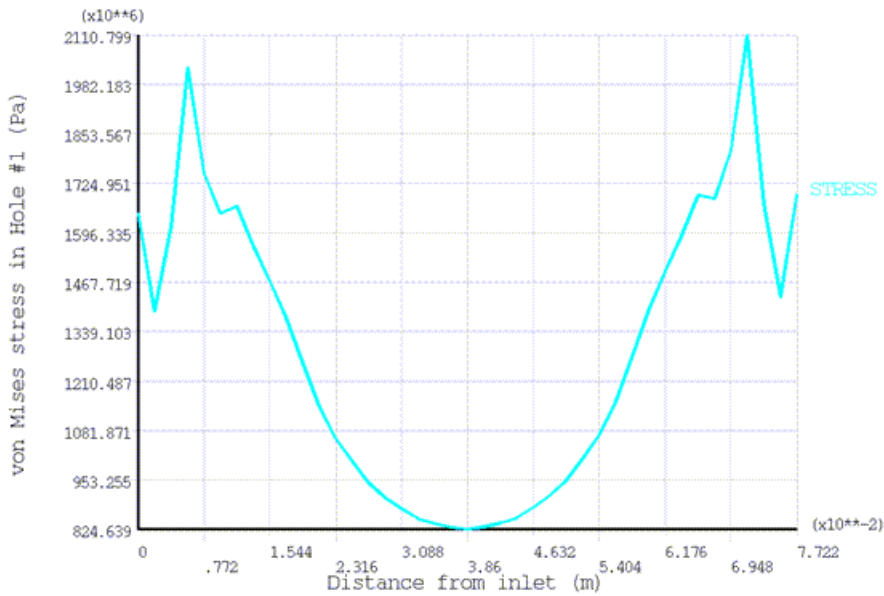
**Figure 6.7: Fluid Temperature Along Path of Hole Number 1****Figure 6.8: Solid Temperature Along Path of Hole Number 1**

The next figure shows the von Mises stresses for the solid region. Maximum stresses occur inside hole number 10.

Figure 6.9: Von Mises Stresses for Solid Region



The following XY plot shows the stress variation in hole 1.

**Figure 6.10: Von Mises Stress Along Path of Hole Number 1**

## 6.8. Recommendations

When performing a similar type of analysis, consider the following hints and recommendations:

- Create surface-effect elements that are much smaller than the fluid elements.

Doing so ensures that all fluid elements are coupled with the surface-effect elements.

- Mapping the surface-effect elements onto the fluid elements (**MSTOLE**) creates the two extra nodes for the surface-effect element.

Three methods are available for mapping: Minimum Centroid Distance, Projection, and Hybrid.

- Use **MSTOLE** with care.

As shown in this analysis, the **MSTOLE** command is applied to each hole. Using a single **MSTOLE** command for multiple holes is inefficient and can lead to incorrect mappings.

- If a hole passage is straight, a single **MSTOLE** command should be sufficient.

If the passage has a serpentine path, several **MSTOLE** commands may be necessary to produce the correct mapping for that hole. For example, if the passage is a U-tube, use the **MSTOLE** command three times.

- When higher-order elements are used for the solid region, the midside nodes on the convecting elements should be dropped.

The lower-order surface-effect element can then be used. Using higher-order surface-effect elements can sometimes lead to an unrealistic temperature distribution.

## 6.9. References

This example problem was based on the following reports:

1. Hylton, L.D. et al. "Analytical and Experimental Evaluation of the Heat Transfer Distribution Over the Surfaces of Turbine Vanes." [NASA CR 168015](#), May 1983.
2. Turner, E. R. et al. "Analytical and Experimental Evaluation of Surface Heat Transfer Distributions with Leading Edge Showerhead Film Cooling." [NASA CR 174827](#), July 1985.
3. Hylton, L. D. et al. "The Effects of Leading Edge and Downstream Film Cooling on Turbine Vane Heat Transfer." [NASA CR 182133](#), Nov. 1988.

## 6.10. Input Files

The following files were used in this problem:

- `turbineblade.dat` -- Input file for the turbine blade thermal-stress analysis.
- `turbinebladestruc.dat` -- Input file for the structural analysis portion of the problem.
- `tblade.cdb` -- The Parasolid file of the meshed turbine blade model (called by `turbineblade.dat`).

The files are available in the `td-6` folder. See [Obtaining the Input Files \(p. xxxv\)](#) for more information.

---

## Chapter 7: Nonlinear Transient Analysis of a Camshaft Assembly

---

This example problem demonstrates the ease with which you can set up and perform an analysis involving both axisymmetric and nonaxisymmetric components. The problem shows how modeling with [general axisymmetric element technology](#) can reduce computational resources significantly while maintaining the same degree of accuracy as a simulation using a full 3-D model.

The following features and capabilities are highlighted:

- Use of general axisymmetric element technology and 3-D element technology in a model consisting of both axisymmetric and nonaxisymmetric parts.
- Generating axisymmetric elements in an assembly having more than one axisymmetric part with multiple axes of symmetry and subjected to nonaxisymmetric loading.
- Use of [contact element](#) technology to couple general axisymmetric elements with standard 3-D elements.
- Use of [joint element](#) technology for applying loading.

Topics related to this example problem follow:

- [7.1. Introduction](#)
- [7.2. Problem Description](#)
- [7.3. Modeling](#)
- [7.4. Material Properties](#)
- [7.5. Boundary Conditions and Loading](#)
- [7.6. Analysis and Solution Controls](#)
- [7.7. Results and Discussion](#)
- [7.8. Recommendations](#)
- [7.9. Input Files](#)

### 7.1. Introduction

Axisymmetric modeling greatly reduces modeling and analysis time when compared to equivalent 3-D modeling. In some cases, however, certain components of the model may be nonaxisymmetric, or the geometry may be axisymmetric but loading is nonaxisymmetric.

#### 7.1.1. Differences Between General Axisymmetric and Harmonic Axisymmetric Elements

[General axisymmetric elements](#) offer much more utility than standard [harmonic axisymmetric elements](#). For example, the elements:

- Introduce the Fourier series into interpolation functions to describe the change of displacements in the circumferential ( $\theta$ ) direction. (The elements can therefore apply to any analysis type, including geometric nonlinear analyses, and can support any load and deformation mode.)
- Can have any axis as the axisymmetric axis.

- Do not require the input of peak loads and multiple load steps for each Fourier term. (Loads can therefore be applied anywhere in 3-D space and only one solve operation is required to obtain the solution.)

With general axisymmetric elements, it is necessary only to define *base elements* (quadrilaterals or triangles) on a *master plane*. (See [General Axisymmetric Element Terminology](#).) The program generates a 3-D mesh (based on a 2-D mesh) on the master plane, after which boundary conditions and loading can be applied at nodes in 3-D space.

## 7.1.2. Where to Find More Information

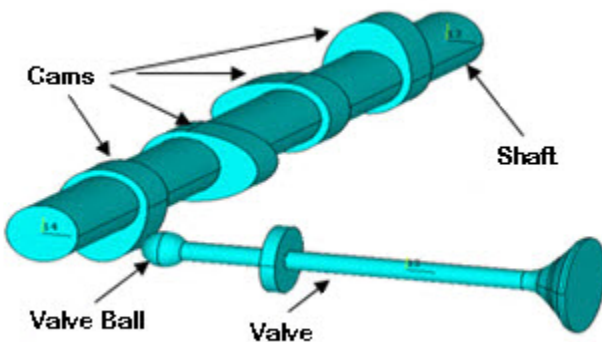
For more information, see the following resources:

- [General Axisymmetric Elements](#) in the *Element Reference*.
- [SOLID272](#) and [SOLID273](#) documentation in the *Element Reference*.
- [SOLID272 - General Axisymmetric Solid with 4 Base Nodes](#) and [SOLID273 - General Axisymmetric Solid with 8 Base Nodes](#) in the *Mechanical APDL Theory Reference*.

## 7.2. Problem Description

The following model is a camshaft assembly, consisting of four cams connected to a shaft:

**Figure 7.1: Full 3-D Geometry of a Camshaft Assembly**



One of the cams is in contact with a valve. As the shaft rotates, the motion of the valve is controlled by the cam, which pushes the valve according to the cam profile.

A transient analysis of the assembly is performed by rotating the shaft for one full rotation.

## 7.3. Modeling

This section covers the following modeling topics:

[7.3.1. Camshaft Modeling](#)

[7.3.2. Contact Modeling](#)

### 7.3.1. Camshaft Modeling

To better demonstrate the benefits of using general axisymmetric elements in models having both axisymmetric and nonaxisymmetric components, two models are analyzed and compared:

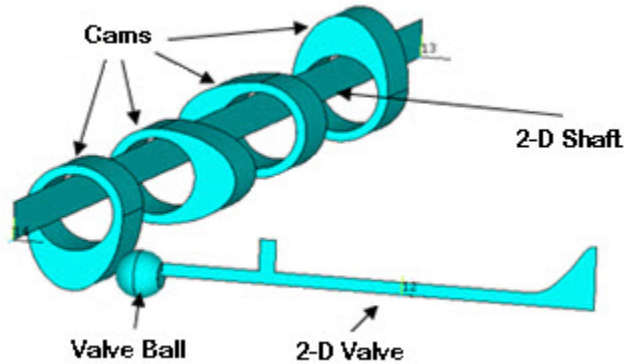
[7.3.1.1. General Axisymmetric Element Model](#)

### 7.3.1.2. Full 3-D Model

#### 7.3.1.1. General Axisymmetric Element Model

Because the shaft and valve components of the camshaft are axisymmetric, but the cams are not, the model is simplified by combining axisymmetric and full 3-D modeling concepts. The following model shows the geometry of the simplified camshaft assembly, which now has a 2-D shaft and a 2-D valve:

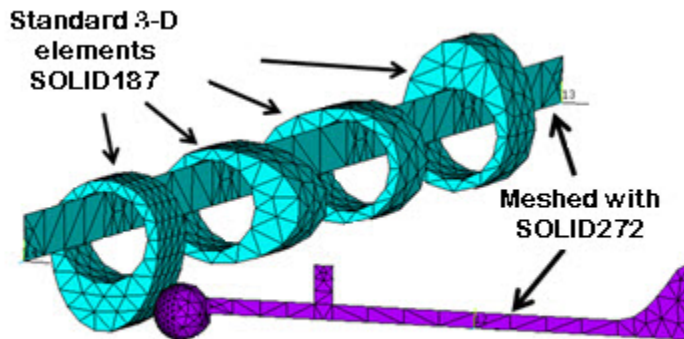
**Figure 7.2: Simplified Geometry of a Camshaft Assembly**



The 2-D valve and 2-D shaft are modeled with general axisymmetric **SOLID272** elements. Because the valve and shaft should not have high localized deformation in the circumferential direction ( $\theta$ ), the number of Fourier nodes is set to 3. (The **SOLID272** element's **KEYOPT(2)** option controls the number of Fourier nodes in the circumferential direction.)

The remaining parts of the assembly such as the valve ball and cams are modeled with standard 3-D elements (**SOLID187** in this case), as shown:

**Figure 7.3: Meshed Camshaft Model Prior to Generating the 3-D Mesh**



Before generating the 3-D mesh (based on the 2-D mesh) on the master plane, axes of symmetry for the valve and shaft are defined separately (via **SECTYPE** and **SECDATA** commands), as follows:

#### Defining valve axis of symmetry:

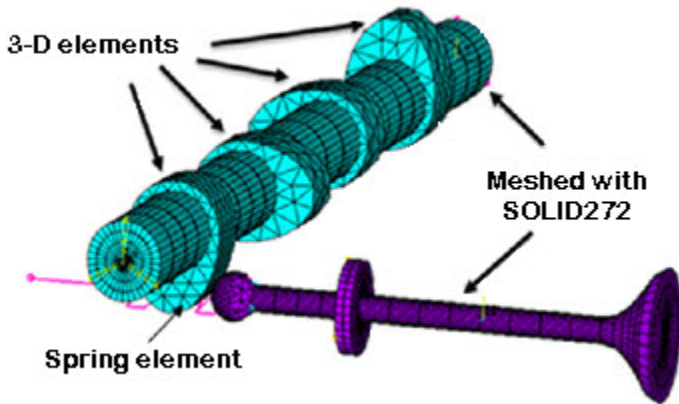
```
SECTYPE,1,AXIS,,valve      ! Here "valve" is a user-specified name
SECDATA,x1,y1,z1,x2,y2,z2 ! Coordinates of two points to define axis of valve
```

#### Defining shaft axis of symmetry:

```
SECTYPE,2,AXIS,,shaft      ! Here "shaft" is a user-specified name
SECDATA,X1,Y1,Z1,X2,Y2,Z2 ! Coordinates of two points to define axis of shaft
```

After defining the axes of symmetry, the **NAXIS** command generates the 3-D mesh, as shown:

**Figure 7.4: Meshed Camshaft Model After Generating the 3-D Mesh**



### 7.3.1.2. Full 3-D Model

This model uses the full camshaft assembly as shown in [Figure 7.1: Full 3-D Geometry of a Camshaft Assembly \(p. 104\)](#). The purpose for analyzing the full 3-D model is simply to better illustrate the efficiency, and to verify the accuracy, of the [general axisymmetric model \(p. 105\)](#).

All components of the assembly are modeled with standard 3-D elements (**SOLID187** in this case), and all boundary conditions, loadings, material properties, solution settings and hardware settings are identical to the general axisymmetric model.

A comparison of the analysis results based on the general axisymmetric model and the full 3-D model appears in [Results and Discussion \(p. 110\)](#).

### 7.3.2. Contact Modeling

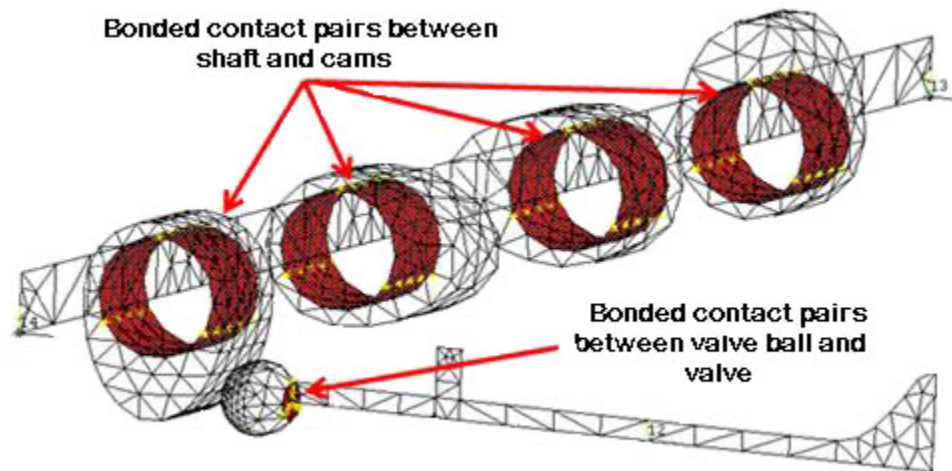
Contact pairs couple general axisymmetric elements with standard 3-D elements. A node-to-surface contact element represents contact between two surfaces by specifying one surface as a group of nodes.

Because the **SOLID272** general axisymmetric element has nodes (and not elements) in 3-D space after the **NAXIS** command has generated the 3-D mesh, the **CONTA175** 2-D / 3-D node-to-surface contact element is a good choice for making contact pairs.

As shown in the following figure, bonded contact pairs with the MPC algorithm are defined to couple the shaft with the cams and the valve ball with the valve. The bonded contact pairs connect the general axisymmetric elements **SOLID272** with the standard 3-D elements **SOLID187**.



Figure 7.5: Bonded Contact Pairs



The following example input shows how to create the contact pairs between the shaft and cams:

```

ET,1,175                ! Define CONTACT175 element
ET,2,170                ! Define TARGET170 element
KEYOPT,1,12,5          ! Bonded Contact
KEYOPT,1,2,2           ! MPC style contact
CMSEL,S,SHAFT_NODES    ! "SHAFT_NODES" is the user-defined nodal component
                        ! which has all the nodes of the shaft that are in
                        ! contact with cams

TYPE,1
REAL,1

! Small loop to create contact elements on selected nodes

NN=0
*GET,NUMN,NODE,,COUNT
*DO,I,1,NUMN
  NN=NDNEXT(NN)
  E,NN                  ! Create contact elements on nodes one by one.
*ENDDO

CMSEL,S,CAM_NODES      ! Select cam nodes and elements at the contact region
ESLN
TYPE,2
REAL,1
ESURF                  ! Create contact pair between shaft and cams

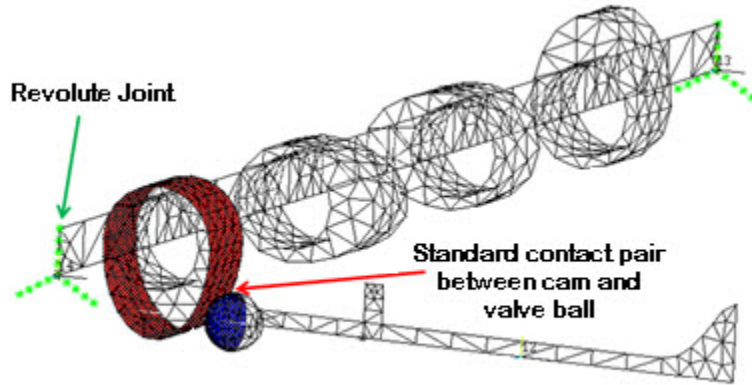
```

Similarly, the other bonded contact pair is defined between the valve and valve ball.

A spring is modeled using the [COMBIN14](#) element (as shown in [Figure 7.4: Meshed Camshaft Model After Generating the 3-D Mesh \(p. 106\)](#)). The spring ensures that the valve maintains contact with the shaft during analysis. One end of the spring is attached to the valve via the bonded contact pair; the other is fixed in all degrees of freedom.

In the following figure, a standard surface-to-surface contact pair using the augmented Lagrangian algorithm is defined between the cam and valve ball. Also shown are two revolute joints (one at either end of the shaft).

**Figure 7.6: Revolute Joints and Surface-to-Surface Contact Pair**



Shown are two revolute joints (one at each end of the shaft) and a surface-to-surface contact pair between the cam and valve ball.

CONTA174 and TARGE170 elements are used in the contact pair between the cam and valve ball. The status of this contact pair changes during analysis.

## 7.4. Material Properties

Material properties considered for the shaft, cams and valve are elastic, as follows:

Shaft, Cams and Valve Material Properties	
Young's Modulus (Nm <sup>-2</sup> )	2.00E + 11
Poisson's Ratio	0.3
Density (Kgm <sup>-3</sup> )	7850

Spring properties are as follows:

Spring Material Properties	
Spring Constant (N / m)	1.00E + .05
Initial Force (N)	1000

## 7.5. Boundary Conditions and Loading

The shaft is allowed to rotate by 360 degrees. Revolute joints are defined at the ends of the shaft with MPC184 joint elements, as shown in Figure 7.6: Revolute Joints and Surface-to-Surface Contact Pair (p. 108). The joints in the shaft allow rotational loading on the shaft to be applied uniformly.

The following example input shows how to create the joint elements:

```
! Creating joint elements

ET,3,184                ! Defines MPC184 element
KEYOPT,3,1,6           ! Selects revolute joint type
KEYOPT,3,4,1           ! Selects Z axis as revolute axis
LOCAL,11,x1,y1,z1...  ! Creates local coordinate system at one end of the shaft
                       ! such that axis of shaft becomes the local z axis
N,99,X1,Y1,Z1         ! Creates node at the centre of the cross section of the shaft at one end.
ET,4,175               ! Defines CONTACT175 element
```

```

ET,5,170                ! Defines TARGET170 element
KEYOPT,4,12,5           ! Bonded Contact
KEYOPT,4,4,2            ! Rigid CERIG style load
KEYOPT,4,2,2            ! MPC style contact
KEYOPT,5,2,1           ! Don't fix the pilot node
KEYOPT,5,4,0            ! Activates all DOF's due to CERIG style
CMSEL,S,SHAFT_NODES    ! Selects all nodes at one end of the shaft.
TYPE,4,
REAL,4

! Creating bonded contact pairs for defining joints

NN=0
*GET,NUMN,NODE,,COUNT
*DO,I,1,NUMN
  NN=NDNEXT(NN)
  E,NN
*ENDDO
ALLSEL,ALL
TYPE,5
REAL,4
TSHAPE,PILOT
EN,999,99                ! Creates target element with pilot node
TSHAPE
CSYS,11
NROT,99
CSYS,0
ALLSEL,ALL
SECTYPE,3,JOINT,REVO,    ! Creates section type for joint elements
SECJOINT,,11,11          ! Defines local coordinate systems at joint element nodes
REAL,3
TYPE,3
SECNUM,3
EN,888,,99                ! Defines body to ground joint (revolute joint)

```

After the joints are defined at both ends of the shaft, loading (360-degree rotation) is applied on the revolute joint at one end of the shaft (via the **DJ** command), as follows:

```

ESEL,S,TYPE,,3          ! Selects joint elements
DJ,ALL,ROTZ,%LOAD%     ! Applies load on joint elements

```

When the shaft rotates, the cams attached to the shaft also rotate. The cam in contact with the valve ball (via the surface-to-surface contact pair) pushes the valve along its axial direction.

The valve moves along its axial direction only and, due to the spring force, it returns to its original position when the cam does not push it further.

To control the movement of the valve, all valve nodes are constrained so that it moves along its axial direction only. To do so, a local coordinate system is defined at the valve such that the local z axis is along the valve axis.

## 7.6. Analysis and Solution Controls

A nonlinear transient analysis is performed on the camshaft assembly.

Large-deflection effects and transient effects are included in the analysis (via **NLGEOM,ON** and **TIMINT** commands, respectively).

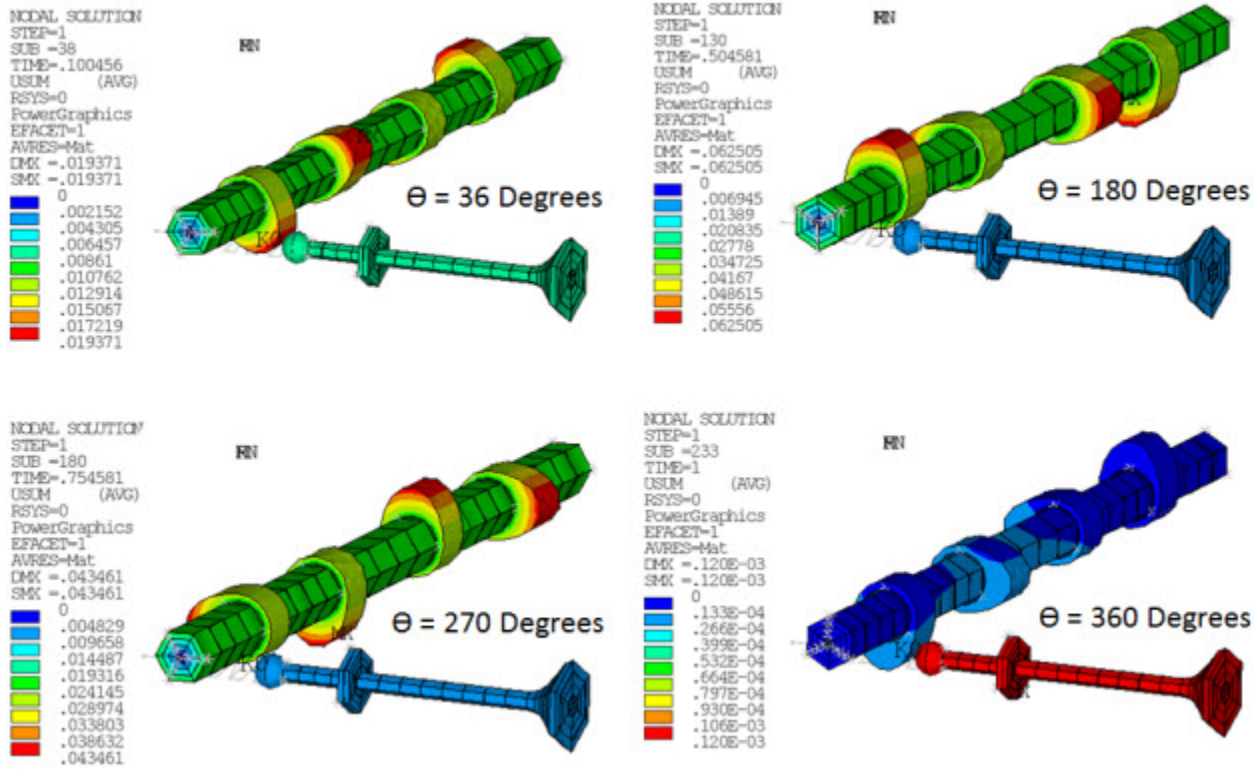
Automatic time stepping is used, with an initial time increment of 3.3 milliseconds.

Solution items are stored in the `.rst` results file for 20 equally spaced time steps.

## 7.7. Results and Discussion

The following illustration shows the deformation plots (USUM) of the camshaft assembly at various time steps during one full rotation ( $\theta = 360$  degrees) of the shaft:

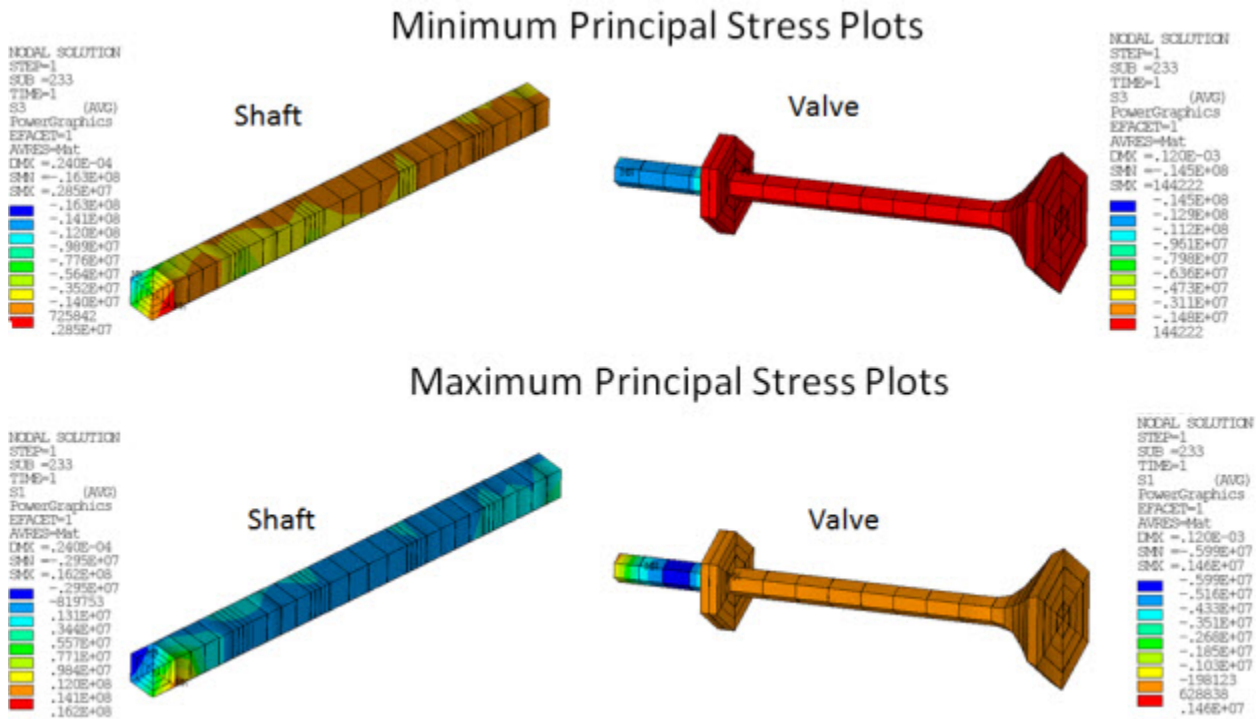
**Figure 7.7: USUM Plots of Camshaft Assembly During Analysis**



The plots show that the valve always remains in touch with the cam throughout the analysis.

The following figure shows the maximum and minimum principal stress plots of the valve and shaft at the end of the analysis:

Figure 7.8: Maximum and Minimum Principal Stress Plots



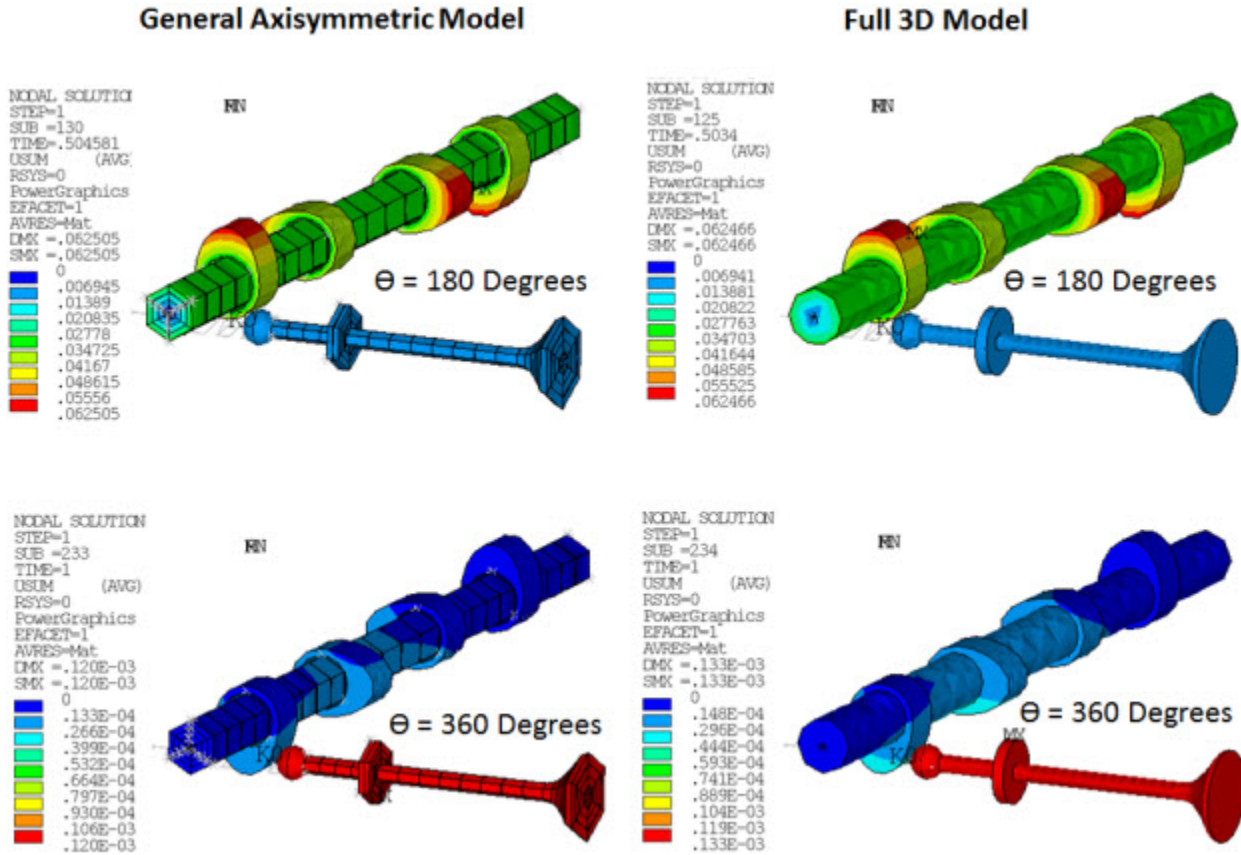
The shaft and valve are subjected to nonaxisymmetric deformation. The results show that general axisymmetric elements are capable of modeling nonlinear general 3-D deformation. The problem also demonstrates how general axisymmetric elements can have any axis as the axisymmetric axis.

### 7.7.1. Results Comparison: General Axisymmetric Model and Full 3-D Model

To verify the accuracy and efficiency of the general axisymmetric element model, a transient analysis was performed on the full 3-D model of the crankshaft assembly. Both the general axisymmetric model and the full 3-D model simulations were run on the same computer. Solution settings for both models were identical.

The following figure shows a direct comparison of results between the full 3-D model and the general axisymmetric model:

**Figure 7.9: Comparison of USUM Plots: General Axisymmetric Model and Full 3-D Model**



In the full 3-D model, the number of degrees of freedom (DOFs) is approximately 300,000. In the general axisymmetric model, the number of DOFs is only 18,000. The smaller number of DOFs in the general axisymmetric model is possible due to the combination of axisymmetric and 3-D modeling.

Following is a comparison of the general axisymmetric model and the full 3-D model in terms of computational efficiency:

FEA Model Details	General Axisymmetric Model [1]	Full 3-D Model [2]
Number of elements in FEA model	4140	8473
Number of elements in valve component	69	1632
Number of elements in shaft component	102	3453
Number of elements in valve ball component	1158	1122
Number of elements in cams	1769	1769
Simulation time	Simulation time for the general axisymmetric model is observed to be approximately 55 percent less than that of the full 3-D model.	

1. In the general axisymmetric model, the valve and shaft components are meshed with general axisymmetric **SOLID272** elements. The remaining components consist of standard 3-D elements.
2. In the full 3-D model, *all* components are meshed with 3-D elements.

The analyses show that using general axisymmetric elements can reduce computational time significantly with no loss of accuracy.

## 7.8. Recommendations

To perform a similar type of analysis, keep the following hints in mind:

- For every axisymmetric part of the assembly, define a separate axis of symmetry (**SECDATA**) *before* generating nodes around the axis of an axisymmetric section (**NAXIS**).
- Choose an appropriate number of Fourier nodes in the circumferential direction to ensure better accuracy and to minimize computational cost.

The KEYOPT (2) option for the general axisymmetric elements (**SOLID272** and **SOLID273**) controls the number of Fourier nodes in the circumferential direction.

If any part of your model which uses general axisymmetric elements does not have high localized deformation in the circumferential direction, the number of Fourier nodes can be set as low as 3.

In the case of high localized deformation in the circumferential direction, the number of Fourier nodes can be set as high as 12, according to your requirements.

- Use a node-to-surface contact pair to connect general axisymmetric elements to standard 3-D elements.

Always create target surfaces on standard 3-D elements.

## 7.9. Input Files

The following files were used in this problem:

- `camshaft_assembly.inp` -- Input file for the transient analysis (used for both the general axisymmetric and the full 3-D models)
- `general_axisymmetric_model.cdb` -- The common database file for the general axisymmetric model (called by the `camshaft_assembly.inp` file).
- `full_3d_model.cdb` -- The common database file for the full 3-D model (called by the `camshaft_assembly.inp` file).

The files are available in the `td-7` folder. See [Obtaining the Input Files \(p. xxxv\)](#) for more information.





---

## Chapter 8: Nuclear Piping System Under Seismic Loading

---

This example demonstrates the advantages of elbow element technology over traditional shell and pipe element technology for modeling pipe bends in a typical nuclear piping system.

Topics related to this example problem follow:

- 8.1. Introduction
- 8.2. Problem Description
- 8.3. Modeling
- 8.4. Material Properties
- 8.5. Boundary Conditions and Loading
- 8.6. Analysis and Solution Controls
- 8.7. Results and Discussion
- 8.8. Recommendations
- 8.9. References
- 8.10. Input Files

### 8.1. Introduction

Nuclear piping systems under seismic loading are typically analyzed in two stages:

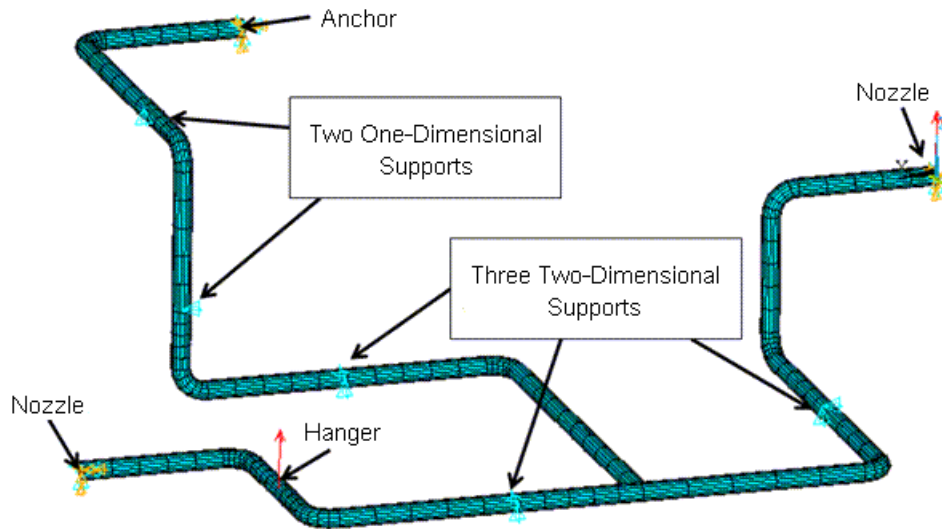
1. A transient analysis is performed with a simplified model of the entire piping system to obtain the global response of the system.
2. Using the global response as the imposed boundary condition, nonlinear static analyses are performed separately on critical parts to investigate local stress and strain responses over time. The critical parts are typically modeled with refined 3-D elements.

This conventional global-local analysis method requires the conversion of results between the global and local models and is usually time-consuming and computationally expensive.

Compared to the straight-pipe segments, curved-pipe bends (elbows) have much greater flexibility and can therefore develop more significant deformation and stresses. ANSYS, Inc. elbow element technology offers a simple 1-D geometry (similar to a standard pipe element) and excellent accuracy (matching that of a 3-D shell element). The elbow can be used directly in both global and local simulation to avoid any cumbersome global-to-local model and boundary-condition conversion.

### 8.2. Problem Description

The problem involves a large-scale nuclear piping system consisting of straight pipes, nine elbows, and a tee:

**Figure 8.1: Large-Scale Nuclear Piping System**

Not shown in the figure is a 1000 kg mass representing a valve.

The system is supported by nozzles, an anchor, three two-directional supports, a horizontal support, a vertical support and a spring hanger [1]. The following analyses are performed on the piping system to study both global and local responses of the system when subjected to seismic loading:

- **Modal analysis** of the entire piping system
- **Nonlinear static analysis** of one of the critical elbows of the piping system using elbow element technology
- **Nonlinear static analysis** of one of the critical elbows of the piping system using shell element technology

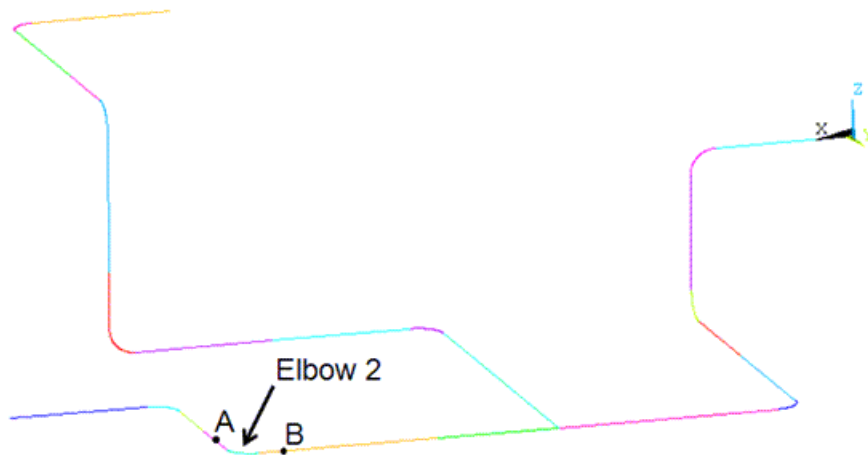
## 8.3. Modeling

Three models are prepared for this problem:

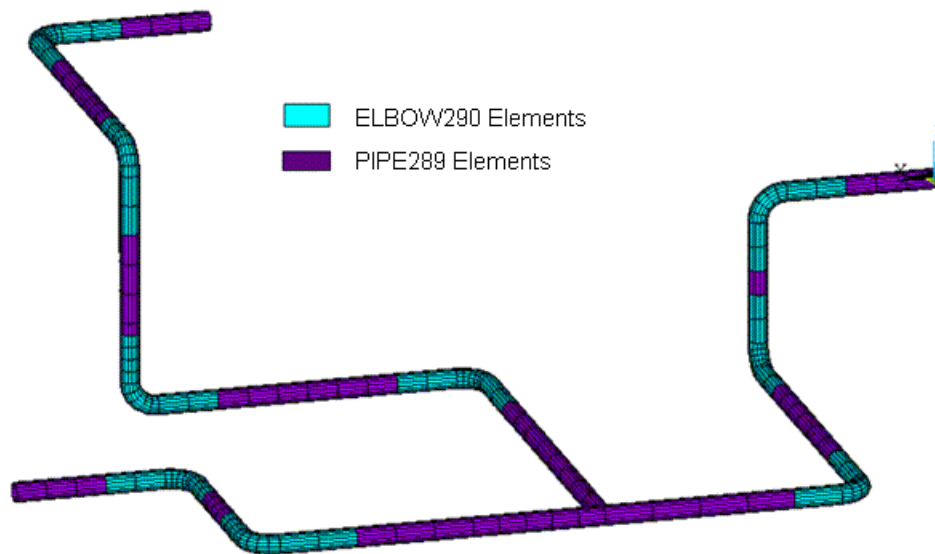
- 8.3.1. Global Nuclear Piping System Model
- 8.3.2. Local Elbow Model Meshed with ELBOW290 Elements
- 8.3.3. Local Elbow Model Meshed with SHELL281 Elements

### 8.3.1. Global Nuclear Piping System Model

The entire piping system is examined in this model. Initially, a line diagram of the piping system is created:

**Figure 8.2: Entire Nuclear Piping System Line Diagram**

Straight segments are meshed with PIPE289 elements, and elbows are meshed with ELBOW290 elements:

**Figure 8.3: Entire Nuclear Piping System Meshed with Pipe and Elbow Elements**

An ELBOW290 element key option controls the level of accuracy in cross-sectional deformation. In this case, KEYOPT(2) = 4 allows general section deformation, including nonuniform radial expansion, ovalization, and warping.

The average diameter and average thickness of the pipes are assigned to ELBOW290 and PIPE289 elements (via SECDATA and SECTYPE commands), as follows:

```
SECTYPE,1,PIPE
SECDATA,Do,T      ! Where Do is the outer diameter and T is thickness of the pipe
                  ! In this example, Do = 219.2 mm and T = 10.38 mm
SECNUM,1
```

Subsequently, to create necessary transition zones from the elbows to straight-pipe segments, the **ELBOW** command automatically converts a few **PIPE289** elements adjacent to the elbows into **ELBOW290** elements, as follows:

```
ELBOW,ON,,,
```

Elbow and pipe elements must have the same pipe section ID for the pipe-to-elbow transition to occur.

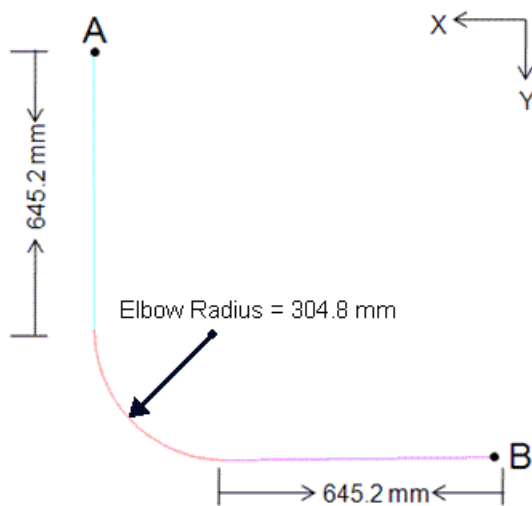
A **modal analysis** is performed on the global model to obtain the fundamental natural frequency. The result is compared to the experimental result given in [1].

### 8.3.2. Local Elbow Model Meshed with **ELBOW290** Elements

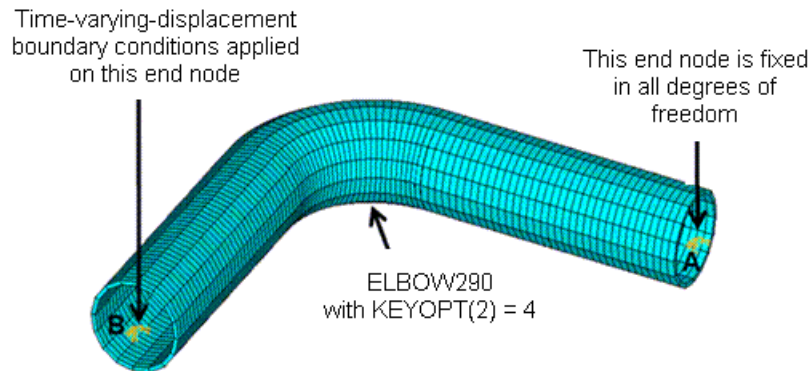
The local nonlinear analysis is focused on the elbow between locations labeled A and B in [Figure 8.2: Entire Nuclear Piping System Line Diagram](#) (p. 117).

Following is the line diagram of this elbow model:

**Figure 8.4: Elbow Model Line Diagram**



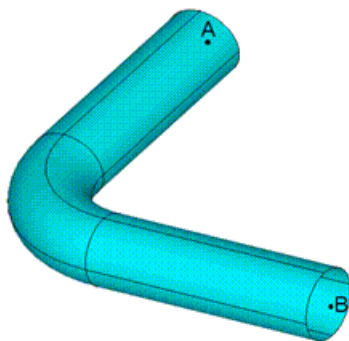
The model has branches that are 645.2 mm long and an elbow with a radius of 304.8 mm (for a total centerline length of 950 mm). The diameter of the pipe is 219.2 mm and the wall thickness is 10.38 mm. The elbow is meshed with **ELBOW290** elements:

**Figure 8.5: Elbow Model Meshed with ELBOW290 Elements**

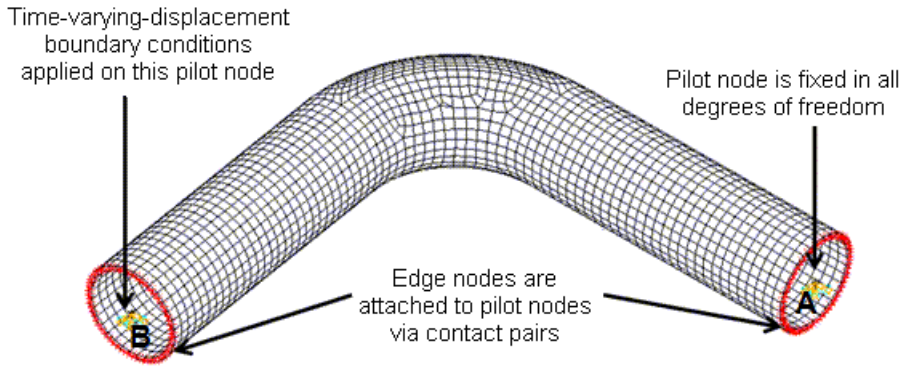
Time-varying-displacement boundary conditions, extracted from a [transient analysis](#) of the entire piping system model under seismic loading, are applied at one end of the model. A [nonlinear static analysis](#) using the [Chaboche material model](#) is performed on this elbow model to obtain the stress and strain response over time.

### 8.3.3. Local Elbow Model Meshed with SHELL281 Elements

An equivalent local 3-D model of the same elbow using [SHELL281](#) elements is used to generate a reference solution. The 3-D surface representation of the elbow and the refined [SHELL281](#) mesh are shown respectively in the following figures:

**Figure 8.6: Midsurface Geometry of Elbow (SHELL281 Model)**

**Figure 8.7: Elbow Model Meshed with SHELL281 Elements**



Material properties and loadings considered in this model are identical to those of the local [ELBOW290](#) model. A conversion of boundary conditions from the global line mesh to the local 3-D shell mesh is necessary, however. Time varying displacement boundary conditions are applied to the pilot node at one end of the model. The pilot nodes are coupled with edge nodes at both ends via contact elements as shown in [Figure 8.7: Elbow Model Meshed with SHELL281 Elements \(p. 120\)](#).

### 8.4. Material Properties

A multilinear [kinematic hardening](#) material model is used in the analysis of the entire nuclear piping system (for both modal and transient analyses).

Following are the material properties for the entire system:

<b>Nuclear Piping System Material Properties</b>	
Young's Modulus (MPa)	1.89E+05
Poisson's Ratio	0.3
<b>Multilinear Kinematic Hardening Material Model</b>	
Strain	Stress (MPa)
0.00146	275.942
0.02184	280.14
0.02701	312.55
0.05	379.34

A [Chaboche nonlinear](#) kinematic hardening material model is used in the nonlinear static analysis of the elbow model (for both the [ELBOW290](#) and [SHELL281](#) models).

Following are the material properties for the elbow model:

<b>Elbow Model Material Properties</b>	
Young's Modulus (MPa)	2.03E+05
Poisson's Ratio	0.3
<b>Chaboche Nonlinear Kinematic Hardening Material Model</b>	
Yield Stress ( $\sigma_y$ )	275.92 MPa

<b>Elbow Model Material Properties</b>	
Material Constant for First Kinematic Model (c1)	65191.29 MPa
Material Constant for First Kinematic Model ( $\gamma_1$ )	1044.83
Material Constant for Second Kinematic Model (c2)	14909.91 MPa
Material Constant for Second Kinematic Model ( $\gamma_2$ )	177.06
Material Constant for Third Kinematic Model (c3)	1653.9 MPa
Material Constant for Third Kinematic Model ( $\gamma_3$ )	2.2

The mass density of the pipe material for all models is 12388 kg / m<sup>3</sup>. All material properties shown are taken from Nie (p. 126).

## 8.5. Boundary Conditions and Loading

Boundary conditions for the three models follow:

8.5.1. Global Nuclear Piping System Model

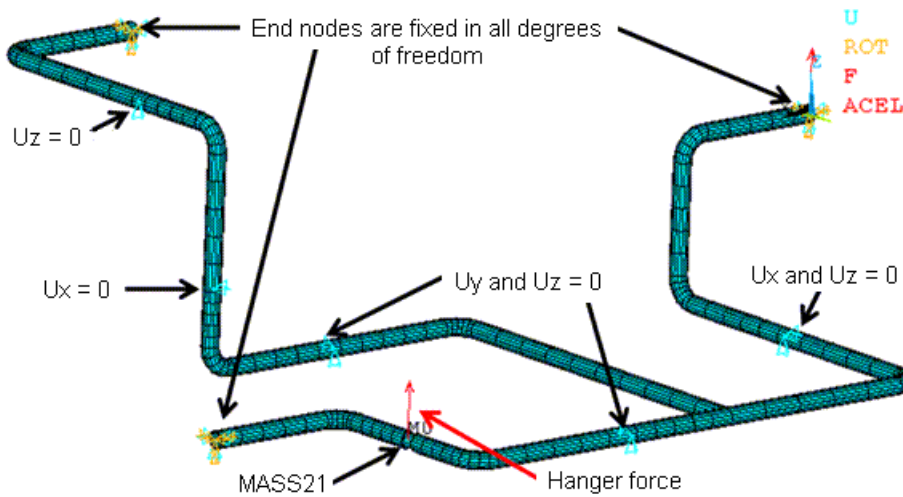
8.5.2. Local Elbow Model Meshed with ELBOW290 Elements

8.5.3. Local Elbow Model Meshed with SHELL281 Elements

### 8.5.1. Global Nuclear Piping System Model

To simulate various types of supports in the system, the following boundary conditions and equivalent loading are applied:

- To simulate the nozzles and anchor supports, the nodes at all three ends of the system are completely constrained.
- To simulate the three two-directional supports, three nodes are constrained in either the Y and Z directions or the X and Z directions.
- To simulate a horizontal support and a vertical support, two nodes are constrained respectively in the X and Z directions.
- A spring hanger support is replaced by an equivalent concentrated force.
- A 1000 kg mass representing a valve is simulated by a **MASS21** element.

**Figure 8.8: Boundary Conditions of Entire Nuclear Piping System**

Internal pressure and gravity load are applied in the model as follows:

```
SFE,ALL,1,PRES,,10.7 ! P (internal pressure) = 10.7 MPa
ACEL,, ,9.8 ! G = 9.8 m/sec^2
```

### 8.5.2. Local Elbow Model Meshed with ELBOW290 Elements

One end of this model is fixed in all degree of freedoms and time varying displacements, representing the seismic loading condition, are applied at the other end of the elbow model, as shown in [Figure 8.5: Elbow Model Meshed with ELBOW290 Elements](#) (p. 119).

Cross-section deformation is not allowed at both ends (**D**). The [input file](#) (p. 126) for this model shows the time-varying-displacement data.

Internal pressure and gravity loads are identical to those applied in the [global model](#) (p. 121).

### 8.5.3. Local Elbow Model Meshed with SHELL281 Elements

Boundary conditions for this model are identical to those applied on the [local elbow model](#) (p. 122) meshed with [ELBOW290](#) elements. In this model, however, the method for applying displacement-time-history data is different.

Pilot nodes are created both ends of the model, at the center of the cross-sections. The pilot nodes are coupled with the edge nodes of the cross-sections via contact pairs. One pilot node is fixed in all degrees of freedoms and time-varying-displacement data are applied at the other pilot node, as shown in [Figure 8.7: Elbow Model Meshed with SHELL281 Elements](#) (p. 120).

## 8.6. Analysis and Solution Controls

This example problem involves the following analyses:

- 8.6.1. Modal Analysis of the Global Piping System Model
- 8.6.2. Nonlinear Static Analyses of the Local Elbow Models



## 8.6.1. Modal Analysis of the Global Piping System Model

A prestressed (**PSTRES**) modal analysis is conducted on the global model.

Initially, a large-deflection (**NLGEOM**) static analysis is performed, followed by the prestressed modal analysis (**PSOLVE**). The Block Lanczos solver (**MODOPT**) extracts the first fundamental mode.

```
PSTRESS,ON
MODOPT,LANB,1
MXPAND,1,,0
PSOLVE,EIGLANB
```

To examine the effect of the prestressed analysis, a modal analysis *without* prestress effects is performed on the same model, as follows:

```
MODOPT,LANB,1
MXPAND,1,,0
SOLVE
```

## 8.6.2. Nonlinear Static Analyses of the Local Elbow Models

A nonlinear static analysis is performed on both of the local elbow (**ELBOW290** and **SHELL281**) models.

A constant time increment of 5 ms is specified to obtain the stress and strain response over a period of 20 seconds.

Large-deflection effects are included.

Results are stored (in the RST file) for all substeps.

## 8.7. Results and Discussion

This section examines the results of both the modal analysis of the global piping system and the nonlinear static analysis of the local elbows:

[8.7.1. Global Piping System: Modal Analysis Results](#)

[8.7.2. Local Elbow Models: Nonlinear Static Analysis Results](#)

### 8.7.1. Global Piping System: Modal Analysis Results

Following is a comparison of the fundamental natural frequency of entire piping system with the expected experimental result [1]:

Fundamental Frequency of Entire Nuclear Piping System		
Modal Analysis Results		Measured Value in Experiment
<i>With Prestress Effects</i>	<i>Without Prestress Effects</i>	
6.3 Hz	6 Hz	5.9 - 6.3 Hz

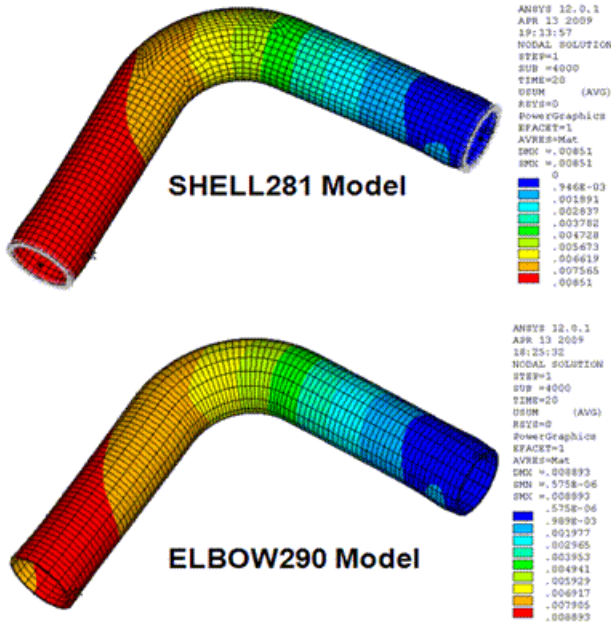
The close agreement between the simulation and the expected results validates the methods used in this analysis:

- Using **PIPE289** and **ELBOW290** separately for the straight and curved segments, respectively.
- Defining transition zones (**ELBOW**) for building the global piping system model.

## 8.7.2. Local Elbow Models: Nonlinear Static Analysis Results

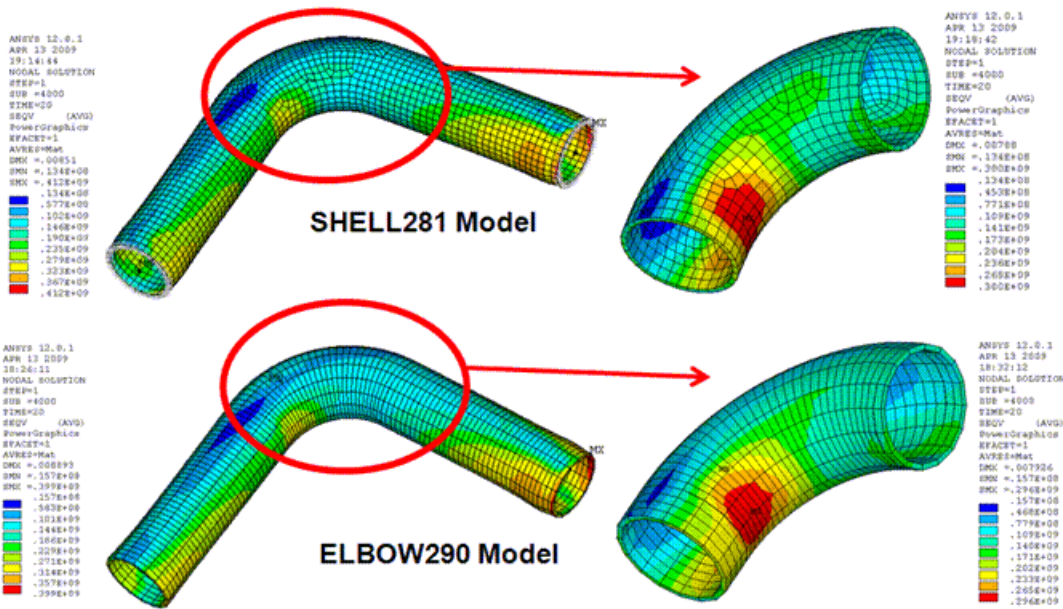
The final deformed shape of the local ELBOW290 model matches closely with that of the local SHELL281 model, as shown:

Figure 8.9: USUM Plot Comparison: Local ELBOW290 and SHELL281 Models

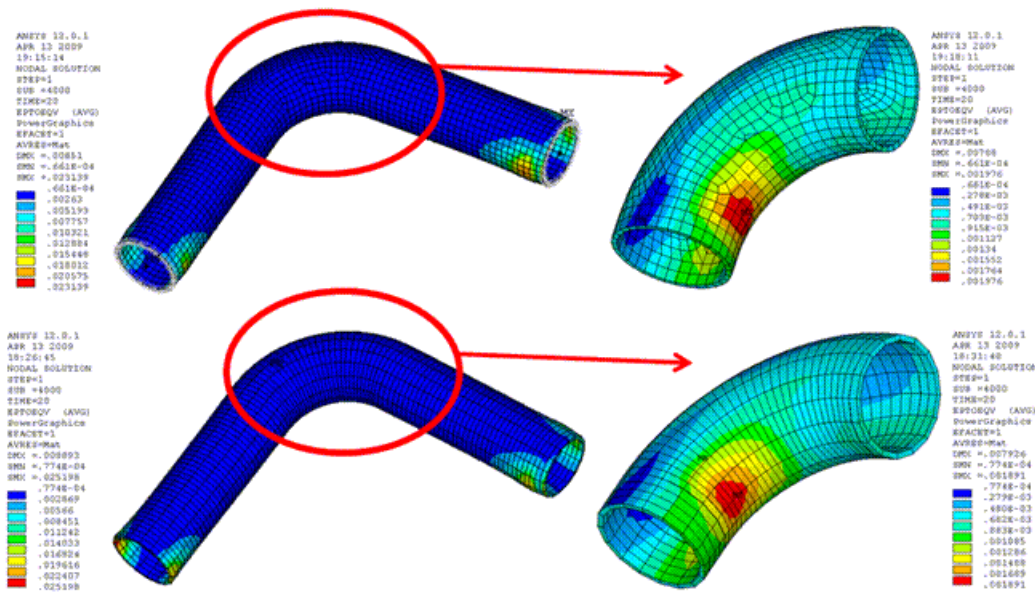


Von Mises stress and total mechanical strain for both models are shown respectively in the following figures:

Figure 8.10: Von Mises Stress Comparison: Local ELBOW290 and SHELL281 Models



**Figure 8.11: Von Mises Strain Comparison: Local ELBOW290 and SHELL281 Models**



Again, the close agreement between the stress and strain results from the two models is apparent.

Following is a comparison of the local [ELBOW290](#) and [SHELL281](#) elbow models in terms of computational efficiency:

	<b>ELBOW290 Local Elbow Model</b>	<b>SHELL281 Local Elbow Model</b>
Number of elements in the FEA model	100	3009
Simulation time required	Simulation time for the <a href="#">ELBOW290</a> model is observed to be approximately 53 percent less than that of the <a href="#">SHELL281</a> model	
Disk usage	Disk space usage for the <a href="#">ELBOW290</a> model is observed to be approximately 64 percent less than that of the <a href="#">SHELL281</a> model.	

While offering simplicity for line-based modeling, the [ELBOW290](#) element is capable of producing an accurate global response as well as detailed local solutions for a piping system. [ELBOW290](#) is ideal for modeling bends in the pipe systems or straight-pipe segments that may undergo significant cross-section deformation.

## 8.8. Recommendations

To perform a similar type of analysis, consider the following hints and recommendations:

- Results accuracy increases as the number of Fourier terms specified increases.

Computational costs also rise sharply as the number of Fourier terms increases.

The [ELBOW290](#) element's KEYOPT(2) setting controls the number of Fourier terms. See the element documentation for more information about specifying an appropriate number of Fourier terms.

- To minimize computational costs, use the [PIPE289](#) element to model straight-pipe segments.

If a straight-pipe segment may be subjected to large cross-sectional deformation, the [ELBOW290](#) element is a better choice.

- Transition zones ([ELBOW](#)) between the curved [ELBOW290](#) and straight [PIPE289](#) elements are generally desirable for obtaining a smooth solution.
- Because the [ELBOW290](#) element is based on shell theory, its applicability is limited to pipes with thin to moderately thick walls.

## 8.9. References

The following references are used in this example problem:

1. Nie, J. et al. "Nonlinear Seismic Correlation Analysis of the JNES/NUPEC Large-Scale Piping System Tests." 2008 ASME Pressure Vessels and Piping Division Conference. PVP2008 Proceedings. CD-ROM. ASME. 2008.

## 8.10. Input Files

The following input files are used in this problem:

- `nuclear_piping_system.dat` -- Combined input file for performing the modal and static analyses of the nuclear piping system.
- `input_file_for_time_varying_displacement_boundary_conditions.dat` -- The input file for the time-varying-displacement boundary conditions.
- `modal_analysis_whole_nuclear_piping_system.cdb` -- The common database file for the modal analysis on the entire piping system.
- `static_analysis_elbow_model_with_ELBOW290.cdb` -- The common database file for the non-linear static analysis of the elbow model using the [ELBOW290](#) element.
- `static_analysis_elbow_model_with_SHELL281.cdb` -- The common database file for the non-linear static analysis of the elbow model using the [SHELL281](#) element.

The files are available in the `td-8` folder. See [Obtaining the Input Files \(p. xxxv\)](#) for more information.

---

## Chapter 9: Reliability Study of a Composite Overwrapped Pressure Vessel

---

This example problem is a reliability study of a composite overwrapped pressure vessel (COPV). The model uses reinforcing fibers in a layered composite. A finite-element simulation of a COPV is performed first to gain insight into its mechanical behaviors, then simulation results are processed using failure analysis to determine the most vulnerable layer. The problem generates linearized stress output for pressure-vessel design optimization and code compliance.

Topics related to this example problem follow:

- 9.1. Introduction
- 9.2. Problem Description
- 9.3. Modeling
- 9.4. Material Properties
- 9.5. Boundary Conditions and Loading
- 9.6. Analysis and Solution Controls
- 9.7. Results and Discussion
- 9.8. Recommendations
- 9.9. References
- 9.10. Input Files

### 9.1. Introduction

Composite overwrapped pressure vessels (COPVs) are manufactured by filament winding, a process involving a continuous application of high-stiffness fibers over a thin metal shell (liner). For their excellent corrosion resistance and high strength-to-mass ratios, COPVs are commonly used for critical applications (such as deep-sea and space missions).

A typical COPV usually contains numerous fiber-reinforced layers and exhibits a complex overall material orthotropy. The material properties may undergo significant changes due to fiber realignment when the COPV is under intense operational load. The material properties and their load-dependent variations are difficult to obtain by experimental means; therefore, finite-element simulations are often conducted by designers and researchers to gain insight into the mechanical behaviors of COPVs.

Further processing of the simulation result is often performed to:

- assess the reliability of the COPV,
- optimize its design, or
- ensure compliance to codes and standards.

### 9.2. Problem Description

A COPV is subjected to a uniform internal pressure and a temperature field with a constant through-the-wall gradient.

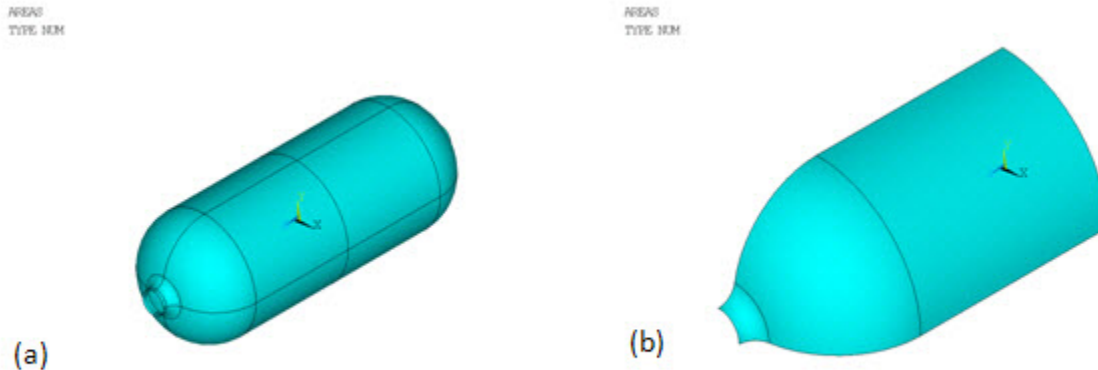
A nonlinear static analysis is performed to obtain stress and strain results of all layers under large-deformation conditions.

Failure criteria (FC) analysis and stress linearization are conducted based on the simulation results.

### 9.3. Modeling

The pressure vessel consists of a cylindrical main tank, and an inlet and an outlet at each end of the tank, as shown below:

**Figure 9.1: COPV Geometry**



The tank wall has a composite construction of one homogeneous aluminum alloy liner and four T800/EPOXY fiber-reinforced layers. The inlet and outlet are made of aluminum alloy only. Due to the symmetry, only one-eighth of the entire geometry is modeled (shown by (b) in the above figure).

For this problem, the composite wall is modeled as two distinct components:

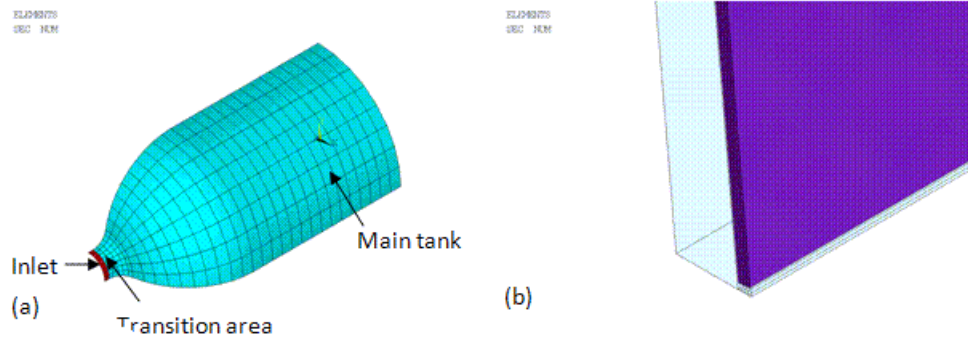
- One isotropic matrix component containing the liner and all bonding material (resin) in the reinforced layers
- Another fiber component representing all reinforcing fibers.

The modeling approach described allows one to independently study the failure limits of the matrix and fiber components based on their own strength characteristics.

The shell element [SHELL281](#) is used for meshing the matrix component.

The [SHELL281](#) mesh is shown by (a) in the following figure:

Figure 9.2: COPV Mesh



The layup of the matrix material is defined using shell sections. Following are the section properties, including material IDs, layer thickness, material orientation (irrelevant if the material is isotropic), and the number of layer integration points:

Section	Layer Thickness	Material ID	Material Orientation Angle	Integration Points
1 (main tank wall)	1.9e-3	1	0	3
	0.1e-3	2	0	3
	0.1e-3	2	0	3
	0.1e-3	2	0	3
	0.1e-3	2	0	3
2 (inlet / outlet wall)	1.9e-3	1	0	3

For proper internal pressure application, the shell sections are offset to the bottom (**SECOFFSET**).

It is assumed that the fibers in each reinforced layer have a unique cross-section area, material property, spacing, and orientation; therefore, a smeared reinforcing approach is used. With smeared reinforcing, the fibers are represented by an equivalent homogeneous layer (instead of the fibers being modeled individually). The smeared approach allows for better computational efficiency. The smeared reinforcing element used is **REINF265**. The fiber properties (material, cross section area, spacing, orientation, and location) are defined via the reinforcing section using the smear subtype (**SECTYPE,REINF,SMEAR**), as follows:

Reinforcing Layer #	Material ID	Fiber Cross-Section Area	Distance Between Two Adjacent Fibers	Fiber Orientation Angle	Layer Location in Base Element
1	3	0.5e-4	1.0	45	2
2	3	0.5e-4	1.0	-45	3
3	3	0.5e-4	1.0	45	4
4	3	0.5e-4	1.0	-45	5

The expanded solid display (**/ESHape**) of both **SHELL281** (shown in translucency) and the embedded **REINF265** elements is shown by (b) in **Figure 9.2: COPV Mesh** (p. 129).

## 9.4. Material Properties

The material properties of the liner are as follows:

<b>Material Properties: Aluminum Liner</b>	
Young's Modulus in x direction (MPa)	72.0e9
Poisson's ratio PRXY	0.29
Secant coefficients of thermal expansion	5.0e-6

The material properties of the bonding matrix and reinforcing fibers are as follows:

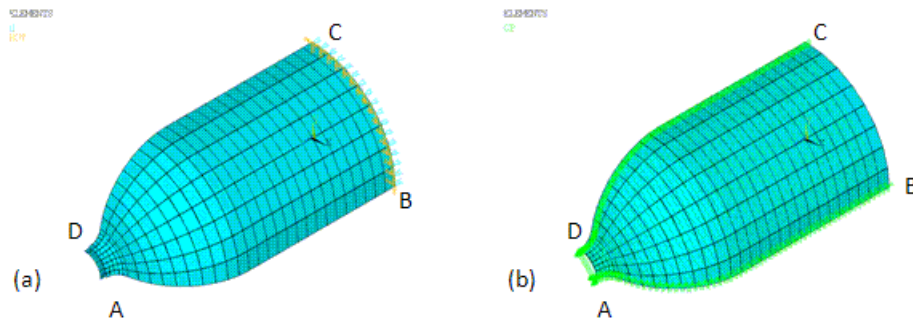
<b>Material Properties:</b>	<b>Bonding Matrix</b>	<b>Reinforcing Fibers</b>
Young's Modulus in x direction (MPa)	8.82e9	161.3e9 - 8.82e9
Young's Modulus in y direction (MPa)	8.82e9	---
Young's Modulus in z direction (MPa)	8.82e9	---
Poisson's Ratio PRXY	0.33	---
Poisson's Ratio PRYZ	0.33	---
Poisson's Ratio PRXZ	0.33	---
Secant coefficient of thermal expansion ALPX	---	1e-6

The fibers have a one-dimensional constitutive relation and are significantly stiffer than the bonding material. For simplicity, it is assumed that all materials in this problem are linear-elastic and temperature-independent.

## 9.5. Boundary Conditions and Loading

Symmetry boundary conditions with respect to the global XY plane are applied to the BC edge, as shown by (a) in the following figure:



**Figure 9.3: COPV Boundary Conditions**

To compensate for the asymmetric section construction, cyclic symmetry conditions (**CP**) are applied for coupling degrees of freedom (DOFs) at the AB edge with the corresponding DOFs at the CD edge (shown by (b) in the above figure).

A uniform pressure of  $13.79 \times 10^6$  Pa is applied to the inner surface of the vessel.

A uniform temperature of  $1000^\circ$  is applied to the inner surface. A  $500^\circ$  temperature gradient is allowed through the wall thickness, resulting in a temperature of  $500^\circ$  at the outer surface.

The temperature at each base shell layer is specified via the **BFE** command. See the **SHELL281** element documentation for more information about defining layered temperature loading.

Temperatures on the reinforcing fibers are automatically determined according to their locations in the shell elements.

## 9.6. Analysis and Solution Controls

A nonlinear static analysis is performed.

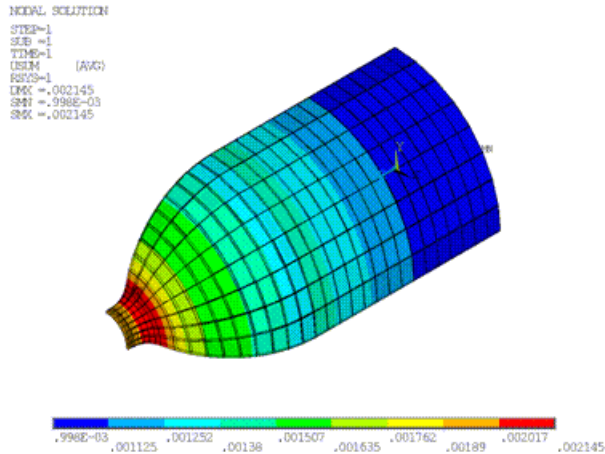
The large-deflection option is activated (**NLGEOM**).

The analysis accounts for fiber realignment.

## 9.7. Results and Discussion

The overall deformation of the vessel is shown in the following figure:

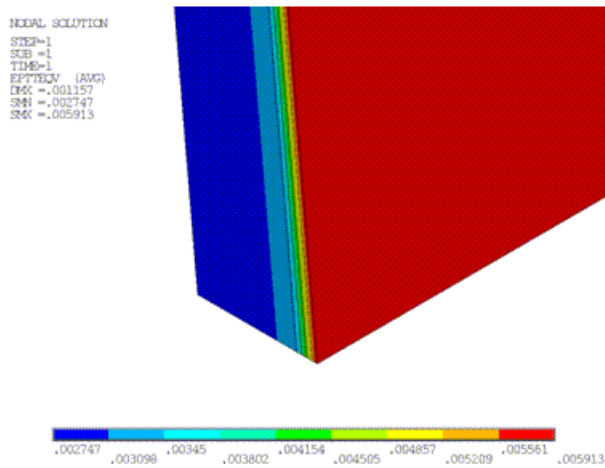
**Figure 9.4: COPV Total Displacement**



The deformation is uniform in the hoop direction; however, a significantly nonuniform pattern is apparent in the meridian direction.

A detailed through-the-wall strain distribution in the matrix component is shown in this figure:

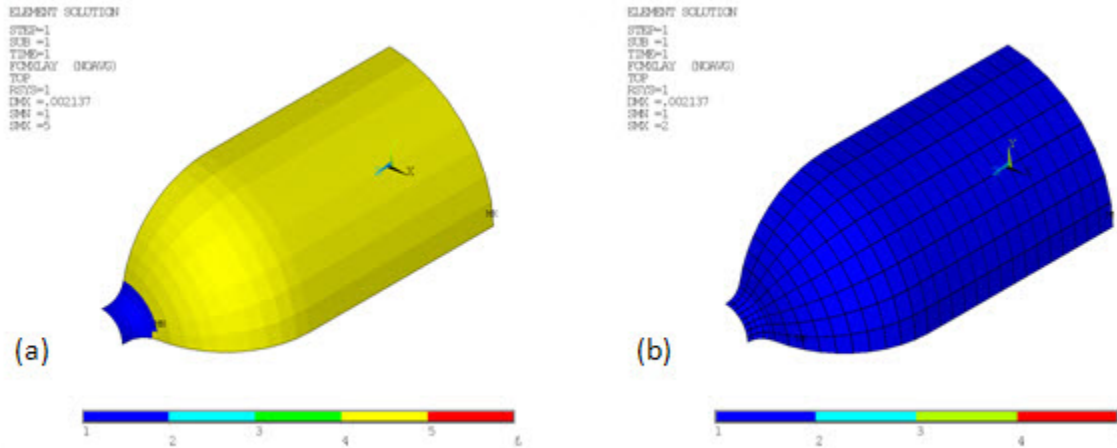
**Figure 9.5: COPV Thickness Strain**



The improved shell formulation of **SHELL281** incorporates the membrane strain effects into the curvature calculation, leading to a more accurate through-the-wall strain distribution. If the matrix is simulated with regular shell elements, strains would be largely uniform through the wall thickness.

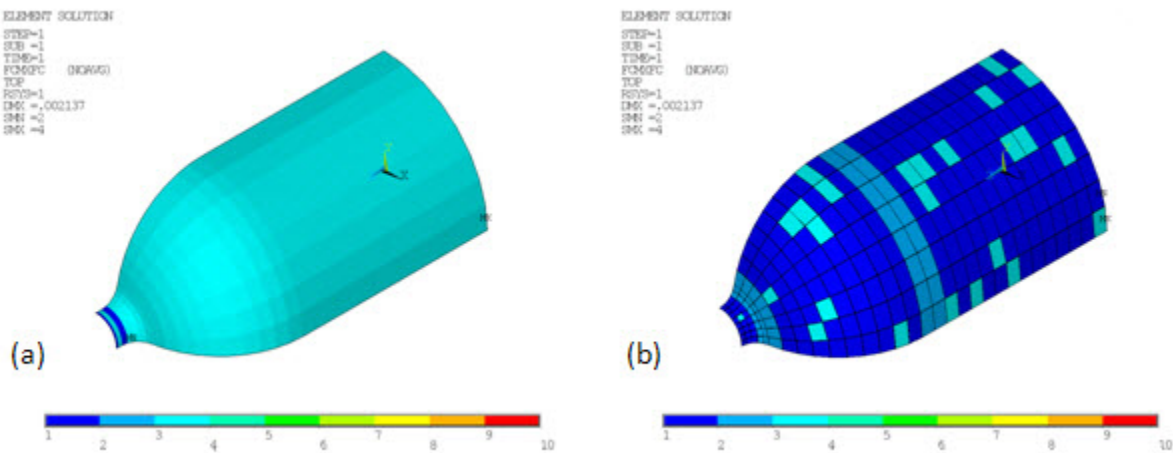
Material-specific strength limits are defined (**FC**) for both matrix and fiber components. The failure-criteria analysis automatically determines the layer with the maximum failure criteria value (or the most vulnerable layer that is likely to fail first). The layer number and failure-criteria value/type of the most vulnerable layer can be listed and plotted (via standard postprocessing listing and visualization commands [**PRESOL** and **PLESOL**]).

The following figure shows that the liner would most likely fail at the inlet, while the bonding material would likely fail at the fourth layer:

**Figure 9.6: Layer with Maximum Failure Criteria in Matrix and Fibers**

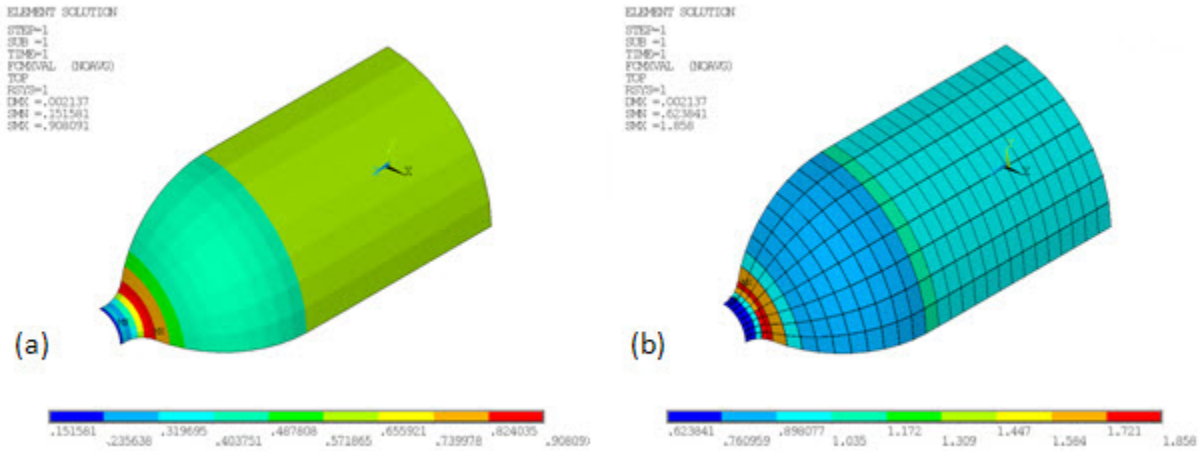
Similarly, according to (b) in the above figure, the fibers would fail first at the first reinforcing layer.

The following figure shows the type of maximum failure criteria on the matrix (a) and fiber (b) components, respectively:

**Figure 9.7: Type of Maximum Failure Criteria in Matrix and Fibers**

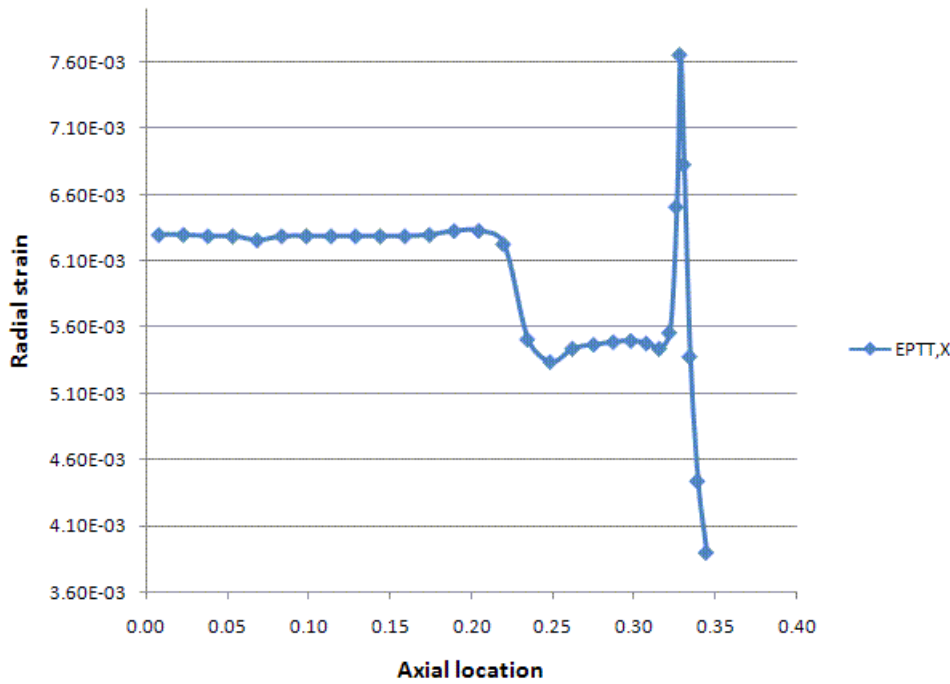
Based on the value of maximum failure criteria, the tank-to-inlet transition region (b) is easily identified as the critical location for the reinforcing fibers (shown by (b) in the following figure):

**Figure 9.8: Value of Maximum Failure Criterion in Matrix and Fibers**



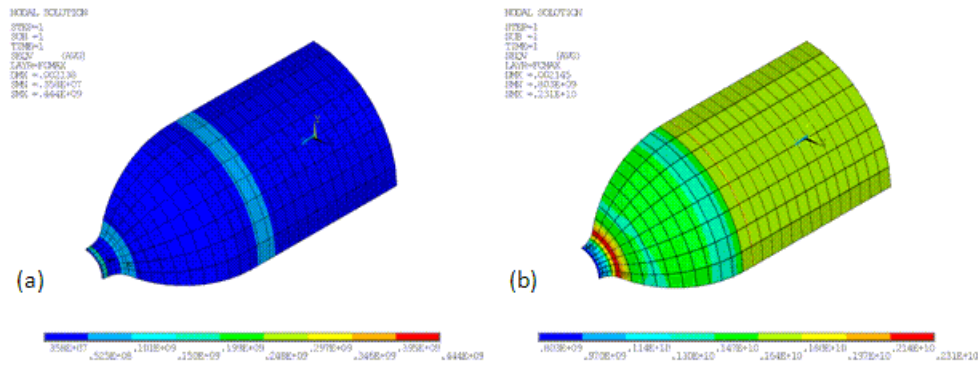
Consistent with the failure criteria analysis results, the fiber strain distribution also shows a spike in this transition region:

**Figure 9.9: Radial Strain Against the Axial Location**

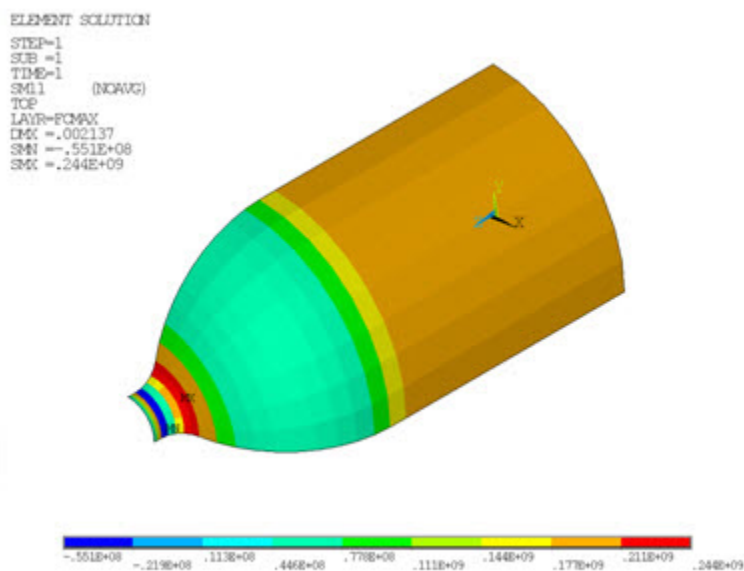


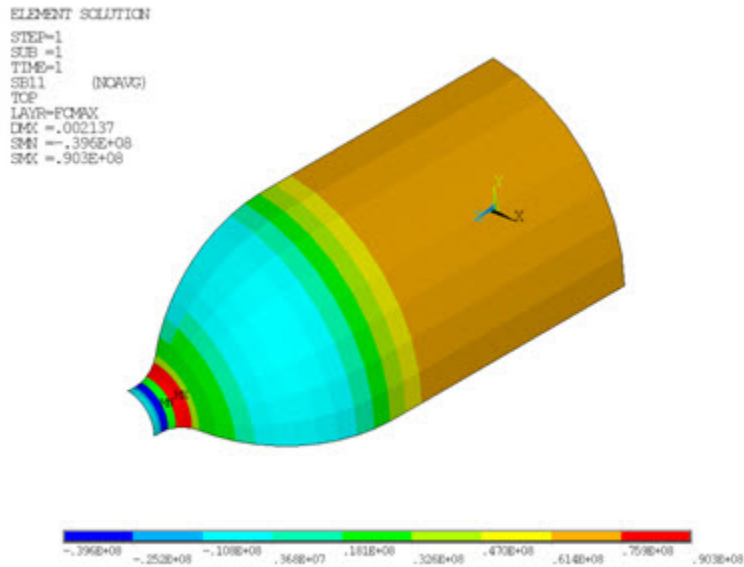
The results indicate that a design modification, either in the liner shape or fiber orientation, is necessary to further strengthen the fibers in this area.

Strains, stresses, and other solution items at the layer of maximum failure criteria can be inspected (**LAYER,FCMAX**, followed by postprocessing listing and visualization commands [**PRESOL** and **PLESOL**]). The following figure shows the equivalent stresses at the layer of maximum failure criteria in the matrix and fiber components, respectively:

**Figure 9.10: Equivalent Stresses at Critical Layer in Matrix and Fibers**

Linearized stresses are commonly cited in boiler and pressure vessel codes and standards. The program computes the linearized stresses, including membrane, bending, and peak stresses, and stores them as the SMISC quantities for [current-technology](#) shell and solid-shell elements. These quantities can be retrieved during postprocessing (**ETABLE** or **\*GET**) for further inspection and code-compliance verification. The following two figures show the membrane and bending stress, respectively, of the matrix component

**Figure 9.11: COPV Membrane Stress in the Element X Coordinate Direction**

**Figure 9.12: COPV Bending Stress in the Element X Coordinate Direction**

## 9.8. Recommendations

To perform a reliability study of a composite overwrapped pressure vessel, consider the following hints and recommendations:

- Fibers in composite materials can be simulated separately using reinforcing elements. In addition to the smeared reinforcing element **REINF265** used in this study, a discrete reinforcing element **REINF264** is also available for modeling individual fibers with arbitrary orientations or nonuniform geometry or materials.
- Use the FCMX item (and accompanying components) available in the postprocessing listing and visualization commands (**PRESOL** and **PLESOL**) to conveniently determine the location, type, and value of the highest failure criteria.
- Select layers of maximum failure criteria for more standard postprocessing (**LAYER,FCMAX**).
- Take advantage of the linearized stress output to optimize the design and to check for code compliance.

## 9.9. References

The following reference was used as the basis of this example problem:

1. Kim, Cheol-Ung et al. "Optimal Design of Filament Wound Structures under Internal Pressure Based on the Semi-geodesic Path Algorithm." *Composite Structures*. 67 (2004): 443-452.

## 9.10. Input Files

The following files were used in this problem:

- `pressure_vessel.dat` -- Input file for the reliability study of a composite overwrapped pressure vessel.
- `pressure_vessel.cdb` -- The common database file used for this problem, called by `pressure_vessel.dat`.

The files are available in the `td-9` folder. See [Obtaining the Input Files \(p. xxxv\)](#) for more information.





---

## Chapter 10: Simulation of a Lumbar Motion Segment

---

This example problem demonstrates the use of [coupled pore-pressure element](#) technology to study the creep response of a lumbar motion segment under compression. The simulation reveals the interaction between the solid phase and the fluid phase in soft tissues.

Topics related to this example problem follow:

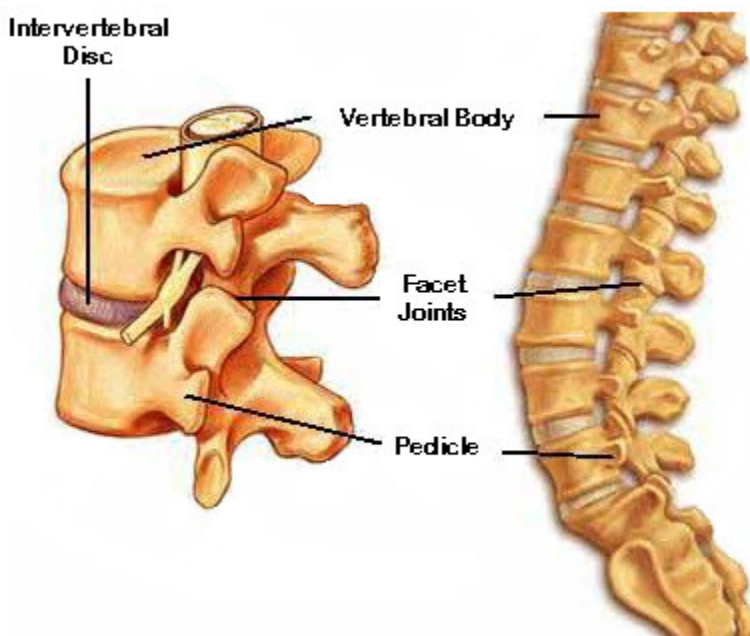
- 10.1. Introduction
- 10.2. Problem Description
- 10.3. Modeling
- 10.4. Material Properties
- 10.5. Boundary Conditions and Loading
- 10.6. Analysis and Solution Controls
- 10.7. Results and Discussion
- 10.8. References
- 10.9. Input Files

### 10.1. Introduction

Approximately 26 million Americans between the ages of 20 and 64 are affected by frequent lower back pain [1], one of the major causes of worker disability. The problem costs the economy roughly \$50-100 billion each year [2].

Most lower back problems involve the intervertebral disc (IVD), shown in this illustration [4]:

**Figure 10.1: Vertebral Body Components**



The IVD is the smallest segment of the spine that exhibits biomechanical characteristics similar to that of the entire spine [3]. The IVD is composed of annulus bulk and nucleus pulposus, both soft tissues.

Finite element analysis (FEA) has been applied in orthopedic biomechanics and spine biomechanics research since 1983. Typically, the IVD is modeled by solid elements. Many experimental observations, however, suggest that it is more realistic to consider soft tissue in the IVD as a biphasic model. For example, when the disc is compressed, fluid flows out from either the entire disc [5] or from disc slices; therefore, one can consider the soft tissues in IVD to be a multiphase system.

Clinical studies shows that back pain is associated with the mechanical behavior of the intervertebral disc. A significant finding is that the degenerated intervertebral disc has lower permeability than a normal disc [3]; therefore, using [coupled pore-pressure elements](#) in a lumbar motion segment simulation provides a realistic model for clinical study of degenerated intervertebral discs.

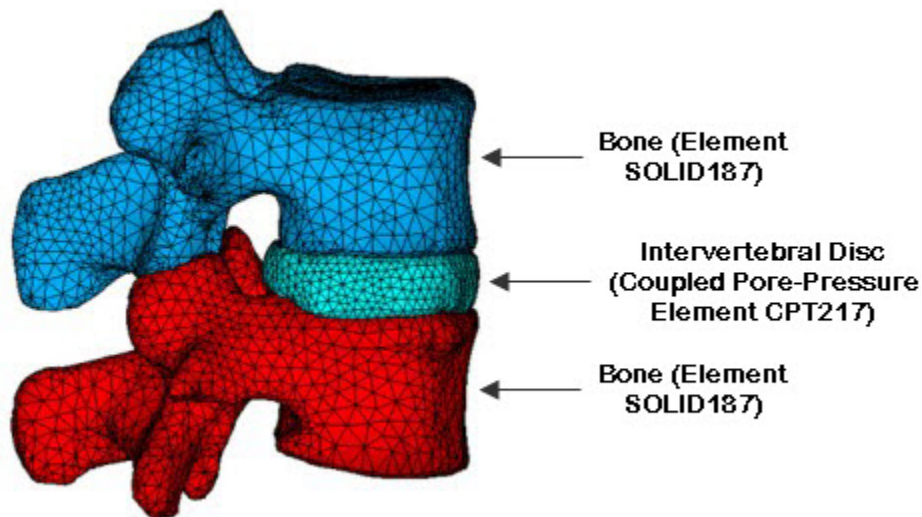
## 10.2. Problem Description

A human vertebral motion segment from *in vitro* measurements is examined. A constant axial force of 500N is applied at the top of the upper vertebra while the lower vertebra is fixed at the bottom. Initially, the full load is applied instantly and maintained in the subsequent creep stage. During the entire loading period, the lateral surfaces of the IVD are permeable [6].

## 10.3. Modeling

Following is finite element model of a lumbar motion segment:

**Figure 10.2: Finite Element Model of a Human Lumbar Motion Segment**



Because the IVD is composed of soft tissue, it is modeled using [CPT217](#) coupled pore-pressure elements. Bones in the segment are modeled using [SOLID187](#) solid elements.

## 10.4. Material Properties

Following are the material properties [6] used in the lumbar motion segment analysis:

Human Vertebral Motion Segment Material Properties			
Property	Annulus Bulk	Nucleus Pulposus	Bone
Elastic Modulus (MPa)	2.5	1.5	3500
Poisson's Ratio	0.1	0.1	0.2
Permeability ( $m^4 N^{-1} s^{-1}$ )	3.0E - 16	3.0E - 16	---

The permeating fluid and the solid phase are both assumed to be incompressible, so the Biot modulus  $\alpha$  is set to 1.

## 10.5. Boundary Conditions and Loading

The lower vertebral body is constrained with all degrees of freedom. The central node in the top surface of the upper vertebral body is given step load 500N.

## 10.6. Analysis and Solution Controls

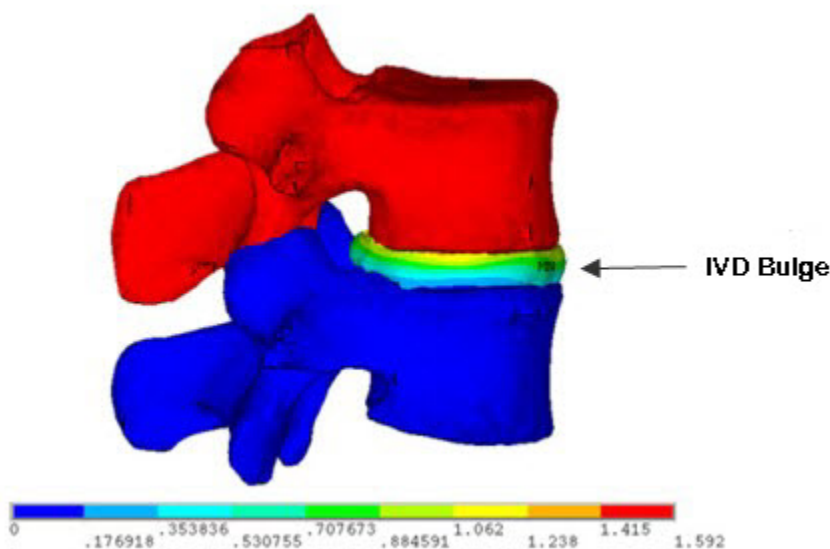
A nonlinear static analysis is performed using the unsymmetric Newton-Raphson option.

Creep is studied over a period of five days (about 4.26E4 seconds). Results show that small time steps induce nonphysical pressure oscillations in the computation; therefore, the entire solution is completed in 100 substeps with no oscillation present.

## 10.7. Results and Discussion

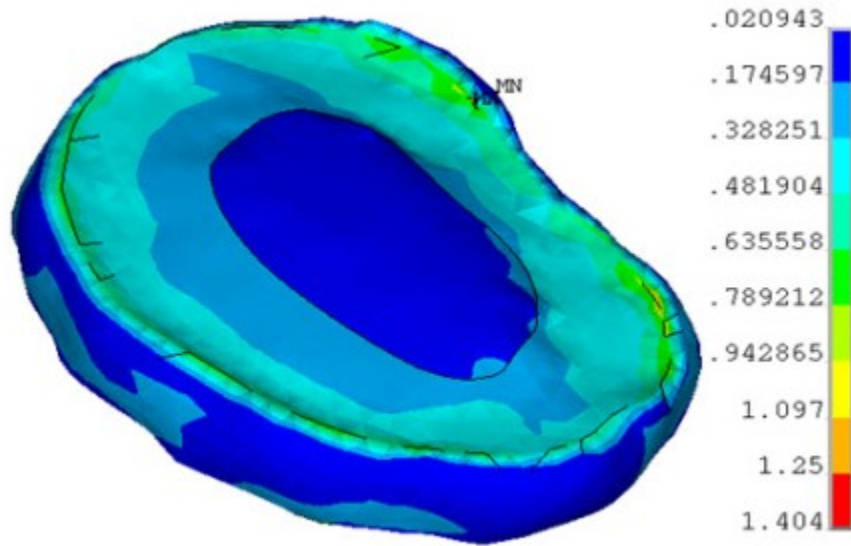
The following figure show the bulging of the IVD, one of the primary deformation modes of an IVD under compression in clinical studies:

**Figure 10.3: IVD Deformation**



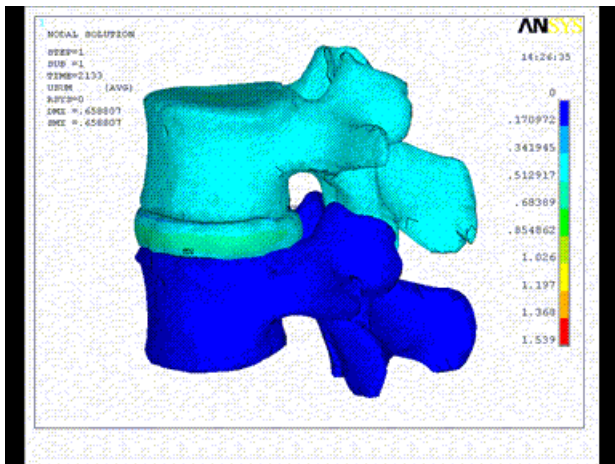
For IVD stresses, the annulus bulk takes more load than the nucleus since it has higher stiffness, as shown in this figure:

**Figure 10.4: IVD von Mises Stresses**



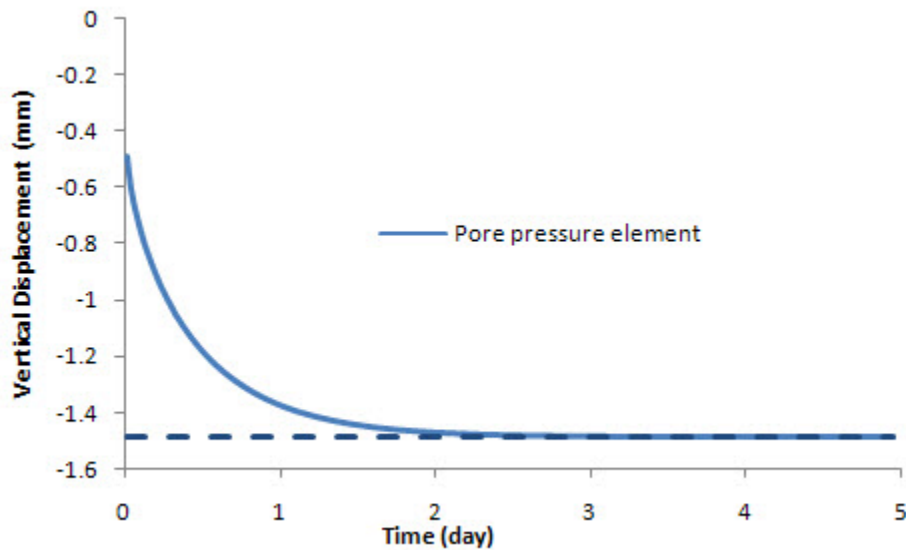
With the IVD modeled using coupled pore-pressure elements, vertical displacement gradually increases with time, as shown in this animation:

**Figure 10.5: Lumbar Motion Segment Animation of Vertical Displacement Increasing with Time**

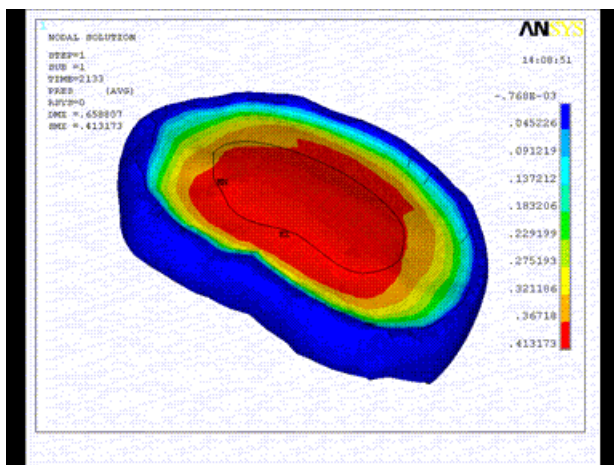


The animation also illustrates the difference between solid elements and coupled pore-pressure elements. With the same loading and boundary conditions, the upper vertebral body modeled with coupled pore-pressure elements drops gradually under compression, as compared to the constant displacement of solid elements. For soft-tissue modeling, coupled pore-pressure elements provide a more realistic simulation.

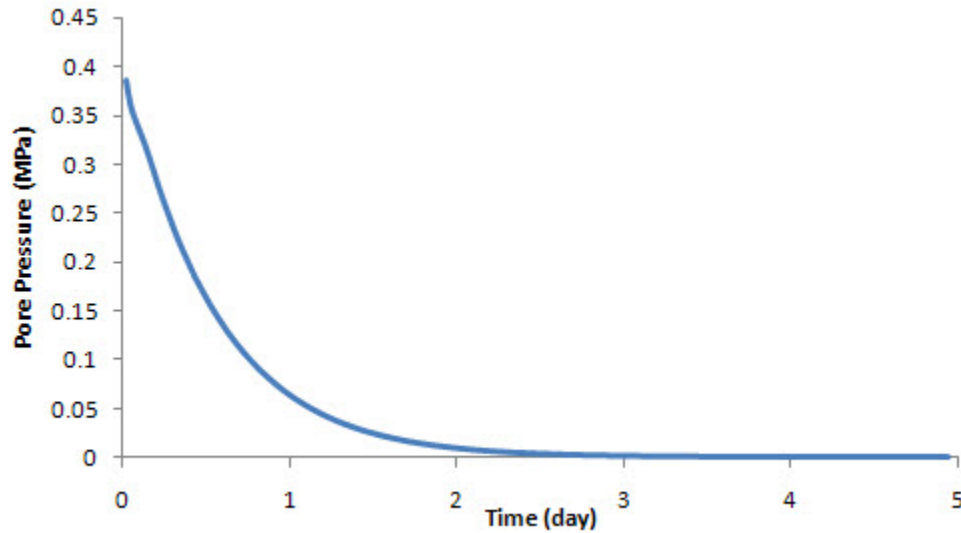
As vertical displacement increases with time, pore pressure dissipates:

**Figure 10.6: Displacements of Vertebral Body Over Time**

The creep response of the lumbar motion segment is due to fluid flowing out of the IVD, as shown:

**Figure 10.7: Lumbar Motion Segment Creep Response**

When the fluid is exhausted, the final displacement is equal to that of an IVD modeled by solid elements only:

**Figure 10.8: IVD Pore-Pressure Dissipation**

The creep response under compression demonstrates the diffusive interaction between the solid matrix and the interstitial fluid in soft tissues.

## 10.8. References

The following references are used in this example problem:

1. *Wikipedia: The Free Encyclopedia*. Tissue (Biology). <[http://en.wikipedia.org/wiki/Biological\\_tissue](http://en.wikipedia.org/wiki/Biological_tissue)>.
2. Paremer, A., S. Fumer, D. P. Rice. *Musculoskeletal Conditions in the United States*. 1st ed. Park Ridge: American Academy of Orthopaedic Surgeons, 1992.
3. Gilbertson, L. G. et al. "Finite Element Methods in Spine Biomechanics Research." *Critical Reviews in Biomedical Engineering*. 23.5-6 (1995): 411-473.
4. Bridwell, K. "Intervertebral Discs." *Spine Universe*. 12 May 2009. <<http://www.spineuniverse.com/displayarticle.php/article1267.html>>.
5. Charnley, J. "Imbibation of Fluid as a Cause of Herniation of the Nucleus Pulposus." *Lancet*. 6699 (1952): 124-127.
6. Argoubi, A., A. Shirazi-Adl. "Poroeleastic Creep Response Analysis of a Lumbar Motion Segment in Compression." *Journal of Biomechanics*. 29.10 (1996): 1331-1339.

ANSYS, Inc. gratefully acknowledges [Materialise NV](#) for providing the vertebral body geometry for this example problem.

## 10.9. Input Files

The following files were used in this problem:

- `vertebral_body_input.dat` -- Input file for the lumbar motion segment simulation.

- `vertebral_body.cdb` -- Common database file for the lumbar motion segment model (called by the `vertebral_body_input.dat` file).

The files are available in the `td-10` folder. See [Obtaining the Input Files \(p. xxxv\)](#) for more information.





---

## Chapter 11: Rocket Nozzle Extension Simulation: Fabrication

---

This is the first of two example problems that simulate a rocket nozzle:

- The example problem presented here simulates thermal stresses during the *manufacturing* (fabrication) stage of the nozzle.
- The second example, [Rocket Nozzle Extension Simulation: Operation](#), simulates thermal stresses induced during the *operation* of the nozzle.

While both examples are based on the same geometry, the assumptions used are different, thus leading to different meshes and different element types.

This example demonstrates how [current](#) structural-shell element technology can accurately model the orthotropic thermal expansion in curved-shell structures. Section offsets are applied when connecting shell elements to shell elements, or shell elements to other element types. An appropriate results-storage option is selected for postprocessing the layered-element solution.

Topics related to this example problem follow:

- [11.1. Introduction](#)
- [11.2. Problem Description](#)
- [11.3. Modeling](#)
- [11.4. Material Properties](#)
- [11.5. Boundary Conditions and Loading](#)
- [11.6. Analysis and Solution Controls](#)
- [11.7. Results and Discussion](#)
- [11.8. Recommendations](#)
- [11.9. References](#)
- [11.10. Input Files](#)

### 11.1. Introduction

Thermal loading can produce different thermal strains in the in-plane and through-the-thickness directions in shell structures with orthotropic thermal expansion coefficients. If the structure is curved, this difference causes shell curvature changes and additional stresses.

Classic shell elements do not account for thickness strains and therefore lack the ability to account for the orthotropic thermal expansion effect [1]. Shell element technology that incorporates the thickness strain in the shell curvature calculation is well suited for this type of simulation.

### 11.2. Problem Description

A thin-walled rocket nozzle extension with a reinforcing ring is first processed at a higher temperature and assumed to be stress-free during processing. The extension is then allowed to cool down to the ambient temperature.

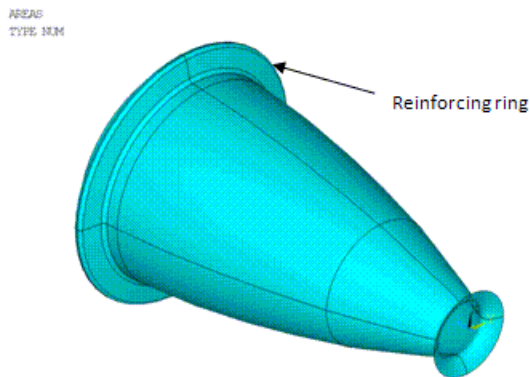
The extension materials exhibit different in-plane and through-the-thickness thermal expansion properties; therefore, the cooling process may induce significant residual stresses, particularly in parts with large curvatures.

A linear static analysis is performed to study the residual stresses on the nozzle extension under this uniform thermal (cooling) load. Special attention is given to the reinforcing ring at the jet exhaust where the highest stresses are expected.

### 11.3. Modeling

The nozzle extension consists of a main curved wall and a reinforcing ring close to the jet exhaust, as shown in this figure:

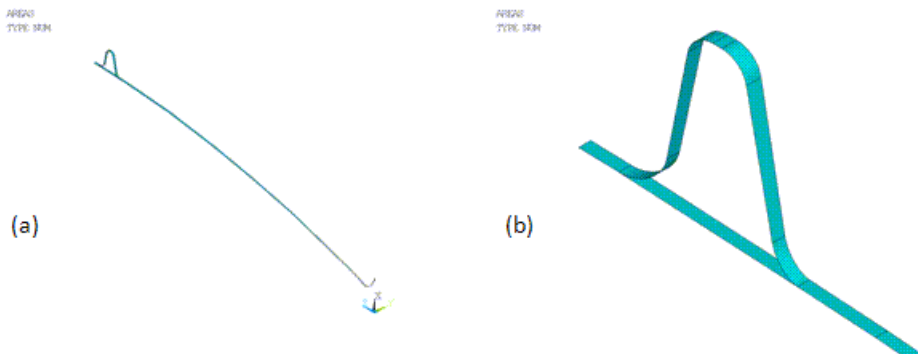
**Figure 11.1: Nozzle Extension Geometry**



Both the wall and the reinforcing ring are made of layered composite materials. To maintain a degree of simplicity for this example, the model uses a single orthotropic material for all layers; however, the material orientation varies from layer to layer.

Because the model exhibits symmetry, optimal computational efficiency is achieved by modeling only a single 1° sector (the base sector) of the entire nozzle extension. The geometry model of the 1° sector is shown in this figure, where (a) is the global geometry and (b) is a detail view of the reinforcing ring:

**Figure 11.2: Nozzle Extension 1° Base Sector Geometry**



The reduced 1° geometry model is meshed with **SHELL281** elements. The following figures show respectively the mesh and the expanded solid representation of the shell mesh (**/ESHAPE**).

Figure 11.3: Ring Element Plot

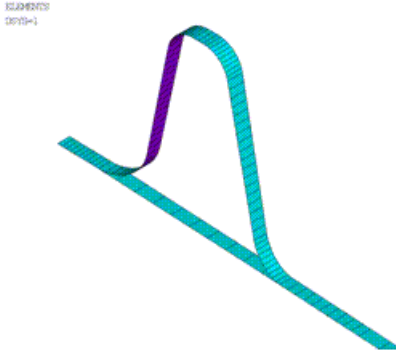
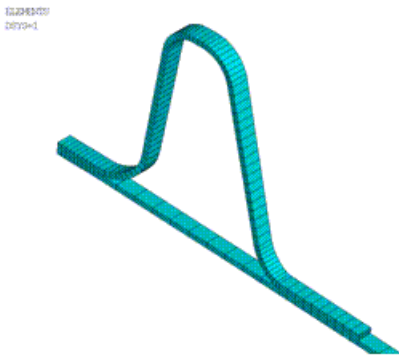


Figure 11.4: Expanded Solid Representation of the Shell Mesh



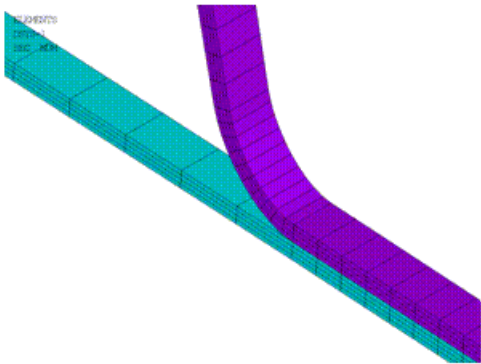
Using the **SHELL281** element's option for improved shell formulation ( $\text{KEYOPT}(2) = 1$ ), the element incorporates initial curvature effects more accurately. With this option, both shell-membrane and thickness strains are accounted for in the calculation of effective shell curvature change. This option is essential for capturing the orthotropic thermal expansion effects in curved shell structures. To properly postprocess a layered solution, layered data storage is set to store results for the tops and bottoms of all layers ( $\text{KEYOPT}(8) = 1$ ).

Shell sections define the layers of the composite material. (The **SECTYPE** command specifies the section type, and the **SECDATA** command specifies the material, thickness, material orientation, and the number of integration points of each layer.) Two sections are created, respectively, for the main wall and the reinforcing ring. The following table summarizes the shell section properties:

Section Number	Layer Thickness	Material Number	Material Orientation	Integration Points	Offset
Section 1 (main wall)	1/4 total thickness	1	0	3	Top of the section
			90		
			0		
			90		
Section 2 (reinforcing ring)	1/4 total thickness	1	0	3	Bottom of the section
			90		
			0		
			90		

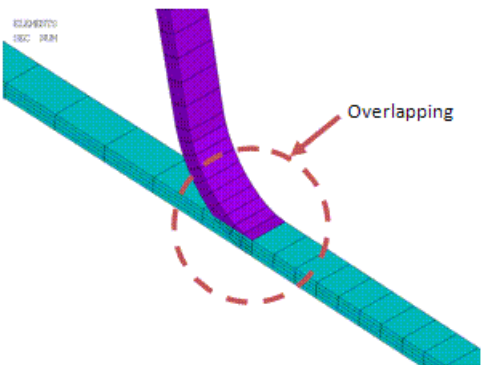
Assume that the reinforcing ring is securely bonded to the outer surface of the main extension wall. The secure bonding is easily simulated via the use of common nodes at the connection areas between the wall and the reinforcing ring. (See [Figure 11.3: Ring Element Plot \(p. 149\)](#).) It is necessary to apply shell offsets, however, so that the wall and the ring can be properly connected. This example offsets the shell section for the main wall to its top, and the shell section for the ring to the bottom (**SECOFFSET**), as shown in this figure:

**Figure 11.5: Nozzle Wall and Ring Connection with Shell Offsets**



Without the offsets, the shell sections are offset to the midplane by default, leading to an incorrectly overlapped model, as shown in this figure:

**Figure 11.6: Nozzle Wall and Ring Connection without Shell Offsets**



To obtain an accurate reference solution, results are compared to a refined 3-D model with multiple quadratic layered solid elements (**SOLID186**) through the wall thickness.

## 11.4. Material Properties

The properties of the single orthotropic material used in the rocket nozzle extension model are as follows:

Orthotropic Material Properties	
Young's Modulus in x direction (MPa)	100000
Young's Modulus in y direction (MPa)	5000
Young's Modulus in z direction (MPa)	5000

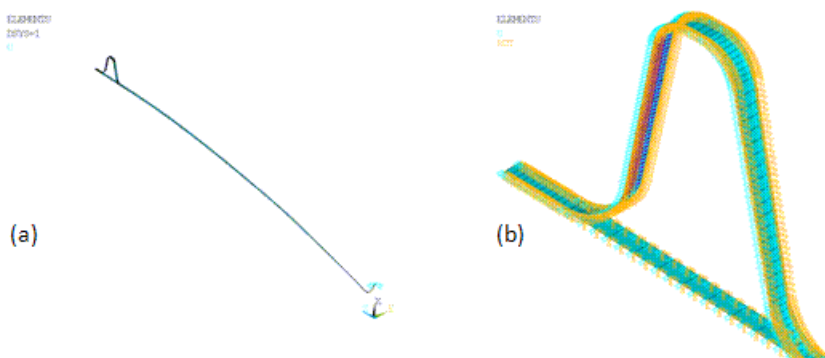
Orthotropic Material Properties	
Poisson's Ratio PRXY	0.40
Poisson's Ratio PRYZ	0.30
Poisson's Ratio PRXZ	0.30
Shear Moduli GXY	3000
Shear Moduli GYZ	2000
Shear Moduli GXZ	2000
Secant coefficient of thermal expansion ALPX	1.6E-05
Secant coefficient of thermal expansion ALPY	1.6E-05
Secant coefficient of thermal expansion ALPZ	6.3E-05

The material is assumed to be linear elastic and temperature-independent. The material has different thermal expansion coefficients in the in-plane (X and Y) and through-the-thickness (Z) directions.

## 11.5. Boundary Conditions and Loading

Two sets of boundary conditions are applied, as shown in this figure:

**Figure 11.7: Nozzle Model Boundary Conditions**



The first set of conditions (a) constrains rigid body motions while allowing free radial wall expansion. The second set of conditions (b) provides necessary symmetry constraints on this reduced sector model.

For the symmetry constraints to work properly, nodal degrees of freedom must be rotated to the cylindrical coordinate system.

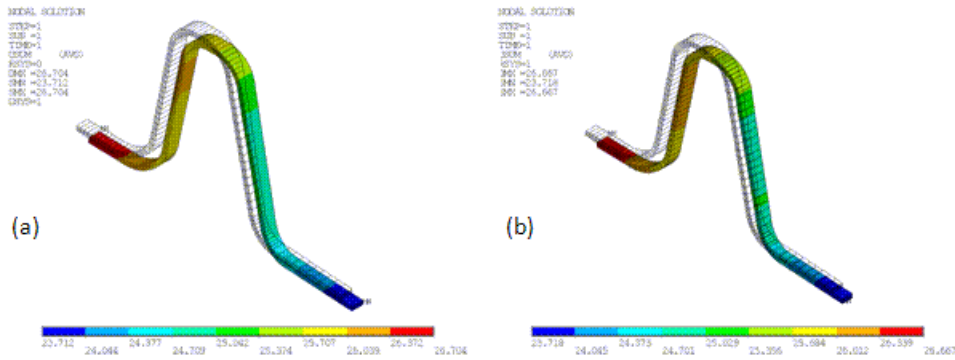
Only thermal loads are considered in this simulation. The uniform cooling of 1600K is specified via the uniform temperature command (**TUNIF**).

## 11.6. Analysis and Solution Controls

A linear static analysis is performed.

## 11.7. Results and Discussion

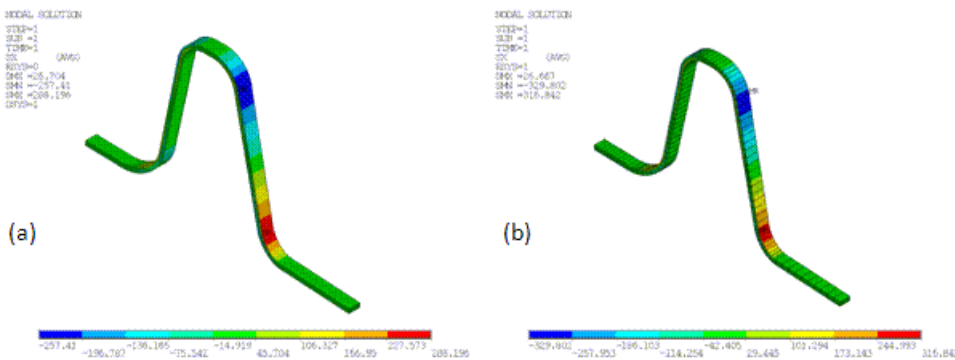
The deformation results from the reference 3-D model (a) and the SHELL281 shell model (b) are shown in this figure:



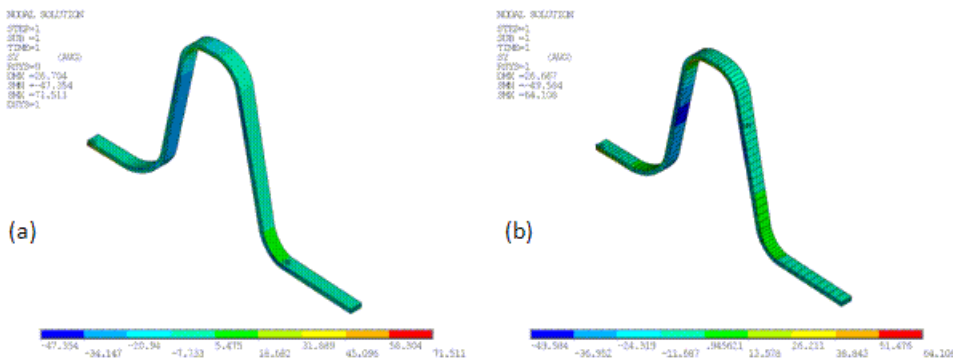
The maximum displacement for the shell model (26.667) nearly matches the reference value (26.704), with an error of only 0.14 percent.

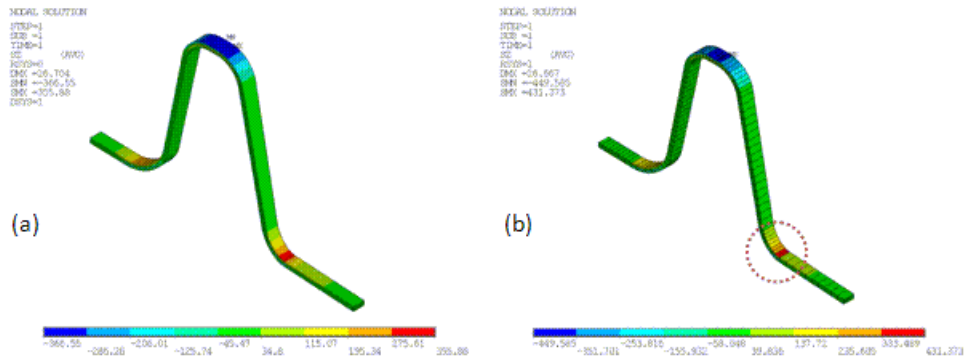
As expected, the highest stresses caused by the thermal load appear in the reinforcing ring, which has the largest curvature and curvature variation. Distributions of all three normal stress components (X - radial, Y - hoop, and Z - axial) agree closely with the reference results, as shown in the following three figures, where (a) refers to the reference 3-D model and (b) refers to the shell model:

**Figure 11.8: Nozzle Radial (X) Stress**



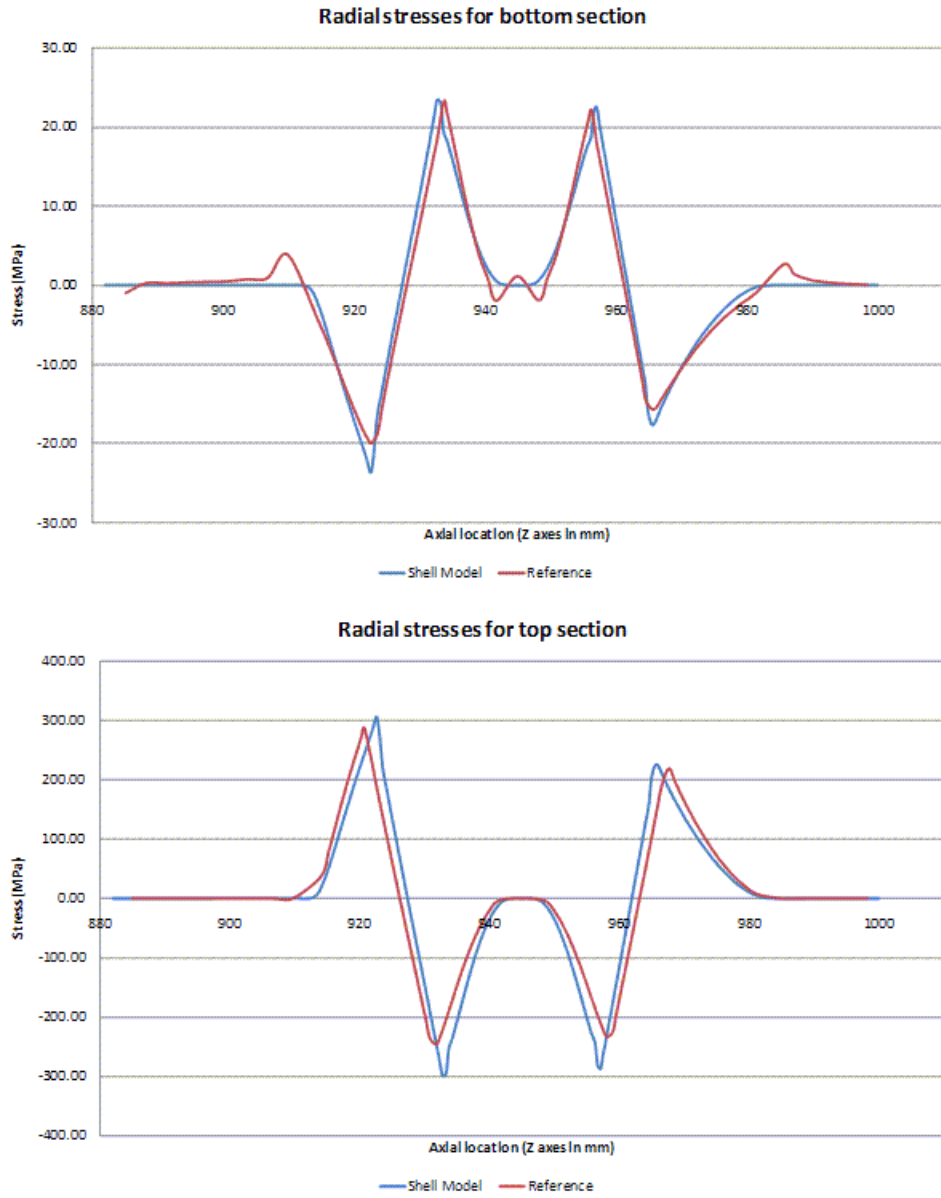
**Figure 11.9: Nozzle Hoop (Y) Stress**



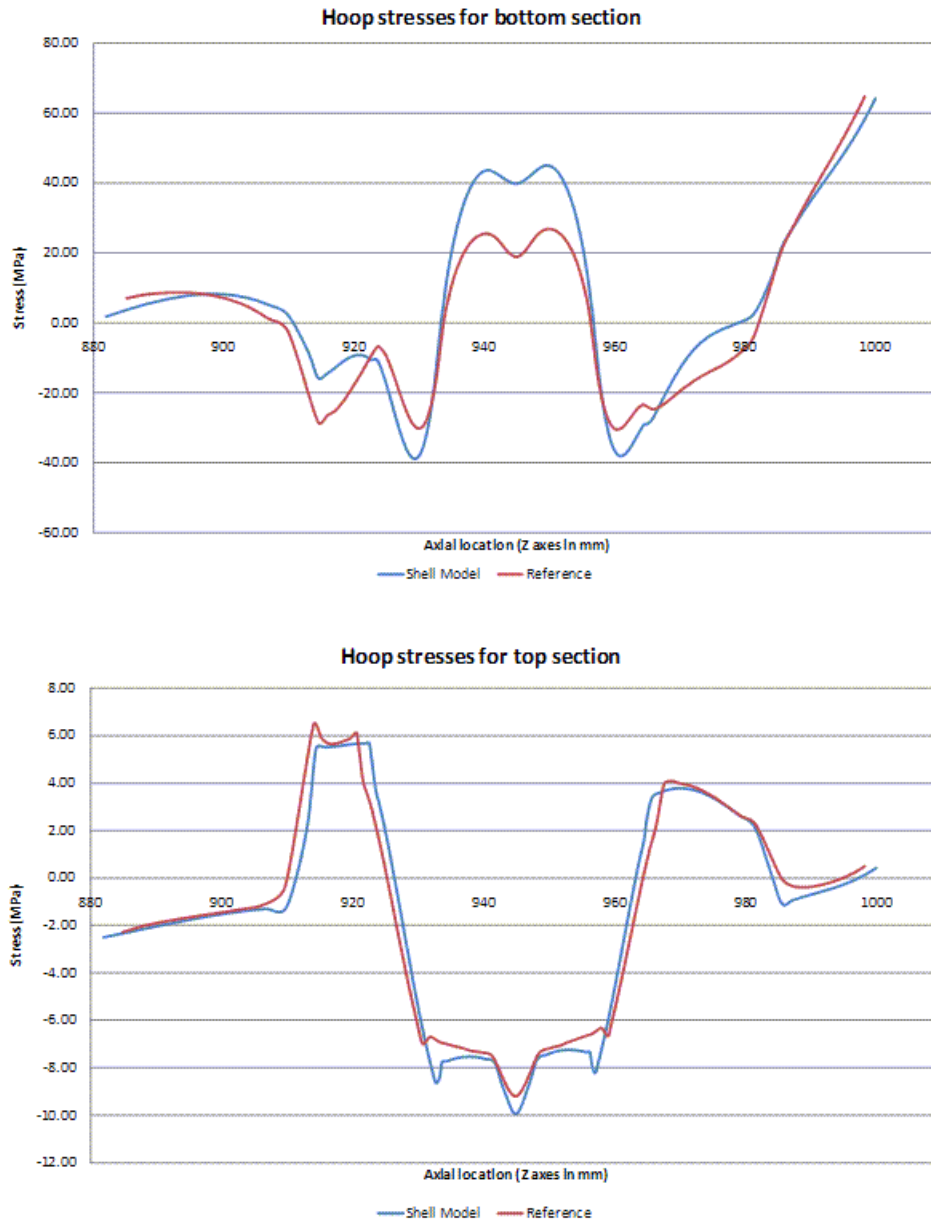
**Figure 11.10: Nozzle Axial (Z) Stress**

The following figures compare the detailed stress distributions from the reference model and the shell model, at both the bottom and top of the reinforcing ring:

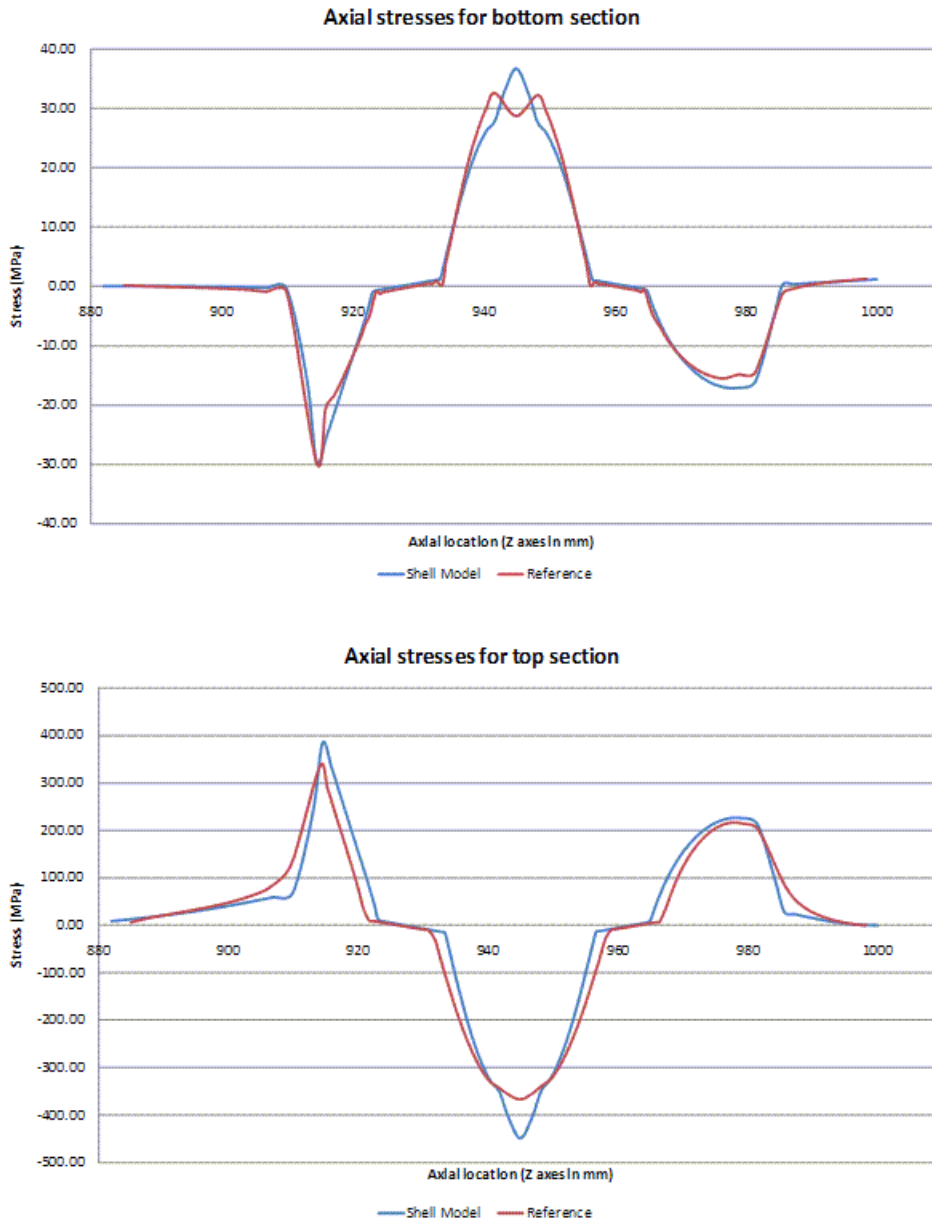
Figure 11.11: Nozzle Radial Stresses (Bottom and Top Sections)





**Figure 11.12: Nozzle Hoop Stresses (Bottom and Top Sections)**

**Figure 11.13: Nozzle Axial Stresses (Bottom and Top Sections)**



The generally accurate agreement between the reference and simulation stress results is clearly observable.

Some small local differences exist in the stress results, particularly at the areas where the ring connects with the main extension wall. The discrepancy is noticeable because the problem applies the [SHELL281](#) element (which is based on the plane stress assumption) to a complex 3-D domain.

If the problem were to be simulated with standard shell elements, no residual stresses would be obtained.

The stress contour display on the [SHELL281](#) model with the expanded solid shapes reveals one graphics irregularity: result averaging may fail where the pseudo expanded interelement connectivity does not match, as shown in the circled area of (b) in [Figure 11.10: Nozzle Axial \(Z\) Stress \(p. 153\)](#). To overcome this issue, use the (default) simple area element display option (`/ESHAPE,0`).

---

## 11.8. Recommendations

To perform a similar type of analysis, consider the following hints and recommendations:

- Select a suitable shell element for simulating initially curved shell structures. Shell element technology that incorporates the thickness strain in the shell curvature calculation (such as [SHELL281](#)) is well suited to this type of simulation.
- Apply appropriate section offsets when connecting shell elements to shell elements, or shell elements to other element types.
- Select the proper results-storage option for postprocessing a layered-element solution.

## 11.9. References

The following reference was used for this example problem:

1. Sach, E. D., G. Fleischmann, W. Ulrich. "Influence of Modeling for Orthotropic Material Properties." [MSC 1999 Aerospace User's Conference Proceedings](#).

## 11.10. Input Files

The following files were used in this problem:

- `nozzle.dat` -- Input file for the orthotropic thermal expansion analysis.
- `nozzle.cdb` -- The common database file used in the orthotropic thermal expansion analysis (called by `nozzle.dat`).

The files are available in the `td-11` folder. See [Obtaining the Input Files \(p. xxxv\)](#) for more information.



---

## Chapter 12: Dynamic Simulation of a Nuclear Piping System Using RSA Methods

---

This example problem is a dynamic simulation of a piping network used in a nuclear power generation system. The problem demonstrates the analysis methods available to account for the effect of higher frequency modes of a structure in a response-spectrum analysis (RSA).

For verification, computational results from the RSA are compared to the full transient analysis results performed on the same model. (In an industrial application, however, a transient analysis approach is computationally intensive and often impractical for analyzing a nuclear piping network.)

The following features and capabilities are highlighted:

- Use of the [missing-mass](#) response to include the responses of the higher modes in the RSA.
- Use of [rigid responses \(Gupta or Lindley-Yow method\)](#) to more accurately combine the modal responses (consisting of both periodic and rigid-response components).

Topics related to this example problem follow:

- 12.1. Introduction
- 12.2. Problem Description
- 12.3. Modeling
- 12.4. Material Properties
- 12.5. Boundary Conditions and Loading
- 12.6. Analysis and Solution Controls
- 12.7. Results and Discussion
- 12.8. Recommendations
- 12.9. References
- 12.10. Input Files

### 12.1. Introduction

The response-spectrum analysis (RSA) is a widely used method for studying seismic responses of structures such as nuclear power plants, boilers, and pressure vessels. The current practice is to calculate only the responses of the modes having a frequency within the frequency range of the input spectrum.

In some cases, however, the responses of the higher modes may not be negligible. The missing-mass method is a convenient, computationally efficient, and accurate method used to account for:

- The contribution of all modes with frequencies above  $f_{ZPA}$  at which the response spectrum returns to the Zero Period Acceleration (ZPA).
- The contribution to support reactions of mass apportioned to system-support points.

**Terms Used**

The following terms are used in this example problem:

Zero Period Acceleration (ZPA) -- The acceleration value (peak) at zero period (or infinite frequency) of an input spectrum. It corresponds to the response of a rigid system.

ZPA frequency ( $f_{ZPA}$ ) -- The minimum frequency beyond which the input spectrum curves for various damping ratios converge towards the same ZPA acceleration.

For frequencies occurring in the amplified region of the response spectrum ( $f < f_{ZPA}$ ), the mode responses generally have both in-phase (periodic) and out-of phase (rigid-response) components.[2]

To separate and combine the response components, the methods proposed by Gupta and Lindley-Yow are applied and the results are compared.[3] The in-phase modal response components and the missing-mass contributions are combined algebraically to produce the total in-phase response component. For the combination of the out-of-phase modal response components, either the Square Root of the Sum of the Squares (SRSS) method or the Der Kiureghian CQC method is applied.

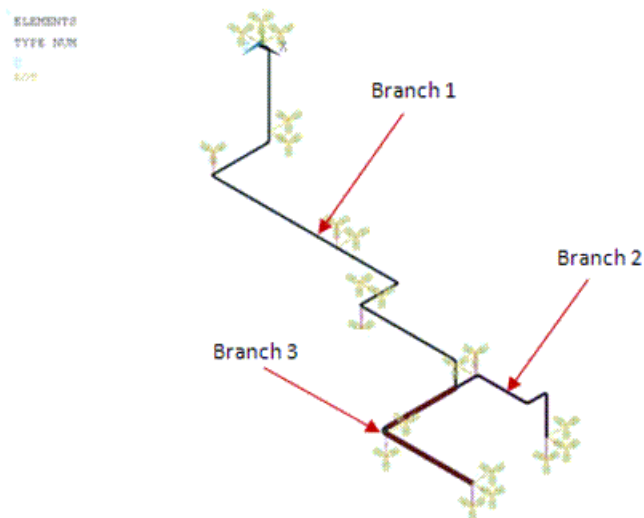
For more information, see the following resources (in the *Mechanical APDL Theory Reference*):

- [Missing-Mass Response](#)
- [Rigid Responses](#)
- [Combination of Modes](#)

## 12.2. Problem Description

The problem uses the BM3 piping system model from an actual nuclear power plant found in the Nuclear Regulatory Commission's report.[1][2] The model consists of three anchors, three piping subsystem branches, and elastic supports, as shown in this figure:

**Figure 12.1: Full Model of the BM3 Nuclear Piping System**



To measure the influence of each effect and compare the response-component combination methods, seven single-point response **spectrum** (SPRS) analyses are performed.

The results of a **full-transient** (direct time-integration) analysis are used as a baseline.

## 12.3. Modeling

The following modeling topics are available:

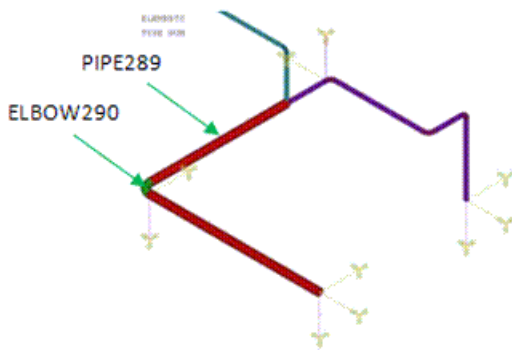
12.3.1. BM3 Piping System Modeling

12.3.2. Elastic Support Modeling

### 12.3.1. BM3 Piping System Modeling

The straight and curved parts of the BM3 model are meshed with pipe (**PIPE289**) and elbow (**ELBOW290**) elements, respectively:

**Figure 12.2: BM3 Model Meshed with PIPE289 and ELBOW290 Elements**



The default settings for the **PIPE289** and **ELBOW290** elements apply.

To more accurately capture the curvature of a bend, it is divided into four parts, and each part is meshed with **ELBOW290**.

The section properties (**SECTYPE** and **SECDATA**) of the pipe and elbow elements are defined via the following input:

#### Branch 1 section properties

```
SECTYPE, SECID1, PIPE, ctube      ! "SECID1" is a user-specified name
SECDATA, 3.5, 0.216              ! Outside diameter and wall thickness
```

#### Branch 2 section properties

```
SECTYPE, SECID2, PIPE, ctube      ! "SECID2" is a user-specified name
SECDATA, 4.5, 0.2370             ! Outside diameter and wall thickness
```

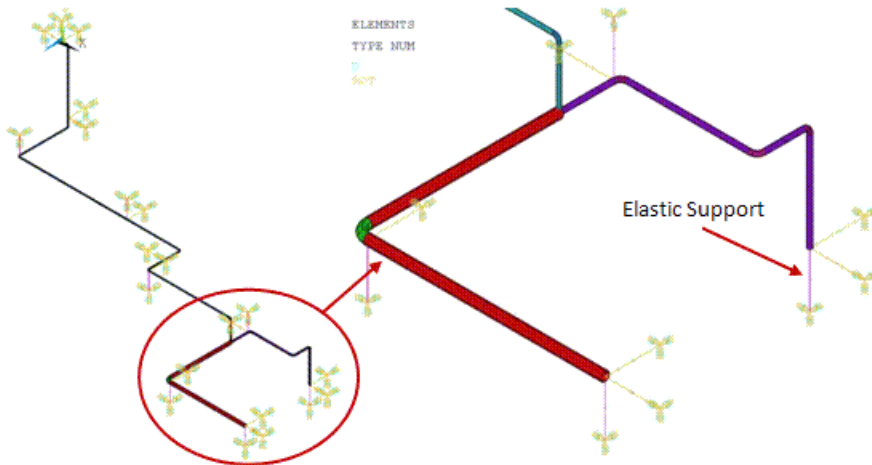
#### Branch 3 section properties

```
SECTYPE, SECID3, PIPE, ctube      ! "SECID3" is a user-specified name
SECDATA, 8.625, 0.322            ! Outside diameter and wall thickness
```

### 12.3.2. Elastic Support Modeling

Each elastic support of the piping system is modeled as a spring element (**COMBIN14**), as shown in this figure:

**Figure 12.3: Elastic Supports Meshed with COMBIN14 Elements**



One-dimensional longitudinal and torsional springs are defined via element key options (KEYOPT(2) = 1 through 6).

## 12.4. Material Properties

Following are the pipe material properties:

Pipe Material Properties	
Branch 1: Density (Kg mm <sup>-3</sup> )	1.043
Branch 2: Density (Kg mm <sup>-3</sup> )	1.107
Branch 3: Density Kg mm <sup>-3</sup> )	1.253
Young's Modulus (MPa)	2.9e+007
Poisson's Ratio	0.3

Following are the spring properties:

Spring Properties	
Direction	Spring Constant (N/m)
UX	1.00E+05
UY	1.00E+08
UZ	1.00E+11
ROT (X, Y, Z)	1.00E+20

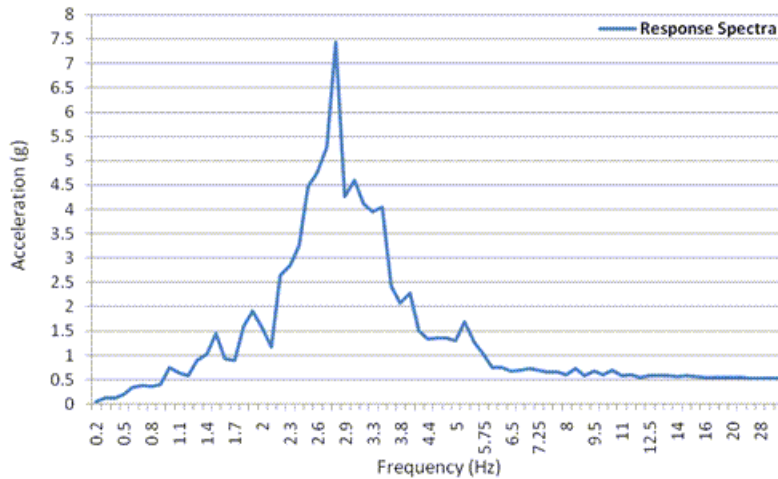


## 12.5. Boundary Conditions and Loading

Fixed support conditions are applied at the second node of each spring, as shown in [Figure 12.3: Elastic Supports Meshed with COMBIN14 Elements](#) (p. 162).

The input spectrum is a one-percent acceleration response spectrum, represented here:

**Figure 12.4: Input-Acceleration Response Spectra (1% X Direction)**

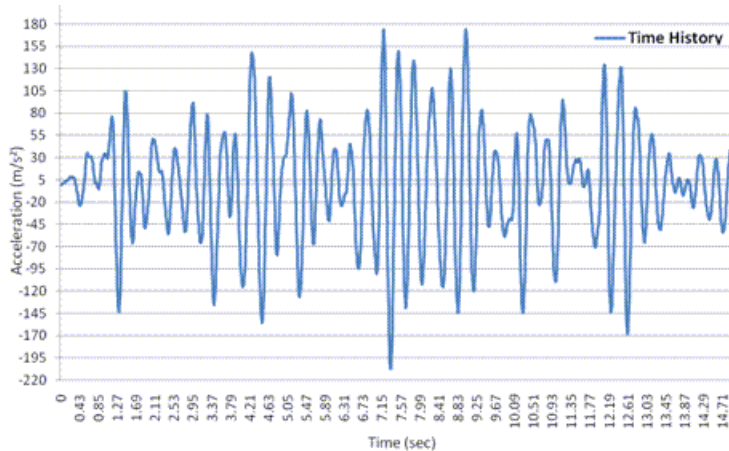


The input-acceleration response is applied in the X direction. It exhibits a sharp, highly amplified peak at the fundamental frequency of the structure/soil system. Its characteristics are  $f_{ZPA} \approx 16.50$  Hz and  $ZPA = 0.54$  g.

Generally, piping systems experience this type of seismic input instead of ground motion associated with broad-banded response spectra. For this study, the unbroadened spectrum is used to provide a direct comparison to the time history analysis results.

Following is the input-acceleration time history along the X direction:

**Figure 12.5: Input-Acceleration Time History (X Direction)**



The ground motion is consistent with the input-acceleration response spectrum shown in [Figure 12.4: Input-Acceleration Response Spectra \(1% X Direction\)](#) (p. 163).

For full-transient and response-spectrum analyses performed using all three-directional inputs, the same input is considered for both horizontal X and Z directions. In the vertical Y direction, the input is considered to be 2/3 of the horizontal input.

## 12.6. Analysis and Solution Controls

The following analysis and solution-control topics are available:

[12.6.1. Response-Spectrum Analysis Summary](#)

[12.6.2. Full-Transient Analysis Summary](#)

### 12.6.1. Response-Spectrum Analysis Summary

Following is a summary of the response-spectrum analyses (RSAs) and corresponding solution controls:

Case	Input Spectra	Mode-Combination Method	Missing-Mass Effect	Rigid-Response Effect	
A1	X-direction input	SRSS	No	No	
A2		CQC	No	No	
A3			No	No	
A4			Yes ( <b>MMASS</b> ,ON, 0.54) <sup>1</sup> (p. 164)	Yes	Yes ( <b>RIGRESP</b> ,ON,LINDLEY,0.54)
A5				Yes	Yes ( <b>RIGRESP</b> ,ON,GUPTA,2.80,11.90) <sup>2</sup> (p. 164)
A6				Yes	Yes ( <b>RIGRESP</b> ,ON,GUPTA,2.80,6) <sup>2</sup> (p. 164)
A7	X-, Y-, and Z-direction inputs	Yes		Yes ( <b>RIGRESP</b> ,ON,LINDLEY,0.54)	

1. The input spectrum unit is g. To transform it into SI units, set  $FACT = 386.4$  on the **SVTYP** command.
2. The rigid-response effect initial frequency is 2.80 Hz ( $VAL1$  on the **RIGRESP** command), and the final frequency is 6 Hz or 11.90 Hz ( $VAL2$ ).

Fourteen modes exist below  $f_{ZPA}$ . All 14 modes are used in all seven spectrum analyses.

### 12.6.2. Full-Transient Analysis Summary

In the transient analysis, the damping coefficients  $\alpha$  (proportional to the mass) and  $\beta$  (proportional to the stiffness) must be specified to reproduce the input spectrum's one-percent constant modal damping.

The equation  $\xi_i = \alpha/2\omega_i + \beta\omega_i/2$  is used for the damping coefficients, where  $\omega_i$  is the natural circular frequency of mode  $i$ .

The coefficients are determined by specifying the target modal damping at the fundamental frequency (2.91 Hz) and at an intermediate frequency between this frequency and  $f_{ZPA}$ . A frequency of 14.32 Hz is chosen to achieve the best fit over the 2.91 Hz to 16.50 Hz range of interest.

The values obtained are  $\alpha = 0.304$  (**ALPHAD**) and  $\beta = 1.85e-4$  (**BETAD**). Small variations of these coefficients have a negligible effect on the results.

Automatic time stepping ensures that the time step is small enough to accurately calculate the higher mode responses. The duration of the analysis is 14.99 seconds.

When performing the time history analysis with three-directional input motions, the individual responses for each input motion (X, Y, and Z directions) are combined using the SRSS method.

## 12.7. Results and Discussion

The following table shows the natural frequencies of the 14 significant modes (below  $f_{ZPA}$ ):

Mode	Frequency (Hz)
1	2.91
2	4.44
3	4.86
4	5.02
5	6.95
6	7.58
7	7.82
8	10.94
9	11.65
10	11.78
11	12.80
12	14.32
13	15.17
14	15.79

### 12.7.1. Results Comparison of the Time-History and Response-Spectrum Analyses

The reactions at the supports obtained in the spectrum analyses A1 through A7 are given in the following topics:

[12.7.1.1. RSAs A1 and A2](#)

[12.7.1.2. RSA A3](#)

[12.7.1.3. RSAs A4 and A5](#)

[12.7.1.4. RSA A6](#)

[12.7.1.5. RSA A7](#)

The ratio of the RSA results to the transient results is reported in separate columns. The mean and standard deviation of these ratios are evaluated at the bottom of each table. This form of representation facilitates easy recognition of over-prediction and under-prediction by the RSA method.

A ratio of 1.0 indicates exact agreement, a ratio of > 1.0 indicates RSA over-prediction, and a ratio of < 1.0 indicates RSA under-prediction.

The absolute acceleration solutions are also compared for the x-direction and 3-direction input motions.

### 12.7.1.1. RSAs A1 and A2

The accuracy of the RSA results using SRSS or CQC combination method is assessed.

The modes are closely spaced, as shown:

Mode Number	Frequency (Hz)	Coupled Modes		Coupling Coefficient
		Mode No.	Freq. (Hz)	
3	4.857	4	5.017	0.276
6	7.581	7	7.816	0.299
9	11.653	10	11.775	0.787
12	14.316	13	15.173	0.106

Because of the closely spaced modes, the CQC results are closer to the reference (transient-analysis results). The mean and standard-deviation values of spectrum results using CQC are 1.57 and 1.11, respectively.

**Table 12.1: X-Direction Input**

S. No.	Reaction Forces	Reference Full Transient	A1 Spectrum (SRSS)	Ratio (A1 / Reference)	A2 Spectrum (CQC)	Ratio (A2 / Reference)
1	FX1	49.94	31.21	0.62	31.33	0.63
2	FY1	4.40	15.54	3.53	12.86	2.92
3	FZ1	5.95	48.91	8.22	24.88	4.18
4	MX1	180.56	1510.42	8.37	763.03	4.23
5	MY1	846.19	1216.04	1.44	929.90	1.10
6	MZ1	817.39	1120.07	1.37	1116.05	1.37
7	FX4	111.33	45.18	0.41	45.00	0.40
8	FZ4	34.74	82.06	2.36	55.61	1.60
9	FY74	10.94	28.26	2.58	16.75	1.53
10	FY11	11.38	18.21	1.60	16.40	1.44
11	FZ11	68.12	43.51	0.64	42.81	0.63
12	FX15	644.57	368.12	0.57	388.15	0.60
13	FY17	28.09	44.59	1.59	46.16	1.64
14	FZ17	64.67	53.49	0.83	55.37	0.86
15	FY36	60.62	161.97	2.67	168.30	2.78
16	FZ36	55.51	81.73	1.47	82.17	1.48
17	FX38	750.51	116.78	0.16	135.75	0.18
18	FY38	40.04	52.38	1.31	54.17	1.35

S. No.	Reaction Forces	Reference Full Transient	A1 Spectrum (SRSS)	Ratio (A1 / Reference)	A2 Spectrum (CQC)	Ratio (A2 / Reference)
19	FZ38	38.43	39.05	1.02	44.45	1.16
20	MX38	787.11	2527.87	3.21	2591.22	3.29
21	MY38	2656.44	2528.86	0.95	2887.73	1.09
22	MZ38	2816.48	3644.84	1.29	3756.73	1.33
23	FX23	259.50	176.84	0.68	193.44	0.75
24	FY23	42.34	144.53	3.41	150.71	3.56
25	FX31	60.09	9.59	0.16	11.23	0.19
26	FY31	13.39	22.28	1.66	24.92	1.86
27	FZ31	15.06	32.85	2.18	33.60	2.23
28	MX31	968.59	2151.45	2.22	2241.86	2.31
29	MY31	546.34	210.58	0.39	236.59	0.43
30	MZ31	2231.74	631.42	0.28	730.46	0.33
<b>Mean of 30 components</b>				1.91	-	1.58
<b>Standard deviation of 30 components</b>				1.95	-	1.12

### 12.7.1.2. RSA A3

To improve accuracy, the missing-mass response is included in the analysis. The standard deviation decreases to 1.05. The mean value of 1.72 still shows over-prediction in the results.

**Table 12.2: X-Direction Input (with Missing-Mass Effect)**

S. No.	Reaction Forces	Reference Full Transient	A3 Spectrum	Ratio (A3 / Reference)
1	FX1	49.94	42.88	0.86
2	FY1	4.40	15.60	3.55
3	FZ1	5.95	25.01	4.20
4	MX1	180.56	765.49	4.24
5	MY1	846.19	935.02	1.10
6	MZ1	817.39	1126.10	1.38
7	FX4	111.33	75.26	0.68
8	FZ4	34.74	56.13	1.62
9	FY74	10.94	16.75	1.53
10	FY11	11.38	16.40	1.44
11	FZ11	68.12	43.86	0.64
12	FX15	644.57	388.85	0.60
13	FY17	28.09	46.16	1.64
14	FZ17	64.67	55.66	0.86
15	FY36	60.62	168.31	2.78
16	FZ36	55.51	86.07	1.55

S. No.	Reaction Forces	Reference Full Transient	A3 Spectrum	Ratio (A3 / Reference)
17	FX38	750.51	583.19	0.78
18	FY38	40.04	54.18	1.35
19	FZ38	38.43	50.26	1.31
20	MX38	787.11	2591.24	3.29
21	MY38	2656.44	3135.26	1.18
22	MZ38	2816.48	3756.91	1.33
23	FX23	259.50	242.94	0.94
24	FY23	42.34	150.77	3.56
25	FX31	60.09	53.26	0.89
26	FY31	13.39	27.91	2.09
27	FZ31	15.06	34.04	2.26
28	MX31	968.59	2252.48	2.33
29	MY31	546.34	390.59	0.71
30	MZ31	2231.74	1822.15	0.82
<b>Mean of 30 components</b>				1.72
<b>Standard deviation of 30 components</b>				1.06

### 12.7.1.3. RSAs A4 and A5

Both missing-mass and rigid-response effects are taken into account in the analyses. The mean and standard-deviation values using the Gupta method are equal to 1.10 and 0.17, respectively. Using the Lindley-Yow method, the mean and standard-deviation values are 1.19 and 0.24, respectively.

**Table 12.3: X-Direction Input (with Missing-Mass and Rigid-Response Effects)**

S. No.	Reaction Forces	Reference Full Transient	A4 Spectrum (Lindley)	Ratio (A4 / Reference)	A5 Spectrum (Gupta)	Ratio (A5 / Reference)
1	FX1	49.94	52.24	1.05	53.42	1.07
2	FY1	4.40	6.08	1.38	3.74	0.85
3	FZ1	5.95	10.23	1.72	5.98	1.01
4	MX1	180.56	317.64	1.76	189.94	1.05
5	MY1	846.19	901.90	1.07	874.82	1.03
6	MZ1	817.39	982.04	1.20	984.43	1.20
7	FX4	111.33	105.26	0.95	102.74	0.92
8	FZ4	34.74	43.09	1.24	42.52	1.22
9	FY74	10.94	11.31	1.03	10.42	0.95
10	FY11	11.38	13.42	1.18	13.32	1.17
11	FZ11	68.12	51.31	0.75	49.51	0.73
12	FX15	644.57	562.49	0.87	546.98	0.85
13	FY17	28.09	35.06	1.25	35.99	1.28
14	FZ17	64.67	52.85	0.82	56.46	0.87

S. No.	Reaction Forces	Reference Full Transient	A4 Spectrum (Lindley)	Ratio (A4 / Reference)	A5 Spectrum (Gupta)	Ratio (A5 / Reference)
15	FY36	60.62	86.27	1.42	72.88	1.20
16	FZ36	55.51	66.54	1.20	68.13	1.23
17	FX38	750.51	751.13	1.00	768.11	1.02
18	FY38	40.04	46.00	1.15	45.76	1.14
19	FZ38	38.43	43.25	1.13	45.96	1.20
20	MX38	787.11	1188.24	1.51	912.70	1.16
21	MY38	2656.44	3008.28	1.13	3208.35	1.21
22	MZ38	2816.48	3236.99	1.15	3229.79	1.15
23	FX23	259.50	323.39	1.25	344.66	1.33
24	FY23	42.34	67.15	1.59	48.83	1.15
25	FX31	60.09	60.53	1.01	62.19	1.03
26	FY31	13.39	17.09	1.28	16.82	1.26
27	FZ31	15.06	20.49	1.36	20.76	1.38
28	MX31	968.59	1316.65	1.36	1380.33	1.43
29	MY31	546.34	511.67	0.94	551.75	1.01
30	MZ31	2231.74	2193.87	0.98	2313.51	1.04
<b>Mean of 30 components</b>				1.19	-	1.10
<b>Standard deviation of 30 components</b>				0.24	-	0.16

Gupta method, with  $f_1 = 2.80$  Hz and  $f_2 = 11.90$  Hz.

The absolute acceleration values at support (node 4) and far from support (nodes 16 and 34) are compared in the following table:

**Table 12.4: X-Direction Input Motion**

Node	Reference Full Transient (absolute)	A5 Spectrum ACC (with RIGRESP)	Error (%)	Reference Full Transient (absolute)	A5 Spectrum ACC (with RIGRESP + MMASS)	Error (%)
16	310.21	285.01	8.12	310.21	277.14	10.66
4	207.54	10.62	<b>94.88</b>	207.54	209.36	0.88
34	226.27	233.43	3.16	226.27	227.20	0.41

It is clearly shown that the absolute acceleration value at node 4 (at support) shows close comparison with the full transient solution after the addition of the missing-mass effect.

### 12.7.1.4. RSA A6

With the Gupta method, there is a limitation lying in the semi-empirical basis of the definition of the rigid-response coefficient  $\alpha_i$ , as a function of  $f_i$ . [2][3] The choice of key parameter  $f_2$  (**RIGRESP**, VAL2), which defines the frequency above which modal responses are combined algebraically, has a significant effect on the predicted response.

To show the effect of the  $f_2$  value, two different values of  $f_2$  are chosen: 6.0 Hz [2 Appendix H] and 11.90 Hz.[4] Both frequencies are within a range where the input acceleration is almost constant and the acceleration value is very close to the ZPA. A value of  $f_1 = 2.80$  Hz is maintained for both analyses. The respective results are shown in the following two tables:

For  $f_2 = 6.0$  Hz, the mean and standard-deviation values are 0.91 and 0.18, respectively, implying under-prediction of the reaction forces. Conversely, for  $f_2 = 11.90$  Hz, the mean and standard-deviation values are 1.10 and 0.17, respectively, implying over-prediction of reaction forces.

**Table 12.5: X-Direction Input (with Missing-Mass and Rigid-Response Effects)**

S. No.	Reaction Forces	Reference Full Transient	A6 Spectrum (Gupta)	Ratio (A6 / Reference)
1	FX1	49.94	51.17	1.02
2	FY1	4.40	3.13	0.71
3	FZ1	5.95	4.04	0.68
4	MX1	180.56	135.93	0.75
5	MY1	846.19	904.65	1.07
6	MZ1	817.39	885.76	1.08
7	FX4	111.33	111.51	1.00
8	FZ4	34.74	34.90	1.00
9	FY74	10.94	9.20	0.84
10	FY11	11.38	9.38	0.82
11	FZ11	68.12	62.10	0.91
12	FX15	644.57	641.25	0.99
13	FY17	28.09	26.35	0.94
14	FZ17	64.67	46.56	0.72
15	FY36	60.62	44.91	0.74
16	FZ36	55.51	56.27	1.01
17	FX38	750.51	757.30	1.01
18	FY38	40.04	42.35	1.06
19	FZ38	38.43	42.26	1.10
20	MX38	787.11	399.46	0.51
21	MY38	2656.44	2936.13	1.11
22	MZ38	2816.48	2995.73	1.06
23	FX23	259.50	302.56	1.17
24	FY23	42.34	16.35	0.39
25	FX31	60.09	60.12	1.00
26	FY31	13.39	13.52	1.01
27	FZ31	15.06	13.16	0.87
28	MX31	968.59	784.84	0.81
29	MY31	546.34	497.54	0.91
30	MZ31	2231.74	2149.85	0.96



S. No.	Reaction Forces	Reference Full Transient	A6 Spectrum (Gupta)	Ratio (A6 / Reference)
Mean of 30 components				0.91
Standard deviation of 30 components				0.18

Gupta Method, with  $f_1 = 2.80$  Hz and  $f_2 = 6.00$  Hz.

### 12.7.1.5. RSA A7

This analysis considers the inputs in the X, Y and Z directions. The mean and standard-deviation values obtained are 1.00 and 0.10, respectively, implying that the correlation between the spectrum-analysis and transient-analysis results is better than for single-directional input. The better spectrum-analysis correlation is a result of the reactions having directions orthogonal to the input, which are not significantly improved by including the missing-mass and rigid-response effect; however, these reactions should remain smaller than the primary reactions.

**Table 12.6: 3-Direction Input (with Missing-Mass and Rigid-Response Effects)**

S. No.	Reaction Forces	Reference Full Transient	A7 Spectrum (Lindley)	Ratio (A7 / Reference)
1	FX1	54.93	56.51	1.03
2	FY1	98.63	98.71	1.00
3	FZ1	37.90	45.23	1.19
4	MX1	722.93	845.20	1.17
5	MY1	1099.20	1207.77	1.10
6	MZ1	1891.99	2013.72	1.06
7	FX4	129.34	117.53	0.91
8	FZ4	318.39	246.76	0.78
9	FY74	120.44	117.45	0.98
10	FY11	226.31	217.24	0.96
11	FZ11	287.89	229.73	0.80
12	FX15	664.97	603.60	0.91
13	FY17	91.60	94.38	1.03
14	FZ17	146.95	153.49	1.04
15	FY36	374.81	348.78	0.93
16	FZ36	830.88	830.99	1.00
17	FX38	751.27	752.08	1.00
18	FY38	181.96	191.64	1.05
19	FZ38	260.43	261.41	1.00
20	MX38	3377.83	3170.57	0.94
21	MY38	11097.98	11184.24	1.01
22	MZ38	7684.11	8443.85	1.10
23	FX23	273.79	336.42	1.23
24	FY23	264.72	233.99	0.88

S. No.	Reaction Forces	Reference Full Transient	A7 Spectrum (Lindley)	Ratio (A7 / Reference)
25	FX31	61.21	61.70	1.01
26	FY31	90.08	92.93	1.03
27	FZ31	138.59	140.44	1.01
28	MX31	9033.85	9045.39	1.00
29	MY31	746.60	714.41	0.96
30	MZ31	2624.24	2584.03	0.98
<b>Mean of 30 components</b>				1.00
<b>Standard deviation of 30 components</b>				0.10

The absolute acceleration values at support (node 4) and far from support (nodes 16 and 34) are compared in the table below:

**Table 12.7: 3-Direction Input Motion**

Node	DOF	Reference Full Transient (absolute)	A7 Spectrum ACC (with RIGRESP)	Error (%)	Reference Full Transient (absolute)	A7 Spectrum ACC (with RIGRESP + MMASS)	Error (%)
16	ACCY	518.55	496.17	4.32	518.55	484.7	6.53
4	ACCX	206.26	11.33	<b>94.51</b>	206.26	208.70	1.19
34	ACCZ	203.95	24.772	<b>87.85</b>	203.95	208.77	2.36

It is clearly shown that the absolute acceleration value at node 4 (at support) shows close comparison with the full transient solution after the addition of the missing-mass effect.

## 12.8. Recommendations

When performing a spectrum analysis that takes into account missing-mass and rigid-response effects, consider the following hints and recommendations:

- Define the ZPA frequency value ( $f_{ZPA}$ ) corresponding to the input spectrum. (This value is the beginning of the frequency range for which the acceleration remains constant and equal to the ZPA.)
- Request all solutions below  $f_{ZPA}$  in the modal analysis.
- Include all modes having a frequency below  $f_{ZPA}$  in the spectrum analysis.
- Choose a CQC mode combination to correctly combine modes with closely spaced frequencies (if any).
- Always include the missing-mass effect in the *first* simulation to verify its significance. (The missing-mass response is the result of a static analysis of the structure, so its computational cost is small.)
- Include the rigid-response effect. The Lindley-Yow method is easier to use, as only the ZPA value must be input.

## 12.9. References

The following references are used in this example problem:

1. Belzer P. et al. "Alternate Modal Combination Methods in Response Spectrum Analysis." [NUREG/CR-5627, BNL](#). October 1990.
2. Morante, R., Y. Wang. "Reevaluation of Regulatory Guidance on Modal Response Combination Methods for Seismic Response Spectrum Analysis." [NUREG/CR-6645, BNL-NUREG-52576](#). December 1999.
3. [U.S. Nuclear Regulatory Commission](#). "Combining Modal Responses and Spatial Components in Seismic Response Analysis." *Regulatory Guide 1.92*. Rev. 2. July 2006.
4. Gupta, A.K. *Response Spectrum Method in Seismic Analysis and Design of Structures*. [CRC](#), 1993.

## 12.10. Input Files

The following files were used in this problem:

### BM3 Model Input

- `BM3model.dat` -- Input file for modeling the BM3 nuclear piping system.
- `1D_time_history` -- Acceleration time history data for X-direction input motion.
- `3D_time_history` -- Acceleration time history data for 3-direction input motion.

### X-Direction Input

- `Response_Spectrum_Analysis_A5.dat` -- Input file for performing the response-spectrum analysis A5 on the BM3 model.
- `Full_Transient_Analysis1.dat` -- Input file for performing the full-transient analysis on the BM3 model.

### 3-D (X,Y,Z) Input

- `Response_Spectrum_Analysis_A7.dat` -- Input file for performing the response-spectrum analysis A7 on the BM3 model.
- `Full_Transient_Analysis2.dat` -- Input file for performing the full-transient analysis on the BM3 model.

The files are available in the `td-12` folder. See [Obtaining the Input Files \(p. xxxv\)](#) for more information.



---

## Chapter 13: Centrifugal Impeller Analysis Using Cyclic Symmetry and Linear Perturbation

---

This example problem demonstrates a centrifugal impeller blade analysis using [cyclic modeling methods](#) and [linear-perturbation](#) solution approaches. The problem includes a modal analysis, a full harmonic analysis, a prestressed modal analysis using linear perturbation, a prestressed full harmonic analysis using linear perturbation, and a prestressed mode-superposition harmonic analysis using linear perturbation.

The results of the cyclic symmetry analysis are verified against reference results obtained from an analysis of the full (360-degree) model.

Topics related to this example problem follow:

- [13.1. Introduction](#)
- [13.2. Problem Description](#)
- [13.3. Modeling](#)
- [13.4. Material Properties](#)
- [13.5. Boundary Conditions and Loading](#)
- [13.6. Analysis and Solution Controls](#)
- [13.7. Results and Discussion](#)
- [13.8. Recommendations](#)
- [13.9. References](#)
- [13.10. Input Files](#)

### 13.1. Introduction

[Cyclic symmetry modeling](#) is a powerful tool for analyzing structures with a repetitive geometric pattern 360 degrees around an axis of symmetry. Cyclic symmetry is found in many civil engineering structures such as domes, cooling towers, and industrial chimneys. It can also be found in mechanical equipment such as milling cutters, turbine blade disks, gears, fans, and pump impellers.

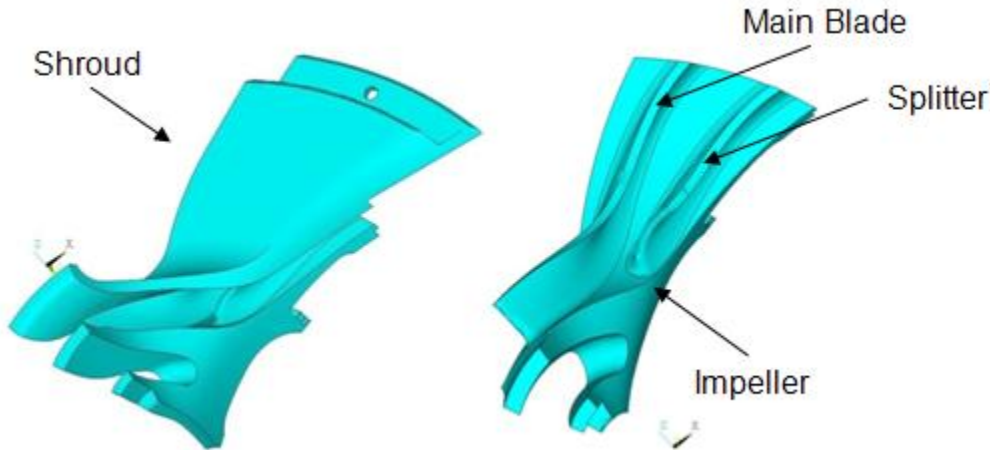
Cyclically symmetric models can be solved using a single portion (called the [basic sector](#)) of the whole structure, enforcing the continuity and compatibility boundary conditions between the cyclic substructures. A cyclic symmetry analysis vastly reduces model sizes and computational cost.

For detailed information, see the [Cyclic Symmetry Analysis Guide](#).

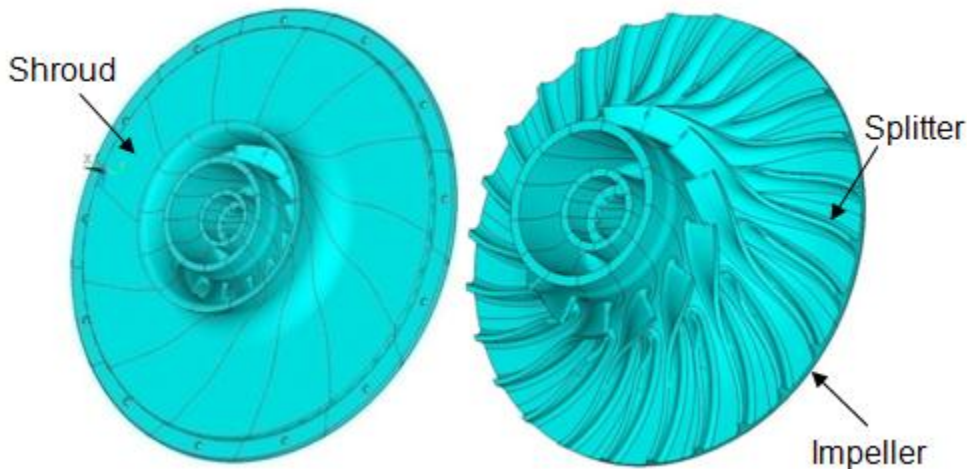
### 13.2. Problem Description

The impeller blade assembly in this example is a subsystem of a gas turbine engine used in aerospace applications.

The following model shows a cyclically symmetric sector of a single centrifugal impeller blade:

**Figure 13.1: Sector Model of Centrifugal Impeller Blade**

The model consists of a shroud and an impeller blade assembly with a sector angle of 27.692 degrees. The full model comprises 13 primary blades and splitters, as shown:

**Figure 13.2: Full Model of Centrifugal Impeller Blade**

Modal, perturbed prestressed modal with linear and nonlinear base static solution, full harmonic, perturbed prestressed full harmonic with nonlinear base static solution, and perturbed prestressed mode-superposition harmonic analyses with nonlinear base static solution are performed on the cyclic-sector model.

The perturbed modal cyclic symmetry analysis includes the initial prestressed condition from both the linear and nonlinear static analyses. The initial stress state with the linear static solution is produced by the spinning impeller assembly as well as the pressure load applied on the impeller blade. The initial stress state with the nonlinear static analysis is produced by the spinning impeller blade, a pressure load applied on the impeller blade, and thermal loading applied on all nodes of the impeller blade assembly model.

The perturbed full harmonic and perturbed mode-superposition harmonic cyclic symmetry analyses include the initial prestressed condition due to the nonlinear static analysis. The initial stress state is produced by the spinning of the impeller assembly and thermal loading applied on all nodes of the impeller blade assembly model.

Modal, perturbed modal, full harmonic, and perturbed full harmonic analyses of the full (360-degree) model are also performed to validate the accuracy of cyclic-sector model results.

## 13.3. Modeling

Following are the topics related to the cyclic symmetry modeling for this problem:

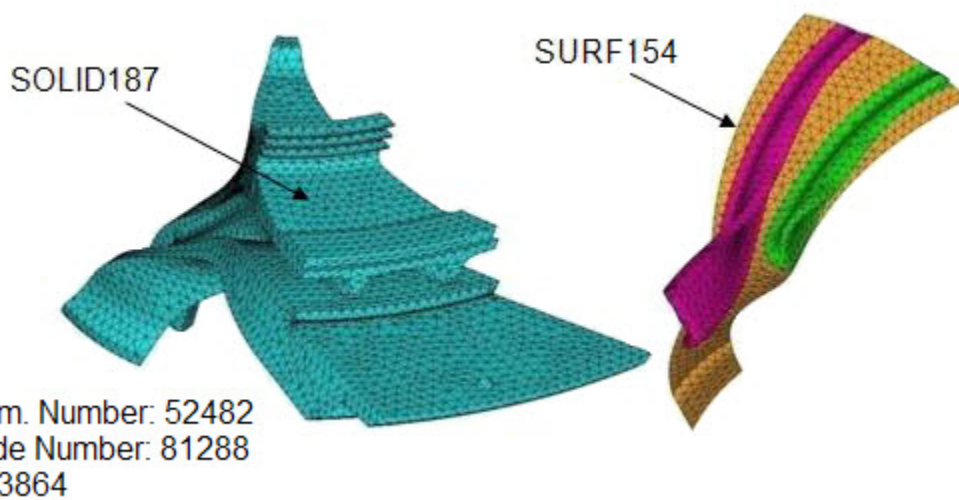
[13.3.1. Impeller Blade Modeling](#)

[13.3.2. Contact Modeling](#)

### 13.3.1. Impeller Blade Modeling

The sector model of a centrifugal impeller blade is meshed with **SOLID187** elements, as shown in this figure:

**Figure 13.3: Element Plot of the Cyclic-Sector Model**

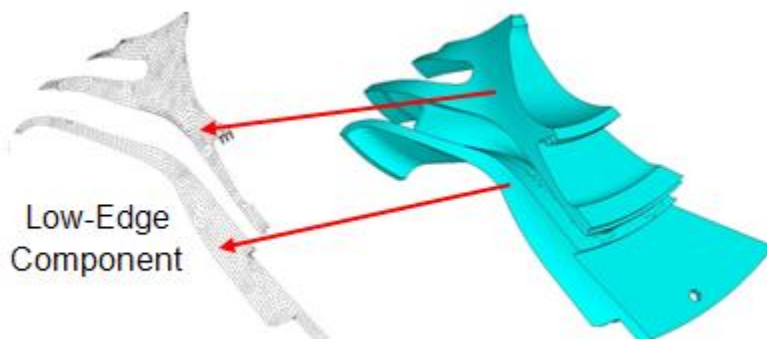


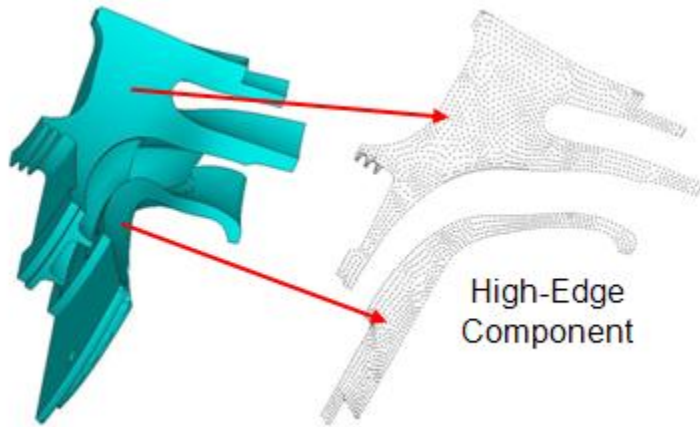
The **SOLID187** element default settings are used.

**SURF154** elements are created on the surface of the impeller blade to apply a pressure load.

The following model shows the **low- and high-edge components** of the cyclic-sector model:

**Figure 13.4: Low-Edge Component of Sector Model of Centrifugal Impeller Blade**



**Figure 13.5: High-Edge Component of Sector Model of Centrifugal Impeller Blade**

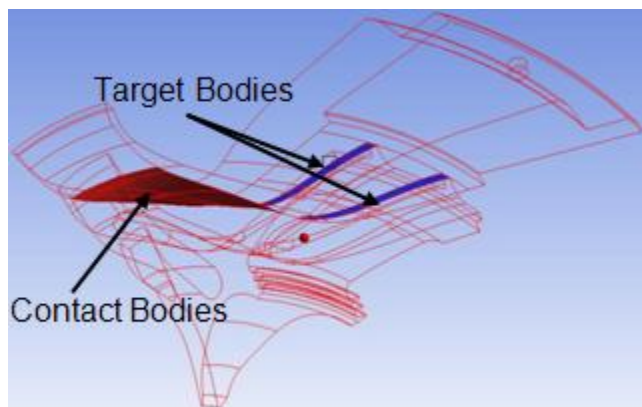
A tetrahedral mesh is used to obtain the matched node pattern along the high and low edges. To ensure the most accurate solution, it is best to have identical node and element face patterns on the low and high edges of the cyclic sector.

If you issue the **CYCLIC** command *before* meshing the cyclic sector (**AMESH** or **VMESH**), the mesh will have identical node and element face patterns on the low and high edges when possible.

For more information about sector low and high edges, see [Edge Component Pairs in the Mechanical APDL Cyclic Symmetry Analysis Guide](#).

### 13.3.2. Contact Modeling

Bonded [surface-to-surface contact](#) pairs are used to define contact between the shroud and impeller blade assembly, as shown in this figure:

**Figure 13.6: Bonded Contact Pair Between the Shroud and Impeller**

The pure penalty contact algorithm is used for bonded contact. Because [MPC](#)-based bonded contact can create overconstraint along the edge of the cyclic sectors (due to the internally generated constraint equations), the pure penalty or augmented Lagrangian penalty methods are preferred for bonded contact when used in conjunction with cyclic symmetry application.

The contact surface is meshed using **CONTA174** elements. The target surface is meshed using **TARGE170** elements.



## 13.4. Material Properties

Following are the material properties considered for modeling the cyclic sector of the impeller blade:

Impeller Blade Material Properties	
Young's Modulus ( $\text{Nm}^{-2}$ )	2.0e+005 MPa
Poisson's Ratio	0.3
Density ( $\text{Kgm}^{-3}$ )	7.85e-006 $\text{kg mm}^{-3}$
Coefficient of Thermal Expansion	1.2e-005 $^{\circ}\text{C}^{-1}$
Reference Temperature	22° C

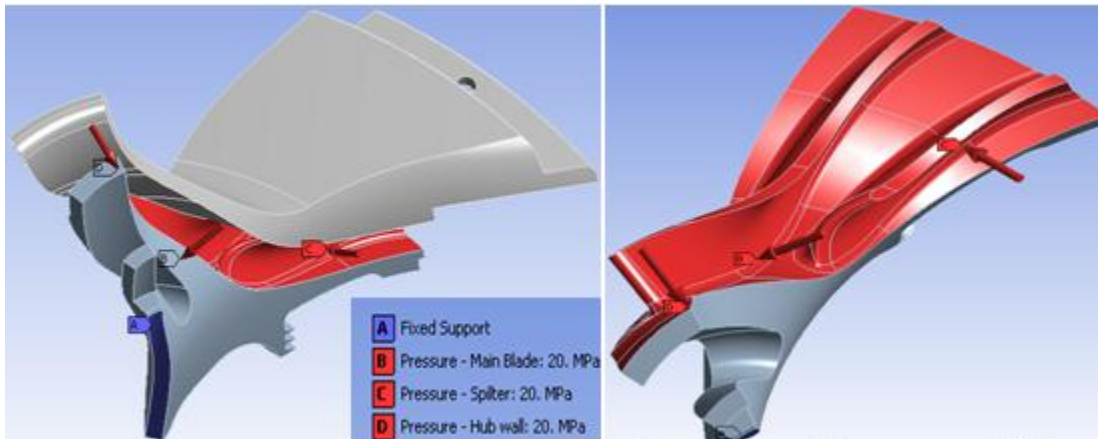
Following is the unit system used in this simulation:

Units	
Unit System	Metric (mm, kg, N, s, mV, mA) Degrees rad/s Celsius
Angle	Degrees
Rotational Velocity	rad/s
Pressure	MPa

## 13.5. Boundary Conditions and Loading

Fixed-support conditions are applied near the hub portion of the cyclic-sector impeller blade model, as shown in this figure:

**Figure 13.7: Static Fluid Pressure Load on Hub Wall, Main Blade, and Splitter**



The following loads are considered for the cyclic-symmetry analyses:

- Fluid pressure applied on the impeller blade
- Centrifugal loads caused by rotational velocity

- Thermal loads caused by the difference in reference temperature and applied temperature and due to thermal coefficient of expansion

The applied load is cyclic in nature. It is also possible to apply **non-cyclic loading** with different loading values on each of the cyclic sectors (**CYCOPT**,**LDSECT**,**SECTOR**).

The rotational velocity (**OMEGA**,0,6000,0) is applied along the global Y axis. The impeller blade assembly is modeled with a thermal coefficient expansion of  $1.2e-005 \text{ } ^\circ\text{C}^{-1}$ . The reference temperature is held at 22° C and a body temperature of 50° C is applied on all nodes of the model to generate the thermal load vector.

The thermal load vector generated from the base static solve can be ignored in the subsequent analysis (**THEXPAND**).

For the full harmonic, perturbed full harmonic, and perturbed mode-superposition harmonic analyses, the pressure load applied on the main blade, splitter, and hub wall is treated as a harmonically varying load.

## 13.6. Analysis and Solution Controls

This section describes the following analyses performed for this problem:

13.6.1. Modal Cyclic Symmetry Analysis

13.6.2. Linear Prestressed Modal Cyclic Symmetry Analysis with Linear Perturbation

13.6.3. Nonlinear Prestressed Modal Cyclic Symmetry Analysis with Linear Perturbation

13.6.4. Full Harmonic Cyclic Symmetry Analysis

13.6.5. Nonlinear Prestressed Full Harmonic Cyclic Symmetry Analysis with Linear Perturbation

13.6.6. Nonlinear Prestressed Mode-Superposition Harmonic Cyclic Symmetry Analysis with Linear Perturbation

For information about linear perturbation, see [Linear Perturbation Analysis](#) in the *Structural Analysis Guide*.

### 13.6.1. Modal Cyclic Symmetry Analysis

To begin a cyclic symmetry analysis, issue the **CYCLIC** command within **/PREP7**, the model-creation preprocessor.

The **CYCLIC** command automatically detects cyclic symmetry model information such as edge components, the number of sectors, the sector angles, and the corresponding cyclic coordinate system.

You can display the fully expanded model in the preprocessor (**/CYCEXPAND**,1,ON).

The Block Lanczos eigensolver is used to extract 10 modes. By default, all harmonic indices (0 to 6 in this case) are calculated (based on  $(N - 1) / 2$ , where N is the number of sectors). You can ignore some harmonic indices if desired (**CYCOPT**,HINDX).

The following input fragment shows the steps in this analysis:

```
/prep7

allsel, all, all
cyclic                ! Default cyclic command detects the number of sectors, the
                    ! sector angle, and the coordinate system

allsel, all, all
finish

/solu
```

```

antype, modal                ! Perform modal solve.
modopt, lanb, 10             ! Use Block Lanczos solver to extract 10 modes.
mxpand, 10                   ! Expand 10 modes, do not evaluate element results.
solve
finish

/post1
set, list,,,,,,,,order      ! Sorts the harmonic index results in ascending order
                              ! of eigen frequencies
finish

```

## 13.6.2. Linear Prestressed Modal Cyclic Symmetry Analysis with Linear Perturbation

The procedure to perform a linear prestressed modal cyclic symmetry analysis is essentially the same as a standard modal analysis, except that you must first prestress the structure by performing a static cyclic symmetry analysis.

To prestress the structure via static cyclic symmetry analysis:

1. Obtain a linear static solution. Enable file writing for performing a subsequent linear perturbation analysis (**RESCONTROL,LINER**).
2. Perform a **linear perturbed** modal analysis where the linear prestress effects are included automatically.
3. Expand the modes and then postprocess the results from `jobname.rstp`.

The following input fragment shows the steps in this analysis:

```

/solu

antype, static                ! Perform Static analysis.
rescontrol,linear,all,1      ! Enable file writing for a subsequent linear
                              ! perturbation analysis

nsub, 10, 10, 10
time, 1.0
omega, 0, 3000, 0           ! Centrifugal load
solve
save, ,db
finish

/solu
antype,static,restart,,,perturb ! Perform a static restart with perturbation
                              ! from the last load step and substep of
                              ! the previous static solve
perturb,modal,,,allkeep      ! Set the analysis options for perturbed modal
                              ! analysis
solve,elform                 ! Reform element matrices
outres,all,all
modopt,lanb,10               ! Use Block Lanczos mode extraction procedure
mxpand,10                    ! Expand the modes
solve
finish

/post1
file, ,rstp                  ! Specify the data file where results are to be found
/out,

set, list,,,,,,,,order      ! Sort the harmonic index results in ascending order
                              ! of eigen frequencies

finish

```

### 13.6.3. Nonlinear Prestressed Modal Cyclic Symmetry Analysis with Linear Perturbation

Following is the general process for performing a nonlinear prestressed modal cyclic symmetry analysis with linear perturbation:

1. Obtain a nonlinear (**NLGEOM,ON**) static solution.
2. Enable the file writing option for multiframe restart from a static analysis (**RESCONTROL**).
3. Perform a **linear perturbed** modal analysis with nonlinear prestress effects.
4. Expand the modes and then postprocess the results from `jobname.rstp`.

To better demonstrate the nonlinear effects in the prestressed model, the rotational velocity is doubled (**OMEGA,0,6000,0**) from the linear prestressed analysis, and thermal loading is added.

The following example input shows the steps in this analysis:

```

/solu

csys,0
antype,static           ! Perform Static analysis
nlgeom,on              ! Include large deformation effects
rescontrol,define,all,1 ! Enable the file writing in multiframe restart
nsub,10,10,10         ! Number of substeps = 10

allsel,all,all
nsle
bf,all,temp,50        ! Define temperature = 50

time,1.0
omega, 0, 6000, 0,    ! Centrifugal load

kbc,0
solve
finish

/solu
antype,static,restart,,perturb ! Perform a static restart with perturb
! from the last load step and substep of the previous
! static solution
perturb,modal,,allkeep      ! Set the analysis options for perturbed modal analysis
solve,elform                ! Reform element matrices

outres,all,all
modopt,lanb,10             ! Use Block Lanczos mode extraction procedure
mexpand,10                 ! Expand the modes
solve

finish

/post1
file, ,rstp                ! Specify the data file where results are to be found
/out,

set,list,,,,,,,,order      ! Sort the harmonic index results in ascending order

finish

```

### 13.6.4. Full Harmonic Cyclic Symmetry Analysis

A full harmonic analysis of the cyclic-sector model is performed in the frequency range of 1200-5500 Hz with 20 substeps. The frequency range of excitation is chosen based on the modal frequency values. With this frequency range, the first few modes of the impeller blade assembly are excited.

The following input fragment shows the steps involved in this analysis:

```
/solu

antype, harm           ! Perform harmonic analysis
harfrq,1200, 5500     ! Frequency range of excitation 1200 - 5500 Hz
hropt, full           ! Perform Full harmonic analysis
kbc, 1                 ! Use Stepped loading
nsub, 20              ! Use substep 20

solve
finish
```

### 13.6.5. Nonlinear Prestressed Full Harmonic Cyclic Symmetry Analysis with Linear Perturbation

To perform a nonlinear prestressed full harmonic cyclic symmetry analysis with linear perturbation, you must first [prestress the structure with nonlinear effects in a static solution \(p. 182\)](#). Then, the perturbed procedure is used to perform a full harmonic analysis from the prestressed stiffness matrix in a manner similar to the standard full harmonic analysis.

---

#### Note

A nonlinear prestressed perturbed full harmonic cyclic symmetric analysis is supported for the following methods (**HROPT**): FULL or VT

---

The following example input shows the steps in this analysis:

```
/solu

csys,0
antype,static          ! Perform Static analysis
nlgeom,on             ! Include large deformation effects
rescontrol,define,all,1 ! Enable the file writing in multiframe restart
nsub,10,10,10         ! Number of substeps = 10

allsel,all,all
nsle
bf,all,temp,50        ! Define temperature = 50

time,1.0
omega, 0, 6000, 0,    ! Centrifugal load
kbc,0
solve
finish

/solu
antype,static,restart,,perturb ! Perform a static restart with perturb
! from the last load step and substep of the previous
! static solution
perturb,harm,,,allkeep ! Set the analysis options for perturbed harmonic analysis
solve,elform

thexpand,off          ! Thermal loading is not included in the load vector
omega, 0, 0, 0

harfrq,1200,5500     ! Frequency range of excitation
```

```

hropt,full           ! Use full harmonic analysis option
kbc,1
nsub,20,20,20
solve
finish

```

### 13.6.6. Nonlinear Prestressed Mode-Superposition Harmonic Cyclic Symmetry Analysis with Linear Perturbation

To perform a nonlinear prestressed mode-superposition harmonic cyclic symmetry analysis with linear perturbation, you must first prestress the structure with nonlinear effects in a static solution. In order to perform a downstream mode-superposition analysis, you must specify `MSUP = ON` with the **CYCOPT** command in a static solution. The perturbed procedure is used to perform a modal analysis from the prestressed state, followed by a mode-superposition harmonic analysis.

The following example input shows the steps in this analysis:

```

/solu

csys,0
antype,static           ! Perform Static analysis
nlgeom,on              ! Include large deformation effects
rescontrol,define,all,1 ! Enable the file writing in multiframe restart
nsub,10,10,10          ! Number of substeps = 10

allsel,all,all
nsle
bf,all,temp,50         ! Define temperature = 50

time,1.0
omega, 0, 6000, 0,     ! Centrifugal load
kbc,0
cycopt,MSUP,1         ! MSUP key is ON
solve
finish

/solu
antype,static,restart,,perturb ! Perform a static restart with perturb
! from the last load step and substep of the previous
! static solution
perturb,modal,,,allkeep ! Set the analysis options for perturbed modal analysis
solve

outres,all,all
modopt,lanb,2
mexpand,2,,,yes

thexpand,off           ! Thermal loading is not included in the load vector
omega, 0, 0, 0

solve
finish

/solu

csys,0
antype,harm
hropt,MSUP             ! Choose MSUP harmonic analysis option

harfrq,1200,5500       ! Frequency range of excitation
nsub,20,20,20
cycfreq,eo,0           ! Engine order = 0
kbc,1
dmpmat,1.0e-002        ! Define constant damping ratio of 1.0%
outres,all,all
solve
finish

```

## 13.7. Results and Discussion

The modal frequencies of the centrifugal impeller blade cyclic-sector model and the full model are compared in the following table:

Mode No.	Full Model (Hz)	Cyclic Sector Model (Hz)	Error (%)
1	1710.30	1710.10	0.01
2	1983.90	1983.80	0.01
3	1984.00	1983.80	0.01
4	2822.20	2823.00	0.03
5	2897.80	2898.20	0.01
6	2898.20	2898.20	0.00
7	4152.20	4152.40	0.00
8	4152.40	4152.40	0.00
9	5373.50	5373.10	0.01
10	5373.90	5373.10	0.01

The linear (**NLGEOM,OFF**) prestressed modal frequencies of the cyclic sector obtained from the linear perturbation analysis also show strong agreement with the full-model results, as shown in the following table:

Mode No.	Full Model (Hz)	Cyclic Sector Model (Hz)	Error (%)
1	1710.90	1710.70	0.01
2	2043.00	2042.90	0.00
3	2043.10	2042.90	0.01
4	2857.50	2858.40	0.03
5	2989.50	2989.80	0.01
6	2989.90	2989.80	0.00
7	4266.10	4266.00	0.00
8	4266.40	4266.00	0.01
9	5505.30	5504.60	0.01
10	5505.80	5504.60	0.02

The nonlinear (**NLGEOM,ON**) prestressed modal frequencies obtained from the linear perturbation analysis match within reasonable tolerance with the corresponding full-model results, as shown in the following table:

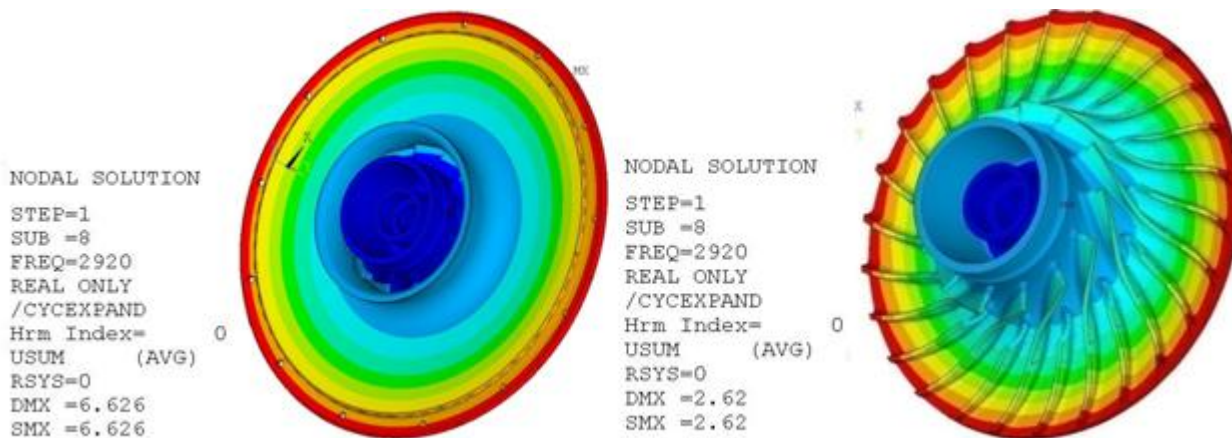
Mode No.	Full Model (Hz)	Cyclic Sector Model (Hz)	Error (%)
1	1707.70	1707.30	0.02
2	2205.10	2204.70	0.02
3	2205.20	2204.70	0.02

Mode No.	Full Model (Hz)	Cyclic Sector Model (Hz)	Error (%)
4	2947.00	2947.50	0.02
5	3239.50	3239.30	0.01
6	3239.90	3239.30	0.02
7	4568.30	4567.70	0.01
8	4568.50	4567.70	0.02
9	5847.60	5846.50	0.02
10	5848.10	5846.50	0.03

The full harmonic analysis postprocessing (/POST1) results of the cyclic-sector model are compared to the results of the full-model analysis:

**Figure 13.8: Total Deformation Pattern at Frequency of 2920 Hz**

**Deformation Pattern: Cyclic Sector Model**



**Deformation Pattern: Full Model**

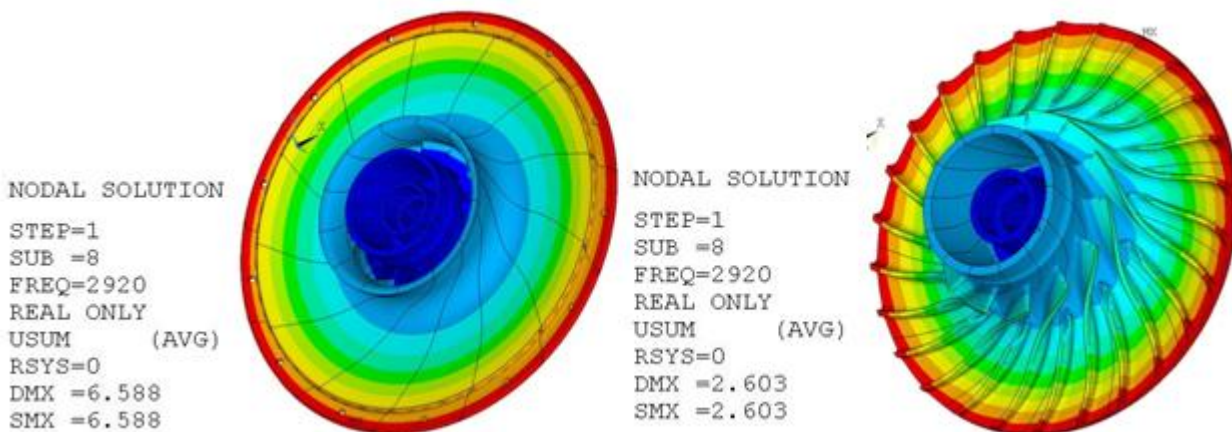
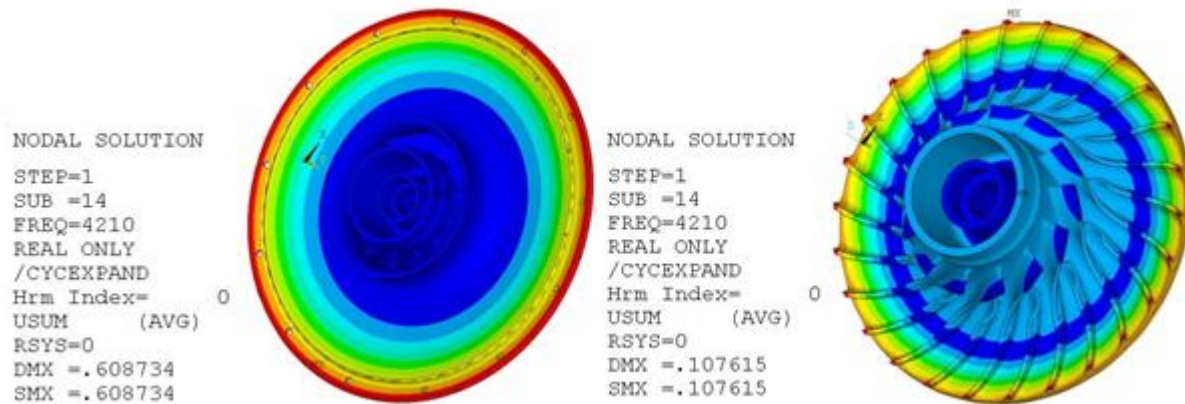


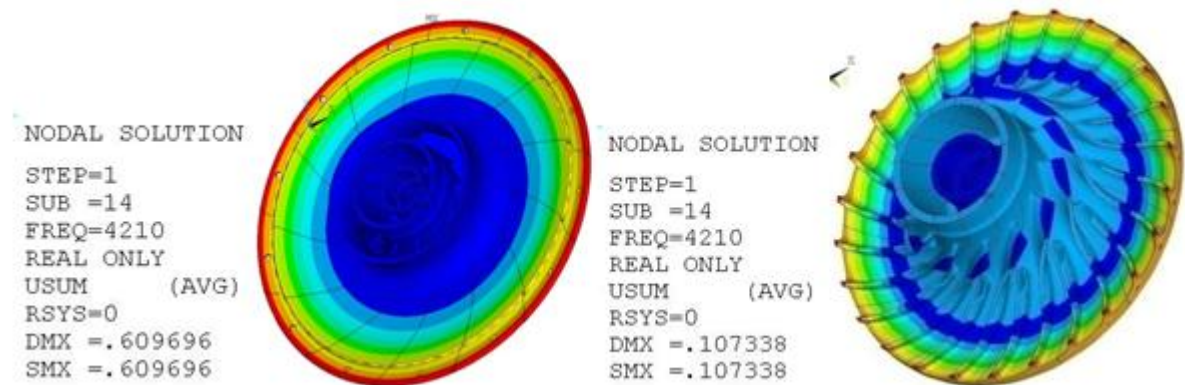


**Figure 13.9: Total Deformation Pattern at Frequency of 4210 Hz**

**Deformation Pattern: Cyclic Sector Model**



**Deformation Pattern: Full Model**

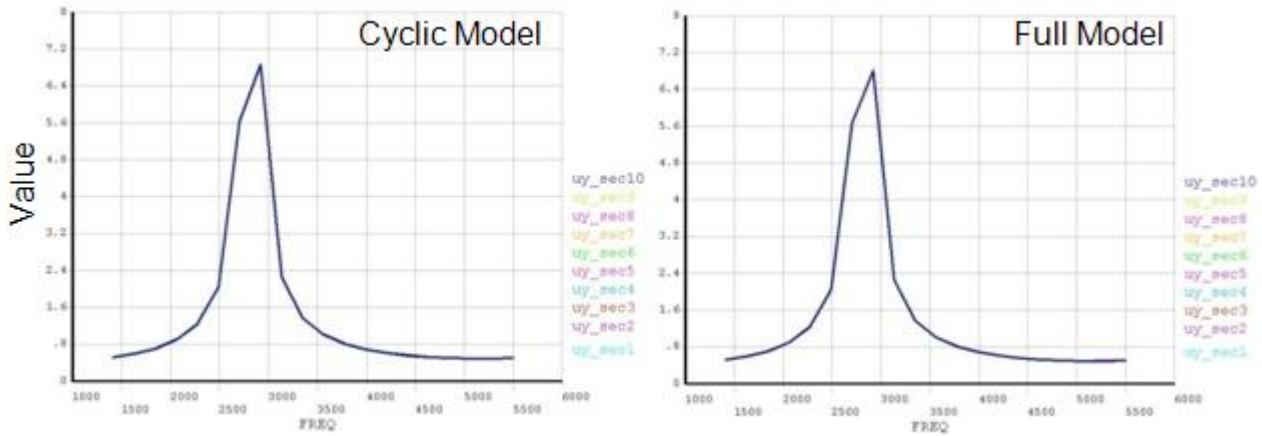


The results show strong agreement between the total deformation plots of the cyclic-sector model and the full model.

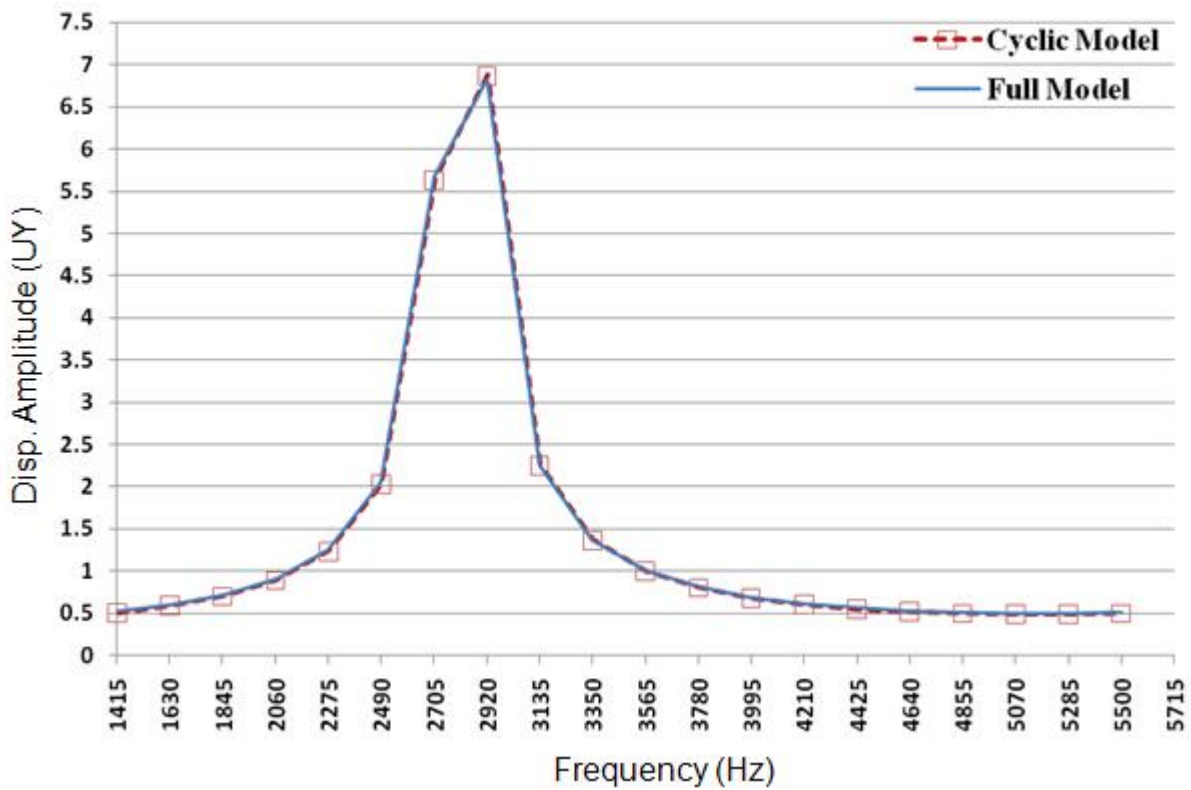
The nodal solution plots (**NSOL**) show the amplitude of a nodal degree-of-freedom (DOF) value with respect to the frequency of excitation:

**Figure 13.10: Nodal Solution Plots with Respect to the Frequency of Excitation**

**(a) Plots of Nodal Amplitude Placed at Symmetric Angular Positions**



**(b) Comparison of Nodal Displacement Amplitude of Cyclic Sector Model and Full Model**



The plots indicate the occurrence of a resonance condition at 2920 Hz. The displacement amplitude of nodes at symmetric angular positions on sectors 1 through 10 is also plotted. The plots show strong agreement between the cyclic and full-model results.

Part (b) of the figure shows the comparison of the nodal solution result (**NSOL**) of a node located at an identical location on the cyclic and full models. The agreement of results is very good and plotted curves are superimposed.

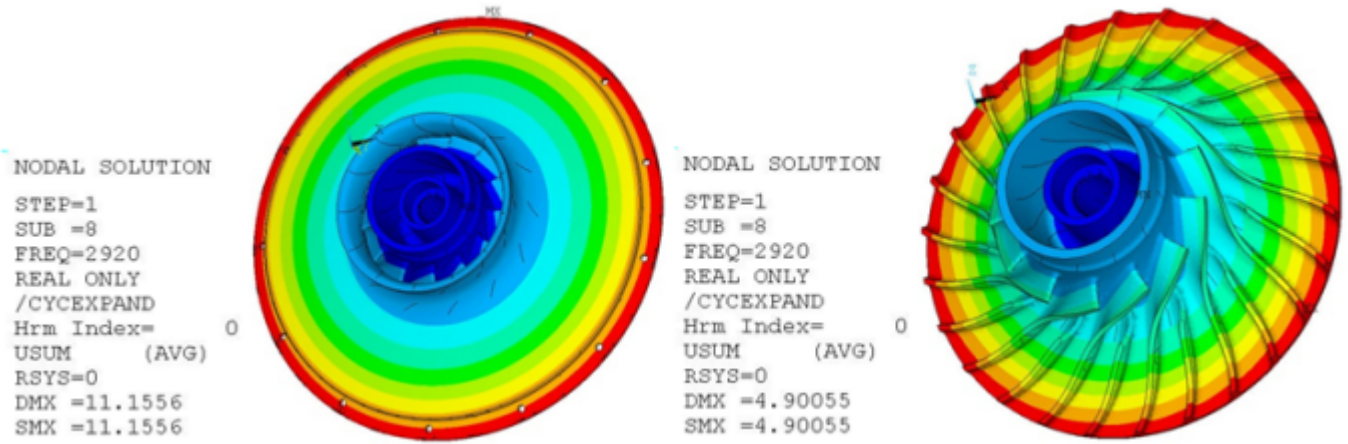
The following table compares the displacement amplitude (UY) of nodes placed symmetrically across each sector at a 2920 Hz frequency excitation. The values show strong agreement between the cyclic-sector and full-model results.

Sector No.	Frequency (Hz)	Full Model	Cyclic Sector Model	Error (%)
1	2920	6.58	6.73	2.31
2	2920	6.57	6.73	2.44
3	2920	6.56	6.73	2.53
4	2920	6.57	6.73	2.48
5	2920	6.58	6.73	2.33
6	2920	6.58	6.73	2.26
7	2920	6.58	6.73	2.33
8	2920	6.57	6.73	2.40
9	2920	6.57	6.73	2.45
10	2920	6.56	6.73	2.54
11	2920	6.57	6.73	2.47
12	2920	6.58	6.73	2.30
13	2920	6.58	6.73	2.26

For the nonlinear prestressed perturbed full harmonic analysis, the following figure compares the postprocessing (/POST1) results of the cyclic-sector model to the results of the full-model analysis:

**Figure 13.11: Total Deformation Pattern at Frequency of 2920 Hz**

**Deformation Pattern: Cyclic Sector Model**



**Deformation Pattern: Full Model**

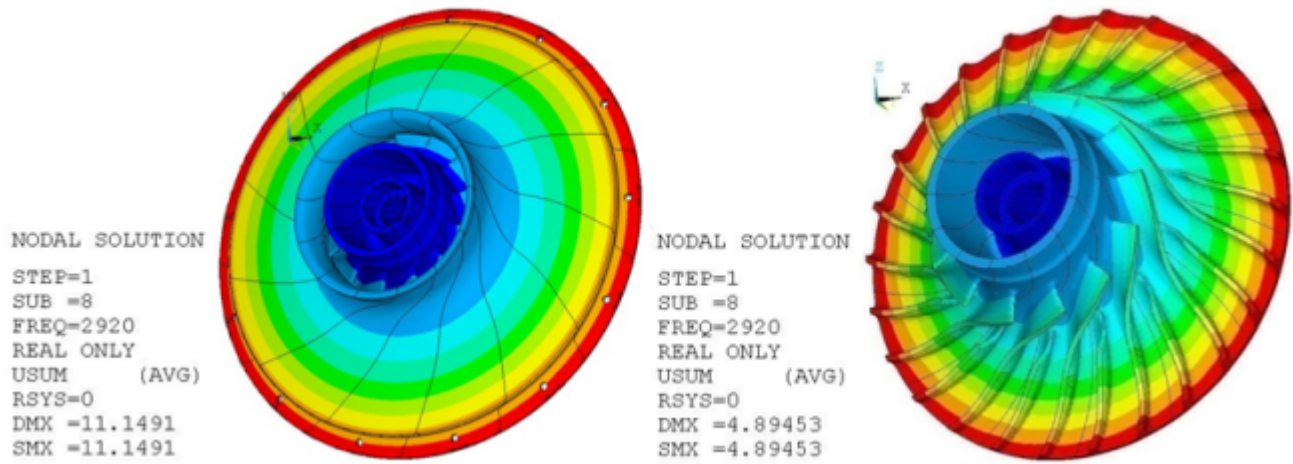
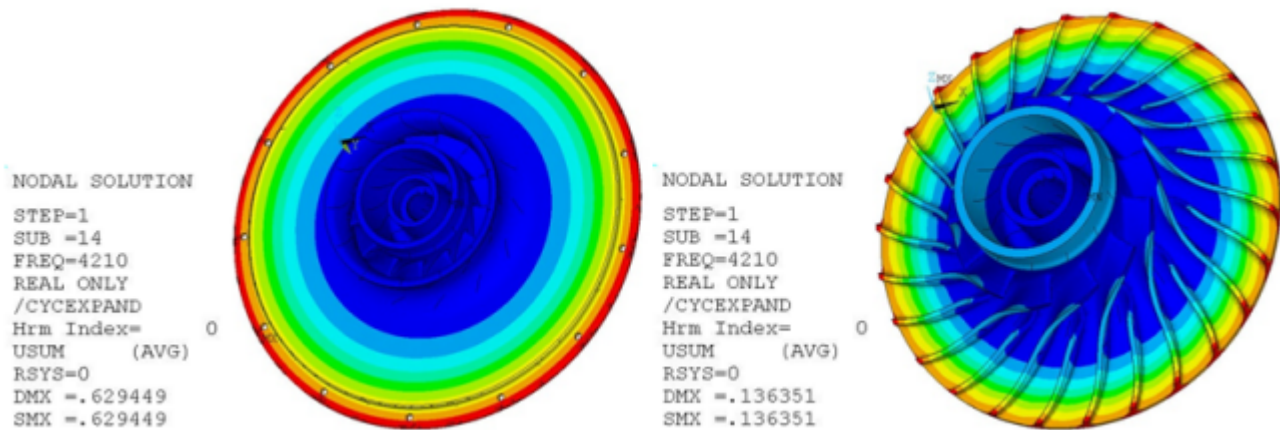
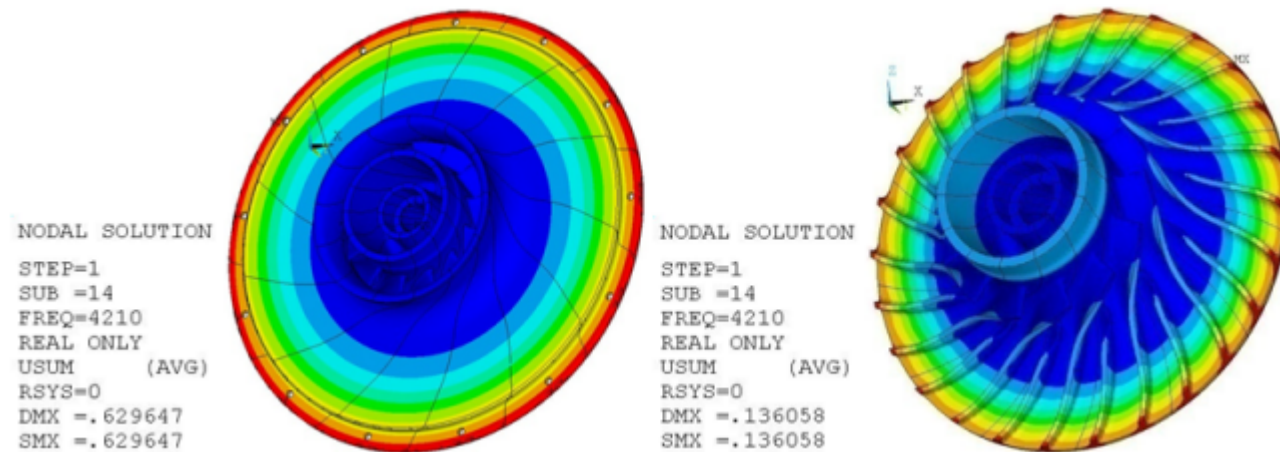


**Figure 13.12: Total Deformation Pattern at Frequency of 4210 Hz**

**Deformation Pattern: Cyclic Sector Model**



**Deformation Pattern: Full Model**

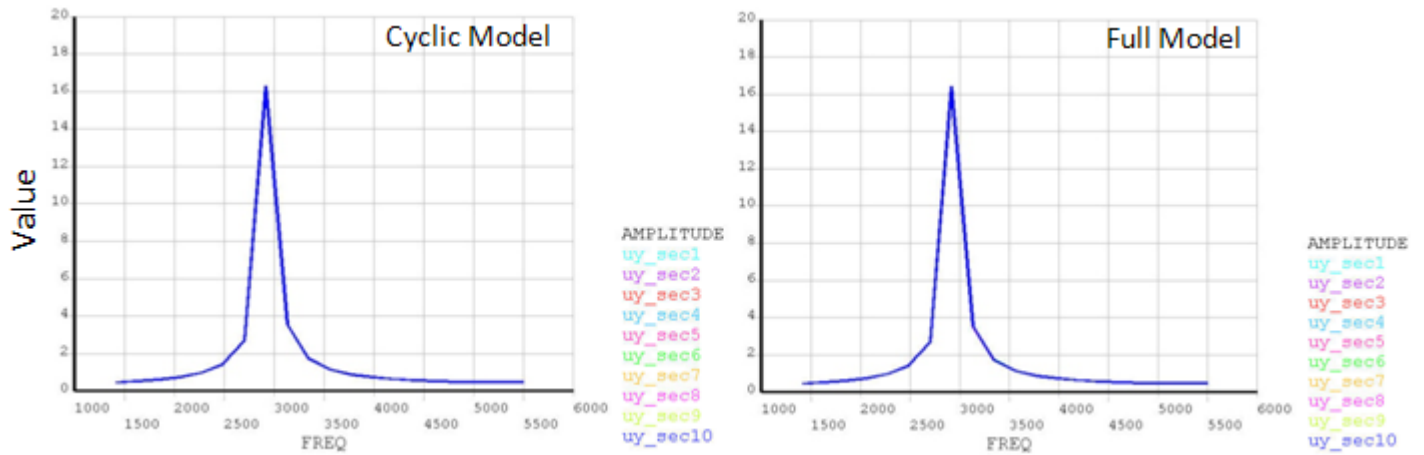


The results show strong agreement between the total deformation plots of the cyclic-sector model and the full model.

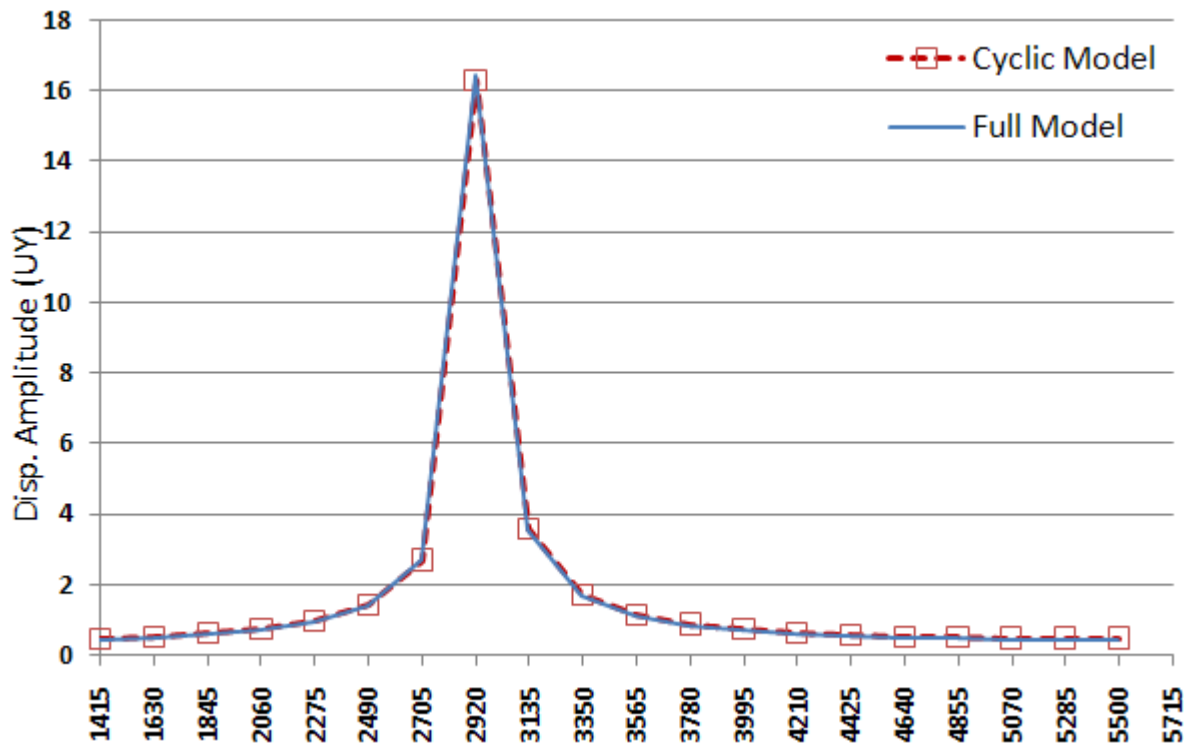
The nodal solution plots (**NSOL**) show the amplitude of a nodal degree-of-freedom (DOF) value with respect to the frequency of excitation:

**Figure 13.13: Nodal Solution Plots with Respect to the Frequency of Excitation**

**(a) Plots of Nodal Amplitude Placed at Symmetric Angular Positions**



**(b) Comparison of Nodal Displacement Amplitude of Cyclic Sector Model and Full Model**



The plots indicate the occurrence of a resonance condition at 2920 Hz. The displacement amplitude of nodes at symmetric angular positions on sectors 1 through 10 is also plotted. The plots show strong agreement between the cyclic and full-model results.

Part (b) of the figure shows the comparison of the nodal solution result (**NSOL**) of a node located at an identical location on the cyclic and full models.

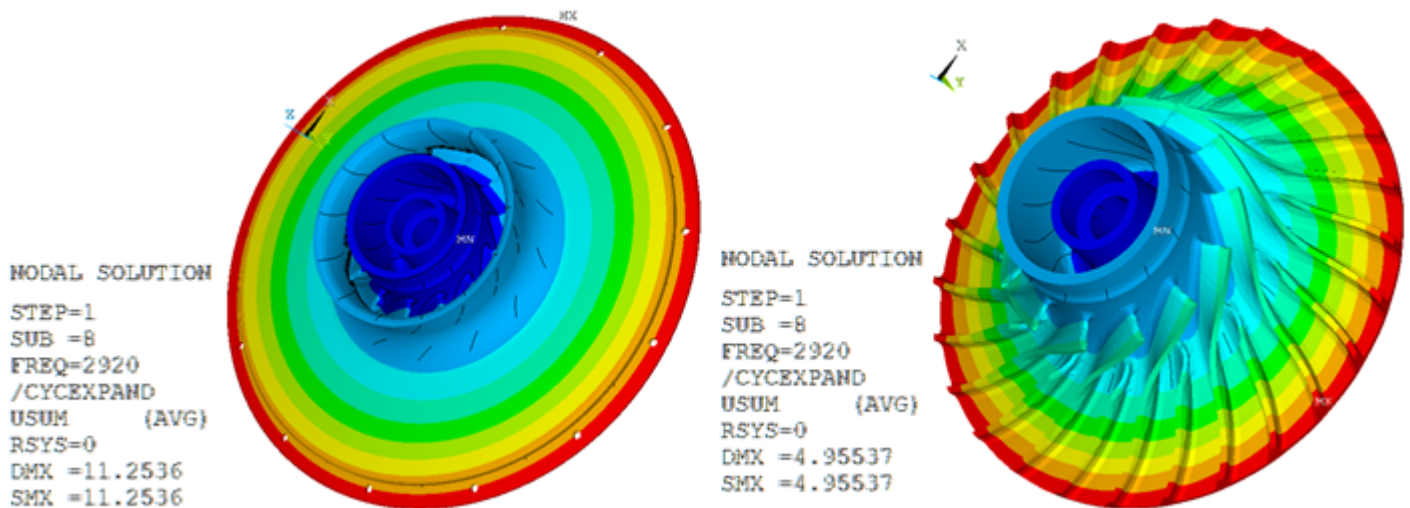
The following table compares the displacement amplitude (UY) of nodes placed symmetrically across each sector at 2920 Hz (frequency of excitation). The values show strong agreement between the cyclic-sector and full-model results.

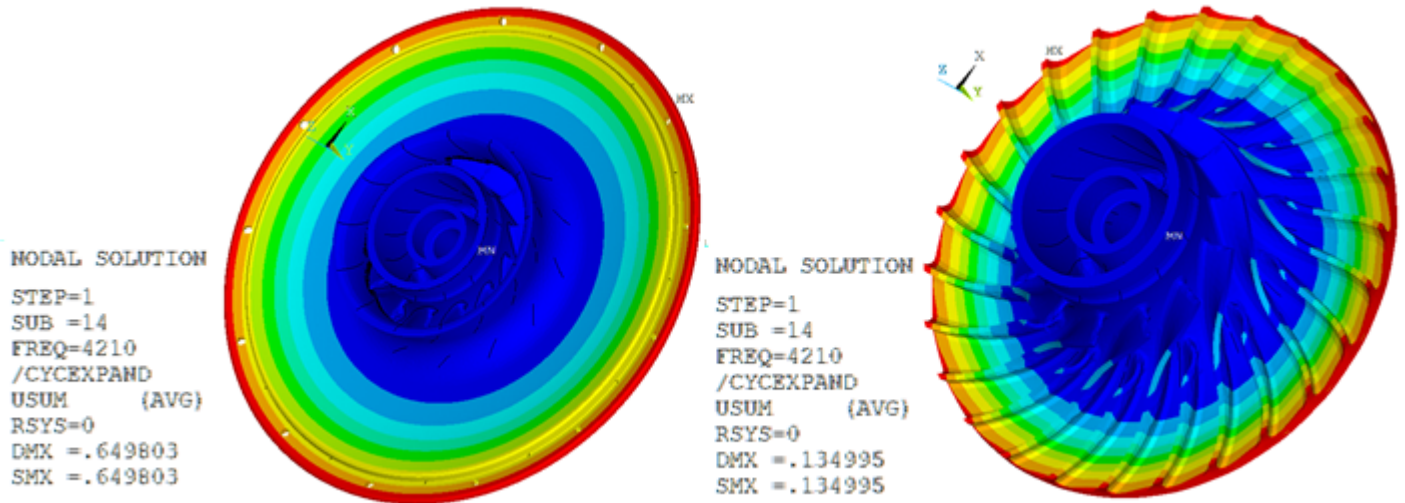
Sector No.	Frequency (Hz)	Full Model	Cyclic Sector Model	Error (%)
1	2920	11.13	11.15	0.18
2	2920	11.14	11.15	0.09
3	2920	11.14	11.15	0.09
4	2920	11.14	11.15	0.09
5	2920	11.14	11.15	0.09
6	2920	11.13	11.15	0.18
7	2920	11.13	11.15	0.18
8	2920	11.13	11.15	0.18
9	2920	11.14	11.15	0.09
10	2920	11.13	11.15	0.18
11	2920	11.13	11.15	0.18
12	2920	11.13	11.15	0.18
13	2920	11.13	11.15	0.18

For the nonlinear prestressed perturbed mode-superposition harmonic analysis, the following figures show the postprocessing (/POST1) results of the cyclic-sector model:

**Figure 13.14: Total Deformation Pattern at Frequency of 2920 Hz**

#### Deformation Pattern: Cyclic Sector Model



**Figure 13.15: Total Deformation Pattern at Frequency of 4210 Hz****Deformation Pattern: Cyclic Sector Model**

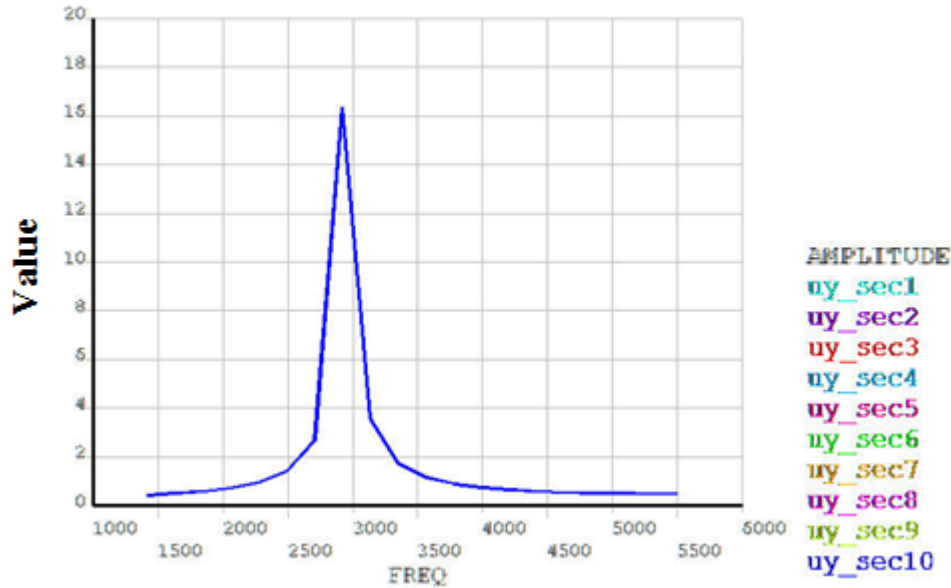
The results show close comparison between the total deformation plots obtained from nonlinear prestressed perturbed mode-superposition harmonic and the nonlinear prestressed perturbed full harmonic analyses.

The nodal solution plots (**NSOL**) show the amplitude of a nodal degree-of-freedom (DOF) value with respect to the frequency of excitation:

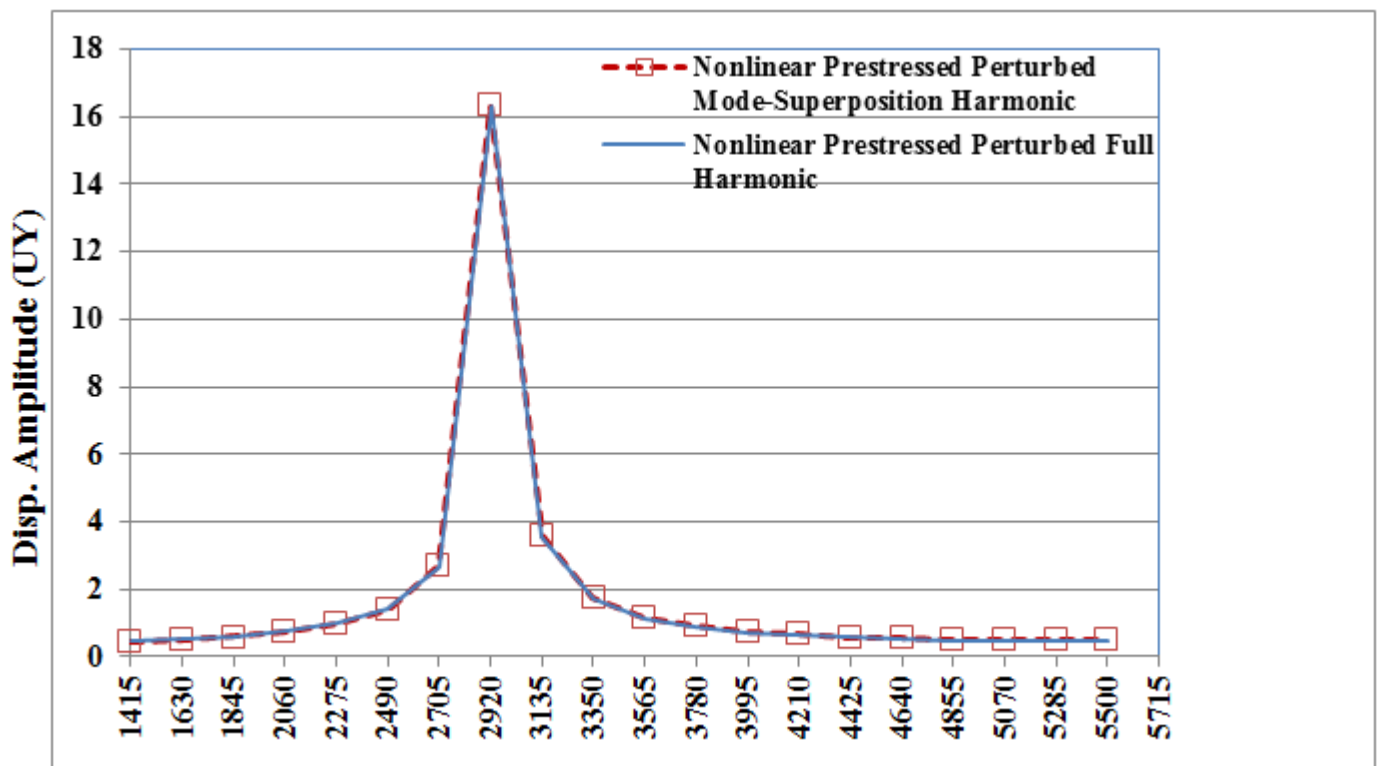


**Figure 13.16: Nodal Solution Plots with Respect to the Frequency of Excitation**

**(a) Plot of Nodal Amplitude Place at Symmetric Angular Positions**



**(b) Comparison of Nodal Displacement Amplitude**



The plots indicate the occurrence of a resonance condition at 2920 Hz. The displacement amplitude of nodes at symmetric angular positions on sectors 1 through 10 is also plotted. The plots show close comparison with the nonlinear prestressed perturbed full harmonic analysis results.

Part (b) of the figure shows the comparison of the nodal solution result (**NSOL**) of a node located at an identical location for the nonlinear prestressed perturbed mode-superposition and nonlinear prestressed perturbed full harmonic analyses.

The following table compares the displacement amplitude (UY) of nodes placed symmetrically across each sector at 2920 Hz (frequency of excitation). The values show close comparison between the nonlinear prestressed perturbed mode-superposition and nonlinear prestressed perturbed full harmonic analyses results.

Sector No.	Frequency (Hz)	Nonlinear Prestressed Perturbed Full Harmonic	Nonlinear Prestressed Perturbed Mode-Superposition Harmonic	Difference (%)
1	2920	11.13	11.24	0.99
2	2920	11.14	11.24	0.90
3	2920	11.14	11.24	0.90
4	2920	11.14	11.24	0.90
5	2920	11.14	11.24	0.90
6	2920	11.13	11.24	0.99
7	2920	11.13	11.24	0.99
8	2920	11.13	11.24	0.99
9	2920	11.14	11.24	0.90
10	2920	11.13	11.24	0.99
11	2920	11.13	11.24	0.99
12	2920	11.13	11.24	0.99
13	2920	11.13	11.24	0.99

### 13.7.1. Performance Benefits of Cyclic Symmetry Analysis

The following table shows that the cyclic-sector model requires far fewer computational resources and much less memory than the full model for the various analyses:

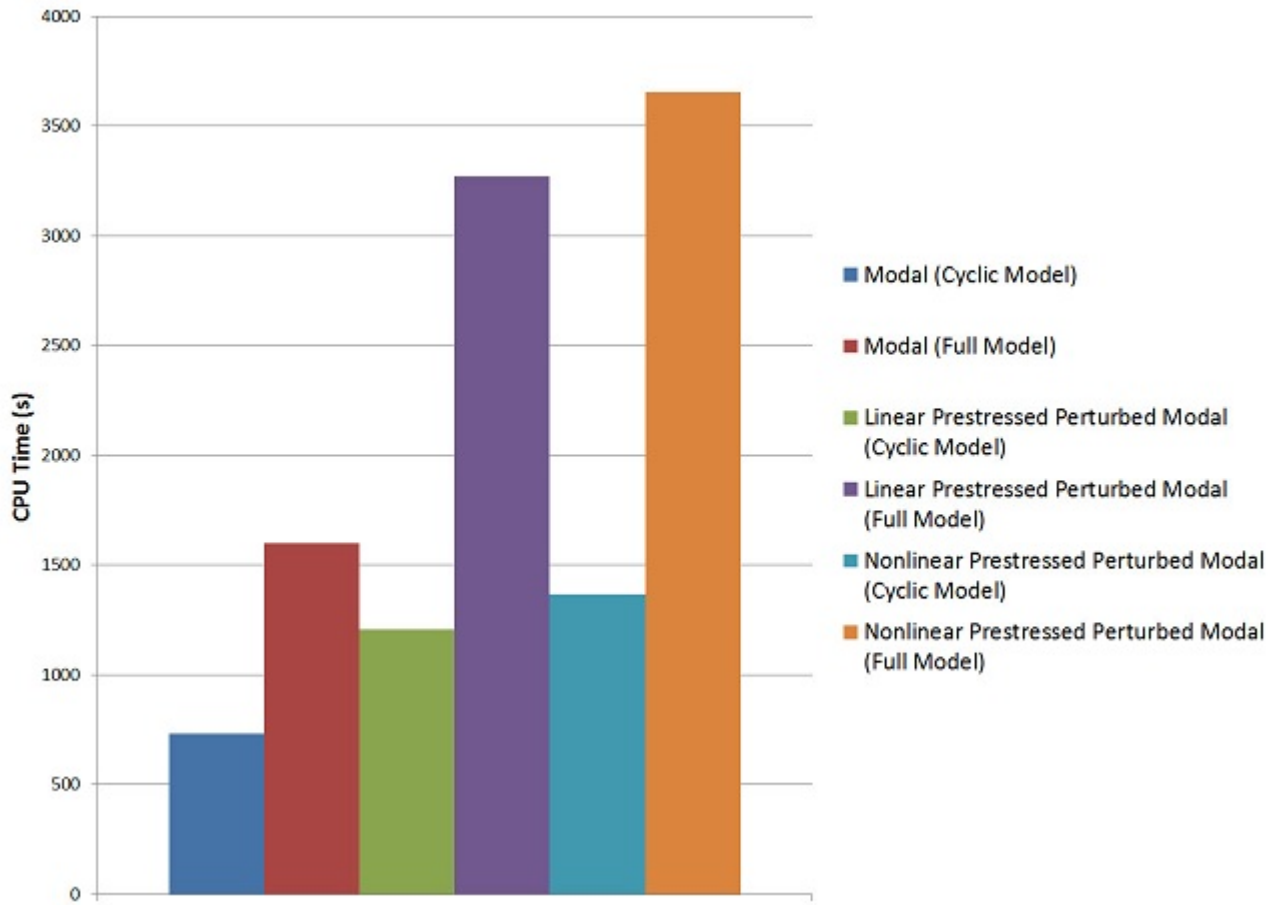
Cyclic-Sector Model CPU and Memory Usage					
	Elements [1 (p. 197)]	Nodes	DOFs	Memory required for in-core (MB)	CPU Time (Sec)
Modal Analysis (p. 180)	48750	81288	243864	1684	731
Linear Prestressed Perturbed Modal Analysis (p. 181)	52482	81288	243864	1026	1208
Nonlinear Prestressed Perturbed Modal Analysis (p. 182)	52482	81288	243864	1038	1364

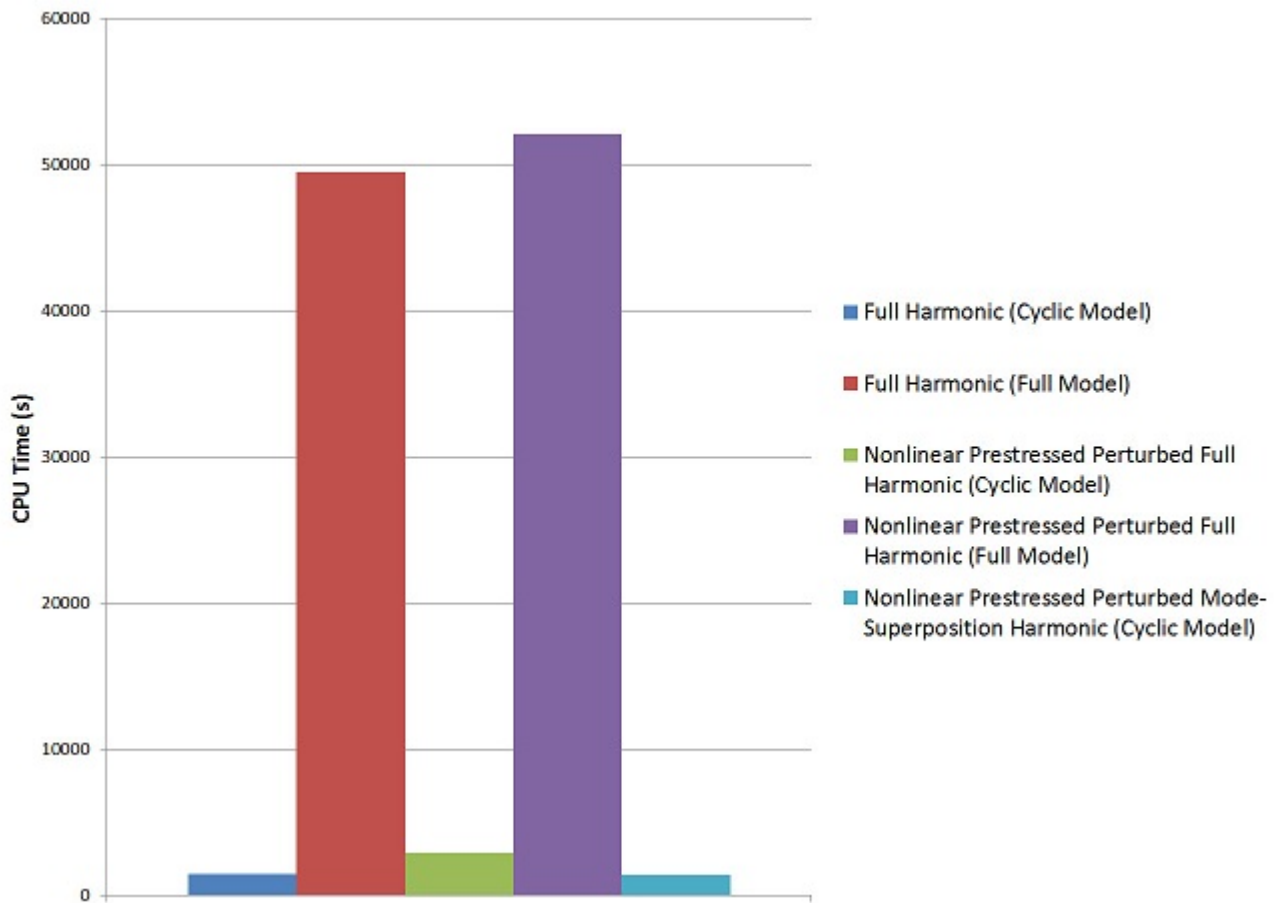
<b>Cyclic-Sector Model CPU and Memory Usage</b>					
Full Harmonic Analysis (p. 183)	52482	81288	243864	1966	1454
Nonlinear Prestressed Perturbed Full Harmonic Analysis (p. 183)	52482	81288	243864	1038	2870
Nonlinear Prestressed Perturbed Mode-Superposition Harmonic Analysis (p. 184)	52482	81288	243864	1038	1376
<b>Full Model CPU and Memory Usage</b>					
	<b>Elements [1 (p. 197)]</b>	<b>Nodes</b>	<b>DOFs</b>	<b>Memory required for in-core (MB)</b>	<b>CPU Time (Sec)</b>
Modal Analysis (p. 180)	273043	439561	1318683	12872	1597
Linear Prestressed Perturbed Modal Analysis (p. 181)	296120	439561	1318683	--	3271
Nonlinear Prestressed Perturbed Modal Analysis (p. 182)	296120	439561	1318683	--	3655
Full Harmonic Analysis (p. 183)	296120	439561	1318683	23405	49485
Nonlinear Prestressed Perturbed Full Harmonic Analysis (p. 183)	296120	439561	1318683	--	52070

1. The difference in the number of elements is due to the surface elements used to apply the pressure load.

The following figure shows the gain in CPU time by solving the analysis via cyclic symmetry modeling:

**Figure 13.17: Comparison of CPU Time Between the Cyclic Sector Model and the Full Model for Various Analyses**



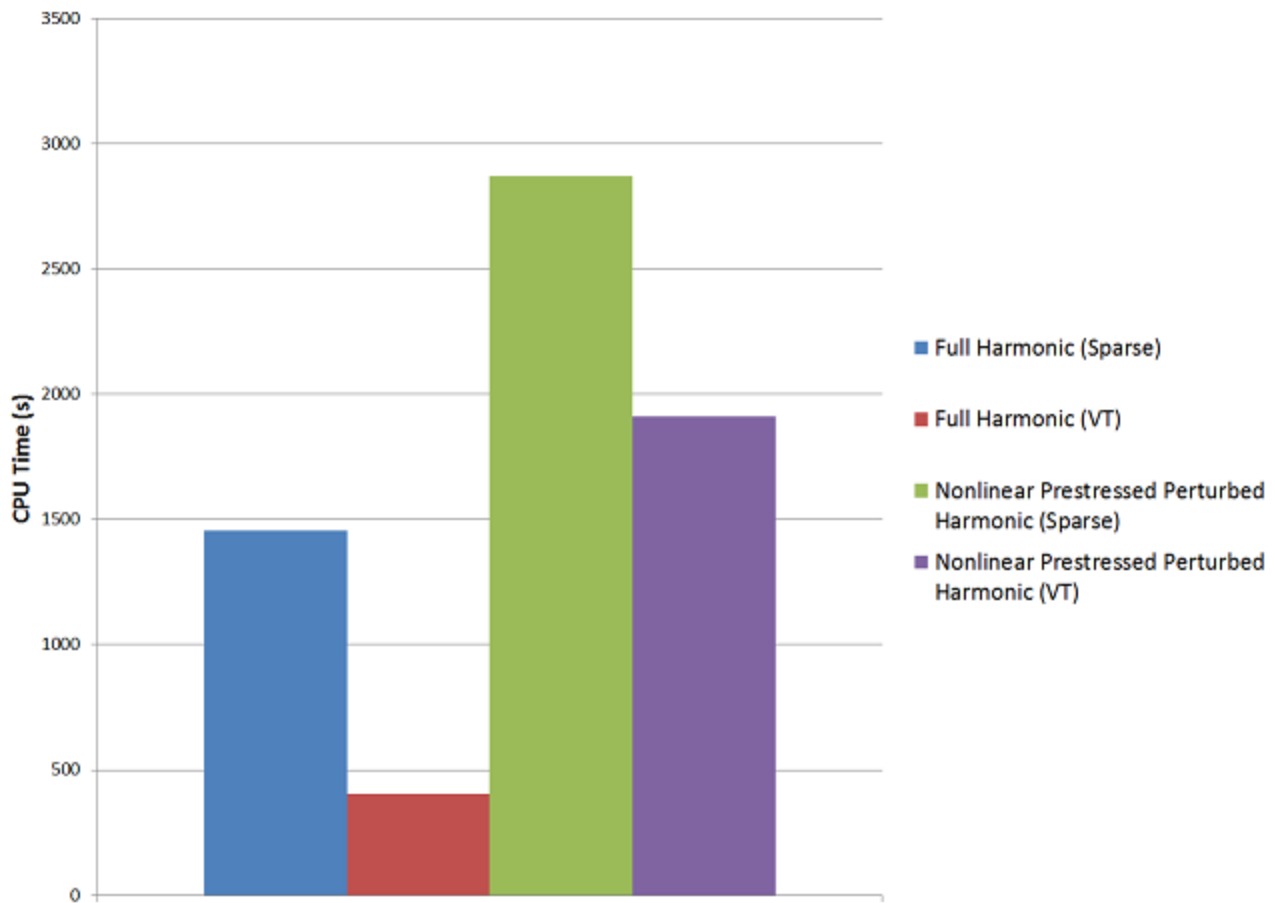


### 13.7.2. Performance Benefits of the Variational Technology (VT) Solver

Use of the Variational Technology solver (*Method* = VT on the **HROPT** command) rather than the sparse solver (*Method* = FULL on the **HROPT** command) can further reduce the computational time of the cyclic symmetry full harmonic analysis, as shown in this table:

Cyclic-Sector Model CPU Usage (Sec.)		
	Sparse Solver	VT Solver
Full Harmonic Analysis	1454	404
Nonlinear Prestressed Perturbed Full Harmonic Analysis	2870	1912

The following figure shows that the VT solver is approximately four times faster than the sparse solver for the full harmonic analysis, and nearly twice as fast for the nonlinear prestressed perturbed full harmonic analysis:

**Figure 13.18: Comparison of CPU Time Between the VT Solver and the Sparse Solver for Harmonic Analysis on the Cyclic Sector Model**

## 13.8. Recommendations

To perform a similar type of analysis, consider the following hints and recommendations:

- Specify a cyclic symmetry analysis (**CYCLIC**) *before* meshing the cyclic sector.

The program can then automatically create matched node pairs at the low and high edges, providing the most accurate results from a cyclic analysis (**AMESH** and/or **VMESH**).

- Use caution when applying boundary conditions on a cyclic sector.

For example, applied boundary conditions (**D**) and/or loading (such as **SF**) on the cut boundaries of a cyclic sector model are not applicable.

- In a harmonic or static cyclic analysis with **non-cyclic loading**, all applicable harmonic index solutions are constructed automatically.

It is not necessary to specify the harmonic indices (**CYCOPT**).

- Use the **linear perturbation** procedure for linear *or* nonlinear prestressed modal analyses and harmonic analyses.

## 13.9. References

The theory behind the cyclic symmetry formulation is available in the following reference:

1. Dickens, John M. *Numerical Methods for Dynamic Substructure Analysis*. Ph.D. Thesis from University of California, Berkeley. 1980.

## 13.10. Input Files

The following input files are used in this problem:

*Cyclic-sector model:*

- `sector_model.cdb` -- The common database file for the cyclic-sector model of the centrifugal impeller blade
- `surf154_gen.dat` -- The common input file for the cyclic-sector model of the centrifugal impeller blade to read `SURF154` elements
- `cyclic_modal_analysis.dat` -- Input file for the cyclic-symmetry modal analysis of the impeller blade
- `cyclic_modal_perturb.dat` -- Input file for the cyclic-symmetry linear prestressed perturbed modal analysis of the impeller blade
- `cyclic_modal_perturb_nonlinear.dat` -- Input file for the cyclic-symmetry nonlinear prestressed perturbed modal analysis of the impeller blade
- `cyclic_model_harmonic.dat` -- Input file for the cyclic-symmetry full harmonic analysis of the impeller blade
- `cyclic_model_nonlinear_perturb_harm.dat` -- Input file for the cyclic-symmetry nonlinear prestressed perturbed full harmonic analysis of the impeller blade
- `cyclic_model_non_pert_msup_harm.dat` -- Input file for the cyclic-symmetry nonlinear prestressed perturbed mode-superposition harmonic analysis of the impeller blade

*Full (360-degree) model:*

- `full_model.cdb` -- The common database file for the full-model analysis of the centrifugal impeller
- `surf154_gen_360_degree.dat` -- The common input file for the full-model analysis of the centrifugal impeller to read `SURF154` elements
- `full_modal_analysis.dat` -- Input file for the modal analysis on the full impeller model
- `full_modal_perturb.dat` -- Input file for the linear prestressed perturbed modal analysis on the full impeller model
- `full_model_perturb_nonlinear.dat` -- Input file for the nonlinear prestressed perturbed modal analysis on the full impeller model
- `full_model_harmonic.dat` -- Input file for the full harmonic analysis on the full impeller model
- `full_model_nonlinear_perturb_harm.dat` -- Input file for the nonlinear prestressed perturbed full harmonic analysis on the full impeller model

The files are available in the `td-13` folder. See [Obtaining the Input Files \(p. xxxv\)](#) for more information.



---

## Chapter 14: Rotordynamics of a Shaft Assembly Based on a Representative Model of Nelson-Vaugh Rotor

---

Rotordynamics plays a crucial role in identifying critical speeds, and to ultimately design rotating structures that tolerate extremely high vibrations. This example illustrates the application of rotordynamics analysis procedures using the [Nelson-Vaugh rotor model \(p. 223\)](#).

A 2-D axisymmetric representation of the 3-D solid model is used to perform a rotordynamic analysis. The results of the 2-D axisymmetric model analyses are compared to the full 3-D solid model results.

This problem demonstrates the following concepts and techniques:

- Axiharmonic meshing of a 3-D geometry
- Disc and bearing modeling
- Gyroscopic effects in rotating structures and modal analysis
- Campbell diagram analysis
- Determination of critical speeds
- Unbalance response analysis
- Orbit plot
- Performance benefits of 2-D axisymmetric models

Topics related to this example problem follow:

- [14.1. Introduction](#)
- [14.2. Problem Description](#)
- [14.3. Modeling](#)
- [14.4. Material Properties](#)
- [14.5. Boundary Conditions and Loading](#)
- [14.6. Analysis and Solution Controls](#)
- [14.7. Results and Discussion](#)
- [14.8. Recommendations](#)
- [14.9. References](#)
- [14.10. Input Files](#)

### 14.1. Introduction

Rotating machines such as steam or gas turbines, turbo-generators, internal combustion engines, motors, and disk drives can develop inertia effects that can be analyzed to improve the design and decrease the possibility of failure. Current trends in rotating equipment design focus on increased speeds, which increase operational problems caused by vibration. At higher rotational speeds, the inertia effects of rotating parts must be consistently represented to accurately predict rotor behavior.

Inertia effects in rotating structures are usually caused by gyroscopic moment introduced by the precise motions of the vibrating rotor as it spins. As spin velocity increases, the gyroscopic moment acting on the rotor becomes critical. Not accounting for inertia effects at the design level can lead to bearing and support structure damage. It is also important to consider bearing stiffness, support structure flexibility, and damping characteristics to understand the stability of a vibrating rotor.

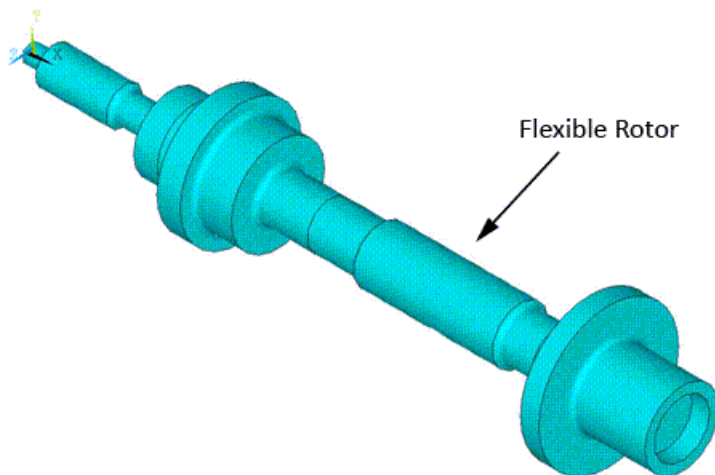
In the sections that follow, modeling details and analysis procedures for a rotating structure are detailed. Generally, a 3-D model directly available from the CAD can be used for the analysis; however, 3-D models result in a large number of nodes and elements models. This example demonstrates how to extract a plane 2-D model from the 3-D model, which can be analyzed using far fewer nodes and elements. The ease of use, accuracy, and performance of 2-D and 3-D model analyses are compared.

For more information about rotordynamics, refer to the *Rotordynamic Analysis Guide* and *Rotating Structure Analysis* in the *Advanced Analysis Guide*.

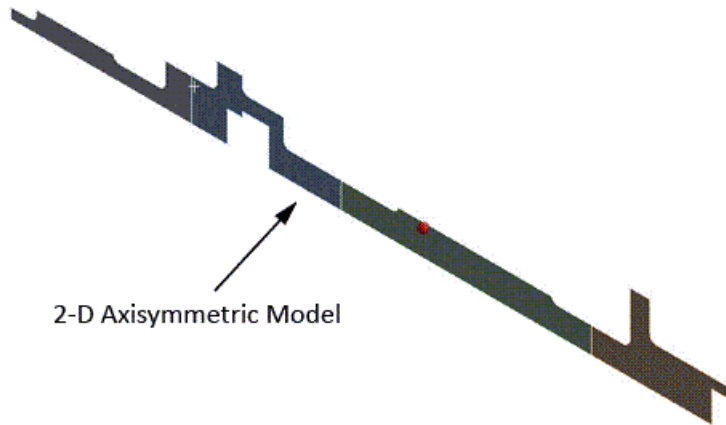
## 14.2. Problem Description

The model for the problem is a 3-D geometry model of a Nelson-Vaugh rotor, as shown in the figure below. The model consists of a flexible rotor with one rigid disk supported by two orthotropic bearings. The modeling details of the original model can be found in Reference [1 (p. 223)].

**Figure 14.1: 3-D Geometry of Nelson-Vaugh Rotor**



Modal, Campbell diagram, and unbalance response analyses are performed on the 2-D axisymmetric model represented in the figure below. The effect of gyroscopic moment on the rotating structure dynamics is observed in each analysis.

**Figure 14.2: 2-D Axisymmetric Geometry of Nelson-Vaugh Rotor**

To validate the accuracy of the results obtained with the 2-D axisymmetric model, the same analyses were performed with the corresponding 3-D solid model. The results are then used as a benchmark for the 2-D axisymmetric model results.

## 14.3. Modeling

The following modeling topics are discussed in this section:

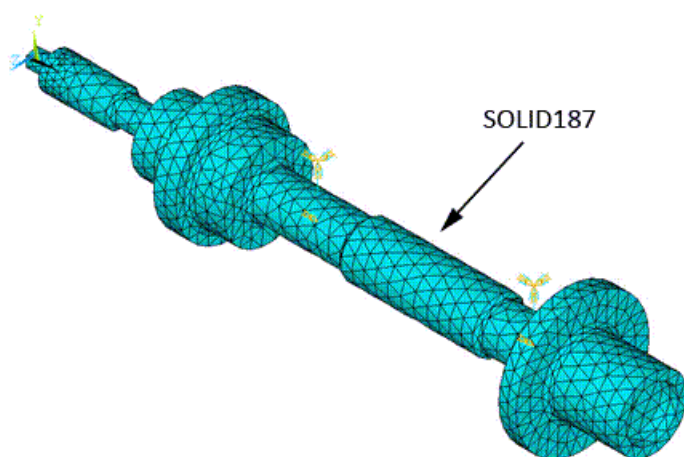
[14.3.1. 3-D Modeling of Flexible Rotor Component](#)

[14.3.2. Axisymmetric Modeling of the Flexible Rotor Component from 3-D Geometry](#)

[14.3.3. Disk and Bearing Modeling](#)

### 14.3.1. 3-D Modeling of Flexible Rotor Component

The 3-D model is meshed with **SOLID187** elements, as shown in the figure below. The default settings of **SOLID187** elements are used.

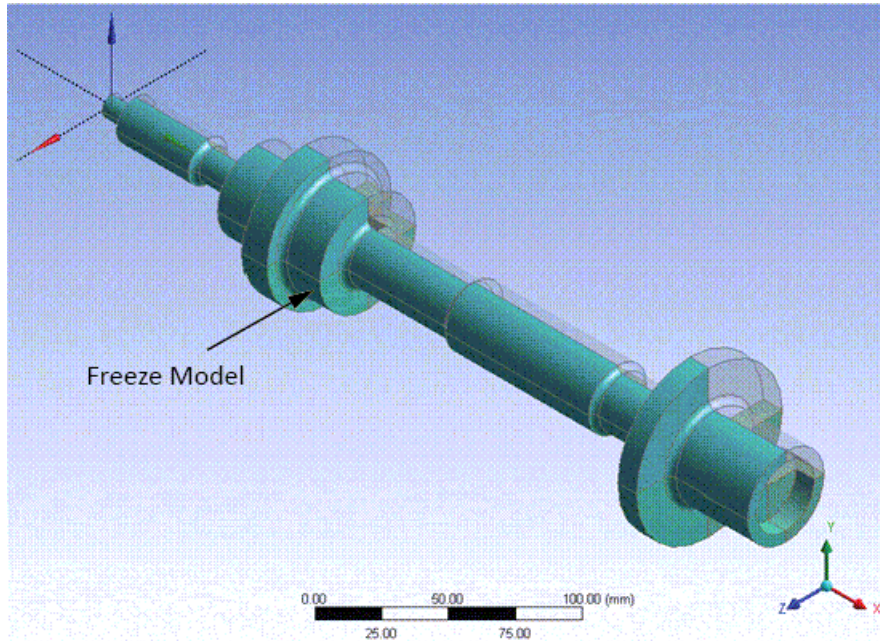
**Figure 14.3: 3-D Model Meshed with SOLID187 Elements**

### 14.3.2. Axisymmetric Modeling of the Flexible Rotor Component from 3-D Geometry

The following process uses the ANSYS Workbench product to extract the 2-D axisymmetric geometry from the 3-D geometry:

1. Freeze the highlighted portion of the model shown below.

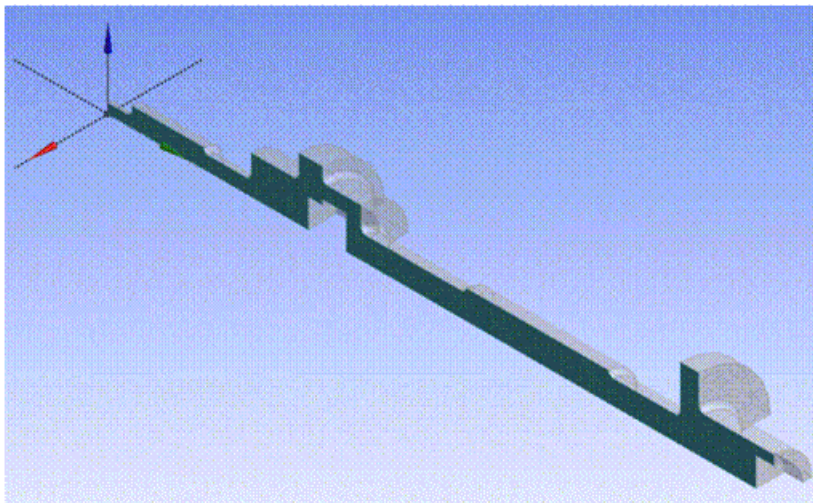
**Figure 14.4: 3-D Geometry**



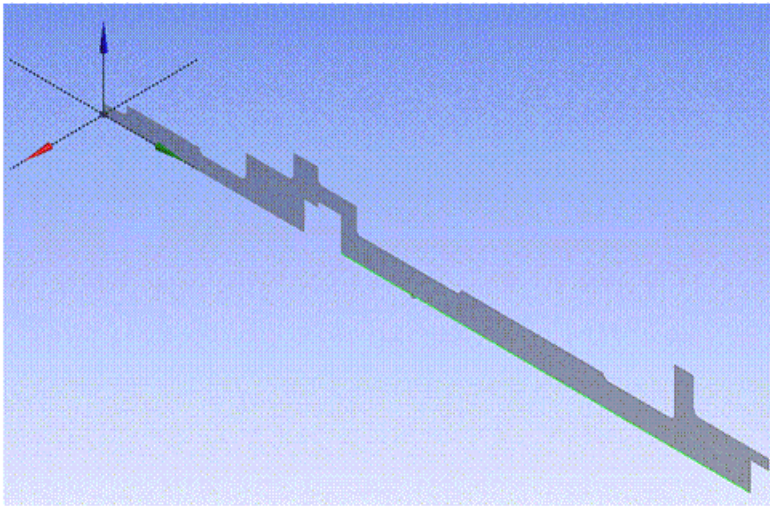
2. Use the Slice by Plane operation on the unfrozen portion of the model as shown below.

**Figure 14.5: 2-D Axisymmetric Geometry Extracted from 3-D Geometry**

#### 3-D Geometry

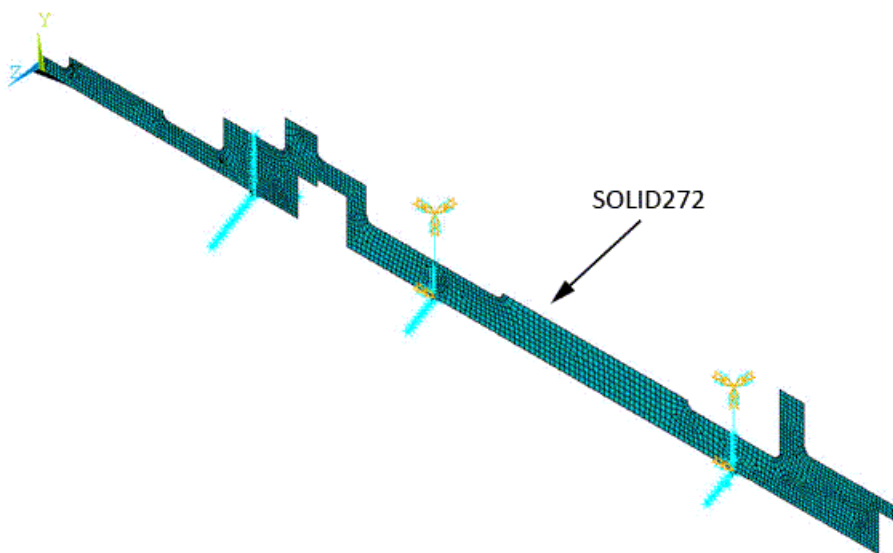


#### Extracted 2-D Axisymmetric Geometry



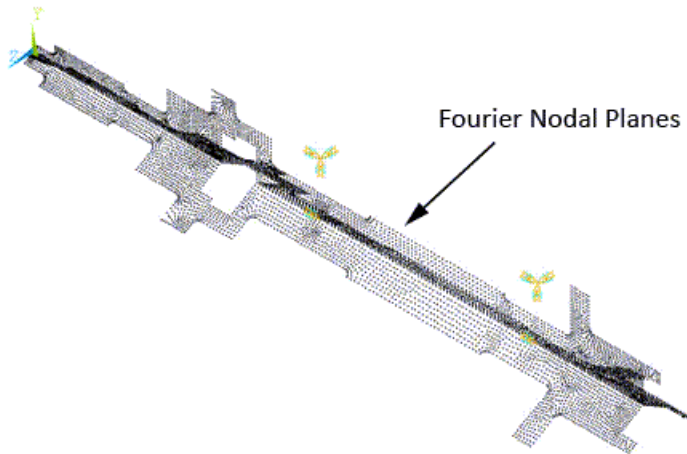
The extracted 2-D geometry is then meshed with the general axisymmetric **SOLID272** elements as shown in the figure below.

**Figure 14.6: 2-D Axisymmetric Geometry Meshed with **SOLID272** Elements**



For modeling, three Fourier nodal planes along the circumferential direction are considered with **KEYOPT(2) = 3** as pictured in the figure below.

**Figure 14.7: 2-D Axisymmetric Model with Fourier Nodal Planes**

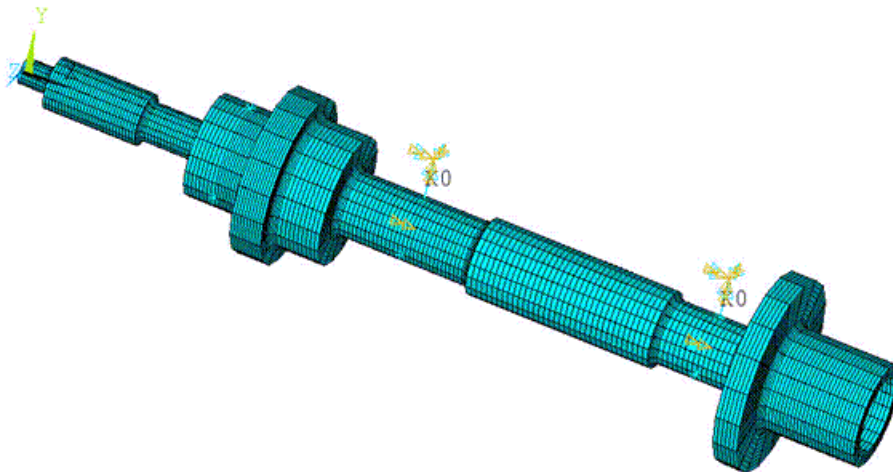


The 3-D mesh is generated based on the 2-D mesh of master planes using the axis of symmetry of the rotor model. It is defined using the **SECTYPE** and **SECDATA** commands as follows:

```
! Define the axis of symmetry  
  
SECT, 1, axis  
SECDATA, 1, x1,y1,z1, x2,y2,z2 ! Coordinates to define the axis of symmetry
```

Finally, using the axis of symmetry and the **NAXIS** command, the 3-D mesh is automatically generated as shown in the figure below.

**Figure 14.8: 3-D View of SOLID272 Mesh**



### 14.3.3. Disk and Bearing Modeling

The following modeling topics are available:

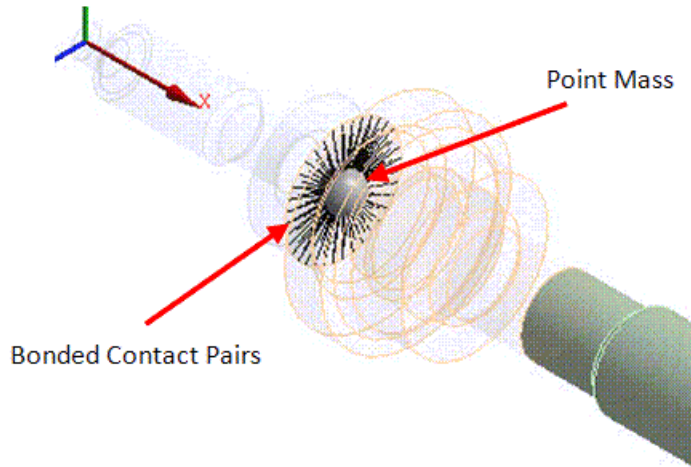
[14.3.3.1. Disk Modeling](#)

[14.3.3.2. Modeling Bearings](#)

### 14.3.3.1. Disk Modeling

The rigid disk is modeled as a concentrated mass using **MASS21** element as shown in the figure below. **KEYOPT(3) = 0** is used to define the 3-D mass with rotary inertia.

**Figure 14.9: Rigid Disk Modeled Using **MASS21** Element (3-D Solid Model)**



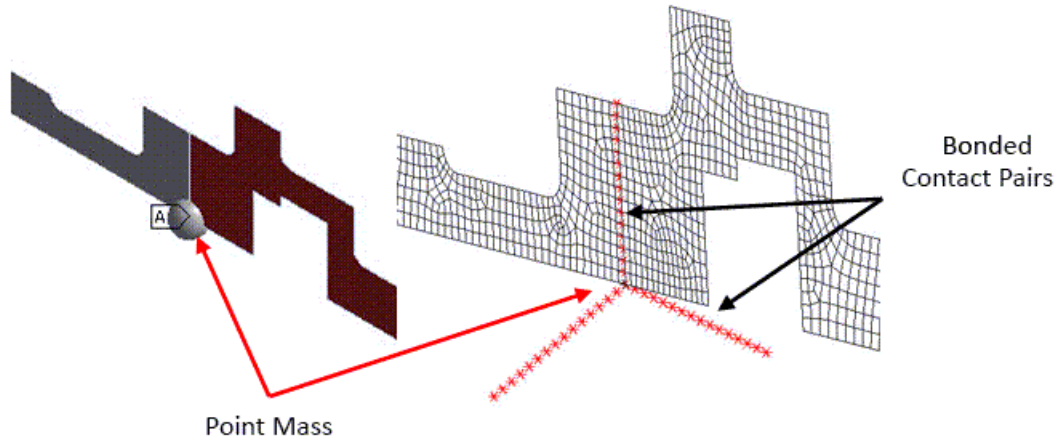
Following is the general process for modeling the rigid disk:

1. Create the contact pairs at the interface corresponding to the location of the rigid disk (the geometry is sliced beforehand at this location).
2. Mesh the contact surfaces of the 3-D solid model with **CONTA174** elements, and contact surfaces of the 2-D axisymmetric model with **CONTA175** elements.
3. Define a pilot node scoped to the surfaces.
4. Create a point mass at this pilot node.

In the case of the 3-D solid model, bonded surface-to-surface contact pairs are used to define contact between the cross sectional elements and the pilot node. The pilot node is located at the center of the cross section. The cross sectional elements and/or contact surfaces are meshed using **CONTA174** elements (3-D 8-node surface-to-surface contact) as shown in the figure above.

Similarly, for the 2-D axisymmetric model, bonded node-to-surface contact pairs are used to define contact between the cross sectional nodes and the pilot node. **CONTA175** elements (2-D/3-D node-to-surface contact) are used to mesh the cross sectional nodes and/or contact surfaces as shown in the figure below.

**Figure 14.10: Disk Modeled Using MASS21 Element (2-D Axisymmetric Model)**



The Multipoint Constraints (MPC) algorithm is used for bonded contact through KEYOPT(2) = 2 when modeling both contact pairs.

TARGE170 elements are used to mesh the pilot node in both models. All degrees of freedom (DOF) of this pilot node are constrained through KEYOPT(4) = 111111.

The following input fragments show the steps involved in creating the contact pairs for the 2-D axisymmetric model:

```

/prep7

et, 1, contal75          ! Define Contact 175 element
et, 2, targel70        ! Define Target 170 element
keyopt, 2, 2, 1         ! Don't fix the pilot node
keyopt, 2, 4, 111111   ! Constrained all DOFs
keyopt, 1, 12, 5        ! Bonded Contact
keyopt, 1, 4, 0         ! Rigid RBE3 style load
keyopt, 1, 2, 2         ! MPC style contact

nselect, s, loc, x, 89.01 ! Select nodes at the user specified location
nplot
cm, contactpl, node

type, 1
real, 1
mat, 1

/com, Creating bonded contact pairs for defining Point Mass

nn = 0
*get, numn, node, , count
*do, i, 1, numn          ! Loop to create contact elements on selected nodes
nn = ndnext(nn)
e, nn                   ! Create contact elements on node one by one
*enddo
allsel, all, all

*set, _npilot, 2        ! Set node 2 as a pilot node (user defined)
type, 2
mat, 1
real, 1
tshape, pilo
e, _npilot              ! Create target element on pilot node
tshape
    
```



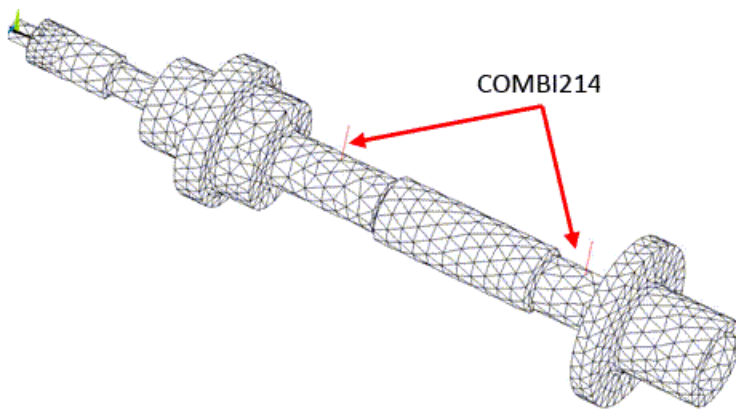
### 14.3.3.2. Modeling Bearings

Bearings are used to support the rotor in the lateral direction. Two identical undamped and linear orthotropic bearings were modeled using **COMBI214** elements, as shown in the figure below and in [Figure 14.13: Bearings Modeled with COMBI214 Elements \(2-D Axisymmetric Model\)](#) (p. 212).

**KEYOPT(2) = 1** is used to define the elements in a plane parallel to the YZ plane. The DOFs of these elements are then UY and UZ.

The X, Y, and Z axes should be added to the following figure (see [Figure 14.4: 3-D Geometry](#) (p. 206) for the directions).

**Figure 14.11: Bearings Modeled with **COMBI214** Elements (3-D solid model)**

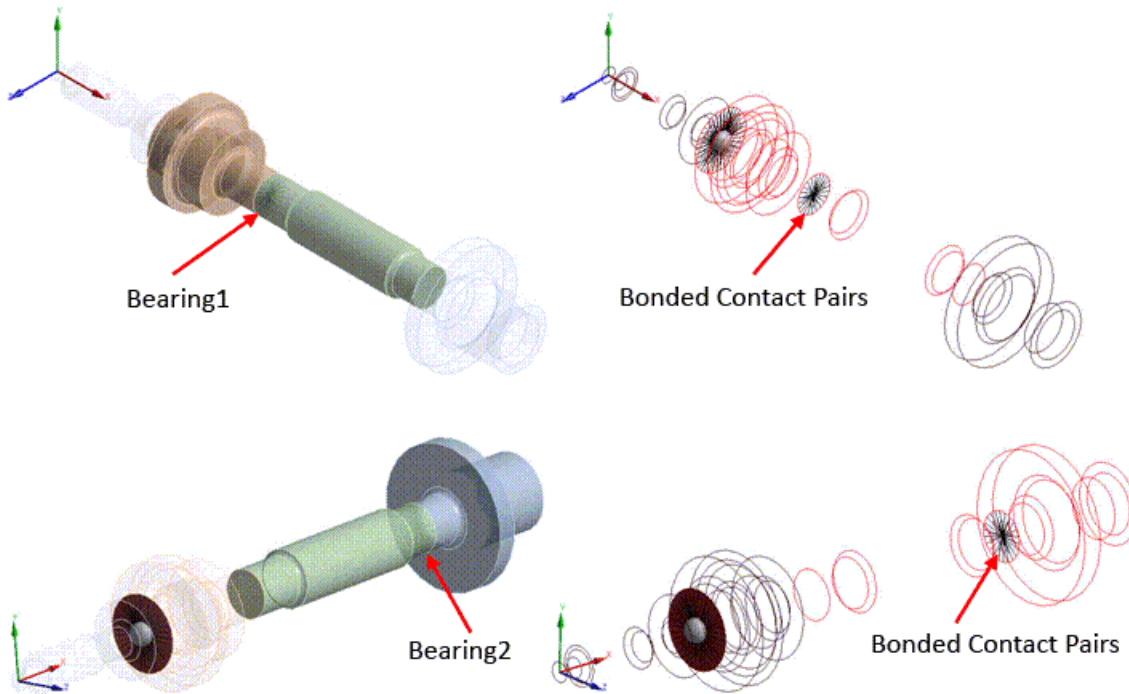


Following is the general process for modeling the bearings:

1. Create the contact pairs at the bearing locations (the geometry is sliced beforehand at these locations).
2. Mesh the contact surfaces with **CONTA174** elements for the 3-D solid model, and **CONTA175** elements for the 2-D axisymmetric model.
3. Create nodes at the center of the cross section of the rotor at each bearing location (i.e. at the pilot node locations). It will represent the second node of the bearing.
4. Create the **COMBI214** elements using these nodes and the pilot nodes.

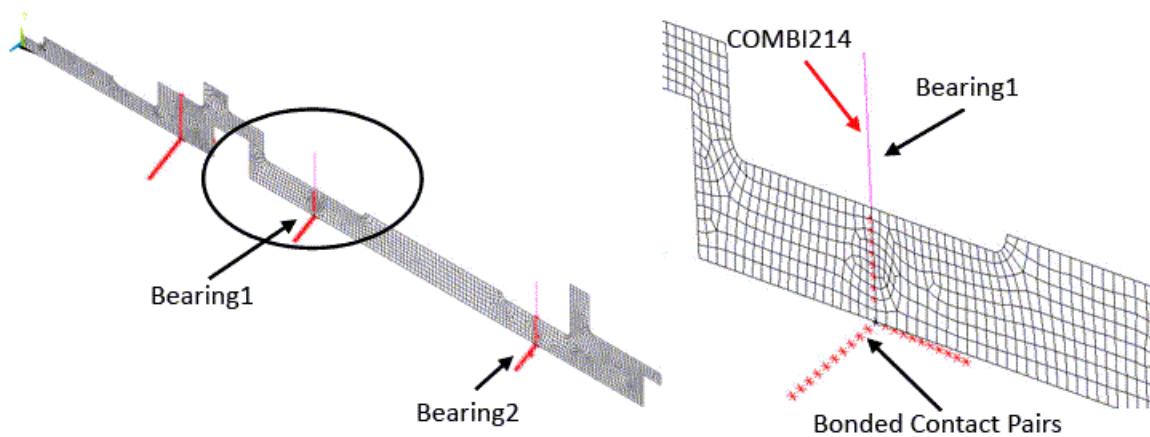
The contact pairs shown in the figure below must be created to model the bearings. The contact pairs are modeled in a similar fashion to the disk modeled in the previous section.

**Figure 14.12: Bonded Contact Pairs at Bearing Locations (3-D Solid Model)**



To model an orthotropic bearing, an additional node is created at the center of the cross section of the rotor at the bearing location. This node is then connected to pilot node using COMBI214 elements. To visualize this element, offset the node along the Y-direction without altering the results as shown in the figure below and in Figure 14.11: Bearings Modeled with COMBI214 Elements (3-D solid model) (p. 211).

**Figure 14.13: Bearings Modeled with COMBI214 Elements (2-D Axisymmetric Model)**



## 14.4. Material Properties

The unit system for this example problem is shown in the table below.

<b>Unit System</b>	Metric (mm, tonne, N)
<b>Angle</b>	Degrees

<b>Rotational Velocity</b>	rad/s
----------------------------	-------

Material properties of the 3-D/2-D Model of a Nelson Rotor are shown in the table below.

<b>Density</b>	7.85e-009 tonne mm <sup>-3</sup>
<b>Young's Modulus</b>	2.0e+005 tonne mm <sup>-2</sup>
<b>Poisson's Ratio</b>	0.3

The properties of the point mass (rigid disk) are shown in the table below.

<b>Mass (X, Y and Z directions)</b>	1.401e-3 tonne
<b>Polar Inertia</b>	2.0 tonne-mm <sup>2</sup>
<b>Diametral Inertia</b>	13.6 tonne-mm <sup>2</sup>

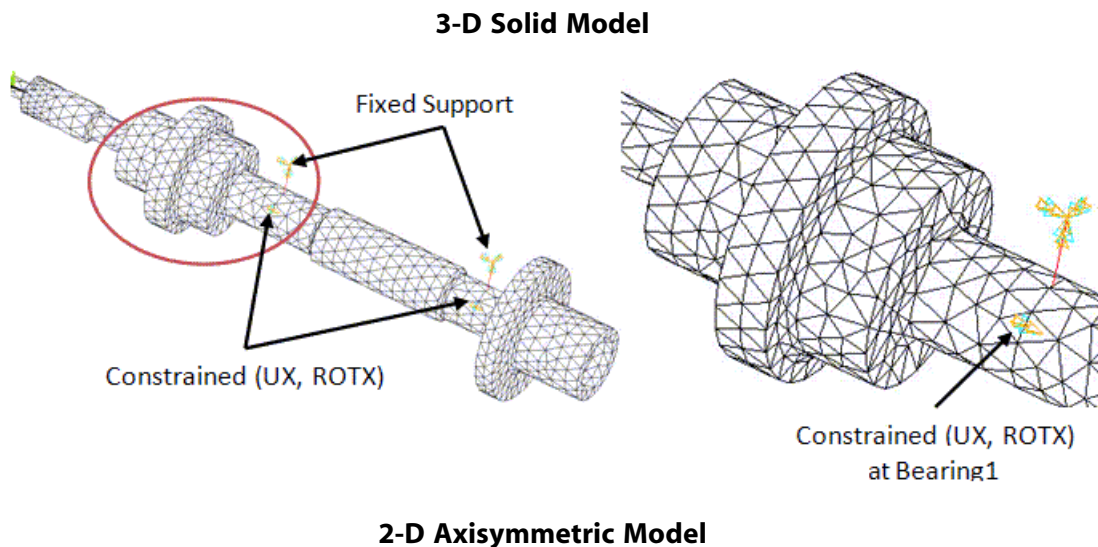
The stiffness properties of the two identical orthotropic bearings are shown in the table below.

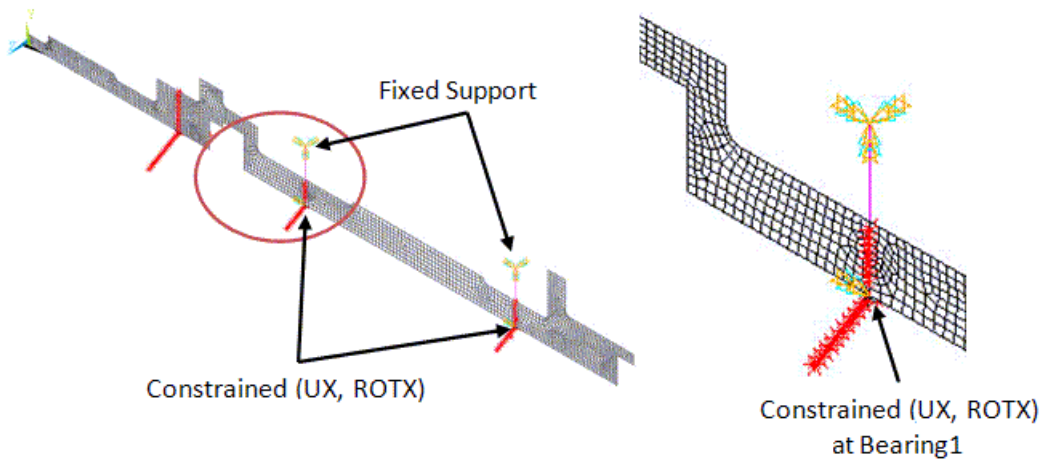
<b>K11 = K22</b>	3.503e+004 N/mm
<b>K12 = K21</b>	-8.756e+003 N/mm

## 14.5. Boundary Conditions and Loading

Fixed support conditions are applied to the second node of the bearing elements, as shown in the figure below. Translational and rotational DOFs about the axis of rotation at the bearing locations are constrained.

**Figure 14.14: Boundary Conditions (3-D Solid Model)**





The effect of the unbalanced mass on the disk is represented by forces acting in the two directions perpendicular to the spinning axis. The forces are applied on a node located on the axis of rotation at the same location as the point mass. The amplitude of the unbalance force is equal to the mass multiplied by the distance of the unbalance mass to the spin axis.

The following input fragment shows the steps to apply the unbalance force:

```
/com, Force, f0 = mass * radius  
  
f0 = 1.90e-3  
nodeUnb = node(89.01, 0, 0)  
  
/com, Applying rotating force in the clockwise direction.  
  
F, nodeUnb, FY, -f0 ! Real FY component at node ' nodeUnb'  
F, nodeUnb, FZ,, f0 ! Imaginary FZ component at node ' nodeUnb'
```

## 14.6. Analysis and Solution Controls

This section discusses the following topics:

- 14.6.1. Modal Analysis
- 14.6.2. Campbell Diagram Analysis
- 14.6.3. Unbalance Response Analysis

### 14.6.1. Modal Analysis

Modal analyses of the 2-D axisymmetric model with and without gyroscopic effects included are discussed in this section.

#### 14.6.1.1. Modal Analysis without Gyroscopic Effects

The modal analysis without gyroscopic effects is performed using the Block Lanczos (LANB) solver, extracting twelve modes.

The following input fragment shows the steps to extract these modes:

```
/solu  
  
antype, modal ! Perform Modal analysis  
modopt, lanb, 12 ! Use Block Lanczos solver to extract 12 modes  
mexpand, 12 ! Expands all the modes  
solve  
finish
```

### 14.6.1.2. Modal Analysis with Gyroscopic Effects

The rotational velocity is specified with the **OMEGA** or **CMOMEGA** command. The gyroscopic effects of the rotating structure are included using the **CORIOLIS** command.

The modal analysis with gyroscopic effects is performed on the model using the complex QRDAMP eigensolver.

The following input fragment shows the steps to perform the modal analysis with gyroscopic effects:

```
/SOLU

/com, Select all the rotating elements supporting Coriolis command

esel,,ename,,272
esel,a,ename,,21
cm,rot_part, elem
esel, all

/com, Specify rotational velocity to the structure/rotating elements.

pival = acos(-1)
spinRpm = 50000           ! Rotational velocity in rpm
spinRds = spinRpm*pival/30
cmomega, rot_part, spinRds ! Apply rotational velocity along rotating velocity (X)

/com, Activate Coriolis command and choose QRDAMP eigensolver

antype, modal           ! Perform Modal analysis
modopt, qrdamp, 12,,, on ! Use QRDAMP solver to extract 12 complex modes
mexpand, 12             ! Expand all the modes
coriolis, on,,, on      ! Last field specifies stationary reference frame
solve
finish
```

### 14.6.2. Campbell Diagram Analysis

Before performing a Campbell diagram analysis, a modal analysis must be performed with multiple load steps corresponding to different angular velocities. A Campbell diagram plot (**PLCAMP** command) shows the evolution of the natural frequencies with respect to the rotational speed. The **PRCAMP** command prints out the critical speeds based on the Campbell diagram plot for a synchronous (unbalanced) or asynchronous force.

The following input fragment shows the steps to perform the Campbell Diagram Analysis:

```
/SOLU

/com, Select all rotating elements supporting Coriolis command

esel,,ename,,272
esel,a,ename,,21
cm, rot_part, elem
esel, all

/com, Activate Coriolis command and pick the QRDAMP eigensolver

antype, modal           ! Perform Modal analysis
modopt, qrdamp, 12,,,on ! Use QRDAMP solver to extract 12 complex modes
mexpand, 12             ! Expand all the modes
coriolis, on,,, on      ! Last field specifies stationary reference frame

/com, Solve modal analysis for different angular velocities

pival = acos(-1)
spinRpm = 0             ! Rotational velocity in rpm
spinRds = spinRpm*pival/30
```

```
cmomega, rot_part, spinRds
solve

spinRpm = 50000          ! Rotational velocity in rpm
spinRds = spinRpm*pival/30
cmomega, rot_part, spinRds
solve

spinRpm = 100000        ! Rotational velocity in rpm
spinRds = spinRpm*pival/30
cmomega, rot_part, spinRds
solve
finish

/com, Post process the Campbell diagram plot

/POST1

prcamp,, 1.0, rpm,, rot_part ! Prints Campbell diagram data
/show, png
/rgb, index, 100, 100, 100, 0 ! Set white background
/rgb, index, 0, 0, 0, 15
plcamp,, 1.0, rpm,, rot_part ! Plots Campbell diagram data
finish
```

### 14.6.3. Unbalance Response Analysis

A harmonic analysis of the 2-D axisymmetric model is performed within a speed range of 0 to 100,000 rpm (a frequency range of 0 to 1666.67 Hz) using 200 substeps. The first seven modes in this frequency range are excited.

In this analysis, the unbalance is considered as loading. (see [Boundary Conditions and Loading \(p. 213\)](#) for more details).

A structural damping coefficient of 1 percent is considered (**DMPSTR**).

The frequency of excitation is specified as synchronous with the rotational velocity (**SYNCHRO**). The rotational velocity (**CMOMEGA**) determines only the rotational velocity direction vector of the rotating component. The spin of the rotor is automatically calculated (**HARFRQ**).

The following input fragment shows the steps to perform the unbalance response analysis:

```
/SOLU

spinRds = 1          ! Rotating velocity of the shaft to specify the spin axis

spinRpm1 = 0        ! Begin speed in rpm
spinRpm2 = 100000   ! End speed in rpm
begin_freq = spinRpm1/60 ! Equivalent begin frequency in Hz
end_freq = spinRpm2/60 ! Equivalent end frequency in Hz

antype, harmic      ! Perform Harmonic analysis
hropt, full         ! Select Full Harmonic analysis option
nsubst, 200
harfrq, begin_freq, end_freq ! Defines the frequency range
kbc, 1

dmpstr, 0.01        ! Specify damping ratio of 1%

synchro,,rot_part  ! Specify synchronous analysis
cmomega,rot_part,spinRds ! Define the rotational velocity direction vector
coriolis,on,,, on  ! Includes gyroscopic effect
solve

finish
```

## 14.7. Results and Discussion

The natural frequencies of the 2-D axisymmetric model without rotation are evaluated and compared with the results of 3-D solid model in the following table.

Mode #	2-D Axisymmetric Model (Hz)	3-D Solid Model (Hz)	Error (%)
1	189.72	189.00	0.38
2	208.96	208.04	0.44
3	639.91	639.59	0.05
4	654.54	653.25	0.20
5	733.26	732.77	0.07
6	807	805.64	0.17
7	990.36	991.73	0.14
8	1780.5	1782.50	0.11
9	1781.1	1785.20	0.23
10	2016.9	2009.60	0.36
11	2092.6	2086.90	0.27
12	3291.7	3287.80	0.12

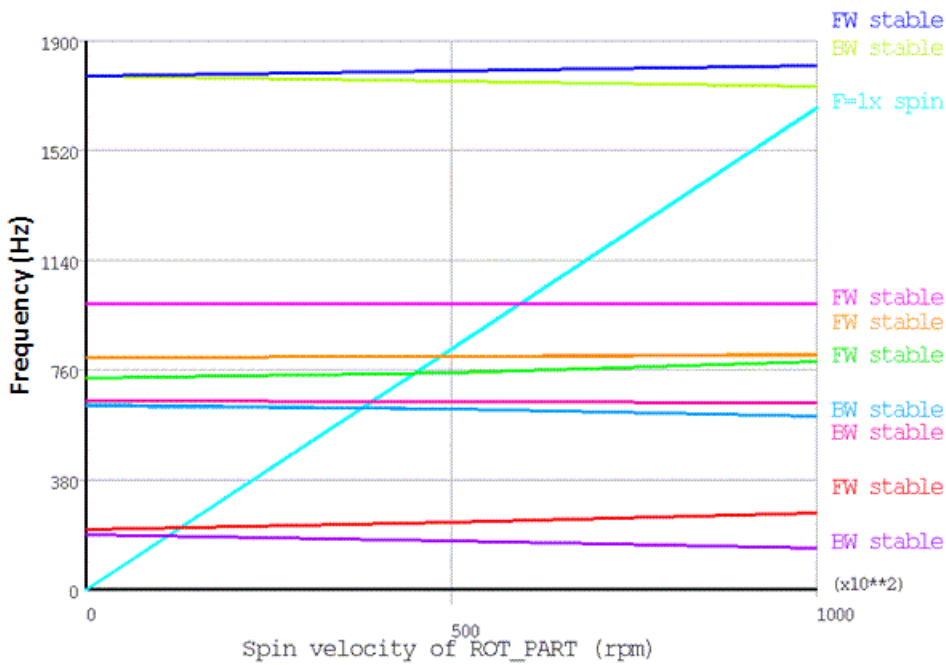
The natural frequencies of the 2-D axisymmetric model in rotation (50,000 rpm) also show good agreement with the 3-D solid model results, as shown in the following table.

Mode #	2-D Axisymmetric Model (Hz)	3-D Solid Model (Hz)	Error (%)
1	169.07	168.25	0.49
2	232.54	231.75	0.34
3	627.97	627.19	0.12
4	652.32	651.39	0.14
5	752.14	751.59	0.07
6	808.51	807.25	0.16
7	990.36	991.73	0.14
8	1763.00	1766.00	0.17
9	1798.90	1802.00	0.17
10	1931.30	1923.50	0.41
11	2192.50	2187.60	0.22
12	3291.70	3287.80	0.12

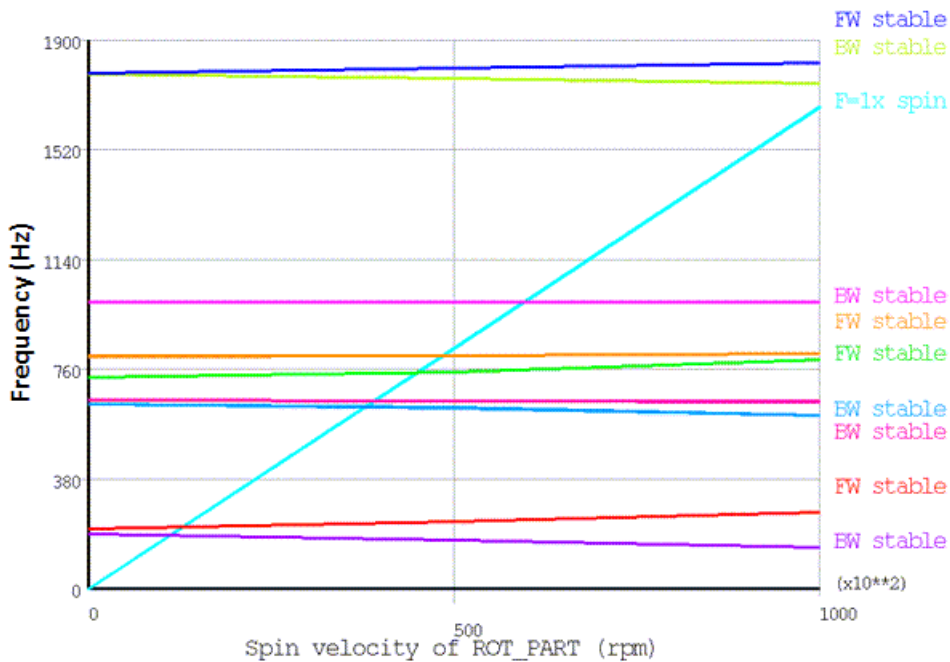
The /POST1 results of the Campbell diagram analysis are shown in the figure that follows.

**Figure 14.15: Campbell Diagram**

### 2-D Axisymmetric Model



### 3-D Solid Model



With the help of the Campbell diagram analysis, we can identify the forward (FW) and backward (BW) whirals, as well as possible unstable frequencies (though none are present in this example). In the table below, the whirals and natural frequencies of the 2-D axisymmetric model at maximum rotational speed (100,000rpm) are compared with the 3-D solid model results.

Mode #	Frequency (Hz)			
	Whirl		100000 RPM	
	2-D Axisymmetric Model	3-D Solid Model	2-D Axisymmetric Model	3-D Solid Model
1	BW	BW	144.98	144.17



Mode #	Frequency (Hz)			
	Whirl		100000 RPM	
	2-D Axisymmetric Model	3-D Solid Model	2-D Axisymmetric Model	3-D Solid Model
2	FW	FW	264.59	263.92
3	BW	BW	602.73	601.48
4	BW	BW	649.45	648.72
5	FW	FW	792.94	791.73
6	FW	FW	814.48	813.99
7	FW	BW	990.36	991.73
8	BW	BW	1745.08	1748.14
9	FW	FW	1817.30	1820.05

The Campbell diagram analysis helps to determine the critical speeds of the rotating structure (**PRCAMP**). Critical speeds are compared in the table below. For a synchronous excitation, the critical speeds correspond to the intersection points between the frequency curves and the 1.0 slope line. The critical speeds of the 2-D axisymmetric and 3-D solid models show strong agreement.

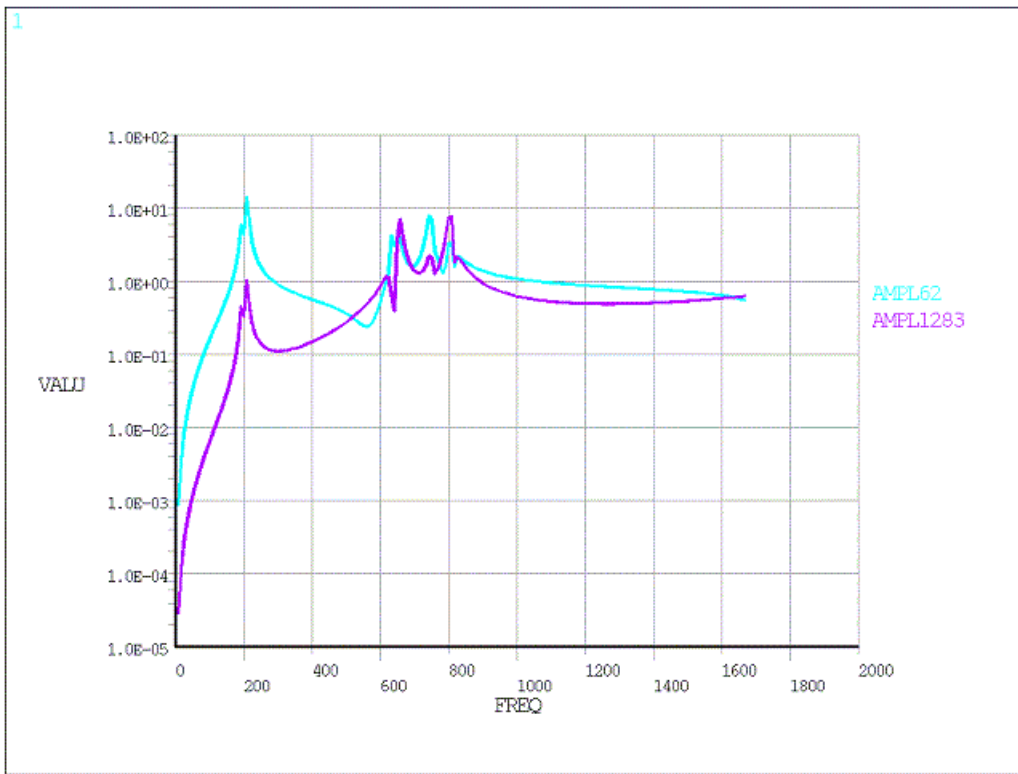
Critical Speeds (RPM)			
Mode #	2-D Axisymmetric Model	3-D Solid Model	Error (%)
1	11107.97	11064.65	0.39
2	12902.64	12847.70	0.43
3	37852.19	37812.80	0.10
4	39167.83	39107.83	0.15
5	45015.50	44982.13	0.07
6	48507.73	48431.91	0.16
7	59421.77	59503.56	0.14
8	none	none	-
9	none	none	-

The results of the unbalance response analysis post processed in /POST26 are shown in the following figure. The logarithmic plots show the variation of the displacement amplitudes of two selected nodes with respect to the frequency of excitation. The first node is located near the rigid disk, and it corresponds to the light blue curve. The second node is located near the bearing location, and it corresponds to the purple curve.

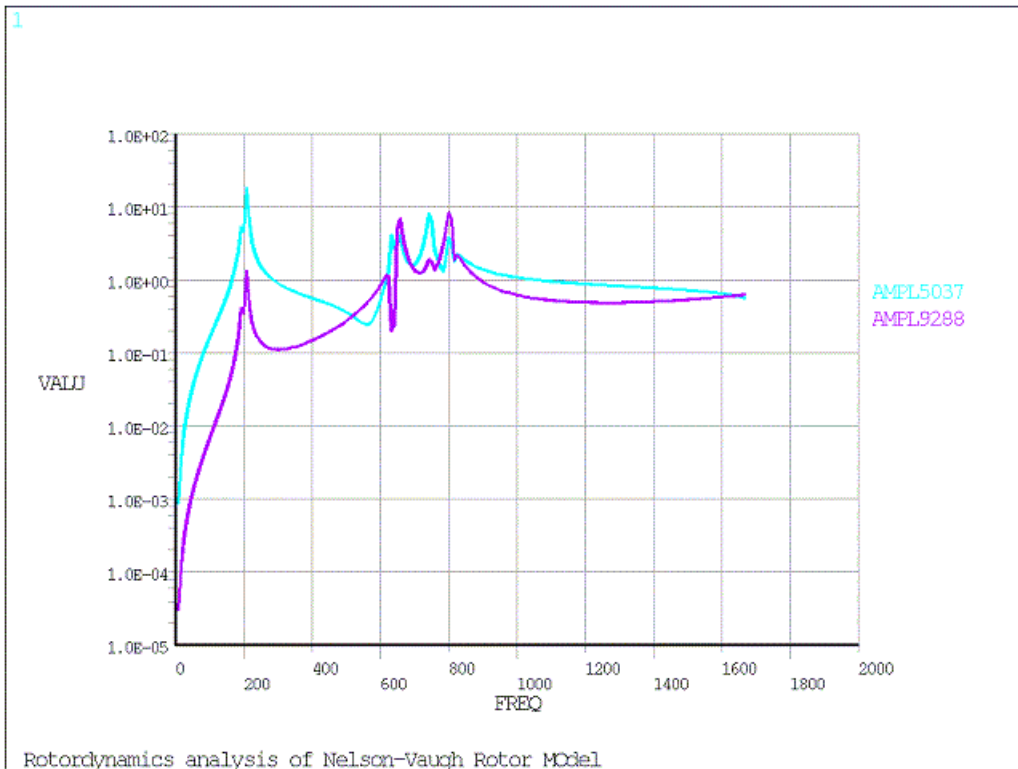
The critical frequencies appear where the amplitudes are largest, and correspond to the critical speeds.

### Figure 14.16: Unbalance Response

#### 2-D Axisymmetric Model



**3-D Solid Model**



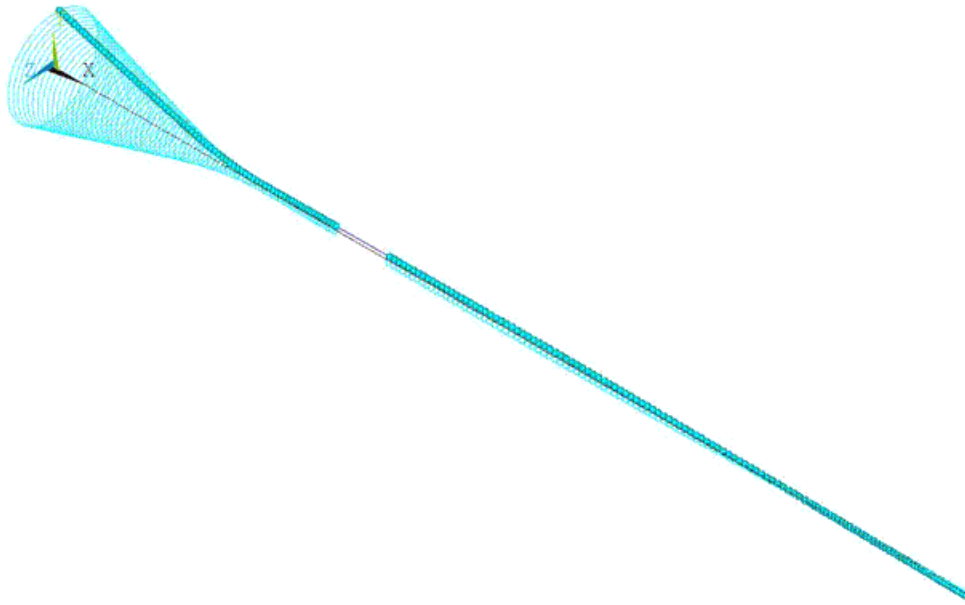
The orbits after a full harmonic analysis can be plotted in POST1 as shown in the figure below (**PLORB** command). For the solid element as well as for the axisymmetric element model, we need to add massless line elements using **BEAM188** on the rotational velocity axis to plot these orbits. The orbits of the 2-D axisymmetric model at a frequency of 1666.67 Hz are shown in the figure below. The rotor line is in dark blue, while the orbits are in light blue.

The following input fragment shows the steps to produce an orbits plot at a given frequency:

```
/POST1
esel,r,ename,, 188 ! Select BEAM188 elements to produce orbits
set,1, 200 ! Visualize orbits at frequency 1666.67 Hz
/view,,1,1,1
plorb ! Displays the orbital motion of a rotating structure
```

**Figure 14.17: Orbits Plot of 2-D Axisymmetric Model**

```
STEP=1
SUB =200
FREQ=1666.67
```



### 14.7.1. Performance Benefits of the 2-D Axisymmetric Model

The memory and CPU usage of the 2-D model is shown in the following table.

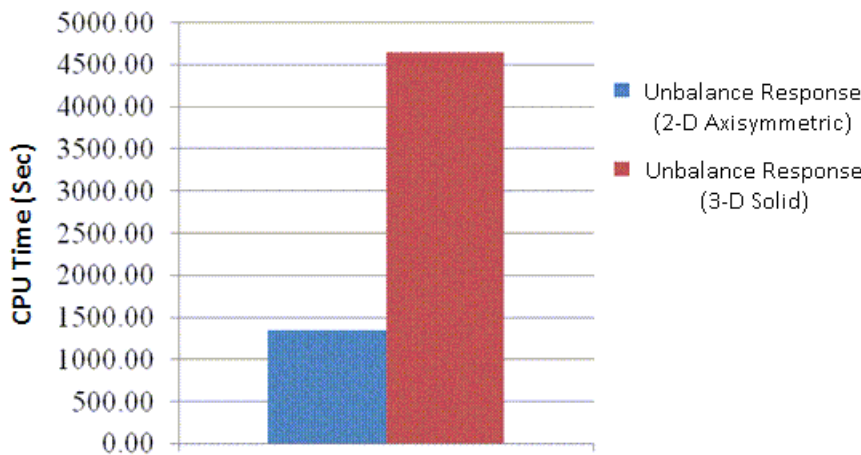
	2-D Axisymmetric Model				
	Elements #	Nodes #	No. of Equations	Memory required for in-core (MB)	CPU Time (Sec)
Campbell Diagram Analysis	2208	6751	20225	53.283	17.30
Unbalance Response Analysis				118.325	1347.53

The memory and CPU usage of the 3-D model is shown in the following table.

	3-D Solid Model				
	Elements #	Nodes #	No. of Equations	Memory required for in-core (MB)	CPU Time (Sec)
Campbell Diagram Analysis	9239	15123	45341	186.141	45.56
Unbalance Response Analysis				605.464	4645.95

The CPU times for the unbalance response analysis are represented in the following bar graph.

**Figure 14.18: CPU Time of 2-D Axisymmetric and 3-D Solid Models (Unbalance Response Analysis)**



## 14.8. Recommendations

- In the CAD geometry, identify the axisymmetric and non-axisymmetric parts. A non axisymmetric part should be considered as follow:
  - If inertia is negligible, create a non-rotating component based on this part. The gyroscopic effect will not be taken into account.
  - If inertia is not negligible, delete the part and create an equivalent axisymmetric geometry so that its gyroscopic effects are included. The simplest way to do this is to add a point mass on the rotational velocity axis. The point mass characteristics are based on the part mass and inertias. Keep in mind that the two rotary inertias perpendicular to the rotational velocity axis must be equal to guaranty the axisymmetry.
- For 3-D and 2-D axisymmetric modeling, the geometry is sliced at rigid disks and bearing locations so that those components are easily created and connected to remote points attached to the interfaces.
- When meshing a 2-D axisymmetric model using [SOLID272](#) or [SOLID273](#), choose an appropriate number of Fourier nodes in the circumferential direction to ensure good accuracy and minimize the computational cost. For typical rotordynamics problems in linear dynamics, three Fourier nodes are sufficient.
- When performing a Campbell diagram of a structure, always check the eigenfrequencies at zero rotational velocity first. If the supports (e.g., bearings or boundary conditions) are symmetric, bending frequencies should appear in pairs. If that is not the case in a 3-D model, try refining the mesh.

- To perform the unbalance response analysis of 3-D and 2-D axisymmetric models, the unbalance response is introduced using complex forces defined at a node on the rotational velocity axis. The unbalance response may be defined using a point mass away from the rotational velocity axis only in the case of a nonlinear transient analysis.

## 14.9. References

The following references are used in this example problem:

1. H.D. Nelson and J.M. Mc Vaugh. *The Dynamics of Rotor-Bearing Systems Using Finite Elements*. Journal of Engineering For Industry. ASME. May 1976.
2. Beley, A., C. Rajakumar, P. Thieffry. "Computational Methods for Rotordynamics Simulation." NAFEMS World Congress, 2009.

## 14.10. Input Files

The following files were used in this problem:

### 2-D Axisymmetric Model Input

- `2-D_axi_symm.cdb` -- The common database file for a 2-D axisymmetric model of the Nelson-Vaugh rotor.
- `2-D_axi_symm_campbell.dat` -- Input file for performing a Campbell diagram analysis of the 2-D axisymmetric model.
- `2-D_axi_symm_harm.dat` -- Input file for performing an unbalance response analysis of the 2-D axisymmetric model.

### 3-D Solid Model Input

- `3D_solid_model.cdb` -- The common database file for a 3-D solid model of the Nelson-Vaugh rotor.
- `3D_solid_campbell.dat` -- Input file for performing Campbell diagram analysis of the 3-D solid model.
- `3D_solid_harm.dat` -- Input file for performing unbalance response analysis of the 3-D solid model.

The files are available in the `td-14` folder. See [Obtaining the Input Files \(p. xxxv\)](#) for more information.



---

# Chapter 15: Calibrating and Validating a Hyperelastic Constitutive Model

---

This example problem demonstrates the [hyperelastic curve-fitting](#) capabilities used to select constitutive model parameters to fit [experimental data](#). Several issues that influence the accuracy of the curve fit are discussed. Validation of the resulting constitutive model is demonstrated by comparison with a tension-torsion experiment.

Topics related to this example problem follow:

- [15.1. Introduction](#)
- [15.2. Problem Description](#)
- [15.3. Material Properties](#)
- [15.4. Analysis and Solution Controls](#)
- [15.5. Results and Discussion](#)
- [15.6. Recommendations](#)
- [15.7. References](#)
- [15.8. Input Files](#)

## 15.1. Introduction

Several hyperelastic constitutive models can be used to model the large deformation behavior of elastic materials; however, it is sometimes difficult to select parameters to adequately match the behavior of the material. The [curve-fitting](#) process fits the hyperelastic constitutive model parameters to a set of experimental data using a least-squares minimization.

Curve fitting is relatively simple, but certain conditions can affect the accuracy of the resulting constitutive model. The constitutive model should therefore be compared with experimental data to ensure that it adequately reproduces the material behavior over the actual range of deformation.

## 15.2. Problem Description

A constitutive model is needed that matches the behavior of a vulcanized natural rubber material up to 100 percent engineering strain in a variety of deformation modes.

In this problem, the experimental data are obtained from a simulation of a hyperelastic test suite (uni-axial, biaxial, and planar tension tests) using common experimental test specimens. Using this data, parameters for a constitutive model are determined using hyperelastic fitting capabilities that focus on use of the three-, five-, and nine-parameter [Mooney-Rivlin hyperelastic](#) models.

After demonstrating the fitting procedure and selecting a suitable constitutive model, a tension-torsion experiment is simulated and compared to the experimental data to validate the predictions for the model.

## 15.3. Material Properties

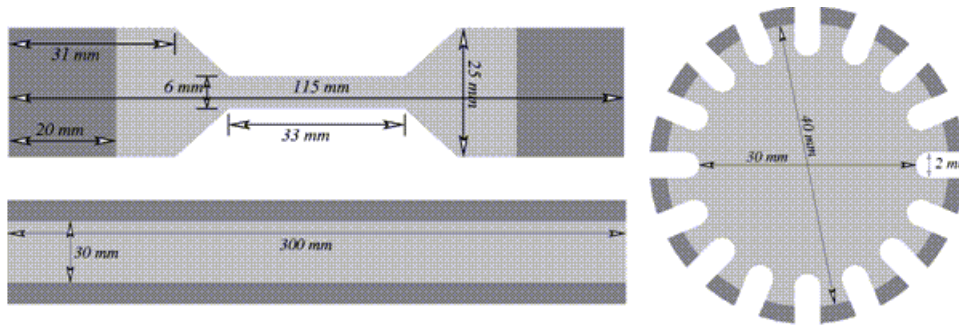
Material properties for the calibration and validation experiments follow:

15.3.1. Calibration Experiments  
 15.3.2. Validation Experiment

### 15.3.1. Calibration Experiments

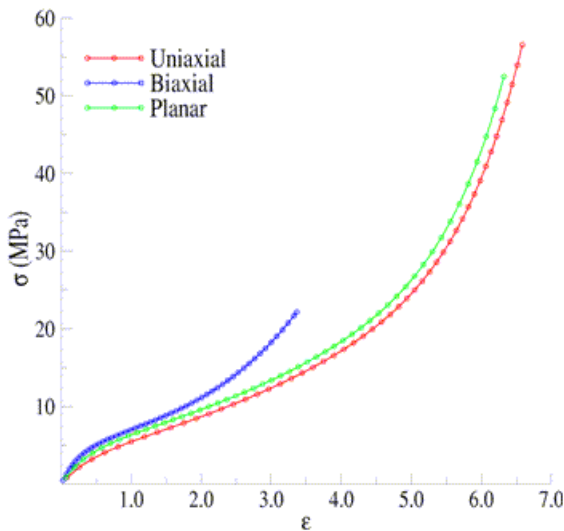
Experimental data was obtained via a simulation of a hyperelastic test suite with an [Ogden hyperelastic](#) material. The test suite specimens are shown here, with the dark areas indicating locations of the clamps:

**Figure 15.1: Hyperelastic Test Suite: Test Specimens**



The engineering-stress vs. engineering-strain results are as follows:

**Figure 15.2: Hyperelastic Test Suite: Experimental Data**



The uniaxial specimen is similar to ASTM D412-C (ASTM Standard D412, 2006).

The crosshead is displaced by 396 mm, giving a measured engineering strain in the gage section of 662 percent and a calculated engineering stress of 58.1 MPa.

The equibiaxial specimen is disc-shaped, with 16 equally spaced tabs about the circumference. The tabs are stretched 127.3 mm, resulting in a measured engineering strain in the gage section of 336 percent and a calculated engineering stress of 22.1 MPa.

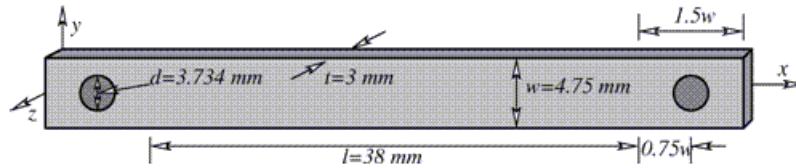
For the planar specimen, the crosshead is displaced by 191.6 mm, giving a calculated engineering strain of 639 percent and a calculated engineering stress of 54.7 MPa.



## 15.3.2. Validation Experiment

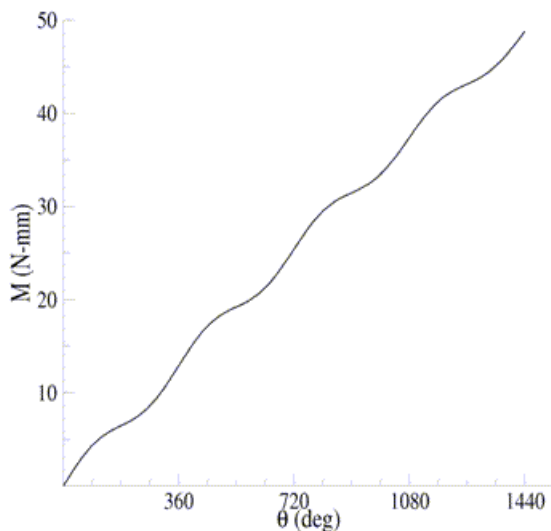
A simulated tension-torsion experiment was performed on a thin strip. The specimen is similar to that specified in ASTM D1043 (ASTM Standard D1043, 2006) and is shown here:

**Figure 15.3: Tension-Torsion Test Specimen**



The experiment consists of clamping each end of the specimen into the test apparatus, then stretching the specimen by 50 percent of its original gage length and twisting one end of the specimen for four complete revolutions. Following is the resulting moment-vs.-rotation data:

**Figure 15.4: Tension-Torsion Experimental Data**



## 15.4. Analysis and Solution Controls

Analysis and solution-control information for calibration and validation follow:

15.4.1. Calibrating Parameters

15.4.2. Validating Parameters

### 15.4.1. Calibrating Parameters

Material parameter calibration occurs using the [curve-fitting tool](#).

The command input shown here is for illustrative purposes only. While curve fitting can be done using command input, ANSYS, Inc. recommends using the graphical user interface (GUI) to perform the curve fitting, or at least visually validating the results using the GUI to ensure a sound fit.

Following is an input example of the commands used to fit a hyperelastic constitutive model to a set of uniaxial stress-strain data:

```

/PREP7
TBFT,FADD,1,HYPER,MOONEY,3
TBFT,EADD,1,UNIA,UNIAX.LOG
TBFT,SOLVE,1,HYPER,MOONEY,3
TBFT,FSET,1,HYPER,MOONEY,3
    
```

The **TBFT,FADD** command initializes the curve-fitting procedure for a hyperelastic, three-parameter, **Mooney-Rivlin model** assigned to material identification number 1.

**TBFT,EADD** reads the uniaxial experimental data in the `uniax.log` file as the fitting data for material number 1. The experimental data in the file is a set of engineering-strain vs. engineering-stress input:

```

0.819139E-01 0.82788577E+00
0.166709E+00 0.15437247E+01
0.253960E+00 0.21686152E+01
0.343267E+00 0.27201819E+01
0.434257E+00 0.32129833E+01
0.526586E+00 0.36589498E+01
0.619941E+00 0.40677999E+01
0.714042E+00 0.44474142E+01
0.808640E+00 0.48041608E+01
0.903519E+00 0.51431720E+01
0.998495E+00 0.54685772E+01
0.109341E+01 0.57836943E+01
    
```

**TBFT,SOLVE** determines the three constitutive parameters for the Mooney-Rivlin model, minimizing the difference between the model and the experimental data.

**TBFT,FSET** assigns the fitted constitutive parameters to material number 1.

For this problem, the fitted parameters for the three-parameter Mooney-Rivlin model are:

$$C_{10} = 1.338856$$

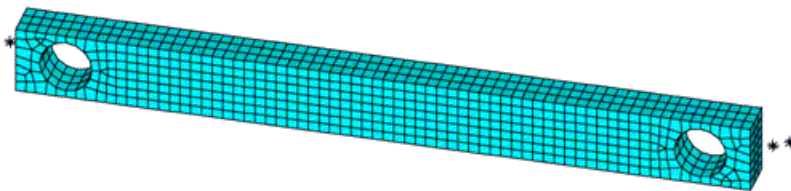
$$C_{01} = 5.236214 \times 10^{-1}$$

$$C_{11} = -1.648364 \times 10^{-2}$$

### 15.4.2. Validating Parameters

Following is a mesh developed to simulate the torsion experiment to validate the fitted constitutive model parameters obtained in [Calibrating Parameters \(p. 227\)](#):

**Figure 15.5: Tension-Torsion Test Specimen Mesh**



The mesh consists of 1,332 **SOLID186** elements using the default formulation (a mixed-displacement pressure formulation with reduced integration).

The attachment of the [test specimen \(p. 226\)](#) to the test apparatus is simulated by boundary conditions applied to the specimen in the region of the clamps, as described here:

- The back-left clamp region is fully restrained.

- The back-right clamp region is attached to a rigid-contact surface and fixed in place.
- The front-left clamp region is attached to a rigid-contact surface and displaced in the z direction to simulate a clamping displacement equal to 25 percent of the specimen thickness. The same is true for the front-right clamp region.

The stretching to 50 percent engineering strain is simulated by displacing the rigid-contact surfaces attached to the right clamp regions while holding left clamp regions fixed.

The torsion of the specimen is simulated by holding the left clamp region in place and twisting the keypoints attached to the right contact surfaces about the longitudinal axis.

## 15.5. Results and Discussion

Results for the calibration and validation operations are discussed below:

[15.5.1. Calibration Results](#)

[15.5.2. Validation Results](#)

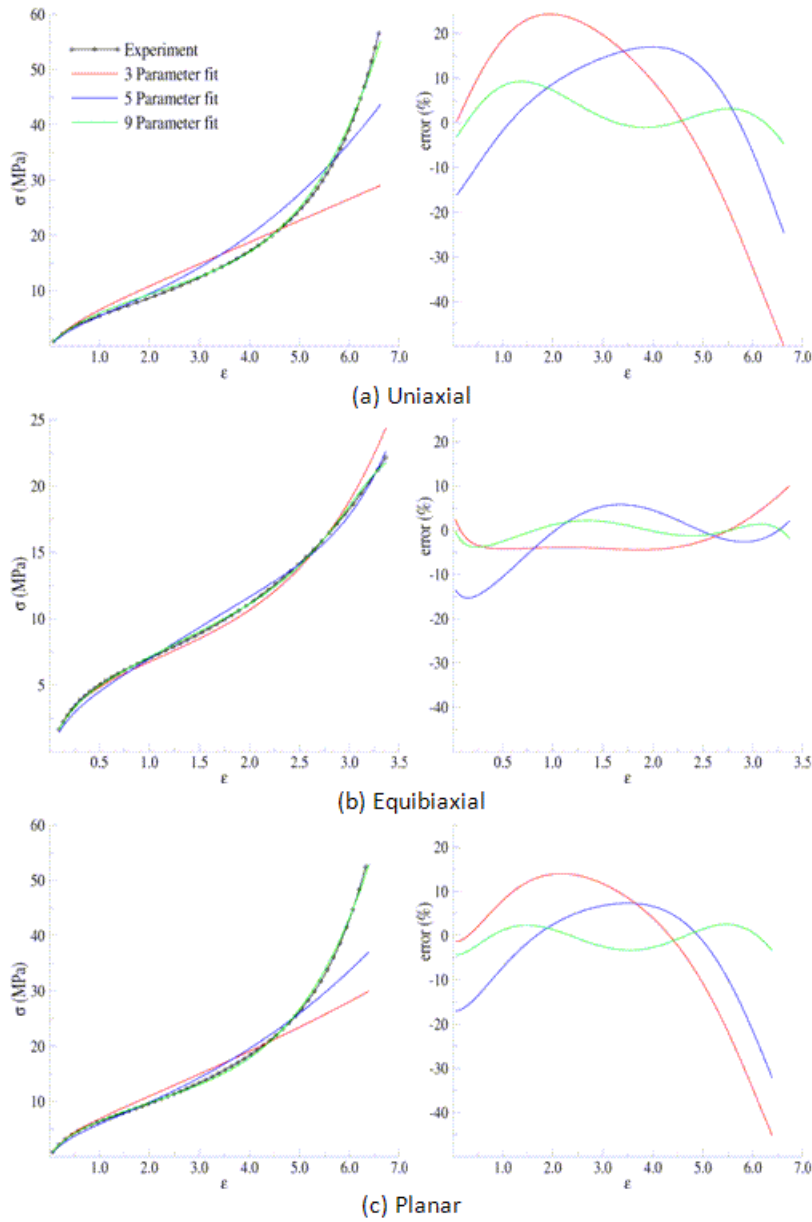
### 15.5.1. Calibration Results

Using all of experimental data shown in [Figure 15.2: Hyperelastic Test Suite: Experimental Data \(p. 226\)](#) to fit the three-, five-, and nine-parameter Mooney-Rivlin models results in the following parameters, fit to the entire range of experimental data:

	Three-Parameter	Five-Parameter	Nine-Parameter
$C_{10}$	1.8785	1.4546	1.7095
$C_{01}$	$-5.7759 \times 10^{-2}$	$7.6677 \times 10^{-2}$	$5.6365 \times 10^{-2}$
$C_{20}$	---	$1.3484 \times 10^{-2}$	$-1.2088 \times 10^{-2}$
$C_{11}$	$1.9589 \times 10^{-3}$	$-4.4337 \times 10^{-3}$	$3.7099 \times 10^{-5}$
$C_{02}$	---	$2.3997 \times 10^{-4}$	$-4.6858 \times 10^{-4}$
$C_{30}$	---	---	$3.5202 \times 10^{-4}$
$C_{21}$	---	---	$6.0562 \times 10^{-6}$
$C_{12}$	---	---	$1.9666 \times 10^{-5}$
$C_{03}$	---	---	$-8.9997 \times 10^{-7}$
$\mu$	3.6415	3.0625	3.5318

The following figure is a comparison of the models to the experimental data:

**Figure 15.6: Comparison of the Data and Fits Over the Entire Range of Data**



Thus far, it is obvious that none of the models provide a suitable fit to the entire range of experimental data. The reason is that the least-squares fitting procedure is minimizing the error over the entire range of data; therefore, it can be detrimental to include data that is not representative of the *actual range of use*.

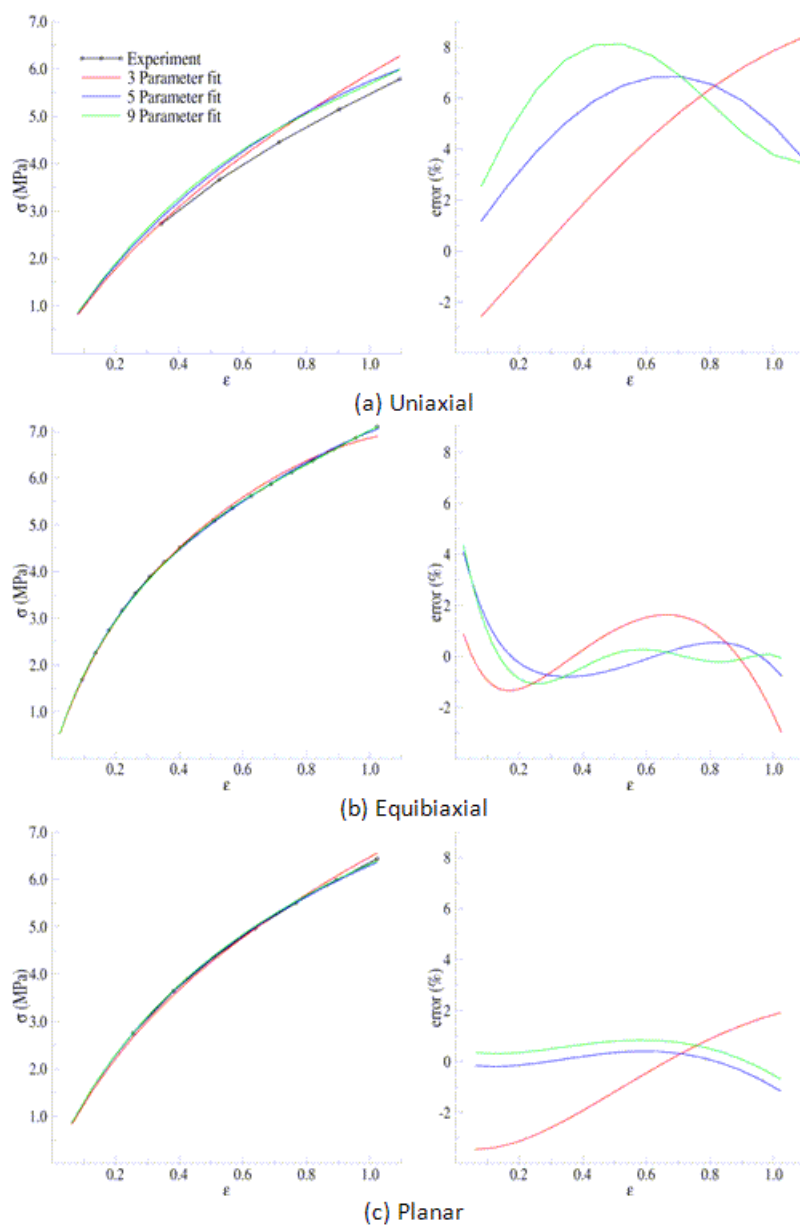
If the experimental data range is limited to about 100 percent strain, however, the fitted parameters shown in the following table are obtained:

	Three-Parameter	Five-Parameter	Nine-Parameter
$C_{10}$	1.6540	1.7874	1.8904
$C_{01}$	$1.2929 \times 10^{-1}$	$5.7229 \times 10^{-2}$	$-3.6352 \times 10^{-2}$
$C_{20}$	---	$-5.8765 \times 10^{-2}$	$-2.3484 \times 10^{-1}$
$C_{11}$	$-1.2726 \times 10^{-2}$	$2.6843 \times 10^{-2}$	$2.6511 \times 10^{-1}$

	Three-Parameter	Five-Parameter	Nine-Parameter
$C_{02}$	---	$-5.1127 \times 10^{-3}$	$-6.8670 \times 10^{-2}$
$C_{30}$	---	---	$5.1742 \times 10^{-2}$
$C_{21}$	---	---	$-8.3262 \times 10^{-2}$
$C_{12}$	---	---	$3.6204 \times 10^{-2}$
$C_{03}$	---	---	$-4.3754 \times 10^{-3}$
$\mu$	3.5665	3.6892	3.7081

The following figure is a comparison of the models with the parameters fit to the modified experimental data:

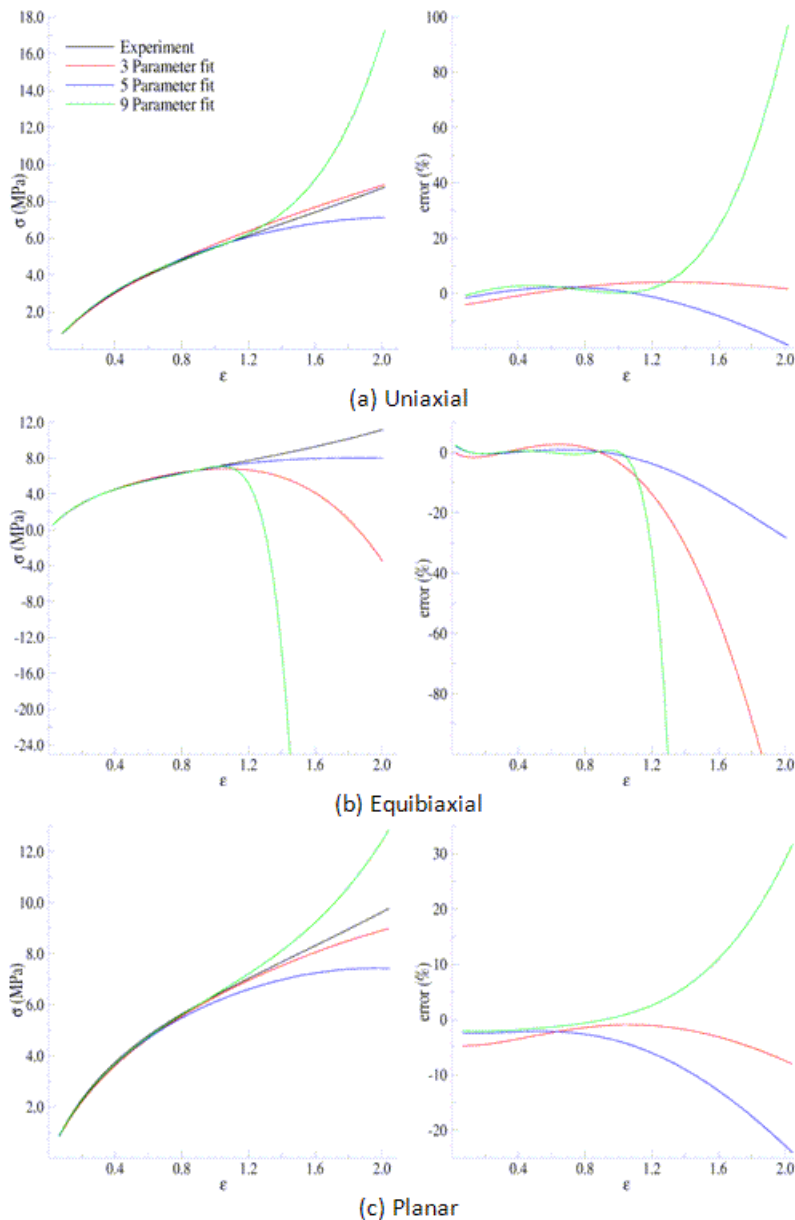
**Figure 15.7: Parameters Fit to Experimental Data to About 100 Percent Strain**



For the equibiaxial and planar experiments, any of the three models might be acceptable; however, the comparison with the uniaxial data might indicate that *none* of the three models are acceptable.

The behavior of the model outside the fitted range can significantly differ from the actual response of the material. For example, the model parameters fit to the experimental data to 100 percent strain have been used to simulate the hyperelastic test suite to strains of about 200 percent, as shown in the following comparisons:

**Figure 15.8: Comparison of the Data and Fits Showing Predictions Outside the Range of Fitted Data**



Beyond 100 percent strain, it becomes apparent that some of the predictions quickly deteriorate. In all three comparisons, the nine-parameter model quickly loses accuracy, and it appears that the three- and nine-parameter Mooney-Rivlin models have lost stability for the biaxial deformation case.

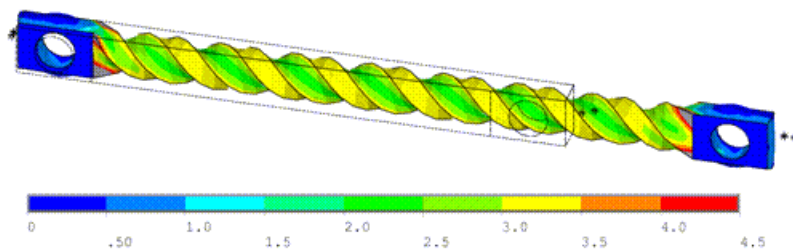
## 15.5.2. Validation Results

The five-parameter Mooney-Rivlin model, fit to the experimental data up to 100 percent strain, is selected as an adequate representation of the material response. The constitutive model is specified via the following input:

```
C10 = 1.787381e+00
C01 = 5.722875e-02
C20 = -5.876502e-02
C11 = 2.684331e-02
C02 = -5.112790e-03
TB, HYPER, 1, , 5, MOONEY
TBDATA, 1, C10, C01, C20, C11, C02
```

The following figure shows a contour plot of the strain energy density at the end of simulation. The plot offers a general idea of the overall deformation of the specimen.

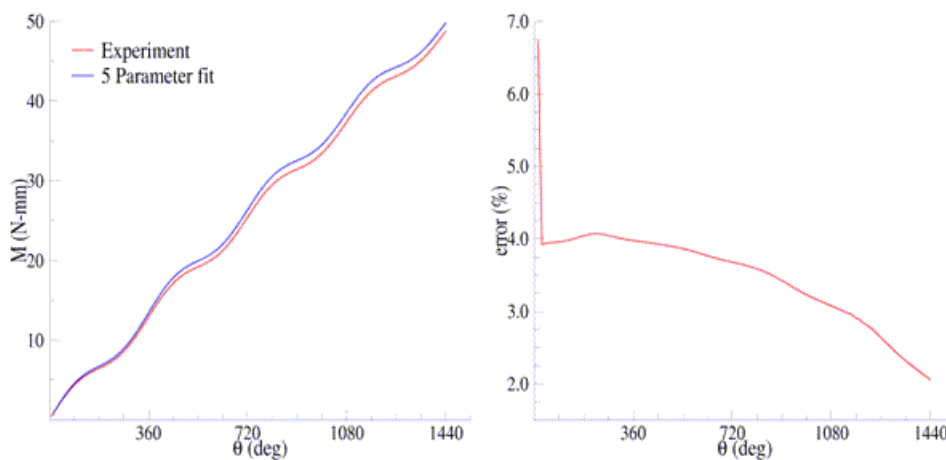
**Figure 15.9: Strain-Energy Density Contours of the Tension-Torsion Test**



With the exception of the clamp regions, the deformation shows a uniform pattern in the gage region along the axis of twisting. Perpendicular to the axis of twisting is a large strain-energy density near the outside edge of the specimen, decreasing toward the center.

The following figure shows a comparison of the model with the experimental moment vs. theta data:

**Figure 15.10: Comparison of Tension-Torsion Experiment to the Five-Parameter Mooney-Rivlin Model**



After a seemingly anomalous first data point, the error between the simulation and experiment is in the range of 2 to 4 percent. Throughout the entire simulation, the five-parameter Mooney-Rivlin model predicts a higher moment for an equivalent twist, which is not entirely expected by the error plots for

the hyperelastic test suite comparisons; nevertheless, a maximum four percent error appears to be a reasonable margin of error for this simulation.

## 15.6. Recommendations

When performing a similar type of calibration and validation, consider the following recommendations:

- Obtain test data from at least two (and preferably all three) of the experiments in the hyperelastic test suite.
- Ensure that the test data covers the range of deformation over which the constitutive model will be used.
- If the error between the experimental data and the constitutive model is too great, try limiting the experimental data to the range of deformation over which the constitutive model will be used.
- Use the constitutive model within the range of fitted data only.
- Use an independent experiment to validate that the constitutive model adequately matches the material behavior.

## 15.7. References

The following references are used in this example problem:

1. [ASTM Standard D1043](#). *Standard Test Method for Stiffness Properties of Plastics as a Function of Temperature by Means of a Torsion Test*. ASTM International. West Conshohocken. 2006.
2. [ASTM Standard D412](#). *Standard Test Methods for Vulcanized Rubber and Thermoplastic Elastomers-Tension*. ASTM International. West Conshohocken. 2006.

## 15.8. Input Files

The following files were used in this problem:

- `tension_torsion.dat` -- Tension-torsion simulation input file.
- `tension_torsion.cdb` -- The common database file containing the model information for this problem (called by `tension_torsion.dat` ).

The files are available in the `td-15` folder. See [Obtaining the Input Files \(p. xxxv\)](#) for more information.



---

## Chapter 16: Evaluation of Mixed-Mode Stress Intensity Factors and T-stress for 3-D Surface Flaws

---

This example problem shows how to evaluate mixed-mode [stress-intensity factors](#), [J-integrals](#), and [T-stresses](#) for cracks in structural components. Analyses of a simple semicircular surface flaw in a rectangular block and a warped flaw along a tubular joint are discussed.

The following features and capabilities are highlighted:

- Evaluating mode-I stress-intensity factors and T-stresses for a semicircular surface flaw in a rectangular block.
- Evaluating mixed-mode stress-intensity factors and T-stresses for a warped semi-elliptical surface flaw in a tubular joint.
- Meshing around a crack front in 3-D structures.

Topics related to this example problem follow:

- [16.1. Introduction](#)
- [16.2. Problem Description](#)
- [16.3. Modeling](#)
- [16.4. Material Properties](#)
- [16.5. Boundary Conditions and Loading](#)
- [16.6. Analysis and Solution Controls](#)
- [16.7. Results and Discussion](#)
- [16.8. Recommendations](#)
- [16.9. References](#)
- [16.10. Input Files](#)

### 16.1. Introduction

Fracture analysis is widely used to predict component failure caused by preexisting small cracks, allowing one to take precautions to prevent further crack growth or to determine the remaining life of the structure.

To assess the fracture damage, stress intensity factors (SIFs) must be evaluated accurately. Because it is difficult to determine accurate SIFs using a closed-form analytical solution for cracks in complex structures, finite-element analysis is used instead.

Two approaches are available for evaluating SIFs:

- **Interaction Integral Method** -- Performs the SIF calculation during the solution phase of the analysis and stores the results for later postprocessing.
- **Displacement Extrapolation Method** -- Performs the SIF calculation during postprocessing. This method is limited to problems involving linear elasticity with homogeneous, isotropic materials near the crack region.

The interaction integral method is used here as it allows for the calculations to be performed during the solution phase. It is also more accurate, as the domain integral expressions are naturally aligned with the FE formulation.

## 16.2. Problem Description

The following two models with surface flaws are considered for analysis:

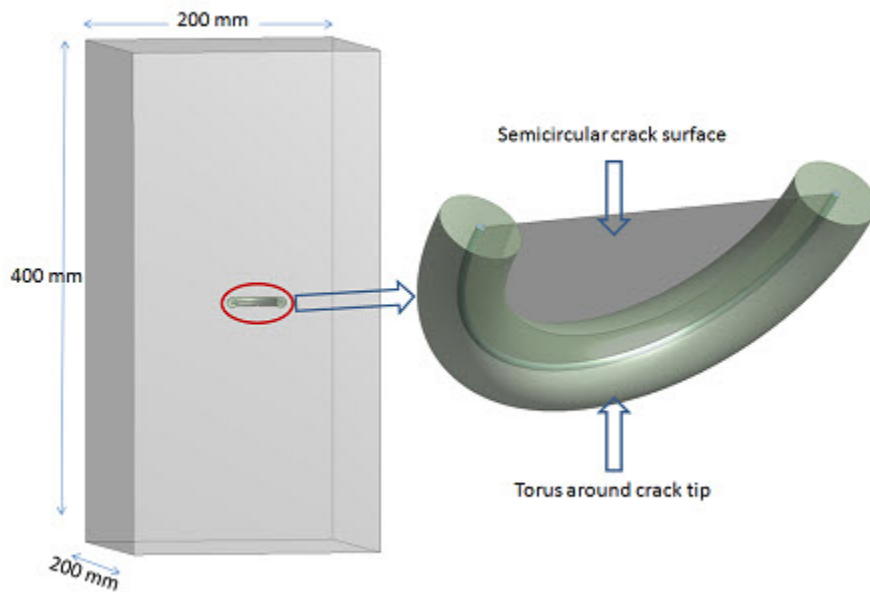
16.2.1. Rectangular Block with a Semicircular Surface Flaw

16.2.2. X-Joint Pipe with Warped Surface Flaw

### 16.2.1. Rectangular Block with a Semicircular Surface Flaw

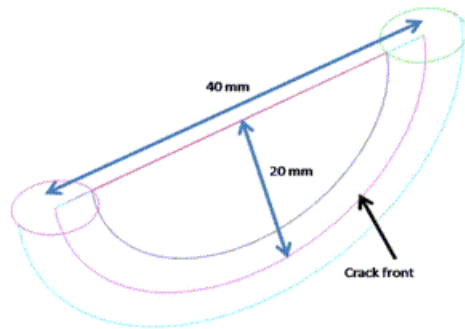
This model is fixed at one face of the block and a pressure load is applied on the opposite face. The block has a semicircular surface flaw at the center of one longitudinal face in the thickness direction--a crack is perpendicular to one of the surfaces of the rectangular block--with a 20 mm radius, as shown:

**Figure 16.1: Rectangular Block Geometry with Semicircular Surface Flaw**



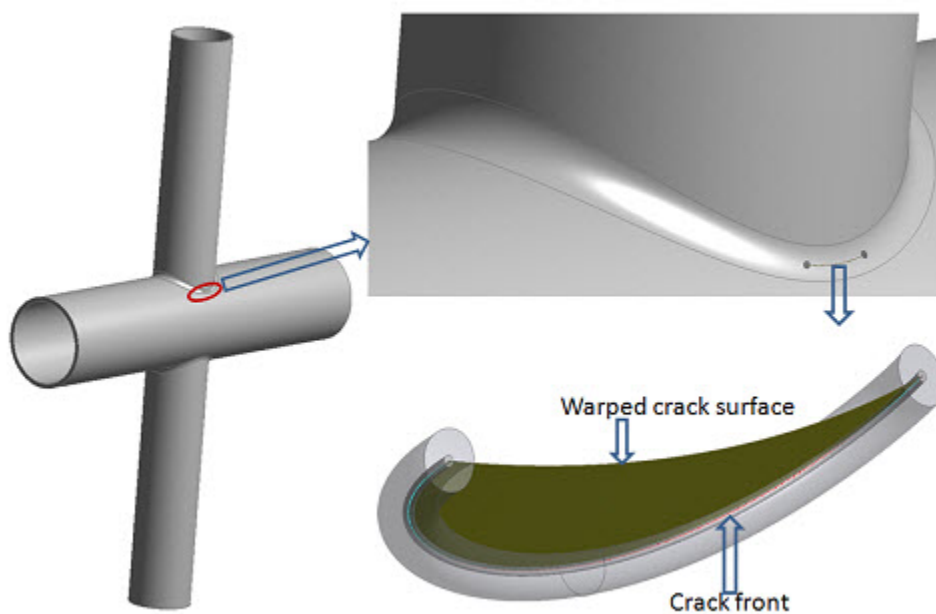
A torus is created around the crack front to control the mesh at the crack front. The objective is to find KI along the crack front and validate the results with reference results.[1][2][3]

Following is the semicircular crack and torus along the crack front used to create a sweep mesh with SOLID186:

**Figure 16.2: Semicircular Crack and Torus Along the Crack Front**

### 16.2.2. X-Joint Pipe with Warped Surface Flaw

A semi-elliptical warped surface flaw at the tubular joint is analyzed to obtain mixed-mode SIFs (KI, KII and KIII) along the crack front:

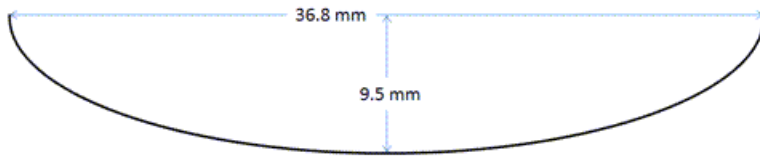
**Figure 16.3: X-Joint Pipe Full Model with Warped Surface Flaw at Welded Joint**

The problem consists of two tubular members attached to each other by a welded joint. The tubular members have outer diameters of 323.85 mm (D1), 219.08 mm (D2), and thicknesses of 15.88 mm (t1) and 8.18 mm (t2), respectively. The semi-elliptical surface crack lies on a plane parallel to the radial direction of the heavier running pipe.

A torus is created around the crack front to control the mesh at the crack front. The semi-elliptical surface crack at the weld toe is warped along the welded joint and it is perpendicular to the outer surface of the 323.85 mm diameter pipe in the thickness direction.

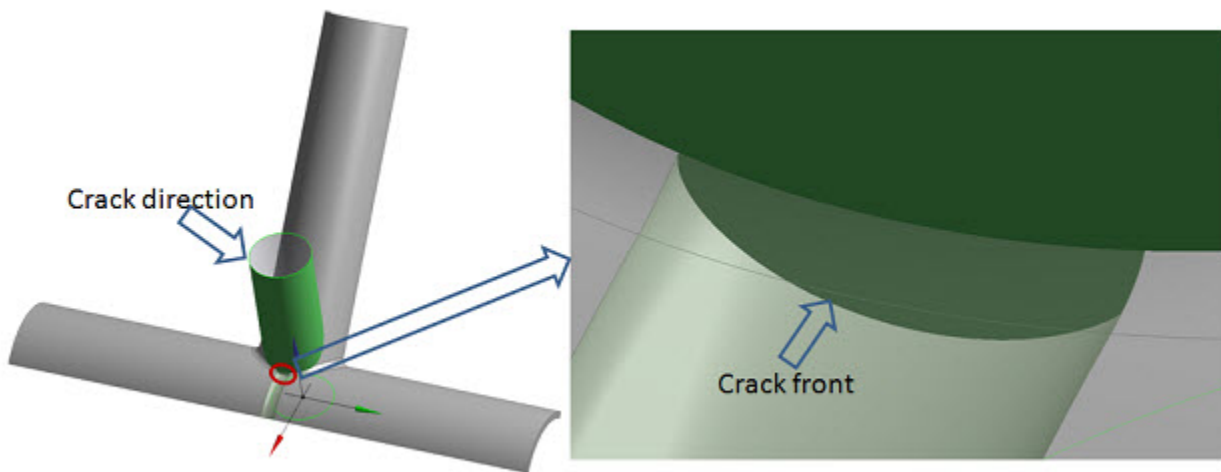
Following are the crack dimensions:

**Figure 16.4: Semi-elliptical Surface Crack Dimensions**



The warped crack profile at the welded joint is created via the interaction of a rotated semi-ellipse on the 323.85 mm diameter pipe and an extruded circle normal to the inner surface of the same pipe at the welded joint, as shown:

**Figure 16.5: Two-plane Symmetry of X-joint Pipe with Warped Surface Flaw Geometry**

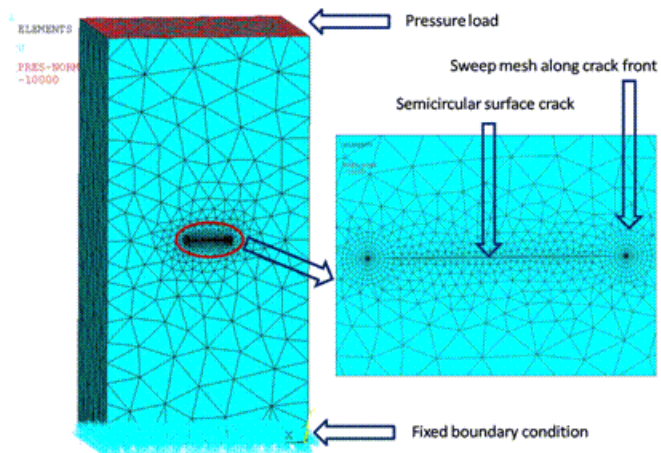


### 16.3. Modeling

For 3-D models, the recommended element type near the crack front is **SOLID186**, the 20-node brick element.

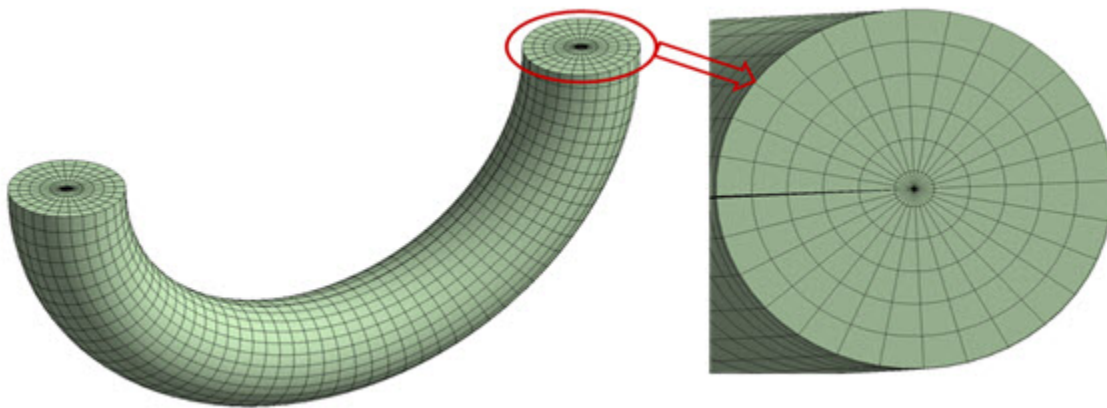
The rectangular block and x-joint pipe models are meshed with **SOLID187** elements (except for the regions around the crack tip), as shown:

**Figure 16.6: Rectangular Block Model with Boundary Conditions and Loading Applied**



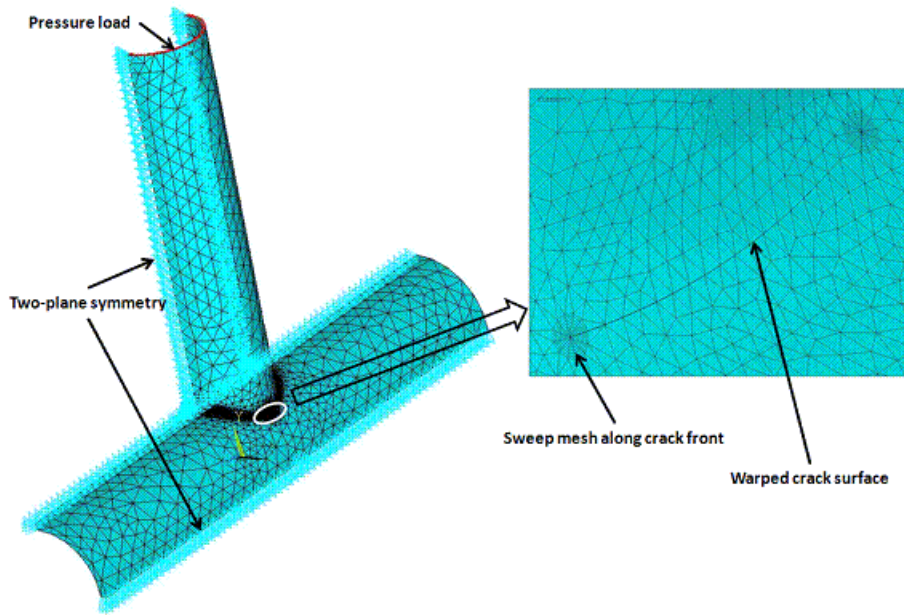
Regions around the crack tips are meshed with **SOLID186**, as shown:

**Figure 16.7: Sweep Mesh with **SOLID186** Around Crack Front**



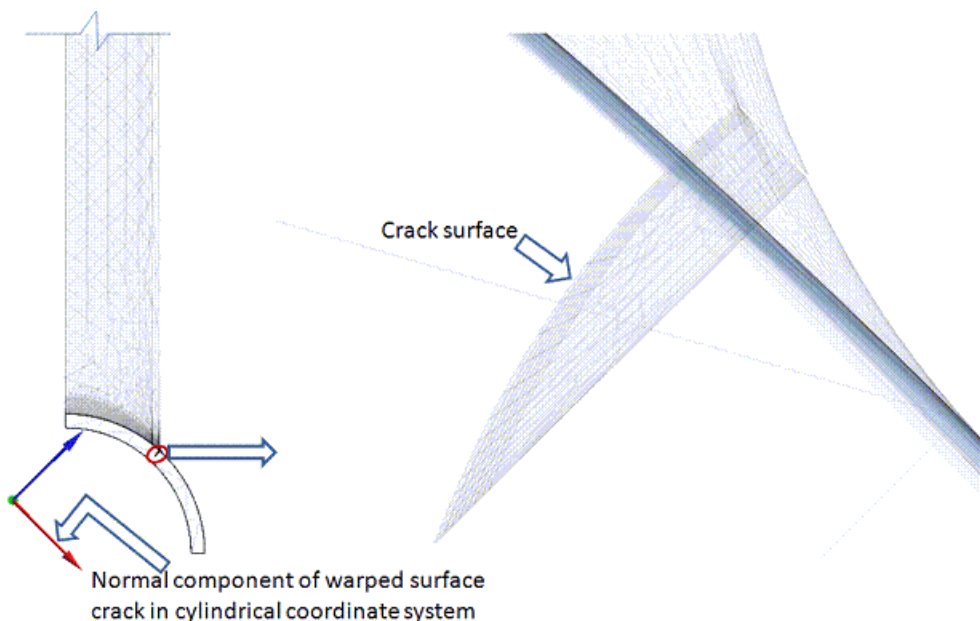
Due to the two-plane symmetry of the x-Joint problem, a quarter model is considered for analysis, as shown:

**Figure 16.8: Two-plane Symmetry of X-joint Pipe with Warped Surface Flaw at Welded Joint**



If the crack surface is not normal to any component in the global coordinate system, a local coordinate system should be created in such a way that one component of this coordinate system is perpendicular to the crack surface. For example, in the x-joint model, a local cylindrical coordinate system is created such that one of its components is normal to the crack surface, as shown:

**Figure 16.9: X-joint Pipe with Warped Surface Flaw at Welded Joint in Thickness Direction.**

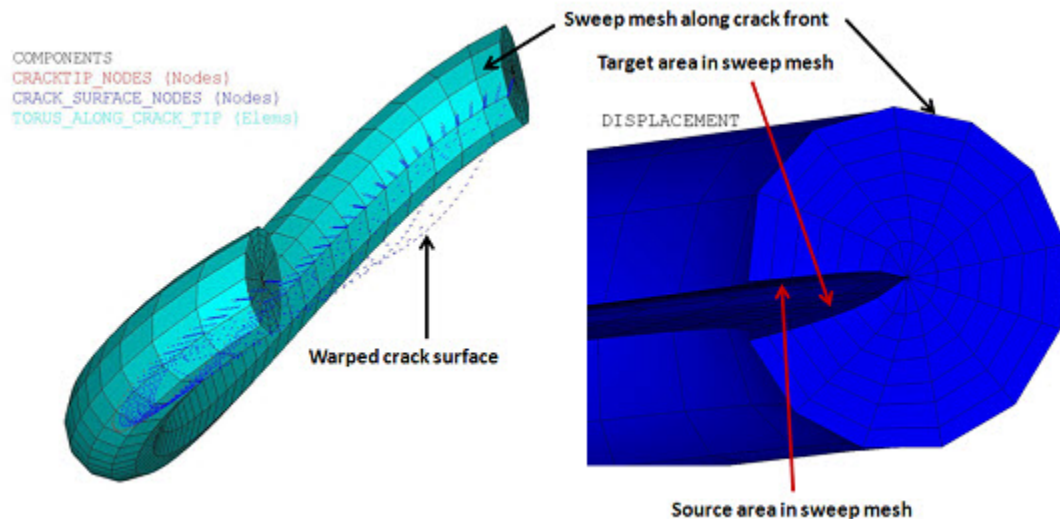


In the x-joint model, the warped crack in the thickness direction is perpendicular to the inner surface of the 323.85 mm diameter pipe.

A torus is created around the crack front to obtain a good sweep mesh (**VSWEEP**). A common area separates the torus and the remaining volume at the interface.

In 3-D models, a fracture has two surfaces with a common edge at the crack front; the same is true for the torus. The two torus surfaces are used to create a clean sweep mesh around the crack front. One surface is defined as the source, the other as the target. In this procedure, the sweep mesh generates brick elements with one layer of prism elements around the crack front. Following is the sweep mesh with **SOLID186** around the crack front in the x-joint pipe model, with the source and target areas for the sweep mesh indicated in the deformed body:

**Figure 16.10: Sweep Mesh with **SOLID186** Around the Crack Front**



The warped surface contains a sweep mesh and a set of nodes, along with source and target areas in the deformed torus body. The source and target areas existed at the same location in the nondeformed structure.

After meshing, crack parameters must be defined. The following example inputs show how to define parameters associated with contour integral calculation:

```
! Initiate a new contour integral calculation and define type
CINT, NEW, 1           ! Initiate new calculation and assign ID
CINT, TYPE, SIFS      ! Replace SIFS with JINT to find J-integral

! Define crack tip nodal component to find SIFs or J-integral for specified flaw
CINT, CTNC, component_name, , 1

! Define symmetry details, number of contours to be calculated
CINT, SYMM, OFF       ! Symmetry off
CINT, NCON, 6         ! Number of contours

! Define crack plane normal
CINT, NORMAL, 0, 2
```

A line component of the crack front lines (**CM**) is created. This component is useful for selecting nodes attached to the crack front (**NSLL**). The nodal component of these nodes is used to define crack tip node components (**CINT,CTNC**), as shown in the following figures:

**Figure 16.11: Crack Tip Nodal Component: Rectangular Block Model**

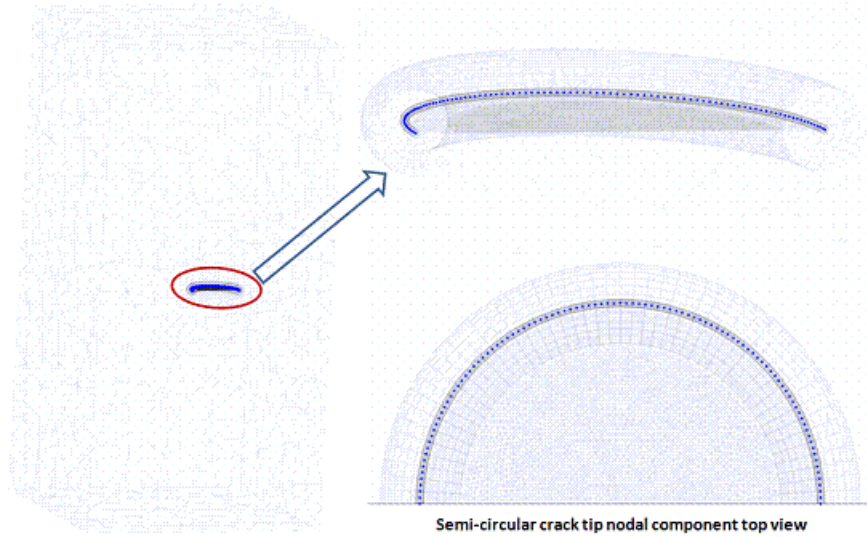
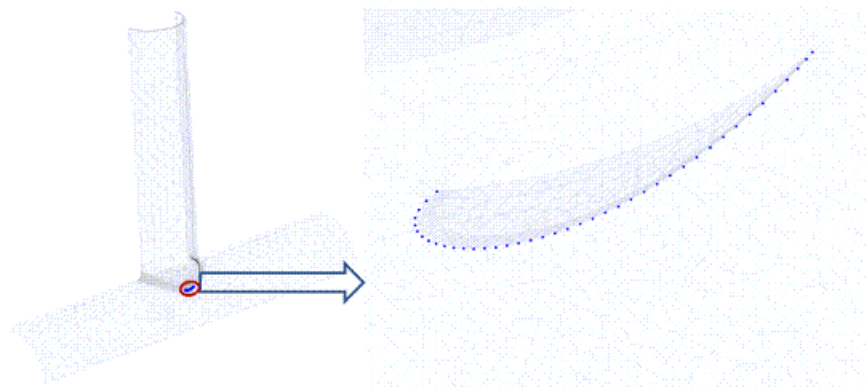


**Figure 16.12: Crack Tip Nodal Component: X-joint Pipe Model**



## 16.4. Material Properties

Material properties for this problem are as follows:

Mixed-Mode Stress-Intensity Factors	
Material Properties	
Young's Modulus (Pa)	2E+11
Poisson's Ratio	0.3

## 16.5. Boundary Conditions and Loading

The rectangular block is fixed at one face. A pressure of  $-10E+3$  MPa is applied on the other face, as shown in [Figure 16.6: Rectangular Block Model with Boundary Conditions and Loading Applied \(p. 239\)](#).

Analysis of the x-joint model is performed with two-sided symmetry. Two-plane symmetric boundary conditions are applied and one midside node at the horizontal plane is constrained in the opposite



direction to restrict rigid-body motion. A pressure load of -1000 MPa is applied on the top of the small-diameter tube, as shown in [Figure 16.8: Two-plane Symmetry of X-joint Pipe with Warped Surface Flaw at Welded Joint](#) (p. 240).

## 16.6. Analysis and Solution Controls

A linear static analysis is performed.

Output controlled (**OUTRES,CINT**) is used to write the SIFs, J-integral, and T-stress results to the results (.rst) file and output files.

The following postprocessing commands can be used to list and/or plot and list the results:

```

/POST1
PLCINT,FRONT,1,,K1    ! Plot KI results
PLCINT,FRONT,1,,K2    ! Plot KII results
PLCINT,FRONT,1,,K3    ! Plot KIII results
PLCINT,FRONT,2        ! Plot J-integral results
PLCINT,FRONT,3,,TSTR  ! Plot T-Stress results

PRCINT,1,ALL,K1       ! Print KI results
PRCINT,1,ALL,K2       ! Print KII results
PRCINT,1,ALL,K3       ! Print KIII results
PRCINT,2,ALL,JINT     ! Print J-integral results
PRCINT,3,ALL,TSTR     ! Print T-Stress

```

## 16.7. Results and Discussion

This section presents the results for both models used in this problem:

16.7.1. Rectangular Block with Semicircular Surface Flaw

16.7.2. X-joint Pipe with Warped Flaw

### 16.7.1. Rectangular Block with Semicircular Surface Flaw

The following two figures show the displacement vector sum (USUM) and the Von Mises Stresses, respectively:

**Figure 16.13: USUM Results (Rectangular Block)**

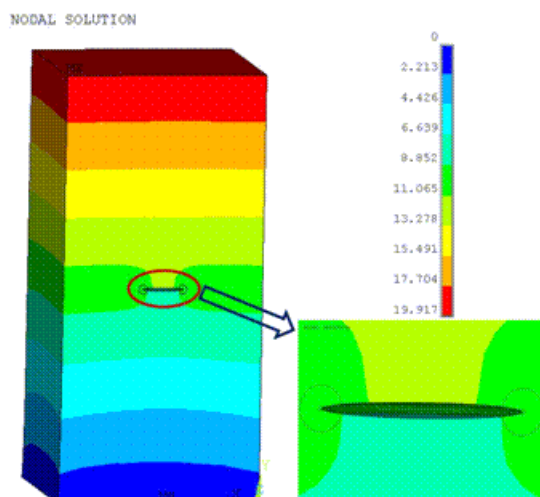
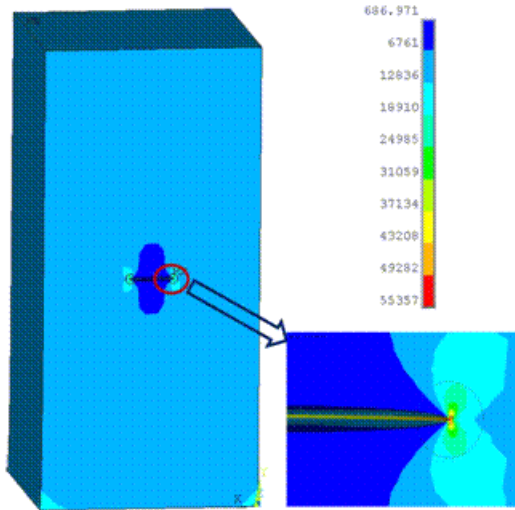


**Figure 16.14: Von Mises Stress Plot (Rectangular Block)**

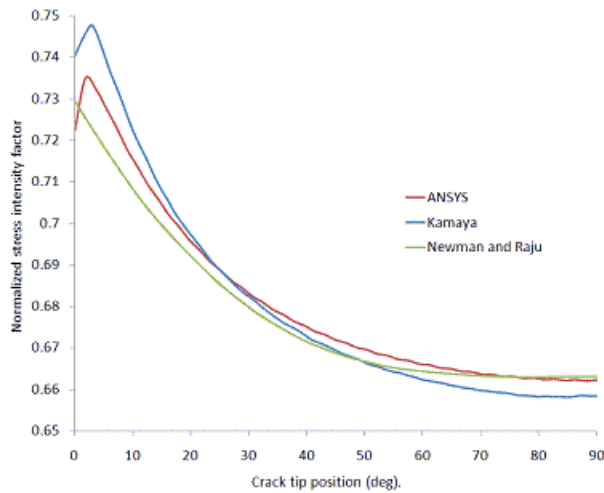


The plot shows the maximum Von Mises stress occurring at the crack tip.

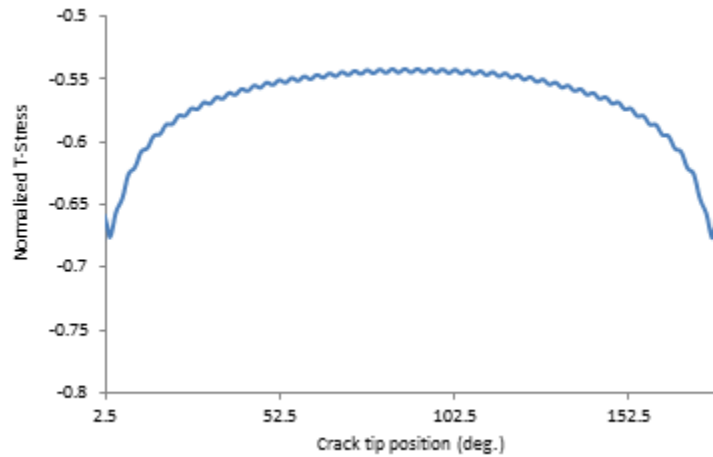
To verify the SIF accuracy obtained via the interaction integral method, the results are compared to analytical results of Newman and Raju (p. 247) and finite-element result of Kamaya (p. 247). The results agree closely with those obtained in the references.

Because the crack exists at the center of the rectangular block, the results for half of the crack are therefore plotted in this figure, where normalized SIF =  $KI / (\sigma_0 \sqrt{(\pi \times \text{initial radius of flaw})})$ :

**Figure 16.15: Normalized KI Results**

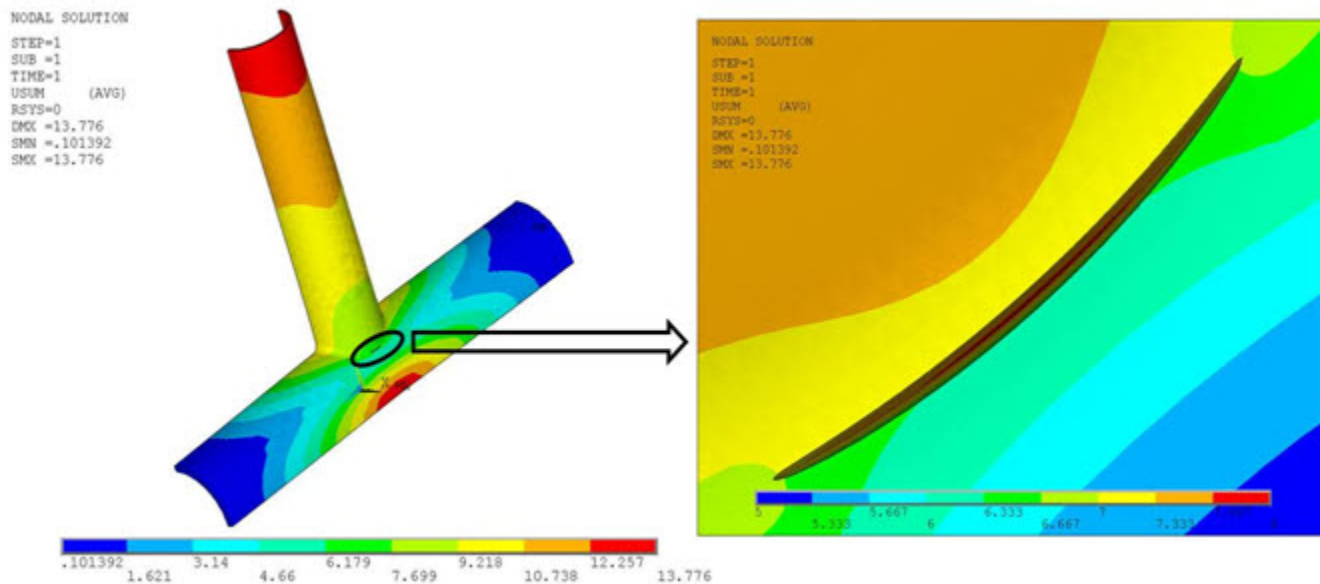


The T-stress results for the semicircular surface flaw are plotted in this figure, where normalized T-stress = T-stress /  $\sigma_0$ :

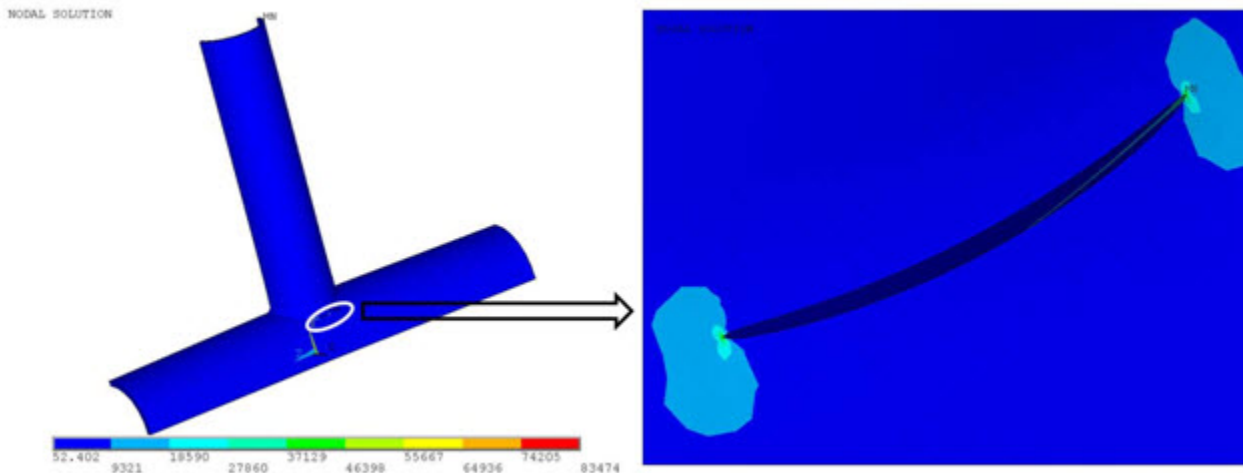
**Figure 16.16: Normalized T-Stress Results: Semicircular Surface Flaw**

### 16.7.2. X-joint Pipe with Warped Flaw

The following figures show the displacement vector sum (USUM) and Von Mises Stresses plot of the x-joint pipe with the warped flaw at the welded joint:

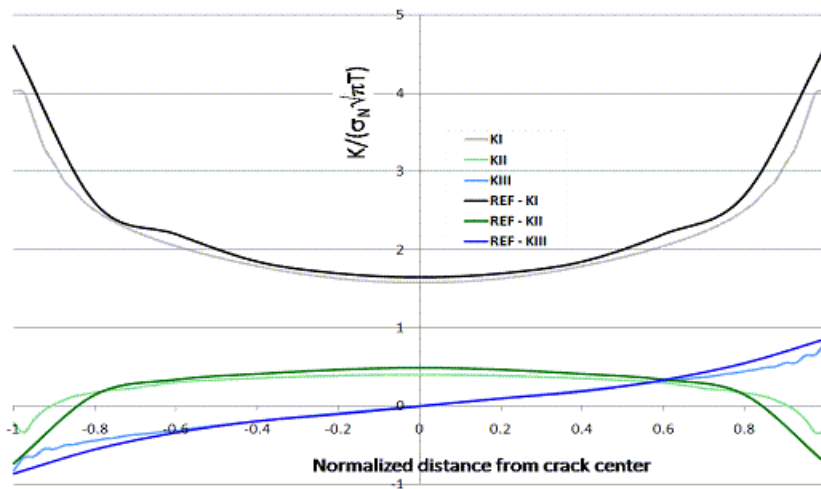
**Figure 16.17: USUM Results (X-joint Pipe)**

**Figure 16.18: Von Mises Stress Plot (X-joint Pipe)**



The SIFs of the mixed-mode 3-D problem with the warped crack surface were compared with those of Chong Rhee.[4] The comparison shows that the normalized KI, KII and KIII results agree well with the reference results near the end points, as shown:

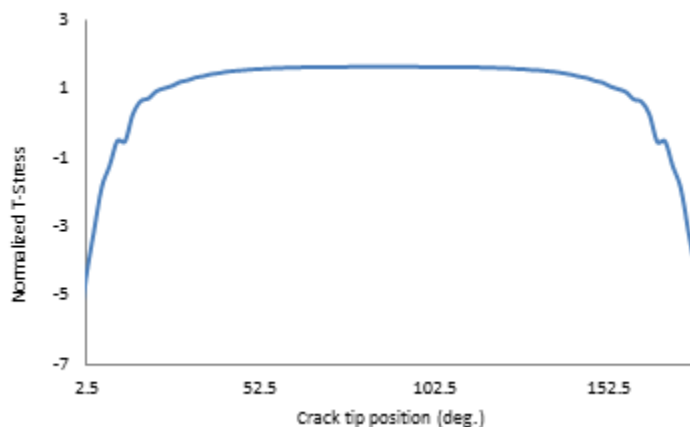
**Figure 16.19: Normalized SIF Results: Comparison with Chong Rhee[4]**



where T is the thickness of the pipe, and the normalized distance is the distance from center of the crack along the crack front divided by half of the crack tip length.

A fine mesh (using meshing bias [**LESIZE**,,,,,*SPACE*]) at the end-point regions improves the results.

The T-stress results for the X-joint pipe with warped flaw are plotted in this figure, where normalized T-stress = T-stress /  $\sigma_0$  :

**Figure 16.20: Normalized T-Stress Results: X-Joint Pipe with Warped Flaw**

## 16.8. Recommendations

When setting up a fracture analysis for 3-D structures, consider the following hints and recommendations:

- The recommended element type for 3-D fracture models along the crack tip is the 20-node brick element [SOLID186](#).
- A fine sweep mesh along the crack front yields more accurate results. Create a torus along the crack front in the model geometry for this purpose.
- If any component in the global coordinate system is not orthogonal to the crack surface, create one local coordinate system with one component normal to the crack surface. This action is necessary to define the crack plane normal ([CINT,NORM](#)).
- For multiple cracks, use unique crack tip IDs and separate sets of [CINT](#) commands for each.
- To determine SIFS *and* J-integrals for the same crack, use two separate [CINT](#) command sets.
- The interaction integral method gives accurate results because the contour integral is evaluated at points far away from the crack-tip. Disregard the first contour results, however, as they are less accurate than the other results due to the nearness of the crack tip.

For more information, see [Introduction to Fracture in the Mechanical APDL Fracture Analysis Guide](#).

## 16.9. References

The following references are used in this example problem:

1. Newman, J. C., Jr., and I. S. Raju. "Analysis of Surface Cracks in Finite Plates Under Tension or Bending Loads." [NASA Technical Paper 1578](#). National Aeronautics and Space Administration (1979).
2. Kamaya, M. "Stress Intensity Factor of Surface Crack with Undulated Front." [JSME International Journal](#) 49.4 (2006): 529-535.
3. Anderson, T.L. *Fracture Mechanics - Fundamentals and Applications* 3rd ed. Boca Raton: [CRC](#), (2005).
4. Rhee H. C. and M. M. Salama. "Mixed-Mode Stress Intensity Factor Solutions of a Warped Surface Flaw by Three-Dimensional Finite Element Analysis." [Engineering Fracture Mechanics](#) 28-2 (1987): 203-209.

## 16.10. Input Files

The following files were used in this problem:

- `semicircular_surface_flaw.dat` -- Input file for the analysis of the semicircular surface flaw in the rectangular plate.
- `semicircular_surface_flaw_model.dat` -- Database file for the finite-element model of the semicircular surface flaw (called by `semicircular_surface_flaw.dat`).
- `xjoint_pipe_with_warped_flaw.dat` -- Input file for the fracture analysis of the x-joint model.
- `xjoint_pipe_with_warped_flaw.cdb` -- Common database file for the x-joint finite-element model (called by `xjoint_pipe_with_warped_flaw.dat`).

The files are available in the `td-16` folder. See [Obtaining the Input Files \(p. xxxv\)](#) for more information.

---

## Chapter 17: Impact of a Metal Bar on a Rigid Wall

---

This example problem demonstrates an impact simulation using a 3-D model of a metal bar hitting a rigid wall. The problem shows the advantages of using impact constraints for modeling contact in a nonlinear transient dynamic analysis.

Several combinations of available time-integration methods and contact algorithms are also investigated, using different material models to show how various choices affect the performance and accuracy of the finite-element solution of impact problems.

Topics related to this example problem follow:

- 17.1. Introduction
- 17.2. Problem Description
- 17.3. Modeling
- 17.4. Material Properties
- 17.5. Boundary Conditions and Loading
- 17.6. Analysis and Solution Controls
- 17.7. Results and Discussion
- 17.8. Recommendations
- 17.9. References
- 17.10. Input Files

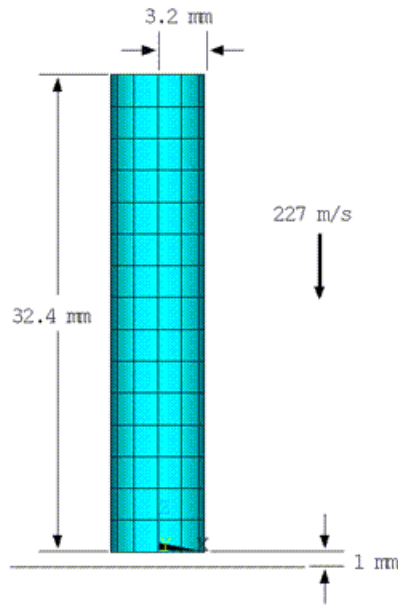
### 17.1. Introduction

Simulating contact in a transient dynamic analysis can be challenging. The presence of inertial forces can adversely affect convergence in contact problems. The simulated response also needs to be accurate to ensure that it remains stable, and consistent with physical behavior, over a long time period.

The impact of a metal bar on a rigid wall is ideal for demonstrating various solution options, as this problem has been [extensively studied and documented \(p. 264\)](#), and there are existing analytical and numerical solutions available for comparison.

### 17.2. Problem Description

A copper bar with a circular cross section having an initial length of 32.4 mm and a radius of 3.2 mm impacts a rigid, frictionless wall. The bar has an initial velocity of 227 m/s along its longitudinal axis and has one end located at a distance of 1 mm from the rigid wall at the start of the analysis, as shown in this figure:

**Figure 17.1: Geometry and FE Model of a Metal Bar Impacting a Rigid Wall**

Several transient analyses are performed, taking into account the following criteria:

- Rigid, elastic, and elastoplastic (p. 251) material behavior for the bar
- Newmark and HHT time-integration methods (with and without damping)
- Element-level time-incrementation controls and impact constraints.

For rigid and elastic material behavior, the results of displacements, velocities, strain energies (SE), and kinetic energies (KE) are compared to the analytical solution. For the elastoplastic material behavior, the results of mushroom radius, final length, equivalent plastic strain, and von Mises stress are compared to a reference solution.

### 17.3. Modeling

The bar is modeled with a 3-D coarse mesh using 495 SOLID186 elements, as shown in Figure 17.1: Geometry and FE Model of a Metal Bar Impacting a Rigid Wall (p. 250).

Frictionless contact between the rigid wall and the end of the bar is modeled using TARGE170 and CONTA174 elements.

The CONTA174 elements have the following settings:

- Augmented Lagrangian formulation (KEYOPT(2) = 0, the default behavior)
- Location of the contact-detection point on the nodal point-normal to target surface is activated (KEYOPT(4) = 2). This setting is required for the rigid-impact case, as geometric irregularities that may exist on the contact surface could create a nonsymmetric contact-force distribution and affect solution convergence adversely.
- Contact stiffness is updated at each iteration (KEYOPT(10) = 2).



The problem uses three separate element-level time-incrementation controls (KEYOPT(7)):

- No control (KEYOPT(7) = 0) -- Time incrementation is based on the response frequency.
- Contact predictions are changed (KEYOPT (7) = 3) -- Maintains the minimum time/load increment whenever a contact status change occurs.
- Impact constraints are used KEYOPT (7) = 4) -- The time increment is adjusted automatically.

The latter two time-incrementation controls (KEYOPT (7) = 3 and KEYOPT (7) = 4) activate time-step size control to capture all contact status changes.

### 17.3.1. Impact Scenarios

Three impact scenarios are examined. Each of these scenarios requires its own finite-element model and its own output of results of interest:

- **Rigid Impact (p. 252)**

The bar is modeled as a rigid body using only [TARGE170](#) elements, with automatically constrained boundary conditions for rigid target nodes (KEYOPT (2) = 1). The target elements are located on the exterior surface of the bar which has been premeshed with [SOLID186](#) elements.

The program builds internal multipoint constraints between the nodes on the exterior surface of the rigid body and a pilot node located at the center of gravity. The pilot node is also shared by a 3-D point mass with rotary inertia (modeled with a [MASS21](#) element).

The location of the center of gravity, and the mass and moments of inertia properties for [MASS21](#), are estimated by performing a single load step solution with the option for precalculating masses ([IRLF,-1](#)).

For more information, see [Modeling Rigid Bodies in a Multibody Analysis](#) in the *Multibody Analysis Guide*.

Before obtaining the solution, the underlying [SOLID186](#) mesh is unselected ([ESEL,U](#) command).

- **Elastic Impact (p. 253)**

The bar is modeled as a flexible body with linear elastic material properties.

- **Elastoplastic Impact (p. 253)**

The bar is modeled as a flexible body with elastoplastic material properties.

## 17.4. Material Properties

The material properties of the copper bar are as follows:

Linear Elastic Material Properties	
Young's Modulus (GPa)	E = 117
Poisson's Ratio ( $\nu$ )	0.35
Plastic Material Properties	
Yield Stress (MPa)	$\sigma_y = 400$

Linear Elastic Material Properties	
Tangent Modulus (MPa)	$E_T = 100$
Density (kg / m <sup>3</sup> )	$\rho = 8930$

## 17.5. Boundary Conditions and Loading

No boundary conditions or loads are applied to the copper bar.

An initial velocity of 227 m/s is applied to all nodes on the bar (including the rigid-body pilot node for rigid impact).

The rigid wall, defined using [TARGE170](#) elements, is internally constrained in all six directions.

## 17.6. Analysis and Solution Controls

Large-strain effects, large displacements, and large rotations are included in the analysis ([NLGEOM,ON](#)).

Automatic time-stepping adjustments (based on element-level time incrementation) are in effect; however, they are overridden if a fixed number of substeps ([NSUBST](#)) or a fixed time-step size ([DELTIM](#)) is specified, or if automatic time stepping is disabled ([AUTOTS,OFF](#)).

For each of the three [impact scenarios](#) (p. 251), three transient analyses are performed using the following settings and commands:

- Full method with the Newmark time-integration scheme and no damping:

```
TRNOPT, FULL, , , , , NMK
TINTP, 0.0
```

- Full method with the Newmark time-integration scheme and damping:

```
TRNOPT, FULL, , , , , NMK
TINTP, 0.1
```

- Full method with the HHT time-integration scheme and damping:

```
TRNOPT, FULL, , , , , HHT
TINTP, 0.1
```

### 17.6.1. Solution Options for Capturing Simulation Results

The solution options for each of the three [impact scenarios](#) (p. 251) are set to fully capture the simulated responses:

[17.6.1.1. Rigid Impact](#)

[17.6.1.2. Elastic Impact](#)

[17.6.1.3. Elastoplastic Impact](#)

#### 17.6.1.1. Rigid Impact

The transient analysis is carried up to time 0.1e-4 seconds with an initial minimum number of substeps of 100, and a maximum number of substeps of 10000:

```
TIME, 0.1e-4
NSUBST, 100, 10000, 100
```

The total time (simulation time) represents a slightly larger time than the time needed for the bar to impact the rigid wall; the bar moving at a velocity of 227 m/s requires about 0.4405e-5 seconds to cover a 1 mm gap before impacting the rigid wall.

The minimum of 100 substeps ensures a smooth response. The maximum of 10000 substeps allows the automatic time-stepping method to cut back the time increment to satisfy the impact constraints. Because the goal in this case is to study the displacement and velocity response of the bar at some points of interest over the total time period, the nodal displacement and velocity solution data is written at every substep to the results file:

```
OUTRES, NSOL, ALL
OUTRES, V, ALL
```

### 17.6.1.2. Elastic Impact

The same solution settings are used as for the [rigid case \(p. 252\)](#) with the only difference being the total time. The total time in this case must take into account the time that the stress wave created from the impact needs to travel back and forth through the elastic bar. The calculated time of impact is 0.4405e-5 seconds and the release time is calculated analytically as 0.223e-4 seconds, so a total time of 0.28e-4 seconds is used for the elastic impact.

### 17.6.1.3. Elastoplastic Impact

The same solution settings are used as in the [rigid \(p. 252\)](#) and [elastic \(p. 253\)](#) cases, except for the total time. Because the bar undergoes large plastic deformation and remains in contact with the rigid wall for a longer time period, the total time is increased to 0.8e-4 seconds.

The nodal-displacement solution data is written to the results file at every substep, and stresses and plastic strains are written at the last substep only, as follows:

```
OUTRES, NSOL, ALL
OUTRES, STRS, LAST
OUTRES, EPPL, LAST
```

## 17.7. Results and Discussion

Following is an examination of the results for each of the three [impact scenarios \(p. 251\)](#):

- 17.7.1. Rigid Impact Results
- 17.7.2. Elastic Impact Results
- 17.7.3. Elastoplastic Impact Results
- 17.7.4. Performance Summary

Key option (KEYOPT) settings are those of the [CONTA174](#) element.

### 17.7.1. Rigid Impact Results

For rigid impact, the bar should hit the rigid wall and bounce back immediately with the same velocity. The total energy after the impact (SE+KE) should be same as the total energy before the impact (239.61 J).

As shown in the following table and subsequent figures, a comparison of the rebound velocity and the total energy at post-impact separation indicates that the rebound velocity is greater than the initial velocity when using either:

- no control (KEYOPT(7) = 0), or

- element-level time-incrementation control (based on contact-status changes (KEYOPT(7) = 3)) without numerical damping.

CONTA174 Key Option Setting	NMK with No Damping (p. 255)		NMK with Damping (p. 256)		HHT with Damping (p. 257)	
	Rebound velocity (m/s)	Total energy after impact (J)	Rebound velocity (m/s)	Total energy after impact (J)	Rebound velocity (m/s)	Total energy after impact (J)
KEYOPT(7) = 0	383.25	683.01	220.32	225.72	311.58	451.43
KEYOPT(7) = 3	450.95	945.63	224.59	234.55	449.99	941.60
KEYOPT(7) = 4	207.31	199.85	204.48	194.43	204.48	194.43
KEYOPT(7) = 4 with Lagrange Multiplier	227.00	239.61	227.00	239.61	227.00	239.61

The greater rebound velocity after impact is related to the absence of energy conservation, evidenced by the increase in the total energy. With impact constraints (KEYOPT(7) = 4), energy conservation is enforced, so there is no increase in the total energy or the rebound velocity.

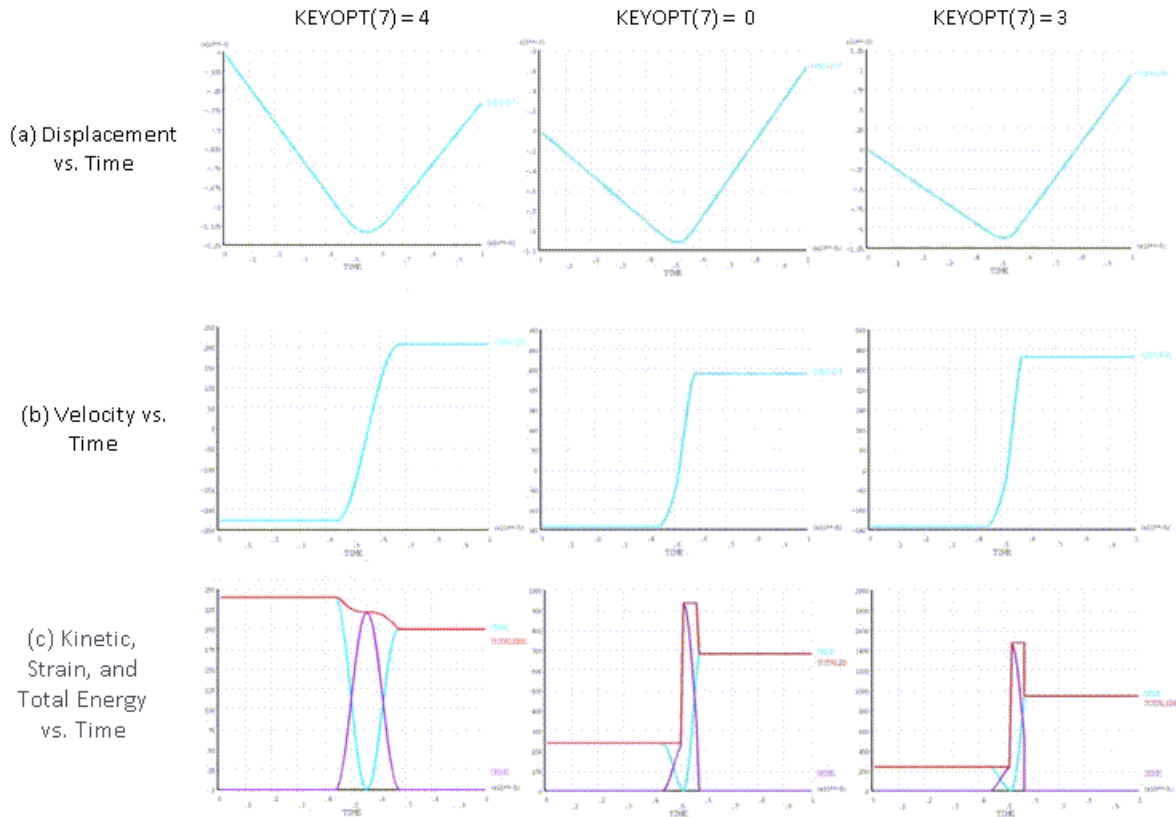
Precise satisfaction of impact constraints is necessary to conserve energy and obtain the same rebound velocity as the initial velocity, as evidenced by a comparison of the results for impact constraints (KEYOPT(7) = 4) with augmented Lagrangian contact (KEYOPT(2) = 0), and Lagrange multiplier contact (KEYOPT(2) = 4).

---

### Note

Lagrange multiplier contact for rigid bodies is generally not recommended due to the possibility of overconstraints. It is used here with [CONTA175](#) at a single node (to avoid overconstraints) to demonstrate that energy conservation is dependent upon the exact satisfaction of impact constraints.

---

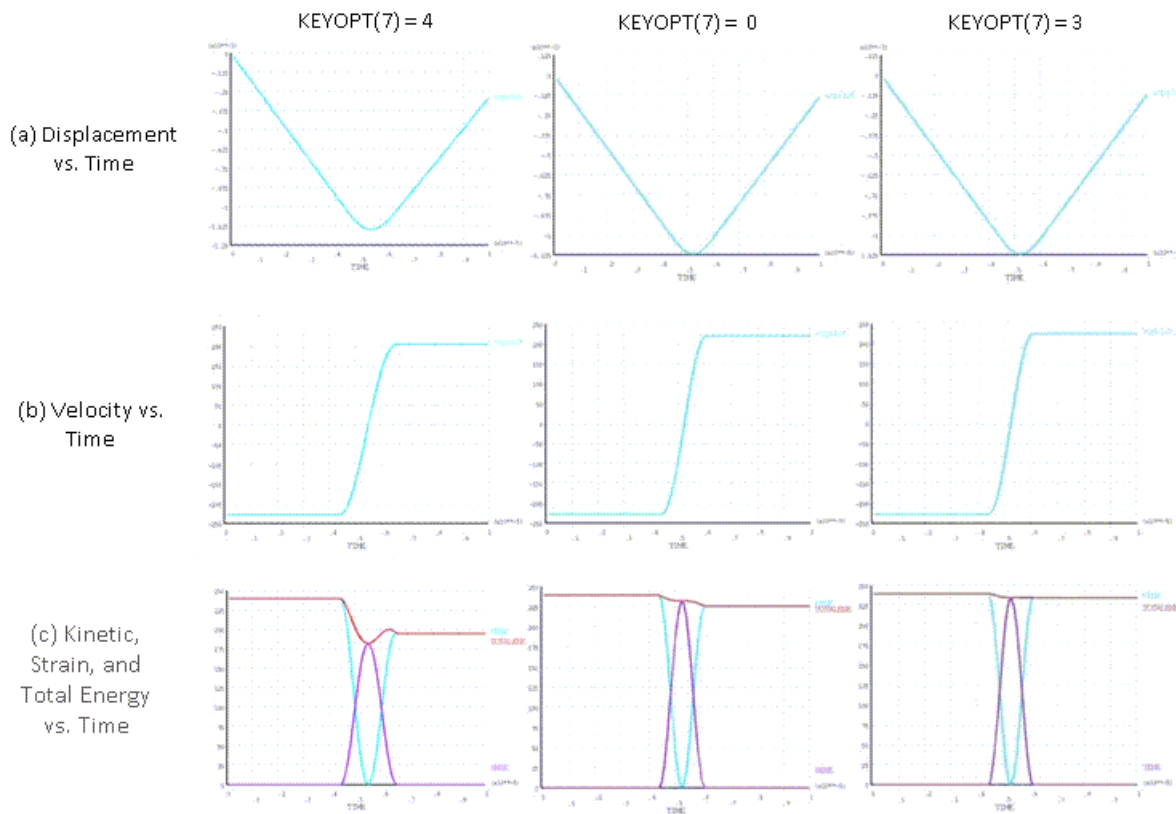
**Figure 17.2: Rigid Impact: Newmark Method with No Damping**

Ranges for Y axis differ to better illustrate results.

As shown in the following figure, adding numerical damping to the Newmark method helps to improve the results when using either:

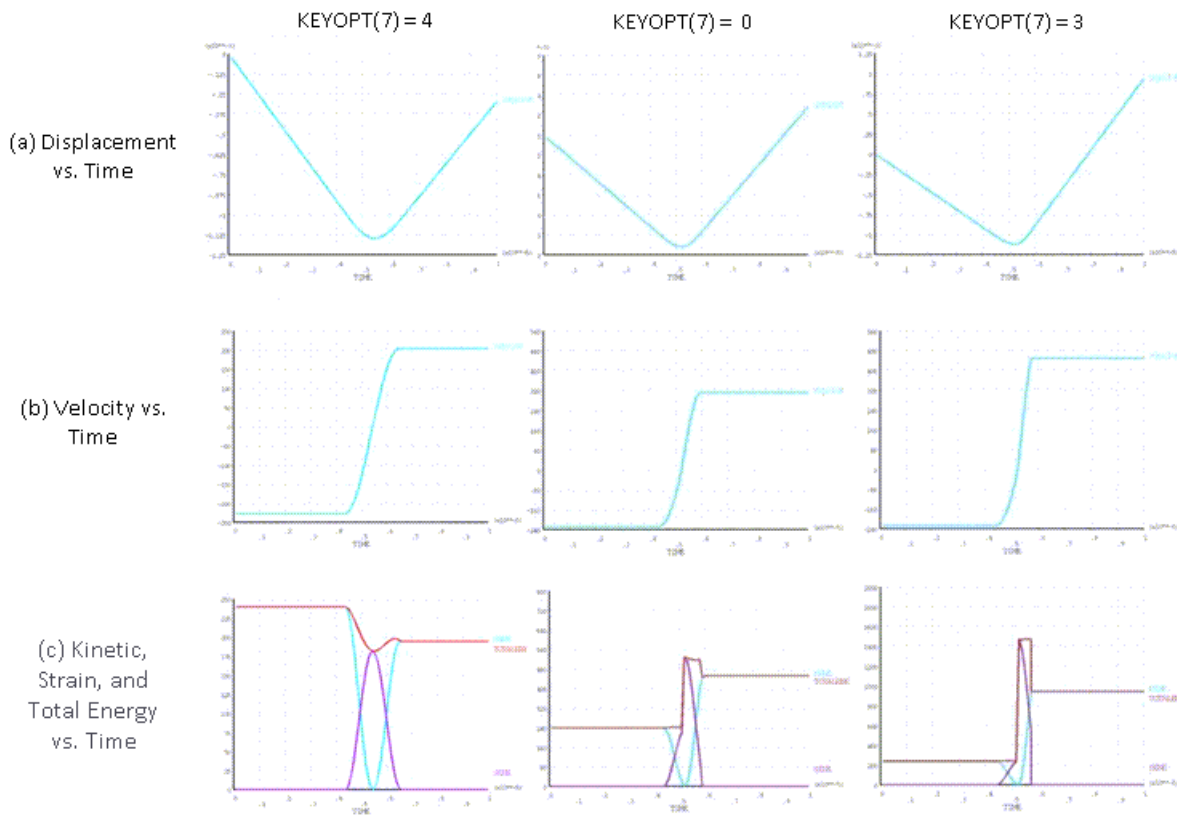
- No control (KEYOPT(7) = 0), or
- Element-level time-incrementation control (based on contact-status changes (KEYOPT(7) = 3)).

Numerical damping removes some of the energy from the system and thus counterbalances the increase in the total energy due to non-energy-conserving time integration, lowering the rebound velocity by a small amount.

**Figure 17.3: Rigid Impact: Newmark Method with Damping**

Ranges for Y axis differ to better illustrate results.

The HHT method removes energy only from the higher frequency modes (which are not dominant in the rigid-impact case). When compared to the Newmark method with damping, therefore, the HHT method does not yield as much improvement when KEYOPT(7) = 0 or 3, as shown in this figure:

**Figure 17.4: Rigid Impact: HHT Method with Damping**

Ranges for Y axis differ to better illustrate results.

Generally, impact constraints yield a close-to-expected or an expected solution, with or without damping. Other types of element-level time-incrementation controls (KEYOPT(7) = 0 or 3) rely heavily on numerical damping for a stable solution.

### 17.7.2. Elastic Impact Results

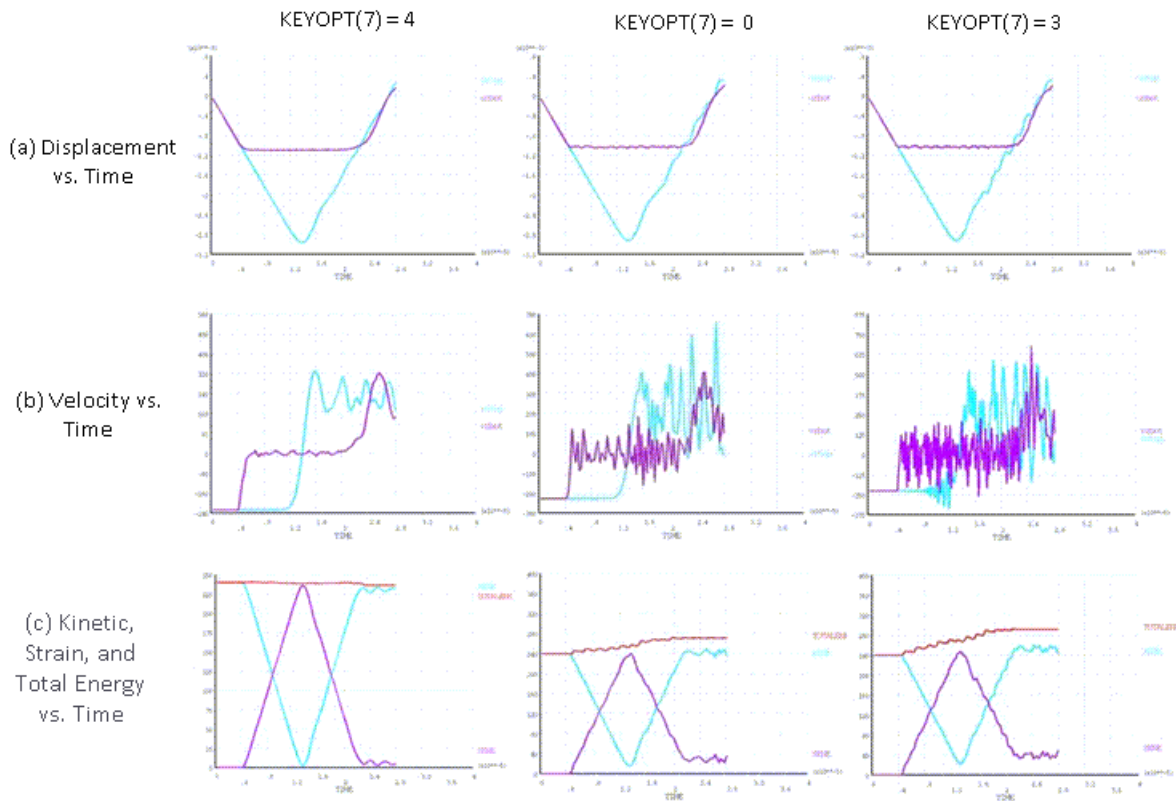
For elastic impact, the flexible bar begins to vibrate as the stress wave from impact with the rigid wall travels through the bar. When the stress wave returns to the impact end, the bar separates from the wall. Because the material is assumed to be elastic, the bar continues to vibrate as it moves away from the wall. Conservation of energy and momentum requires that the total energy in the bar after impact (SE+KE) remain equal to the total energy before impact (KE). Some of the initial kinetic energy (KE) is converted to strain energy (SE) after impact, so the rebound velocity after impact (spatially averaged velocity for rigid body motion) is slightly lower than the velocity before impact.

CONTA174 Key Option Setting	NMK with No Damping (p. 255)		NMK with Damping (p. 256)		HHT with Damping (p. 257)	
	Rebound velocity (m/s)	Total energy after impact (J)	Rebound velocity (m/s)	Total energy after impact (J)	Rebound velocity (m/s)	Total energy after impact (J)
KEYOPT(7) = 0	221.49	270.8	211.98	216.30	216.48	246.90

KEYOPT(7) = 3	225.39	291.60	218.73	239.67	220.84	275.20
KEYOPT(7) = 4	222.67	236.31	216.46	221.80	221.10	230.30

Finite-element discretization introduces additional nonphysical high-frequency modes into the structural response of the flexible bar. When using no control (KEYOPT(7) = 0) and no numerical damping, the displacement and velocity responses of the flexible bar become corrupted by high-frequency modes after impact, as shown in this figure:

**Figure 17.5: Elastic Impact: Newmark Method with No Damping**

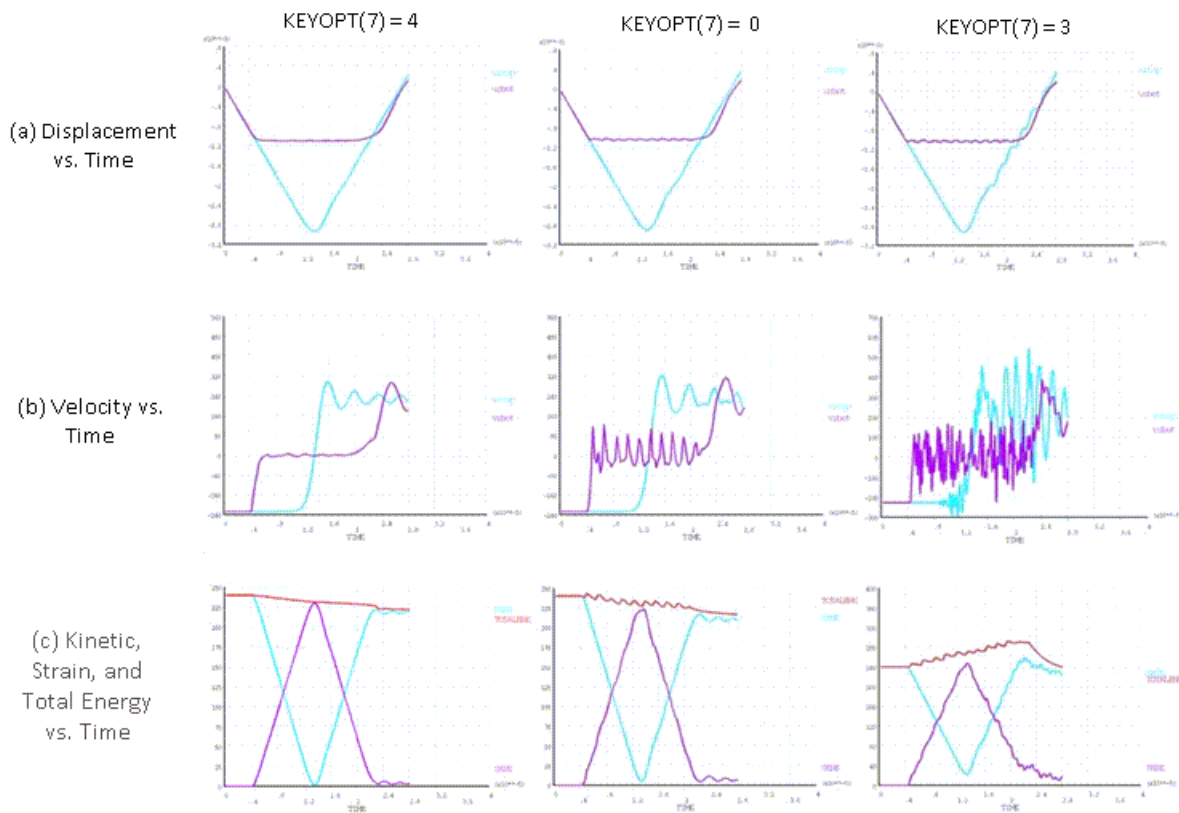


Ranges for Y axis differ to better illustrate results.

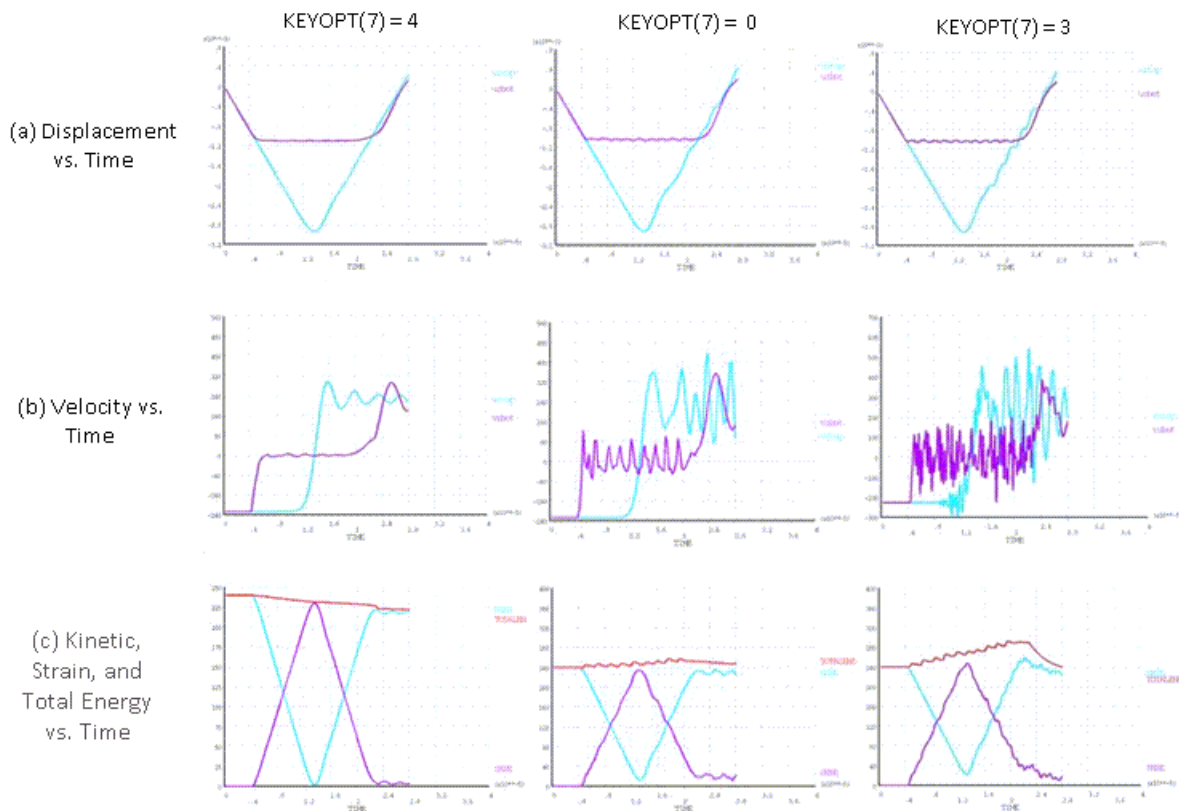
The higher modes are excited due to absence of enforcement of energy conservation, as evidenced by the total energy output. The response becomes worse over time due to the continued increase in the total energy.

Adding numerical damping stabilizes the response by dissipating some of the extra energy, as shown in [Figure 17.6: Elastic Impact: Newmark Method with Damping \(p. 259\)](#) and [Figure 17.7: Elastic Impact: HHT Method with Damping \(p. 260\)](#). Eliminating higher modes, however, requires a great deal of numerical damping, which can yield a solution that is significantly different from the expected physical response.



**Figure 17.6: Elastic Impact: Newmark Method with Damping**

Ranges for Y axis differ to better illustrate results.

**Figure 17.7: Elastic Impact: HHT Method with Damping**

Ranges for Y axis differ to better illustrate results.

Element-level time-incrementation control (based on contact-status changes (KEYOPT(7) = 3)) forces the analysis to use smaller time increments; however, this option leads to excitation of the higher modes which would otherwise be suppressed due to larger time increments. As seen from the results presented in this section, the solution is much noisier than it is with no control (KEYOPT(7) = 0).

Using impact constraints (KEYOPT(7) = 4) ensures energy conservation implicitly at the contact interface, preventing excitation of higher modes. Exact energy conservation is possible only when the impact constraints are satisfied exactly. When using the augmented Lagrangian or penalty-contact options (KEYOPT(2) = 0 or 1), a slight violation of constraints exists, leading to a small loss of energy. The energy loss is minimized via the program's automatic time-increment adjustments; however, the adjustment decreases the rebound velocity after separation by only a small amount, giving a stable and smooth response much closer to the expected physical response and other published results for similar problems.[1]

### 17.7.3. Elastoplastic Impact Results

For elastoplastic impact, the impact end of the bar deforms plastically upon impact. The bar stays in contact with the wall while undergoing plastic deformation in radial and longitudinal directions. The separation occurs when the material cannot deform (plastically) anymore and the stress wave reaches the impact end.

Numerical simulation of an elastoplastic impact is less sensitive to the choice of time-integration method or the amount of numerical damping, as shown in this comparison of the mushroom radius (R), final length (L), maximum equivalent plastic strain ( $\epsilon^{Pl}_{eqv}$ ), and maximum von Mises stress ( $\sigma_{eqv}$ ):

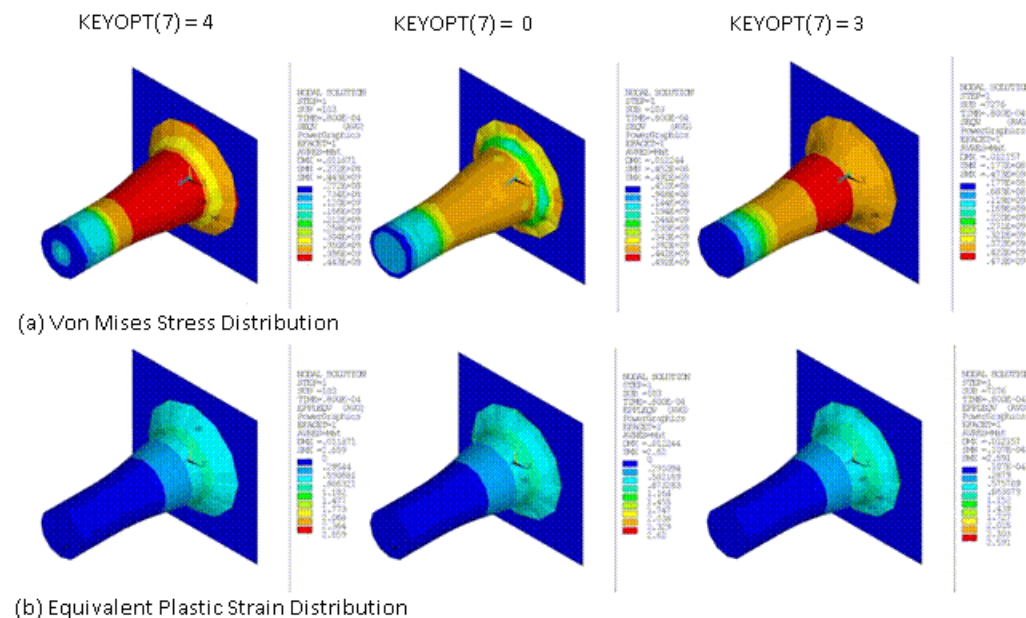
CONTA174 Key Option Setting	NMK with No Damping (p. 255)				NMK with Damping (p. 256)				HHT with Damping (p. 257)			
	R	L	$\sigma_{eqv}$	$\epsilon^{Pl}_{eqv}$	R	L	$\sigma_{eqv}$	$\epsilon^{Pl}_{eqv}$	R	L	$\sigma_{eqv}$	$\epsilon^{Pl}_{eqv}$
KEYOPT(7) = 0	7.3	20.15	491.6	2.62	7.36	20.57	458.5	2.64	7.37	20.49	489.8	2.64
KEYOPT(7) = 3	7.17	20.24	472.9	2.59	7.24	20.34	465.6	2.62	7.19	20.28	469.1	2.59
KEYOPT(7) = 4	7.3	20.53	442.6	2.66	7.35	20.61	439.4	2.64	7.36	20.57	442.2	2.65
Reference[2]	7.02	21.66	476	3.24	7.02	21.66	476	3.24	7.02	21.66	476	3.24

In the table above, R and L are expressed in mm, and  $\sigma_{eqv}$  is expressed in MPa.

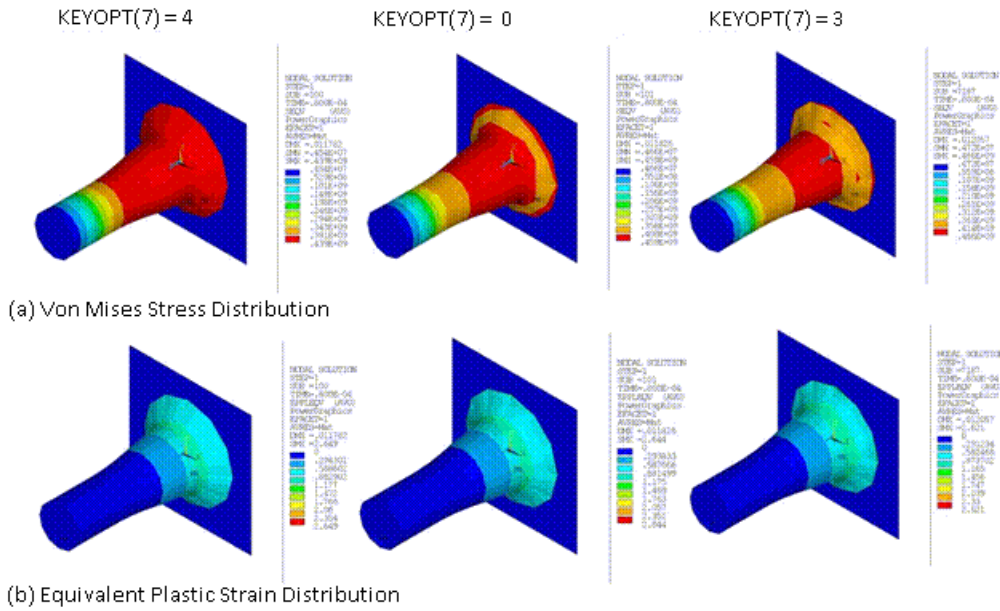
The numerical response is stable because the plastic dissipation of the total energy in the bar is much more significant than the jump in energy due to either non-conservation of energy during time integration or the dissipation of energy because of added numerical damping.

Although the peak values for stresses and strains are comparable for different choices, the contour plots for equivalent plastic strain and von Mises stress indicate that satisfaction of impact constraints (which conserves energy for the contact interface) gives a better distribution of the stresses and strains, as shown in the following figures:

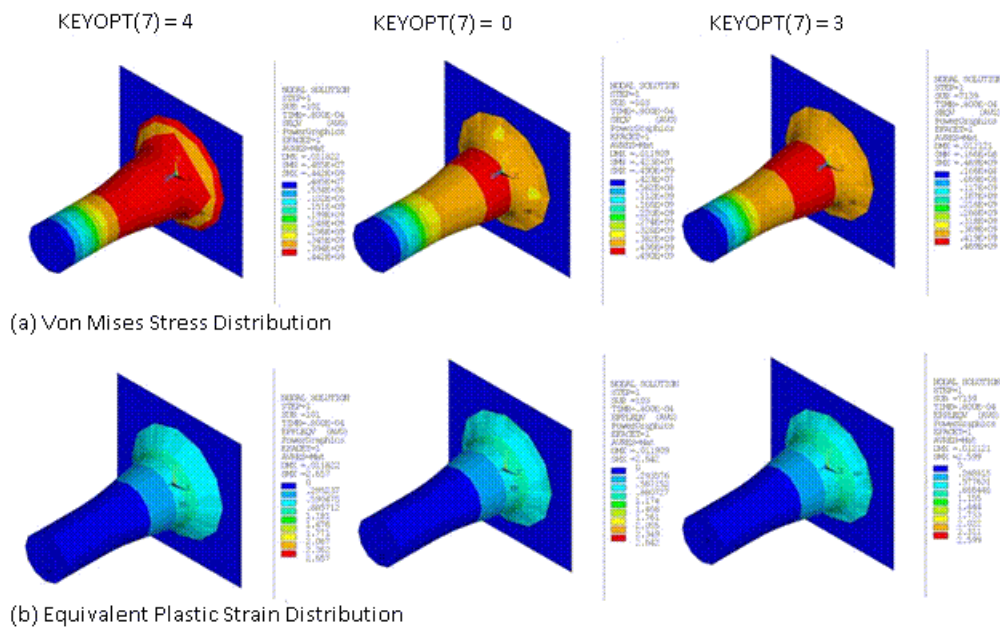
**Figure 17.8: Elastoplastic Impact: Newmark Method with No Damping**

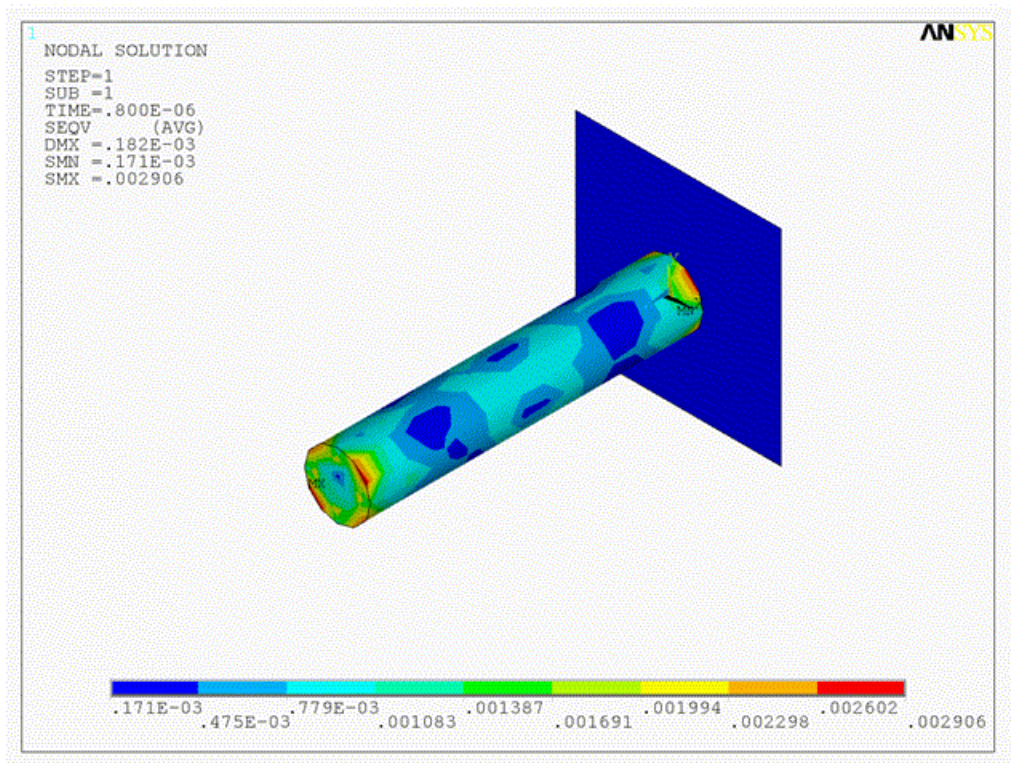


**Figure 17.9: Elastoplastic Impact: Newmark Method with Damping**



**Figure 17.10: Elastoplastic Impact: HHT Method with Damping**



**Figure 17.11: Animation: Elastoplastic Impact Using the HHT Method with Damping**

### 17.7.4. Performance Summary

Simulation time for the bar impact depends on the material model being used. The rigid-impact simulation requires the least amount of time, followed by the elastic-impact and then the elastoplastic-impact simulations. For each model, computational time (CPU time) depends most noticeably on the element-level time-incrementation controls used (KEYOPT(7) = 0, 3 or 4 on the [CONTA174](#) element).

In the following table, a comparison of computational times (in seconds) indicates that using impact constraints with automatic time-increment adjustment (KEYOPT(7) = 4) requires the least amount of time in all cases:

CONTA174 Key Option Setting	NMK with No Damping (p. 255)	NMK with Damping (p. 256)	HHT with Damping (p. 257)
<b>Rigid Impact</b>			
KEYOPT(7) = 0	39	42	45
KEYOPT(7) = 3	179	321	190
KEYOPT(7) = 4	45	41	44
KEYOPT(7) = 4 with Lagrange Multiplier	38	41	41
<b>Elastic Impact</b>			
KEYOPT(7) = 0	783	638	753
KEYOPT(7) = 3	12186	11511	13091
KEYOPT(7) = 4	404	413	507
<b>Elastoplastic Impact</b>			

KEYOPT(7) = 0	976	697	834
KEYOPT(7) = 3	24048	23330	25976
KEYOPT(7) = 4	591	556	621

By using impact constraints with automatic time-increment adjustment, fewer substeps and equilibrium iterations are necessary to obtain the transient response.

With no control (KEYOPT(7) = 0), more analysis time is required, as more substeps and equilibrium iterations are required. The absence of energy conservation at the contact interface forces smaller time increments.

Using element-level time-incrementation control based on contact status changes (KEYOPT(7) = 3) requires the most time, as smaller time increments are necessary to avoid sudden changes in the contact status.

## 17.8. Recommendations

When performing a similar type of impact simulation, consider the following recommendations for obtaining better accuracy and faster performance:

- Activate impact constraints (KEYOPT(7) = 4 on the [CONTA174](#) element) to enforce energy conservation at the contact interface. This option helps to maintain accuracy of the nonlinear transient response over long simulation times.
- For rigid- or elastic-impact scenarios, use the HHT time-integration method with small numerical damping (0.1) to damp out high-frequency noise.

## 17.9. References

The following references are used in this example problem:

1. Carpenter, N.J., R.L. Taylor, and M.G. Katona. "Lagrange constraints for transient finite element surface contact." *International Journal for Numerical Methods in Engineering*. 32 (1991): 103-128.
2. Hallquist, J.O. and D.J. Benson. "DYNA3D User's Manual." Report No. [UCID-19592](#) (1987). Rev. 3. Lawrence Livermore National Laboratory.
3. Kamoulakos, A. "A Simple 'Benchmark' for Impact." *Bench Mark*. (1990): 31-35.
4. Simo, J.C. "Algorithms for Static and Dynamic Multiplicative Plasticity that Preserve the Classical Return Mapping Schemes of the Infinitesimal Theory." *Computer Methods in Applied Mechanics and Engineering*. 68 (1998): 1-31.
5. Wilkins, M.L. and M.W. Guinan. "Impact of Cylinders on a Rigid Boundary." *Journal of Applied Physics*. 44.3 (1973): 1200-1206.

## 17.10. Input Files

The following files were used in this problem, with each file corresponding to one of the [three impact scenarios](#) (p. 251) examined:

- `impact_rigid.dat` -- Input file for the rigid-impact scenario.
- `impact_elastic.dat` -- Input file for the elastic-impact scenario.

- `impact_plastic.dat` -- Input file for the elastoplastic scenario.
- `impact_rigid.cdb` -- Common database file for the rigid-impact simulation (called by `impact_rigid.dat` ).
- `impact_elastic.cdb` -- Common database file for the elastic-impact simulation (called by `impact_elastic.dat`).
- `impact_plastic.cdb` -- Common database file for the elastoplastic-impact simulation (`impact_plastic.dat`).

The files are available in the `td-17` folder. See [Obtaining the Input Files \(p. xxxv\)](#) for more information.





---

## Chapter 18: Viscoelastic Analysis of an All-Ceramic Fixed Partial Denture

---

This example problem demonstrates the fictive-temperature material model using the Tool-Narayananaswamy (TN) *shift function* to examine residual stresses in an all-ceramic fixed partial denture (FPD). A coupled-field solution process, including transient thermal and nonlinear structural analyses, is used in the problem simulation.

The following capabilities are highlighted:

- Using the fictive temperature model for viscoelastic material.
- Running a transient thermal analysis to determine the temperature profile at various time steps.
- Applying thermal analysis results as temperature loads for structural analysis.
- Running a nonlinear structural analysis to determine residual stresses due to thermal loading.

Topics related to this example problem follow:

- 18.1. Introduction
- 18.2. Problem Description
- 18.3. Modeling
- 18.4. Material Properties
- 18.5. Boundary Conditions and Loading
- 18.6. Analysis and Solution Controls
- 18.7. Results and Discussion
- 18.8. Recommendations
- 18.9. References
- 18.10. Input Files

### 18.1. Introduction

Materials are generally considered to be viscoelastic if they have an elastic and viscous behavior. The elastic behavior is typically rate-independent and represents the recoverable deformation due to loading, while the viscous behavior is typically rate-dependent and represents dissipative mechanisms within the material.

A wide range of materials (such as polymers, glassy materials, soils, biological tissue, and textiles) exhibit viscoelastic behavior. Viscoelastic materials exhibit viscous fluid behavior at high temperatures and solid behavior at low temperatures.

For most viscoelastic materials, the effect on the material properties caused by changes in temperature is similar to that of the effect caused by changes in the time scale. Such materials are considered to be thermorheologically simple. A general material property called the *shift function* can reduce the constitutive relation at a reference temperature and shifted time. The shift function can lessen the amount of experimentation needed to determine the material parameters.

The following *shift functions* are available for representing thermorheologically simple materials:

- **Williams-Landel-Ferry (WLF)** -- Suitable for many types of polymers.
- **Tool-Narayanaswamy (TN)** -- Suitable for glassy materials.
- **TN with fictive temperature** -- Suitable for the melting and solidification process of viscoelastic materials such as glass and stiff polymers.

The shift functions reproduce the behavior of a wide range of viscoelastic materials. For special requirements, [user-defined shift functions](#) can also be defined.

The *fictive temperature* is the temperature at which the current microstructure of glass is in an equilibrium state. For the TN shift function with fictive temperature model, the fictive temperature is used to model materials containing an intrinsic equilibrium temperature that typically differs from the ambient temperature of the material. The fictive temperature relaxes toward the ambient temperature similar to the way that deviatoric and volumetric stiffness constants of the viscoelastic material relax toward the long time-elastic constants.

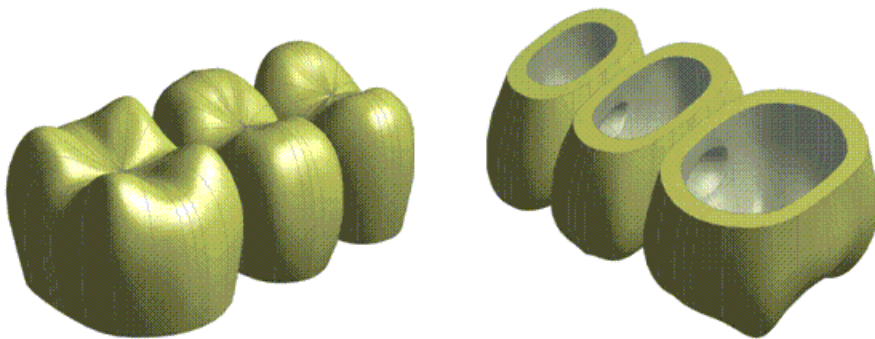
With the shift function, the evolution of the fictive temperature for any thermal history can be calculated. As the fictive temperature approaches the actual temperature, the viscoelastic material becomes more relaxed. The fictive temperature model is often used to model the melting and solidification process of viscoelastic materials such as glass and stiff polymers. This problem uses a fixed partial denture (FPD) model to determine the residual stresses due to the solidification of a glass veneer on a ceramic core material.

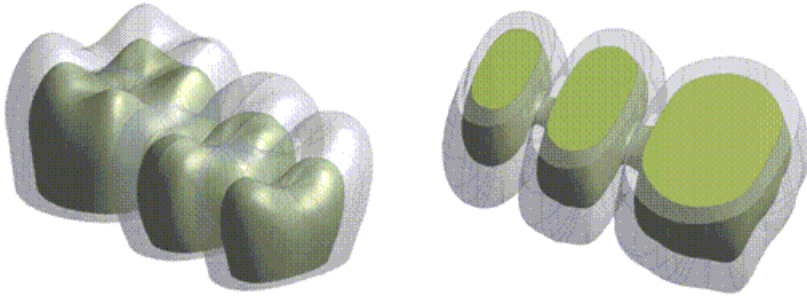
Metal-free ceramic materials are biocompatible, chemically durable, and aesthetically desirable. Such materials are therefore ideal for FPDs. Thermal loading during the glass layer manufacturing process causes residual stresses in FPDs. Higher residual stresses caused by thermal contraction incompatibility between the veneer and core materials can lead to failure under occlusal loading in the oral cavity.[1] The ability to determine residual stresses in an FPD subjected to thermal loading is useful for predicting the life of the FPD.

## 18.2. Problem Description

The FPD is a combination of glass veneer and ceramic core, as shown in the following two figures, respectively:

**Figure 18.1: FPD Viscoelastic (Glass) Veneer Geometry**



**Figure 18.2: FPD Ceramic Core Geometry (Inside the Veneer)**

A 3-D model of the FPD is constructed from the digitized scanning data of a reference FPD.[1] Because the original model is unavailable, a similar geometry of a three-unit FPD is created in ANSYS Design-Modeler for use in this problem.

**Sintering** is commonly used for glass coatings. The high temperatures ( $\sim 700^\circ\text{C}$ ) used during sintering are reduced to room temperature ( $30^\circ\text{C}$ ) via free convection. Initially, some free thermal expansion occurs in the core material due to the high temperature; however, this free expansion may not affect stresses developed during free convection of the veneer and core together. For demonstration purposes, a uniform initial temperature for both the veneer and the core is assumed, with no initial thermal expansion of the ceramic core.

The temperature distribution in the FPD is needed to determine the thermal residual stresses in the veneer and core. A transient thermal analysis with a duration of 600 seconds is performed on the FPD. The initial temperature is  $700^\circ\text{C}$ , and free convection cools the FPD to a room temperature of  $30^\circ\text{C}$ . A convective heat transfer coefficient of  $3.4\text{E-}5\text{ W/mm}^2\text{ }^\circ\text{C}$  is specified on all free surfaces, reducing sintering temperature to the steady-state room temperature.

The temperature results are stored every 60 seconds. The results are used as input for a subsequent nonlinear structural analysis to determine the residual stresses.

## 18.3. Modeling

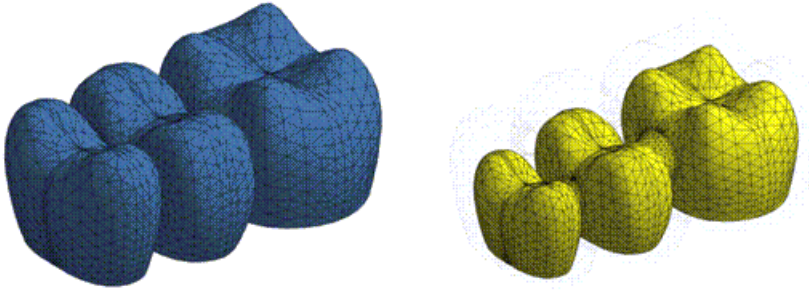
Following are the modeling topics available for this problem:

[18.3.1. Denture Modeling](#)

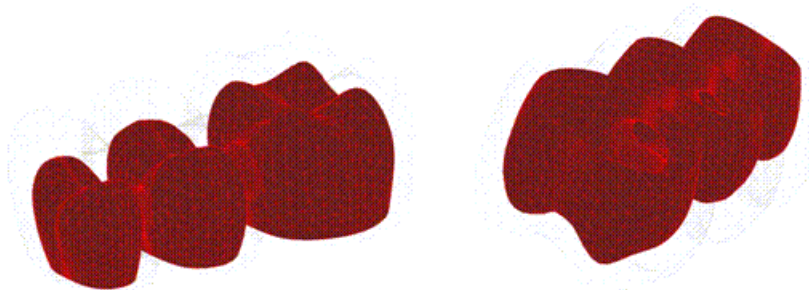
[18.3.2. Contact Modeling](#)

### 18.3.1. Denture Modeling

For both the veneer and core meshes, thermal element **SOLID87** is used for the transient thermal analysis, as shown in this figure:

**Figure 18.3: FPD Veneer and Core Mesh (SOLID87)**

A 3-D surface-to-surface contact is used for creating the contact pair. The contact between veneer and core is meshed with **CONTA174** and **TARGE170** elements, as shown in the following figure:

**Figure 18.4: Contact Between Veneer and Core (CONTA174 and TARGE170)**

The temperature profile (obtained in the thermal analysis) is used in a nonlinear structural analysis to determine the residual stress in the veneer. The temperature results are read in as thermal loads at different time steps (**LDREAD**).

The structural analysis requires the same mesh as that used for the thermal analysis. It is therefore necessary to change the thermal elements to structural elements (**ETCHG**). In this case, thermal element **SOLID87** is converted to structural solid element **SOLID187**. The contact **CONTA174** and target **TARGE170** elements are compatible with **SOLID187**, so those elements remain; contact element *options* are modified as necessary (**KEYOPT**).

The following example input changes the element type:

```
ETCHG,TTS           ! Change thermal elements to structural elements
KEYOPT,3,1,0       ! Change degrees of freedom for TEMP to UX, UY, and UZ
```

The FPD model contains 164,041 nodes. The model has 110,275 3-D 10-node tetrahedral structural solid elements (56,811 veneer elements and 53,464 core elements), and 10,568 3-D 8-node surface-to-surface contact elements.

### 18.3.2. Contact Modeling

Bonded surface-to-surface contact pairs define the contact between the veneer and the core. The contact pair modeled for the thermal analysis is converted for the structural analysis (**ETCHG**).

The following example input creates the element pair:

```

/COM, CONTACT PAIR CREATION - START
ET,3,170          ! Define TARGET170 element
ET,4,174          ! Define CONTACT174 element
KEYOPT,4,1,2      ! Select temperature degree of freedom for thermal analysis
REAL,3           ! Set the element real constant
RMODIF,3,14,4e-005 ! Define Thermal Contact Conductance (TCC)

! Generate the target surface
NSEL,S,,,VENEER.TGT ! Selected user-defined nodal component for target
TYPE,3             ! Element type for target elements
ESLN,S,0          ! Select elements attached to nodal component
ESURF            ! Generate target mesh on the free faces of selected elements
ALLSEL,ALL

! Generate the contact surface
NSEL,S,,,CORE.CNT ! Selected user-defined nodal component for contact
TYPE,4            ! Element type for contact elements
ESLN,S,0          ! Select elements attached to nodal component
ESURF            ! Generate contact mesh on the free faces of selected elements
ALLSEL

/COM, CONTACT PAIR CREATION - END

```

## 18.4. Material Properties

The veneer is represented by viscoelastic material behavior while the core is assumed to behave elastically.

The following material property data is available for this problem:

[18.4.1. Transient Thermal Analysis Material Properties](#)

[18.4.2. Static Structural Analysis Material Properties](#)

### 18.4.1. Transient Thermal Analysis Material Properties

The following material properties are used for the transient thermal analysis:

Temperature (°C)	Conductivity (W/mm <sup>2</sup> °C)	Specific Heat (J/kg °C)	Density (kg/mm <sup>3</sup> )
<b>Core</b>			
30	0.004002012	914.540	2.514E-6
200	0.003254307	1119.296	
500	0.002973238	1284.875	
700	0.003255384	1347.341	
<b>Veneer</b>			
30	0.010005623	742.274	2.531E-6
200	0.006603368	947.144	
500	0.004560125	1105.625	
700	0.004299903	1167.299	

The thermal contact conductance is 4E-05 J/(sec-°C).

### 18.4.2. Static Structural Analysis Material Properties

The following material properties are used for the static structural analysis:

#### Core

Young's Modulus (GPa)	Poisson's Ratio	Density (kg/mm <sup>3</sup> )	Temperature (°C)	Coefficients of Thermal Expansion
96	0.24	2.514E-6	30	1.00E-05
			40	9.87E-06
			50	9.68E-06
			60	9.51E-06
			100	8.90E-06
			200	8.20E-06
			300	8.65E-06
			400	1.02E-05
			500	1.30E-05
			700	2.20E-05

### Veneer

Young's Modulus (GPa)	Poisson's Ratio	Density (kg/mm <sup>3</sup> )	Reference Temperature T <sub>ref</sub> (°C)	H/R (° K) *
65	0.26	2.531E-6	700	46400

\* H/R = activation energy / ideal gas constant

Prony Series		Shift Function Constants		
G <sub>i</sub> / G <sub>0</sub>	τ <sub>i</sub>	Fictive Temperature (°C)	Weight	Relaxation Time (Sec)
0.48844	1.58E-05	750	0.25	1.58E-05
0.44003	0.000163	726	0.25	0.000163
0.03576	0.003853	705	0.25	0.003853
0.00487	0.008050	687	0.25	0.008050

Following are the polynomial coefficients for glass and liquid thermal expansion:

$$\alpha_{g0} = 10.7510E-6 \text{ ppm / } ^\circ\text{C}$$

$$\alpha_{g1} = -2.4208E-8 \text{ ppm / } ^\circ\text{C}$$

$$\alpha_{g2} = 5.7267E-11 \text{ ppm / } ^\circ\text{C}$$

$$\alpha_{l0} = -39.1180E-6 \text{ ppm / } ^\circ\text{C}$$

$$\alpha_{l1} = 1.1526E-7 \text{ ppm / } ^\circ\text{C}$$

## 18.5. Boundary Conditions and Loading

The following boundary and loading condition data is available for this problem:

[18.5.1. Thermal Analysis BC and Loading](#)

[18.5.2. Structural Analysis BC and Loading](#)

### 18.5.1. Thermal Analysis BC and Loading

An initial temperature of 700° C is applied on all nodes. A convective heat-transfer coefficient of 3.4E-5 W/mm<sup>2</sup> °C is specified on all free surfaces of the FPD.

The following example input defines the initial temperature and convection coefficient:

```

NSEL,ALL                ! Select all nodes
IC,ALL,TEMP,700         ! Specifies initial temperature at nodes

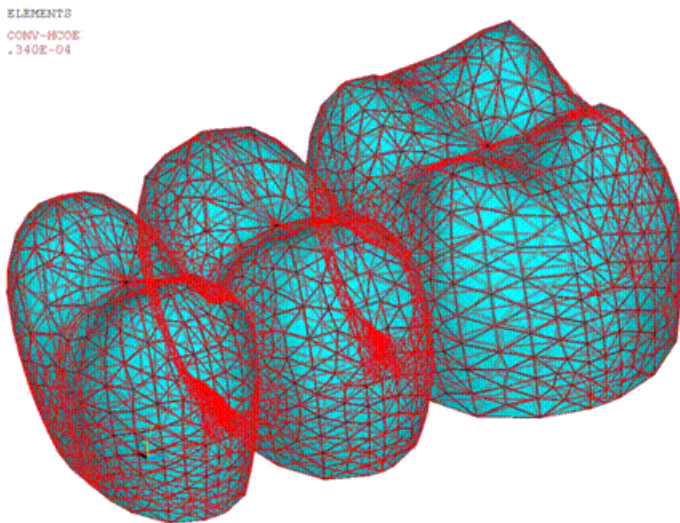
!           Apply convection on the outer areas of the FPD

CMSEL,S,VOAN,NODE       ! Select veneer outer area nodes
CMSEL,A,BAN,NODE        ! Select FPD bottom area nodes
SF,ALL,CONV,3.4E-5,30   ! Convection

```

The following figure shows the model with the initial temperature and convection on the FPD surface applied:

**Figure 18.5: FPD Boundary Conditions: Thermal Analysis**



For the contact pair, a thermal contact conductance of 4E-05 J/(sec-°C) is used for heat conduction between the veneer and the core.

### 18.5.2. Structural Analysis BC and Loading

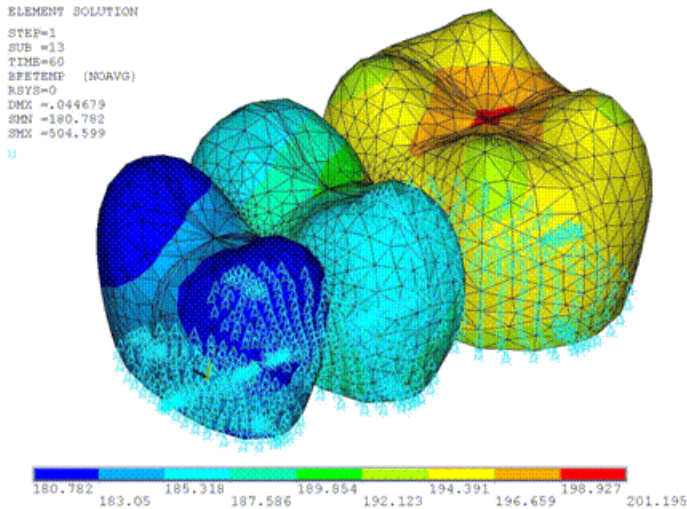
Rigid body motion is constrained with appropriate displacement constraints at the midline of the FPD base. Vertical displacement constraints are applied to all base nodes. The thermal load is applied (**LDREAD**).

The following example input reads the temperature from the thermal analysis results:

```
LDREAD,TEMP,,,TIME,0,'thermal','rth' ! Read temperature from thermal analysis results file
```

The temperature is read at every load step (**LDREAD**). The *TIME* value represents the final solution time of each load step.

The following figure shows the displacement boundary conditions and body force at *TIME* = 60 seconds.

**Figure 18.6: FPD Boundary Conditions: Structural Analysis**

## 18.6. Analysis and Solution Controls

A transient thermal analysis is performed to determine the temperature distribution and a linear static analysis is run to determine the residual stress.

### Thermal Analysis Solution

The analysis type is defined as a transient thermal analysis (**ANTYPE,TRANS**).

The following example input obtains the solution for the thermal analysis:

```
ANTYPE,TRANS           ! Perform a transient analysis
TRNOPT,FULL           ! Specifies transient analysis options
TIME,600              ! Final time for solution
OUTRES,ALL,-10       ! Saved results at every 60 seconds
```

### Structural Analysis Solution

A linear static analysis (**ANTYPE,STATIC**) is performed. For the stress analysis, **SOLID87** elements are converted to **SOLID187** elements.

The Tool-Narayanaswamy (TN) shift function with fictive temperature is used with the viscoelastic constitutive model. As with other time-temperature superposition models, the shift function is accessible via the **TB,SHIFT** command, as shown in the following input example:

```
TB,SHIFT,1,1,4,FICT           ! Specify Tool-Narayanaswamy shift function
TBDATA, 1,700,46400,0.3       ! TN constants - Reference temperature, H/R and X
TBDATA, 4, 750, 0.25, 1.58E-5 ! Fictive T, weight, relaxation time
....
TBDATA, 16, 10.7510E-6, -2.4208E-8, 5.7267E-11 ! glass CTE coefficients

! Time-dependent behavior of shear and bulk modulus can be
! represented via Prony series. Prony series for deviatoric
! Maxwell elements is defined as follows:

TB,PRONY,1,1,4,SHEAR
TBDATA,1, 0.48844 , 1.58E-5    ! Prony pairs
....
```



According to the reference results, volume relaxation for glass occurs much less rapidly than the shear relaxation.[1] The Prony series input for volume decay is therefore not considered in this problem.

### 18.6.1. Adjusting the Time Step

A full simulation based on the time stepping from the reference input file requires approximately 3.5 hours (using eight processors). You can adjust the time-step increment according to your needs:

- A larger increment accelerates the simulation but is less accurate.
- A small increment is more computationally intensive, requiring a longer analysis time, but offers greater accuracy.

---

#### Important

The structural portion of the analysis requires 10 solve operations. The *first* solution (time = 1 - 60) requires more time to converge than the remaining nine; however, it is not good practice to increase the time increment for the first solution.

---

## 18.7. Results and Discussion

The following three figures show the distribution of temperature at different time steps in both the FPD veneer and core, with the temperature for both reaching the steady-state room temperature at 600 seconds:

**Figure 18.7: Temperature Distribution in Veneer and Core at 60 Seconds**

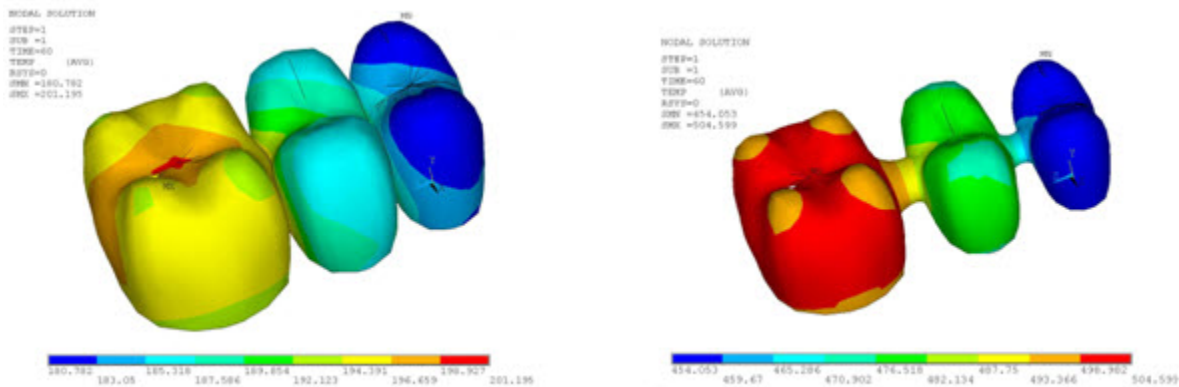


**Figure 18.8: Temperature Distribution in Veneer and Core at 300 Seconds**

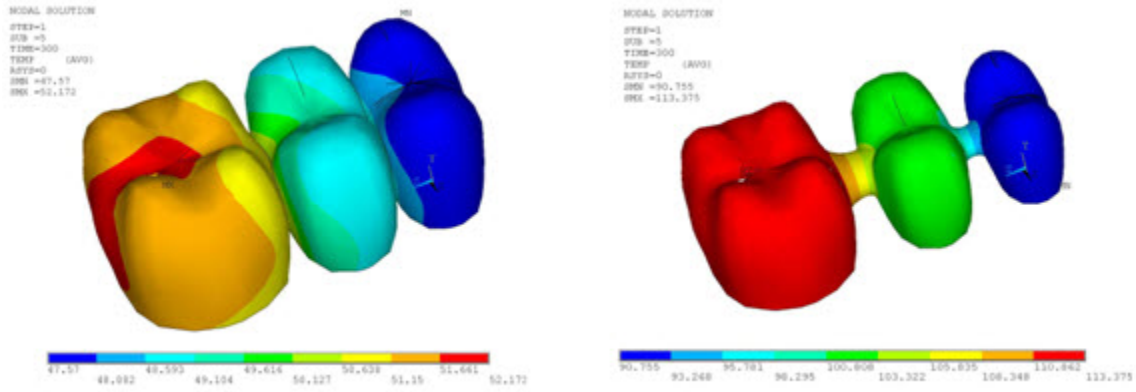
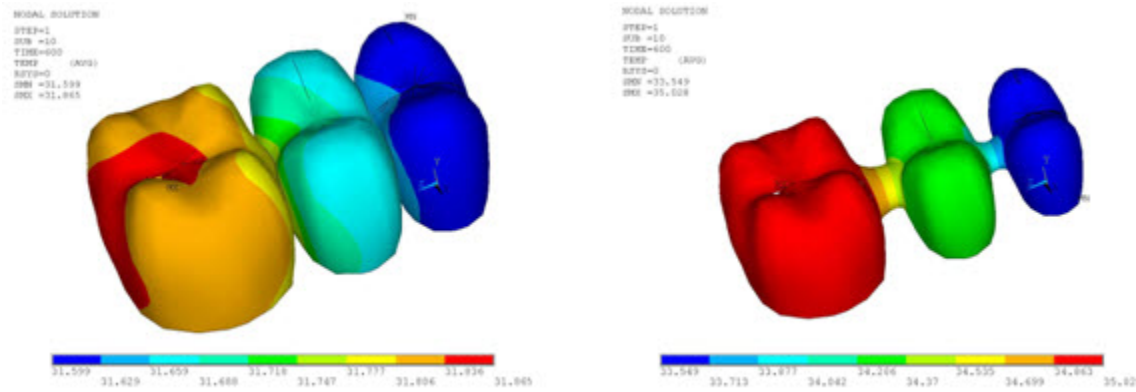
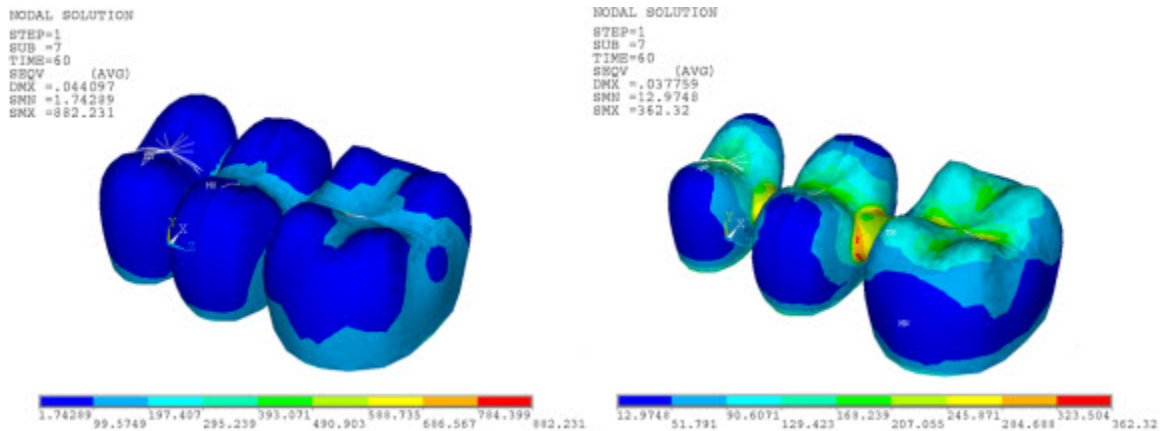


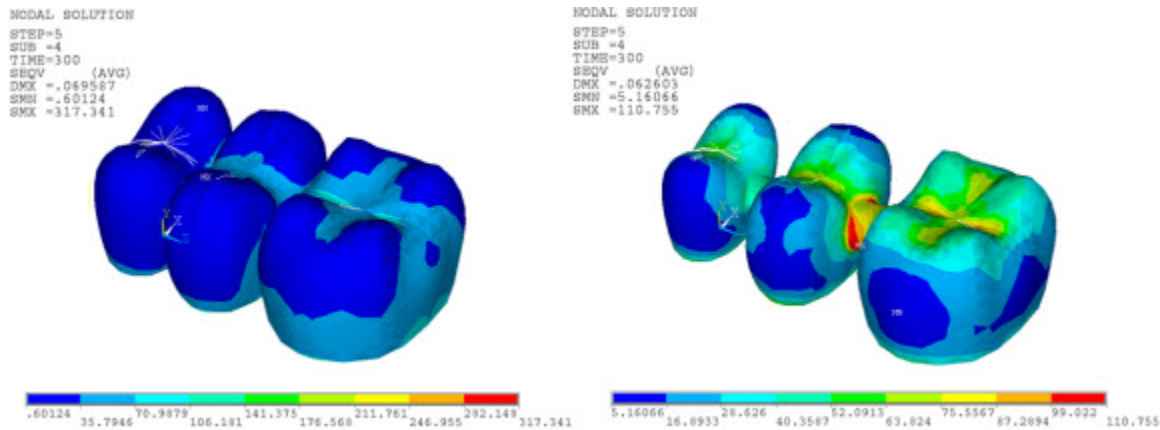
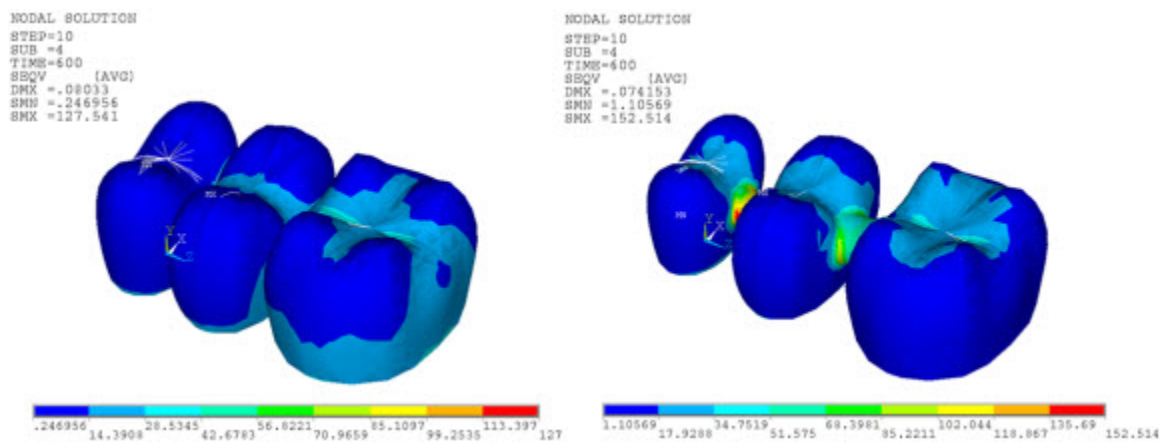
**Figure 18.9: Temperature Distribution in Veneer and Core at 600 Seconds**



The following three figures show the von Mises stress distribution at different time steps in both the FPD veneer and core:

**Figure 18.10: Von Mises Stress in Veneer and Core at 60 Seconds**



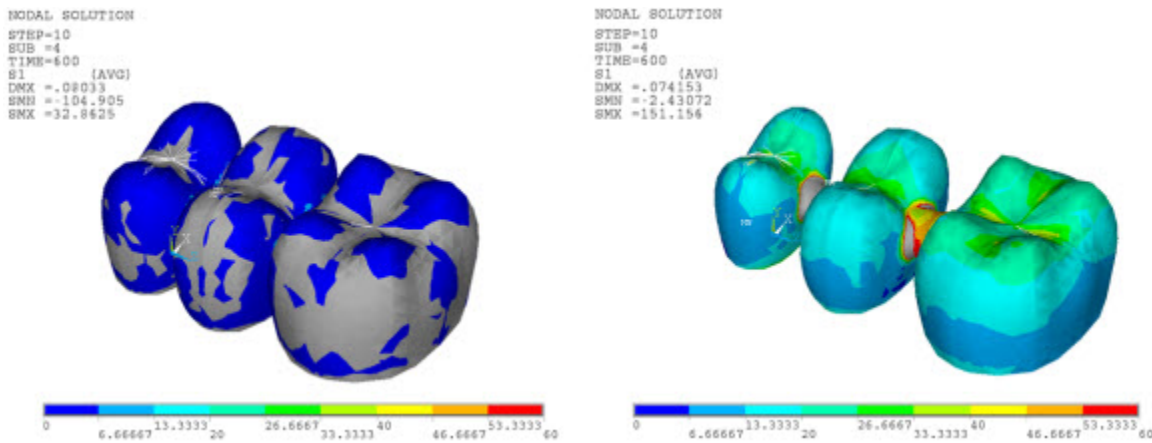
**Figure 18.11: Von Mises Stress in Veneer and Core at 300 Seconds****Figure 18.12: Von Mises Stress in Veneer and Core at 600 Seconds**

The von Mises stresses in both veneer and core change with temperature due to natural convection on the veneer surface. The stresses correspond to temperature loadings at 60, 300 and 600 seconds. At high temperatures, the von Mises stresses are very high in the veneer as compared to the core.

As the veneer cools through the transition, the elastic moduli no longer relax on the time scale of the cooling and--due to the different thermal contraction coefficients of the veneer and core--a jump in the stress distribution occurs at the veneer-core interface, bringing the higher von Mises stresses in the veneer close to the core stress at room temperature.

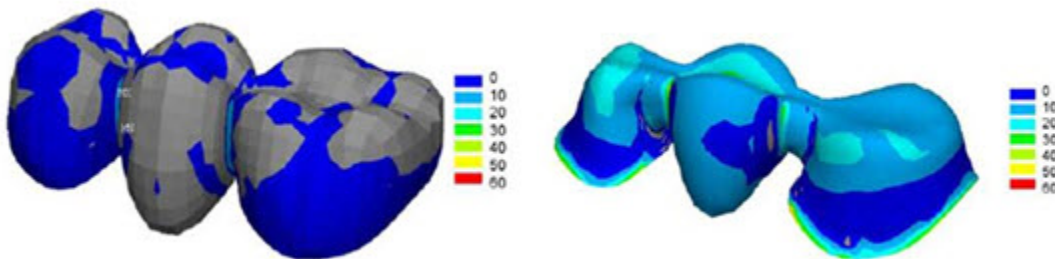
Stresses in the inner veneer surface at the interface are not significantly different from the core outer surface stresses due to the stabilized fictive temperature (equal to the actual temperature) at lower temperatures.

The following figure shows tension in the core and compression in the veneer at the room temperature residual stress pattern:

**Figure 18.13: Residual Principal Stress Distribution in Veneer and Core 600 Seconds**

The tension is present because the surface cools most rapidly and becomes rigid, while the inner surface of the veneer (at interface with the core) is still at a higher temperature. When the interface becomes rigid and cools, it forces the surface under more compression. These residual stresses can be used for analyzing FPDs under occlusal loading in the oral cavity and subsequently to predict the life of the FPDs.[1]

The following figure shows the maximum residual principal stress distribution in the veneer and the core from the reference results [1], which agree closely with the simulated results from this problem:

**Figure 18.14: Reference Results: Residual Principal Stress Distribution in Veneer and Core**

## 18.8. Recommendations

To perform a similar type of viscoelastic analysis, consider the following hints and recommendations:

- Save the thermal analysis results (**OUTRES**) at required time steps so that the temperatures can be read in for the structural analysis.
- Specify the correct path for the thermal analysis results (.rth file) during the structural analysis (**LDREAD**).
- The sum of the fictive-temperature relaxation coefficients (specified in the table data activated via the **TB,SHIFT,,,FICT** command) should be 1.0.

For more information, see *Viscoelasticity* in the *Material Reference* and *Shift Functions* in the *Mechanical APDL Theory Reference*.

---

## 18.9. References

This analysis was based on the following reference work:

1. DeHoff, Paul H. et al. "Viscoelastic Finite Element Analysis of an All-Ceramic Fixed Partial Denture." *Journal of Biomechanics*. 39 (2006): 40-48.

## 18.10. Input Files

The following files were used in this problem:

- `denture_model.cdb` -- Common database file for the fixed partial denture (FPD) finite-element model and contact pair.
- `denture_thermal.dat` -- Input file for the transient thermal analysis.
- `denture_structural.dat` -- Input file for structural analysis.

The files are available in the `td-18` folder. See [Obtaining the Input Files \(p. xxxv\)](#) for more information.



---

## Chapter 19: Transient Dynamic Analysis of a Digger-Arm Assembly

---

This example problem uses a digger-arm assembly to show how to perform a [transient dynamic analysis](#) of a [multibody system](#).

The following techniques and capabilities are highlighted:

- Defining joints, rigid parts, and flexible parts during modeling.
- Mitigating overconstraints due to improper joint definitions.
- Representing flexible parts using [component mode synthesis](#) (CMS).

The example also uses transient dynamic analyses for the following three cases:

- All parts of the multibody system are assumed to be rigid.
- Some of the parts are flexible and the remainder are rigid.
- The flexible parts are modeled using CMS superelements.

Topics related to this example problem follow:

- [19.1. Introduction](#)
- [19.2. Problem Description](#)
- [19.3. Modeling](#)
- [19.4. Material Properties](#)
- [19.5. Boundary Conditions and Loading](#)
- [19.6. Analysis and Solution Controls](#)
- [19.7. Results and Discussion](#)
- [19.8. Recommendations](#)
- [19.9. Input Files](#)

### 19.1. Introduction

A multibody system is an assembly of bodies or parts in which some or all parts move relative to one another. These assemblies may be simple or complex and may be composed of all rigid bodies or a combination of rigid and flexible parts. The parts are constrained to each other by a set of kinematically admissible constraints modeled as joints.

Common examples of multibody systems include land transportation systems, aviation systems, nautical systems, and robotic systems.

The components of a multibody system may experience finite-strain effects and large displacements and/or large rotations.

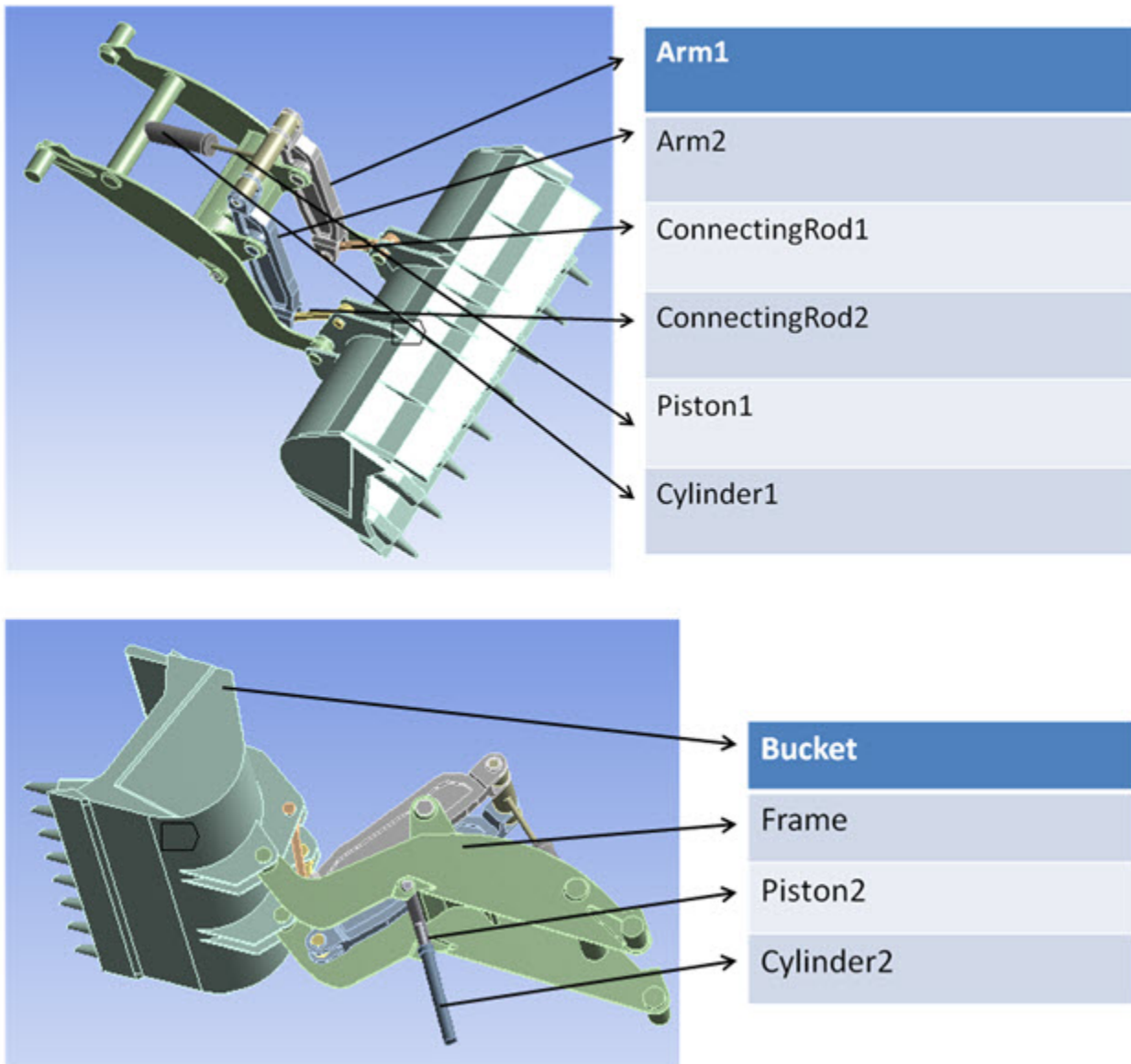
Dynamic analysis of a multibody system allows one to understand the interaction of the parts, evaluate the stress and deformation fields in the parts, and calculate the fatigue life of critical components.

For further information about multibody systems, see the [Multibody Analysis Guide](#).

## 19.2. Problem Description

The following figure shows the digger-arm assembly with all parts identified:

**Figure 19.1: Dagger-Arm Assembly**



A mass of 500 kg (not shown) is attached to the bucket to simulate the load the bucket carries.

The various parts of the digger-arm assembly are connected to each other using [joints](#). Actuation of the two piston-cylinder arrangements causes the frame, arms, and connecting rods to move, thereby causing the bucket to move as well. The entire system has essentially two free degrees of freedom.

The motion of the frame, arms, connecting rods, and the bucket are dependent on the two free degrees of freedom. For this problem, the motion of the digger-arm is restricted to in-plane motion.

Transient dynamic analyses are conducted on the multibody system as follows:

- The first analysis assumes that all parts are rigid.



- The second analysis assumes that the connecting rods are flexible and all other parts are rigid. The flexible parts are modeled using 3-D finite elements.
- The third analysis is a variation of the second analysis. The flexible connecting rods are now modeled as CMS superelements.

## 19.3. Modeling

The finite-element models for simple 2-D and 3-D problems are usually generated via the Mechanical APDL command interface. For complicated assemblies, the ANSYS Workbench product is used, as it allows one to define the geometry natively and to set up a project workflow that allows the entire analysis, from model generation to results processing, to occur in a well-defined manner.

In this problem, the digger-arm assembly is modeled using ANSYS Workbench. The modeling description identifies the relevant Mechanical APDL features that define the eventual finite-element model for analysis.

The following modeling topics for the digger-arm assembly are available:

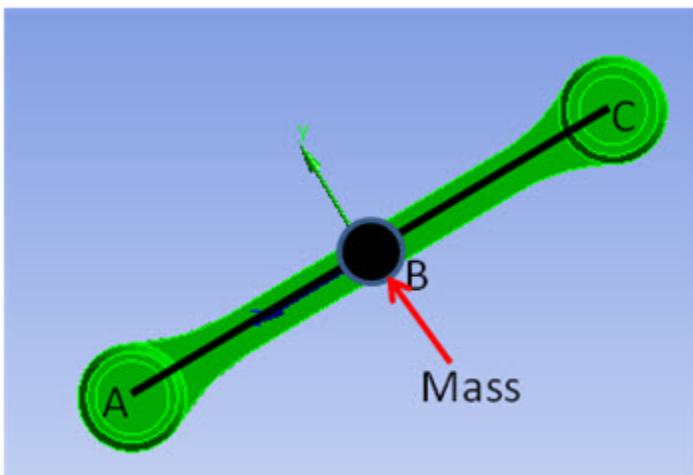
- 19.3.1. Modeling Rigid Parts
- 19.3.2. Modeling Joints
- 19.3.3. Modeling Flexible Parts
- 19.3.4. Modeling Flexible Parts with CMS Superelements

For details about the ANSYS Workbench program, see *Workbench User's Guide*.

### 19.3.1. Modeling Rigid Parts

Rigid parts are modeled using the MPC-based rigid target definition, as shown in this example of a connecting rod:

**Figure 19.2: Rigid Modeling of the Connecting Rod**



The connecting rod is modeled as a rigid part as follows:

1. A mass element, with mass equal to the mass of the connecting rod, is defined at the center of mass (B) of the part.

2. The node defining the mass element location (B) is identified as a pilot node using the **TARGE170** element.
3. The locations at which the rod is connected to other parts are identified (A and B).
4. **TARGE170** elements are defined between the mass element and the identified locations (A-B and B-C).
5. Points A and B are used in the joint definitions when connecting to other parts.

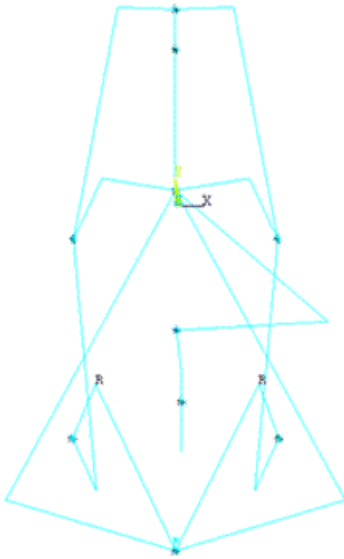
For further information, see [Modeling Rigid Bodies in a Multibody Analysis](#) in the *Multibody Analysis Guide*.

The following example input creates the rigid part:

```

!node definitions
n, A, x,y,z          ! node definition for mass node A
n, B, x,y,z          ! node definition for point B
n, C, x,y,z          ! node definition for point C
!
!Mass element definition at point A
et,1,MASS21          ! element type
keyo,1,2,1           ! moments of inertia in nodal coordinates
keyo,1,3,0           ! 3-D mass with rotary inertia
r,1, m, , , Ixx, Iyy, Izz
local,11,0,0, 0,     ! local coordinate system to define the inertias
csys,11
nrot,A               ! align local cs
csys,0
mat,1
real,1
type,1
en,elem#, A
!
!Pilot node definition at Point A
et, 2, 170           ! define target element
keyo, 2, 2, 1        ! set mpc target element do not fix pilot
keyo, 2, 4, 0        ! create constraint equations for all degrees of freedom
type, 2
mat, 2
real, 2
tshape,pilo          ! define element to be pilot node element
en,elem#, A
!
!Target elements for line segments A-B and B-C
type,2
mat,2
real,2
tshap, line          ! define 3-D line segment
en,elem#, A, B
en,elem#, B, C
    
```

All rigid parts of the digger-arm assembly are essentially modeled in the same manner. The ANSYS Workbench program automates the process for modeling the complicated geometries of the digger-arm assembly. The following figure shows the entire rigid model for the assembly as generated by ANSYS Workbench:

**Figure 19.3: Rigid Representation of the Digger-Arm Assembly**

### 19.3.2. Modeling Joints

The various parts of the multibody system are connected or constrained to each other via kinematically admissible constraints implemented as [joint elements](#).

Two nodes define a joint element. The relative motion between the two nodes is characterized by six relative degrees of freedom. A joint element is defined based on the type of constraints imposed on these relative degrees of freedom.

So that the constraints can be suitably imposed, local coordinate systems must be defined at the nodes of the joint elements. In Mechanical APDL, the constraints are implemented via the [Lagrange multiplier method](#).

The joint capability offers the following features:

- Stops and locks on the free degrees of freedom of the joint
- Stiffness, damping, and frictional behavior in the joint
- Joint actuation

This problem implements joint actuation only.

The following example input creates a [revolute joint element](#):

```

n, n1, x,y,z
n, n2, x,y,z
local,12,0,x1,y1,z1,...           ! defines a local coordinate system
et, etid#,184                     ! MPC184 element
keyopt, etid#,1,6                 ! revolute joint
keyopt, etid#,4,1                 ! Z axis is revolute axis
sectype,secid#, joint, revo, RevJoint ! identify joint section and subtype
secjoint,,12,12                   ! associate local cs with joint nodes
mat, matid#
real,realid#
type, etid#

```

```
secnum,secid#
en,elem#,n1,n2                ! define revolute joint element
```

The parts of the assembly are connected to each other by various types of joints, depending on the interaction between the parts. For example, the piston-cylinder arrangement requires a translational joint; other interactions between parts seem to indicate that one part rotates relative to another about an axis, requiring a revolute joint. Thus, as a first attempt, the joints between the parts are defined as follows:

Interacting Parts	Joint Type	Constraints
Frame-Ground	Revolute	5
Frame-Cylinder1	Revolute	5
Cylinder1-Piston1	Translational	5
Piston1-Arm1	Revolute	5
Piston1-Arm2	Revolute	5
Arm1-Frame	Revolute	5
Arm2-Frame	Revolute	5
Arm1-ConnectingRod1	Revolute	5
Arm2-ConnectingRod2	Revolute	5
ConnectingRod1- Bucket	Revolute	5
ConnectingRod2-Bucket	Revolute	5
Frame-Bucket-1	Revolute	5
Frame-Bucket-2	Revolute	5
Piston2-Frame	Revolute	5
Cylinder2-Piston2	Translational	5
Cylinder2-Ground	Revolute	5

After the joints between parts have been defined, the kinematic behavior of the assembly must be verified. The wrong choice of joints can cause either of the following conditions in the system:

- *Overconstraint* – More constraints exist than are required, leading to a stiff response of the system.
- *Underconstraint* – Fewer constraints exist than are required, leading to unnecessary deformation modes.

In either case, the result is inconsistent kinematic behavior, and the joints must be redefined to obtain a proper kinematic response.

To check whether a multibody system model is overconstrained or underconstrained due to improper joint definition, the free degrees of freedom in the system are counted. All parts are assumed to be rigid for this calculation. The calculated number must match the expected value. If a mismatch exists, the joints must be replaced by other joints of similar behavior such that the mathematical modeling of the system shows consistent kinematic behavior.

The free degrees of freedom for the digger-arm assembly are calculated as follows:

10 rigid bodies x 6 degrees of freedom per rigid body	+60
14 revolute joints x 5 constraints	-70

2 prismatic joints x 5 constraints	-10
<b>Number of free degrees of freedom</b>	<b>-20</b>

The number of free degrees of freedom should be 2; therefore, the calculation shows that the Digger-Arm model is severely overconstrained due to improper joint definitions.

The overconstraints can be minimized by redefining the joints between the various parts. Some experimentation may be required. For example, consider the constraints in the joints between the following part pairs (as shown in [Figure 19.4: Connections Between Piston, Cylinder, and Arms \(p. 287\)](#)):

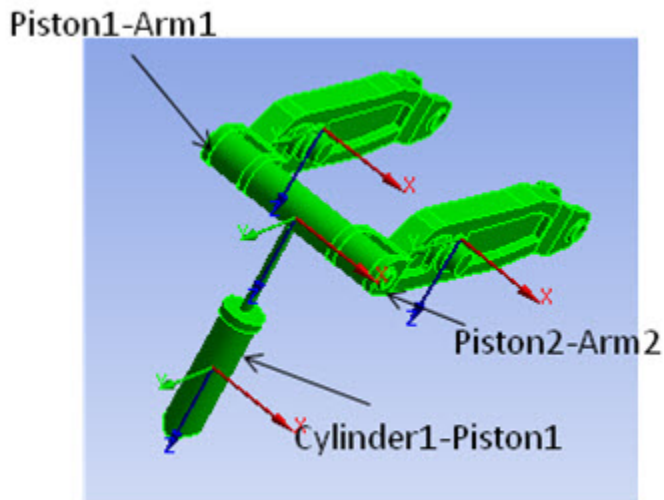
- **Translational joint between Piston1-Cylinder1**

- Free degrees of freedom -- 1 relative displacement along translational axis
- Constrained degrees of freedom -- 2 relative displacements, 3 relative rotations

- **Revolute joints between Piston1-Arm1 and Piston1-Arm2**

- Free degrees of freedom – 1 relative rotation along revolute axis
- Constrained degrees of freedom – 3 relative displacements, 2 relative rotations

**Figure 19.4: Connections Between Piston, Cylinder, and Arms**



It is apparent that Piston1 does not rotate with respect to Cylinder1 due to the rotational constraints in the translational joint; therefore, the rotational constraints in the revolute joints between Piston1-Arm1 and Piston1-Arm2 are not required. The relative displacement constraints between these parts must be maintained, however, and so the revolute joint can be replaced by a [spherical joint](#). The spherical joint provides the same relative displacement constraints but allows the relative rotations to be unconstrained.

In a similar way, other joints are replaced as necessary. The new joint definitions between the various parts are as follows:

Interacting Parts	Joint Type	Constraints
Frame-Ground	Cylindrical	4
Frame-Cylinder1	Spherical	3
Cylinder1-Piston1	Translational	5
Piston1-Arm1	General	2
Piston1-Arm2	Spherical	3
Arm1-Frame	Cylindrical	4
Arm2-Frame	Cylindrical	4
Arm1-ConnectingRod1	Spherical	5
Arm2-ConnectingRod2	Spherical	5
ConnectingRod1- Bucket	Revolute	5
ConnectingRod2-Bucket	Revolute	5
Frame-Bucket-1	General	2
Frame-Bucket-2	General	2
Piston2-Frame	Cylindrical	4
Cylinder2-Piston2	Translational	5
Cylinder2-Ground	Spherical	3

The redefinition of joints outlined in the table is not necessarily unique; however, it meets the objective of ensuring that a joint does not unnecessarily constrain motion in a particular direction which has been otherwise constrained.

With the new joint definitions, the free degrees of freedom in the model are now calculated as follows:

10 rigid bodies x 6 degrees of freedom per rigid body	+60
2 revolute joints x 5 constraints	-10
2 translational joints x 5 constraints	-10
4 cylindrical joints x 4 constraints	-16
5 spherical joints x 3 constraints	-15
2 prismatic joints x 5 constraints	-6
<b>Number of free degrees of freedom</b>	<b>+2</b>

The number of free degrees of freedom in the model matches the required number of degrees of freedom. A transient dynamic analysis of the digger-arm assembly, with all parts rigid and joints redefined, exhibits the correct kinematic response.

In this problem, the joints as defined above are used for all subsequent analyses.

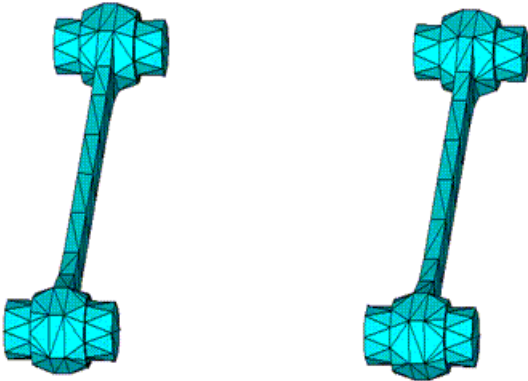
For further information, see [Connecting Multibody Components with Joint Elements](#) in the *Multibody Analysis Guide* and [Constraints and Lagrange Multiplier Method](#) in the *Mechanical APDL Theory Reference*.

### 19.3.3. Modeling Flexible Parts

Frequently, a part or component may be modeled as flexible if its material behavior is defined as non-linear (for example, with plasticity or hyperelasticity) or the part is expected to undergo large deformation. A wide variety of continuum and structural elements is available to model the flexibility.

The two connecting rods are defined to be flexible for this analysis. The flexible parts are meshed with **SOLID185** elements. A total of 876 **SOLID185** elements are used in the analysis. The following figure shows the finite-element mesh:

**Figure 19.5: Connecting Rods Modeled with **SOLID185** Elements**



For further information, see [Modeling Flexible Bodies in a Multibody Analysis](#) in the *Multibody Analysis Guide*.

### 19.3.4. Modeling Flexible Parts with CMS Superelements

Flexible bodies are often modeled with **component mode synthesis (CMS) superelements** to reduce computational requirements. The advantage of CMS is that the many degrees of freedom in a flexible multibody system are replaced by a limited set of degrees of freedom, thereby reducing the computational time required. The CMS superelement represents the stiffness and mass of the flexible body and is used in place of a standard element in the analysis phase.

Following is the general process for generating and using a CMS superelement:

1. Prepare a full model of the flexible multibody system (including joint loads).
2. Define components for each flexible body to be represented as a CMS superelement:
  - Create a node component (the master component) that defines the master degrees of freedom.
  - Create a component of elements (the slave component) that are dependent on the master degrees of freedom.
3. Generate a CMS substructure file (in the generation pass) characterizing the dynamic flexibility of the body.
4. Use the CMS substructure information (in the use pass) in a standard analysis.

The CMS substructure information is used to define a CMS superelement representing the flexible body.

5. Expand the results of the analysis (in the expansion pass) to all elements in the flexible body to recover its stress and deformation fields.
6. Postprocess the results for stress and deformation fields in the model.

For the analysis requiring a CMS superelement representation of the flexible part, the two connecting rods are once again defined as flexible. The rods are then modeled as CMS superelements.

The following example input creates the master and slave components:

```
/com,***** Create Components for CMS *****
nset,none ! create nodal component of master nodes
nset,a,node,,Node#, ! add pilot node attached to this body
nset,a,node,,Node#, ! add pilot node attached to this body
cm,COMPONENT_master,node
esel,s,elem,,COMPONENT
nsls ! select any nodes touching these bodies in the user component
esln ! add in any touching elements such as contact and surf effect
cm,COMPONENT_slave,elem
allsel
```

The following example input creates the CMS substructure file:

```
/solu
antype,substr ! perform a substructure analysis
seopt,Component,2 ! CMS substructure file name and generate stiffness and mass matrices
cmsopt,free,30 ! specify CMS analysis options with free-interface method
mdelete,all,all ! delete any previously generate master dofs
cmsel,s,COMPONENT_MASTER ! select the master component
m,all,all ! define master degrees of freedom
cmsel,s,COMPONENT_SLAVE ! select the slave component
nsls
save
solve
finish
```

Because the analysis phase considers both the lower and higher modes of vibration to be equally important, the free-interface method (**CMSOPT,FREE**) is used to generate the substructure files.

The following example input defines and uses the CMS superelement during the analysis phase:

```
/filnam,FILENAME
resume, ! resumes database

/prep7
cmsel,u,Component_slave ! unselect the flexible elements
cmsel,a,Component_master ! make sure the master nodes are selected

et,100,50 ! define substructure element type using available itype number
type,100
real,100
mat,100
mp,mu,100,0.0
se,ConnectRod1 ! define substructure element

/solu
antype,trans
nlgeom, on
...
...
finish
```

The following example input shows expands the results to the full flexible body:

```
/filnam,FILENAME
resume

/solu
```



```

expass,on
seexp,Component,FILENAME      ! substructure name and the use pass jobname
numexp,all,,,yes      ! Expand all time points
solve
finish

```

For further information, see [Using Component Mode Synthesis Superelements in a Multibody Analysis in the \*Multibody Analysis Guide\*](#).

## 19.4. Material Properties

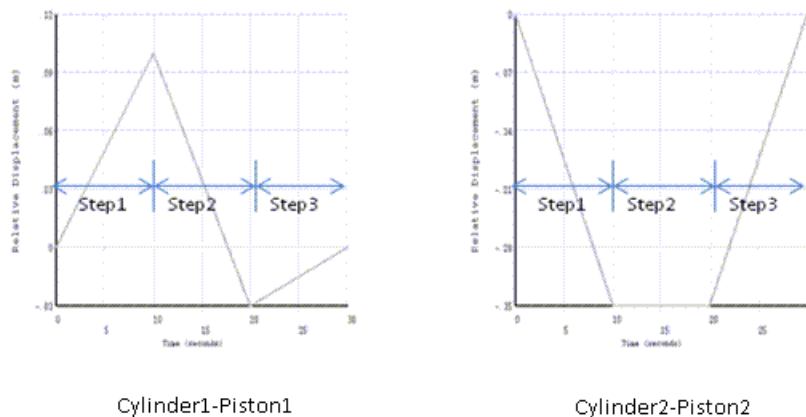
Following are the material properties used for the flexible bodies:

Flexible Body Material Properties	
Young's Modulus (Nm <sup>-2</sup> )	2.00E + 11
Poisson's Ratio	0.3
Density (Kgm <sup>-3</sup> )	7850

## 19.5. Boundary Conditions and Loading

The entire digger-arm model is subjected to acceleration to account for gravity. The two piston-cylinder arrangements are also activated simultaneously. In the finite-element model, these piston-cylinder arrangements are represented as translational joints. Displacement boundary conditions are applied on the free relative degree of freedom of the translational joints. The displacements are applied over three load steps, as shown:

**Figure 19.6: Relative Displacement Specifications for Cylinders and Pistons**



The following example input applies the acceleration and displacement loading (**ACEL** and **DJ**):

```

acel,%_acelx%,%_acely%,%_acelz%      ! apply acceleration loading via table
esel,s,type,, id1#                    ! select the first translational joint
dj,all,ux,%_load1%                    ! apply loads defined by table
esel,all
esel,s,type,, id2#                    ! select the other translational joint
dj,all,ux,%_load2%                    ! apply loads defined by table

```

## 19.6. Analysis and Solution Controls

Three **nonlinear transient dynamic analyses** (**ANTYPE,TRANS**) are performed on the digger-arm assembly. Finite-deformation and large-rotation effects are included in the analysis (**NLGEOM**).

An analysis is performed for each of the following cases:

- All parts are considered to be rigid.
- The connecting rods are modeled as flexible with **SOLID185** elements.
- The flexible connecting rods are now modeled as **CMS superelements**.

In general, automatic time-stepping schemes are preferred over fixed-time stepping schemes, as the program is allowed to cut back when the problem does not converge; when the convergence rate is good, larger time increments are used to achieve faster convergence. For this problem, however, fixed time-stepping with a time increment of 0.2 seconds is used so that the results at additional time points can be captured. Three load steps, each having a 10-second duration, are used, for a total analysis time of 30 seconds.

A default numerical damping of 0.1 is set (**TINTP**), and the HHT time-integration method is selected (**TRNOPT**).

The following example input performs the essential tasks in the analysis process:

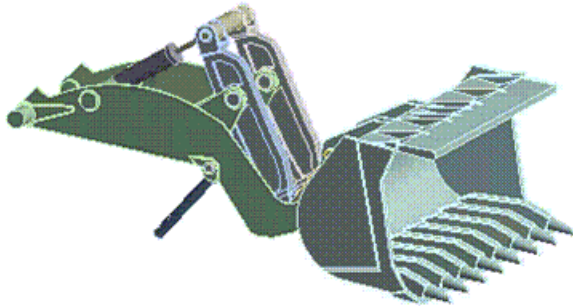
```

/solu
antype,4                ! transient analysis
nlgeom,on              ! activate large-deformation effects
trnopt,full,,,,,hht   ! HHT time-integration method
tintp,0.1              ! numerical damping
autots,off             ! automatic time-stepping disabled
deltim,0.1,0.1,0.1    ! set time increments
time,10.               ! set total time
timint,on              ! activate time-integration effects
outres,all,all         ! output all results at all time points
!
solve                  ! solve for 1st load step
time, 20.
solve                  ! solve for 2nd load step
time, 30.
solve                  ! solve for 3rd load step
finish

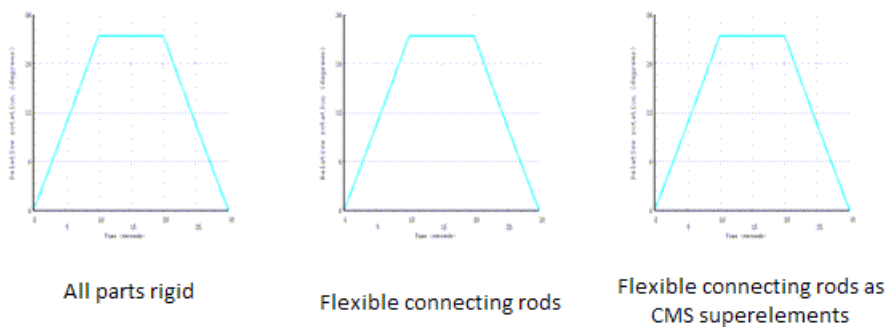
```

## 19.7. Results and Discussion

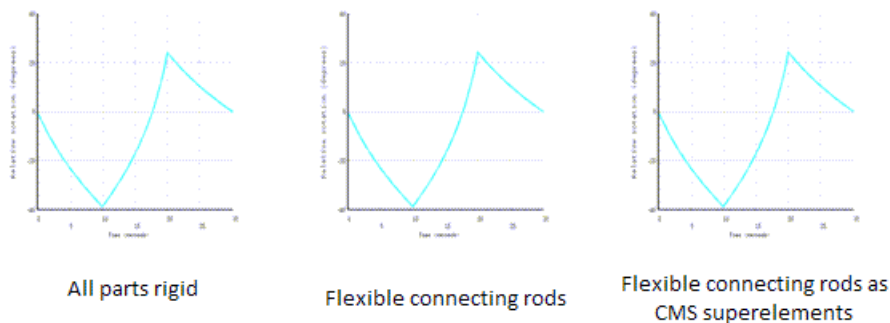
The following animation (generated in ANSYS Workbench) shows the motion of the digger-arm assembly:

**Figure 19.7: Digger-Arm Assembly Animation**

The following figure shows the rotation of the frame with respect to ground for all three transient dynamic analysis cases. The motion of the frame (due to the activation of the piston-cylinder assemblies) is the same in all three cases.

**Figure 19.8: Relative Rotation at Cylindrical Joint (Ground-to-Frame)**

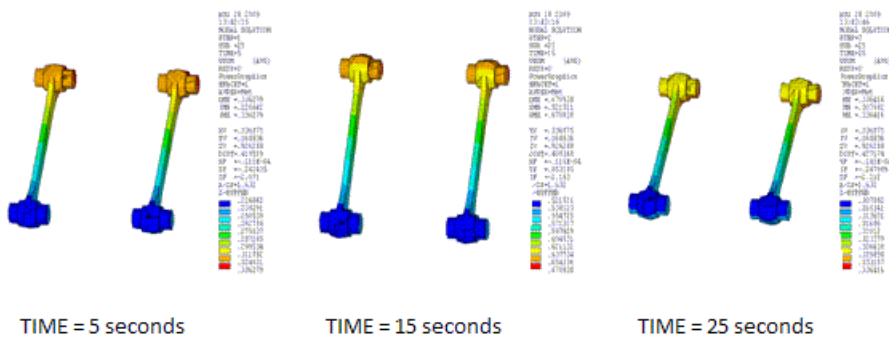
The following figure compares the relative rotation of the bucket with respect to the frame for the three analysis cases. The rotations in the three cases are nearly identical.

**Figure 19.9: Relative Rotation at General Joint Along Local Z Axis (Bucket-Frame)**

Both relative-rotation figures shown above indicate that the kinematic behavior of the digger-arm assembly, whether modeled as entirely rigid or as a rigid/flexible combination, exhibit the same behavior. When flexibility is involved in an analysis, modeling the assembly as though it consisted of rigid parts, and ensuring that the joints are defined correctly, allows the engineer to focus on other issues.

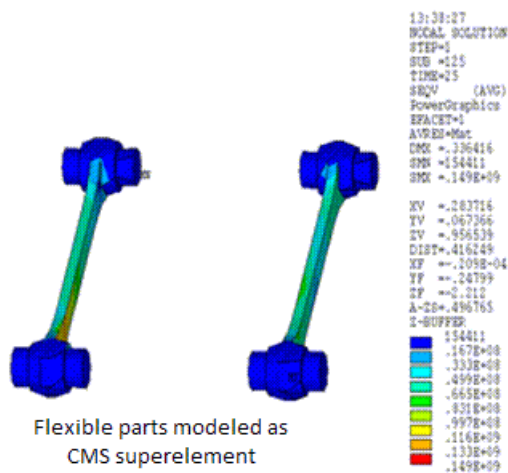
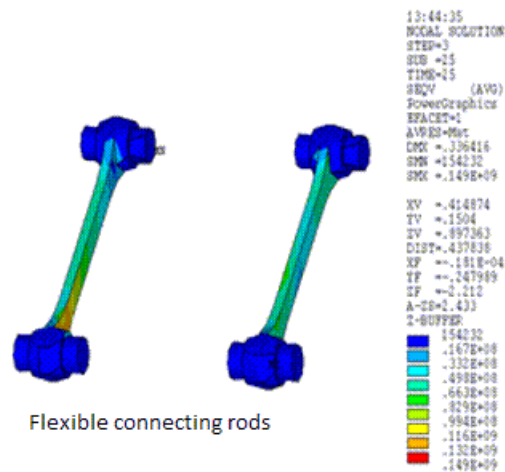
The stresses and deformation fields can be evaluated when the connecting rods are made flexible. The following figure shows the deformation plots (USUM) of the connecting rods when the rods are modeled as flexible:

**Figure 19.10: USUM Plots of Connecting Rods**



The following figure shows the equivalent stresses in the connecting rods when the rods are modeled using SOLID185 elements and as CMS superelements, respectively.

Figure 19.11: Equivalent Stress Plots of Connecting Rods



The time point is at 25 seconds (load step 3, substep 25). The equivalent stress plots show good agreement with each other.

The following table shows the CPU time comparisons between the three analysis cases.

	All Rigid Parts	Flexible and Rigid Parts	CMS and Rigid Parts
Total degrees of freedom	606	2874	702
Total iterations	458	489	436
Generation time (with original database saved)	---	---	2.38 seconds
Use pass time	---	---	46.8 seconds
Total CPU time (including full-model save, generation pass,	42.5 seconds	372.68 seconds	78.06 seconds

	All Rigid Parts	Flexible and Rigid Parts	CMS and Rigid Parts
use pass, expansion pass, and results processing)			

In all cases, shared memory parallel with two CPUs is used. The results are reported for a 64-bit Linux system.

The table and the other results discussed illustrate some essential analysis considerations:

- It is worthwhile to verify the kinematic behavior of the multibody system by assuming all parts as rigid, as the time and resources required for the rigid analysis are small.
- Modeling the flexible bodies using CMS superelements results in significant time savings.
- Analysis of the assembly when the flexible part is modeled with 3-D finite elements necessarily requires more time due to the increased number of degrees of freedom. Such an analysis, however, should be performed only when the flexible part undergoes large deformations, either due to nonlinear material behavior or to nonlinear geometric effects.

## 19.8. Recommendations

To perform a similar transient dynamic analysis of a multibody system, consider the following hints and recommendations:

- Ensure that the motion and behavior of the model is kinematically consistent by modeling all parts as rigid bodies connected to each other by joints.
- Relax overconstraints due to joints by selecting joints of similar behavior. Use a spherical or cylindrical joint instead of a revolute joint if some constraints are deemed unnecessary.
- When modeling flexible parts, build the model incrementally and verify that the motion and behavior are consistent with expected behavior.
- Use full modeling of the parts only when detailed information about the stress and deformation fields is required.
- For reduced run times, model the flexible parts as CMS superelements whenever possible.

For additional recommendations, see [Troubleshooting a Flexible Multibody Analysis](#) in the *Multibody Analysis Guide*.

## 19.9. Input Files

The following files were used in this problem:

- `DiggerArm-Rigid.dat` -- Input file for all parts modeled as *rigid*.
- `DiggerArm-Rigid.inp` -- Rigid model information (called by `DiggerArm-Rigid.dat`).
- `DiggerArm-Flexible.dat` -- Input file for connecting rods modeled as *flexible* using `SOLID185` elements.
- `DiggerArm-Flexible.inp` -- Flexible model information (called by `DiggerArm-Flexible.inp`).

- `DiggerArm-CMS.dat` -- Input file for modeling the flexible connecting rods as CMS superelements.
- `DiggerArm-CMS.inp` -- CMS superelement model information (called by `DiggerArm-CMS.dat`).

The files are available in the `td-19` folder. See [Obtaining the Input Files \(p. xxxv\)](#) for more information.





---

## Chapter 20: Dynamic Simulation of a Printed Circuit Board Assembly Using Modal Analysis Methods

---

This example demonstrates the use of [residual vectors](#) to improve the solution accuracy in modal subspace based analysis methods, such as [modal superposition](#) and [power spectral density \(PSD\)](#) analyses. The problem includes a study of the computational efficiency of the results-expansion procedure used to obtain the full model solution.

Topics related to this example problem follow:

- [20.1. Introduction](#)
- [20.2. Problem Description](#)
- [20.3. Modeling](#)
- [20.4. Material Properties](#)
- [20.5. Boundary Conditions and Loading](#)
- [20.6. Analysis and Solution Controls](#)
- [20.7. Results and Discussion](#)
- [20.8. Recommendations](#)
- [20.9. References](#)
- [20.10. Input Files](#)

### 20.1. Introduction

Portable electronic devices such as digital cameras, mobile phones, and PDAs use printed circuit boards (PCBs). Due to increased demands for convenience and multi-functionality, these devices are designed with a focus on miniaturization to accommodate a higher density and smaller dimensions of integrated circuit (IC) packages. These design constraints require smaller solder joints with finer pitch, contributing to the vulnerability of interconnections at the board level. Exposure to harsh dynamic loading environments during transportation and customer use are a critical issue for PCBs. [PSD analysis](#) simulates the random excitations with unknown loading encountered in these harsh conditions.

The modal superposition method efficiently solves a large linear dynamic system by transforming it into a set of uncoupled equations using the normal modes of the system. The first step in the modal superposition method is to obtain the eigen frequencies and eigen modes of the system through [modal analysis](#). The downstream modal transient, modal harmonic, and spectral analyses are then performed.

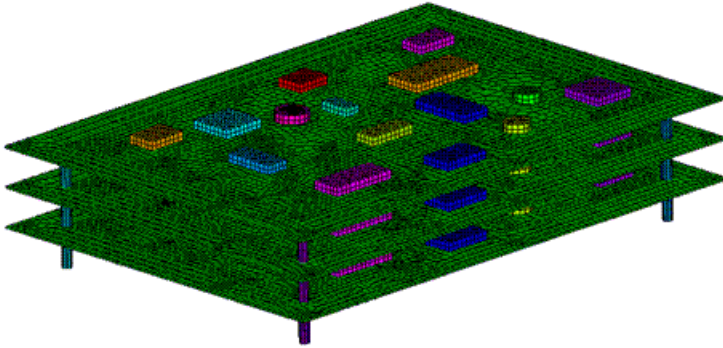
In the modal analysis, only a subset of the lower frequencies is usually extracted, truncating the higher frequency modes. As a result, the accuracy of the modal subspace based solution is not guaranteed, though accuracy can be improved using [residual vectors](#). The residual vectors are calculated and normalized to the modes extracted, and can then be used in all the downstream analyses (e.g., modal transient, modal harmonic, and spectral analyses).

The efficiency of the modal superposition expansion pass has been improved using a direct combination approach of stress/strain modes. You can activate the expansion in the modal analysis by applying the [element results expansion option](#).

## 20.2. Problem Description

The model below is a PCB assembly consisting of three PCBs stacked together. A PSD analysis with base excitation using acceleration response spectrum is performed on this model. The aim is to determine the  $1-\sigma$  displacement solution and compare the accuracy of results with and without the residual vectors. Improvement of the computational efficiency is verified via modal superposition expansion (**MXPAND**).

**Figure 20.1: Full 3-D Geometry of a PCB assembly**



## 20.3. Modeling

This section describes the detailed modeling of the PCB assembly. The following modeling topics are covered:

### 20.3.1. Modeling of the PCB Structure

#### 20.3.2. Contact Modeling

### 20.3.1. Modeling of the PCB Structure

The assembly consists of three PCBs stacked together. Each PCB consists of a circuit board with IC packages on top. The board is a 0.20m×0.28m rectangular surface body with a 1 mm uniform thickness. The IC packages are 3-D structures, each with a thickness of 5 mm. The board is modeled with **SHELL181**, which is suitable for analyzing thin to moderately thick shell structures. The IC packages are modeled with **SOLID186**, which is a 3-D 20 noded solid element, exhibiting quadratic displacement behavior. The stack is connected together by five vertical columns. These are thick beam structures (length/diameter  $\approx 10$ ), and they are modeled using **BEAM188**.

**BEAM188** uses Timoshenko beam theory, which includes shear deformation effects, and is one of the most accurate beam elements for analyzing moderately stubby beam structures. A hexahedral dominant mesh is used to mesh the board and the solids, resulting in each PCB having 14600 nodes. Both the board and the IC packages are made of polyethylene material. The supporting columns are made of aluminum alloy. The total number of nodes for the model is 44097 with 26046 elements.

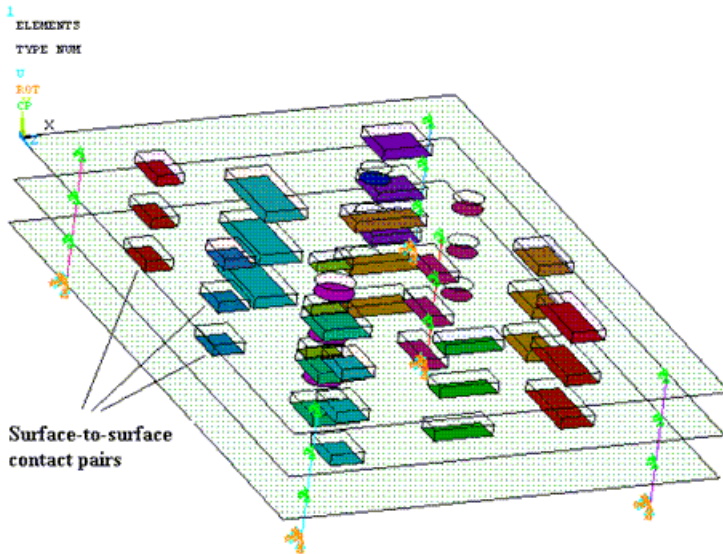
### 20.3.2. Contact Modeling

Bonded and flexible surface-to-surface contact pairs are used to define the contact between the IC packages and the circuit board. Contact and target surfaces are used to connect the IC packages to the board. The contact surface is modeled with **CONTA174** elements and the target surfaces are modeled using **TARGE170** elements. The surface-to-surface contact elements have the following advantages over the node-to-node elements:

- Support for lower and higher order elements on the contact and target surfaces. (SHELL181 is a linear element, whereas SOLID186 is a quadratic element)
- No restrictions on the shape of the target surface. Surface discontinuities can result from manufacturing flaws or mesh discretization.

For each board, fifteen contact pairs are identified, as seen in the figure below.

**Figure 20.2: Bonded Contact Pairs Between IC Packages and Circuit Boards**



## 20.4. Material Properties

Material properties for the supporting columns, board, and IC packages are as follows:

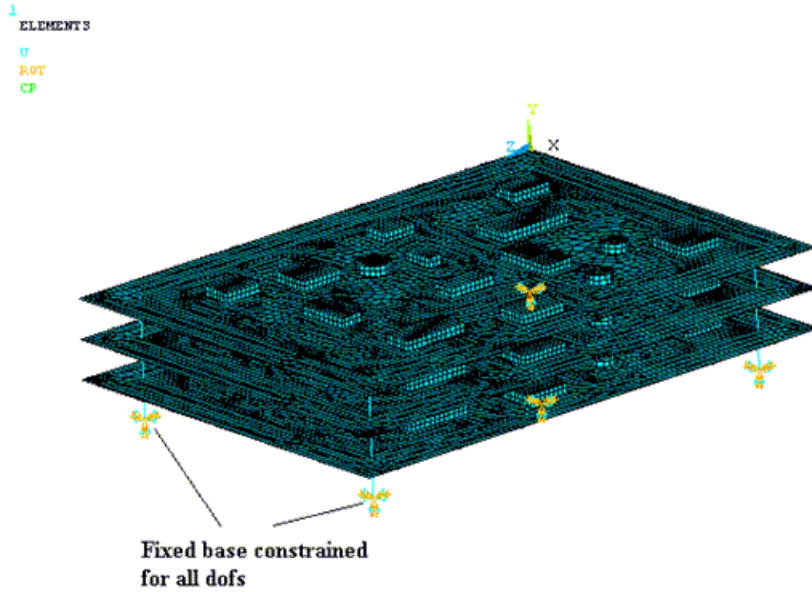
Supporting Column Material Properties	
Young's Modulus (ton/s <sup>2</sup> mm)	71.0e3
Poisson's Ratio	0.33
Density (ton/mm <sup>3</sup> )	2.77e-009

Board and IC Packages Material Properties	
Young's Modulus (ton/s <sup>2</sup> mm)	1.1e3
Poisson's Ratio	0.42
Density (ton/mm <sup>3</sup> )	9.5e-010

## 20.5. Boundary Conditions and Loading

The boards of the PCB assembly are connected with five supporting columns. The base of the columns ( $y = -60$ ) are constrained on all degrees of freedom as shown in the figure below:

**Figure 20.3: PCB Boundary Conditions**



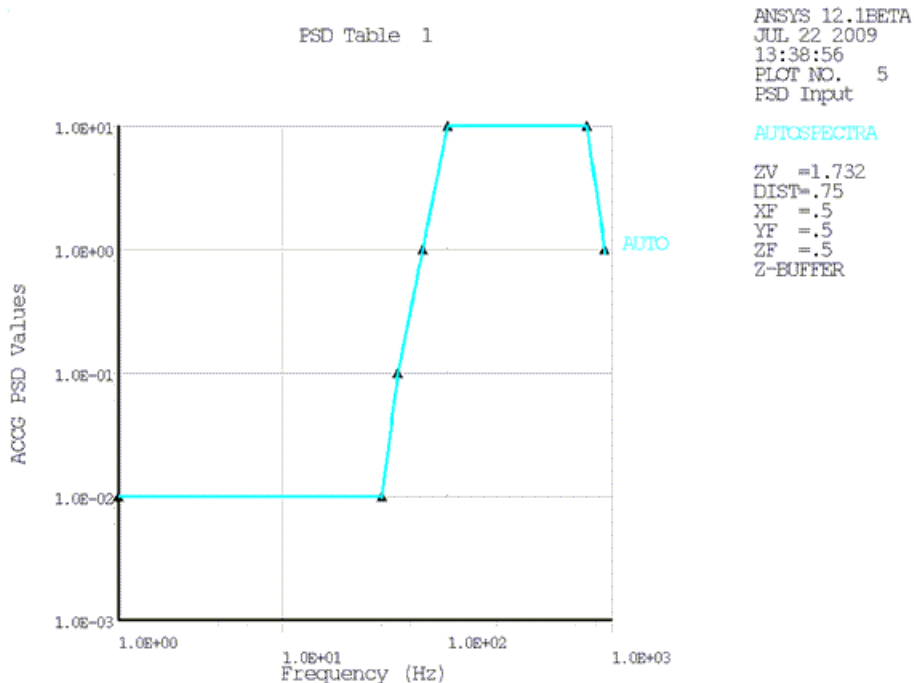
The following example input shows how the fixed constraints are applied:

```
CM, N_BASE_EXCITE, NODE          ! Group the set of nodes at the base of the columns as a component  
D, ALL, ALL                       ! Apply displacement and rotation constraints to this set
```

N\_BASE\_EXCITE in the input above specifies the nodes at the junction of the supporting columns with the base. For PSD analysis, the loading is applied in the form of base excitation on the set N\_BASE\_EXCITE.

The PSD values for the input spectrum at different frequency points are shown in the figure below. The input segment between 1.0E-02 and 1.0E+01 has 2 intermediate points in order to obtain a good fit for the curve-fitting polynomial used in the PSD integration process.

Figure 20.4: PSD Base Excitation Values



The following example input shows how base excitation is applied:

```

/SOLU
ANTYPE, SPECTR          ! Perform a spectral analysis
SPOPT, PSD              ! Use power spectral density (PSD) as the spectrum
                          ! type
PSDUNIT, 1, ACCG, 9.81*1000 ! Use input table 1 with acceleration spectrum in
                          ! terms of acceleration due to gravity
PSDFRQ, 1, , 1, 40, 50, 70.71678, 100, 700, 900, 1E3 ! Define the frequency points in the input table 1
PSDVAL, 1, 0.01, 0.01, 0.1, 1, 10, 10, 1, 1 ! Define the PSD values in the input table 1
PSDGRAPH, 1            ! Display the input PSD curve from table 1
DMPRAT, 0.05          ! Set the damping ratio as 5%
D, N_BASE_EXCITE, UY, 1 ! Apply base excitation on the set of nodes
                          ! N_BASE_EXCITE in the y direction from table 1

```

## 20.6. Analysis and Solution Controls

This section describes the solution controls and analysis settings for the modal and PSD analyses with the use of the residual vectors and modal expansion.

The [modal analysis](#) is performed using the [Block Lanczos](#) mode extraction method with the residual vector. (For additional information on the residual vector method, refer to [Residual Vector Method](#) in the [Mechanical APDL Theory Reference](#) and [Residual Vector Method](#) in [Structural Analysis Guide](#))

Linear acceleration loading is applied in the y direction ([ACEL](#)), as it is needed to generate the residual vector in conjunction with the downstream PSD analysis. Acceleration loading in the global y direction is chosen to generate the residual vector because in the subsequent PSD analysis, base excitation is applied in the same direction. The example input below shows how residual vectors are generated in the modal analysis:

```

NUM_MODES=50            ! Number of modes to be extracted = 50
/SOLU
ANTYPE, MODAL          ! Perform a modal analysis
MODEOPT, LANB, NUM_MODES ! Use block Lanczos to extract the modes

```

## Methods

---

```
RESVEC, ON           ! Calculate the residual vectors
ACEL,0,1,0          ! Set the linear acceleration of the reference frame along the global Y axis
```

For power spectral density (PSD) analysis, base excitation is applied in the form of acceleration in the vertical y direction, which is represented in terms of the acceleration due to gravity. The PSD values for the input spectrum at different frequency points are given previously in [Figure 20.4: PSD Base Excitation Values \(p. 303\)](#) and a damping ratio of 0.05 is selected.

### 20.6.1. Residual Vector Method

In the modal superposition analysis, the dynamic response will be approximate if the applied loading excites the modes of a structure more than the modal analysis. The residual vector method is used to improve the accuracy of the dynamic response. The residual vectors are calculated using the static displacement response of the loads applied on the structure, which represent the linear combination of the truncated high frequency modes. The residual vectors are orthogonalized with respect to the eigenmodes extracted in the modal analysis to form orthogonalized residual vectors. The orthogonalized residual vectors are then used in modal superposition transient, harmonic, and spectral analyses to obtain more accurate modal based analyses results.

Because of the improved convergence properties of this method, fewer eigenmodes are required from the eigensolution. The dynamic response of the structure can be divided into two parts: contributions from the lower modes, and contributions due to the higher modes, which can be expressed as a combination of residual vectors.

The response power spectral density (RPSD) 1- $\sigma$  displacement solutions are obtained with and without the residual vectors. The residual vectors are calculated in the modal analysis, and subsequently used in the PSD analysis with the same [procedure](#). The sample input below shows how residual vectors are used in a PSD analysis:

```
/SOLU
ANTYPE,SPECTR      ! Perform a spectral analysis
RESVEC, ON        ! Include the residual vectors
ACEL,0,0,0        ! Initialize the linear acceleration of the ref frame to zero
SPOPT,PSD         ! Use power spectral density (PSD) as the spectrum type.
                  ! Rest of the code is same as in the previous section
```

### 20.6.2. Mode Expansion

Element results are written in the `Jobname.mode` file prior to the expansion pass of the subsequent mode-superposition by using the parameter `MSUPkey` in the modal analysis with **MXPAND**. Results in `Jobname.mode` are written as a linear combination of the modal element results. This saves a significant amount of time for the downstream modal transient, harmonic, and PSD analyses, as the expansion pass does not need to execute element routines due to prior information being available.

Full model modal analysis is carried out with and without storing the element results for the PSD analysis, and their efficiencies are compared.

## 20.7. Results and Discussion

The following topics are discussed in this section:

[20.7.1. Computational Efficiency](#)

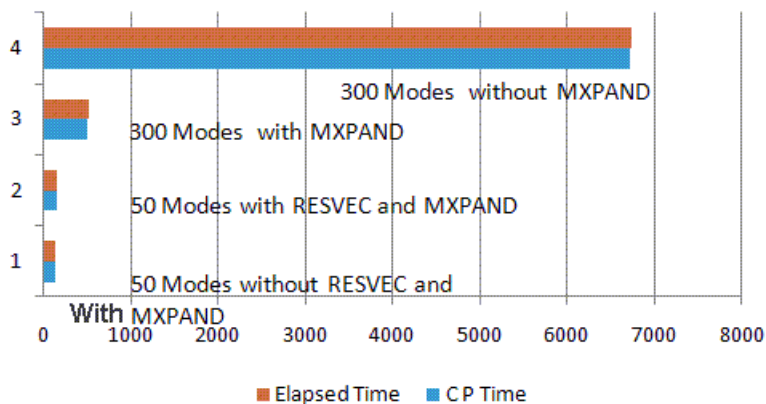
[20.7.2. Accuracy of Results](#)

## 20.7.1. Computational Efficiency

PSD analysis is performed with a large number of modes first. Using the **MXPAND** command (*MSUPkey* = YES) to store the modal element results significantly improves the efficiency in the downstream modal superposition expansion pass. Reduction of the number of modes used also reduces the solution time, but at the expense of accuracy. Accuracy can be improved without a significant increase in the solution time by using residual vectors.

The figure below shows the elapsed and CPU times with and without the residual vector method and the expansion of the modes. Significant reduction in the solution time is achieved with the use of *MSUPkey* = YES.

**Figure 20.5: Solution Times With and Without MXPAND**

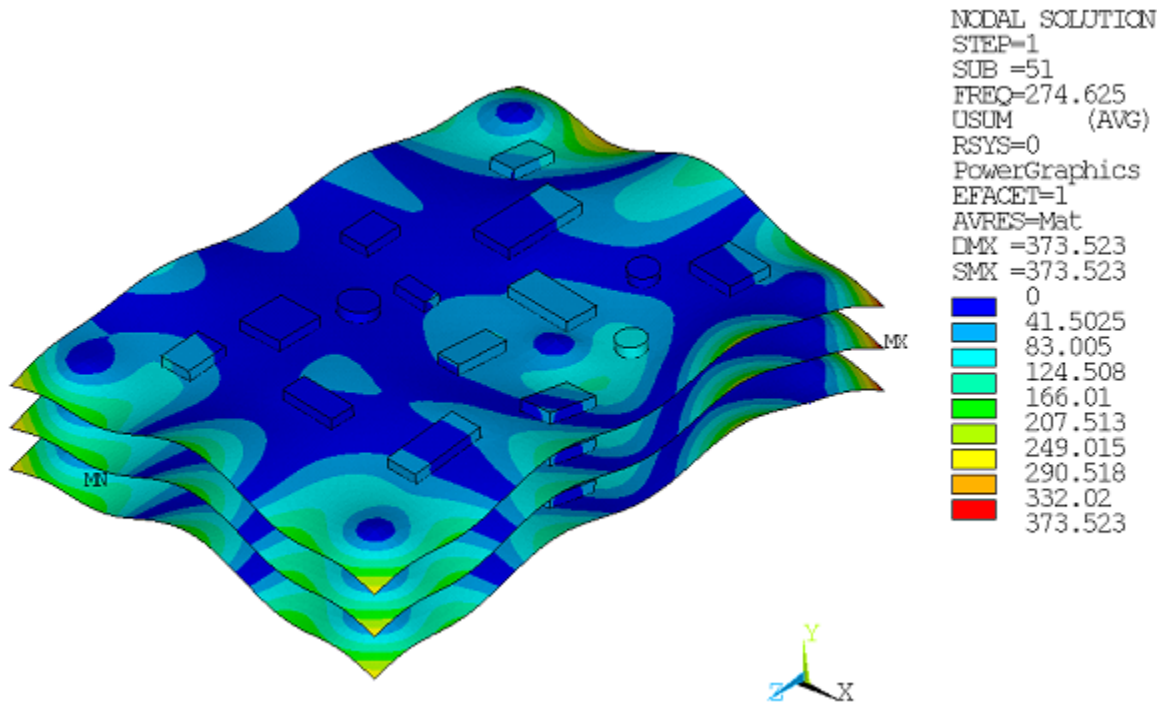


The solution time is slightly increased with the residual vector. For 50 modes, the elapsed time with and without the residual vector are 143.00 and 137.42 seconds, respectively.

## 20.7.2. Accuracy of Results

The mode shape of the residual vector obtained using 50 modes (the 51th mode being the residual vector) is shown in the figure below. Note that the residual vector corresponds to a displacement in the y direction.

**Figure 20.6: Mode Shape of the Residual Vector**



The residual vector method uses an additional vector computed in the modal analysis pass in addition to the eigenvectors in the modal transformation. This increases the accuracy of the response solution. RPSD displacement solutions with and without the residual vector are listed in the table below. For 50 modes without the residual vector, accuracy of the results is poor, as shown in column A in the following table. Accuracy is significantly improved with the use of the residual vector, as shown in column B.

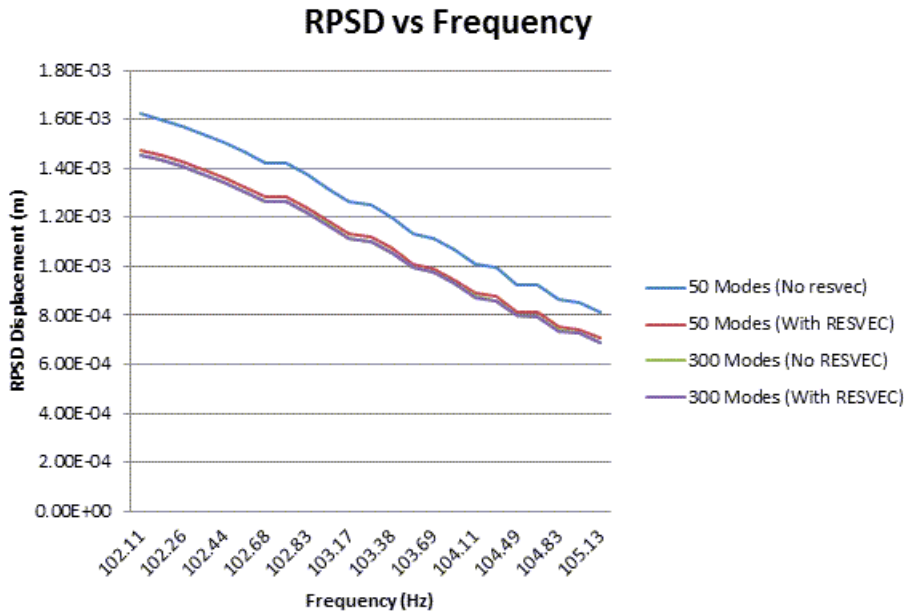
Frequency	Number of Modes			% Diff with Column C	
	50 (No RESVEC) Column A	50 (With RESVEC) Column B	300 (Full Model) Column C	50 (No RESVEC)	50 (With RESVEC)
102.11	1.62 x 10 <sup>-3</sup>	1.48 x 10 <sup>-3</sup>	1.46 x 10 <sup>-3</sup>	1.114	1.013
102.18	1.60 x 10 <sup>-3</sup>	1.45 x 10 <sup>-3</sup>	1.43 x 10 <sup>-3</sup>	1.115	1.014
102.26	1.57 x 10 <sup>-3</sup>	1.43 x 10 <sup>-3</sup>	1.41 x 10 <sup>-3</sup>	1.116	1.014
102.35	1.54 x 10 <sup>-3</sup>	1.40 x 10 <sup>-3</sup>	1.38 x 10 <sup>-3</sup>	1.117	1.014
102.44	1.50 x 10 <sup>-3</sup>	1.36 x 10 <sup>-3</sup>	1.34 x 10 <sup>-3</sup>	1.119	1.014
102.56	1.46 x 10 <sup>-3</sup>	1.33 x 10 <sup>-3</sup>	1.31 x 10 <sup>-3</sup>	1.121	1.014



Frequency	Number of Modes			% Diff with Column C	
	50 (No RESVEC) Column A	50 (With RESVEC) Column B	300 (Full Model) Column C	50 (No RESVEC)	50 (With RESVEC)
102.68	1.42 x 10 <sup>-3</sup>	1.29 x 10 <sup>-3</sup>	1.27 x 10 <sup>-3</sup>	1.123	1.015
102.68	1.42 x 10 <sup>-3</sup>	1.28 x 10 <sup>-3</sup>	1.27 x 10 <sup>-3</sup>	1.123	1.015
102.83	1.37 x 10 <sup>-3</sup>	1.24 x 10 <sup>-3</sup>	1.22 x 10 <sup>-3</sup>	1.125	1.015
102.99	1.32 x 10 <sup>-3</sup>	1.19 x 10 <sup>-3</sup>	1.17 x 10 <sup>-3</sup>	1.128	1.015
103.17	1.26 x 10 <sup>-3</sup>	1.13 x 10 <sup>-3</sup>	1.12 x 10 <sup>-3</sup>	1.132	1.016
103.21	1.25 x 10 <sup>-3</sup>	1.12 x 10 <sup>-3</sup>	1.10 x 10 <sup>-3</sup>	1.132	1.016
103.38	1.20 x 10 <sup>-3</sup>	1.07 x 10 <sup>-3</sup>	1.06 x 10 <sup>-3</sup>	1.136	1.016
103.61	1.13 x 10 <sup>-3</sup>	1.01 x 10 <sup>-3</sup>	9.94 x 10 <sup>-4</sup>	1.141	1.017
103.69	1.11 x 10 <sup>-3</sup>	9.92 x 10 <sup>-4</sup>	9.75 x 10 <sup>-4</sup>	1.142	1.017
103.88	1.07 x 10 <sup>-3</sup>	9.45 x 10 <sup>-4</sup>	9.29 x 10 <sup>-4</sup>	1.147	1.018
104.11	1.01 x 10 <sup>-3</sup>	8.91 x 10 <sup>-4</sup>	8.75 x 10 <sup>-4</sup>	1.152	1.019
104.17	9.94 x 10 <sup>-4</sup>	8.78 x 10 <sup>-4</sup>	8.62 x 10 <sup>-4</sup>	1.154	1.019
104.49	9.27 x 10 <sup>-4</sup>	8.14 x 10 <sup>-4</sup>	7.98 x 10 <sup>-4</sup>	1.162	1.020
104.51	9.23 x 10 <sup>-4</sup>	8.10 x 10 <sup>-4</sup>	7.94 x 10 <sup>-4</sup>	1.162	1.020
104.83	8.64 x 10 <sup>-4</sup>	7.53 x 10 <sup>-4</sup>	7.38 x 10 <sup>-4</sup>	1.170	1.021
104.89	8.53 x 10 <sup>-4</sup>	7.43 x 10 <sup>-4</sup>	7.28 x 10 <sup>-4</sup>	1.172	1.021
105.13	8.14 x 10 <sup>-4</sup>	7.07 x 10 <sup>-4</sup>	6.91 x 10 <sup>-4</sup>	1.178	1.022

The following figure shows a subset of these values. The figure also contains RPSD values for 300 modes with the residual vector. As the frequency of this residual vector (1489 Hz) falls outside the range of the input frequency, there is hardly any change in result for 300 modes. Hence, this is taken as the baseline for the analysis. Generally residual vectors should be used to increase accuracy and reduce the number of modes whose frequency is most likely to fall within the input frequency range for spectral analysis.

**Figure 20.7: Improved Accuracy of RPSD Values with Residual Vectors for 50 Modes**



## 20.8. Recommendations

To perform a similar type of analysis, consider the following hints and recommendations:

- If a subsequent MSUP analysis will be performed (for example, a modal superposition transient, harmonic, spectrum or PSD analysis after modal analysis), write the element result to the mode file for use in the expansion pass in the subsequent analysis (**MXPAND,,,,,YES**).
- The **Residual Vector Method** is recommended in the subsequent MSUP analysis if the excitation is known prior to a modal analysis. The residual vector may be insignificant if sufficient modes are extracted.

## 20.9. References

The following references are used in this example problem:

1. Bo Zhang, Han Ding, XinJun Sheng. "Modal analysis of board-level electronic package." *Microelectronic Engineering*. 85: 610-620. 2008.
2. Ying-Chih Lee, Bor-Tsuen Wang, Yi-Shao Lai, Chang-Lin Yeh, Rong-Sheng Chen. "Finite element model verification for packaged printed circuit board by experimental modal analysis." *Microelectronics Reliability*. 48: 1837-1846. 2008.

## 20.10. Input Files

The following files were used in this problem:

- `Electronics_PCB.cdb` -- PCB model information for a single layer (called by other .dat files). The .dat files generate the 3 three-layered PCB structure.
- `psd_full_with_mxpand.dat` -- Input file for the PSD analysis with the full model (300 modes) using `MSUPkey = YES` in **MXPAND**.
- `psd_full_No_mxpand.dat` -- Input file for the PSD analysis with the full model (300 modes) using `MSUPkey = NO` in **MXPAND**.
- `psd_reduced_with_resvec.dat` -- Input file for the PSD analysis using reduced model (50 modes) with residual vector and `MSUPkey = YES` in **MXPAND**.
- `psd_reduced_No_resvec.dat` -- Input file for the PSD analysis using reduced model (50 modes) with no residual vector and `MSUPkey = YES` in **MXPAND**.
- `psd_full_with_resvec.dat` -- Input file for the PSD analysis using full model (300 modes) with residual vector and `MSUPkey = YES` in the **MXPAND** command.

The files are available in the `td-20` folder. See [Obtaining the Input Files \(p. xxxv\)](#) for more information.



---

## Chapter 21: Buckling and Post-Buckling Analysis of a Ring-Stiffened Cylinder Using Nonlinear Stabilization

---

This example demonstrates how to perform a [nonlinear buckling](#) and post-buckling analysis using [nonlinear stabilization](#). The problem uses a stiffened cylinder subjected to uniform external pressure to show how to find the nonlinear buckling loads, achieve convergence at the post-buckling stage, and interpret the results.

Topics related to this example problem follow:

- [21.1. Introduction](#)
- [21.2. Problem Description](#)
- [21.3. Modeling](#)
- [21.4. Material Properties](#)
- [21.5. Boundary Conditions and Loading](#)
- [21.6. Analysis and Solution Controls](#)
- [21.7. Results and Discussion](#)
- [21.8. Recommendations](#)
- [21.9. References](#)
- [21.10. Input Files](#)

### 21.1. Introduction

Buckling analysis is crucial to successful structure design and simulation, especially when thin structures such as shells and beams are involved. While linear buckling analysis is comparatively straightforward, it is limited by approximations and cannot simulate post-buckling phenomena. [Nonlinear buckling analysis](#) does not have these limitations and is therefore preferred, even if it is a little more complicated and requires some trial-and-error experimentation.

By analogy, it is also difficult in the physical world to determine the initiation of buckling. "From a scientific and engineering point of view, the interesting phases of buckling phenomena generally occur before the deformations are very large when, to the unaided eye, the structure appears to be undeformed or only slightly deformed." [1] To perform a nonlinear buckling analysis, special nonlinear analysis techniques are necessary to overcome the convergence difficulties, and a few trials are usually needed.

The following techniques are available for solving instability or buckling problems:

- **Nonlinear stabilization**

This capability deals with both local and global instabilities of buckling and can be used with any other nonlinear technique except the arc-length method.

- **Arc-length method**

This method deals only with global instability or buckling when forces are applied, and can simulate the negative slope region of a load-displacement curve.

- **Running a static problem as a "slow dynamic" analysis**

This technique uses the dynamic effect to prevent divergence, but can be difficult to use.

For more information, see [Unstable Structures](#) in the *Structural Analysis Guide*.

This example uses a ring-stiffened cylinder under external hydrostatic pressure to demonstrate how to predict buckling loads and simulate post-buckling phenomena with the aid of nonlinear stabilization. The numerical simulation results are compared to the reference experimental results.[2]

## 21.2. Problem Description

A circular cylinder made of bare 2024-T3 aluminum alloy is stiffened inside with five Z-section rings. Its ends are closed with thick aluminum bulkheads. A riveted L section exists between the top plate and the top ring and the bottom plate and bottom ring.

The cylinder is subjected to a differential external pressure. The pressure causes a local buckling phenomenon characterized by buckling of the skin between stiffening rings, leading eventually to collapse. The buckling pressure, buckling and collapse pattern, number of waves into which the cylinder buckled, and load-displacement curve are examined and compared to the [reference results](#) (p. 332).

The following table shows the dimensions of the cylinder, ring spacing, and the thicknesses of both cylinder and Z-section rings. The dimensions chosen are based on the reference model.

Dimension	Value (mm)
Cylinder Radius (r)	355.69
Cylinder length (L)	431.8
Ring Spacing (bs)	95.3
Skin thickness (ts)	1.034
Ring thickness (tw)	0.843
Ratio of r/ts	344
Plate thickness	25
Plate diameter	760

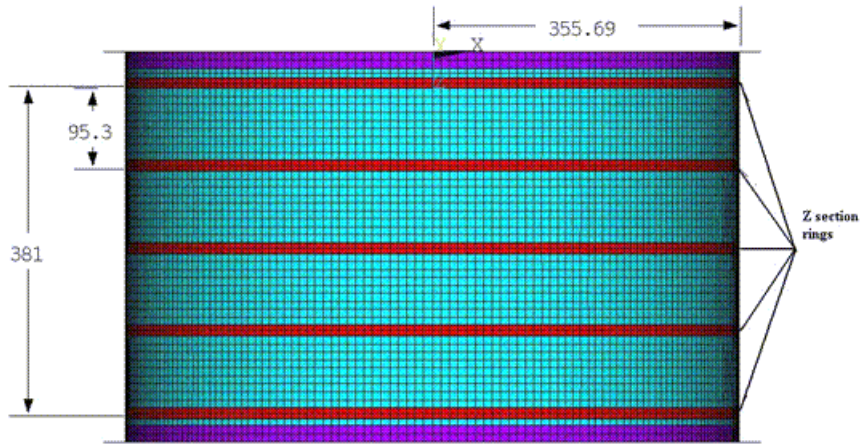
## 21.3. Modeling

The finite element model of the ring stiffened cylinder is meshed with 26,796 [SHELL281](#) elements with an element size of 10 mm. The fine mesh is required for buckling analysis, and a full 360-degree model is necessary because the deformation is no longer axisymmetric after buckling occurs.

All shell elements have uniform thickness. Five sections are created in the model with no offsets, so the shell sections are offset to the midplane by default.

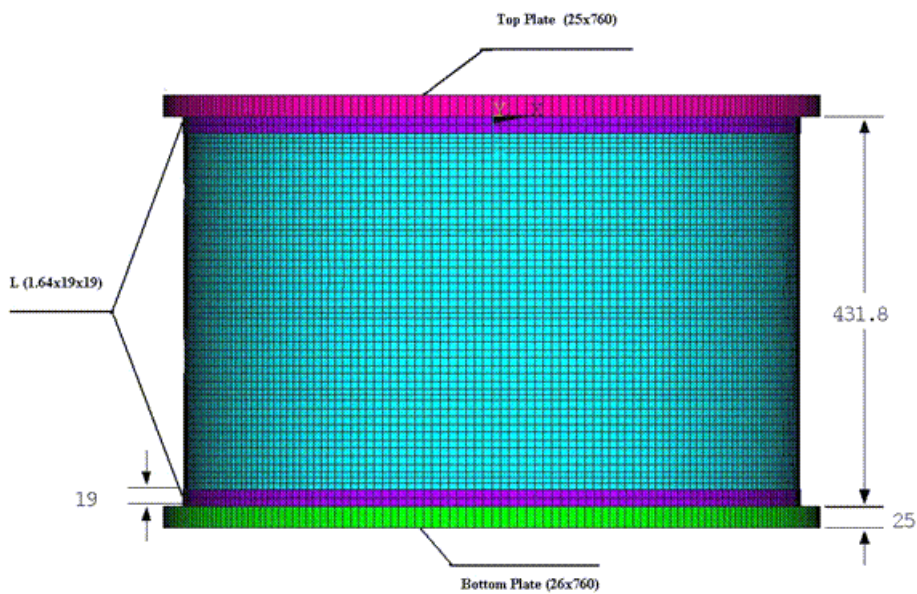
The following figure shows the mesh (a) and the expanded solid representation (b) of the shell mesh ([/ESHape](#)):

**Figure 21.1: Geometry and Finite-Element Model**



a)

Meshed shell model (**/ESHAPE,0**)

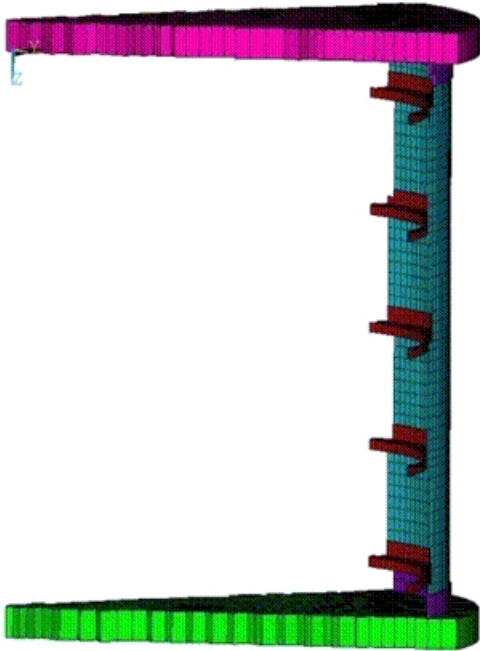


b)

Expanded solid representation of the shell mesh (**/ESHAPE,1**)

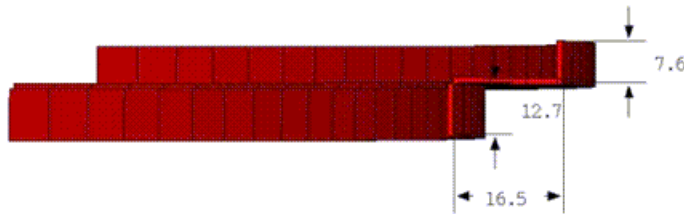
This figure shows a cylinder sector of 45 degrees of the cylinder, plates and Z rings:

**Figure 21.2: Inside View of a 45-Degree Sector**



This figure shows the stiffening ring detail and its dimensions:

**Figure 21.3: Stiffening Ring Detail with Dimensions**



## 21.4. Material Properties

The cylinder, rings and plates are made of 2024-T3 sheet aluminum alloy and have the following material properties (according to AMS 4037 property data):

Cylinder, Ring, and Plate Material Properties	
Young's Modulus (GPa)	$E = 73$
Poisson's Ratio ( $\nu$ )	0.33

The plastic part of the material is modeled using the von Mises yield criteria coupled with an isotropic hardening (**TB,BISO**), described by a bilinear stress-strain curve with the following constants:

Plastic Material Properties	
Yield Stress (MPa)	$\sigma_y = 268.9$
Tangent Modulus (MPa)	$E_T = E / 1000 = 73$



The tangent modulus is assumed, as no data is provided for this property in the reference information. Because the reference [2] does not provide all necessary material data, some of the material data are obtained from other publications detailing the properties of the same material.

## 21.5. Boundary Conditions and Loading

The cylinder type for this problem is used extensively for supporting external pressure loads in submarine hulls and in aerospace applications; therefore, the reference experiment models the cylinder as a free floating object for testing.

For this numerical analysis, the only required boundary conditions are those to prevent the six rigid body motions. A total of six displacements are therefore applied to three nodes located on the top plate at 0, 90, and 270 degrees; the nodes are restricted so that all rigid translations and rotations are not possible for the cylinder.

Loading consists of a uniformly distributed external differential pressure:  $P_{\text{ext}} = 0.24 \text{ MPa}$

## 21.6. Analysis and Solution Controls

In most cases, a linear buckling analysis provides only an upper limit to the buckling behavior of an actual structure. It is generally preferable, therefore, to perform a nonlinear buckling analysis, which can account for the influence of nonlinear material behavior and large-deflection response.

The following analysis and solution-control topics are available:

[21.6.1. Performing the Nonlinear Buckling Analysis](#)

[21.6.2. Post-Buckling Analysis](#)

[21.6.3. Applying Nonlinear Stabilization](#)

### 21.6.1. Performing the Nonlinear Buckling Analysis

The method for obtaining the nonlinear buckling and collapse of the ring-stiffened cylinder is based on the following sequence of actions:

1. [Run a Linear \(Eigenvalue\) Buckling Analysis \(p. 315\)](#)
2. [Generate Imperfections \(p. 316\)](#)
3. [Run the Nonlinear Buckling Analysis \(p. 316\)](#)

#### 21.6.1.1. Run a Linear (Eigenvalue) Buckling Analysis

This preliminary analysis predicts the theoretical buckling pressure of the ideal linear elastic structure (perfect cylinder) and the buckled mode shapes used in the next step to generate the imperfections. It is also an efficient way to check the completeness and correctness of modeling.

To run the linear buckling analysis, a static solution with prestress effects must be obtained, followed by the eigenvalue buckling solution using the [Block Lanczos](#) method and mode expansion, as shown in the following example input:

```

/solu
pstres,on           ! Activate the prestress option
solve
finish
/solu
outres,all,all
antype,buckle      ! Buckling analysis

```

```
bucopt,lanb,10,      ! Mode extraction is Block Lanczos
mxpand,10           ! Expand mode shapes
solve
finish
```

### 21.6.1.2. Generate Imperfections

If a structure is perfectly symmetric (that is, its geometry—including the mesh patterns—and loading are both symmetric), nonsymmetric buckling does not occur numerically, and a nonlinear buckling analysis fails because nonsymmetric buckling responses cannot be triggered.

In this problem, the geometry, elements, and pressure are all axisymmetric. It is not possible, therefore, to simulate nonaxisymmetric buckling with the initial model. To overcome this problem, small geometric imperfections (similar to those caused by manufacturing a real structure) must be introduced to trigger the buckling responses.

Although small perturbation loads can also be introduced to serve the same purpose, it is not an ideal method because it is difficult to determine how large the loads should be and where to apply them. Also, a perturbation load that is too large can change the problem completely.

The geometric imperfections can be generated either in the shape of the buckling mode or in a given shape with a random amplitude:

- The imperfections in the buckling mode shapes are obtained by running a [preliminary linear buckling analysis \(p. 315\)](#), then updating the geometry of the finite-element model to the deformed configuration. This technique is done by adding the displacements of the mode shapes reduced by a scaling factor. It is safe to add a few mode shapes to avoid any bias in the imperfections.
- Introduce pseudo-random imperfections by modifying the coordinates of the nodes with a random number (using the RAND parametric function).

The imperfection magnitudes are generally dependent on the geometry and should be in the same range as the manufacturing tolerance (typically less than one percent) so that they do not change the problem during analysis.

For this problem, the imperfections are added as a sum of the first 10 modes shapes extracted in the preliminary buckling analysis. (While random imperfections can also be used, their disadvantage is that they cannot be repeated; therefore, the results would differ each time the analysis is run.)

Because the radius of the cylinder is 355.69 mm and the maximum displacement of a mode shape is 1 mm, a factor of 0.1 is applied when updating the geometry with mode shapes. The factor assumes the manufacturing tolerance of the radius to be on the order of 0.1. The following input example shows how the imperfections are added:

```
/prep7
*do,i,1,10
upgeom,0.1,1,i,buckling,rst      ! Add imperfections as a tenth of each mode shape
*enddo
finish
```

### 21.6.1.3. Run the Nonlinear Buckling Analysis

The nonlinear buckling analysis is a static analysis performed after adding imperfections with large deflection active (**NLGEOM,ON**), extended to a point where the stiffened cylinder can reach its limit load.

To perform the analysis, the load must be allowed to increase using very small time increments so that the expected critical buckling load can be predicted accurately.

The following example input runs the nonlinear buckling analysis:

```

/solu                                ! Run static analysis
antype,static
nlgeom,on                            ! Specify large deflection
pred,off                             ! No prediction occurs
time,1
nsubst,100,500,10                   ! Minimum time increment is 2e-3
rescontrol,define,all,1              ! Write all files for multiframe restart
outres,all,all                       ! Write all solution items to the database
solve
finish

```

Some convergence difficulty at or after buckling is expected, so it is useful to have all restart files available for resuming the analysis with nonlinear stabilization. It is best to have the restart files at each substep (**RESCONTROL,DEFINE,ALL,1**)--or at least for every few substeps--as it is virtually impossible to know for certain when the buckling is initiated and therefore when to activate the stabilization via the restart.

## 21.6.2. Post-Buckling Analysis

An unconverged solution of the nonlinear static analysis could mean that buckling has occurred, but that is not always the case. The buckling begins to occur *before* the deformations become very large, when the structure appears to be undeformed or only slightly deformed.

Buckling initiation is difficult to detect by visual inspection but can be observed by plotting a load-displacement curve or by a monitor file inspection. To detect the moment of buckling initiation, carefully study the monitor file at this stage, as shown in this figure:

**Figure 21.4: Monitor File of Initial Run**

LOAD STEP	SUB-STEP	NO. ATMP	NO. ITER	TOTL ITER	INCREMENT TIME/LFACT	TOTAL TIME/LFACT	VARIAB 1 MONITOR CPU	VARIAB 2 MONITOR MxDs	VARIAB 3 MONITOR MxPl
1	1	1	2	2	0.10000E-01	0.10000E-01	0.0000	-0.22232E-01	0.78886E-30
1	2	1	2	4	0.10000E-01	0.20000E-01	0.0000	-0.44472E-01	0.78886E-30
1	3	1	2	6	0.15000E-01	0.35000E-01	0.0000	-0.77846E-01	0.78886E-30
1	4	1	2	8	0.22500E-01	0.57500E-01	0.0000	-0.12794	0.78886E-30
1	5	1	2	10	0.33750E-01	0.91250E-01	0.0000	-0.20319	0.78886E-30
1	6	1	3	13	0.50625E-01	0.14188	0.0000	-0.31633	0.78886E-30
1	7	1	3	16	0.75938E-01	0.21781	0.0000	-0.48706	0.78886E-30
1	8	1	3	19	0.10000	0.31781	0.0000	0.94592	0.78886E-30
1	9	1	4	23	0.10000	0.41781	0.0000	1.5706	0.78886E-30
1	10	1	5	28	0.10000	0.51781	0.0000	2.5921	0.78886E-30
1	11	3	3	39	0.20250E-01	0.53806	0.0000	2.7732	0.78886E-30
1	12	2	3	47	0.91125E-02	0.54717	0.0000	2.8471	0.78886E-30
1	13	2	4	55	0.41006E-02	0.55128	0.0000	2.8782	0.78886E-30

From the monitor file, several observations can be made to help determine if buckling has started to occur and at what time, as follows:

- **Difficulties in convergence occur.** The program bisects the load-step increment and attempts a new solution at a smaller load
- **The maximum displacement monitored has an instantaneous change in value.** This is a good indicator of large displacement for a smaller load increment specific to buckling.
- **The maximum displacement monitored has an instantaneous change in sign.** This is another good indication that buckling has begun to occur.

In this example, the change in time (or load) increment, and displacement value, occurs between substeps 10 and 11, which corresponds to TIME = 0.51781 and TIME = 0.53806 and to a pressure between 0.124 MPa and 0.129 MPa. It is therefore very likely that buckling occurred at this time; to be sure, the analysis is continued. The goal is to verify the assessment made at this stage by obtaining the load-displacement behavior over a larger range.

If the convergence difficulty is caused by buckling, resuming the analysis means starting a post-buckling analysis. Because the post-buckling state is unstable, special techniques are necessary to compensate. In a static analysis, **nonlinear stabilization** is the best option. When local buckling or time-dependent material exists, it is the *only* option.

A substep experiencing convergence difficulty in the initial run (13 in this case) should generally be avoided as the substep from which to restart; therefore, to continue with a post-buckling analysis, stabilization is activated from substep 10. If convergence occurs at this substep, and assuming minimal stabilization energy, this solution can be accepted.

The following example input runs the post-buckling analysis:

```
/solu                                ! Run static analysis
antype,,restart,1,10                 ! Perform multiframe restart at substep 10
nsubst,100,10000,10
stabilize,constant,energy,0.000143  ! Use energy method with constant option
solve
finish
```

If convergence does not occur, an earlier substep should be tried.

### 21.6.3. Applying Nonlinear Stabilization

Two methods are available for controlling the stabilization force:

- Apply a damping factor (**STABILIZE,,DAMPING,,,**)
- Apply an energy ratio (**STABILIZE,,ENERGY,,,**)

Selecting which method to use, and then choosing the right value for the energy or damping factor, are not trivial decisions. The best option and value to use depends on the type of instability, the type and size of the elements used in the model, and the end time and number of substeps used for the load step. In most cases, the decision is based on a trial-and-error correction process. The goal is to achieve convergence with the smallest stabilization force, which can be controlled in turn by either an energy ratio or damping factor.

For more information, see [Using Nonlinear Stabilization](#) in the *Structural Analysis Guide*.

The following topics describe the nonlinear stabilization methods tried in the ring-stiffened cylinder problem:

[21.6.3.1. Damping Method](#)

[21.6.3.2. Energy Method](#)

#### 21.6.3.1. Damping Method

The first trial is typically done using the *energy* option because:

- It has a specific range of values that can be used (between 0 and 1), and
- After running, it calculates a damping factor at the beginning of the next substep, providing a reference value for the damping factors that can be used (if damping is chosen as the stabilization method).

The first energy value tried provided a damping factor of 0.1e-2, which helped convergence but without producing significant buckling. The damping values were then gradually reduced to 0.1e-5 and, even though in each case convergence was achieved, the collapse due to buckling did not occur. A value of 0.1e-6 did not result in convergence and the trials for applying the damping factor method ceased.

The observed is due to the localized phenomena inherent in this problem. When damping is applied, the specified value is used for all elements. When the applied damping value is too large, too much stabilization force is applied to the structure, so the system is too stiff and converges easily without much deformation. Conversely, when the applied damping is too small, the unstable elements do not benefit from sufficient stabilization forces, so the solution diverges.

The conclusion is that the damping option is not ideal for problems involving significant local buckling.

### **21.6.3.2. Energy Method**

Because this problem is characterized by local rather than global instabilities, the energy method for stabilization is more helpful. The energy method uses different damping values for different elements, so elements with large instability have higher damping values and elements with little instability have small damping values. It is therefore possible to compensate for the instability without the system becoming too stiff.

After determining that this problem should use stabilization via the energy method, several trials were performed using energy ratios in a range from 0.001 to 0.0001. The trials showed that larger energy ratios result in convergence, but with no significant deformation and excessive stabilization energy, and smaller energy ratios result in no convergence.

The smallest stabilization energy ratio to offer convergence was found to be 0.000143. With that value, the analysis converges and the full loading is reached, while significant buckling is observed and global stabilization energy is kept at the lowest possible level.

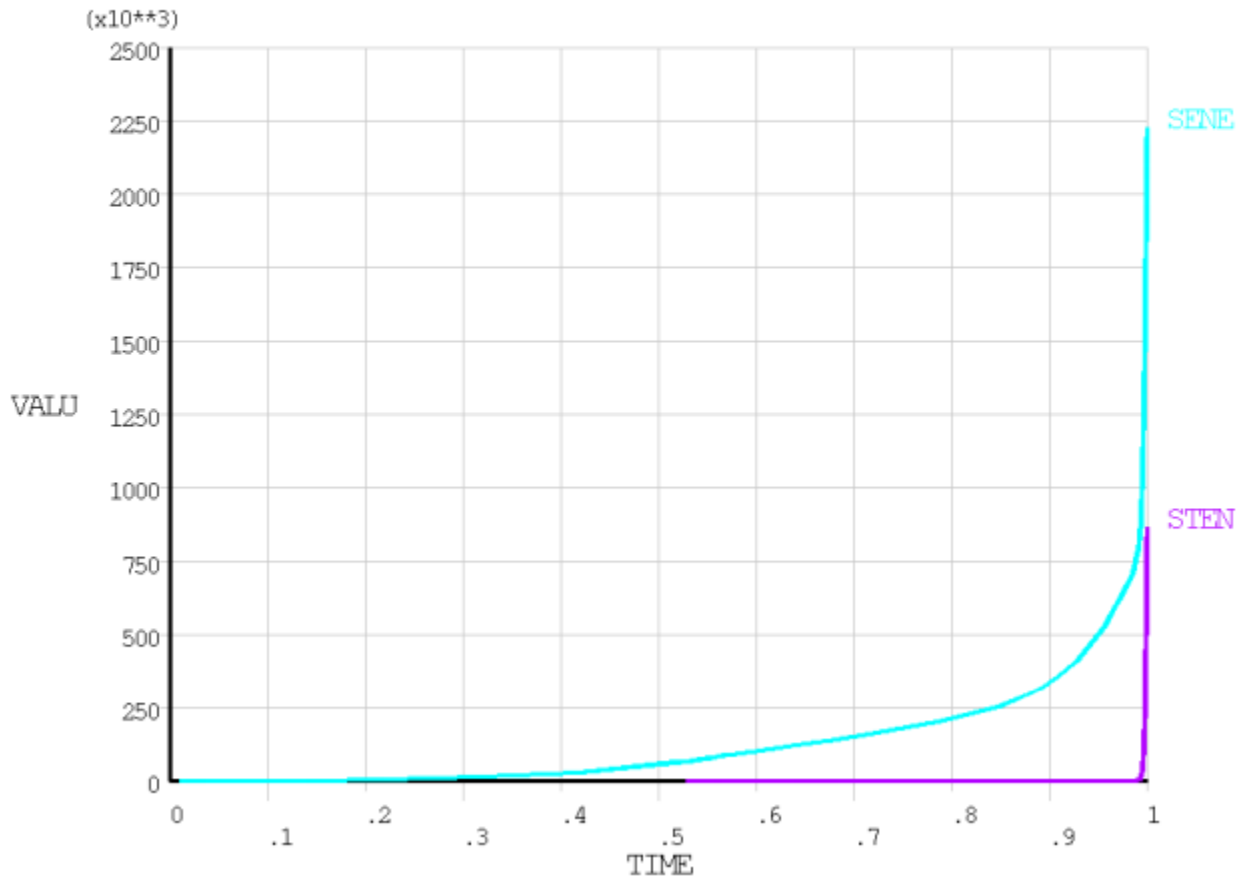
The following figure shows a time-history plot of the stiffness and stabilization energies:

**Figure 21.5: Time-History Plot of Stiffness Energy (SENE) and Stabilization Energy (STEN)**

POST26

SENE

STEN



## 21.7. Results and Discussion

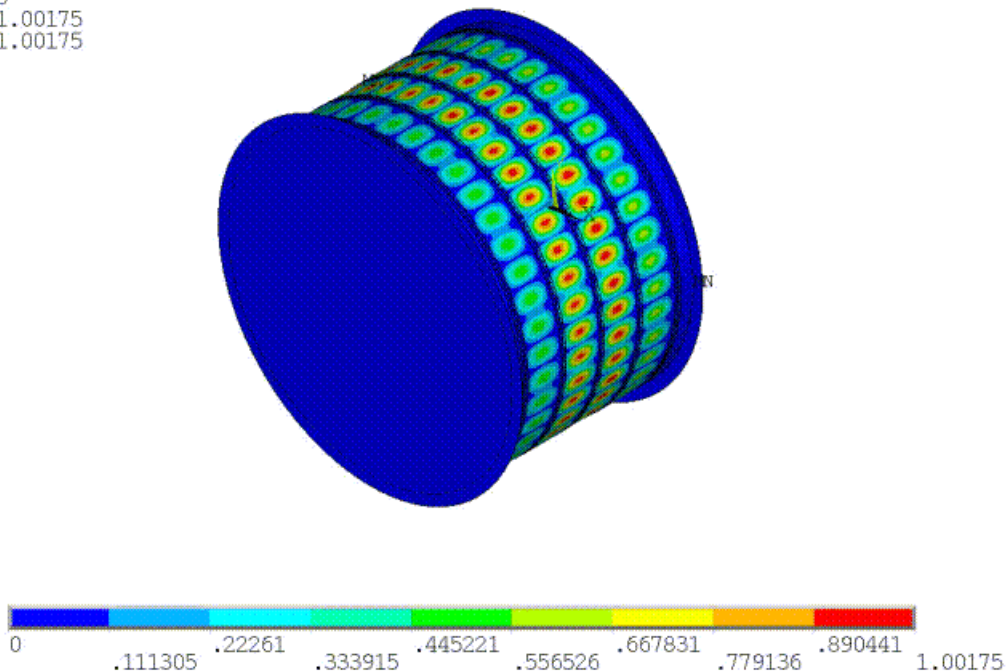
In the following figure, the linear buckling analysis results show 40 circumferential full waves at buckling:

**Figure 21.6: Load Factor and Mode Shape for the First Eigenvalue**

```

NODAL SOLUTION
STEP=1
SUB =1
FREQ=.625712
USUM      (AVG)
RSYS=0
DMX =1.00175
SMX =1.00175

```



The number of waves is more than the number obtained in the reference experiments, predicted by theory, or obtained by the current nonlinear buckling analysis together with post-buckling analysis.

All extracted eigenvalues cluster around a critical value of 0.63, which is equivalent to a buckling pressure of 0.15 MPa. This behavior is expected and is characteristic of a highly symmetrical system such as a ring-stiffened cylinder under hydrostatic pressure. As is the case in this problem, a completely symmetrical system is known to be very sensitive to imperfections because many different modes are associated with the same eigenvalue or closely spaced eigenvalues.[1]

Generally, the results from the nonlinear buckling analysis with stabilization agree with the reference results, as follows:

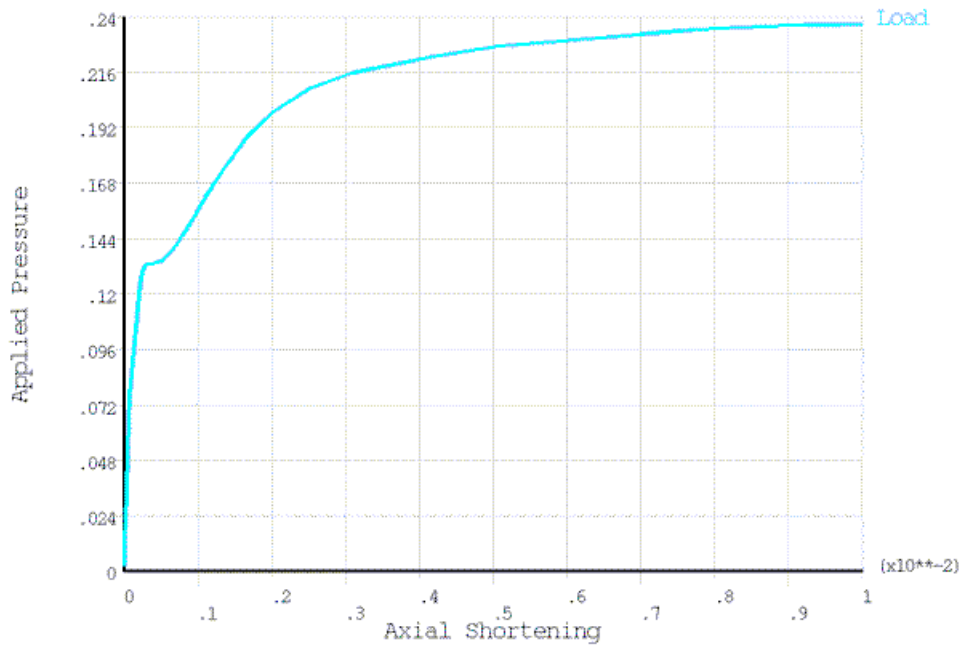
- 21.7.1. Buckling Behavior Is Expected
- 21.7.2. Number of Buckles Decreases
- 21.7.3. Buckle Size and Behavior Is Consistent with Reference Results
- 21.7.4. Plasticity Affects Buckling Results Insignificantly

### 21.7.1. Buckling Behavior Is Expected

Buckling occurs between TIME = 0.5178 and TIME = 0.559, which translates into pressures between 0.124 and 0.134 MPa. These values correlate closely to the reference buckling pressure of 0.121 MPa.

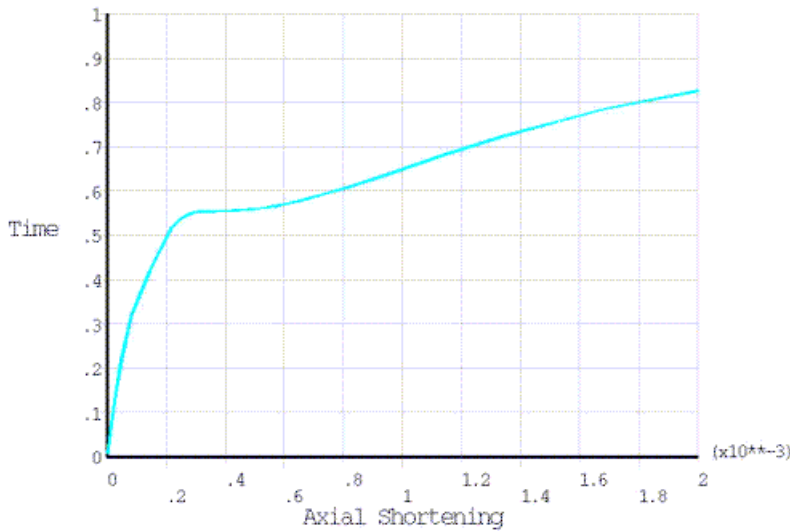
The results can be verified from the plots of applied pressure versus axial shortening for a node located under the first ring. The following figure shows (a) the applied load versus axial shortening for one node, and (b) the axial shortening with time for the same node but using a shorter range of strain (up to 0.002):

Figure 21.7: Applied Pressure and Axial Shortening



a)

Applied pressure vs. axial shortening



b)

Time vs. axial shortening

The shorter range of strain used in plot (b) in the figure above allows changes in the slope of the curve to be easily observed and buckling time (pressure) to be easily predicted. Buckling occurs when the slope of load-displacement curve (the pressure-axial shortening curve in this case) becomes zero or reduces suddenly and significantly.

The displacement is almost constant between times 0.5178 and 0.559, where the load-vs.-displacement slope is zero or slightly negative. As the load approaches the maximum value, the rate of deformation increases very quickly until the cylinder fails.



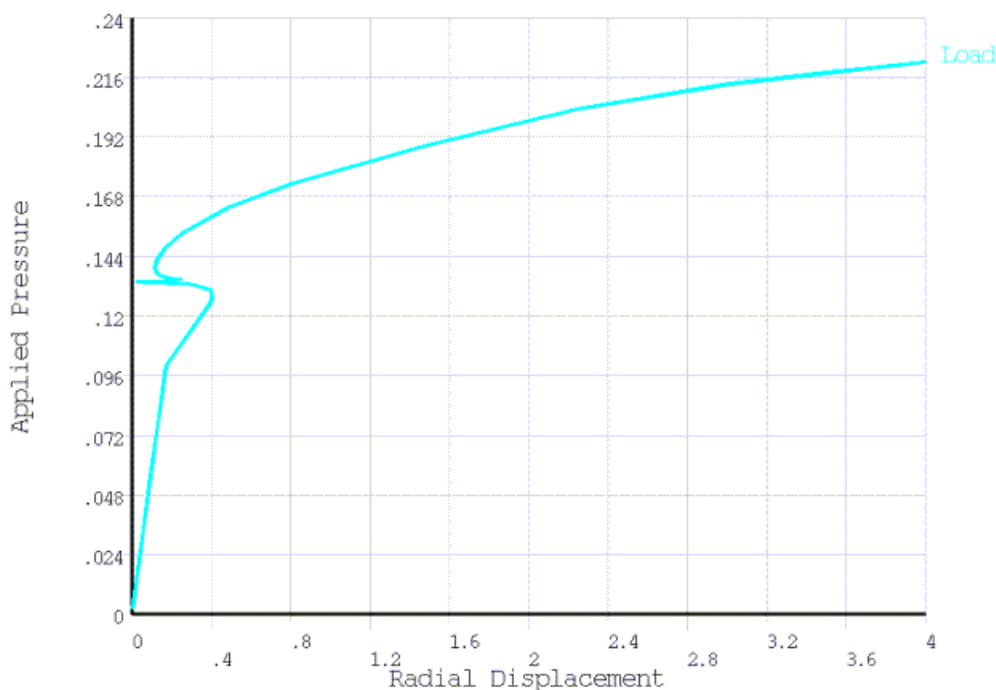
From TIME = 0.98 to TIME = 1, the total deformation increases from 11.2 to 47.7 mm, at which point the rings and the skin between rings fails. The curves agree closely with the experimental results.

### Note

Some material properties are not reported in the reference, and the cylinder used to obtain the reference results may have had defects in addition to the geometric imperfections. Any additional imperfections or differences in material data would of course affect the comparison to the experimental results.[2]

The following figure offers a much better view of the buckling phenomenon, given by the applied pressure vs. radial displacement curve for the node with maximum deformation:

**Figure 21.8: Applied Pressure vs. Radial Displacement**

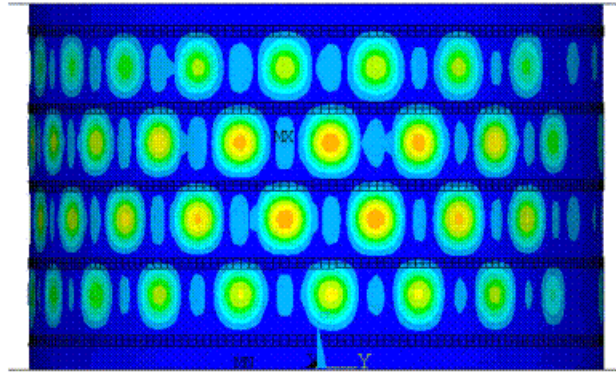


A complex buckling mechanism is evident. Buckling clearly begins to occur at approximately 0.129 MPa, when the displacement ceases to be linear and the slope inverses its direction. The displacement continues with changes in the slope sign (from negative to positive), corresponding to inward and outward displacements of the buckles up to 0.22 MPa. At this point, the displacement increases dramatically and leads to failure.

The following figure shows the total deformation at TIME = 0.5178 (buckling pressure 0.124 MPa) when buckling is initiated; the deformation is hardly detectable by visual inspection, yet the buckling has already occurred:

**Figure 21.9: Total Deformation at the Time of Buckling Initiation**

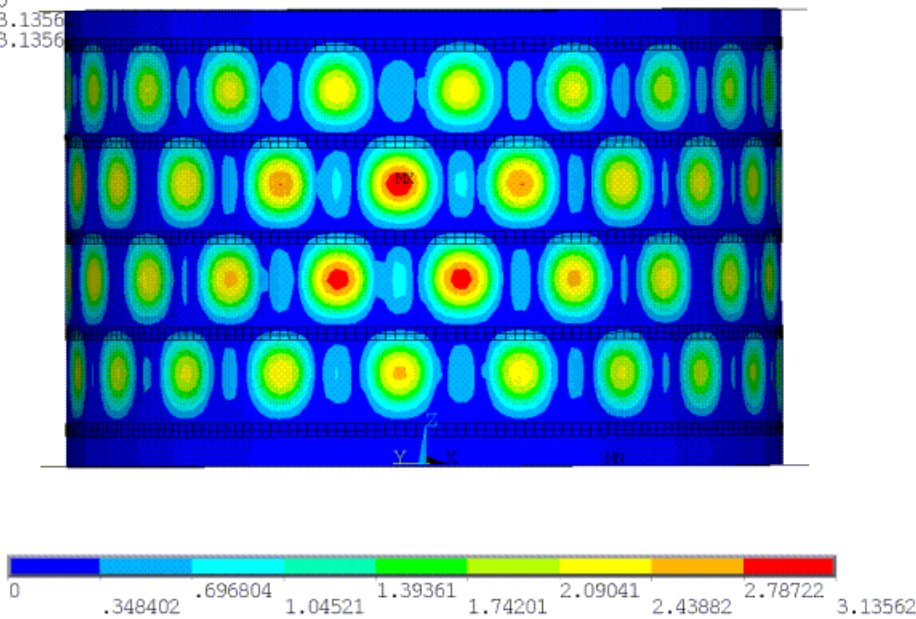
```
NODAL SOLUTION  
STEP=1  
SUB =10  
TIME=.517813  
USUM (AVG)  
RSYS=0  
DMX =2.73935  
SMX =2.73935
```



The following figure shows the deformation at TIME = 0.559 (pressure 0.134 MPa), corresponding to the zero-slope plateau on the applied pressure-axial shortening curve (p. 322). The results are comparable to the reference data and observations.

**Figure 21.10: Total Deformation at Zero Slope on the Load-Deformation Curve**

```
MODAL SOLUTION  
STEP=1  
SUB =18  
TIME=.55955  
USUM (AVG)  
RSYS=0  
DMX =3.1356  
SMX =3.1356
```

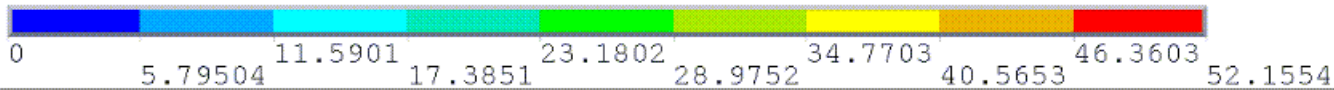
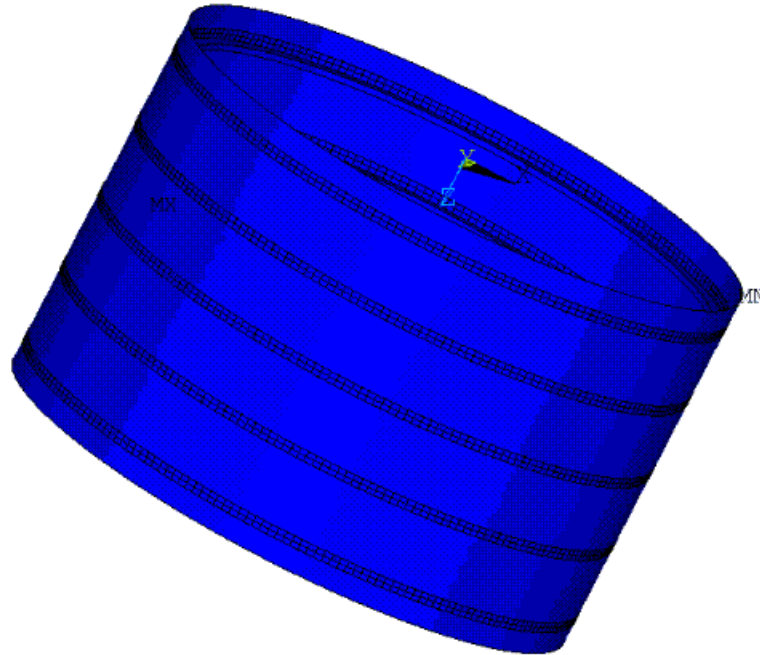


### 21.7.2. Number of Buckles Decreases

As shown in the following animation, the number of buckles decreases throughout the simulation (a behavior also observed in the reference experiment results):

1

```
NODAL SOLUTION  
STEP=1  
SUB =1  
TIME=.01  
USUM (AVG)  
RSYS=0  
DMX =.01538  
SMX =.01538
```



The number of buckles (20) is consistent with theory (20) and close to the reference results (19).

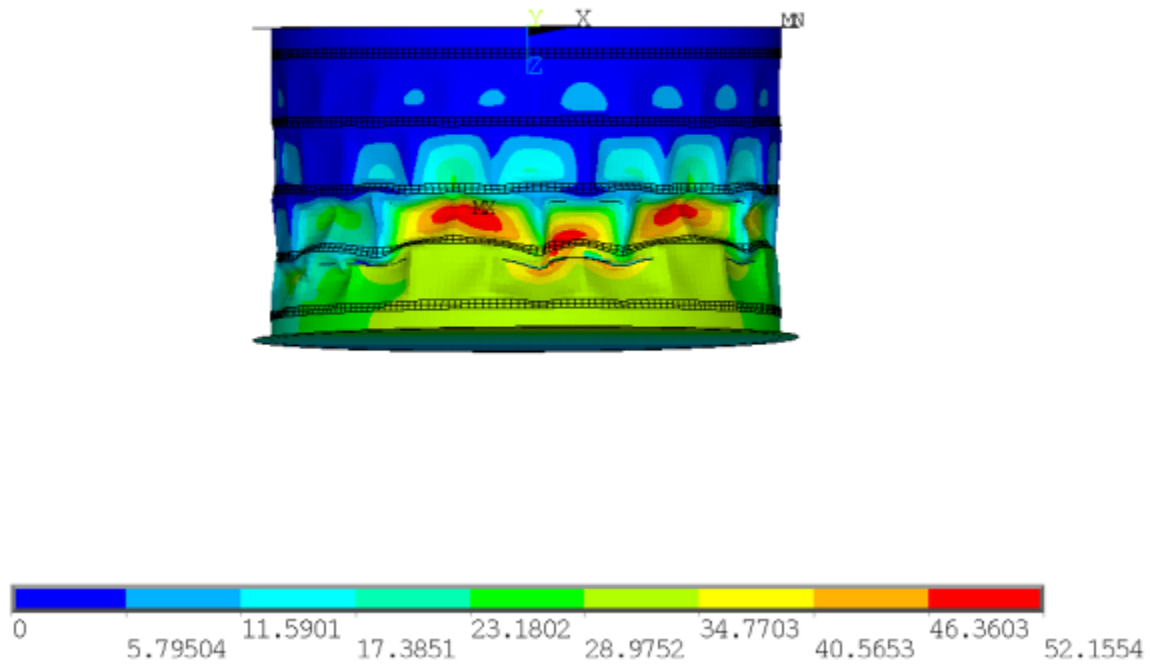
### 21.7.3. Buckle Size and Behavior Is Consistent with Reference Results

The deepest buckles are merged from two waves and are located between the second and third ring. The size of the deepest buckles at collapse is 260 mm (close to the reference size of 300 mm).

The size of the buckles between the first and second ring and the third and fourth ring is 140 mm, which is in good agreement with the corresponding buckle size of 140 mm from the reference results.

**Figure 21.11: Total Deformation at the End of the Post-Buckling Analysis**

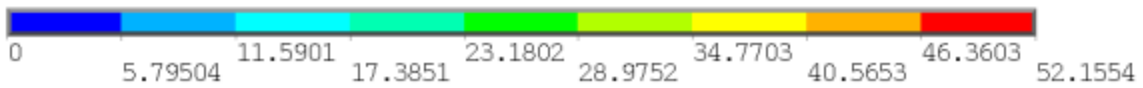
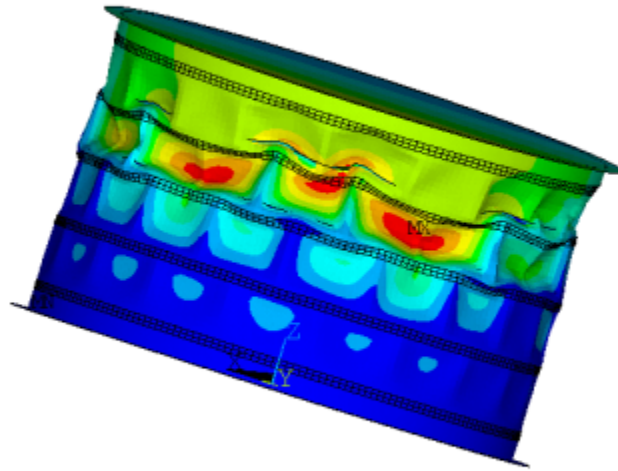
```
NODAL SOLUTION
STEP=1
SUB =88
TIME=1
USUM      (AVG)
RSYS=0
DMX =52.1554
SMX =52.1554
```



The buckles formed on one side of the cylinder before the other side, which is consistent with the reference observations.

**Figure 21.12: Another Total Deformation View**

```
NODAL SOLUTION  
STEP=1  
SUB =88  
TIME=1  
USUM (AVG)  
RSYS=0  
DMX =52.1554  
SMX =52.1554
```

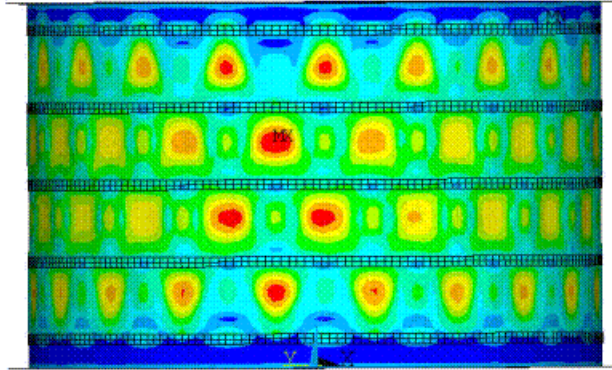


### 21.7.4. Plasticity Affects Buckling Results Insignificantly

Plasticity was not observed to have influenced the reference results nor the simulation results. The von Mises stresses are lower than the yield stress (269 MPa) at buckling, as shown in this figure:

**Figure 21.13: Von Mises Stress Distribution at Buckling Initiation**

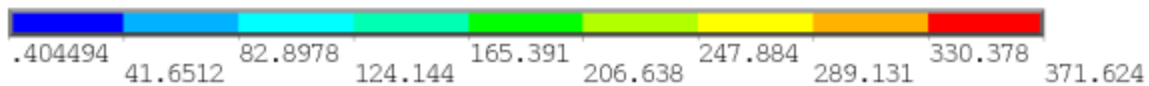
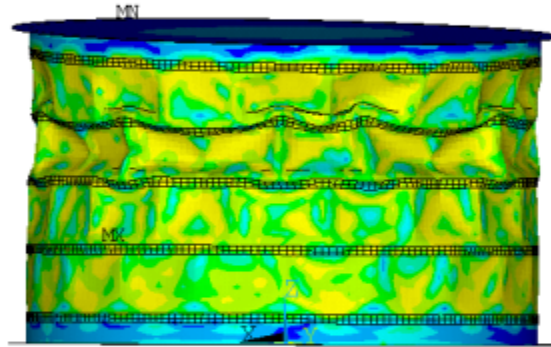
```
NODAL SOLUTION
STEP=1
SUB =10
TIME=.517813
SEQV (AVG)
DMX =2.73935
SMN =.595289
SMX =249.116
```



Only localized areas of high stresses exist at the failure locations between the rings, as shown in this figure:

**Figure 21.14: Von Mises Stress Distribution at the End of the Analysis**

```
NODAL SOLUTION
STEP=1
SUB =88
TIME=1
SEQV      (AVG)
DMX =52.1554
SMN =.404494
SMX =371.624
```



## 21.8. Recommendations

When setting up a similar nonlinear buckling and post-buckling analysis, consider the following hints and recommendations:

- 21.8.1. Buckling Analysis Guidelines
- 21.8.2. Nonlinear Stabilization Guidelines

### 21.8.1. Buckling Analysis Guidelines

When performing the [nonlinear buckling analysis](#), consider the following hints and recommendations:

- **Understand that a nonlinear buckling analysis can be complex.**

A nonlinear buckling or post-buckling analysis is not a single-run analysis but a *set* of analyses. Some advanced nonlinear techniques such as stabilization are necessary in the static analysis which may require trial-and-error experimentation.

- **Perform a linear buckling analysis first.**

It is best to start with a linear buckling analysis to verify the correctness and completeness of the model, and to get a general idea of how large the buckling load may be. In the linear analysis, the mode shapes can be expanded to predict the buckled mode shapes (used for introducing geometric imperfections later).



- **Geometric imperfections or perturbation loads should be introduced.**

Geometric imperfections introduced with modes from the linear buckling analysis are recommended. The magnitude of imperfection should be within the range of manufacturing tolerances.

- **Examine the monitor file.**

When nonlinear analysis stops due to convergence difficulty, the monitor file should be inspected carefully. Many bisections in the substeps indicate instability, and a significant change in the displacement values could mean that buckling is starting to occur.

- **Restart the analysis using nonlinear stabilization.**

To verify the nonlinear buckling load and to perform post-buckling analysis, the analysis should be restarted using some advanced nonlinear technique to examine the load-displacement behavior for a larger range of loads. In a static analysis, nonlinear stabilization is preferred and is the *only* option if local buckling or time-dependent materials exist.

- **Determine the optimal displacement to find the buckling load on the load-displacement curve.**

The buckling load is the load at which the slope of the load-displacement curve reduces significantly. For which node and for which direction the displacement should be chosen depends upon the problem being solved, and a few trials may be necessary to find the optimal displacement. Some displacements show the start of buckling more clearly than others.

## 21.8.2. Nonlinear Stabilization Guidelines

To apply [nonlinear stabilization](#) to achieve convergence in the post-buckling analysis, consider the following guidelines:

- **Establish what type of buckling (local or global) is present.**

The buckling type helps to determine which stabilization method to use (damping or energy). For local buckling, the energy method is the only option. For global buckling, either the energy or damping method can be used.

- **Always try the energy method first using a small value.**

Obtain the damping factor value and use it as a reference value if damping is the desired method to control the stabilization.

Energy is the preferred method in the post-buckling analysis. Because the energy ratio ranges only from 0 to 1, however, damping can be used to obtain very fine control of stabilization forces if necessary. The damping factor can be any positive number, but should not stray too far from the reference value.

When different energy ratios are tried, do not change the number of substeps or time, as this will affect your comparison and therefore your decision as to which stabilization method you should use.

- **Use the smallest damping factor or energy ratio possible.**

The specified energy ratio or damping factor should be large enough to circumvent divergence and small enough to avoid excessive stiffness. The best solution should be the one converged using the smallest energy ratio or damping factor.

- **Activate stabilization via a multiframe restart.**

Although you can activate nonlinear stabilization at the beginning of the solution, in most cases it is more efficient and accurate to activate stabilization in a multiframe restart.

If you do so, save the restart files and restart from the substep *before the last converged substep*. If the substep has many bisections or a large number of iterations, try one substep before, or the substep at which monitored displacement shows significant change (as it is likely the point where buckling starts).

- **Check results after applying stabilization.**

Accuracy can be affected if the stabilization damping or energy values are excessive. The stabilization energy should be much less than the strain energy. Results checking can be done in either the POST1 (/POST1) or POST26 (/POST26) postprocessor.

## 21.9. References

The following references are used in this example problem:

1. Bushnell, D. *Computerized Buckling Analysis of Shells*. New York: Springer, 1985.
2. Dow, Donaldson A. "Buckling and Postbuckling Tests of Ring-Stiffened Circular Cylinders Loaded by Uniform External Pressure." [NASA Technical Note NASA TN D-3111](#). Langley Research Center: November, 1965.

## 21.10. Input Files

The following files were used in this problem:

- `buckling.dat` -- The input file used for the buckling/post-buckling analysis.
- `buckling.cdb` -- The common database file containing the model information for this problem (called by `buckling.dat`).

The files are available in the `td-21` folder. See [Obtaining the Input Files \(p. xxxv\)](#) for more information.

---

## Chapter 22: Modal and Harmonic Frequency Analyses of an Automotive Suspension Assembly Using CMS

---

This example problem shows how to use [component mode synthesis](#) (CMS) to generate dynamic super-elements for use in downstream linear dynamic analyses. The example demonstrates how CMS technology can greatly reduce the use of computational resources and maintain a level of accuracy similar to that of the full model in [modal](#) and [harmonic](#) analyses.

Topics related to this example problem follow:

- [22.1. Introduction](#)
- [22.2. Problem Description](#)
- [22.3. Modeling](#)
- [22.4. Material Properties](#)
- [22.5. Boundary Conditions and Loading](#)
- [22.6. Analysis and Solution Controls](#)
- [22.7. Results and Discussion](#)
- [22.8. Recommendations](#)
- [22.9. References](#)
- [22.10. Input Files](#)

### 22.1. Introduction

Automotive suspension systems contribute to a car's handling and braking to improve safety, and keep vehicle occupants comfortably isolated from road noise, bumps, and vibrations. When a car moves on uneven terrain, the wheels are subjected to base excitation. For analysis purposes, this can be approximated as harmonic excitation. Because the suspension forms part of the chassis in a car, response of the suspension system to harmonic displacement excitation is a critical subject for analysis.

[Component mode synthesis](#) (CMS) is a form of substructure-coupling analysis frequently used in structural dynamics. CMS enables the behavior of the entire assembly to be derived from its constituent components. First, the dynamic behavior of each component is formulated. Then, the dynamic characteristics of the full system model are formed by enforcing equilibrium and compatibility along component interfaces. CMS is more accurate than the Guyan reduction for modal, harmonic, and transient analyses because CMS includes truncated sets of normal mode generalized coordinates, which capture the basic modal characteristics of the components.

For more information, see the following resources:

- [Benefits of Substructuring in the \*Mechanical APDL Substructuring Analysis Guide\*](#)
- [Component Mode Synthesis in the \*Mechanical APDL Substructuring Analysis Guide\*](#)
- [Component Mode Synthesis \(CMS\) in the \*Mechanical APDL Theory Reference\*](#)

## 22.2. Problem Description

The model used in this analysis is a slightly asymmetric [automotive suspension assembly](#) (p. 334). The analysis calculates the response of two points attached to a link on the body due to a harmonic (sinusoidally varying) displacement excitation at the bottom of the wheels. The displacements of the response points are determined for a specified frequency range. Modal and harmonic analyses are performed. Results using the CMS generated models are compared to results for a full (non-substructure) model.

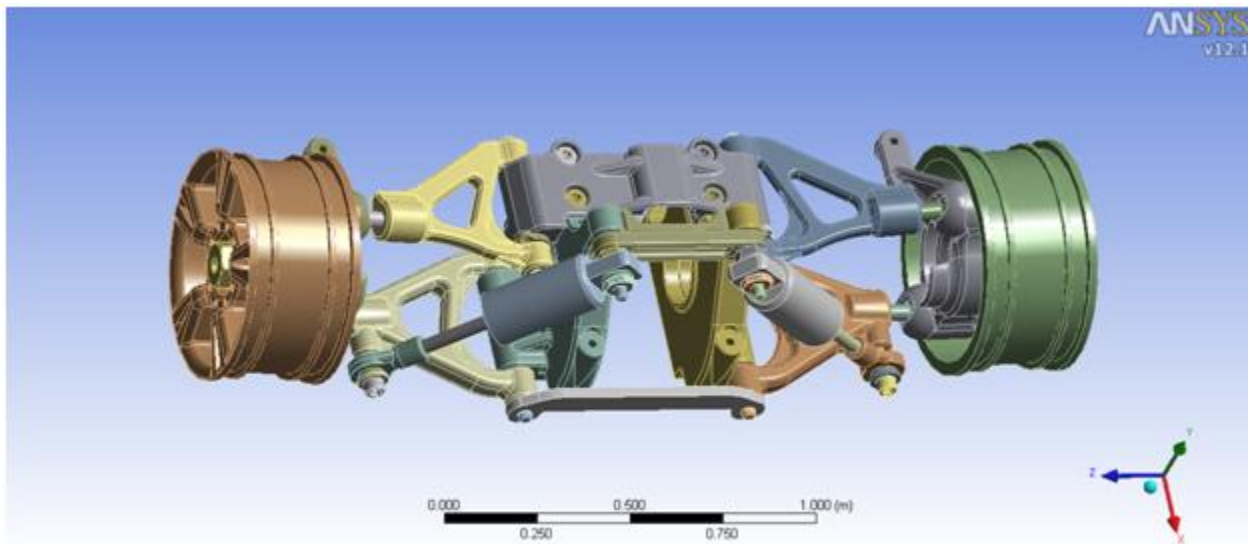
## 22.3. Modeling

The assembly shown in [Figure 22.1: 3-D Suspension Model](#) (p. 334) consists of two wheels and a body. A wheel consists of 11 parts, and the wheels are attached to the body via shafts. The body consists of 53 parts, and the dimension of the overall bounding box is  $0.79594 \times 0.79324 \times 2.5252$  (in meters).

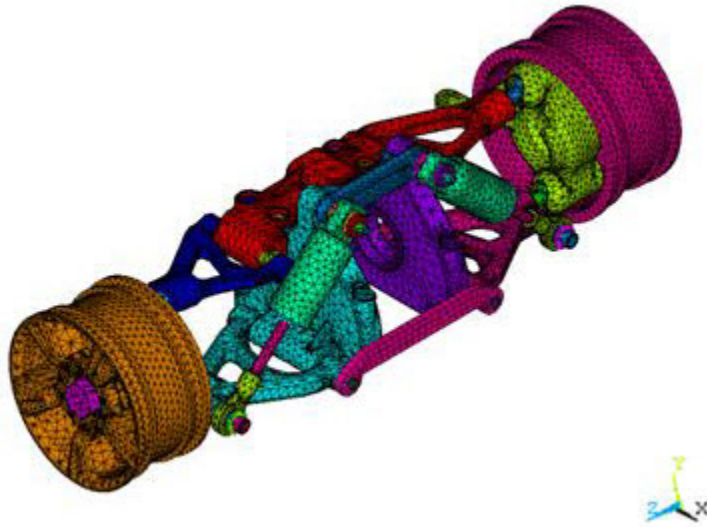
The model uses [SOLID186](#), [SOLID187](#), and [BEAM188](#) elements. [SOLID186](#) is a 3-D 20-node solid element exhibiting quadratic displacement behavior suitable for modeling homogeneous structural solids. [SOLID187](#) is a 3-D 10-node element that exhibits quadratic displacement behavior, but is suitable for modeling irregular meshes. [BEAM188](#) is a 3-D 2-node linear element used for linear elements to create general welds between different parts in contact. Bonded contact is assumed. This contact prevents relative displacement between the different parts of the assembly.

The parts of the model are made of structural steel and have a combined mass of 1250.1 kg.

**Figure 22.1: 3-D Suspension Model**



Tetrahedral and hexahedral dominant meshes are used to mesh the assembly. The model has 305,968 nodes and 165,901 elements. [Figure 22.2: Meshed Suspension Model](#) (p. 335) shows the meshed model of the assembly.

**Figure 22.2: Meshed Suspension Model**

## 22.4. Material Properties

Isotropic linear elastic materials are used to model all parts.

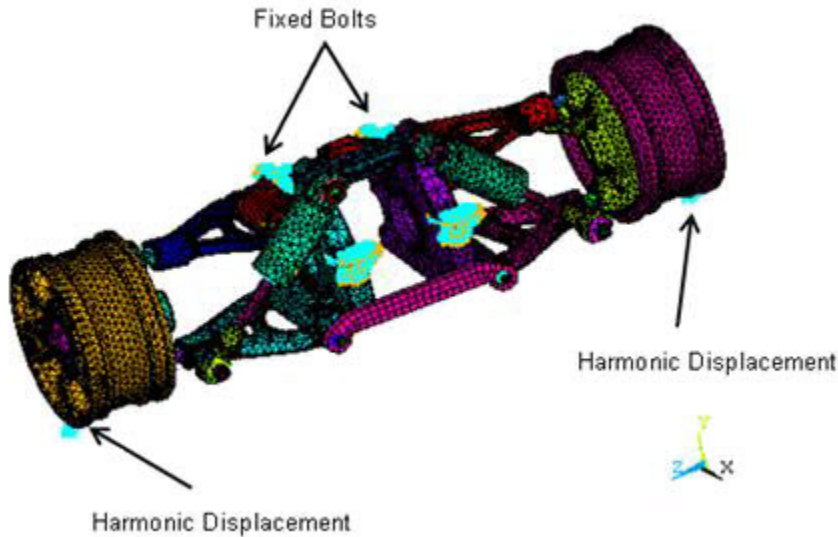
Material properties for all components of the suspension assembly	
Young's Modulus (N/m <sup>2</sup> )	2.0 E+11
Poisson's Ratio	0.30
Density (Kg/m <sup>3</sup> )	7850

For the harmonic analysis, a constant damping ratio of 5 percent is used to prevent possible large-response amplitudes.

## 22.5. Boundary Conditions and Loading

As shown in the following figure, the six bolts on top of the body are constrained in all directions. Sinusoidal displacement excitation is applied at three nodes at the bottoms of both wheels.

**Figure 22.3: Suspension Assembly with Boundary Conditions and Displacement Loading**



The following example input shows how the boundary conditions are applied in the generation pass of the CMS model:

```

/FILNAME, BODY
/SOLU
/COM, SELECT A SUBSET OF THESE NODES
CMSEL, S, BOLT1      ! Select a new subset of components named Bolt1
CMSEL, A, BOLT2      ! Additionally select a set Bolt2 and extend the current set
CMSEL, A, BOLT3      ! Additionally select a set Bolt3 and extend the current set
CMSEL, A, BOLT4      ! Additionally select a set Bolt4 and extend the current set
CMSEL, A, BOLT5      ! Additionally select a set Bolt5 and extend the current set
CMSEL, A, BOLT6      ! Additionally select a set Bolt6 and extend the current set
ESLN                ! Select the elements attached to the selected nodes
NSLE                ! Select the nodes attached to the selected elements
D, ALL, ALL         ! Constrain the nodes for all degrees of freedom
    
```

The loading is applied in the form of harmonic displacement in the vertical y direction on a selected set of nodes on both the wheels. The sample input shows how the displacement loading is applied in the full harmonic analysis:

```

/COM, NODES AT THE BOTTOM OF THE FIRST WHEEL FOR EXCITATION
N1=NODE(-0.13838, -0.28280, 1.0714) ! Node #191882
N2=NODE(-0.13733, -0.28293, 1.0501) ! Node #192365
N3=NODE(-0.13786, -0.28287, 1.0608) ! Node #210243

/COM, NODES AT THE BOTTOM OF THE SECOND WHEEL FOR EXCITATION
N4=NODE(-0.14007, -0.28151, -1.3531) ! Node #260357
N5=NODE(-0.14043, -0.28140, -1.3638) ! Node #278577
N6=NODE(-0.14079, -0.28129, -1.3744) ! Node #259968
FINISH

/SOLU
ANTYPE, HARMONIC    ! Perform a harmonic analysis
HROPT, FULL        ! Employ the full method
KBC, 1             ! Use the same value of the load for each substeps
DMPRAT, 0.05      ! Set a constant damping ratio of 5%

HARFRQ, 160, 200   ! Choose the frequency range between 160 and 200 Hz
NSUBST, 20        ! Number of substeps = 20

/COM, LOCATION OF THE LOAD ON THE FIRST WHEEL

NSEL, S, NODE, , N1 ! Select the node n1 as a new subset
    
```

```

NSEL, A, NODE, , N2 ! Additionally select the node n2 and extend the current set
NSEL, A, NODE, , N3 ! Additionally select the node n3 and extend the current set

/COM, LOCATION OF THE LOAD ON THE SECOND WHEEL

NSEL, A, NODE, , N4 ! Additionally select the node n4 and extend the current set
NSEL, A, NODE, , N5 ! Additionally select the node n5 and extend the current set
NSEL, A, NODE, , N6 ! Additionally select the node n6 and extend the current set

D, ALL, UY, 100 ! Define a displacement degree of freedom on these nodes in the y
                ! direction. This harmonic displacement amplitude = 100.
NSEL, ALL      ! Restore the full set of nodes before solving
SOLVE         ! Solve the full model for harmonic analysis
FINISH

```

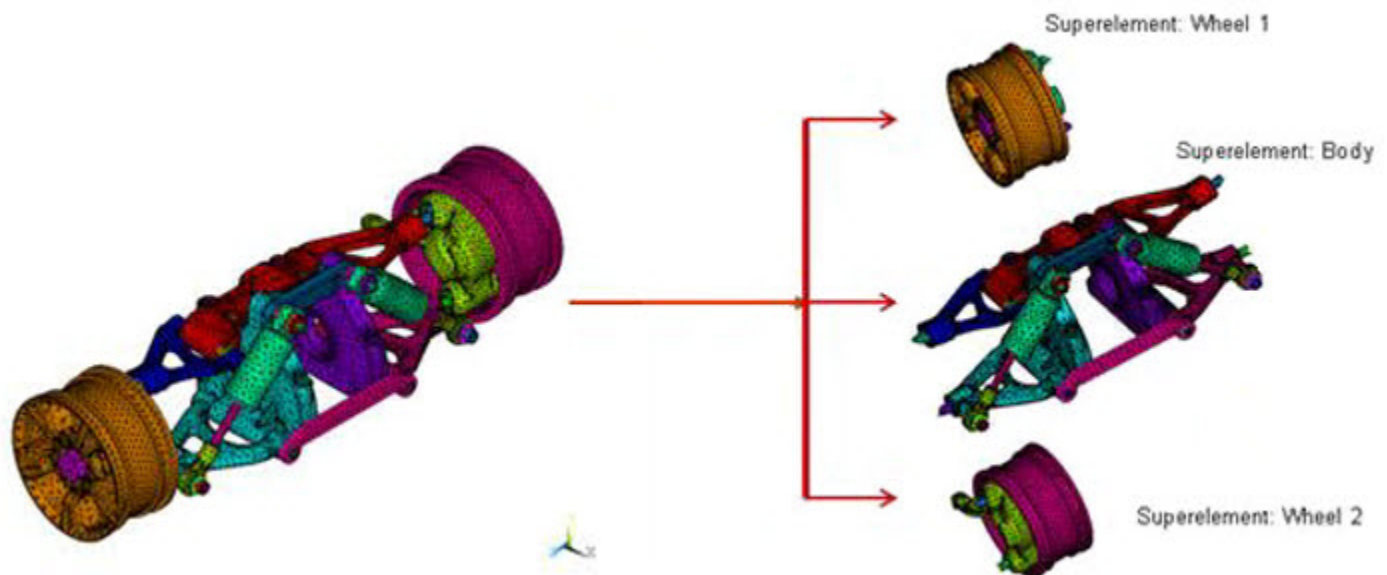
## 22.6. Analysis and Solution Controls

The solution control and analysis settings are different for the full and CMS models. CMS generates substructures with generalized modal coordinates. This section describes substructure and CMS techniques for modal and harmonic analyses with the relevant analysis settings and solution controls.

### 22.6.1. Substructure

Substructuring is a procedure that condenses a group of finite elements into one element represented as a matrix. The single-matrix element is called a superelement. The substructure analysis uses the technique of matrix reduction to reduce the system matrices to a smaller set of degrees of freedom (DOFs). The use pass of a substructure reduces the computer time and enables the solution of very large problems with limited computer resources. The following figure shows how the suspension assembly is divided into three superelements: Wheel1, Wheel2, and Body.

**Figure 22.4: Superelements of the Suspension Assembly**



A substructure analysis involves three distinct steps called passes: the generation pass, the use pass, and the expansion pass.

#### 1. Generation pass

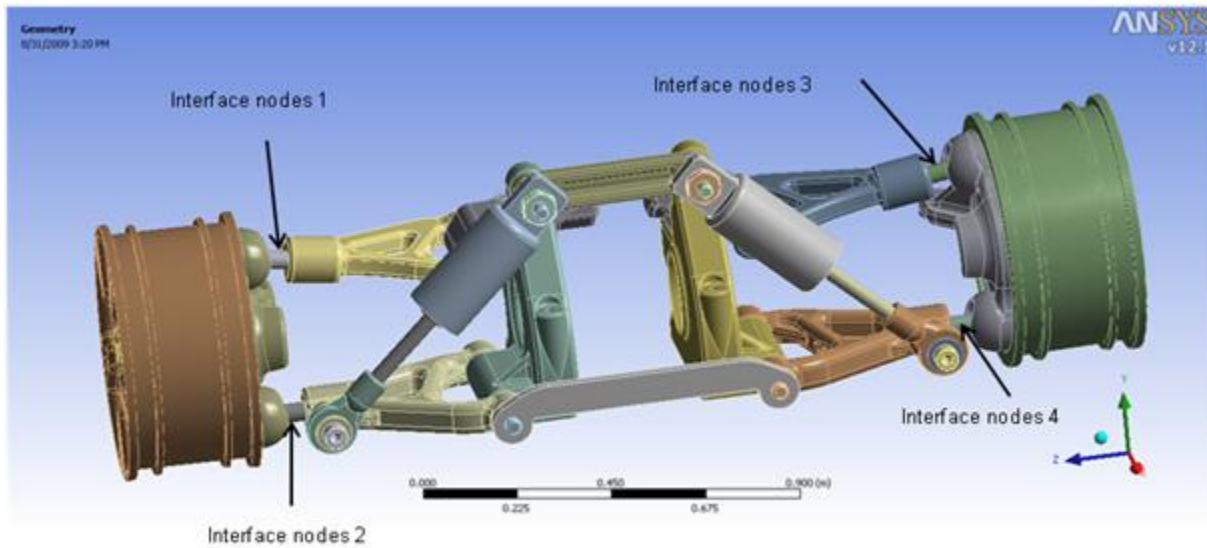
The objective of the generation pass is to condense a group of standard finite elements into a single superelement. The elements are condensed by identifying a set of master degrees of freedom

(MDOFs) known as *master nodes*. Master nodes are used to define the interface between the super-element and the other elements and to capture the characteristics for the dynamic analyses.

Proper choice of the interface master nodes is important to maintain continuity among the super-elements and the other parts of the model. To optimize solution time, select the interface with the fewest nodes that still maintains continuity. For a 3-D model, select the interface at a region of minimum cross-sectional area. For a 2-D model, you would select the interface at a region of minimum length.

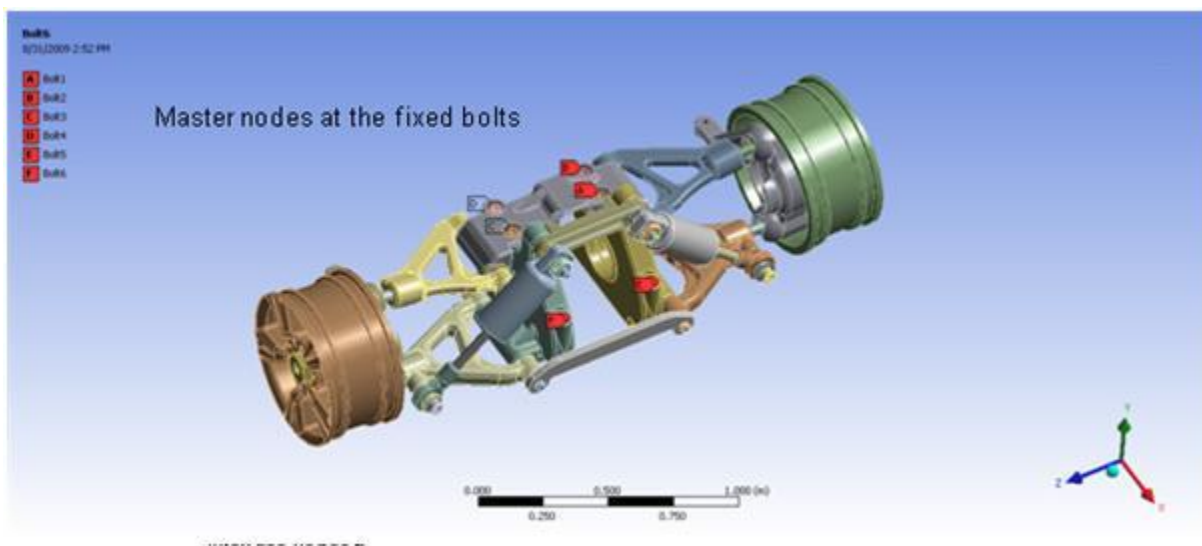
As shown in the following figure, the interface master nodes are defined on the shafts connecting the wheels and the body because the cross-sectional areas of the shafts are minimal compared to the other parts.

**Figure 22.5: Interface Master Nodes Between the Superelements of the Suspension Assembly**



The Master nodes are also defined where boundary conditions or constraint equations are applied, as shown in the following figure:

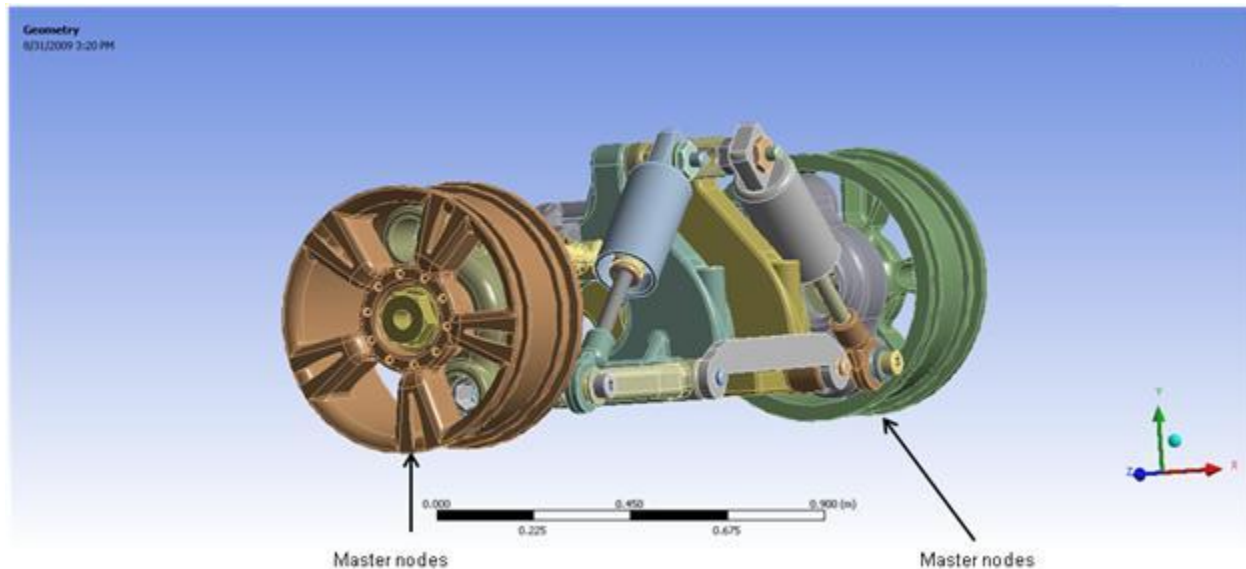
**Figure 22.6: Master Nodes Defined at Fixed Bolts**





For the harmonic analysis, the points of load application are also defined as master nodes, as shown in this figure:

**Figure 22.7: Master Nodes Defined at Points of Application of Harmonic Displacement**



In the use pass (described below), the master nodes are the only nodes available for a superelement. The interface master nodes associated with Wheel1 and Body are named component “master1.” Master nodes associated with Wheel2 and Body are named component “master2.” In the substructure analysis, the superelement Wheel1 consists of the first wheel and the attached shafts up to “master1” and is termed Wheel1\_for\_solve. Likewise, the superelement Wheel2 consists of the second wheel and the attached shafts up to “master2” and is termed Wheel2\_for\_solve.

The following example input shows how the superelement of the first wheel is created after defining the master nodes:

```

/FILNAME, FIRSTWHEEL ! Name of the Superelement is FirstWheel
/SOLU
CMSEL, S, MASTER1, NODE ! Select a new set of interface nodal components named master1
M, ALL, ALL ! Define them as master nodes

/COM, SELECT A SET OF NODES FOR POINT OF APPLICATION OF HARMONIC DISPLACEMENT ON THE FIRST WHEEL
NSEL, S, NODE, , N1 ! Select the node n1 as a new subset
NSEL, A, NODE, , N2 ! Additionally select the node n2 and extend the current set
NSEL, A, NODE, , N3 ! Additionally select the node n3 and extend the current set
M, ALL, ALL ! Define them as master nodes

ALLSEL, ALL
CMSEL, ALL

NUM_MODES = 100 ! Number of modes to extract for each component = 100
/SOLU
ANTYPE, SUBSTR ! Perform a substructure analysis
SEOPT, FIRSTWHEEL, 2 ! Generate the stiffness and mass matrices
CMSOPT, FIX, NUM_MODES, 0, 100000 ! Use fixed-interface method to extract 100 modes between 0 and a
! large number
CMSEL, S, WHEEL1_FOR_SOLVE ! Select a new subset of components to create the superelement
! associated with the first wheel and the attached shaft
ESLN, S ! Select a new set of elements attached to the selected nodes
SOLVE
FINISH
SAVE

```

## 2. Use pass

The superelement is used to make it a part of the whole model. The entire model may be a superelement, or the superelement may be connected to non-superelements.

The solution from the use pass consists of only the reduced solution for the superelement, which is the DOF solution only at the MDOF, and the complete solution for non-superelements.

### 3. Expansion pass

The results at all DOFs in the superelement are calculated at the start of the expansion pass. If multiple superelements are used in the use pass, a separate expansion pass will be required for each superelement.

The reduced solution obtained from the use pass is applied to the model as displacement boundary conditions, and the complete solution within the superelement is solved.

The expansion pass logic for substructuring analysis searches for the superelement .LN22 file and, if found, uses the sparse solver to perform a back-substitution.

You can specify a load step and a substep for expanding a particular frequency (**EXP SOL**).

## 22.6.2. Component Mode Synthesis

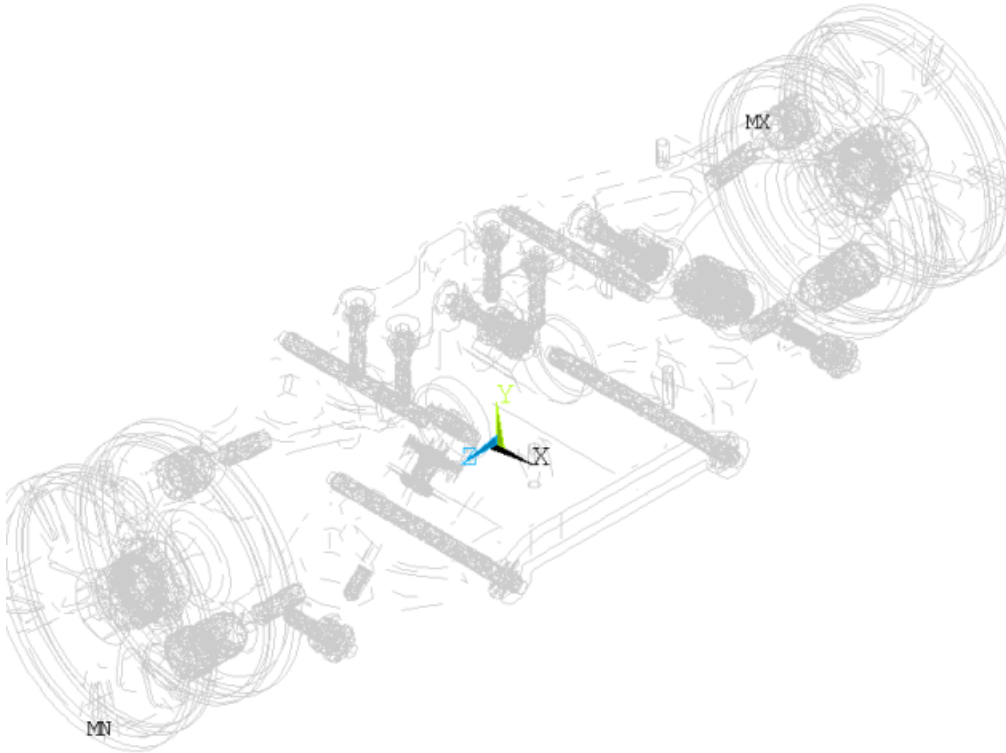
Using **component mode synthesis** (CMS), the dynamic characteristics of the full system model are formed by first formulating the dynamic behavior of each of the components, and then enforcing equilibrium and compatibility along component interfaces.

The generated substructure information in CMS is in the .sub file, which is all that is required in the use pass. Because the internal details of the structure are not exposed using CMS, specialized teams can work on the same structure without having to provide detailed or proprietary information about the component. The superelements created in the generation pass are combined in the use pass with knowledge of master nodes. The superelements are given a new element type: **MATRIX50**.

The following sample input shows how the superelements are combined in the use pass.

```
/FILENAME, USE
/PREP7
*GET, MAX_ETYPE, ETYP, , NUM, MAX ! Retrieve the value of the maximum element type number
! and store it as MAX_ETYPE
ET, MAX_ETYPE+1, 50 ! Define Matrix50 as the next element type number
TYPE, MAX_ETYPE+1 ! Assign this type number to the elements
MAT, 1 ! Assign 1 as the material number to subsequently defined
! elements
REAL, MAX_ETYPE+1 ! Set the element real constant set attribute pointer
SE, FIRSTWHEEL ! Define the superelement associated with the Wheel1
SE, BODY ! Define the superelement associated with the Body
SE, SECONDWHEEL ! Define the superelement associated with the Wheel2
FINISH
```

The following figure shows the resulting superelements:

**Figure 22.8: Superelement of the Suspension Model After the Use Pass**

A CMS substructure can be advantageous over a basic substructure because it is more accurate than a Guyan reduction for model, harmonic, and transient analyses. CMS includes truncated sets of normal modal generalized coordinates that characterize the behavior of the components of the structural model.

A typical use of CMS involves modal analysis of a large, complicated structure (such as an aircraft or nuclear reactor) where various teams are in charge of the design of a component of the structure. With CMS, design changes to a single component affect only that component; therefore, additional generation passes are necessary only for the modified substructure.

The following CMS options are available:

- Fixed-interface (**CMSOPT,FIX**), where interface nodes are constrained during the CMS superelement generation pass.
- Free-interface (**CMSOPT,FREE**), where interface nodes remain free during the CMS superelement generation pass.
- Residual-flexible free-interface (**CMSOPT,RFFB**), where interface nodes remain free during the CMS superelement generation pass.

The fixed-interface CMS method is preferable for most analyses. The free-interface method and the residual-flexible free-interface method are useful when an analysis requires more accurate eigenvalue computation at the mid to high end of the spectrum. As in substructuring, a component mode synthesis analysis involves three distinct steps or passes. In CMS generation pass, a group of finite elements are condensed into a single CMS superelement that includes a set of master degrees of freedom (MDOFs) and truncated sets of normal mode generalized coordinates. The MDOFs serve to define the interface between the superelements and the other elements. The CMS use pass and expansion pass utilize the same procedure as a basic substructure analysis.

As multiple superelements were used for the present model in the use pass, a separate expansion pass would usually be required for each of them. However, since the response nodes belong to the superelement Body, expansion of this superelement is sufficient.

### 22.6.3. Modal Analysis

A modal analysis determines the natural frequencies and mode shapes of a structure. These are important parameters in the design for dynamic loading conditions, and required to perform a spectrum, mode-superposition harmonic, or transient analysis. Several mode-extraction methods are available: Block Lanczos, Supernode, PCG Lanczos, unsymmetric, damped, and QR damped. The damped and QR damped methods allow inclusion of damping in a structure. The QR damped method also allows for the unsymmetrical damping and stiffness matrices.

Modal analysis is a linear analysis aimed at finding the eigensolution; therefore, no force is involved in the modal analysis. Nonlinearities, such as plasticity and contact (gap) elements, are ignored even if they are defined. In this model, the Block Lanczos method is used to extract the modes with the boundary conditions shown in [Figure 22.6: Master Nodes Defined at Fixed Bolts \(p. 338\)](#).

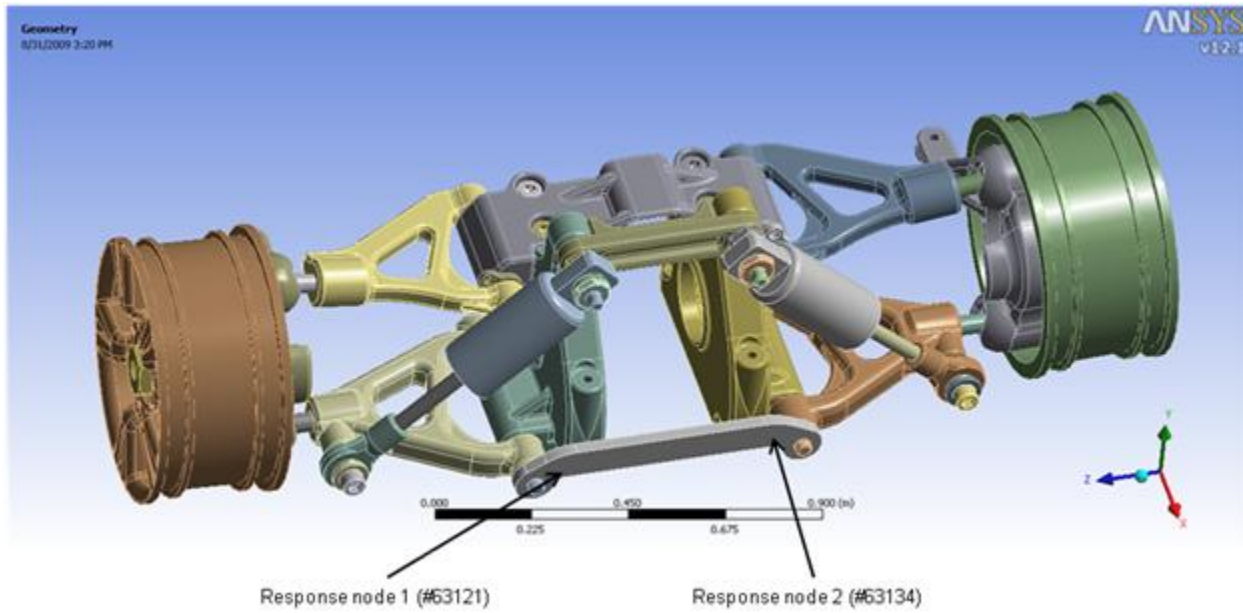
### 22.6.4. Harmonic Analysis

A harmonic analysis determines the steady-state response of a linear structure to loads that vary sinusoidally (harmonically) with time. The structure's response is determined over a range of frequencies and a response quantity (usually displacements) is plotted versus frequency. Peak responses are then identified on the graph, and stresses are reviewed at those peak frequencies.

This analysis technique calculates only the steady-state, forced vibrations of a structure. The transient vibrations, which occur at the beginning of the excitation, are not accounted for in a harmonic analysis. Harmonic analysis is typically linear. Some nonlinearities, such as plasticity are ignored, even if they are defined; however, unsymmetric system matrices (such as those encountered in a fluid-structure interaction problem ) can be accommodated in the harmonic analysis.

In the present model, base excitation is applied in the form of sinusoidal displacement in the vertical y-direction at selected nodes on both wheels. Those nodes are defined as master nodes in the generation pass (as shown in [Figure 22.3: Suspension Assembly with Boundary Conditions and Displacement Loading \(p. 336\)](#) and [Figure 22.7: Master Nodes Defined at Points of Application of Harmonic Displacement \(p. 339\)](#)).

The response is calculated at the response nodes specified during the expansion pass, as shown in this figure:

**Figure 22.9: Non-Master Nodes for Response Calculation in the Expansion Pass**

As the response nodes belong to only one of the superelements (Body), the results file of Body is used for the response calculation. The following example input performs the expansion pass with postprocessing:

```

/CLEAR, NOSTART
/FILNAME, BODY ! Change the jobname to Body
RESUME, , ! Resume the database file Body.db
/SOLU
EXPASS, ON ! An expansion pass will be performed
OUTRES, ALL, ALL ! Write the solution of the specified solution results item for
! every substep in the database
SEEXP, BODY, USE ! Specify the name of the dsub file as use, containing the
! superelement degree-of-freedom (DOF) solution
NUMEXP, ALL, , , ! Expand all substeps with element results
SOLVE
SAVE
FINISH

/post26

/COM, NODES FOR RESPONSE CALCULATION
N7 = NODE(0.22701, -0.98593E-01, -0.35058) ! Select the node #63121 defined by the coordinates
N8 = NODE(0.22701, -0.98292E-01, 0.42245E-01) ! Select the node #63134 defined by the coordinates

/VIEW, 1, 1, 1, 1 ! Define the viewing direction as isometric
/SHOW, PNG ! Creates PNG (Portable Network Graphics) files that are
! named Body001.png onwards
ALLSEL, ALL
NSOL, 7, N7, U, Y ! Store the nodal data for N13 for y-displacement into the
! variable 7
NSOL, 8, N8, U, Y ! Store the nodal data for N14 for y-displacement into the
! variable 8
PLVAR, 7 ! Plot the data for variable 7
PLCPLX, 0 ! Plot the amplitude of the complex variable
PLVAR, 8 ! Plot the data for variable 8
PLCPLX, 0
PLVAR, 7, 8 ! Plot the data for variables 7 and 8 in the same plot
PLCPLX, 0

/SHOW, CLOSE
FINISH

```

## 22.7. Results and Discussion

Both the modal and harmonic analyses are performed using full and CMS models, and their solution times are noted. Significant improvement in the solution time is observed for the CMS model with very little loss of accuracy.

### 22.7.1. Modal Analysis Comparison of Accuracy and Efficiency

Before the harmonic analysis, a modal analysis with the same boundary conditions is performed using both the full and CMS models. The following table compares the first 50 eigenfrequencies obtained using both methods:

**Table 22.1: Comparison of Eigenfrequencies for Full and CMS Models**

Mode #	Full Model	CMS Fixed Interface	% Diff	Mode #	Full Model	CMS Fixed Interface	% Diff
1	31.12	31.31	0.59	26	421.43	421.11	0.08
2	33.13	33.12	0.03	27	438.35	437.67	0.16
3	44.66	44.69	0.08	28	441.79	441.03	0.17
4	53.17	53.10	0.12	29	452.46	452.13	0.07
5	87.88	88.18	0.34	30	496.92	496.10	0.17
6	88.63	88.97	0.38	31	513.90	513.11	0.15
7	144.61	144.55	0.04	32	539.43	538.38	0.19
8	146.77	146.41	0.24	33	553.06	552.27	0.14
9	187.22	187.23	0.01	34	557.25	557.39	0.03
10	223.63	223.70	0.03	35	570.47	571.11	0.11
11	237.48	237.41	0.03	36	620.15	619.67	0.08
12	251.83	251.69	0.06	37	633.79	634.34	0.09
13	256.42	256.48	0.02	38	647.02	647.11	0.01
14	263.33	263.05	0.10	39	675.83	675.73	0.01
15	272.06	271.91	0.06	40	707.77	708.04	0.04
16	274.79	274.68	0.04	41	708.81	709.53	0.10
17	357.55	358.10	0.15	42	714.94	715.58	0.09
18	368.37	368.17	0.06	43	716.93	716.76	0.02
19	368.47	368.26	0.06	44	726.62	726.06	0.08
20	368.50	368.30	0.06	45	734.91	734.39	0.07
21	368.77	368.56	0.06	46	734.93	734.41	0.07
22	372.73	372.32	0.11	47	734.97	734.43	0.07
23	387.18	386.90	0.07	48	734.99	734.44	0.07
24	391.96	391.67	0.08	49	751.62	751.70	0.01
25	415.22	414.77	0.11	50	768.84	768.93	0.01

The following table shows the elapsed and CPU times for modal analysis using the full and CMS models for 100 frequencies. Significant improvement in solution time is achieved during the use pass via the CMS method.

**Table 22.2: Comparison of CPU and Elapsed Times for Modal Analysis**

Number of Modes = 100	Full Model	CMS Fixed Interface	
		CPU Time (s)	2034.280
		Use Pass	4.630
Elapsed Time (s)	1291.000	Gen Pass	1336.000
		Use Pass	3.000

## 22.7.2. Full Harmonic Analysis Comparison of Accuracy and Efficiency

The harmonic analysis is conducted over the frequency range of 160 Hz to 200 Hz in 20 substeps. The following table compares the CMS and full model response amplitudes for the two response nodes.

**Table 22.3: Comparison of Response Amplitudes for Full and CMS Models**

Freq (Hz)	Node # 63121			Freq (Hz)	Node # 63134		
	Full Model	CMS Fixed Interface	% Diff		Full Model	CMS Fixed Interface	% Diff
162	39.65	39.7493	0.25	162	44.1064	43.7604	0.78
164	40.8758	40.896	0.05	164	48.6884	48.237	0.93
166	41.9754	41.9335	0.10	166	52.4358	51.9039	1.01
168	43.5616	43.4692	0.21	168	56.0015	55.4024	1.07
170	45.9102	45.7711	0.30	170	59.7247	59.0597	1.11
172	48.9518	48.7638	0.38	172	63.5063	62.7696	1.16
174	52.2104	51.9681	0.46	174	66.7185	65.905	1.22
176	54.7814	54.4813	0.55	176	68.2576	67.3727	1.30
178	55.668	55.3164	0.63	178	67.0837	66.1534	1.39
180	54.4876	54.1044	0.70	180	63.1036	62.1716	1.48
182	51.7678	51.3783	0.75	182	57.3466	56.4547	1.56
184	48.4247	48.0481	0.78	184	51.1398	50.3119	1.62
186	45.1665	44.8127	0.78	186	45.3776	44.6201	1.67
188	42.3427	42.0154	0.77	188	40.4304	39.7395	1.71
190	40.0521	39.7523	0.75	190	36.3475	35.7165	1.74
192	38.2657	37.9946	0.71	192	33.0387	32.4621	1.75
194	36.8948	36.6556	0.65	194	30.3676	29.8435	1.73
196	35.8121	35.6126	0.56	196	28.1851	27.7175	1.66

Node # 63121				Node # 63134			
Freq (Hz)	Full Model	CMS Fixed Interface	% Diff	Freq (Hz)	Full Model	CMS Fixed Interface	% Diff
198	34.8474	34.7009	0.42	198	26.3318	25.9327	1.52
200	33.7753	33.7011	0.22	200	24.6321	24.3226	1.26

The following table shows the elapsed and CPU times for harmonic analysis using full and CMS models for 20 substeps. The use pass includes the expansion. Significant improvement in solution time is achieved via the CMS method.

**Table 22.4: Comparison of CPU and Elapsed Times for Harmonic Analysis**

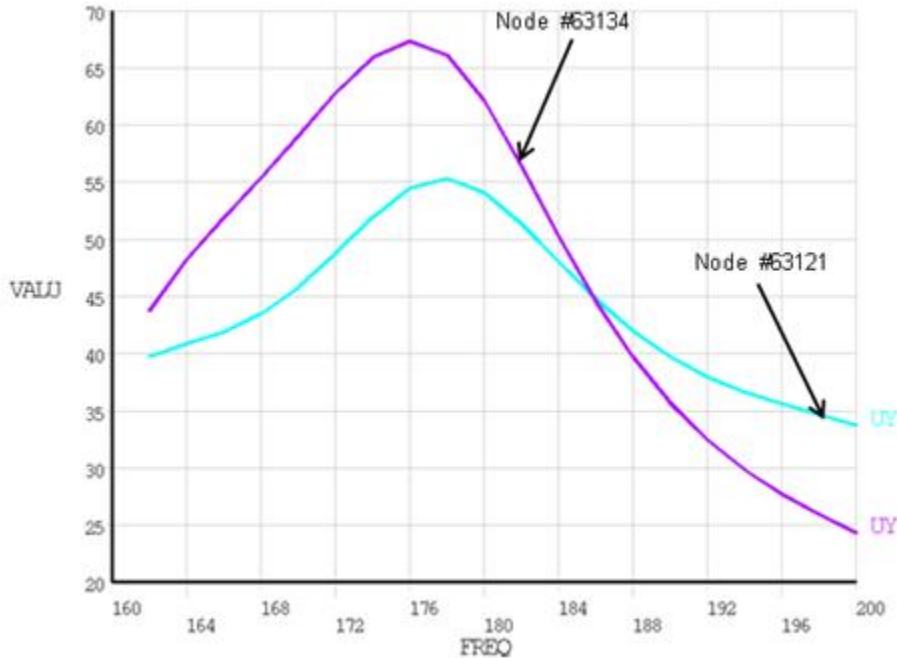
Number of Modes = 20	Full Model	CMS Fixed Interface	
CPU Time (s)	13580.800	Gen Pass	2022.670
		Use Pass	1758.800
Elapsed Time (s)	7866.000	Gen Pass	1336.000
		Use Pass	1764.000

### 22.7.3. Analysis of Peak Response

As shown in the following figure, the response amplitude plots for the two nodes show distinctive peaks (p. 347) at ~176 Hz.



**Figure 22.10: Nodal Responses Due to Harmonic Displacement Excitation at the Bottom of the Wheels**



The peaks are explained by observing the mode shape at the undamped natural frequency of 187.22 Hz (Figure 22.11: Mode Shapes at the Undamped Natural Frequency of 187.22 Hz (p. 347)). The figure shows the configuration of the structure at two extreme deflections. The mode shape at this frequency has tilting vibrations of the wheels (in phase) about the x axis with the associated deflection of part of the body. Harmonic displacement at the bottom of the wheels in the Y-Direction excites this mode, resulting in peaks at nearby frequencies.

Mode shapes for nearby higher frequencies (223.63 Hz and 237.48 Hz) do not involve significant tilting of the wheels or deflection of the links attached to the response nodes. Figure 22.12: Mode Shapes at the Undamped Natural Frequency of 223.63 Hz (p. 348) and Figure 22.13: Mode Shapes at the Undamped Natural Frequency of 237.48 Hz (p. 348) show the mode shapes at these frequencies.

**Figure 22.11: Mode Shapes at the Undamped Natural Frequency of 187.22 Hz**

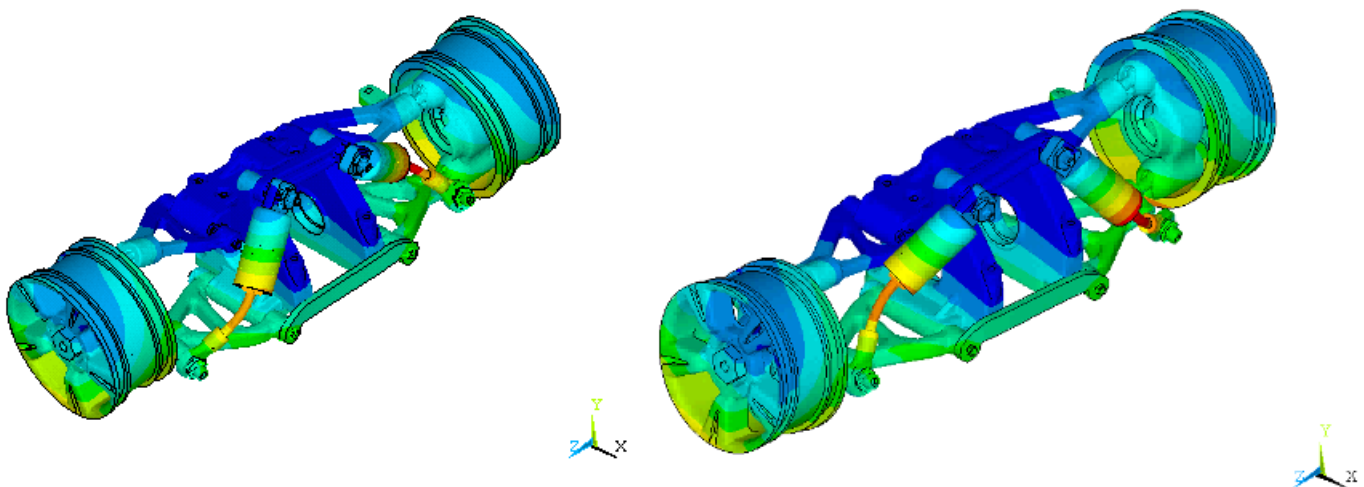


**Figure 22.12: Mode Shapes at the Undamped Natural Frequency of 223.63 Hz**

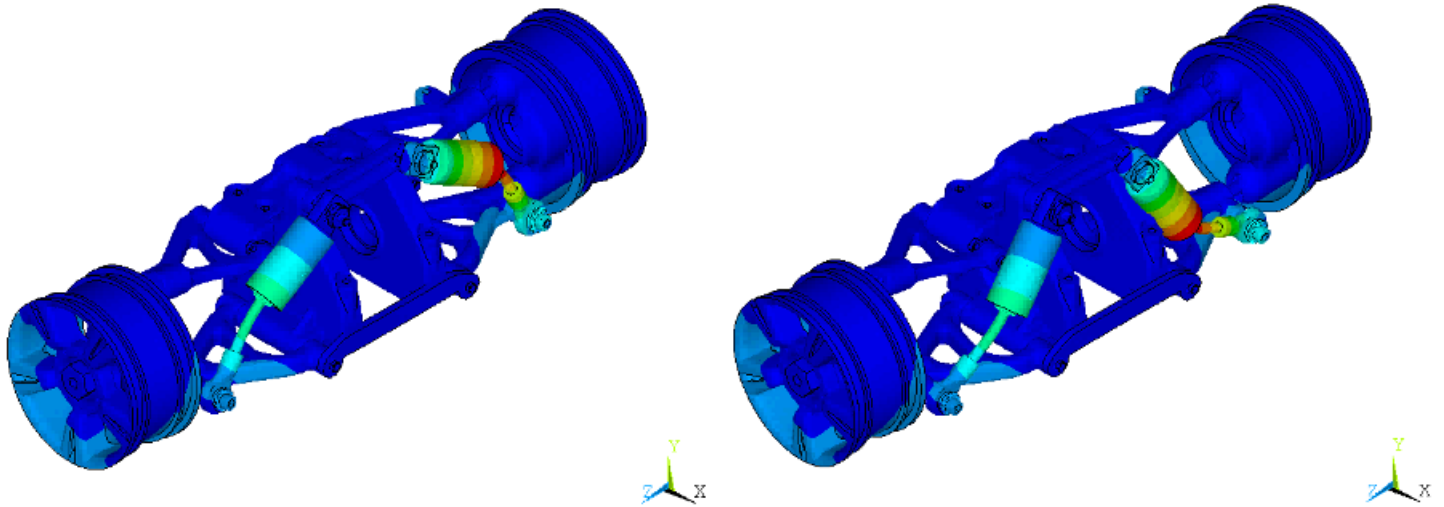
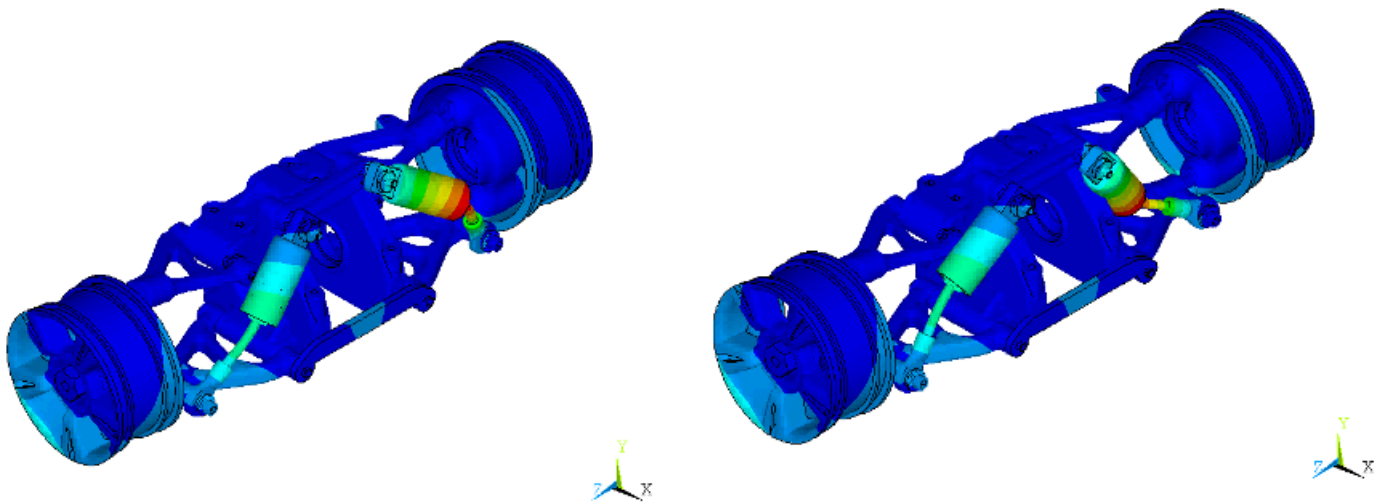


**Figure 22.13: Mode Shapes at the Undamped Natural Frequency of 237.48 Hz**



## 22.8. Recommendations

To perform a similar type of analysis, keep the following hints in mind:

- The computational benefits gained from CMS analysis can be increased by reducing the number of interface degrees of freedom defined. For maximum benefit, define as few as possible.
- CMS analysis is more efficient if only part of the structure is redesigned.
- CMS analysis can take advantage of repetitive geometry or parts to make the analysis more efficient

## 22.9. References

The following references are used in this example problem:

1. Craig, R.R. and M. D. D. Bampton. "Coupling of Substructures for Dynamic Analysis." *AIAA Journal*. 6.7 (1968): 1313-1319.
2. Craig, R.R. "A Review of Time Domain and Frequency Domain Component Mode Synthesis Methods." *International Journal of Analytical and Experimental Modal Analysis*. 2.2 (1987): 59-67.

## 22.10. Input Files

The following files were used in this problem:

- `Suspension.dat` -- Contains FE model details of automotive suspension assembly.
- `FullModel.dat` -- Modal and harmonic analysis on the suspension assembly.
- `CMSModel.dat` -- Modal and harmonic analysis on the suspension assembly using CMS method.

The files are available in the `td-22` folder. See [Obtaining the Input Files \(p. xxxv\)](#) for more information.



---

## Chapter 23: Modal Analysis of a Wind Turbine Blade Using Beam Elements

---

This example problem demonstrates how [current-technology](#) beam elements can be used effectively in the simulation of slender composite structures such as a wind turbine blade.

The following features and capabilities are highlighted:

- The [meshed beam-section subtype](#) for conveniently representing the built-up sections with complex geometry and nonuniform materials.
- The [tapered-beam section type](#) for defining varying cross-section geometry.
- Cubic interpolation option for improving computational efficiency and accuracy.
- The nonaveraged results file format for storing results from an analysis involving composite materials.

Topics related to this example problem follow:

- [23.1. Introduction](#)
- [23.2. Problem Description](#)
- [23.3. Modeling](#)
- [23.4. Material Properties](#)
- [23.5. Boundary Conditions and Loading](#)
- [23.6. Analysis and Solution Controls](#)
- [23.7. Results and Discussion](#)
- [23.8. Recommendations](#)
- [23.9. Input Files](#)

For related information, see [Beam and Pipe Cross Sections](#) in the *Structural Analysis Guide*.

### 23.1. Introduction

Wind turbines play an important role in harvesting alternative sources of energy. The turbine blade is the critical component in a wind turbine. An optimal blade design is crucial to the ultimate efficiency and strength of the turbine.

For their excellent formability and density to strength ratios, fiber-reinforced composite materials are now extensively used in the blade construction. Compared to their conventional counterparts, composite materials introduce a number of additional design parameters, such as the matrix and fiber material properties, laminar thicknesses, and fiber orientations.

Each blade design must be carefully verified. For example, to avoid a catastrophic failure, a design must not lead to a natural frequency close to any of the resonance frequencies. Without the aid of an effective simulation tool for design verification, the design process of a composite blade can be excessively time-consuming.

Because of the complex blade geometry, a typical strategy is to create a 3-D finite-element model of the turbine blade using shell or solid elements. With a detailed 3-D model, both global and local

mechanical responses of the blade can be adequately predicted with shell or solid elements. The *disadvantage* of using shells or solids becomes apparent when design changes are necessary.

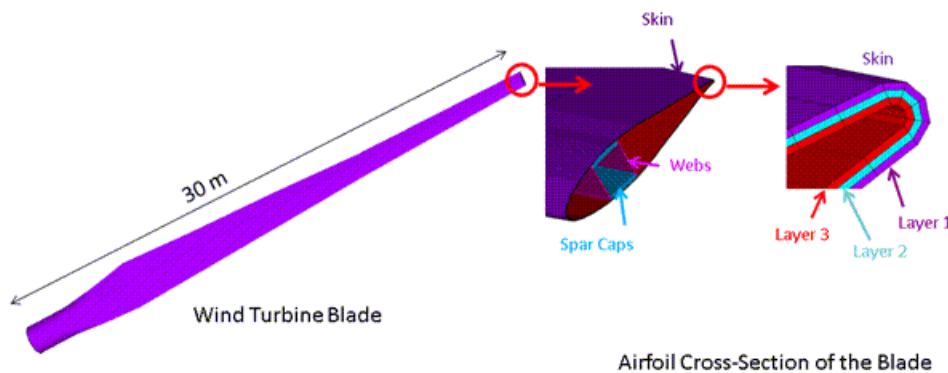
A small variation in the design can lead to partial or even complete reconstruction of the 3-D model. Because 3-D models are generally difficult to build and modify, frequent modifications during the design process may be impractical.

In some circumstances, especially during the preliminary design stage, only the global mechanical responses of the blade are sought. A simplified model, such as a 1-D beam model, is more desirable for such situations. The [current-technology](#) beam elements, with their advanced beam-section modeling capabilities, can be used to accurately predict natural frequencies of a typical composite turbine blade with minimal modeling effort and computational costs.

## 23.2. Problem Description

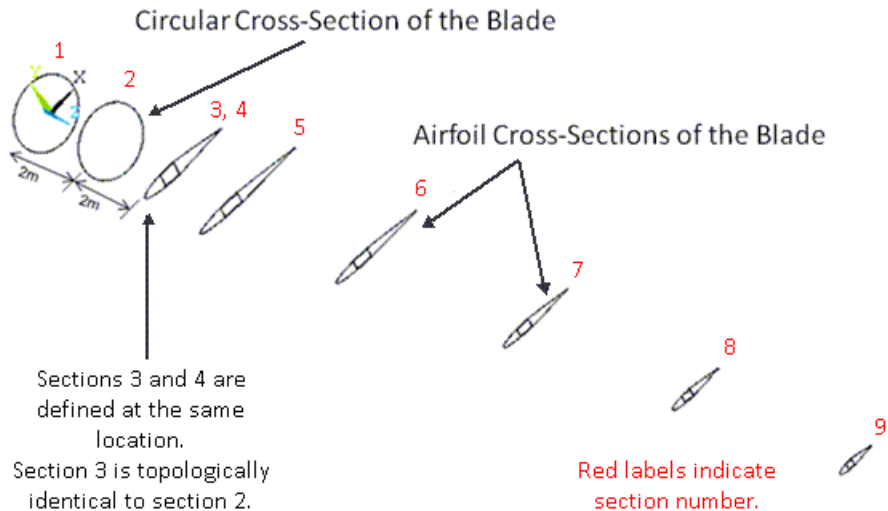
The following figure shows a model of a single turbine blade with a length of 30 meters, consisting of three primary structural components (the skin, the spar caps, and the shear webs):

**Figure 23.1: Wind Turbine Blade Geometry and Structural Components**



In an actual application, all three components of the blade can be made using layered composites. For illustrative purposes, this problem adopts a three-layered construction for the skin only, with homogeneous and orthotropic materials used for the spar caps and shear webs.

The blade geometry is defined via representative cross-sections at eight locations along the longitudinal axis, as shown in this figure:

**Figure 23.2: Representative Blade Cross-Section Areas at Various Locations**

The geometry is assumed to be linearly tapered between each pair of adjacent cross-sections. The natural frequencies and modes of the blade are analyzed using three comparative models:

- A **BEAM188** model with linear interpolation ( $\text{KEYOPT}(3) = 0$ ) and a fine mesh
- A **BEAM188** model with cubic interpolation ( $\text{KEYOPT}(3) = 3$ ) and a coarse mesh
- A detailed 3-D reference model using **SHELL281** elements

## 23.3. Modeling

The following models for the wind turbine blade are described:

23.3.1. Wind Turbine Blade: **BEAM188** Models

23.3.2. Wind Turbine Blade: **SHELL281** Reference Model

### 23.3.1. Wind Turbine Blade: **BEAM188** Models

Following is the general process for modeling the wind turbine blade using beam elements:

#### 1. Create the geometry models of the representative blade cross sections.

For this problem, the geometry was created using DesignModeler.

The *root part* is contained within the first two round sections (the area between sections #1 and #2). The root part is made of the skin material only.

Two sections (sections #3 and #4) are defined at the same location. While section #4 and the remaining sections consist of all three section components (skin, spar caps, and shear webs), section #3 contains only the skin component. Because sections #2 and #3 are topologically consistent, a *transition part* is defined between sections #2 and #3, connecting the root part to the airfoil part.

The airfoil part starts at section #4 and ends at section #9.

#### 2. Mesh the section-area geometry.

The section-area geometry is meshed using **MESH200** elements in a quadrilateral shape with eight nodes (**KEYOPT(1) = 7**), and appropriate material property types are assigned to different components within the sections.

The section meshes are output to external files (**SECWRITE**).

The following example input stores the mesh information for section #1:

```
CMSEL, s, areal          ! Select area component of first blade cross-section.
ALLSEL, below, area     ! Select everything below the selected area
SECWRITE, mesh1,sect,,1 ! Output mesh to file "mesh1.sect"
```

**3. Define constant beam sections types(BEAM), each with a meshed subtype (MESH).**

Beam sections with a mesh subtype are defined (**SECTYPE**), and the section meshes from the prior step are restored (**SECREAD**).

The following example input reads the mesh information contained in the mesh1.sect file and associates it with beam section #1:

```
SECTYPE,1,beam,mesh     ! Specify beam section 1 with mesh subtype
SECREAD,mesh1,sect,,mesh ! Import mesh from file "mesh1.sect"
```

**4. Define seven tapered-beam section types (TAPER).**

Using the constant previously defined beam sections, define seven beam sections (**SECTYPE**) of section type TAPER.

The sections are assigned later to beam elements in the various blade parts (root, transition, and airfoil).

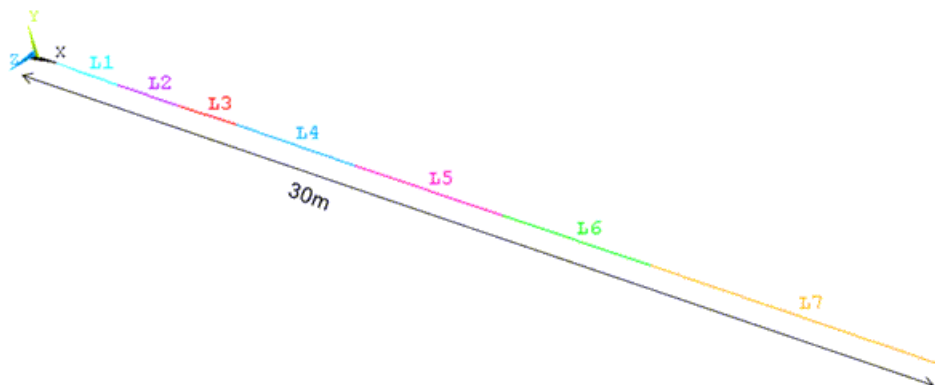
The following example input defines section #11 for the transition part:

```
SECTYPE,11,taper       ! Specify tapered-beam section type
SECDATA,2,2.0          ! Put BEAM section 2 at global X location 2.0 as the starting section
SECDATA,3,4.0         ! Put BEAM section 3 at global X location 4.0 as the ending section
```

**5. Create a line diagram of the blade model.**

Following is a line diagram of the blade model:

**Figure 23.3: Line Diagram of Wind Turbine Blade Model**





Line segments end where the constant beam sections are defined so that no elements are split by the sections.

## 6. Generate both beam meshes.

Two **BEAM188** meshes are generated, one a fine mesh with the linear interpolation option (**KEYOPT(3) = 0**), the other a coarse mesh with the cubic interpolation option (**KEYOPT(3) = 3**). The following two figures show both models, respectively:

**Figure 23.4: BEAM188 Blade Model with Fine Mesh and Linear Interpolation**

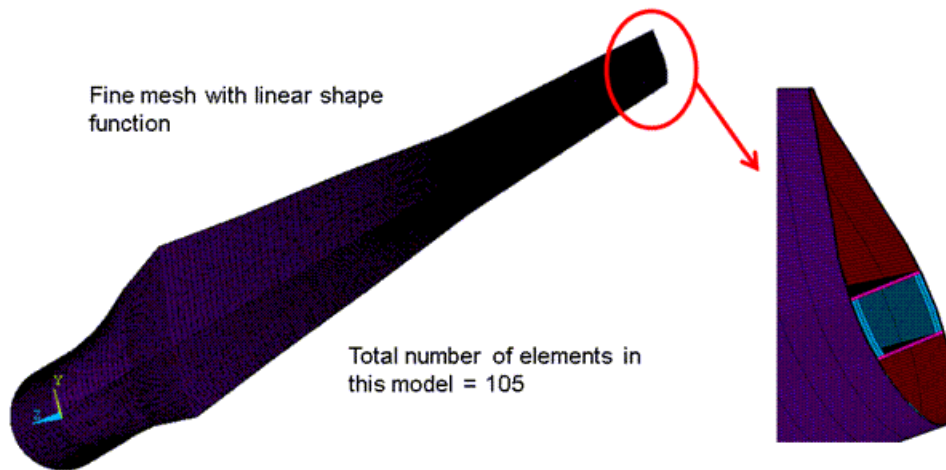
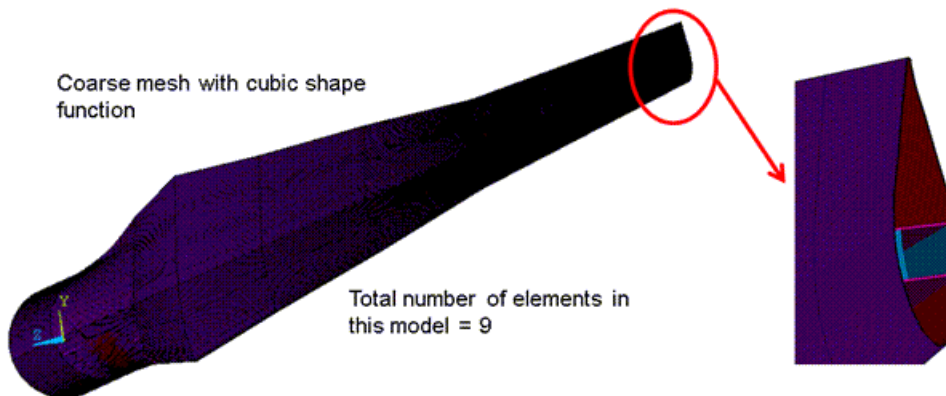


**Figure 23.5: BEAM188 Blade Model with Coarse Mesh and Cubic Interpolation**



The elements are visualized with the expanded solid display option (**/ESHAPE**) to show the 3-D section details.

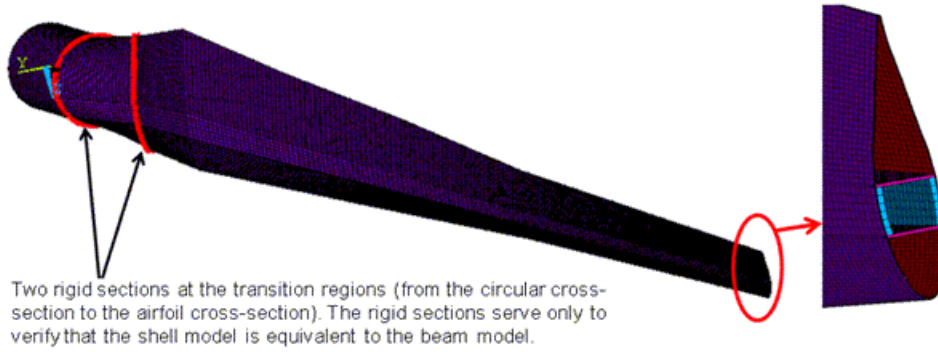
The following example input meshes line #3, representing the transition part:

```
SECNUM,11          ! Set the current section as section 12
LMESH,3           ! Mesh line number 3
```

## 23.3.2. Wind Turbine Blade: SHELL281 Reference Model

To generate a reference solution, an equivalent 3-D model is created using **SHELL281** elements, as shown in the following figure:

**Figure 23.6: SHELL281 Reference Blade Model**



Material properties (p. 356) and boundary conditions (p. 356) in this model are identical to those of the BEAM188 models.

### 23.4. Material Properties

Five orthotropic materials are used for the three layers in the skin, the shear webs, and the spar caps, respectively. The material properties are as follows:

Material Constants	Skin Layer 1	Skin Layer 2	Skin Layer 3	Spar Caps	Shear Webs
$E_x$ (N/m <sup>2</sup> )	1.39E+10	1.20E+10	1.48E+10	1.66E+10	1.59E+10
$E_y$ (N/m <sup>2</sup> )	1.39E+10	1.20E+10	1.48E+10	1.66E+10	1.59E+10
$E_z$ (N/m <sup>2</sup> )	1.05E+10	9.50E+09	1.10E+10	1.21E+10	1.15E+10
$\nu_{xy}$	0.43	0.38	0.48	0.40	0.52
$\nu_{yz}$	0.15	0.18	0.13	0.15	0.10
$\nu_{xz}$	0.15	0.18	0.13	0.15	0.10
$G_{xy}$ (N/m <sup>2</sup> )	1.09E+10	9.30E+09	1.10E+10	1.24E+10	1.19E+10
$G_{yz}$ (N/m <sup>2</sup> )	5.48E+09	6.03E+09	5.03E+09	4.08E+09	4.48E+09
$G_{xz}$ (N/m <sup>2</sup> )	5.48E+09	6.03E+09	5.03E+09	4.08E+09	4.48E+09
Density (kg/m <sup>3</sup> )	1900	1750	2000	1800	1850

### 23.5. Boundary Conditions and Loading

Boundary conditions for the beam and the reference shell models are given separately, as follows:

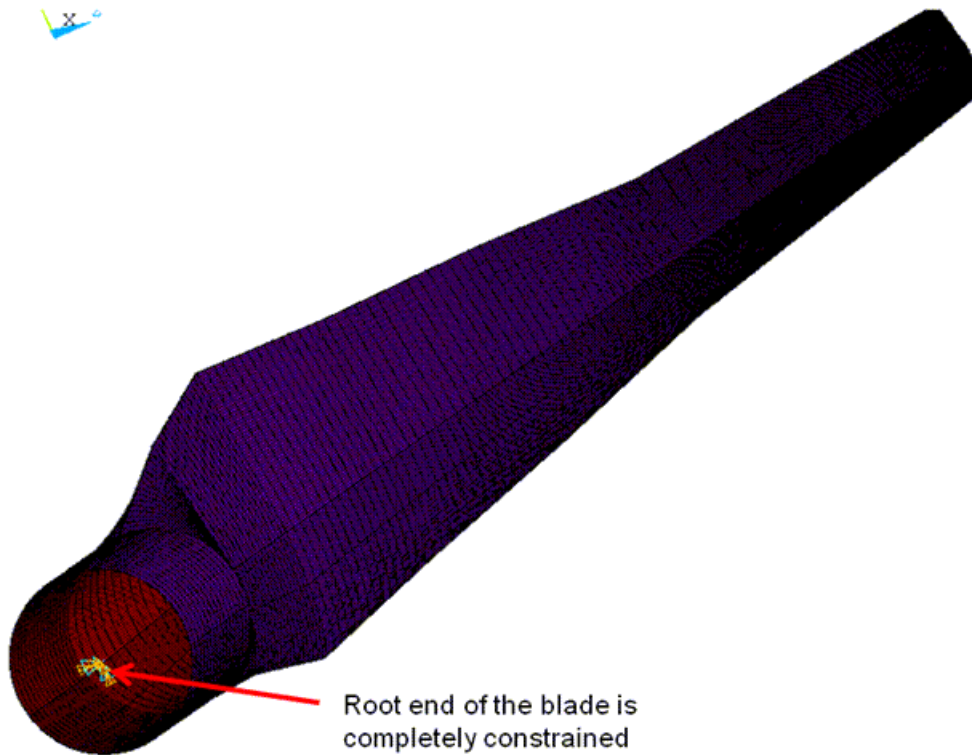
23.5.1. BEAM188 Blade Model Boundary Conditions

23.5.2. SHELL281 Blade Model Boundary Conditions

#### 23.5.1. BEAM188 Blade Model Boundary Conditions

For the beam models (p. 353), the root end of the blade is completely constrained, as shown in the following figure:

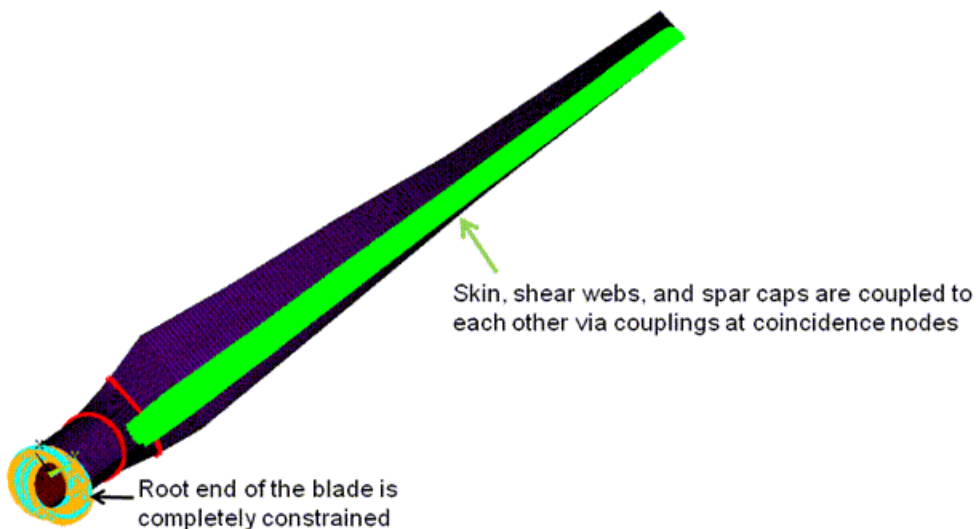
**Figure 23.7: Boundary Conditions on the BEAM188 Blade Model**



### 23.5.2. SHELL281 Blade Model Boundary Conditions

For the reference shell model (p. 355), the root end of the blade is also completely constrained, as shown in this figure:

**Figure 23.8: Boundary Conditions on the Reference SHELL281 Blade Model**



Extensive constraint equations (CEs) are used for properly assembling the three structural components (indicated by the green areas in the figure above).

As a result of the simplified model, an abrupt section-property change exists from the three-component airfoil section to the skin-only transition section. Significant section deformation is expected at this connection location.

While the SHELL281 reference model can simulate the section deformation, the same capability in the BEAM188 models is greatly limited due to basic beam characteristics. To create a comparable reference model, an artificially rigid plane is inserted at this location, indicated by the red symbols in the figure above. Similarly, another rigid plane is inserted at the connection of the root part and the transition part.

This technique does not invalidate the beam modeling, as these types of sudden section-property changes do not exist in actual blade designs.

### 23.6. Analysis and Solution Controls

Modal analyses are conducted with the three wind turbine blade models. The Block Lanczos solver is used to extract the first ten natural frequencies and mode shapes, as shown by the following example input:

```

ANTYPE, modal
MODOPT, lanb,10
MXPAND, 10, , ,yes
SOLVE
    
```

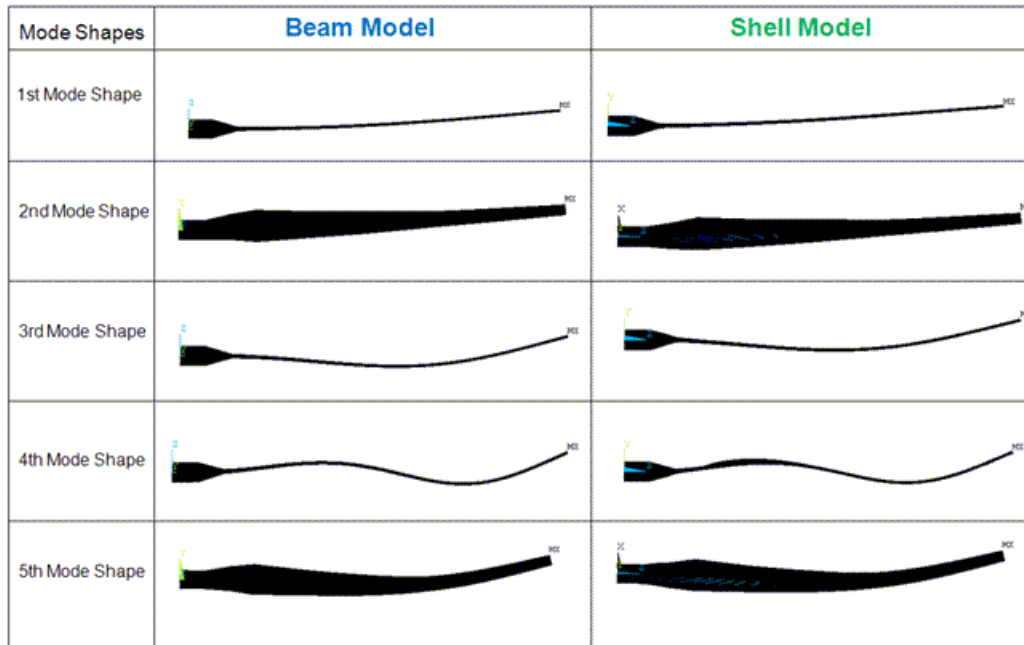
### 23.7. Results and Discussion

The following table summarizes the natural frequency results from the analyses of the three blade models:

Blade Length (m) ----->	30.000			Error (%) between beam model (with linear function) and shell model	Error (%) between beam model (with cubic function) and shell model
Natural Frequencies	Shell Model	Beam Model with Linear Function	Beam Model with Cubin Function		
1st Natural Frequency	0.2597	0.2559	0.2561	1.4403	1.3710
2nd Natural Frequency	0.9558	0.9259	0.9259	3.1303	3.1261
3rd Natural Frequency	1.1307	1.1211	1.1216	0.8490	0.8048
4th Natural Frequency	2.8979	2.8225	2.8205	2.6019	2.6709
5th Natural Frequency	3.7873	3.6892	3.6884	2.5902	2.6114
6th Natural Frequency	4.9235	5.2931	5.2854	7.5069	7.3505
7th Natural Frequency	5.9331	8.5089	8.4901	43.4141	43.0972
8th Natural Frequency	6.4775	9.6953	9.6797	49.6766	49.4357
9th Natural Frequency	7.0154	9.7862	9.7895	39.4960	39.5430
10th Natural Frequency	7.4022	12.4240	12.4030	67.8420	67.5583

The first five frequencies predicted by the three comparative models are consistent within a range of five percent. The difference increases in higher modes.

The following figure shows the mode shapes of the first five matching frequencies:

**Figure 23.9: Comparison of Mode Shapes Predicted by BEAM188 and SHELL281 Models**

In the [SHELL281](#) reference model, local deformation is evident in higher modes.

The current-technology beams are shown to be effective for simulating slender structures. Compared to 3-D modeling using shell and solid elements, beam modeling greatly reduces model-creation time and effort while generally leading to acceptable overall results.

The applicability of current-technology beam elements, however, is bound by the first-order shear-deformation (or Timoshenko) theory. Beam elements are therefore not suitable for extremely stubby structures or structures that may undergo large section deformation (as shown in the higher modes predicted in the [SHELL281](#) model).

With the aid of the mesh (MESH) section subtype, current-technology beam elements can be used for certain types of composite structures. Consider the applicability of beam elements carefully before adopting them for composite-structure simulation. When modeled with beam elements, composite structures introduce these restrictions:

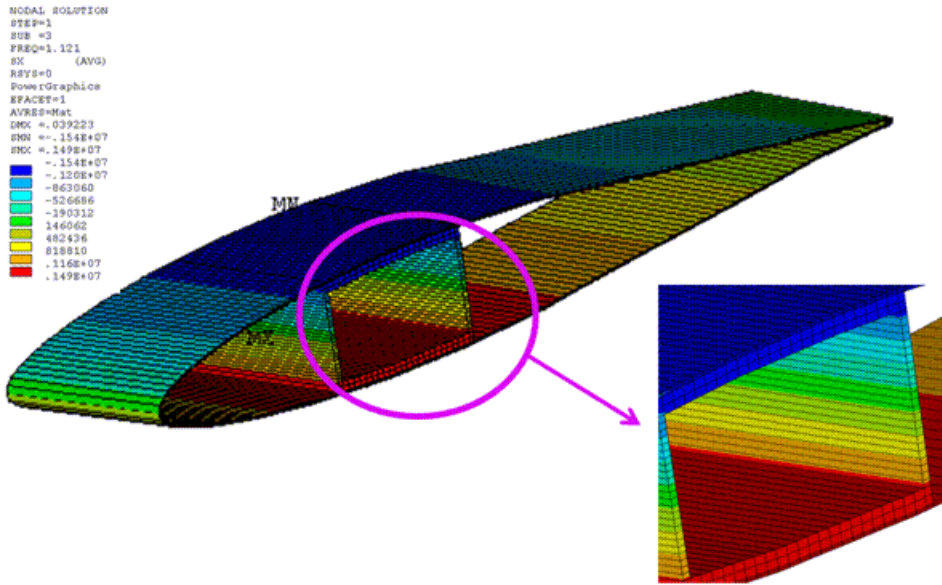
- The materials must be oriented in the beam solution coordinate system.
- The material properties should not exhibit great variation within the section
- Because of beam-theory limitations, some material properties such as Poisson's ratio, and the coupling between axial stiffness and twisting/transverse shear stiffness, are ignored in beam elements.

The tapered-beam section type (TAPER) can be used with all standard (and even user-defined) beam sections, making it a powerful and flexible tool for modeling structures with complex and varying cross-section geometry.

The cubic interpolation option enables the [BEAM188](#) model to generate an equally accurate solution with far fewer elements than the [BEAM188](#) model with the linear option. Cubic interpolation is also required for modeling partially distributed or pointed loads within the element.

The typical beam-bending stress results ( $S_{xx}$ ) with different results-file formats (KEYOPT(15) in current-technology beam and pipe elements) are shown in the following two figures:

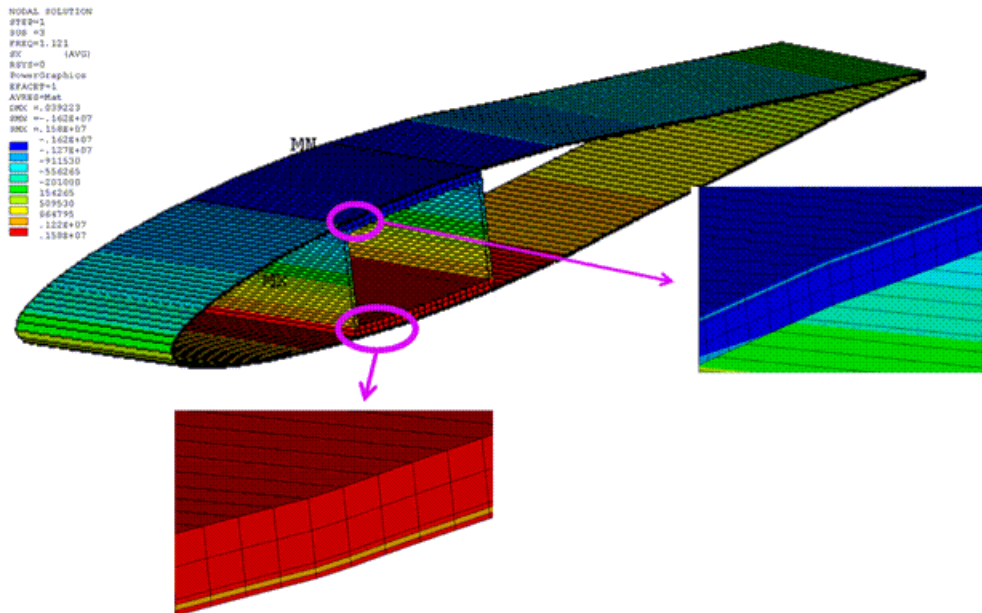
**Figure 23.10: Averaged Bending-Stress Distribution (Corresponding to Third Mode Shape at Location  $x = 15\text{m}$ )**



With the averaged result format (KEYOPT(15) = 0), continuous bending stress is observed even across the interfaces between two different materials.

For beams with built-up sections, the nonaveraged format (KEYOPT(15) = 1) is appropriate. As shown in the following figure, the stress discontinuity in heterogeneous media is properly captured using the nonaveraged format:

**Figure 23.11: Nonaveraged Bending-Stress Distribution (Corresponding to Third Mode Shape at Location  $x = 15\text{m}$ )**



## 23.8. Recommendations

To perform a similar analysis for a slender composite structure, consider the following hints and recommendations:

- When applicable, use [current-technology](#) beam elements (such as [BEAM188](#)) to achieve better computational efficiency and to simplify model creation and modification. Verify that all modeling requirements, such as slenderness ratio and material orientation, are satisfied.
- Use the meshed beam-section subtype ([SECTYPE,,BEAM,MESH](#)) and/or the tapered-beam section type ([SECTYPE,,TAPER](#)) for modeling structures with complex section geometry and profiles.
- Select higher-order interpolation options in [BEAM188](#) if nonuniform deformation along the length is expected. Because higher-order interpolation options introduce invisible internal elements nodes, however, carefully inspect boundary conditions and loading to avoid inconsistency.
- Select the nonaveraged results file format for proper postprocessing of the simulation results.

## 23.9. Input Files

The following files were used in this problem:

- `blade_188_linear.inp` -- Input file for the modal analyses of the wind turbine blade modeled with linear [BEAM188](#) elements.
- `blade_188_linear.cdb` -- Common database file containing the model data for the wind turbine blade modeled with linear [BEAM188](#) elements (called by `blade_188_linear.inp`).
- `blade_188_cubic.inp` -- Input file for the modal analyses of the wind turbine blade modeled with cubic [BEAM188](#) elements.
- `blade_188_cubic.cdb` -- Common database file containing the model data for the wind turbine blade modeled with cubic [BEAM188](#) elements (called by `blade_188_cubic.inp`).
- `blade_281.inp` -- Input file for the modal analyses of the wind turbine blade modeled with [SHELL281](#) elements.
- `blade_281.cdb` -- Common database file containing the model data for the wind turbine blade modeled with [SHELL281](#) elements (called by `blade_281.inp`).

The files are available in the `td-23` folder. See [Obtaining the Input Files \(p. xxxv\)](#) for more information.





---

## Chapter 24: Hydrostatic Fluid Analysis of an Inflating and Rolling Tire

---

This example problem demonstrates how to model a fluid that is fully enclosed by a solid (the container). The problem shows how loading on the container and container deformation affect the pressure, volume, density and mass of the contained fluid.

The following features and capabilities are highlighted:

- Modeling hydrostatic fluid elements with negative and positive volumes
- Use of a gas material model
- Reinforcing

A [transient analysis](#) of an inflated and rolling tire shows the tire deformation through various load steps.

Topics related to this example problem follow:

- [24.1. Introduction](#)
- [24.2. Problem Description](#)
- [24.3. Modeling](#)
- [24.4. Material Properties](#)
- [24.5. Boundary Conditions and Loading](#)
- [24.6. Analysis and Solution Controls](#)
- [24.7. Results and Discussion](#)
- [24.8. Recommendations](#)
- [24.9. Input Files](#)

### 24.1. Introduction

Hydrostatic fluid elements are well suited for calculating fluid volume and pressure for coupled problems involving fluid-solid interaction. Modeling with a hydrostatic fluid allows one to study the changes in fluid behavior when it is contained within a solid upon which various loads are imposed.

Such an analysis is useful in the example problem presented here, where it is possible to examine the changing pressure, density and volume of the air inside of a tire during inflation and rolling. Another example application involves the volume and pressure changes of a fluid contained within a cylinder in which a piston is moving.

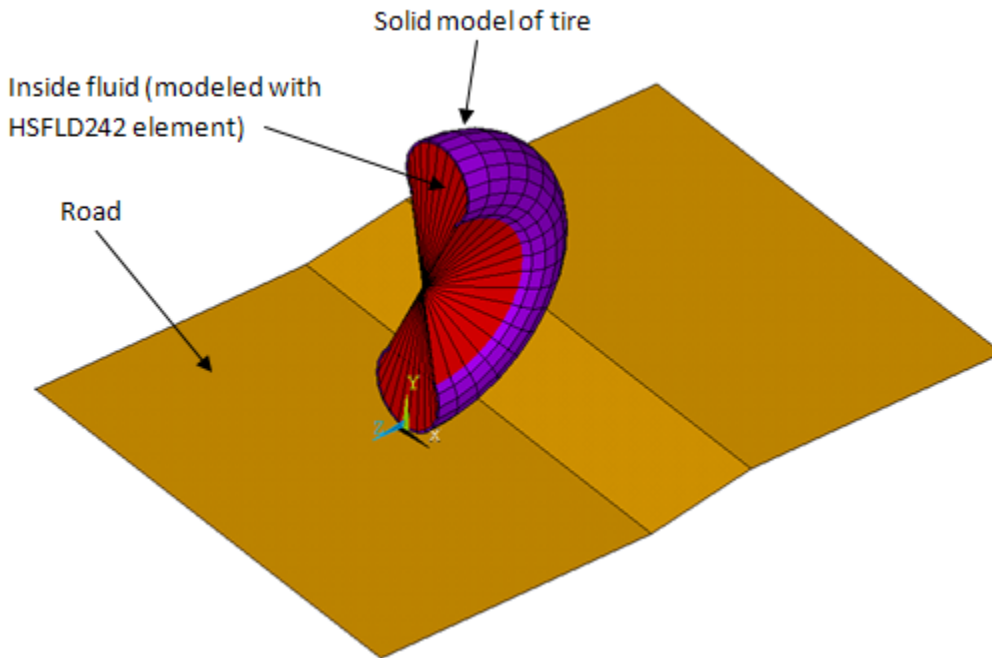
The automobile industry strives to improve fuel economy and to lessen power loss, both of which are affected by the rolling resistance of a vehicle's tires. To do so, it is necessary to accurately predict the changing fluid conditions within a rolling, deformed tire.

### 24.2. Problem Description

A 3-D tire model is inflated and pressed against the road surface and then rolled over a bump on the road. The tire is modeled with hyperelastic material and reinforcing elements. The air inside is modeled

with a hydrostatic fluid element, and the pressure, volume and density is monitored as loads are applied to the tire.

**Figure 24.1: 3-D Model of an Inflated Tire and a Road Surface**



The tire is inflated to 36 psi and a mass of 1 ton is added at the axle to simulate the portion of the vehicle's mass resting on that axle.

The analysis occurs over five load steps, as follows:

1. Apply a gravity load and set the reference temperature for the air.
2. Inflate the tire.
3. Move the tire down to seat it on the road surface.
4. Remove displacement and pressure boundary conditions.
5. Apply an acceleration boundary condition to roll the tire over a bump.

Load steps 1 through 4 are performed statically, while load step 5 is performed as a transient analysis to study the loading effect on vertical acceleration.

## 24.3. Modeling

To simulate actual conditions, the tire dimensions approximate those of a P215/65R16 car/minivan tire.

An incompressible hyperelastic material model is used for the tire. Reinforcing elements are embedded into the solid elements to model steel reinforcing within the tire structure.

Modeling for this problem involves the following tasks:

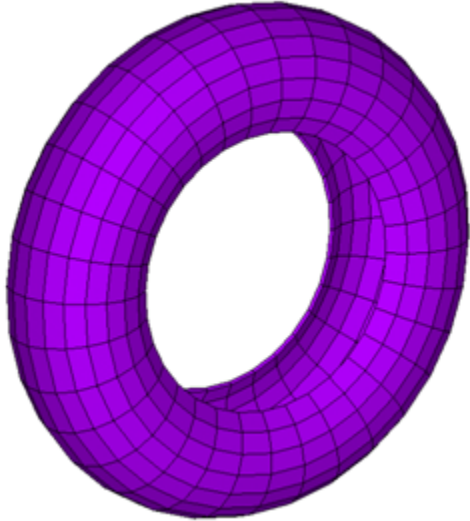
- [24.3.1. Model the Tire as a Solid](#)
- [24.3.2. Model the Air Inside of the Tire](#)

- 24.3.3. Model the Tire Reinforcing
- 24.3.4. Model the Tire Rim
- 24.3.5. Model Tire Contact with the Road Surface

### 24.3.1. Model the Tire as a Solid

The tire is modeled with **SOLID186** solid elements by rotating a 2-D meshed area around an axis defined by two key points, as shown:

**Figure 24.2: 3-D Tire Model Using a Solid Element**

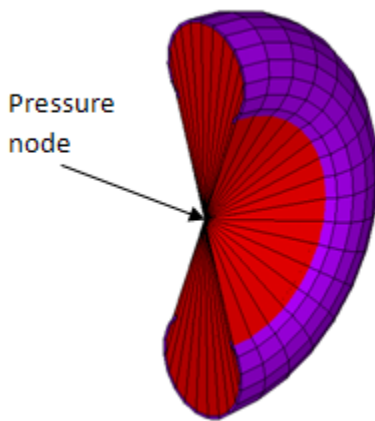


### 24.3.2. Model the Air Inside of the Tire

The air inside of the tire is modeled with **HSFLD242** hydrostatic fluid elements. The elements are generated (**ESURF**) with a pressure node ID over the solid elements to enclose the air.

The following figure shows the fluid elements generated over the solid elements:

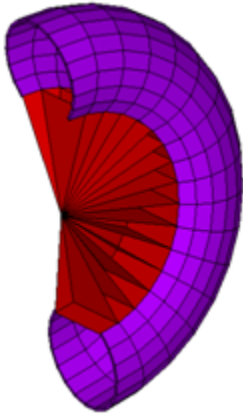
**Figure 24.3: Hydrostatic Fluid Element with Positive Volume**



Because the fluid elements are pyramid shaped with common vertices at each pressure node ID, the fluid elements cover some undesired volumes as well. So that fluid elements exist only in the region

where air should be present, fluid elements having a negative volume in the undesired region are used, as shown in this figure:

**Figure 24.4: Hydrostatic Fluid Element with Negative Volume**



This technique involves manually generating fluid elements with the nodes ordered in a clockwise direction.

The following input example shows how to model the air inside of the tire using hydrostatic fluid element **HSFLD242**:

```

! Defining hydrostatic fluid element
Et,3,242          ! Hydrostatic fluid element
keyopt,3,5,1     ! Fluid mass calculated based on the volume
!               of the fluid element
type,3
mat,2            ! Gas material model used to model the inside fluid
real,3
r,3,0.10156     ! Initial air pressure (atmospheric) = 0.10156 N/mm^2
n,1,0.,340.,0. ! Define pressure node

! Selecting solid elements to enclose the fluid
lsel,s,line,,52
lsel,a,line,,53,123,5
lsel,a,line,,130
lsel,a,line,,131,201,5
lsel,a,line,,208
lsel,a,line,,209,279,5
lsel,a,line,,282
lsel,a,line,,283,311,2
nsll,s,1
esln
esurf,1         ! Generate the hydrostatic fluid element over the solid
!             elements with pressure node.
allsel,all
! Generate the hydrostatic fluid element with negative volume
e,60,284,283,59, ! Order the node in clockwise direction
emore,1
e,61,285,284,60,
emore,1         ! Similarly more elements are generated in undesired volume

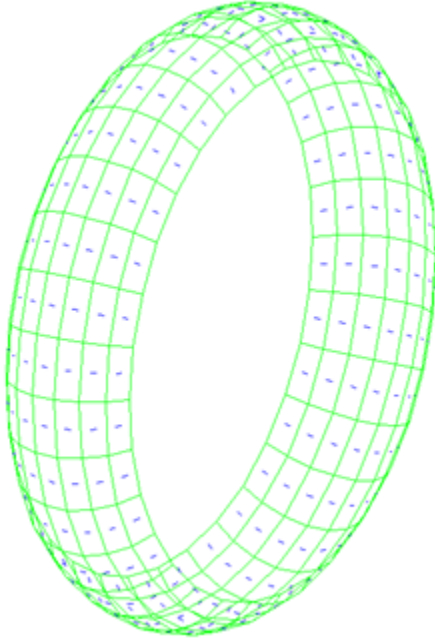
```

For more information about modeling, see [Modeling Hydrostatic Fluids and Example Model Using Hydrostatic Fluid Elements](#) in the *Structural Analysis Guide*.

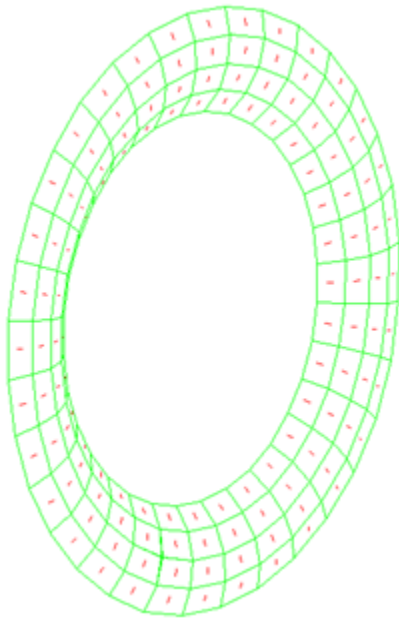
### 24.3.3. Model the Tire Reinforcing

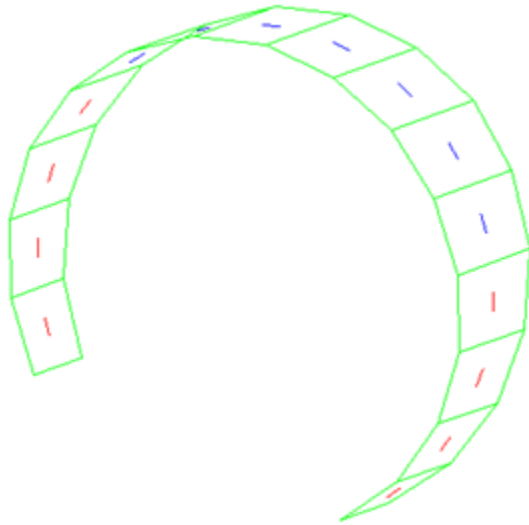
Tire reinforcing is modeled with reinforcing element [REINF265](#). Different material models are used to define the reinforcing in the road contact area and the side walls, as shown in the following figures:

**Figure 24.5: Tire Reinforcing: Road Contact Area**



**Figure 24.6: Tire Reinforcing: Side Wall**



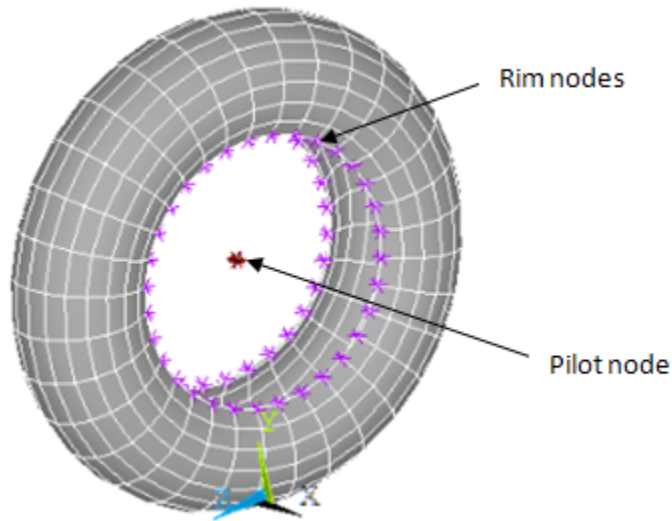
**Figure 24.7: Tire Reinforcing: Sectional View**

The following input example shows how to model tire reinforcing using [REINF265](#):

```
! Section definition for reinf1
sectype,13,reinf,smear,reinf13 ! Define section type and
!                               sub type(smear), 13 is section id number
secdata,4,4,2,,,ELEf,3,0.5    ! Define section data
! For more information, see SECDATA command documentation
!
vsel,s,volu,,5,11              ! Select base element
vsel,a,volu,,20,26
eslv,s
esel,r,type,,2
secn,13                        ! Assign section to reinforcing element
ereinf                          ! Generate reinforcing element
!
! Reinforcing elements are generated similarly in other sections
```

### 24.3.4. Model the Tire Rim

A rim is modeled as a rigid body using a multipoint constraint (MPC) algorithm (rigid constraints), as shown in this figure:

**Figure 24.8: Rim Model with Tire**

Node-to-surface contact elements (**CONTA175**) are used for the rim nodes and a target element (**TARGE170**) is used to define a pilot node at the center of the tire, as shown in the following figure:

The following input example shows how to model the rim:

```

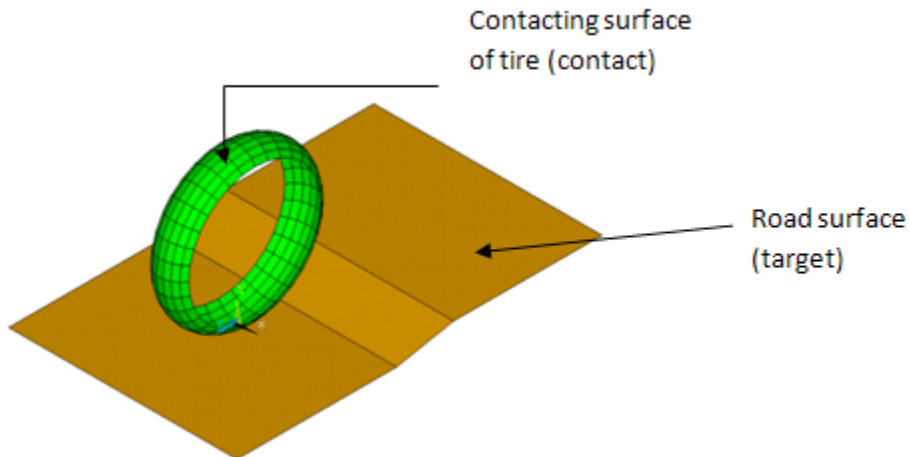
et,4,175          ! Select contact element
et,5,170          ! Select target element
keyopt,4,2,2      ! Use MPC constraints
keyopt,4,4,0      ! Use rigid surface constraint
keyopt,4,12,5     ! Always bonded
n,1026,0.,340.,0. ! Make node at axle (pilot node)

! Define target element at pilot node
tshap,pilot
type,5
real,4
e,1026
! Contact element definition
type,4
real,4
! Select contact surface (rim nodes)
lsel,s,line,,51
lsel,a,line,,124
lsel,a,line,,129
lsel,a,line,,202
lsel,a,line,,207
lsel,a,line,,280
lsel,a,line,,281
lsel,a,line,,312
nsl1,s,1
esurf             ! Generate contact element
allsel,all

```

### 24.3.5. Model Tire Contact with the Road Surface

A surface-to-surface contact pair is modeled between the road and tire, as shown in this figure:

**Figure 24.9: Model of Tire Contact with Road Surface**

The **CONTA174** element is used to model the part of the tire's surface which comes in contact with the road. The road is modeled as a rigid target (**TSHAP,QUAD**). Impact constraints (**KEYOPT(7) = 4**) are specified for the contact element.

## 24.4. Material Properties

Following are the properties for the tire, air and reinforcing materials.

### Tire Material Properties

Tire Rubber	
Young's Modulus	6894.8 MPa
Poisson's Ratio	0.5
Density	2.67E-9 Kg/mm <sup>3</sup>
Mooney-Rivlin Material Model Constants	
C10	0.551584 MPa
C01	0.137896 MPa
D	0

### Fluid Material Properties

Air is used as the inside fluid, modeled using a compressible gas model.

Internal Air	
Initial Density	1.225E-12 Kg/mm <sup>3</sup>
Reference Temperature	20°C
Temperature Offset	274°C

### Reinforcing Material Properties

Steel is used as a reinforcing material.



Reinforcing in Contact with the Road Surface	
Young's Modulus	2.0E5 MPa
Poisson's Ratio	0.3
Reinforcing in the Side Walls	
Young's Modulus	2.0E4 MPa
Poisson's Ratio	0.3

## 24.5. Boundary Conditions and Loading

Because this problem is solved in five load steps, different boundary conditions (BCs) and loadings are imposed in each load step.

### 24.5.1. BCs and Loading in Load Step 1

The pilot node, representing the gravity center of axle, is constrained. To simulate vehicle mass, one ton of gravity load is applied. An initial temperature of 20°C is applied at the pressure node.

```
d,1026,all           ! 1026 represents the pilot node
accel,0.,9810,0.
bf,1,temp,20        ! 1 is the pressure node
```

### 24.5.2. BCs and Loading in Load Step 2

To inflate the tire, the pressure node is constraint by applying a pressure boundary condition (hydrostatic pressure of 36 psi (0.2482128 N/mm<sup>2</sup>)). The constraint is equivalent to applying a surface load on the underlying solid surface.

```
d,1,hdsp,0.2482128
```

### 24.5.3. BCs and Loading in Load Step 3

The tire is moved down to make contact with the road surface by applying the displacement boundary condition to the pilot node.

```
d,1026,uy,-50
```

### 24.5.4. BCs and Loading in Load Step 4

All pressure and displacement boundary conditions are removed.

```
ddel,1026,uy,,,force      ! Remove boundary conditions
ddel,1026,rotx,,,force
ddel,1026,roty,,,force
ddel,1026,rotz,,,force
ddel,1,hdsp                ! Remove pressure boundary condition
```

### 24.5.5. BCs and Loading in Load Step 5

An acceleration boundary condition is applied to the pilot node.

```
d,1026,accz,-1400.0
```

## 24.6. Analysis and Solution Controls

A nonlinear [transient analysis](#) is performed using the HHT time-integration method. Load steps 1 through 4 are performed statically. Transient effects are included in load step 5.

```
antype,trans           ! Select transient analysis
nlgeom,on             ! Include geometric nonlinearities
trnopt,full, , , ,HHT ! Use HHT algorithm to include transient effect
tintp,0.15           ! Specify amplitude decay factor
```

## 24.7. Results and Discussion

The time-history response shows changes to the tire's internal air pressure, volume, density and mass during each load step.

A comparison to the expected results (obtained via an analytical solution) validates the simulation of the air using the hydrostatic fluid element [HSFLD242](#).

### 24.7.1. Expected Results

The volume of the gas inside the tire is defined by the underlying solid, so it is considered a given. Expected pressure, density, and mass are calculated as follows:

Density:  $\rho_f = \rho_o * P_f / P_o$

Pressure:  $P_f = P_o * V_o / V_f$  when mass is constant during load step

Mass:  $\text{mass} = \text{density} * \text{volume}$

The following table shows the expected results at each load step:

Time (Sec)	Pressure (N/mm <sup>2</sup> )	Volume (mm <sup>3</sup> )	Density (Kg/mm <sup>3</sup> )	Mass (Kg)
1	0	0.326285E+08	0.1225E-11	0.3997E-04
2	0.248213	0.329565E+08	0.4219E-11	0.139E-03
3	0.248213	0.327078E+08	0.4219E-11	0.1379E-03
4	0.253812	0.319862E+08	0.43141E-11	0.1379E-03
5	0.252676	0.321300E+08	0.42947E-11	0.1379E-03

### 24.7.2. Simulation Result Using Hydrostatic Fluid Element HSFLD242

Hydrostatic pressure can be output as the HDSP degree-of-freedom solution. The NMISC output quantities (TVOL, DENSITY, and TMAS) provide results for the entire fluid volume, so all hydrostatic fluid elements sharing the pressure node have the same output value.

The following table shows the simulation results at each load step:

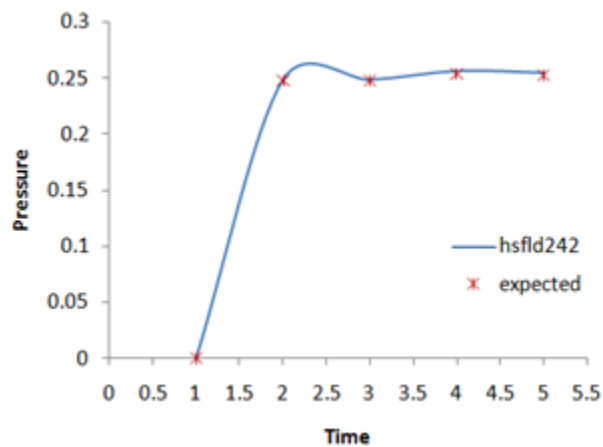
Time (Sec)	Pressure - HDSP (N/mm <sup>2</sup> )	Volume - TVOL (mm <sup>3</sup> )	Density - DENSITY (Kg/mm <sup>3</sup> )	Mass - TMAS (Kg)
1	.967073E-5	0.326285E+08	0.12251E-11	0.3997E-04
2	0.248213	0.329565E+08	0.42189E-11	0.1390E-03

Time (Sec)	Pressure - HDSP (N/mm <sup>2</sup> )	Volume - TVOL (mm <sup>3</sup> )	Density - DENSITY (Kg/mm <sup>3</sup> )	Mass - TMAS (Kg)
3	0.248213	0.327078E+08	0.42189E-11	0.1379E-03
4	0.256104	0.319862E+08	0.43140E-11	0.1379E-03
5	0.254482	0.321300E+08	0.42945E-11	0.1379E-03

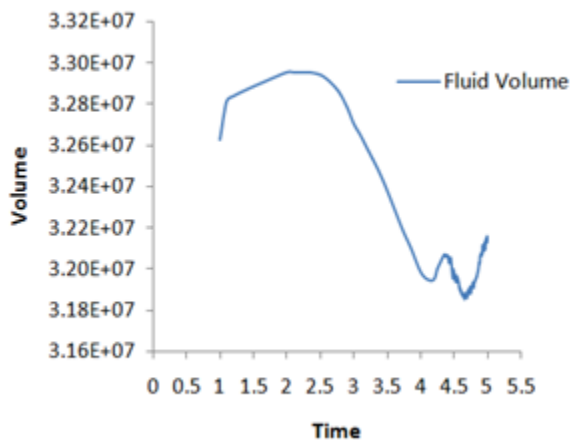
### 24.7.3. Time-History Response

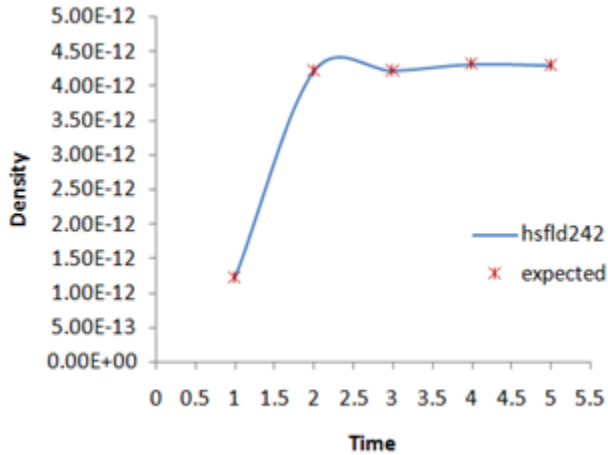
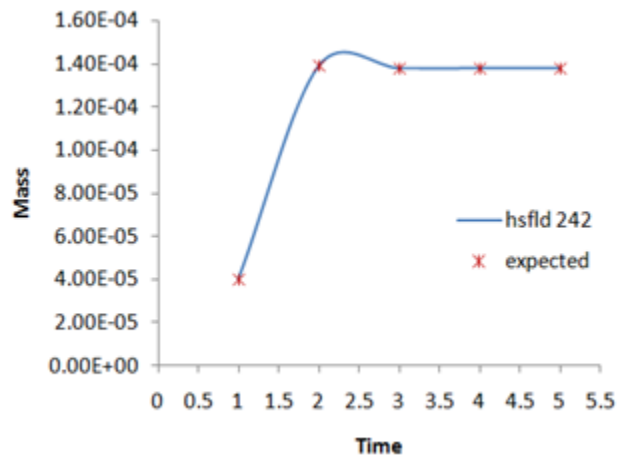
The following figures shows the condition of the inside air and its effect on the axle through each load step:

**Figure 24.10: Fluid Pressure Variation**



**Figure 24.11: Fluid Volume Variation**



**Figure 24.12: Fluid Density Variation****Figure 24.13: Fluid Mass Variation**

Most importantly, the figures indicate a good agreement with the expected results, validating the use of hydrostatic fluid element [HSFLD242](#) to model the air inside of the tire.

### 24.7.4. Tire Deformation Simulation

The following animation shows the tire deformation through all load steps:

**Figure 24.14: Tire Deformation (All Load Steps)**

## 24.8. Recommendations

To perform a similar analysis of a fluid that is fully enclosed within a solid container, consider the following hints and recommendations:

- **Verify the fluid elements.**

After creating the fluid elements (**ESURF**), note whether they have positive or negative volumes. Fluid elements have negative volumes if nodes are ordered in a clockwise direction, or if the normal of the container is oriented outward from the pressure node.

- **Introduce the fluid mass based on the volume of the fluid element.**

Set KEYOPT(5) = 1 for the hydrostatic fluid. No mass is added if the volume becomes negative.

- **Specify the fluid compressibility type.**

Set KEYOPT(6) = 0 for the hydrostatic fluid to model compressible fluid (default), or KEYOPT(6) = 1 to model incompressible fluid.

- **Determine the pressure node location carefully.**

The pressure node can be located anywhere within the fluid volume. If the fluid volume is bounded by one or more symmetry lines or planes, however, the pressure node must be on the line or plane of symmetry, or on the intersecting corner or line of multiple symmetry lines or planes, and it must have symmetrical boundary conditions.

- **Use impact constraints appropriately.**

For contact, specify impact constraints (KEYOPT(7) = 4). This option includes automatic time-increment adjustments for standard (default) or rough contact (KEYOPT(12) = 0 or 1, respectively) in a transient dynamic analysis.

- **Display the reinforcing elements.**

To display the reinforcing elements, issue the following commands:

```
/psymb,layr,1
/device,vector,1
```

## 24.9. Input Files

The following files were used in this problem:

- `tire_hsfld242.dat` -- Input file for the tire analysis problem.
- `tire_hsfld242.cdb` -- The common database file containing the model information for this problem (called by `tire_hsfld242.dat`).

The files are available in the `td-24` folder. See [Obtaining the Input Files \(p. xxxv\)](#) for more information.



---

## Chapter 25: Cardiovascular Stent Simulation

---

This example problem demonstrates how to simulate stent-artery interaction during and after stent placement in an occluded artery. The analysis uses advanced modeling techniques including [contact](#), [element birth and death](#), [mixed u-P formulation](#), and [nonlinear stabilization](#).

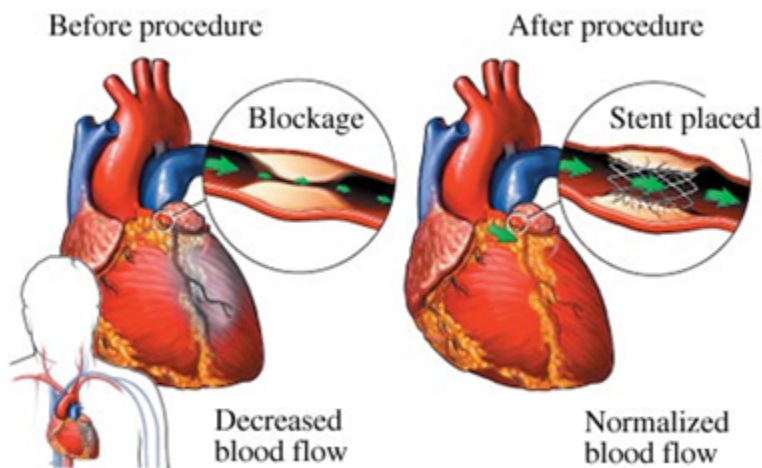
Topics related to this example problem follow:

- 25.1. Introduction
- 25.2. Problem Description
- 25.3. Modeling
- 25.4. Material Properties
- 25.5. Boundary Conditions and Loading
- 25.6. Analysis and Solution Controls
- 25.7. Results and Discussion
- 25.8. Recommendations
- 25.9. References
- 25.10. Input Files

### 25.1. Introduction

A bare metal stent, as shown in the following figure (courtesy of [Lakeview Center](#)) is an effective device for opening atherosclerotic arteries and other blockages:

**Figure 25.1: Effect of Stent Placement in Increasing Blood Flow**



The success of stenting depends largely on how the stent and the artery interact mechanically. In both the stent-design process and in pre-clinical patient-specific evaluations, computer simulation using finite element analysis (FEA) has become an accepted tool for studying stent-artery interaction.

A viable stent-artery finite element model must properly reflect the nonlinear nature of the phenomenon, such as the biological tissue properties, large arterial wall deformation, and the sliding contact between

the stent and the artery wall. This example problem shows how to use appropriate technologies to overcome these modeling challenges.

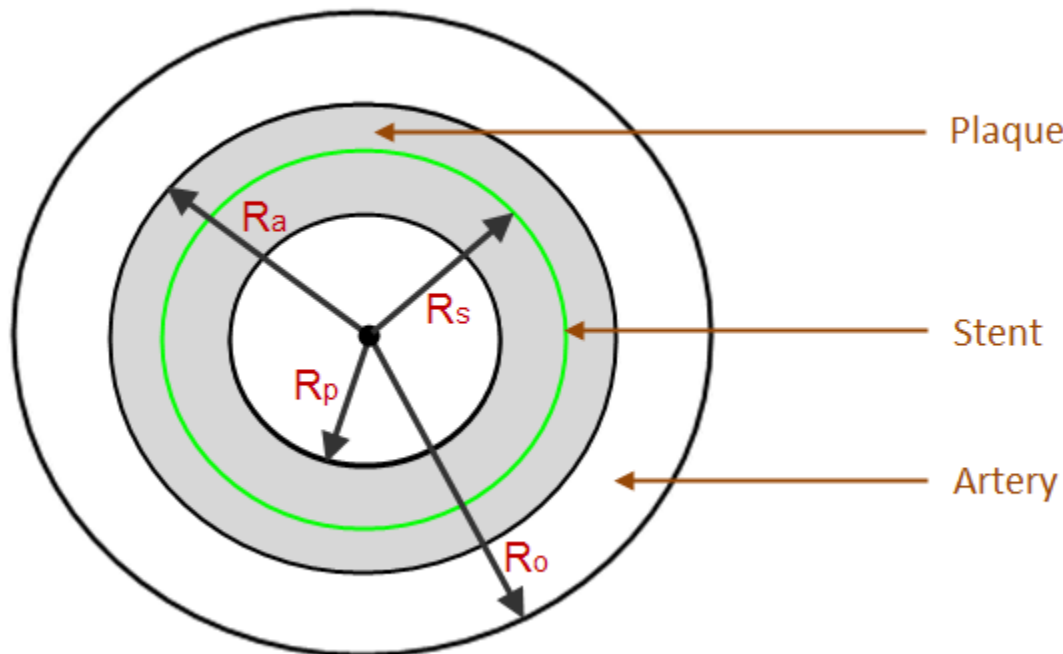
## 25.2. Problem Description

A Medtronic Driver<sup>®</sup> (formerly S7) coronary stent and a severely occluded coronary artery are modeled.

The artery is simplified as a two-layered straight cylinder, with one layer representing the artery wall and the other representing the calcified plaque.

The following figure shows the general dimensions of the artery and stent:

**Figure 25.2: Cross-sectional View of Unloaded Artery and Stent**



$R_a$  (inner artery radius) = 2.1 mm

$R_s$  (stent radius) = 1.75 mm

$R_p$  (inner plaque radius) = 1.6 mm

$R_o$  (outer artery radius) = 2.6 mm

A nonlinear static analysis is performed to simulate the three-step stenting procedure:

1. Expand the artery using elevated pressure (balloon angioplasty).
2. Place the stent.
3. Contract the artery using mean blood pressure and creating contact between the stent and the artery wall.

## 25.3. Modeling

Cardiovascular stent modeling involves three components:

[25.3.1. Stent Modeling](#)

[25.3.2. Artery and Plaque Modeling](#)

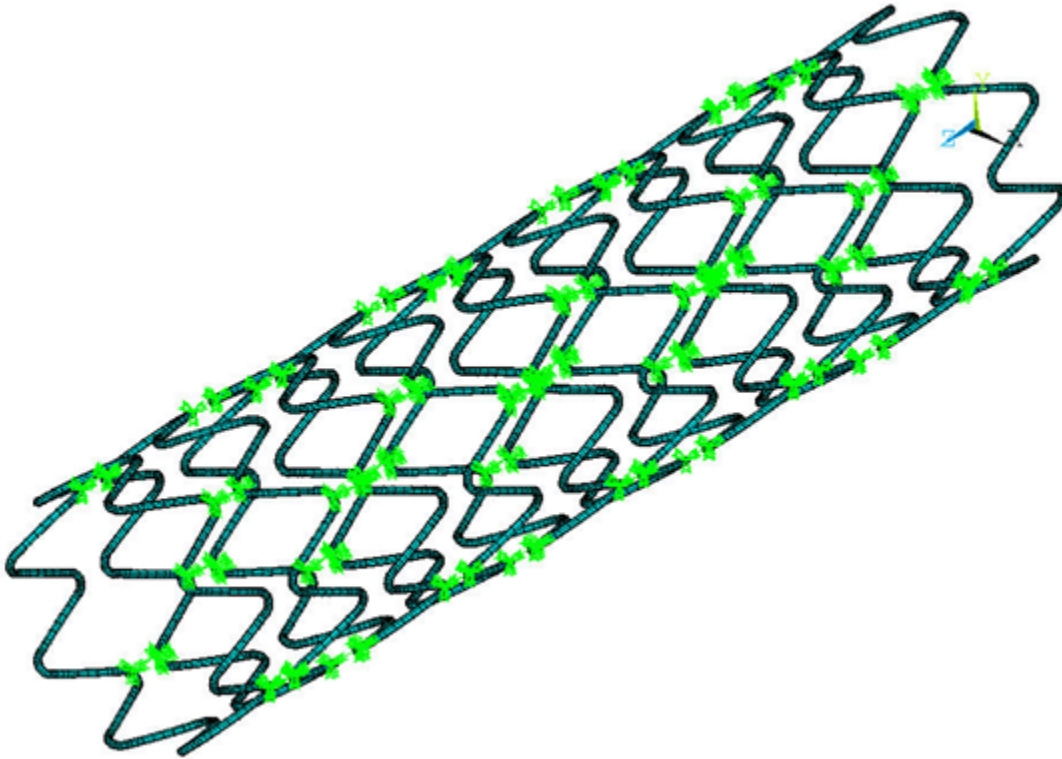


### 25.3.3. Stent-Plaque Contact Modeling

#### 25.3.1. Stent Modeling

A line model of the stent is created and then meshed with 1,760 BEAM189 beam elements, as shown in the following figure:

**Figure 25.3: Stent Model 3-D Expanded Solid Display**



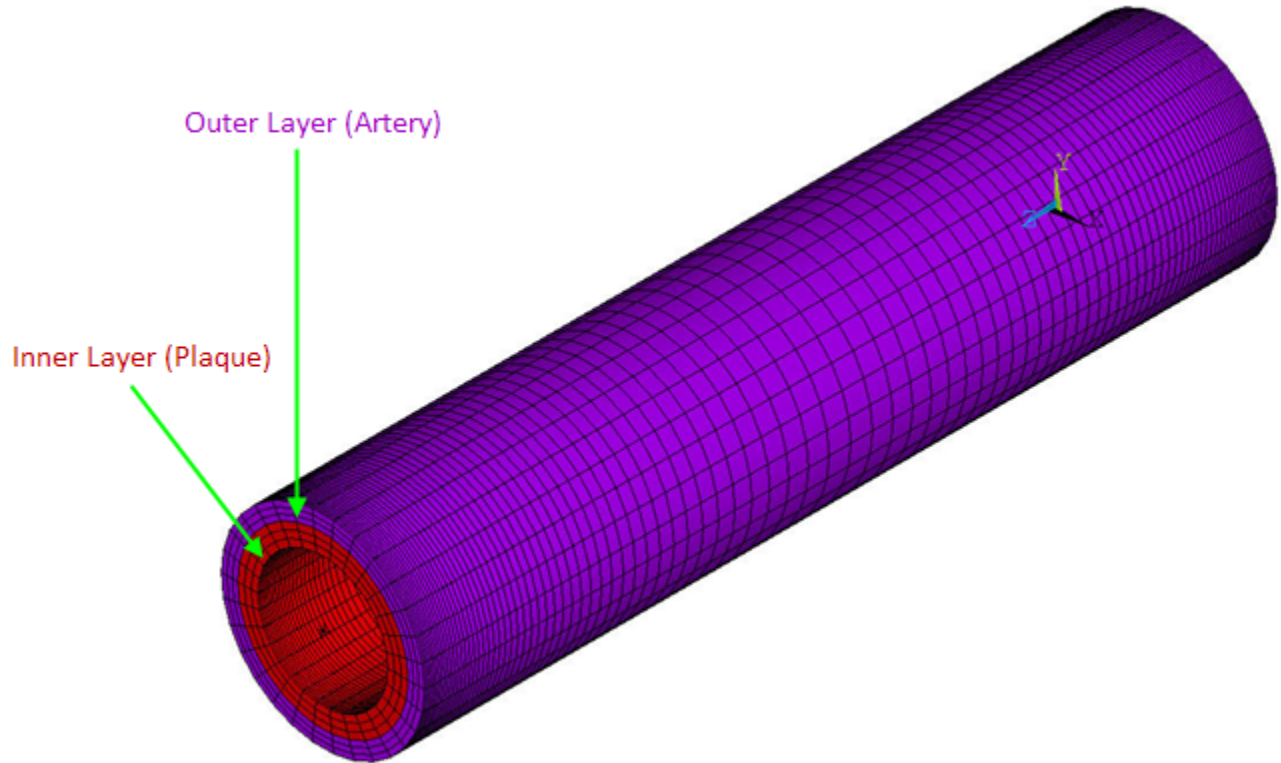
For modeling simplicity and computational efficiency, beam elements are preferred over solid elements.

The stent assembly has a 3.5 mm diameter, a 15 mm length, and 8 crowns. The wire for constructing the stent has a circular cross-section with an outer diameter of 0.1 mm.

Although Nitinol material is commonly used for the stent, the nonlinear material behavior of Nitinol requires a separate discussion. For the purposes of this problem, therefore, the model uses linear elastic 316L steel instead.

#### 25.3.2. Artery and Plaque Modeling

The simplified two-layer artery and plaque model is meshed with 3-D solid elements, as shown in this figure:

**Figure 25.4: Simplified Atherosclerotic Artery Model**

The artery layer is meshed with 9,000 **SOLID185** layered structural solid elements with the simplified enhanced strain formulation ( $\text{KEYOPT}(2) = 3$ ). Mixed u-P formulation ( $\text{KEYOPT}(6) = 1$ ) is used to overcome the volumetric locking typically associated with incompressible biological tissue.

The plaque layer is also meshed with 9,000 **SOLID185** elements. Full integration with the  $\bar{B}$  method is used for the plaque elements, as the material of the calcified plaque is considered to be linear elastic.

A coincident mesh is created at the artery-plaque interface to enforce a secure bond between the artery and the plaque.

Based on St. Venant's principle, both the artery and plaque are extended by 3 mm to reduce end effects. Fine elements are used near the two ends to mitigate any convergence difficulty caused by large localized deformation.

### 25.3.3. Stent-Plaque Contact Modeling

Contact between the inner plaque wall and stent from arterial contraction is modeled as **line-to-surface contact**.

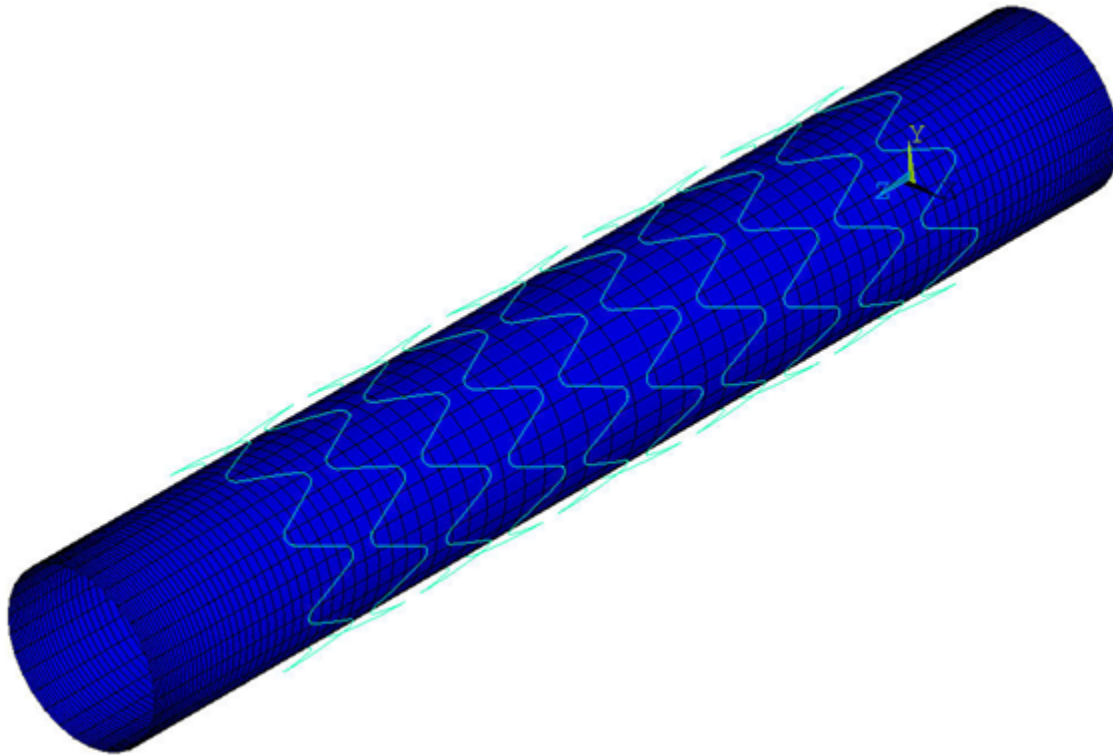
The stent lines are meshed with **CONTA177** contact elements.

A Lagrangian multiplier method on contact normals and penalty tangent method on target normals is used ( $\text{KEYOPT}(2) = 3$ ), along with automatic bisection ( $\text{KEYOPT}(7) = 1$ ) and standard contact behavior ( $\text{KEYOPT}(12) = 0$ ).

The inner plaque wall surface is meshed with **TARGE170** target elements. Zero-friction behavior is assumed [1].

The following figure illustrates the stent-plaque contact:

**Figure 25.5: Standard Line-to-Surface Contact Between Stent and Inner Plaque Wall**



## 25.4. Material Properties

Material properties [1] for the stent, artery, and plaque are as follows:

	Linear Elastic		Mooney-Rivlin Hyperelastic			
	EX (N/mm <sup>2</sup> )	PRXY	C10 (N/mm <sup>2</sup> )	C01 (N/mm <sup>2</sup> )	C20 (N/mm <sup>2</sup> )	C11 (N/mm <sup>2</sup> )
<b>Stent</b>	2.00E+05	0.3				
<b>Artery</b>			1.89E-02	2.75E-03	5.90E-01	8.57E-01
<b>Plaque</b>	2.19	0.49				

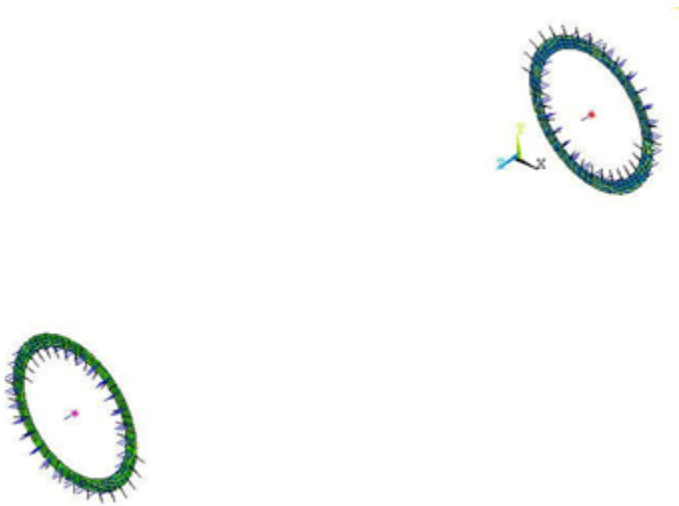
## 25.5. Boundary Conditions and Loading

The following topics concerning boundary conditions and loading for the cardiovascular stent simulation are available:

- 25.5.1. Artery Boundary Conditions
- 25.5.2. Stent Boundary Conditions
- 25.5.3. Plaque Wall Loading

### 25.5.1. Artery Boundary Conditions

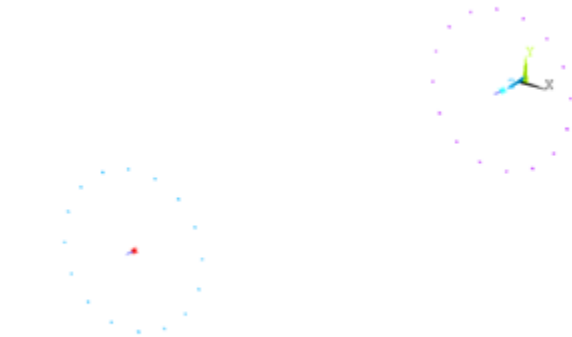
A [multipoint constraint \(MPC\)](#), force-distributed constraint is applied to the proximal and distal surfaces of the artery by specifying KEYOPT(2) = 2, KEYOPT(4) = 1 and KEYOPT(12) = 5 for the [CONTA174](#) elements, as shown in the following figure:

**Figure 25.6: Artery Boundary Conditions**

MPC pilot nodes (TARGE170) are fixed in all six degrees of freedom. The boundary conditions allow for radial arterial expansion, while adequately preventing rigid body motion of the artery.

### 25.5.2. Stent Boundary Conditions

As with the artery, an MPC-based, force-distributed constraint is applied to selected nodes on the proximal and distal ends of the stent (CONTA175), as shown in this figure:

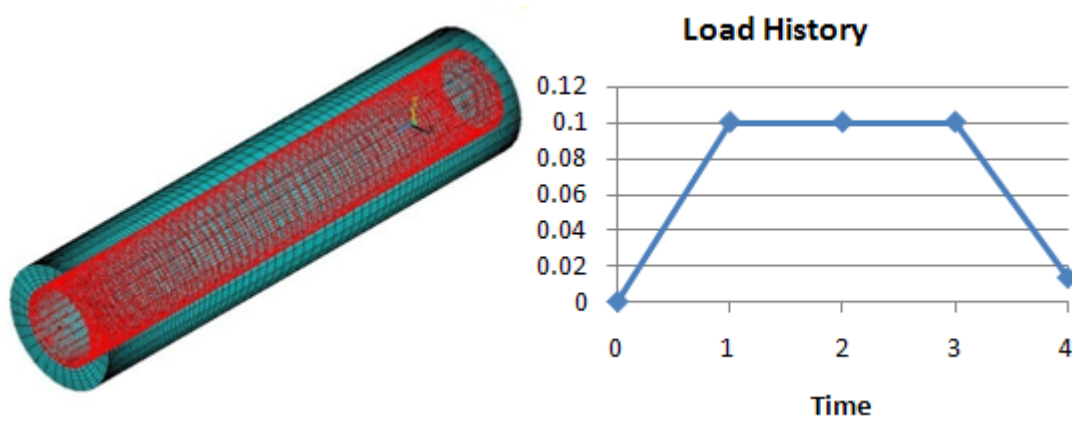
**Figure 25.7: Stent Boundary Conditions**

MPC pilot nodes (TARGE170) are fixed in all six degrees of freedom.

### 25.5.3. Plaque Wall Loading

Surface pressure loads are applied to all nodes on the inner plaque wall, representing the balloon expansion pressure in the first load step ( $0.1 \text{ N/mm}^2$ ) and blood pressure in the fourth load step ( $0.0133 \text{ N/mm}^2$ ).

The following figure illustrates the load surface and load history:

**Figure 25.8: Uniform Pressure Loading on the Inner Plaque Wall (a) and Load History (b)**

(a)

(b)

## 25.6. Analysis and Solution Controls

A nonlinear static analysis (**ANTYPE,STATIC**) with large-deflection effects (**NLGEOM,ON**) is specified. Contact parameters are optimized (**CNCHECK,AUTO**) to achieve better convergence based on overall contact-pair behaviors.

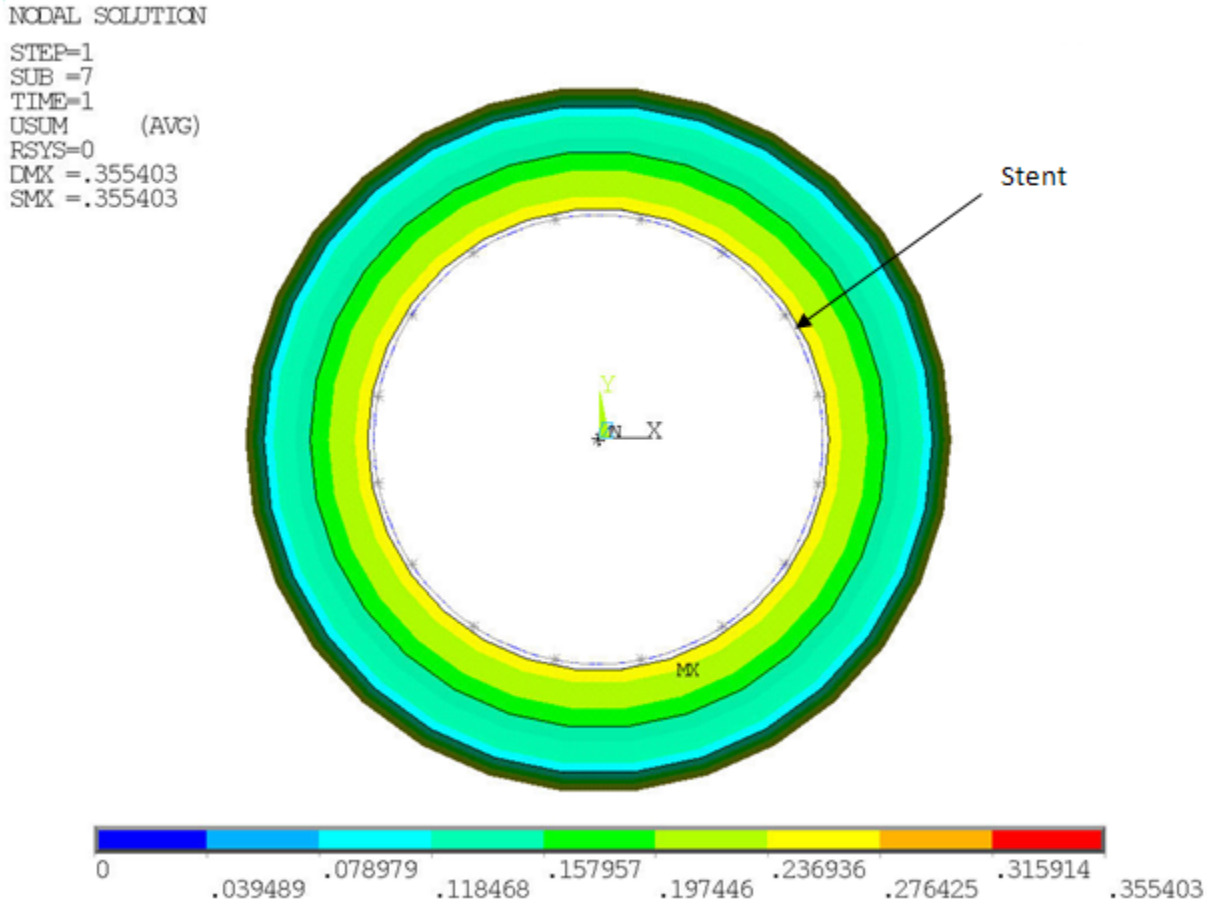
### Load Step 1

During the first load step, an elevated blood pressure of  $0.1 \text{ N/mm}^2$  is applied to the inner surface of the plaque wall to cause sufficient radial wall expansion for subsequent stent placement.

Stent contact elements (**CONTA177**) are killed (**EKILL**) to remove the effects of the stent.

This load step uses a maximum of 20 substeps with 20 initial substeps (**NSUBST,20,20**).

The following figure shows the effects of the first load step:

**Figure 25.9: Cross-Sectional View of Artery and Stent After Balloon Angioplasty (Load Step 1)**

### Load Steps 2 and 3

Load steps 2 and 3 use three total substeps to allow the **Newton-Raphson** residuals (from the nonlinear expansion in load step 1) to equilibrate after the stent contact elements are reactivated (**EALIVE**).

### Load Step 4

In the fourth load step, blood pressure is ramped to a magnitude of  $0.0133 \text{ N/mm}^2$ , which represents the mean arterial blood pressure (100 mmHg).

Under this reduced load, the atherosclerotic artery collapses onto the stent scaffold.

This load step uses 200 initial substeps, 2000 maximum substeps, and 20 minimum substeps to obtain contact convergence (**NSUBST,200,2000,20**).

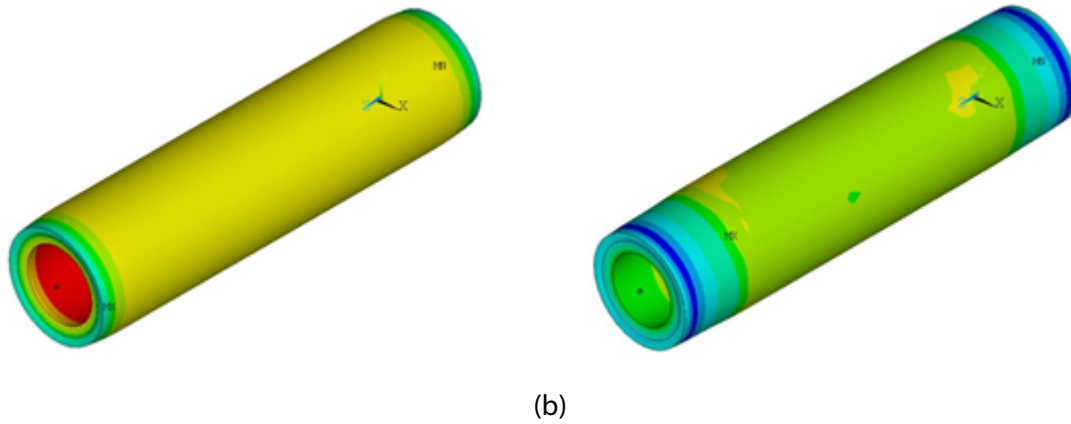
**Nonlinear stabilization** (**STABILIZE,CONST,ENERGY,0.1**) helps to achieve solution convergence during this load step.

## 25.7. Results and Discussion

Proper element technologies and solution options allow a successful nonlinear simulation of stent-artery interaction. The analysis generates detailed information about the post-insertion artery wall deformation, wall stresses, and stent retraction.

The positive effect of stenting is evident in the following figure, which shows the artery wall configurations before and after stent placement:

**Figure 25.10: Arterial Wall Deformation During Balloon Angioplasty (a) and After Stent Placement (b)**



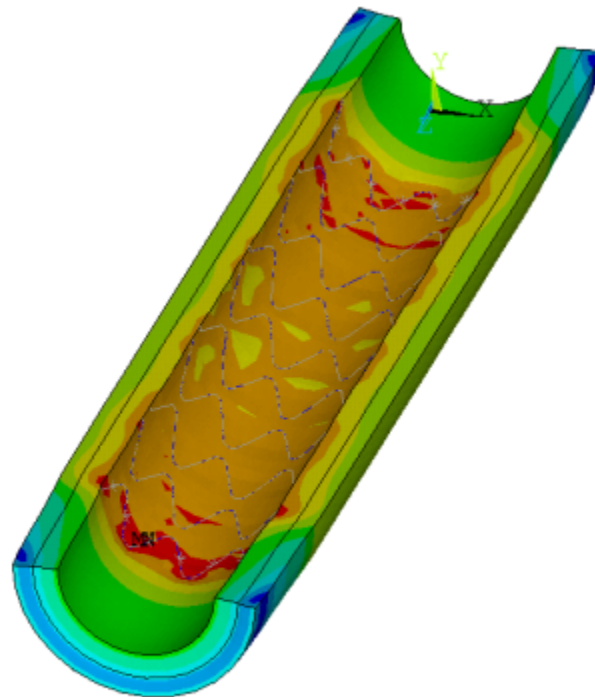
The following figure clearly shows the expected tissue prolapse (tissue extension into the gaps in the stent):

**Figure 25.11: Arterial Wall Displacement and Tissue Prolapse Results**

```

NODAL SOLUTION
STEP=4
SUB =59
TIME=4
USUM      (AVG)
RSYS=0
DMX = .185574
SMN = .172E-03
SMX = .185574

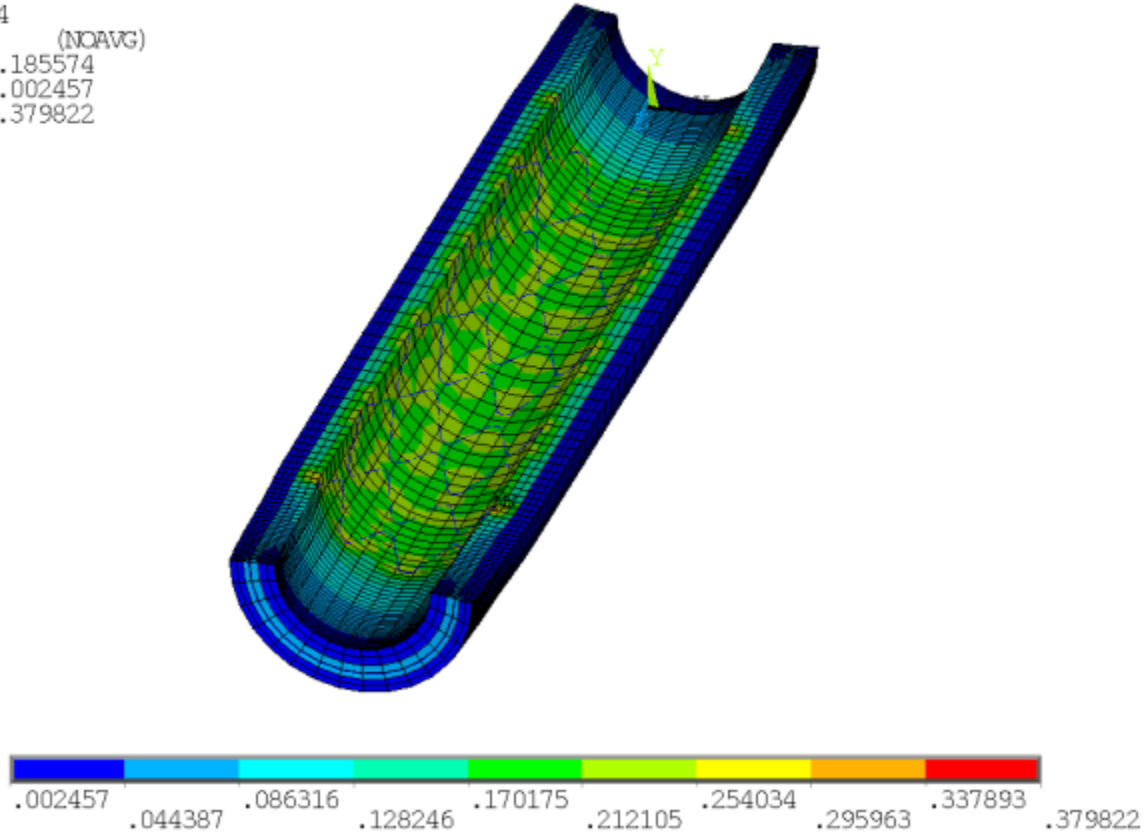
```



This figure shows the detailed stress distribution on the inner artery wall, with an expected pattern matching the stent geometry:

**Figure 25.12: Arterial Wall von Mises Stress Results**

ELEMENT SOLUTION  
STEP=4  
SUB =59  
TIME=4  
SEQV (NOAVG)  
DMX =.185574  
SMN =.002457  
SMX =.379822



Finally, the stent retraction under compressive load from the occluded artery wall is shown in this figure:

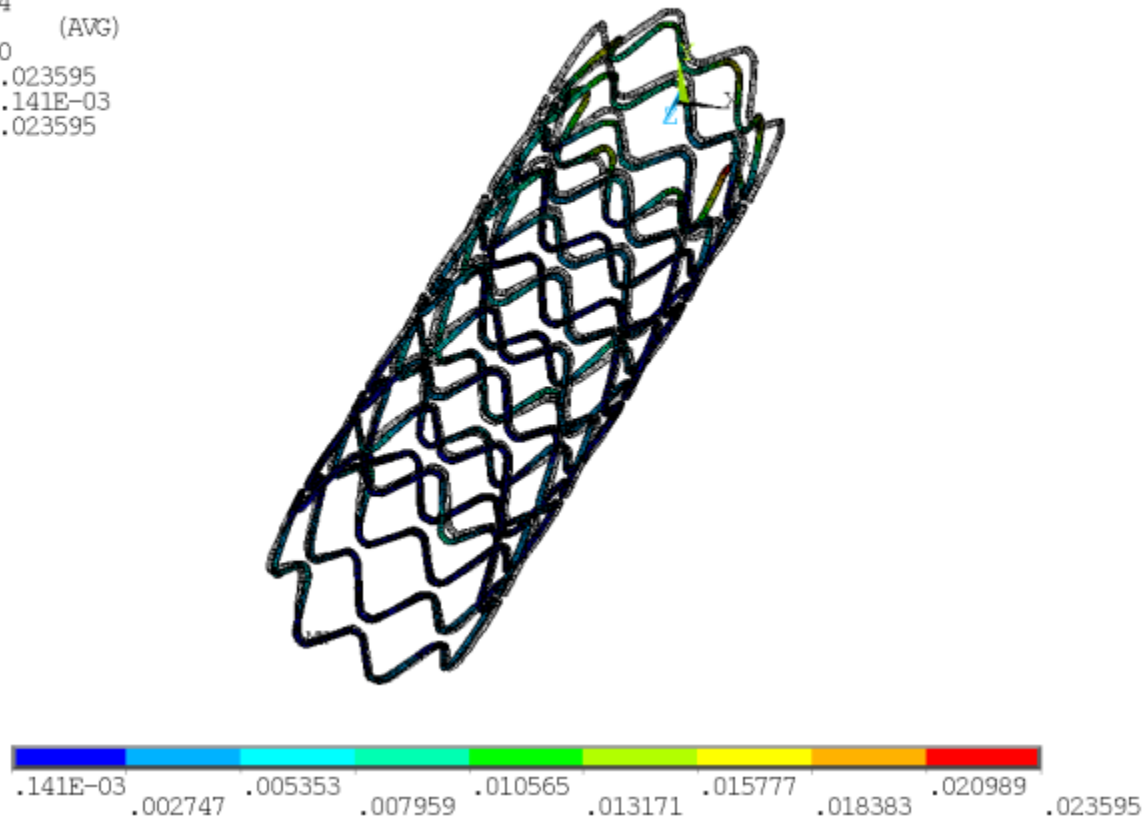


**Figure 25.13: Stent Retraction Resulting from Arterial Compression**

```

NODAL SOLUTION
STEP=4
SUB =59
TIME=4
USUM      (AVG)
RSYS=0
DMX =.023595
SMN =.141E-03
SMX =.023595

```



The simulation results agree well with those in the published literature [1].

FEA-based simulation is capable of quickly generating accurate and detailed information about stent-artery interaction. Finite element modeling is being used not only to develop state-of-the-art stent innovations, but also for pre-clinical patient-specific assessment and customization.

## 25.8. Recommendations

To perform a similar stent-artery interaction analysis, consider the following hints and recommendations:

- Compared to surface-to-surface contact with a full solid model, [line-to-surface contact](#) can provide similar results using significantly less solution time.
- [Multipoint constraints](#) (MPCs) provide biologically accurate boundary conditions.
- The choice of units is critical for avoiding numerical difficulties. For biological problems, millimeters-micron units are preferred.
- To achieve faster solutions, coincident nodes and surfaces are preferred over bonded contact.
- [Stabilization](#) mitigates convergence issues in unstable nonlinear problems.

## 25.9. References

The following reference is used in this example problem:

1. Lally, C., F. Dolan, P.J. Pendergrast. [Journal of Biomechanics]. "Cardiovascular stent design and vessel stresses: a finite element analysis." 38 (2005): 1574-1581.

## 25.10. Input Files

The following files were used in this problem:

- `stent.dat` -- Input file for the cardiovascular stent problem.
- `stent.cdb` -- The common database file containing the model information for this problem (called by `stent.dat`).

The files are available in the `td-25` folder. See [Obtaining the Input Files \(p. xxxv\)](#) for more information.

---

## Chapter 26: Nonlinear Analysis of a Rubber Boot Seal

---

This example problem demonstrates the capabilities and advantages of the surface-projection-based contact method in a highly nonlinear problem. This analysis of a rubber boot seal model includes geometric, material, and changing status nonlinearities (contact).

The following features and capabilities are highlighted:

- 3-D surface-to-surface contact element technology
- Surface-projection-based contact
- Geometric nonlinearities
- Neo-Hookean hyperelastic material

Topics related to this example problem follow:

- 26.1. Introduction
- 26.2. Problem Description
- 26.3. Modeling
- 26.4. Material Properties
- 26.5. Boundary Conditions and Loading
- 26.6. Analysis and Solution Controls
- 26.7. Results and Discussion
- 26.8. Recommendations
- 26.9. Input Files

### 26.1. Introduction

Rubber boot seals are used in many industrial applications to protect the flexible joint between two bodies. In the automotive industry, rubber boot seals cover constant velocity joints on the drive shaft to protect them from the outside elements (dust, humidity, mud, etc.). These rubber boots are designed to accommodate the maximum possible swing angle of the joints and to compensate for changes in the shaft length.

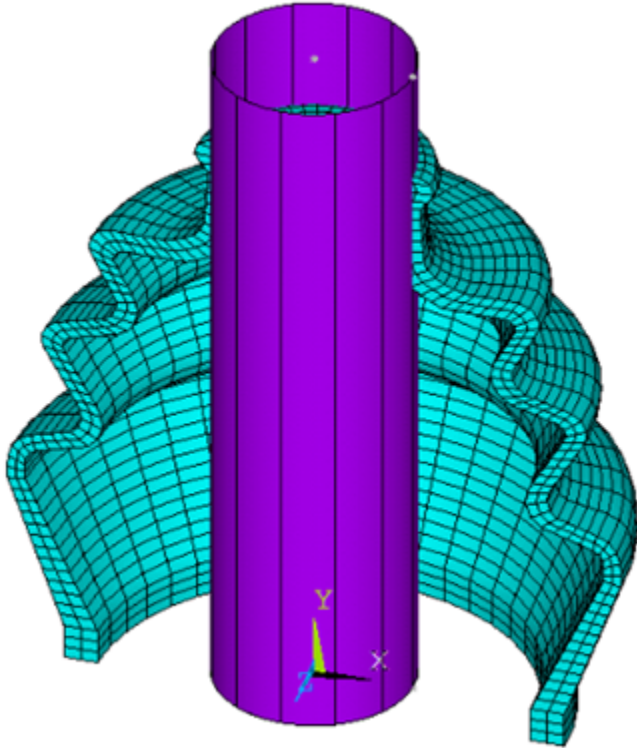
This rubber boot seal example demonstrates geometric nonlinearities (large strain and large deformation), nonlinear material behavior (rubber), and changing status nonlinearities (contact). The objective of this example is to show the advantages of the surface-projection-based contact method and to determine the displacement behavior of the rubber boot seal, stress results, and location of the contact point on the outer surface and inner surface of the boot during the shaft motion.

Surface-projection-based contact can be defined by setting `KEYOPT(4) = 3` for the contact elements. This option enforces contact constraints on an overlapping region of contact and target surfaces rather than on individual contact nodes or gauss points. The contact penetration/gap is computed over the overlapping region in an average sense.

## 26.2. Problem Description

A rubber boot seal with half symmetry is considered for this analysis. There are three contact pairs defined; one is rigid-flexible contact between the rubber boot and cylindrical shaft, and the remaining two are self contact pairs on the inside and outside surfaces of the boot.

**Figure 26.1: 3-D Model of Rubber Boot Seal and Rigid Shaft**



The problem is solved in three load steps:

1. Initial interference between the cylinder and boot
2. Vertical displacement of the cylinder (axial compression in the rubber boot)
3. Rotation of the cylinder (bending of the rubber boot)

## 26.3. Modeling

Due to the symmetry of the structure, only half of the rubber boot is modeled. For the rubber boot, the hyperelastic material model is used. The shaft is considered as a rigid body.

Modeling for this problem involves the following tasks:

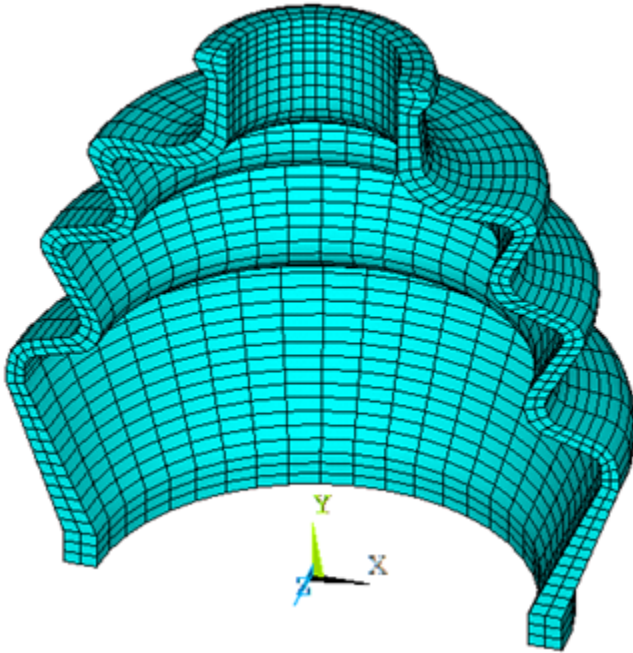
[26.3.1. Model the Rubber Boot Seal](#)

[26.3.2. Model the Contact Pairs](#)

### 26.3.1. Model the Rubber Boot Seal

The 3-D model is generated by using the rubber boot seal profile. **SOLID185** elements are used to model the actual 3-D structure of the rubber boot as shown in the figure below. This model has 3387 elements.

**Figure 26.2: Half Symmetry Model of the 3-D Rubber Boot Seal**



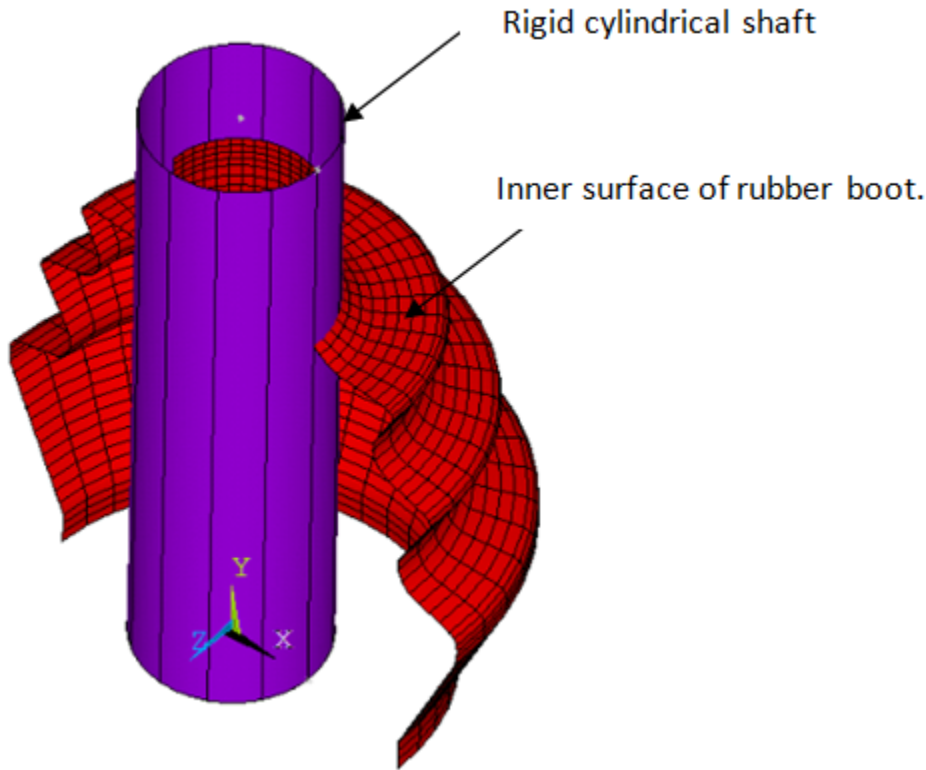
### 26.3.2. Model the Contact Pairs

Three contact pairs are defined to simulate contact occurring in the rubber boot during the shaft movement:

- Rigid flexible contact between the rigid cylindrical shaft and the inner surface of the rubber boot.
- Self contact at the inner surface of the rubber boot using the surface-projection-based contact method.
- Self contact at the outer surface of the rubber boot using the surface-projection-based contact method.

#### 26.3.2.1. Rigid-flexible Contact Pair between Rigid Shaft and Rubber Boot

The rigid cylindrical shaft is modeled by the **TARGE170** element with the **TSHAP,CYLI** command. The radius of the cylindrical shaft is 14 mm. This rigid cylinder is in initial interference with the internal surface of the rubber boot.

**Figure 26.3: Rigid-Flexible Contact Pair**

The following contact settings are used for the contact elements, [CONTA173](#):

- KEYOPT(9) = 2 to include interference with ramped effects
- KEYOPT(4) = 0 to set the location of the contact detection point at the gauss integration point
- KEYOPT(10) = 2 to update contact stiffness at each iteration

The following commands illustrate the contact settings of the rigid flexible contact pair:

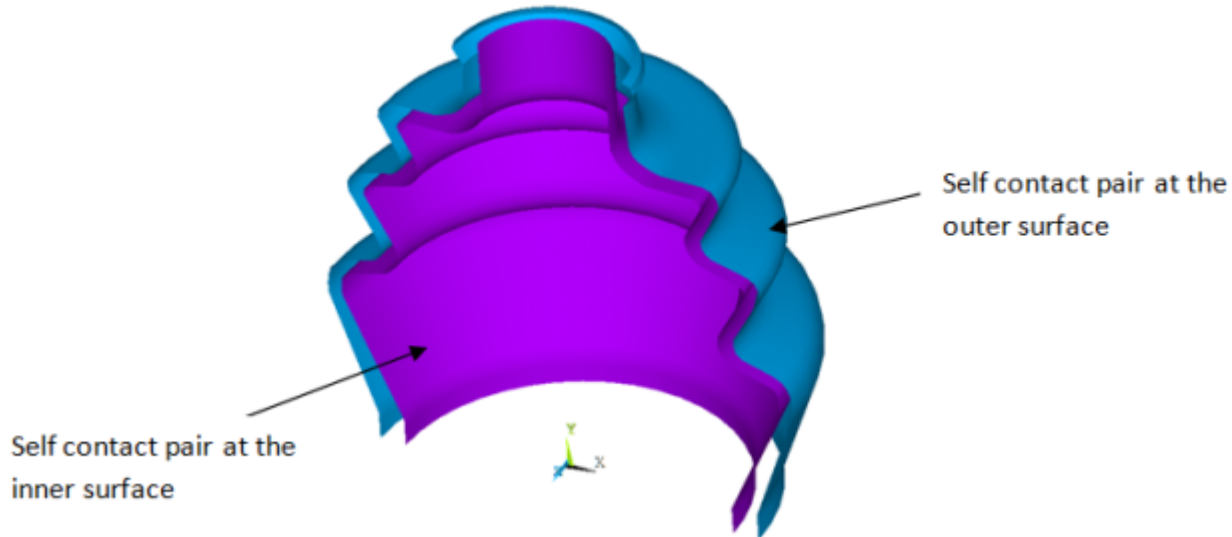
```

et,2,170           ! Target element to define rigid cylinder
et,3,173           ! Contact element for rigid-flexible contact pair
keyopt,3,9,2       ! Include interference with ramped effects
keyopt,3,4,0       ! Gauss point contact detection algorithm
keyopt,3,10,2      ! Update contact stiffness at each iteration
r,2
rmodif,2,1,14      ! Radius of the cylinder = 14 mm
rmodif,2,3,1.0

```

### **26.3.2.2. Self Contact Pairs at Inner and Outer Surfaces of Rubber Boot**

To model a self contacting pair, both the target and contact surfaces are the same. KEYOPT(4) = 3 is used to define surface-projection-based contact, and KEYOPT(10) = 2 is used to update contact stiffness at each iteration.

**Figure 26.4: Self Contact Pairs**

## 26.4. Material Properties

The rubber boot is made of a rubber material that exhibits an elastic response up to the large strain. Therefore, the Neo-Hookean model, an incompressible hyperelastic material model, is used for the rubber material.

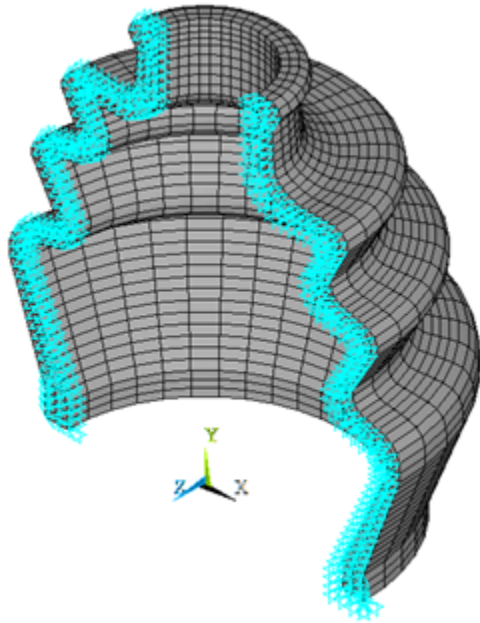
Constants for Neo-Hookean Model	
Initial shear modulus ( $\mu$ )	1.5 MPa
Incompressibility parameter (d)	0.026 MPa <sup>-1</sup>

In addition, the coefficient of friction for the rubber material is set to 0.2.

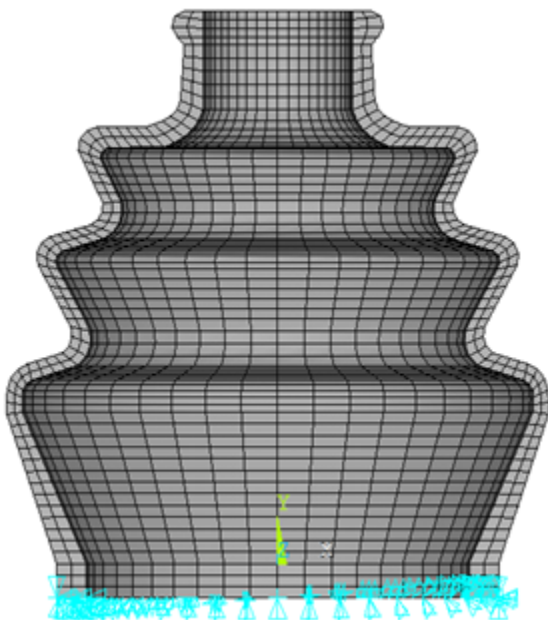
## 26.5. Boundary Conditions and Loading

The model is constrained at the symmetry plane by restricting the out-of-plane translation as shown in [Figure 26.5: Boundary Conditions at a Symmetry Plane \(p. 394\)](#). The bottom portion of the rubber boot is restricted in axial and radial directions as shown in [Figure 26.6: Boundary Conditions at the Bottom of the Rubber Boot \(in the Axial Direction\) \(p. 394\)](#) and [Figure 26.7: Boundary Conditions at the Bottom of the Rubber Boot \(in the Radial Direction\) \(p. 395\)](#).

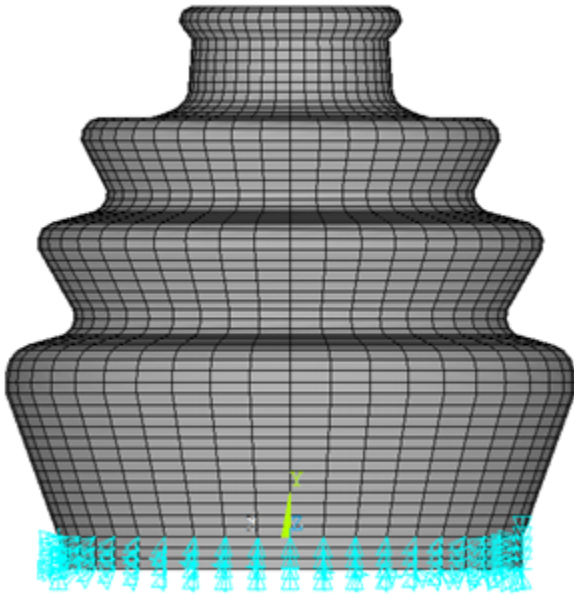
**Figure 26.5: Boundary Conditions at a Symmetry Plane**



**Figure 26.6: Boundary Conditions at the Bottom of the Rubber Boot (in the Axial Direction)**





**Figure 26.7: Boundary Conditions at the Bottom of the Rubber Boot (in the Radial Direction)**

The load is applied in terms of displacements and rotations through different load steps.

- **Load Step 1**

Base node (pilot node) at the end of the shaft's center axis is constrained in all direction as follows:

```
RIGID_BASE=1
RIGID_TOP =2
n,RIGID_BASE,0,0,0      ! Base node at the end of the
                        ! shaft's center axis
n,RIGID_TOP,0,97,0     ! Top node at the shaft's center axis
d,RIGID_BASE,all
```

- **Load Step 2**

Boot seal gets compressed when the shaft moves down. The vertical movement of the shaft is governed by the displacement applied to the base node (pilot node) at the end of the shaft's center axis. The following displacement is applied at the pilot node for the 2nd load step.

```
d,RIGID_BASE,uy,-10
```

- **Load Step 3**

Shaft is rotated by giving certain amount of rotation about z-axis to the base node (pilot node) at the end of the shaft's center axis, as follows:

```
d,RIGID_BASE,rotz,0.55
```

## 26.6. Analysis and Solution Controls

A nonlinear static analysis is performed in three load steps. Large-deflection effects are included in the analysis via the command **NLGEOM,ON**.

```

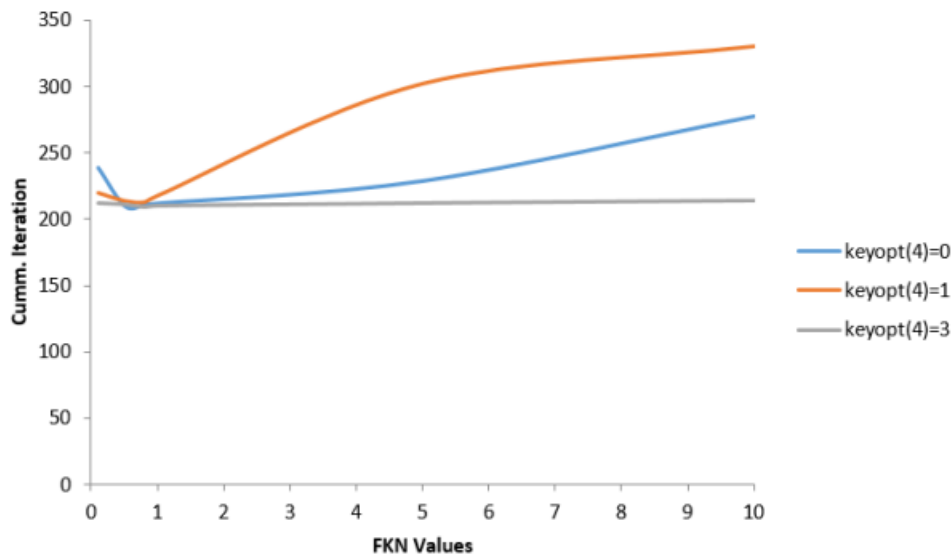
antype,static      ! select static analysis
nlgeom,on         ! include geometric nonlinearities
    
```

## 26.7. Results and Discussion

Figure 26.8: Comparison of Cumulative Iterations for Different Contact Detection Methods (p. 396) and Table 26.1: Simulation Statistics for Different Contact Detection Methods (p. 397) illustrate the following advantages of the surface-projection-based contact method by comparing it with other available contact detection algorithms.

- Compared to other methods, the surface-projection-based contact method (KEYOPT(4) = 3) requires the least number of cumulative iterations to solve this problem.
- Convergence of the problem is less sensitive to the normal contact stiffness factor (FKN) when using the surface-projection-based contact method (KEYOPT(4) = 3).

**Figure 26.8: Comparison of Cumulative Iterations for Different Contact Detection Methods**



The surface-projection-based contact method (KEYOPT(4) = 3) produces smoother contact forces than other contact detection algorithms. It is less sensitive to the magnitude of the contact stiffness.

For smaller values of FKN (0.1 to 1.0), the variation in cumulative iterations is less for all contact detection methods. But for the higher values of FKN (1 to 10), the variation in cumulative iterations for the surface-projection-based method is much less compared to the other contact detection methods. FKN = 1 is optimal for nonlinear analysis. This can be observed in Figure 26.8: Comparison of Cumulative Iterations for Different Contact Detection Methods (p. 396).

In general, the surface-projection-based contact method is much more expensive in computational time. In this particular model, the total number of iterations and substeps used with this method is less

than for other contact detection algorithms. The overall performance using the surface projection method turns out to be better. This can be observed in the table below:

**Table 26.1: Simulation Statistics for Different Contact Detection Methods**

	KEYOPT(4) = 0; Gauss Point	KEYOPT(4) = 1; Nodal Point	KEYOPT(4) = 3; Surface Projection
<b>Substeps</b>	45	45	45
<b>Cumulative Iterations</b>	212	218	210
<b>Simulation Time (sec)</b>	1223	1218	1097

Figure 26.9: Displacement Vector Sum at the Maximum Shaft Angle (p. 397) shows the displacement position of the boot at maximum shaft angle.

**Figure 26.9: Displacement Vector Sum at the Maximum Shaft Angle**

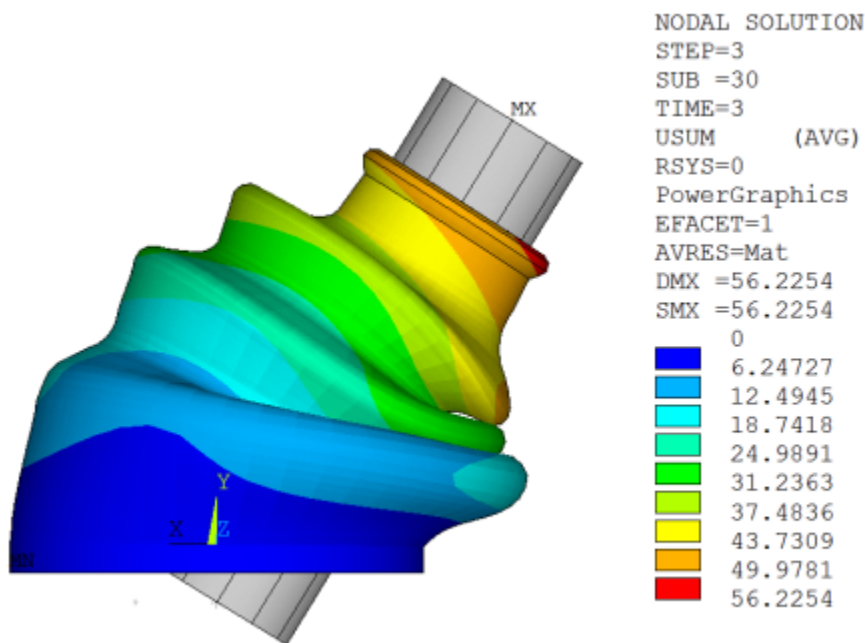
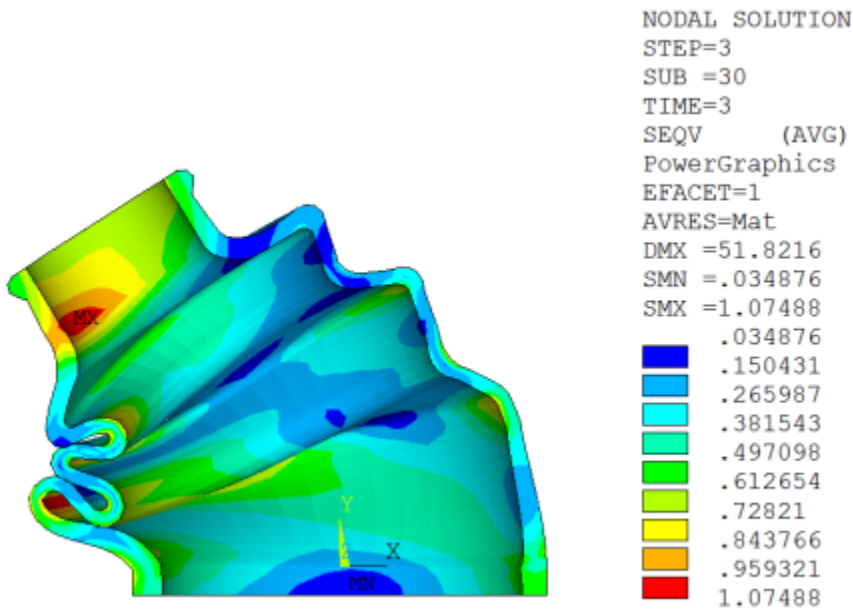


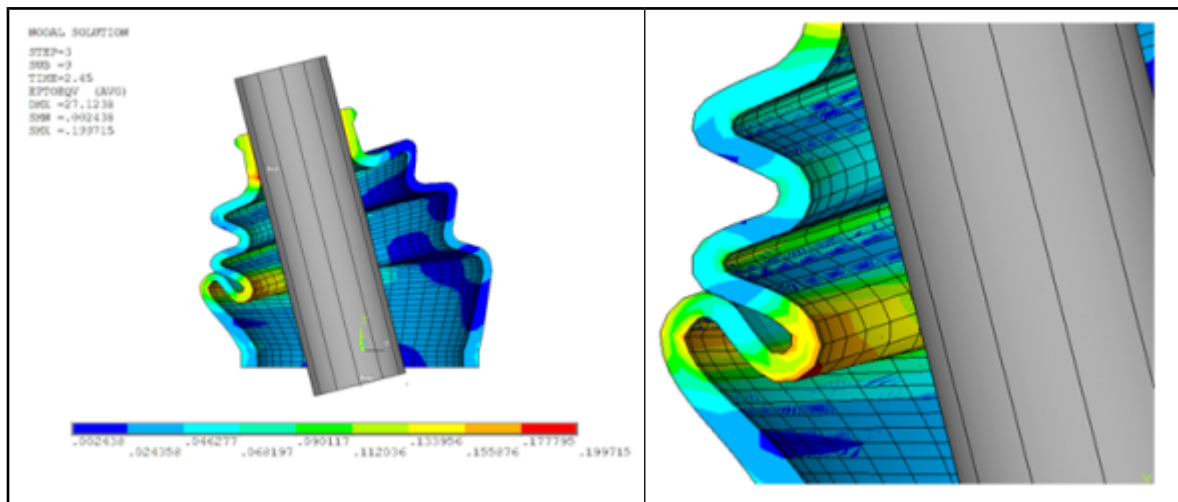
Figure 26.10: Von Mises Stress at the Maximum Shaft Angle (p. 398) illustrates the location of the critical zones where the maximum stress occurs in the boot at maximum shaft angle. In spite of the fact that it is low, and considering the fatigue effects of the material after a given number of cycles, it is clear that these areas are the most likely to fail under fatigue loads.

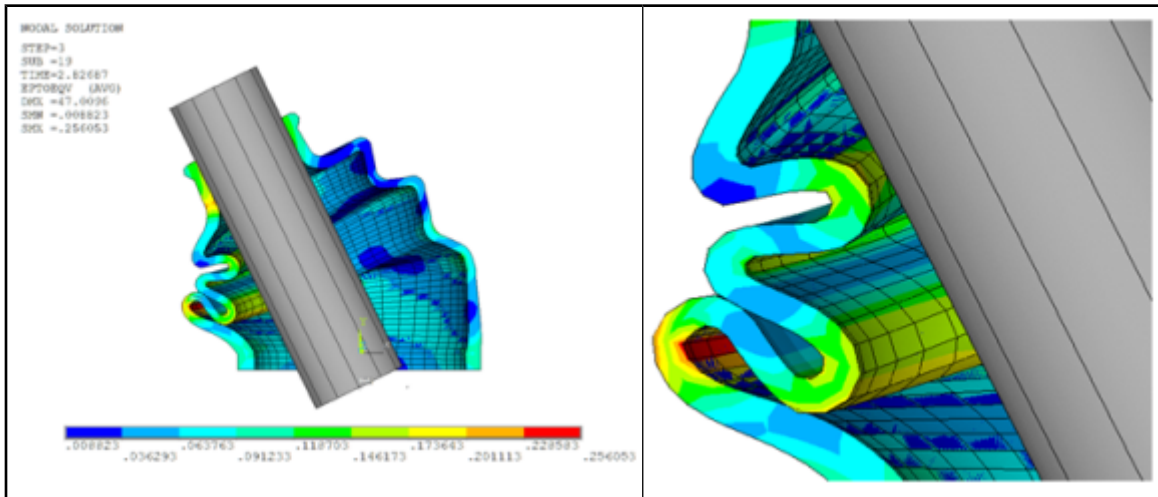
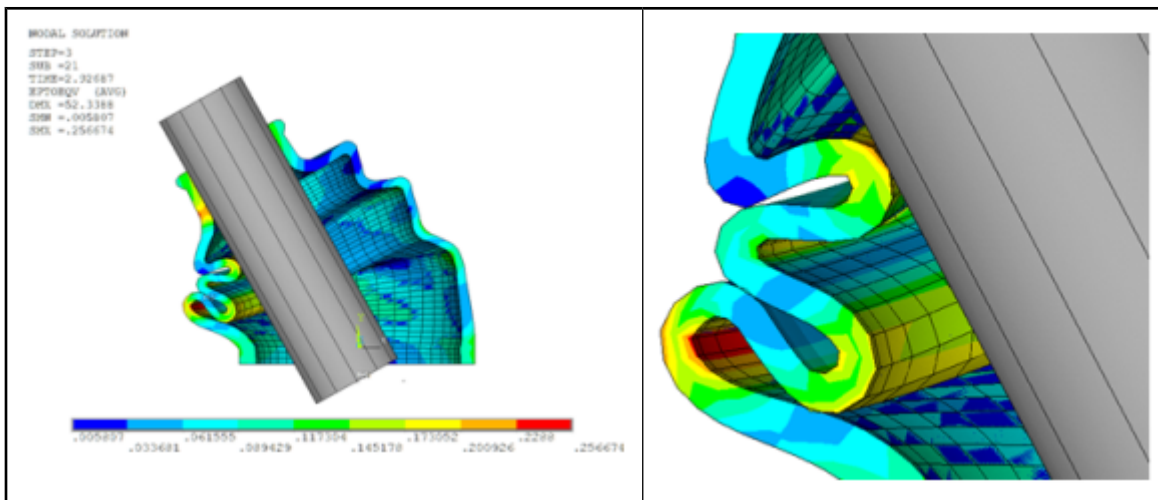
**Figure 26.10: Von Mises Stress at the Maximum Shaft Angle**



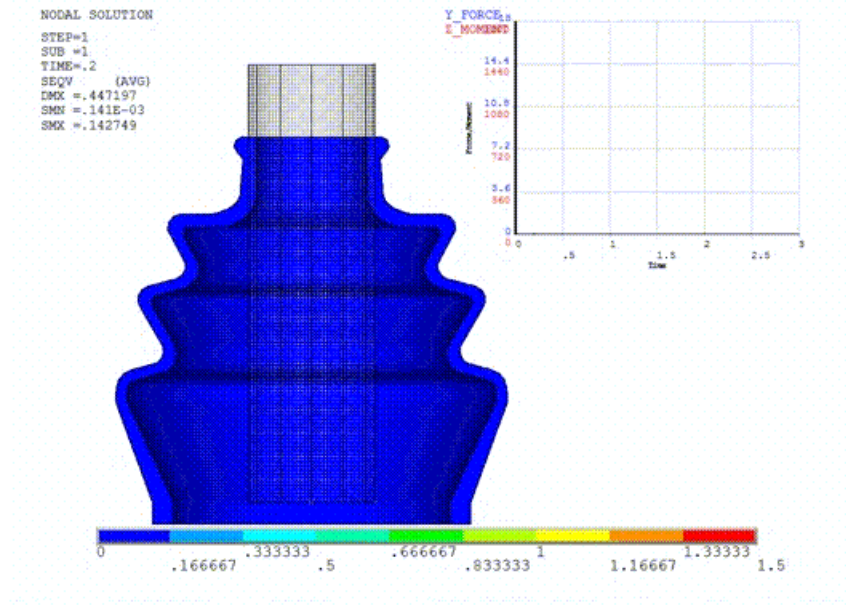
The following figures show total strain at different points of contact occurring in the rubber boot at different shaft angles. The first instance of contact occurs between the outer plaits of the rubber boot. After that, stretching is noticed in the first contact zone, and the second contact occurs between the inner plaits of the rubber boot. Finally, the third contact occurs between the inner plaits of the rubber boot and the shaft.

**Figure 26.11: Total Strain at First Contact between Outer Plaits of Rubber Boot**



**Figure 26.12: Total Strain at Second Contact between Inner Plaits of Rubber Boot****Figure 26.13: Total Strain at Third Contact between Inner Plaits of Rubber Boot and Shaft**

The following animation shows the von Mises stress, reaction force in the Y direction, and moment about the Z-axis through all load steps.

**Figure 26.14: Animated Results**

## 26.8. Recommendations

The following are recommendations for performing this type of analysis:

- Note that the surface-projection-based method (KEYOPT(4) = 3) is not used to define contact between the rigid shaft and the rubber boot because this method does not support rigid surfaces defined by primitive target segments.
- For problems such as an interference fit, over-penetration is expected. These problems often have convergence difficulties if the initial penetration is step-applied in the first load step. You may overcome convergence difficulties by ramping the total initial penetration over the first load step using KEYOPT(9) = 2.

## 26.9. Input Files

The following files were used in this problem:

- `bootseal_3d.dat` -- Input file for the nonlinear analysis of the rubber boot seal using surface-projection-based contact.
- `bootseal_3d.cdb` -- Common database file containing the model information for this problem (called by `bootseal_3d.dat`).
- `bootseal3d.anf` -- File containing geometry information for the 3-D rubber boot seal model.

The files are available in the `td-26` folder. See [Obtaining the Input Files \(p. xxxv\)](#) for more information.

---

## Chapter 27: Hot-Rolling Structural Steel Analysis with 3-D Rezoning

---

This example problem demonstrates the use of rezoning in a 3-D large-deformation problem. In large-deformation analyses (such as rolling, forging, and extrusion), elements are subject to excessive deformation, which can eventually cause the analysis to terminate.

The following features and capabilities are highlighted:

- [Rezoning](#) in 3-D problems
- Use of [contact technology](#) in complex problems
- User-defined [symmetric expansion](#) options

Topics related to this example problem follow:

- [27.1. Introduction](#)
- [27.2. Problem Description](#)
- [27.3. Modeling](#)
- [27.4. Material Properties](#)
- [27.5. Boundary Conditions and Loading](#)
- [27.6. Analysis and Solution Controls](#)
- [27.7. Results and Discussion](#)
- [27.8. Recommendations](#)
- [27.9. Input Files](#)

For more information about rezoning and the methods for repairing or replacing a distorted mesh, see [Rezoning](#) in the *Advanced Analysis Guide*.

### 27.1. Introduction

Hot-rolling is a metal-forming process occurring above the recrystallization temperature of the material. Many types of hot-rolling processes exist, including structural shape rolling, where a component is passed through rollers to achieve the desired shape and cross section.

Structural steel is the most common hot-rolled material. Common shapes for structural steel include I-beams, H-beams, T-beams, U-beams, and channels. I-beams have an I-shaped cross-section. The horizontal elements of the cross section are called *flanges*, and the vertical element is called the *web*.

In this example problem, the hot-rolling process to form the I-beam is simulated statically using [rezoning](#).

#### 27.1.1. Description of the Hot-Rolling Process

The hot-rolling process consists of two primary phases, *unsteady* and *steady*. The starting and the ending of the hot-rolling process represent the unsteady phase, while the rest of the process represents the steady-state phase.

In the unsteady phase, the billet (rectangular bar of steel) comes into contact with the rollers and fills the gap between the rollers before moving through the rollers. When the billet begins to move through the rollers, the process is considered to be in a steady state until the end face of the billet comes into contact with the rollers.

### 27.1.2. Hot-Rolling Process Simulation

Although a transient analysis is often used to simulate the hot-rolling process, a static analysis is generally preferred when dynamic effects are unimportant or when a transient analysis may require excessive resources. This example shows how both the unsteady and steady phases of the hot-rolling process can be simulated via a static analysis.

The static analysis is performed in two load steps: the first builds up the rolling process, and hot-rolling occurs in the second.

In the first load step, the billet moves toward rigid rollers to establish contact with the rollers and to fill the gap between the rollers. In order to build up the rolling process, the billet should partially fill the gap between rollers so that when rollers begin to rotate, they can pull the billet in via friction.

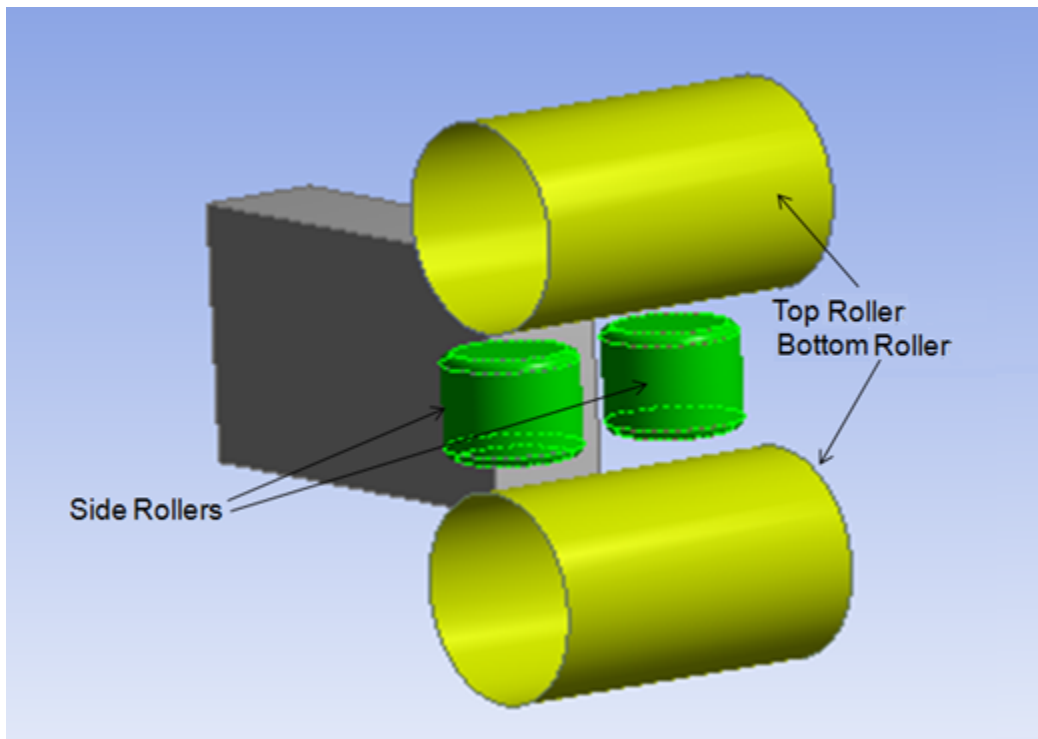
In the second load step, the rollers pull the billet in and eventually shape the rectangular billet into an I-section block.

In this example, the simulation terminates at near the end of the first load step due to mesh distortion. A [rezoning](#) operation repairs the distorted mesh, and the analysis resumes and continues to completion using the new mesh.

## 27.2. Problem Description

A rectangular block is passed through set of rollers to obtain an I-shaped beam, as shown in the following figure:



**Figure 27.1: Hot-Rolling Model**

Two types of rollers are used:

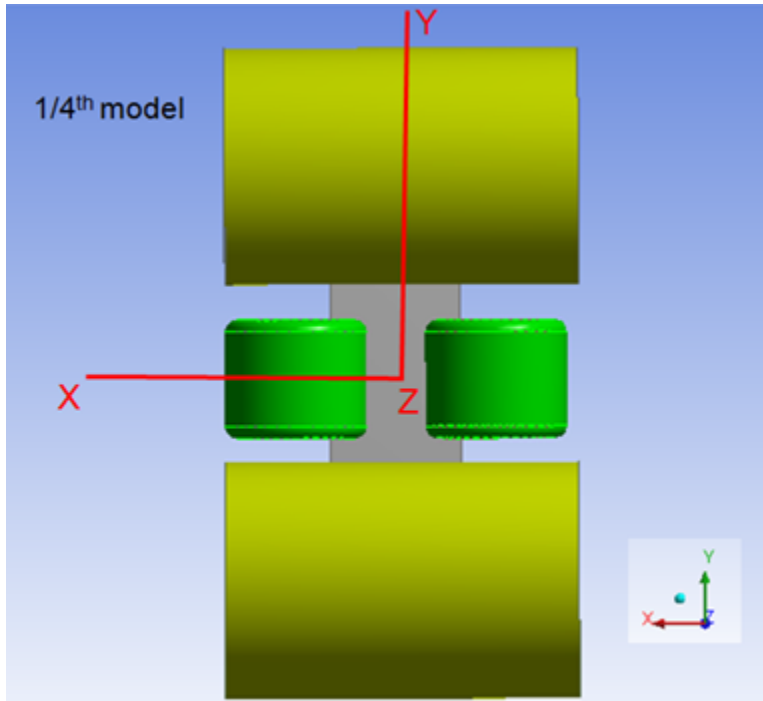
- **Top and bottom rollers**

Horizontal cylindrical rollers pull the block from the top and bottom to increase the width and reduce the depth of the block. The rollers control the width of the flange parts of the I-shape; they are modeled using rigid target elements.

- **Side rollers**

Vertical cylindrical rollers with small fillets at either end. The fillets are necessary to ensure smooth material flow. The side rollers pull the block from the sides to create the I-shaped cross section. They control the width of the web part of the I-shape. As with the top and bottom rollers, the side rollers are modeled using rigid target elements.

The following figure shows that the problem is symmetrical about two planes (XZ and YZ):

**Figure 27.2: Symmetric Hot-Rolling Model**

To reduce modeling and computational time, therefore, only one quarter of the model is analyzed. After the analysis has completed, however, the results are viewable in the full model by performing symmetry expansion about two planes of symmetry.

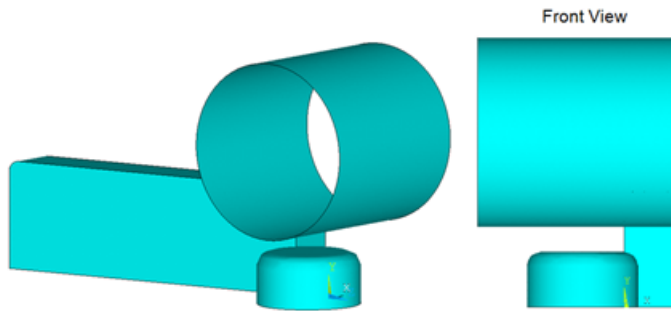
The simulation is performed statically in two load steps. In the first load step, the block is moved towards fully constrained rigid rollers in order to build up the rolling process. In the second load step, hot-rolling is performed by rotating the rollers about their axes of rotation, and the block is free to move in the horizontal direction (Z).

As the rollers rotate, the block passes through them due to the high level of friction between the rollers and the block. Eventually, the full block passes through the rollers to achieve the I-shaped cross section. In such large-deformation problems, however, mesh distortion is common, leading to convergence difficulties or eventual analysis termination.

The analysis diverges in the first load step due to excessive distortion in a few elements. A rezoning operation repairs the distorted mesh and allows the analysis to continue.

### 27.3. Modeling

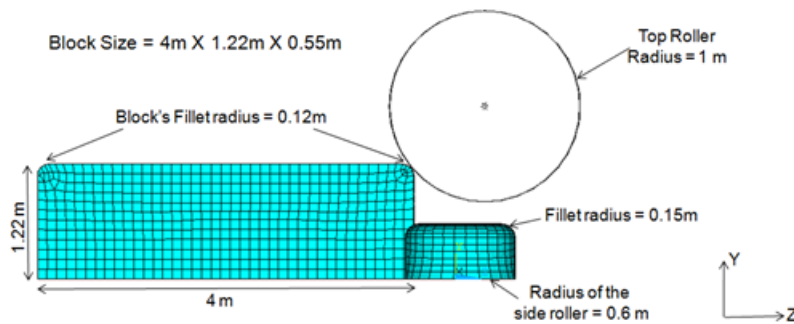
The following figure shows one-quarter of the model, all that is necessary for this analysis:

**Figure 27.3: Hot-Rolling Quarter Model Geometry**

The geometry of the block is 1/4 of the full geometry of the block shown in [Figure 27.1: Hot-Rolling Model](#) (p. 403). Appropriate geometries for the rollers are also considered in the quarter model.

### 27.3.1. Modeling the Block

Geometry of the block is created in DesignModeler and meshed with **SOLID185** (with mixed u-P formulation ( $KEYOPT(6) = 1$ )) elements. The following figure shows the dimensions and mesh of the block:

**Figure 27.4: Meshed Model with Dimensions**

Notice that the block has small fillets at either end of the top face. The fillet helps to establish contact with the top roller. Without the fillet, the sharp corner of the block would cause local singularities, and the analysis would diverge.

### 27.3.2. Modeling the Rollers

Dimensions for both roller pairs are shown in [Figure 27.4: Meshed Model with Dimensions](#) (p. 405). The rollers are modeled as rigid target surfaces.

Two methods are available for creating rigid target surfaces:

- **Generate Target Elements via Primitives**

Use this method if the shape of the target surface matches any of the available primitives (circle, cylinder, cone, and sphere). You can also combine primitive segments with general segments (lines, parabolas, triangles, and quadrilaterals) to define a target surface.

You must first specify the shape of the target elements (**TSHAP**), then define the radius via real constants. Create nodes (**N**) and elements (**E**) directly. The elements will have their shapes already defined.

- **Mesh the Areas with TARGE170 Target Elements**

Use this method when target surfaces cannot be modeled with primitives. Because the side rollers have fillets at either end, they cannot be modeled using primitives. In this case, CAD geometry of the side roller is created in DesignModeler and then meshed with TARGE170 elements to create the contact pair with the block.

For more information, see [Defining the Target Surface in the Mechanical APDL Contact Technology Guide](#).

### 27.3.3. Contact Modeling

The following two contact pairs are created:

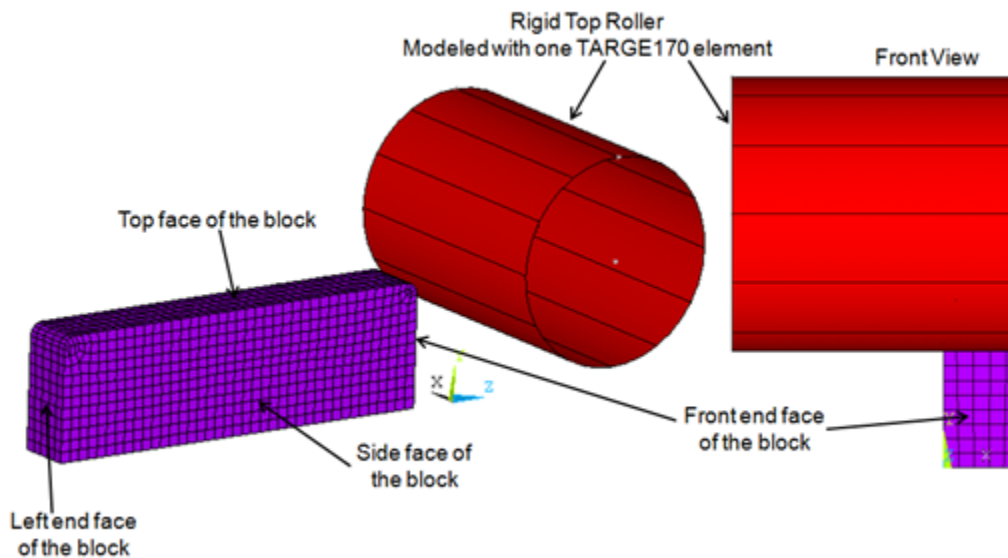
27.3.3.1. Contact Pair Between Block and Top Roller

27.3.3.2. Contact Between Block and Side Roller

#### 27.3.3.1. Contact Pair Between Block and Top Roller

A standard rigid-flexible contact pair is created between the top roller and the block. As shown in the following figure, four faces of the block are contact surfaces:

**Figure 27.5: Contact Between Block and Top Roller**



The contact surfaces are modeled via CONTA174 elements.

The rigid top roller is modeled using one TARGE170 element and primitives (TSHAP, CYLI).

One pilot node is created and associated with the top roller (the rigid target surface). The pilot node governs the motion of the entire target surface. (Think of a pilot node as a sort of handle for the rigid target surface.) Forces/moments or rotations/displacements for the entire target surface should generally be specified via the pilot node. The location of the pilot node is important when rotation or moment loading is required. In this case, the pilot node is created at the center of the mass of the top roller, as the roller must be rotated in the second load step.

The augmented Lagrangian algorithm is used in this contact pair. The following example input shows how the contact pair is modeled:

```

et,2,CONTA174
KEYOPT,2,10,2 ! Select option to update contact stiffness in each iteration
et,3,TARGE170

cmsel,s,tn.cnt ! Select the nodal component of 4 faces of the block
nplot
type,2          ! Select element type 2 (CONTA174)
real,3         ! Use Real Constant 3
esurf         ! Generate contact elements
allsel,all

! Model rigid top roller with primitives

n,9997,0.55,1.85,0.30 ! Create two nodes to define the axis of the cylinder
n,9998,-1.55,1.85,0.30

tshap,cylin     ! Select "Cylinder" primitive shape
type,3         ! Select element type 3 (TARGE170)
real,3         ! Use same real constant 3
r,3,1         ! Define Radius = 1 m
e,9997,9998    ! Generate one element, cylindrical shaped top roller

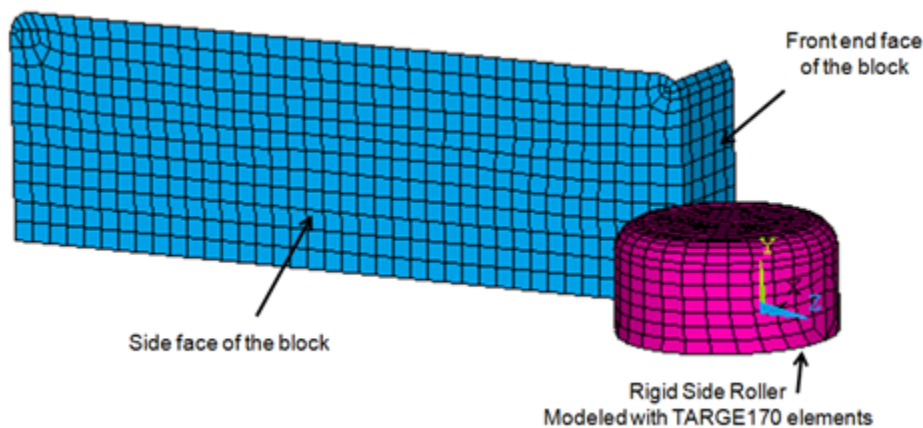
! Create and attach pilot node to this rigid target surface (top roller)
type,3
real,3
n,9999,-0.5,1.85,0.30
tshap,pilot
e,9999
allsel,all

```

### 27.3.3.2. Contact Between Block and Side Roller

A standard rigid-flexible contact pair is created between the side roller and the block. As shown in the following figure, the contact pair is created between two faces (front and side faces) of the block and side rollers:

**Figure 27.6: Contact Between Block and Side Roller**



Contact surfaces are modeled with **CONTA174** elements and the rigid side roller is modeled with **TARGE170** elements. As with the [previous contact pair](#) (p. 406), one pilot node is created at the center of the mass of the side roller. The pilot node governs the motion of the side roller.

The following example input shows how the contact pair is modeled:

```

et,4,CONTA174
KEYOPT,2,10,2 ! Select option to update contact stiffness in each iteration
et,5,TARGE170
cmsel,s,tn2.cnt ! Select the nodal component of 2 faces of the block

```

```

nplot
type,4      ! Select element type 4 (CONTA174)
real,5      ! Use Real Constant 5
esurf       ! Generate contact elements
allsel,all
! Model rigid side roller by meshing the area of side roller
type,5      ! Select element type 5 (TARGE170)
real,5      ! Use same real contact 5
aatt,1,5,5  ! Assign attributes to the areas of side roller
amesh,all   ! Mesh geometry of the side roller with TARGE170 elements
allsel,all
esel,s,type,,5 ! The target normals are not oriented correctly, so we must
              !reverse the direction of normals
esurf,,reverse ! Reverse the direction of the normals on target elements
allsel,all
! Create and attach pilot node to this rigid target surface (side roller)
type,5
real,5
n,20999,-0.4461,0.4337,0.0456
tshap,pilot
e,20999
allsel,all

```

## 27.4. Material Properties

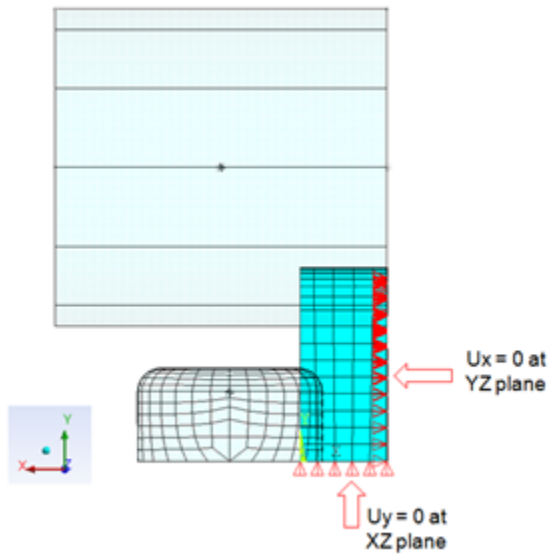
The model uses structural steel with elastoplastic behavior. A [bilinear isotropic hardening](#) material model (**TB,BISO**) is used with the following temperature-independent material properties:

Material Properties for Hot-Rolling Analysis	
Young's Modulus	200 Gpa
Poisson's Ratio	0.3
Tangent Modulus	2 Gpa
Yield Stress	70 Mpa [1]
Coefficient of friction [2]	0.6

1. A hot-rolling problem uses a low-yield stress value.
2. Between rollers and block during the rolling process.

## 27.5. Boundary Conditions and Loading

Symmetric boundary conditions are applied on both symmetry planes of the block, as shown in the following figure:

**Figure 27.7: Symmetric Boundary Conditions on the Block**

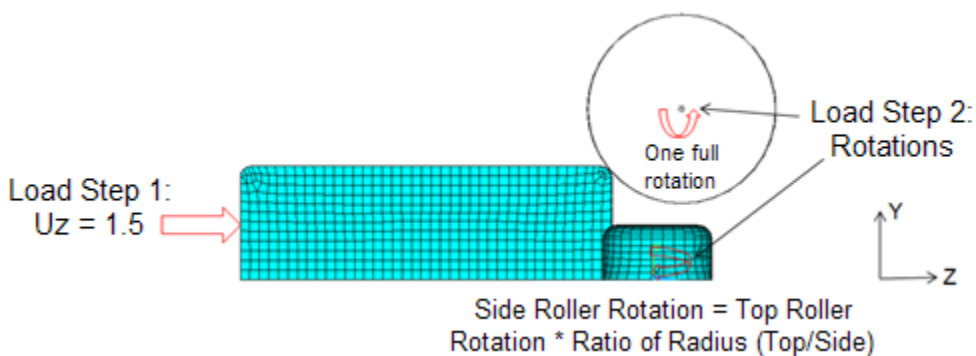
To showcase the usefulness of rezoning in 3-D problems, this problem is solved statically in two load steps:

27.5.1. Load Step 1: Establish Contact with Rollers

27.5.2. Load Step 2: Hot-Rolling

### 27.5.1. Load Step 1: Establish Contact with Rollers

The block is allowed to move towards the rollers and establish contact with them. The displacement ( $U_z = 1.5$  m) is applied on the left end face of the block, as shown in the following figure:

**Figure 27.8: Loadings**

Both the rigid rollers (top and side) are constrained in all directions with the use of pilot nodes. No friction is used.

The following input applies the boundary conditions and loading used in the first load step:

```
!Load Step 1
!Boundary Conditions
cmsel,s,ux_node    ! Select node on symmetry plane (YZ plane)
d,all,ux          ! Apply symmetry boundary conditions
cmsel,s,uy_node    ! Select node on symmetry plane (XZ plane)
```

```

d,all,uy      ! Apply symmetry boundary conditions
d,9999,all    ! Constrain top roller in all degrees of freedom
d,20999,all   ! Constrain side roller in all degrees of freedom
allsel,all
! Loadings
cmsel,s,uz_node ! Select the nodes of the left end face of the block
d,all,uz,1.5    ! Apply prescribed displacement (Uz =1.5m)
mp,mu,1,0      ! Use zero value of friction

```

## 27.5.2. Load Step 2: Hot-Rolling

Hot-rolling occurs in this load step. The rollers are allowed to rotate, and the block is free to move in the Z direction. A high value of friction ( $\mu = 0.6$ ) is used.

Because the top and side rollers are different sizes, different rotations are given to the rollers in order to maintain continuity. Based on the size of top roller, the friction coefficient, and the block length, one full rotation is applied to the top roller (as shown in [Figure 27.8: Loadings \(p. 409\)](#)).

No forward or backward slip is considered while calculating the rotation value of the side roller. Rotation of the side roller is calculated using this formula:

$$\text{Rotation of side roller} = \text{Rotation of top roller} * (\text{Radius of top roller} / \text{Radius of side roller})$$

The following input applies the boundary conditions and loading used in the second load step:

```

!Load Step 2
cmsel,s,uz_node ! Select the nodes of the left end face of the block
ddel,all,uz     ! Free the block to move in Z direction
nset,s,,,9999
d,all,rotx,-6.28 ! Rotate top roller
nset,s,,,20999
d,all,roty,-10.47 ! Rotate side roller
mp,mu,1,0.6     ! Use high value of friction
allsel,all

```

## 27.6. Analysis and Solution Controls

A nonlinear static analysis is performed in two load steps of one second each. The analysis diverges in the first load step, rezoning occurs, and the analysis resumes.

Restart files are saved at each substep, as rezoning requires a restart file, and the substep at which rezoning is required is still unknown. Results items are also stored at each substep.

For illustrative purposes, restart files and results items are saved at each and every substep, despite the considerable memory requirements for doing so. In most cases, it is sufficient to save them at every few substeps instead.

The following input applies the solution settings for the run:

```

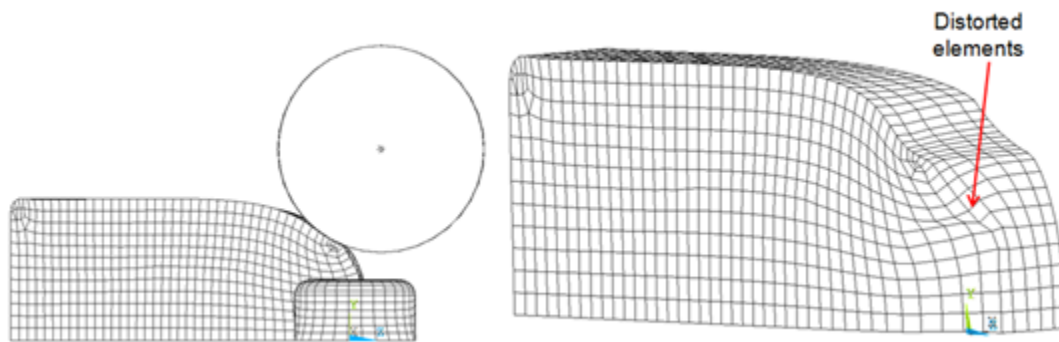
/solu
time,1          ! Define time for first load step
nlgeom,on      ! Enable nonlinear geometry effects
OUTRES,ALL,ALL ! Save the results data for each substep
RESCONTRL,DEFINE,ALL,ALL,0 ! Save restart files for each substep
NSUBST,100,1000000,20 ! Define initial, maximum and minimum substeps
solve         ! Solve the first load step

```



The initial run diverges in the first load step at TIME = .7718. The following figure shows the deformed shape of the model at the last converged substep:

**Figure 27.9: Deformation in First Load Step, 40th Substep**



Element shape checking of the deformed model suggests that the mesh is overly distorted at the location indicated.

**Rezoning** repairs the distorted mesh and allows the analysis to continue. Rezoning is applied to this problem as described in the following topics:

- 27.6.1. Rezoning Initiated at the 30th Substep
- 27.6.2. Distorted Mesh Replaced by an Imported New Mesh
- 27.6.3. Solution Items Mapped from Original Mesh to New Mesh
- 27.6.4. Analysis Resumes Using the New Mesh

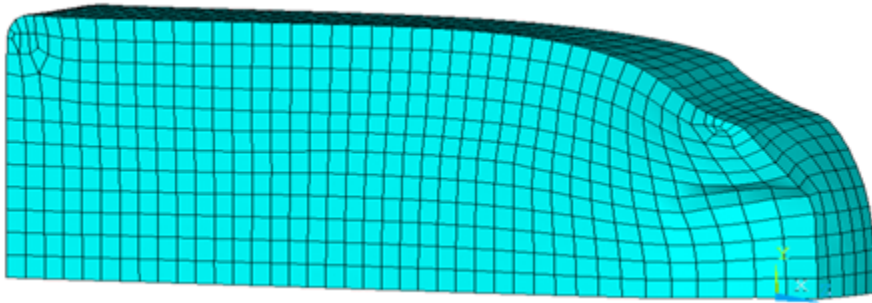
### 27.6.1. Rezoning Initiated at the 30th Substep

The **best substep at which to initiate rezoning** is determined by examining the deformed model and the physics of the simulation.

The analysis diverges after the 40th substep at TIME = .7718. Very little time (from TIME = .77 to .7718) occurs between the 31st to the 40th substeps, however, indicating that severe distortion of the mesh begins to occur at the 31st substep.

Because rezoning should be attempted at one or more substeps *before* the substep where mesh deformation occurs, the 30th substep is a logical choice at which to initiate rezoning. **Shape-checking (SHPP or CHECK)** of the deformed mesh at the 30th substep confirms the choice, as the deformed mesh violates no error limits.

The following figure shows the deformed mesh at the 30th substep:

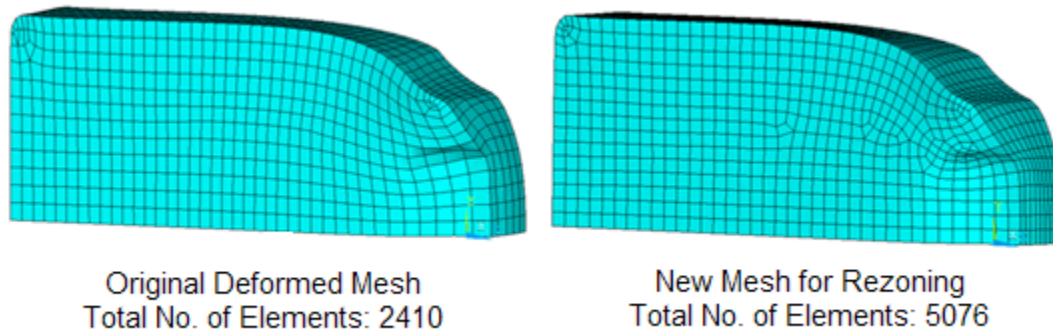
**Figure 27.10: Deformed Mesh of the Block at 30th Substep of First Load Step**

### 27.6.2. Distorted Mesh Replaced by an Imported New Mesh

Various [remeshing options](#) are available for rezoning. Because this is a 3-D problem, however, a [new mesh is read in](#) to replace the original, distorted mesh.

The new mesh can be generated in Workbench or by other third-party software by first creating the deformed geometry from the deformed mesh, then meshing the deformed geometry with new settings to obtain a new, good mesh. The new mesh [must be better than the original mesh](#); otherwise, rezoning cannot improve convergence.

The following figure shows the original, deformed mesh and the new, good mesh:

**Figure 27.11: Original Deformed Mesh and Imported New Mesh**

Original Deformed Mesh  
Total No. of Elements: 2410

New Mesh for Rezoning  
Total No. of Elements: 5076

The following input initiates rezoning at the 30th substep and reads in the new mesh:

```
/solu
rezone,manual,1,30          ! Start rezoning at the 30th substep
remesh,start               ! Start "remeshing" process
remesh,read,Rezone_Mesh,cdb ! Read new mesh in "cdb" format
remesh,finish              ! Transfer boundary conditions and loadings from the
!                           old mesh to the new mesh, and recreate contact
!                           pairs (if any)
```

After remeshing (**REMESH,FINISH**), the program transfers surface loads, forces, boundary conditions, and contact pairs (if any) from the original, deformed old mesh to the new, good mesh. It is good practice to [check the model after remeshing](#) to verify that all such transfers to the new mesh were successful.

### 27.6.3. Solution Items Mapped from Original Mesh to New Mesh

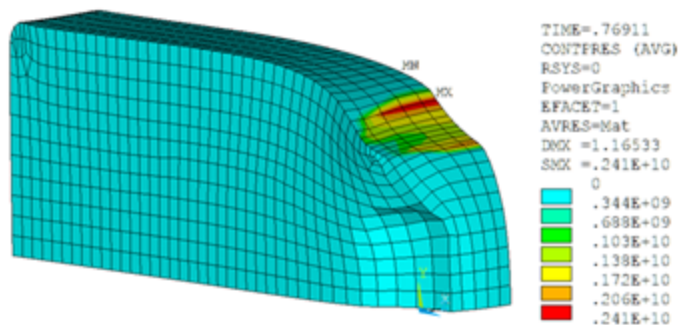
After remeshing, solution and results items from the original mesh are mapped to the new mesh, and the resulting residual forces are rebalanced (**MAPSOLVE**). The following input performs the mapping operation:

```
mapsolve,500 ! Use maximum 500 substeps. The default value is 5.
```

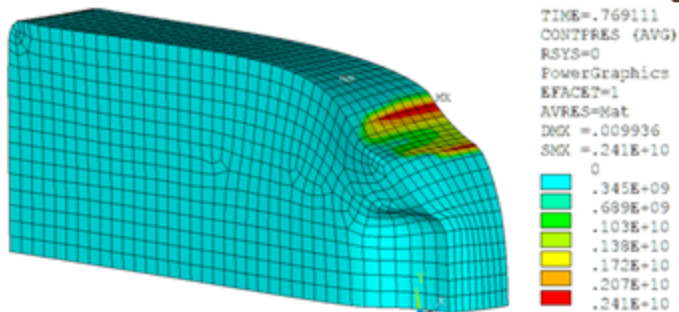
The following figure shows the contact pressure results for the top roller contact pair, first from the 30th substep (where rezoning is performed), and after mapping variables and balance residuals from the original mesh to the new mesh:

**Figure 27.12: Comparison of Contact Pressure Results Before and After Rezoning**

#### Contact Pressure Results From Initial Run at 30th Substep



#### Contact Pressure Results After Rezoning



The mapping operation concludes the rezoning process, and a standard multiframe restart resumes solution processing using the new mesh.

### 27.6.4. Analysis Resumes Using the New Mesh

After mapping quantities from the old to the new mesh and rebalancing the residual forces, a multiframe restart (**ANTYPE,,RESTART,,CONTINUE**) resumes the nonlinear solution with the new mesh.

The following input restarts the analysis:

```
/clear,nostart
/file,Hot_Rolling_Model ! Give same job name as initial run
/solu
antype,,restart ! Specify analysis type (restart)
solve ! Solve first load step

! Load Step2: Rotate rollers
time,2 ! Define time for second load step
esel,s,ename,,185
allsel,below,element ! Select the nodes of the block
```

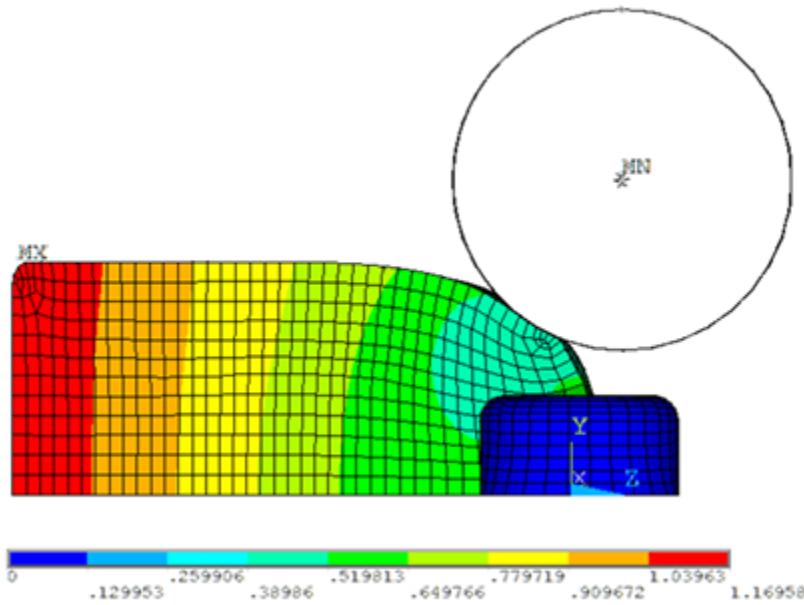
```

ddel,all,uz          ! Free the block to move in Z direction
allsel,all
nsel,s,,,9999
d,all,rotx,-6.28    ! Rotate top roller
nsel,s,,,20999
d,all,roty,-10.47   ! Rotate side roller
allsel,all
mp,mu,1,0.6         ! Use high value of friction
OUTRES,ALL,10       ! Save results items at every 10th substep
RESCONTRL,DEFINE,ALL,30,0 ! Save restart files at every 30th substep
NSUBST,1000,100000,20
solve                ! Solve second load step
    
```

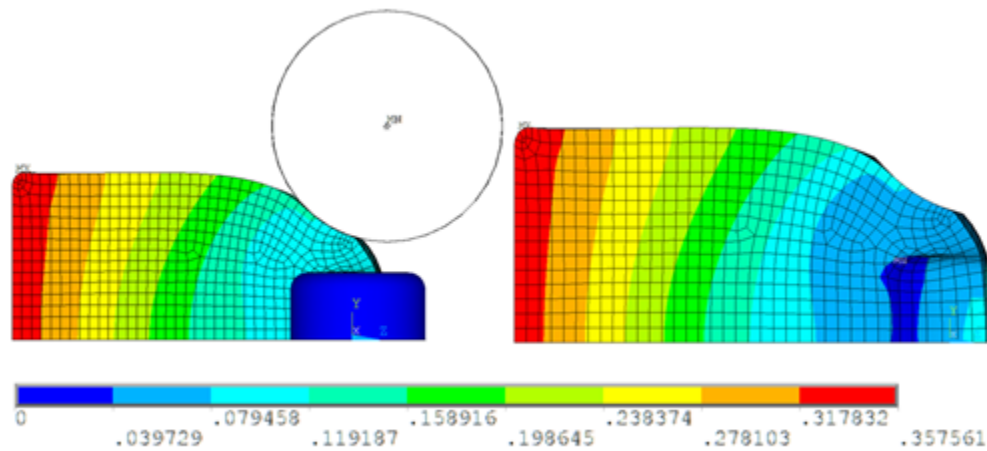
## 27.7. Results and Discussion

The following figure shows the deformation plot (USUM) of the initial run at the last converged substep (TIME = .7718).

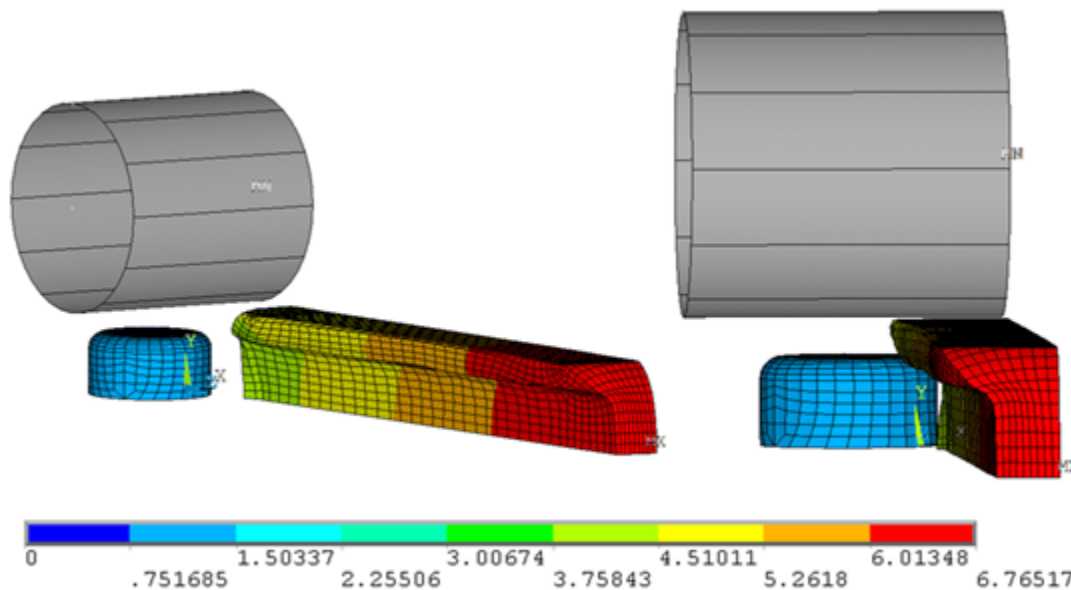
**Figure 27.13: USUM Plots: Initial Run at Last Converged Substep**



Following the successful rezoning, the following figure shows the deformation plot (USUM) of the model after building up the rolling process (at the end of the first load step):

**Figure 27.14: USUM Plots: After Building Up the Rolling Process**

The hot-rolling process is performed in the second load step by rotating the rollers and using high-friction contact between the rollers and the billet. The following figure shows the deformation plot (USUM) of the model at the end of the second load step:

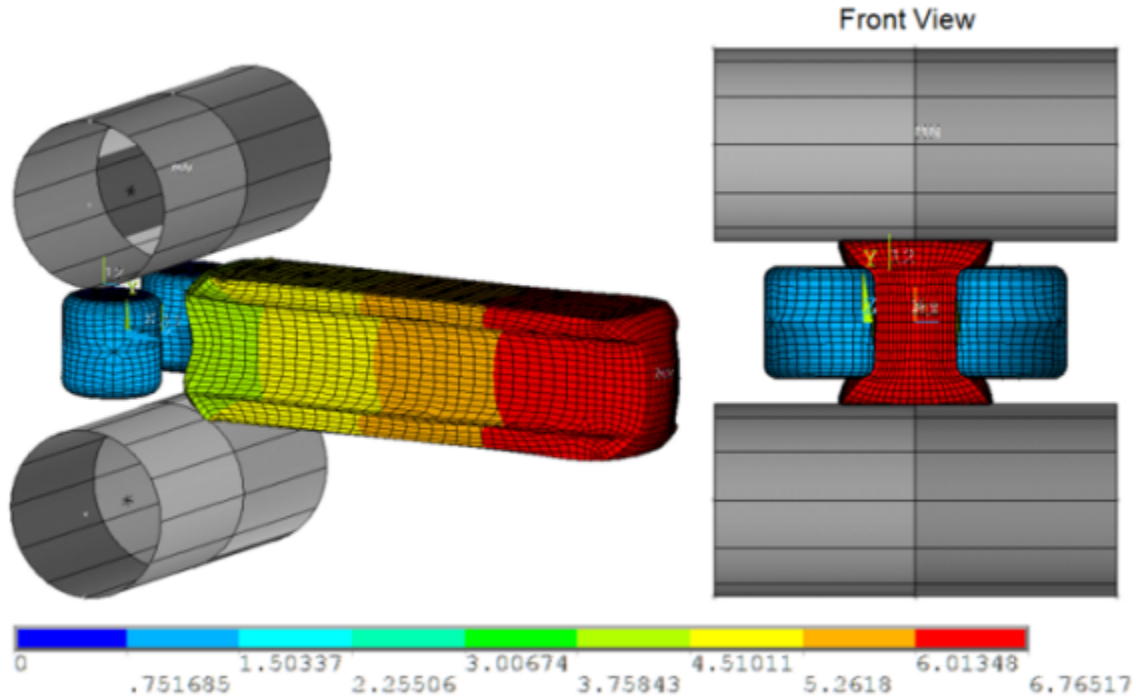
**Figure 27.15: USUM Plots: End of Analysis (After Second Load Step)**

To view the full-model results, two symmetric expansions (**/EXPAND**) are performed. The following input performs the symmetric expansion:

```
CS,11,0,28752,29076,28734,1,1 ! Create local Cartesian coordinate system (using three nodes) on YZ symmetry plane
/EXPAND,1,LRECT,HALF,,.000001,,1,LRECT,HALF,,,,.000001,,RECT,FULL
```

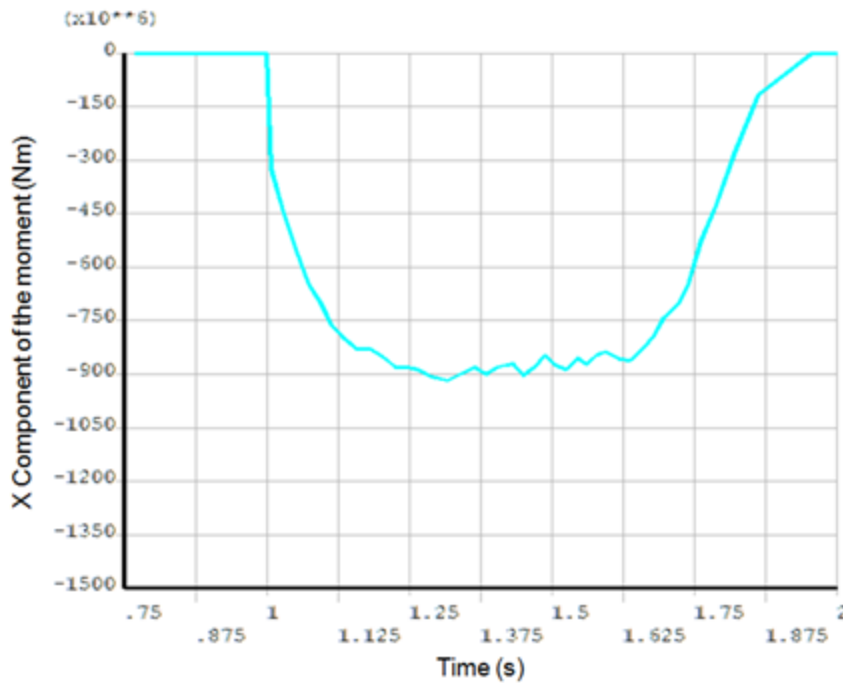
The following figure shows the deformation plot in the fully expanded model, where the rectangular block becomes an I-shaped beam:

**Figure 27.16: USUM Plot of Full Model after Symmetry Expansion**



The following figure shows the variation of the X component of the moment along with the time for the top roller:

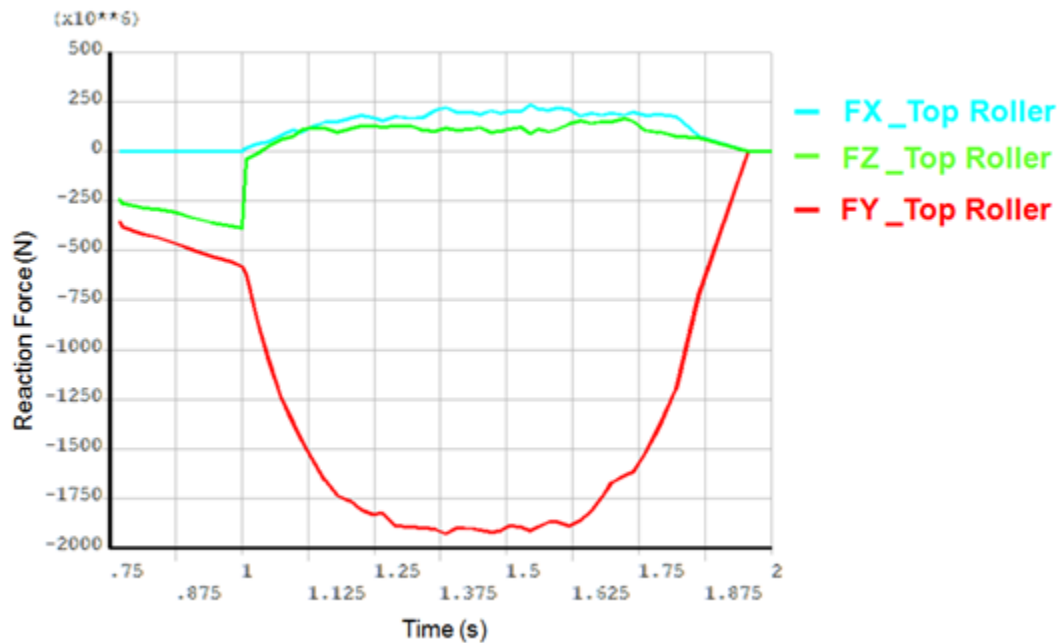
**Figure 27.17: Variation of the Moment (Mx) of the Top Roller**



The plot suggests that rolling moment varies little from TIME = 1.25s to TIME = 1.6. The hot-rolling process during this time range can be considered to be steady state.

Similarly, the following figure shows the variation of the force components of the top roller:

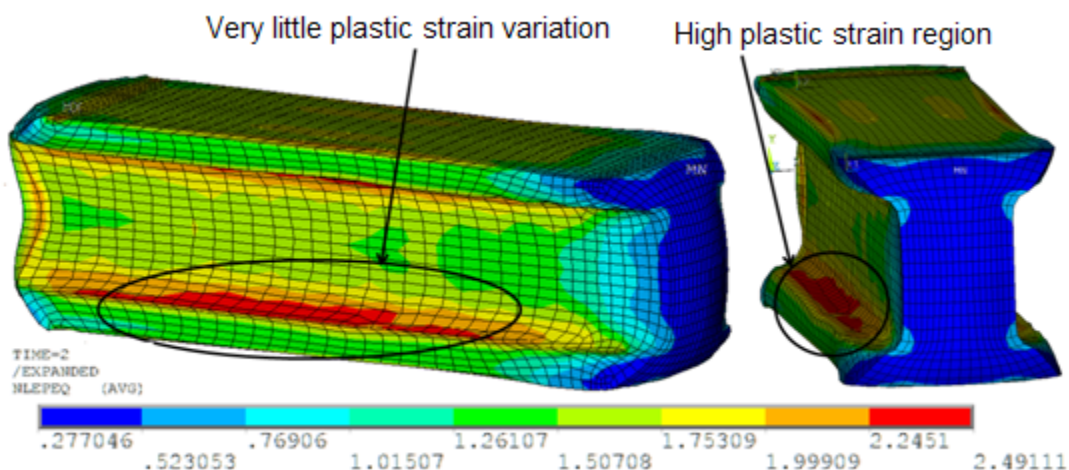
**Figure 27.18: Variation of the Reaction Forces of the Top Roller**



The plot also shows that forces vary little from TIME = 1.25 to TIME = 1.6s. As would be expected from the top roller, the Y component of the force (that is, the downward force) is dominant in the rolling process.

The following figure shows the equivalent plastic strain plot in the fully expanded model:

**Figure 27.19: Equivalent Plastic Strain Plot in the Full Expanded Model**



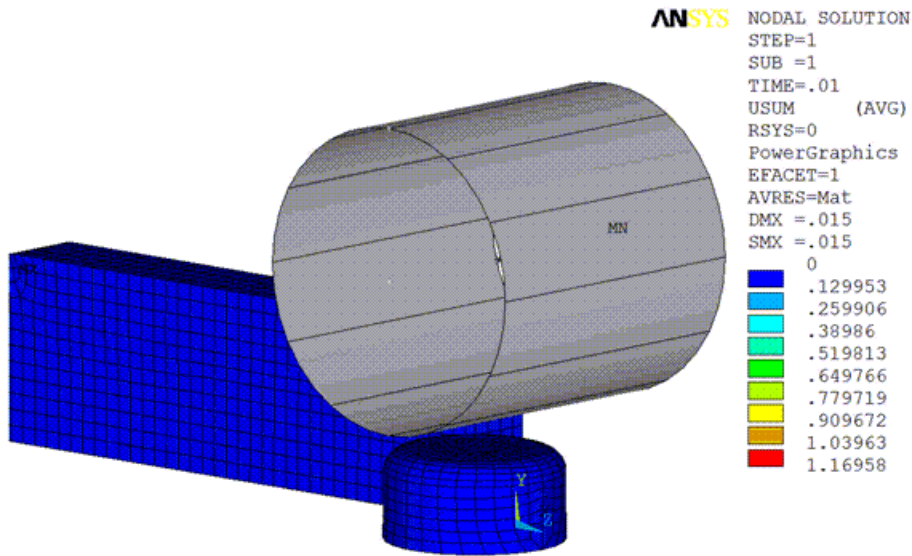
As expected, the high plastic strain region is observed at the location where the web and flange components of the I-beam are connected.

For some duration in the rolling process, the plastic strain varies little over time in the high plastic strain region. This behavior occurs during the steady-state (rolling) phase of the simulation.

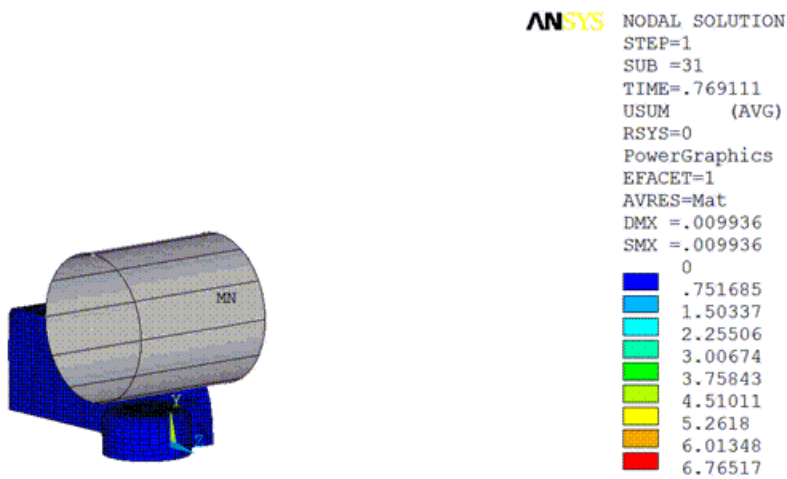
### 27.7.1. Deformation Animations

The following animations show the deformations occurring in the hot-rolling problem:

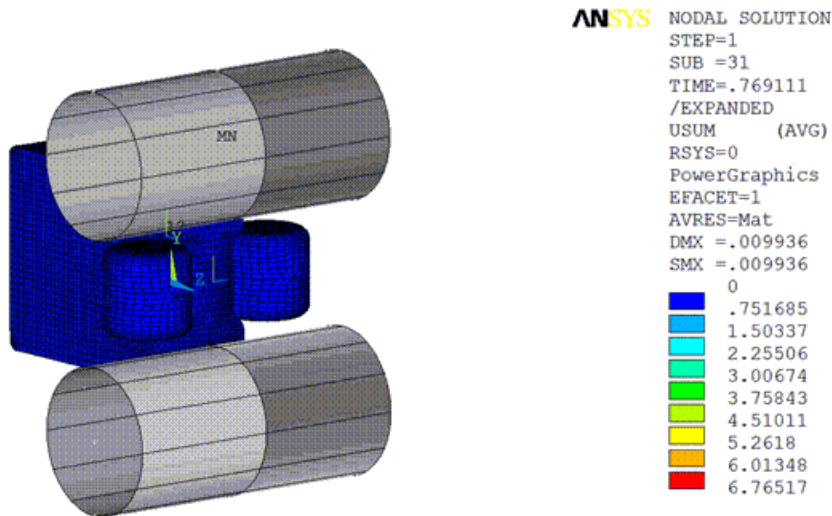
**Figure 27.20: Deformation (USUM) in the Initial Run**



**Figure 27.21: Deformation (USUM) After Rezoning**





**Figure 27.22: Deformation (USUM) After Rezoning in the Expanded Model**

## 27.8. Recommendations

To perform a similar 3-D simulation using rezoning, consider the following hints and recommendations:

- The hot-rolling process can be simulated via static analysis in two load steps. The first load step pushes the billet until it establishes contact with the rollers, and the second pulls the billet by rotating the rollers.
- Before rezoning, back up results and restart files associated with the initial run in a separate directory. Rezoning updates results and restart files, so the original files are no longer available should you wish to try rezoning at another substep.
- If rezoning is performed at a substep where the original mesh is too distorted (where shape-checking [**SHPP** or **CHECK**] indicates errors), then rezoning will not work. Rezoning should therefore be **performed at an earlier substep**.
- A new mesh that is too fine as compared to the original mesh may cause mapping (**MAPSOLVE**) errors. The primary requirement for the new mesh is that it should **properly capture the outer surface geometry** of the deformed model.
- Check the model after remeshing (**REMESS,FINISH**) to verify that all boundary conditions, contact pairs, and loadings have transferred correctly from the original mesh to the new mesh.
- After rezoning, if the analysis diverges again *after* passing the initial run's diverged time, **multiple rezonings may be necessary**. If the analysis diverges again *before* passing the initial run's diverged time, then either the new mesh is of insufficient quality, or **other problems** unrelated to mesh distortion (such as geometry and material instabilities) exist.

## 27.9. Input Files

The following files were used in this problem:

- `Hot_Rolling_Model.dat` -- Hot-rolling model input file.
- `Hot_Rolling_Model.cdb` -- Common database file containing the hot-rolling model information (called by `Hot_Rolling_Model.dat`).
- `Initial_Mesh.cdb` -- Common database file for the original mesh used in the hot-rolling problem.
- `New_Mesh.cdb` -- Common database file for the new mesh used for rezoning in the hot-rolling problem.
- `Roller_Geometry.iges` -- Geometry file for the side rollers.

The files are available in the `td-27` folder. See [Obtaining the Input Files \(p. xxxv\)](#) for more information.

---

## Chapter 28: Friction Stir Welding (FSW) Simulation

---

This example problem demonstrates how to simulate the friction stir welding (FSW) process. Several characteristics of FSW are presented, including tool-workpiece surface interaction, heat generation due to friction, and plastic deformation. A nonlinear direct coupled-field analysis is performed, as thermal and mechanical behaviors are mutually dependent and coupled together during the FSW process.

Because it is often difficult to find a full set of engineering data to simulate the FSW process, the problem emphasizes the simulation rather than the numerical results. A simplified version of the model created by Zhu and Chao [1 (p. 442)] illustrates the FSW simulation method.

The following features and capabilities are highlighted:

- Direct [structural-thermal analysis](#) using [coupled-field solid elements](#)
- [Plastic heat generation](#) in coupled-field elements
- Frictional heat generation using [contact elements](#)
- [Surface-projection-based contact method](#)
- Contact elements with bonding capability

Topics related to this example problem follow:

- [28.1. Introduction](#)
- [28.2. Problem Description](#)
- [28.3. Modeling](#)
- [28.4. Material Properties](#)
- [28.5. Boundary Conditions and Loading](#)
- [28.6. Analysis and Solution Controls](#)
- [28.7. Results and Discussion](#)
- [28.8. Recommendations](#)
- [28.9. References](#)
- [28.10. Input Files](#)

### 28.1. Introduction

Friction stir welding (FSW) is a solid-state welding technique that involves the joining of metals without filler materials. A cylindrical rotating tool plunges into a rigidly clamped workpiece and moves along the joint to be welded. As the tool translates along the joint, heat is generated by friction between the tool shoulder and the workpiece. Additional heat is generated by plastic deformation of the workpiece material. The generated heat results in thermal softening of the workpiece material. The translation of the tool causes the softened workpiece material to flow from the front to the back of the tool where it consolidates. As cooling occurs, a solid continuous joint between the two plates is formed. No melting occurs during the process, and the resulting temperature remains below the solidus temperature of the metals being joined. FSW offers many advantages over conventional welding techniques, and has been successfully applied in the aerospace, automobile, and shipbuilding industries.

Thermal and mechanical behaviors are mutually dependent during the FSW process. Because the temperature field affects stress distribution, this example uses a fully thermo-mechanically coupled model. The model consists of a coupled-field solid element with structural and thermal degrees of freedom. The model has two rectangular steel plates and a cylindrical tool. All necessary mechanical and thermal [boundary conditions \(p. 428\)](#) are applied on the model. The simulation occurs over three load steps, representing the [plunge, dwell, and traverse phases \(p. 429\)](#) of the process.

The temperature rises at the contact interface due to frictional contact between the tool and workpiece. FSW generally occurs when the temperature at the weld line region reaches 70 to 90 percent of the melting temperature of the workpiece material [[3 \(p. 442\)](#)]. The temperature obtained around the weld line region in this example falls within the range reported by Zhu and Chao [[1 \(p. 442\)](#)] and Prasanna and Rao [[3 \(p. 442\)](#)], while the maximum resulting temperature is well below the melting temperature of the workpiece.

The calculated frictional heat generation and plastic heat generation show that the friction between the tool shoulder and workpiece is responsible for generating most of the heat. A bonding temperature is specified at the contact interface of the plates to model the welding behind the tool. When the temperature at the contact surface exceeds this bonding temperature, the contact is changed to bonded.

## 28.2. Problem Description

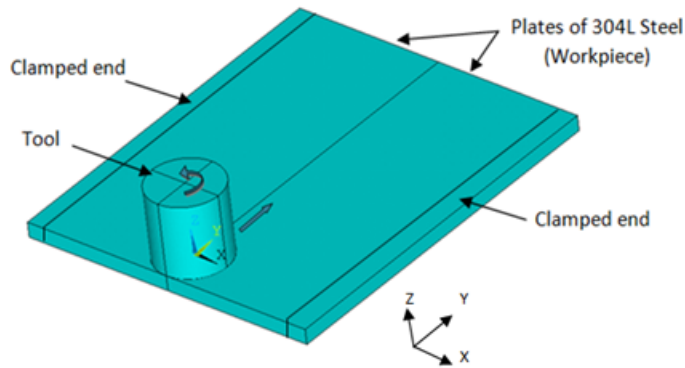
### **The Zhu and Chao Thermo-Mechanical Model**

The model used in this example is a simplified version of the thermo-mechanical model developed by Zhu and Chao [[1 \(p. 442\)](#)] for FSW with 304L stainless steel. Zhu and Chao presented nonlinear thermal and thermo-mechanical simulations using the finite element analysis code WELDSIM. They initially formulated a heat-transfer problem using a moving heat source, and later used the transient temperature outputs from the thermal analysis to determine residual stresses in the welded plates via a 3-D elastoplastic thermo-mechanical simulation.

A direct coupled-field analysis is performed on a reduced-scale version of the Zhu and Chao model [[1 \(p. 442\)](#)]. Also, rather than using a moving heat source as in the reference model, a rotating and moving tool is used for a more realistic simulation.

The tool pin is ignored. The heat generated at the pin represents approximately two percent of the total heat and is therefore negligible.

The simulation welds two 304L stainless steel plates (workpiece) with a cylindrical shape tool, as shown in the following figure:

**Figure 28.1: 3-D Model of Workpiece and Tool**

The FSW process generally requires a tool made of a harder material than the workpiece material being welded. In the past, FSW was used for soft workpiece materials such as aluminium. With the development of tools made from super-abrasive materials such as polycrystalline cubic boron nitride (PCBN), FSW has become possible with high-temperature materials such as stainless steel [4 (p. 443)]. A cylindrical PCBN tool is modeled in this case.

The workpiece sides parallel to the weld line are constrained in all the directions to simulate the clamping ends. The bottom side of the workpiece is constrained in the perpendicular (z) direction to simulate support at the bottom. Heat losses are considered on all the surfaces of the model. All [boundary conditions](#) (p. 428) are symmetric across the weld centerline.

The simulation is performed in three load steps, each representing a respective phase ([plunge](#), [dwell](#), and [traverse](#) (p. 429)) of the FSW process.

## 28.3. Modeling

Modeling is a two-part task, as described in these topics:

[28.3.1. Workpiece and Tool Modeling](#)

[28.3.2. Contact Modeling](#)

### 28.3.1. Workpiece and Tool Modeling

Two rectangular shaped plates (similar to those used in the reference model) are used as the workpiece. Dimensions have been reduced to decrease the simulation time.

The plate size is 3 x 1.25 x 0.125 in (76.2 x 31.75 x 3.18 mm). The tool shoulder diameter is 0.6 in (15.24 mm).

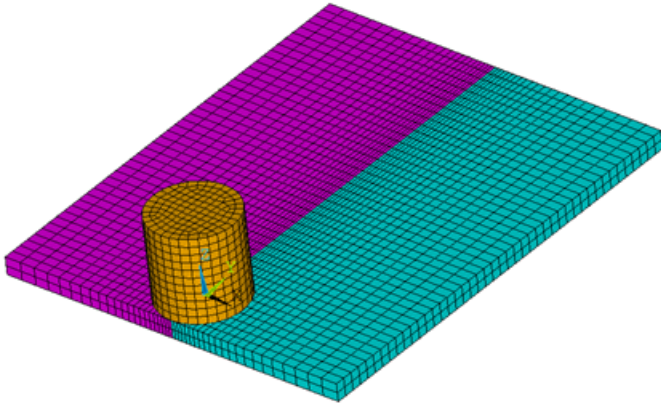
Plate thickness remains the same as that of the reference model, but the plate length and width are reduced. The plate width is reduced because the regions away from the weld line are not significantly affected by the welding process, and this example focuses primarily on the heat generation and temperature rise in the region nearest the weld line.

The height of the tool is equal to the shoulder diameter. Both the workpiece (steel plates) and the tool are modeled using coupled-field element [SOLID226](#) with the structural-thermal option (KEYOPT(1) = 11).

A hexahedral mesh with dropped midside nodes is used because the presence of midside nodes (or quadratic interpolation functions) can lead to oscillations in the thermal solution, leading to nonphysical

temperature distribution. A hexahedral mesh is used instead of a tetrahedral mesh to avoid mesh-orientation dependency. For more accurate results, a finer mesh is used in the weld-line region. The following figure shows the 3-D meshed model:

**Figure 28.2: 3-D Meshed Model of Workpiece and Tool**



## 28.3.2. Contact Modeling

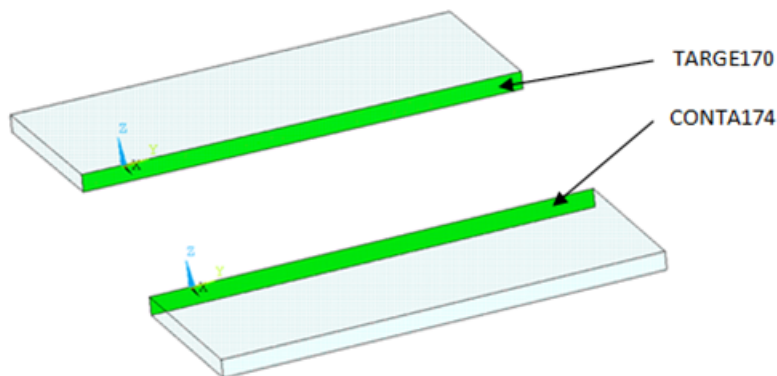
Contact is modeled as follows for the FSW simulation:

- 28.3.2.1. Contact Pair Between the Plates
- 28.3.2.2. Contact Pair Between Tool and Workpiece
- 28.3.2.3. Rigid Surface Constraint

### 28.3.2.1. Contact Pair Between the Plates

During the simulation, the surfaces to be joined come into contact. A standard surface-to-surface contact pair using **TARGE170** and **CONTA174**, as shown in the following figure:

**Figure 28.3: Contact Pair Between Plates**



The **surface-projection-based contact method** (**KEYOPT(4) = 3** for contact elements) is defined at the contact interface. The surface-projection-based contact method is well suited to highly nonlinear problems that include geometrical, material, and contact nonlinearities.

The problem simulates welding using the bonding capability of contact elements. To achieve continuous bonding and simulate a perfect thermal contact between the plates, a high thermal contact conductance

(TCC) of  $2E06 \text{ W/m}^2 \text{ }^\circ\text{C}$  is specified. (A small TCC value yields an imperfect contact and a temperature discontinuity across the interface.) The conductance is specified as a real constant for **CONTA174** elements.

The maximum temperature ranges from 70 to 90 percent of the melting temperature of the workpiece material. Welding occurs after the temperature of the material around the contacting surfaces exceeds the bonding temperature (approximately 70 percent of the workpiece melting temperature). In this case,  $1000 \text{ }^\circ\text{C}$  is considered to be the bonding temperature based on the reference results. The bonding temperature is specified using the real constant **TBND** for **CONTA174**. When the temperature at the contact surface for closed contact exceeds the bonding temperature, the contact type changes to bonded. The contact status remains bonded for the remainder of the simulation, even though the temperature subsequently decreases below the bonding value.

The following example input defines the contact settings of the contact pair:

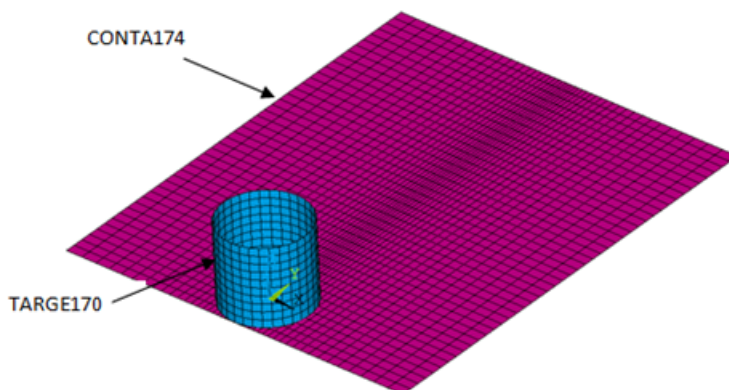
```
.
et,6,TARGE170
et,7,CONTA174
keyopt,7,1,1      ! Displacement and Temp DOF
keyopt,7,4,3      ! To include Surface projection based method

rmodif,6,14,2e06  ! A real constant TCC, thermal contact
                  ! conductance coeff. b/w the plates, W/m2'C
rmodif,6,35,1000  ! A real constant TBND,bonding temp for
                  ! welding, 'C
```

### 28.3.2.2. Contact Pair Between Tool and Workpiece

The tool plunges into the work piece, rotates, and moves along the weld line. Because the frictional contact between the tool and workpiece is primarily responsible for heat generation, a standard surface-to-surface contact pair is defined between the tool and workpiece. The **CONTA174** element is used to model the contact surface on the top surface of the workpiece, and the **TARGE170** element is used for the tool, as shown in this figure:

**Figure 28.4: Contact Pair Between Tool and Workpiece**



Two real constants are specified to model friction-induced heat generation. The fraction of frictional dissipated energy converted into heat is modeled first; the **FHTG** real constant is set to 1 to convert all frictional dissipated energy into heat. The factor for the distribution of heat between contact and target surfaces is defined next; the **FWGT** real constant is set to 0.95, so that 95 percent of the heat generated from the friction flows into the workpiece and only five percent flows into the tool [2 (p. 442)].

A low TCC value ( $10 \text{ W/m}^2 \text{ }^\circ\text{C}$ ) is specified for this contact pair because most of the heat generated transfers to the workpiece. Some additional heat is also generated by plastic deformation of the workpiece material. Because the workpiece material softens and the value of friction coefficient drops as the temperature increases [3 (p. 442)], a variable coefficient of friction (0.4 to 0.2) is defined (**TB,FRIC** with **TBTEMP** and **TBDATA**).

The following example input specifies the settings for the contact pair:

```
et,4,TARGE170
et,5,CONTA174
keyopt,5,1,1      ! Displacement & Temp DOF
keyopt,5,5,3      ! Close gap/reduce penetration with auto cnof
keyopt,5,9,1      ! Exclude both initial penetration or gap
keyopt,5,10,2     ! Contact stiffness update each iteration based

rmodif,5,9,500e6  ! Max friction stress, N/m2
rmodif,5,14,10    ! Thermal contact conductance b/w tool and
                  ! workpiece, W/m2'C
rmodif,5,15,1     ! A real constant FHTG,the fraction of
                  ! frictional dissipated energy converted
                  ! into heat
rmodif,5,18,0.95  ! A real constant FWGT, weight factor for
                  ! the distribution of heat between the
                  ! contact and target surfaces
```

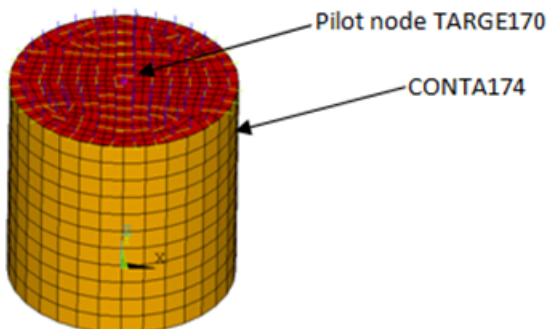
### 28.3.2.3. Rigid Surface Constraint

The workpiece remains fixed in all stages of the simulation. The tool rotates and moves along the weld line. A pilot node is created at the center of the top surface of the tool in order to apply the rotation and translation on the tool. The motion of the pilot node controls the motion of the entire tool. A rigid surface constraint is defined between the pilot node (**TARGE170**) and the nodes of the top surface of the tool (**CONTA174**). A multipoint constraint (MPC) algorithm with contact surface behavior defined as bonded always is used to constrain the contact nodes to the rigid body motion defined by the pilot node.

The following contact settings are used for the **CONTA174** elements:

- To include MPC contact algorithm: **KEYOPT(2) = 2**
- For a rigid surface constraint: **KEYOPT(4) = 2**
- To set the behavior of contact surface as bonded (always): **KEYOPT(12) = 5**

**Figure 28.5: Rigid Surface Constrained**





## 28.4. Material Properties

Accurate temperature calculation is critical to the FSW process because the stresses and strains developed in the weld are temperature-dependent. Thermal properties of the 304L steel plates [1 (p. 442), 3 (p. 442)] such as thermal conductivity, specific heat, and density are temperature-dependent. Mechanical properties of the plates such as Young's modulus and the coefficient of thermal expansion are considered to be constant due to the limitations of data available in the literature.

It is assumed that the plastic deformation of the material uses the von Mises yield criterion, as well as the associated flow rule and the work-hardening rule (Zhu and Chao [1 (p. 442)]). Therefore, a bilinear isotropic hardening model (**TB**, BISO) is selected.

The following table shows the material properties of the workpiece:

**Table 28.1: Workpiece Material Properties**

Material Properties of the Plates						
Young's modulus	193 GPa					
Poisson's ratio	0.3					
Coefficient of thermal expansion	18.7 $\mu\text{m/m } ^\circ\text{C}$					
Bilinear Isotropic Hardening Constants ( <b>TB</b> ,BISO)						
Yield stress [1]	290 MPa					
Tangent modulus [1]	2.8 GPa					
Temperature Dependent Material Properties						
Temperature ( $^\circ\text{C}$ )	0	200	400	600	800	1000
Thermal Conductivity (W/m $^\circ\text{C}$ )	16	19	21	24	29	30
Specific Heat (J/Kg $^\circ\text{C}$ )	500	540	560	590	600	610
Density (Kg/m <sup>3</sup> )	7894	7744	7631	7518	7406	7406

1. The **TB**DATA command defines the yield stress and tangent modulus.

The fraction of the plastic work dissipated as heat during FSW is about 80 percent [2 (p. 442)]. Therefore, the fraction of plastic work converted to heat (Taylor-Quinney coefficient) is set to 0.8 (**MP**,QRATE) for the calculation of plastic heat generation in the workpiece material.

To weld a high-temperature material such as 304L stainless steel, a tool composed of hard material is required. Tools made from super-abrasive materials such as PCBN are suitable for such processes [4 (p. 443)], and so a cylindrical PCBN tool is used here. The material properties of the PCBN tool are obtained from the references ([5 (p. 443), 6 (p. 443)]).

The following table shows the material properties of the PCBN tool:

**Table 28.2: Material Properties of the PCBN Tool**

Young modulus	680 GPa
Poisson's ratio	0.22
Thermal Conductivity	100 W/m $^\circ\text{C}$
Specific Heat	750 J/Kg $^\circ\text{C}$

Density	4280 Kg/m <sup>3</sup>
---------	------------------------

## 28.5. Boundary Conditions and Loading

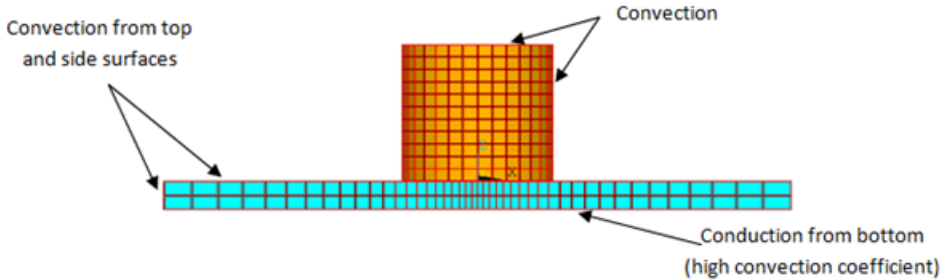
This section describes the thermal and mechanical boundary conditions imposed on the FSW model:

- 28.5.1. Thermal Boundary Conditions
- 28.5.2. Mechanical Boundary Conditions
- 28.5.3. Loading

### 28.5.1. Thermal Boundary Conditions

The frictional and plastic heat generated during the FSW process propagates rapidly into remote regions of the plates. On the top and side surfaces of the workpiece, convection and radiation account for heat loss to the ambient [1 (p. 442)]. Conduction losses also occur from the bottom surface of the workpiece to the backing plate.

**Figure 28.6: Thermal Boundary Conditions**



Available data suggest that the value of the convection coefficient lies between 10 and 30 W/m<sup>2</sup> °C [1 (p. 442), 2 (p. 442), 3 (p. 442)] for the workpiece surfaces, except for the bottom surface. The value of the convection coefficient is 30 W/m<sup>2</sup>°C for workpiece and tool. This coefficient affects the output temperature. A lower coefficient increases the output temperature of the model. A high overall heat-transfer coefficient (about 10 times the convective coefficient) of 300 W/m<sup>2</sup> °C is assumed for the conductive heat loss through the bottom surface of the workpiece. As a result, the bottom surface of the workpiece is also treated as a convection surface for modeling conduction losses. Because the percentage of heat lost due to radiation is low, radiation heat losses are ignored. An initial temperature of 25 °C is applied on the model. Temperature boundary conditions are not imposed anywhere on the model.

The following example input defines the thermal boundary conditions:

```
! Convection heat loss from the workpiece surfaces
vsel,s,volume,,1,2      ! Selecting the workpiece
allsel,below,volume
nselect,r,loc,z,0
nselect,a,loc,x,-w      ! w is the width of each plate
nselect,a,loc,x,w
nselect,a,loc,y,-l1
nselect,a,loc,y,l2
sf,all,conv,30,25

! Convection (high)heat loss from the workpiece bottom
nselect,s,loc,z,-t      ! t is the thickness of each plate
sf,all,conv,300,25
allsel,all

! Convection heat loss from the tool surfaces
vsel,u,volume,,1,2      ! Selecting the tool
allsel,below,volume
```

```

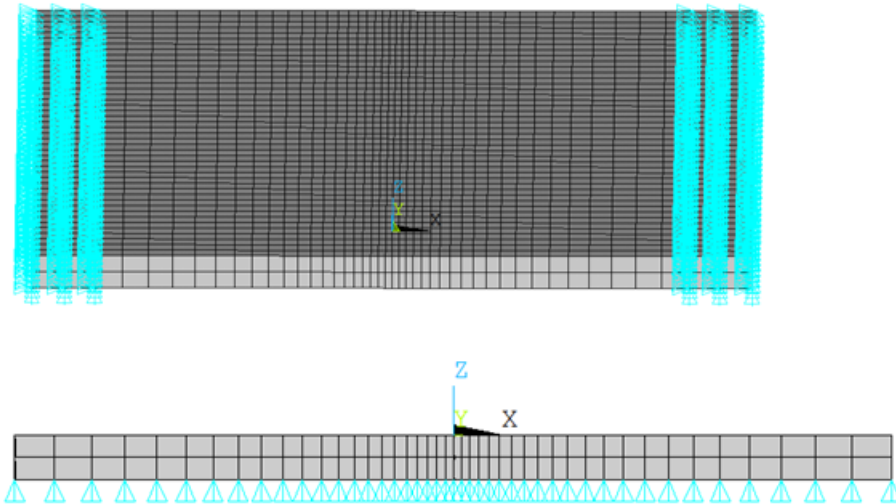
csys,1
nsel,r,loc,x,r1      ! r1 is the tool shoulder radius
nsel,a,loc,z,h      ! h is the height of the tool
sf,all,conv,30,25

```

## 28.5.2. Mechanical Boundary Conditions

The workpiece is fixed by clamping each plate [1 (p. 442)]. The clamped portions of the plates are constrained in all directions. To simulate support at the bottom of the plates, all bottom nodes of the workpiece are constrained in the perpendicular direction (z direction).

**Figure 28.7: Mechanical Boundary Conditions**



The following example input defines the mechanical boundary conditions:

```

! Mechanical Boundary Conditions
! 20% end of the each plate is constraint
nsel,s,loc,x,-0.8*w,-w
nsel,a,loc,x,0.8*w,w
d,all,uz,0      ! Displacement constraint in x-direction
d,all,uy,0      ! Displacement constraint in y-direction
d,all,ux,0      ! Displacement constraint in z-direction
allsel,all
! Bottom of workpiece is constraint in z-direction
nsel,s,loc,z,-t
d,all,uz      ! Displacement constraint in z-direction
allsel,all

```

## 28.5.3. Loading

The FSW process consists of three primary phases:

1. **Plunge** -- The tool plunges slowly into the workpiece
2. **Dwell** -- Friction between the rotating tool and workpiece generates heat at the initial tool position until the workpiece temperature reaches the value required for the welding.
3. **Traverse (or Traveling)** -- The rotating tool moves along the weld line.

During the traverse phase, the temperature at the weld line region rises, but the maximum temperature values do not surpass the melting temperature of the workpiece material. As the temperature drops, a solid continuous joint appears between the two plates.

For illustrative purposes, each phase of the FSW process is considered a separate load step. A rigid surface constraint is already defined for applying loading on the tool.

The following table shows the details for each load step.

**Table 28.3: Load Steps**

Load Step	Time Period (sec)	Loadings on Pilot Node	Boundary Condition
1	1	Displacement boundary condition	UZ = -7.95E-07 m
2	5.5	Rotational boundary condition	ROTZ = 60 RPM
3	22.5	Displacement and rotational boundary conditions together on the pilot node	ROTZ = 60 RPM UY = 60.96E-03 m

The tool plunges into the workpiece at a very shallow depth, then rotates to generate heat. The depth and rotating speeds are the critical parameters for the weld temperatures. The parameters are determined based on the experimental data of Zhu and Chao. The tool travels from one end of the welding line to the other at a speed of 2.7 mm/s.

## 28.6. Analysis and Solution Controls

A nonlinear transient analysis is performed in three load steps using structural-thermal options of [SOLID226](#) and [CONTA174](#).

FSW simulation includes factors such as nonlinearity, contact, friction, large plastic deformation, structural-thermal coupling, and different loadings at each load step. The solution settings applied consider all of these factors.

The first load step in the solution process converges within a few substeps, but the second and third load steps converge only after applying the proper solution settings shown in the following table:

**Table 28.4: Solution Settings**

Solution Setting	Description of Setting and Comments
<a href="#">ANTYPE,4</a>	Transient analysis.
<a href="#">LNSRCH,ON</a>	For contact problems, this option is useful for enhancing convergence.
<a href="#">CUTCONTROL, PLSLIMIT,0.15</a>	Controls the time-step cutback during a nonlinear solution and specifies the maximum equivalent plastic strain allowed within a time-step. If the calculated value exceeds the specified value, the program performs a cutback (bisection). PLSLIMIT is set at 15 percent (from the default five percent) because solution-control support is not available.

Solution Setting	Description of Setting and Comments
<b>NLGEOM,ON</b>	Includes large-deflection effects or large strain effects, according to the element type.
<b>NROPT,UNSYM</b>	Recommended for contact elements with high friction coefficients.
<b>TIMINT,OFF,STRUC</b>	To speed up convergence in a coupled-field transient analysis, the structural dynamic effects are turned off. These structural effects are not important in the modeling of heat generation due to friction; however, the thermal dynamic effects are considered here.
<b>KBC,0</b>	The loads applied to intermediate substeps within the load step are ramped because the structural dynamic effects are set to off.

To allow for a faster solution, automatic time-stepping is activated (**AUTOTS,ON**). The initial time step size (**DELTIM**) is set to 0.1, and the minimum time step is set to 0.001. The maximum time step is set as 0.2 in load steps 2 and 3. A higher maximum time-step size may result in an unconverged solution.

The time step values are determined based on mesh or element size. For stability, no time-step limitation exists for the implicit integration algorithm. Because this problem is inherently nonlinear and an accurate solution is necessary, a disturbance must not propagate to more than one element in a time step; therefore, an upper limit on the time step size is required. It is important to choose a time step size that does not violate the subsequent criterion (minimum element size, maximum thermal conductivity over the whole model, minimum density, and minimum specific heat).

The following example input defines the solution settings:

```

/solu
lnsrch,on          ! Activating a line search to be used with
                  ! Newton-Raphson (for contact problem)
cutcontrol,plslimit,0.15 ! Controls time-step cutback during a
                  ! solution,Maximum equivalent plastic
                  ! strain allowed within a time-step is 15%
                  !
kbc,0             ! Ramped loading within a load step
antype,4         ! Transient analysis
nlgeom,on        ! Activate large-deformation effects
timint,off, struc ! Structural dynamic effects are disabled

nropt,unsym      ! Use full Newton-Raphson with
                  ! unsymmetric matrices of elements

```

## 28.7. Results and Discussion

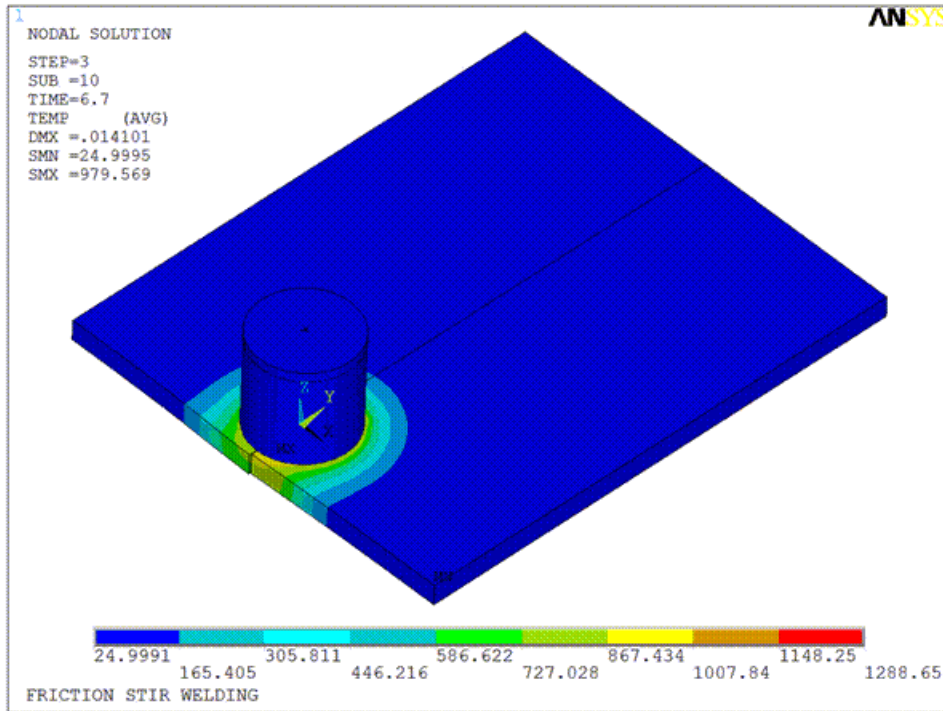
The following results topics for the FSW simulation are available:

[28.7.1. Deformation and Stresses](#)

[28.7.2. Temperature Results](#)

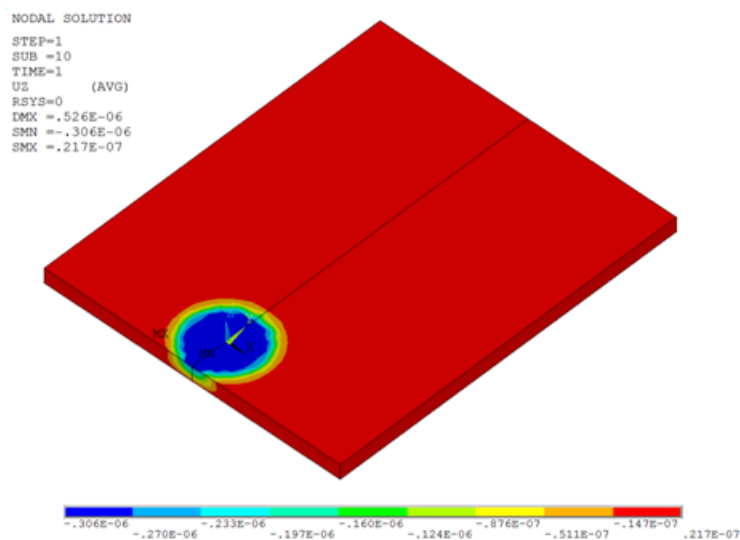
[28.7.3. Welding Results](#)

[28.7.4. Heat Generation](#)

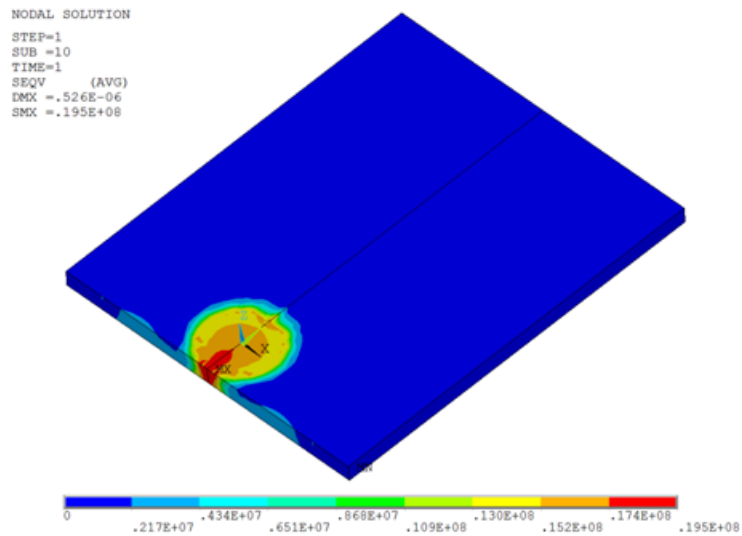
**Figure 28.8: Friction Stir Welding Animation**

### 28.7.1. Deformation and Stresses

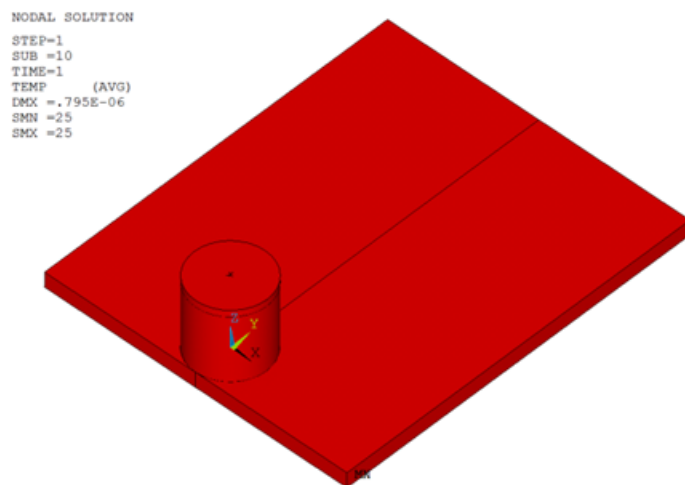
It is important to observe the change in various quantities around the weld line during the FSW process. The following figure shows the deflection of the workpiece due to plunging of the tool in the first load step:

**Figure 28.9: Deflection at Workpiece After Load Step 1**

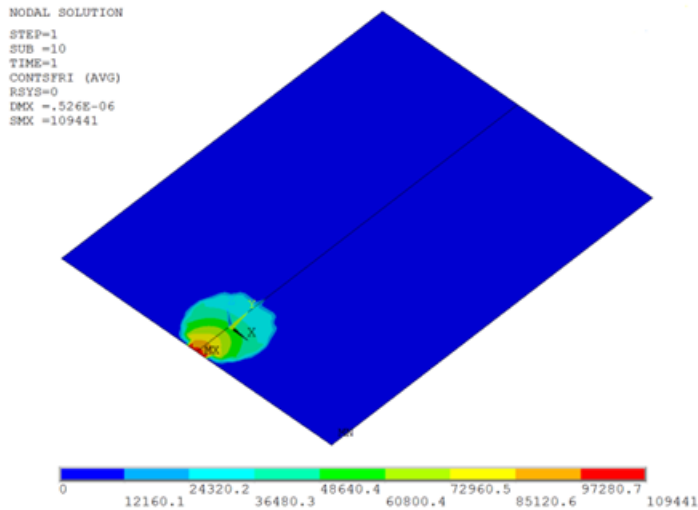
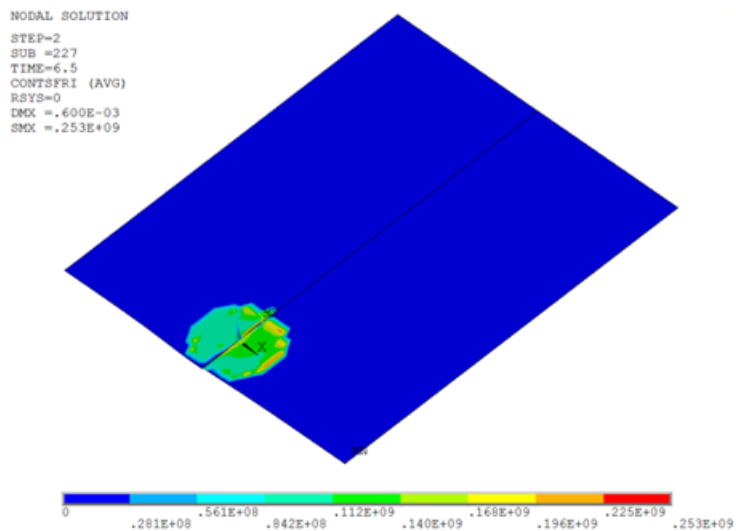
The deflection causes high stresses to develop on the workpiece beneath the tool, as shown in this figure:

**Figure 28.10: von Mises Stress After Load Step 1**

Following load step 1, the temperature remains unchanged (25 °C), as shown in this figure:

**Figure 28.11: Temperature After Load Step 1**

As the tool begins to rotate at this location, the frictional stresses develop and increase rapidly. The following two figures show the increment in contact frictional stresses from load step 1 to load step 2:

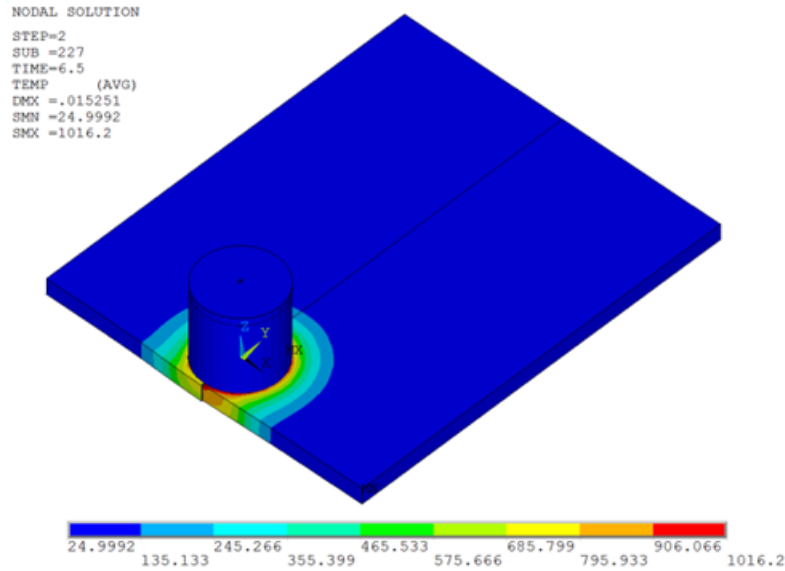
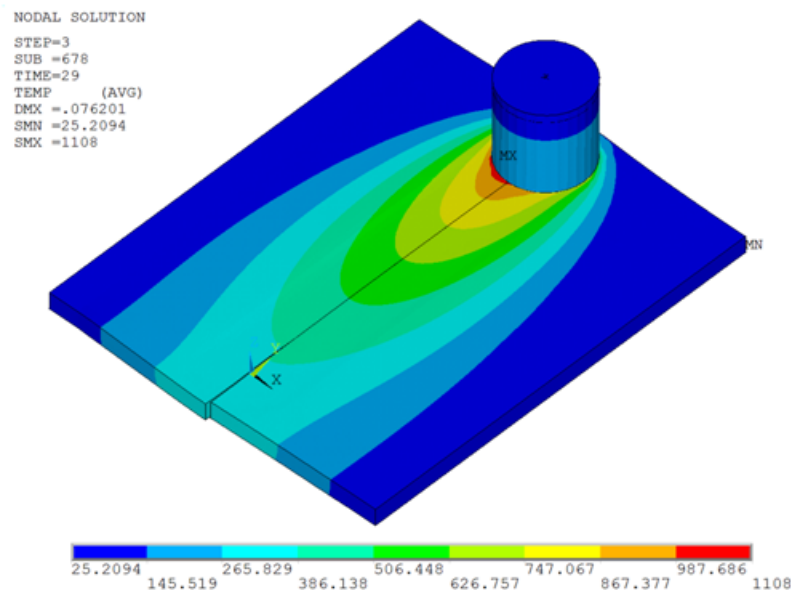
**Figure 28.12: Frictional Stress After Load Step 1****Figure 28.13: Frictional Stress After Load Step 2**

All frictional dissipated energy is converted into heat during load step 2. The heat is generated at the tool-workpiece interface. Most of the heat is [transferred to the workpiece \(p. 425\)](#) (FWGT is specified to 0.95). As a result, the temperature of the workpiece increases rapidly compared to that of the tool.

### 28.7.2. Temperature Results

The following two figures shows the temperature rise due to heat generation in the second and third load steps:



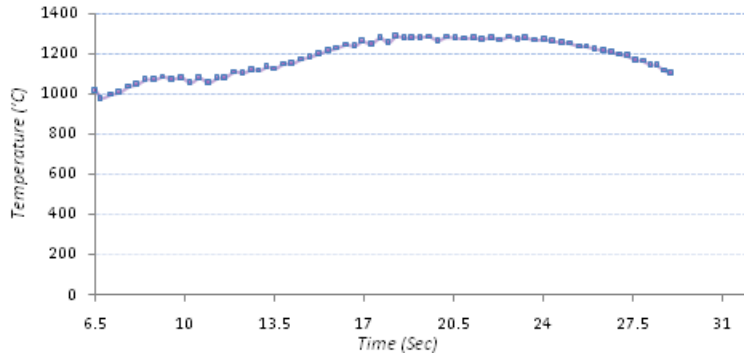
**Figure 28.14: Temperature After Load Step 2****Figure 28.15: Temperature After Load Step 3**

The maximum temperature on the workpiece occurs beneath the tool during the last two load steps. Heat generation is due to the mechanical loads. No external heat sources are used. As the temperature increases, the material softens and the coefficient of friction decreases. A temperature-dependent coefficient of friction (0.4 to 0.2) helps to prevent the maximum temperature from exceeding the material melting point.

The observed temperature rise in the model shows that heat generation during the second and third load steps is due to friction between the tool shoulder and workpiece, as well as plastic deformation of the workpiece material.

The melting temperature of 304L stainless steel is 1450 °C. As shown in the following figure, the maximum temperature range at the weld line region on the workpiece beneath the tool is well below the melting temperature of the workpiece material during the second and third load steps, but above 70 percent of the melting temperature:

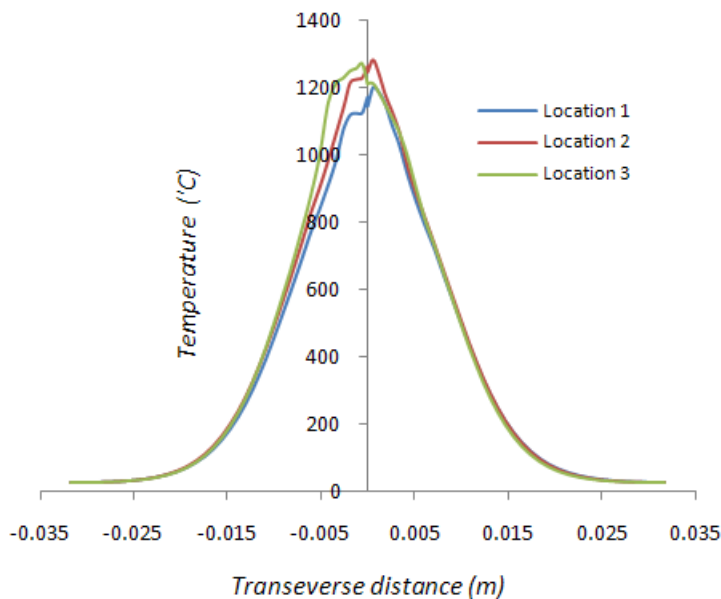
**Figure 28.16: Maximum Temperature (on Workpiece Beneath the Tool) Variation with Time**



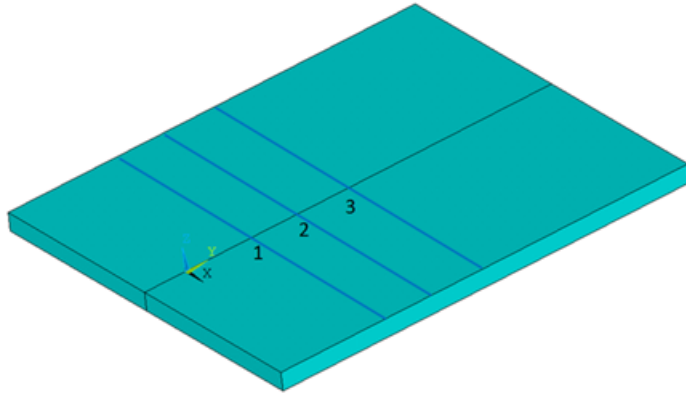
The two plates can be welded together within this temperature range.

The following figure shows the temperature distributions on the top surface of the workpiece along the transverse distance (perpendicular to the weld line):

**Figure 28.17: Temperature Distribution on the Top Surface of Workpiece at Various Locations**

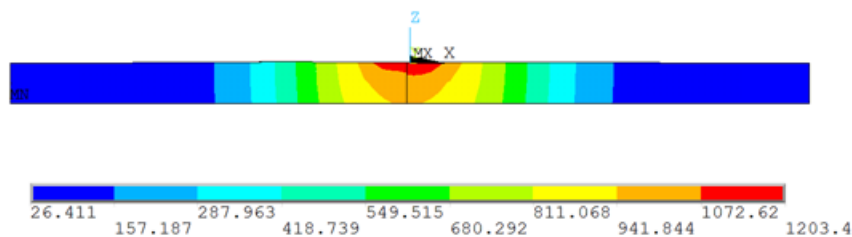


As shown in the following figure and table, the temperature plots indicate the temperature distribution at various locations on the weld line when the maximum temperature occurs at those locations:

**Figure 28.18: Various Locations on the Workpiece****Table 28.5: Locations on Weld Line**

Location Number	Distance on the Weld Line in y Direction	Time When Maximum Temperature Occurs
1	0.016 m	15.25 Sec
2	0.027 m	19.2 Sec
3	0.040 m	24 Sec

The following figure shows the temperature distribution in the thickness direction at location 1:

**Figure 28.19: Temperature Distribution in Thickness Direction at Location 1**

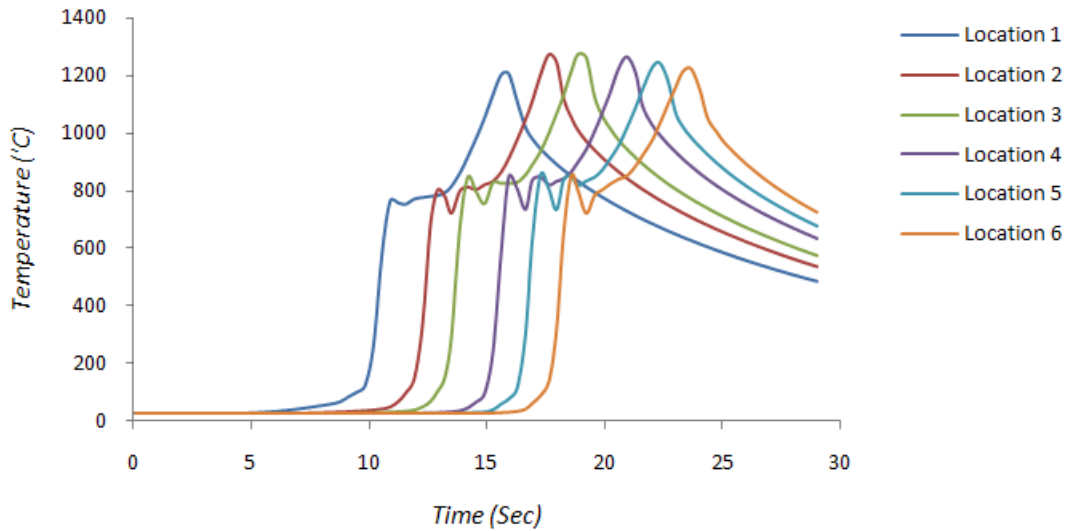
As expected, the highest temperature caused by heat generation appears around the weld line region. By comparing the above temperature results with the reference results, it can be determined that the temperatures obtained at the weld line are well below the melting temperature of the workpiece material, but still sufficient for friction stir welding.

The following table and figure show the time-history response of the temperature at various locations on the weld line:

Location Number	Distance on the Weld Line
1	0.018 m
2	0.023 m
3	0.027 m
4	0.032 m

Location Number	Distance on the Weld Line
5	0.035 m
6	0.039 m

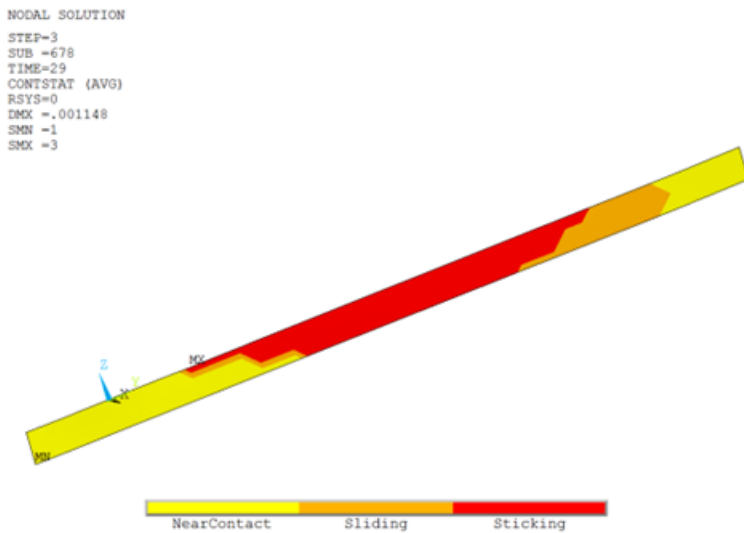
**Figure 28.20: Temperature Variation with Time on Various Joint Locations**



### 28.7.3. Welding Results

A bonding temperature of 1000 °C is already defined for the welding simulation at the interface of the plates. The contact status at this interface after the last load step is shown in the following figure:

**Figure 28.21: Contact Status at Interface with Bonding Temperature 1000 °C**



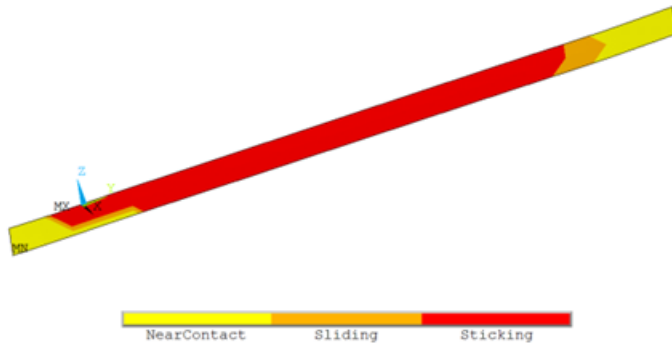
The sticking portion of the interface shows the bonding or welding region of the plates. If the bonding temperature was assumed to be 900 °C, then the welding region would increase, as shown in this figure:

**Figure 28.22: Contact Status at Interface with Bonding Temperature 900 °C**

```

NODAL SOLUTION
STEP=3
SUB =682
TIME=29
CONSTAT (AVG)
RSYS=0
DMX =.001076
SMN =1
SMX =3

```

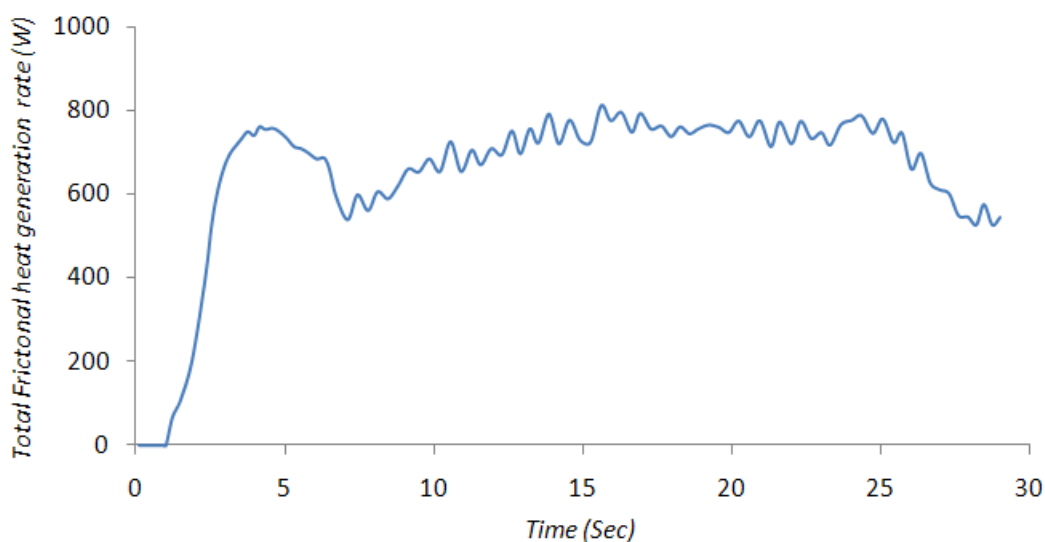


### 28.7.4. Heat Generation

Friction and plastic deformation generate heat. A calculation of frictional and plastic heat generation is performed. The generation of heat due to friction begins in the second load step.

The [CONTA174](#) element's FDIS (SMISC item) output option is used to calculate frictional heat generation on the workpiece. This option gives the frictional energy dissipation per unit area for an element. After multiplying this value with the corresponding element area, the friction heat-generation rate for an element is calculated. By summing the values from each [CONTA174](#) element of the workpiece, the total frictional heat generation rate is calculated for a given time.

It is possible to calculate the total frictional heat-generation rate at each time-step ([ETABLE](#)). The following figure shows the plot of total frictional heat generation rate on the workpiece with time:

**Figure 28.23: Total Frictional Heat Rate Variation with Time**

The plot indicates that the frictional heat starts from the second load step (after 1 second).

The element contact area can be calculated using the [CONTA174](#) element CAREA (NMISC, 58) output option.

The following example input defines the frictional heat calculations:

```

/post1
set,last
*get,nst,active,,set,nset ! To get number of data sets on result file

! Total frictional heat rate
esel,s,real,,5
esel,r,ename,,174 ! Selecting the contact elements on workpiece
*dim,fht,array,nst,1
*do,i,1,nst,1
set,,,,,i
etable,fri,smisc,18 ! Frictional energy dissipation per unit
! area for an element, FDIS
etable,arel,nmisc,58 ! Area of each contact element
smult,frri,fri,arel ! Multiplying Fri. energy dissipation
! per unit area with the area of
! corresponding element
ssum
*get,frhi,ssum,,item,frri ! Total Frictional heat rate on
! workpiece at a particular time

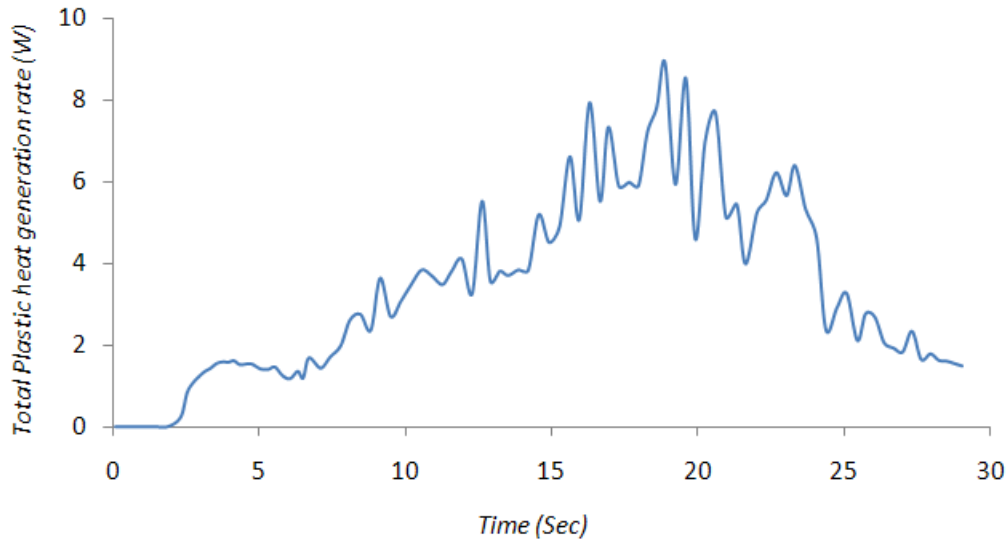
fht(i,1)=frhi
*enddo
parsav,all
allsel,all
finish

/post26
file,fsw,rst
numvar,200
solu,191,ncmit ! Solution summary data per substep to be
! stored for cumulative no. of iterations.
store,merge ! Merge data from results file
filldata,191,,,1,1
realvar,191,191
parres,new,'fsw','parm'
vput,fht,11,,,fric_heat
plvar,11 ! Plot of frictional heat rate against time
finish

```

A similar calculation is performed to check the heat generation from plastic deformation on the workpiece. The [SOLID226](#) element's output option PHEAT (NMISC, 5) gives the plastic heat generation rate per unit volume. After multiplying this value with the corresponding element volume, the plastic heat generation rate for an element is calculated. By summing the values from each element ([SOLID226](#)) of the workpiece, the total plastic heat generation rate is calculated for a particular time.

It is possible to calculate the total frictional heat generation rate at each time-step ([ETABLE](#)). The following figure shows the plot of the total plastic heat-generation rate with time.

**Figure 28.24: Total Plastic Heat Rate Variation with Time**

The following example input defines the plastic heat calculations:

```

/post1
set,last
*get,nst,active,,set,nset !To get number of data sets on result file

! Total Plastic heat rate
esel,s,mat,,1           !Selecting the coupled elements on workpiece
etable,vlml,volu       !Volume of the each element
*dim,pha,array,nst,1
*do,i,1,nst,1
set,,,,,,i
etable,pi,nmisc,5      !Plastic heat rate per unit volume on
                       !each element, PHEAT
smult,psi,pi,vlml      !Multiplying Pl. heat rate per unit
                       !volume with the volume of
                       !corresponding element
ssum                   !Summing up the Plastic heat rate
*get,ppi,ssum,,item,psi !Total Plastic heat rate on workpiece
                       !at a particular time

pha(i,1)=ppi
*enddo
parsav,all
allsel,all

/post26
file,fsw,rst
numvar,200
solu,191,ncmit        !solution summary data per substep to be
                       !stored for cumulative no. of iterations.
store,merge           !Merge data from results file
filldata,191,,,,1,1
realvar,191,191
parres,new,'fsw','parm'
vput,pha,10,,,pheat_nmisc
plvar,10              !Plot of Plastic heat rate against time
finish

```

Figure 28.23: Total Frictional Heat Rate Variation with Time (p. 439) and Figure 28.24: Total Plastic Heat Rate Variation with Time (p. 441) clearly show that friction is responsible for generating most of the heat needed, while the contribution of heat due to plastic deformation is less significant. Because the tool-penetration is shallow and the tool pin is ignored, the plastic heat is small compared to frictional heat.

## 28.8. Recommendations

To perform a similar FSW analysis, consider the following hints and recommendations:

- FSW is a coupled-field (structural-thermal) process. The temperature field affects the stress distribution during the entire process. Also, heat generated in structural deformation affects the temperature field. The direct method of coupling is recommended for such processes. This method involves just one analysis that uses a coupled-field element containing all necessary degrees of freedom. Direct coupling is advantageous when the coupled-field interaction involves strongly-coupled physics or is highly nonlinear.
- A nonlinear transient analysis is preferable for simulations where the objective is to study the transient temperature and transient heat transfer.
- The dynamic effects of different physics should be controlled. In this problem, for example, the dynamic effects of the structural degrees of freedom are disabled as they are unimportant.
- Separating the solution process into three load steps helps you to understand the physics and solve the problem.
- The contact between the two plates must be nearly perfect to maintain temperature continuity. For a perfect thermal contact, specify a high thermal contact conductance (TCC) coefficient between workpiece plates. A high coefficient results in temperature continuity across the interface.
- Because the problem is nonlinear, proper solution settings are required. Set the following analysis controls to the appropriate values to achieve the converged solution: **LNSRCH**, **CUTCONTROL**, **KBC**, **NEQIT**, **NROPT**, and **AUTOTS**.
- Convergence at the second and third load steps is difficult to achieve. The depth of penetration of the tool on the workpiece (uz), rotational speed of the tool (rotz), and time-step size play crucial roles in the convergence of the second load step. Use a very small time-step size if the rotational speed is higher than 60 RPM.
- A symmetric mesh (about the joint line) is preferred to capture the exact outputs and their effects on the workpiece. A hex mesh with dropped midside nodes is recommended for the workpiece as well as the tool. This approach helps to maintain symmetry and prevent the temperature from reaching negative values during the simulation.
- A minimum of two element layers is required in the thickness direction. A fine sweep mesh near the weld line yields more accurate results; however, too fine a mesh increases computational time. A fine mesh is unnecessary on the tool side. To minimize computational time, the tool can be considered to be rigid with no temperature degrees of freedom.

## 28.9. References

The following references are used in this example problem:

1. Zhu, X. K., and Y. J. Chao. "Numerical Simulation of Transient Temperature and Residual Stresses in Friction Stir Welding of 304L Stainless Steel." *Journal of Materials Processing Technology*. 146.2 (2004): 263-272.
2. Chao, Y.J., X. Qi, and W. Tang. "Heat Transfer in Friction Stir Welding - Experimental and Numerical Studies." *Journal of Manufacturing Science and Engineering-Transactions of the ASME*. 125.1 (2003): 138-145.
3. Prasanna, P., B. S. Rao, and G. K. Rao. "Finite Element Modeling for Maximum Temperature in Friction Stir Welding and its Validation." *Journal of Advanced Manufacturing Technology*. 51 (2010): 925-933.



4. Sorensen, C.D., and T.W. Nelson. "Friction Stir Welding of Ferrous and Nickel Alloys." *Friction Stir Welding and Processing*. Ed. M. W. Mahoney and R. S. Mishra. Materials Park: ASM International, 2007. 111-121.
5. Ozel, T., Y. Karpuz, and A. Srivastava. "Hard Turning with Variable Micro-Geometry Pcbn Tools." *CIRP Annals - Manufacturing Technology*. 57 (2008): 73-76.
6. Mishra, R. S. *Friction Stir Welding and Processing*. Ed. R. S. Mishra and M. W. Mahoney. Materials Park, OH: ASM International, 2007.

## 28.10. Input Files

The following files were used in this problem:

- `fs_w.dat` -- Input file for the friction stir welding (FSW) problem.
- `fs_w.cdb` -- Common database file containing the FSW model information (called by `fs_w.dat`)

The files are available in the `td-28` folder. See [Obtaining the Input Files \(p. xxxv\)](#) for more information.



---

## Chapter 29: Rocket Nozzle Extension Simulation: Operation

---

This is the second of two example problems that simulate a rocket nozzle:

- The first example, [Rocket Nozzle Extension Simulation: Fabrication](#), demonstrates how to simulate the thermal stresses during the *manufacturing* stage of the nozzle.
- The second example problem that follows demonstrates how to simulate thermal stresses induced during the *operation* of the rocket nozzle.

While both examples are based on the same geometry, the assumptions are different, thus leading to different meshes and different element types.

For this problem, it is assumed that the rocket has been launched and hot gases are flowing through the nozzle, subjecting the inside and outside of the nozzle body to convection heat loading. The heat loading leads to a significant thermal gradient through the thickness of the body that manifests as high thermal stresses.

Solid thermal and structural elements accurately simulate the multiphysics of the problem. While a fully coupled element could solve the problem, a loose coupling method is used instead. Because the body material could be homogeneous or a layered composite, the simulation requires a solid element type with both homogeneous and layered material capabilities.

Topics related to this example problem follow:

- [29.1. Introduction](#)
- [29.2. Problem Description](#)
- [29.3. Modeling](#)
- [29.4. Material Properties](#)
- [29.5. Boundary Conditions and Loading](#)
- [29.6. Analysis and Solution Controls](#)
- [29.7. Results and Discussion](#)
- [29.8. Recommendations](#)
- [29.9. Input Files](#)

### 29.1. Introduction

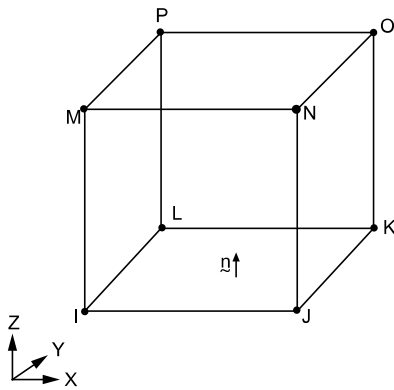
The shell element model gives accurate stresses in most regions; however, through-the-thickness stresses are not as accurate, especially where the reinforcement joins with the nozzle body. Solid elements are used for this analyses to improve the accuracy of through-the-thickness stresses. This problem therefore demonstrates some of the features of the solid layered thermal elements ([SOLID279](#)). The geometry for this example problem has already been meshed and stored in a `cdb` file.

For this example, it is assumed that the material behavior is orthotropic (both structurally and thermally). As such, it is important to define material properties along certain orthogonal directions within the elements. This underscores the need to define an element coordinate system within each element. While there is a good argument for defining material directions independent of the underlying elements, this is currently restricted by the available technology.

All elements have default element coordinate systems, but these defaults may not always be convenient. Material directions could be misaligned with respect to the element coordinate system (**ESYS**) and, as such, you may need to modify them. You can typically accomplish this with the following steps:

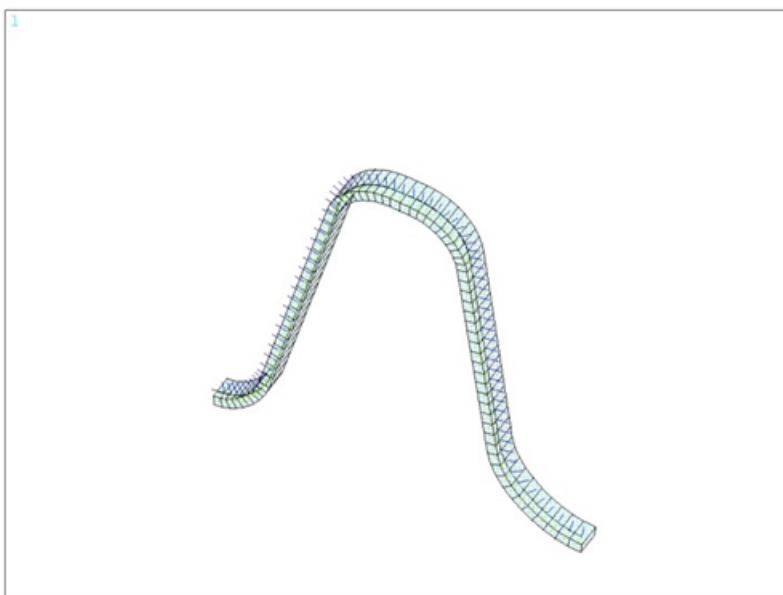
1. **Define the element coordinate system** - Due to rapidly changing curvature, each element in this model must have its own element coordinate system defined. (Consider using **LOCAL** and **EMODIF** commands for a given brick mesh.) As a result, the element z axis is aligned with the thickness direction, and the element x axis is aligned with the curvature. This makes it very convenient to define material properties along preferred directions.
2. **Adjust the element connectivity** - Because solid elements are being used, you must adjust the element connectivity so that the IJKL face is aligned with the element coordinate z axis. This ensures that the layer definition is parallel to face 1 (the IJKL face normal  $n$ ) of the element and is normal to the ESYS z axis. (Consider using **EORIENT** to accomplish this for any arbitrary mesh with a defined element coordinate system.)

**Figure 29.1: Element Coordinate System**



Both of these steps have already been accomplished for the model provided in this example.

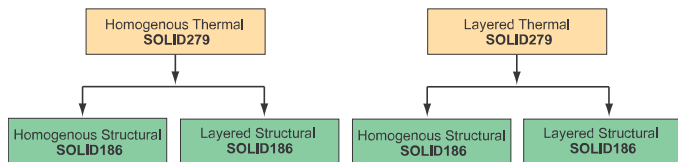
**Figure 29.2: 3-D Solid Element Model**



Thermal stresses can be obtained using an element with TEMP and DISP degrees of freedom (DOFs) that are fully coupled (strong coupling). Alternately, stresses can be obtained using a thermal run and then a structural run (loose coupling). The advantages and disadvantages of these methodologies are not fully detailed here. Instead, this example uses the loose coupling method to demonstrate the flexibility that it offers.

In this example a static thermal analysis is run using element **SOLID279**, and then temperatures are transferred to a static structural analysis using the **LDREAD** command. For the structural run, **SOLID279** is converted into **SOLID186**. For the thermal run, it is assumed that the material can be homogeneous or layered. A similar assumption is made for the structural run, thus allowing you to use the temperatures from either a homogeneous or layered run for a structural run, as illustrated in the figure below:

**Figure 29.3: Thermal-Structural Analysis**



A material could be treated as "homogeneous" for a thermal run and "layered" for a structural run. This allows you the flexibility to mix and match the runs at your own discretion. A strongly coupled solution would not provide this level of flexibility and freedom.

## 29.2. Problem Description

A 1° sector of the full geometry is modeled. It is assumed that the thermal and structural solution are axisymmetric. This example uses the same geometry used in the [first rocket nozzle example problem \(p. 147\)](#); however, 3-D solid elements with the capability to model layers are used instead of 2-D shell elements with the axisymmetric option.

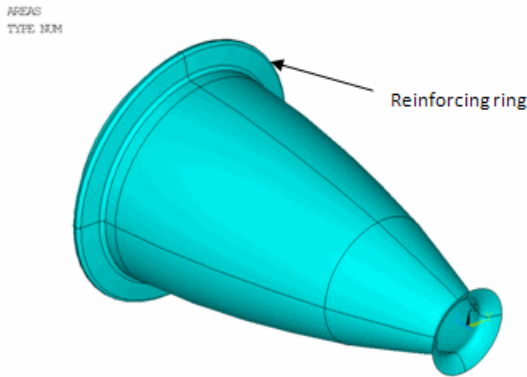
A thermal analysis is performed using a homogeneous material option, followed by an analysis using the 4-layer material option. The solutions from these analyses serve as the loads for a structural analysis (both homogeneous and 4-layer material option). A total of four structural solutions will be obtained.

To ensure an axisymmetric solution for the thermal run, the TEMP is constrained to be the same along the theta direction (**CE** command). Axisymmetry DOF constraints are specified to ensure an axisymmetric solution for the structural run (**DSYM**). While there are many different ways to accomplish axisymmetry for a sector model, this method was selected for its ease of implementation.

## 29.3. Modeling

The nozzle extension consists of a main curved wall and a reinforcing ring close to the jet exhaust, as shown in [Figure 29.4: Nozzle Extension Geometry \(p. 448\)](#)

**Figure 29.4: Nozzle Extension Geometry**

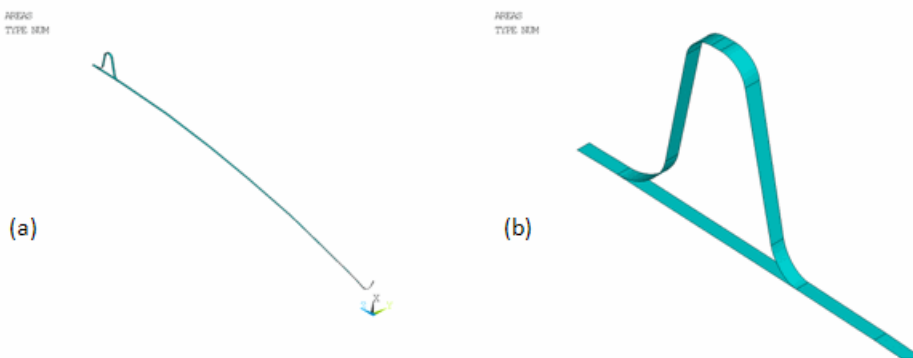


Both the wall and the reinforcing ring are made of layered composite materials. The model uses a single orthotropic material for all layers; however, the material orientation varies from layer to layer. The material is assumed to be homogeneous for both the thermal and mechanical analysis. This simplification could speed up the computations and provide a reasonable solution.

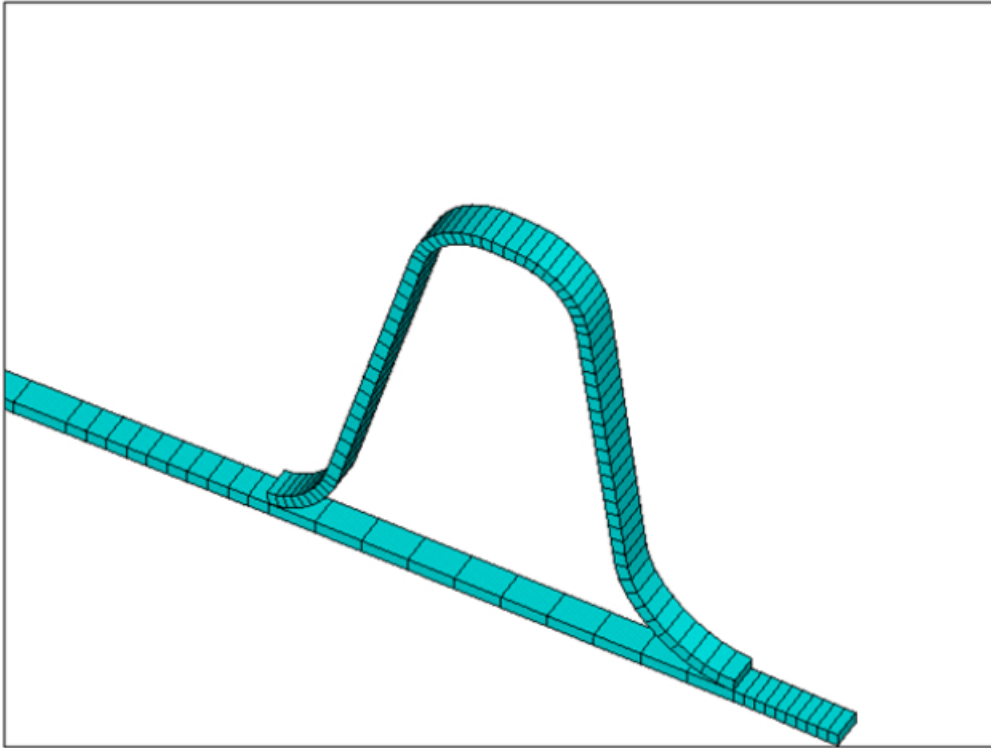
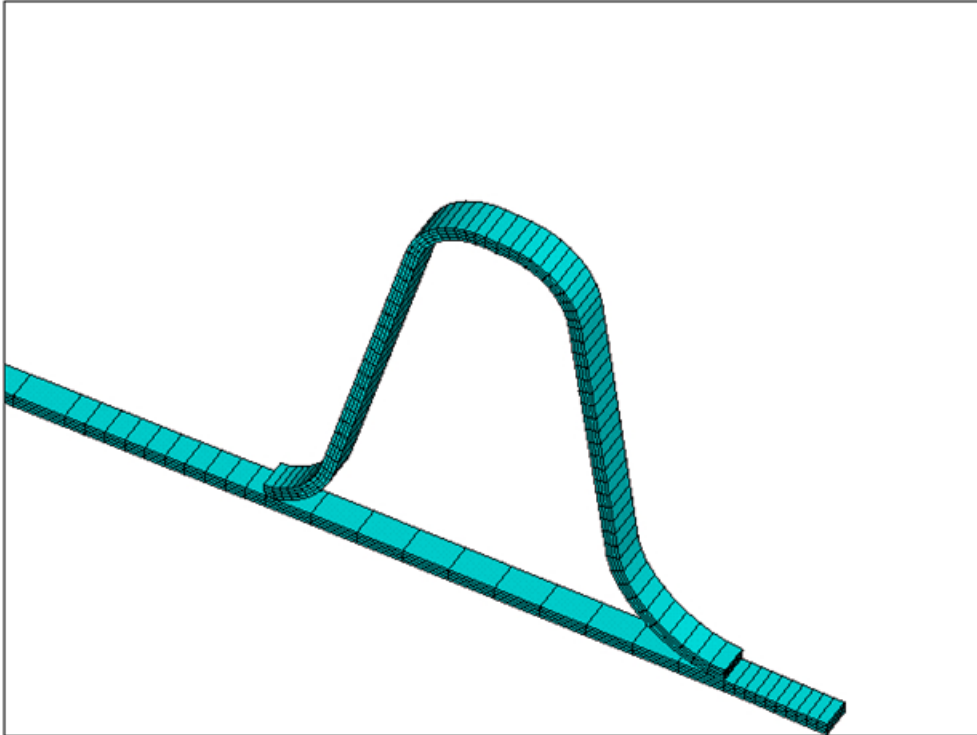
Because the model exhibits symmetry, optimal computational efficiency is achieved by modeling only a single 1° sector (the base sector) of the entire nozzle extension. The geometry model of the 1° sector is shown in [Figure 29.5: Nozzle Extension 1° Base Sector Geometry \(p. 448\)](#), where (a) is the global geometry and (b) is a detail view of the reinforcing ring.

Since the thermal solution exhibits cyclic symmetry for temperature, **CE** can be used to accomplish this. The **CE** command could be used for the structural cyclic symmetry, but in this example, the **DSYM** command is used to demonstrate the different ways to accomplish a task in ANSYS.

**Figure 29.5: Nozzle Extension 1° Base Sector Geometry**



The reduced 1° geometry model is meshed with **SOLID279** elements. [Figure 29.6: Ring Element Plot \(p. 449\)](#) and [Figure 29.7: Expanded Layer Representation of the Solid Mesh \(p. 449\)](#) respectively show the mesh and the layer solid representation of the solid mesh (**/ESHAPE**).

**Figure 29.6: Ring Element Plot****Figure 29.7: Expanded Layer Representation of the Solid Mesh**

Using the **SOLID279** element it is possible to make the element behave like a homogeneous material or a layered material (**KEYOPT**(3) = 0 or 1). Shell sections define the layers of the composite material. (The **SECTYPE** command specifies the section type, and the **SECDATA** command specifies the material, thickness, material orientation, and the number of integration points of each layer.) Two sections are

created: one for the main wall and another for the reinforcing ring. The following table summarizes the shell section properties:

Section Number	Layer Thickness	Material Number	Material Orientation	Integration Points
Section 1 (main wall)	1/4 total thickness	1	0	3
			90	
			0	
			90	
Section 2 (reinforcing ring)	1/4 total thickness	1	0	3
			90	
			0	
			90	

Assume that the reinforcing ring is securely bonded to the outer surface of the main extension wall. The secure bonding is easily simulated (**CE/CP** commands).

## 29.4. Material Properties

The properties of the single orthotropic material used in the rocket nozzle extension model are as follows:

Orthotropic Material Properties	
Young's Modulus in x direction (MPa)	100000
Young's Modulus in y direction (MPa)	5000
Young's Modulus in z direction (MPa)	5000
Poisson's Ratio PRXY	0.40
Poisson's Ratio PRYZ	0.30
Poisson's Ratio PRXZ	0.30
Shear Moduli GXY	3000
Shear Moduli GYZ	2000
Shear Moduli GXZ	2000
Secant coefficient of thermal expansion ALPX	1.6E-05
Secant coefficient of thermal expansion ALPY	1.6E-05
Secant coefficient of thermal expansion ALPZ	6.3E-05

The material is assumed to be linear elastic and temperature-independent. The material has different thermal expansion coefficients in the in-plane (X and Y) and through-the-thickness (Z) directions.



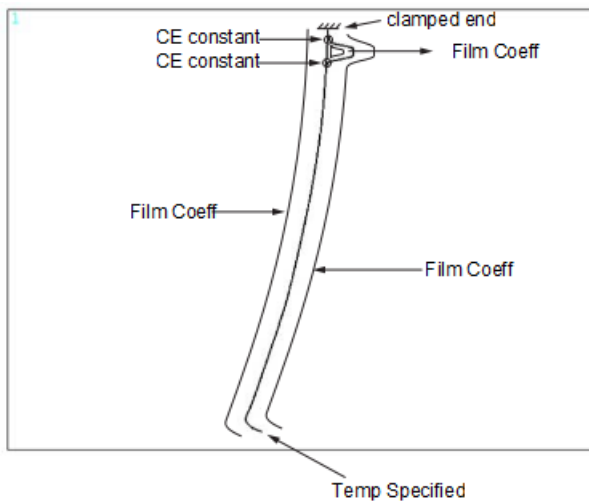
## 29.5. Boundary Conditions and Loading

For the thermal model, four types of boundary conditions are used (see [Figure 29.8: Thermal Boundary Conditions](#) (p. 451)):

- TEMP specified at the clamped end
- Three different film convection boundary conditions for different regions of the model
- Constraint equations to bond the reinforcement to the nozzle body
- Constraint equations to enforce cyclic symmetry

A realistic thermal model may have film coefficients that were derived from empirical correlations. Constant values are used here for simplicity. It is possible to specify heat flux boundary conditions instead of convection boundary conditions.

**Figure 29.8: Thermal Boundary Conditions**

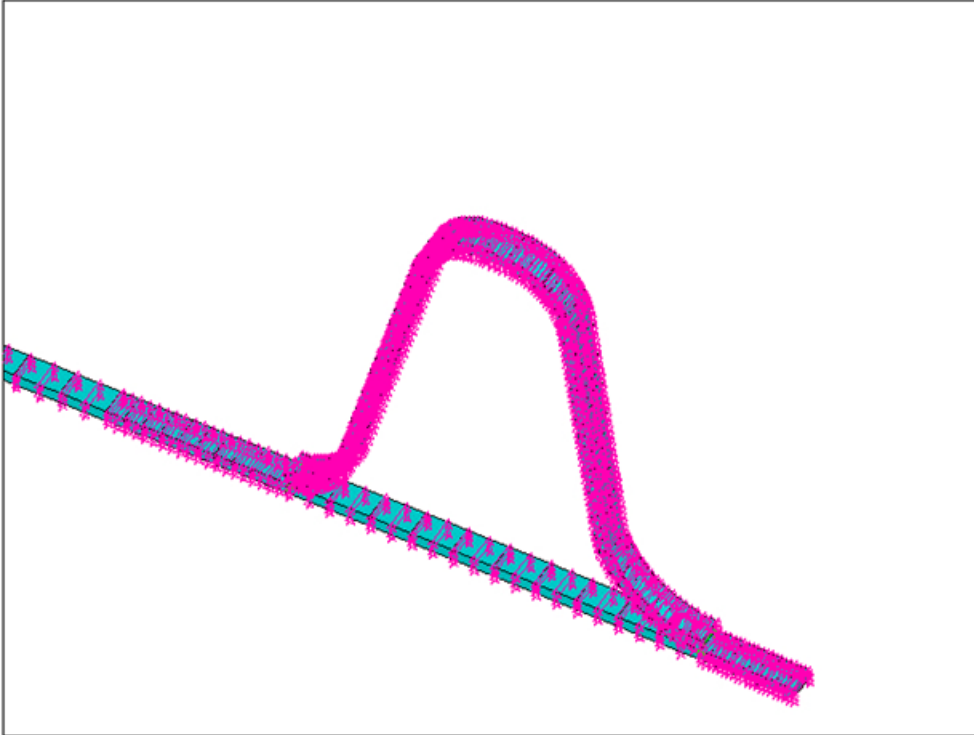


For the structural model, three types of boundary conditions are used (see [Figure 29.9: Structural Boundary Conditions](#) (p. 452)):

- Displacements specified at the clamped end
- Constraint equations to bond the reinforcement to the nozzle body
- Symmetry conditions to enforce cyclic symmetry

In addition to the aforementioned boundary conditions, thermal loads are applied to the structural model (**LDREAD**). This accomplishes loose coupling, as described in the introduction.

It should be noted that for the structural analysis other mechanical loads could be active that have been ignored in this analysis (e.g., pressure and shearing stresses due to gaseous flows). A realistic simulation would have to account for all possible loads that could be a major contributor to stress.

**Figure 29.9: Structural Boundary Conditions**

## 29.6. Analysis and Solution Controls

A linear static analysis is performed for the thermal model using the homogeneous and layered options (2 different model options).

This is followed by a linear static analysis for the structural model using the homogeneous and layered options (4 different analyses). As mentioned in the introduction, temperatures must be transferred from the first two analyses to the last four analyses (**LDREAD**) when the loosely coupled method is used.

## 29.7. Results and Discussion

For the thermal analysis using the layered option, the results for the reinforcing ring are shown in the following three figures. It is important to note the layered analysis solution within each layer. For example, the peak TEMP gradient may occur in layer 2, while the peak Von Mises stress may occur in layer 3.

Figure 29.10: Layered Temperature Results

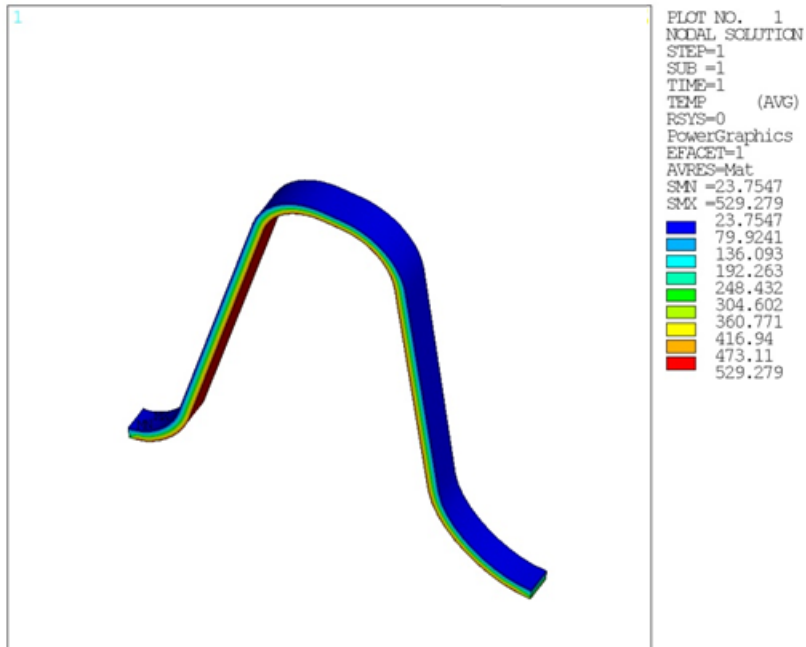
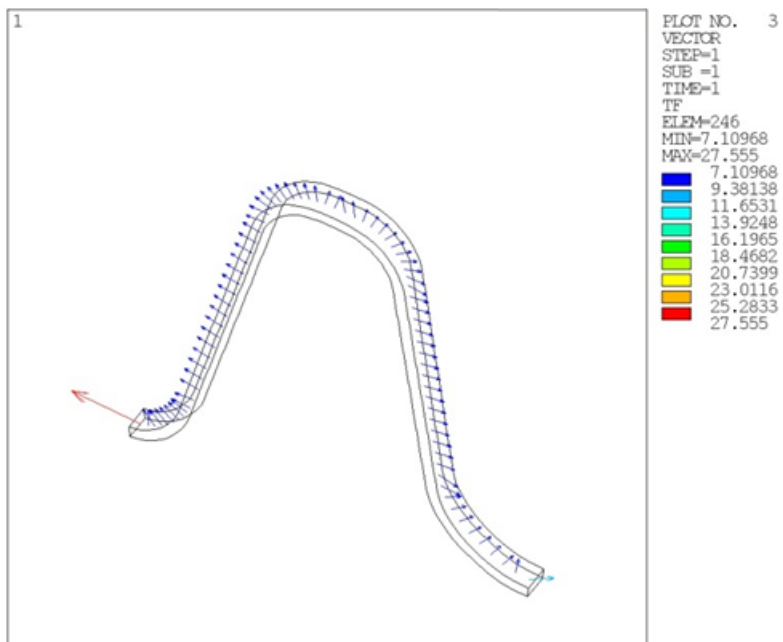
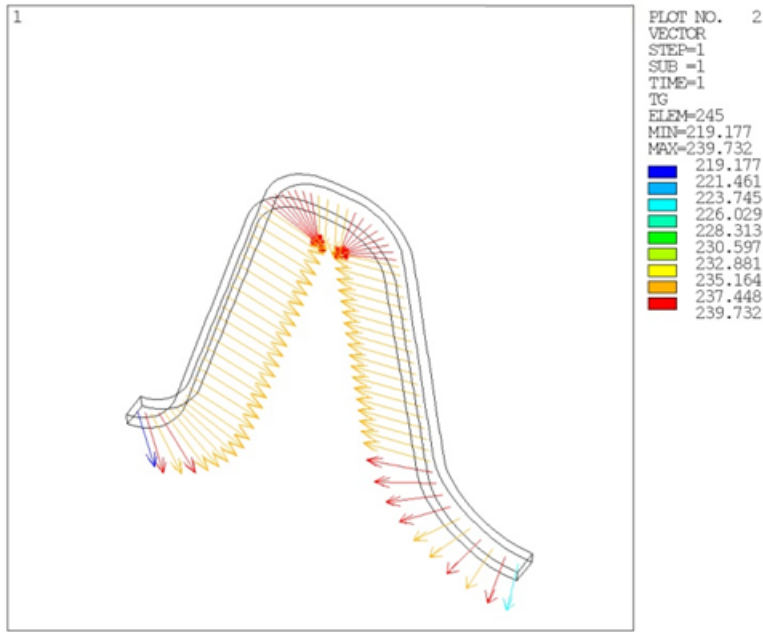


Figure 29.11: Layered TF Results



**Figure 29.12: Layered Temperature Gradient Results**



An additional complication to consider when postprocessing elements with layers, is that while regular postprocessing commands can be used, the results will be based on the corner node values, and the values within each layer will be ignored. For example, the **PLNSOL,TEMP** command will create a contour plot based on the 8 nodes of the element, but it does not reveal how the temperature varies within the 4 layers. To postprocess layer by layer, activate each individual layer, then issue the relevant post-processing command.

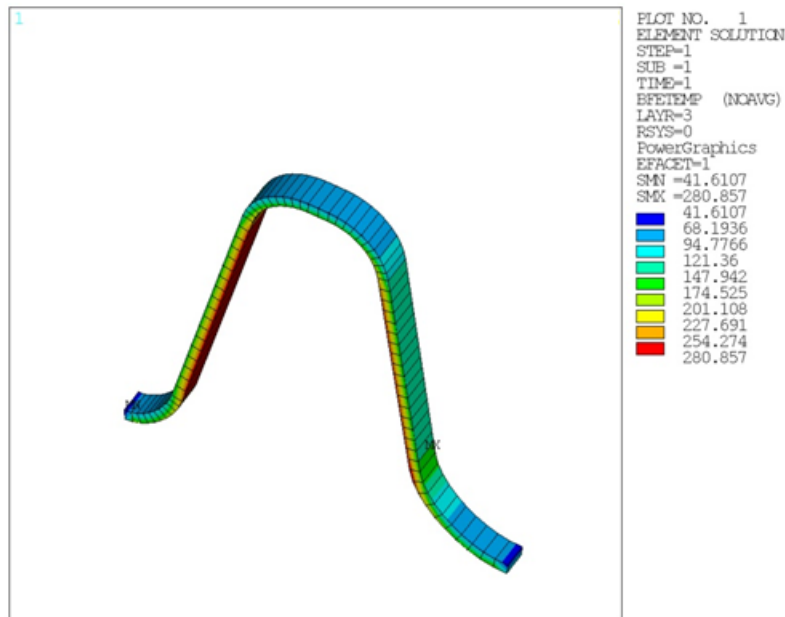
The TEMP in layer 3 of the reinforcing ring is shown in [Figure 29.13: Layer 3 Temperature Results \(p. 455\)](#). You can generate this by issuing the following command in /POST1:

```
Layer,3      !activate the layer for postprocessing
presol,bfe,temp ! plot the element stored layer temp
```

You can also force the layer TEMP onto the 8 corner nodes of the element and then contour the element solution (**LAYER**). This ensures that the element solution plotted is the actual layer solution in the figure.

To view the layer heat flux and temp gradient issue the **PLESOL** command after the **LAYER** command.

By default the layer value is 0. This implies that the postprocessed quantities are top of top layer and bottom of bottom layer.

**Figure 29.13: Layer 3 Temperature Results**

The following figures show the displacement solution for the four analyses of the reinforcing ring. These are all element based plots (i.e., the **LAYER** command was not used, which is the same as **LAYER,0**). The maximum displacement in all cases occurs where the reinforcing ring is bonded with the nozzle body. The figures show the original geometry superposed on the displacement plot. The following commands can be used in /POST1 to accomplish this:

```
PLDI,1
PLNS,U,SUM
```

Note that the displacement solution for the layered cases do not vary significantly. As a result, using homogeneous or layered thermal loading for the layered mechanical problem does not appear to have a significant effect. A similar conclusion can be drawn for the displacement solution of the homogeneous cases; however, this may not be true for stresses. General conclusions should not be drawn based on this model, as each model should be analyzed based on its loading conditions and assumptions.

Figure 29.14: homogeneous Thermal - homogeneous Structural Results

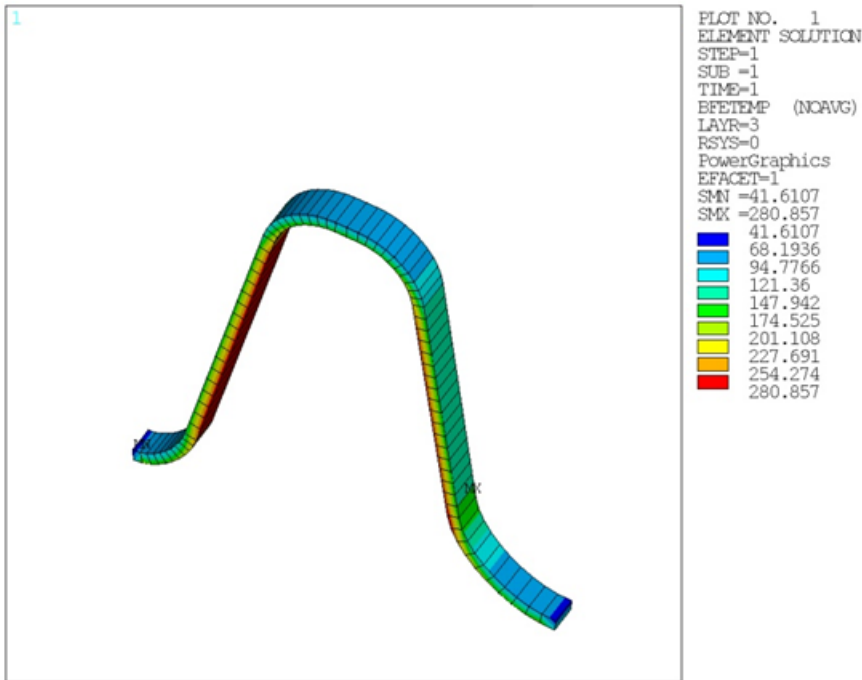
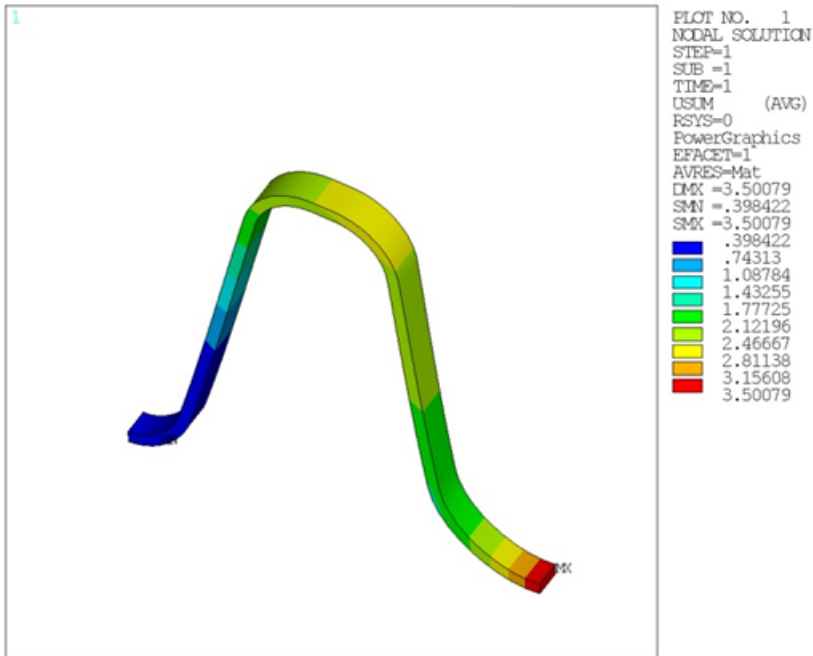


Figure 29.15: homogeneous Thermal - Layered Structural Results



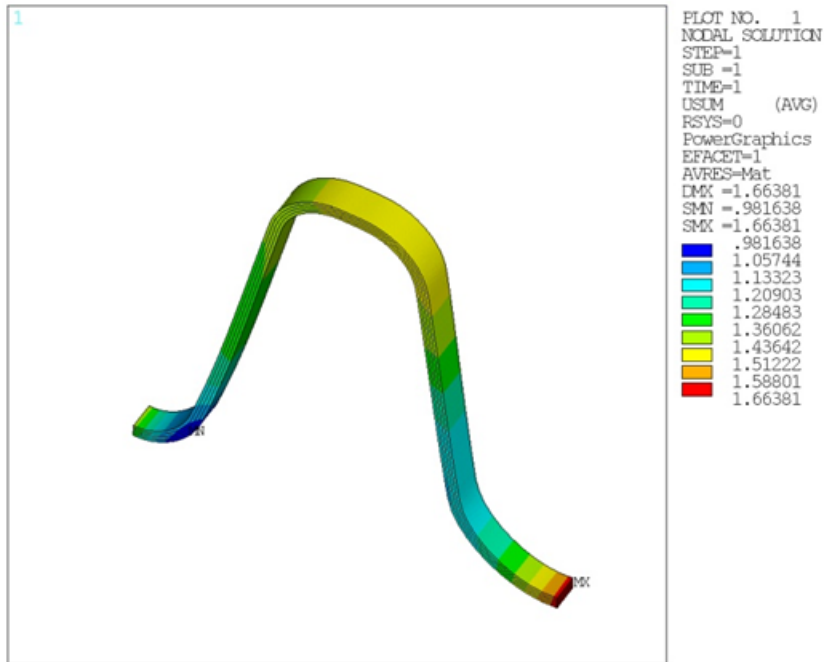
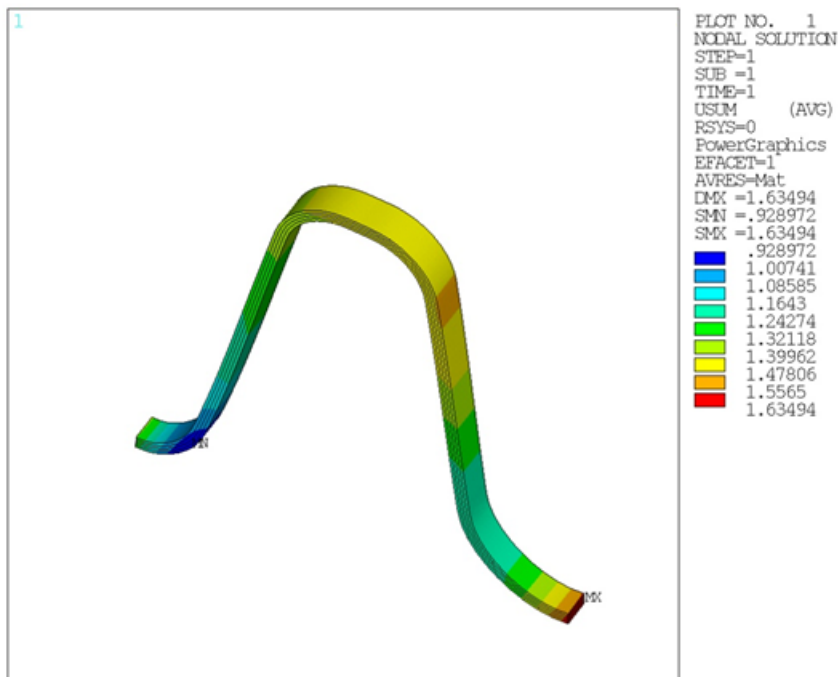
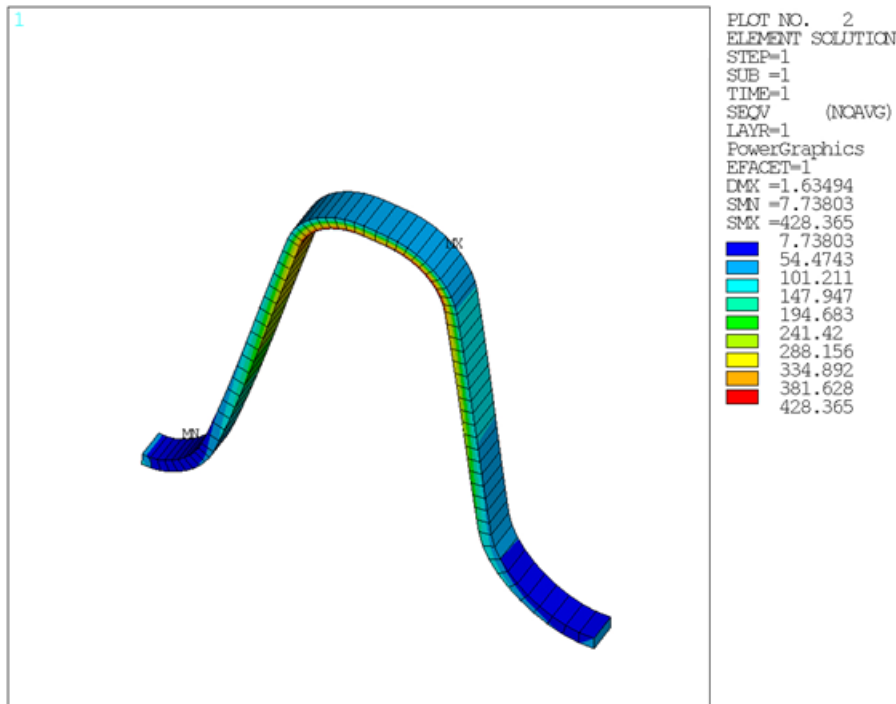
**Figure 29.16: Layered Thermal - homogeneous Structural Results****Figure 29.17: Layered Thermal - Layered Structural Results**

Figure 29.18: Layer 1 Equivalent Stresses (p. 458) shows the equivalent stresses in layer 1. The figure shows that stresses do not peak near the bonded region for layer 1 as might be expected. This underscores the need to analyze the solution layer by layer rather than element by element. Consider changing the ring shape, material, number of layers, or layer orientations to shift the peak stresses to acceptable levels.

When the equivalent stresses in layer 2, 3, and 4 are plotted, the location of peak stresses noticeably shifts. This underscores the need to study each layer carefully and refrain from drawing immediate

conclusions about other layers. For example, peak stresses in layer 4 shift to the bonded region, which could not have been predicted from the layer 1 solution alone.

**Figure 29.18: Layer 1 Equivalent Stresses**

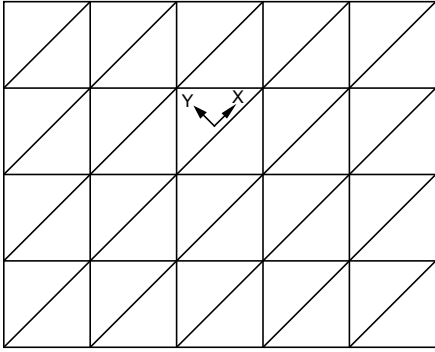
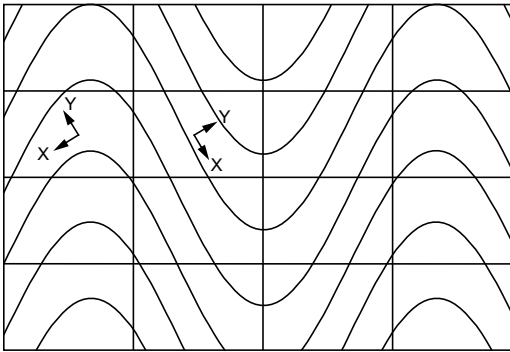


## 29.8. Recommendations

To perform a similar type of analysis, consider the following hints and recommendations:

- Consider refining the mesh near bonded regions of the mesh, as well as near high curvature regions. This recommendation is based on the observed peak stress regions of all the layers.
- By default all layer information is written to the results file. For large meshes it would be wise to select the proper KEYOPT(8) setting to minimize storage requirements with the layered option for [SOLID279](#) or [SOLID186](#) elements. The downside of reducing the file size is that it will not be possible to postprocess the individual layers. You will need to decide what is appropriate for your analysis.
- For a mesh that has not been swept, it is difficult to see if the element coordinate system z axis is normal to the IJKL face of the layered solid [SOLID279/SOLID279](#) or [SOLID185/SOLID186](#) element. Consider using the **EORIENT** command to accomplish this. This is emphasized in the introduction. Also keep the following points in mind when performing a layered analysis:
  - The layers must be parallel to the IJKL face.
  - The element coordinate system z axis must also be normal to the IJKL face (face 1).
- For complex material fibres, it is convenient to align the element coordinate system axis with the fibre direction. In this case, consider defining a unique element coordinate system for each element using a combination of **LOCAL** and **EMODIF,ALL,ESYS** commands as detailed in the introduction. In [Figure 29.19: Single Element Coordinate System](#) (p. 459) below, only one **LOCAL** command is required. In [Figure 29.20: Multiple Element Coordinate Systems](#) (p. 459) below, each element must have a distinct element coordinate system, implying multiple **LOCAL** commands.



**Figure 29.19: Single Element Coordinate System****Figure 29.20: Multiple Element Coordinate Systems**

## 29.9. Input Files

The following files were used in this problem:

- `nozzle.dat` -- Input file for the rocket nozzle extension operation simulation.
- `nozzle_cdbfile.cdb` -- Common database file containing the rocket nozzle extension model information (called by `nozzle.dat`)

The files are available in the `td-29` folder. See [Obtaining the Input Files \(p. xxxv\)](#) for more information.



---

## Chapter 30: Acoustic Analysis of a Small Speaker System

---

This example problem demonstrates the use of acoustic elements coupled with structural elements to examine the performance of a speaker assembly.

The following features and capabilities are highlighted:

- Structural-acoustic coupling using [fluid-structure interaction \(FSI\)](#) in 3-D
- Use of a symmetric FSI algorithm
- Use of perfectly matched layers (PML) to absorb outgoing acoustic waves
- Postprocessing sound pressure level (SPL) and velocity
- Far-field postprocessing of acoustic field
- User-defined symmetric expansion options

For more information about acoustic fluid-structure interaction, see [Accounting for Acoustic Fluid-Structure Interaction \(FSI\)](#) in the *Acoustic Analysis Guide*.

Topics related to this example problem follow:

- [30.1. Introduction](#)
- [30.2. Problem Description](#)
- [30.3. Modeling](#)
- [30.4. Material Properties](#)
- [30.5. Boundary Conditions and Loading](#)
- [30.6. Analysis and Solution Controls](#)
- [30.7. Results and Discussion](#)
- [30.8. Recommendations](#)
- [30.9. Input Files](#)

### 30.1. Introduction

A dynamic loudspeaker includes a speaker connected to a frame via a suspension system. The speaker has a cone and voice coils that are excited by a driver magnet. The suspension system includes the surround, which holds the cone centered, and the spider, which provides a restoring mechanism of the cone to the frame.

When designing a speaker, material selection (material properties), component thickness, and other parameters can be changed to alter performance characteristics over a frequency range. Ideally, constant performance is obtained in the operating frequency range (bass, midrange, and treble).

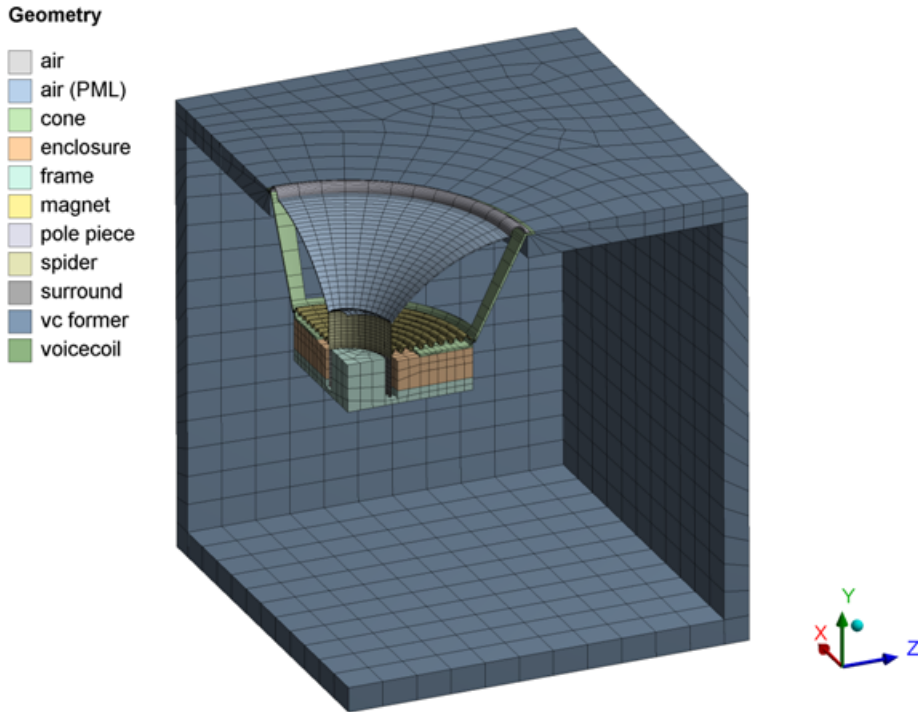
The movement of the structure (speaker) imparts energy into a fluid (air) and generates acoustic waves. The impedance of the fluid influences the structural behavior in turn. To properly characterize the acoustic response, a coupled structural-acoustic analysis is performed, wherein structural and acoustic equations are solved simultaneously.

The magnetic force characterization and the air inside the enclosure are ignored. Attention is focused on the acoustic response of the system.

### 30.2. Problem Description

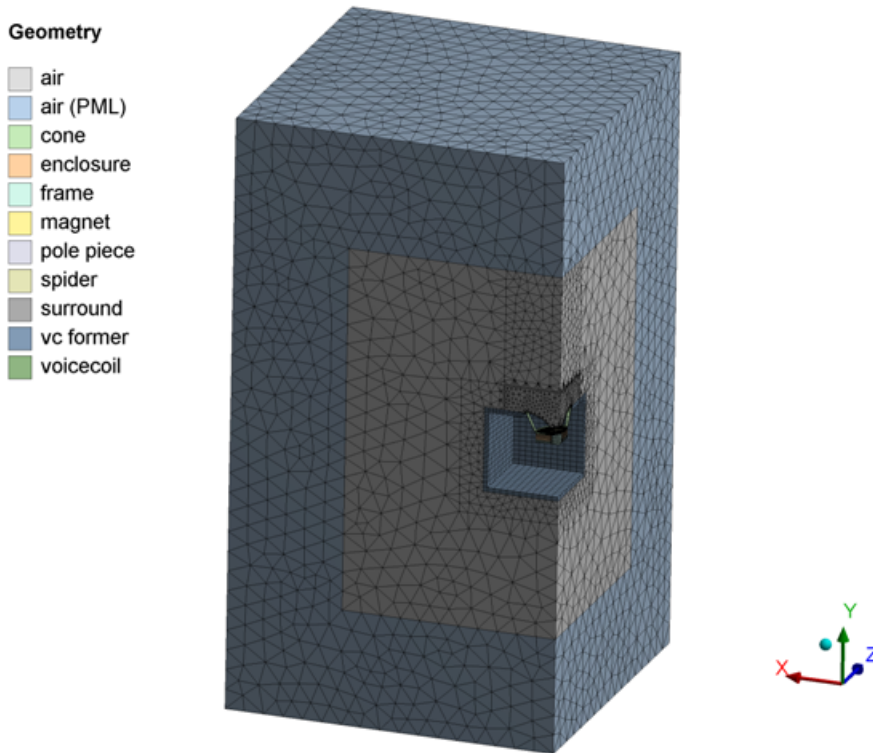
The following figure shows the structural components of the speaker:

**Figure 30.1: 3-D Model of the Speaker Assembly**



Components include the cone, surround, spider, frame, magnet, and voice coil. A 1/4 symmetry model is used. The air inside the cabinet is ignored.

As shown in the following figure, the acoustic fluid elements are outside of the cabinet:

**Figure 30.2: Acoustic Fluid Elements**

Perfectly matched layer (PML) elements are used on the outermost region to absorb outgoing acoustic waves.

### 30.3. Modeling

The 1/4 3-D model of the structure is created in ANSYS DesignModeler and meshed with **SOLID186** elements. Flexible components such as the surround, cone, and spider are meshed with finer elements because they are of high importance. Stiffer components such as the frame, magnet, pole piece, and enclosure are meshed with coarser elements.

The acoustic elements used are **FLUID220** and **FLUID221**. Both unsymmetric and symmetric formulations are available for fluid-structure interaction (controlled via **KEYOPT(2)**). The symmetric algorithm (**KEYOPT(2) = 3**) is used because it requires less memory and computational time. (If using the symmetric formulation, *all* acoustic fluid elements must have this setting, regardless of whether the elements are adjacent to structural elements.)

The PML region is specified using acoustic elements with **KEYOPT(4) = 1**. Approximately six elements are included in the PML region. The region between the PML region and the structure, or the “buffer” region, also includes approximately six elements. A minimum of four elements should exist in both the buffer region and the PML region. Using more elements improves accuracy (at an increase in computational cost).

Vibroacoustic problems should use shared nodes between the structural and acoustic domains. Avoid using dissimilar meshes at the interface and contact elements.

The force applied on the voice coil is modeled using **SURF154** surface effect elements. A tangential load per unit area in the element’s coordinate system is applied (**KEYOPT(2) = 1**).

## 30.4. Material Properties

The material properties for each component are as follows:

Description	Density	Young's Modulus	Poisson's Ratio	Damping Ratio	Speed of Sound
Air	1.2	--	--	--	343
Cone	1350	3.20+09	0.3	0.01	--
Enclosure	800	9.00+09	0.35	0.1	--
Frame	8000	2.10+11	0.3	0.005	--
Magnet	7800	1.50+11	0.3	0.001	--
Pole Piece	7850	2.00+11	0.3	0.001	--
Spider	650	7.00+08	0.3	0.1	--
Surround	1100	2.70+06	0.49	0.1	--
VC Former	2700	7.00+10	0.33	0.005	--
Voice Coil	8900	1.10+11	0.34	0.005	--

## 30.5. Boundary Conditions and Loading

Structural and acoustic boundary conditions and loads are applied:

[30.5.1. Structural Loads and Boundary Conditions](#)

[30.5.2. Acoustic Loads and Boundary Conditions](#)

### 30.5.1. Structural Loads and Boundary Conditions

A unit force is applied on the voice coil using surface effect element [SURF154](#). A resulting load per unit area of 2425.21892 is applied on face 2. The value is constant with respect to frequency. Structural symmetry boundary conditions are applied to the  $x = 0$  and  $z = 0$  locations. The cabinet is assumed to be free to move and is unconstrained.

### 30.5.2. Acoustic Loads and Boundary Conditions

The outermost PML faces are constrained, with the pressure degree of freedom set to 0 to specify the truncated domain location. The naturally occurring boundary condition in acoustics is a symmetry boundary condition, so no specification on the acoustic elements is necessary to designate a symmetry plane.

In the following example input, an FSI flag is applied to predefined nodal component "FSI" to designate acoustic faces that have fluid-structure interaction calculations activated:

```
d,PML,pres,0
esel,s,ename,,220,221
sf,FSI,fsi
allsel,all
cmset,all
```

The acoustic elements must be selected first, as the FSI flag is applied only to acoustic element faces, and not structural element faces that share the same nodes.

## 30.6. Analysis and Solution Controls

A harmonic analysis is performed from 700 to 1000 Hz in 20 Hz increments. The structural load is step-applied, which means that it is a constant unit force value across the range of frequency (unit force for 1/4 symmetry model).

The sparse direct solver was chosen for this model. Vibroacoustic harmonic problems can also be efficiently solved with the Quasi-Minimal Residual (QMR) iterative solver.

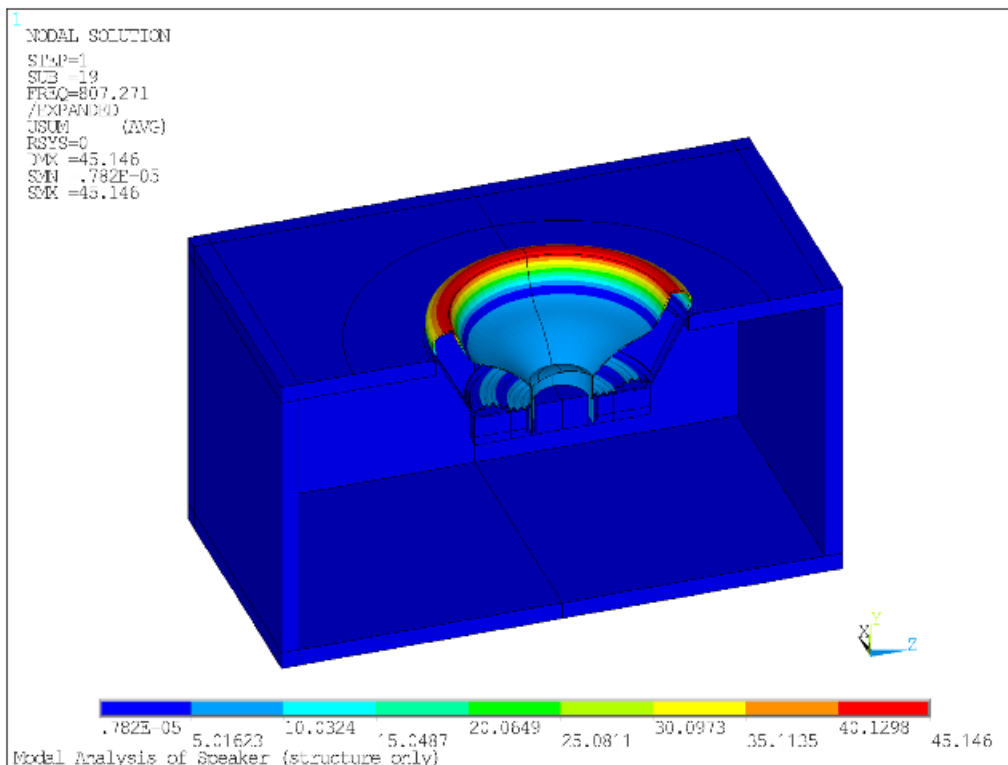
## 30.7. Results and Discussion

The following topics related to the acoustic analysis results are available:

### 30.7.1. Structural-Only Modes

A modal analysis of only the structure (acoustic fluid elements and element types deleted) is performed. The following figure shows a mode within the 700-1000 Hz range (807 Hz):

**Figure 30.3: Modal Analysis at 807 Hz**

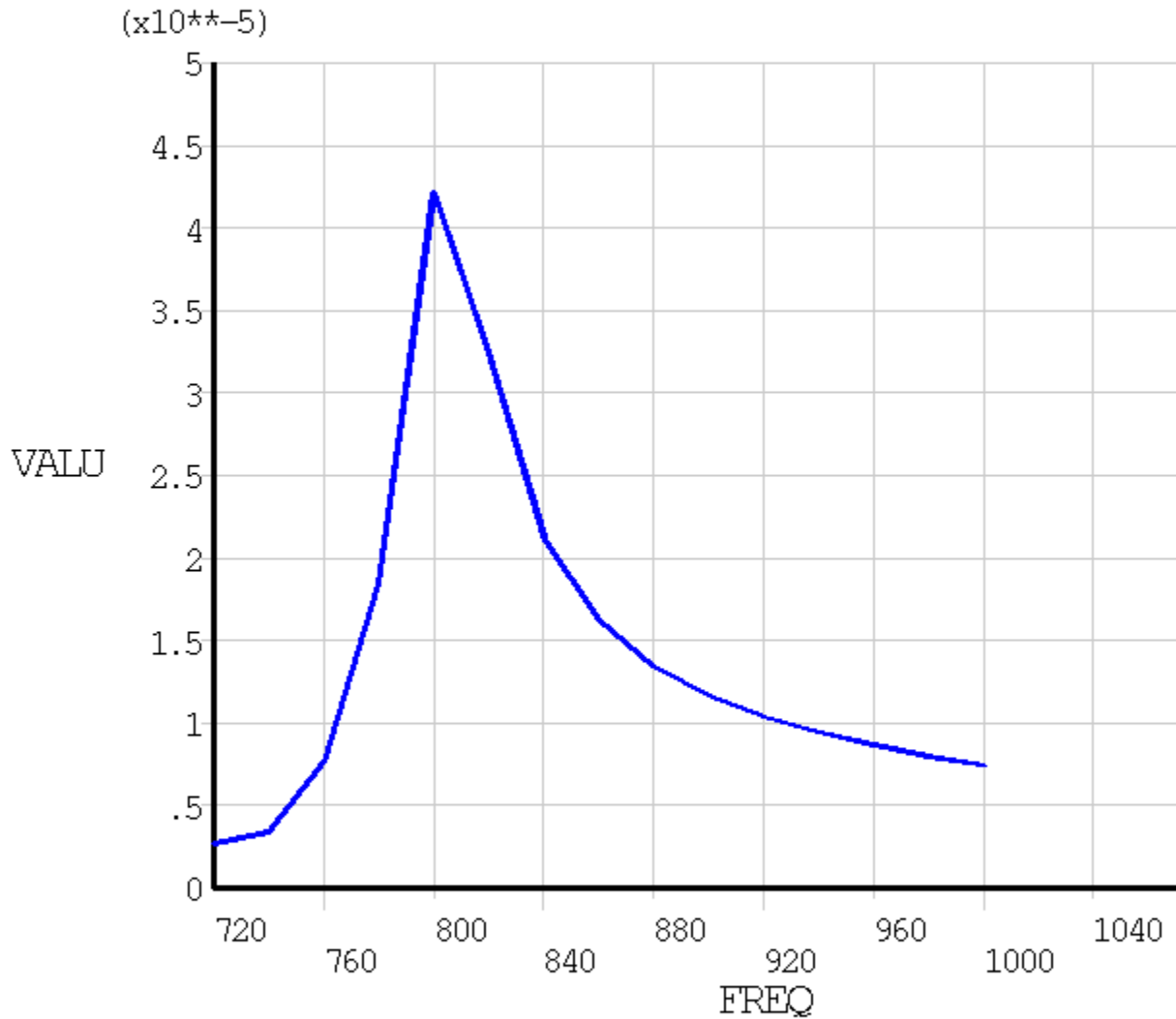


### 30.7.2. Plotting Sound Pressure Levels

The frequency response plot of displacement at the center of the dust cap is shown in the following figure:

**Figure 30.4: Displacement Frequency Response Plot**

POST26  
 AMPLITUDE



About XY Plane at 1 m @ 860 Hz

Note the peak response at 800 Hz, which coincides with the structural mode discussed in [Structural-Only Modes](#) (p. 465). Because the frequency spacing is 20 Hz, additional frequency points would need to be solved to obtain the actual peak in the harmonic analysis.

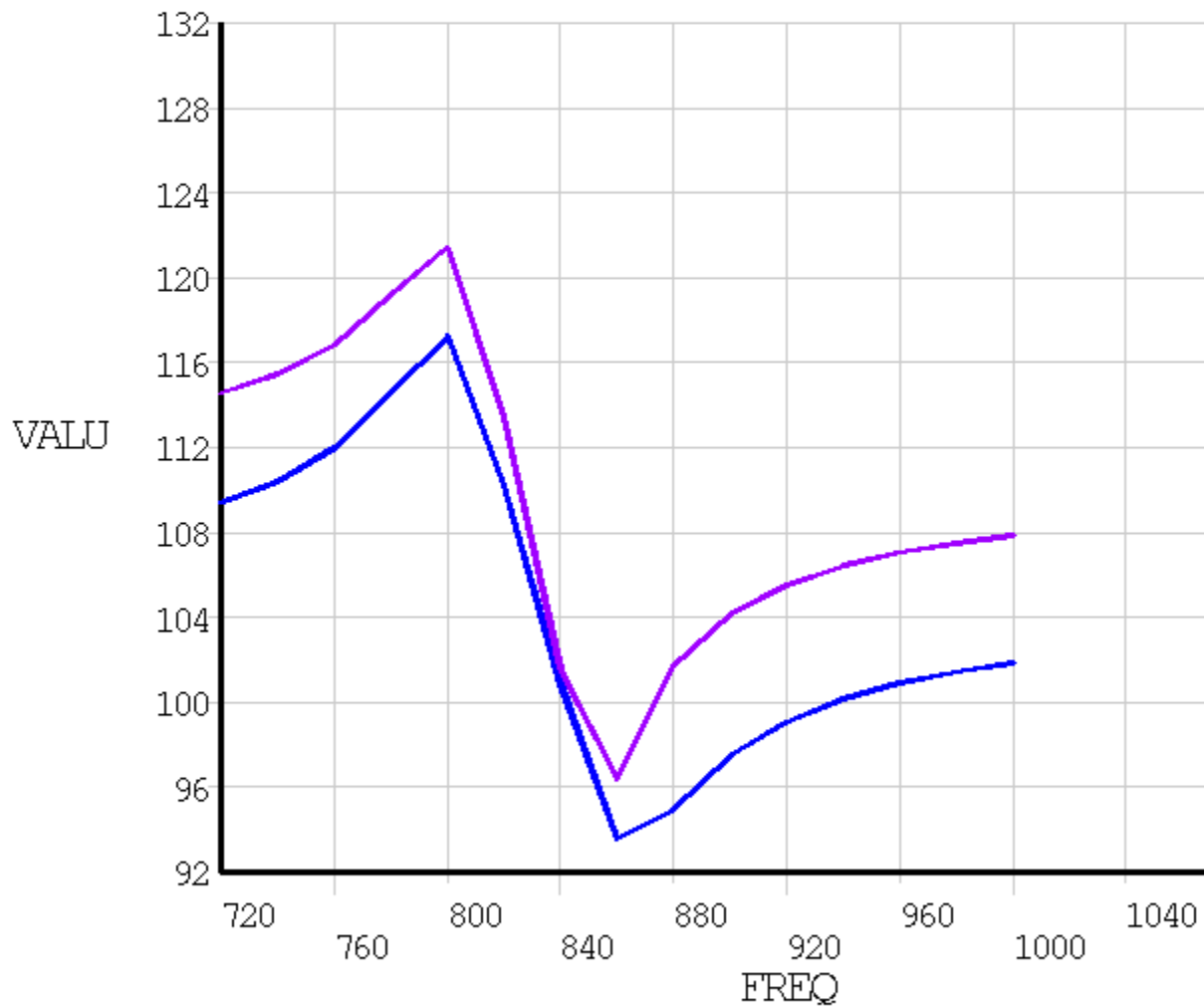
The SPL at approximately 50 mm from the speaker at 0° and 30° off-axis are shown this figure:



**Figure 30.5: SPL at 50 mm**

POST26

AMPLITUDE



### About XY Plane at 1 m @ 860 Hz

The acoustic response shows a maximum value at the structural resonance; however, the SPL drops suddenly at 860 Hz.

The reference pressure for SPL calculations is taken from the real constant value, which defaults to 20  $\mu\text{Pa}$ . SPL in the time-history postprocessor (**/POST26**) can be plotted (**NSOL**).

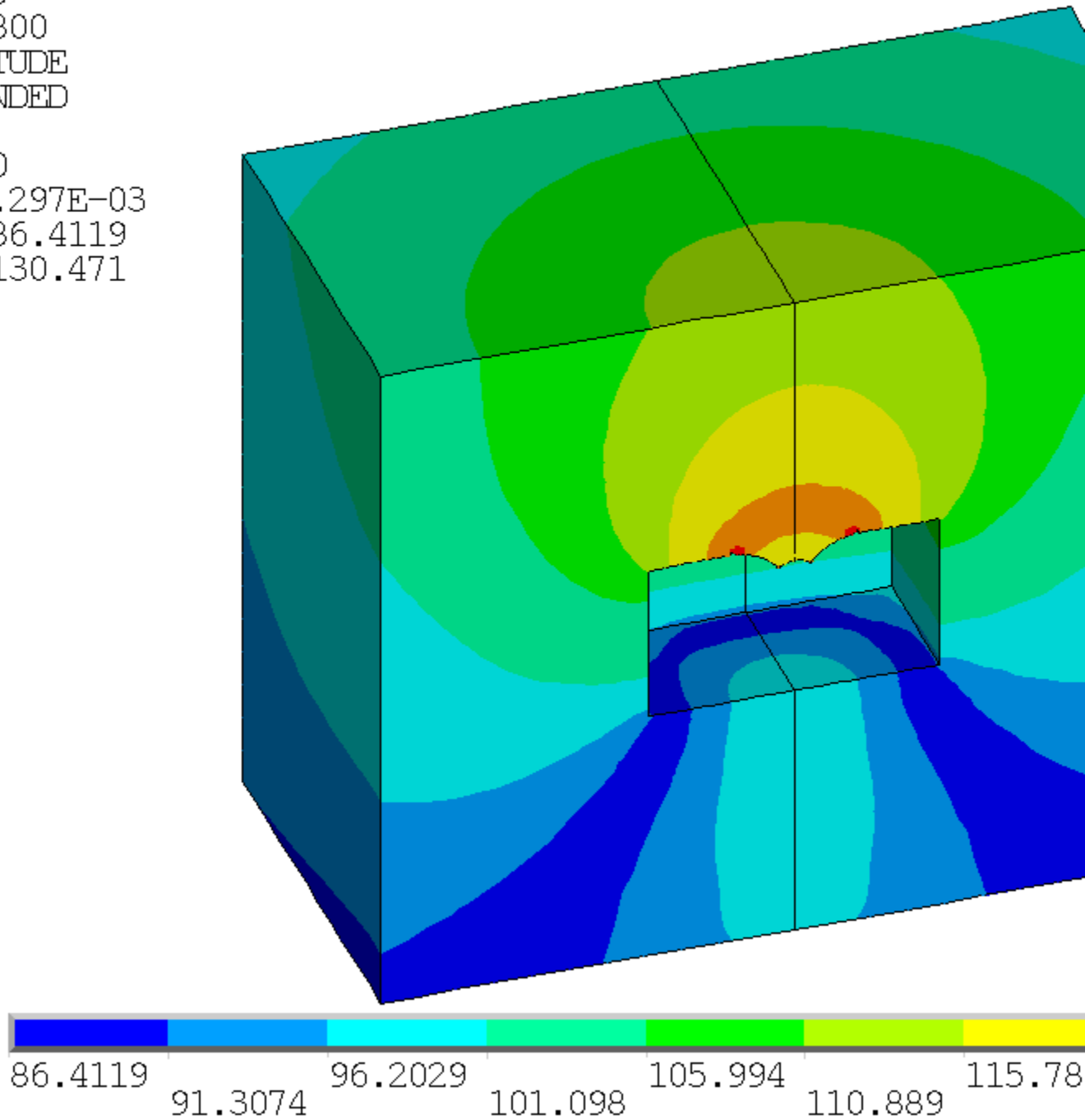
SPL can be listed (**PRNSOL** command) or plotted (**PLNSOL** command) in the general postprocessor.

The following figure shows a plot of SPL at 800 Hz:

**Figure 30.6: SPL at 800 Hz**

NODAL SOLUTION

```
STEP=1  
SUB =5  
FREQ=800  
AMPLITUDE  
/EXPANDED  
SPL  
RSYS=0  
DMX =.297E-03  
SMN =86.4119  
SMX =130.471
```



SPL @ 800 Hz

This figure shows the SPL values at 860 Hz:

**Figure 30.7: SPL at 860 Hz**

NODAL SOLUTION

STEP=1

SUB =8

FREQ=860

AMPLITUDE

/EXPANDED

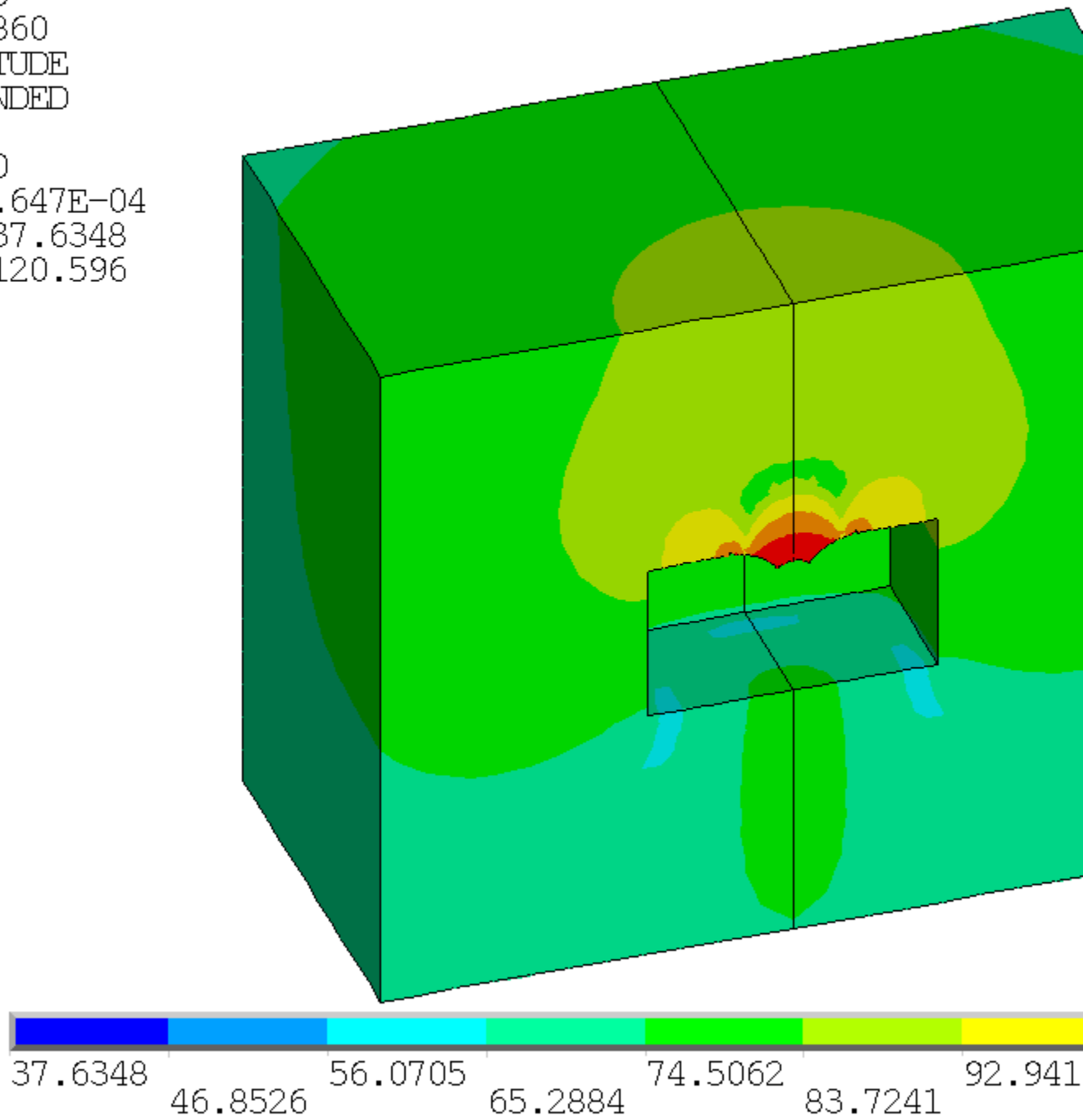
SPL

RSYS=0

DMX =.647E-04

SMN =37.6348

SMX =120.596



SPL & 860 Hz

Displacement of the cone should ideally generate the acoustic waves. [Figure 30.3: Modal Analysis at 807 Hz \(p. 465\)](#) shows that the structural resonance at 807 Hz involves the surround rather than the cone, which explains why the 800 Hz SPL results show larger pressure values near the surround in [Figure 30.6: SPL at 800 Hz \(p. 468\)](#).

The resulting nonuniform frequency response plot shown in [Figure 30.4: Displacement Frequency Response Plot \(p. 466\)](#) indicates that the surround design should be modified or the speaker should not operate at this frequency.

### 30.7.3. Plotting Velocities

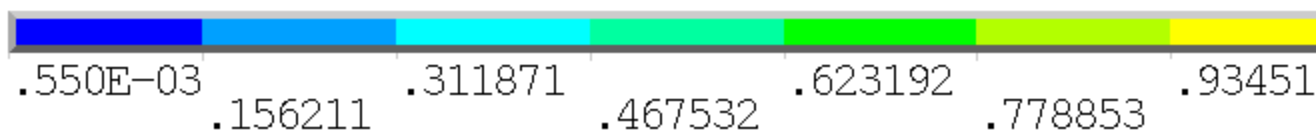
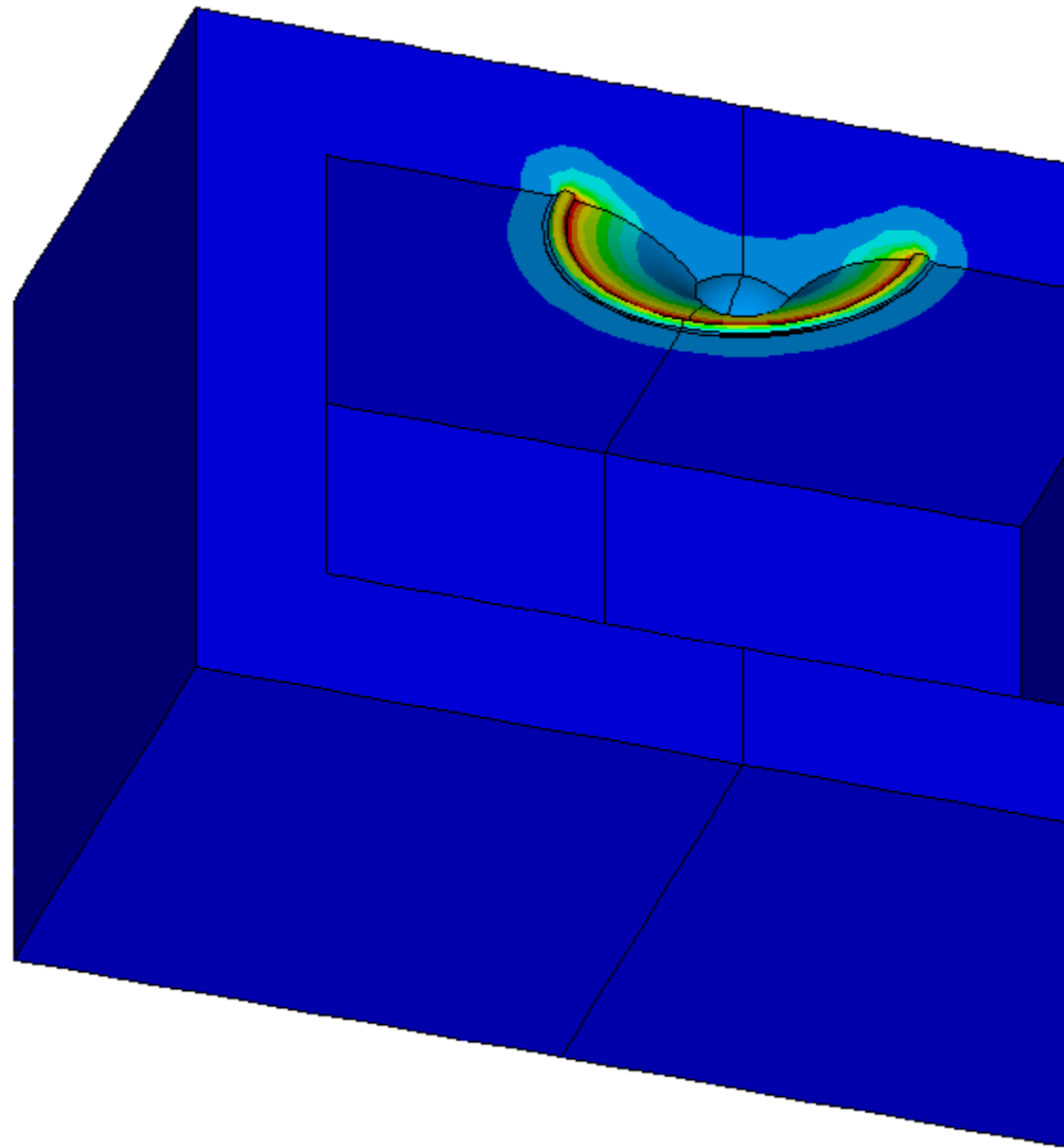
Nodal velocity output is available for acoustic elements in modal and harmonic analyses. The output label item is PG for **PLNSOL**, **PRNSOL**, **PLVECT**, **PLESOL**, and **PRESOL** commands.

In the following figure, the velocity magnitude is displayed as a contour plot, where the bottom of acoustic elements adjacent to the cone are displayed (and only a subset of the fluid domain is shown for the sake of clarity):

**Figure 30.8: Velocity Magnitude Contour Plot**

NODAL SOLUTION

STEP=1  
 SUB =5  
 FREQ=800  
 AMPLITUDE  
 /EXPANDED  
 PGSUM (AVG)  
 RSYS=0  
 DMX =.297E-03  
 SMN =.550E-03  
 SMX =1.40149



Velocities @ 800 Hz

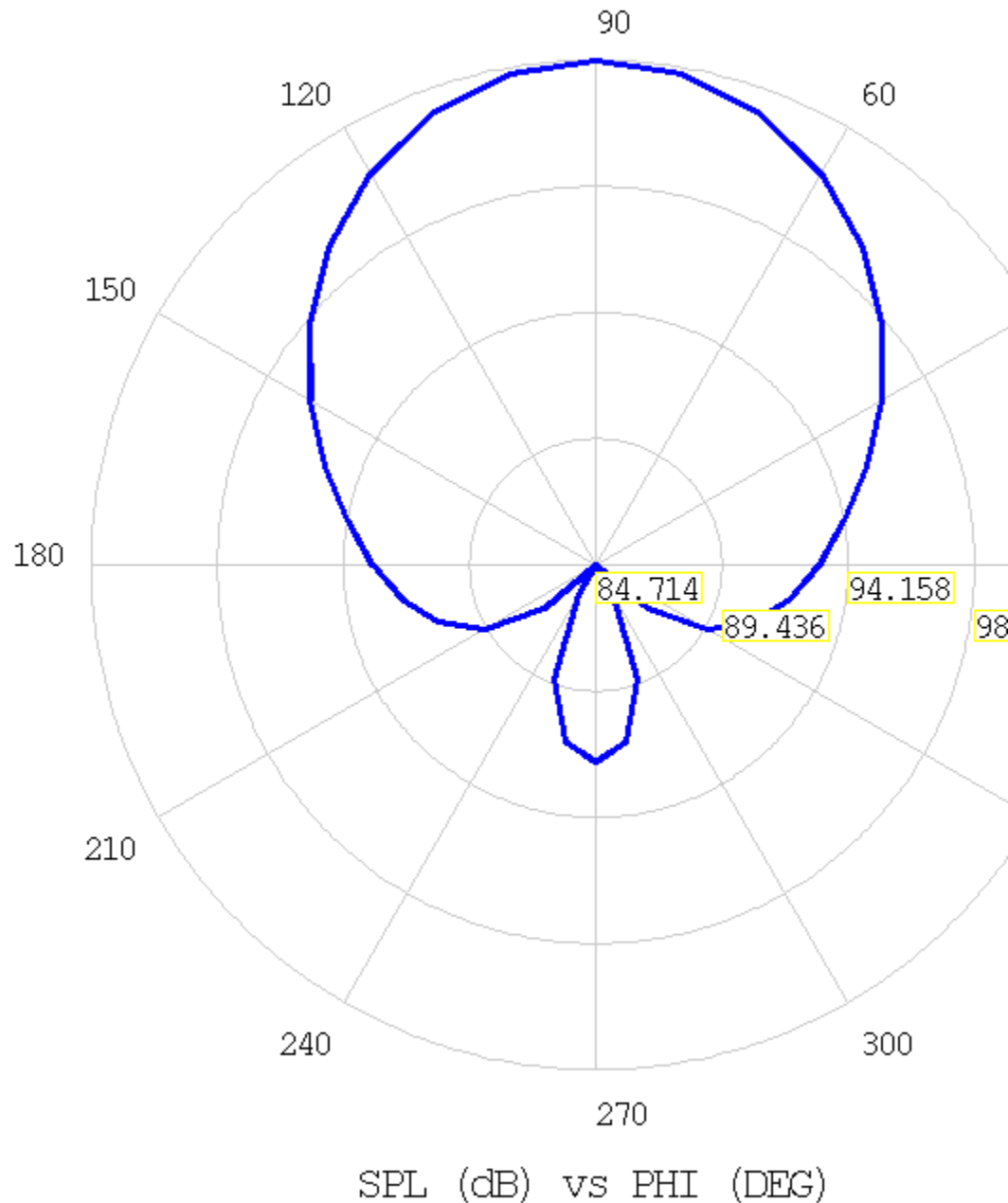
### 30.7.4. Plotting Far-Field Results

Near-field (**PLNEAR**) and far-field (**PLFAR**) pressure results can be plotted. Because only a quarter of the speaker was modeled, the **HFSYM** command defines symmetry planes to allow near-field or far-field plots of the full model.

The following figure shows a polar plot (PLFAR,PRES,SPLP) of SPL at 800 Hz:

**Figure 30.9: SPL Polar Plot at 800 Hz**

FAR-FIELD SOUND PRESSURE LEVEL AT R = 1



About XY Plane at 1 m @ 800 Hz

The plot of directivity can be used to determine how focused the acoustic signal is and to evaluate speaker performance. Directivity influences how on-axis or off-axis listeners hear the sound generated by the speaker.

## 30.8. Recommendations

To perform a similar type of acoustic analysis, consider the following hints and recommendations:

[30.8.1. Harmonic Sweep and Mesh Generation](#)

[30.8.2. GPU Accelerator](#)

### 30.8.1. Harmonic Sweep and Mesh Generation

At least six elements per wavelength should be used with higher-order acoustic elements ([FLUID220](#), [FLUID221](#)). Buffer and PML regions should have more than four elements between the boundaries.

If a large frequency range is solved, the lowest frequency solved has a large wavelength and the highest frequency solved has a small wavelength. To solve for a large frequency range and satisfy the two requirements stated above, it may be necessary to use very large PML and buffer regions (to address low frequency requirements) meshed with very small elements (to satisfy high frequency requirements). This can be computationally expensive.

Because the element size depends on wavelength, acoustic analyses benefit greatly from parametric models where each frequency is solved with a mesh that is optimal for that configuration. Parametric models can be generated using the APDL command language, or they can be generated within ANSYS Workbench using ANSYS DesignModeler and Workbench Mechanical.

### 30.8.2. GPU Accelerator

With supported graphics cards, GPU Accelerator can speed up solutions when used with the sparse direct solver. A run of this example problem is tabulated below with total elapsed time normalized to the baseline case of a single core without GPU Accelerator.

Cores	GPU	Speedup
1	off	1.00
2	off	1.52
4	off	2.12
1	on	2.24
2	on	2.68
4	on	2.99

In this case, use of GPU Accelerator resulted in a solution time 1.76 times faster for two cores using this particular hardware configuration.

## 30.9. Input Files

The following files were used in this problem:

- `speaker.dat` -- Input file for the speaker analysis.
- `speaker.cdb` -- Common database file for the original mesh used in the speaker analysis (called by `speaker.dat`).

The files are available in the `td-30` folder. See [Obtaining the Input Files \(p. xxxv\)](#) for more information.





---

## Chapter 31: Fitting Parameters for a Chaboche Kinematic Hardening Model

---

This example problem demonstrates how to determine material parameters for a third-order [Chaboche](#) kinematic hardening model using the [curve-fitting tool](#).

A method is presented to estimate the initial parameters and obtain a least-squares best fit to the data. The fitted parameters are validated by conducting uniaxial simulations using a single element and comparing the results with the experimental data.

The following features and capabilities are highlighted:

- [Material curve fitting](#)
- [Chaboche nonlinear kinematic hardening model](#)

Topics related to this example problem follow:

- [31.1. Introduction](#)
- [31.2. Modeling](#)
- [31.3. Results and Discussion](#)
- [31.4. Recommendations](#)
- [31.5. References](#)
- [31.6. Input Files](#)

### 31.1. Introduction

The [Chaboche model](#) is a nonlinear kinematic hardening model commonly used to model the plastic deformation of metals. A phenomenon associated with kinematic hardening is *ratcheting*, the progressive accumulation of plastic strain during cyclic loading.

Ratcheting is observed, for example, in high-pressure piping systems in nuclear power plants subject to seismic loading. A primary concern is that the *accumulated* plastic strain could lead to catastrophic failure, even though the loading amplitude from individual cycles is not expected to cause failure.

### 31.2. Modeling

Commonly used plasticity models for ratcheting are based on the von Mises yield criterion and a kinematic hardening rule. The von Mises yield criterion for kinematic hardening is:

$$f(\bar{\sigma}, \sigma_y) = \sqrt{\frac{3}{2} \left( \bar{\sigma} : \bar{\sigma} - \frac{1}{3} \text{tr}(\bar{\sigma})^2 \right)} - \sigma_y = 0 \quad (31.1)$$

where  $\sigma_y$  is the isotropic hardening yield stress, and  $\bar{\sigma}$  is the center of the yield surface which is a function of the stress tensor  $\sigma$  and back stress tensor  $\alpha$ :

$$\bar{\sigma} = \sigma - \alpha$$

The back stress tensor results in a shifting of the yield surface in stress space. A bias in this shift over repeated loading causes the progressive accumulation of plastic strain ([ratcheting \(p. 475\)](#)).

Experimental data and the [curve-fitting tool](#) are used to determine a set of material parameters for the Chaboche kinematic hardening model. A third-order Chaboche kinematic hardening model is used, as it provides sufficient variation to calibrate the nonlinear behavior of the material and can account for ratcheting behavior. More parameters can be used but, for the data used in this problem, a third order is sufficient.

The following related topics are available:

[31.2.1. Chaboche Nonlinear Kinematic Hardening Model](#)

[31.2.2. Determining Material Parameters](#)

### 31.2.1. Chaboche Nonlinear Kinematic Hardening Model

Chaboche [1][2] proposed the decomposed kinematic hardening model, expressed as:

$$\alpha = \sum_{i=1}^n \alpha_i \tag{31.2}$$

$$\dot{\alpha}_i = \frac{2}{3} C_i \dot{\epsilon}^{pl} - \gamma_i \dot{\epsilon}^{pl} \alpha \tag{31.3}$$

where:

*n* = number of back stress components

$\dot{\epsilon}^{pl}$  = magnitude of plastic strain rate

$\alpha$  = back stress

$\dot{\alpha}_i$  = *i*<sup>th</sup> component of back stress rate

$\dot{\epsilon}^{pl}$  = plastic strain rate

*C<sub>i</sub>* and  $\gamma_i$  are material parameters

Each of the back stress terms of the Chaboche model have the form of an Armstrong-Frederick rule, where the parameters *C<sub>i</sub>* represent a plastic modulus and  $\gamma_i$  serve as the parameters for history dependence. For accurate ratcheting predictions, specify at least three components [3].

For a stable hysteresis of strain-controlled cyclic loading, the solution for the back stress in the uniaxial direction is:

$$\alpha_i = \frac{C_i}{\gamma_i} \left( 1 - 2 \exp[-\gamma_i (\epsilon_x^{pl} - (-\epsilon_L^{pl}))] \right), \quad i=1,2 \tag{31.4}$$

$$\alpha_3 = C_3 \epsilon_x^{pl} \tag{31.5}$$

where:

$\epsilon_x^{pl}$  = plastic strain in the uniaxial direction

$\epsilon_L^{pl}$  = strain limit of the hysteresis loop

The uniaxial yield stress is the sum of the initial yield stress and the back stress component in the uniaxial direction, expressed as:

$$\sigma_x = \sigma_0 + \sum_{i=1}^n \alpha_i \quad (31.6)$$

Using Equation 31.4 (p. 476) and Equation 31.5 (p. 476) for plastic strains at or near the strain limit  $\varepsilon_L^{pl}$ , Equation 31.6 (p. 477) for a third-order Chaboche model becomes:

$$\frac{C_1}{\gamma_1} + \frac{C_2}{\gamma_2} + \sigma_0 = \sigma_x - \frac{C_3}{2} (\varepsilon_x^{pl} - (-\varepsilon_L^{pl})) \quad (31.7)$$

### 31.2.2. Determining Material Parameters

The model requires six material parameters:  $C_1$ ,  $\gamma_1$ ,  $C_2$ ,  $\gamma_2$ ,  $C_3$ , and  $\gamma_3$  as well as the initial yield stress,  $\sigma_0$ .

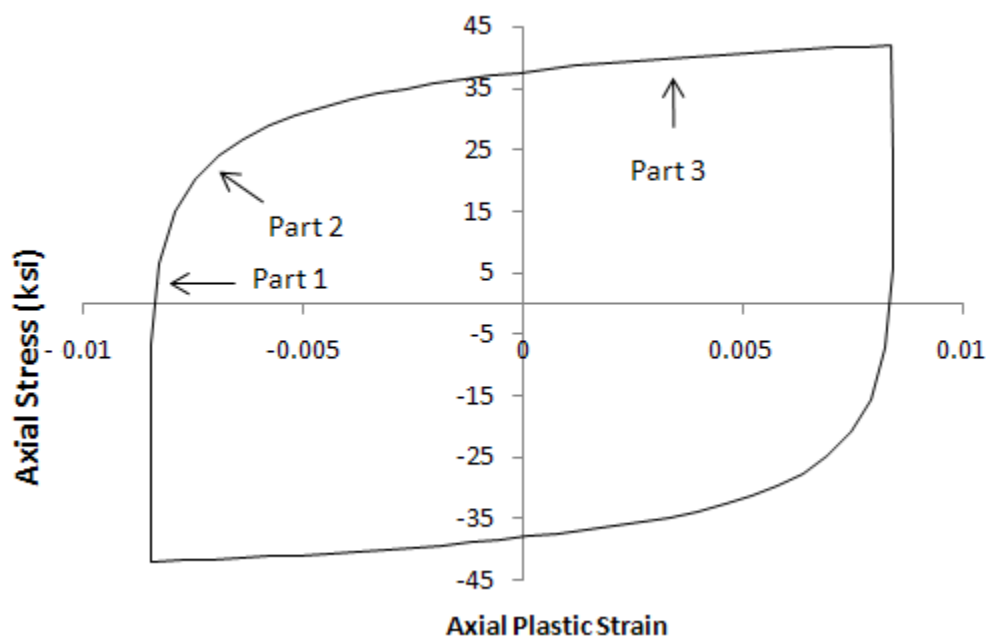
The parameters must be determined so that the model closely matches the material behavior. One method for doing so is to obtain data from stabilized strain-controlled and stress-controlled ratcheting experiments and use that data with the [curve-fitting tool](#) to determine material parameters that minimize the error between the data and the model predictions.

The nonlinear curve-fitting method used by the curve-fitting tool is an iterative process and requires initial values for each of the material parameters. The success and quality of the fit depends on how far the initial values are from the values that give a good fit. A procedure is developed using stabilized hysteresis stress-strain data to determine a good estimate for the initial parameters.

Stabilized hysteresis stress-strain data is obtained by cycling a specimen under strain-controlled loading with symmetric tension-compression amplitude. A cyclically stabilized hysteresis response is achieved when a cycle of stress-strain response remains unchanged through subsequent cycles.

The following figure shows a typical stable strain-controlled hysteresis curve:

**Figure 31.1: Stable Hysteresis Strain-Controlled Data**



Three distinct regions are noted. Part 1 is the initial onset of yielding, Part 2 is the knee of the hysteresis curve, and Part 3 is the constant modulus segment.

For fitting purposes, the individual components of back stress for the model ( $\alpha_1$ ,  $\alpha_2$ , and  $\alpha_3$ ) are chosen to represent the three regions of the strain-controlled stable hysteresis loop. In each region, the corresponding  $C_i$  is chosen to approximately match the plastic modulus. The  $\gamma_i$  parameters are chosen to accommodate the history dependence defined by Equation 31.4 (p. 476) and the relationship defined by Equation 31.7 (p. 477).

Using the described heuristic method, the initial material parameters can be estimated as follows:

1.  $\sigma_0$  is the initial yield stress of the material.
2.  $C_1$  is the slope in Part 1 of the stress-strain curve at the transition from elastic to plastic deformation. This value is approximately the plastic modulus at yielding.
3. Using Equation 31.4 (p. 476),  $\gamma_1$  should be large enough that the exponential term quickly diminishes so that  $\alpha_1$  is approximately constant outside of Part 1.
4.  $C_2$  is chosen as a slope from Part 2.
5.  $\gamma_2$  is calculated from the chosen  $C_2$  and the ratio  $C_2 / \gamma_2$  that satisfies Equation 31.7 (p. 477).
6.  $C_3$  is the slope of the stress-strain curve in Part 3.
7.  $\gamma_3$  is not included in Equation 31.4 (p. 476) through Equation 31.7 (p. 477) and is assigned a small positive value.

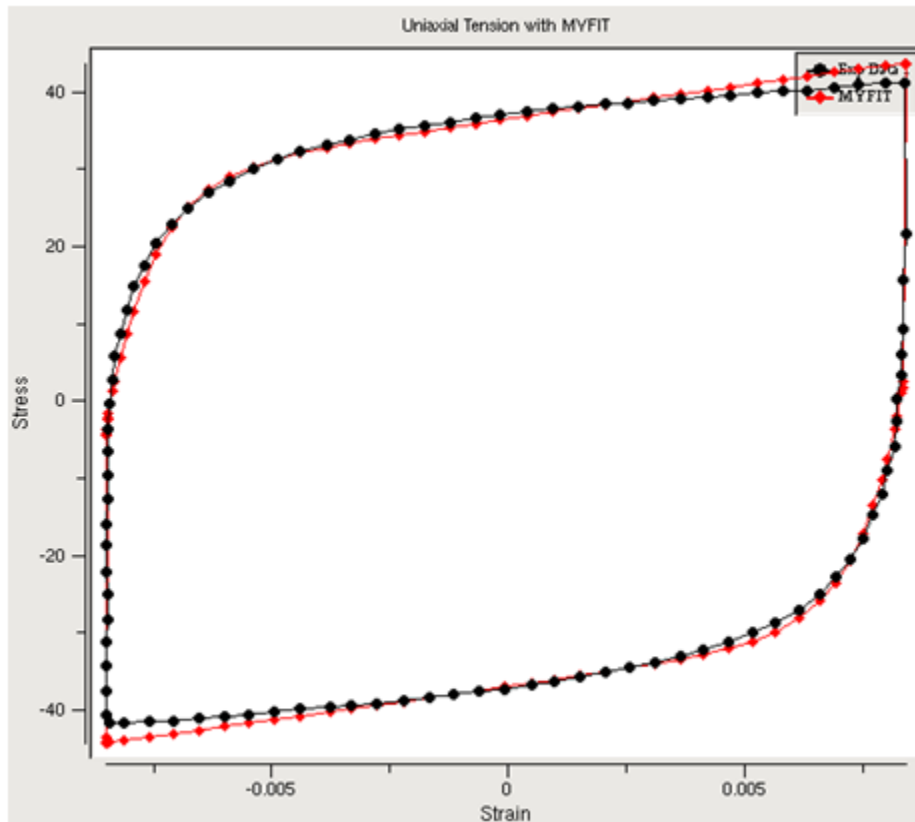
The procedure was developed from a trial-and-error method used to fit the material parameters [4] and usually gives a set of initial parameters that allows the curve-fitting tool to obtain a good fit.

The initial yield stress of the material is generally known, and in this problem it is fixed and does not affect the error minimization performed by the curve-fitting tool.

$\gamma_3$  is chosen as a small positive value because it does not enter into the closed-form equations, and experience indicates that this is generally a good choice. While the fitting procedure iterates to a value of  $\gamma_3$  that best fits the data, this value is often difficult to estimate based on stabilized hysteresis strain-controlled data. The value of this parameter affects the amount of ratcheting in each cycle of a stress-controlled experiment and is best determined using that data.

Although the procedure for estimating the initial material parameters was developed for stabilized hysteresis strain-controlled data, it can be applied to a single cycle of stress-controlled data; however, the quality of the resulting fit should be checked carefully.

The curve-fitting tool provides a comparison of the data used for fitting and the model's prediction. It is good practice, however, to compare the experimental data with a simulation of the entire experimental load history to validate the fitted parameters, as shown in this figure:

**Figure 31.2: Plot Comparing Curve-Fitting Tool Results**

### 31.3. Results and Discussion

Curve fitting is performed for data from a strain-controlled stable hysteresis loop, as well as for data from a stress-controlled loop, and then for the combined set of data. The experimental data is taken from Bari and Hassan [4]. The initial parameters are estimated as described in [Determining Material Parameters](#) (p. 477).

To verify that the parameters from the curve-fitting tool give a good match to experimental data over the entire loading history, uniaxial single-element tension-compression simulations are performed.

The following related topics are available:

- [31.3.1. Uniaxial Strain-Controlled Experiment](#)
- [31.3.2. Uniaxial Stress-Controlled Experiment](#)
- [31.3.3. Fitting to Multiple Data Sets](#)
- [31.3.4. Fitting the Ratcheting Strain](#)

#### 31.3.1. Uniaxial Strain-Controlled Experiment

The curve-fitting and simulation portions of the uniaxial strain-controlled experiment are described here.

##### 31.3.1.1. Curve Fitting

The initial parameters are determined (p. 477) using the experimental strain-controlled data (p. 477).

Because the initial yield stress for the material is well known, the value is fixed.

The value for  $\gamma_3$  does not significantly affect the model predictions for the stable hysteresis loop, and it is best fit to cyclic stress ratcheting data. In this problem, the value is fixed because allowing it to vary in the fitting procedure produced a poor set of material coefficients.

The following table shows the initial parameters and those determined via the curve-fitting tool:

**Table 31.1: Initial and Fitted Parameters for the Strain-Controlled Experiment**

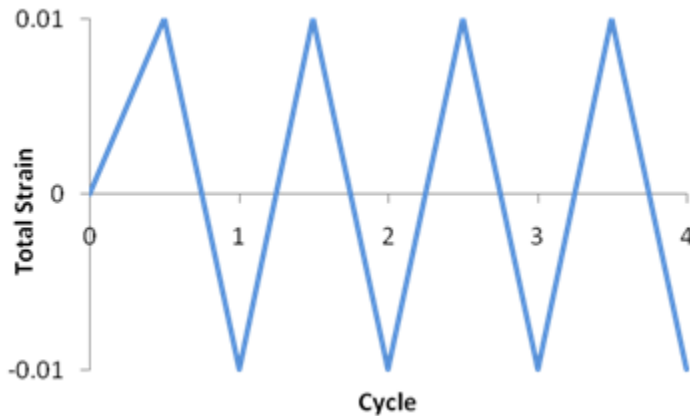
Parameter	Initial Parameters	Fitted Parameters
$C_1$ (ksi)	60000	5174000
$\gamma_1$	20000	4607500
$C_2$ (ksi)	13850	17155
$\gamma_2$	996.1	1040
$C_3$ (ksi)	450	895.18
$\gamma_3$	9	9
$\sigma_0$ (ksi)	18.8	18.8

### 31.3.1.2. Simulation

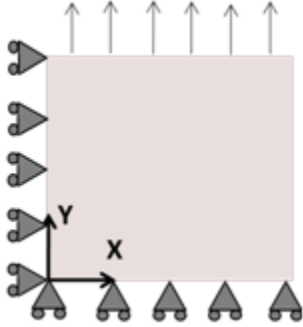
To simulate the loading history over the entire uniaxial strain-controlled experiment, a single SOLID185 element is used with quarter symmetry boundary conditions and uniaxial displacement in the Y direction. Elastic properties are a Young’s modulus of 26300 ksi and a Poisson’s ratio of 0.302. The nodes are given a displacement value to simulate a strain cycle with an amplitude of 0.01.

The following figure shows the loading history for the entire experiment:

**Figure 31.3: Loading History for Strain-Controlled Experiment**



This figure shows a schematic of the model:

**Figure 31.4: Schematic for Single-Element Uniaxial Test**

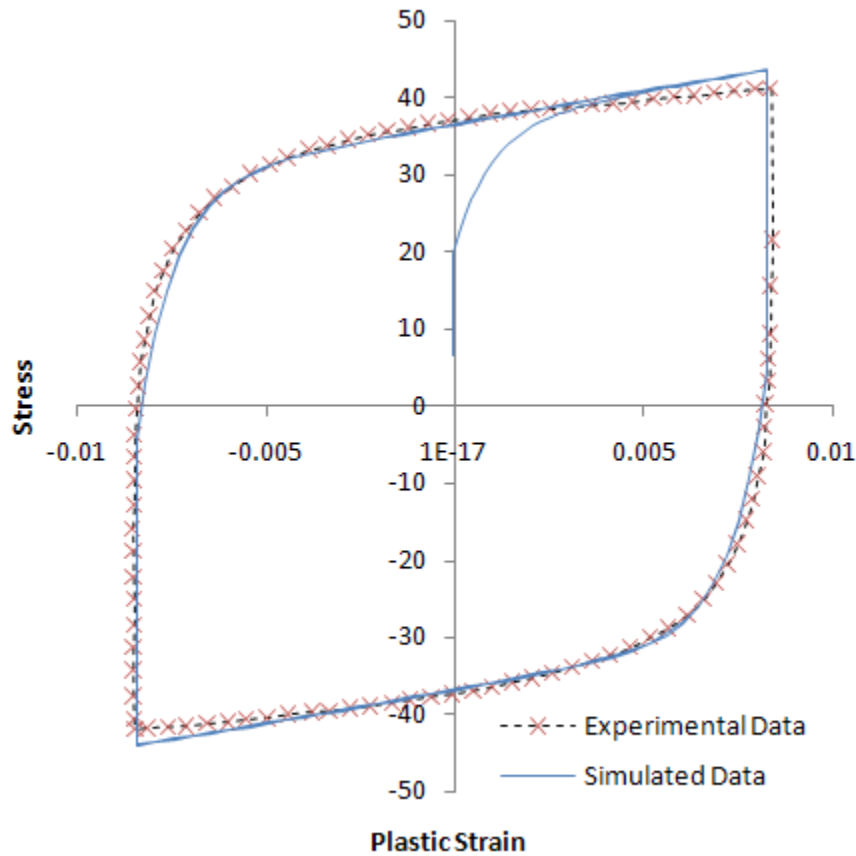
The following table compares the simulated results at the maximum negative plastic strain to the experimental data:

**Table 31.2: Comparison of Strain-Controlled Experimental Data with Simulated Data**

	<b>Simulated</b>	<b>Experimental</b>	<b>Ratio</b>
<b>Maximum Stress (ksi)</b>	43.6	41.1	1.06
<b>Plastic Strain at Maximum Stress</b>	0.00829	0.00837	0.990

Following is a plot of the stress-strain history:

**Figure 31.5: Plot Comparing Strain-Controlled Experimental Data with Simulation Data**



The model predictions indicate that little evolution occurs in the stress-strain plot after the initial cycle and the hysteresis loop has stabilized. If the hysteresis continues to evolve over several loading cycles, the model prediction from the curve-fitting tool will not correspond to the stabilized hysteresis predicted by the model.

To alleviate the inconsistency, try inputting multiple copies of the same experimental data. The curve-fitting algorithm can then minimize the error from the model prediction over multiple cycles.

### 31.3.2. Uniaxial Stress-Controlled Experiment

The curve-fitting and simulation portions of the uniaxial stress-controlled experiment are described here.

#### 31.3.2.1. Curve Fitting

The initial parameters are determined (p. 477) using the stress-controlled experimental data from Bari and Hasan [4]. The following table shows the initial parameters and those determined via the curve-fitting tool:

**Table 31.3: Initial and Fitted Parameters for the Stress-Controlled Experiment**

Parameter	Initial Parameters	Fitted Parameters
$C_1$ (ksi)	100000	29214



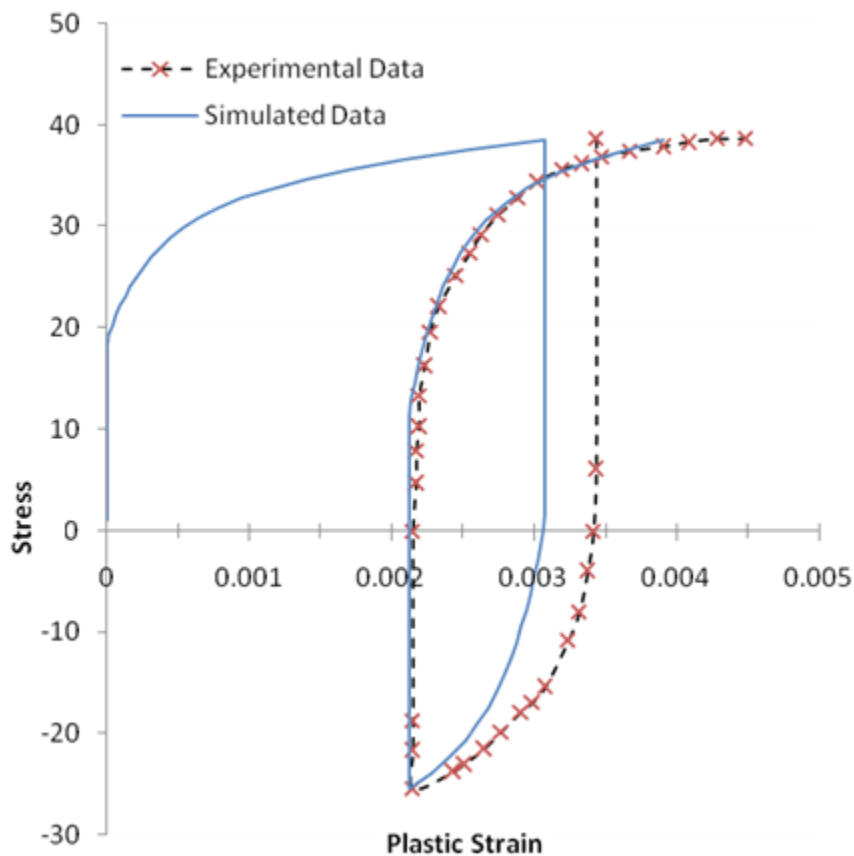
Parameter	Initial Parameters	Fitted Parameters
$\gamma_1$	10000	4608.9
$C_2$ (ksi)	10000	11315
$\gamma_2$	1000	1261.8
$C_3$ (ksi)	1000	1517.8
$\gamma_3$	10	10
$\sigma_0$ (ksi)	18.8	18.8

While the heuristic procedure for determining the initial parameters was developed for stabilized hysteresis strain-controlled data, using the procedure on a single load cycle of stress-controlled data often gives an adequate set of initial parameters. It may be necessary to adjust the initial parameters, however, if a good fit is not evident after comparing the results from the fitted model to the experimental data.

### 31.3.2.2. Simulation

The same finite element model is used as that for the simulation of the strain-controlled experiment. The loading is changed to a uniaxial stress cycle between 38.68 ksi and -25.45 ksi. The results from the single element simulation are compared with the experimental data in the following figure:

**Figure 31.6: Plot Comparing Stress-Controlled Experimental Data with Simulation Data**



### 31.3.3. Fitting to Multiple Data Sets

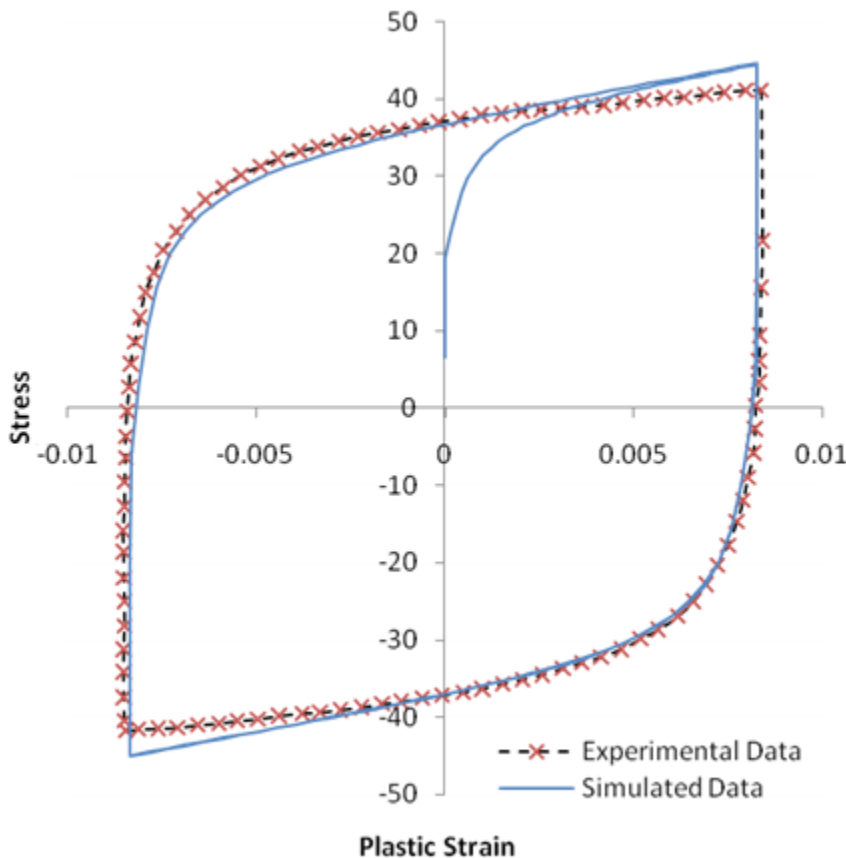
The curve-fitting tool can use more than one data set in the fitting procedure. The stabilized hysteresis data has been used to estimate the initial parameters. The curve-fitting tool then uses both the stabilized hysteresis and stress-controlled experimental data to generate the fitted parameters. The following table shows the initial and fitted parameters:

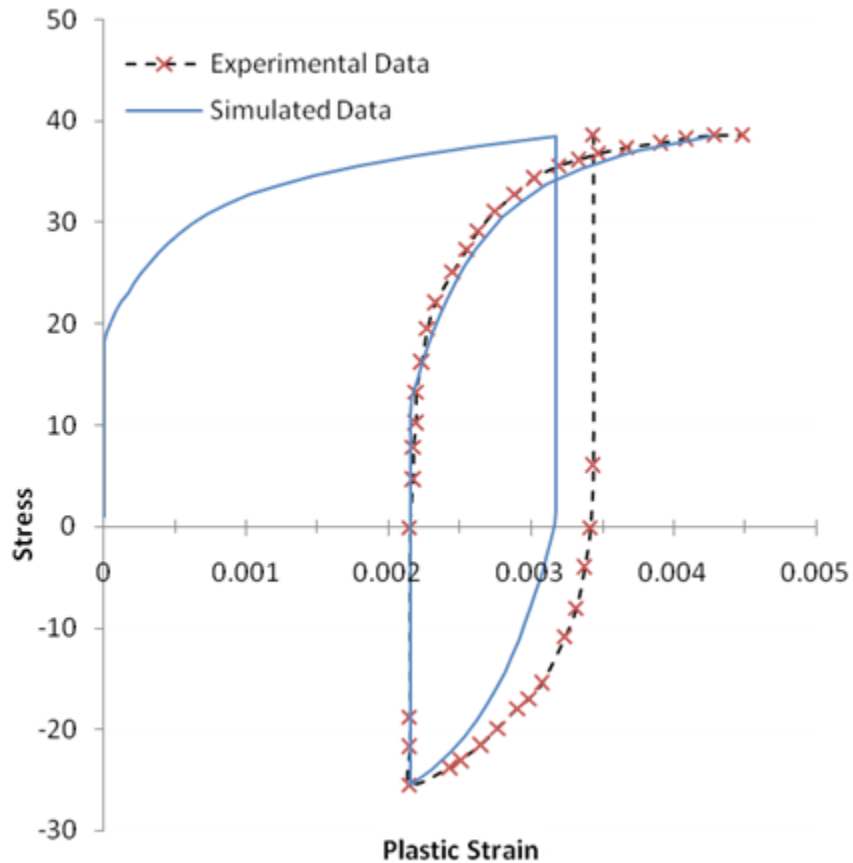
**Table 31.4: Initial and Fitted Parameters for Fit to Both Data Sets**

Parameter	Initial Parameters	Fitted Parameters
$C_1$ (ksi)	60000	26291
$\gamma_1$	20000	2409.8
$C_2$ (ksi)	13850	3781.0
$\gamma_2$	996.1	537.58
$C_3$ (ksi)	450	976.46
$\gamma_3$	9	9
$\sigma_0$ (ksi)	18.8	18.8

The comparison of the experimental data sets and the model predictions data for the fit to multiple data sets are shown in the following two figures:

**Figure 31.7: Plot Comparing Stabilized Hysteresis Data to Fit of Multiple Data Sets**



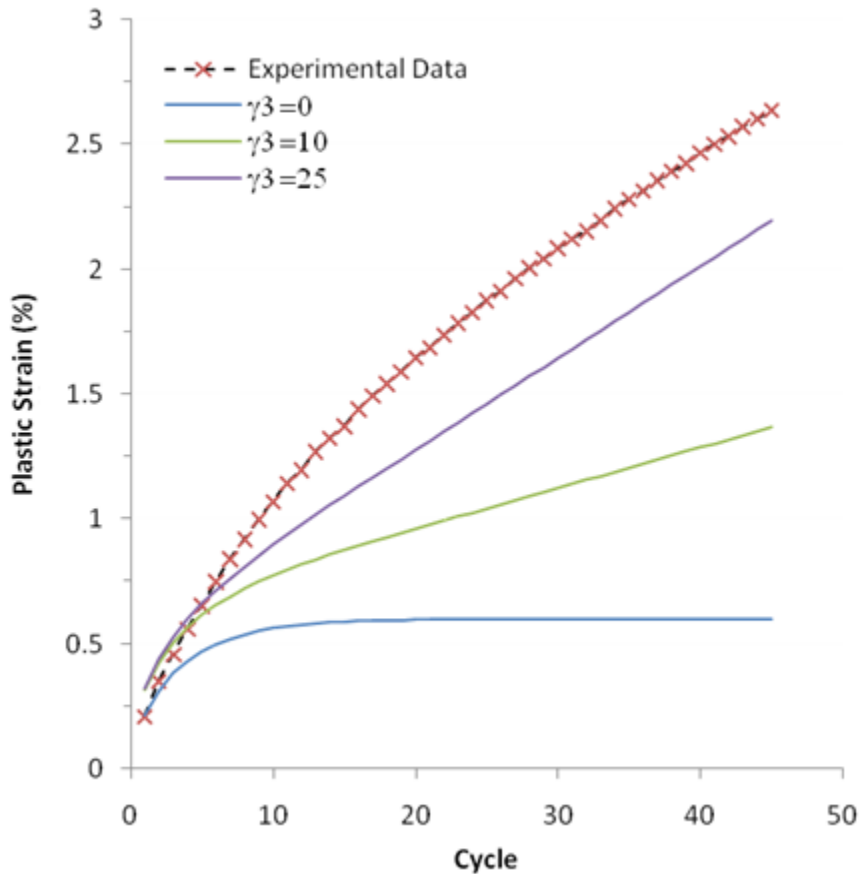
**Figure 31.8: Plot Comparing Stress Data to Fit of Multiple Data Sets**

The stabilized hysteresis comparison shows a slightly better fit in the unloading knee and a change in the data fit for the loading knee. The predictions at the maximum and minimum plastic strain points are not significantly affected, however. The stress-controlled data comparison also shows a shift in the reloading knee region, but the plastic strain prediction in the initial unloading point still shows significant error.

### 31.3.4. Fitting the Ratcheting Strain

Using the three back stress components to fit the three parts of the stress-strain behavior (as described in [Determining Material Parameters \(p. 477\)](#)), it is difficult to fit the value of  $\gamma_3$  using either the stabilized hysteresis or the stress-controlled data. The value of  $\gamma_3$ , however, can be used to match the rate at which plastic strain accumulates over a number of loading cycles.

The following figure shows data from Bari and Hassan [4] that illustrates the accumulation of plastic strain over 45 cycles of loading:

**Figure 31.9: Plot Comparing Ratcheting Strain Data to Prediction from Fitted Chaboche Model**

The load cycle is the same as that used for the [stress-controlled data](#) (p. 482). Also shown are predictions from the model using the parameters from the fit to multiple data sets, except that three different values for  $\gamma_3$  are used. The plot shows that the rate of plastic strain accumulation after about 10 cycles of loading is nearly linear with the value of  $\gamma_3$  controlling this rate of ratcheting.

For a value  $\gamma_3 = 25$ , the rate of ratcheting approximately matches the experimental data; however, the total amount of plastic strain from the model does not match the experimental data. One reason is that the plastic strain in the early part of the load history is affected by the isotropic hardening behavior, which quickly saturates after a few loading cycles.

Selecting a value for  $\gamma_3$  to match the ratcheting rate is a manually iterative process, as a fixed value is set and a new fit to the other Chaboche parameters is obtained via the curve-fitting tool.

### 31.4. Recommendations

When fitting a Chaboche nonlinear kinematic model to experimental data using the curve-fitting tool, consider the following recommendations:

- Use stabilized hysteresis strain-controlled data for estimating initial parameters. Refer to the heuristic procedure described in [Determining Material Parameters](#) (p. 477).
- Stress-controlled data can be used for estimating initial parameters, but the resulting fit should be carefully compared to the experimental data. When using stress-controlled data, omitting the elastic-plastic transition

region helps to limit the effect of isotropic hardening in the experimental data and can result in a better fit for the kinematic hardening parameters.

- The experimental data should be arranged such that the first point is the initial (0,0) stress-strain point. Although this value is not required in the experimental data, the fitting algorithm simulates the experimental data starting from the (0,0) stress-strain point.
- Smooth noisy experimental data.
- Use a small nonzero value for  $\gamma_3$  for the initial estimate. If stress-controlled ratcheting data are available,  $\gamma_3$  can be manually adjusted or automatically fit to control the rate of ratcheting.
- The initial values of the constants  $C_1, \gamma_1, C_2, \gamma_2, C_3, \gamma_3$  should be of decreasing order.
- Compare the results of the fitted model to the experimental data to verify the fit. If the fit is poor, modify the values for the initial parameters and try the fit again.
- If the model cannot be made to fit the entire range of experimental data, it may be necessary to sacrifice the fit quality in some regions of the loading history in order to fit other regions of the loading history.
- Use caution when extrapolating model predictions to loading histories outside of the available experimental data, as the results may be of limited value.

## 31.5. References

The following references are used in this example problem:

1. Chaboche, J.L.. "Constitutive Equations for Cyclic Plasticity and Cyclic Viscoplasticity." *International Journal of Plasticity* 5:3 (1989): 247-302.
2. Chaboche, J.L.. "On Some Modifications of Kinematic Hardening to Improve the Description of Ratcheting Effects." *International Journal of Plasticity* 7 (1991): 661-678.
3. Rezaiee-Pajand M. and S. Sinaie. "On the Calibration of the Chaboche Hardening Model and a Modified Hardening Rule for Uniaxial Ratcheting Prediction." *International Journal of Solids and Structures*. 46 (2009): 3009-3017. [CRC](#), (2005).
4. Bari, S. and T. Hassan. "Anatomy of Coupled Constitutive Models for Ratcheting Simulation." *International Journal of Plasticity* 16 (2000): 381-409.

## 31.6. Input Files

The following files were used in this problem:

- `fit_chaboche_strain.dat` -- Input file to fit the model to stabilized hysteresis strain-controlled experimental data and simulate a uniaxial, strain-controlled experiment.
- `fit_chaboche_stress.dat` -- Input file to fit the model to a cycle of stress-controlled experimental data and simulate a uniaxial, stress-controlled experiment.
- `fit_chaboche_combined.dat` -- Input file to fit the model to stabilized hysteresis strain-controlled experimental data, and to fit the model to a cycle of stress-controlled experimental data and simulate a uniaxial, stress-controlled experiment.

The files are available in the `td-31` folder. See [Obtaining the Input Files \(p. xxxv\)](#) for more information.

---

## Chapter 32: Anterior Cruciate Ligament (ACL) Simulation

---

This example problem simulates the response of an anterior cruciate ligament (ACL) of a human knee subjected to tension, flexion, and rotation. The problem uses an [anisotropic hyperelastic](#) material model with [viscoelasticity](#).

Topics related to this example problem follow:

- [32.1. Introduction](#)
- [32.2. Problem Description](#)
- [32.3. Modeling](#)
- [32.4. Material Properties](#)
- [32.5. Boundary Conditions and Loading](#)
- [32.6. Analysis and Solution Controls](#)
- [32.7. Results and Discussion](#)
- [32.8. Recommendations](#)
- [32.9. References](#)
- [32.10. Input Files](#)

### 32.1. Introduction

Sports and automobile accidents are significant causes of ligament injury, and injury to the anterior cruciate ligament (ACL) is the most common ligament injury [1]. Of the many ligaments holding the human knee joint together, the ACL is of special importance because it maintains knee stability and helps to prevent damage to the knee by limiting joint motion [2].

The ACL is composed mostly of densely packed collagen fibers that connect the femur and tibia [6]. The ACL lies inside the knee joint, as shown in this figure:

**Figure 32.1: Human Knee Components**

Courtesy of Hughston Research and Education

Because of large deformations and rotations, the ACL exhibits highly nonlinear and anisotropic behavior, and shows a clear strain rate dependency [1]. The anisotropic behavior is caused by collagen fiber families arranged in a matrix of soft material.

Ligaments are viscoelastic and thus display time-dependent and load-history-dependent mechanical behavior [2]. The viscoelastic behaviors for ligaments have clinical significance as they help to prevent fatigue failure of the ligaments.

The problem presented here uses an [anisotropic hyperelastic](#) material model with [viscoelasticity](#) to model the anisotropy, nonlinear behavior, large strains, high compliance for bending loading and incompressibility. The exponential strain energy potential is used for anisotropic hyperelasticity with a Prony series viscoelastic model.

## 32.2. Problem Description

The ACL is one of the four primary stabilizing ligaments of the knee. It limits the movement of the tibia with respect to the femur when subjected to flexion, extension and rotation.

As shown in [Figure 32.1: Human Knee Components \(p. 490\)](#), the ACL attaches to the knee-end of the femur (at the back of the joint) and passes down through the knee joint to the front of the flat upper surface of the tibia. It passes across the knee joint in a diagonal direction.

The primary objective of this simulation is to investigate the behavior of the ACL in relation to the movement of the femur; therefore, a section of the ACL is constructed. The femur is modeled as a rigid surface. The length of the ACL is specified as 31 mm. The ACL is assumed to exhibit visco-anisotropic hyperelastic behavior. Several analyses are performed to simulate various femur movements.

The ACL has no stress-free state. At all knee flexions, stress is present in the ligament [2]. The precise experimental distribution of the stress field is unknown; therefore, the simulation is performed without prestressing the ACL.

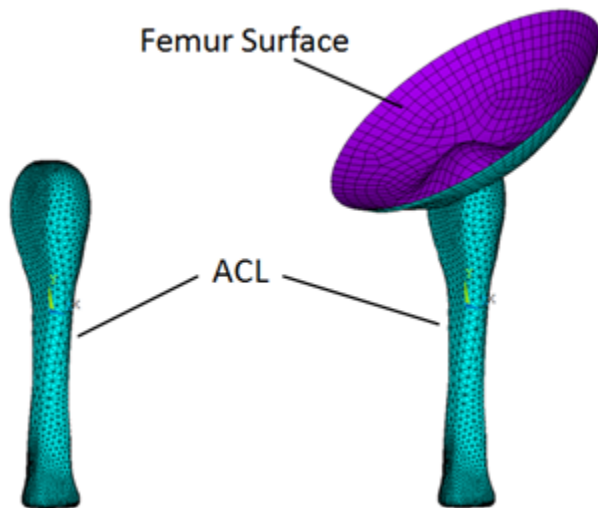


A constant strain rate is applied with displacement at the top of the ACL, while the lower part is fixed at the bottom. The behavior of the ACL under knee flexion of 45 degrees and rotation of 11.25 degrees is also examined.

### 32.3. Modeling

The ACL model geometry is similar to the geometry used by the Open Knee Project [8], but with different dimensions. It is an approximate model with nonuniform geometry, where the midsection cross-sectional area is smaller than that of the insertions. A typical ACL has bundles of collagen fibers, but the model used here is a solid model with anisotropic material properties.

**Figure 32.2: Finite Element Model of an ACL**



A tetrahedral mesh of the ACL is built with **SOLID187** elements. A rigid surface is modeled to represent the action of the femur. A standard contact behavior ( $\text{KEYOPT}(12) = 0$ ) is defined between the femur surface and the upper part of the ACL. A pilot node is also defined for the rigid surface to give the rotations.

### 32.4. Material Properties

An anisotropic hyperelastic material model is used with viscoelasticity for the ACL simulation. Anisotropic hyperelasticity is a potential-based-function with parameters to define the volumetric part, the isochoric part, and the material directions.

The exponential strain energy potential is used for characterizing the isochoric part.

The strain energy potential for anisotropic hyperelasticity is given by:

$$W = W_v(J) + W_d(\bar{C}, A \otimes A, B \otimes B)$$

where:

$J$  = Determinant of the elastic deformation gradient

$\bar{C}$  = Cauchy-Green tensor

$A, B$  = Constitutive material directions

The volumetric strain energy is given by:

$$W_v(J) = \frac{1}{d} (J-1)^2$$

The exponential-function-based strain energy potential is given by:

$$W_d(\bar{C}, A \otimes A, B \otimes B) = \sum_{i=1}^3 a_i (\bar{I}_1 - 3)^i + \sum_{j=1}^3 b_j (\bar{I}_2 - 3)^j + \frac{c_1}{2c_2} \left\{ \exp[c_2 (\bar{I}_4 - 1)^2] - 1 \right\} + \frac{e_1}{2e_2} \left\{ \exp[e_2 (\bar{I}_6 - 1)^2] - 1 \right\}$$

The constants a1, c1, and c2 are taken from Peña, et al. [1], and the compressibility parameter d is considered to be small.

Anisotropic Hyperelastic Material Properties	
a <sub>1</sub>	1.5 (MPa)
c <sub>1</sub>	4.39056 (MPa)
c <sub>2</sub>	12.1093
d	0.001 (MPa <sup>-1</sup> )
Viscoelastic Material Properties	
α <sub>1</sub> <sup>G</sup>	0.3
τ <sub>1</sub> <sup>G</sup>	0.3 (sec)
α <sub>2</sub> <sup>G</sup>	0.4
τ <sub>2</sub> <sup>G</sup>	9.0 (sec)

The following example input defines the material properties:

```
! Anisotropic Hyperelastic Material
A1=1.5
A2=0
A3=0
B1=0
B2=0
B3=0
C1=4.39056
C2=12.1093
E1=0
E2=0
d=1E-03

TB,AHYPER,1,,10,EXP
TBDATA,1, A1,A2,A3,B1,B2,B3
TBDATA,7, C1,C2,E1,E2

TB,AHYPER,1,,AVEC      ! aligned with uniaxial strain direction
TBDATA,1, 0, 1, 0

TB,AHYPER,1,,PVOL
TBDATA,1, d

! Viscoelasticity
alpha1=0.30
alpha2=0.4
tau1=0.3
tau2=9.0
```

```
TB,PRONY,1,,2,SHEAR
TBDATA,1,alpha1,tau1
TBDATA,3,alpha2,tau2
```

The preferred orientation of the collagen fibers of the ACL induces the transversely isotropic symmetry of the ligament [5]; therefore, only the direction vector aligned with the loading (-y) axis is considered for performing the uniaxial extension simulation.

## 32.5. Boundary Conditions and Loading

Because the purpose of this problem is to show the anisotropic, hyperelastic, and viscoelastic behavior of the ACL, a simplified model is used. The problem focuses on the ACL part of the knee only. Instead of using a complex model with the femur, tibia, and fibula parts, only the boundary conditions are considered accordingly.

The femur is modeled with a rigid contact surface to enable modeling of the bending and twisting behavior of the ACL. In the analyses, the tibia (bottom) side of the ACL model remain fixed and is constrained with all degrees of freedom.

The knee joint works in flexion, extension, and rotation. The simulations therefore show the behavior of the ACL under the uniaxial flexion, tension, and rotation.

In the first case, a uniaxial displacement loading is applied at the top surface of the ACL with total stretch of 1.12. A high constant strain rate of 50 percent per second with an elongation rate of 15.5 mm/sec is maintained. The following example input specifies the loading:

```
Ly = 31           ! length of the ACL (mm)
erat = 15.5      ! elongation rate (mm/s)
ts = 1.12       ! total stretch
dl = (ts-1)*Ly  ! total displacement (mm)
tt = dl/erat    ! total time (sec)
```

In the second case, a flexion of 45 degrees is applied.

In the third case, a rotation of 11.25 degrees is applied using the femur surface in a small time period of 1.5 seconds.

## 32.6. Analysis and Solution Controls

Nonlinear static analyses are performed under uniaxial loading, bending and twisting.

Large-deflection effects are included in the analysis (**NLGEOM,ON**). Automatic time stepping is in effect, with an initial time increment of 0.001 seconds.

## 32.7. Results and Discussion

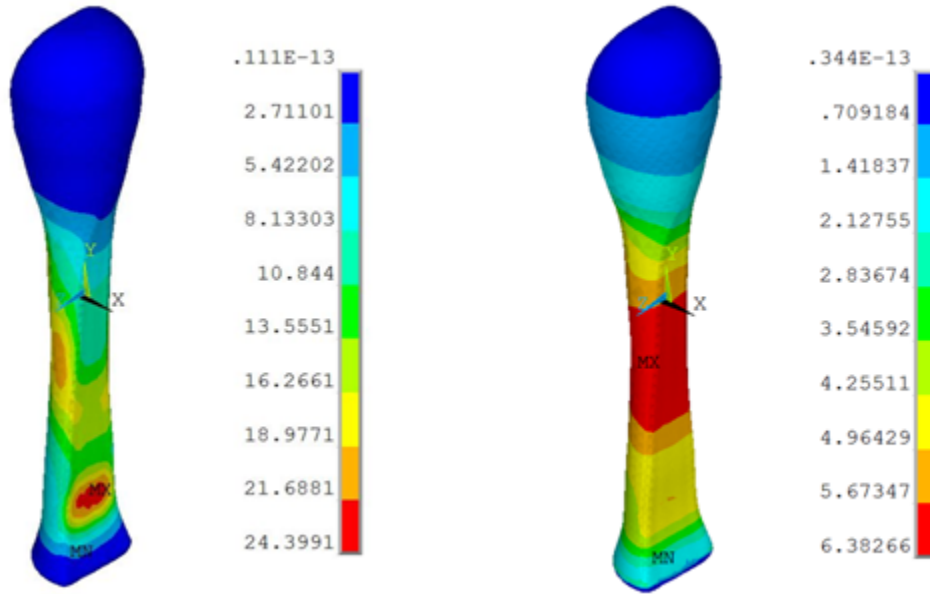
The following ACL simulation result discussion topics are available:

- [32.7.1. Uniaxial Loading](#)
- [32.7.2. Knee Flexion](#)

### 32.7.1. Uniaxial Loading

Because the ACL transmits tensile forces, experimental studies of this tissue are generally performed in uniaxial tension. The following figure shows the von Mises stress distribution for the ACL under the uniaxial tension at constant strain rate of 50 percent per second for anisotropic visco-hyperelastic and Neo-Hookean viscoelastic models:

**Figure 32.3: Von Mises Stress (Anisotropic Visco-Hyperelastic and Neo-Hookean Viscoelastic)**

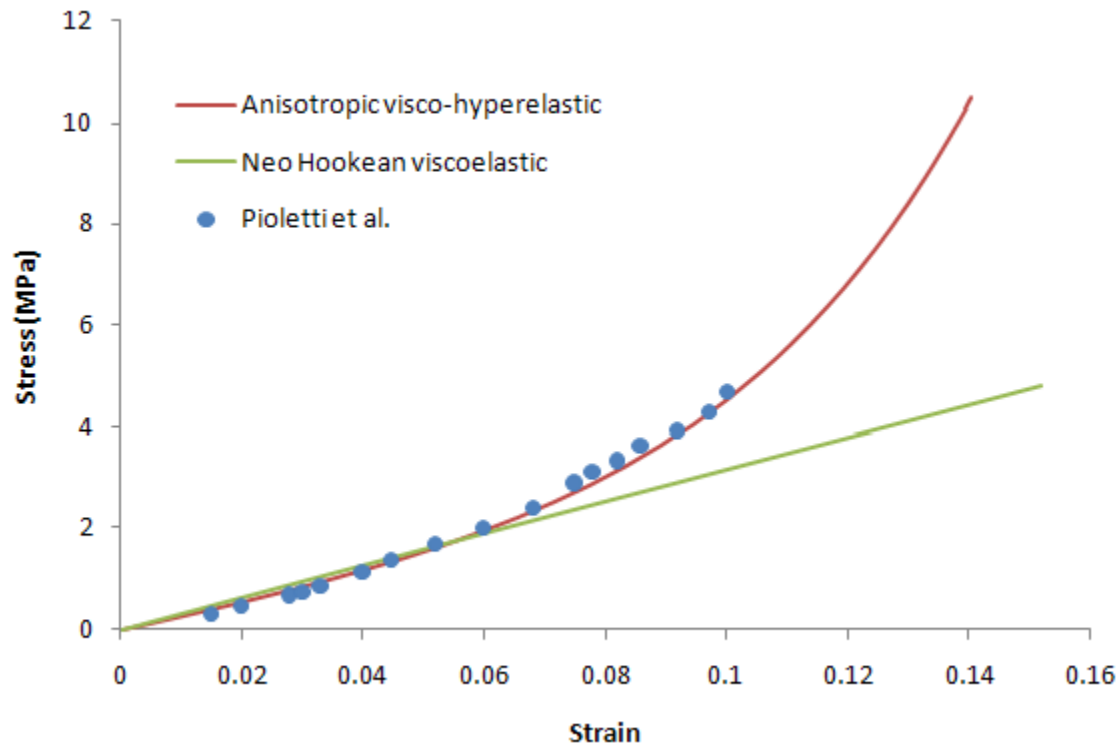


In the anisotropic visco-hyperelastic model, the peak stresses in the ACL are seen near the insertion sites, suggesting that this area could be susceptible to injury.

Ligaments are highly anisotropic due to their fibrous structure [7]. The collagen fibers in the cruciate ligaments of the knee are highly aligned with the long axis; therefore, an anisotropic model is required to show the behavior of the ACL under deformation.

The strain rate during injury is a significant factor in determining the magnitude of the lesion. The stress-strain behavior of the ligament is therefore essential in order to examine the importance of the strain rates during the ACL movement.

The following figure shows the stress-strain behavior of the ACL under uniaxial tension for visco-anisotropic, visco-hyperelastic, and Neo-Hookean viscoelastic material models along with the experimental results of Pioletti et al. [3]:

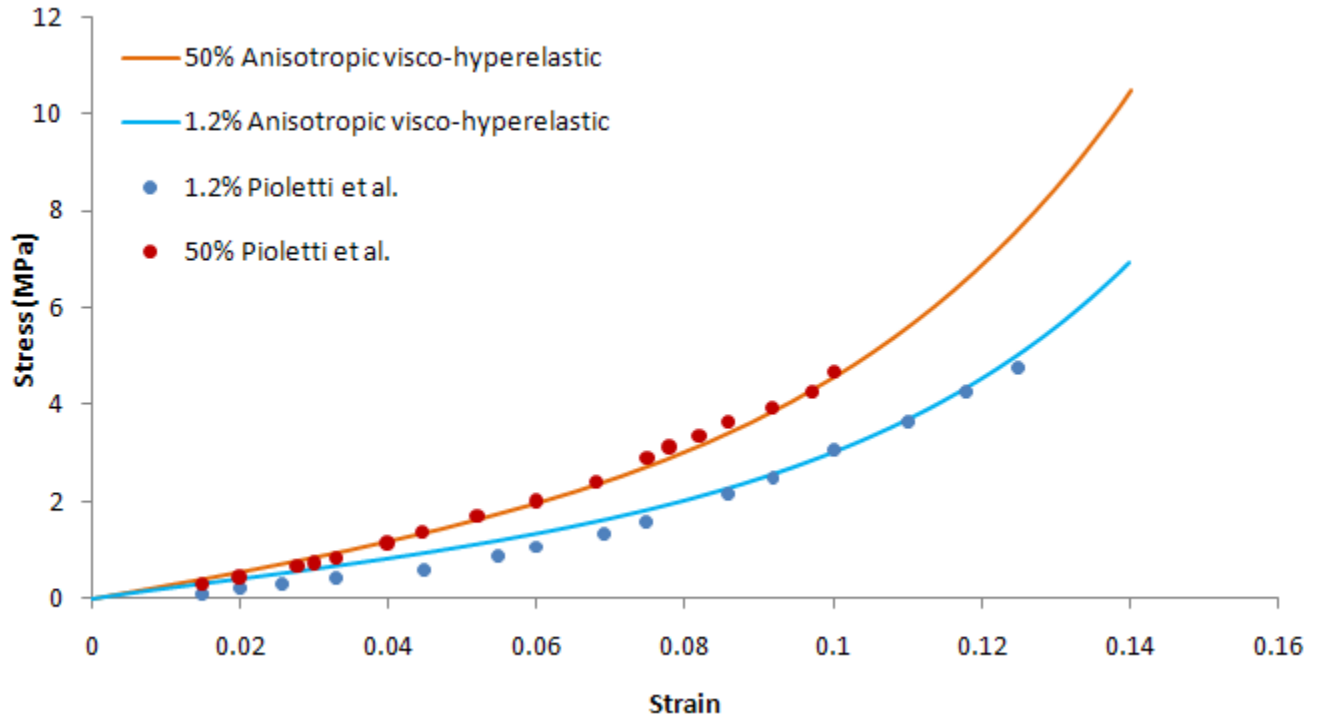
**Figure 32.4: ACL Stress-Strain Plot**

The stress and strain values are the average values on the cross-sectional area of the ACL.

The anisotropic visco-hyperelastic ACL model used in this problem exhibits a response closer to the experimental data when the ACL is subjected to uniaxial loading.

The following figure shows the stress- strain behavior of the ACL under uniaxial tension for the anisotropic visco-hyperelastic model with differing strain rates:

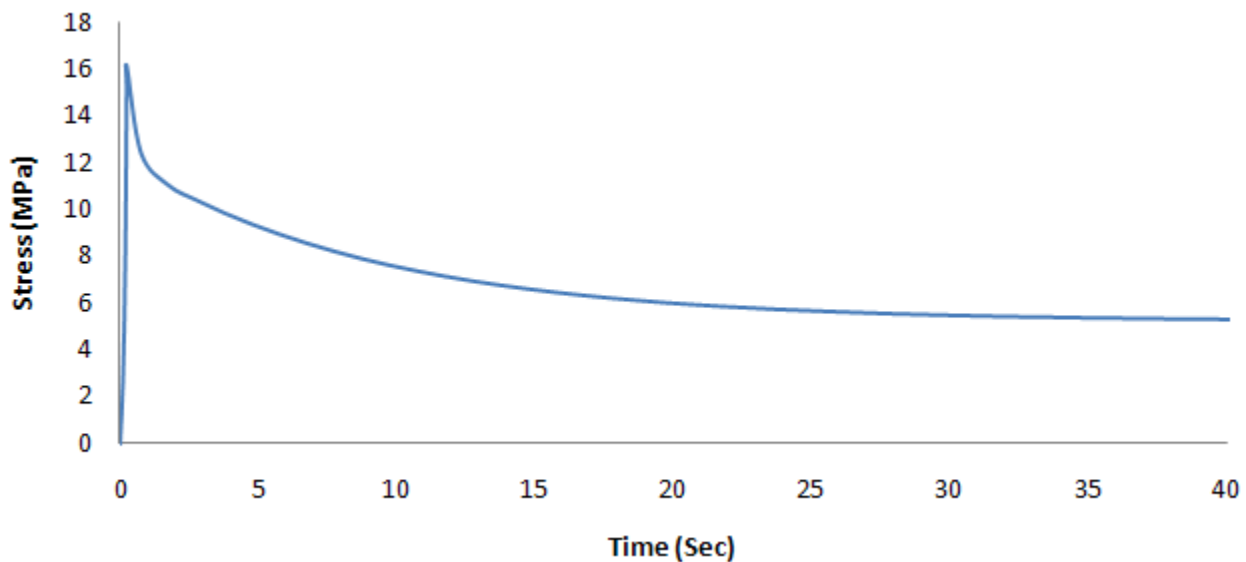
**Figure 32.5: Stress-Strain at Differing Strain Rates**



At high strain rates, the results are closer to the experimental results. It is known that damage in mature ligaments typically occurs at high load rates. The variation of ligament stress-strain behavior with strain rate is an indicator of the viscoelastic nature of the tissue.

An important viscoelastic characteristic of ligaments is stress relaxation (a decline in stress over time under a constant deformation), and so a relaxation test is simulated. A uniaxial deformation is applied up to a stretch ratio of 1.12 for a very small time period (0.24 seconds) and is then allowed to relax for 50 seconds. The following figure demonstrates viscoelasticity in stress relaxation for the ACL model:

**Figure 32.6: Stress Relaxation**

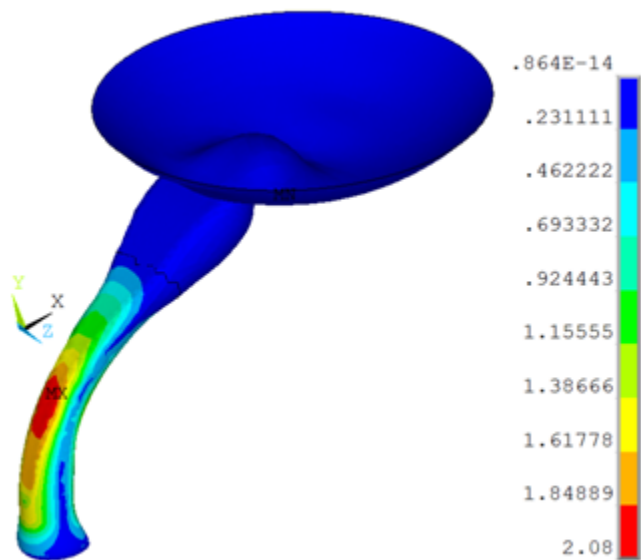


### 32.7.2. Knee Flexion

The ACL can be injured or torn in a number of different ways. Some of the common ways are flexion and internal rotation of femur on tibia. As a soft tissue, the ACL cannot resist compressive loads. An assumption of isotropy is therefore invalid for the ACL model when analyzing knee flexion [4].

The following figure shows the stress variation in the ACL under knee flexion:

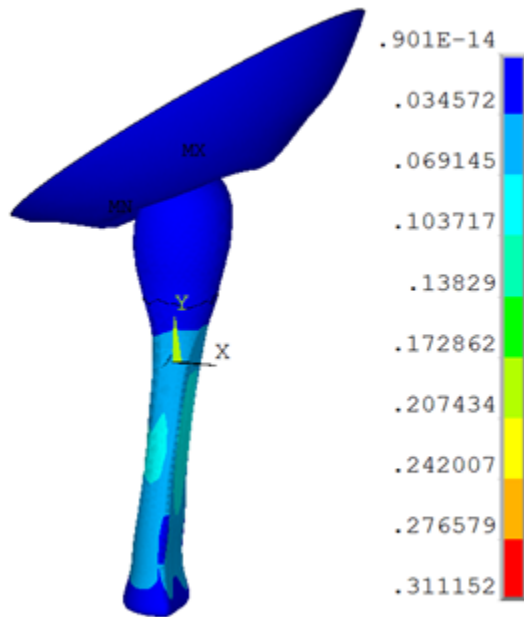
**Figure 32.7: Von Mises Stresses Under 45° Knee Flexion**



The femur surface rotates about the z axis, and the tibia side (the bottom part of the ACL) remains fixed. During knee flexion, an increase in von Mises stress occurs near the minimum cross sectional area of the ACL.

The femoral and tibial insertion zones are not considered, as this model emphasizes only the ACL behavior irrespective of the insertion zones. If one also considers the insertion zones, more accurate stresses near the femoral insertion zone can be expected.

The knee joint enables leg rotation along its longitudinal axis. The cruciate ligaments limit the internal rotation [2]. The following figure shows the stress variation in the ACL under the knee rotation:

**Figure 32.8: Von Mises Stresses Under 11.25° Knee Rotation**

The femur surface rotates about the vertical y axis, and the tibia side remains fixed. The stress in the ligament is increased with the internal rotation of the femur.

## 32.8. Recommendations

To perform a similar type of analysis using anisotropic hyperelasticity and viscoelasticity, consider the following recommendations:

- The ACL has irregular and complex geometry; therefore, the ideal element type for ACL simulation is the 10-node tetrahedral element **SOLID187**. It is well suited to modeling irregular geometries (such as those created using CAD/CAM systems).
- The fiber directions in the ACL can be defined using the vectors (A,B) in the anisotropic hyperelastic material model. The ligaments are highly anisotropic because of their strongly unidirectional fibrous structure and provide primary resistance to the tensile loading; therefore, only the direction vector aligned with the long axis is considered.
- Although a simplified model of ACL is used in this problem, femur and tibia sides with insertion zones can also be considered in an ACL simulation. In such a case, a fine mesh yields more accurate results. Too fine a mesh, however, increases computational time; to minimize the computational cost, the femur and tibia sides can be considered to be rigid.

## 32.9. References

The following references are used in this example problem:

1. Peña, E. et al. "An Anisotropic Visco-Hyperelastic Model for Ligaments at Finite Strains. Formulation and Computational Aspects." *International Journal of Solids and Structures* 44 (2007): 760-778.
2. Pioletti, D.P. (1997) *Viscoelastic Properties of Soft Tissues: Application to Knee Ligaments and Tendons*. Ph.D. Thesis. École Polytechnique Fédérale de Lausanne: Switzerland.



3. Pioletti, D. et al. "Viscoelastic Constitutive Law in Large Deformations: Application to Human Knee Ligaments and Tendons." *Journal of Biomechanics*. 31 (1998): 753-757.
4. Song, Y. et al. "A Three Dimensional Finite Element Model of the Human Anterior Cruciate Ligament: A Computational Analysis with Experimental Validation." *Journal of Biomechanics* 37 (2004): 383-390.
5. Limbert, G., M. Taylor, J. Middleton. "Three Dimensional Modeling of the Human ACL: Simulation of Passive Knee Flexion with a Stressed and Stress-Free ACL." *Journal of Biomechanics* 37:11 (2004): 1723-1731.
6. Borotikar, B.S. (2009) *Subject Specific Computational Models of the Knee to Predict Anterior Cruciate Ligament Injury*. Ph.D. Thesis. Cleveland State University: USA.
7. Haghpanahi, M. and F. Jalayer. "Three-Dimensional Finite Element Analysis of the Human ACL." Paper presented at the 1st WSEAS International Conference on Biomedical Electronics and Biomedical Informatics: Rhodes, Greece (August, 2008).
8. Erdemir, A. and S. Sibole. "Open Knee: A Three-Dimensional Finite Element Representation of the Knee Joint." Computational Biomodeling Core and Department of Biomedical Engineering, Lerner Research Institute, Cleveland Clinic: Cleveland, USA.

## 32.10. Input Files

The following files were used in this problem:

- `acl_tension.dat` -- Input file for the analysis of the ACL under uniaxial tension loading.
- `acl_tension.cdb` -- Database file for the finite-element model of the ACL under uniaxial tension (called by `acl_tension.dat`).
- `acl_flexion.dat` -- Input file for the analysis of the ACL under flexion.
- `acl_flexion.cdb` -- Database file for the finite-element model of the ACL under flexion (called by `acl_flexion.dat`).
- `acl_rotation.dat` -- Input file for the analysis of the ACL under rotation.
- `acl_rotation.cdb` -- Database file for the finite-element model of the ACL under rotation (called by `acl_rotation.dat`).

The files are available in the `td-32` folder. See [Obtaining the Input Files \(p. xxxv\)](#) for more information.



---

## Chapter 33: Analysis of a Piezoelectric Flextensional Transducer in Water

---

This example problem demonstrates the coupling of structural, piezoelectric, and acoustic elements to analyze the acoustic response of a flextensional transducer to voltage excitation.

The following features and capabilities are highlighted:

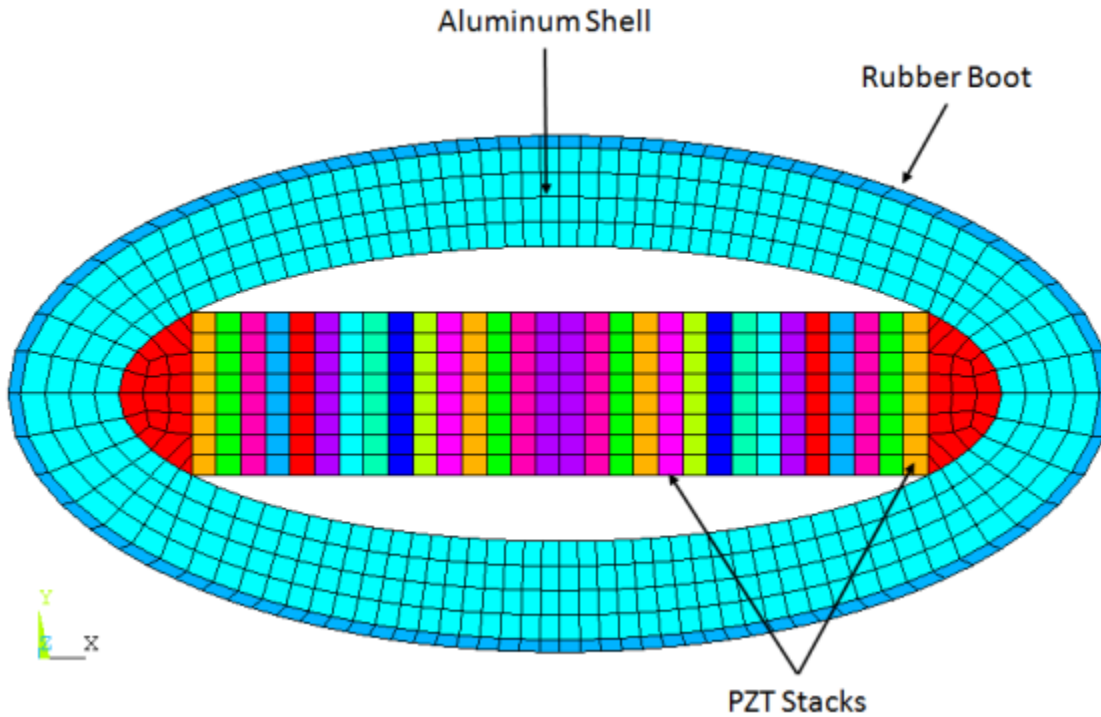
- Structural-acoustic coupling using [fluid-structure interaction \(FSI\)](#) in 2-D and 3-D
- Use of [piezoelectric materials](#)
- Use of [infinite acoustic elements](#) to absorb outgoing acoustic waves in 2-D
- Use of the [Robin boundary condition](#) to absorb outgoing acoustic waves in 3-D
- Far-field postprocessing of an acoustic field in 2.5-D models

Topics related to this example problem follow:

- [33.1. Introduction](#)
- [33.2. Problem Description](#)
- [33.3. Modeling](#)
- [33.4. Material Properties](#)
- [33.5. Boundary Conditions and Loading](#)
- [33.6. Analysis and Solution Controls](#)
- [33.7. Results and Discussion](#)
- [33.8. Recommendations](#)
- [33.9. References](#)
- [33.10. Input Files](#)

### 33.1. Introduction

Flextensional transducers usually operate in the low- or mid-frequency range and are attractive because they can generate high-power output. A [Class IV type](#) of flextensional transducer, shown in the following figure, contains a stack of piezoelectric ceramics in an elliptically-shaped shell that is covered with rubber to isolate it from the surrounding water:

**Figure 33.1: Class IV Flextensional Underwater Acoustic Transducer Shell**

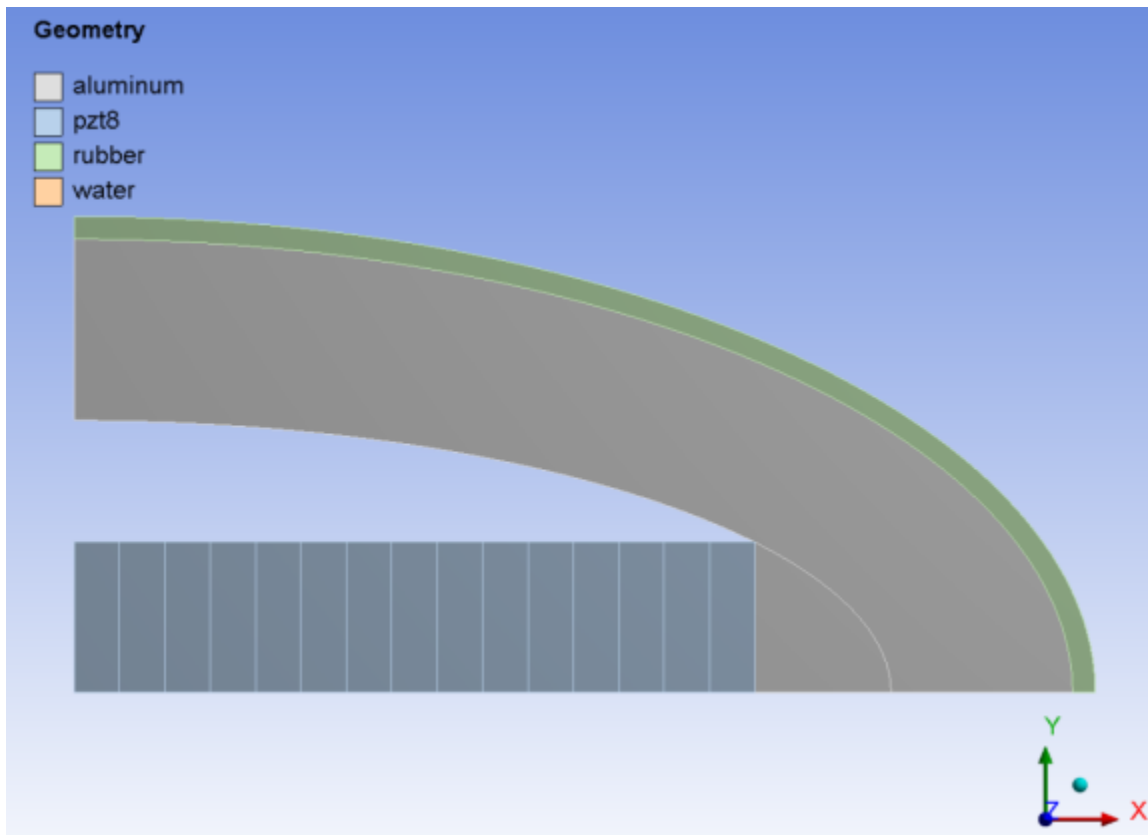
Voltage applied to the piezoelectric ceramics causes motion along the x axis (major axis), which in turn causes amplified motion along the y axis (minor axis). This behavior produces large-volume displacement and thus high-power output. The Class IV flextensional transducer produces a roughly omnidirectional radiation pattern, although there reduced output occurs along the minor axis.

Transducer design can include changing material properties or dimensions to obtain the desired resonant frequency or response amplitude (quadrupole bending mode).

For this example, the flextensional transducer is idealized as a 2-D planar model and excited at 1400 Hz. Results of 2-D analyses are compared to a 3-D (2.5-D) model. The term *2.5-D* describes a single layer of extruded 3-D elements used to mimic 2-D planar behavior. The example also uses advanced 3-D capabilities, such as wave-absorption conditions and far-field postprocessing, to model 2-D analyses.

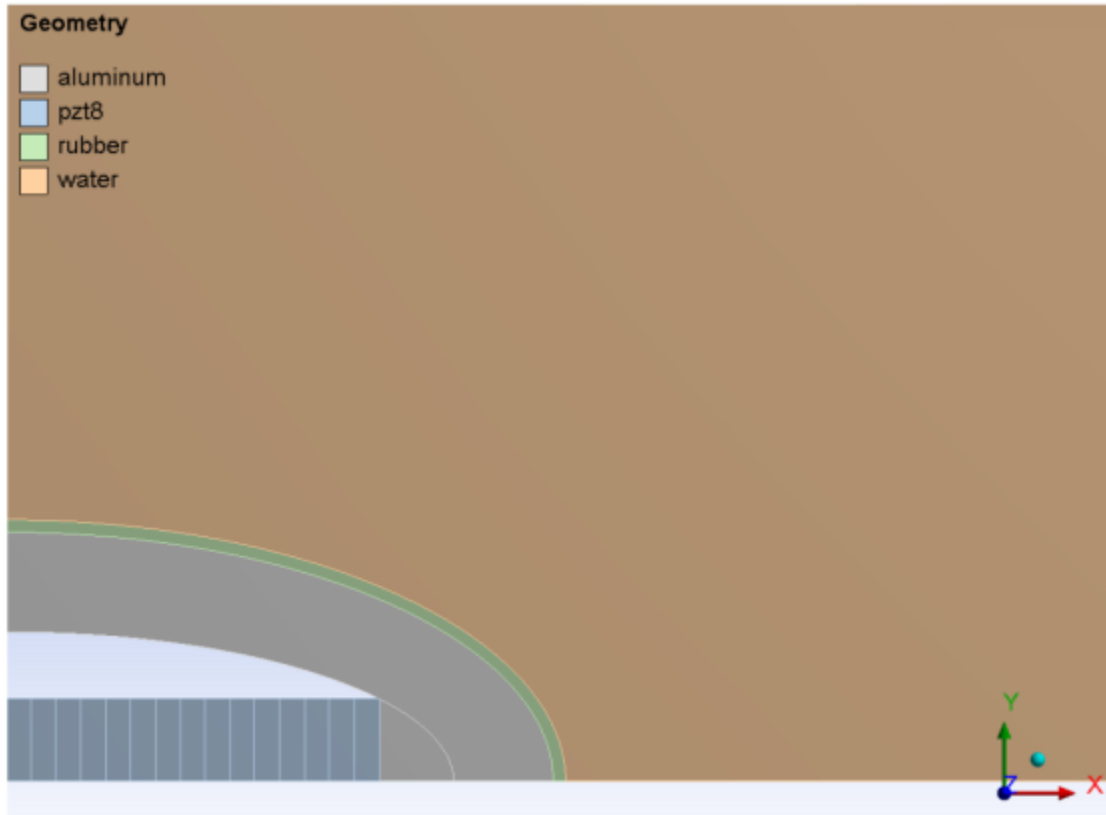
## 33.2. Problem Description

As shown in the following figure, the model exhibits  $\frac{1}{4}$  symmetry, so one quarter of the geometry is analyzed:

**Figure 33.2: Flextensional Transducer Components**

The quarter-symmetry model has 15 piezoelectric stacks (and 30 in the full model). The polarization direction is defined as the element's x axis (aligned with the global X axis), and the element coordinate system x-axes alternate between each piezoelectric ceramic.

Water surrounds the transducer, as shown in the following figure:

**Figure 33.3: Transducer Surrounded by Water**

The acoustic waves are assumed to radiate outward freely.

### 33.3. Modeling

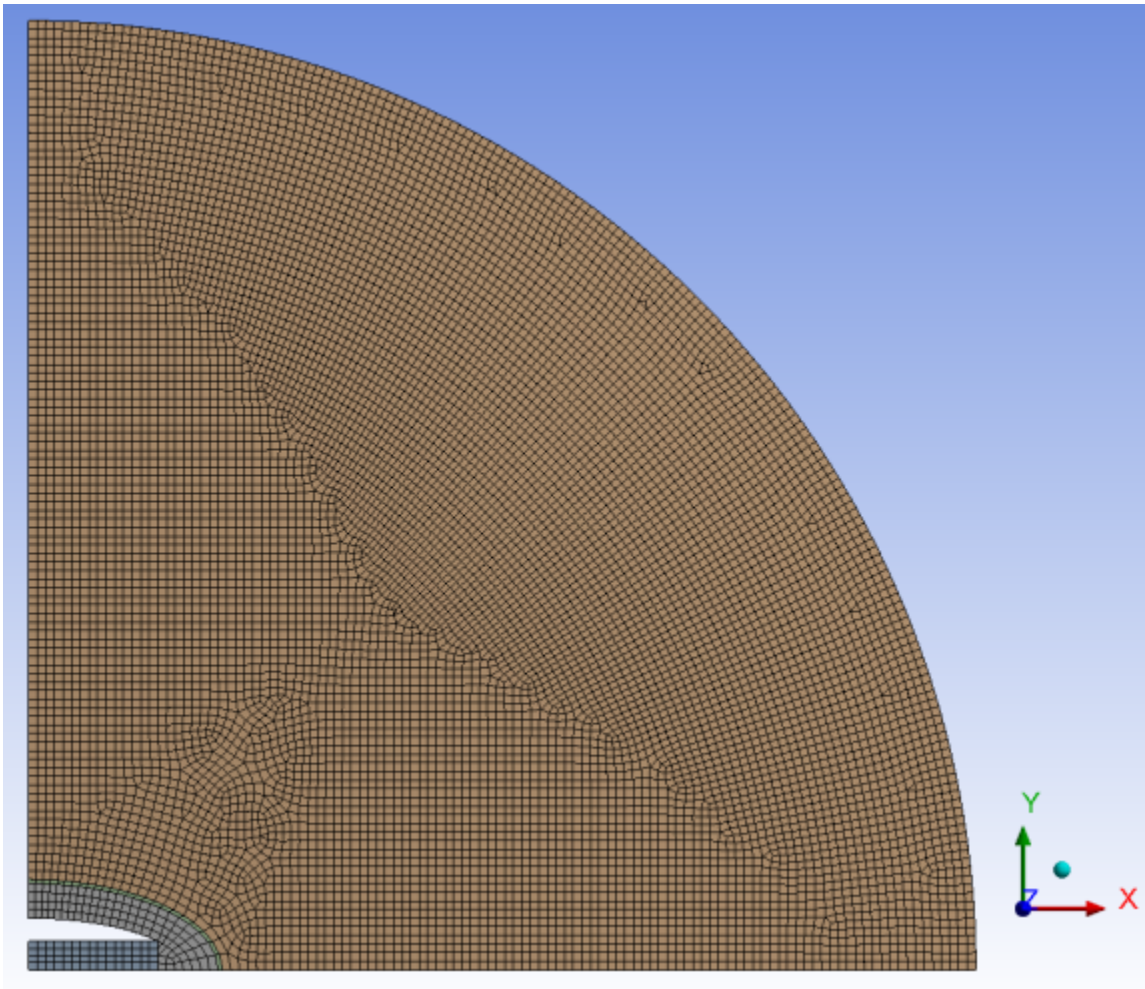
The 2-D (p. 504) and 3-D (p. 505) transducer models are created in ANSYS DesignModeler and meshed in the ANSYS Mechanical application. The major axis length is 450 mm and the minor axis length is 210 mm.

#### 33.3.1. 2-D Transducer Model

The 2-D transducer is meshed with **PLANE223** coupled-field (piezoelectric) elements with dropped midside nodes for the piezoelectric ceramics. **PLANE182** structural elements are used for the aluminum shell and rubber boot.

The surrounding water is a circular region meshed with **FLUID29** acoustic elements with a distance of 1.1 m. The truncated boundary defined by the 1.1 m circular arc is meshed with **FLUID129** infinite fluid elements to absorb outgoing acoustic waves.

The following figure shows the final mesh with an average element size of 10 mm:

**Figure 33.4: 2-D Transducer Model Mesh**

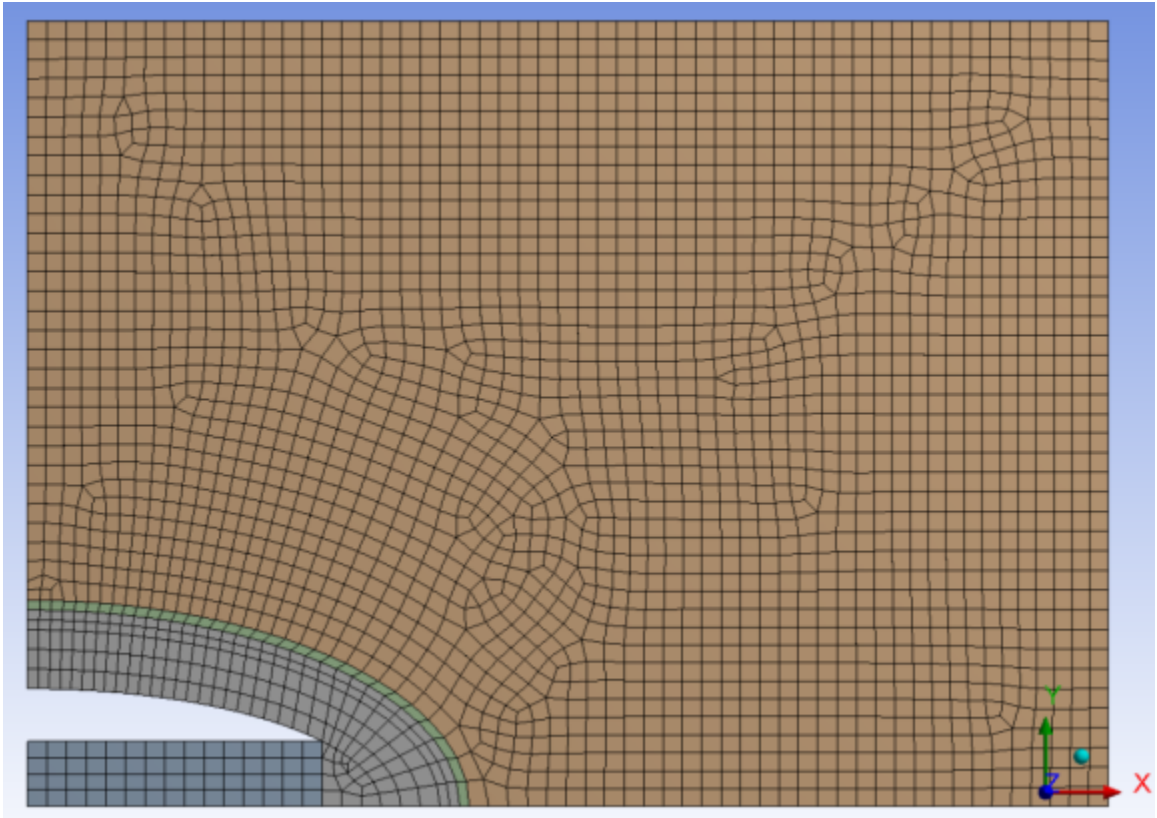
### 33.3.2. 3-D Transducer Model

The 3-D transducer's ceramic stacks are modeled with [SOLID226](#) coupled-field (piezoelectric) elements with dropped midside nodes. The aluminum shell and rubber boot are modeled with [SOLID185](#) structural elements.

A rectangular region 300 mm from the sides of the transducer represents the surrounding water. The model is extruded 10 mm in the out-of-plane (z-axis) direction to create a 2.5-D representation.

The following figure shows the final mesh with an average element size of 10 mm:

**Figure 33.5: 3-D Transducer Model Mesh**



### 33.4. Material Properties

Following are the material properties for the aluminum shell and rubber boot:

Material Property	Material	
	Aluminum	Rubber
Young's Modulus (Nm <sup>-2</sup> )	68.9E9	30E6
Poisson's Ratio	.3	.49
Density (kg/m <sup>-3</sup> )	2710	1100

The water density is assumed to be 1000 kg/m<sup>3</sup>, and its speed of sound is 1500 m/s.

Following are the material properties of the piezoelectric ceramic (PZT8), where the polarization direction is along the element x axis:

Material Property	Piezoelectric Ceramic Material
Density (kg/m <sup>-3</sup> )	7600
Elastic Moduli	EX: 74.07E9 Pa EY, EZ: 86.96E9 Pa PRXY: 0.303 PRYZ: 0.356 PRXZ: 0.322 GYX, GXZ: 31.35E9 Pa GYZ: 32.89E9 Pa



Material Property	Piezoelectric Ceramic Material			
	X	Y	Z	
Piezoelectric Stress Matrix [e] (C/m <sup>2</sup> )	X	13.911	0	0
	Y	-3.8754	0	0
	Z	-3.8754	0	0
	XY	0	10.3448	0
	YZ	0	0	0
	XZ	0	0	10.3448
Dielectric Permittivity (Relative)	PERX: 561 PERY, PERZ: 904			

## 33.5. Boundary Conditions and Loading

Following are the boundary conditions and loading applied to the piezoelectric flextensional transducer model:

- 33.5.1. Structural Boundary Conditions
- 33.5.2. Acoustic Boundary Conditions and Flags
- 33.5.3. Piezoelectric Boundary Conditions

### 33.5.1. Structural Boundary Conditions

Because a quarter of the model is analyzed, two symmetry boundary conditions are applied along the x and y axes. The 3-D model has an additional z constraint on both planes at z = 0 and 0.01 m.

### 33.5.2. Acoustic Boundary Conditions and Flags

The naturally occurring boundary condition is a rigid wall or a symmetry plane, so no acoustic boundary conditions are necessary on the two symmetry planes at x = 0 and y = 0. In the 3-D case, the planar surfaces at z = 0 and 0.01 m are rigid walls.

To active the vibroacoustic coupling, the FSI flag is specified to the nodal component N\_FSI .

#### 33.5.2.1. 2-D Acoustic Wave-Absorption Condition

For the 2-D case, [FLUID129](#) infinite acoustic element is used to model the wave-absorption condition. Typically, the fluid domain can be truncated around a quarter of the wavelength away from the object of interest. Because far-field postprocessing is not supported for 2-D [FLUID29](#) elements, however, the calculated results at 1 m must be included in the computational domain. [FLUID129](#) elements are therefore positioned in a circular arc 1.1 m from the center.

#### 33.5.2.2. 3-D Acoustic Wave-Absorption Condition

For the 3-D case, the modeled domain is Cartesian. A Robin radiation flag ([SF,,INF](#)) is applied to the outermost (+x and +y) surfaces to model the wave-absorption condition. Because far-field postprocessing is supported in 3-D, it is not necessary for the computational domain to extend 1 m in distance.

### 33.5.3. Piezoelectric Boundary Conditions

Between each piezoelectric ceramic is a terminal (not modeled). Because each terminal is equipotential, voltages of 0 V and 1 V are applied in an alternating fashion between each piezoelectric ceramic part.

### 33.6. Analysis and Solution Controls

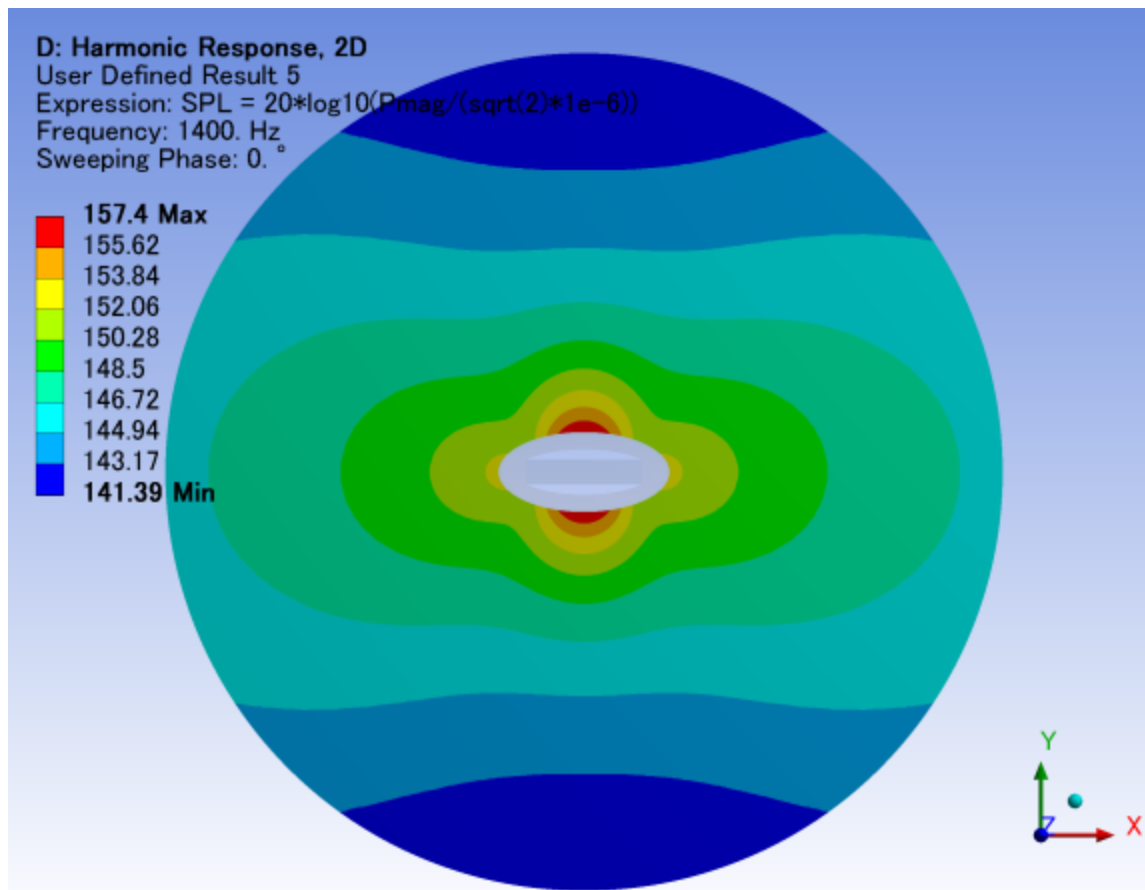
A harmonic response analysis is performed using the full method at a single frequency of 1400 Hz.

The direct sparse solver is used for this model. Because the number of degrees of freedom in the model is not large due to the 2-D simplification of the transducer, the solution completes in a few seconds.

### 33.7. Results and Discussion

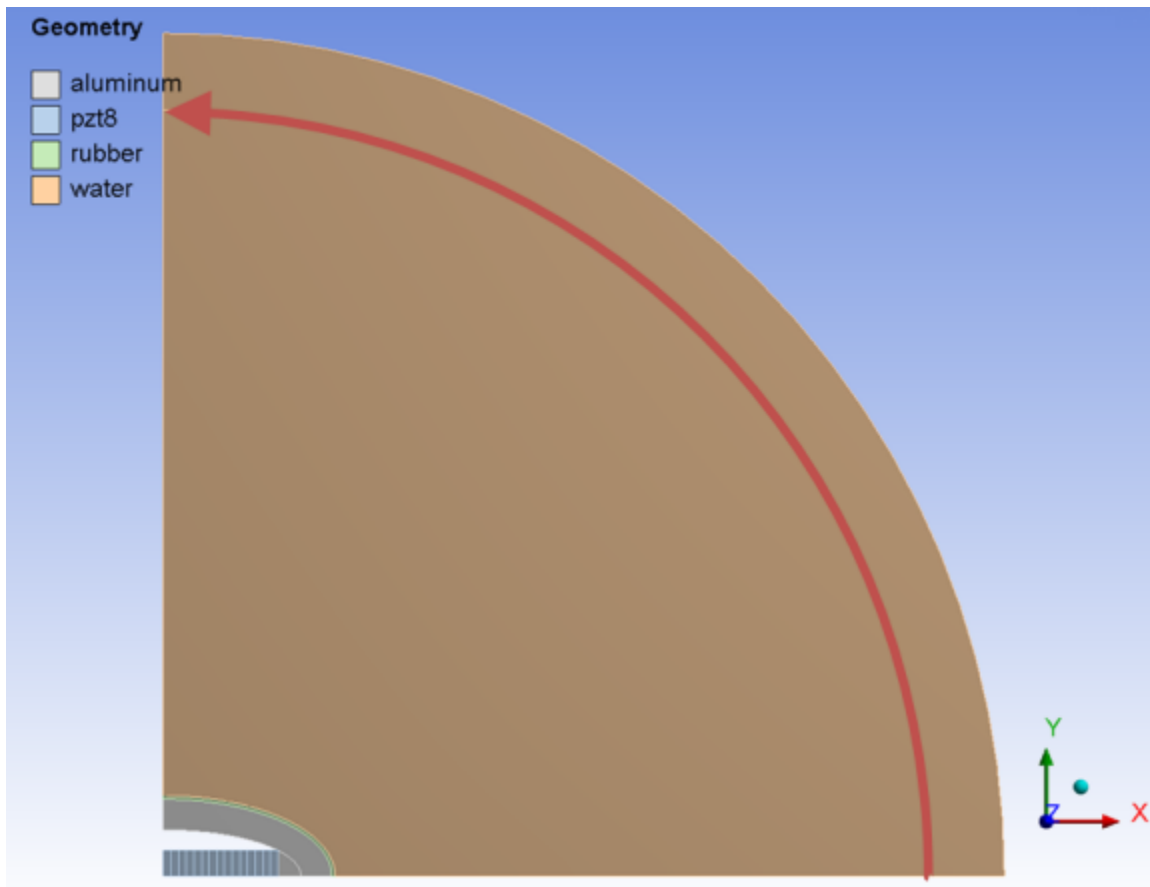
Following is a plot of the sound pressure level (SPL) on the full model:

**Figure 33.6: SPL Plot of Full Transducer Model**



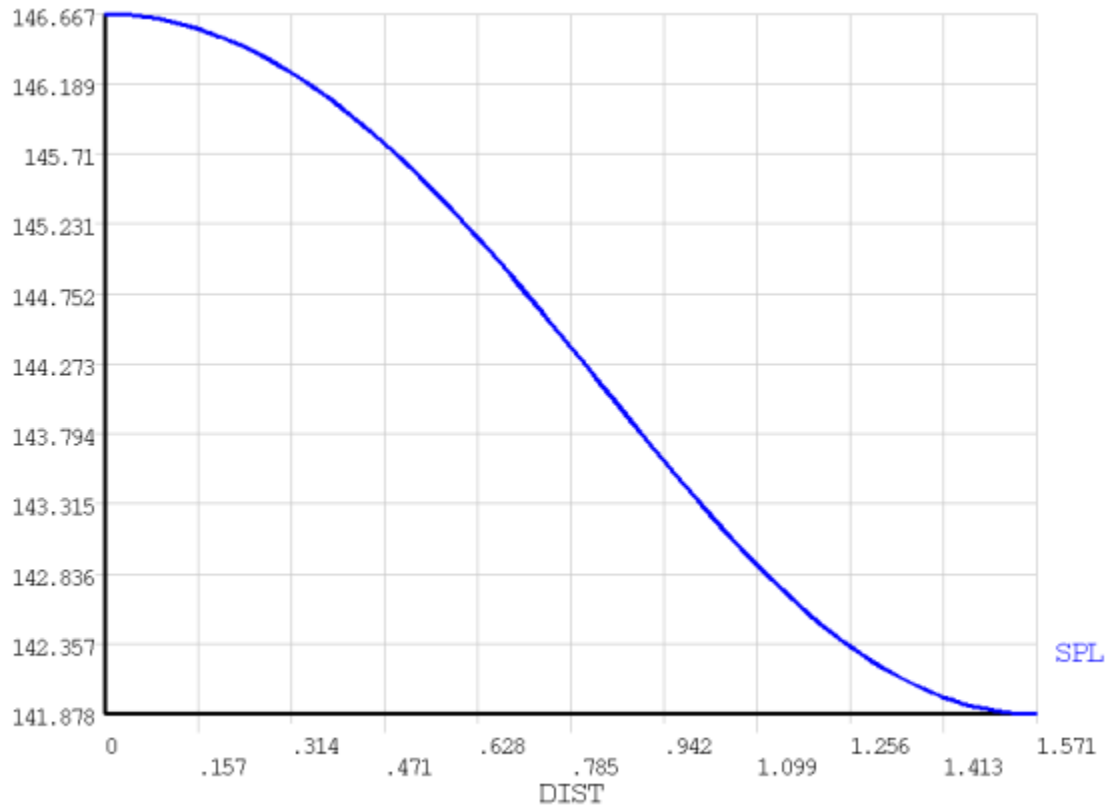
Notice that while the maximum SPL is at the surface of the transducer's minor axis, the SPL near the truncated boundary is lower along the minor axis.

This SPL plot along an arc 1 m from the center shows the direction of the arc from the x axis towards the y axis:

**Figure 33.7: SPL Plot Along an Arc 1 m from Center**

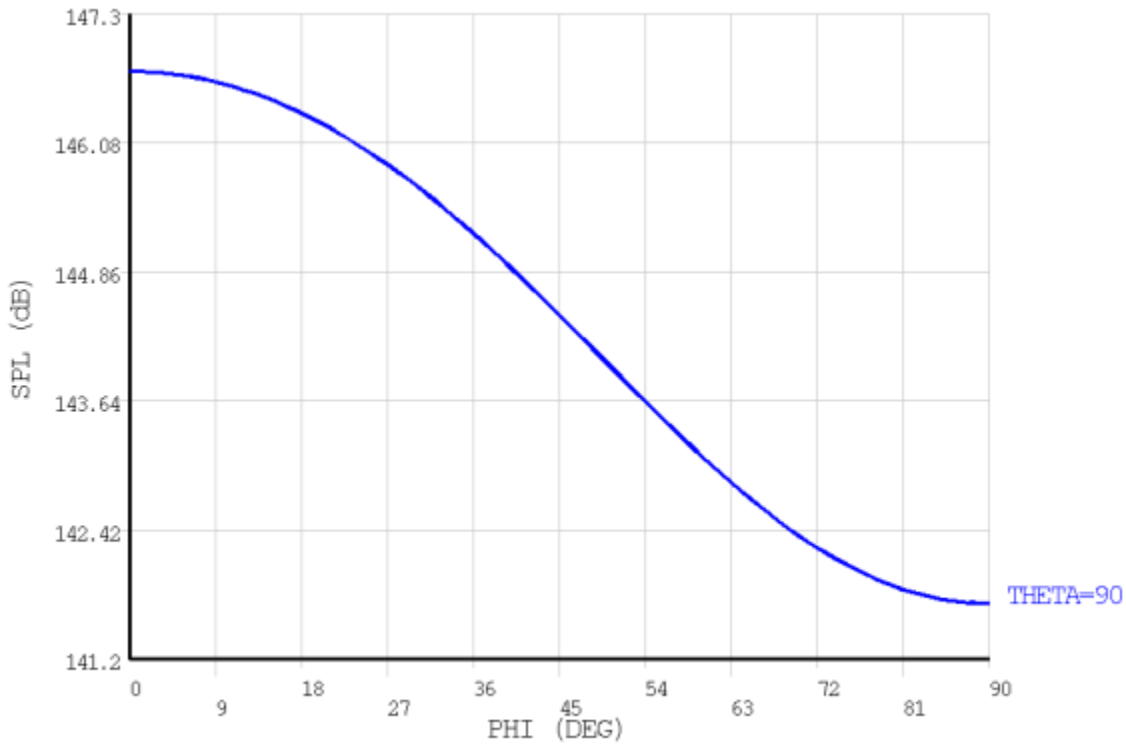
The following figures show the 2-D and 3-D plots followed by the two plots overlaid:

**Figure 33.8: 2-D SPL Plot**

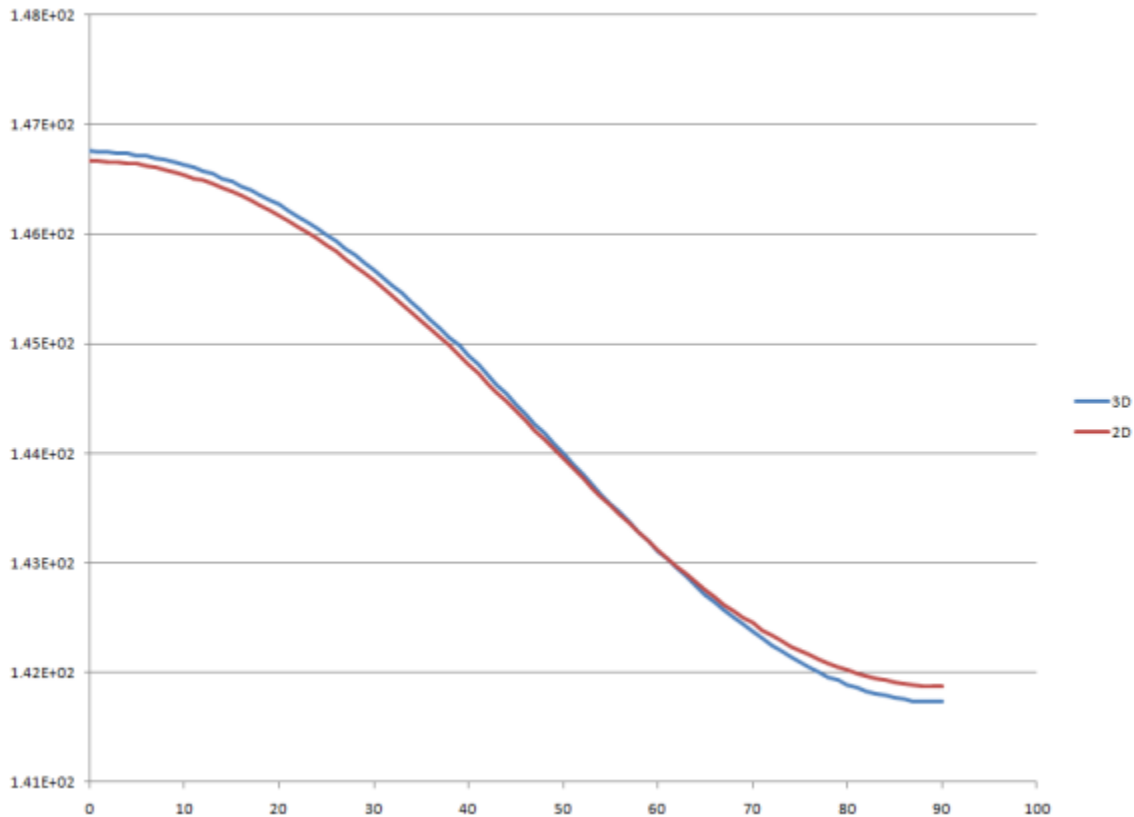


Plot of SPL at 1m distance (2D)

**Figure 33.9: 3-D SPL Plot**



Far-field plot of SPL at 1m (3D)

**Figure 33.10: Overlaid 2-D and 3-D Plots**

The plot overlay indicates good correlation between the 2-D and 3-D models.

---

### Note

The meshes for both cases were not identical, so some variation in the results was expected.

---

## 33.8. Recommendations

To perform a similar type of piezoelectric flextensional transducer analysis, consider the following hints and recommendations:

- For both the [FLUID129](#) infinite fluid element (2-D) and the Robin boundary condition (3-D), include at least a quarter-wavelength of fluid in a given direction, where the wavelength is based on the lowest frequency of interest.
- For linear (lower-order) fluid elements, use approximately 14-16 elements per wavelength, where the wavelength is based on the highest frequency of interest.

## 33.9. References

Theory behind the analysis of a flextensional transducer can be found in this resource:

1. Kang, K. and Y. Roh (1980). "Optimization of Structural Variables of a Flextensional Transducer by the Statistical Multiple Regression Analysis Method." *Journal of the Acoustical Society of America*. Ph.D. Thesis. University of California, Berkeley: USA.

## 33.10. Input Files

The following files were used in this problem:

- `xducer2d.dat` -- Input file for the 2-D analysis.
- `xducer2d.cdb` -- Common database file for the 2-D mesh (called by `xducer2d.dat`).
- `xducer3d.dat` -- Input file for the 3-D analysis.
- `xducer3d.cdb` -- Common database file for the 3-D mesh (called by `xducer3d.dat`).

The files are available in the `td-33` folder. See [Obtaining the Input Files \(p. xxxv\)](#) for more information.

---

## Chapter 34: Dynamic Simulation of a Nuclear Island

---

This example problem demonstrates a [power spectral density \(PSD\)](#) analysis of a nuclear island component of a nuclear power plant. The problem shows the analysis methods available to simulate the response of the nuclear island to a seismic event, taking into account motion incoherency and wave-passage effects.

The following features and capabilities are highlighted:

- Modal analysis of a large shell-type structure with high modal density.
- PSD analysis using enforced displacement.
- Capturing both motion incoherency and wave-passage effects.

Topics related to this example problem follow:

- [34.1. Introduction](#)
- [34.2. Problem Description](#)
- [34.3. Modeling](#)
- [34.4. Material Properties](#)
- [34.5. Boundary Conditions and Loading](#)
- [34.6. Analysis and Solution Controls](#)
- [34.7. Results and Discussion](#)
- [34.8. Recommendations](#)
- [34.9. References](#)
- [34.10. Input Files](#)

### 34.1. Introduction

Power spectral density (PSD) analysis is a widely used method for studying the responses of structures subjected to a random input. It is a statistical measure defined as the limiting root-mean square (RMS) value of a structure's response. In this analysis approach, the magnitudes of the response can be specified only by probability distribution functions that show the probability of the magnitude taking a particular value. It is assumed that the random input has a zero mean and that its values are Gaussian distributed.

The problem presented here uses PSD analysis to simulate the response of a nuclear island (NI) component of a nuclear power plant (NPP) to a seismic event, taking into account the partial correlation between ground motions occurring at various locations of the basemat. This effect is known as ground motion incoherency (GMI), and is of particular significance in cases where nearby faults generate short-duration, high-frequency waves.

GMI consists of spatial variation of both horizontal and vertical ground motions. The horizontal spatial variation of seismic ground motion is the result of the combination of three phenomena:

- Wave-passage effect, which is the difference in the arrival times of seismic waves at different locations.
- The incoherence effect, resulting from reflection and refraction of waves through the soil during their propagation, as well as the superposition of waves arriving from an extended source at various locations.

- The local effect, due to local soil conditions at each location.

Ground motions in recorded earthquake events exhibit spatial incoherency in high-frequency contents.[1][2] It is therefore important to account for these effects to accurately predict the response of the structure. By considering rock-like soil condition, the spatial variation due to both the wave-passage effect and the incoherency effect can be observed.

The method applied here could also be used to estimate structure-borne sound radiated into buildings such as concert halls when located within the immediate vicinity of railway lines. More generally, the same method can be applied to any simulation involving an incident field and/or wave with known statistical properties (involving frequency and space), such as an automotive windshield or a rocket nozzle.

For more information, see the following topics in the [Mechanical APDL Theory Reference](#):

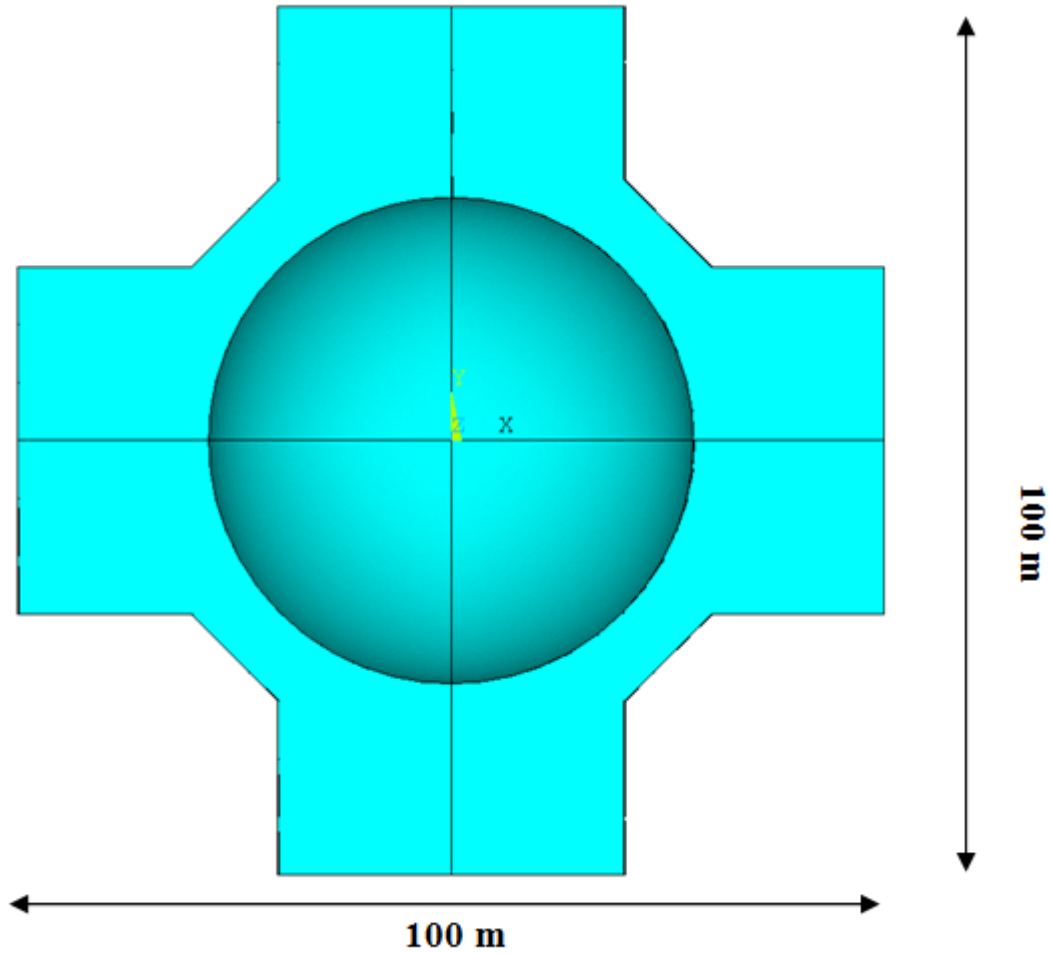
- [Spatial Correlation](#)
- [Wave Propagation](#)

## 34.2. Problem Description

An analysis of a structure excited by uniform base motion is a common task usually performed using tools such as response spectrum analysis (RSA). Accounting for ground motion incoherency effects requires additional modeling effort and computational resources, the benefit being a reduction of the response at the spectrum high frequency. This example demonstrates the determination of the reduction ratio using PSD analysis.

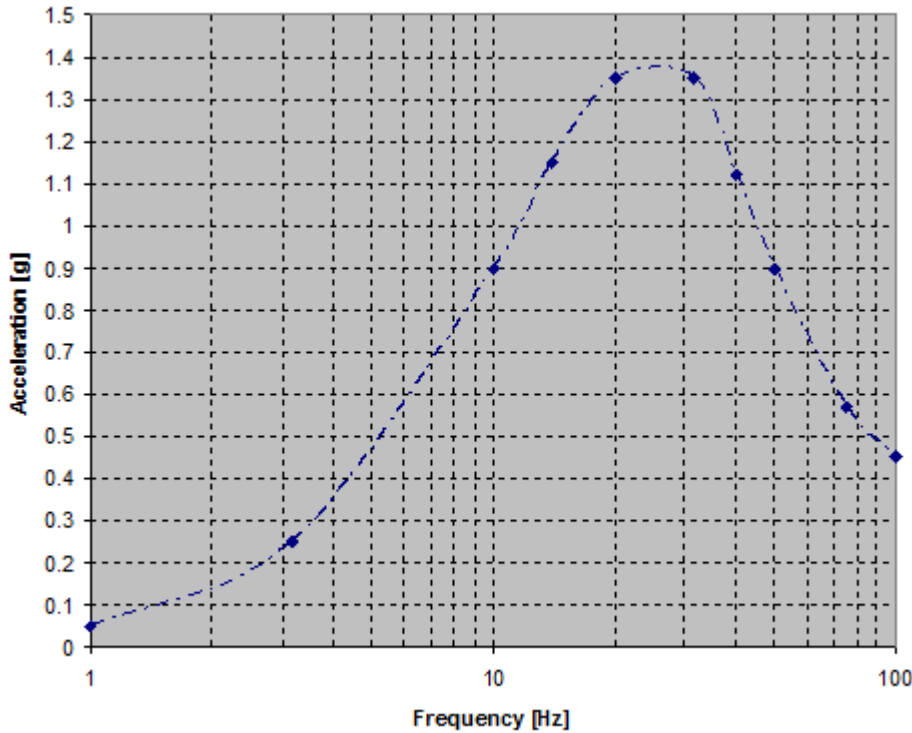
A nuclear island (NI) component of a typical modern nuclear power plant (NPP) is modeled. The model consists of one reactor building and four auxiliary buildings, all located on a single basemat. Each building encompasses five floor levels. Overall plan dimensions are 100 x 100 m<sup>2</sup>. The building height range is 40-50 m.



**Figure 34.1: NPP Structure Footprint**

The structure is excited by a typical base motion generated by a nearby fault. The event generates a high-amplitude, short-duration, high-frequency quake. Such loading is commonly applied in the form of a ground motion response spectrum (GMRS), which provides the peak response of a series of single-degree-of-freedom (SDOF) systems. The GMRS selected by Xu and Samaddar [1 (p. 533)] is used here and is shown in the following figure:

**Figure 34.2: Ground Motion Response Spectrum (5%)**



The GMRS typical of eastern United States sites is characterized by a high energy content in the high-frequency range (>10 Hz).

The GMI effects on responses can be incorporated using either the stochastic approach or the deterministic approach [6 (p. 533)]. The deterministic approach is used here. The following coherency functions describe the relationship between ground motions at separate locations as a function of the separation distance and the frequency of the ground motion [2]:

- The lagged coherency function.
- The plane-wave coherency function.
- The unlagged coherency function.

The plane-wave coherency function is used for this example, as it applies to rock-like soil conditions. The function is expressed as:

$$\gamma_{PW} = \left[ 1 + \left( \frac{F}{a_1 f_c} \tanh(a_3 \xi) \right)^{n_1} \right]^{-\frac{1}{2}} \left[ 1 + \left( \frac{F}{a_2 f_c} \tanh(a_3 \xi) \right)^{n_2} \right]^{-\frac{1}{2}}$$

where  $\gamma_{pw}$  is the plane wave coherency representing the random horizontal spatial variation of ground motion,  $F$  is the ground motion frequency,  $\xi$  is the separation distance between locations in meters,

and  $\tanh$  is the hyperbolic tangent function. All other parameters are given in the following table for horizontal and vertical ground motion:

**Table 34.1: Coherency Function Coefficients**

Coefficient	Horizontal Ground Motion	Vertical Ground Motion
$a_1$	1.647	3.15
$a_2$	1.01	1.0
$a_3$	0.4	0.4
$n_1$	7.02	4.95
$n_2$	$5.1 - 0.51\ln(\xi + 10)$	1.685
$f_c$	$-1.886 + 2.221\ln(4000 / (\xi + 1) + 1.5)$	$\exp[2.43 - .025\ln(\xi + 1) - 0.048 (\ln(\xi + 1))^2]$

Coherency functions are plotted as a function of frequency for various separation distances, as shown in [Figure 34.5: EPRI-TR 1014101 -- Plane Wave Coherency Model for Horizontal Direction \(p. 520\)](#).

### 34.3. Modeling

The entire building is meshed using four-node structural shell elements ([SHELL181](#)). Shell thickness is uniform (1 m) for the wall and slab, and the basemat thickness is 2 m.

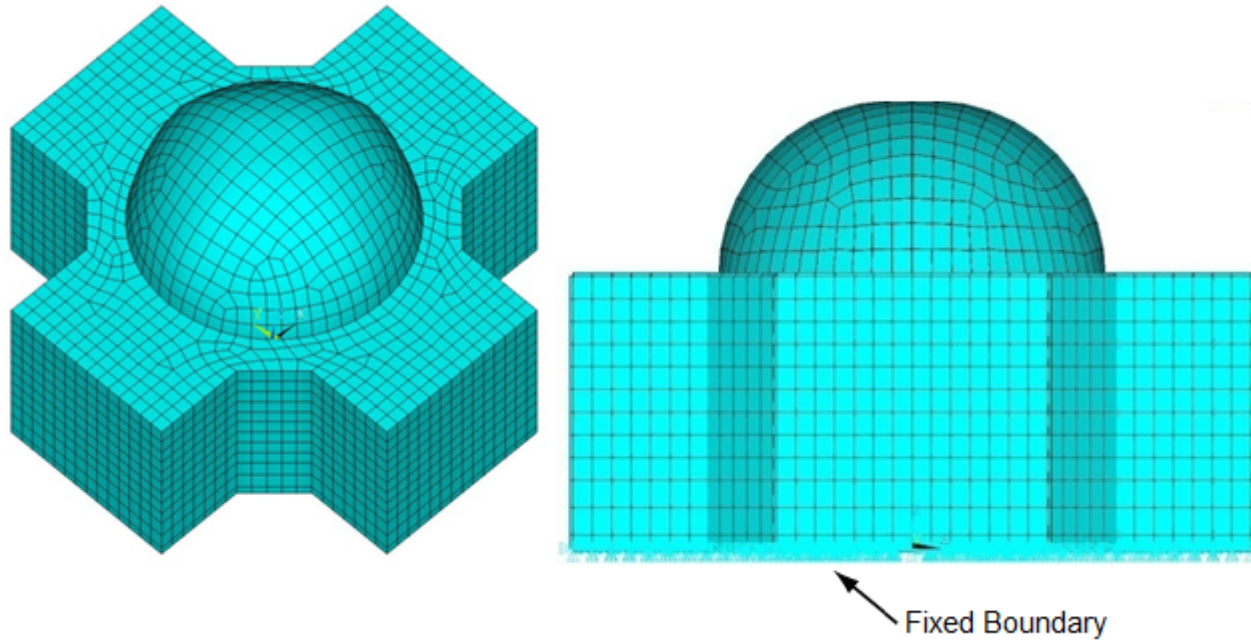
Mesh size is based on the shortest wavelength to be resolved. In this case, the flexural wavelengths can be predicted using the classical formula [[3 \(p. 533\)](#)]:

$$\lambda_b = 2\pi \left[ \frac{B}{\left(\frac{\omega^2}{m''}\right)} \right]^{\frac{1}{4}}$$

where  $\lambda_b$  is the flexural wavelength,  $B$  is the plate bending inertia per unit-length,  $\omega$  is the circular frequency, and  $m''$  is the plate mass per unit-length.

A cutoff frequency of 50 Hz is specified, which gives a bending wavelength of about 12 m. Using six elements per wavelength is sufficient and results in a mesh size of 2 m.

**Figure 34.3: NPP Structures FEM (Mesh Size Adapted to 50 Hz Cutoff Frequency)**



To simplify the problem in order to better illustrate the method, the following assumptions apply:

- **Soil structure-interaction (SSI) effects are ignored**

Ignored effects include the effects of waves reflected back to the soil/structure interface, and waves radiated following the structural motion. This assumption is conservative for very stiff, rock-like soil situations. The loading can be modeled as an enforced displacement (or acceleration) at the boundaries.

- **Damping is homogeneous within the structure.**

A rigorous treatment would require a distinction between prestressed (external shell and dome) and reinforced concrete parts damping. Because most of the structure is made of reinforced concrete, uniform damping is applied. This assumption is valid because the high-frequency seismic events are not expected to damage the building significantly. High-frequency events are less harmful to large, ductile concrete structures, but more detrimental to smaller, stiffer objects such as secondary components.

### 34.4. Material Properties

A material model typical of undamaged reinforced concrete is used:

Reinforced Concrete Material Properties	
Young's Modulus	35000 MPa
Poisson's Coefficient	0.2
Density	2500 kg/m <sup>3</sup>
Damping Ratio	0.04 (corresponding to stress level 1) [4 (p. 533)]

Reinforced Concrete Material Properties	
Soil Shear Wave Velocity	3000m/s (hard rock site)

## 34.5. Boundary Conditions and Loading

Boundary conditions are considered to be fixed (zero displacements) at all degrees of freedom (DOFs) of the basemat nodes, as shown in [Figure 34.3: NPP Structures FEM \(Mesh Size Adapted to 50 Hz Cutoff Frequency\)](#) (p. 518). It is assumed that the basemat follows the free-field ground motion exactly.

### 34.5.1. Loading

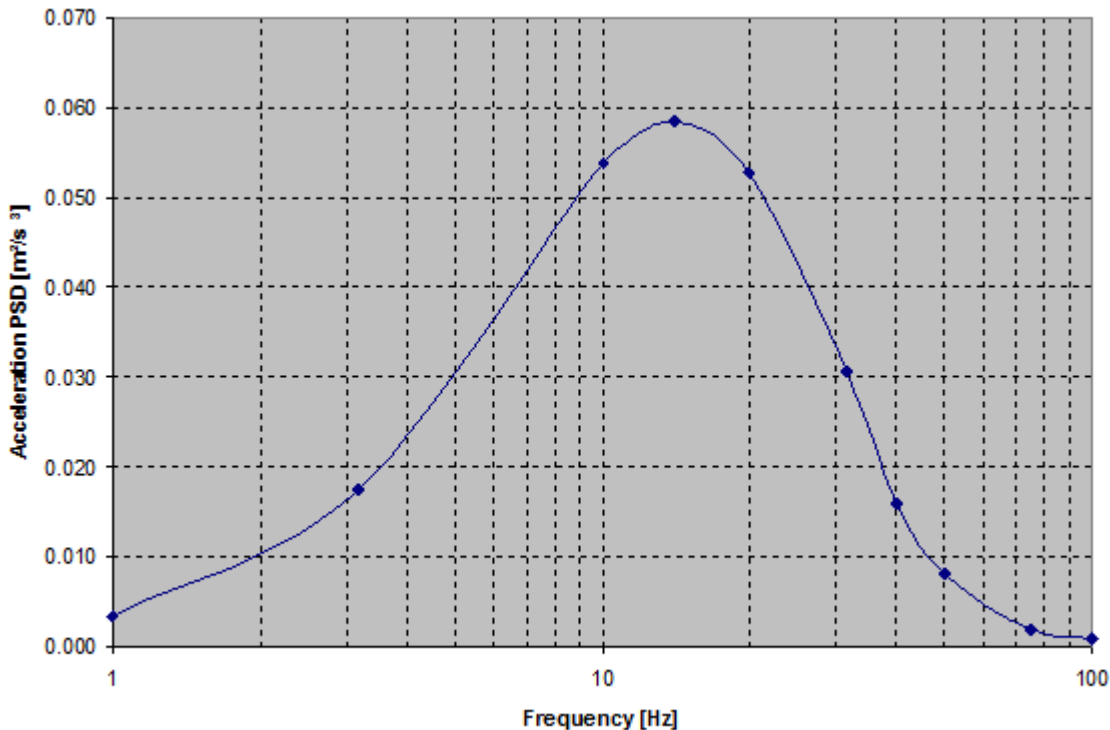
The probable SDOF system peak responses (response spectrum) is related to the PSD of the input signal using the following relationship [5 (p. 533)]:

$$G = \frac{2\xi}{\pi F} \frac{S_a^2(F, \xi)}{\ln(2FT_0)}$$

where  $G$  is the one-sided ground-motion acceleration PSD ( $(\text{m/s}^2)^2/\text{Hz}$ ),  $\xi$  is the damping ratio,  $F$  is the excitation frequency,  $S_a(F, \xi)$  is the acceleration response spectrum, and  $T_0$  is the earthquake duration (s).

The following acceleration PSD can be obtained assuming a 5 s duration earthquake:

**Figure 34.4: Ground Motion Power Spectral Density (Acceleration PSD)**

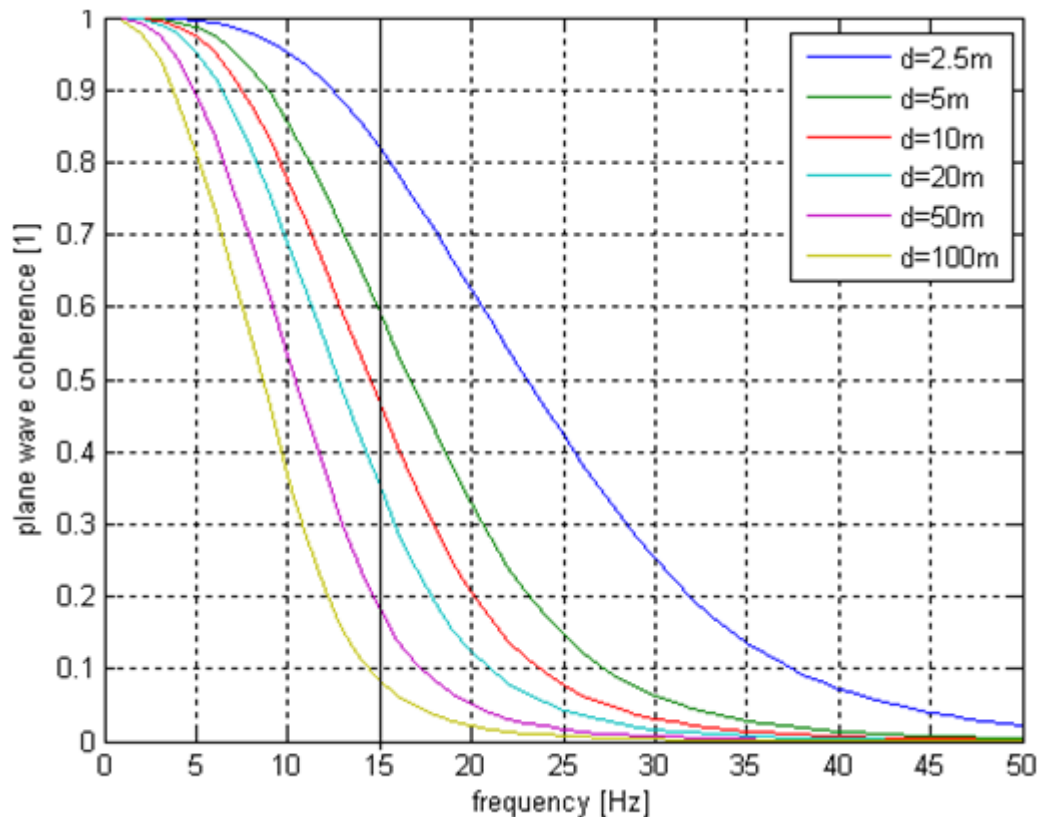


The acceleration PSD is required to run a single point (coherent) PSD analysis. In the case of multiple partially coherent excitations, it is necessary to perform these additional tasks:

- Calculate the participation factor pertaining to each region being used.
- Calculate the direct and cross participation of each pair of regions to the overall response.

A suitable region size should be selected based on the central frequency and the spatial coherency model used. The coherence curve shown in the following figure is used to determine the minimum size of the region:

**Figure 34.5: EPRI-TR 1014101 -- Plane Wave Coherency Model for Horizontal Direction**



By definition, the coherence function is unity for coherent input. The figure shows that the coherence function is near unity at low frequencies (less than 5 Hz), and that it decreases with frequency and separation distance between the observations points in the free-field. A decrease in response amplitudes for high-frequency vibration modes can therefore be expected.

At a given frequency, two points experience correlated motion if the coherence value is close to unity (or approximately above 0.6).

At a frequency of 15 Hz (the peak of PSD curve), two points distant by more than 5 m would exhibit a coherency below 0.6. To be rigorous, a region size of 5 m should be used; for a 100 x 100 m square basemat,  $20 \times 20 = 400$  regions would therefore be required. Here, a 10 m region size is used to moderate the problem size while capturing the primary phenomena.

To capture wave-passage effects, a region size smaller than the wavelength should be used. To simplify the analysis, it is assumed that the NPP is excited by a wave exhibiting a horizontally propagating direction, with the wavelength equal to:

$$\lambda = \frac{c_s}{F_{cut}}$$

where  $\lambda$  is the wavelength,  $F_{cut}$  is the cutoff frequency, and  $C_s$  is the soil shear wave velocity.

With a cutoff frequency of 50 Hz and a soil shear wave velocity of 3000 m/s, the resulting dominant wavelength is 60 m. Based on a minimum of six regions per wavelength, the region size is input as 10 m.

## 34.6. Analysis and Solution Controls

The PSD analysis occurs in three steps:

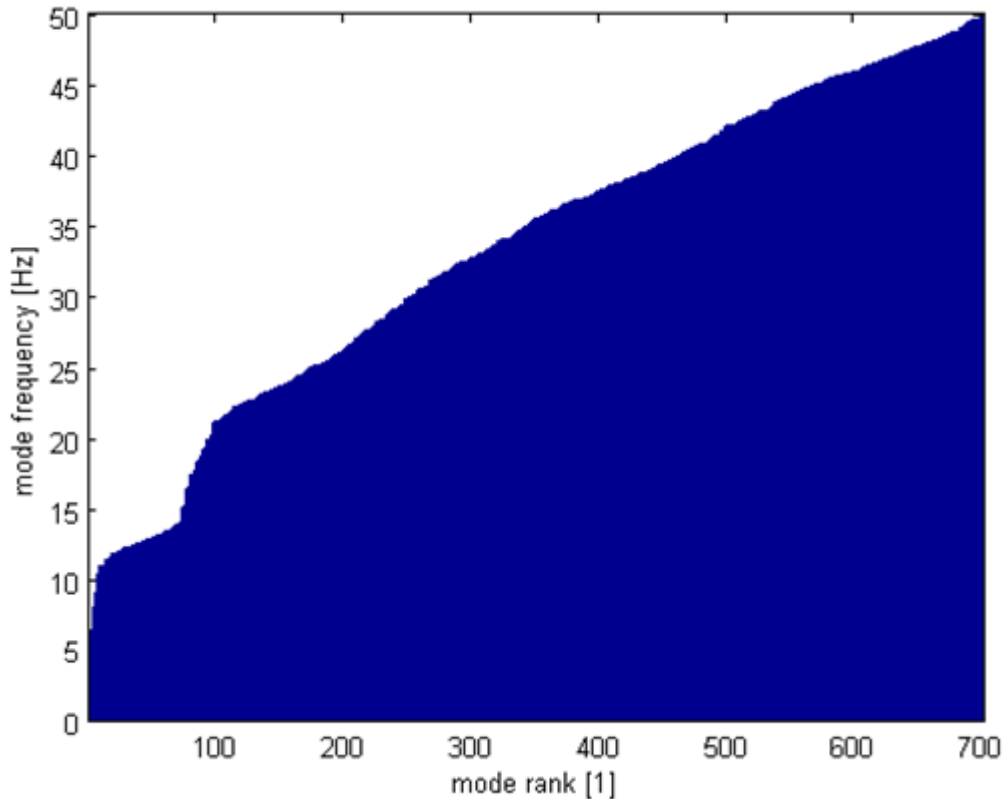
1. Perform a modal analysis of the entire NI. (p. 521)
2. Perform a PSD analysis using enforced displacements. (p. 522)
3. Evaluate the response PSD (RPSD). (p. 523)

### 34.6.1. Step 1: Modal Analysis

A modal analysis is performed using the Block Lanczos eigensolver, which is well suited for extracting a medium number of modes (a few hundred) from a moderate-sized model (< 50K DOFs in this case).

Because no element results are needed, only nodal solutions (nodal displacements and rotations) are requested.

As a general rule, plate-type structures exhibit constant modal density in the medium frequency range. As shown in the following figure, the number of modes within a given frequency range is approximately constant above 22 Hz:

**Figure 34.6: Constant Modal Density Checking**

The following input fragment shows the analysis steps involved:

```

/solu

antype,modal                ! Perform modal solve
modopt,lanb,150,-1.0,50    ! Use Block Lanczos eigensolver to extract 150
                             ! modes with begin frequency FREQB = -1 Hz and with end frequency, FREQE = 50 Hz

outres,all,none
outres,nsol,all            ! Only nodal solution data written to the database
solve
finish

/com, Modes selection based on mode coefficients (ModSelMethod=MODC)
/solu
antype,modal,restart
mxpand,150,,,NO,,,modc    ! Expand all modes and do not evaluate element results
outres,all,none
outres,nsol,all
solve
fini

```

### 34.6.2. Step 2: PSD Analysis

PSD analyses are performed on the NI using:

- Fully coherent input motion with no wave passage effect.
- Partial coherent input motion with no wave passage effect.
- Partial coherent input motion with wave passage effect.



In each analysis type, the same ground input motion is considered.

For each region (elementary excitation), a unit nodal displacement is input (**D**), and then modal participation factors are evaluated (**PFACT**). This is most easily achieved by using an APDL do-loop.

Elementary excitation must be defined for each region using PSD tables. The magnitude-vs.- frequency data can be input with a PSD table (via **PSDFRQ**, which defines the frequency points of an input spectrum, and **PSDVAL**, which defines the PSD values of an input spectrum). The PSD curve as defined in [Figure 34.4: Ground Motion Power Spectral Density \(Acceleration PSD\) \(p. 519\)](#) must be used as an input spectrum. Additionally, the input motion has a unit of acceleration (defined via **PSDUNIT**).

For cross excitations, PSD co-spectral values are obtained by multiplying the original (direct) PSD values with the plane-wave coherence value, as defined in [Figure 34.5: EPRI-TR 1014101 -- Plane Wave Coherency Model for Horizontal Direction \(p. 520\)](#), frequency by frequency (**COVAL**).

For cases where wave-passage effects must be considered, cross PSDs have both a real part (defined via **COVAL**) and an imaginary part (defined via **QDVAL**). Both terms are equal to the previous cross-PSD value multiplied by a phasor of unit amplitude, and have an argument equal to the phase shift between the two locations considered. The relationship can be expressed as [2]:

$$PSD_{WavePassage}(F, d_{ij}) = PSD_{PlaneWave}(F, d_{ij}) e^{-i2\pi f \frac{(d_{ij})N}{c_s}}$$

where  $PSD_{WavePassage}$  is the co-spectral values of cross PSDs with wave-passage effect,  $PSD_{PlaneWave}$  is the spectral values of cross PSDs with no wave-passage effect, and  $d_{ij}$  is the distance between the two locations  $i$  and  $j$ .

The distance  $d_{ij}$  depends on whether the incoherency or the wave-passage effects are being considered:

- For incoherency,  $d_{ij}$  is the Euclidian distance between the two locations (that is, the conventional distance).
- For wave-passage effects,  $d_{ij}$  is the distance along the propagation (orientation) vector. It is the dot product of the vector  $d_{ij} \cdot N$ , where  $d_{ij}$  is the vector between nodes  $i$  and  $j$ , and  $N$  is the unitary orientation vector defining the propagation direction).

For simplicity, wave-propagation along the global X-axis is assumed .

Because the absolute acceleration result is the only quantity of interest, only this single calculation is requested (**PSDRES**).

### 34.6.3. Step 3: Response PSD (RPSD) Calculation

The response PSD of absolute acceleration quantity is calculated in the POST26 postprocessor (**RPSD**) and plotted on log-log scale to derive the frequency-by-frequency reduction ratio, as shown in [Figure 34.9: PSD Reduction Due to Incoherency and Wave-Passage Effects \(p. 528\)](#).

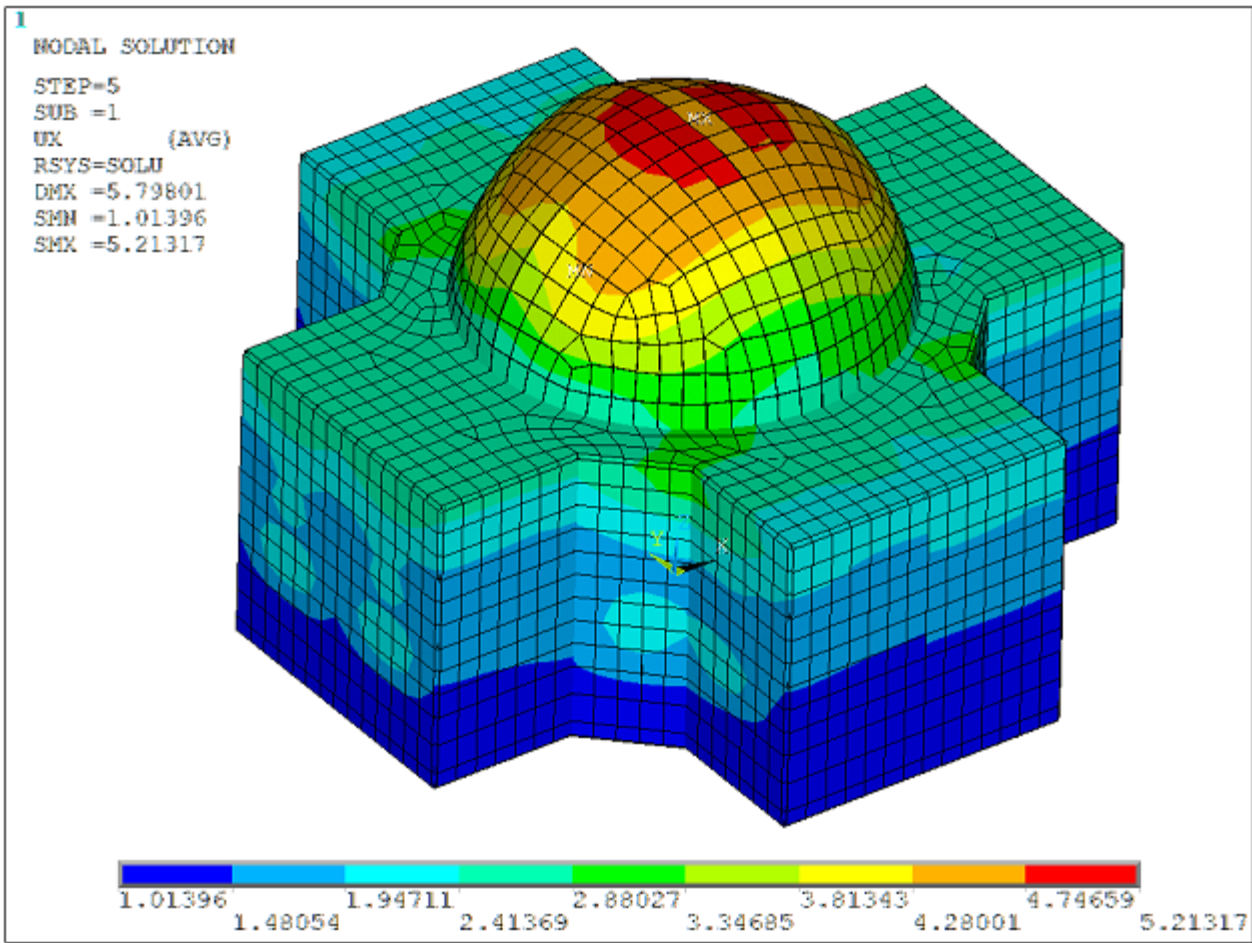
## 34.7. Results and Discussion

The primary results are obtained as RMS acceleration values on the entire structure via the POST1 postprocessor (**SET,5,1**).

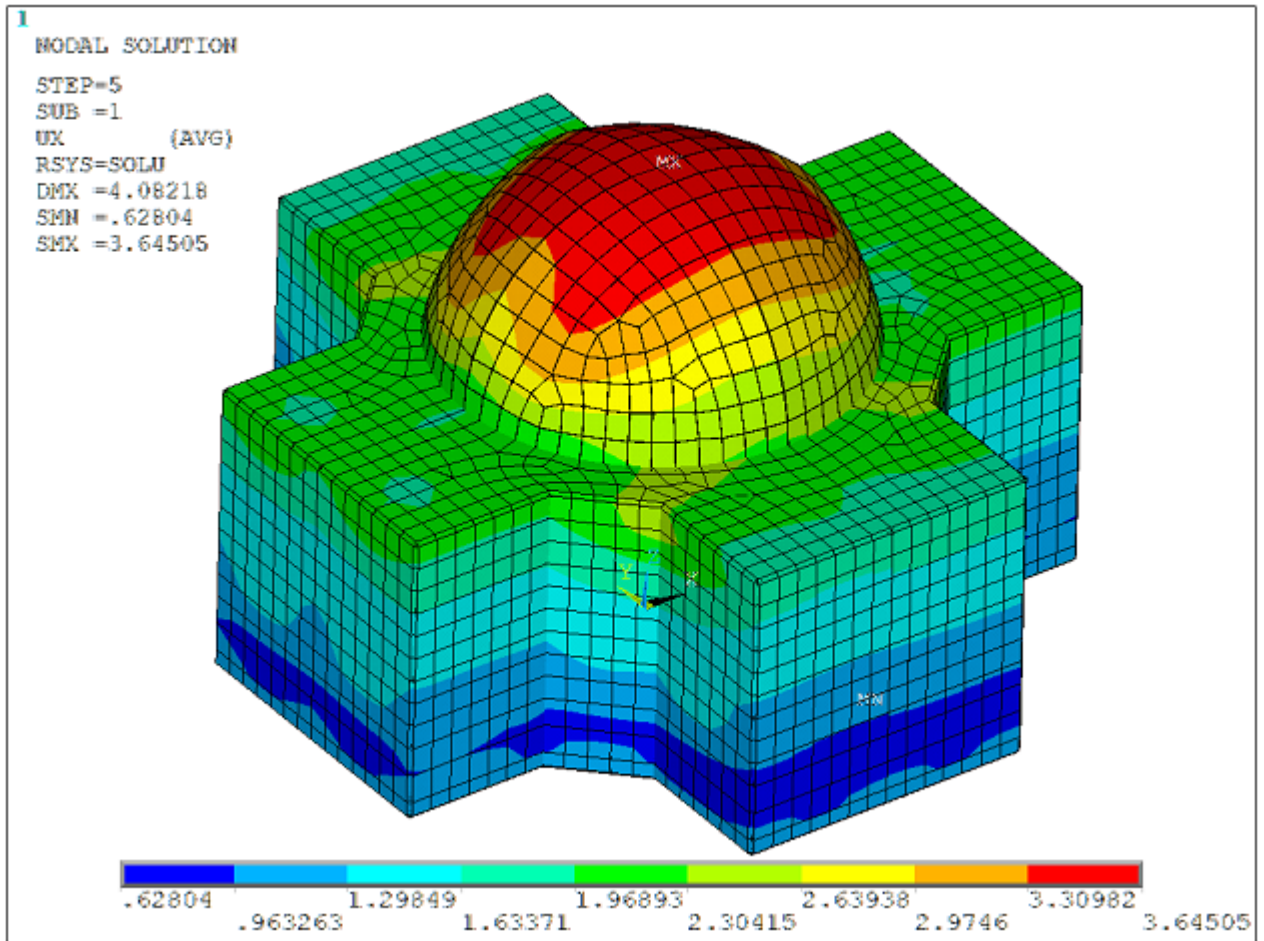
**Figure 34.7: 1- $\sigma$  Absolute Acceleration Values on NPP**

(A) and (B) show that the motion incoherency effects on the nodal solutions are significant, and that the overall response has been reduced. (B) and (C) reveal that the consideration of wave-passage effects further reduces the overall response.

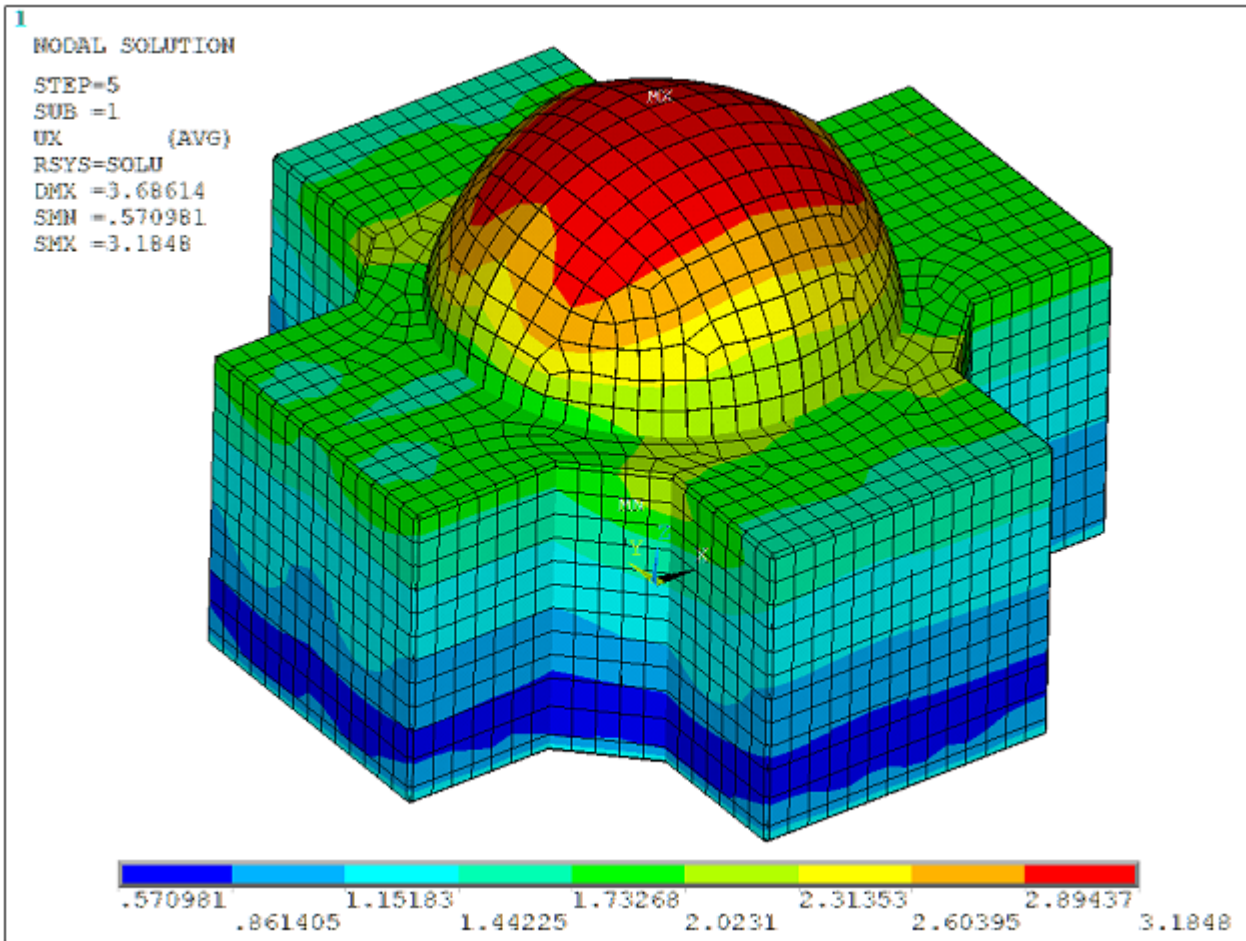
**(A) Fully Coherent Input with No Wave Passage Effect**



**(B) Partially Coherent Input with No Wave Passage Effect**

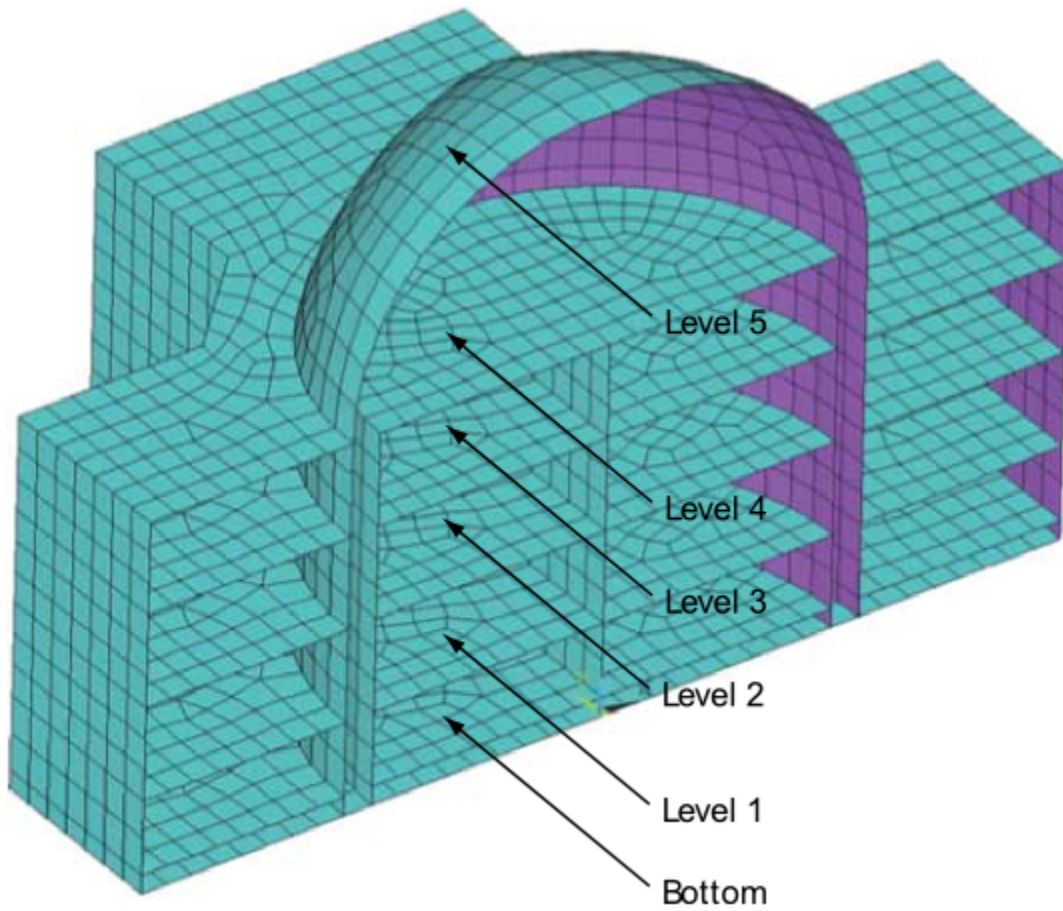


(C) Partially Coherent Input with Wave Passage Effect



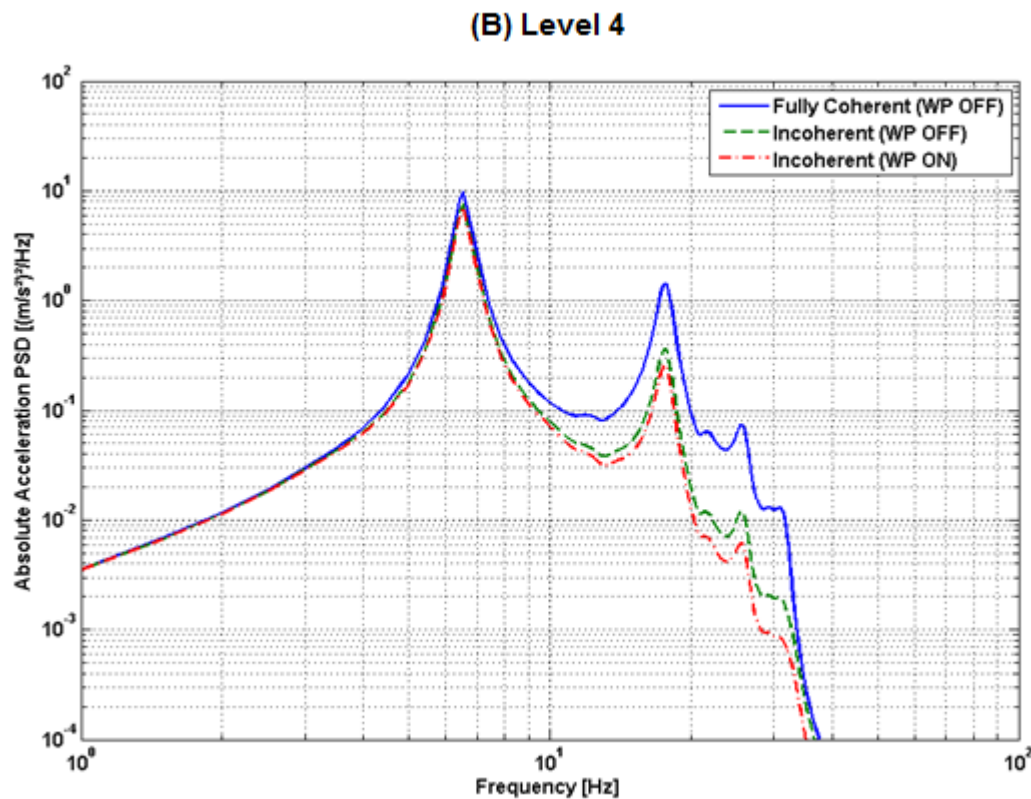
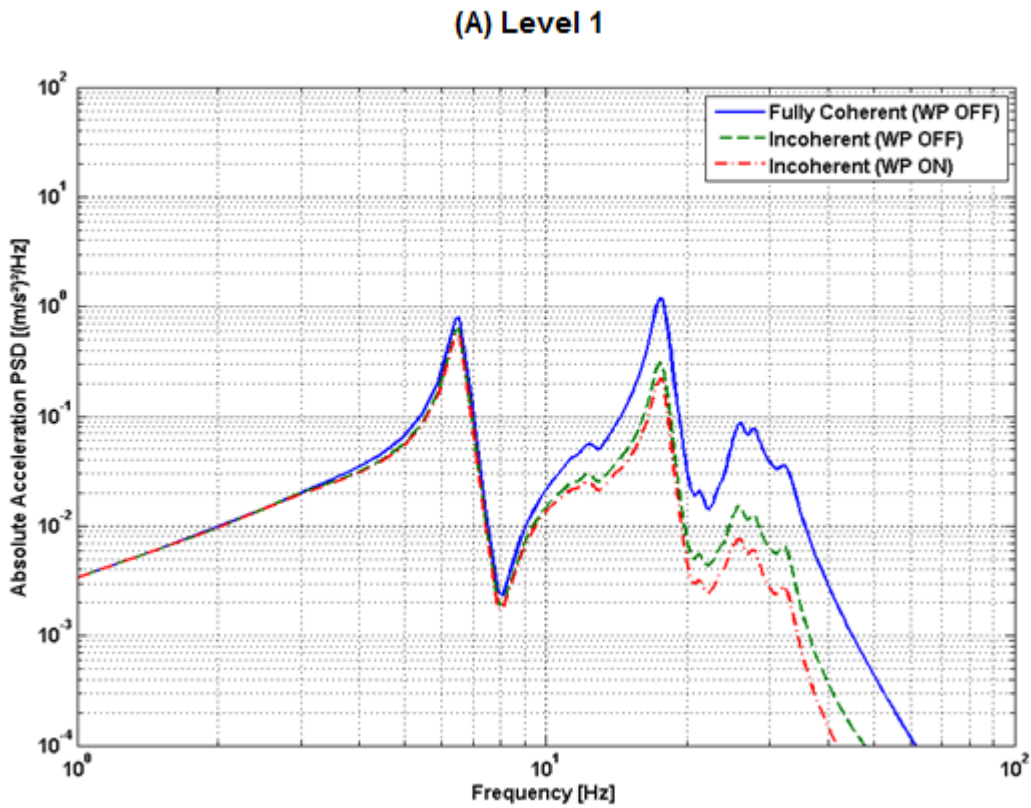
The plots provide information about the overall response reduction only. To derive the frequency-by-frequency reduction ratio, the acceleration response PSDs at various locations of the structure using both coherent and incoherent inputs are compared.

The following figure shows a comparison of response PSDs obtained at the building centerline at five different elevations (**RPSD**):

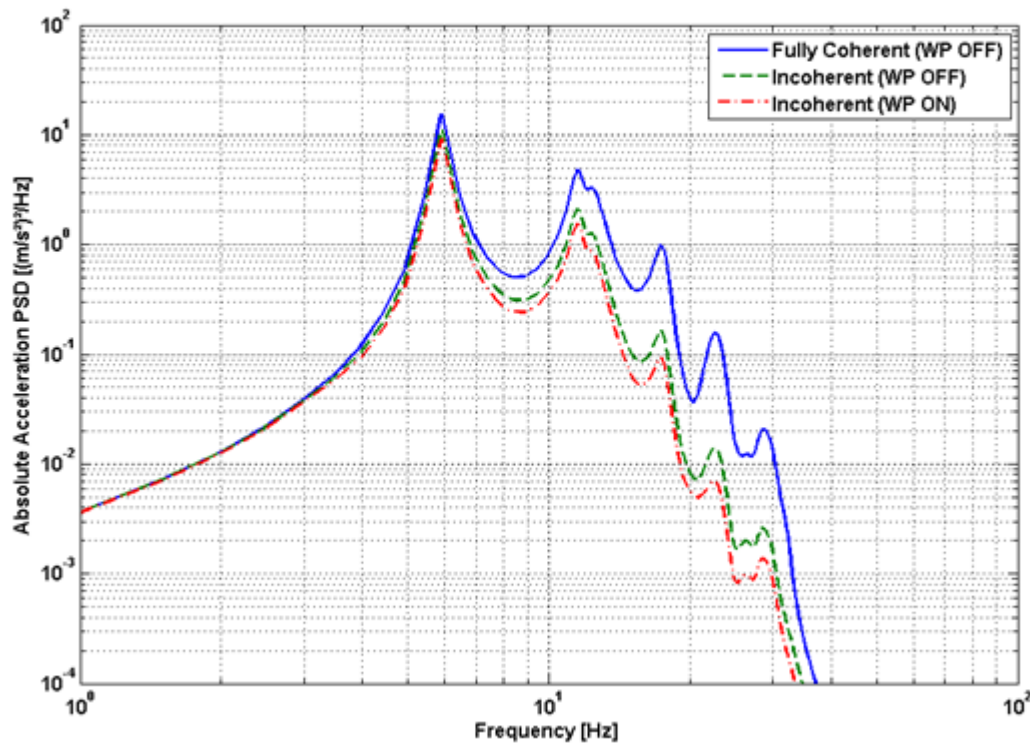
**Figure 34.8: Keypoints Location for Estimation of PSD Reduction**

The following figure shows the results for levels 1, 4, and 5:

Figure 34.9: PSD Reduction Due to Incoherency and Wave-Passage Effects



(C) Level 5 (Top of the Dome)



The observations are as follows:

- In Eastern United States rock sites, ground motions generally exhibit high energy content for frequencies 10 Hz and above. When high-frequency ground motion is applied to the NPP model, it is expected that out-of-phase high-frequency modes will be randomly distributed across the foundation footprint in accordance with the specified coherency function. The incoherency effect should therefore reduce the high-frequency responses.
- The motion incoherency effects reduce the responses for all frequency ranges, especially in the high-frequency range above 10 Hz. For frequencies below 10 Hz, the responses are virtually identical for incoherent and coherent ground inputs.
- The combined effects of motion incoherency and wave-passage effects are significant, and they further reduce the responses in the high-frequency range.
- The points situated farthest from the excitation location are affected more by incoherent input as a result of the smearing effect due to numerous contributors.

### 34.7.1. Performance Evaluation

To expose the parallelism of the analysis procedure, both Mechanical APDL R14.0 and R14.5 are used. Shared-memory parallelism (SMP) is initially activated with two processing cores (invoked via the `-np` command in batch runs).

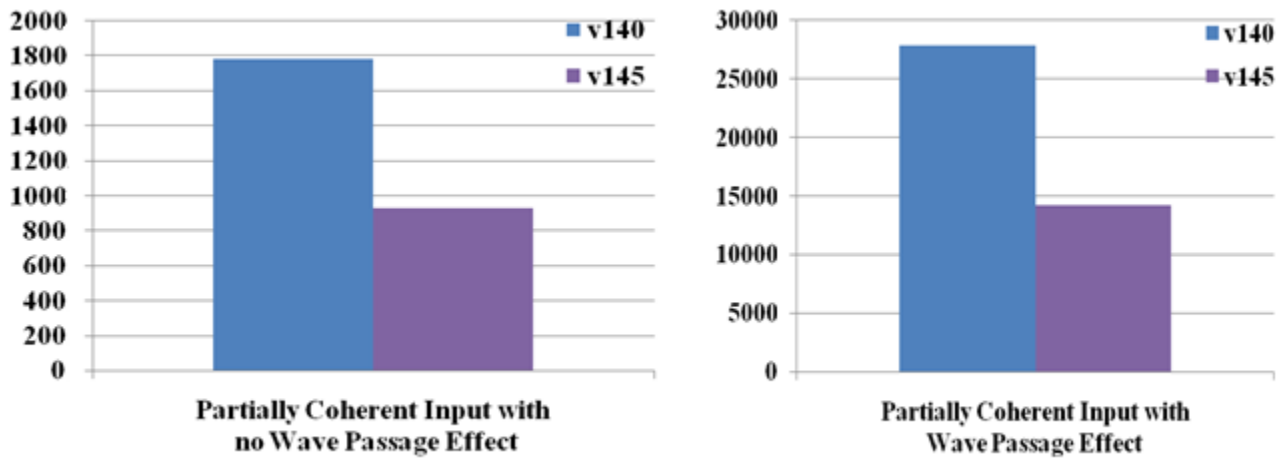
The following table shows the performance gains:

**Table 34.2: Comparison of Wall Time**

	Fully Coherent Input with No Wave Passage Effect			Partially Coherent Input with No Wave Passage Effect			Partially Coherent Input with Wave Passage Effect		
	Solution Time (Sec)	PSD Table	Post-Processing Time (Sec)	Solution Time (Sec)	PSD Table	Post-Processing Time (Sec)	Solution Time (Sec)	PSD Table	Post-Processing Time (Sec)
<b>R14.0</b>	12	1	10	1785	21	1908	27852	68	31519
<b>R14.5</b>	10	1	6	927	21	723	14196	68	14196

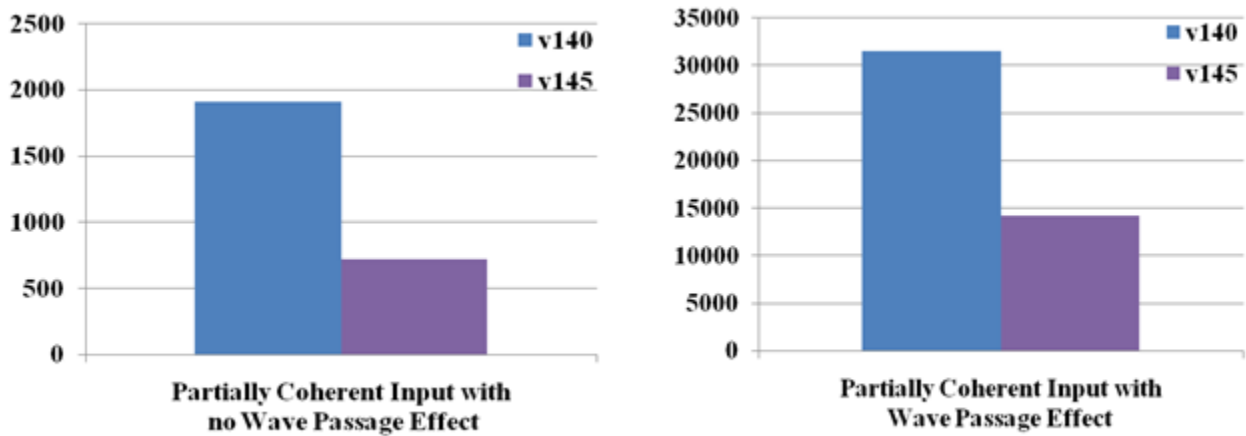
The following figure shows the solution time (the covariance matrix calculation) required for the PSD analyses with partially coherent input motion with and without the wave-passage effect:

**Figure 34.10: Comparison of Wall Time Spent on Solution**



The following figure shows the time required for the response PSD calculation (the POST26 elapsed time) or the PSD analyses with partially coherent input motion with and without the wave-passage effect:



**Figure 34.11: Comparison of Wall Time for RPSD Calculation (POST26 Postprocessing Time)**

Both figures show that the elapsed time for solution and postprocessing is substantially lower in Mechanical APDL R14.5.

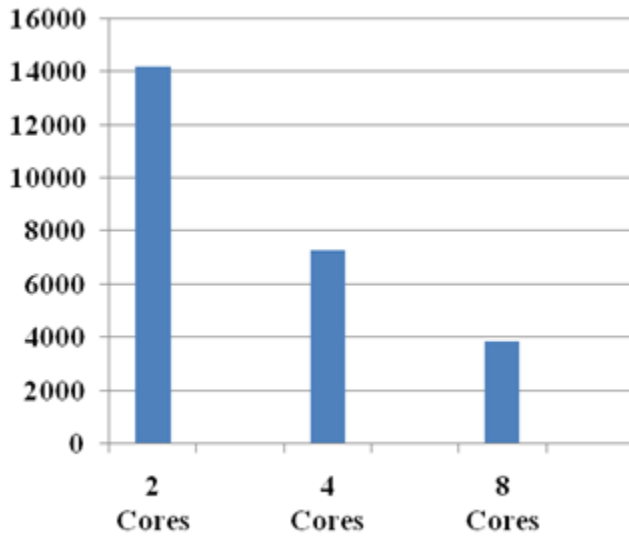
It is of interest to evaluate the scalability of SMP on Mechanical APDL R14.5 using various numbers of cores, with a maximum of 8 cores.

The following table shows the wall time of the PSD analyses with partially coherent input motion with wave-passage effect for various numbers of cores:

**Table 34.3: Comparison of Wall Time for Various Numbers of Cores (R14.5)**

	2 Cores		4 Cores		8 Cores	
<b>Partially Coherent Input with Wave Passage Effect</b>	Solution Time (Sec)	Postprocessing Time (Sec)	Solution Time (Sec)	Postprocessing Time (Sec)	Solution Time (Sec)	Postprocessing Time (Sec)
	14196	14196	7316	7274	3867	3728

The following figure shows the solution time (covariance matrix calculation) required using various numbers of cores:

**Figure 34.12: Comparison of Wall Time of Solution for Various Numbers of Cores**

The same trend is observed for the POST26 postprocessing wall time.

Computational time spent on solution and postprocessing for four cores is nearly half that of two cores, meaning that a performance increase up of about 2x is achieved. Similar comparisons have also been observed with eight-core and four-core runs. It can therefore be concluded that the scalability of the SMP-based solver is good.

## 34.8. Recommendations

The following recommendations are suggested for PSD analyses that account for the effects of motion incoherency and wave-passage effect:

- Select proper input ground motion based on site conditions. The input ground motion considered here is for rock-like soil conditions.
- Choose coherency functions based on the knowledge of time lags between the locations per the site conditions.
- The mesh size should be able to resolve the shortest wavelength.
- Select a suitable region size based on the coherency model used, central frequency, and the problem type. The size of regions should be such that they capture motion incoherency and wave-passage effects.
- Include a suitable number of modes in the analysis based on the cutoff frequency and the study of modal density.
- Execute a few test runs using a minimal number of modes, as the cost of the analysis can grow rapidly. The growth ratio is governed by the number of regions (or more specifically, the number of PSD tables) to the power of 2, as well as the number of modes, also to the power of 2. The total analysis duration is therefore predictable after a single test run. Parallelization is recommended.

## 34.9. References

The following references are used in this example problem:

1. Xu, J. and S. Samaddar. "Case Study: Effect of Soil-Structure Interaction and Ground Motion Incoherency on Nuclear Power Plant Structures." *ASME 2009 Pressure Vessels and Piping Conference*. 26-30 July 2009, Prague. Vol. 8. Seismic Engineering, 2009. 369-377.
2. Abrahamson, N. "Program on Technology Innovation: Spatial Coherency Models for Soil-Structure Interaction." Electric Power Research Institute. TR 1012968. 2006.
3. Cremer, L., M. Heckl, and E.E. Ungar. *Structure Borne Sound*. 2nd ed. Berlin: Springer-Verlag, 1990.
4. American Society of Civil Engineers. *Seismic Analysis of Safety-Related Structures and Commentary*. 1999.
5. Preumont, A. *Random Vibrations and Spectral Analysis*. Dordrecht; Boston: Kluwer, 1994.
6. Ghiocel, D. M. "Stochastic Simulation Methods in Engineering Predictions." *Engineering Design Reliability Handbook*. Eds. Nikolaidis, Ghiocel and Singhal. New York: CRC Press, Taylor & Francis, 2005.

## 34.10. Input Files

The following files are used in this example problem:

### Nuclear Island Model:

- `Dummy_NPP.db` -- Database for the nuclear island model.
- `EPRI_TR1014101.MAC` -- Macro for calculating plane-wave coherency values, per EPRI-TR 101401 Tables 3-4 and 3-5.

### PSD Analyses:

- `PSD_fully_correlation_no_wave_passage.dat` -- Input file for fully coherent input PSD with no wave passage effect.
- `PSD_partial_correlation_no_wave_passage.dat` -- Input file for partial coherent input PSD with no wave passage effect.
- `PSD_partial_correlation_wave_passage.dat` -- Input file for partial coherent input PSD with wave passage effect.

The files are available in the `td-34` folder. See [Obtaining the Input Files \(p. xxxv\)](#) for more information.



---

## Chapter 35: Elastoplastic Creep Analysis of Lead-Free Solder Bumps

---

This example problem demonstrates a thermo-mechanical analysis of lead-free solder bumps subjected to cyclic thermal loading.

The following features and capabilities are highlighted:

- Obtaining implicit creep material constants using experimental data.
- Using creep and plasticity material models to simulate viscoplastic behavior.
- Determining accumulated creep strain due to thermal loading.

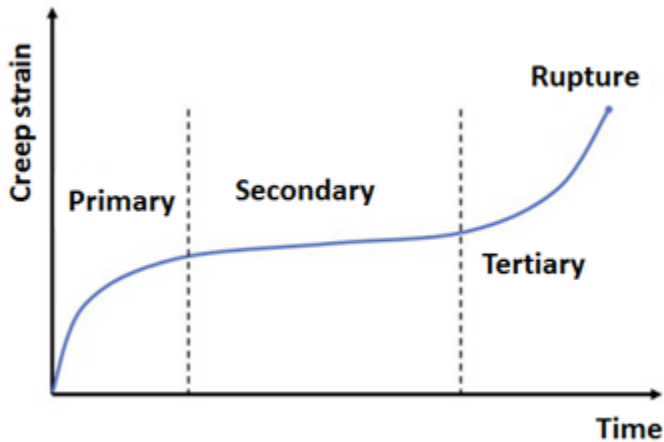
Topics related to this example problem follow:

- 35.1. Introduction
- 35.2. Problem Description
- 35.3. Modeling
- 35.4. Material Properties
- 35.5. Boundary Conditions and Loading
- 35.6. Analysis and Solution Controls
- 35.7. Results and Discussion
- 35.8. Recommendations
- 35.9. References
- 35.10. Input Files

### 35.1. Introduction

Creep is a **rate-dependent** material nonlinearity in which the material continues to deform under a constant load. Creep occurs as a result of long-term exposure to a high level of stress that does not exceed the yield strength of the material. Creep is more severe in materials subjected to heat for long periods. The creep strain rate can be a function of stress, time, temperature, and neutron flux level.

Under constant load, the uniaxial strain-vs.-time creep behavior is illustrated in the following figure:

**Figure 35.1: Creep Stages**

In the primary stage, which tends to occur over a comparatively short period, the strain rate decreases with time. The secondary stage exhibits an associated constant strain. In the tertiary stage, the strain rate increases rapidly until failure (rupture). Typically, the primary and secondary stages of creep are usually of greatest interest.

In static or transient structural analysis, creep can be simulated via implicit creep models. Compared to other creep methods, implicit creep is preferred as it is computationally faster and more accurate. The primary and secondary stages of creep can be simulated using different implicit creep material models, as shown in the following table:

**Table 35.1: Implicit Creep Models**

Creep Equation Description	Type
Strain Hardening	Primary
Time Hardening	Primary
Generalized Exponential	Primary
Generalized Graham	Primary
Generalized Blackburn	Primary
Modified Time Hardening	Primary
Modified Strain Hardening	Primary
Generalized Garofalo	Secondary
Exponential Form	Secondary
Norton	Secondary
Combined Time Hardening	Both
Rational Polynomial	Both
Generalized Time Hardening	Primary
User-Defined Creep	Any

The creep model can be selected based on available experimental data.

The temperature fluctuations endured by flip chip packages can cause progressive damage in solder joints. Damage accumulation beyond certain limits results in electrical failure. Such failures are typically

the result of thermal-expansion mismatches between the materials used [1]. The mismatches lead to a complex deformation behavior, and are associated with irreversible, temperature- and strain-rate or time-dependent inelastic characteristics, producing viscoplastic deformation in and around the solder joints. Deformation behavior can be simulated via viscoplastic material models, or by a creep model used with a plasticity material model.

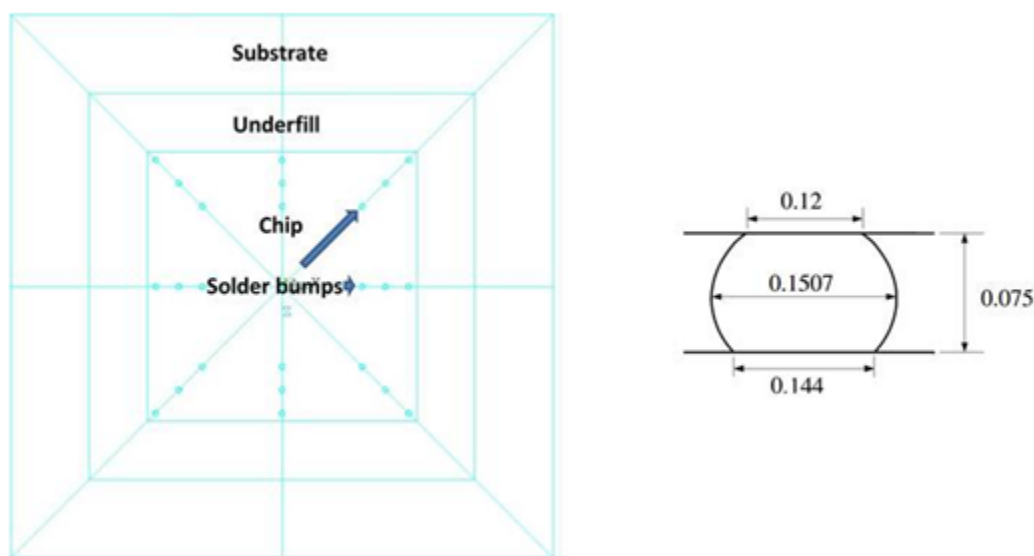
In the electronics industry, a primary goal of thermo-mechanical analysis is to simulate the stress and strain responses of the solder joint to better predict its service reliability. The problem presented here is a thermo-mechanical analysis of flip chip packages using creep and plasticity material models.

Because the harmful health-related effects of lead has forced electronic manufacturers to reduce their use of toxic heavy metals (including lead) in solders, thermo-mechanical analysis for solder joints becomes increasingly important as reliable alternative solders to replace lead-based solders are explored [2]. This example uses a lead-free solder 96.5Sn-3.5Ag.

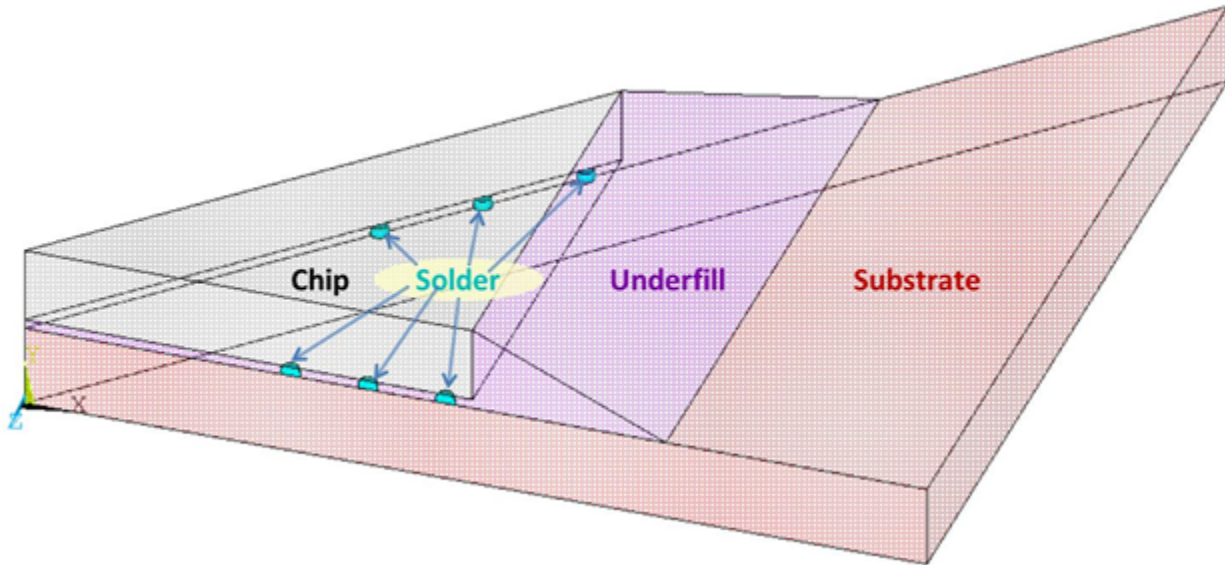
## 35.2. Problem Description

The flip chip package comprises chip, underfill, substrate, and solder as shown in the following figures:

**Figure 35.2: Distribution of Solder Bumps in Full Flip Chip Model and Size of Solder Bump**



The size of the chip is 6.95 mm × 6.95 mm × 0.6 mm. The size of the substrate is 14 mm × 14 mm × 0.65 mm. The distance between chip and substrate is 0.075 mm. The diameter of the upper pad, the diameter of the lower pad, and the width of the solder bump are 0.12 mm, 0.144 mm, and 0.1507 mm, respectively.

**Figure 35.3: 1/8 Symmetry of Flip Chip Pack**

To minimize the number of degrees of freedom, and therefore the computational resources required for the thermo-mechanical analysis, a 1/8 symmetry of the full model is used. To determine the cyclic thermal load effect on the solder joint, a generalized Garofalo creep model is used for the secondary stage of the creep analysis.

## 35.3. Modeling

The following modeling work is necessary for this example problem:

[35.3.1. Flip Chip Modeling](#)

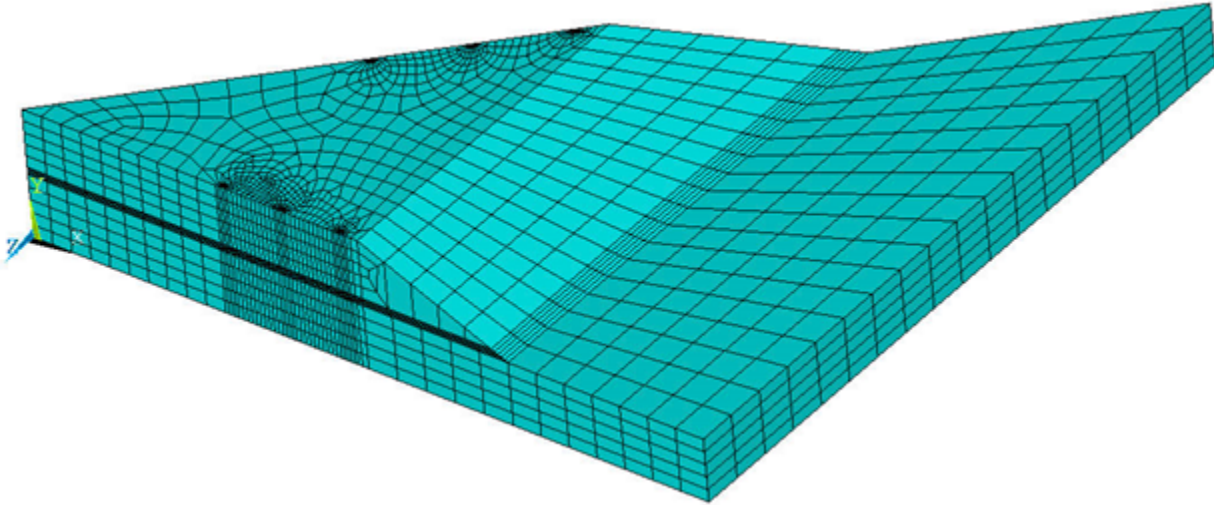
[35.3.2. Contact Modeling](#)

The completed model contains 57,134 nodes and 11,558 3-D 20-node hexahedron structural solid elements.

### 35.3.1. Flip Chip Modeling

Thermal element [SOLID90](#) is used for all parts of the flip chip model as shown in this figure:



**Figure 35.4: Flip Chip Mesh with SOLID90 for Thermal and SOLID186 for Structural Analysis**

Temperature profiles at different time steps, obtained from transient thermal analysis, are used in nonlinear structural analysis to predict residual creep strains in solder bumps. The analysis requires the same mesh used for thermal analysis. It is therefore necessary to convert thermal element **SOLID90** to structural element **SOLID186** (**ETCHG**).

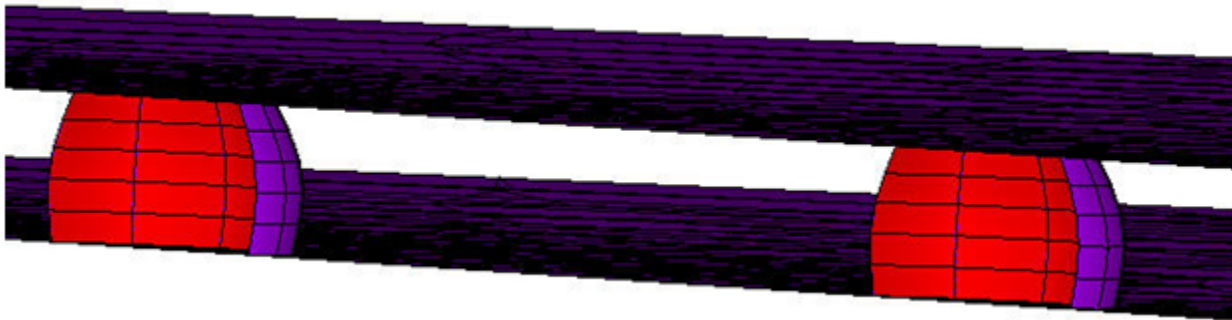
Contact and target elements **CONTA174** and **TARGE170**, respectively, are compatible with structural element **SOLID186**, so those elements are not changed. Contact element options can be modified if necessary (**KEYOPT**).

The following input converts the element types:

```
ETCHG,TTS      ! Change thermal elements to structural elements
KEYOPT,3,1,0  ! Change degrees of freedom for TEMP to UX, UY and UZ
```

### 35.3.2. Contact Modeling

Surface-to-surface contact pairs are created between flip chip parts using **CONTA174** and **TARGE170** elements, as shown in this figure:

**Figure 35.5: Contact Between Solder, Chip, Underfill, and Substrate**

The following input creates a contact pair:

```
/COM, CONTACT PAIR CREATION - START
ET,2,170      ! Define TARGE170 element
ET,3,174      ! Define CONTA174 element
```

```
KEYOPT,3,1,2 ! Select temperature degree of freedom for thermal analysis
REAL,2      ! Set the element real constant
RMODIF,2,14, 319.186992 ! Define Thermal Contact Conductance (TCC)

! Generate the target surface
CMSEL,S,CHIP_DOWN.TGT,NODE ! Selected user-defined nodal component for target.
TYPE,2      ! Element type for target elements
ESLN,S,0    ! Select elements attached to nodal component
ESURF      ! Generate target mesh on the free faces of selected elements.
ALLSEL,ALL

! Generate the contact surface
CMSEL,S,SOLDER_TOP.CNT ! Selected user-defined nodal component for contact.
TYPE,3      ! Element type for contact elements
ESLN,S,0    ! Select elements attached to nodal component
ESURF      ! Generate contact mesh on the free faces of selected elements.
ALLSEL

/COM, CONTACT PAIR CREATION - END
```

Similarly, contact pairs are created between other parts of the flip chip.

### 35.4. Material Properties

The rate-dependent plasticity material behavior is used for solder bumps, while the other parts are assumed to be linear elastic and temperature-independent.

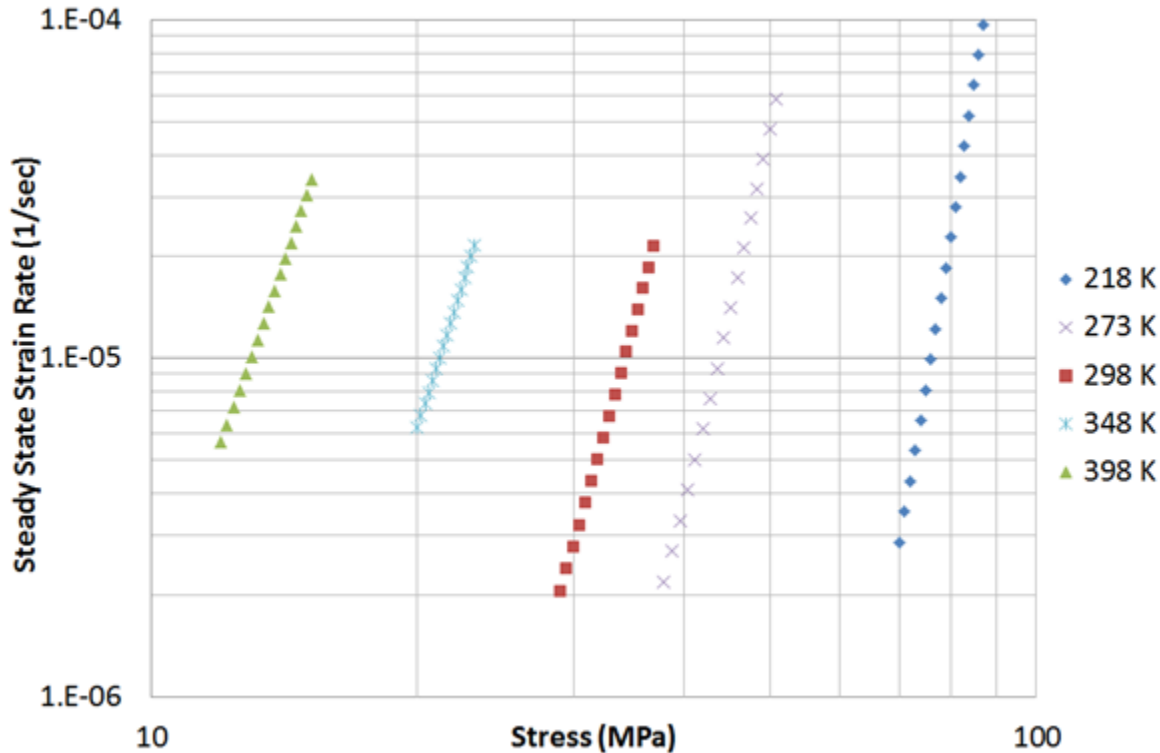
The generalized Garofalo model is used to simulate creep behavior. The creep strain rate of the model is expressed as:

$$\dot{\epsilon}_{cr} = C_1 [\sinh(C_2 \hat{\sigma})]^{C_3} e^{-C_4/T}$$

where  $\dot{\epsilon}_{cr}$  is the change in equivalent creep strain with respect to time,  $\hat{\sigma}$  is the equivalent stress, T is the temperature,  $C_1$  through  $C_4$  are the constants, t is the time at the end of the substep, and e is the natural logarithm base.

The following experimental data are used with the [curve-fitting tool for creep materials](#) to find the creep model constants:

Figure 35.6: Creep Experimental Data [4-6] at Different Temperatures Used for Curve Fitting



The curve-fitting method is nonlinear, so an iterative process is used to obtain a good fit with the experimental data; therefore, initial values for each material parameter are required. The following input finds the generalized Garofalo material constants:

```

/COM, Read experimental data saved in dat files
TBFT,EADD,1,CREEP,temp218.dat ! Read experimental data at 218 K temperature
TBFT,EADD,1,CREEP,temp273.dat ! Read experimental data at 273 K temperature
TBFT,EADD,1,CREEP,temp298.dat ! Read experimental data at 298 K temperature
TBFT,EADD,1,CREEP,temp348.dat ! Read experimental data at 348 K temperature
TBFT,EADD,1,CREEP,temp398.dat ! Read experimental data at 398 K temperature

/COM, Perform material curve-fitting operations.
TBFT,FADD,1,CREEP,GGAR, ! Define a constitutive model generalized Garofalo
TBFT,SET,1,CREEP,GGAR,,1,1e-5 ! Initialize C1 coefficients (C1 > 1)
TBFT,SET,1,CREEP,GGAR,,2,1e-5 ! Initialize C2 coefficients
TBFT,SET,1,CREEP,GGAR,,3,5.0 ! Initialize C3 coefficients
TBFT,SET,1,CREEP,GGAR,,4,0 ! Initialize C4 coefficients
TBFT,SET,1,CREEP,GGAR,,tdep,1 ! Set temperature dependency ON
TBFT,SET,1,CREEP,GGAR,,tref,all ! Set reference temperature
TBFT,SOLVE,1,CREEP,GGAR,,1,5000,0,0 ! Solve for coefficients with 5000 iterations
TBFT,FSET,1,CREEP,GGAR, ! Write constants to the material database

```

Table 35.2: Generalized Garofalo Creep Constants from Curve Fitting and Reference

Temperature (K)	Constant	Reference [3]	Curve Fitting
218	C1	26.00917	7.19E-11
	C2	0.037486	3.75E-02
	C3	5.5	5.50E+00
	C4	5802	0.00E+00

Temperature (K)	Constant	Reference [3]	Curve Fitting
273	C1	17.14286	1.01E-08
	C2	0.044852	4.49E-02
	C3	5.5	5.50E+00
	C4	5802	0.00E+00
298	C1	14.19463	4.97E-08
	C2	0.049251	4.93E-02
	C3	5.5	5.50E+00
	C4	5802	0.00E+00
348	C1	9.568966	5.50E-07
	C2	0.061269	6.13E-02
	C3	5.5	5.50E+00
	C4	5802	0.00E+00
398	C1	6.105528	2.85E-06
	C2	0.081046	8.10E-02
	C3	5.5	5.50E+00
	C4	5802	0.00E+00

For more information, see [Creep Material Curve Fitting](#) in the *Material Reference*.

The following material properties [3] are used for the thermo-mechanical analysis of the flip chip:

**Table 35.3: Flip Chip Material Properties**

Properties	Solder	Chip	Underfill	Substrate
Conductivity (W/m-K)	33	110	1.6	13
Specific Heat (J/Kg-K)	226	712	674	879
Density (Kg/m <sup>3</sup> )	7400	2330	6080	1938
Young's Modulus (MPa)	[1]	162000	14470	18200
Poisson's Ratio	0.4	0.28	0.28	0.25
Coefficients of Thermal Expansion (ppm/K)	22.36	2.3	20	19

1. Young's modulus for solder is  $E(T) = 52708 - 67.14T - 0.0587T^2$  MPa.

**Table 35.4: Temperature-Dependent Properties**

Temperature (K)	273	323	373
Yield Stress	21	16	10

Elastic and perfectly plastic material behavior is assumed. Bilinear isotropic hardening is used to define the solder plasticity to compare results.

## 35.5. Boundary Conditions and Loading

Analysis of the flip chip is performed via a 1/8 symmetry model. A symmetric boundary condition is applied to two cut planes in both the thermal and the structural analyses.

The following related topics are available:

[35.5.1. Thermal Analysis](#)

[35.5.2. Structural Analysis](#)

### 35.5.1. Thermal Analysis

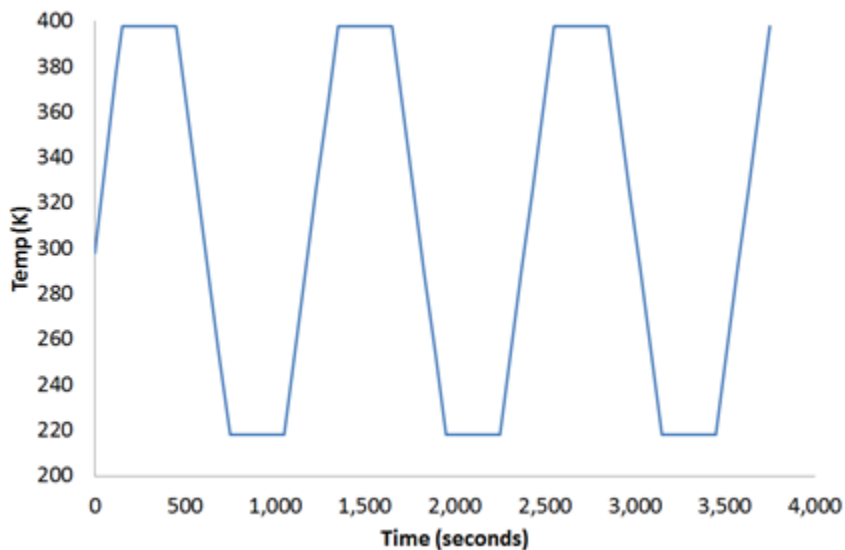
An initial temperature of 298 K is applied on all nodes.

The temperature on the free surface of the chip is increased at a constant rate for 150 seconds to 398 K.

The same constant temperature is maintained in the next load step for 300 seconds, then cooled to 218 K in 300 seconds.

The following figure illustrates each heating phase and each cooling phase, and the constant temperature maintained for 300 seconds between each phase:

**Figure 35.7: Temperature Cycle History**



The following input defines the initial temperature:

```
NSEL,ALL      ! Select all nodes
IC,ALL,TEMP,298  ! Specifies initial temperature at nodes
```

Temperature degree-of-freedom constraints are used to apply loading on the chip surface, as shown in the following input:

```
NSEL,S,LOC,Y,1.325  ! Select free surface nodes of chip
D,ALL,TEMP,218      ! Applied temperature
ALLSEL,ALL
```

### 35.5.2. Structural Analysis

The temperature profile at different time steps (obtained from a transient thermal analysis) is used in nonlinear structural analysis to predict residual creep strains in solder. The following command reads thermal analysis temperature results as thermal loads at different time steps:

```
LDREAD,TEMP,,,TIME,0,'thermal','rth' ! Read temperature from thermal analysis results file
```

Issue the **LDREAD** command at every substep to read the temperature at the appropriate time. Change the *TIME* value to the final solution time of a given substep. A linear variation in the solder temperature between load steps is observed; therefore, the thermal load is applied at the end of each load step rather than to each substep.

Rigid body motion is constrained with displacement of all degrees of freedom at the center of a substrate bottom node.

### 35.6. Analysis and Solution Controls

A transient thermal analysis (**ANTYPE,TRANS**) obtains the temperature distribution, and a linear static analysis (**ANTYPE,STATIC**) obtains the residual creep strains in the lead-free solder.

The following input shows the solution commands used for the thermal analysis:

```
TRNOPT,FULL ! Specifies transient analysis options.
TIME,150 ! Final time for solution.
OUTRES,ALL,ALL ! Saved results at each substep.
SOLVE
```

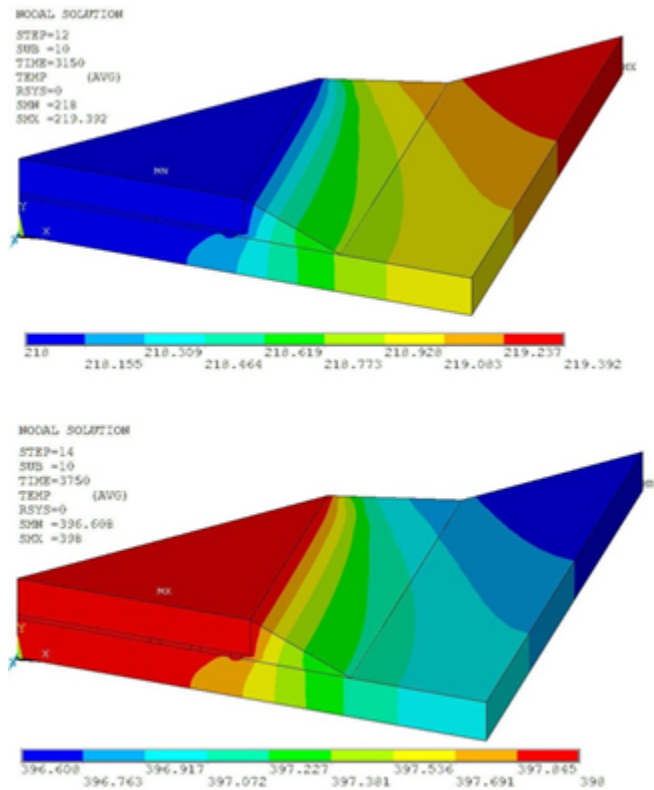
The following shows the solution commands used for the structural analysis:

```
! RAMP (LOAD STEP 2)
NLGEOM,ON ! Includes large-deflection effects
RATE,ON ! Perform implicit creep analysis
TIME,150 ! Set load step end time
KBC,0 ! Loads are ramped
LDREAD,TEMP,,,TIME,0,'THERMAL','RTH'
SOLVE

! DWELL (LOAD STEP 3)
NLGEOM,ON ! Includes large-deflection effects
AUTOTS,ON ! Turn on auto time step
KBC,1 ! Loads are step changed
TIME,450 ! Set load step end time
SOLVE ! Solve load step
```

### 35.7. Results and Discussion

The following figure shows the temperature distribution at the end of the 12th and 14th load steps:

**Figure 35.8: Temperature Distribution in Flip Chip at 3150 Seconds and 3750 Seconds**

Temperature on the chip is reduced from 398 K to 218 K in the 12th load step, and increased from 218 K to 398 K in the 14th load step.

The temperature distribution is nearly uniform in all load steps, due to assumed perfect thermal contact between parts of the flip chip and a high thermal contact conductance value. These results are used in the structural analysis as thermal loading.

The reference structural analysis [3] results using the generalized Garofalo creep model constants are compared to the structural analysis results with creep curve-fitting constants. The following two figures show the displacement vector sum of both analyses:

**Figure 35.9: USUM Results from Creep Curve Fitting Constants and Reference Constants at the End of 12th Load Step (3150 Seconds)**

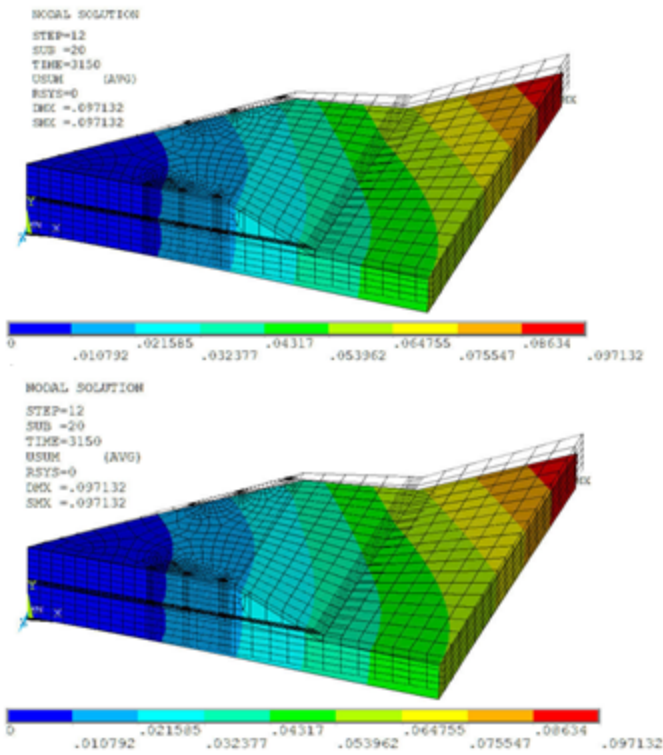
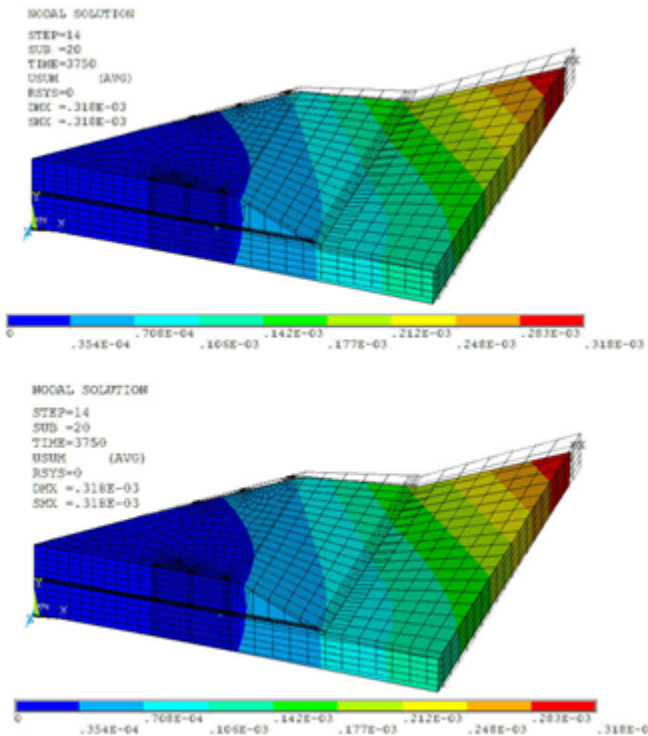


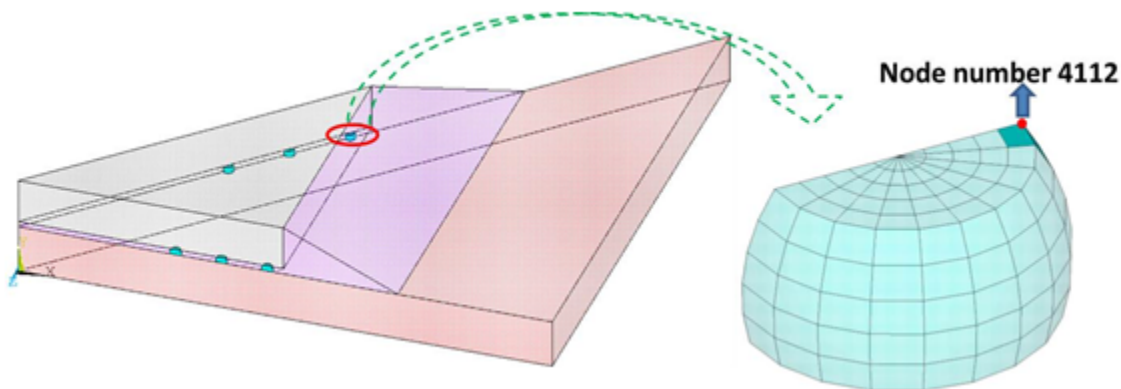
**Figure 35.10: USUM Results from Creep Curve Fitting Constants and Reference Constants at the End of 14th Load Step (3750 Seconds)**





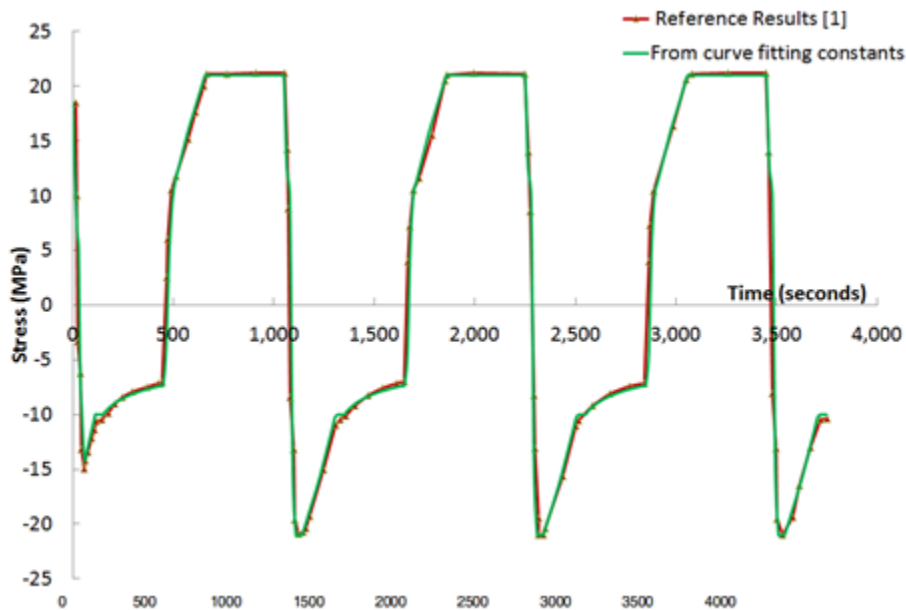
All time-history results are plotted for solder element results at node 4112, positioned at the end of outmost solder and near the chip, as shown in the following figure:

**Figure 35.11: Node Used for Plotting Post Process Results**



The equivalent stress result at the node is compared to the reference results. The sign for Von Mises stress above room temperature is changed to represent compressive stresses developed due to resistance in thermal expansion. Results from curve-fitting constants matching well with the reference result, as shown in this figure:

**Figure 35.12: Time History Post Process Results of Equivalent Stress: Comparison with Wen-Ren Jong [3]**

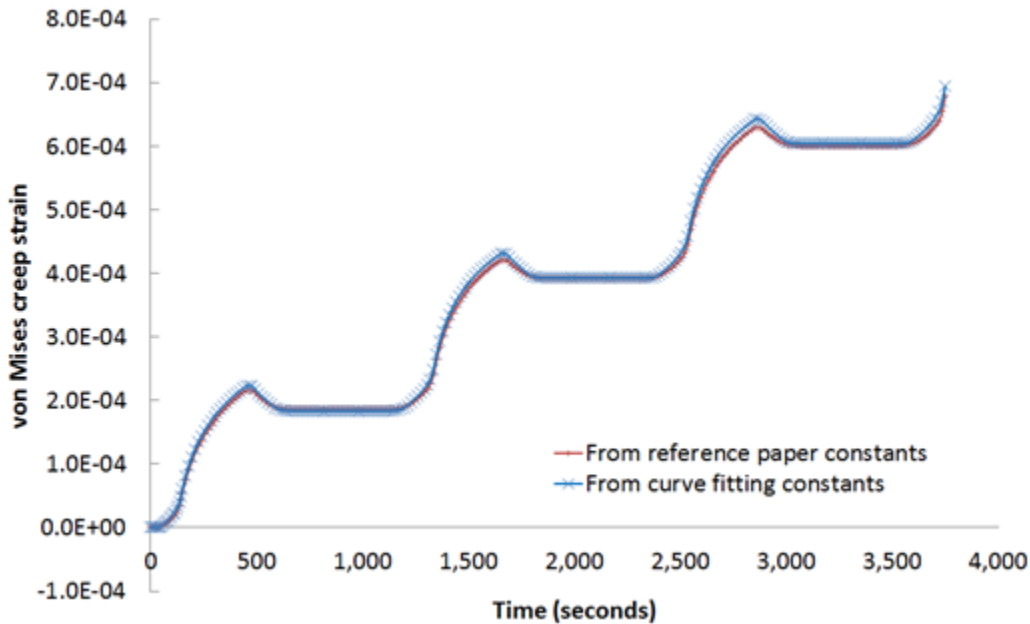


Due to unavailable thermal contact conductance and plasticity behavior used in the reference analysis, the following assumptions apply to this problem:

- Perfect thermal contact between parts of the flip chip.
- Elastic and perfectly plastic behavior with isotropic hardening in the structural analysis.

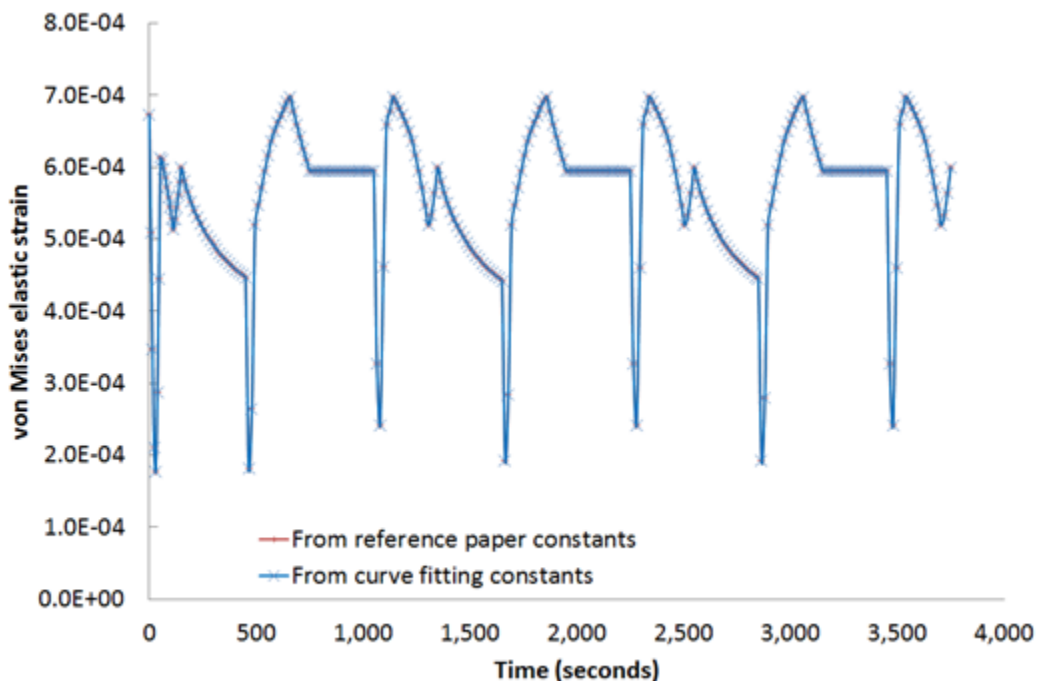
The results based on the curve-fitting creep constants are therefore compared to another analysis using the reference creep constants and run with the same assumptions, as shown in this figure:

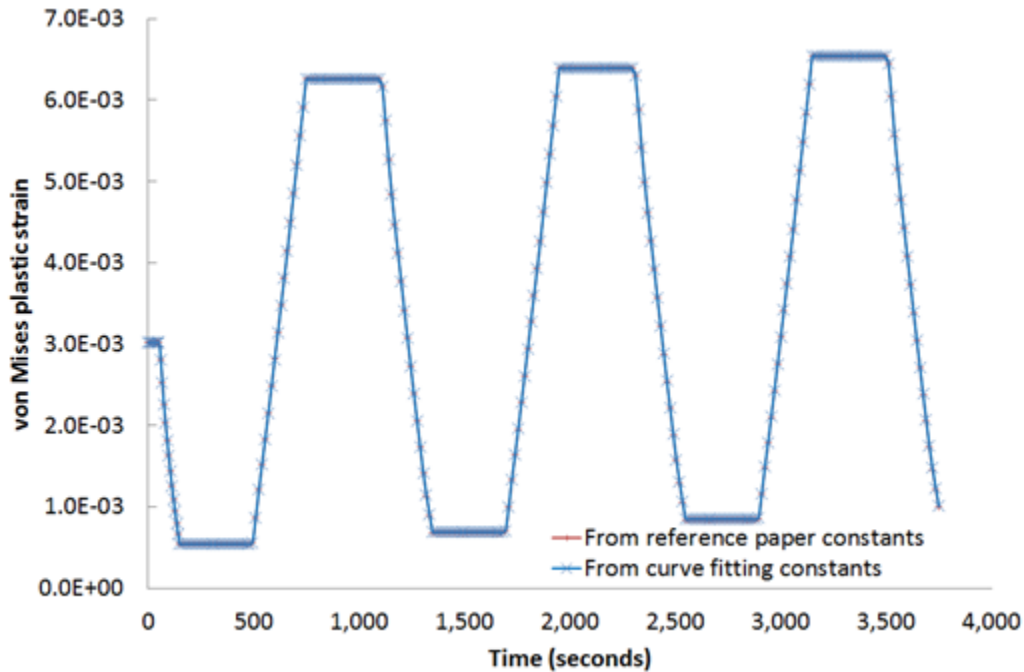
**Figure 35.13: Von Mises Creep Strain at Node Number 4112**



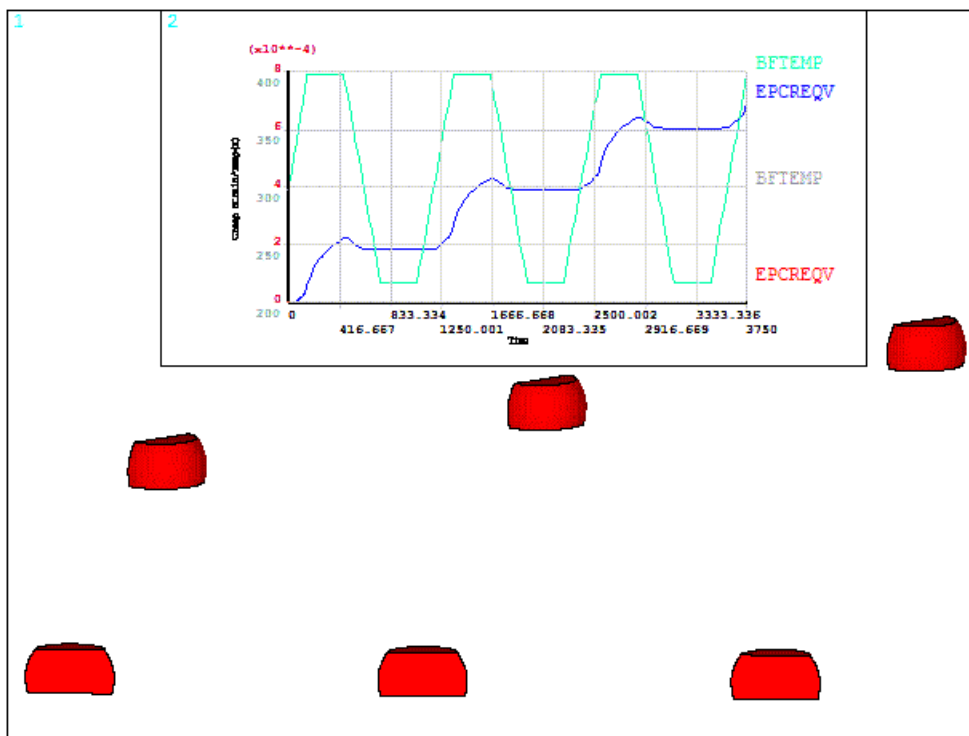
In the following figure, von Mises creep strain results from the curve-fitting constants match closely with the material constants used in the reference solution. Elasticity and plasticity constants in both models are identical, so von Mises elastic strain and von Mises plastic strain match exactly, as shown in the following two figures:

**Figure 35.14: Von Mises Elastic Strain at Node Number 4112**

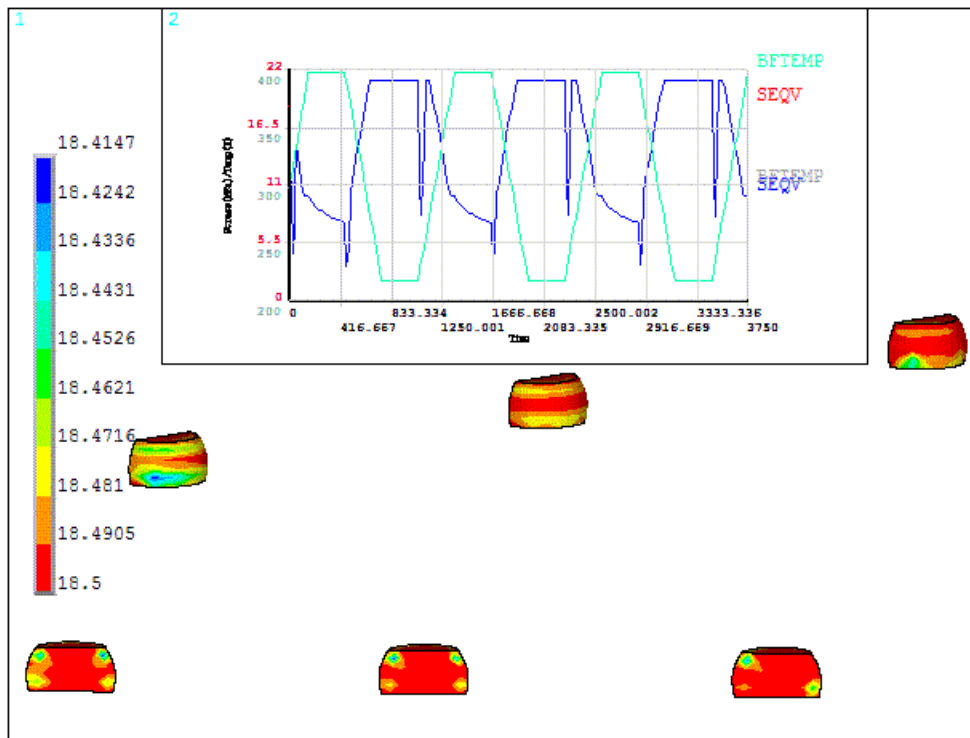


**Figure 35.15: Von Mises Plastic Strain at Node Number 4112**

The following animations show the von Mises creep strain and von Mises stress animation (respectively) along with the time-history postprocessing of the results at node 4112.

**Figure 35.16: Von Mises Creep Strain Animation of Solder with Time-History Results at Node Number 4112**

**Figure 35.17: Figure 17: Von Mises Stress Animation of Solder with Time-History Results at Node Number 4112**



One can observe the increase in creep strain with cyclic load steps.

## 35.8. Recommendations

To perform a similar elastoplastic creep analysis, consider these recommendations:

- Save the thermal analysis results (**OUTRES**) at the desired time steps. Use the temperature results for input loading in the subsequent structural analysis.
- Select the creep model based on available experimental data.
- For better results, the stress/strain rate and temperature range of the application should fall within the considered experimental data range. Using too much additional experimental data outside the required range also leads to more complexity in finding material constants and reduces accuracy within the desired range of strains. Engineering judgment is therefore necessary to select an experimental data range for curve fitting.
- Because the curve-fitting procedure is a numerical technique for obtaining material constants without considering the physics of the material model, material model knowledge is required to judge the constants obtained from curve fitting in order to avoid solution inconsistency.
- Provide accurate experimental test data to obtain valid curve-fitting results.
- For more information, see [Rate-Dependent Plasticity \(Viscoplasticity\)](#) in the *Material Reference* and [Rate-Dependent Plasticity \(Including Creep and Viscoplasticity\)](#) in the *Mechanical APDL Theory Reference*.

## 35.9. References

The following references are used in this example problem:

1. Kornain, Z., A.Jalar, N.Amin, R.Rasid, C.S.Foong. "Comparative Study of Different Underfill Material on Flip Chip Ceramic Ball Grid Array Based on Accelerated Thermal Cycling." *American Journal of Engineering and Applied Sciences* 3.1 (2010): 83-89.
2. Shangguan, Dongkai. "Lead-Free Solder Interconnect Reliability." Materials Park, OH: ASM International, 2005.
3. Jong, Wen-Ren, Chien-Chia Chiu, Hsin-Chun Tsai, Hsiu-Tao Chung., "Elastic-Plastic-Creep Analysis of Lead and Lead-Free Solder Bumps in FC." Annual Technical Conference (ANTEC) of the Society of Plastics Engineers (2005): 1665-1669.
4. Darveaux, Robert and Corey Reichman. "Mechanical Properties of Lead-Free Solders." 57th Electronic Components and Technology Conference (2007): 695-706.
5. Clech, John Paul. "Sn-Ag Properties and Creep Data." Material Measurement Laboratory. Web. 15 January 2013. <[http://www.metallurgy.nist.gov/solder/clech/Sn-Ag\\_Bulk.htm](http://www.metallurgy.nist.gov/solder/clech/Sn-Ag_Bulk.htm)>.
6. Lau, John H. and Stephen H. Pan. "Creep Behaviors of Flip Chip on Board with 96.5Sn-3.5Ag and 100In Lead-Free Solder Joints." *International Journal of Microcircuits and Electronic Packaging* 24 (2001): 11-18.

## 35.10. Input Files

The following files were used in this problem:

- `Lead_Free_Solder.cdb` -- Finite element model of the flip chip.
- `Thermal.dat` -- Input file for the transient thermal analysis.
- `Structural.dat` -- Input file for the structural analysis.

The files are available in the `td-35` folder. See [Obtaining the Input Files](#) (p. xxxv) for more information.



---

## Chapter 36: VCCT-Based Crack-Growth Simulation of a Composite Laminated T-Joint

---

This example problem demonstrates the [virtual crack closure technique \(VCCT\)](#) to simulate the interfacial crack growth of a laminated T-Joint. The simulation involves growing an existing crack along a predefined path using interface elements.

The following features and capabilities are highlighted:

- VCCT for energy calculations
- Crack-growth simulation

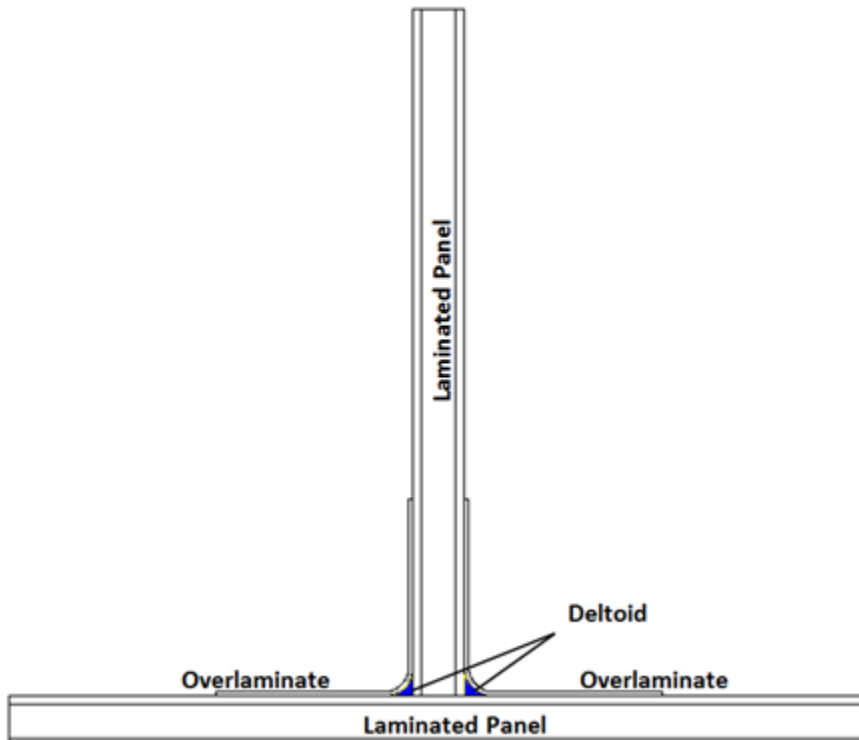
Topics related to this example problem follow:

- [36.1. Introduction](#)
- [36.2. Problem Description](#)
- [36.3. Modeling](#)
- [36.4. Material Properties](#)
- [36.5. Boundary Conditions and Loading](#)
- [36.6. Analysis and Solution Controls](#)
- [36.7. Results and Discussion](#)
- [36.8. Recommendations](#)
- [36.9. References](#)
- [36.10. Input Files](#)

### 36.1. Introduction

Composite T-joints are used in a wide variety of applications, from fuselage stiffeners in aerospace structures to load-transmission joints between the hull and bulkhead in oceangoing vessels [1].

The following figure shows a typical T-joint geometry:

**Figure 36.1: T-Joint**

The T-Joint consists of laminated panels connected via composite overlaminates and deltoids (gap fillers).

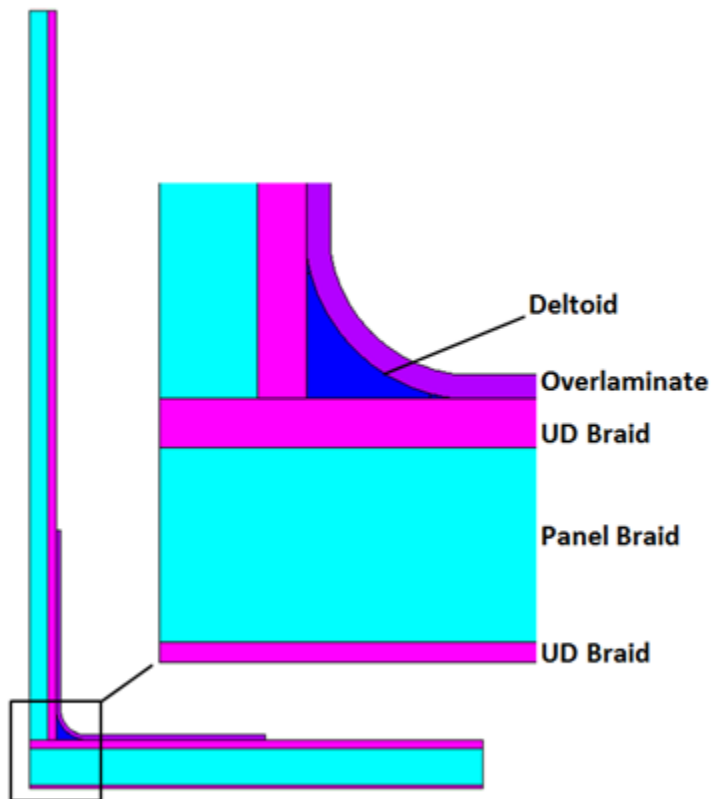
Because the overlaminates and the deltoid comprise the load-transmission path between a vessel's hull and bulkhead, the strength of the joints depends on the strength of both components. Due to the variable quality of the interfaces and the presence of defects, overlaminates can be the primary source of delamination [2].

The T-Joint simulation shows delamination propagation under a mechanical pull-off load case using VCCT-based crack growth. The energy-release-rate calculations using VCCT are based on the assumption that the energy needed to separate a surface is the same as the energy needed to close the same surface, and therefore that the crack-growth criteria is the energy-release rate. Because cracks generally grow along interfaces, VCCT-based crack-growth simulation is an effective technique for simulating interface delamination of laminate composites.

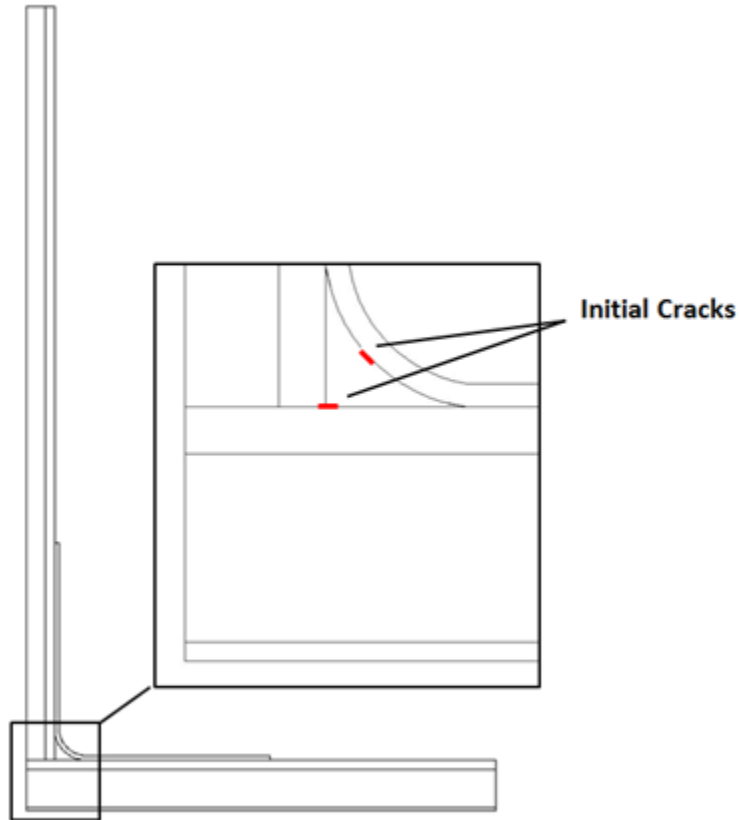
## 36.2. Problem Description

The 2-D T-Joint model is a carbon-fiber-based braided composite with two panels of laminated braids and the deltoid. A half model is used for the simulation due to the symmetry. The following figure shows a schematic configuration of the laminates with layup details.



**Figure 36.2: T-Joint Layup Configuration**

The dominant delamination occurs along the interface between the deltoid and overlaminat in the curve area first and then grows up to the end of laminate. During the first delamination process, a second delamination also starts between two panels which completely separate the panels. Based on the study of T-Joint failure, therefore, two critical locations of higher interlaminar stresses are considered as the initial failure points. For the simulation, two small cracks are defined at these critical locations, as shown in this figure:

**Figure 36.3: T-Joint with Initial Cracks**

The fracture energy and interlaminar material strength are based on reference results [3].

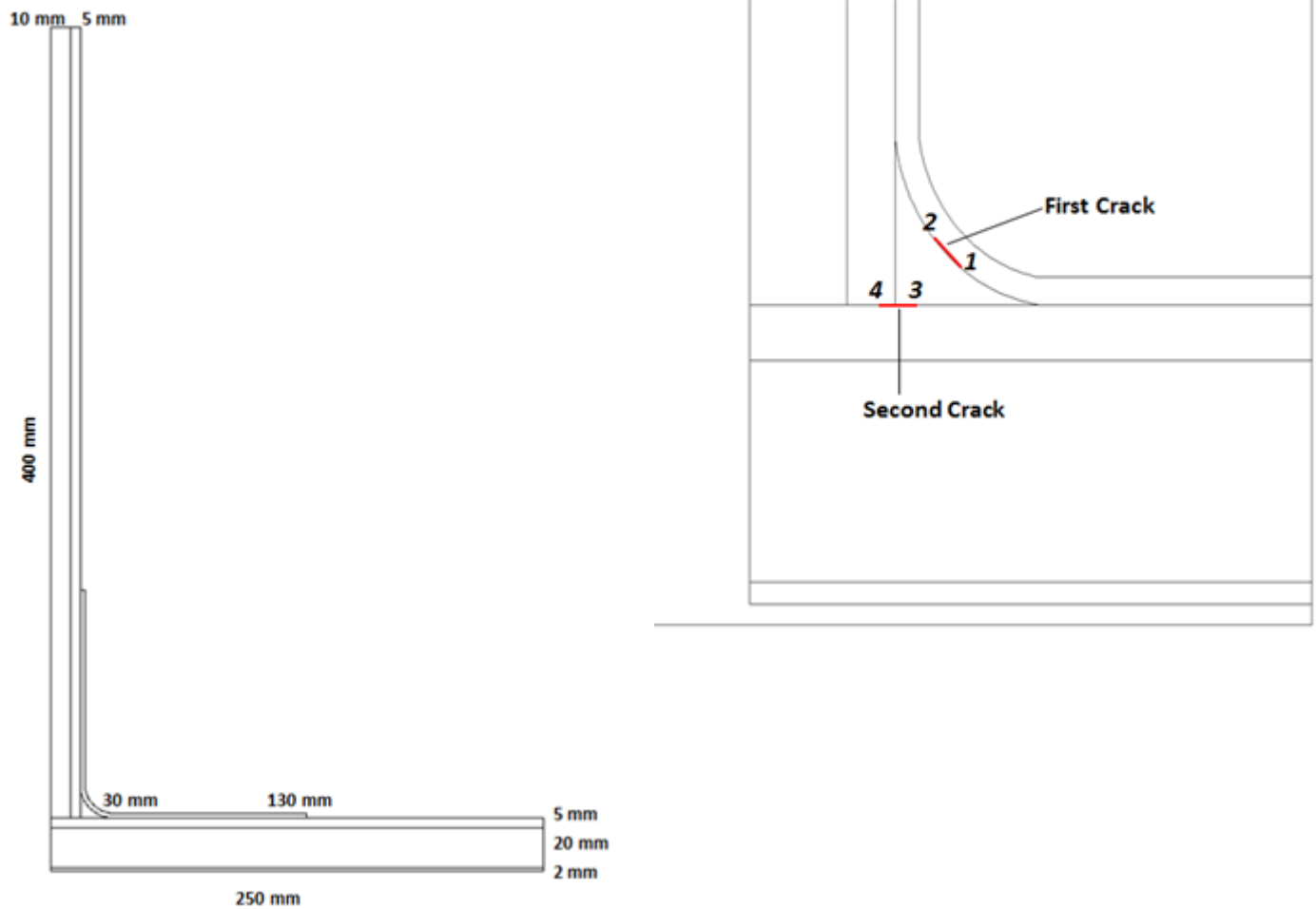
A VCCT-based crack-growth simulation requires the following operations:

- Specifying 2-D interface elements (**INTER202**).
- Calculating the energy-release rate (**CINT**).
- Defining the crack-growth set, fracture criterion, crack-growth path, and solution-control parameters (**CGROW**).

### 36.3. Modeling

Tensile test simulations are performed on the models having the dimensions shown in part (a) of the following figure:

**Figure 36.4: T-Joint Dimensions (a) and Cracks with Crack Tip IDs (b)**



(a)

(b)

Dimensions are based on the specimen used in the reference study [4].

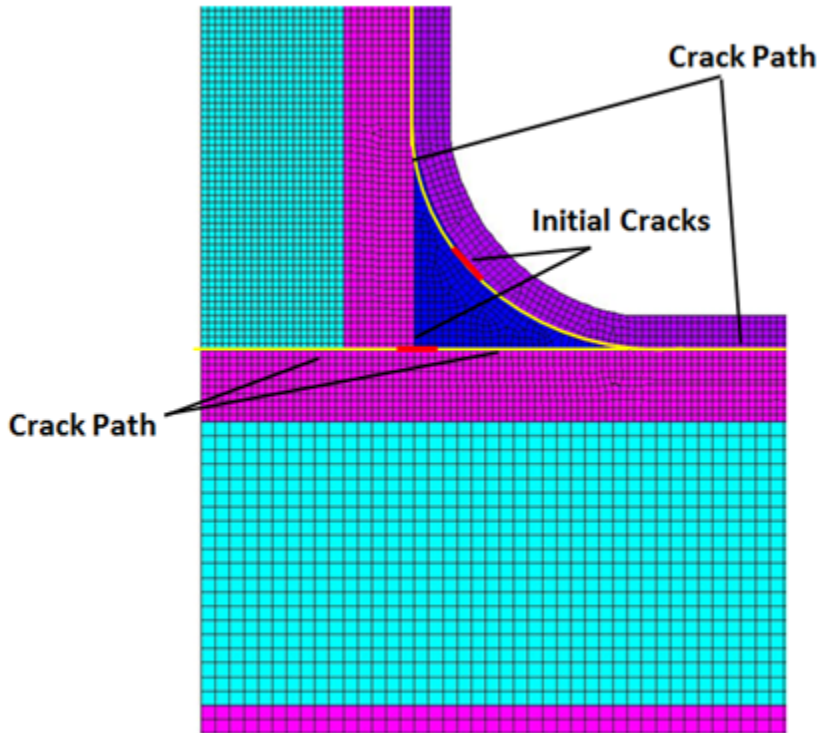
Part (b) of the figure shows the crack tip IDs.

Because plane strain is simulated, the finite element model is created using the 2-D structural solid element [PLANE182](#) (KEYOPT (1) = 2, KEYOPT(3) = 2).

The various components are bonded to each other using standard bonded contact definitions, except along the crack paths.

Crack paths are defined using the interface elements [INTER202](#). To avoid crack surface interpenetrations, contact is also defined along the crack paths. The mesh around the crack paths is finer than around other sections of the model, as shown in the following figure:

**Figure 36.5: T-Joint Finite Element Model with Initial Cracks and Crack Paths**



### 36.4. Material Properties

The material is a braided carbon fiber composite. The following table provides the material properties of each layer:

<b>UD Braid and Overlaminates: Linear Elastic Material 1</b>	
Young's Modulus in X direction (GPa)	160
Young's Modulus in Y direction (GPa)	9.7
Young's Modulus in Z direction (GPa)	9.7
Poisson's Ratio (PRXY)	0.33
Poisson's Ratio (PRYZ)	0.28
Poisson's Ratio (PRXZ)	0.33
Shear Modulus GXY (GPa)	5.9
Shear Modulus GYZ (GPa)	4.7
Shear Modulus GXZ (GPa)	5.9
<b>Deltoid: Linear Elastic Material 2</b>	
Young's Modulus in X direction (GPa)	9.7
Young's Modulus in Y direction (GPa)	152
Young's Modulus in Z direction (GPa)	9.7
Poisson's Ratio (PRXY)	0.021
Poisson's Ratio (PRYZ)	0.33

Poisson's Ratio (PRXZ)	0.28
Shear Modulus GXY (GPa)	5.9
Shear Modulus GYZ (GPa)	5.9
Shear Modulus GXZ (GPa)	4.7
<b>Panel Braids: Linear Elastic Material 3</b>	
Young's Modulus in X direction (GPa)	65.8
Young's Modulus in Y direction (GPa)	46.1
Young's Modulus in Z direction (GPa)	9.7
Poisson's Ratio (PRXY)	0.421
Poisson's Ratio (PRYZ)	0.48
Poisson's Ratio (PRXZ)	0.28
Shear Modulus GXY (GPa)	25.8
Shear Modulus GYZ (GPa)	4.7
Shear Modulus GXZ (GPa)	4.7

For VCCT-based crack-growth simulation, isotropic, orthotropic or anisotropic materials can be used with several fracture criteria (including a user-defined option). Multiple cracks are also allowed.

For this simulation, a linear fracture criterion is defined for crack onset and subsequent crack growth. The linear option assumes that the fracture criterion is a linear function of the Mode I (GI), Mode II (GII), and Mode III (GIII) energy-release rates, expressed as:

$$f = \frac{G_I}{G_I^C} + \frac{G_{II}}{G_{II}^C} + \frac{G_{III}}{G_{III}^C}$$

<b>Critical Energy-Release Rate</b>	
Critical Mode I energy-release rate, $G_I^C$ (N/mm )	0.3
Critical Mode II energy-release rate, $G_{II}^C$ (N/mm)	1.0
Critical Mode III energy-release rate, $G_{III}^C$ (N/mm )	1.0

The following example input defines the fracture criterion:

```

C1=0.3
C2=1.0
C3=1.0

TB,CGCR,6,,3,LINEAR      ! Linear fracture criterion
TBDATA,1,C1,C2,C3

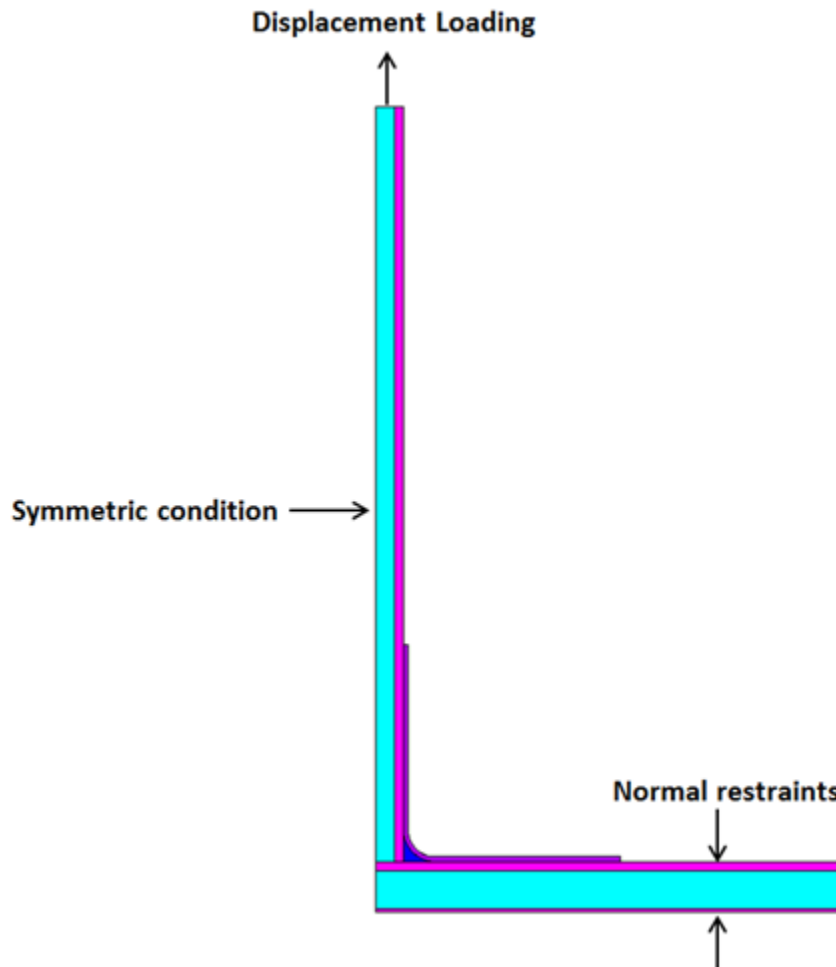
TB,CGCR,7,,3,LINEAR      ! Linear fracture criterion
TBDATA,1,C1,C2,C3

```

## 36.5. Boundary Conditions and Loading

Due to the model's symmetry, symmetric boundary conditions are used on one side. The tension displacement loading is applied at the top of the vertical panel surface, and two points of the horizontal panel are constrained, as shown in the following figure:

**Figure 36.6: T-Joint Model Boundary Conditions and Loading**



## 36.6. Analysis and Solution Controls

Because crack growth is typically a nonlinear phenomenon, a nonlinear static analysis is performed. For a VCCT-based crack-growth simulation, it is also necessary to perform both of the following tasks at each crack tip:

- Calculate the energy-release rate (p. 561) (**CINT**).
- Grow the crack when the assumed fracture criterion is satisfied (p. 561) (**CGROW**).

For more detailed information, see *VCCT Energy-Release Rate Calculation* in the *Mechanical APDL Fracture Analysis Guide* and *VCCT-Based Crack-Growth Simulation* in the *Mechanical APDL Fracture Analysis Guide*.

### 36.6.1. Energy Release-Rate Calculation Setup

The following commands initiate the new energy-release rate calculation:

**CINT,NEW,1** -- Assigns an energy-release rate calculation ID of 1 (*Par1* = 1).  
**CINT,TYPE,VCCT** -- Specifies a VCCT-based energy-release-rate calculation (*Par1* = VCCT).

VCCT calculation requires the finite element mesh to be in the crack-extension direction. The crack tip component, normal of crack plane, and crack-extension direction provide the data necessary for the calculation:

**CINT,CTNC,CRACK\_RIGHTR** -- Assigns the crack tip component name (*Par1* = CRACK\_RIGHTR).  
**CINT,NORM,0,2** -- Specifies the global Cartesian coordinate system (*Par1* = 0 [default]) and the Cartesian Y axis of the coordinate system (*Par2* = 2 [default]).

Crack-plane and crack-extension directions are defined in relation to the global Cartesian coordinate system by assuming the flat crack plane.

### 36.6.2. Crack-Growth Calculation Setup

The following commands initiate the crack-growth calculation:

**CGROW,NEW,1** -- Assigns a crack-growth data set ID of 1.  
**CGROW,CID,1** -- The contour-integral calculation ID, the same value specified for **CGROW,NEW**.  
**CGROW,CPATH,CPATH\_RIGHTR** -- The interface element component name for the crack path.  
**CGROW,FCOPTION,MTAB,6** -- Specifies the linear fracture criterion for crack growth (as defined in the material table by **TB,CGCR,,,,LINEAR**) and material ID 6.

The following commands specify the solution controls for crack growth:

**CGROW,DTIME,1E-3** -- Initial time step when crack growth is detected.  
**CGROW,DTMIN,1E-4** -- Minimum time step allowed when crack growth is detected.  
**CGROW,DTMAX,2E-2** -- Maximum time step allowed when crack growth is detected.  
**CGROW,FCRAT,1** -- Fracture-criterion ratio ( $f_c$ , generally around 1).

### 36.6.3. Input for Defining Energy-Release Rate and Crack Growth

The following example input defines the energy-release rate and crack-growth simulation set for crack tip 1:

```
! Energy Release Rate
CINT,NEW,1
CINT,TYPE,VCCT
CINT,CTNC,CRACK_RIGHTR
! Define a local coordinate system. Use neighboring nodes.
CS,21,0,229,228,1171
! Use the y axis the crack normal.
CINT,NORM,22,2

! Crack-Growth Simulation Set
CGROW,NEW,1
CGROW,CID,1
CGROW,CPATH,CPATH_RIGHTR
```

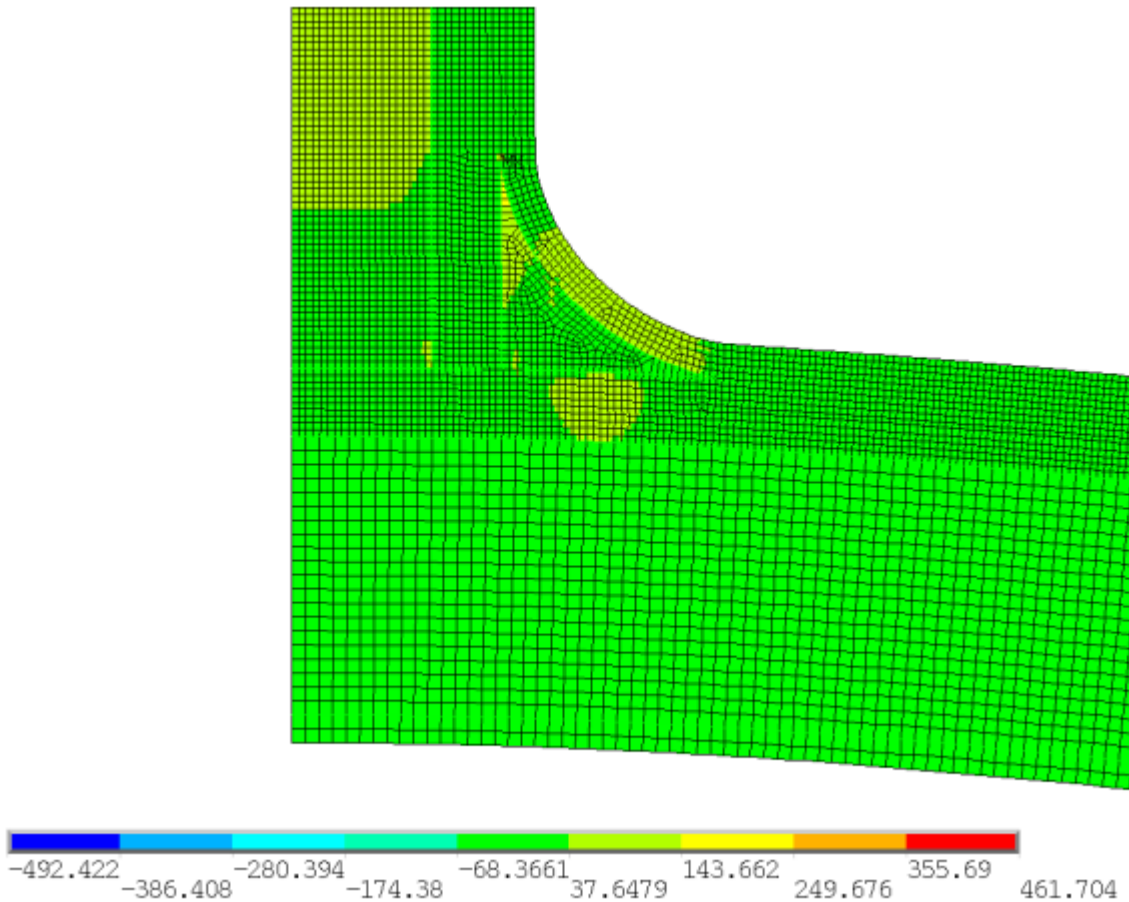
```

CGROW,FCOP,MTAB,6      ! Crack-growth fracture criterion used with the
                        ! material data table
CGROW,DTIME,1E-3       ! Initial time step when crack growth is detected
CGROW,DTMIN,1E-4       ! Minimum time step allowed when crack growth is
                        ! detected
CGROW,DTMAX,2E-2       ! Maximum time step allowed when crack growth is
                        ! detected
CGROW,FCRAT,1          ! Fracture-criterion ratio
    
```

### 36.7. Results and Discussion

The following figure shows the distribution of the y-component of stresses at approximately the same time step:

**Figure 36.7: Distribution of Y-Component of Stresses**



Initially, the stresses become high around the crack tips, especially near the crack (located at the curve area). As the stress increases, the energy-release rate at the crack tip also increases and reaches the critical value. Fracture occurs when the following fracture criterion is met:

$$f \geq f_c$$

where  $f_c$  is the fracture-criterion ratio. The recommended ratio is 0.95 through 1.05. The default is 1.0.

The following table shows the energy-release-rate values for the crack tips in the model at two different time steps, before and at the time of crack growth:

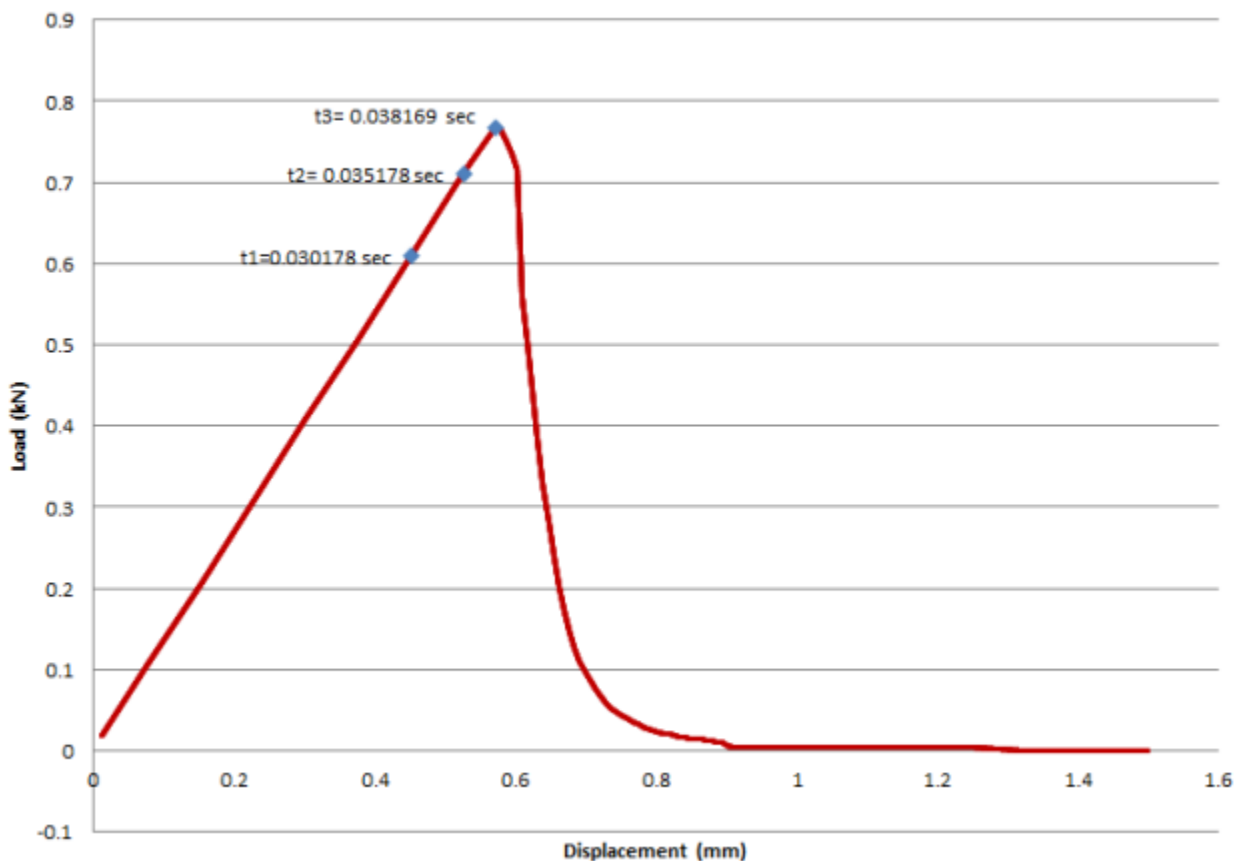


Energy-Release Rate and Fracture-Criterion Ratio					
Crack ID	Time	$G_I$	$G_{II}$	$f = \frac{G_I}{G_I^c} + \frac{G_{II}}{G_{II}^c} + \frac{G_{III}}{G_{III}^c}$	$f_c$ (default = 1)
1	0.030178	7.17E-02	0.43018	0.66920333	$f < f_c$
	0.035178	0.79123	2.4774	5.11483333	$f > f_c$
2	0.030178	0.073927	0.37991	0.62633333	$f < f_c$
	0.035178	0.45969	1.9227	3.455	$f > f_c$
3	0.030178	0.055529	0.43103	0.61612667	$f < f_c$
	0.035178	0.29733	0.9005	1.8916	$f > f_c$
4	0.030178	0.023272	0.67118	0.74875333	$f < f_c$
	0.035178	0.07832	1.6736	1.93466667	$f > f_c$

The table data show that crack growth occurs first at crack tips 1 and 2, whereas crack growth at crack tips 3 and 4 occurs a little later. This behavior indicates that the dominant delamination occurs along the interface between the deltoid and overlamine in the curve area first, then between the UD braid and the deltoid. Also for crack tip 1, 2 and 4, the fracture criteria ratio is much higher than after crack growth is initiated, indicating an unstable crack growth. To avoid overpredicting the maximum loading, use a smaller minimum time step (DTMIN) value.

The following figure shows the energy-release rate increasing until failure occurs:

**Figure 36.8: Y-Force vs. Y-Displacement**

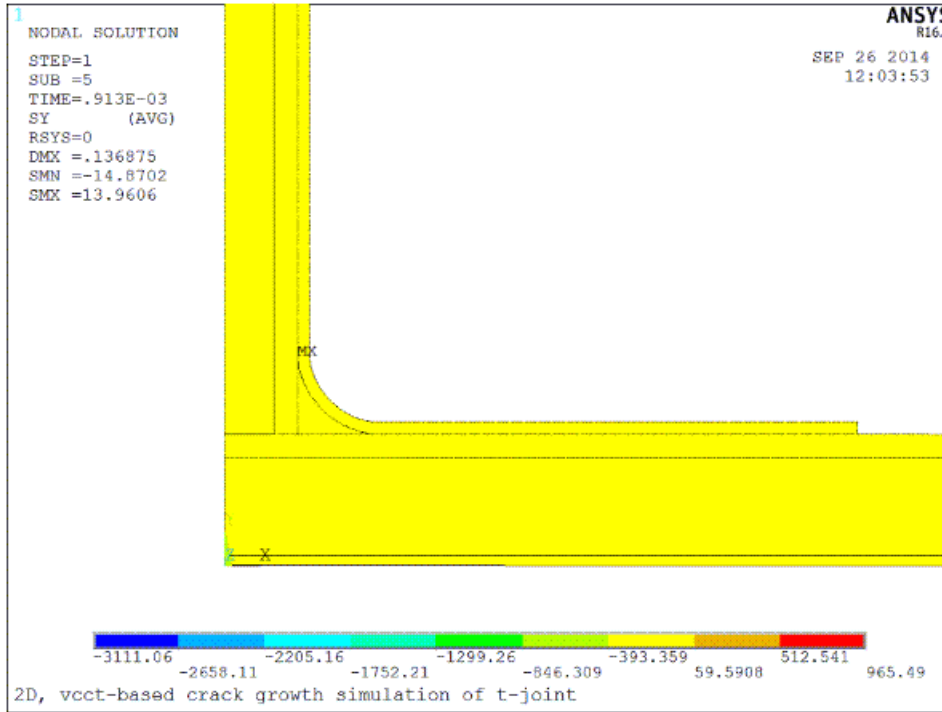


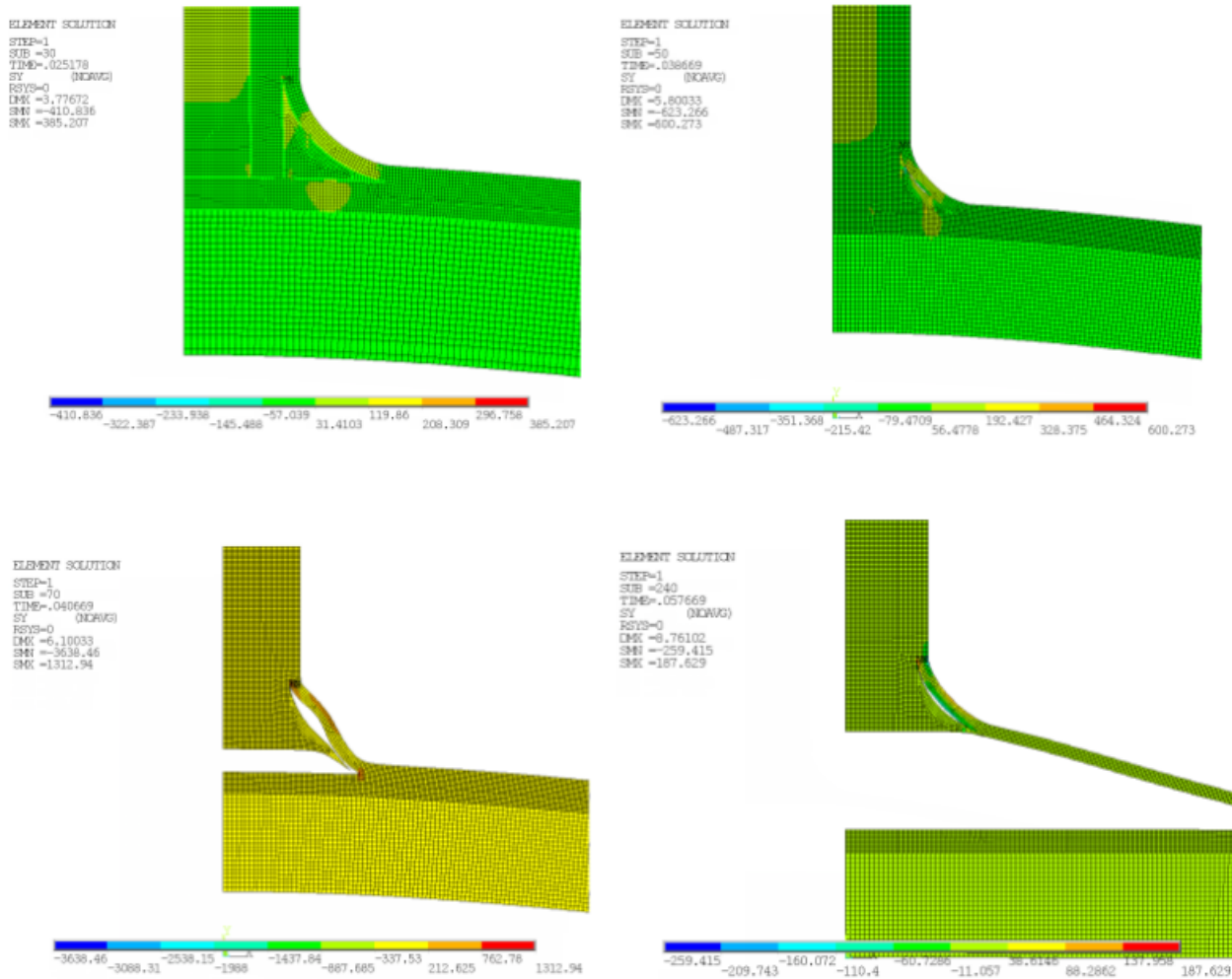
The figure shows the variation of reaction force with the displacement in the Y direction. The response of the T-joint model at times t1, t2 and t3 indicates that the reaction force increases first and reaches the maximum value before crack-growth initiation. After time t3, almost all cracks begin to grow. When crack growth begins, the force drops suddenly and decreases steadily.

Delamination is easily observed by the deformation of interface elements or by hiding the interface elements from the model in postprocessing.

The following figures show the delamination of the panels at various time steps:

**Figure 36.9: Animation: T-Joint Panel Delamination**



**Figure 36.10: Crack Growth**

The crack growth from crack tips 1 and 3 eventually merge, thereby separating the laminated panels.

### 36.7.1. Comparison to the Debonding Capability

The T-joint is analyzed using the existing debonding capability with contact elements. A cohesive zone model (CZM) describes the behavior of the contact interface. The model uses an option to define bilinear material behavior with tractions and critical fracture energies ( $TB,CZM,,,,TBOPT = CBDE$ ).

The boundary conditions and loading are the same as in the VCCT model, and predefined crack models are used with the same crack sizes.

The following table shows the input parameters for the CZM model:

CZM T-Joint Model Parameters		
Maximum normal contact stress (MPa)	$\sigma_{\max}$	45
Critical fracture energy for normal separation (N/mm)	$G_{cn}$	0.3
Maximum equivalent tangential contact stress (MPa)	$\tau_{\max}$	35
Critical fracture energy for tangential slip (N/mm)	$G_{ct}$	1.0
Artificial damping coefficient (sec)	$\eta$	5E-04

CZM T-Joint Model Parameters		
Flag for tangential slip under compressive normal contact stress	$\beta$	1

The following example input defines the cohesive zone model:

```

C1=45
C2=0.3
C3=35
C4=1.0
C5=5E-04
C6=1

TB,CZM,6,,,CBDE           ! Cohesive zone material
TBDATA,1,C1,C2,C3,C4,C5,C6

TB,CZM,7,,,CBDE           ! Cohesive zone material
TBDATA,1,C1,C2,C3,C4,C5,C6
    
```

The following figures show the Y-component stresses in the VCCT and CZM models with identical meshes.

**Figure 36.11: Distribution of Y-Component Stresses: VCCT Model**

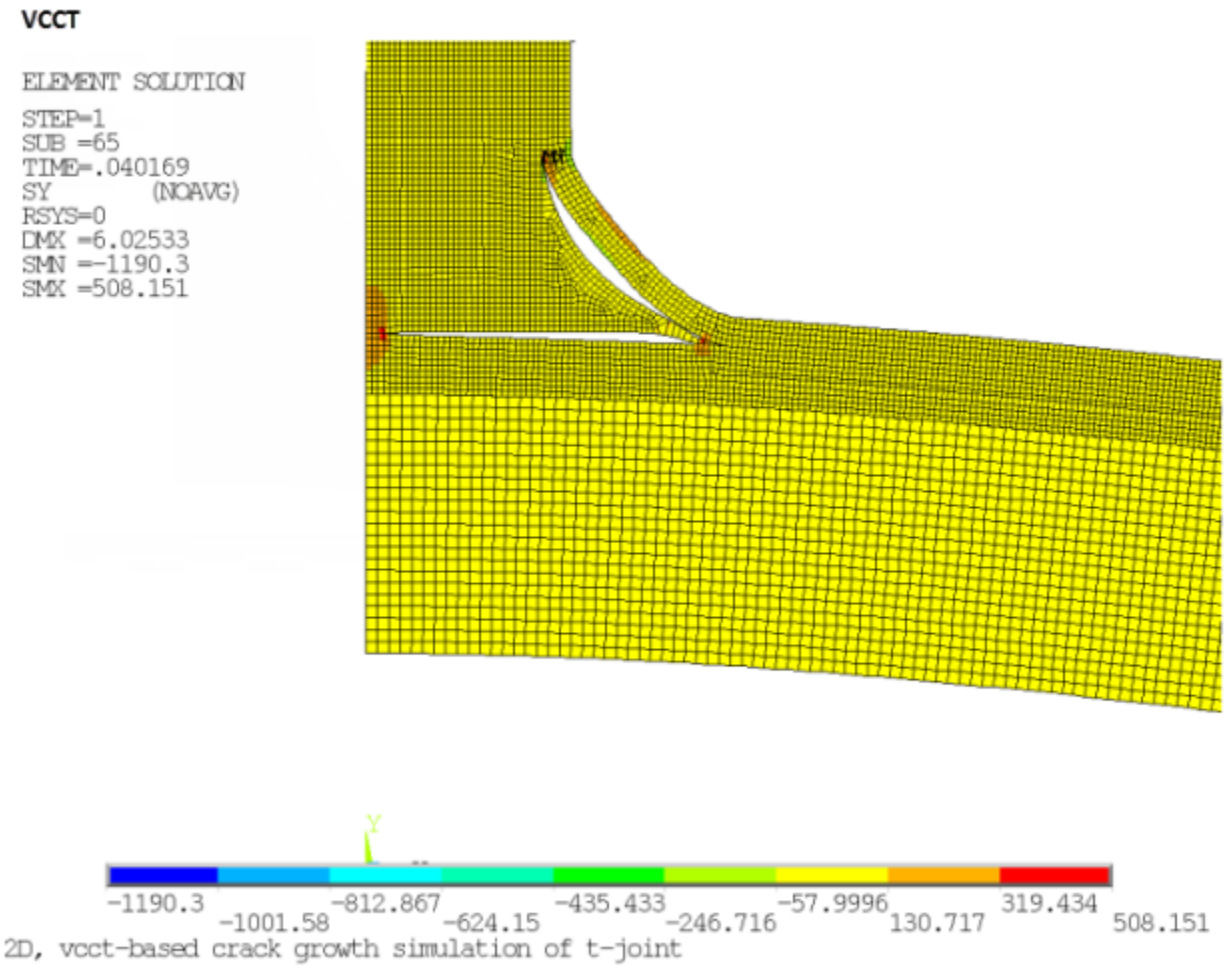


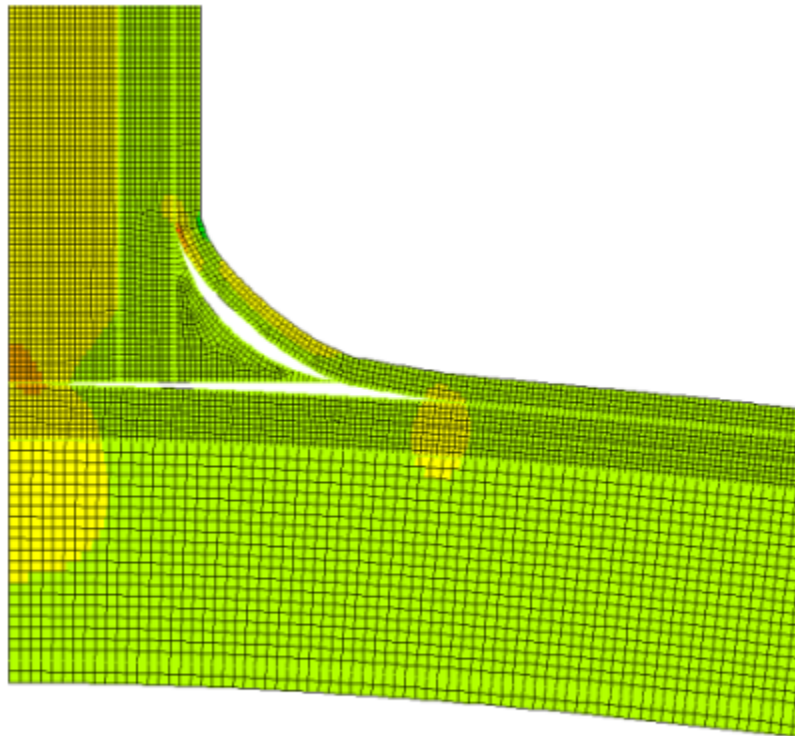
**Figure 36.12: Distribution of Y-Component Stresses: CZM Models****CZM**

## ELEMENT SOLUTION

```

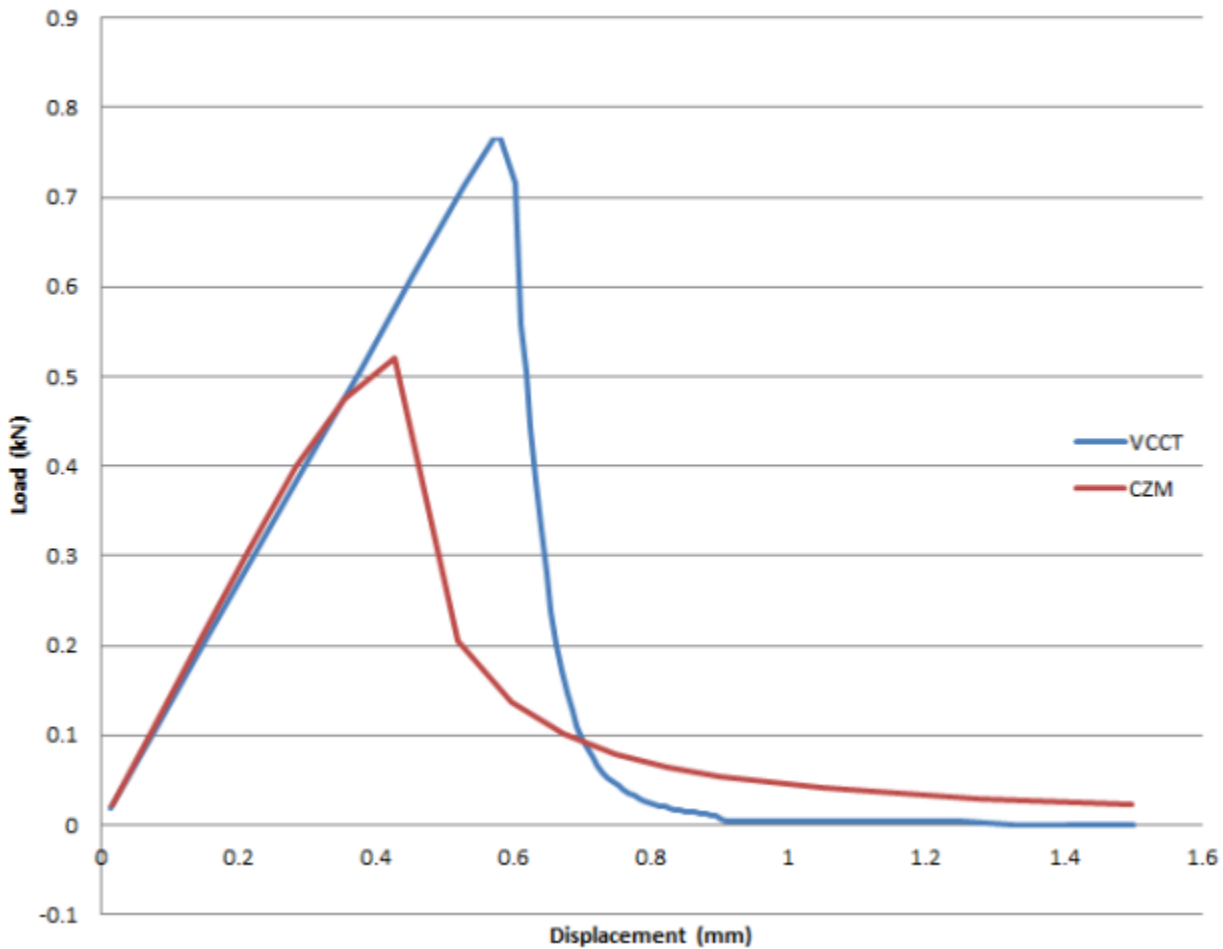
STEP=1
SUB =35
TIME=.030178
SY (NOAVG)
RSYS=0
DMX =4.52672
SMN =-443.839
SMX =243.418

```



Similar to the VCCT model, the debonding in CZM starts from the curved crack portion, then merges with the debonding from the horizontal cracked portion, thereby separating the laminated panels.

The following figure shows the force-deflection (Y-force vs. Y-displacement) response of delamination for the two models:

**Figure 36.13: T-Joint Y-Force vs. Y-Displacement: VCCT and CZM Models**

For both models, the force increases with the applied displacement and peaks quickly before the crack begins to grow. The reaction force then decreases rapidly at the initial phase of crack growth, then slows with the subsequent crack growth.

A slight difference in the results is observed because the fracture criterion used for VCCT crack growth is linear and critical fracture energy based only, while the delamination for CZM model is based on interlaminar strengths along with critical energy. An artificial damping coefficient also affects the convergence of the CZM model. Furthermore, in the VCCT model, the nodes separate instantaneously when the fracture criterion is reached, implying that the load-carrying capacity drops more rapidly than it does in the CZM model.

## 36.8. Recommendations

When setting up a VCCT-based crack-growth analysis, consider the following hints and recommendations:

- Differences in the size of the elements ahead of and behind the crack tip/front affect the accuracy of the energy-release-rate calculation. Use equally sized meshes for elements along the predefined crack path whenever possible.
- The mesh size itself also affects the solution. Examine mesh-size convergence before attempting the finite element solution.
- To ensure accuracy of the energy-release-rate calculation, define the crack extension carefully.

- The following assumptions apply to the VCCT calculation:
  - The strain energy released when a crack advances by a small amount is the same as the energy required to close the crack by the same amount.
  - The crack tip field/deformation at the crack tip/front location is similar to that which occurs when the crack extends by a small amount.

Neither assumption applies when crack growth approaches the boundary, or when the two cracks approach each other; therefore, when using the VCCT calculation for problems such as T-joints where the two cracks approach each other, examine the analysis results carefully.

- In the case of unstable crack growth or a rapid extension of the crack, specify smaller DTMAX and DTMIN values (**CGROW**) to allow time for load rebalancing.

## 36.9. References

The following references are used in this example problem:

1. Dharmawan, F., S. Rodney, et al. "Geometry and Damage Effects in a Composite Marine T-Joint." *Composite Structures* 66 (2004): 181-187.
2. Dharmawan, F. (2008) *Structural Integrity and Damage Tolerance of Composite T-Joints in Naval Vessels*. Ph.D. Thesis. School of Aerospace, Mechanical and Manufacturing Engineering, RMIT University: Melbourne, Victoria, Australia.
3. Chen, J., Eric Ravey. "Prediction of Delamination in Braided Composite T-Piece Specimens." *Journal of Composites Science and Technology* 69 (2009): 2363–2367.
4. DiBella, G., C. Borsellino. "Experimental and Numerical Study of Composite T-Joints for Marine Applications." *International Journal of Adhesion and Adhesives* 30 (2010): 347-358.

## 36.10. Input Files

The following files were used in this problem:

- `vcct2d.dat` -- Input file for the VCCT-based 2-D analysis of the T-joint.
- `vcct2d.cdb` -- Common database file for the VCCT-based 2-D finite-element T-joint model (called by `vcct2d.dat`).
- `czm2d.dat` -- Input file for the CZM-based 2-D analysis of the T-joint.
- `vcct2d.cdb` -- Common database file for the CZM-based 2-D finite-element T-joint model (called by `czm2d.dat`).

The files are available in the `td-36` folder. See [Obtaining the Input Files \(p. xxxv\)](#) for more information.





---

## Chapter 37: Bolt Thread Simulation

---

This example problem demonstrates a simplified modeling technique for bolt thread simulation via the [bolt section](#) method. This method delivers approximate results with the near accuracy of the true threaded bolt model, but without the need for detailed thread geometry and refined mesh discretization. The bolt section method also offers a significant savings in simulation time.

The following features and capabilities are highlighted:

- Modeling of 2-D/3-D bolt thread by assigning the bolt section to [contact elements](#).
- Use of [pretension](#) loading.

Topics related to this example problem follow:

- [37.1. Introduction](#)
- [37.2. Problem Description](#)
- [37.3. Modeling](#)
- [37.4. Material Properties](#)
- [37.5. Boundary Conditions and Loading](#)
- [37.6. Analysis and Solution Controls](#)
- [37.7. Results and Discussion](#)
- [37.8. Recommendations](#)
- [37.9. Input Files](#)

### 37.1. Introduction

A bolted joint is used to hold two or more parts together to form an assembly of a mechanical structure. In order to achieve expected physical behaviors of a bolted joint structure, a detailed three-dimensional bolt model, which fully includes the bolt pretension effect and the frictional behavior at contact interfaces, is desirable. However, for a large, complex structure, detailed modeling of bolted joints is difficult because of problem size restrictions and computational costs associated with analyzing the entire structure.

The bolt thread modeling technique available for 2-D and 3-D contact elements offers simplified modeling with accuracy close to that of a true threaded bolt model. Bolt threads can be simulated by assigning a bolt section (defined by the **SECTYPE** command) to contact elements that are overlaid on a smooth cylindrical bolt surface. To approximate the behavior of the bolt, calculations are performed internally based on the user-specified thread geometry data and the end points of the bolt axis (input via the **SECDATA** command).

The bolt thread modeling technique is useful for system level modeling where the primary bolt function is to transfer a load. The absence of geometric details and refined mesh discretization in the thread region also makes it a computationally inexpensive method. This technique can be applied to 3-D models and 2-D axisymmetric models

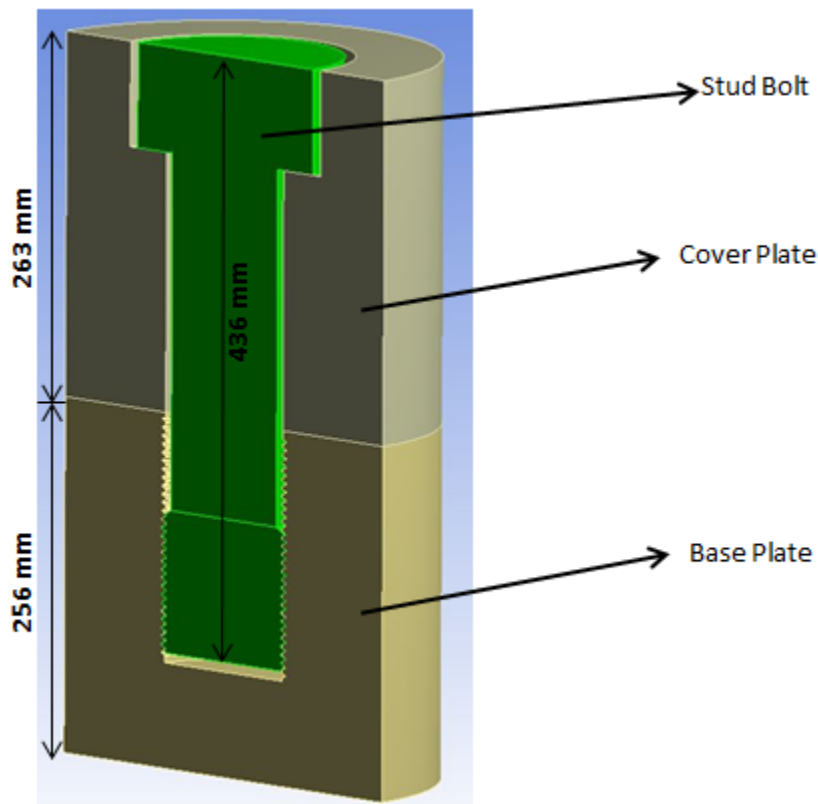
## 37.2. Problem Description

The two primary characteristics in a bolted joint are pretension and mating part contact. To simulate the bolt configuration, a stud M120 bolt is modeled with a cover and a base plate. The bolt is subjected to a pretension load of 256446 N to simulate the actual bolt phenomenon. Three frictional contact pairs (FCP) are defined: one in the thread region, another between the bolt head and the cover plate, and the third between the cover plate and the base plate.

A pressure load of 50 MPa (which is less than the equivalent pretension load) is applied to the upper surface of the cover plate after applying pretension to the bolt. The resulting bolt shank stress (stress in the region between the bolt head and the bolt thread) due to the pretension load and the inclusion of frictional contact behavior are the major concerns during the bolt simulation.

The objective of this problem is to show that the bolt section method simplifies the modeling of this bolt joint and produces approximate thread behavior and shank stress that are comparable to the true threaded bolt model.

**Figure 37.1: 3-D Half Model of a Bolted Joint**



This problem is simulated by three methods:

### 1. True thread simulation

This method is the most accurate bolt simulation. The detailed modeling of threads provides accurate thread behavior in the model. Very refined mesh discretization is required in the thread region, which makes this method computationally expensive.

### 2. Bolt section method (simplified bolt thread modeling technique)

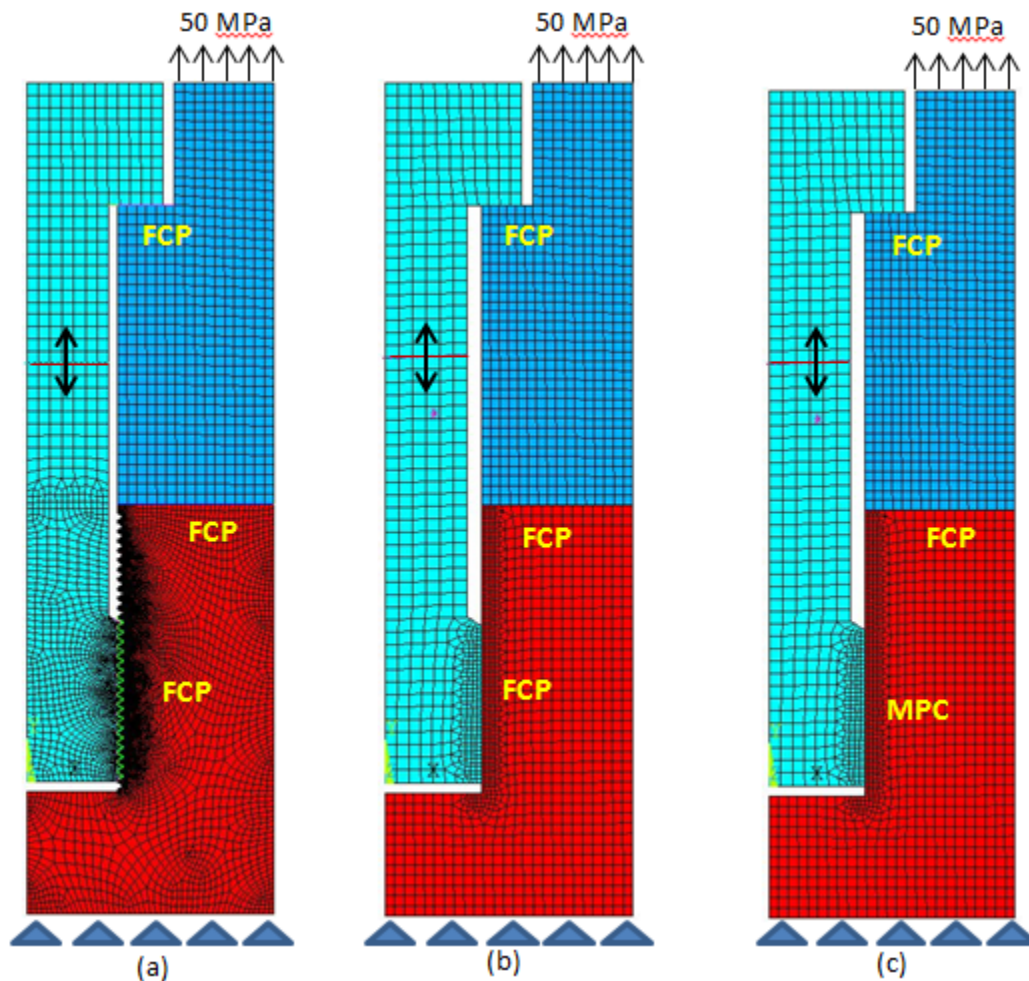
In this method, the bolt thread is simulated by assigning a bolt section to the contact elements overlaid on the smooth cylindrical bolt surface. (No detailed thread geometry is required.) Calculations are performed internally based on the thread parameters given by the **SECDATA** command to approximate the behavior of the bolt. This method is computationally inexpensive.

### 3. MPC method (bonded behavior in thread region)

In this method, MPC bonded behavior is defined in the thread region. (No detailed thread geometry is required.) This method is very fast computationally, but thread behavior can be lost.

Both 2-D axisymmetric and 3-D models are used to compare these three methods. The 2-D model setup for all three methods is shown in the figure below.

**Figure 37.2: 2-D Axisymmetric Problem Setup for (a) True Thread, (b) Bolt Section, (c) MPC Bonded Method**



## 37.3. Modeling

An M120 structural steel bolt with standard thread dimensions is modeled with a cover plate and a base plate of reasonable dimensions. Both 2-D and 3-D bolt thread modeling is performed. A bilinear isotropic plastic material model is used for the bolt and the plates.

Modeling of this problem is done through the following steps:

### 37.3.1. Model the Bolt with Cover Plate and Base Plate

37.3.2. Model the Pretension Section

37.3.3. Model the Contact Pairs

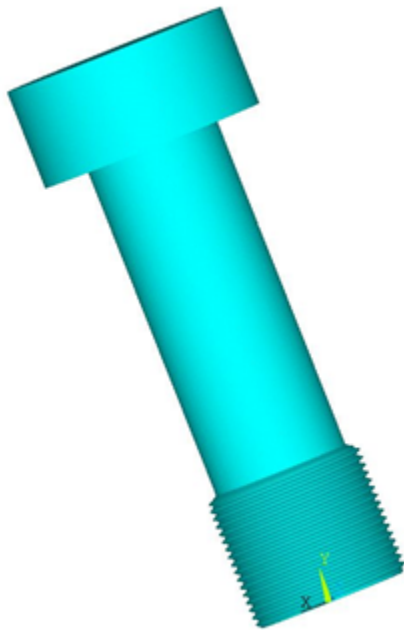
### 37.3.1. Model the Bolt with Cover Plate and Base Plate

Two models, one with a threaded bolt surface and another with a smooth bolt surface, are created to demonstrate the simplicity and advantage of the bolt section method over the true thread simulation method.

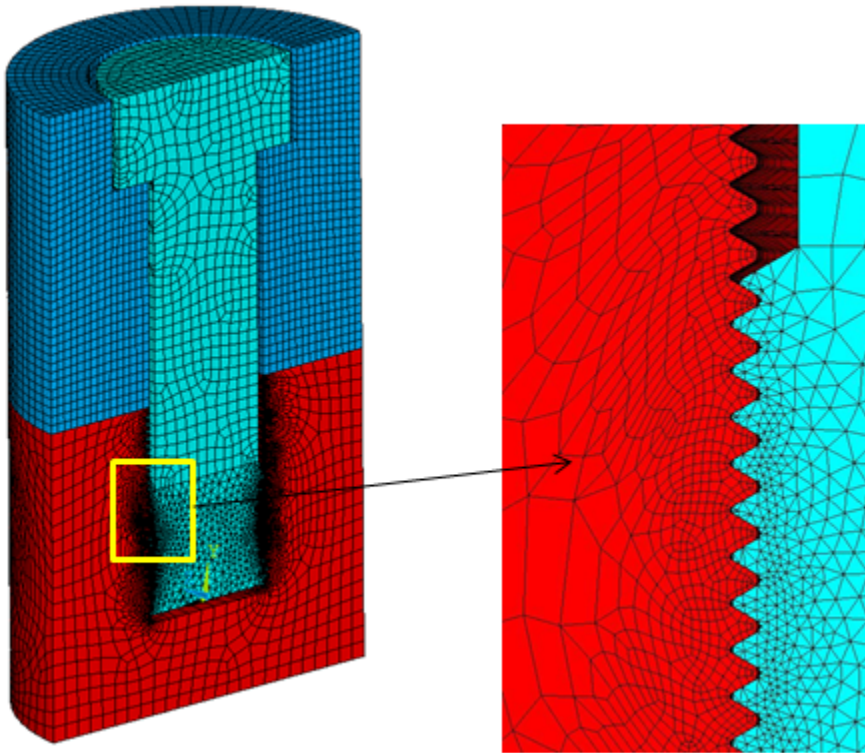
#### 37.3.1.1. Model the True Threaded Bolt with Cover Plate and Base Plate

The 3-D threaded bolt model represents a single start M120 bolt with a cover plate and a base plate. The bolt has a maximum diameter of 120 mm, a pitch diameter of 116 mm, a 6 mm pitch, and a half thread angle of 30 degrees (according to the standard thread profile).

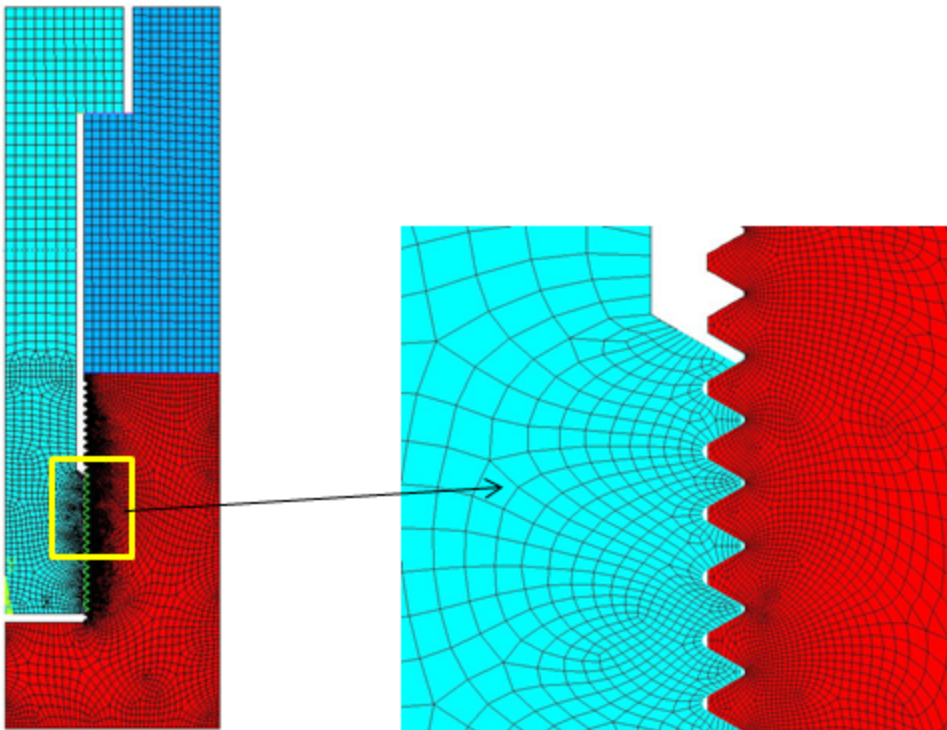
**Figure 37.3: 3-D Model of a Threaded M120 Bolt**



The model is meshed with **SOLID186** and **SOLID187** elements. Mesh refinement is performed in the thread region.

**Figure 37.4: 3-D Half Model of a Threaded Bolt Joint with Mesh Details**

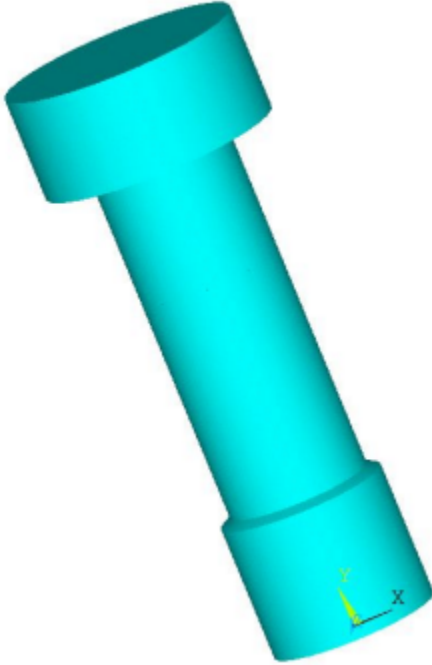
The 2-D surface geometry is extracted from the 3-D thread geometry. The 2-D model is meshed with PLANE183 axisymmetric elements (KEYOPT(3) = 1).

**Figure 37.5: 2-D Axisymmetric Model of a True Threaded Bolt Joint with Mesh Details**

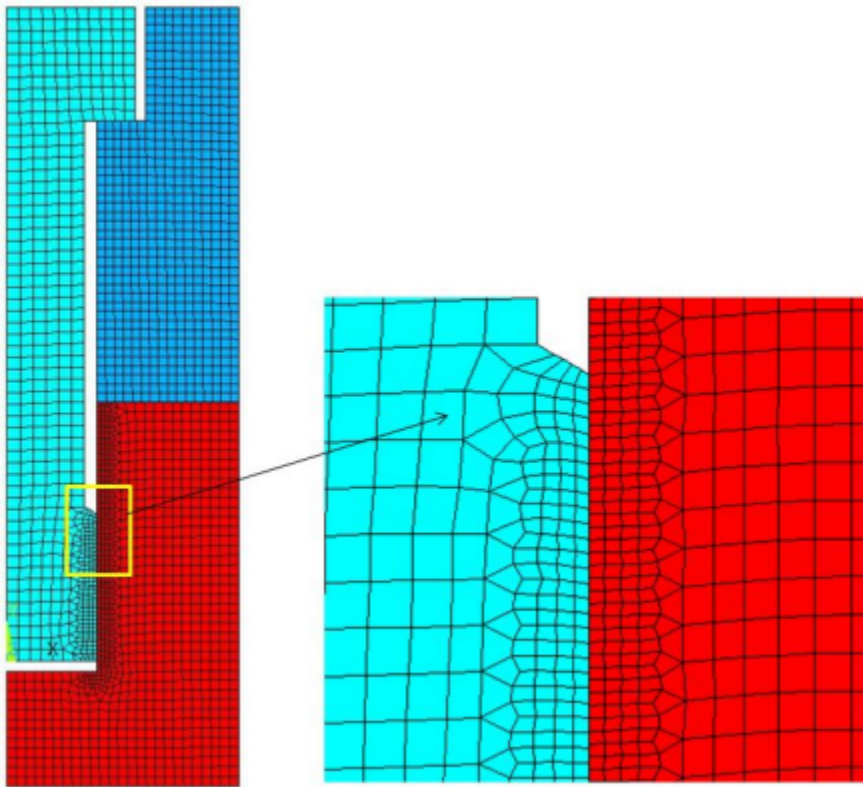
### **37.3.1.2. Model the Simplified Bolt with Cover Plate and Base Plate**

Instead of modeling a true threaded bolt, smooth cylindrical surfaces are created for both the bolt and base plate.

**Figure 37.6: Simplified 3-D Model of an M120 Bolt**

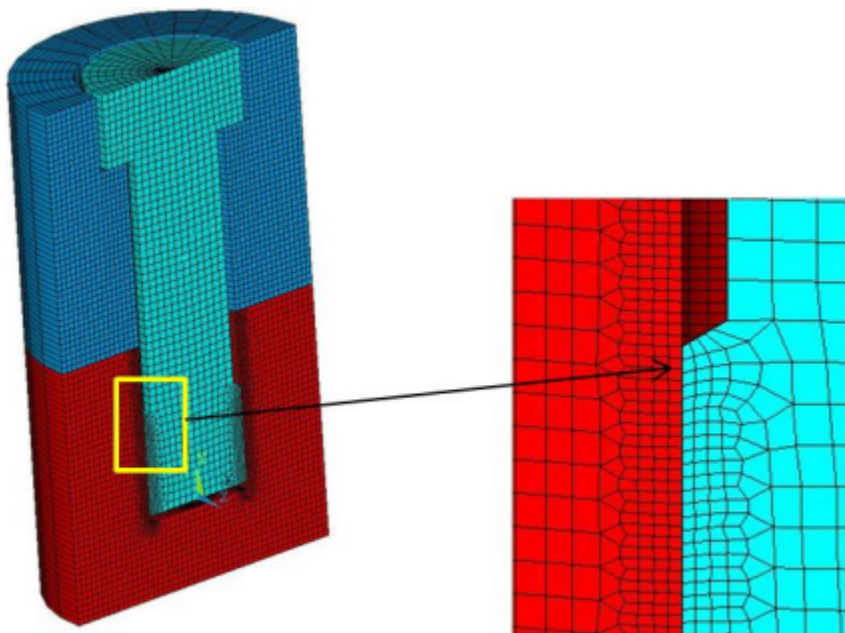


A 2-D axisymmetric model is created and meshed with **PLANE183** axisymmetric elements (KEYOPT(3) = 1).

**Figure 37.7: 2-D Axisymmetric Model of a Simplified Bolt Joint with Mesh Details**

The 3-D model is generated with **SOLID186** elements by extruding the 2-D axisymmetric model about the Y-axis with the **EEXTRUDE** command.

```
eextrude,,30,,,360 !creates 3-D model by rotating 2-D axisymmetric model about y-axis
```

**Figure 37.8: 3-D Half Model of a Simplified Bolt Joint with Mesh Details**

### 37.3.2. Model the Pretension Section

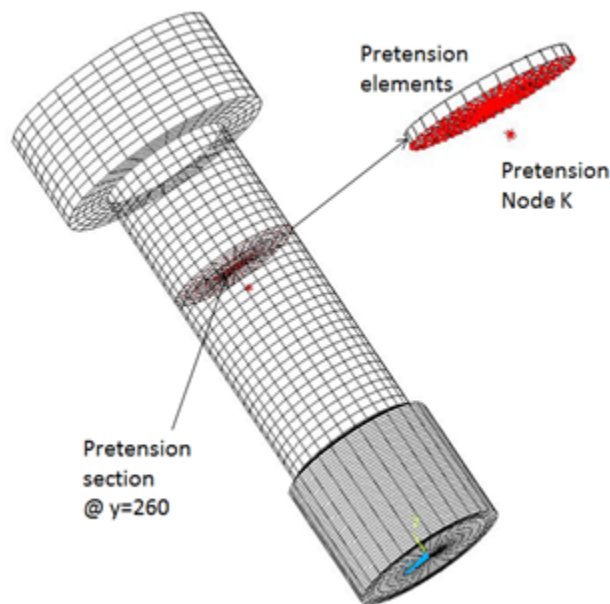
Pretension is the most important aspect of the simulation of the bolted structure. It transfers the load in the model while sustaining only a small part of the external load on the bolt. The preload on the bolt is caused by the tightening of the bolt to fasten the cover plate to the base plate. Pretension in the bolt is modeled by cutting the bolt into two segments and pulling each segment toward the other.

The following steps and commands illustrate the [procedure to simulate pretension](#) in the bolt:

1. Mesh the bolt, then cut the mesh and insert [PRETS179](#) elements to form the pretension section. The [PSMESH](#) command is used to create pretension elements in the bolt at  $y = 260$  mm.

```
ESEL,S,TYPE,,<type number> !selection of bolt elements by element type number
PSMESH,,,,ALL,,,Y,260,,,,ECOMP,NCOMP !automatically generate the pretension elements @ y = 260
```

**Figure 37.9: Pretension Section in the Bolt Model at  $y = 260$  mm**



2. The [SLOAD](#) command is used to apply the pretension load. In the first load step, the pretension load is applied as a force to node K. In the second load step the force locks, allowing additional loads. The effect of the initial load is preserved as a displacement after it is locked.

```
SLOAD,1,PL01,lock,FORC,2544690,1,2
```

### 37.3.3. Model the Contact Pairs

Three frictional contact pairs are defined to simulate the contact interfaces in the model. The coefficient of friction in the contact region is 0.15. Contact regions are meshed with [CONTA174](#) elements for the 3-D case and with [CONTA172](#) elements for the 2-D axisymmetric case. The augmented Lagrange algorithm is used ([KEYOPT\(2\) = 0](#)). Target surfaces are meshed with [TARGE170](#) elements for the 3-D case and [TARGE169](#) elements for the 2-D axisymmetric case.

Contact pairs are modeled in the following regions:

- 37.3.3.1. [Contact in the Thread Region](#)
- 37.3.3.2. [Contact Between the Bolt Head and the Cover Plate](#)
- 37.3.3.3. [Contact Between the Cover Plate and the Base Plate](#)



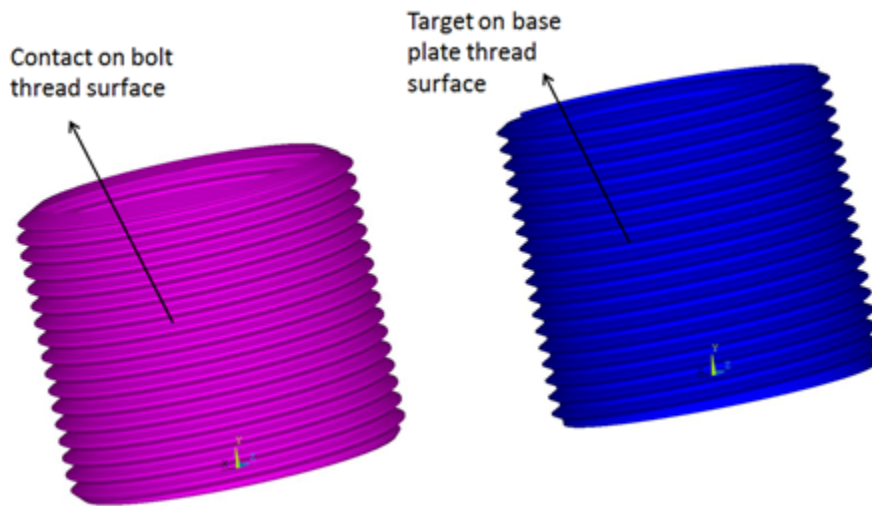
### 37.3.3.1. Contact in the Thread Region

A surface-to-surface contact pair is defined between the bolt and the base plate. Contact in the thread region is modeled differently for each of the three simulation methods.

#### 37.3.3.1.1. Contact in the Thread Region for the True Thread Simulation Method

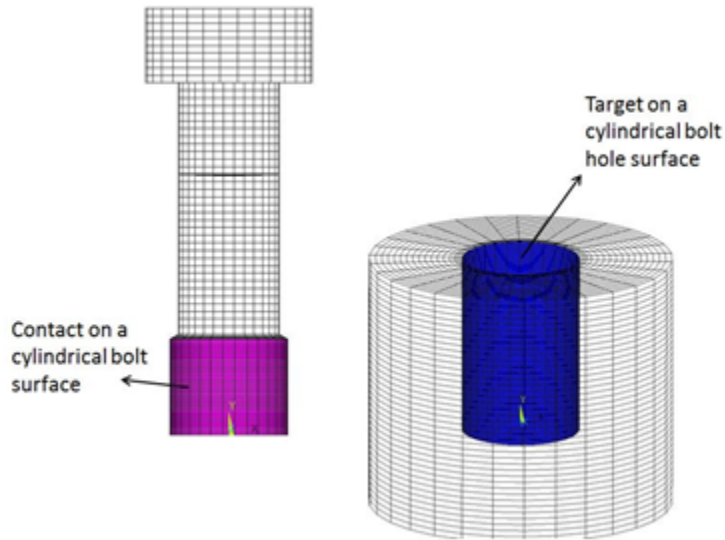
A frictional contact pair is defined between the bolt thread surface (the contact surface) and the base plate thread surface (target surface). The surface projection contact detection method (KEYOPT(4) = 3) is used because it provides more accurate contact tractions and stresses for underlying elements compared with other contact detection methods.

**Figure 37.10: Contact and Target Surfaces at the Bolt Thread and the Base Plate Thread**



#### 37.3.3.1.2. Contact in the Thread Region for Bolt Section Simulation Method

Contact elements (CONTA174 for the 3-D case, CONTA172 for the 2-D case) are generated on the smooth cylindrical bolt surface. A bolt section is assigned to the contact elements to simulate the thread. The contact region is computed internally based on the user-specified thread geometry data and the two end points of the bolt axis. Target elements (TARGE170 for the 3-D case, TARGE169 for the 2-D case) are overlaid on the smooth cylindrical hole of the base plate.

**Figure 37.11: Contact and Target Surfaces at the Bolt Surface and Base Plate**

The **SECTYPE** and **SECDATA** section commands are used to define the bolt section for contact elements. The format for these commands is shown below.

```
SECTYPE, SECID, CONTACT, BOLT
SECDATA, Dm, P, ALPHA, N, X1, Y1, Z1, X2, Y2, Z2
```

where

$D_m$  = Mean pitch diameter,  $d_m$

$P$  = Pitch distance,  $p$

$ALPHA$  = Half-thread angle,  $\alpha$

$N$  = Number of starts (defaults to 1)

$X1, Y1, Z1, X2, Y2, Z2$  = Two end points of the bolt axis in global Cartesian coordinates

The following commands illustrate the procedure for bolt thread modeling using the bolt section commands:

```
et,100,174           ! Define contact element type
keyopt,100,4,3      ! Define surface projection based contact detection method
keyopt,100,10,2     ! Update stiffness at each iteration
mp,mu,100,.15      ! Frictional co-efficient
sectype,5,contact,bolt
secdata,116,6,30,,0,0,0,0,162,0
et,101,170         ! Define target element type
r,100,
cmsel,s,bolt_thread,node
type,100
mat,100
real,100
secn,5            ! Assign the section to contact elements
esurf
cmsel,s,bottomplate_thread,node
type,101
mat,100
real,100
secn,0
esurf
allsel,all
```

### 37.3.3.1.3. Contact in the Thread Region for the MPC Simulation Method

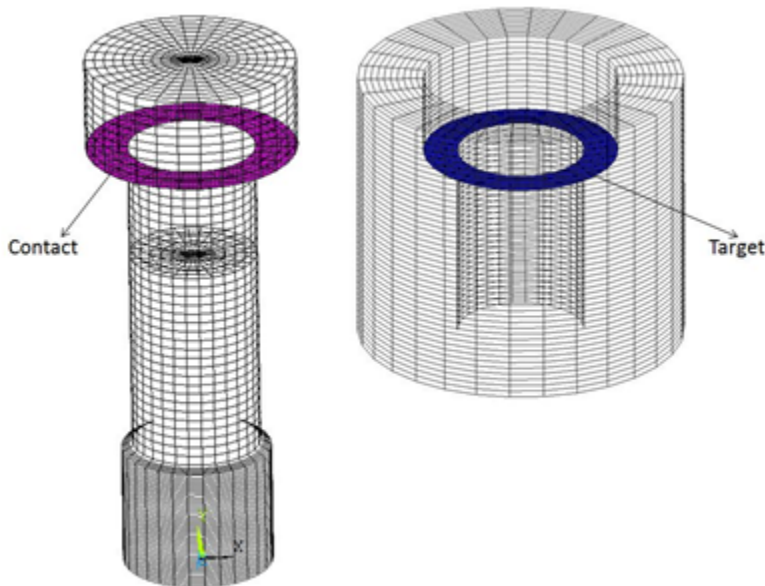
In this method, MPC bonded contact behavior is defined between the smooth cylindrical bolt surface and the smooth base plate. There is no thread behavior defined. To define MPC contact, the following contact elements KEYOPT settings are used:

KEYOPT(2) = 2 - MPC algorithm  
 KEYOPT(4) = 2 - Nodal contact detection  
 KEYOPT(12) = 5 - Always bonded behavior

### 37.3.3.2. Contact Between the Bolt Head and the Cover Plate

A frictional contact pair is defined between the bolt head (the contact surface) and the cover plate (the target surface). The surface projection contact detection method (KEYOPT(4) = 3) is used for this contact pair.

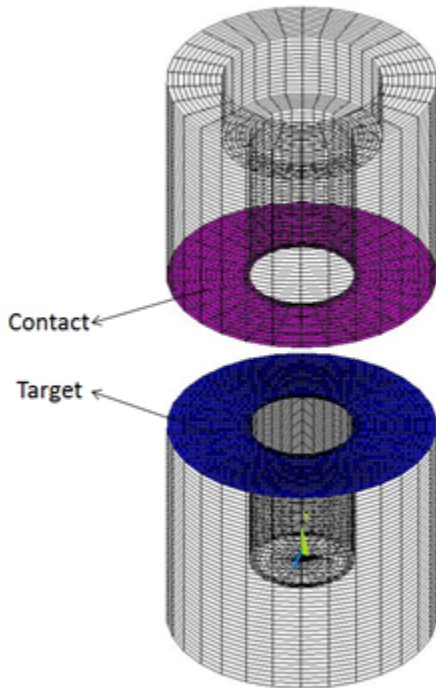
**Figure 37.12: Contact and Target Surfaces at the Bolt Head and Cover Plate**



### 37.3.3.3. Contact Between the Cover Plate and the Base Plate

A frictional contact pair is defined between the cover plate (the contact surface) and the base plate (the target surface). The surface projection contact detection method (KEYOPT(4) = 3) is used for this contact pair.

**Figure 37.13: Contact and Target Surfaces at the Cover Plate and Base Plate**



### 37.4. Material Properties

Structural steel with the bilinear isotropic hardening model (TB,BISO) is used to model the bolt and plates.

**Table 37.1: Material Properties of Bolt**

Elastic Material Properties	
Young's Modulus	2.00E5 MPa
Poisson's Ratio	0.3
Density	7.85E-9 tonne/mm <sup>3</sup>
Bilinear Isotropic Hardening Constants (TB,BISO)	
Yield stress	450 MPa
Tangent modulus	2.00E4 MPa

**Table 37.2: Material Properties of Cover Plate and Base Plate**

Elastic Material Properties	
Young's Modulus	2.00E5 MPa
Poisson's Ratio	0.3
Density	7.85E-9 tonne/mm <sup>3</sup>
Bilinear Isotropic Hardening Constants (TB,BISO)	
Yield stress	280 MPa
Tangent modulus	2.00E4 MPa

## 37.5. Boundary Conditions and Loading

The bottom surface of the base plate is constrained in all directions. A pressure load is applied to the upper surface of the cover plate after preloading the bolt.

- In the first load step, pretension loading of 2544690 N is applied to the pretension section through the **SLOAD** command.

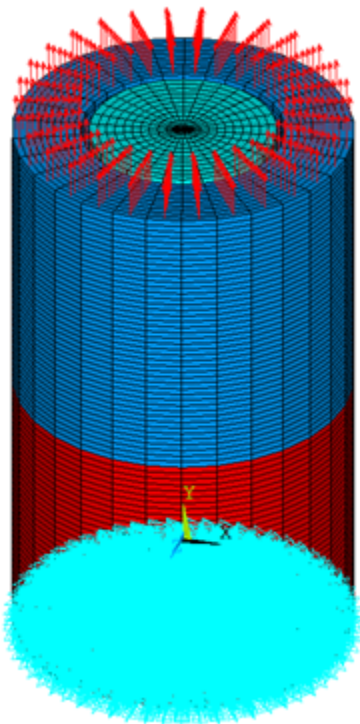
```
sload,1,p101,lock,forc,2544690,1,2 ! pretension load of 2544690 N
```

- In the second load step, a pressure load of 50 MPa (which is less than the equivalent pretension load) is applied to the upper surface of the cover plate.

```
sf,sfload_nn,pres,-50 ! pressure load of 50 MPa on upper surface of cover plate
```

**Figure 37.14: Boundary Conditions and Loading on the 3-D Model**

Pressure of 50 MPa



## 37.6. Analysis and Solution Controls

A nonlinear static analysis is performed in two load steps. Large-deflection effects (**NLGEOM**) are included in the analysis.

```
antype,static !selecting analysis
nlgeom,on !including geometric nonlinearity
```

## 37.7. Results and Discussion

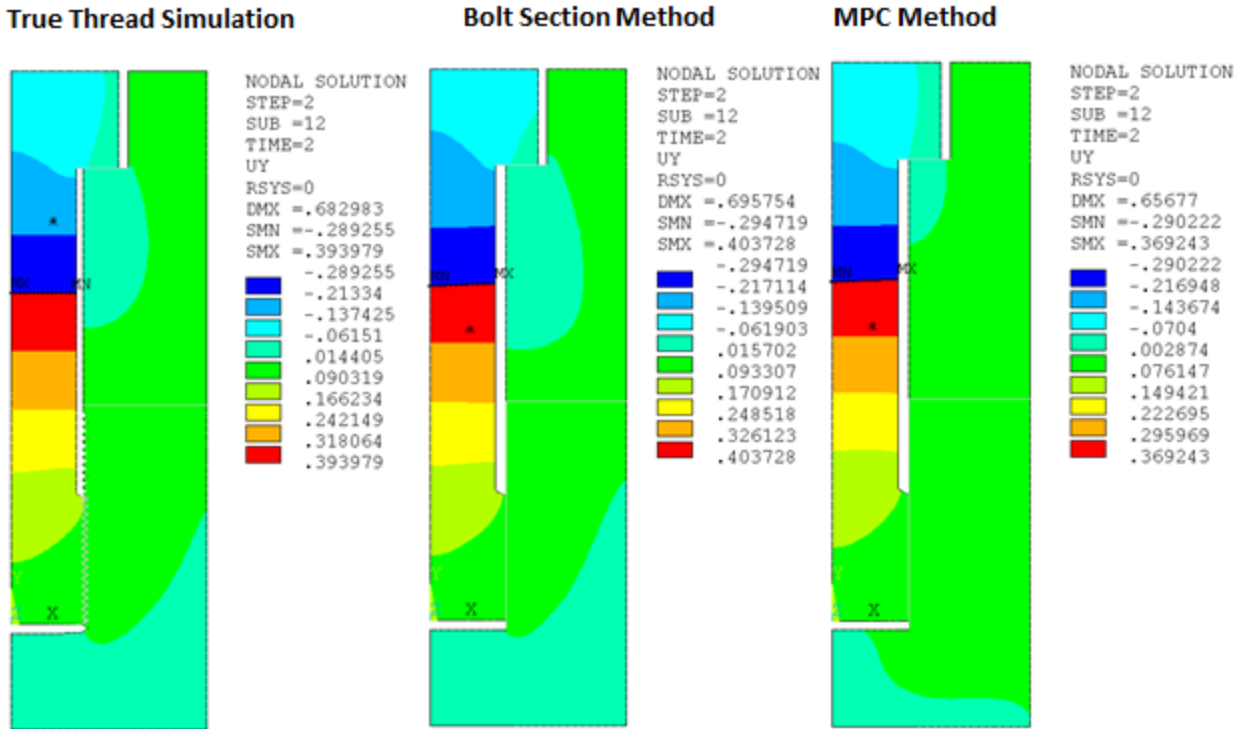
A comparative study of all three methods shows the effectiveness and simplicity of the bolt section method.

### 37.7.1. Results for 2-D Models

#### Axial (UY) Displacement

The pretension effects can be observed in the following figure in which two segments of the bolt are pulling against each other.

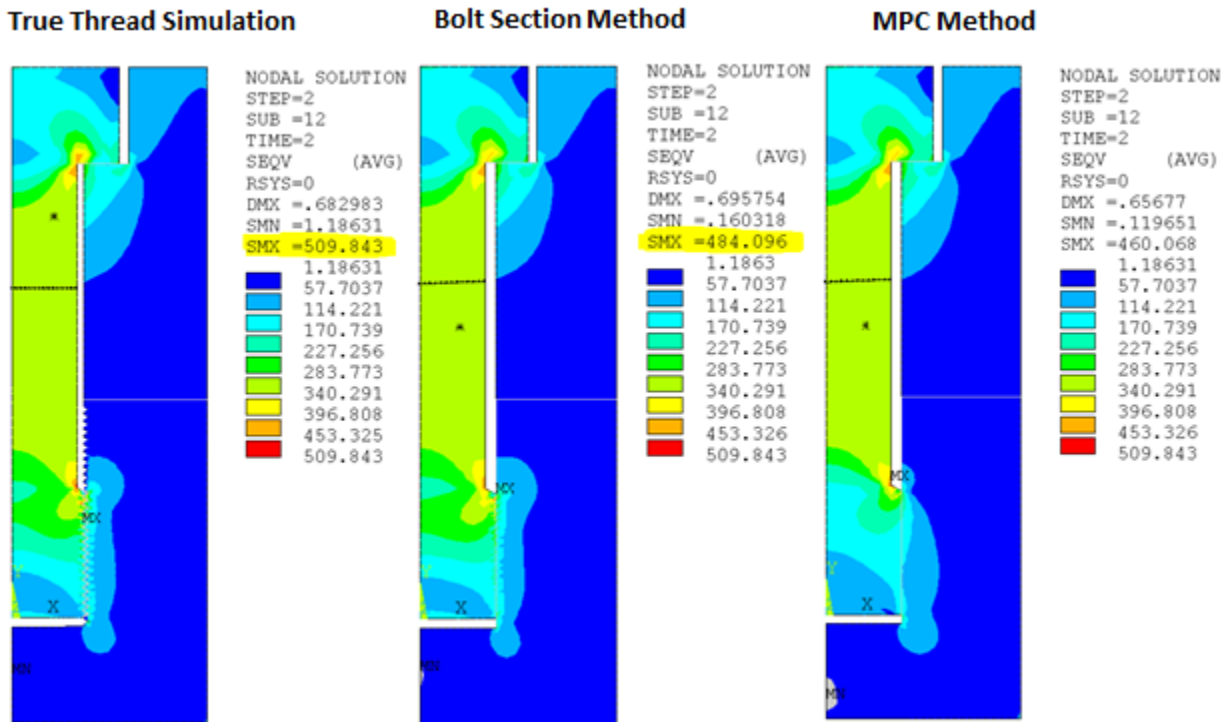
Figure 37.15: UY Displacement in the 2-D Axisymmetric Model for all Three Methods



#### von Mises Stress

The von Mises stress plots below show that shank stress is similar in all three methods. User-specified contour values are used for the purpose of comparison. Variations are observed only in the local areas such as the thread region or near the bolt head and cover plate contact region.

Figure 37.16: von Mises Stress in the 2-D Axisymmetric Model for all Three Methods

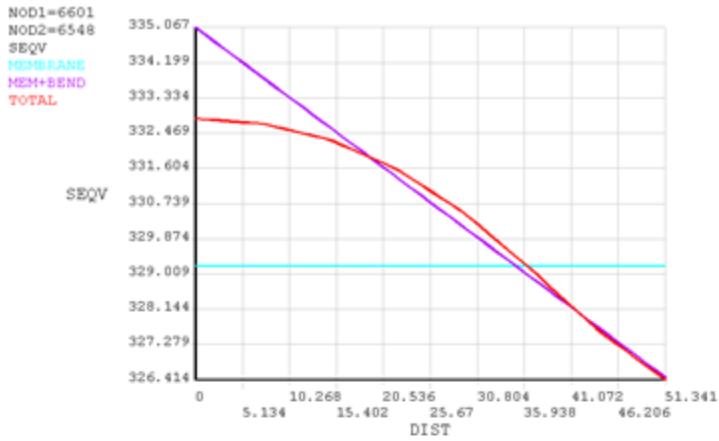


The stress plot of the thread region for the bolt section method closely matches the stress plot for the true thread simulation, and the MPC method plot varies. The comparison between stress plots demonstrates that accurate simulation of thread behavior and shank stress in the bolt can be achieved by using the bolt section method.

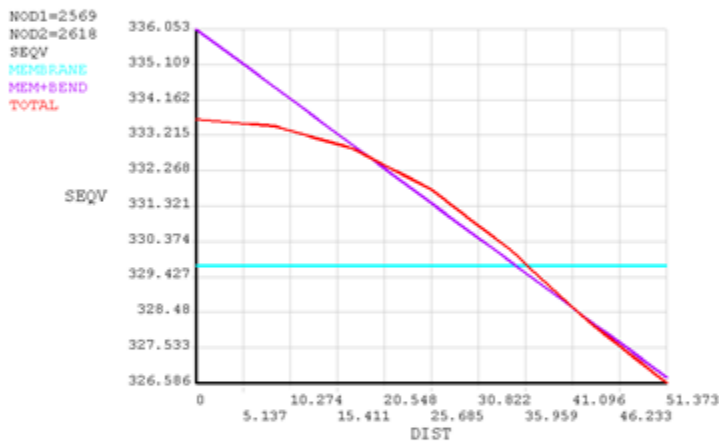
### **Linearized Stress Along a Path**

Linearized stress in the bolt shank along the path at  $y = 280$  is similar for all three methods. The values are 329.2 MPa for the true thread simulation, 329.7 MPa for the bolt section method, and 330.10 MPa for the MPC method.

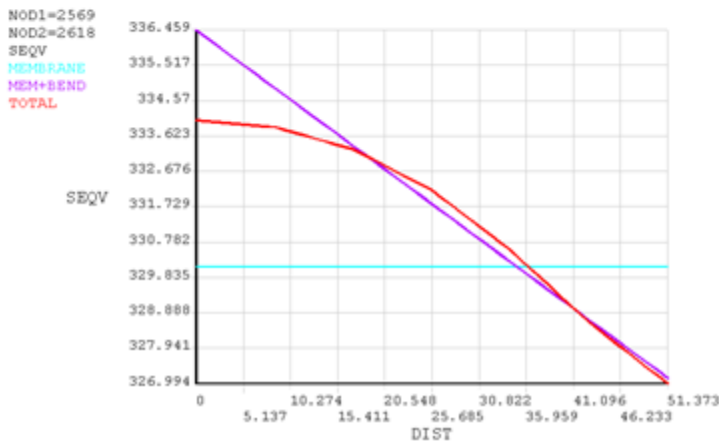
**Figure 37.17: Linearized Stress in the Bolt Shank Along a Path at y = 280 for all Three Methods.**



**True Thread Simulation**



**Bolt Section Method**



**MPC Method**

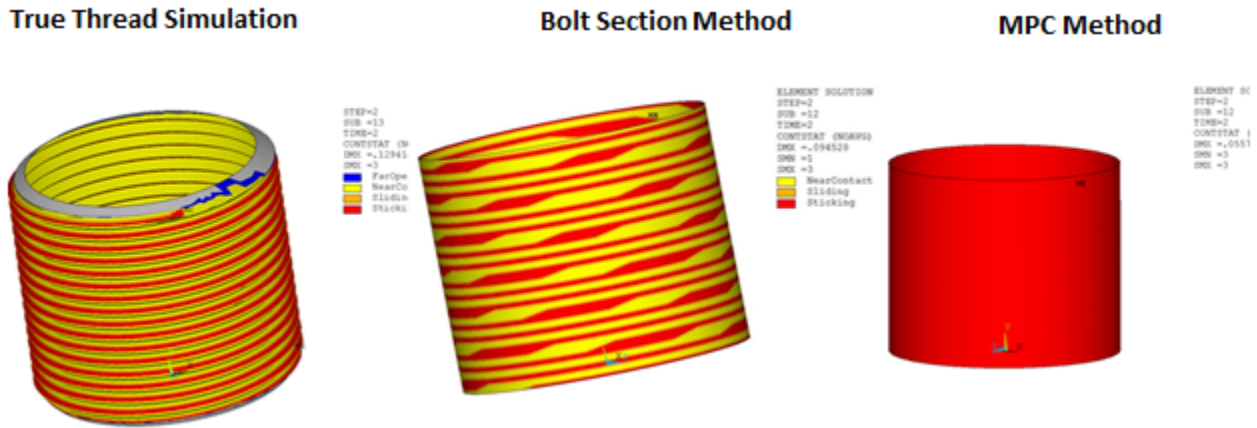
## 37.7.2. Results for 3-D Models

### Contact Status

A helix pattern can be observed in the contact status plot of the bolt section method. If the mesh is sufficiently refined in the thread region, a more accurate helix pattern can be obtained.



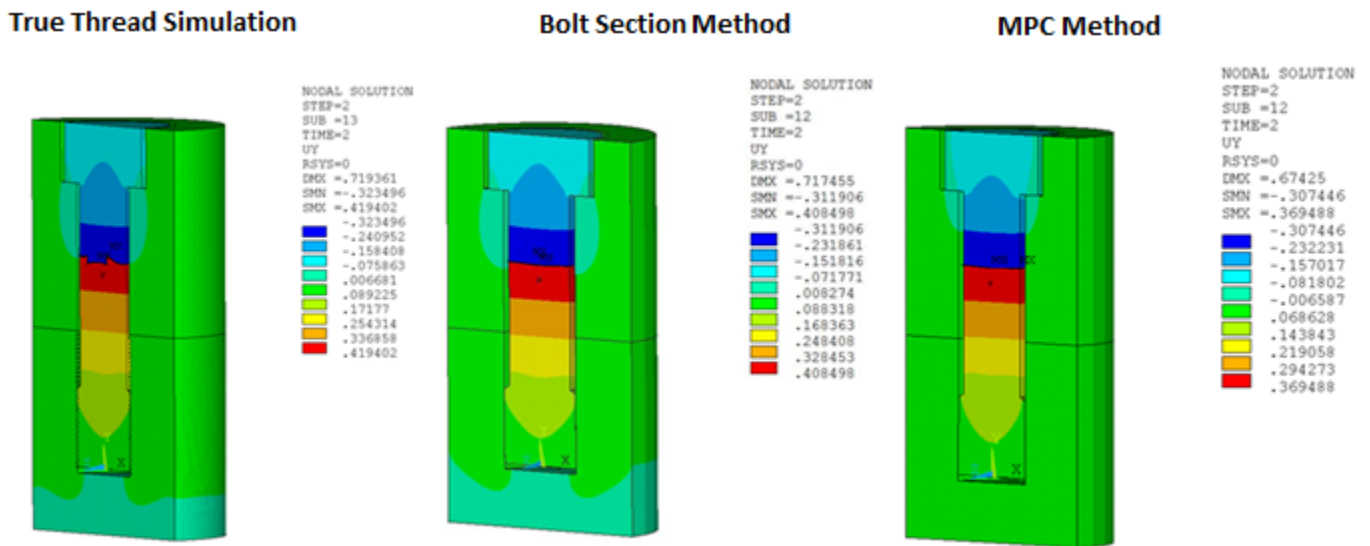
**Figure 37.18: Contact Status in the Thread Region for all Three Methods**



**Axial (UY) Displacement**

The pretension effects can be observed in the following figure in which two segments of the bolt are pulling against each other.

**Figure 37.19: UY Displacement in the 3-D Half Model for all Three Methods**



**von Mises Stress**

Similar to the 2-D case, the von Mises plots for the 3-D models show that shank stress is similar in all three methods, and variations are observed only in the local areas.

**Figure 37.20: von Mises Stress in the 3-D Half Model for all Three Methods**

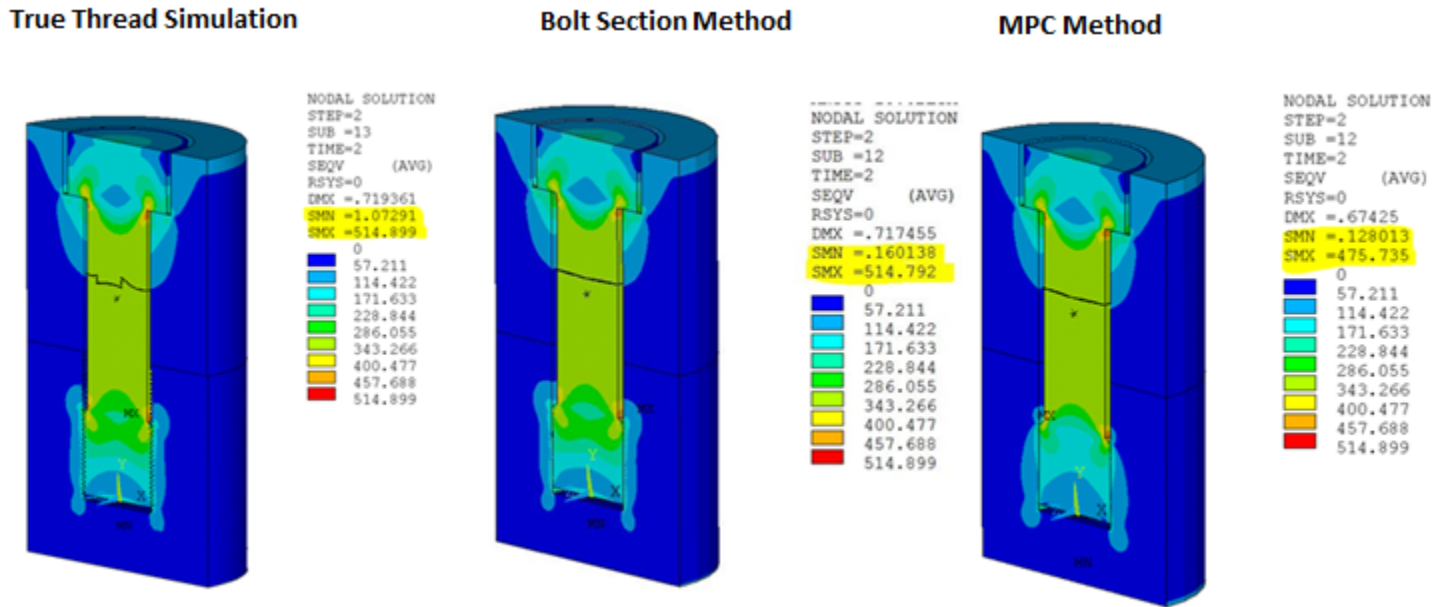
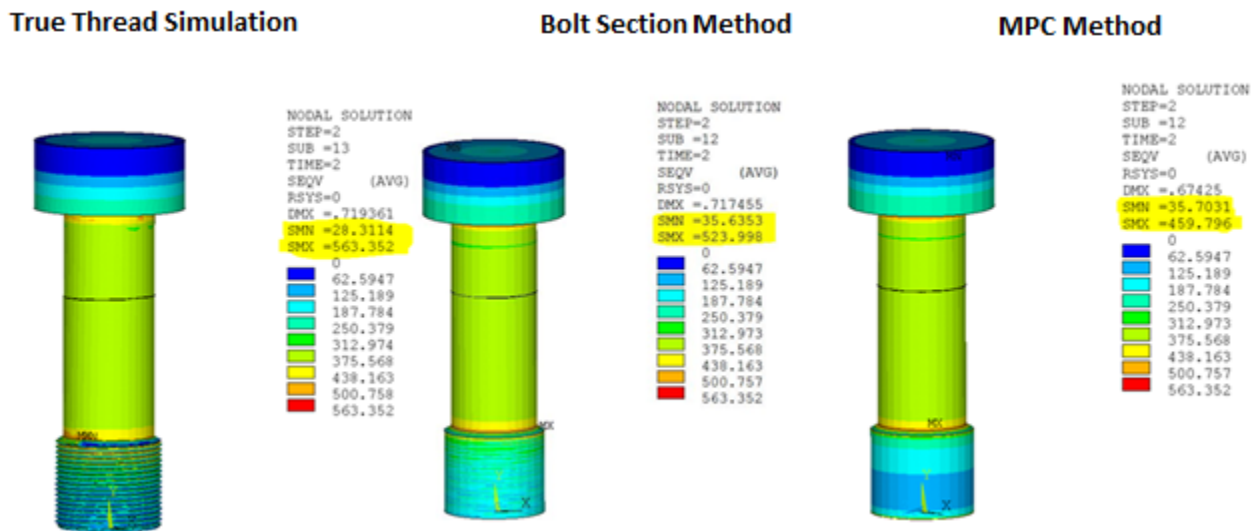


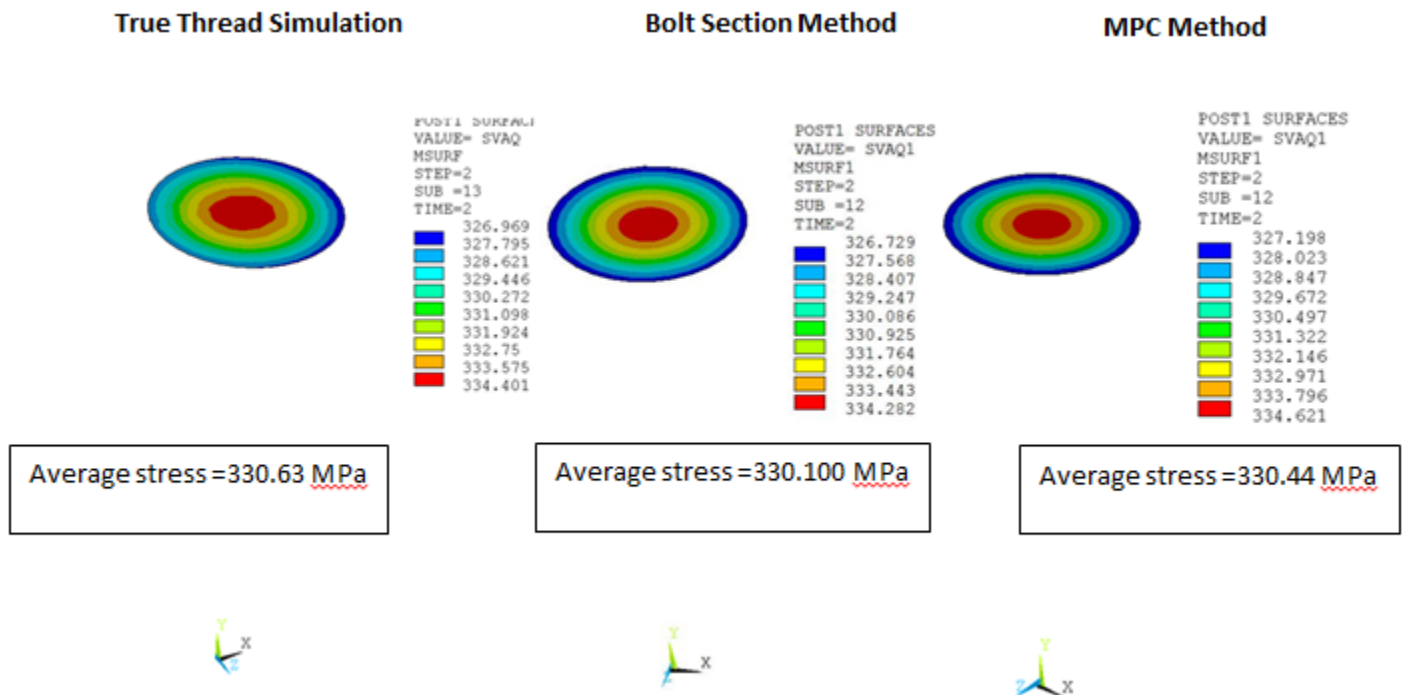
**Figure 37.21: von Mises Stress in the Bolt for all Three Methods**



The stress plot of the thread region for the bolt section method closely matches the stress plot for the true thread simulation, and the MPC method plot varies. This validates the conclusion that the bolt section method achieves accuracy near to that of the true thread simulation.

**von Mises Stress at Section**

Average von Mises stress in the bolt shank at section  $y = 280$  is similar for all three methods. The values are 330.63 MPa for the true thread simulation, 330.10 MPa for the bolt section method, and 330.44 MPa for the MPC method.

**Figure 37.22: von Mises Stress in the Bolt Shank at Section y = 280 for all Three Methods**

### 37.7.3. Comparison of Computation Time

From the tables below it is clear that the bolt section method is less computationally expensive than the true thread simulation. The MPC method is the least computationally expensive, but thread effects are lost.

**Table 37.3: Simulation Time and Cumulative Iterations for 2-D Models**

	Computation time	Elapsed time	Cumulative iterations	Number of Elements
<b>True thread simulation</b>	182.942	186	31	12642
<b>Bolt section method</b>	38.439	41	28	2297
<b>MPC method</b>	35.646	38	28	2297

**Table 37.4: Simulation Time and Cumulative Iterations for 3-D Models**

	Computation time	Elapsed time	Cumulative iterations	Number of Elements
<b>True thread simulation</b>	731625.968	415326	29	1111133
<b>Bolt section method</b>	44451.254	45912	25	69061
<b>MPC method</b>	41255.852	41948	25	69061

Comparisons of von Mises stress and computation time demonstrate that accurate simulation of thread behavior and shank stress results in the bolt can be achieved by the bolt section method, with the added benefit of significant savings of simulation time.

## 37.8. Recommendations

The following points are important for bolt thread modeling:

- The bolt cylindrical surface should be the contact surface, and the bolt section should be assigned to the contact elements.
- Coordinates of the axis data points (required for **SECDATA**) should be on the bolt axis and defined in the global coordinate system.
- In order to achieve better accuracy, the mesh size in the thread region should be less than the pitch distance.
- We recommend you use of a nodal contact detection method (**KEYOPT(4) = 1 or 3**).
- This technique is valid only for standard, straight threads. It is not applicable for nonstandard threads such as tapered threads or buttress threads.
- The maximum stress in the thread region may vary with mesh density. However, the overall stress distribution remains similar in pattern.

## 37.9. Input Files

The following files were used in this problem:

- `boltSimulation_2-D` — Input file for 2-D axisymmetric analysis of bolt thread simulation for all three methods.
- `boltSimulation_3-D` — Input file for 3-D full model analysis of bolt thread simulation for all three methods.
- `truethread2-D.cdb` — Common database of true threaded 2-D model.
- `nothread2-D.cdb` — Common database of non-threaded 2-D model.
- `truethread_3-D.cdb` — Common database of true threaded 3-D model.

The files are available in the `td-37` folder. See [Obtaining the Input Files \(p. xxxv\)](#) for more information.

---

## Chapter 38: Large-Deformation Neo-Hookean Analysis (via UserMat Subroutine)

---

This problem formulates a 3-D large deformation, hyperelastic material to demonstrate the user material capability in nonlinear geometry analyses. Details are given for stress and material tangent calculations and formulation in a co-rotated frame, as well as conversion of tensor quantities to Voigt notation. The problem also serves as a usage example of the `UserMat` subroutine, a user-programmable feature for developing a custom, constitutive model to define the stress-strain behavior of a material.

Topics related to this example problem follow:

- 38.1. Introduction
- 38.2. Problem Description
- 38.3. Modeling
- 38.4. Material Properties
- 38.5. Boundary Conditions and Loading
- 38.6. Analysis and Solution Controls
- 38.7. Results and Discussion
- 38.8. Recommendations
- 38.9. References
- 38.10. Input Files

### 38.1. Introduction

The `UserMat` subroutine is a user-programmable feature for developing a custom, constitutive model to define the stress-strain behavior of a material. User-defined materials can be used with current-technology elements that have a displacement-based element formulation.

Called at each element integration point, the incremental and total deformations are passed into the `UserMat` subroutine, along with stress and state variables from the previous increment. You must develop an algorithm which updates the material state and stress at the end of the increment, as well as calculates the algorithmic material tangent. In analyses with nonlinear geometry (`NLGEOM,ON`), the user material is formulated in a co-rotational frame, and the stress and algorithmic tangent must be calculated in this co-rotated frame.

### 38.2. Problem Description

In this problem, a 3-D, large-deformation, hyperelastic user material is developed and implemented. The constitutive model is the Neo-Hookean hyperelastic model, which closely reproduces the Neo-Hookean model already available as a standard material within the program.

To demonstrate the user material model, the shearing of a 1 x 1 x 1 block is simulated, and the effective stress versus effective strain is reported. The model is recast in the co-rotated frame (required by the user material subroutine), and an algorithm for the determination of the co-rotated frame rotation via polar decomposition of the deformation gradient is also presented. The stress, material tangent, and change of basis operations from are converted from full tensor form to Voigt notation.

### 38.3. Modeling

The following modeling topics are available:

- 38.3.1. Neo-Hookean Model
- 38.3.2. Co-rotational Frame
- 38.3.3. Voigt Notation

#### 38.3.1. Neo-Hookean Model

The strain energy potential for a nearly incompressible hyperelastic material is:

$$W \equiv \Phi(\bar{C}) + \phi(J) \quad (38.1)$$

where:

$C = \bar{F}^T \bar{F}$  = the isochoric right Cauchy-Green deformation tensor

$\bar{F} = J^{-1/3} F$  = the isochoric deformation gradient

$F$  = the deformation gradient

$J = \det(F)$

The 2<sup>nd</sup> Piola-Kirchhoff stress is:

$$S = 2 \frac{\partial W}{\partial C} = 2 \frac{\partial \Phi}{\partial C} + \frac{\partial \phi}{\partial J} J C^{-1} \quad (38.2)$$

The material stiffness tensor is:

$$C = 2 \frac{\partial S}{\partial C} = 4 \frac{\partial^2 \Phi}{\partial C \partial C} + 2 \frac{\partial}{\partial C} \left( \frac{\partial \phi}{\partial J} \right) \otimes J C^{-1} + 2 \frac{\partial \phi}{\partial J} \frac{\partial}{\partial C} (J C^{-1}) \quad (38.3)$$

For a Neo-Hookean model:

$$\begin{aligned} \Phi(\bar{C}) &= \frac{\mu}{2} (\bar{I}_1 - 3) \\ \phi(J) &= \frac{K}{2} (J - 1)^2 \end{aligned} \quad (38.4)$$

where:

$\bar{I}_1 = \text{trace}(\bar{C})$

$\mu$  = Neo-Hookean shear moduli

$K$  = Neo-Hookean bulk moduli

The 1<sup>st</sup>-order derivatives in the above equations are:

$$\begin{aligned} \frac{\partial \Phi}{\partial C} &= \frac{\mu}{2} J^{-2/3} \left( I - \frac{1}{3} C^{-1} \right) \\ \frac{\partial \phi}{\partial J} &= K (J - 1) \\ \frac{\partial}{\partial C} (J C^{-1}) &= J (C^{-1} \otimes C^{-1} - 2J) \end{aligned} \quad (38.5)$$

where:

$$I_1 = \text{trace}(C)$$

$I = 2^{\text{nd}}$ -order identity tensor

$\mathcal{J} = \text{a } 4^{\text{th}}$ -order tensor with components  $\mathcal{J}_{ijkl} = C_{ik}^{-1}C_{jl}^{-1}$

The  $2^{\text{nd}}$ -order derivatives in the above equations are:

$$\begin{aligned} \frac{\partial^2 \phi}{\partial C \partial C} &= \frac{\mu}{2} \frac{J^{-2/3}}{3} \left[ -C^{-1} \otimes I + \frac{I_1}{3} C^{-1} \otimes C^{-1} - I \otimes C^{-1} + I_1 \mathcal{J} \right] \\ \frac{\partial}{\partial C} \left( \frac{\partial \phi}{\partial J} \right) &= \frac{J}{2} K C^{-1} \end{aligned} \quad (38.6)$$

### 38.3.1.1. Stress

Substituting the  $1^{\text{st}}$ -order derivatives of the potential from Equation 38.5 (p. 592) into Equation 38.2 (p. 592), the  $2^{\text{nd}}$  Piola-Kirchhoff stress becomes:

$$S = \mu J^{-2/3} \left( I - \frac{I_1}{3} C^{-1} \right) + K J (J - 1) C^{-1} \quad (38.7)$$

The Cauchy stress is:

$$\sigma = \frac{1}{J} \tau = \frac{1}{J} F S F^T = \frac{1}{J} \mu \left( \bar{b} - \frac{\bar{I}_1}{3} I \right) + K (J - 1) I \quad (38.8)$$

where:

$\tau = \text{Kirchhoff stress}$

$b = F F^T = \text{the left Cauchy-Green deformation tensor}$

$\bar{b} = \bar{F} \bar{F}^T$

### 38.3.1.2. Tangent Stiffness

Substituting the  $1^{\text{st}}$ - and  $2^{\text{nd}}$ -order derivatives from Equation 38.5 (p. 592) and Equation 38.6 (p. 593) into Equation 38.3 (p. 592), the material tangent stiffness is:

$$\mathcal{C} = \frac{2}{3} \mu J^{-2/3} \left[ -C^{-1} \otimes I - I \otimes C^{-1} + I_1 \mathcal{J} + \frac{I_1}{3} C^{-1} \otimes C^{-1} \right] + J^2 K C^{-1} \otimes C^{-1} + K J (J - 1) (C^{-1} \otimes C^{-1} - 2J) \quad (38.9)$$

which can be simplified to:

$$\mathcal{C} = \frac{2}{3} \mu J^{-2/3} \left[ -C^{-1} \otimes I - I \otimes C^{-1} + I_1 \mathcal{J} + \frac{I_1}{3} C^{-1} \otimes C^{-1} \right] + K J [(2J - 1) C^{-1} \otimes C^{-1} - 2(J - 1) J] \quad (38.10)$$

Using the Piola transform, the spatial tangent is:

$$c = \frac{2}{3} \mu J^{-1} \left[ -\bar{b} \otimes I - I \otimes \bar{b} + \bar{I}_1 i + \frac{\bar{I}_1}{3} I \otimes I \right] + K [(2J - 1) I \otimes I - 2(J - 1) i] \quad (38.11)$$

where:

$i = \text{a } 4^{\text{th}}$ -order identity tensor with components  $i_{ijkl} = I_{ik} I_{jl}$

### 38.3.2. Co-rotational Frame

Large deformation is formulated in a co-rotated frame given by the rotation, R, from the polar decomposition of the deformation gradient:

$$F=RU \tag{38.12}$$

where:

$$U=\text{stretch tensor}$$

The rotation of the co-rotated frame is then:

$$R=FU^{-1} \tag{38.13}$$

The stress and tangent stiffness tensors are returned in the co-rotated frame.

#### 38.3.2.1. Polar Decomposition

Given the deformation gradient, the rotation is determined from the closed-form solution of the inverse stretch (see [1]):

$$U^{-1}=\frac{1}{III_U} [C-I_U U+II_U I] \tag{38.14}$$

where  $I_U$ ,  $II_U$ , and  $III_U$  are the principle invariants of U. The stretch tensor is given in closed form by:

$$U=\frac{1}{I_U II_U - III_U} [-C^2+(I_U^2-II_U)C+I_U III_U I] \tag{38.15}$$

The eigenvalues of U are the square root of the eigenvalues of C. The principal invariants of U in terms of the eigenvalues of C are:

$$\begin{aligned} I_U &= \sqrt{\lambda_1} + \sqrt{\lambda_2} + \sqrt{\lambda_3} \\ II_U &= \sqrt{\lambda_1 \lambda_2} + \sqrt{\lambda_2 \lambda_3} + \sqrt{\lambda_1 \lambda_3} \\ III_U &= \sqrt{\lambda_1 \lambda_2 \lambda_3} \end{aligned}$$

where  $\lambda_1$ ,  $\lambda_2$ , and  $\lambda_3$  are the eigenvalues of C given by the roots of the characteristic polynomial:

$$P(\lambda)=-\lambda^3+I_1\lambda^2-I_2\lambda+I_3 \tag{38.16}$$

where the principle invariants are:

$$\begin{aligned} I_1 &= \text{trace}(C) \\ I_2 &= \frac{1}{2} (I_C^2 - \text{trace}(C^2)) \\ I_3 &= \det(C) = J^2 \end{aligned}$$

C is a symmetric, positive-definite, rank 3 matrix. The characteristic polynomial has three positive real roots given by:

$$\begin{aligned} \lambda_i &= \frac{1}{3} \left( I_1 + 2\sqrt{I_1^2 - 3I_2} \cos\left(\frac{\beta+(i-1)2\pi}{3}\right) \right) \text{ where } i=1,2,3 \\ \beta &= \arccos \frac{2I_1^3 - 9I_1 I_2 + 27I_3}{2(I_1^2 - 3I_2)^{3/2}} \end{aligned} \tag{38.17}$$



### 38.3.2.2. Stress

The constitutive model defined by the Neo-Hookean hyperelastic material gives the stress in the spatial configuration by direct evaluation of Equation 38.8 (p. 593). No rate form is used and no integration is required. The Cauchy stress in the co-rotated frame is returned by the user material subroutine.

### 38.3.2.3. Tangent Stiffness

The co-rotational rate relative to the co-rotated frame is called the Green-Naghdi rate. The constitutive response of the Neo-Hookean material described in the previous sections is in terms of the Lie derivative, or Truesdell rate, of the Kirchhoff stress:

$$\mathcal{L}\tau = Jcd \quad (38.18)$$

where:

$c$  = spatial tangent

$$\mathcal{L}\tau = \dot{\tau} - L\tau - \tau L^T$$

$$L = \dot{F}F^{-1} = d + w$$

$$d = \frac{1}{2}(L + L^T)$$

$$w = \frac{1}{2}(L - L^T)$$

The superimposed dot indicates the time derivative in the reference configuration.

The Jaumann rate is a convenient approximation of the Green-Naghdi rate:

$$\overset{\nabla}{\sigma} = \dot{\sigma} + \sigma w - w\sigma \quad (38.19)$$

Using the Jaumann rate, the constitutive response in the co-rotated frame is given by:

$$\overset{\nabla}{\sigma} = c^J d \quad (38.20)$$

where  $c^J$  is the Jaumann tangent stiffness tensor and is implicitly defined by:

$$\overset{\nabla}{\sigma} = cd + d\sigma + \sigma d \quad (38.21)$$

### 38.3.3. Voigt Notation

Voigt notation is a reduced order representation of tensors and is the form required for the stress and tangent stiffness tensors. Voigt notation is given by converting pairs of indices to a single index via  $\{11\ 22\ 33\ 12\ 23\ 31\} = \{11\ 22\ 33\ 21\ 32\ 13\} \Rightarrow \{1\ 2\ 3\ 4\ 5\ 6\}$  and redefining the rate of deformation tensor as:

$$d \Rightarrow \begin{pmatrix} d_1 \\ d_2 \\ d_3 \\ d_4 \\ d_5 \\ d_6 \end{pmatrix} \equiv \begin{pmatrix} d_{11} \\ d_{22} \\ d_{33} \\ 2d_{12} \\ 2d_{23} \\ 2d_{31} \end{pmatrix} \quad (38.22)$$

In component form:

$$\overset{\nabla}{\sigma}_\alpha = c^J_{\alpha\beta} d_\beta \text{ where } \alpha, \beta = 1, 2, \dots, 6 \quad (38.23)$$

where:

$$\sigma_{\alpha}^{\nabla} = \begin{Bmatrix} \nabla \sigma_{11} \\ \nabla \sigma_{22} \\ \nabla \sigma_{33} \\ \nabla \sigma_{12} \\ \nabla \sigma_{23} \\ \nabla \sigma_{31} \end{Bmatrix}$$

$$c_{\alpha\beta}^J = \begin{bmatrix} c_{1111}^J & c_{1122}^J & c_{1133}^J & c_{1112}^J & c_{1123}^J & c_{1131}^J \\ c_{2211}^J & c_{2222}^J & c_{2233}^J & c_{2212}^J & c_{2223}^J & c_{2231}^J \\ c_{3311}^J & c_{3322}^J & c_{3333}^J & c_{3312}^J & c_{3323}^J & c_{3331}^J \\ c_{1211}^J & c_{1222}^J & c_{1233}^J & c_{1212}^J & c_{1223}^J & c_{1231}^J \\ c_{2311}^J & c_{2322}^J & c_{2333}^J & c_{2312}^J & c_{2323}^J & c_{2331}^J \\ c_{3111}^J & c_{3122}^J & c_{3133}^J & c_{3112}^J & c_{3123}^J & c_{3131}^J \end{bmatrix}$$

Minor symmetry with respect to the index pairs is required for this conversion. The 4<sup>th</sup>-order identity  $i$  and the Jaumann tangent stiffness lack minor symmetry. To ensure minor symmetry, they are redefined as:

$$i_{ijkl} \equiv \frac{1}{2} (I_{ik}I_{jl} + I_{il}I_{jk})$$

$$c_{ijkl}^J \equiv c_{ijkl} + \frac{1}{2} (I_{ik}\sigma_{jl} + \sigma_{ik}I_{jl} + I_{il}\sigma_{jk} + \sigma_{il}I_{jk}) \tag{38.24}$$

Converting to Voigt notation:

$$I \Rightarrow \{111000\}$$

$$i \Rightarrow \begin{bmatrix} 1 & 0 & 0 & 0 & 0 & 0 \\ 0 & 1 & 0 & 0 & 0 & 0 \\ 0 & 0 & 1 & 0 & 0 & 0 \\ 0 & 0 & 0 & \frac{1}{2} & 0 & 0 \\ 0 & 0 & 0 & 0 & \frac{1}{2} & 0 \\ 0 & 0 & 0 & 0 & 0 & \frac{1}{2} \end{bmatrix} \tag{38.25}$$

$$I \otimes I \Rightarrow \begin{bmatrix} 1 & 1 & 1 & 0 & 0 & 0 \\ 1 & 1 & 1 & 0 & 0 & 0 \\ 1 & 1 & 1 & 0 & 0 & 0 \\ 0 & 0 & 0 & 0 & 0 & 0 \\ 0 & 0 & 0 & 0 & 0 & 0 \\ 0 & 0 & 0 & 0 & 0 & 0 \end{bmatrix}$$

### 38.3.3.1. Stress

The Cauchy stress in Voigt notation is:

$$\sigma \Rightarrow \frac{\mu}{J} \begin{pmatrix} \bar{b}_1 - \frac{\bar{I}_1}{3} \\ \bar{b}_2 - \frac{\bar{I}_1}{3} \\ \bar{b}_3 - \frac{\bar{I}_1}{3} \\ \bar{b}_4 \\ \bar{b}_5 \\ \bar{b}_6 \end{pmatrix} + K \begin{pmatrix} J-1 \\ J-1 \\ J-1 \\ 0 \\ 0 \\ 0 \end{pmatrix} \quad (38.26)$$

### 38.3.3.2. Tangent Stiffness

The terms  $\bar{b} \otimes I$  and  $I \otimes \bar{b}$  in Voigt notation are:

$$\bar{b} \otimes I \Rightarrow \begin{bmatrix} \bar{b}_1 & \bar{b}_2 & \bar{b}_3 & \bar{b}_4 & \bar{b}_5 & \bar{b}_6 \\ \bar{b}_1 & \bar{b}_2 & \bar{b}_3 & \bar{b}_4 & \bar{b}_5 & \bar{b}_6 \\ \bar{b}_1 & \bar{b}_2 & \bar{b}_3 & \bar{b}_4 & \bar{b}_5 & \bar{b}_6 \\ 0 & 0 & 0 & 0 & 0 & 0 \\ 0 & 0 & 0 & 0 & 0 & 0 \\ 0 & 0 & 0 & 0 & 0 & 0 \end{bmatrix}$$

$$I \otimes \bar{b} \Rightarrow \begin{bmatrix} \bar{b}_1 & \bar{b}_1 & \bar{b}_1 & 0 & 0 & 0 \\ \bar{b}_2 & \bar{b}_2 & \bar{b}_2 & 0 & 0 & 0 \\ \bar{b}_3 & \bar{b}_3 & \bar{b}_3 & 0 & 0 & 0 \\ \bar{b}_4 & \bar{b}_4 & \bar{b}_4 & 0 & 0 & 0 \\ \bar{b}_5 & \bar{b}_5 & \bar{b}_5 & 0 & 0 & 0 \\ \bar{b}_6 & \bar{b}_6 & \bar{b}_6 & 0 & 0 & 0 \end{bmatrix} \quad (38.27)$$

The spatial tangent in Voigt notation is:

$$c \Rightarrow \frac{2}{3} \mu J^{-1} \begin{bmatrix} -2\bar{b}_1 + \frac{4}{3}\bar{I}_1 & -\bar{b}_2 - \bar{b}_1 + \frac{\bar{I}_1}{3} & -\bar{b}_3 - \bar{b}_1 + \frac{\bar{I}_1}{3} & -\bar{b}_4 & -\bar{b}_5 & -\bar{b}_6 \\ -\bar{b}_1 - \bar{b}_2 + \frac{\bar{I}_1}{3} & -2\bar{b}_2 + \frac{4}{3}\bar{I}_1 & -\bar{b}_3 - \bar{b}_2 + \frac{\bar{I}_1}{3} & -\bar{b}_4 & -\bar{b}_5 & -\bar{b}_6 \\ -\bar{b}_1 - \bar{b}_3 + \frac{\bar{I}_1}{3} & -\bar{b}_2 - \bar{b}_3 + \frac{\bar{I}_1}{3} & -2\bar{b}_3 + \frac{4}{3}\bar{I}_1 & -\bar{b}_4 & -\bar{b}_5 & -\bar{b}_6 \\ -\bar{b}_4 & -\bar{b}_4 & -\bar{b}_4 & \frac{\bar{I}_1}{2} & 0 & 0 \\ -\bar{b}_5 & -\bar{b}_5 & -\bar{b}_5 & 0 & \frac{\bar{I}_1}{2} & 0 \\ -\bar{b}_6 & -\bar{b}_6 & -\bar{b}_6 & 0 & 0 & \frac{\bar{I}_1}{2} \end{bmatrix} +$$

$$K \begin{bmatrix} 1 & 2J-1 & 2J-1 & 0 & 0 & 0 \\ 2J-1 & 1 & 2J-1 & 0 & 0 & 0 \\ 2J-1 & 2J-1 & 1 & 0 & 0 & 0 \\ 0 & 0 & 0 & -J+1 & 0 & 0 \\ 0 & 0 & 0 & 0 & -J+1 & 0 \\ 0 & 0 & 0 & 0 & 0 & -J+1 \end{bmatrix} \quad (38.28)$$

The stress terms in the Jaumann tangent stiffness are:

$$\begin{aligned} & \frac{1}{2} (I_{ik}\sigma_{jl} + \sigma_{ik}I_{jl} + I_{il}\sigma_{jk} + \sigma_{il}I_{jk}) = \frac{1}{2} (I_{ik}\sigma_{jl} + \sigma_{ik}I_{jl}) + \frac{1}{2} (I_{il}\sigma_{jk} + \sigma_{il}I_{jk}) \\ \Rightarrow & \frac{1}{2} \begin{bmatrix} 2\sigma_1 & 0 & 0 & \sigma_4 & 0 & \sigma_6 \\ 0 & 2\sigma_2 & 0 & \sigma_4 & \sigma_5 & 0 \\ 0 & 0 & 2\sigma_3 & 0 & \sigma_5 & \sigma_6 \\ \sigma_4 & \sigma_4 & 0 & \sigma_2 + \sigma_1 & 0 & 0 \\ 0 & \sigma_5 & \sigma_5 & 0 & \sigma_3 + \sigma_2 & 0 \\ \sigma_6 & 0 & \sigma_6 & 0 & 0 & \sigma_1 + \sigma_3 \end{bmatrix} + \frac{1}{2} \begin{bmatrix} 2\sigma_1 & 0 & 0 & \sigma_4 & 0 & \sigma_6 \\ 0 & 2\sigma_2 & 0 & \sigma_4 & \sigma_5 & 0 \\ 0 & 0 & 2\sigma_3 & 0 & \sigma_5 & \sigma_6 \\ \sigma_4 & \sigma_4 & 0 & 0 & \sigma_6 & \sigma_5 \\ 0 & \sigma_5 & \sigma_5 & \sigma_6 & 0 & \sigma_4 \\ \sigma_6 & 0 & \sigma_6 & \sigma_5 & \sigma_4 & 0 \end{bmatrix} \\ = & \begin{bmatrix} 2\sigma_1 & 0 & 0 & \sigma_4 & 0 & \sigma_6 \\ 0 & 2\sigma_2 & 0 & \sigma_4 & \sigma_5 & 0 \\ 0 & 0 & 2\sigma_3 & 0 & \sigma_5 & \sigma_6 \\ \sigma_4 & \sigma_4 & 0 & \frac{\sigma_2 + \sigma_1}{2} & \frac{\sigma_6}{2} & \frac{\sigma_5}{2} \\ 0 & \sigma_5 & \sigma_5 & \frac{\sigma_6}{2} & \frac{\sigma_3 + \sigma_2}{2} & \frac{\sigma_4}{2} \\ \sigma_6 & 0 & \sigma_6 & \frac{\sigma_5}{2} & \frac{\sigma_4}{2} & \frac{\sigma_1 + \sigma_3}{2} \end{bmatrix} \end{aligned} \quad (38.29)$$

With simplification, the Jaumann tangent stiffness becomes:

$$\begin{aligned} c^J \Rightarrow & \frac{2}{3} \mu J^{-1} \begin{bmatrix} \bar{b}_1 + \frac{I_1}{3} & -\bar{b}_2 - \bar{b}_1 + \frac{I_1}{3} & -\bar{b}_3 - \bar{b}_1 + \frac{I_1}{3} & \frac{\bar{b}_4}{2} & -\bar{b}_5 & \frac{\bar{b}_6}{2} \\ -\bar{b}_1 - \bar{b}_2 + \frac{I_1}{3} & -\bar{b}_2 + \frac{I_1}{3} & -\bar{b}_3 - \bar{b}_2 + \frac{I_1}{3} & \frac{\bar{b}_4}{2} & \frac{\bar{b}_5}{2} & -\bar{b}_6 \\ -\bar{b}_1 - \bar{b}_3 + \frac{I_1}{3} & -\bar{b}_2 - \bar{b}_3 + \frac{I_1}{3} & \bar{b}_3 + \frac{I_1}{3} & -\bar{b}_4 & \frac{\bar{b}_5}{2} & \frac{\bar{b}_6}{2} \\ \frac{\bar{b}_4}{2} & \frac{\bar{b}_4}{2} & -\bar{b}_4 & \frac{3}{4}(\bar{b}_1 + \bar{b}_2) & \frac{3}{4}\bar{b}_6 & \frac{3}{4}\bar{b}_5 \\ -\bar{b}_5 & \frac{\bar{b}_5}{2} & \frac{\bar{b}_5}{2} & \frac{3}{4}\bar{b}_6 & \frac{3}{4}(\bar{b}_2 + \bar{b}_3) & \frac{3}{4}\bar{b}_4 \\ \frac{\bar{b}_6}{2} & -\bar{b}_6 & \frac{\bar{b}_6}{2} & \frac{3}{4}\bar{b}_5 & \frac{3}{4}\bar{b}_4 & \frac{3}{4}(\bar{b}_1 + \bar{b}_3) \end{bmatrix} + \\ & K \begin{bmatrix} 2J-1 & 2J-1 & 2J-1 & 0 & 0 & 0 \\ 2J-1 & 2J-1 & 2J-1 & 0 & 0 & 0 \\ 2J-1 & 2J-1 & 2J-1 & 0 & 0 & 0 \\ 0 & 0 & 0 & 0 & 0 & 0 \\ 0 & 0 & 0 & 0 & 0 & 0 \\ 0 & 0 & 0 & 0 & 0 & 0 \end{bmatrix} \end{aligned} \quad (38.30)$$

### 38.3.3.3. Change of Basis

For an arbitrary change of basis given by the orthogonal tensor T, the components of the 2<sup>nd</sup>-order stress tensor and the 4<sup>th</sup>-order tangent stiffness tensor transform as:

$$\begin{aligned} \sigma'_{ij} &= T_{im} \sigma_{mn} T_{jn} \\ c'_{ijkl} &= T_{im} T_{jn} c_{mnop} T_{ko} T_{lp} \end{aligned} \quad (38.31)$$

In Voigt notation, Equation 38.31 (p. 598) becomes:

$$\begin{aligned} \sigma'_\alpha &= Q_{\alpha\xi} \sigma_\xi \\ c'_{\alpha\beta} &= Q_{\alpha\xi} c_{\xi\eta} Q_{\beta\eta} \end{aligned} \quad (38.32)$$

Comparing the tensor and Voigt notation transformations, the change of basis tensor Q is given by:

$$Q[T] = \begin{bmatrix} [P_1] & 2[P_2] \\ [P_3] & [P_4] \end{bmatrix} \quad (38.33)$$

where:

$$\begin{aligned} [P_1] &= \begin{bmatrix} T_{11}^2 & T_{12}^2 & T_{13}^2 \\ T_{21}^2 & T_{22}^2 & T_{23}^2 \\ T_{31}^2 & T_{32}^2 & T_{33}^2 \end{bmatrix} \\ [P_2] &= \begin{bmatrix} T_{11}T_{12} & T_{12}T_{13} & T_{11}T_{13} \\ T_{21}T_{22} & T_{22}T_{23} & T_{21}T_{23} \\ T_{31}T_{32} & T_{32}T_{33} & T_{31}T_{33} \end{bmatrix} \\ [P_3] &= \begin{bmatrix} T_{11}T_{21} & T_{12}T_{22} & T_{13}T_{23} \\ T_{21}T_{31} & T_{22}T_{32} & T_{23}T_{33} \\ T_{31}T_{11} & T_{32}T_{12} & T_{33}T_{13} \end{bmatrix} \\ [P_4] &= \begin{bmatrix} T_{11}T_{22} + T_{12}T_{21} & T_{12}T_{23} + T_{13}T_{22} & T_{11}T_{23} + T_{13}T_{21} \\ T_{21}T_{32} + T_{22}T_{31} & T_{22}T_{33} + T_{23}T_{32} & T_{21}T_{33} + T_{23}T_{31} \\ T_{31}T_{12} + T_{32}T_{11} & T_{32}T_{13} + T_{33}T_{12} & T_{31}T_{13} + T_{33}T_{11} \end{bmatrix} \end{aligned}$$

For a change of basis from the spatial frame to the co-rotated frame,  $T = R^T$ .

## 38.4. Material Properties

Material properties for the user material routine are input in a data table using the **TB** command with *Lab* = USER. The material parameters for the Neo-Hookean model are the Neo-Hookean Young's modulus and Poisson's ratio.

Material Properties	
Young's Modulus (Nm <sup>-2</sup> )	30 x 10 <sup>6</sup>
Poisson's Ratio	0.3

## 38.5. Boundary Conditions and Loading

This problem simulates shear on a cube with dimensions 1 x 1 x 1. Boundary conditions are zero displacement in the X- and Y-direction for nodes at Y = 0, and zero displacement in the Z-direction for nodes at Z = 0.

The shear is simulated by displacing the nodes at Y = 1 in the X-direction by a distance of 1 unit and preventing any displacement in the Y-direction for these nodes. The nodes are then returned to their original position to simulate one cycle of shear deformation.

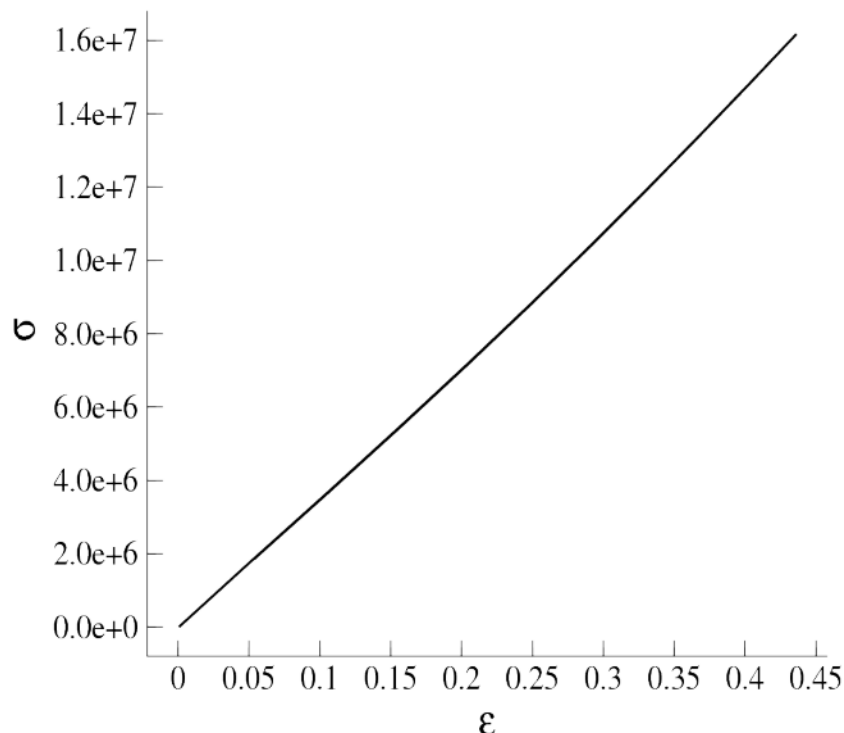
## 38.6. Analysis and Solution Controls

The analysis uses nonlinear geometry (**NLGEOM,ON**). A fixed number of 10 substeps are used for both the loading step and the unloading step, for a total of 20 substeps in the analysis.

## 38.7. Results and Discussion

Equivalent stress and strain are extracted for the node at the center of the mesh and the results are written to an output file. The following table shows the results:

Time	Stress	Strain
0.100000E+00	0.18511346E+07	0.53645216E-01
0.200000E+00	0.36665547E+07	0.10602121E+00
0.300000E+00	0.54384537E+07	0.15643180E+00
0.400000E+00	0.71593019E+07	0.20437866E+00
0.500000E+00	0.88222967E+07	0.24957578E+00
0.600000E+00	0.10422123E+08	0.29193486E+00
0.700000E+00	0.11955693E+08	0.33153319E+00
0.800000E+00	0.13422645E+08	0.36857480E+00
0.900000E+00	0.14825551E+08	0.40335214E+00
0.100000E+01	0.16169843E+08	0.43621175E+00
0.110000E+01	0.14825540E+08	0.40324373E+00
0.120000E+01	0.13422581E+08	0.36836731E+00
0.130000E+01	0.11955591E+08	0.33123410E+00
0.140000E+01	0.10422004E+08	0.29155654E+00
0.150000E+01	0.88221827E+07	0.24913378E+00
0.160000E+01	0.71592219E+07	0.20389315E+00
0.170000E+01	0.54384351E+07	0.15592898E+00
0.180000E+01	0.36666162E+07	0.10553450E+00
0.190000E+01	0.18512794E+07	0.53215926E-01
0.200000E+01	0.46409597E-08	0.66716967E-03

**Figure 38.1: Stress-vs.-Strain Plot**

## 38.8. Recommendations

To perform a similar analysis, consider the following hints and recommendations:

- For constitutive models that require a stress integration algorithm, ensure that the algorithm is accurate. Exercise the user material in simple simulations to determine if it is producing accurate stress results for the types of simulations that will use the user material routine. The accuracy of the stress update directly affects the accuracy of the finite element solution.
- The material tangent returned by the user material routine should be the algorithmic tangent in the co-rotated frame. For a Newton-Raphson solution, the material tangent affects the convergence rate and an algorithmic material tangent will generally give a quadratic convergence rate for iterations that are close to the solution.
- The user material routine is available only for displacement-based element formulations. Since it is not available for the mixed-uP formulations, materials that are nearly incompressible need to use a penalty formulation for the volumetric behavior. This can cause convergence difficulty and errors in the pressure calculation when the volumetric behavior is very stiff. Therefore, the user material subroutine should not be used for nearly incompressible materials when the volumetric behavior is important.

## 38.9. References

The following reference is used in this example problem:

1. Simo, J. C. and T. J. R. Hughes. *Computational Inelasticity*. Springer-Verlag: New York (1998).

## 38.10. Input Files

The following files were used in this problem:

- `usermat3d.F` -- Fortran user material subroutine for the Neo-Hookean material.
- `sample_usr.dat` -- Input file for a shear simulation with the Neo-Hookean user material.

The `stressstrain_usr.log` output file is also included to verify that the `UserMat` subroutine and custom executable are producing the expected Neo-Hookean results.

The files are available in the `td-38` folder. See [Obtaining the Input Files \(p. xxxv\)](#) for more information.



---

## Chapter 39: Wire Bonding Ultrasonic Transducer

---

This example problem simulates electrical excitation of an ultrasonic transducer used for wire bonding applications. The model includes piezoelectric material definition as well as prestressed modal and harmonic response analyses.

Topics related to this example problem follow:

- [39.1. Introduction](#)
- [39.2. Problem Description](#)
- [39.3. Modeling](#)
- [39.4. Material Properties](#)
- [39.5. Boundary Conditions and Loading](#)
- [39.6. Analysis and Solution Controls](#)
- [39.7. Results and Discussion](#)
- [39.8. Recommendations](#)
- [39.9. References](#)
- [39.10. Input Files](#)

### 39.1. Introduction

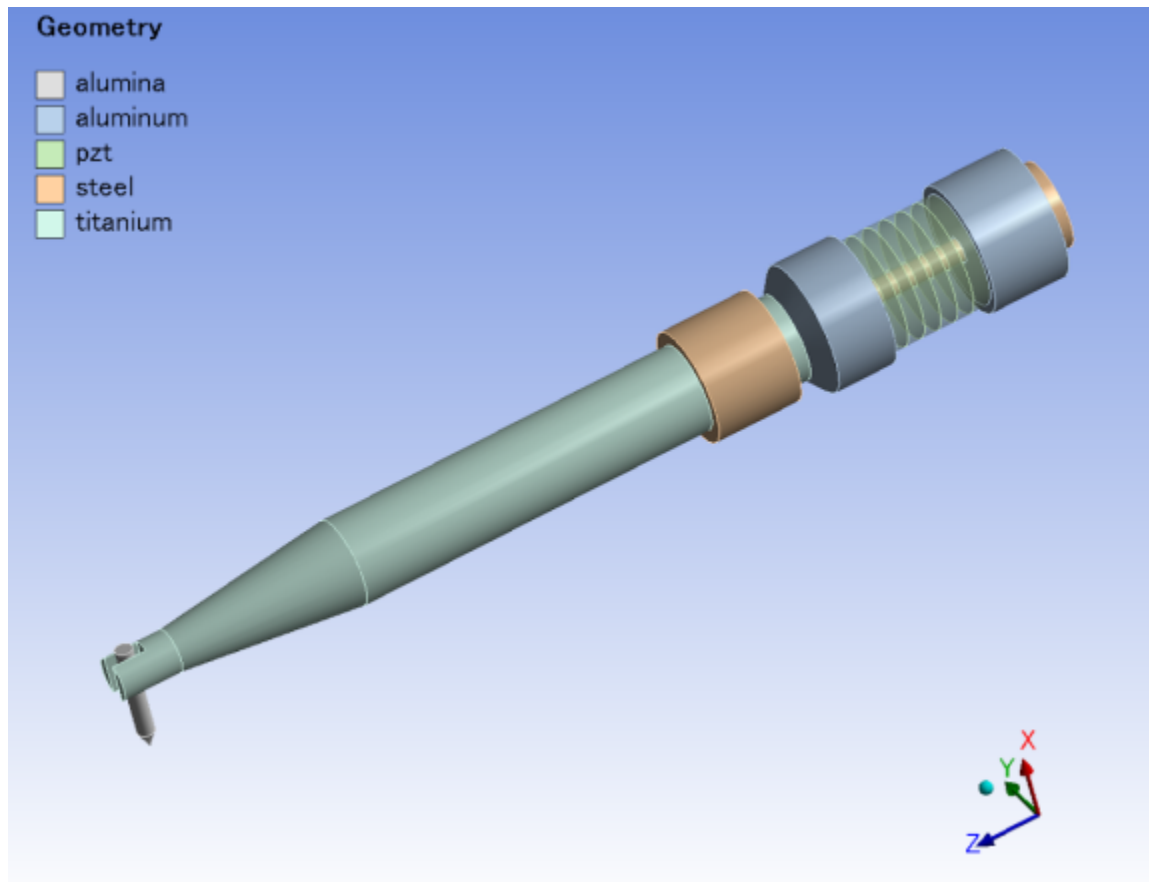
Wire bonding is the most commonly-used process for creating interconnects between the integrated circuit (IC) and its package using fine metal (such as gold or aluminum) wires [1, 2]. In wedge bonding, ultrasonic energy, pressure, and heat are applied to form a bond; the process avoids introducing impurities and provides flexibility in material choice. For larger diameter wires, the frequency is often around 50-60 kHz whereas, for finer diameter wires, the frequency is much higher, up to as much as 200 kHz.

The design of the transducer includes examining the natural frequencies associated with its longitudinal motion. Changes in geometry, for example, can influence the vibration and electrical characteristics of the device.

In piezoelectric ceramics, an applied voltage induces strain (displacement) in the material and vice-versa, demonstrating the coupling of the electric and structural fields. Piezoelectric ceramics are very brittle in tension, so a preload is needed to keep the ceramics in a compressive state of stress in operation.

### 39.2. Problem Description

The following figure shows the ultrasonic transducer used in this example:

**Figure 39.1: Ultrasonic Transducer Model**

The bonding tool, made of alumina, is shown at the far left. It is connected to the titanium horn by small screws (not modeled). The horn is connected to the piezoelectric driver assembly. The driver assembly consists of piezoelectric rings sandwiched between aluminum front and back plates, which are connected together with a steel bolt that provides prestress. The transducer is mounted to the machine via a steel holder.

The holder should be placed at the nodal point of the transducer for optimal performance. A modal analysis is performed without the holder, and the first longitudinal mode is determined.

As shown in the following figure, a plot of the z displacement with contour range -1 to 1 provides an idea of the appropriate location to position the holder:

**Figure 39.2: Approximate Location for Positioning the Holder**

```

NODAL SOLUTION
STEP=1
SUB =10
FREQ=21687.4
USUM      (AVG)
RSYS=0
DMX  =26.8362
SMX  =26.8362

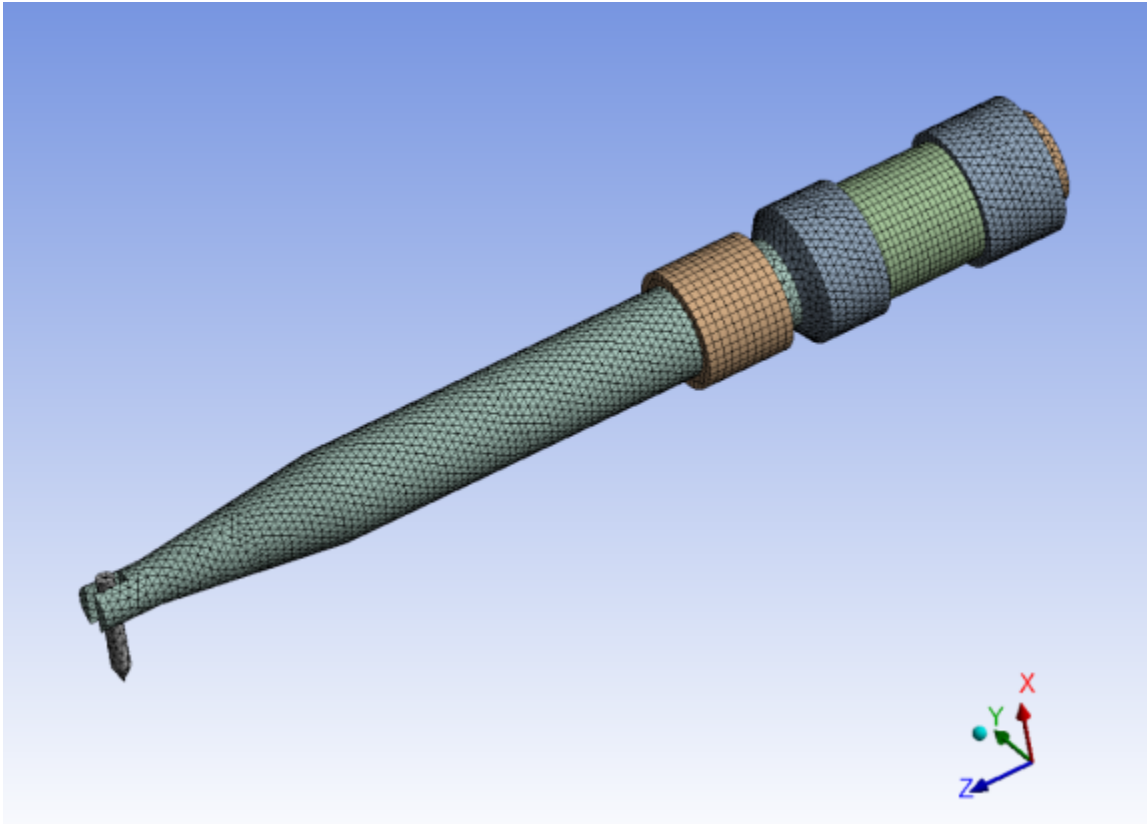
```



First axial mode of interest ("node" designated in color)

### 39.3. Modeling

The 3-D model of the transducer is created in ANSYS DesignModeler and meshed in ANSYS Mechanical, as shown in the following figure:

**Figure 39.3: Meshed Ultrasonic Transducer Model**

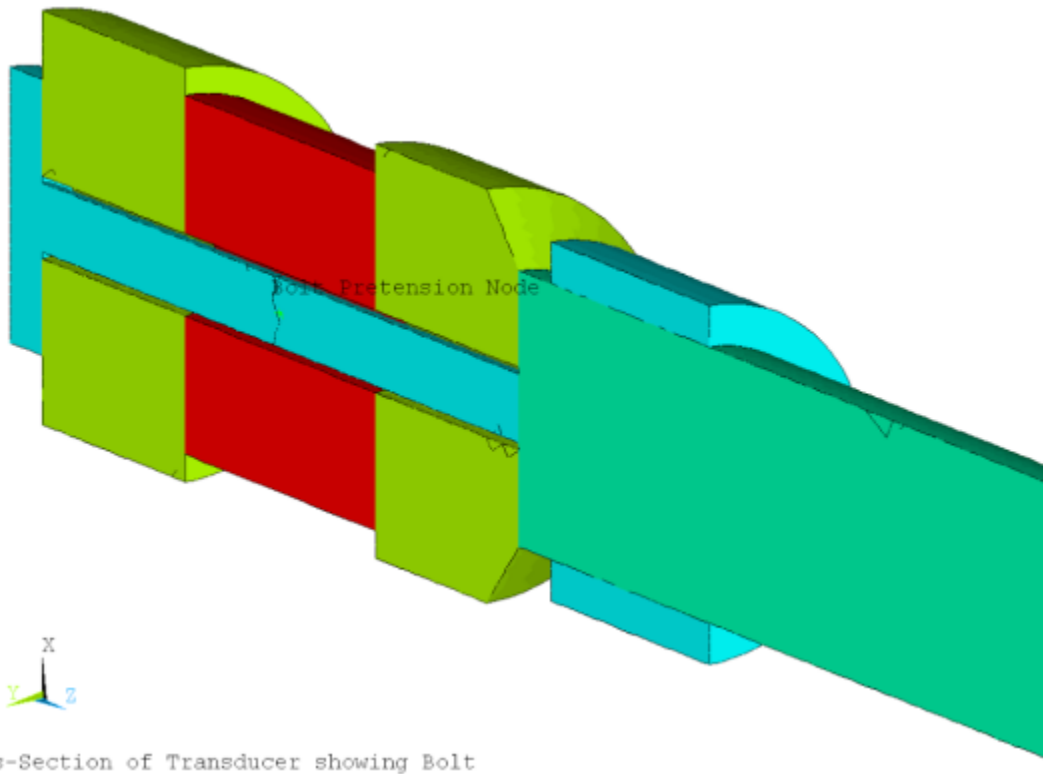
The piezoelectric elements are meshed with [SOLID226](#), and the other parts are meshed with [SOLID186](#) and [SOLID187](#) elements. The total number of elements is 67,756 and the total number of nodes is 115,414.

The coupled-field element [SOLID226](#) supports many physics types. In this case, `KEYOPT(1) = 1001` specifies piezoelectric behavior. Piezoelectric elements are orthotropic, so each of the piezoelectric rings assume z-axis polarization with alternating z-axis orientation.

Although copper terminals lie between the piezoelectric rings, they are omitted here for simplicity. Other details and features (such as small screws or wire holes) are also omitted, as they have no effect on the overall response.

The parts are connected via shared nodes along the interfaces. Although contact elements can be used for piezoelectric analyses, they are unnecessary for such a simple geometry in this case.

A bolt connects the top and bottom plates of the driver, as shown in the following figure:

**Figure 39.4: Top and Bottom Plate Connection**

The fastener is split in half with PRETS179 pretension elements connecting the two halves together. The amount of preload or adjustment is controlled via the pretension node.

## 39.4. Material Properties

The structural material properties used in this problem (taken from Yan [1]) are as follows:

Material	Elastic Modulus (Pa)	Poisson's Ratio	Density (Kg/m <sup>3</sup> )
Alumina	3e11	.2	3720
Aluminum	7e10	.3	2700
PZT	9.2e10	.33	7700
Steel	2.1e11	.3	7800
Titanium	1.1e11	.32	4430

Piezoelectric materials typically have orthotropic material properties, although isotropic materials are assumed in this example, as they are defined in that manner in the reference.

The piezoelectric materials properties (taken from Berlincourt [3]) are as follows:

Relative permittivity in x, y	762
Relative permittivity in z	663
Piezoelectric constant $e_{13}$	-5.2028

Piezoelectric constant $e_{23}$	-5.2028
Piezoelectric constant $e_{33}$	15.0804
Piezoelectric constant $e_{52}$	12.7179
Piezoelectric constant $e_{61}$	12.7179

A system damping ratio of 0.1 percent is assumed for the model, as the ultrasonic transducer has very little damping.

## 39.5. Boundary Conditions and Loading

Both structural and electric boundary conditions are applied:

[39.5.1. Structural Boundary Condition](#)

[39.5.2. Voltage Coupling and Boundary Condition](#)

### 39.5.1. Structural Boundary Condition

The outside diameter of the holder is constrained in all structural degrees of freedom.

A static analysis is performed to calculate the prestress due to the tightening of the bolt to the driver assembly. A preload force of 50 N is applied to the pretension node. For the subsequent dynamic analyses, the adjustment is changed to 0.0.

Although the actual pretension adjustment (change in grip length) is non-zero, the static analysis is performed only to create the stress-stiffening matrix that influences the overall stiffness matrix. In a harmonic response analysis, all loads are applied sinusoidally, so imposing a preload force or non-zero adjustment creates a harmonically-varying bolt load, which is incorrect. The effect of the bolt preload to the stiffness of the driver is considered in the linear perturbation analysis, so the actual adjustment is not required to be applied in the dynamic analysis.

### 39.5.2. Voltage Coupling and Boundary Condition

Between each piezoelectric ring is an electric terminal. The rings are polarized in opposite directions, so the positive and negative terminals alternate.

Because the terminal is equipotential, all of the voltage degrees of freedom for each terminal are coupled, leaving two independent voltage degrees of freedom at the terminal locations. One voltage is specified as ground (voltage of 0).

In the modal analysis, the positive terminal is left unconstrained. In the harmonic response analysis, a voltage of 5V constant with respect to frequency is applied to the positive terminal.

## 39.6. Analysis and Solution Controls

Two additional analyses are performed for this problem:

[39.6.1. Prestressed Modal Analysis with Linear Perturbation Method](#)

[39.6.2. Prestressed Full Harmonic Response Analysis](#)

### 39.6.1. Prestressed Modal Analysis with Linear Perturbation Method

A static analysis with one terminal grounded and a bolt preload of 50 N is performed. A prestressed modal analysis using linear perturbation method and the Block Lanczos eigensolver is then executed, where the first 40 modes are requested. The bolt adjustment is changed to zero.

The linear perturbation method for modal analyses is described in [Applying Prestress Effects in a Modal Analysis](#) in the *Structural Analysis Guide*.

### 39.6.2. Prestressed Full Harmonic Response Analysis

A static analysis (p. 609) as described above is run first. A prestressed harmonic response analysis using the full method is used to calculate the frequency response between 57 and 60 kHz with 30 substeps. In this harmonic response analysis, the linear perturbation method is used to include prestress effects. The bolt adjustment is changed to zero, and the applied voltage is 5V.

The linear perturbation method for full harmonic response analyses is described in [Prestressed Harmonic Analysis](#) in the *Structural Analysis Guide*.

## 39.7. Results and Discussion

The following topics concerning the analyses results are available:

[39.7.1. Results from Prestressed Modal Analysis with Linear Perturbation Method](#)

[39.7.2. Results from Prestressed Full Harmonic Response Analysis](#)

### 39.7.1. Results from Prestressed Modal Analysis with Linear Perturbation Method

Prior to solving a harmonic response analysis, it is important to understand the frequency content of the system, and the modal analysis provides this valuable information.

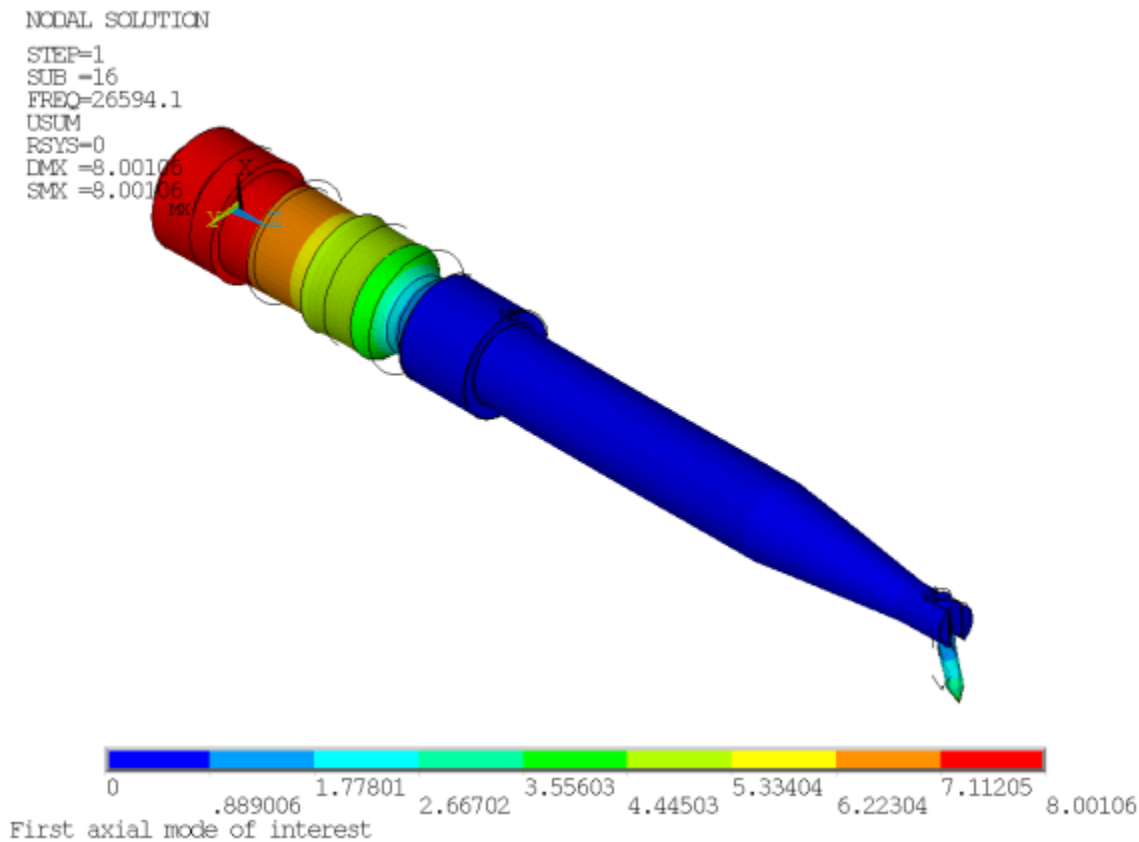
In the solver output, the participation factors in the z (longitudinal) direction are listed at the end of the modal analysis, as follows:

***** PARTICIPATION FACTOR CALCULATION ***** Z DIRECTION							
MODE	FREQUENCY	PERIOD	PARTIC.FACTOR	RATIO	EFFECTIVE MASS	CUMULATIVE MASS FRACTION	RATIO EFF.MASS TO TOTAL MASS
1	1947.47	0.51349E-03	0.13955E-03	0.000974	0.194730E-07	0.469851E-06	0.391044E-06
2	1948.16	0.51331E-03	0.39207E-05	0.000027	0.153722E-10	0.470222E-06	0.308693E-09
3	4427.05	0.22588E-03	0.90019E-05	0.000063	0.810341E-10	0.472177E-06	0.162727E-08
4	4427.86	0.22584E-03	-0.46883E-05	0.000033	0.219797E-10	0.472708E-06	0.441383E-09
5	9304.53	0.10747E-03	-0.22162E-05	0.000015	0.491135E-11	0.472826E-06	0.986266E-10
6	9320.90	0.10729E-03	-0.96822E-03	0.006760	0.937453E-06	0.230920E-04	0.188253E-04
7	11382.1	0.87857E-04	0.17053E-05	0.000012	0.290807E-11	0.230921E-04	0.583979E-10
8	11385.3	0.87833E-04	0.53578E-05	0.000037	0.287058E-10	0.230928E-04	0.576451E-09
9	14535.4	0.68797E-04	0.94644E-06	0.000007	0.895743E-12	0.230928E-04	0.179877E-10
10	15206.9	0.65760E-04	-0.14972E-05	0.000010	0.224167E-11	0.230929E-04	0.450157E-10
11	19129.1	0.52276E-04	-0.72228E-04	0.000504	0.521688E-08	0.232187E-04	0.104762E-06
12	19211.2	0.52053E-04	-0.17198E-01	0.120072	0.295763E-03	0.715948E-02	0.593931E-02
13	21192.5	0.47187E-04	-0.13350	0.932096	0.178230E-01	0.437200	0.357911
14	23711.4	0.42174E-04	0.15719E-04	0.000110	0.247096E-09	0.437200	0.496203E-08
15	23712.1	0.42172E-04	0.20055E-03	0.001400	0.402200E-07	0.437201	0.807671E-06
16	26594.1	0.37602E-04	-0.14323	1.000000	0.205145E-01	0.932181	0.411958
17	28705.8	0.34836E-04	0.42418E-05	0.000030	0.179930E-10	0.932181	0.361324E-09
18	29154.9	0.34300E-04	0.10645E-01	0.074323	0.113319E-03	0.934915	0.227559E-02
19	30305.6	0.32997E-04	0.10060E-04	0.000070	0.101211E-09	0.934915	0.203245E-08
20	30312.8	0.32989E-04	0.49382E-04	0.000345	0.243859E-08	0.934915	0.489702E-07
21	34346.4	0.29115E-04	-0.52235E-05	0.000036	0.272853E-10	0.934915	0.547926E-09
22	36793.2	0.27179E-04	0.51304E-02	0.035820	0.263215E-04	0.935550	0.528571E-03
23	44385.1	0.22530E-04	0.22402E-05	0.000016	0.501871E-11	0.935550	0.100782E-09

24	47898.2	0.20878E-04	0.32907E-05	0.000023	0.108290E-10	0.935550	0.217460E-09
25	51110.3	0.19566E-04	-0.82738E-06	0.000006	0.684562E-12	0.935550	0.137469E-10
26	52122.9	0.19185E-04	-0.82532E-06	0.000006	0.681147E-12	0.935550	0.136783E-10
27	52211.6	0.19153E-04	0.43101E-02	0.030092	0.185766E-04	0.935999	0.373043E-03
28	56171.7	0.17803E-04	-0.56272E-05	0.000039	0.316656E-10	0.935999	0.635887E-09
29	56183.0	0.17799E-04	-0.47378E-04	0.000331	0.224465E-08	0.935999	0.450755E-07
30	58861.0	0.16989E-04	0.41097E-01	0.286934	0.168899E-02	0.976751	0.339171E-01
31	60374.9	0.16563E-04	0.41351E-04	0.000289	0.170992E-08	0.976751	0.343375E-07
32	60377.6	0.16562E-04	-0.46874E-04	0.000327	0.219718E-08	0.976751	0.441223E-07
33	62900.6	0.15898E-04	0.58571E-05	0.000041	0.343061E-10	0.976751	0.688912E-09
34	65167.8	0.15345E-04	0.60328E-05	0.000042	0.363949E-10	0.976751	0.730858E-09
35	69986.8	0.14288E-04	0.21853E-02	0.015257	0.477544E-05	0.976866	0.958973E-04
36	72005.0	0.13888E-04	-0.24739E-02	0.017272	0.612022E-05	0.977014	0.122902E-03
37	79771.7	0.12536E-04	-0.56816E-05	0.000040	0.322802E-10	0.977014	0.648229E-09
38	82189.3	0.12167E-04	0.76951E-05	0.000054	0.592144E-10	0.977014	0.118910E-08
39	87256.5	0.11460E-04	0.30865E-01	0.215495	0.952651E-03	1.00000	0.191305E-01
40	88526.3	0.11296E-04	-0.47219E-04	0.000330	0.222963E-08	1.00000	0.447739E-07
-----							
sum					0.414450E-01		0.832272
-----							

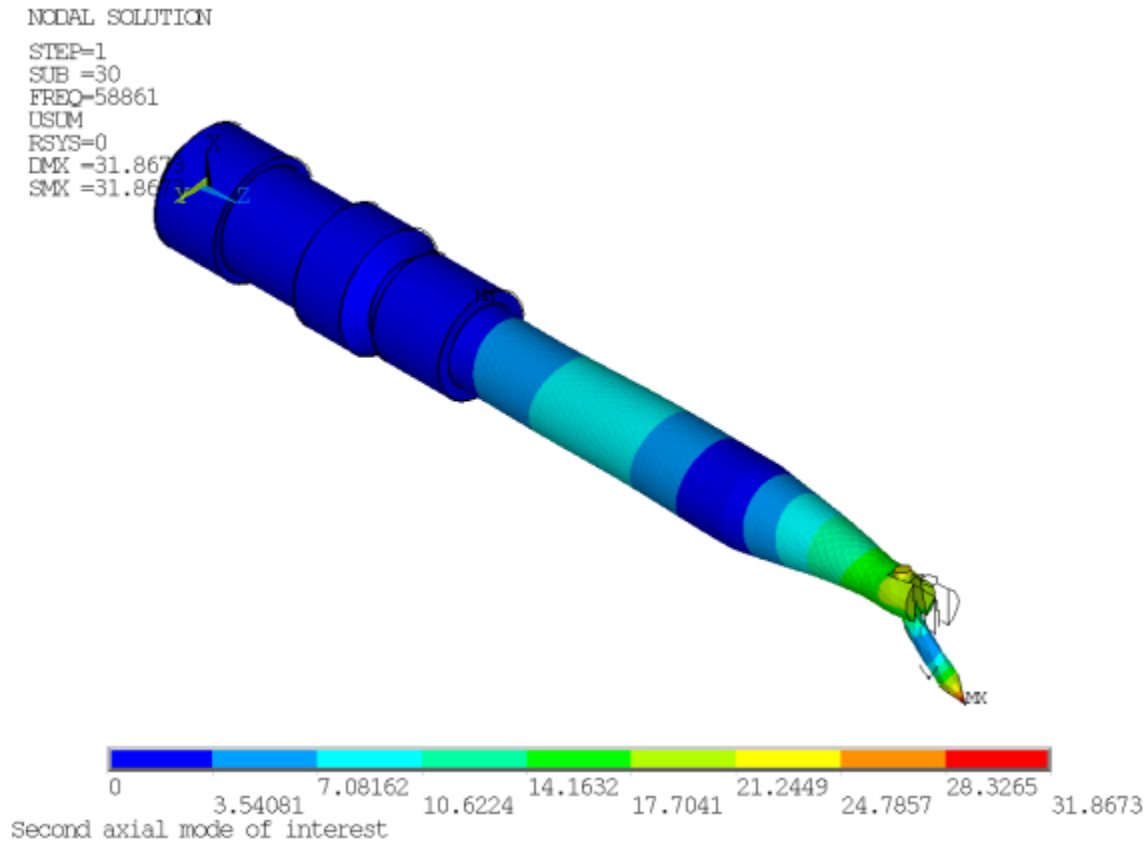
Modes having high participation factors in the z direction are candidates for evaluation as desirable longitudinal modes. Also examine the mode shapes to determine whether excessive transverse motions exist, as those modes should not be excited during transducer operation. Upon examination of the results in this case, modes 16, 30 and 39 are the modes of interest, as shown in the following three figures.

**Figure 39.5: First Longitudinal Mode of Interest (16) at 26.6 kHz**

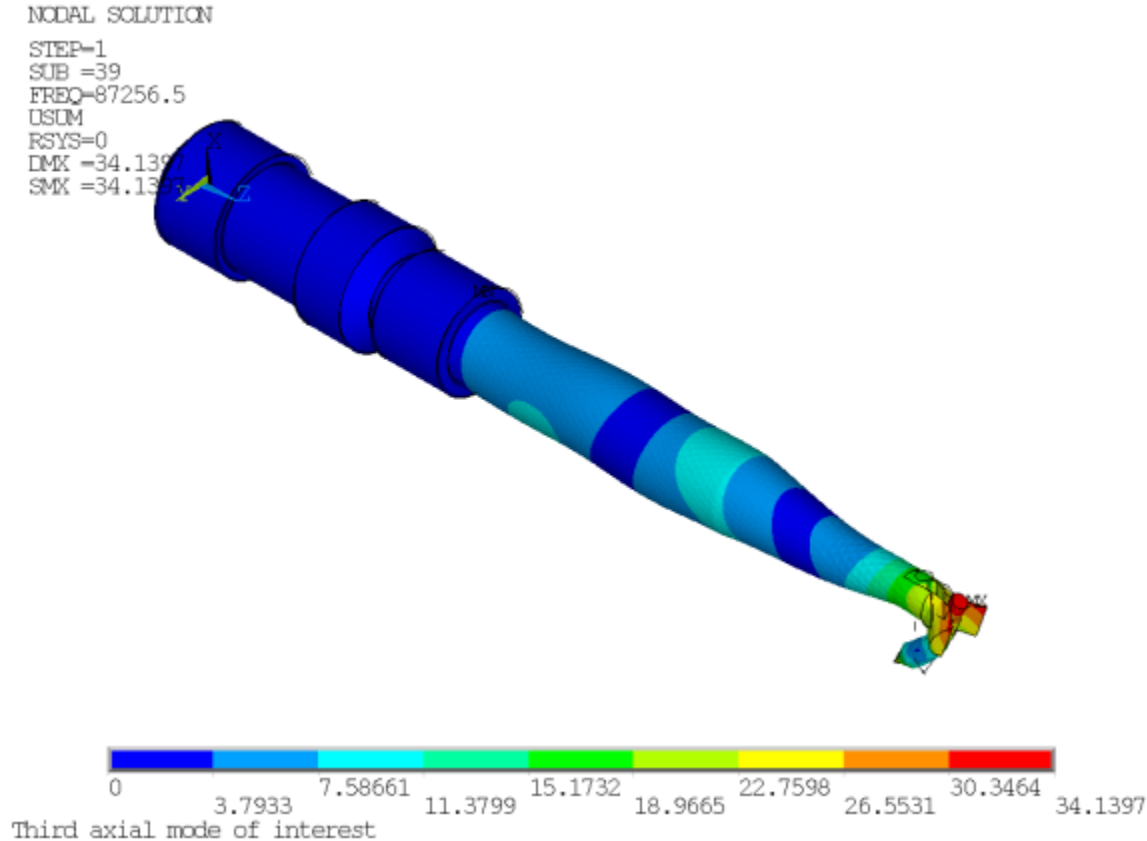


This second mode of interest is the one to be investigated in the subsequent harmonic response analyses:



**Figure 39.6: Second Longitudinal Mode of Interest (30) at 58.9 kHz**

It is worth noting that if the transducer were to be used for a higher-frequency application, the third mode of interest is at 87.3 kHz:

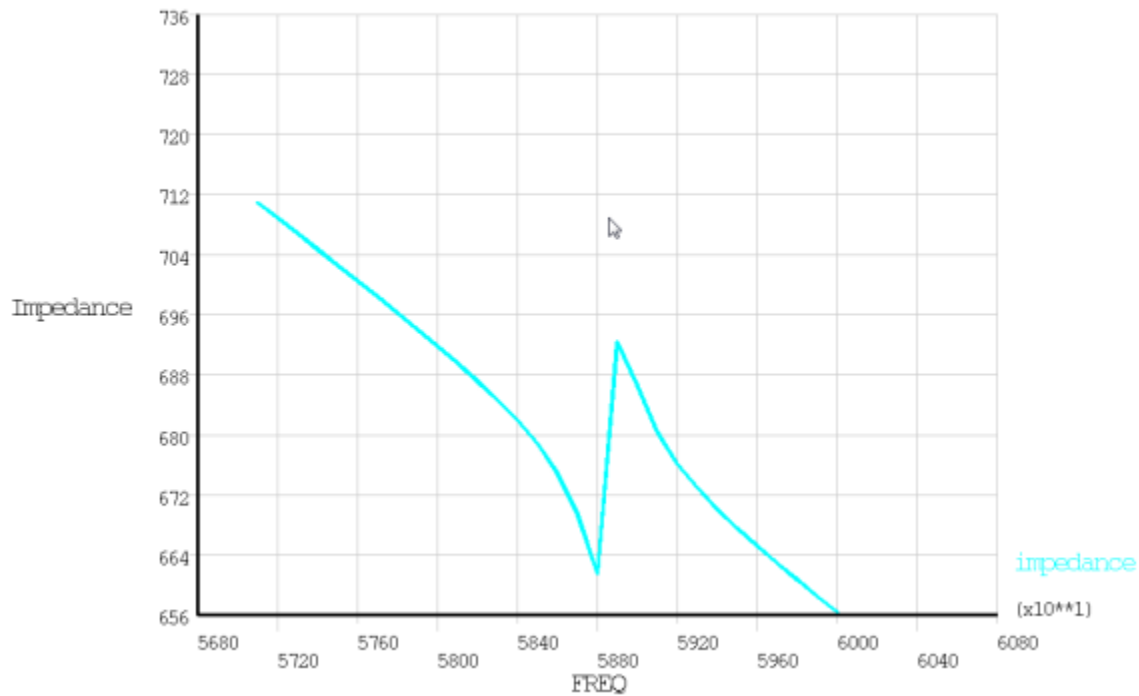
**Figure 39.7: Third Longitudinal Mode of Interest (39) at 87.3 kHz**

In all modes, the tip of the bonding tool has little motion in the x and y directions as compared to the z direction, necessary for proper wire bonding to occur. Also, the frequencies of the second and third modes are roughly twice and thrice that of the first mode, as expected.

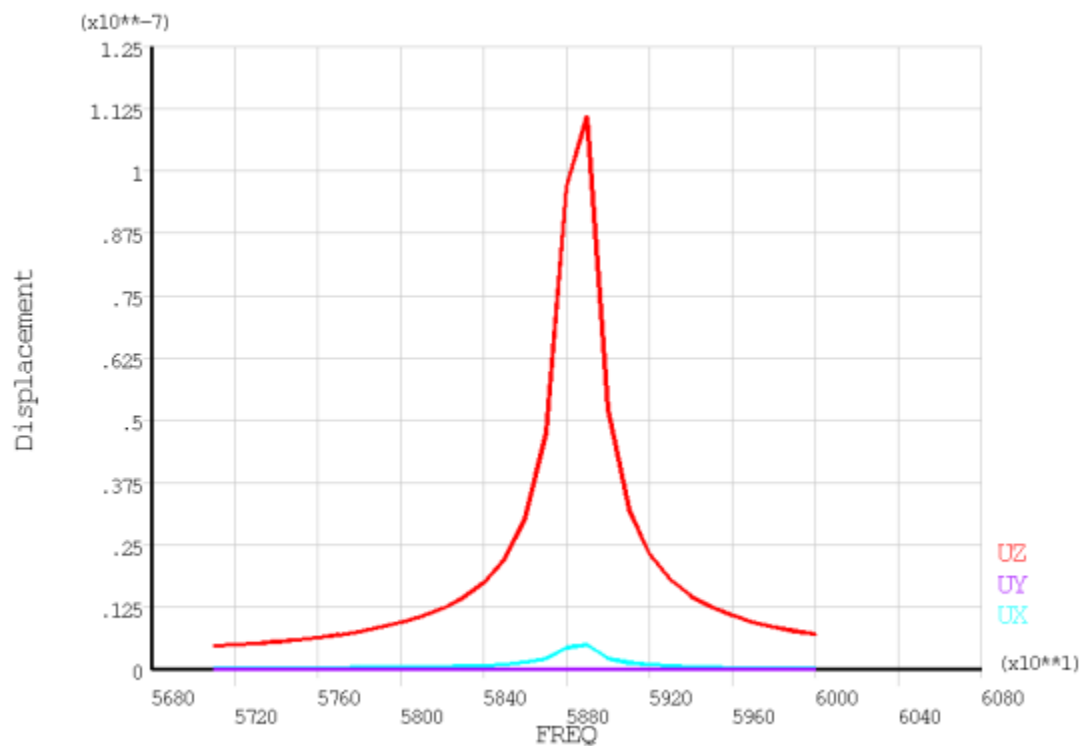
### 39.7.2. Results from Prestressed Full Harmonic Response Analysis

For wire bonding, the transducer can operate in the 50-60 kHz range. Although the modal analysis determined that the second longitudinal mode of interest is 58.9 kHz, it is necessary to determine the actual amplitude and impedance values, and so a harmonic response analysis is performed.

The “reaction force” for voltage degrees of freedom is charge. In the POST26 time-history postprocessor (**/POST26**), the charge Q is retrieved at the terminal. As current  $I = \frac{dQ}{dt}$  and  $Q = Q_0 e^{j\omega t}$ , then  $I = \omega Q_0 e^{j\omega t} j$ . This operation can be performed via the **CFACT** and **PROD** commands to calculate current based on the charge. Impedance  $Z = \frac{V}{I}$  is calculated and plotted as follows:

**Figure 39.8: Electrical Impedance**

The tip x, y and z displacements are output directly in POST26 and plotted as follows:

**Figure 39.9: Tip Displacement**

As indicated, the lateral motion (x and y) is much less than the longitudinal motion (z). The displacement for this applied voltage is a little more than 0.1 micron.

## 39.8. Recommendations

To perform a similar analysis, consider the following hints and recommendations:

- For piezoelectric materials, ensure that the polarization direction (defined by the element coordinate system) is correct. Regardless of the element axis (x, y or z) chosen as the polarization direction, all orthotropic material and piezoelectric constants must be defined accordingly.
- For piezoelectric constants, the piezoelectric stress matrix ([e] form) or the piezoelectric strain matrix ([d] matrix) can be used. If using the piezoelectric strain matrix, however, the elastic properties must be input via the **TB,ANEL** command. Also, IEEE standards list the coefficients based on (x, y, z, yz, xz, xy) ordering, while ANSYS input requires (x, y, z, xy, yz, xz) ordering. For more information, see [Piezoelectric Matrix](#) in the *Coupled-Field Analysis Guide*.
- When calculating the electrical impedance, the current is calculated from the “reaction” charge, as indicated in [Results from Prestressed Full Harmonic Response Analysis \(p. 612\)](#). Each node with voltage degrees of freedom constrained returns a portion of the “reaction” charge. Instead of summing all “reaction” charges for the terminal nodes, however, if the voltage degrees of freedom are coupled, then the total “reaction” charge can be obtained at the master degree of freedom (MDOF). This method provides much simpler postprocessing, as results from only a single node (MDOF) need to be queried.
- In a harmonic response analysis, all loads and boundary conditions are applied in sinusoidally. Consequently, if pretension elements ([PRETS179](#)) are present, constrain their adjustment to zero during the harmonic response portion of the analysis.
- For linear perturbation analyses, use the **RESCONTROL,LINEAR** command in the base linear static analysis to generate the files needed for the multiframe restart (.Rnnn, .RDB, .ESAV). Linear perturbation analyses require use of multiframe restart files, but the restart files are not created for linear static analyses unless the **RESCONTROL** command is issued.

## 39.9. References

The following references are used in this example problem:

1. Yan, T-H et al. “[Design of a Smart Ultrasonic Transducer for Interconnecting Machine Applications.](#)” *Sensors*. 9.6 (2009): 4986-5000.
2. Or, S.W. et al. “[Performance Study of an Ultrasonic Transducer Used for Wire Bonding.](#)” *Electron Devices Meeting*. Hong Kong: 1998.
3. Berlincourt, D. and H. H. A. Krueger. Rev C. Near. “[Properties of Morgan Electro Ceramic Ceramics.](#)” *Properties of Piezoelectricity Ceramics*. Technical Publication TP-226.

## 39.10. Input Files

The following files are used in this problem:

- `wirebond.cdb` -- Common database for the original mesh.
- `wirebond1.dat` -- Input file for modal analysis with no holder.
- `wirebond2.dat` -- Input file for static and linear perturbation modal analysis.
- `wirebond3.dat` -- Input file for static and linear perturbation full harmonic response.

The files are available in the `td-39` folder. See [Obtaining the Input Files \(p. xxxv\)](#) for more information.



---

## Chapter 40: Shape Memory Alloy (SMA) with Thermal Effect

---

This example problem presents two shape memory alloy (SMA) simulations: a spinal spacer implant and a spring actuator.

The following features and capabilities are highlighted:

- The [SMA material model](#) using martensite and austenite (nitinol)
- SMA behavior with thermal loading

Topics related to this example problem follow:

- [40.1. Introduction](#)
- [40.2. SMA Phase Transformation Theory](#)
- [40.3. SMA Thermal Effect Simulations](#)
- [40.4. Recommendations](#)
- [40.5. References](#)
- [40.6. Input Files](#)

### 40.1. Introduction

A shape memory alloy (SMA) is a material that, after being subjected to mechanical loading/unloading cycles, is able to undergo large deformations without showing residual strains (pseudoelasticity) or that can recover from large deformations via temperature change (shape memory effect).

Pseudoelasticity and the shape memory effect are material characteristics especially useful for aeronautical, biomedical, and structural engineering applications. Although much progress has been made with SMA material analysis and design, many challenges still exist for precisely controlling SMAs due to highly nonlinear hysteretic transformation, material degradation, and thermo-mechanical fatigue. Finite element analysis has been widely used to simulate SMA material and provides a valuable tool for designing products using SMA materials.

### 40.2. SMA Phase Transformation Theory

The second order tensor,  $\mathbf{E}_{in}$ , is defined as transformation strain to measure the strain associated with the phase transformation:

$$0 \leq \|\mathbf{E}_{in}\| \leq \varepsilon_L \quad (40.1)$$

where  $\varepsilon_L$  is a maximum value norm of  $\mathbf{E}_{in}$  in the phase transformation after fully transformed.

The stress,  $\sigma$ , is therefore expressed in terms of strain:

$$\sigma = \mathbb{L} : (\mathbf{E} - \mathbf{E}_{in}) \quad (40.2)$$

During the transformation, the transformation stress is defined as:

$$X_{tr} = \sigma' - \left[ \tau_M(T) + h \|\mathbf{E}_{in}\| + \gamma \right] \frac{\mathbf{E}_{in}}{\|\mathbf{E}_{in}\|} \quad (40.3)$$

where  $\tau_M(T) = \langle \beta(T - T_0) \rangle^+$  is a positive and monotonically increasing function of the room temperature,  $T$ , and the material-dependent temperature,  $T_0$ , below which no twinned martensite occurs.  $\beta$  is a material parameter. The material parameter  $h$  is associated with the hardening of the material in the phase transformation.

$$\gamma \text{ is defined by } \begin{cases} \gamma = 0 & \text{if } 0 < \|E_{in}\| < \varepsilon_L \\ \gamma \geq 0 & \text{if } \|E_{in}\| = \varepsilon_L \end{cases}$$

The evolutionary equation for  $\mathbf{E}_{in}$  has the following form:

$$E_{in} = E_{in}(n) + \Delta\xi \frac{\partial F}{\partial \sigma} \quad (40.4)$$

where the limit function  $F$  is given in terms of the transformation stress  $\mathbf{X}_{tr}$  and the elastic domain radius  $R$  in the form of the Prager-type limit function:

$$F(X_{tr}) = \sqrt{2J_2} + m \frac{J_3}{J_2} - R \quad (40.5)$$

where:

$$J_2 = \frac{1}{2} (X_{tr}^2 : 1)$$

$$J_3 = \frac{1}{3} (X_{tr}^3 : 1)$$

Thus, the governing equations for the phase transformation are expressed as:

$$\begin{cases} \sigma = \mathbb{L} : (E - E_{in}) \\ X_{tr} = \sigma' - [\tau_M(T) + h\|E_{in}\| + \gamma] \frac{E_{in}}{\|E_{in}\|} \\ \gamma \geq 0 \\ E_{in} = E_{in}(n) + \Delta\xi \frac{\partial F}{\partial \sigma} \\ \|E_{in}\| \leq \varepsilon_L \\ F(X_{tr}) = \|X_{tr}\| + \frac{2MJ_3}{\|X_{tr}\|^2} - R \leq 0 \\ \Delta\xi \geq 0 \\ \Delta\xi F(X_{tr}) = 0 \end{cases} \quad (40.6)$$

In addition to the Young's modulus and Poisson's ratio of martensite and austenite, six other parameters are defined:  $M$ ,  $R$ ,  $h$ ,  $T_0$ ,  $\beta$ , and  $\varepsilon_L$ .

### 40.3. SMA Thermal Effect Simulations

The following examples demonstrate typical SMA-based applications with thermal loading:

40.3.1. Simulation of a Spinal Spacer Implant

40.3.2. Simulation of a Spring Actuator

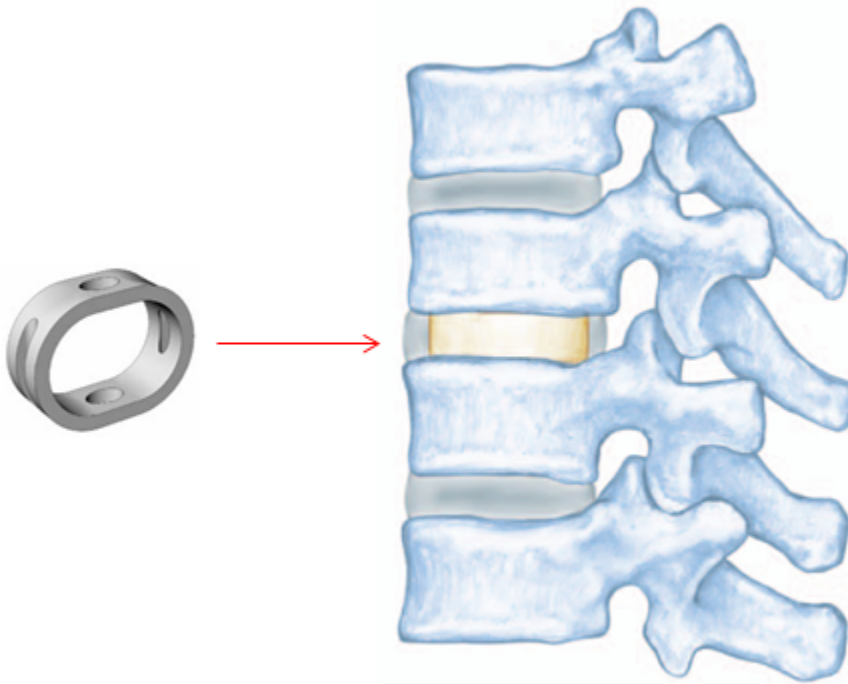
The spinal vertebrae spacer is simulated via [SOLID187](#) elements, and the spring actuator is simulated via [BEAM188](#) and [SOLID185](#) elements.



### 40.3.1. Simulation of a Spinal Spacer Implant

Approximately 20 percent of Americans between the ages of 20 and 64 have back pain problems [1], most of which are associated with intervertebral disc (IVD) degeneration. In some cases, a degenerated IVD is surgically replaced with a spinal spacer inserted into the space between vertebrae, as shown:

**Figure 40.1: Spinal Spacer Implant**



Spinal spacers restore disc space height, alignment, and the spine's ability to bear weight, any or all of which can be lost due to IVD degeneration. Finite element analysis of implant function can help improve the design and quality of the spinal spacer.

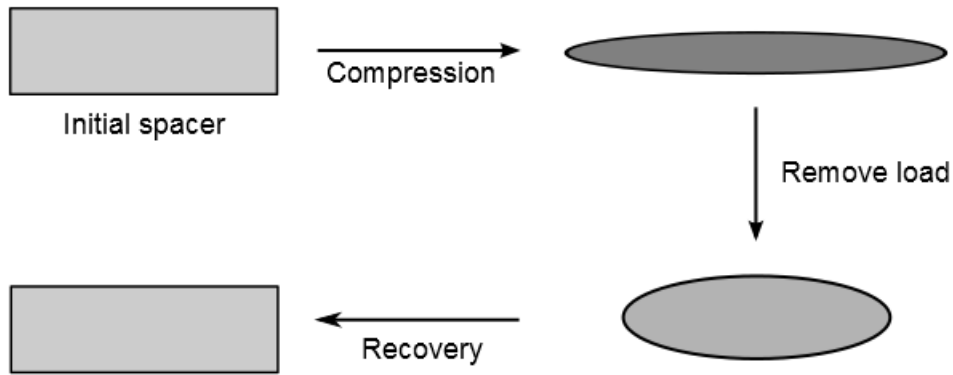
The following topics related to this example simulation are available:

- [40.3.1.1. Problem Description](#)
- [40.3.1.2. Modeling](#)
- [40.3.1.3. Material Properties](#)
- [40.3.1.4. Boundary Conditions and Loading](#)
- [40.3.1.5. Analysis and Solution Controls](#)
- [40.3.1.6. Results and Discussion](#)

#### 40.3.1.1. Problem Description

To simulate the function of a spinal spacer implant, the spacer is initially loaded at room temperature 297 K. The spacer is compressed from the top by a rigid surface to a thickness of 3.375 mm. The compression is then removed, and the spacer undergoes elastic recovery. To remove the residual strain, the spacer is heated to 326 K and then cooled to body temperature 311 K.

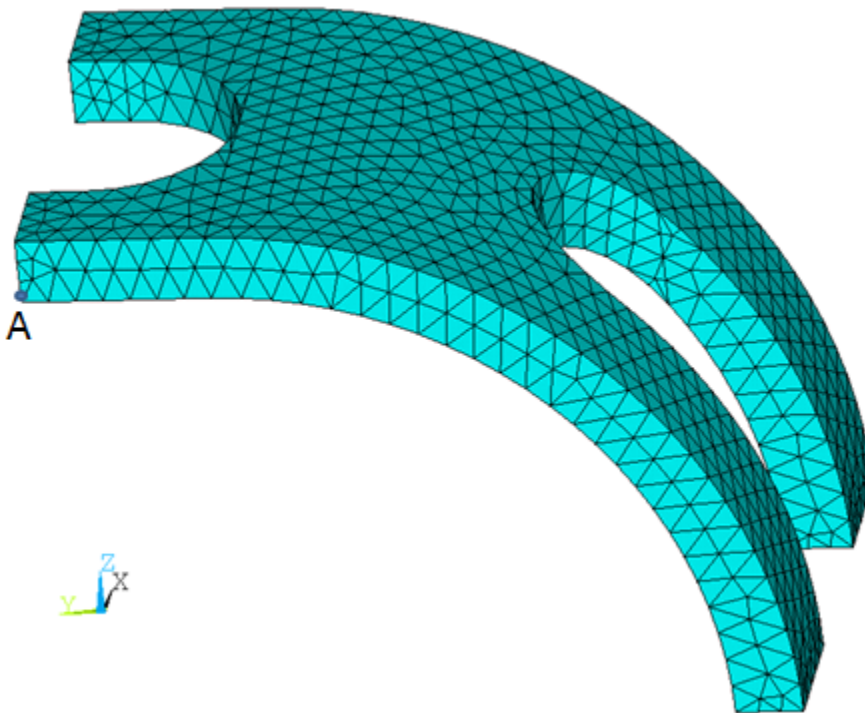
**Figure 40.2: Loading and Recovery of a Spinal Spacer Implant**



**40.3.1.2. Modeling**

A 3-D geometry of the spinal spacer is created in Unigraphics, using dimensions found in Petrini 2005 [2]. The geometry is imported into Mechanical APDL and meshed with SOLID187 elements. Because the spacer is symmetrical, only 1/4 of the spacer is studied.

**Figure 40.3: Spinal Spacer 1/4 Model**



**40.3.1.3. Material Properties**

The spinal spacer analysis uses the following material properties [2]:

<b>Spinal Spacer Material Properties</b>	
Elastic modulus for austenite phase (MPa)	70,000
Elastic modulus for martensite phase (MPa)	70,000

Spinal Spacer Material Properties	
Poisson's ratio	0.3
H (MPa)	500
R (MPa)	120
B (MPa · K <sup>-1</sup> )	8.3
T0 (K)	311
M	0

#### 40.3.1.4. Boundary Conditions and Loading

Symmetrical conditions are applied to the 1/4 model of the spinal spacer. A rigid surface contacts the top of the model, and a compressing displacement is applied to that surface. After the displacement is removed, a thermal load is applied to the whole model.

#### 40.3.1.5. Analysis and Solution Controls

A nonlinear static analysis is performed with large deformation enabled (**NLGEOM,ON**). After the mechanical loading is applied, thermal loading is applied over three steps (4 - 6) (p. 622) for quicker convergence.

In step 4, the temperature is increased from 297 K to 311 K. Convergence is achieved quickly as this temperature is below T0.

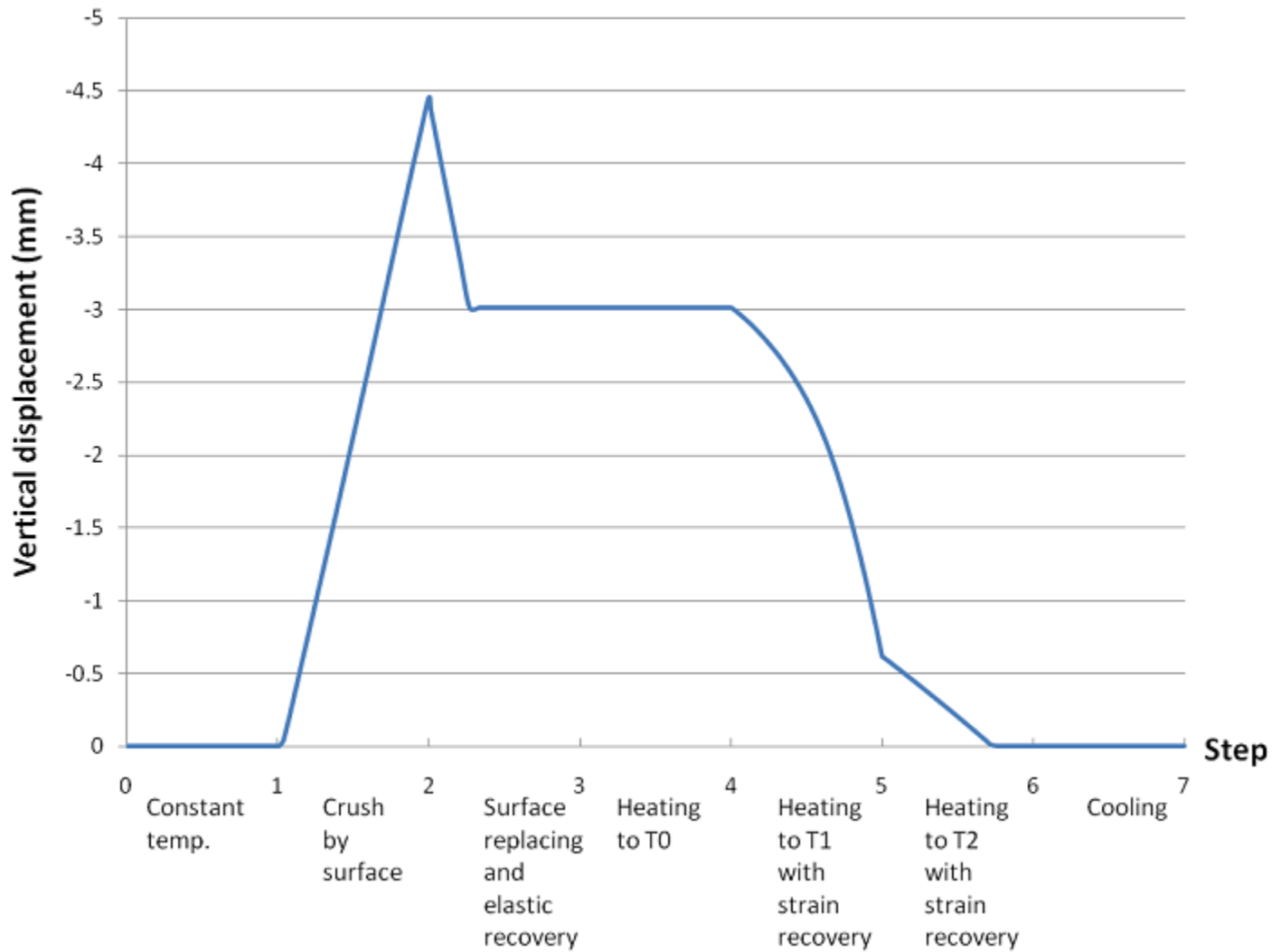
In step 5, the temperature is again increased from 311 K to 324 K. The major phase transformation does not occur in this step, so convergence is again achieved quickly.

In step 6, the temperature is increased above 324 K, and the shape memory effect occurs, so convergence is slower.

#### 40.3.1.6. Results and Discussion

Following is the displacement of central point A (shown in [Figure 40.3: Spinal Spacer 1/4 Model \(p. 620\)](#)):

**Figure 40.4: Displacements of Central Node A of the Spinal Spacer**

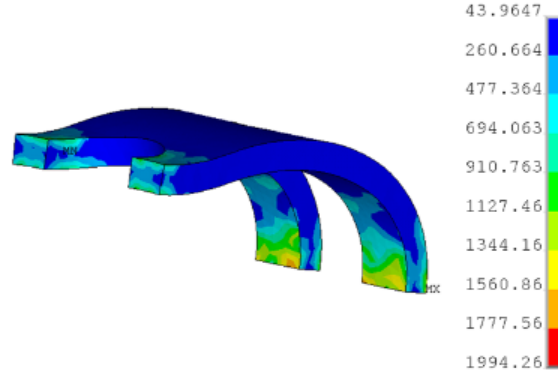
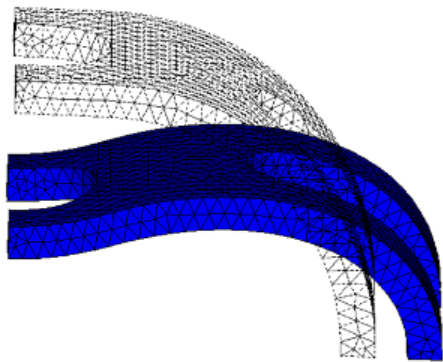


The following figure shows the deformation of the spacer at each step:

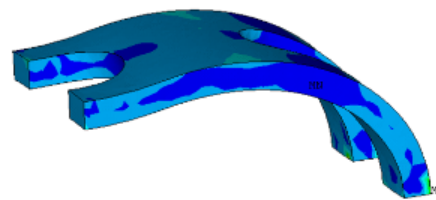
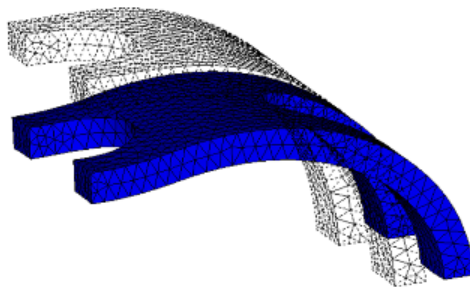
Figure 40.5: Spinal Spacer Deformation and Stress

## Displacement Contour (mm)

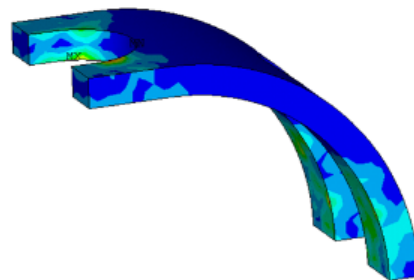
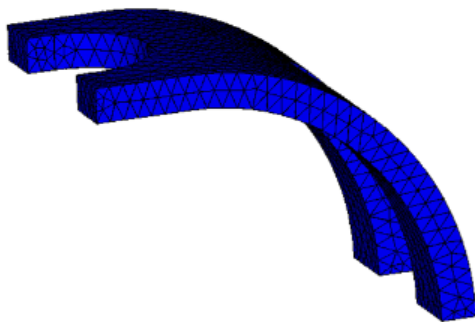
## Stress Contour (MPa)



Results at step 2



Results at step 3



Results at step 6

In step 2, the displacement is 4.5 mm and the stress is 1994 MPa. After elastic recovery, the peak displacement decreases to 3.0 mm and the stress is 579 MPa. In the final step, displacement and stress approaches zero, indicating that the spacer has returned to its original shape.

The simulation accurately depicts the spacer under load (step 2), during elastic recovery (step 3), and at full recovery due to SMA thermal effects (step 6).

### 40.3.2. Simulation of a Spring Actuator

Because of their large-strain capabilities and high force-to-weight ratios, SMAs are used widely as compact, flexible actuators in a variety of industries. For example, SMAs can be used as combination sensor-actuators in thermal bridges for cryogenic coolers, variable-area exhaust nozzles for turbomachinery, and active clearance controls for blade shrouds. A prominent aircraft manufacturer has integrated SMAs into their variable geometry chevrons for engine noise control.

In this problem, a vertical helical spring is simulated to repeat its two-way motion due to the shape memory effect. The following related topics are available:

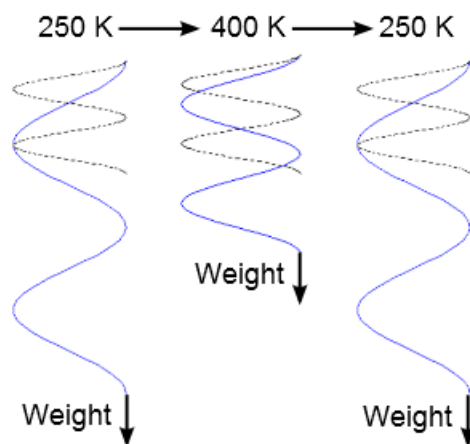
- 40.3.2.1. Problem Description
- 40.3.2.2. Modeling
- 40.3.2.3. Material Properties
- 40.3.2.4. Boundary Conditions and Loading
- 40.3.2.5. Analysis and Solution Controls
- 40.3.2.6. Results and Discussion

#### 40.3.2.1. Problem Description

A vertical helical spring is simulated with shape memory effect using two different models, a [BEAM188](#) element model and a [SOLID185](#) element model.

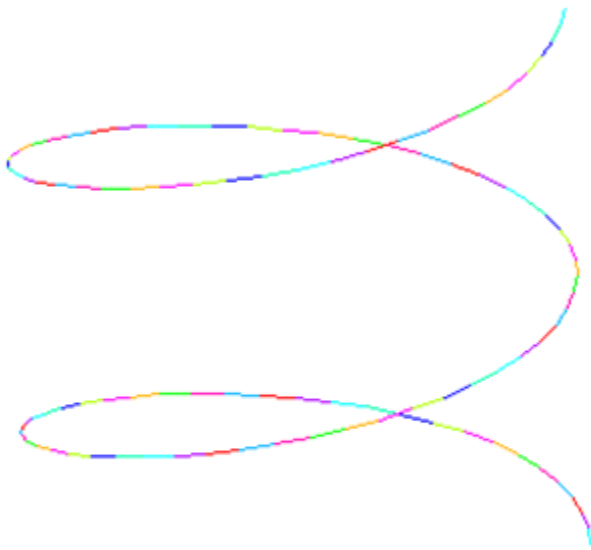
The spring is loaded by a weight of 1830 N in the martinsite state at a temperature of 250 K, then heated to 400 K. At the increased temperature, the spring lifts the weight. The spring is then cooled back to 250 K and stretches again. A repeatable, two-way motion occurs, as shown in this figure:

**Figure 40.6: Motion of a Vertical Helical Spring**

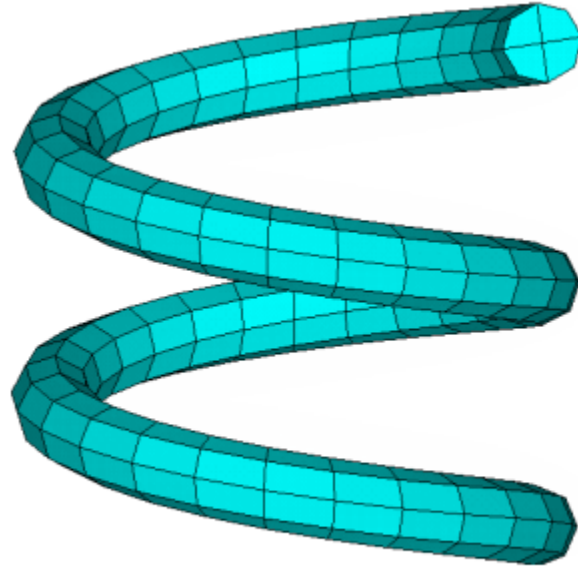


#### 40.3.2.2. Modeling

The geometry of the spring actuator is created in Mechanical APDL with a wire diameter of 4 mm, a spring external diameter of 24 mm, a pitch size of 12 mm, with two coils, and an initial length of 28 mm, as shown in the following figure:

**Figure 40.7: Finite Element Models of a Spring Actuator**

Beam model with BEAM188 elements



3-D model with SOLID185 elements

The corresponding finite element model is created using **BEAM188** elements. A 3-D model is generated by extruding the initial finite element model and meshing with **SOLID185** elements.

#### 40.3.2.3. Material Properties

The following material properties [3], typical of nitinol, are used in the spring actuator simulation:

Material Properties for a Spring Actuator	
Elastic modulus for austenite phase (MPa)	51,700
Elastic modulus for martensite phase (MPa)	51,700
Poisson's ratio	0.3
H (MPa)	1000
R (MPa)	140
B (MPa·K <sup>-1</sup> )	5.6
T <sub>0</sub> (K)	250
M	0

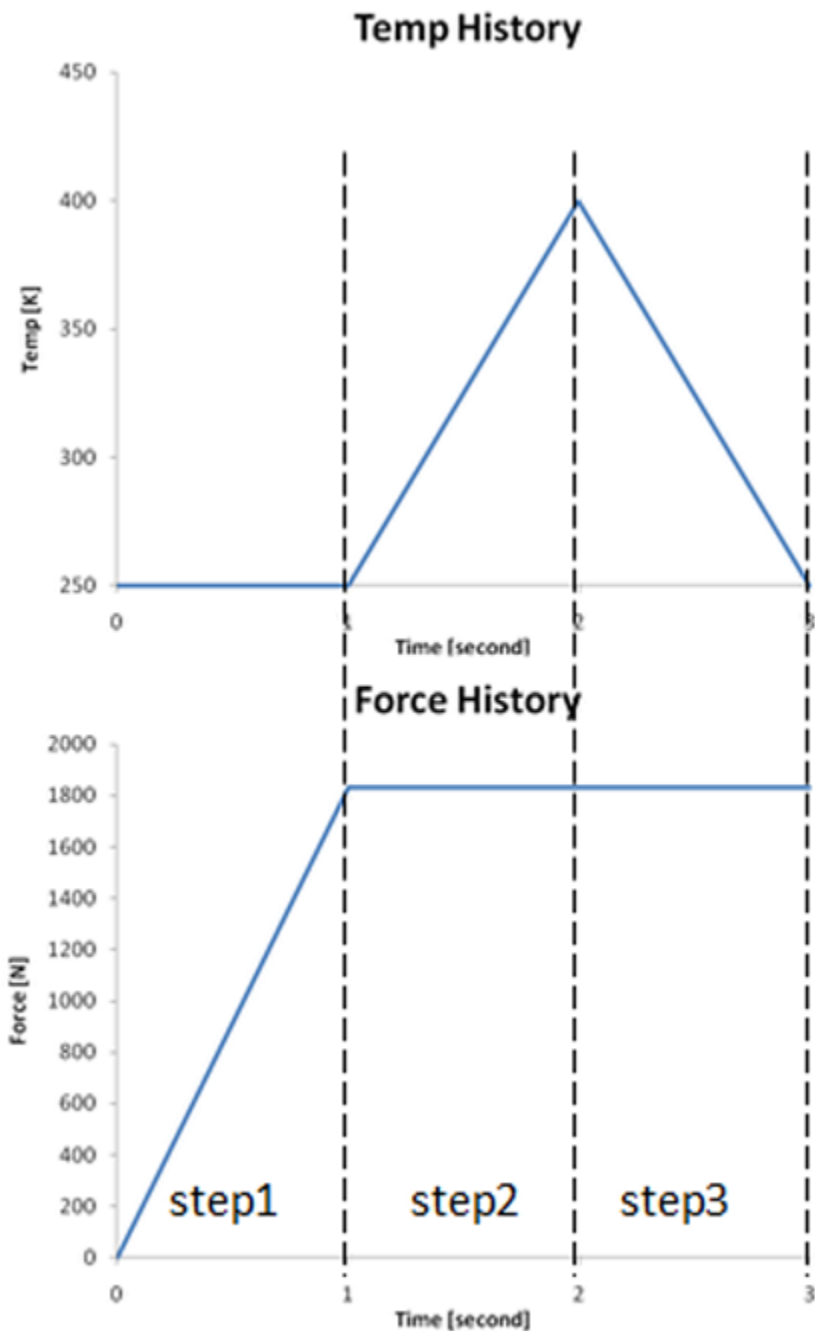
#### 40.3.2.4. Boundary Conditions and Loading

The top of the spring actuator is fixed, and the bottom is loaded with a weight of 1830 N. Displacements are constrained in the X and Y directions. After the spring is stretched by the weight at temperature 250 K, the temperature is raised to 400 K to lift the weight, and the is reduced back to 250 K to lower the weight.

### 40.3.2.5. Analysis and Solution Controls

A nonlinear static analysis is performed using large-deformation (**NLGEOM,ON**) and unsymmetric matrices for the full Newton-Raphson method (**NROPT,UNSYM**). The whole solution is completed in three load steps, as shown in this figure:

**Figure 40.8: Temperature and Force Load Steps**

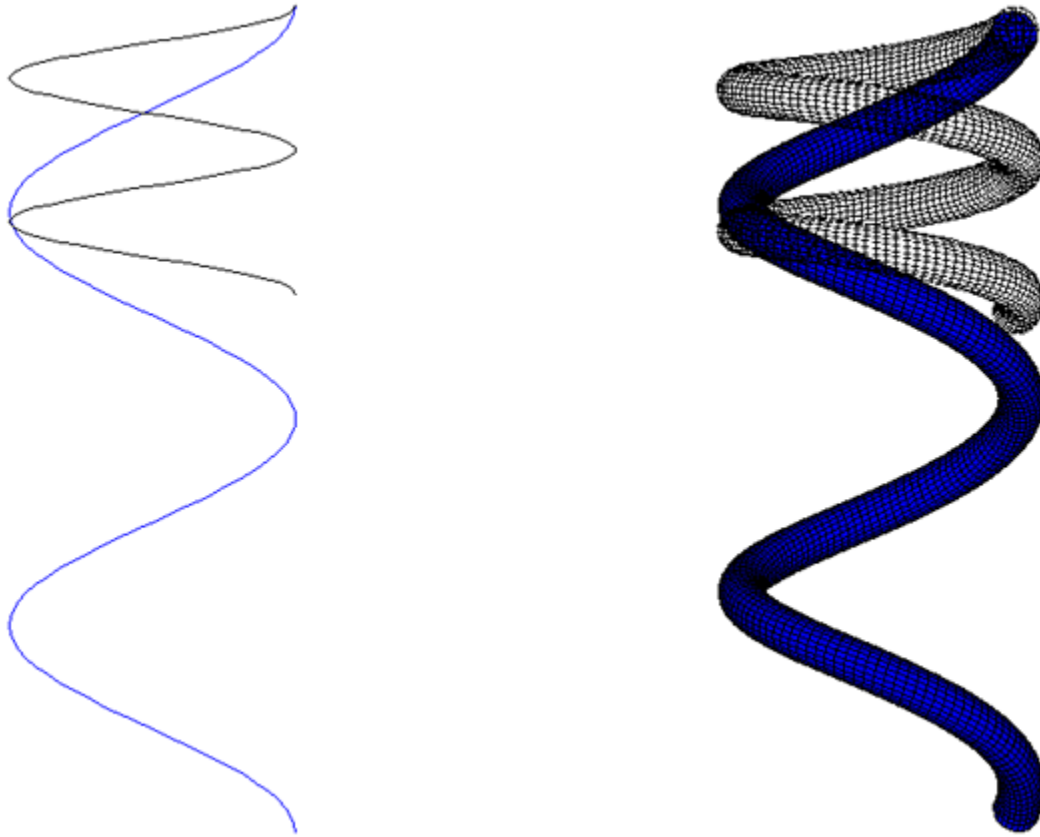


The results from the **BEAM188** and **SOLID185** models are compared.

### 40.3.2.6. Results and Discussion

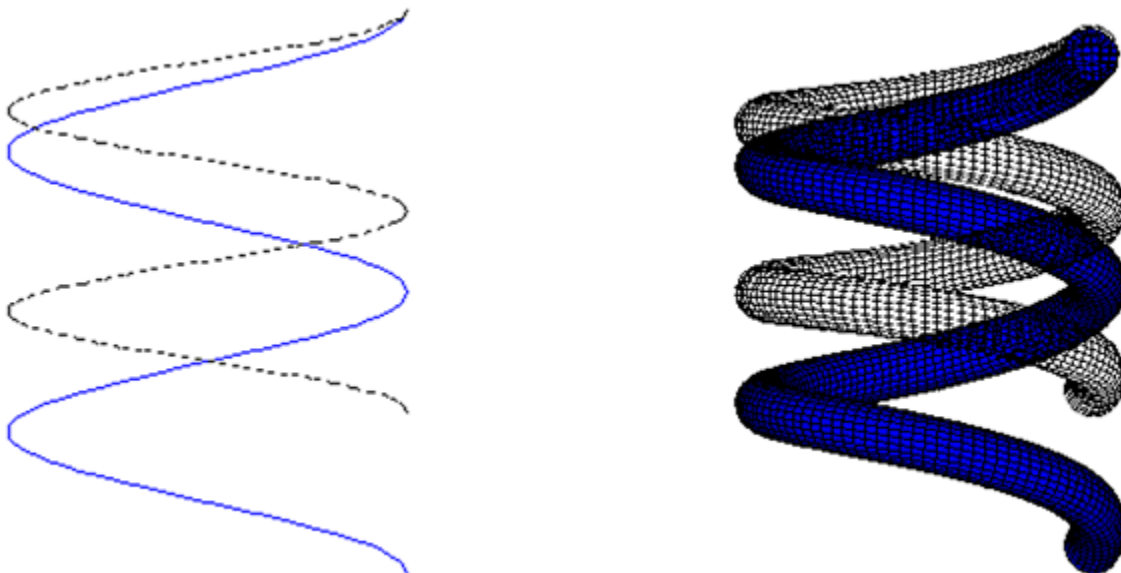
The spring actuator stretched by load  $W$  in step 1 is shown in this figure:



**Figure 40.9: Spring Actuator Deformation at Step 1**

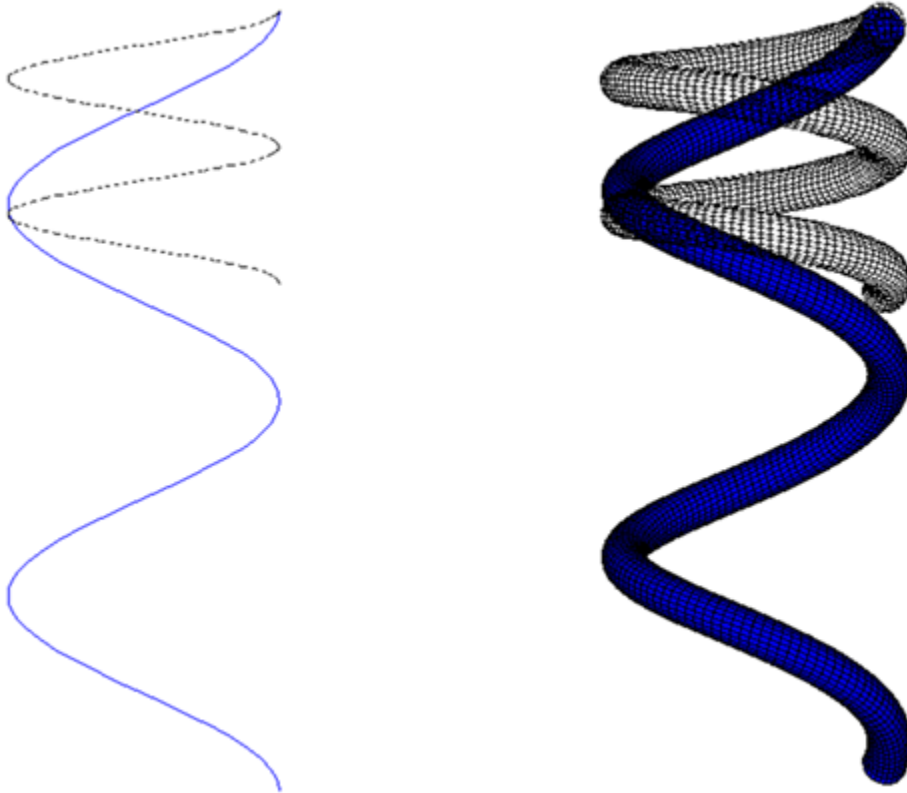
The maximum displacement is 43 mm, greater than the original length of 28 mm.

In step 2, after heating with the shape memory effect, the spring actuator recovers to a maximum displacement of 10 mm. The deformation is in the martensite state to support the weight, as shown here:

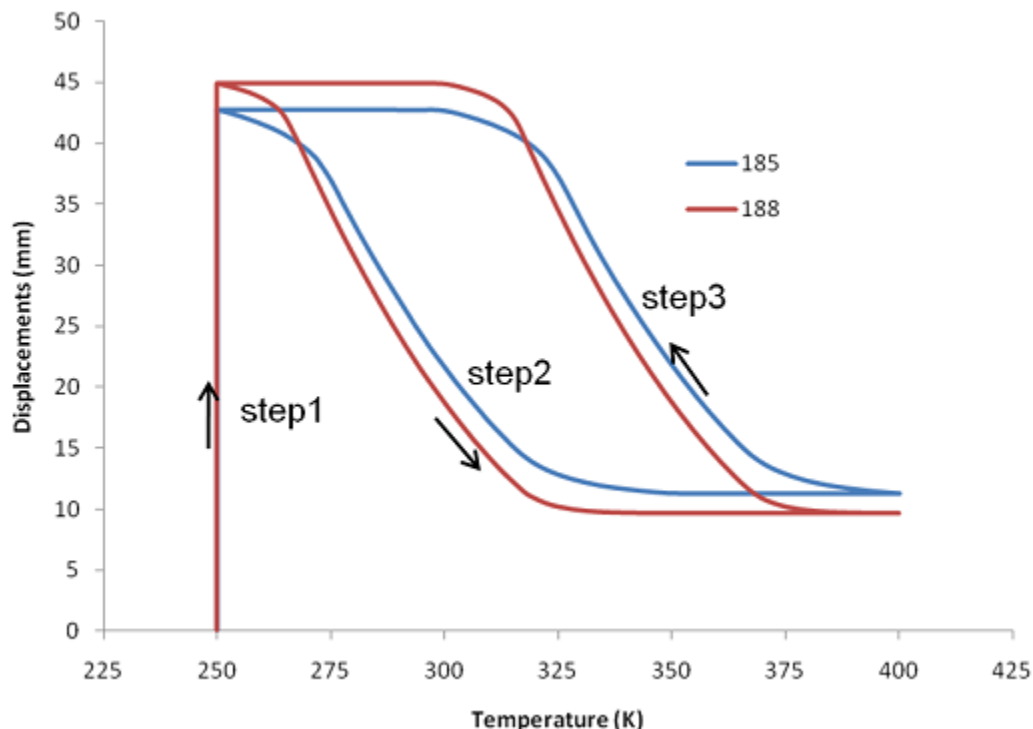
**Figure 40.10: Spring Actuator Deformation at Step 2**

In step 3, after cooling to 250 K, the spring actuator stretches back to its original length:

**Figure 40.11: Spring Actuator Deformation at Step 3**



Following is the displacement history of the actuator:

**Figure 40.12: Displacement History: Bottom of a Spring Actuator with Temperature**

The displacement history indicates that the [BEAM188](#) and [SOLID185](#) models have similar results. The [BEAM188](#) model is much more efficient, however, requiring about an hour to complete. In comparison, the [SOLID185](#) model requires more than eight hours to complete.

## 40.4. Recommendations

To perform similar types of analyses involving SMAs, consider the following:

- The stiffness of the material model is generally unsymmetrical, but a symmetric matrix is used in the solution by default. If convergence difficulty occurs during the solution, specify the unsymmetric solver option (**NROPT,UNSYM**).
- SMA phase transformation involves a transformation stage and the saturated transformation. Because convergence is more difficult to achieve during the transformation stage, break the transformation loadstep up into smaller ones and use smaller time steps.
- The superelasticity option ( $TBOPT = SUPE$ ) of the material model (**TB,SMA**) supports only 3-D, plane strain, and axisymmetric stress states. The memory option ( $TBOPT = MEFF$ ) of the material model supports most of the stress states including beam, shell, plane strain, axisymmetric, and 3-D stress states. The [LINK180](#) element is not supported for either material option.

## 40.5. References

The following references are used in this example problem:

1. Paremer, A., S. Fumer, D. P. Rice. *Musculoskeletal Conditions in the United States*. 1st ed. Park Ridge: American Academy of Orthopaedic Surgeons, 1992.

2. Petrini, L., F. Migliavacca, et al. "Computational Studies of Shape Memory Alloy Behavior in Biomedical Applications." *Journal of Biomedical Engineering*. 127 (2005): 716-725.
3. Arghavani, J., F. Auricchio, R. Naghdabadi. "A finite strain kinematic hardening constitutive model based on Hencky strain: General framework, solution algorithm, and application to shape memory alloys." *International Journal of Plasticity*. 27 (2011): 940-961.

## 40.6. Input Files

The following files are used in this problem:

- `td-40.dat` -- Input file for this analysis.
- `spinal_spacer_input.dat` -- Input for the spinal space portion of the analysis.
- `spacer.db` -- Database file containing the spinal spacer model.
- `actuator_beam_input.dat` -- Input file for the spring actuator portion of the analysis (using beam elements).
- `td-40b.cdb` -- Common database file containing the spring actuator model (using beam elements).
- `actuator_solid_input.dat` -- Input file for the spring actuator portion of the analysis (using solid elements).
- `td-40c.cdb` -- Common database file containing the spring actuator model (using solid elements).
- ...

The files are available in the `td-40` folder. See [Obtaining the Input Files \(p. xxxv\)](#) for more information.

---

## Chapter 41: Acoustic Analysis of a Viscothermal Resonator

---

This example problem demonstrates the use of acoustic elements and viscothermal losses comparing a boundary layer impedance (BLI) model and a low reduced frequency (LRF) model to analyze the noise reduction of sound-absorbing trim panels with quarter-wave resonators.

The following features and capabilities are highlighted:

- 3-D acoustic elements
- Normal surface velocity
- Boundary layer impedance (BLI) model
- Low reduced frequency (LRF) model
- Ports definition
- Absorption coefficient postprocessing

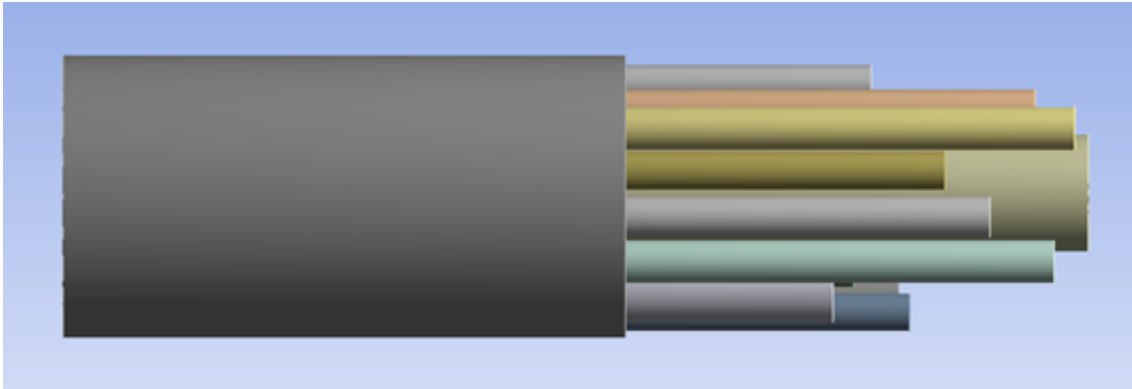
Topics related to this example problem follow:

- 41.1. Introduction
- 41.2. Problem Description
- 41.3. Modeling
- 41.4. Material Properties
- 41.5. Boundary Conditions and Loading
- 41.6. Analysis and Solution Controls
- 41.7. Results and Discussion
- 41.8. Recommendations
- 41.9. References
- 41.10. Input Files

### 41.1. Introduction

Development of systems for minimizing noise is an ongoing process, as noise is a factor that can quickly and adversely affect comfort. In an aircraft cabin, for example, the turbulent boundary layer surrounding the fuselage is a primary source of noise in the mid- to high-frequency range (500-2000 Hz). To reduce the sound pressure level in the cabin, an effective solution consists of quarter-wave resonator panels made of an assembly of tubes of varying diameters and lengths. The absorption capability of the resonator panel is the result of a combined effect of the quarter-wave phenomenon and viscothermal loss.

**Figure 41.1: 3-D Model of a Resonator Panel**



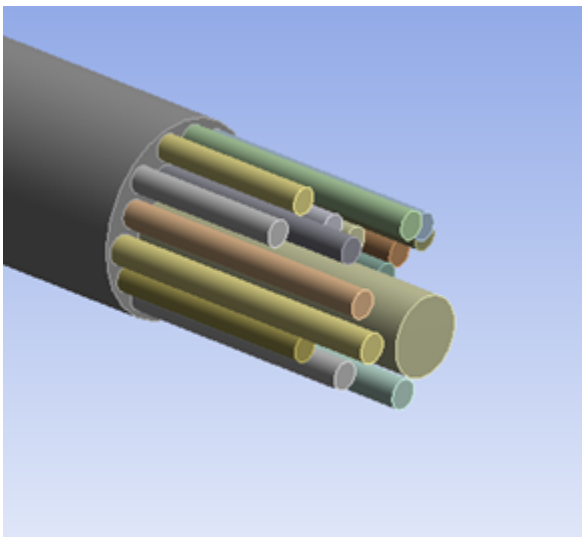
The problem presented here calculates the absorption coefficient of an example resonator panel.

## 41.2. Problem Description

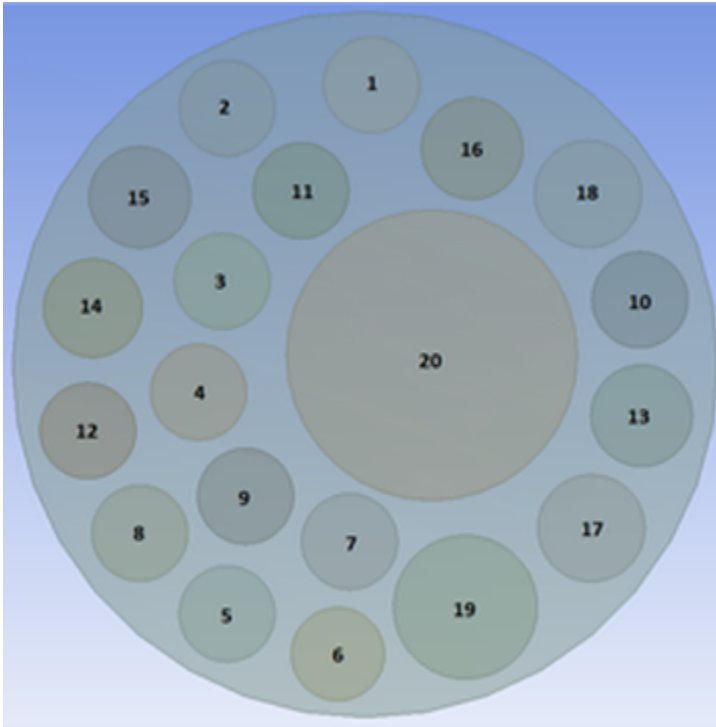
To reduce noise in an aircraft cabin, viscothermal quarter-wave resonator panels can be positioned within the cabin. Resonator tube lengths and diameters are optimized to maximize the sound absorption in the frequency range of interest. The resonator model described here is thus tested experimentally and numerically using the impedance tube method.

The following figure shows the geometry of the resonator model used in this simulation:

**Figure 41.2: 3-D Model of a Quarter-Wave Tubes Resonator**



This figure shows the resonator composed of tubes with variable diameters and lengths, resulting in an optimized absorption for all frequencies:

**Figure 41.3: Resonator Cross-Section**

Radii and length for each tube are defined with the following values [1]:

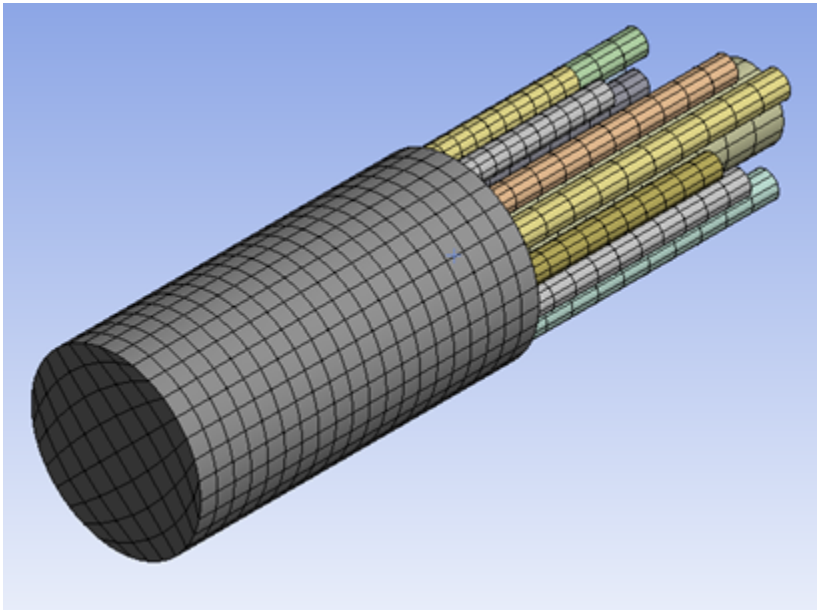
Tube Number	Radius (mm)	Length (mm)
1	3.4	43.6
2	3.4	43.6
3	3.4	45.4
4	3.4	46.8
5	3.4	48.6
6	3.3	50.5
7	3.4	40.6
8	3.4	52.1
9	3.4	54.4
10	3.4	56.7
11	3.4	59.0
12	3.4	61.7
13	3.6	64.7
14	3.5	66.9
15	3.6	69.8
16	3.6	72.9
17	3.8	76.1
18	3.8	79.8
19	5.1	36.8

Tube Number	Radius (mm)	Length (mm)
20	10.3	82.3

### 41.3. Modeling

The 3-D model of the structure is created in ANSYS DesignModeler and meshed with FLUID220 and FLUID221 3-D acoustic elements, with pressure as a unique degree of freedom (KEYOPT(2) = 1).

**Figure 41.4: 3-D Mesh of Resonator Panel**



A normal velocity and a nonreflective radiation boundary are applied on the impedance tube inlet, simulating the sound generated experimentally by a speaker.

Boundary layer impedance (BLI) and low reduced frequency (LRF) models are successively applied on the resonator tubes to analyze viscous and thermal effects.

The element size chosen ensures at least six elements per wave length for the highest frequency of interest.

All bodies are grouped in a single part for node connectivity at the body's interfaces.

### 41.4. Material Properties

The material properties used for all bodies are as follows:

Density	$1.22 \text{ kg} \cdot \text{m}^{-3}$
Speed of Sound	$343.3 \text{ m} \cdot \text{s}^{-1}$
Dynamic Viscosity	$1.829\text{e-}5 \text{ Pa} \cdot \text{s}$
Bulk Viscosity	$1.098\text{e-}5 \text{ Pa} \cdot \text{s}$
Thermal Conductivity	$0.02518 \text{ W} \cdot \text{m}^{-1} \cdot \text{K}^{-1}$



Specific Heat at Constant Pressure	$975.3 \text{ J} \cdot \text{kg}^{-1} \cdot \text{K}^{-1}$
Specific Heat at Constant Volume	$693.8 \text{ J} \cdot \text{kg}^{-1} \cdot \text{K}^{-1}$

The following input defines the material properties:

```
*GET,iMaxMat,MAT,0,NUM,MAX
MP,SONC,iMaxMat+1,343.3
MP,DENS,iMaxMat+1,1.22
MP,VISC,iMaxMat+1,1.829E-05
MP,BVIS,iMaxMat+1,1.098E-05
MP,KXX,iMaxMat+1,0.02518
MP,C,iMaxMat+1,975.3
MP,CVH,iMaxMat+1,693.8
```

## 41.5. Boundary Conditions and Loading

Only acoustic boundary conditions and loads are applied, as the model uses only acoustic elements.

A **normal surface velocity** is applied on the exterior. A **transparent port** and a **radiation boundary** are also applied on the same face:

```
CMSEL,S,source
ESEL,S,ENAME,,220
ESEL,A,ENAME,,221
SF,ALL,SHLD,-1,0
SF,ALL,PORT,1
SF,ALL,INF
```

Another **port**, used to calculate the absorption coefficient, is defined on the extremities of the tubes:

```
CMSEL,S,ends
ESEL,S,ENAME,,220
ESEL,A,ENAME,,221

SF,ALL,PORT,2
```

Two models are available for simulating the viscothermal losses in narrow tubes:

- A **boundary layer impedance** (BLI) model is defined on the tube faces in order to account for the viscothermal effects:

```
CMSEL,S,res
ESEL,S,ENAME,,220
ESEL,A,ENAME,,221
SF,ALL,BLI
```

- A **low reduced frequency** (LRF) model is defined for each tube via the **TB,AFDM,,,,CIRC** material model:

```
TB,AFDM,1,,CIRC
TBDATA,1,Rtube
```

Generally, the LRF model applies to layers and tubes below the cut-off frequency, and the BLI model applies to geometries that are large compared to the viscothermal boundary layer thickness.

## 41.6. Analysis and Solution Controls

A full harmonic analysis is performed from 1000 to 2000 Hz in 10 Hz increments. The acoustic load is step-applied (that is, with a constant unit velocity value across the range of frequency).

The following input sets up the analysis:

```
antype,harm
harfrq,1000.,2000.
hropt,full
kbc,1
nsubst,101
```

The `sparse direct solver` is used for this problem.

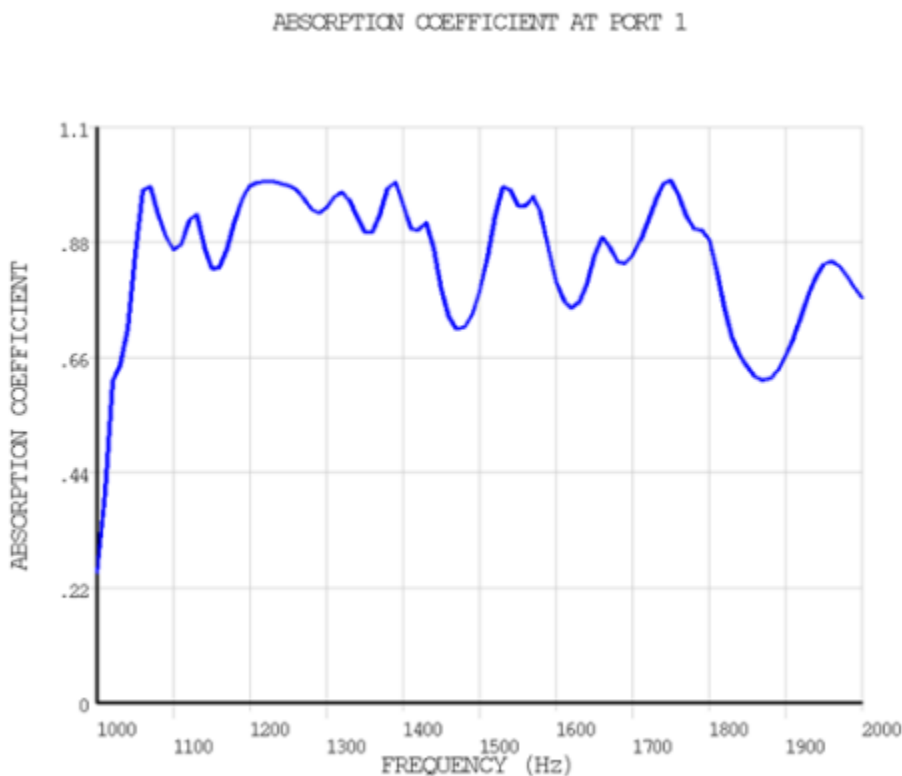
## 41.7. Results and Discussion

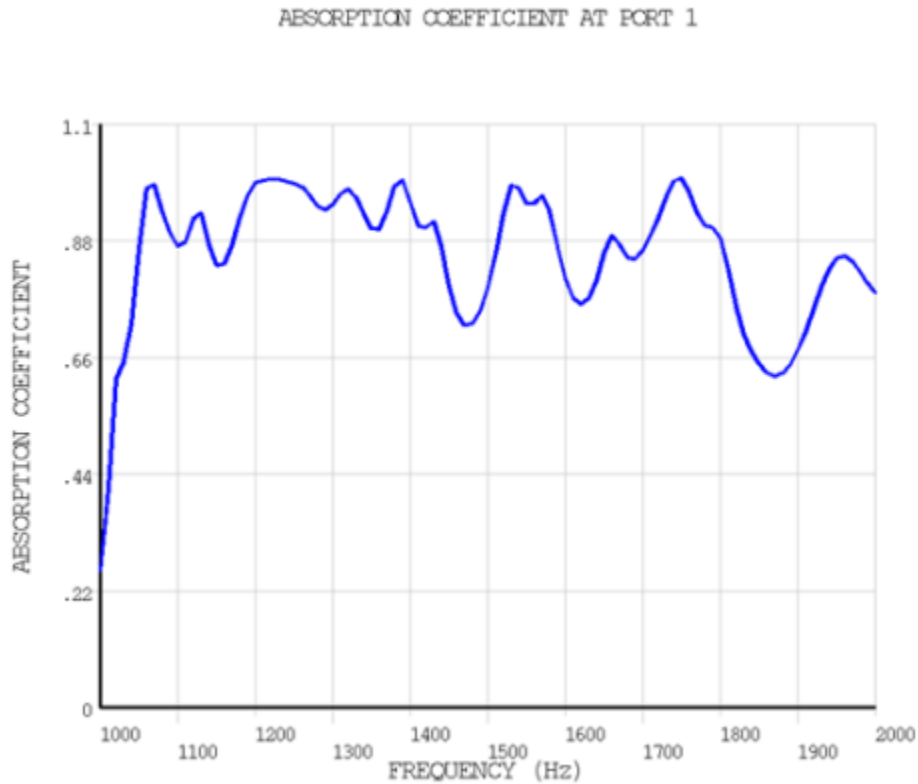
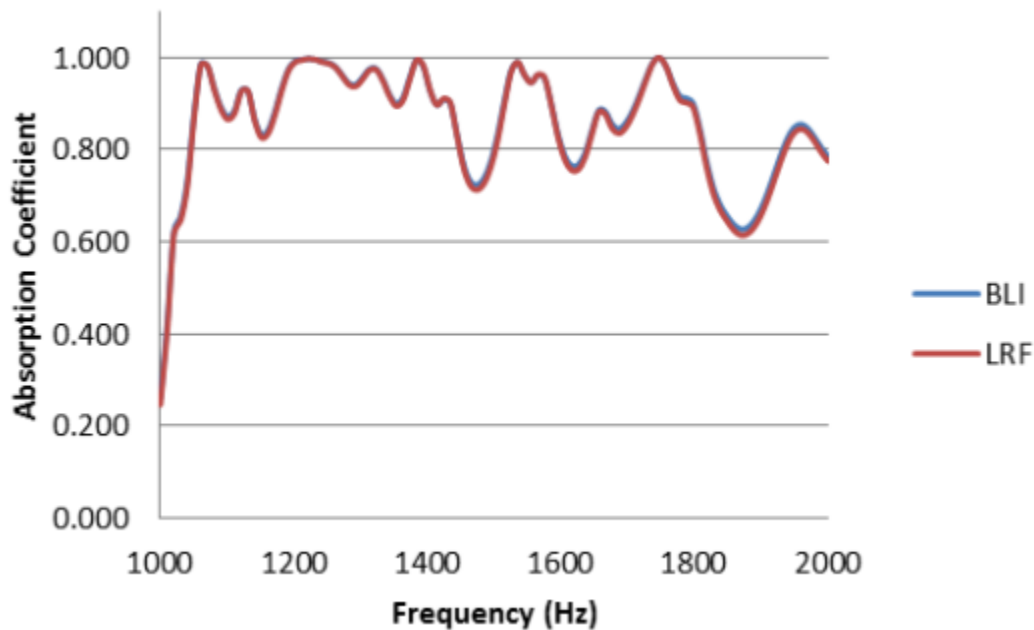
The performance of a sound reducer is determined by the amount of sound energy that it absorbs. A perfect resonator would have a constant absorption coefficient of 1 over the frequency range, meaning that all noise entering the system is absorbed.

The `SPOWER` is issued to postprocess the absorption coefficient of the system.

To analyze the absorption coefficient, the boundary layer impedance (BLI) and low reduced frequency (LRF) models are compared, as shown in the following figures:

**Figure 41.5: Absorption Coefficient of the Resonator: BLI Model**



**Figure 41.6: Absorption Coefficient of the Resonator: LRF Model****Figure 41.7: BLI and LRF Results Comparison**

Both models give close results.

The results show that (except for a lower initial absorption at 1000 Hz) this resonator is efficient, as the absorption coefficient is close to 1 over the frequency range.

## 41.8. Recommendations

To perform a similar analysis involving an acoustic viscothermal model, consider the following recommendations:

- Ensure at least six elements per wave length for the highest frequency of interest by [adapting the mesh element size \(p. 634\)](#) to the frequency range of the analysis.
- Select one of the available viscothermal models: the [low reduced frequency \(LRF\)](#) model applies to layers and tubes below the cut-off frequency, and the [boundary layer impedance \(BLI\)](#) model applies to geometries that are large compared to the viscothermal boundary layer thickness.
- Issue the **SPOWER** command to postprocess the absorption coefficient of the system.

## 41.9. References

The following reference is used in this example problem:

1. Hannink, M. H. C., Y.H. Wijnant, A. de Boer. "Optimised Sound Absorbing Trim Panels for the Reduction of Aircraft Cabin Noise." *11th International Congress on Sound and Vibration*. ICSV 11. St. Petersburg, Russia. (2004)

## 41.10. Input Files

The following files are used in this problem:

- `visco_resonator_BLI.dat` -- Input file for the viscothermal resonator analysis using the BLI model.
- `visco_resonator_BLI.cdb` -- Common database file for the original mesh used in the BLI model (called by `visco_resonator_BLI.dat`).
- `visco_resonator_LRF.dat` -- Input file for the viscothermal resonator analysis using the LRF model.
- `visco_resonator_LRF.cdb` -- Common database file for the original mesh used in the LRF model (called by `visco_resonator_LRF.dat`).

The files are available in the `td-41` folder. See [Obtaining the Input Files \(p. xxxv\)](#) for more information.

---

## Chapter 42: Wire Crimping Modeled with General Contact

---

This example problem demonstrates the ease of contact modeling via the [general contact](#) method. This method offers automated contact creation and requires minimal user input. The general contact procedure is especially useful when a large number of contacting surfaces are involved in the model and the geometry makes it difficult to determine contact pairs.

The following features and capabilities are highlighted:

- Automatic generation of general contact elements by the **GCGEN** command.
- Contact property definitions by the **GCDEF** command.
- Rigid-flexible and flexible-flexible contact modeled by general contact, including surface-to-surface, edge-to-surface, and edge-to-edge contact configurations.

Topics related to this example problem follow:

- [42.1. Introduction](#)
- [42.2. Problem Description](#)
- [42.3. Modeling](#)
- [42.4. Material Properties](#)
- [42.5. Boundary Conditions and Loading](#)
- [42.6. Analysis and Solution Controls](#)
- [42.7. Results and Discussion](#)
- [42.8. Recommendations](#)
- [42.9. Input Files](#)

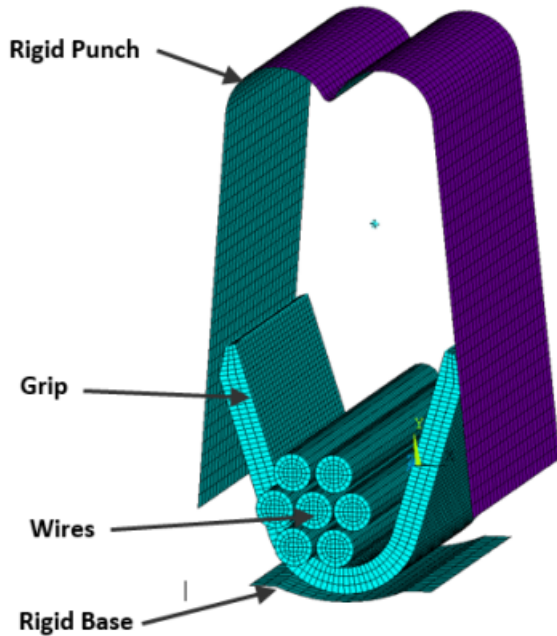
### 42.1. Introduction

In this example, a multi-strand wire is joined to an electrical terminal (connector) through a mechanical deformation process known as crimping. The U-shaped portion of the connector (the grip) is folded around the wires by a rigid punch, forming a B-shaped crimp which provides connectivity between the wires and the electric terminal.

Due to the complexity of this model, defining all possible contact surfaces by the pair-based contact method would be a difficult and time-consuming task. By using the general contact method, contact surfaces are created automatically; only a limited number of contact surfaces require the specification of non-default contact properties. Both flexible-flexible and rigid-flexible contact are modeled.

### 42.2. Problem Description

Following is a figure of the crimp joint model. The rigid punch is moved downward to fold the grip around the wires. The grip is resting on another fixed rigid surface. The rigid punch is moved 7.6822 mm downward in the Y direction through small time steps.

**Figure 42.1: 3-D Crimp Joint Model**

A transient analysis is performed to  $3.4 \times 10^{-4}$  seconds in order to capture the occurrence of all possible contact (surface-to-surface, edge-to-surface, and edge-to-edge) defined by general contact.

## 42.3. Modeling

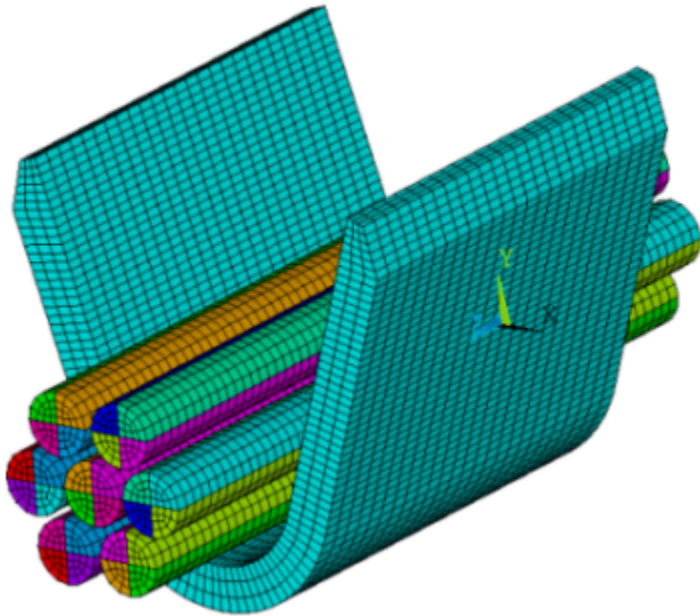
The 3-D crimp joint model consists of a 0.5 mm thick grip and seven stranded wires, with each wire having a 0.725 mm diameter. The grip and wires are made of a copper alloy which is modeled by the multi-linear isotropic hardening plasticity material model. The model also includes a rigid punch and a rigid support.

The steps to create this model are broken down as follows:

- 42.3.1. Model the Grip and Wire
- 42.3.2. Model the Rigid Punch and Base Support
- 42.3.3. Model the Contact Using the General Contact Method

### 42.3.1. Model the Grip and Wire

The grip and the seven stranded wires are modeled with **SOLID186** (3-D structural solid) elements.

**Figure 42.2: 3-D Meshed Model of Grip with Seven Stranded Wires**

### 42.3.2. Model the Rigid Punch and Base Support

The rigid punch and rigid base supports are modeled with **TARGE170** (3-D target segment) elements.

The rigid target surfaces are taken from a pair-based contact model and converted to general contact. To include these target surfaces in the general contact definition, a zero real constant ID and a zero material ID are assigned via the **EMODIF** command with *I1* = GCN. A unique section ID (**SECNUM**) and a unique element type ID (**TYPE**) are also assigned via the **EMODIF** command. The same ID number is used for the section and element type IDs.

```

! Defining the rigid punch as a general contact surface

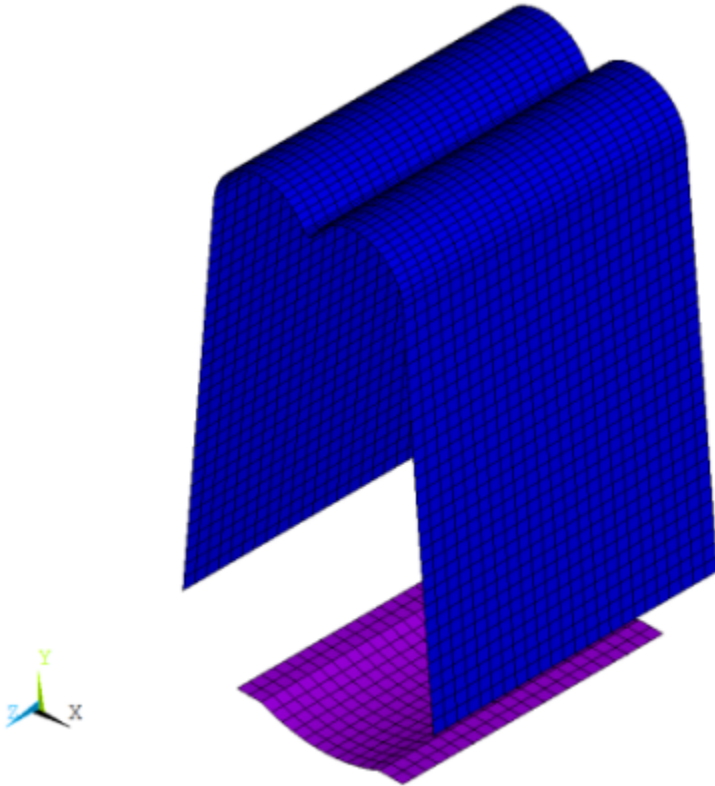
ESEL,S,REAL,,32          ! Select the existing rigid surface for the punch
EMODIF,ALL,SECNUM,32     ! Assign a unique section ID (same as type ID)
EMODIF,ALL,REAL,GCN     ! Assign a 0 REAL ID by inputting the GCN label
EMODIF,ALL,MAT,GCN      ! Assign a 0 MAT ID by inputting the GCN label
ESURF,ALL,REVE          ! Reverse the normal for proper definition

! Defining the rigid base as a general contact surface

ESEL,S,REAL,,35          ! Select the existing rigid surface for the base
EMODIF,ALL,SECNUM,35     ! Assign a unique section ID (same as type ID)
EMODIF,ALL,REAL,GCN     ! Assign a 0 REAL ID by inputting the GCN label
EMODIF,ALL,MAT,GCN      ! Assign a 0 MAT ID by inputting the GCN label
ALLSEL,ALL

```

Alternatively, you could generate these target surfaces via the **AMESH** command if you were modeling this structure from scratch.

**Figure 42.3: Rigid Punch and Rigid Base**

### 42.3.3. Model the Contact Using the General Contact Method

After building a complete finite element model and defining rigid targets, the next step is to generate general contact surfaces via the **GCGEN** command. This command automatically generates 3-D surface-to-surface elements (**CONTA174**) on exterior faces of the base elements and splits them into different contact surfaces (each having a unique section ID) if the angle between the normal of adjacent faces is greater than the feature angle defined on **GCGEN** (*FeatureANGLE* = 20). It also generates 3-D line contact elements (**CONTA177**) on the feature edges between split surfaces based on the setting *EdgeKEY* = 1 on **GCGEN**.

The value 20 is used for feature angle in order to achieve the desired split of the contact surfaces and edges between them. In this model, only the top edges of the grip are considered, and the rest are deleted.

```

allsel,all
gngen,,20,1,      ! Automatically generate CONTA174 elements on
                  ! exterior faces & CONTA177 on feature edges

! Only the top edges of the grip are considered, and the rest are deleted

esel,s,real,gcn   ! Select general contact elements
esel,r,ename,,177 ! Reselect the edge elements, CONTA177
esel,u,sec,,95,96 ! Unselect the top edge elements
esel,u,sec,,109,112 ! Unselect the top edge elements
edele,all,all     ! Delete the selected edge elements except top
                  ! edge elements

allsel,all

! Define the contact force-based model for CONTA177

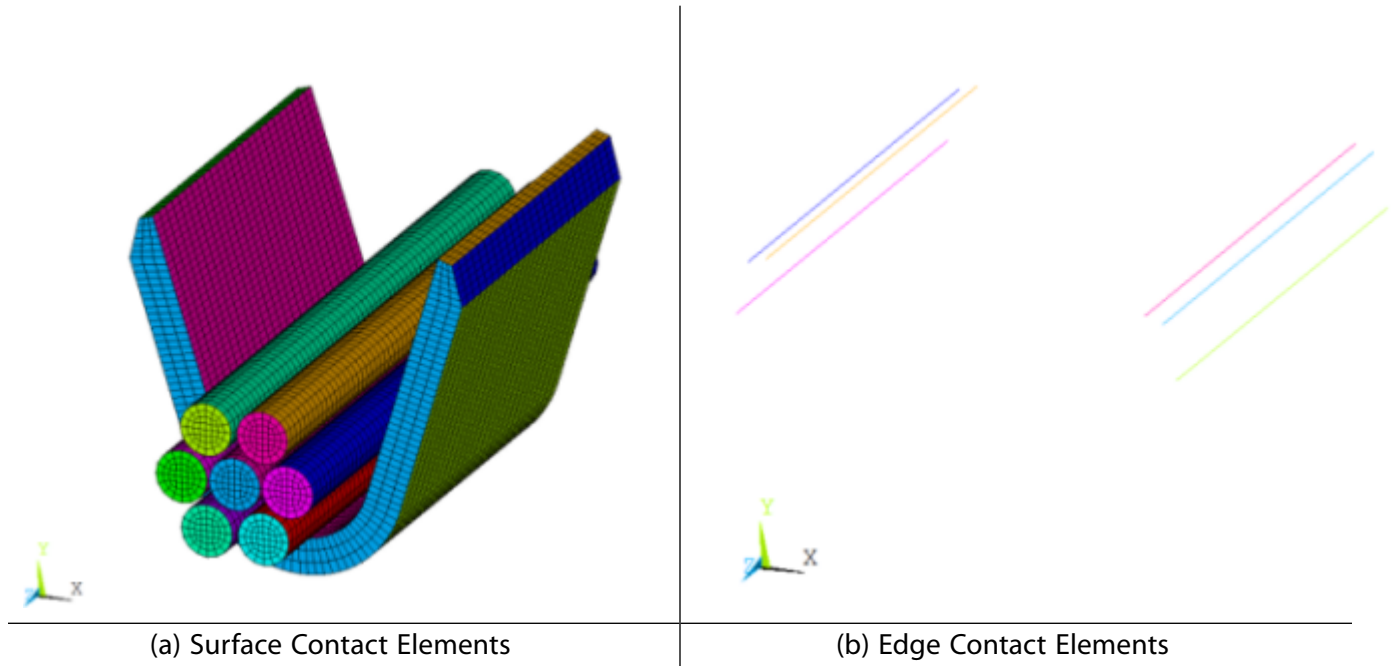
keyopt,95,3,0
keyopt,96,3,0

```



```
keyopt,109,3,0
keyopt,110,3,0
keyopt,111,3,0
keyopt,112,3,0
```

**Figure 42.4: Surface Contact Elements (a) and Edge Contact Elements (b)**



Next, the contact interactions are defined via the **GCDEF** command. By default, frictionless standard contact is assumed among all general contact surfaces. To override this default, the command **GCDEF,AUTO,ALL,ALL,100,100** is used to define frictional contact for all contact surfaces. Additional **GCDEF** commands are used to exclude some surfaces that may cause spurious contact.

```
! Define interactions between general contact surfaces via the GCDEF command

gndef,auto,all,all,100,100 ! Define auto asymmetric frictional contact
                           ! among all surfaces defined by material ID 100
mp,mu,100,.1              ! Define friction coefficient for material ID 100
tb,inter,100,,standard   ! Define standard contact behaviour
tbdata,1,0                ! Include penetration and gap

r,100
rmodif,100,3,1           ! Define FKN for real ID 100

! Exclude contact between some surfaces via the GCDEF command
! to avoid spurious contact

gndef,exclude,grip_zp_face,all_face
gndef,exclude,grip_zn_face,all_face
gndef,exclude,grip_zp_face,all_edge
gndef,exclude,grip_zn_face,all_edge
gndef,exclude,gripTop_xn_face,grip_inner_face
gndef,exclude,75,77
gndef,exclude,gripTop_xp_face,grip_inner_face
gndef,exclude,76,79
allsel,all

gndef,list                ! List all defined interactions between
                           ! general contact surfaces
```

## 42.4. Material Properties

The grip and wires are made of a copper alloy which is modeled with the multilinear isotropic hardening (plastic) material model.

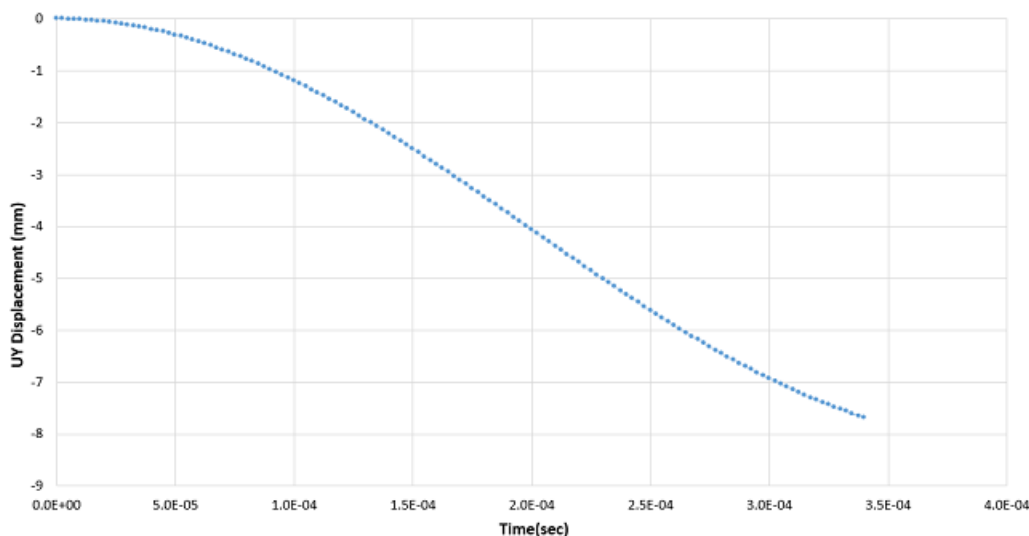
**Table 42.1: Material Properties of Grip and Wire**

Elastic Material Properties	
Young's Modulus	1.32e5 MPa
Poisson's Ratio	0.34
Density	8.9E-9 tonne/mm <sup>3</sup>
Multilinear Isotropic Hardening Constants (TB,PLASTIC,,,,MISO)	
Strain Value	Stress Value
0	261.12
0.0019	320.63
0.0537	401.94
0.1573	520.57
0.3153	627.00
0.5563	699.87
0.9814	735.18
1.303	740.60
1.903	742.39

## 42.5. Boundary Conditions and Loading

The rigid base of the punch assembly is constrained in all directions. One end of each wire is constrained in all translation directions (but not rotations) and the other end of each wire is free. A remote displacement is used to apply a downward displacement of 7.6822 mm to the punch over 3.4e-4 seconds. Displacement with respect to time is applied via tabular input.

**Figure 42.5: UY Time Varying Remote Displacement**



## 42.6. Analysis and Solution Controls

A nonlinear transient analysis is performed to  $3.4 \times 10^{-4}$  seconds. Large-deflection effects are included in the analysis (**NLGEOM,ON** command). This problem undergoes a large plastic deformation; therefore a large plastic limit is introduced as a cutback factor (**CUTCONTROL** command) to automatically reduce the step size when the solution encounters convergence difficulties during the nonlinear analysis.

```

antype,4                ! Analysis type is transient
nlgeom,on               ! Include geometric nonlinearities
trnopt,full,,,,hht     ! HHT time integration method
tintp,0.15             ! Numerical Damping
cutcontrol,plslimit,.9 ! Cutback criterion

```

## 42.7. Results and Discussion

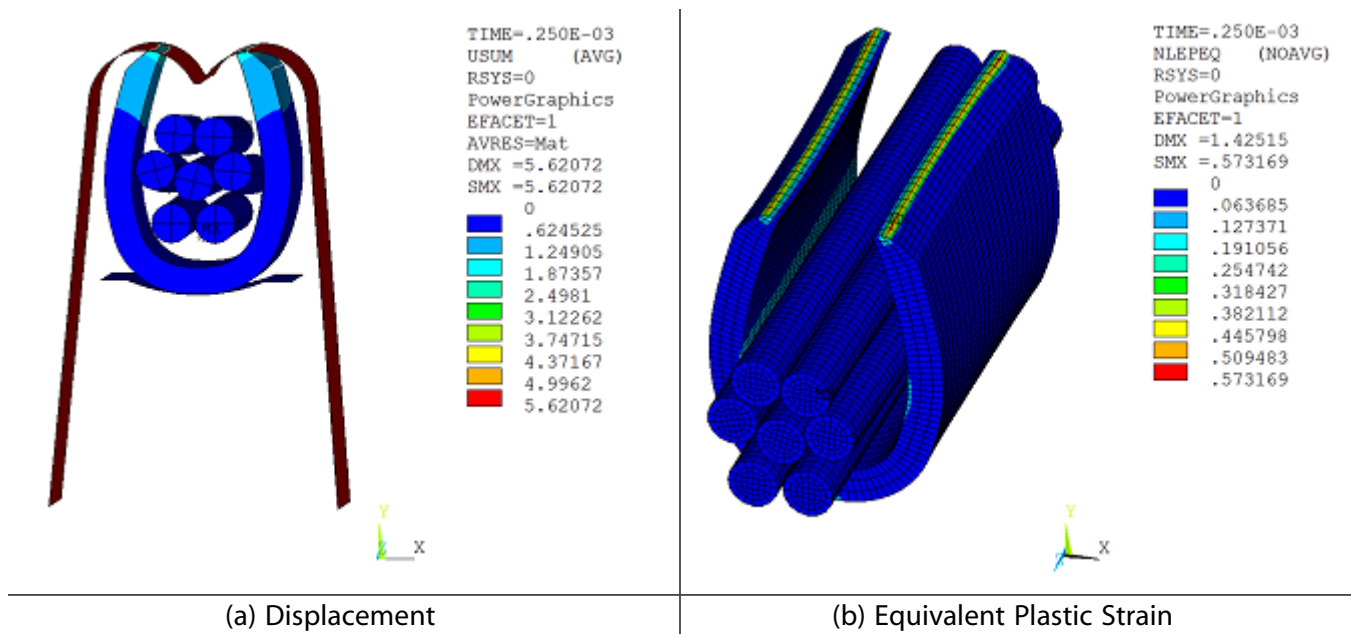
Results are presented at two time points:  $2.5 \times 10^{-4}$  seconds and  $3.4 \times 10^{-4}$  seconds.

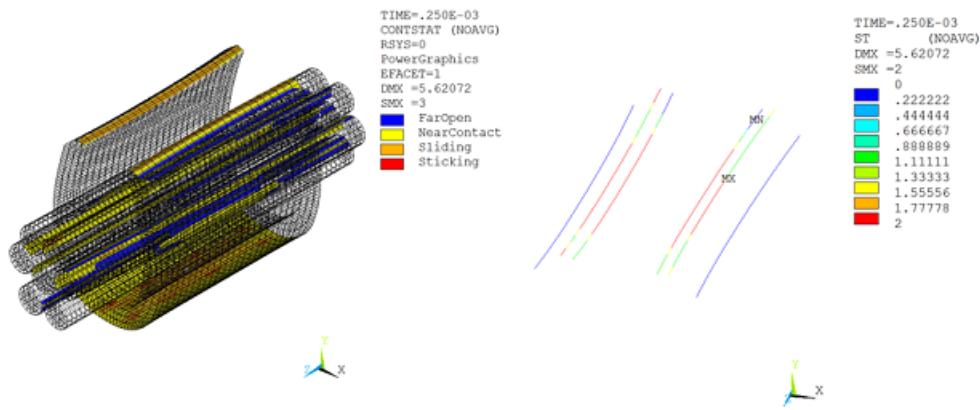
### Results at $2.5 \times 10^{-4}$ Seconds

The following results at  $2.5 \times 10^{-4}$  seconds are shown in the figure:

- Displacement of the rigid punch and deformed shape of the grip
- Equivalent plastic strain; the maximum is at the top edge of the grip as it comes in contact with the rigid punch
- Contact status plots of both surface-to-surface and edge-to-surface contact during the solution

**Figure 42.6: Results at  $2.5 \times 10^{-4}$  Seconds: (a) Displacement, (b) Equivalent Plastic Strain, (c) Contact Status**





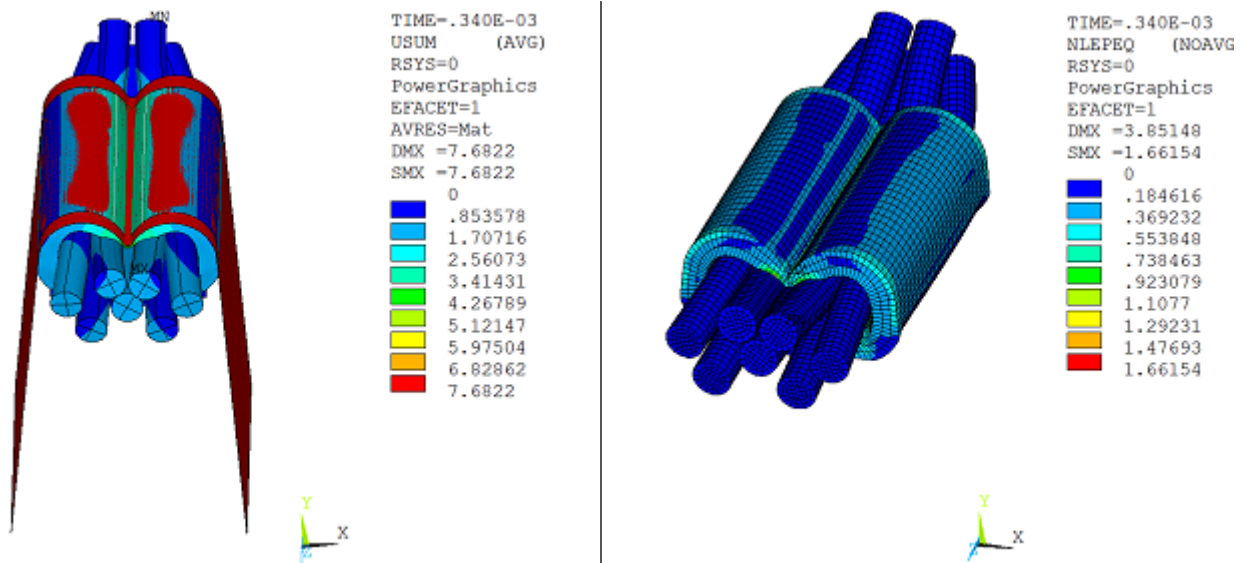
(c) Contact Status

**Results at 3.4 e-4 Seconds**

The following results at 3.4e-4 seconds are shown in the figure:

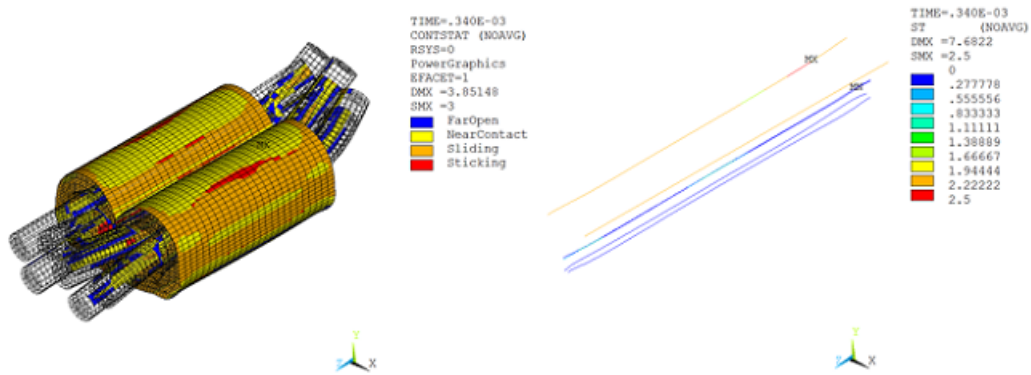
- (a) Displacement of the rigid punch and the final deformed shape of the grip
- (b) Equivalent plastic strain; the maximum is at the grip
- (c) Contact status plots of surface-to-surface, edge-to-surface, and edge-to-edge contact during the solution

**Figure 42.7: Results at 3.4e-4 Seconds: (a) Displacement, (b) Equivalent Plastic Strain, (c) Contact Status**



(a) Displacement

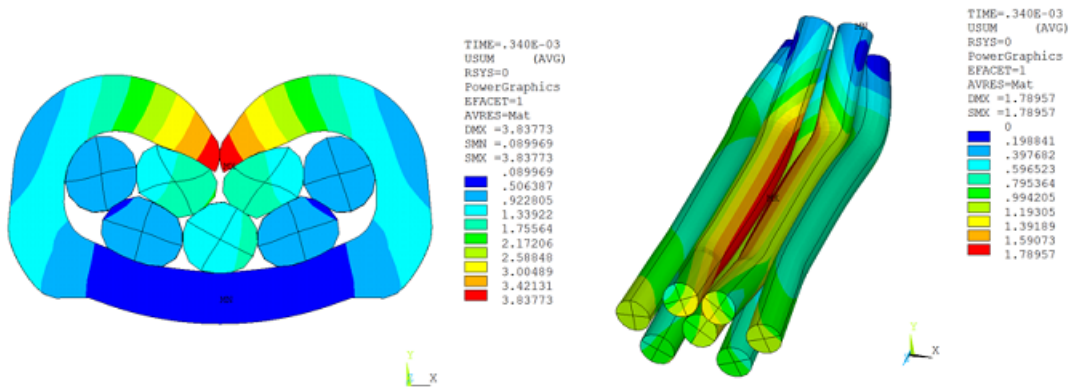
(b) Equivalent Plastic Strain



(c) Contact Status

Figure (a) below shows the cross-sectional view of the B-shaped crimp which is finally formed at the end of the deformation. Observe that the grip is completely folded around the wires and is in contact with the wires. Figure (b) shows the final deformed shape of the wires and their out-of-plane extrusion.

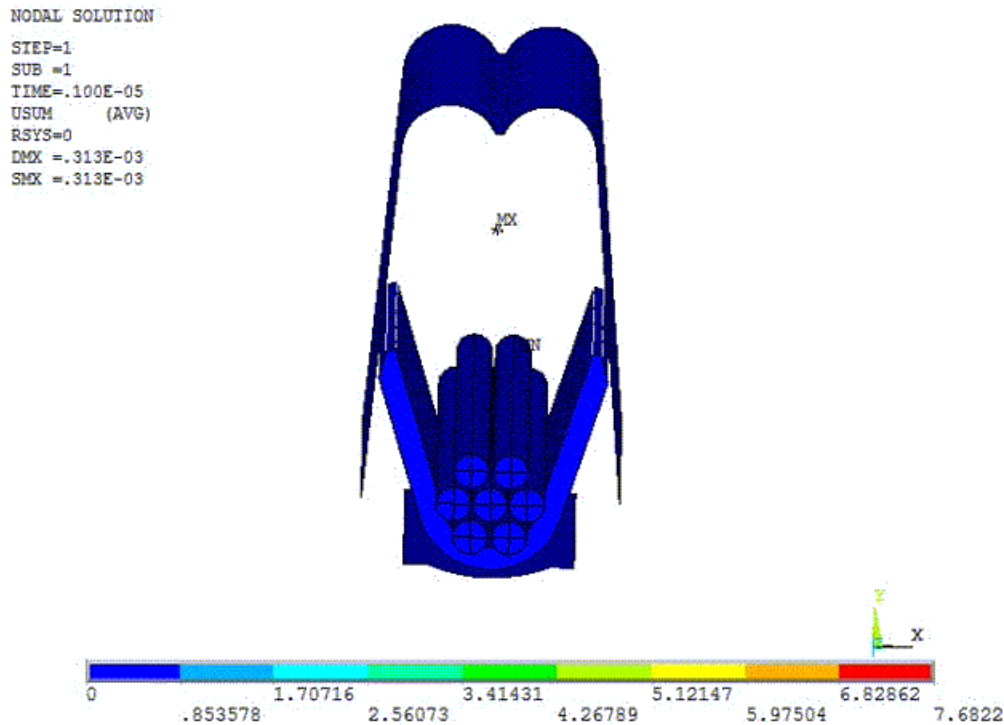
**Figure 42.8: Detailed Views of Deformed Wires**



(a) Cross Section

(b) Deformed Wires

The following animation shows the deformation over time of the grip as it is folded around the wires by the rigid punch to form a B-shaped crimp.

**Figure 42.9: Animation of Crimping Process**

## 42.8. Recommendations

When setting up a general contact analysis, consider the following hints and recommendations:

- Carefully consider the feature angle used on the **GCGEN** command. Choose a value that will produce the desired contact surfaces and edges.
- When using the exclude option on the **GCDEF** command along with node components (to identify surfaces), use the **\_FACE** component name extension to exclude only surface contact. Otherwise, both surface and edge elements will be excluded by default.
- Always check the normal direction of the rigid surface target elements.

## 42.9. Input Files

The following files are used in this problem:

- `wirecrimp.dat` -- Input file for wire crimping process modeled with the general contact method.
- `wirecrimp_fe.dat` -- FE model of wire crimp joint.

The files are available in the `td-42` folder. See [Obtaining the Input Files \(p. xxxv\)](#) for more information.

---

## Chapter 43: Contact Surface Wear Simulation

---

This example problem demonstrates the simulation of wear at a contact surface. The wear occurs at the interface between a hemispherical ring rotating over a flat ring. The following characteristics of wear are demonstrated: removal of material due to wear, changes in contact pressure and area due to wear, and a continuous decrease of the wear rate in steady state conditions.

The following features and capabilities are highlighted:

- [Contact surface wear](#)
- [Mesh nonlinear adaptivity based on a wear criterion](#)
- [User-defined wear](#)

Topics related to this example problem follow:

- [43.1. Introduction](#)
- [43.2. Problem Description](#)
- [43.3. Modeling](#)
- [43.4. Material Properties](#)
- [43.5. Boundary Conditions and Loading](#)
- [43.6. Analysis and Solution Controls](#)
- [43.7. Results and Discussion](#)
- [43.8. Recommendations](#)
- [43.9. Input Files](#)

### 43.1. Introduction

Wear is the progressive loss of material from the surface of a solid body when in contact with another body. The program approximates this loss of material by repositioning the contact nodes at the contacting surface. The new node locations are determined by a wear model which calculates how much and in what direction a contact node is to be moved to simulate wear based on the contact results.

This example shows use of the [Archard Wear model](#) and also demonstrates the [user-defined subroutine for modeling wear \(userwear\)](#).

Since wear involves material removal, the element quality of solid elements underlying the contact elements becomes progressively worse with increasing wear. Remeshing is required to successfully simulate large amounts of wear. This example demonstrates how manual rezoning or mesh nonlinear adaptivity can be used to improve mesh quality when a model undergoes large amounts of wear.

### 43.2. Problem Description

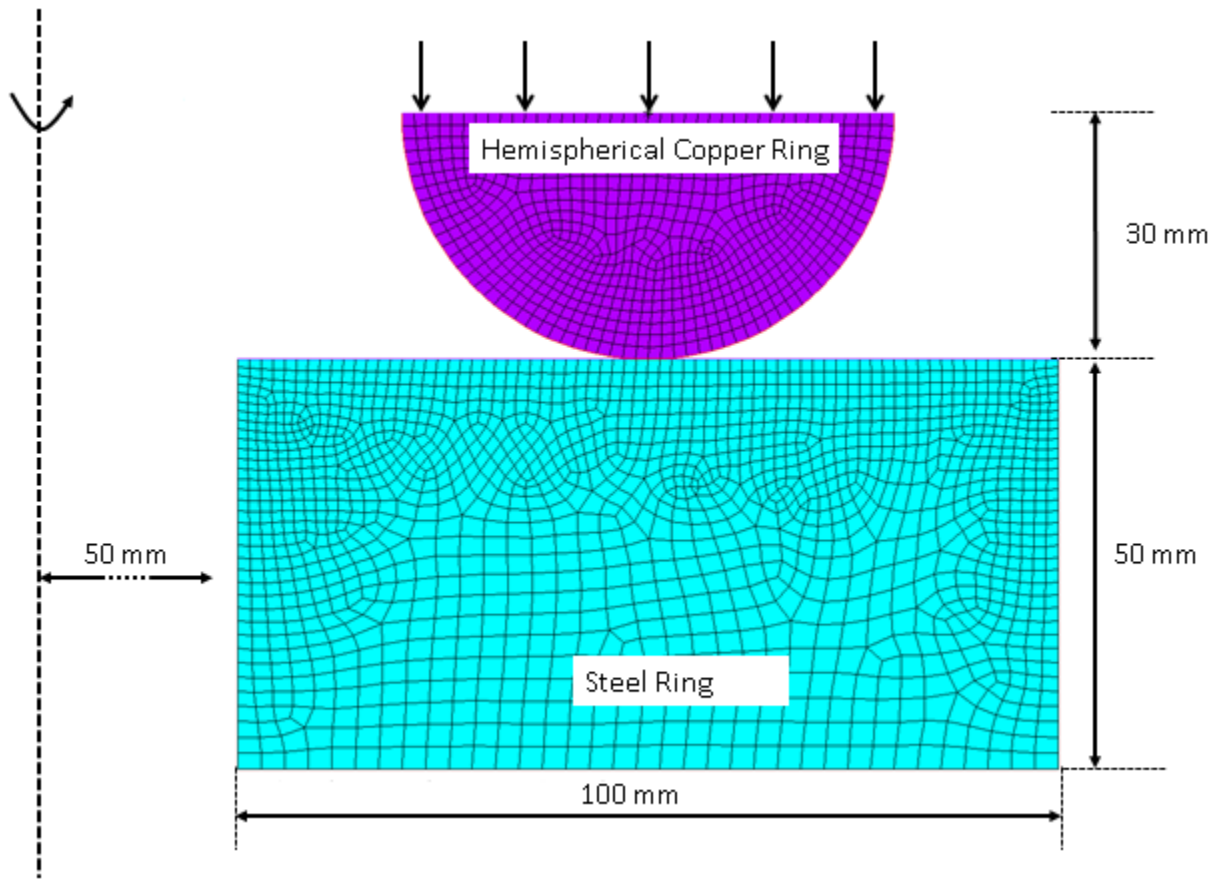
A hemispherical ring of copper with radius = 30 mm rotates on a flat ring of steel with inner radius = 50 mm and outer radius = 150 mm. The hemispherical ring touches the flat ring at the center from the axis of rotation (at 100 mm).

The hemispherical ring is subjected to a pressure load of  $4000 \text{ N/mm}^2$  and is rotating with a frequency of 100,000 revolutions/sec. Sliding of the hemispherical ring on the flat ring causes wear in the rings.

### 43.3. Modeling

A 2-D axisymmetric model representing the two rings is meshed and loaded as shown in the figure.

**Figure 43.1: 2D Axisymmetric Model of a Hemispherical Ring Rotating on a flat Ring**



The rings are meshed with 2-D axisymmetric [PLANE182](#) elements ( $\text{KEYOP}(3) = 1$ ). Frictionless contact is modeled between the two rings by overlaying the surfaces with contact elements ([CONTA171](#)) and target elements ([TARGE169](#)).

Two versions of this model are created, one with asymmetric contact and the other with symmetric contact. The first model uses asymmetric contact to simulate wear only on the top hemispherical ring; contact elements are defined on the top ring and target elements are defined on the bottom ring. In the second model, wear is simulated on both rings by defining symmetric contact between them; contact and target elements are defined on the surfaces of both rings.

Since wear can be modeled only on surfaces that have contact elements, the first example exhibits wear only on the hemispherical ring and the second example exhibits wear on both rings.

The [CONTA171](#) elements have the following settings:

- Augmented Lagrangian formulation ( $\text{KEYOPT}(2) = 0$ , the default behavior)
- Contact stiffness is updated at each iteration ( $\text{KEYOPT}(10) = 2$ )



- Location of the contact detection point: nodal point, normal to target surface (KEYOPT(4) = 2)

Since simulating wear requires repositioning of the contact nodes, the contact detection point must be at nodes (KEYOPT(4) = 1 or 2) , or projection-based contact can be used (KEYOPT(4) = 3).

### 43.3.1. Defining the Wear Model

Wear is simulated by defining a wear model (**TB,WEAR** command) and assigning it to the contact elements. You can specify a generalized form of the Archard wear model as implemented in the program, or you can define your own wear model via the `userwear` subroutine. Example input is provided for both methods.

Contact elements must be defined on the surface undergoing wear. A wear model is then associated with those contact elements via a **TB,WEAR** material definition. The following command is used to define the Archard wear model:

```
TB,WEAR,MATID,,,ARCD
```

where *MATID* is the material ID associated with the contact elements.

#### Simulating Wear via the Archard Wear Model

The Archard wear model is specified by inputting constants C1 through C4 on the **TB,WEAR** command. These constants represent the wear coefficient (K), material hardness (H), the contact pressure exponent (m), and the sliding velocity exponent (n).

The wear coefficient K can sometimes be scaled to simplify modeling. As an example, consider this ring-on-ring problem in which the rings are rotating at constant speed. The only effect of this rotation/sliding at the contact surface is to produce wear (friction is absent). The wear coefficient K can be scaled such that the rotation is not explicitly modeled, but its effect is included in the computation of wear. This greatly reduces the simulation time and effort.

More specifically, if a linear dependence of wear rate on the sliding velocity is assumed, the wear coefficient K can be scaled by the sliding velocity. In this example, sliding velocity is  $2\pi N \cdot R$ , where  $N = 100,000$  revolutions/sec and  $R$  is the distance from the axis of rotation. Scaling K by  $2\pi N \cdot R$  results in the wear rate being linearly dependent upon the sliding velocity without explicitly modeling the sliding. The distance from the axis of rotation ( $R$ ) is assumed to be constant for all points and is taken as 100 mm (the distance of the center of the ring from the axis of rotation).

To more accurately model the sliding velocity, you can program a user-defined wear model (via the `userwear` subroutine) that includes sliding velocity based on the distance from the axis of rotation.

Three example inputs are prepared to demonstrate different approaches to modeling wear:

- 43.3.1.1. Wear on One Contact Surface (Asymmetric Contact)
- 43.3.1.2. Wear on Both Contact Surfaces (Symmetric Contact)
- 43.3.1.3. User-Defined Wear (userwear Subroutine)

#### 43.3.1.1. Wear on One Contact Surface (Asymmetric Contact)

Asymmetric contact is used to model wear in the hemispherical copper ring only. For this case, contact elements are defined on the copper ring while target elements are defined on the steel ring. The Archard wear model is defined as a material associated with the contact elements.

The material data for wear is defined using **TB,WEAR** commands. The wear properties for the copper ring are as follows:

Wear Properties for the Copper Ring		
Property	TBDATA Constant	Value
Wear Coefficient (K)	C1	kcopper = $10e-13 * 2\pi * 1e5 * 100$ (scaled by sliding velocity $2\pi N * R$ )
Hardness (H)	C2	1 MPa
Pressure exponent (n)	C3	1
Velocity Exponent (m)	C4	0

To initiate wear after a steady state has been reached with respect to loading, **TB,WEAR** is used in conjunction with **TBFIELD,TIME**. The problem is simulated in two load steps. In the first load step, pressure is ramped to the desired level and wear is inactive during this load step. To achieve this **TB,WEAR** is defined as follows:

```
TB,WEAR,3,,ARCD           ! Mat #3 = material for wear of contact element on copper ring
TBFIELD,TIME,0            ! Time at the beginning of load step 1
TBDATA,1,0,1,1,0,0       ! C1 = 0 results in no wear for load step 1
TBFIELD,TIME,1           ! Time at the end of load step 1
TBDATA,1,0,1,1,0,0       ! C1 = 0 results in no wear for load step 1
```

In the second load step, the pressure is held constant and wear is defined as follows:

```
TBFIELD,TIME,1.01        ! Time at the beginning of load step 2
TBDATA,1,kcopper,1,1,0,0 ! Value of wear coefficient resulting in initiation of wear
TBFIELD,TIME,4           ! Time at the end of load step 2
TBDATA,1,kcopper,1,1,0,0 ! Wear coefficient kept constant during load step 2
```

### 43.3.1.2. Wear on Both Contact Surfaces (Symmetric Contact)

To model wear in both rings, symmetric contact definitions are used with contact elements on both of the contacting rings, and wear properties for both the copper ring and the steel ring are defined.

The wear properties for the copper ring are as presented in the asymmetric example described above. The wear properties for the steel ring are as follows:

Wear Properties for the Steel Ring		
Property	TBDATA Constant	Value
Wear Coefficient (K)	C1	ksteel = $1e-13 * 2\pi * 1e5 * 100$ (scaled by sliding velocity $2\pi N * R$ )
Hardness (H)	C2	1 MPa
Pressure exponent (n)	C3	1
Velocity Exponent (m)	C4	0

A symmetric contact definition between dissimilar meshes and materials can lead to a non-smooth contact pressure distribution. Thus, the option to use nodal stresses of the underlying solid element to calculate the wear increment (C5 = 1 on **TBDATA**) is recommended and is used in the symmetric example.

Wear for the copper ring is defined as in the asymmetric example with the addition of C5 = 1:

```
TB,WEAR,3,,ARCD           ! Mat #3 = material for wear of contact element on copper ring
TBFIELD,TIME,0            ! Time at the beginning of load step 1
TBDATA,1,0,1,1,0,1       ! C1 = 0 results in no wear for load step 1; C5 = 1 = nodal stress
TBFIELD,TIME,1           ! Time at the end of load step 1
TBDATA,1,0,1,1,0,1       ! C1 = 0 results in no wear for load step 1; C5 = 1
TBFIELD,TIME,1.01        ! Time at the beginning of load step 2
TBDATA,1,kcopper,1,1,0,1 ! Value of wear coefficient resulting in initiation of wear; C5 = 1
```

```
TBFIELD,TIME,7          ! Time at the end of load step 2
TBDATA,1,kcopper,1,1,0,1 ! Wear coefficient kept constant during load step 2; C5 = 1
```

Wear for the steel ring is defined as follows:

```
TB,WEAR,4,,ARCD        ! Mat #4 = material for wear of contact element on steel Ring
TBFIELD,TIME,0         ! Time at the beginning of load step 1
TBDATA,1,0,1,1,0,1    ! C1 = 0 results in no wear for load step 1; C5 = 1 = nodal stress
TBFIELD,TIME,1         ! Time at the end of load step 1
TBDATA,1,0,1,1,0,1    ! C1 = 0 results in no wear for load step 1; C5 = 1
TBFIELD,TIME,1.01      ! Time at the beginning of load step 2
TBDATA,1,ksteel,1,1,0,1 ! Value of wear coefficient resulting in start of wear; C5 = 1
TBFIELD,TIME,4         ! Time at the end of load step 2
TBDATA,1,ksteel,1,1,0,1 ! Wear coefficient kept constant during load step 2; C5 = 1
```

### 43.3.1.3. User-Defined Wear (*userwear* Subroutine)

The *userwear* subroutine is also demonstrated for this problem and uses a model similar to the Archard wear model. In this example, the input material data for *userwear* is similar to that of the Archard model with the addition of angular speed being passed in.

The *userwear* subroutine uses five input properties defined via **TBDATA**. C1 through C4 are the same as for the Archard wear law, and C5 passes in the rotational speed (10,000 rotations/sec). The example *userwear* subroutine calculates position-dependent sliding velocity using the distance of the contact point from the axis of rotation (R) and defines wear increment accordingly, thus avoiding explicit modeling of the sliding motion.

Asymmetric contact is considered in this example. The wear is defined as follows for the copper ring:

```
ang_velocity=2 1e5      ! angular velocity to be passed into userwear to calculate
                        ! accurate sliding velocity
TB,WEAR,3,,5,USER      ! Mat #3 = material for wear of contact element on copper ring
TBFIELD,TIME,0         ! Time at the beginning of load step 1
TBDATA,1,0,1,1,0,ang_velocity ! C1 = 0 results in no wear for load step 1
TBFIELD,TIME,1         ! Time at the end of load step 1
TBDATA,1,0,1,1,0, ang_velocity ! C1 = 0 results in no wear for load step 2
TBFIELD,TIME,1.01      ! Time at the beginning of load step 2
TBDATA,1,kcopper,1,1,0,ang_velocity ! Value of wear coefficient resulting in initiation of wear
TBFIELD,TIME,4         ! Time at the end of load step 2
TBDATA,1,kcopper,1,1,0, ang_velocity ! Wear coefficient kept constant during load step 2
```

### 43.3.2. Improving Mesh Quality During the Solution

Modeling wear involves repositioning contact surface nodes to simulate the material removal process. As a result, the element quality of the solid elements underlying the contact elements can quickly deteriorate. The examples show two ways of addressing this issue to enable simulating large amounts of wear.

#### Mesh Nonlinear Adaptivity

One way to [improve the mesh](#) is to use the [mesh nonlinear adaptivity](#) feature. A wear-based contact criterion is used to trigger mesh nonlinear adaptivity whenever the mesh is distorted. The user defines the critical ratio between the amount of wear and the underlying solid element's height. When this criterion is reached, mesh nonlinear adaptivity is triggered.

Both the asymmetric example and the symmetric example use mesh nonlinear adaptivity, which requires the following steps:

- Create a component that contains the contact elements that are undergoing wear.

- Issue the **NLADAPTIVE** command to trigger adaptivity based on a wear criterion.

In both examples, the component name is “conreal”, and the following command triggers mesh adaptivity:

```
NLADAPTIVE,conwearel,add,contact,wear,0.50 ! Wear criterion is 50% of element height.
```

In this case adaptivity occurs whenever wear at any contact point exceeds 50% of the average height of the solid element underlying the contact element. Each time the criterion is reached, the analysis is stopped, the mesh quality is improved by morphing the mesh, history-dependent variables and boundary conditions are mapped, and the analysis is restarted with an improved mesh. This process is done automatically.

### Manual Rezoning

**Manual rezoning** is another method that enables you to remesh the distorted mesh and continue the wear simulation with an improved mesh. This method, which requires more user intervention, is demonstrated in the user-defined wear example input file (see [Input Files \(p. 662\)](#)).

## 43.4. Material Properties

Linear elastic material behavior is assumed for both the copper ring and the steel ring.

Property	Copper	Steel
Young's Modulus (GPa)	130	210
Poisson's Ratio	0.3	0.3

## 43.5. Boundary Conditions and Loading

The bottom of the flat steel ring is fixed in the X and Y directions.

Contact elements are used to define a **rigid surface constraint** between the nodes on the top surface of the hemispherical ring and a pilot node which is constrained in the X direction. A force is applied on the pilot node that is equivalent to a pressure of 4000 N/mm<sup>2</sup>.

The equivalent pressure is ramped during the first load step from 0 to 4000 N/mm<sup>2</sup> and is kept constant at 4000 N/mm<sup>2</sup> during the second load step. Wear is activated in the second load step.

## 43.6. Analysis and Solution Controls

A nonlinear static analysis is performed in two load steps. Geometric nonlinearity is included in the analysis, and automatic time increments are used.

The repositioning of contact nodes during wear can result in changing contact status. If the wear increment is too large, all contact elements may go from a closed status to an open status, resulting in rigid body motion. To prevent this, a very small time increment is used so that the wear increment is also small and changes in contact status are minimized.

The following **DELTIM** command is used to set a small time increment size in the second load step:

```
DELTIM,0.01,1e-6,0.02
```

## 43.7. Results and Discussion

The results are analyzed to study the effect of wear on the contact conditions (contact pressure and contact area) and how wear evolves with time under steady state loading. The following topics are available:

[43.7.1. Effect of Wear on Contact Pressure](#)

[43.7.2. Effect of Wear on Stress and Element Quality](#)

[43.7.3. Evolution of Wear with Time](#)

### 43.7.1. Effect of Wear on Contact Pressure

#### Axisymmetric Contact; Wear on Hemispherical Ring Only

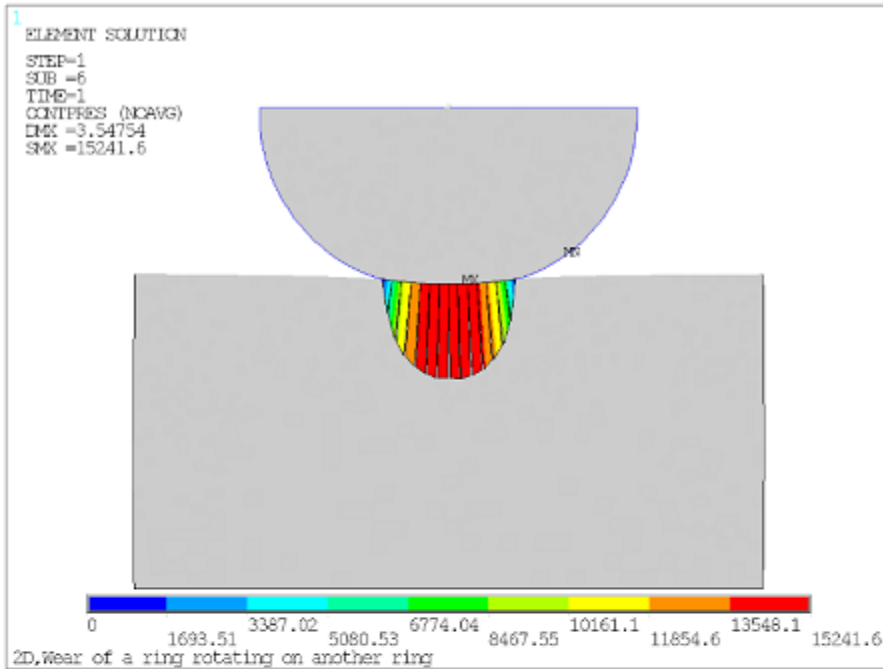
For the axisymmetric contact example, the contact condition is similar to the classical Herzian contact at the end of load step 1 (see figure below). Wear in the hemispherical ring is activated in the second load step. The figure shows the contact pressure at the end of 300,000 rotations (3 seconds) of the hemispherical copper ring over the steel ring.

Since the amount of wear is proportional to the contact pressure, the regions with initially high contact pressure wear more and local curvature is reduced, thereby reducing the contact pressure in those regions. This also leads to increasing area of the ring coming in contact and increases contact pressure in regions that had low contact pressure at the beginning of the wear.

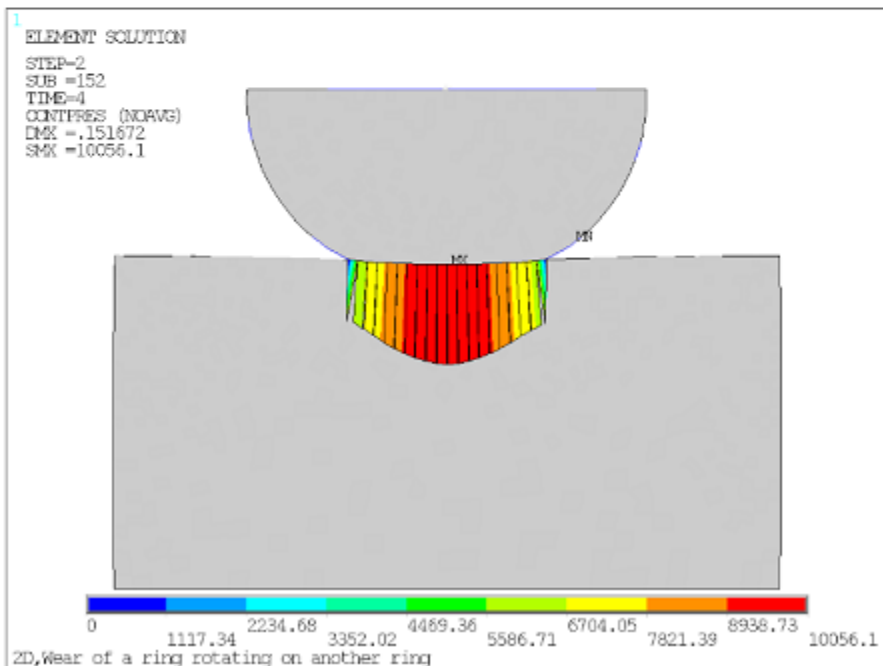
Thus the simulation captures the physical process of wear and results in an increased contact area and more uniform contact pressure; maximum contact pressure goes down with wear and minimum contact pressure goes up with wear. That is, wear makes contact pressure more uniform as shown in the figure below.

**Figure 43.2: Contact Pressure Before and After Wear of Hemispherical Ring (Axisymmetric Contact)**

### Contact pressure before wear



### Contact pressure after wear

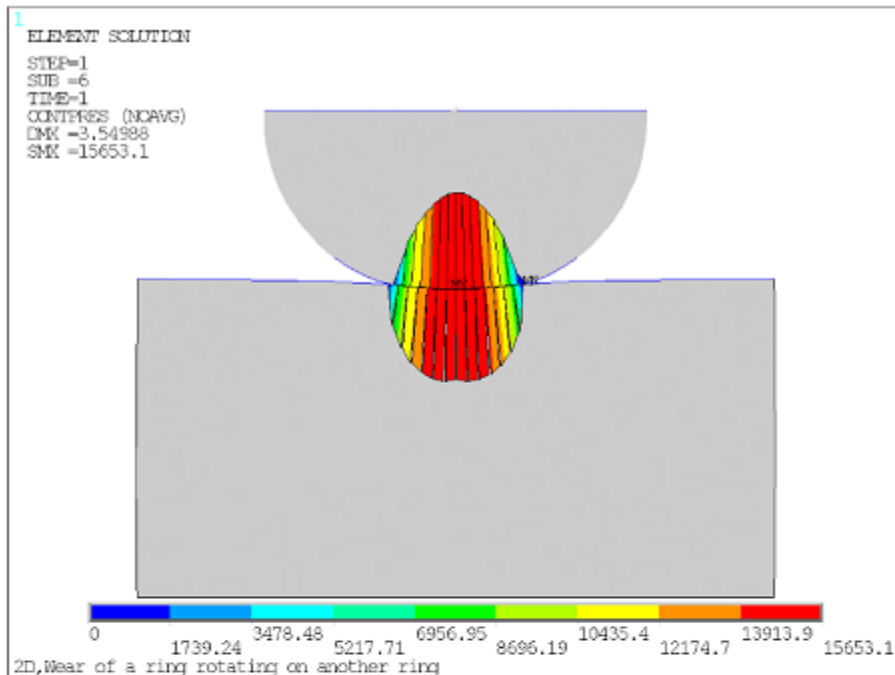


#### Symmetric Contact; Wear on Both Rings

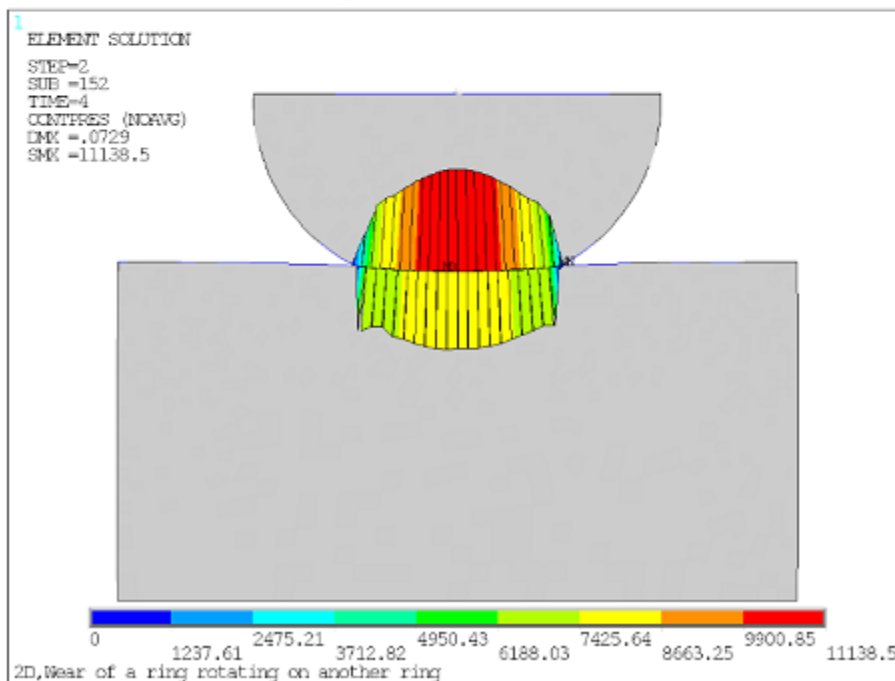
For the symmetric contact example, wear occurs on the top hemispherical ring and on the bottom flat ring. As shown in the figure below, the wear results in similar effects, making contact pressure more uniform on both sides of the contact surfaces and increasing contact area.

**Figure 43.3: Contact Pressure Before and After Wear of Both Rings (Symmetric Contact)**

### Contact pressure before wear



### Contact pressure after wear

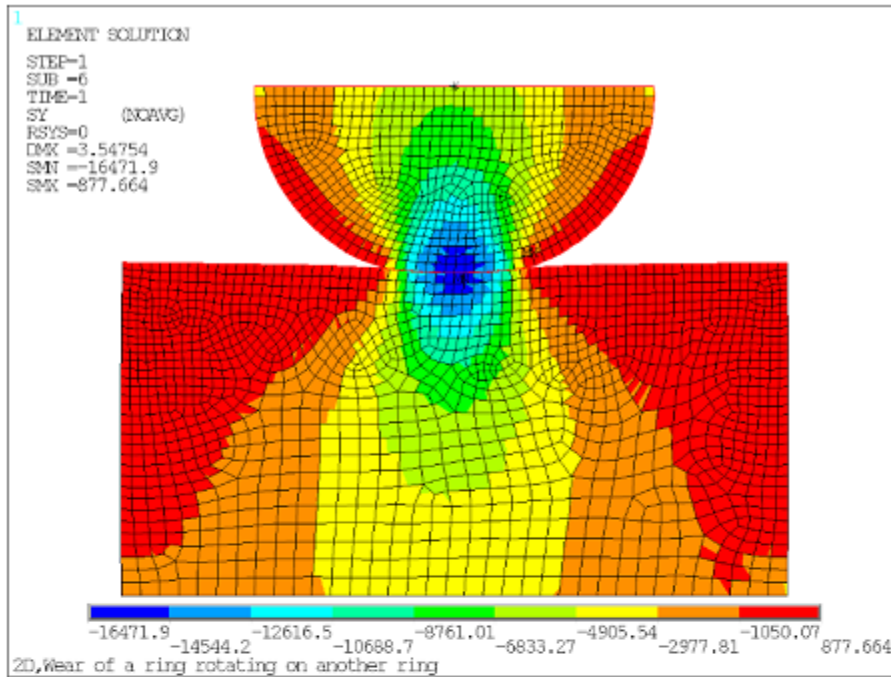


### 43.7.2. Effect of Wear on Stress and Element Quality

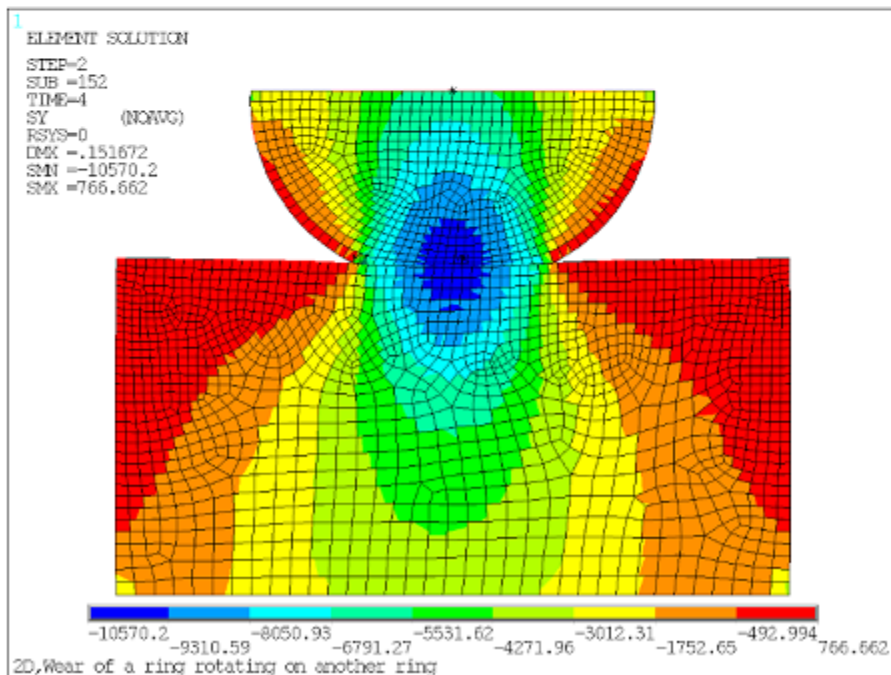
The stress in the loading (Y) direction is affected by wear in a similar way. The maximum stress decreases and the minimum stress increases, while the stress gradient is reduced. This is demonstrated in the plots of stress before and after wear for the asymmetric contact example. The element distortions due to wear at the interface are also evident in the figure.

**Figure 43.4: Stress in the Loading Direction (Y) Before and After Wear of Hemispherical Ring**

### Stress in Y before wear



### Stress in Y after wear

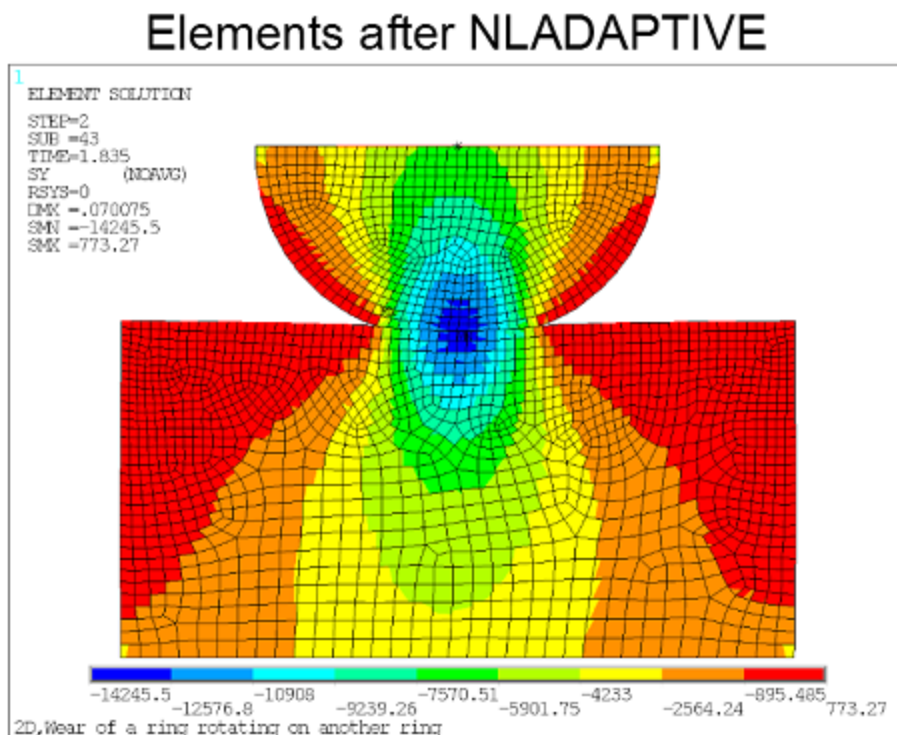
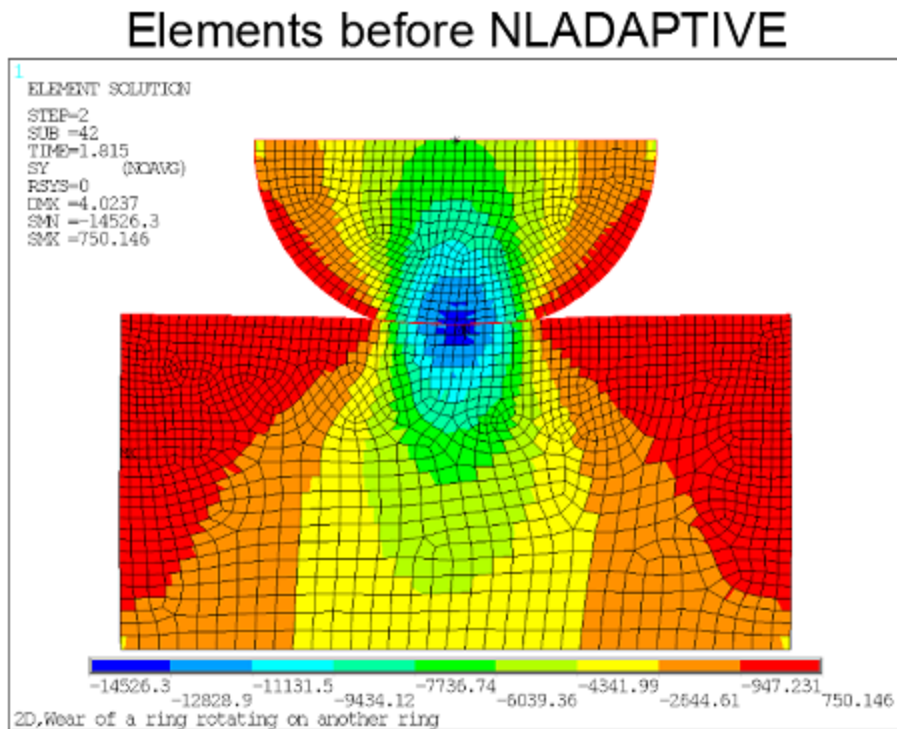


Mesh nonlinear adaptivity improves the mesh quality during wear in this analysis. The specified wear-based criterion is 0.50, which means mesh morphing occurs whenever wear causes the underlying solid element to lose 50% of its height.

The axisymmetric contact example undergoes mesh nonlinear adaptivity four times. The figure below shows the stress in the loading direction and the element quality before and after the first mesh nonlinear adaptivity process.

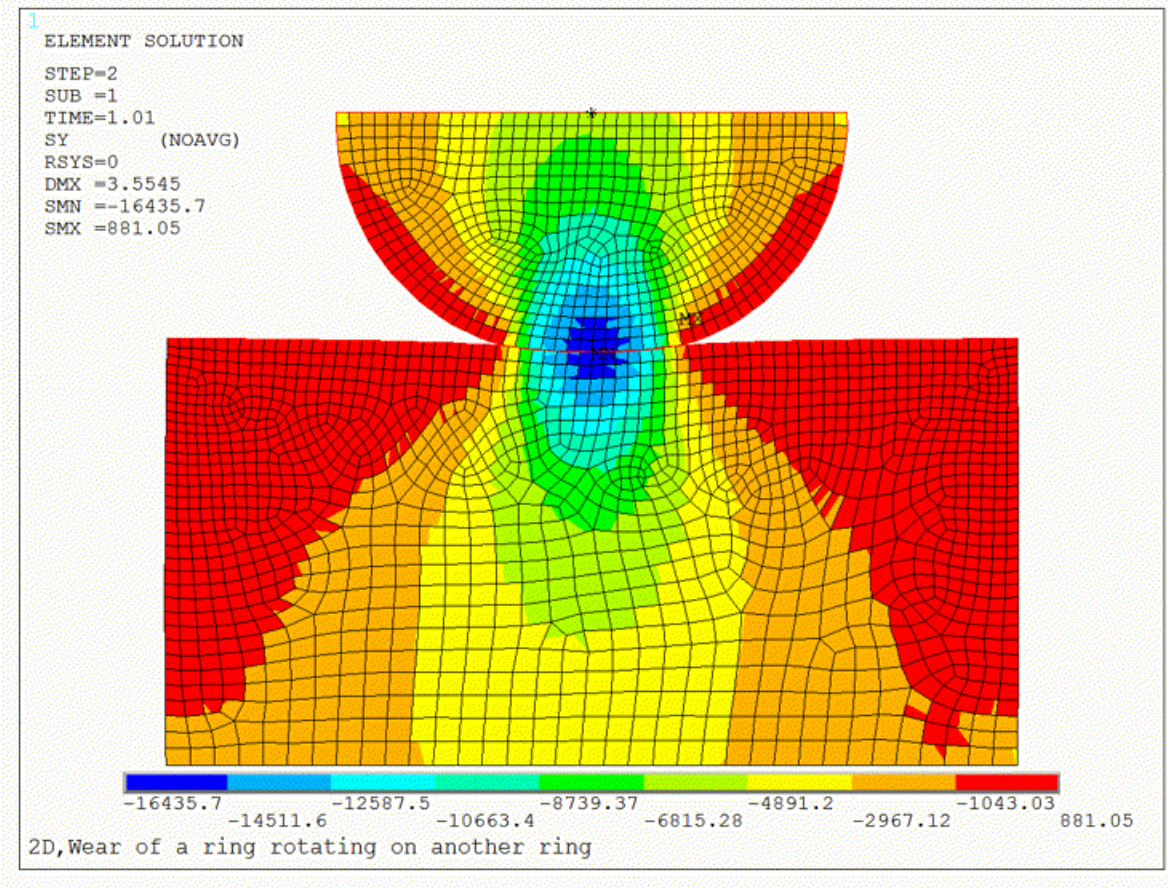


**Figure 43.5: Stress in the Loading Direction (Y) and Element Shapes Before and After Mesh Morphing**

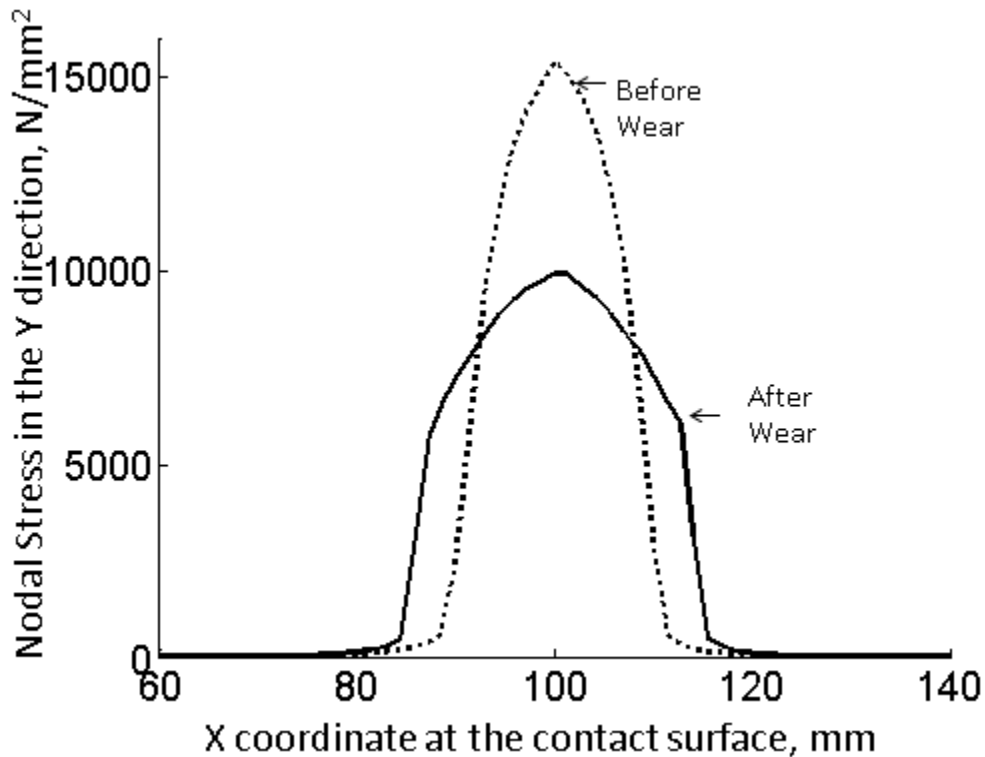


The following animation provides a visualization of the changing stress distribution throughout the second load step, as well as the remeshing of elements due to mesh morphing.

**Figure 43.6: Animation of Stress in the Loading Direction During Load Step 2**

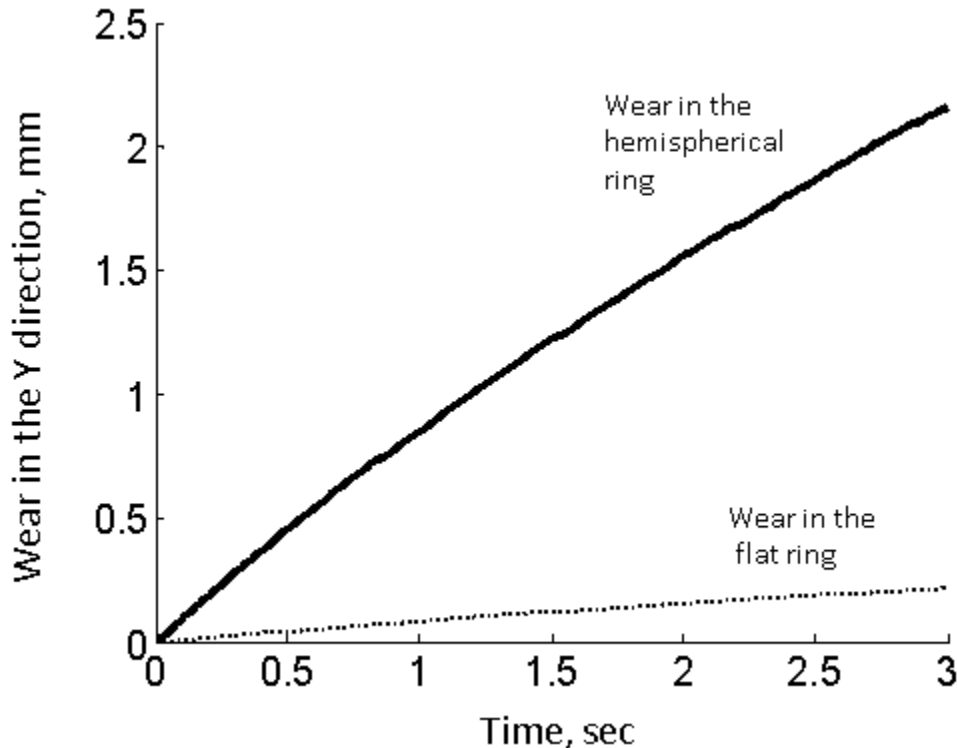


The stress in the loading direction along the contact interface before and after wear is shown in the figure below. Note that the wear makes the stress more uniform.

**Figure 43.7: Stress in the Loading Direction (Y) Along the Contact Interface Before and After Wear**

### 43.7.3. Evolution of Wear with Time

The figure below shows the evolution of wear in the Y direction at the initial point of contact in the symmetric contact example. The wear occurs more in the hemispherical copper ring than the flat steel ring. This is because the wear coefficient of copper is defined as 10 times that of the steel. Furthermore, it can be seen that the rate of wear is continuously decreasing under the constant external load.

**Figure 43.8: Time Evolution of Wear in Y Direction at the Initial Point of Contact**

## 43.8. Recommendations

When performing wear simulations, consider the following recommendations:

- Use one of the following contact algorithms: augmented Lagrangian or penalty function (KEYOPT(2) = 0 or 1). Modeling wear with the pure Lagrangian contact algorithm can result in convergence problems and is not recommended.
- Use very small substeps so that the wear increment is small. A large wear increment can abruptly change the contact status and cause convergence difficulties.
- In general, you should use asymmetric contact to model wear on only one side of the contact interface. However, you can use symmetric contact if wear is desired on both sides of the interface. In this case, define contact elements on both sides of the interface and use the option for the nodal-stress-based wear calculation (C5 of Archard wear model = 1 on **TBDATA**) to achieve better results.
- Simulating a large amount of wear can result in severe mesh distortions. In such cases, use the wear-based nonlinear adaptivity criterion to improve the mesh quality via mesh morphing.

## 43.9. Input Files

The following files are used in this problem:

- RingOnRingWear\_Asym.dat -- Input file using the Archard wear model and asymmetric contact.
- RingOnRingWear\_Asym.cdb -- Database file for the asymmetric contact analysis (called by RingOnRingWear\_Asym.dat).

- 
- `RingOnRingWear_Sym.dat` -- Input file using the Archard wear model with nodal stresses for wear and symmetric contact.
  - `RingOnRingWear_Sym.cdb` -- Database file for the symmetric contact analysis (called by `RingOnRingWear_Sym.dat`).
  - `RingOnRingWear_User.dat` -- Input file demonstrating a user-defined wear model.
  - `RingOnRingWear_User.cdb` -- Database file for the analysis demonstrating a user-defined wear model (called by `RingOnRingWear_User.dat`).
  - `Userwear.F` -- User-defined wear model.

The files are available in the `td-43` folder. See [Obtaining the Input Files \(p. xxxv\)](#) for more information.



---

## Chapter 44: C\*-integral Evaluation for 3-D Surface Flaws

---

This example problem shows how to evaluate the [C\\*-integral](#) for cracks in structural components. C\*-integral characterizes the crack tip conditions in homogenous materials undergoing a secondary (steady-state) creeping deformation.

Analyses of a simple semicircular surface flaw in a rectangular block and a warped flaw along a tubular joint are discussed.

The following features and capabilities are highlighted:

- Evaluating the C\* integral for a semicircular surface flaw in a rectangular block.
- Evaluating the C\* integral for a warped semi-elliptical surface flaw in a tubular joint.
- Meshing around a crack front in 3-D structures.
- Analysis controls for secondary creep deformation dominating the crack tip domain.

Topics related to this example problem follow:

- [44.1. Introduction](#)
- [44.2. Problem Description](#)
- [44.3. Modeling](#)
- [44.4. Material Model and Material Properties](#)
- [44.5. Boundary Conditions and Loading](#)
- [44.6. Analysis and Solution Controls](#)
- [44.7. Results and Discussion](#)
- [44.8. Recommendations](#)
- [44.9. References](#)
- [44.10. Input Files](#)

For more information, see [C\\*-integral Calculation in the Mechanical APDL Fracture Analysis Guide](#).

### 44.1. Introduction

Structural components operating at high temperatures may fail due to the slow extension of a pre-existing crack in the structure over a period of time. For an elastic-secondary power law creeping material model, the stress and strain singularities at the crack tip can be controlled by a time-dependent loading parameter.[1] For long-term loading, the C\*-integral parameter can be path-independent and applies to cracks only when the body with the crack undergoes extensive steady-state creep.

### 44.2. Problem Description

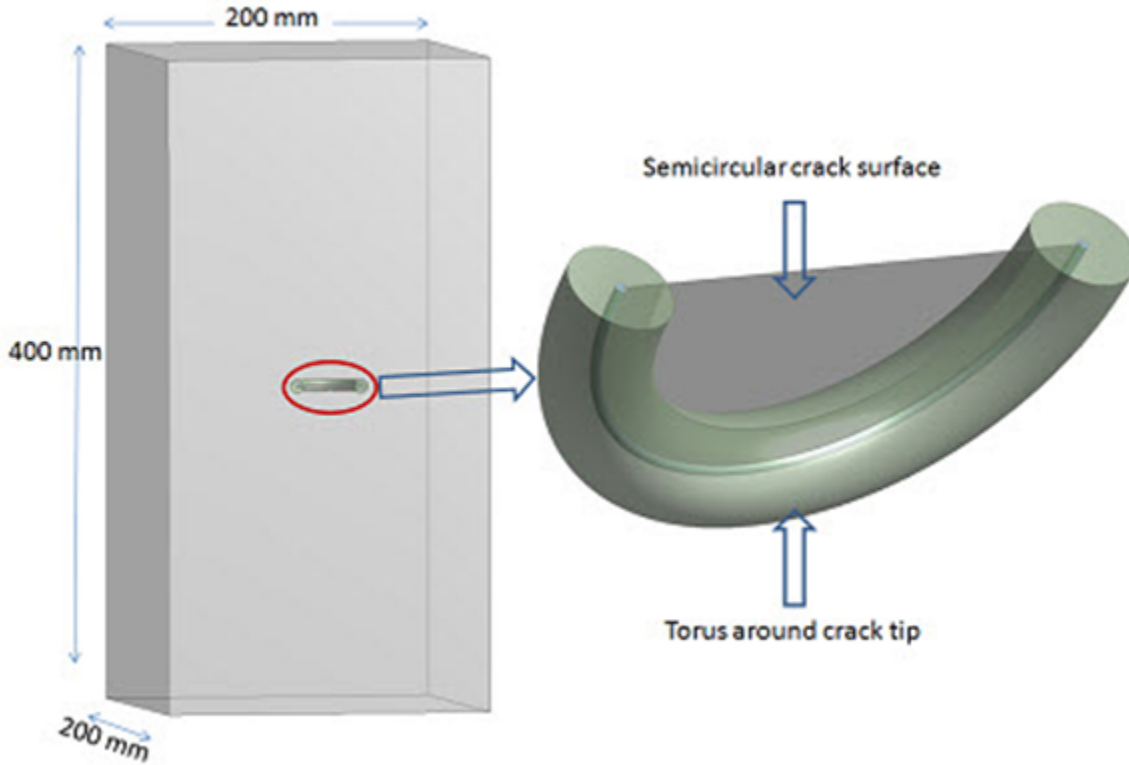
Two models with surface flaws are considered for analysis:

- [44.2.1. Rectangular Block with a Semicircular Surface Flaw](#)
- [44.2.2. X-Joint Pipe with Warped Surface Flaw](#)

### 44.2.1. Rectangular Block with a Semicircular Surface Flaw

This model is fixed at one face of the block. A pressure load is applied on the opposite face. The block has a semicircular surface flaw with a 20 mm radius at the center of one longitudinal face in the thickness direction; the crack is perpendicular to one of the surfaces of the rectangular block.

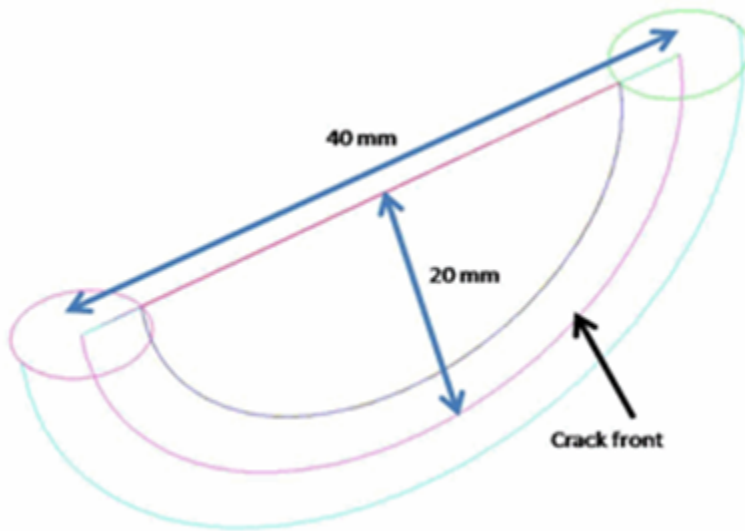
**Figure 44.1: Rectangular Block Geometry with Semicircular Surface Flaw**



A torus is created around the crack front to control the mesh at the crack front. Following is the semi-circular crack and torus along the crack front used to create a sweep mesh with the [SOLID186](#) 3-D 20-node structural solid (brick) element:



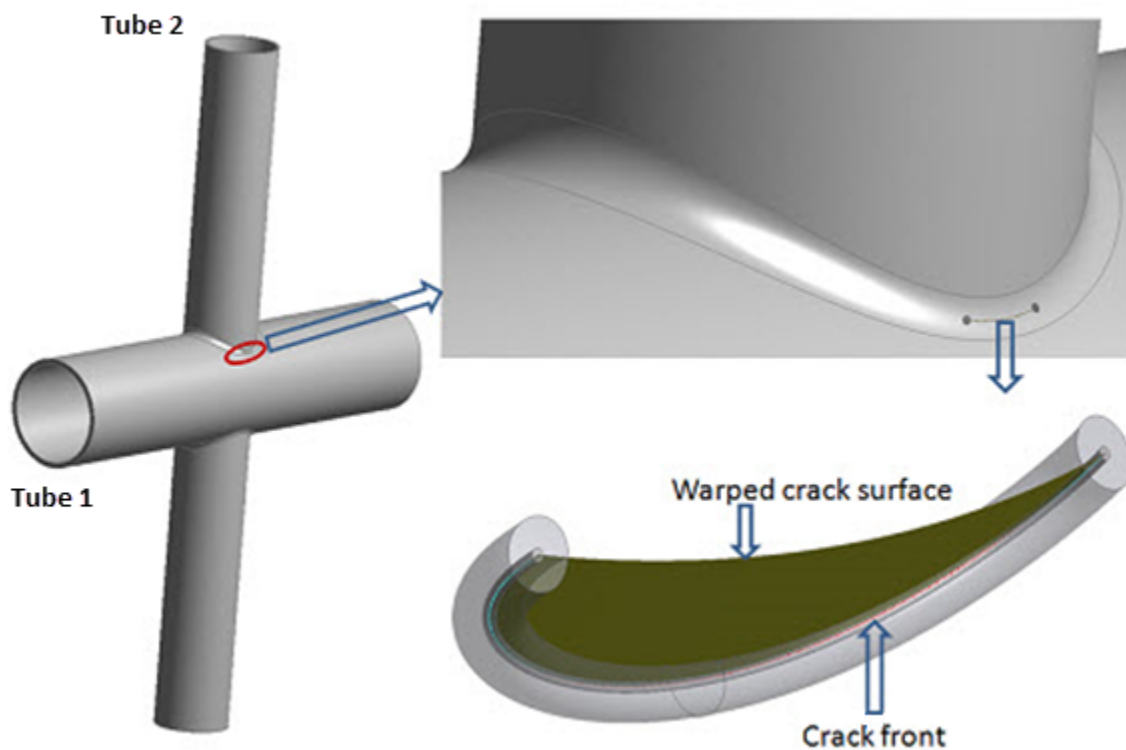
**Figure 44.2: Semicircular Crack and Torus Along the Crack Front**



### 44.2.2. X-Joint Pipe with Warped Surface Flaw

A semi-elliptical warped surface flaw at the tubular joint is analyzed to obtain the  $C^*$ -integral along the crack front:

**Figure 44.3: X-Joint Pipe Full Model with Warped Surface Flaw at Welded Joint**

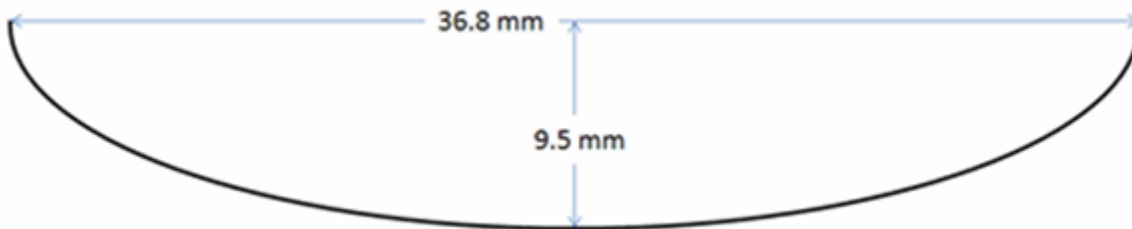


The problem consists of two tubular members attached to each other by a welded joint. The tubular members (labeled Tube 1 and Tube 2) have outer diameters of 323.85 mm ( $D_1$ ) and 219.08 mm ( $D_2$ ),

and thicknesses of 15.88 mm ( $t_1$ ) and 8.18 mm ( $t_2$ ), respectively. The semi-elliptical surface crack lies on a plane parallel to the radial direction of the heavier running pipe.

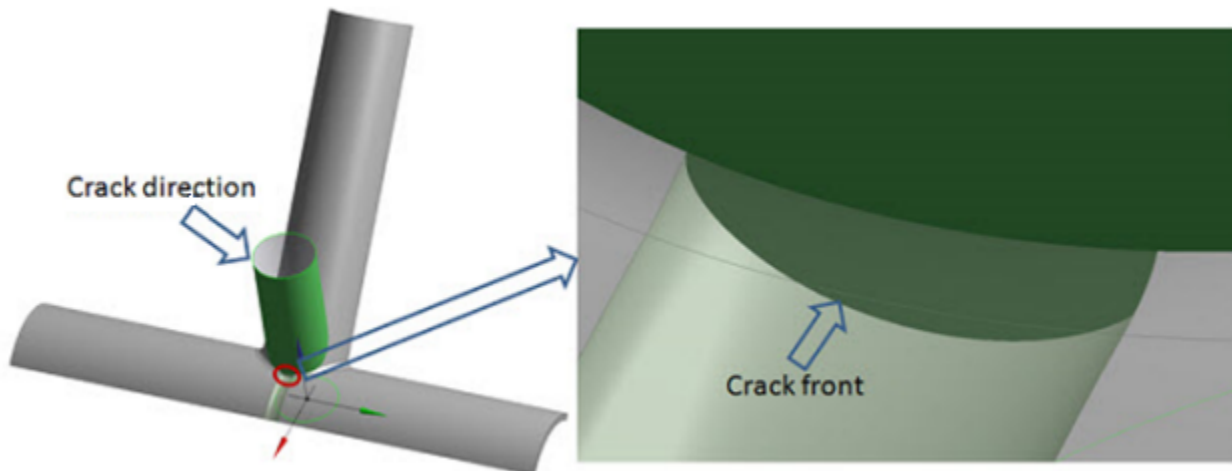
A torus is created around the crack front to control the mesh at the crack front. The semi-elliptical surface crack at the weld toe is warped along the welded joint and it is perpendicular to the outer surface of the 323.85 mm diameter pipe in the thickness direction.

**Figure 44.4: Semi-elliptical Surface Crack Dimensions**



The warped crack profile at the welded joint is created via the interaction of a rotated semi-ellipse on the 323.85 mm diameter pipe and an extruded circle normal to the inner surface of the same pipe at the welded joint:

**Figure 44.5: Two-plane Symmetry of X-joint Pipe with Warped Surface Flaw Geometry**

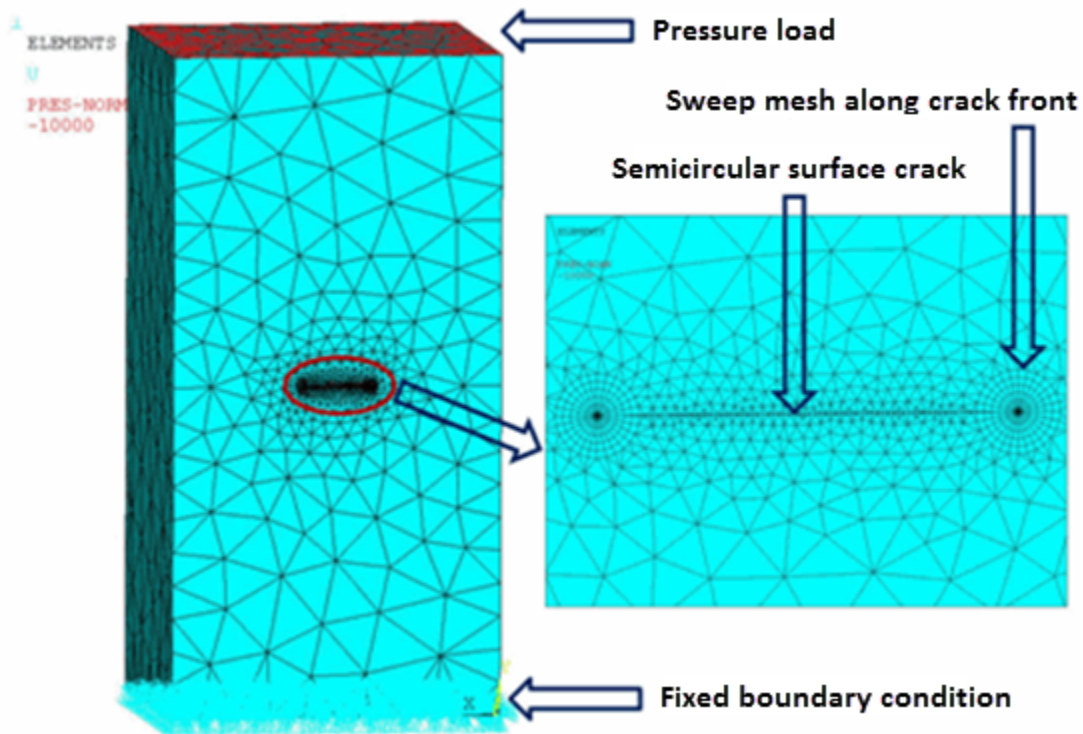


### 44.3. Modeling

For 3-D models, the recommended element type near the crack front is **SOLID186**, the 3-D 20-node structural solid (brick).

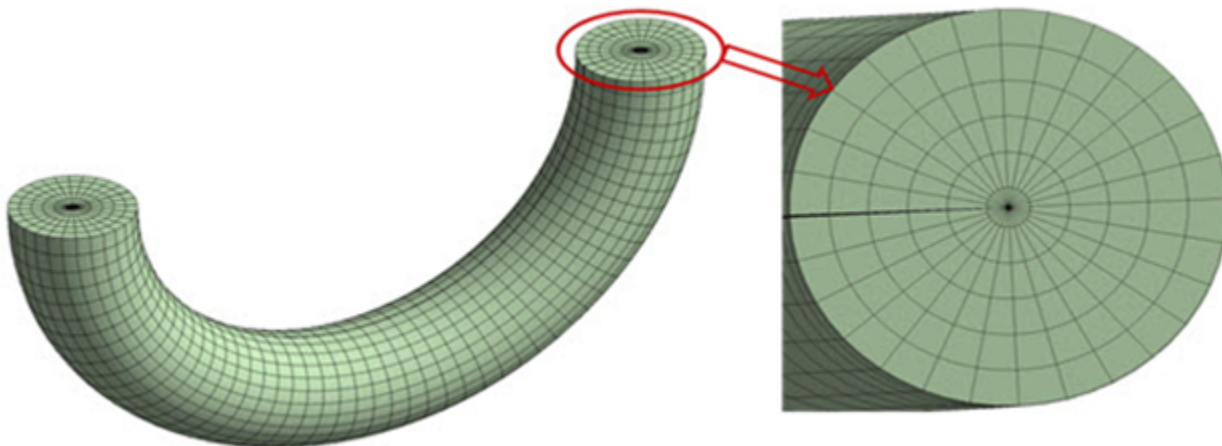
The rectangular block and x-joint pipe models are meshed with **SOLID187** 3-D 10-node tetrahedral structural solid elements (except for the regions around the crack tip).

**Figure 44.6: Rectangular Block Model with Boundary Conditions and Loading Applied**



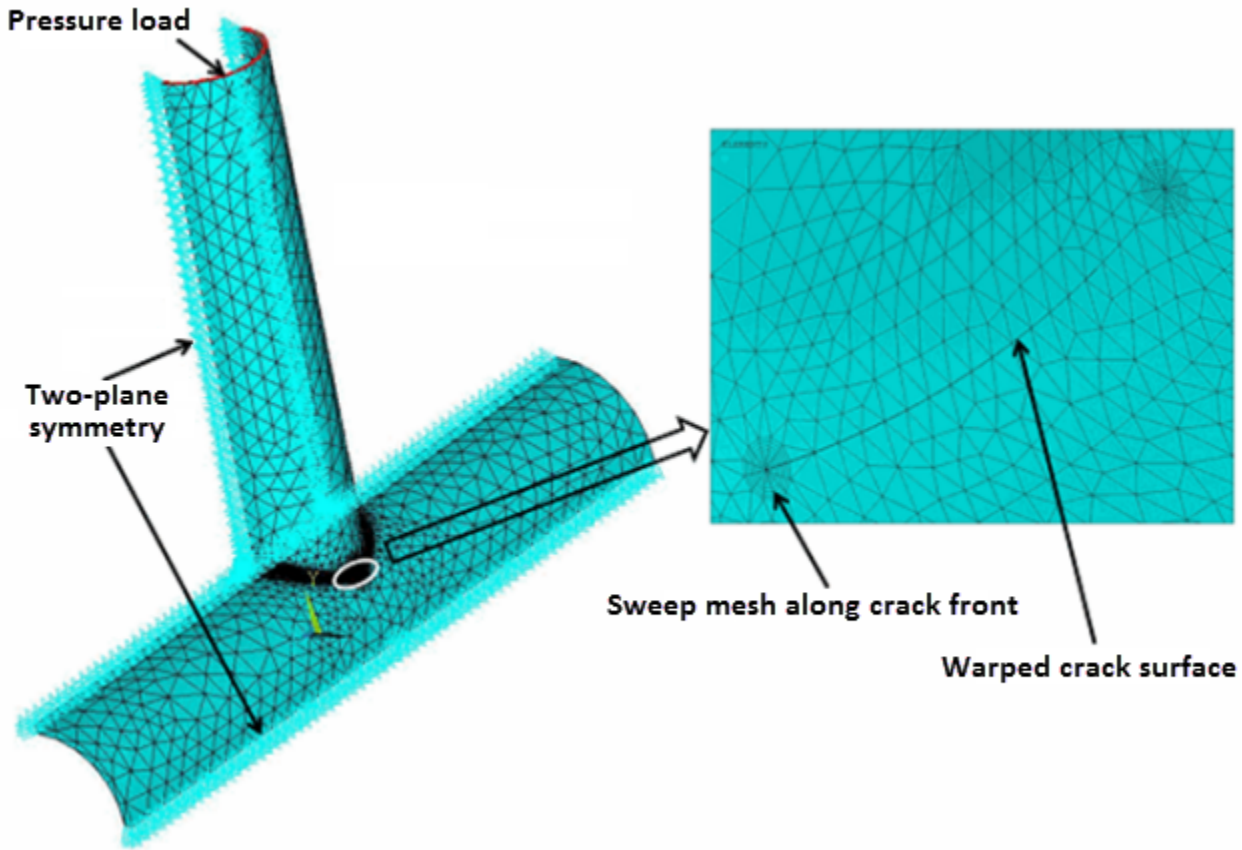
Regions around the crack tips are meshed with **SOLID186**:

**Figure 44.7: Sweep Mesh with **SOLID186** Around Crack Front**



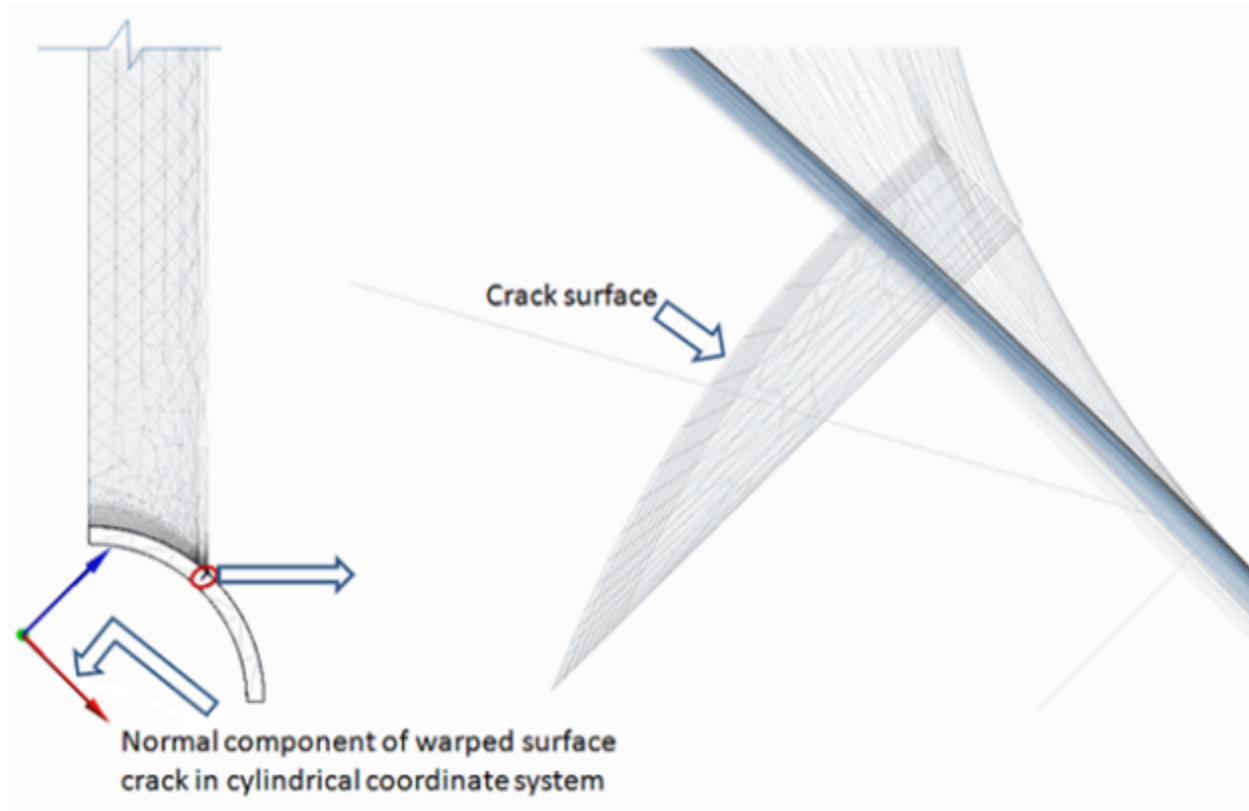
Because of the two-plane symmetry inherent to the X-joint problem, a quarter model is considered for analysis:

**Figure 44.8: Two-plane Symmetry of X-joint Pipe with Warped Surface Flaw at Welded Joint**



If the crack surface is not normal to any component in the global coordinate system, a local coordinate system should be created in such a way that one component of the coordinate system is perpendicular to the crack surface. For example, in the X-joint model, a local cylindrical coordinate system is created such that one of its components is normal to the crack surface:

**Figure 44.9: X-joint Pipe with Warped Surface Flaw at Welded Joint in Thickness Direction**

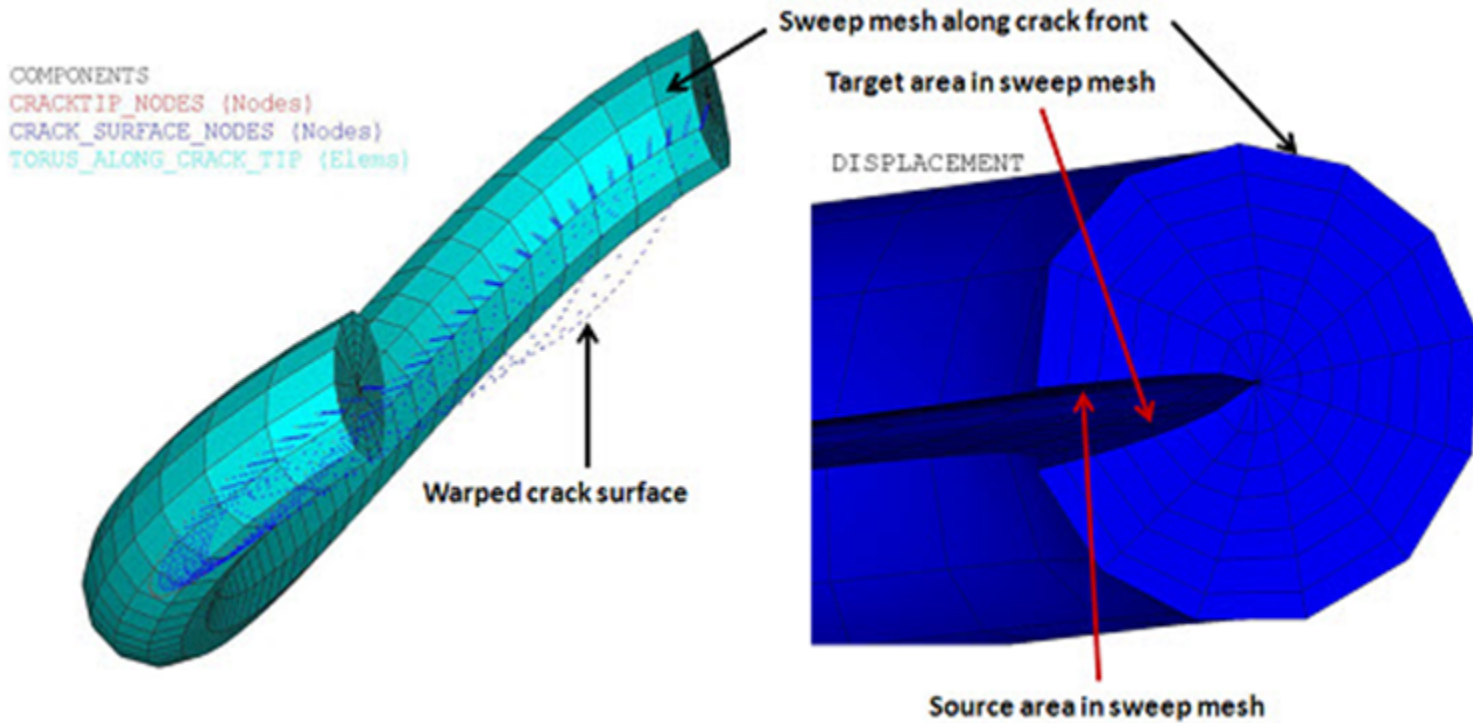


In the X-joint model, the warped crack in the thickness direction is perpendicular to the inner surface of the 323.85 mm diameter pipe.

A torus is created around the crack front to obtain a good sweep mesh (**VSWEEP**). A common area separates the torus and the remaining volume at the interface.

In 3-D models, a fracture has two surfaces with a common edge at the crack front; the same is true for the torus. The two torus surfaces are used to create a clean sweep mesh around the crack front. One surface is defined as the source, the other as the target. In this procedure, the sweep mesh generates brick elements with one layer of prism elements around the crack front. Following is the sweep mesh with **SOLID186** around the crack front in the x-joint pipe model, with the source and target areas for the sweep mesh indicated in the deformed body:

**Figure 44.10: Sweep Mesh with SOLID186 Around the Crack Front**



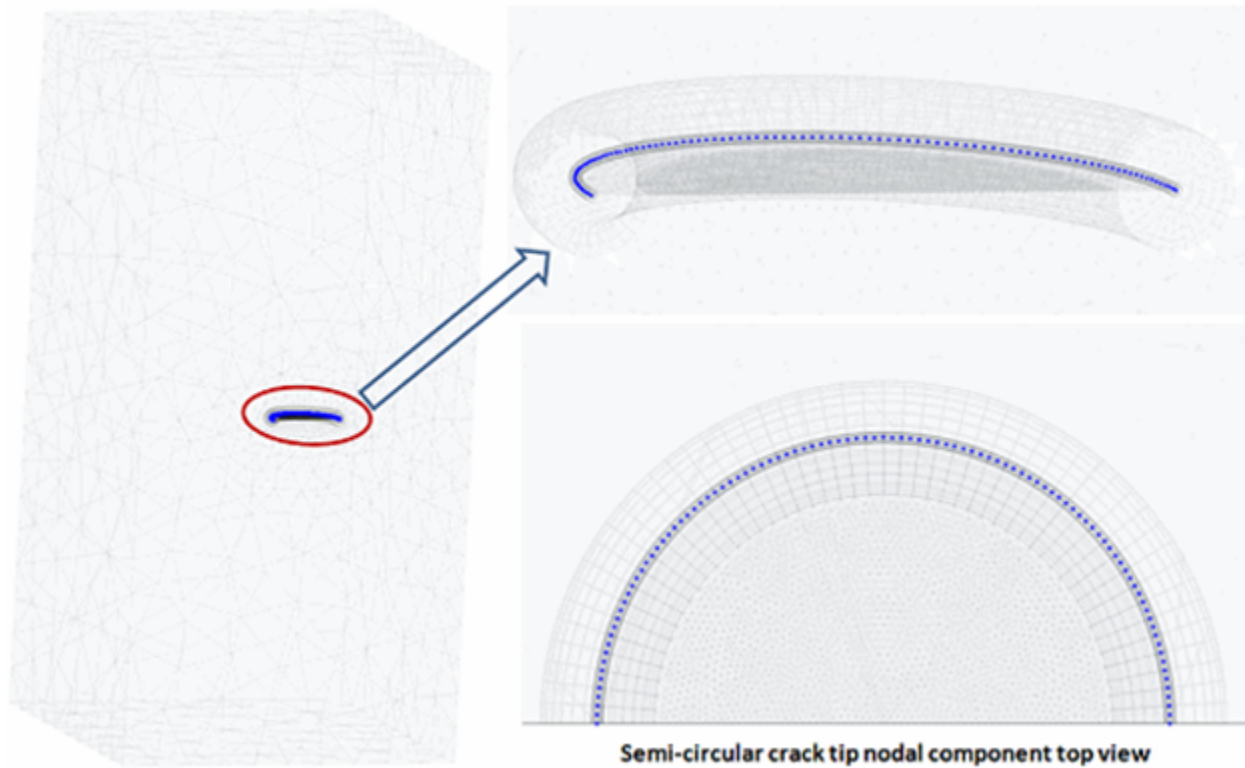
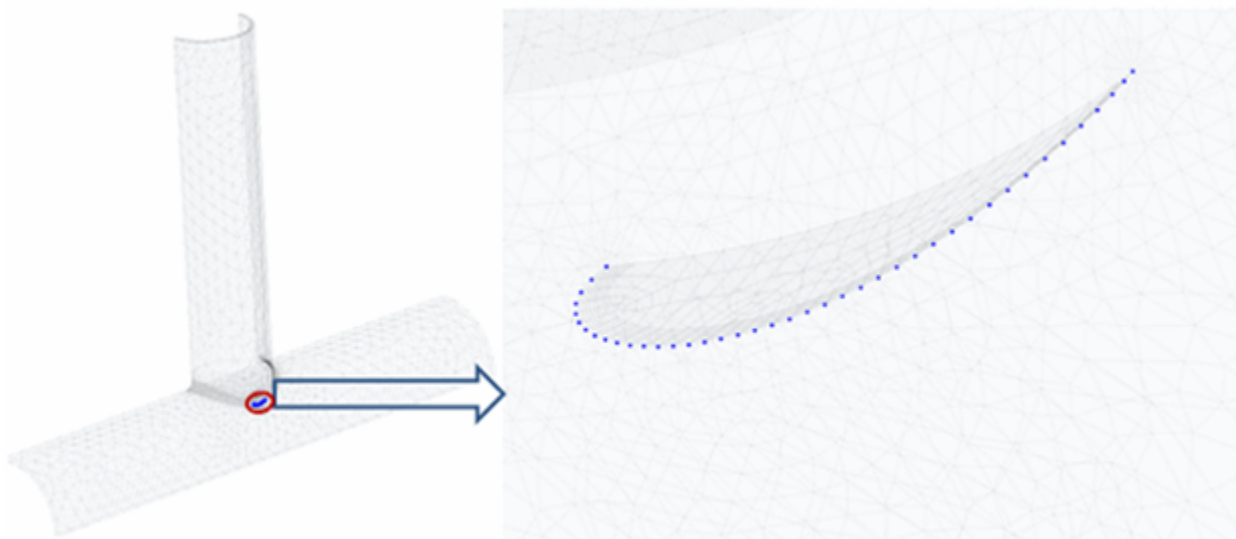
The warped surface contains a sweep mesh and a set of nodes, along with source and target areas in the deformed torus body. The source and target areas existed at the same location in the non-deformed structure.

The crack parameters are defined after meshing:

**Example 44.1: Defining Parameters Associated with Contour Integral Calculation**

```
! Initiate a new contour integral calculation and define type
CINT, NEW, 1           ! Initiate new calculation and assign ID
CINT,TYPE,CSTAR       ! Define calculation of C*-integral
```

A line component of the crack front lines (**CM**) is created. The component is useful for selecting nodes attached to the crack front (**NSLL**). The nodal component of those nodes is used to define crack tip node components (**CINT,CTNC**), as shown in the following figures:

**Figure 44.11: Crack Tip Nodal Component: Rectangular Block Model****Figure 44.12: Crack Tip Nodal Component: X-joint Pipe Model**

## 44.4. Material Model and Material Properties

The specimen is simulated with the strain hardening creep material model. Material constants are selected to ensure that steady-state behavior dominates:

```
C*** PARAMETRIC INPUT FOR CREEP CONSTANTS ! (SECONDARY CREEP)***
*SET,C1,5.E-12
*SET,C2,3
*SET,C3,0
```

```
*SET,C4,0
TB, CREEP,1,,,1
TBDATA,1,C1,C2,C3,C4
```

Material Constants for Creep Material Model	
Young's Modulus (MPa)	200E3
Poisson's Ratio	0.3
C1	5E-12
C2	3
C3	0
C4	0

### 44.5. Boundary Conditions and Loading

The rectangular block is fixed at one face. A pressure of -2E+2 MPa is applied on the other face, as shown in [Figure 44.6: Rectangular Block Model with Boundary Conditions and Loading Applied \(p. 669\)](#).

Analysis of the X-joint model is performed with two-sided symmetry. Two-plane symmetric boundary conditions are applied and one midside node at the horizontal plane is constrained in the opposite direction to restrict rigid-body motion. A pressure load of -10 MPa is applied on the top of the small-diameter tube, as shown in [Figure 44.8: Two-plane Symmetry of X-joint Pipe with Warped Surface Flaw at Welded Joint \(p. 670\)](#).

### 44.6. Analysis and Solution Controls

Because C\*-integral calculation is based on creep materials, a nonlinear static analysis is performed. For a C\*-integral calculation, it is necessary to perform both of the following tasks at each crack tip:

- 44.6.1. Nonlinear Static Analysis
- 44.6.2. C\*-integral Calculation (CINT)

#### 44.6.1. Nonlinear Static Analysis

A nonlinear static analysis is performed. The load is applied instantaneously and then held constant until steady-state creep conditions are reached. Typically, a response of 500~2000 hours is sufficient to reach a steady-state condition.

#### Example 44.2: Applying a Load in 1E-7 Hours for Elastic Response

```
NSUB,2,5,2,OFF
TIME,1.E-007
RATE,OFF
NLGEOM,ON
SOLVE

!ENABLE CREEP RELAXATION AND WAIT FOR STEADY-STATE

*SET,HOUR,2000
AUTOTS,ON
NSUB,50,100,10
TIME,HOUR
OUTRES,ERASE
OUTRES,ALL,ALL
RATE,ON
NLGEOM,ON

SOLVE
```



## 44.6.2. C\*-integral Calculation (CINT)

To obtain the C\*-integral value, a crack tip and its parameters must be defined.

### Example 44.3: Defining Parameters for C\*-integral Calculation

```
! INITIATE A NEW CONTOUR INTEGRAL, AND DEFINE TYPE AS CSTAR
CINT,NEW,4
CINT,TYPE,CSTAR
!
! DEFINE CRACK TIP NODAL COMPONENT
CINT,CTNC,cmCrackTipNodes,,1
!
! DEFINE SYMMETRY DETAILS AND NUMBER OF CONTOURS TO BE CALCULATED
CINT,NCON,4
CINT,SYMM,ON
```

## 44.7. Results and Discussion

This section discusses the results for both models used in this problem:

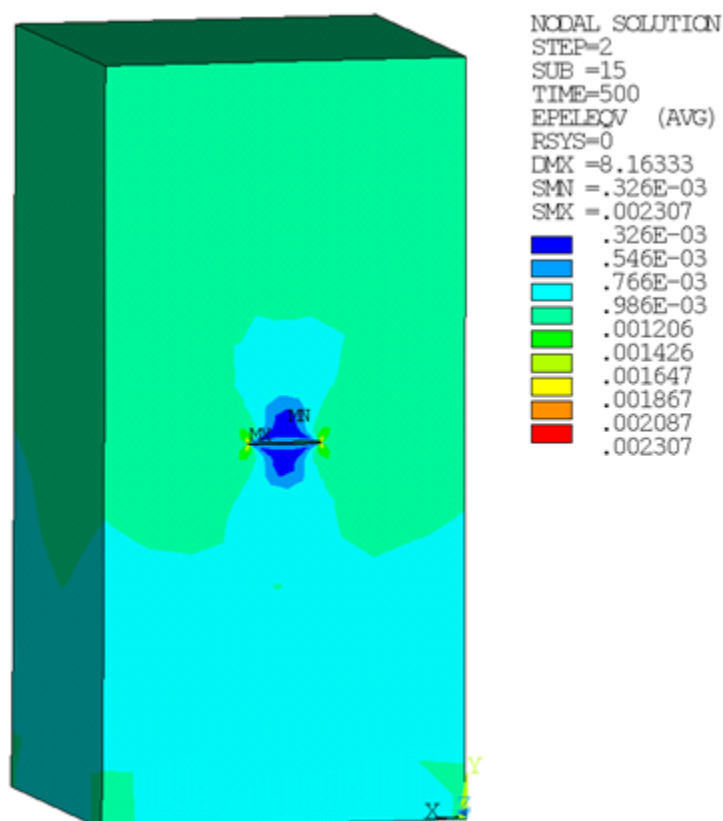
44.7.1. Rectangular Block with Semicircular Surface Flaw

44.7.2. X-joint Pipe with Warped Flaw

### 44.7.1. Rectangular Block with Semicircular Surface Flaw

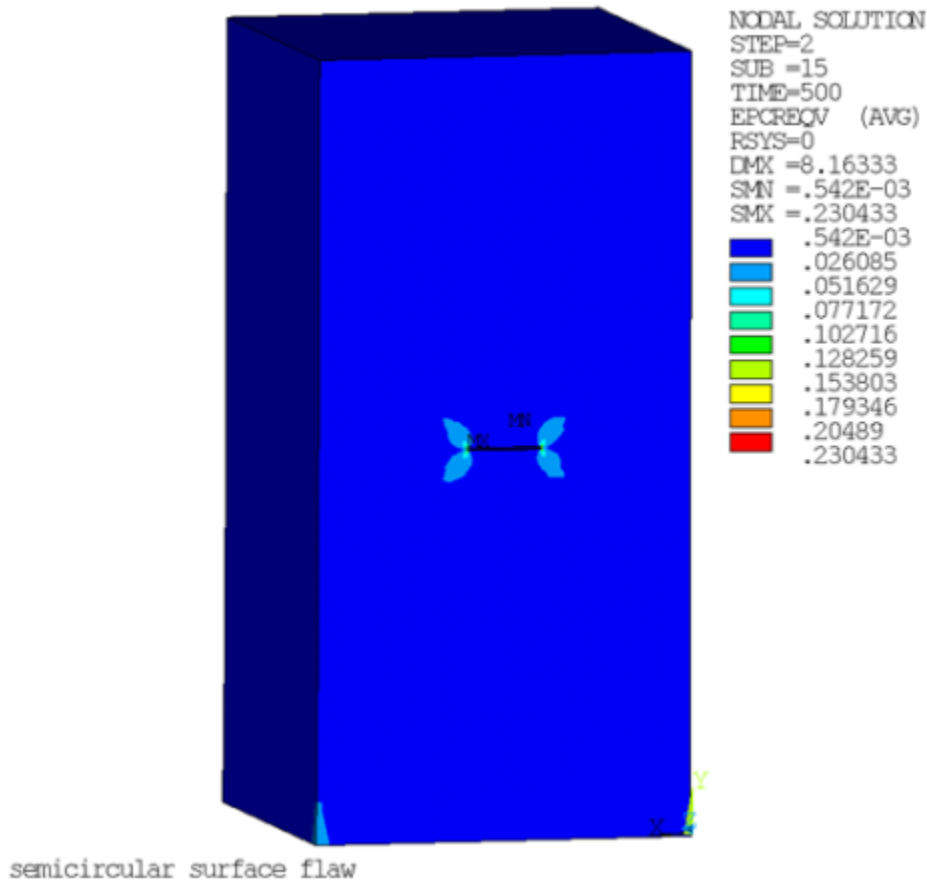
The following figures show the equivalent elastic strain and equivalent creep strain:

**Figure 44.13: Equivalent Elastic Strain -- Rectangular Block**



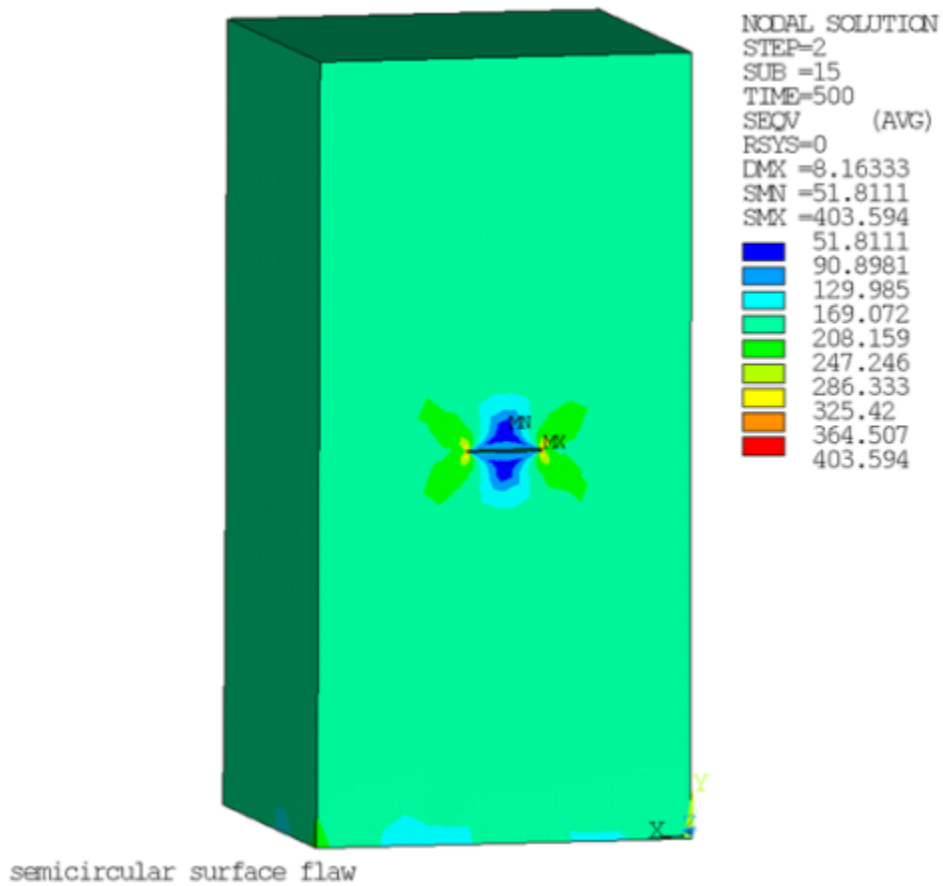
semicircular surface flaw

**Figure 44.14: Equivalent Creep Strain -- Rectangular Block**



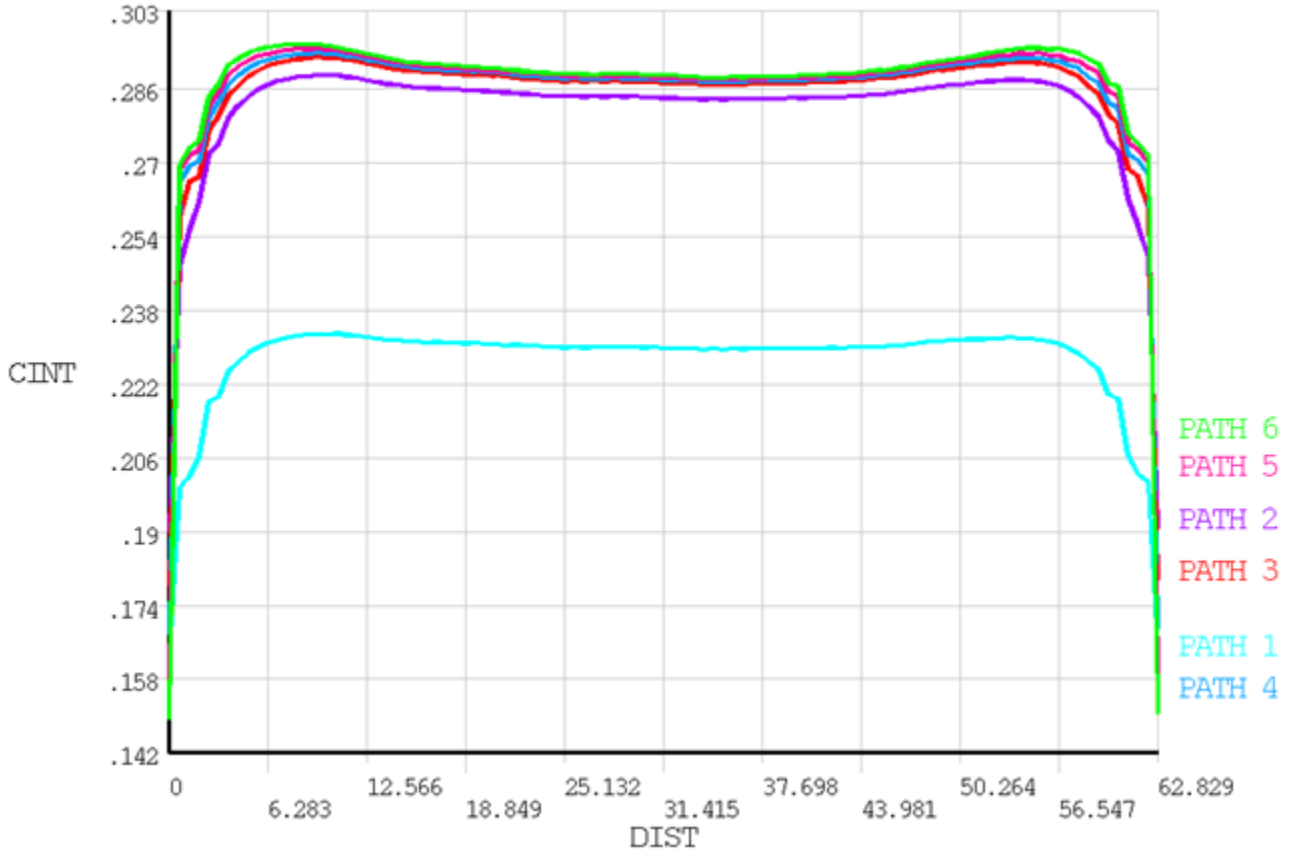
The creep strain is approximately 100 times larger than the elastic strain in the secondary creep stage, which dominates the entire specimen at the end of the simulation.

Following is the maximum Von Mises stress occurring at the crack tip:

**Figure 44.15: Von Mises Stress -- Rectangular Block**

The following figure shows the  $C^*$ -integral along the crack front for different contours, where the path-independence appears after path 3:

**Figure 44.16: C\*-integral Along the Crack Front -- Rectangular Block**



### 44.7.2. X-joint Pipe with Warped Flaw

The following figures show the equivalent elastic strain, equivalent creep strain, and von Mises stress of the X-joint pipe with the warped flaw at the welded joint:

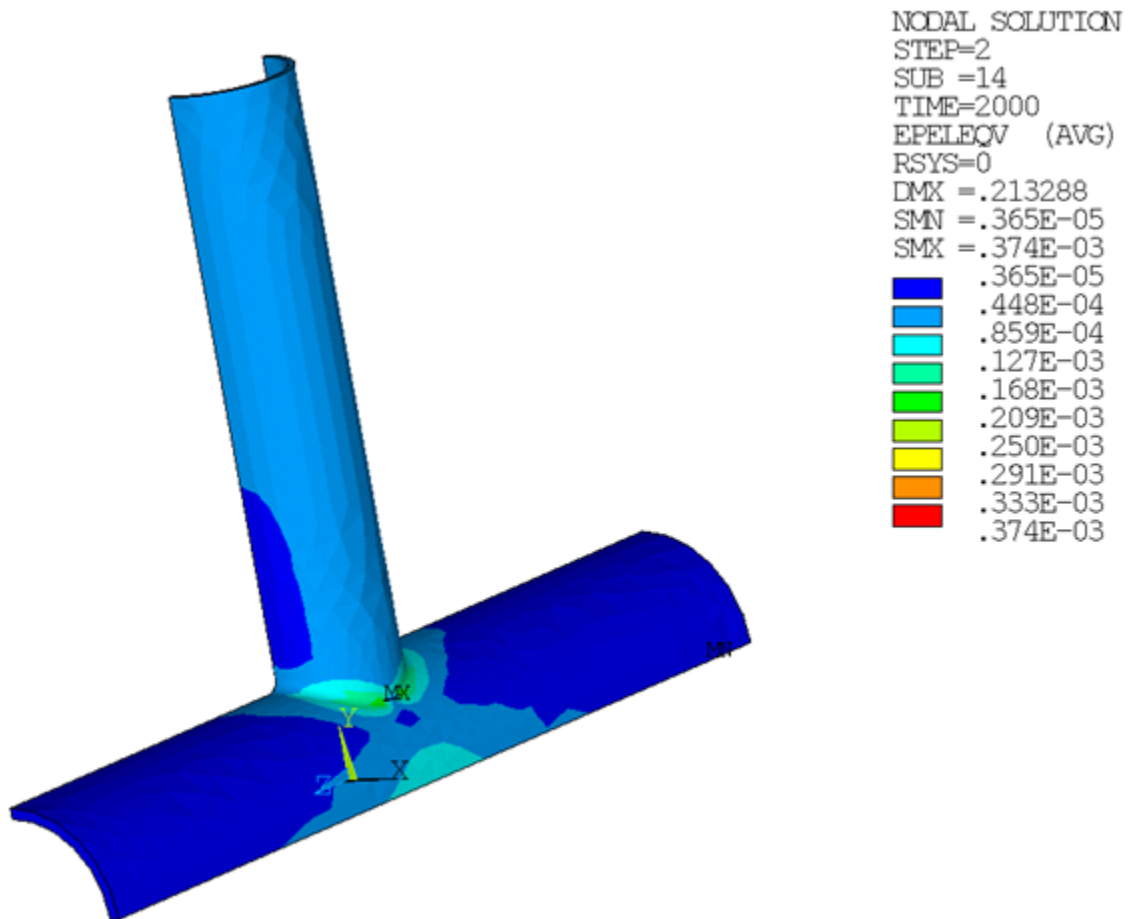
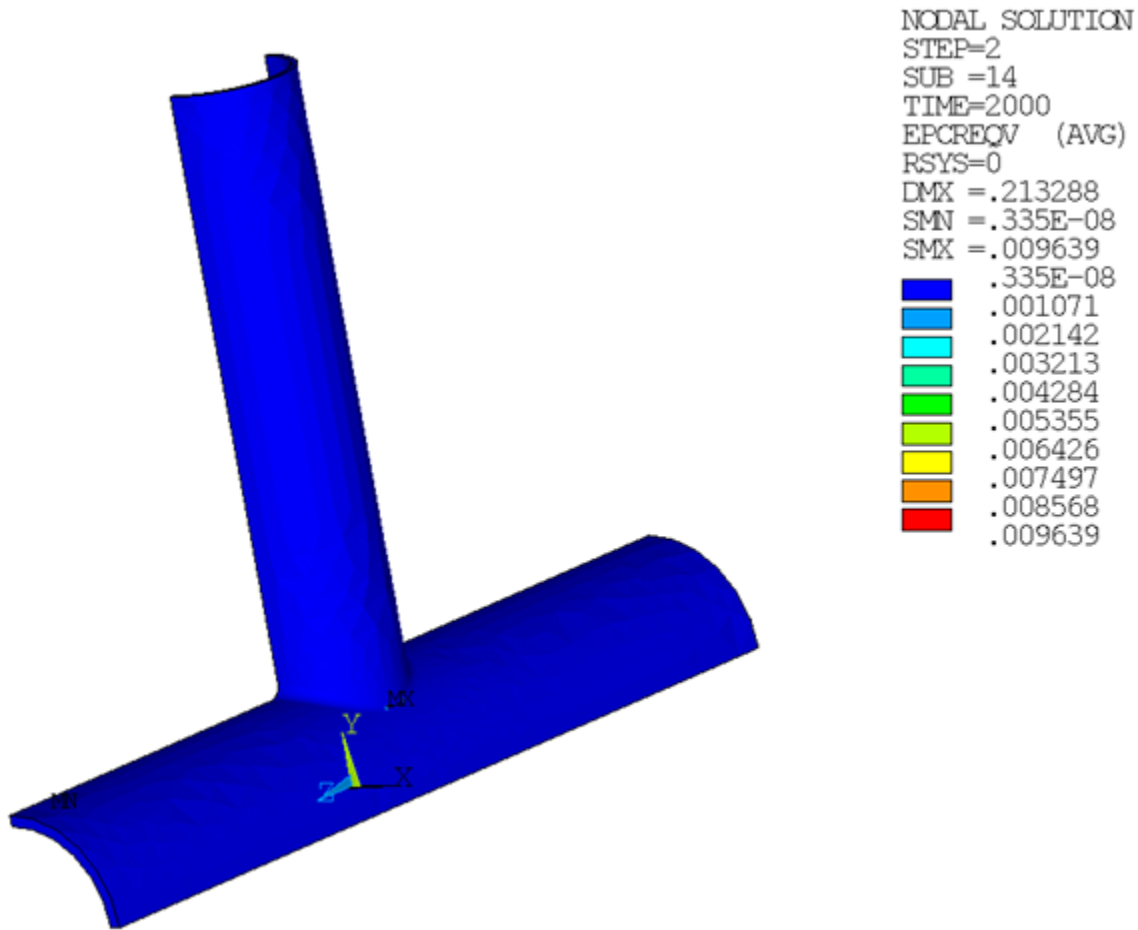
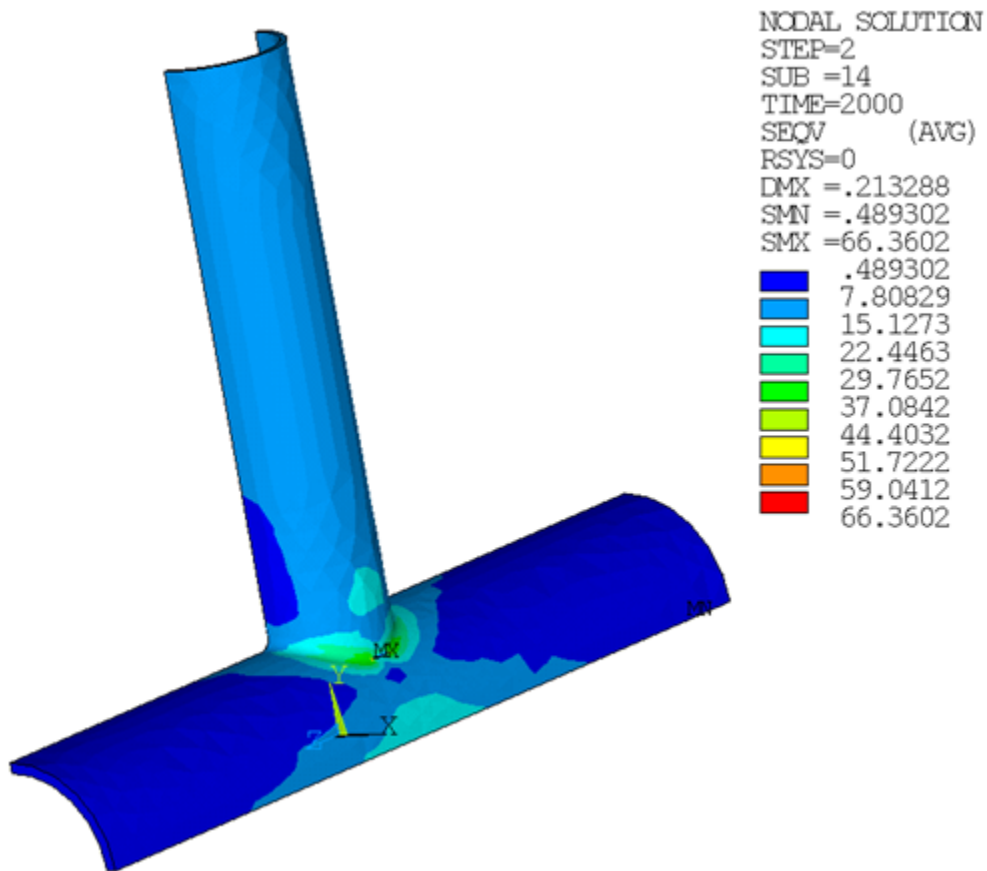
**Figure 44.17: Equivalent Elastic Strain -- X-joint Pipe**

Figure 44.18: Equivalent Creep Strain -- X-joint Pipe

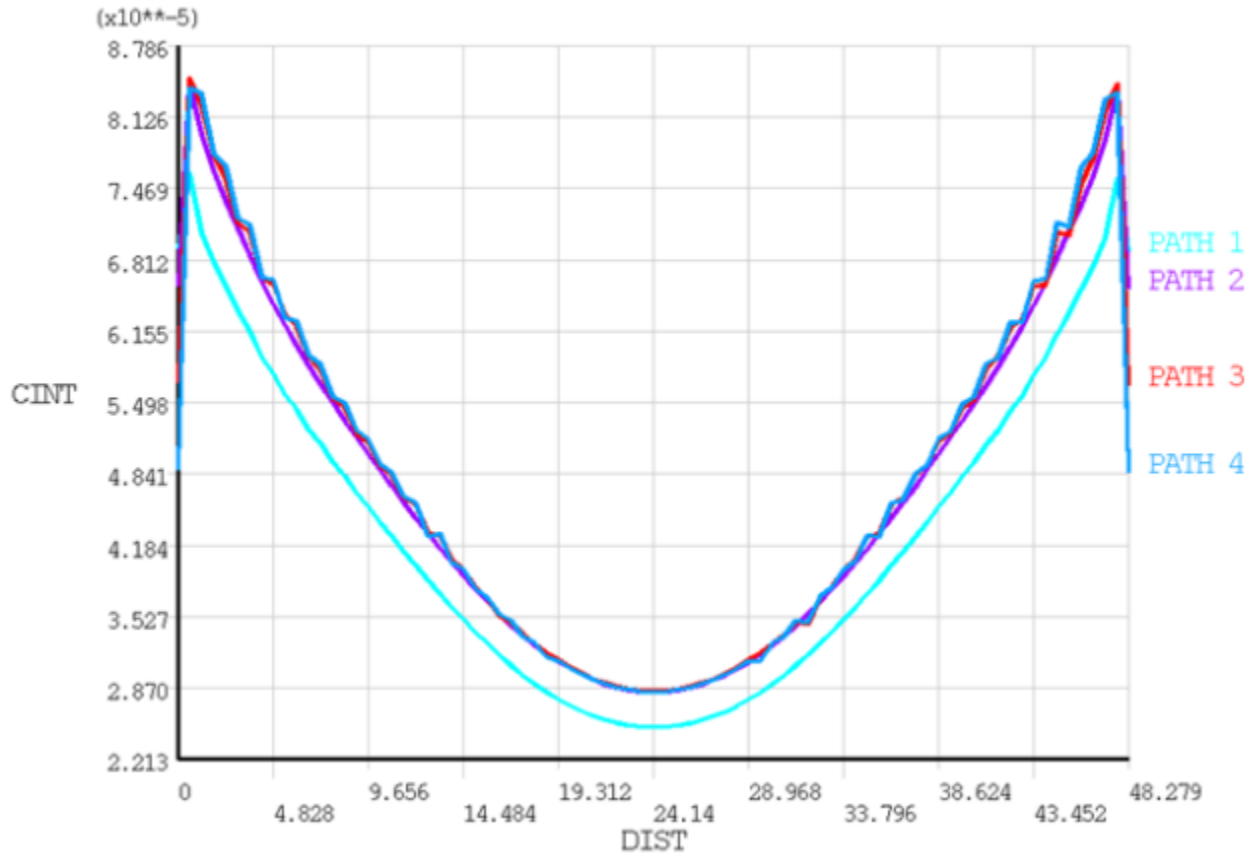


**Figure 44.19: Von Mises Stress -- X-joint Pipe**



The creep strain is approximately 30 times larger than the elastic strain in the secondary creep stage, which dominates the local region of specimen at the end of the simulation.

The following shows the C\*-integral values along the crack front, which gradually becomes path-independent after path 2.

**Figure 44.20: C\*-integral Along the Crack Front -- X-Joint Pipe with Warped Flaw**

## 44.8. Recommendations

When setting up a C\*-integral calculation, consider the following hints and recommendations:

- The recommended element type for 3-D fracture models along the crack tip is the 3-D 20-node structural solid (brick) element **SOLID186**.
- A fine sweep mesh along the crack front yields more accurate results.
- When contour results begin with the first ring of elements around crack tip nodes (PATH 1 in Figure 44.16: C\*-integral Along the Crack Front -- Rectangular Block (p. 678) and Figure 44.20: C\*-integral Along the Crack Front -- X-Joint Pipe with Warped Flaw (p. 682)), the first contour result is discarded. In such cases, experience has shown that the first contour it is less accurate than other contours due to highly concentrated local deformation.
- The C\*-integral could be path-independent only when steady-state creep deformation dominates the integration domain around the crack tip.

## 44.9. References

The following references are used in this example problem:

1. Goldman, H.L., J.W. Hutchinson. "Fully Plastic Crack Problems: The Center-Cracked Strip Under Plane Strain." *International Journal of Solids and Structures*. 11 (1975): 575-591.



2. Riedel, H. "Creep Deformation at Crack Tips in Elastic-viscoplastic Solids." *Journal of the Mechanics and Physics of Solids*. 29 (1981): 35-49.
3. Riedel, H., J. R. Rice. "Tensile Cracks In Creeping Solids." *Fracture Mechanics: Twelfth Conference*. ASTM STP 700 (1980): 112-130.
4. Kumar, V., M. D. German, C. F. Shih. "An Engineering Approach For Elastic-plastic Fracture Analysis." Report NP-1931, 1981.
5. Kanninen, M. F., C. H. Popelar. *Advanced Fracture Mechanics*. New York: Oxford University Press, 1985.

## 44.10. Input Files

The following files are used in this problem:

- `semicircular_surface_flaw_model.dat` -- Input file for the analysis of the semicircular surface flaw in the rectangular plate.
- `xjoint_pipe_with_warped_flaw.dat` -- Input file for the fracture analysis of the x-joint model.
- `xjoint_pipe_with_warped_flaw.cdb` -- Common database file for the x-joint finite-element model (called by `xjoint_pipe_with_warped_flaw.dat`).

The files are available in the `td-44` folder. See [Obtaining the Input Files \(p. xxxv\)](#) for more information.



---

## Chapter 45: Forced Response Analysis of a Mistuned Bladed Disk

---

This example problem demonstrates the free vibration and forced response analyses of a tuned and mistuned NASA Rotor 67 fan using [cyclic modeling methods](#) and [linear perturbation](#) solution approaches. The problem includes a modal analysis, a prestressed modal analysis using linear perturbation, and a prestressed mode-superposition harmonic analysis using linear perturbation. The analyses include pressures acting on the model as a result of unsteady flow imported from ANSYS CFX.

The results of the cyclic symmetry analysis are verified against reference results obtained from an analysis of the full 360° model.

Topics related to this example problem follow:

- [45.1. Introduction](#)
- [45.2. Problem Description](#)
- [45.3. CFD Modeling](#)
- [45.4. Structural Modeling](#)
- [45.5. Structural Material Properties](#)
- [45.6. Boundary Conditions and Loading](#)
- [45.7. Analysis and Solution Controls](#)
- [45.8. Results and Discussion](#)
- [45.9. Recommendations](#)
- [45.10. References](#)
- [45.11. Input Files](#)

### 45.1. Introduction

Turbine engine rotors and bladed disks, which play a crucial role in the energy supply and mobility industries, are dynamic systems that are known to suffer from severe vibration problems. These vibrations may be introduced by aerodynamic forces. Hence, it is important to study the aeroelastic behavior of the blades in turbomachinery design.

Aeroelastic phenomena can be classified into two categories: forced response and flutter. Typically, flutter is an asynchronous self-excited vibration, generally occurring at a frequency corresponding to one of the lower blade or coupled blade-disk natural frequencies. On the other hand, forced response resonance of rotor blades generally results from periodic aerodynamic forcing functions with frequencies of integer multiples of the natural frequency of the system.

In general, a bladed disk is designed to have identical blades, but there are always random deviations among individual blades due to manufacturing tolerances, wear, and other causes. This is known as mistuning.

Though mistuning is typically small, mistuned bladed disks can have drastically larger forced response levels than the ideal tuned design, which can cause blades to fail prematurely due to high cycle fatigue (HCF). HCF is a major cost, safety, and reliability issue for gas-turbine engines. It is clearly of great interest to be able to predict, and ultimately to limit, the increases in maximum blade response caused by mistuning.

Comprehensive modeling, analysis, and understanding of bladed disk vibration is thus critical to reduce the occurrence of HCF and to improve the performance and reliability of turbomachinery.

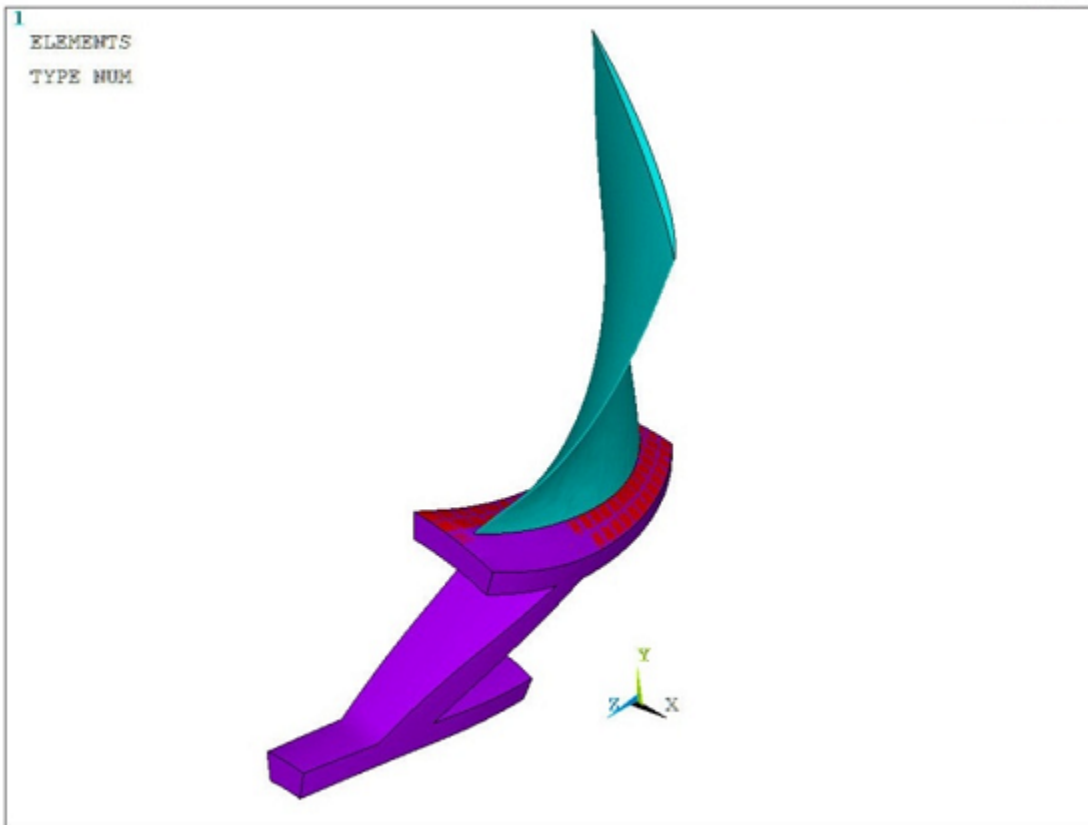
For more information, see the [Cyclic Symmetry Analysis Guide](#).

## 45.2. Problem Description

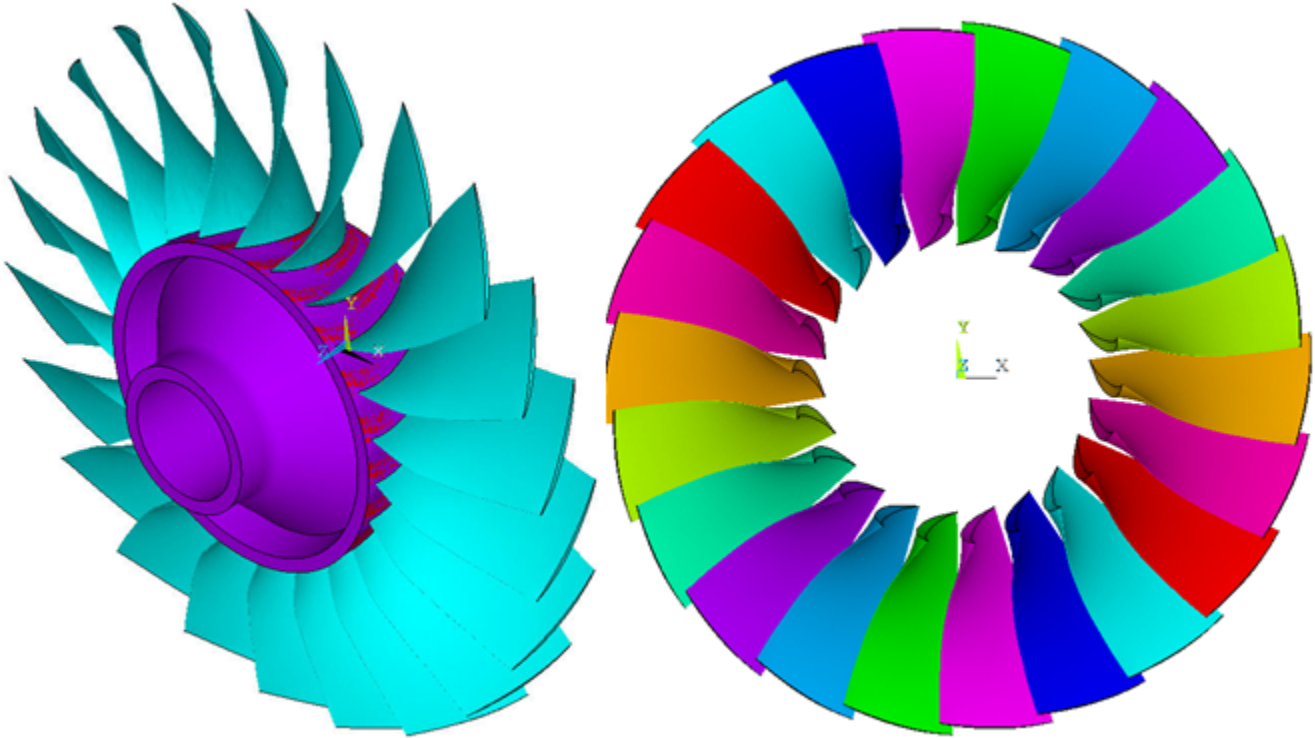
The NASA Rotor 67 fan bladed disk in this example is a subsystem of a turbofan's compressor set used in aerospace engine applications. This model represents a challenging and industrial example for which the detailed geometry and flow information is available in the public domain.

The following figure shows a cyclically symmetric sector of the Rotor 67 fan:

**Figure 45.1: Sector Model of the NASA Rotor 67 Fan**



The model consists of a disk and a fan blade with a sector angle of 16.364 degrees. The full model consists of 22 fan blades, as shown:

**Figure 45.2: Full Model of the NASA Rotor 67 Fan**

The following analyses are performed on the cyclic-sector model:

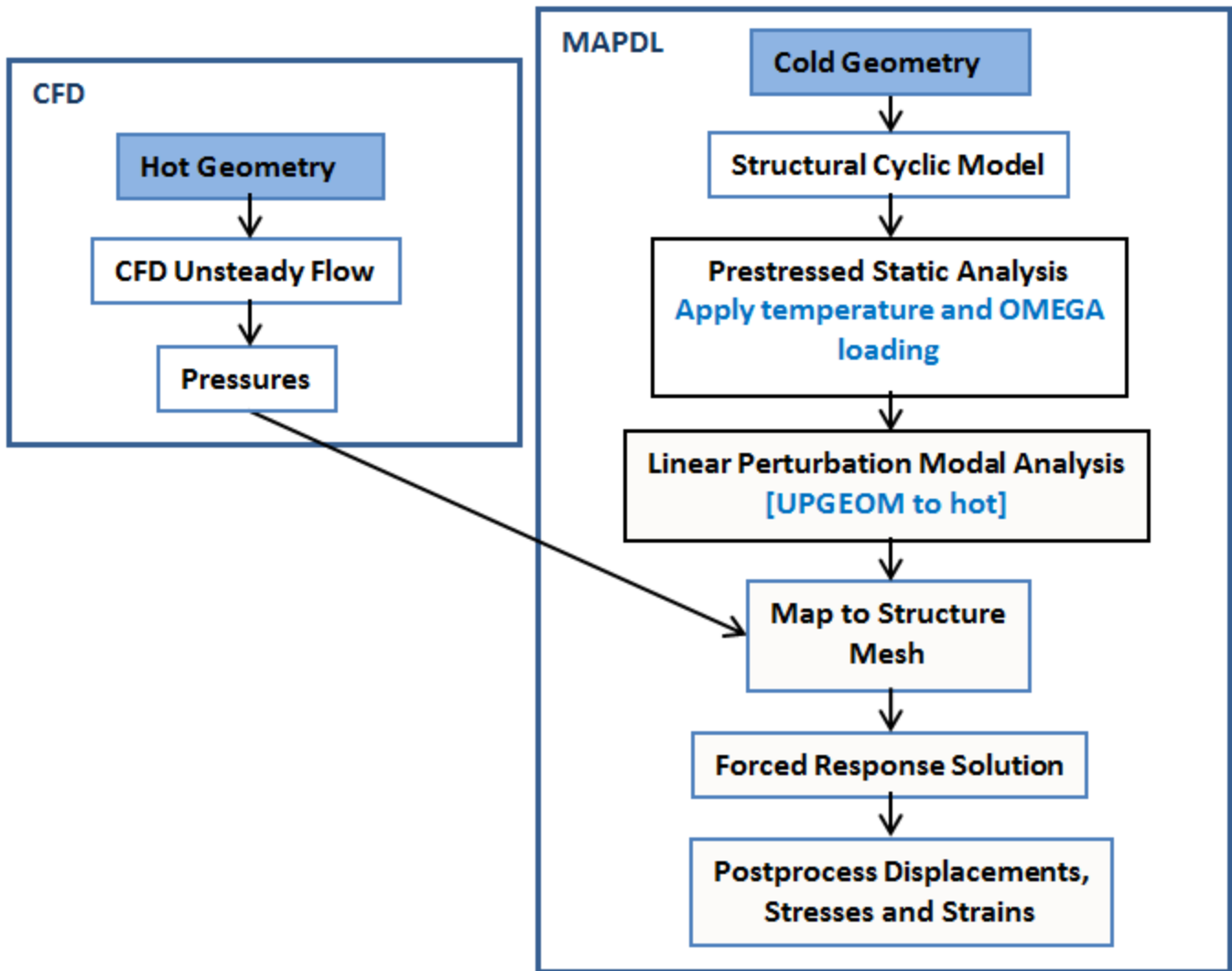
- Modal
- Perturbed prestressed modal following a nonlinear base static solution
- Perturbed prestressed mode-superposition harmonic following a nonlinear base static solution

The perturbed modal and perturbed mode-superposition harmonic cyclic symmetry analyses include the initial prestressed condition from nonlinear static analysis. The initial stress state from the nonlinear static analysis is produced by considering the rotational effects on the fan and the thermal loading applied on all nodes of the fan model.

In addition, the perturbed mode-superposition harmonic cyclic symmetry analysis also includes unsteady flow pressure that is acting on the fan blades. This unsteady flow pressure is calculated for the 3-D viscous flow of air modeled as an ideal gas for a fan running at 16043 RPM with a 10% inlet distortion using ANSYS CFX.

Modal, perturbed modal, and perturbed mode-superposition harmonic analyses of the full 360° model are also performed to validate the accuracy of the cyclic-sector model results.

The complete workflow to perform the forced response analysis is as follows:



### 45.3. CFD Modeling

The following topics concern the computational fluid dynamics (CFD) modeling of this problem that have been carried out on the bladed disk in order to retrieve the unsteady flow pressure:

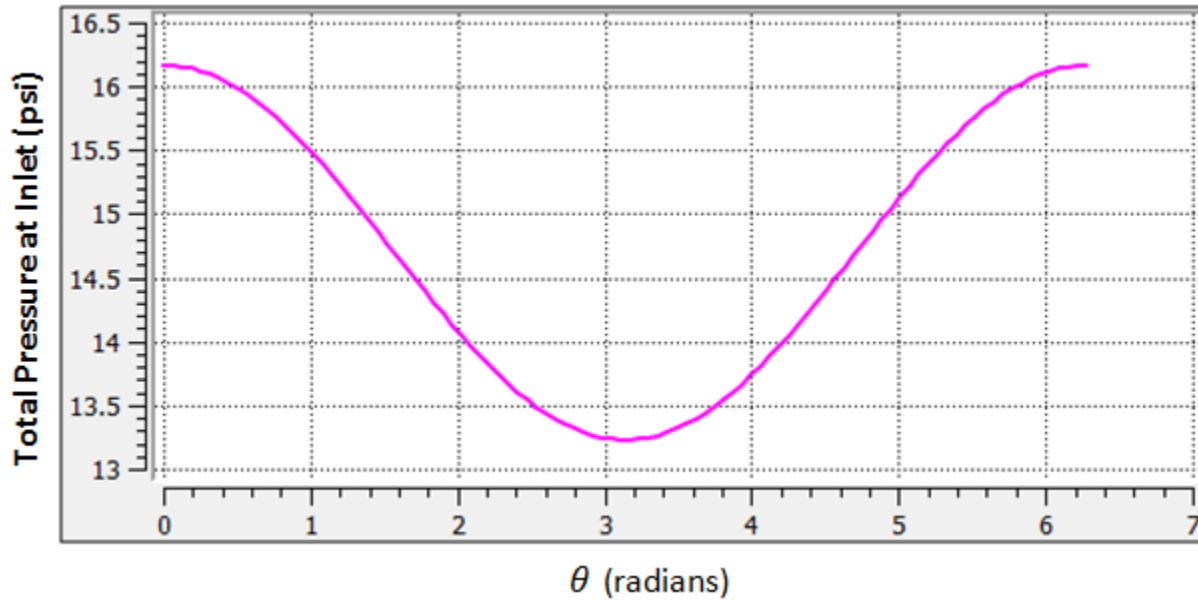
- 45.3.1. Problem Description and Setup
- 45.3.2. Solution Monitor Plots and Convergence Pattern
- 45.3.3. Unsteady Pressure Results

#### 45.3.1. Problem Description and Setup

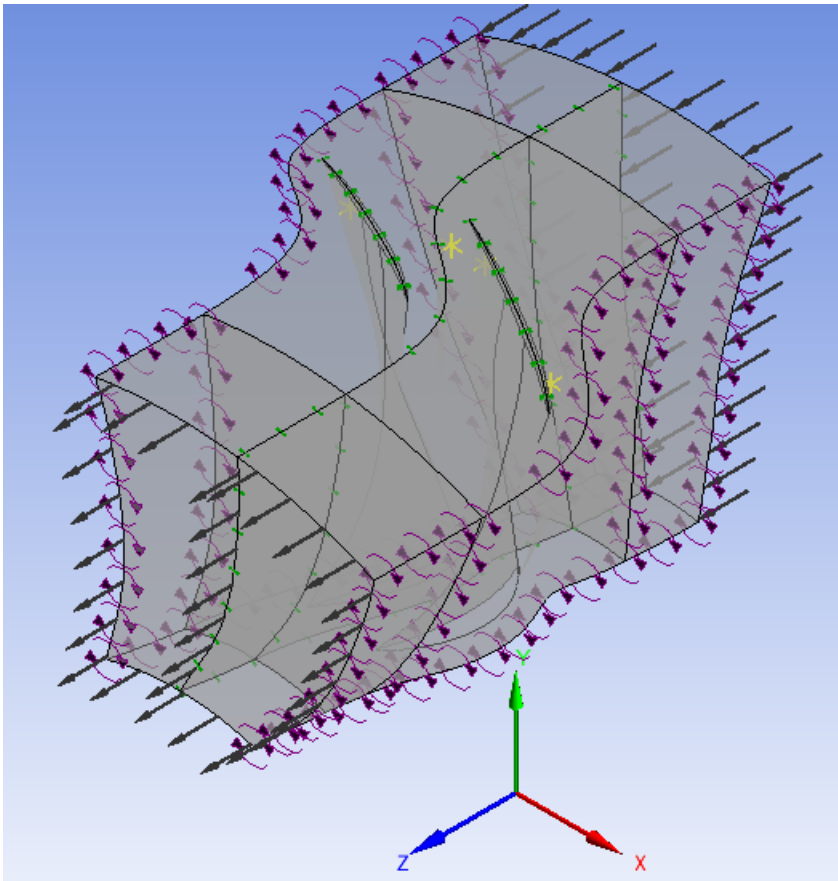
The unsteady flow pressures which act on the fan blade are required for the structural analysis. The unsteady fluid calculations are carried out using ANSYS CFX. The unsteady pressures on the blades arise due to the one per revolution distortion signal at the inlet as well as the rotation of the blades in a pressure field. The expression used to generate the 10% inlet distortion is:

$$1[\text{atm}] \times (1 + 0.1 \times \cos \theta)$$

This expression is plotted in the following figure:

**Figure 45.3: One Per Revolution Signal Excitation**

For the CFX analysis only two blades are considered, as shown below:

**Figure 45.4: CFX Model Showing the Domain of the NASA Rotor 67 Fan**

The Fourier Transformation Inlet Disturbance method is used in this analysis. This method belongs to the ANSYS Transient Blade Row (TBR) family of transient methods for obtaining a full wheel representation of the solution data by solving on a few passages per blade row, thereby providing substantial

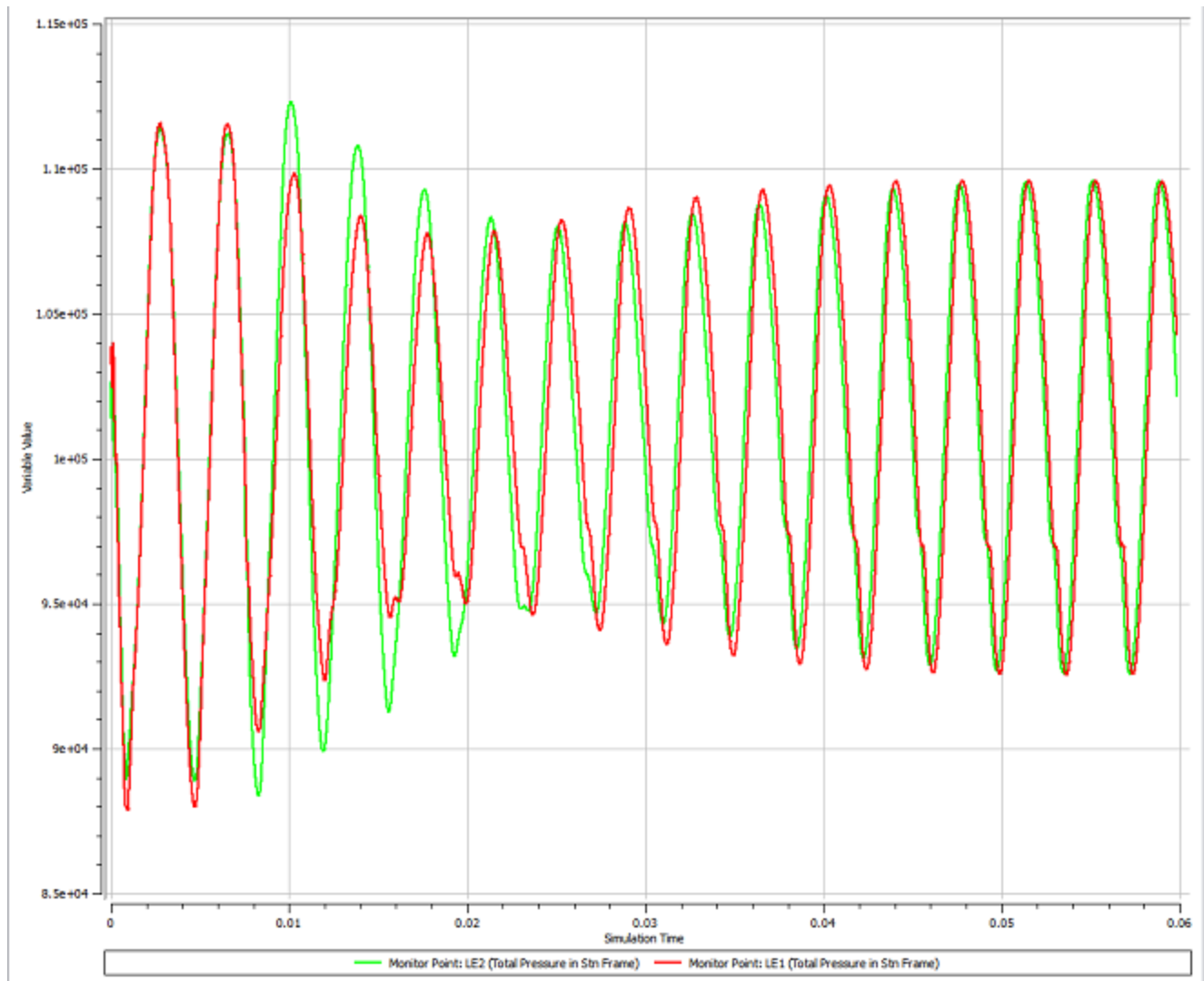
savings in solution time. The Fourier Transformation Inlet Disturbance method used in this study employs a Double Passage strategy, where the Fourier coefficients are collected on a sampling plane at the interface between the two rotors. Though this increases the domain size, it has been found to provide a faster convergence than the single passage method.

A steady-state solution is carried out before the transient analysis is performed, and the results from the steady-state solution are used to provide a good initial condition for the transient case. The transient solution is carried out for a few revolutions of the blade until the periodicity of the solution is achieved. The real and imaginary pressures on the blade surfaces are exported at the required engine order in a .CSV format, which is read into ANSYS Mechanical for carrying out the forced response analysis.

### 45.3.2. Solution Monitor Plots and Convergence Pattern

The convergence of the solution is monitored by creating monitor points at important locations in the domain. One such example is shown below:

**Figure 45.5: Solution Convergence Pattern of the NASA Rotor 67 Fan**



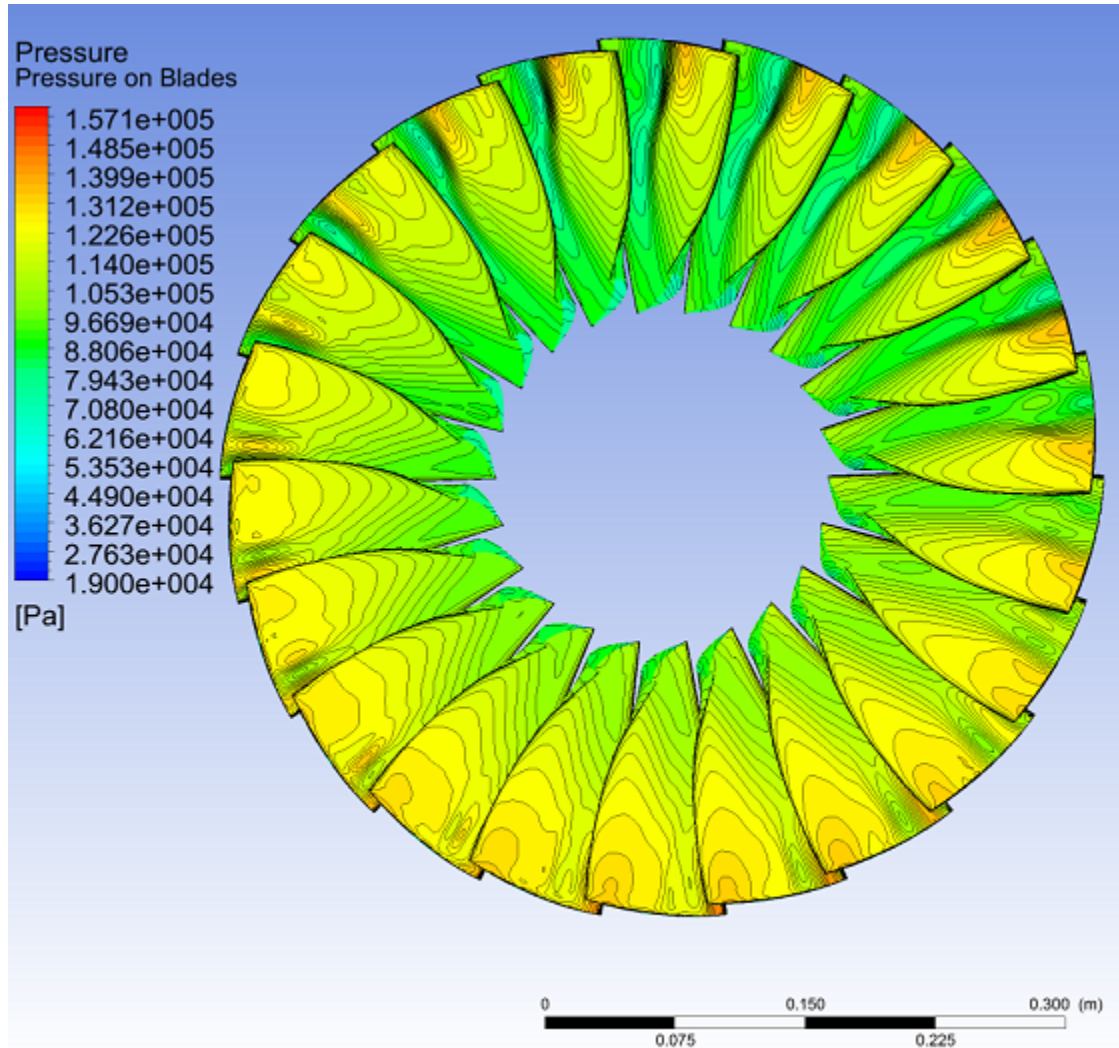
The solution is deemed to be converged when the monitor plots attain periodicity. In addition, it is also important to check the conservation of mass, momentum, and energy before accepting the final solution.



### 45.3.3. Unsteady Pressure Results

The unsteady pressure data has been calculated using two blade rows in this analysis. This data is easily expanded to obtain the full wheel variation of pressure using CFD-Post, as shown in the following figure:

**Figure 45.6: Unsteady Pressure Plots Obtained from TBR Analysis**



These unsteady pressures define the aerodynamic forcing due to the fluid forces. These aerodynamic data can be written to a file in the .CSV format at a specified engine order to perform further analysis using ANSYS Mechanical.

## 45.4. Structural Modeling

The following topics are related to the cyclic symmetry modeling for this problem:

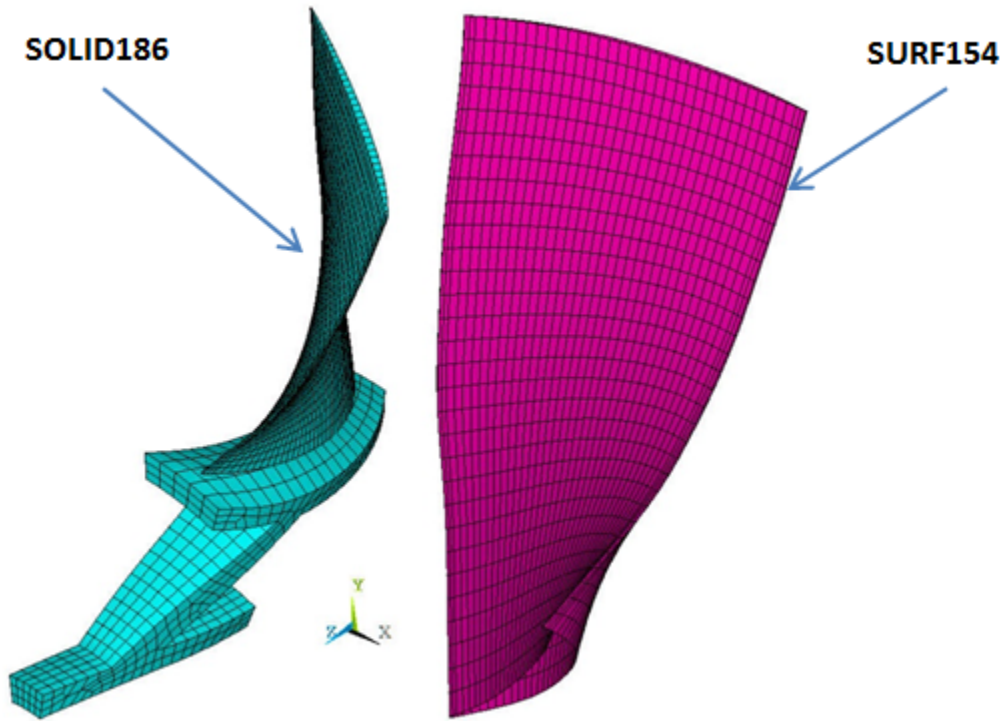
[45.4.1. Rotor 67 Fan Blade Modeling](#)

[45.4.2. Contact Modeling](#)

### 45.4.1. Rotor 67 Fan Blade Modeling

The sector model of a Rotor 67 fan bladed disk is meshed with SOLID186 elements, as shown in the following figure:

**Figure 45.7: Element Plot of the Cyclic-Sector Model**



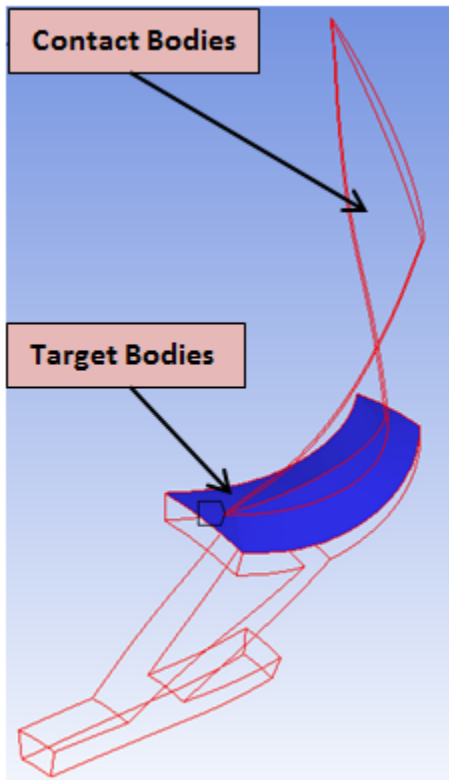
The disk and blade geometries are meshed separately so that the blade elements and the node interface separate the blade from the disk.

The default element settings for **SOLID186** are used.

**SURF154** elements are created on the surface of the fan blade to apply the pressure load.

### **45.4.2. Contact Modeling**

Bonded (always) **surface-to-surface contact pairs** are used to define the contact between the disk and the fan blade, shown in the following figure:

**Figure 45.8: Bonded Contact Pair Between the Disk and the Fan Blade**

The MPC-based contact algorithm is used for bonded contact.

The contact surface is meshed with **CONTA174** elements. The target surface is meshed with **TARGE170** elements.

## 45.5. Structural Material Properties

The following are the material properties for modeling the cyclic sector of the NASA Rotor 67 fan blade:

NASA Rotor 67 Fan Blade Material Properties	
Young's Modulus	$2.2 \times 10^{11}$ Pa
Poisson's Ratio	0.30
Density	$7840 \text{ kg}\cdot\text{m}^{-3}$
Coefficient of Thermal Expansion	$1.2 \times 10^{-5}$
Reference Temperature	22 °C

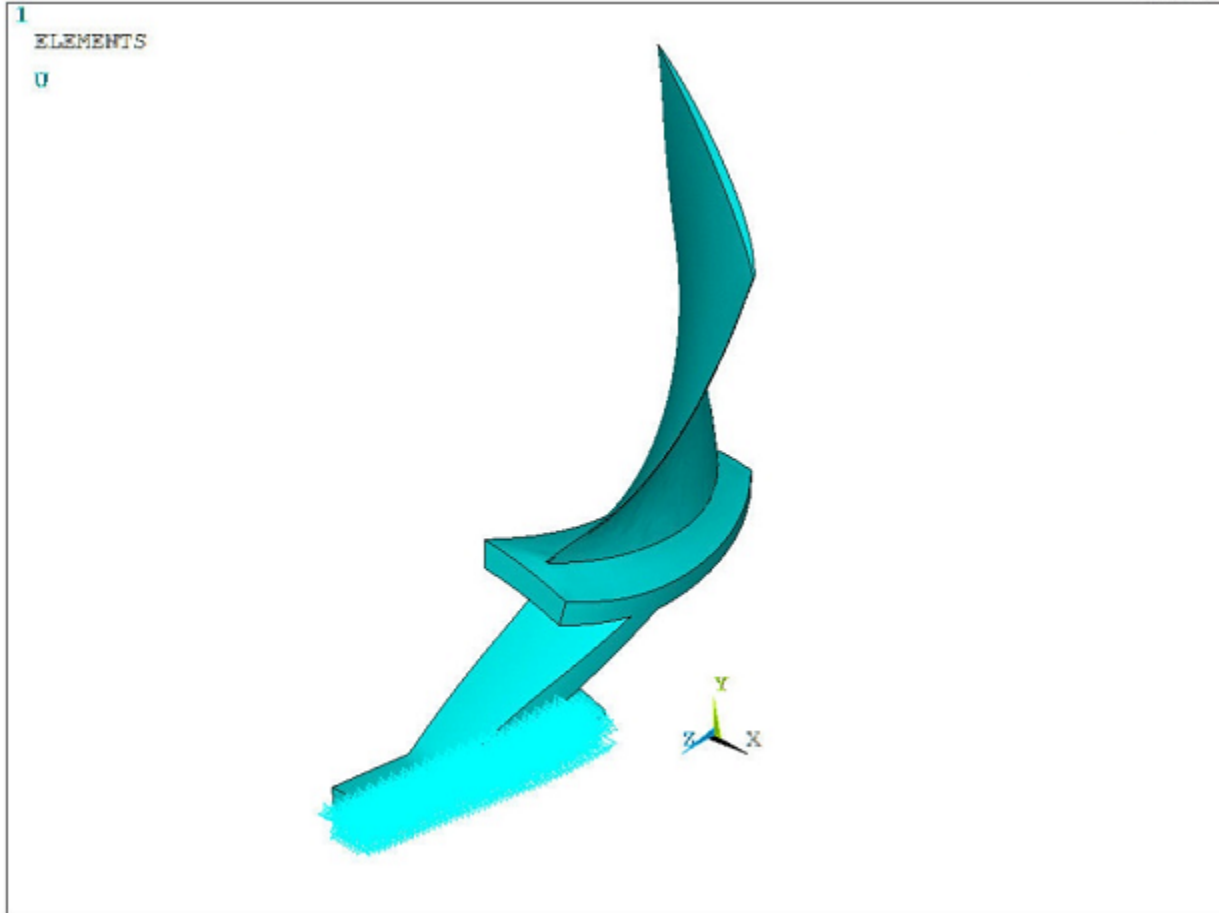
The following unit system is used in this simulation:

Units	
Unit System	Metric (m, kg, N, s, V, A)
Angle	Degrees
Rotational Velocity	rad/s
Temperature	Celsius
Pressure	Pa

## 45.6. Boundary Conditions and Loading

Fixed-support conditions are applied near the disk portion of the cyclic-sector fan blade model, as shown in the following figure:

**Figure 45.9: Fixed Support Condition Near Disk**



The following loads are considered for the cyclic symmetry analyses:

- Centrifugal loads caused by rotational velocity
- Thermal loads due to the difference in reference and operating temperature
- Unsteady flow pressure applied on the fan blade (imported from CFX)

The rotational velocity (**CGOMGA**,0,0,1680) is applied along the global Z-axis. The bladed disk is modeled with a coefficient of thermal expansion of  $1.2 \times 10^{-5} \text{ } ^\circ\text{C}^{-1}$ . The reference temperature is held at 22 °C and an operating temperature of 50 °C is applied on all nodes of the model to generate the thermal load vector.

The thermal load vector generated from the base static solve can be ignored in the subsequent analysis (**THEXPAND**).

The unsteady flow pressures, which are imported from ANSYS CFX, are generated for EO = 2 engine order excitation at a rotational frequency of 534.76 Hz. These pressure data are then mapped to the

structural rotor fan blade model in ANSYS Mechanical APDL using its mapping capabilities via the **/MAP** processor.

The following example input shows the steps involved in this mapping procedure:

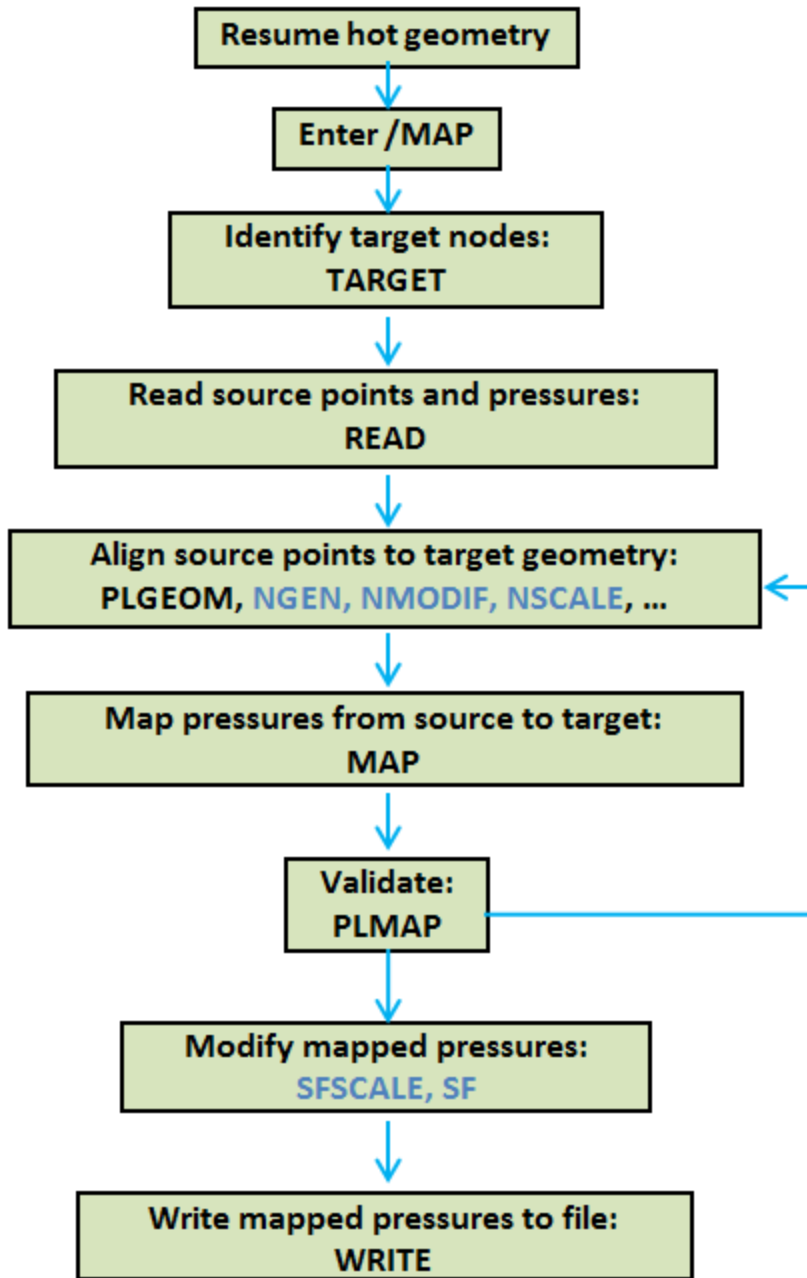
```
/map                                ! Mapping processor
target, nbfl                        ! Specifies target nodes for mapping pressures onto
                                   ! surface effect elements
FTYPE, cfxtbr,1                     ! Specifies file and pressure type for the
                                   ! subsequent import of source points and pressures
READ,CFX_ExportResults_FT_10P_EO2.csv' ! Read coordinate and pressure data from a file

allsel,all,all
csys,0

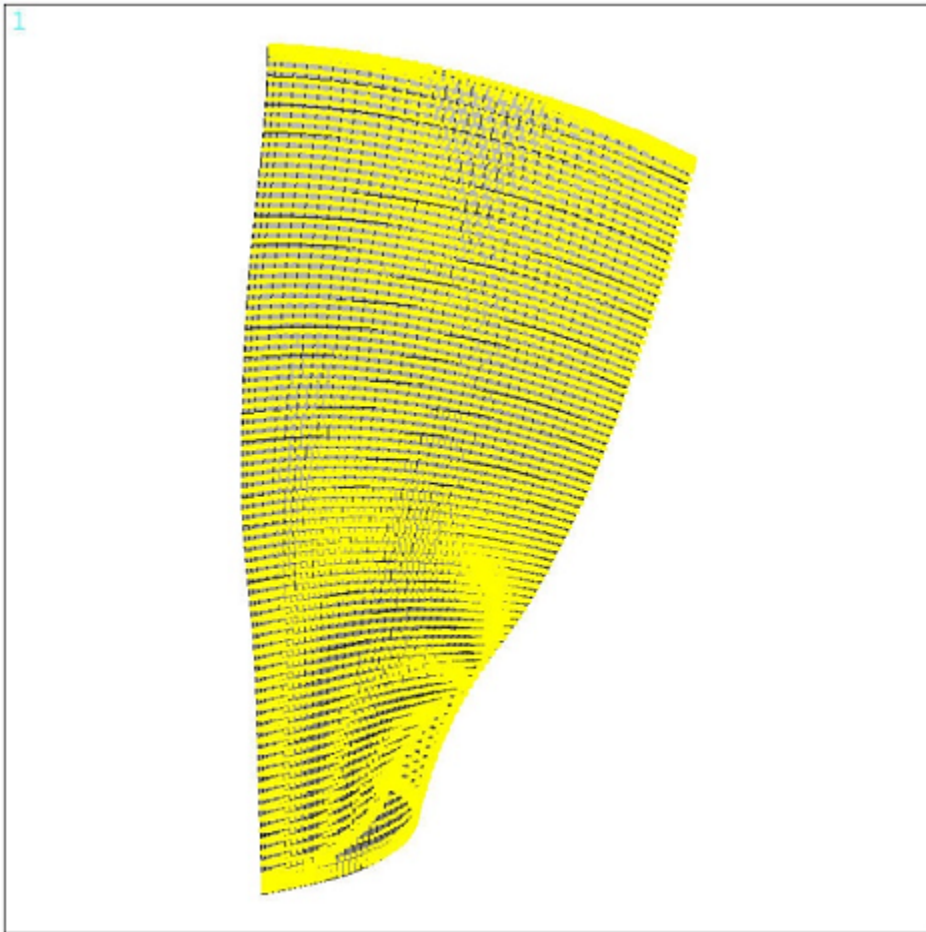
/show, jpeg, rev
plgeom                              ! Plots source and target geometries
MAP,,2,,1,                          ! Map pressures from source points to target surface elements
plmap,target                        ! Plot target and source pressure
plmap,target,,,1
/show,close
WRITEMAP,'mapped_on_cyclic_model.dat' ! Write interpolated pressure
                                   ! data to a file

finish
```

To illustrate the step-by-step mapping procedure, the complete workflow in Mechanical APDL is shown below:

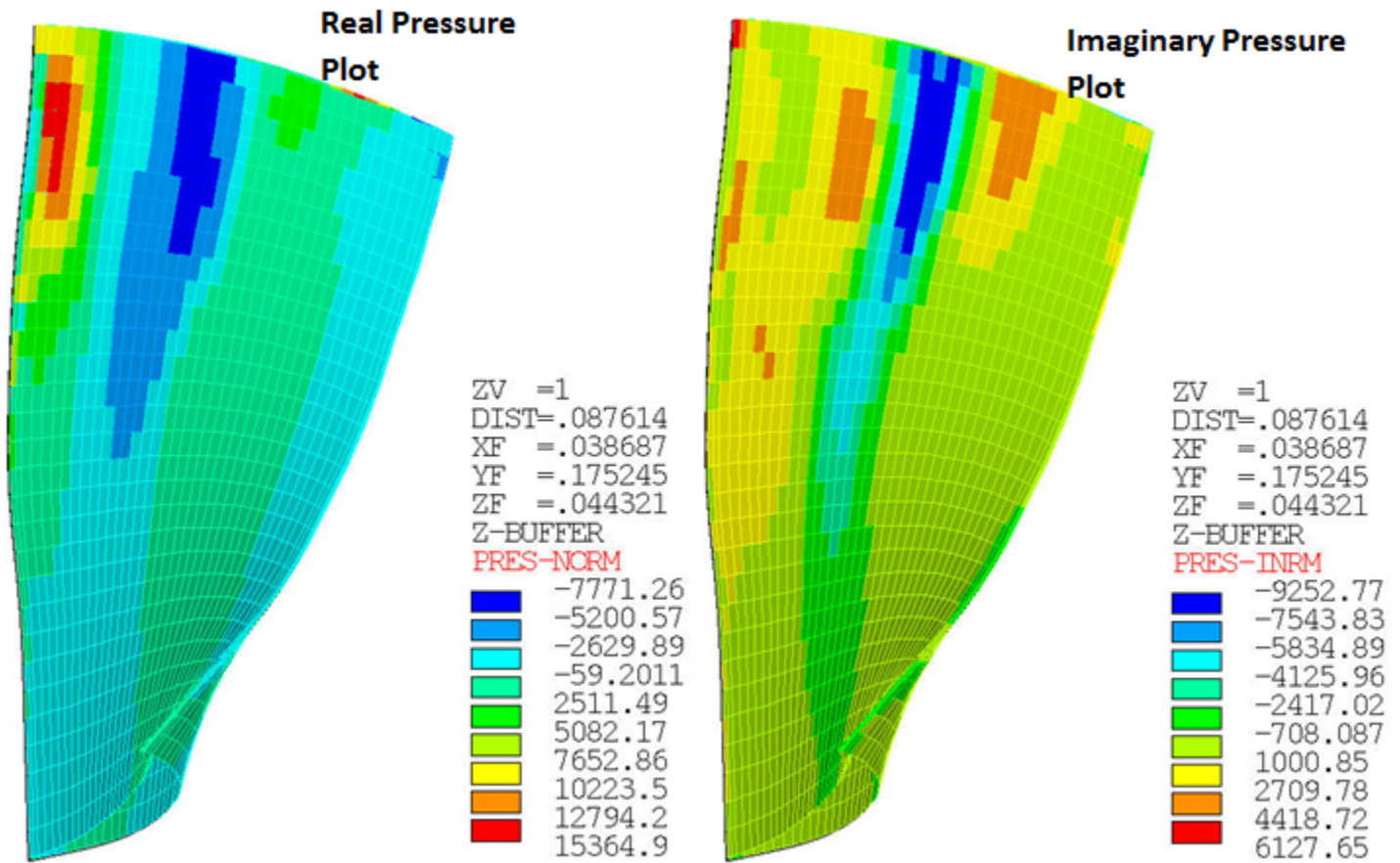


Using the **PLGEOM** command, the target and source geometries can be plotted as shown:

**Figure 45.10: Target and Source Geometries of the Rotor Fan Blade**

The real and imaginary components of mapped target pressure are plotted using the **PLMAP** command, as shown:

**Figure 45.11: Mapped Target Pressure Plots on the Rotor Fan Blade Surface**



In the case of a mistuned bladed disk, blades are subjected to engine order (EO) excitation. Engine order excitation is the effective traveling wave excitation that a bladed disk experiences as it passes through disturbances in the flow-field for each revolution. For example, one disturbance in the flow field results in an  $EO = 1$  excitation; two disturbances in the flow field result in an  $EO = 2$  excitation.

In Mechanical APDL, the engine order excitation is applied using the **CYCFREQ** command with *Option* = EO. Internally, the program computes the aliased engine order, including its sign. The aliased engine order  $\hat{C}$  is determined from the input engine order  $C$  as follows:

**Table 45.1: Aliased Engine Order (Excited Harmonic Index)**

Engine Order $C$		Aliased Engine Order $\hat{C}$
N Even	N Odd	
$C \leq N / 2$	$C \leq (N - 1) / 2$	$C$
$N / 2 < C \leq N - 1$	$2(N + 1) \leq C \leq N$	$N - C$
$N \leq C \leq 3N / 2$	$N \leq C \leq (3N - 1) / 2$	$C - N$
$3N / 2 \leq C \leq 2N$	$(3N + 1) / 2 \leq C \leq 2N$	$2N - C$
...	...	...

where  $N$  = number of sectors.

For the case of mistuned forced response analysis, the forcing/excitation frequency expressed in terms of EO is as follows:



$$f_{\text{excite}} = \text{EO} \times \frac{\Omega}{60}$$

where  $f_{\text{excite}}$  is in Hz and  $\Omega$  is in RPM.

The excitation frequency is specified with the **HARFRQ** command.

In general, mistuning in bladed disks is typically modeled as small, random perturbations to the stiffness of the blade DOF. The deviation in stiffness for blade  $n$  is expressed as follows:

$$E_n = (1 + \delta_n)E$$

where  $\delta_n$  is the mistuning parameter for blade  $n$ .

The mistuning parameters are provided in an array parameter of size  $N \times 1$ , where  $N$  is the number of blades. These mistuning parameters are defined using the **CYCFREQ** command with *Option* = MIST and *Value1* = K.

For the perturbed mode-superposition harmonic analysis, the unsteady flow pressures applied as per the engine order excitation on the fan blade are treated as a harmonically varying load.

## 45.7. Analysis and Solution Controls

This section describes the following analyses performed for this problem:

45.7.1. Nonlinear Prestressed Mode-Superposition Harmonic Cyclic Symmetry Analysis with Linear Perturbation - Tuned Response

45.7.2. Nonlinear Prestressed Mode-Superposition Harmonic Cyclic Symmetry Analysis with Linear Perturbation - Mistuned Response

For procedure and solution controls for the [modal cyclic symmetry](#) (p. 180) analysis and [nonlinear prestressed modal cyclic symmetry analysis with linear perturbation](#) (p. 182), refer to [Analysis and Solution Controls](#) (p. 180) for the [Centrifugal Impeller Analysis Using Cyclic Symmetry and Linear Perturbation](#) (p. 175).

For general information about linear perturbation, see [Linear Perturbation Analysis](#) in the *Structural Analysis Guide*.

### 45.7.1. Nonlinear Prestressed Mode-Superposition Harmonic Cyclic Symmetry Analysis with Linear Perturbation - Tuned Response

In a tuned analysis, which is an idealization of the real structure, all the blades are considered to be identical in terms of blade properties (for example, stiffness).

To perform a nonlinear prestressed mode-superposition harmonic cyclic symmetry analysis with linear perturbation, you must first prestress the structure with nonlinear effects in a static solution. In order to perform a downstream mode-superposition analysis, you must specify *OPTION* = MSUP and *Value1* = ON with the **CYCOPT** command in a static solution. The perturbed procedure is used to perform a modal analysis from the prestressed state, followed by a mode-superposition harmonic analysis.

For this analysis, the  $\text{EO} = 2$  engine order excitation is applied using the **CYCFREQ** command with *Option* = EO and *Value1* = 2.

The frequency range of excitation, 513.76 - 538.76 Hz with 50 substeps is chosen based on the modal frequencies for the mode-superposition harmonic analysis. With this frequency range, the first few modes of the bladed disk are excited.

The following example input shows the steps in this analysis:

```

/solu

csys,0
antype,static           ! Perform Static analysis
nlgeom,on              ! Include large deformation effects
rescontrol,define,all,1 ! Enable the file writing in multiframe restart
nsub,10,10,10          ! Number of substeps = 10

allsel,all,all
nsle
bf,all,temp,50         ! Define temperature = 50
allsel,all,all

csys,1
cgoomega, 0, 0, 1680,  ! Centrifugal load

cycopt,msup,1          ! MSUP key is ON
time,1.0

solve
finish

/solu
antype,static,restart,,perturb ! Perform a static restart with perturb from the last ! substep of the previous s
perturb,modal,,DZEROKEEP      ! Set the analysis options for perturbed modal analysis
solve,elform

modopt,lanb,50,0,14000
mxpand,,,,yes,,yes

cycopt,hindex,2,2,2
/input,'mapped_on_cyclic_model',dat ! Apply mapped pressure data to generate a
! load vector

solve
fini

/solu
antype,harmonic
hropt,msup,,,yes           ! MSUP Harmonic, Write modal coordinates
outres,all,all

harfrq,513.76,538.76
nsubs,50,50,50

cycfreq,eo,2              ! EO = 2

/com, Zeroing Prestressed loads
thexpand,off
cgom, 0, 0, 0
sfedele,all,all,all

lvscale,1,1              ! Scale the load vector
kbc,1

dmpstr,0.01             ! Structural damping

solve
finish

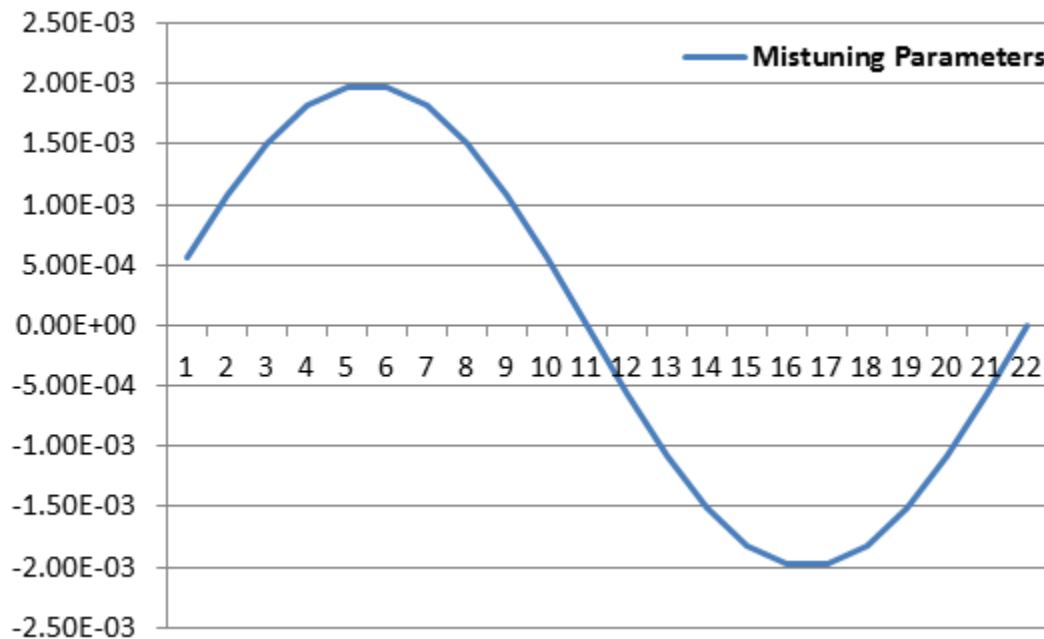
```

## 45.7.2. Nonlinear Prestressed Mode-Superposition Harmonic Cyclic Symmetry Analysis with Linear Perturbation - Mistuned Response

In a mistuned response analysis, which is a realistic case, deviations in blade properties such as stiffness is considered.

To perform this analysis with linear perturbation, the procedure is identical to the procedure described in [Nonlinear Prestressed Mode-Superposition Harmonic Cyclic Symmetry Analysis with Linear Perturbation - Tuned Response](#) (p. 699), except in this procedure mistuning parameters are defined. These mistuning parameters are specified as an array input using the **CYCFREQ** command with *Option* = MIST. For this analysis, a small mistuning of 0.2% (assumed to be a sine wave) is considered:

**Figure 45.12: Mistuning in the NASA Rotor 67 Fan Blade**

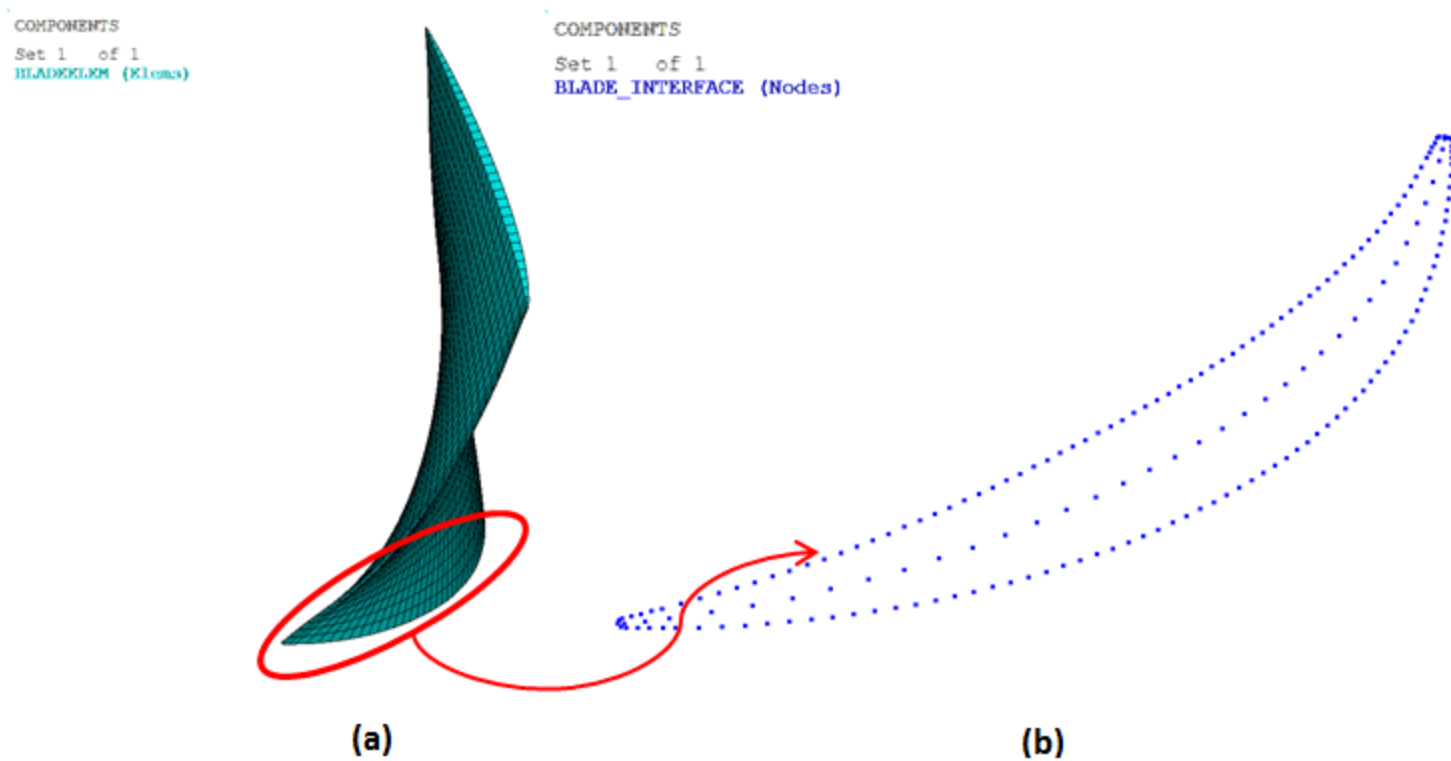


The  $EO = 2$  engine order excitation is applied using the **CYCFREQ** command with *Option* = EO and *Value1* = 2.

The cyclic mode-superposition harmonic analysis with mistuning requires a CMS reduction on the blade alone. For this, you need to provide the blade information using the **CYCFREQ** command with *Option* = BLADE. This blade information comprises the name of the nodal component containing the blade boundary nodes at the blade-to-disk interface, the name of the element component containing the blade elements, and the number of blade modes to include in the CMS reduction.

The following figure shows the element component of the fan blade and the blade boundary nodes at the blade-to-disk interface:

**Figure 45.13: (a) Element Component of Fan Blade; (b) Blade Boundary Nodes at the Blade-to-Disk Interface**



The frequency range of excitation is the same as in the tuned response analysis (513.76 - 538.76 Hz with 50 substeps).

The following example input shows the different steps in this analysis:

```

/solu
antype,harmonic
hropt,msup,,,yes           ! MSUP Harmonic, Write modal coordinates
outres,all,all

harfrq,513.76,538.76
nsubs,50,50,50

cycfreq,eo,2               ! EO = 2

thexpand,off              ! Prestressed load
cgom,0,0,0                ! Prestressed load
sfedele,all,all,all

lvscale,1,1               ! Scale the load vector

/com, Mistuning parameter values
_pi = 4*atan(1)
theta = 2*_pi/22

*do,i,1,22
m%i% = (2e-3)*sin(theta*i)   ! Mistuning = 0.2%
*enddo

*dim,kmist,array,22,1
kmist(1,1) = m1,m2,m3,m4,m5,m6,m7,m8,m9,m10,m11           ! Stiffness mistuning
kmist(12,1) = m12,m13,m14,m15,m16,m17,m18,m19,m20,m21,m22

cycfreq,blade,blade_interface,bladeelem,50,,,
cycfreq,mist,k,kmist
    
```

```
kbc,1
dmpstr,0.01
```

```
! Structural damping
```

```
solve
finish
```

## Note

For an ideal/tuned cyclic bladed disk, engine order excitation will excite only those modes with a number of nodal diameters that match the harmonic index of the excitation. For a mistuned bladed disk, the modes have multiple harmonic contents so that many modes will be excited by engine order excitation.

## 45.8. Results and Discussion

The modal frequencies of the NASA Rotor 67 fan blade cyclic sector model and the full model are compared in the following table:

**Table 45.2: Comparison of Modal Frequencies**

Mode No.	Cyclic Sector Model (Hz)	Full 360° Model (Hz)	Error (%)
1	370.17	370.17	0.00
2	370.17	370.17	0.00
3	376.70	376.70	0.00
4	376.70	376.70	0.00
5	377.12	377.12	0.00
6	377.12	377.12	0.00
7	377.41	377.41	0.00
8	378.93	378.92	0.00
9	378.93	378.93	0.00
10	380.42	380.42	0.00
11	380.42	380.42	0.00
12	381.65	381.65	0.00
13	381.65	381.65	0.00
14	382.65	382.65	0.00
15	382.65	382.65	0.00

The nonlinear (**NLGEOM,ON**) prestressed modal frequencies of the cyclic sector obtained from the linear perturbation analysis also show strong agreement with the full-model results, as shown in the following table:

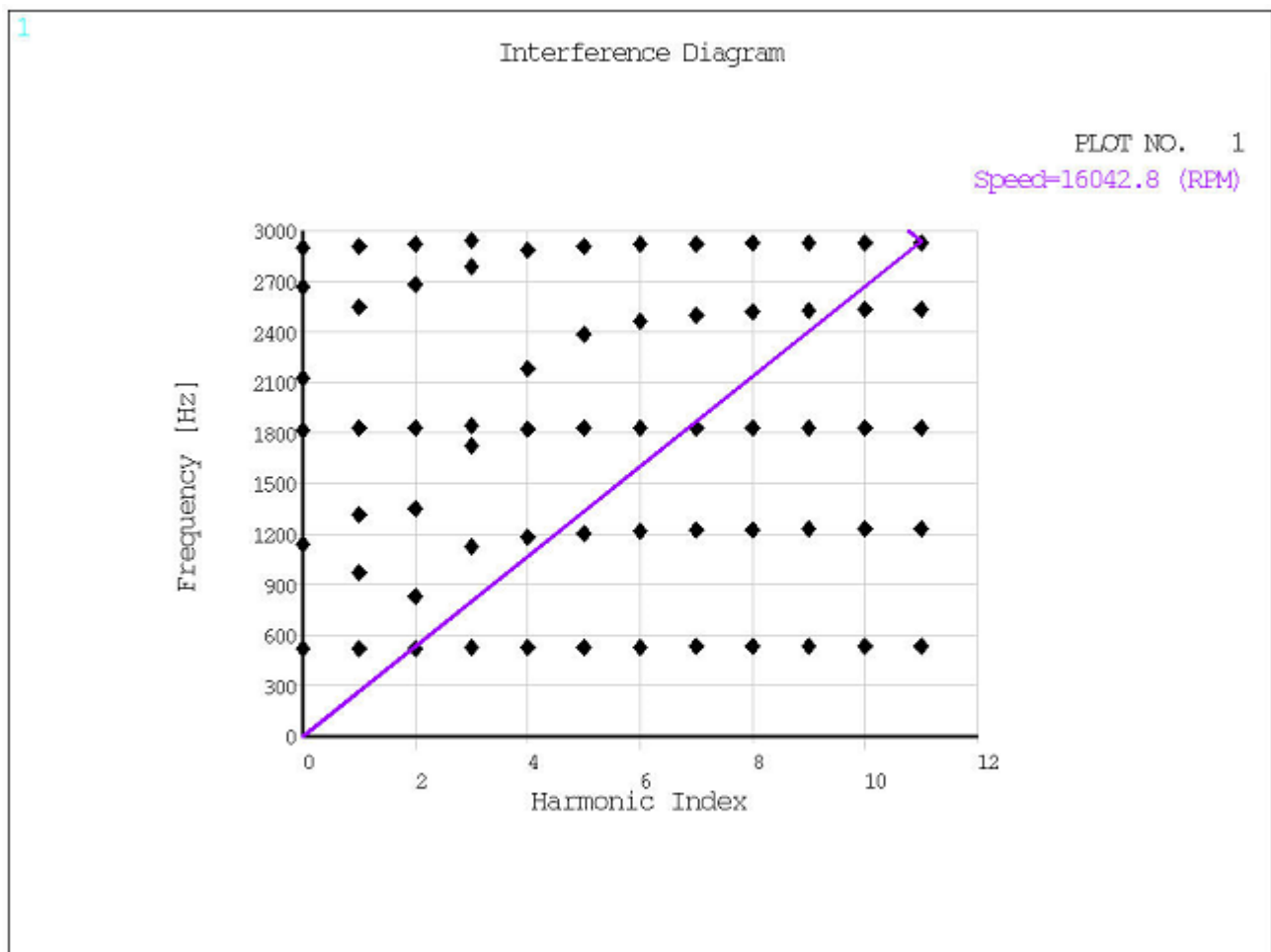
**Table 45.3: Comparison of Prestressed Modal Frequencies**

Mode No.	Cyclic Sector Model (Hz)	Full 360° Model (Hz)	Error (%)
1	519.09	519.09	0.00
2	521.05	521.05	0.00
3	521.05	521.05	0.00
4	522.69	522.70	0.00

Mode No.	Cyclic Sector Model (Hz)	Full 360° Model (Hz)	Error (%)
5	522.70	522.70	0.00
6	526.38	526.39	0.00
7	526.39	526.39	0.00
8	528.12	528.12	0.00
9	528.12	528.12	0.00
10	529.65	529.65	0.00
11	529.65	529.65	0.00
12	531.07	531.07	0.00
13	531.07	531.07	0.00
14	532.29	532.29	0.00
15	532.29	532.29	0.00

The prestressed modal frequencies can be plotted as a function of the number of harmonic index (nodal diameter) using the **PLZZ** command:

**Figure 45.14: Interference Diagram of NASA Rotor 67 Fan Blade Model**



Modes dominated by blade motion tend to appear in a tight frequency range in the plot. In contrast, the modal stiffness of a disk increases rapidly as the harmonic index (nodal diameter) increases, and so

disk-dominated system modes appear as slanted dotted lines in the plot. This plot is also known as a SAFE diagram or a ZZENF diagram and indicates potential frequencies where resonance may occur.

To postprocess the results of a cyclic symmetry mode-superposition harmonic analysis, you must first issue the **CYCFILES** command in **/POST1**.

For the nonlinear prestressed tuned response analysis, the following figures compare the postprocessing results of the cyclic-sector model to the full 360° model:

**Figure 45.15: Total Deformation Pattern (Real Only) at Frequency of 522.76 Hz**

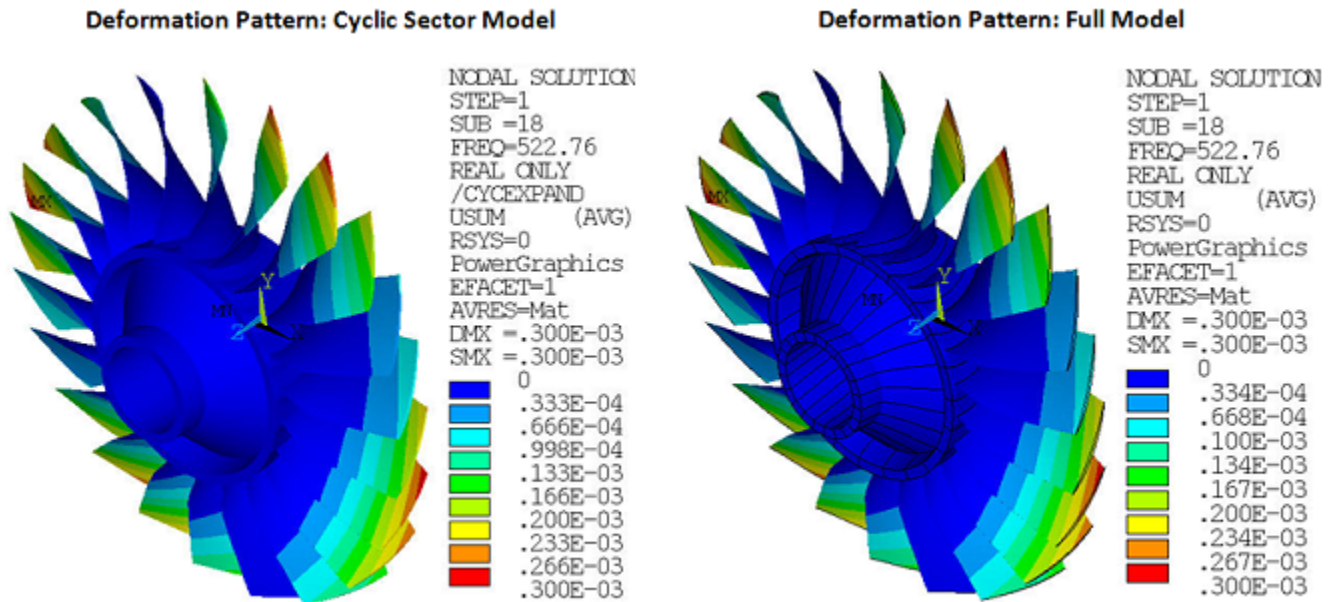


**Figure 45.16: Equivalent Stress Pattern (Real Only) at Frequency of 522.76 Hz**

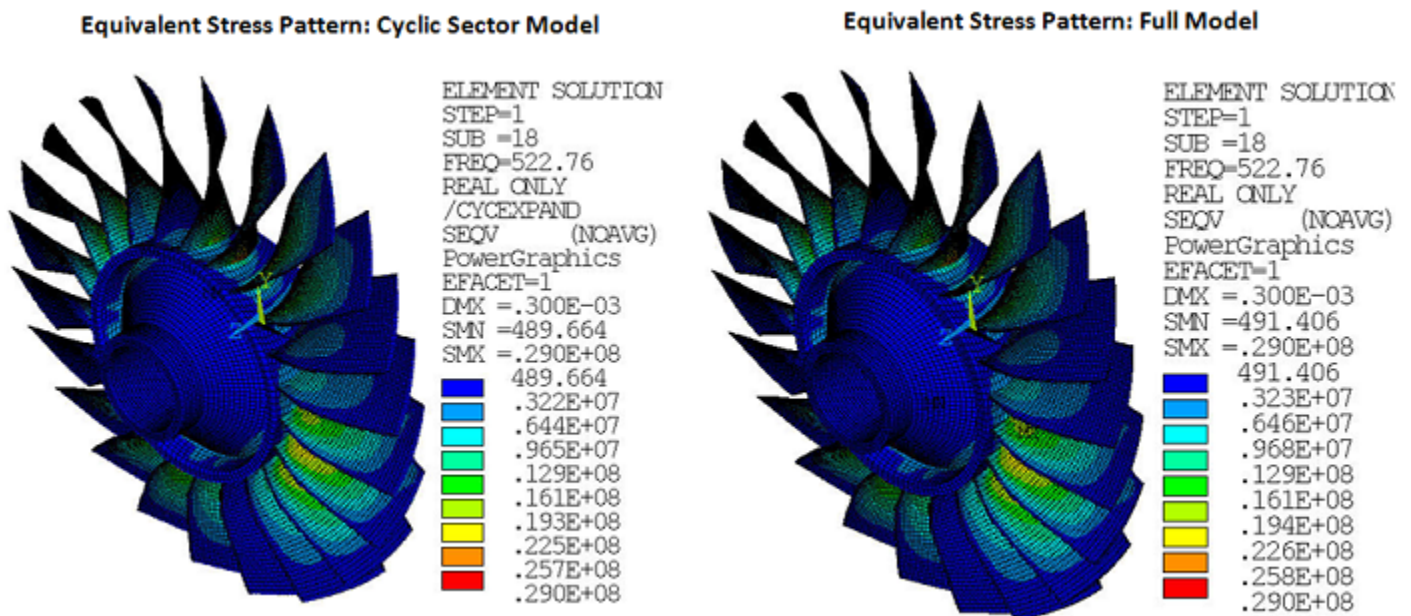
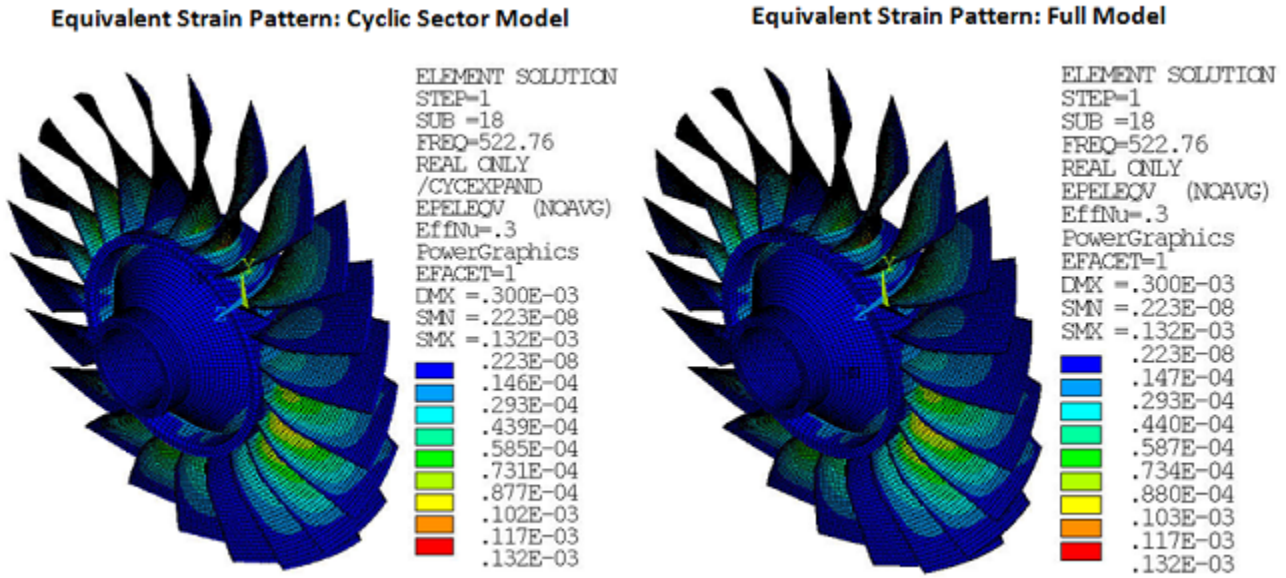
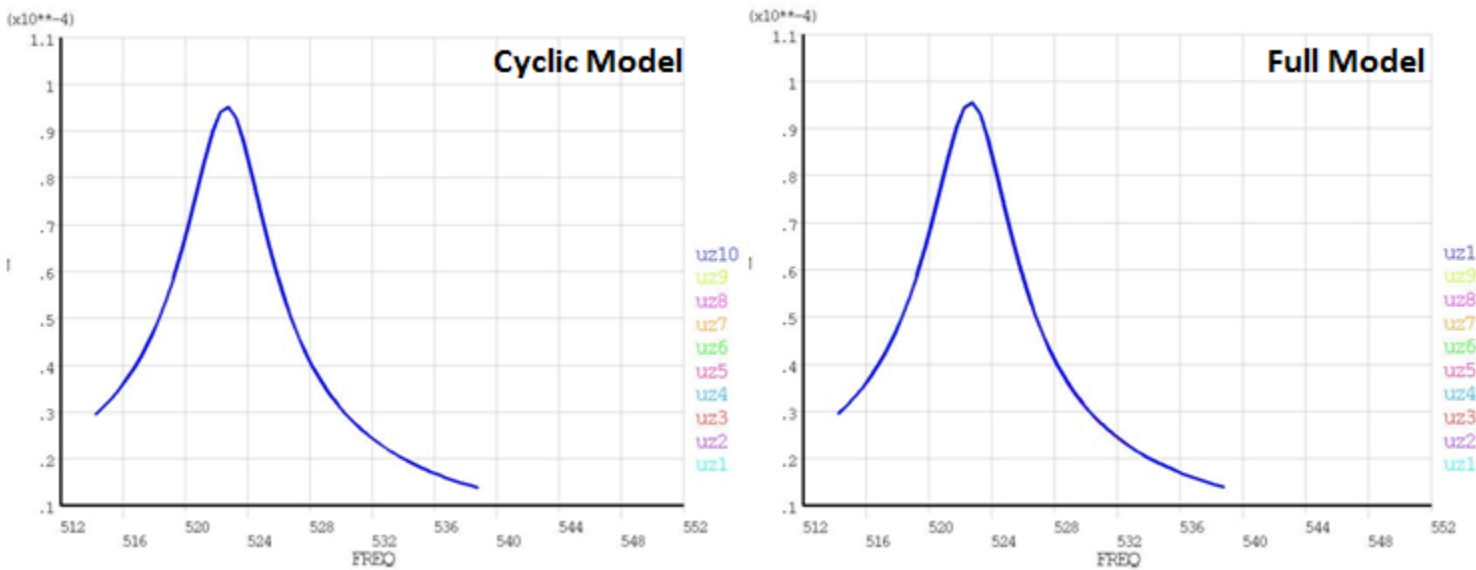


**Figure 45.17: Equivalent Strain Pattern (Real Only) at Frequency of 522.76 Hz**



These results show strong agreement between the cyclic-sector model and the full 360° model. The nodal solution plots (NSOL) show the amplitude of a nodal degree-of-freedom (DOF) value with respect to the frequency of excitation:

**Figure 45.18: Nodal Solution Plots with Respect to the Frequency of Excitation**



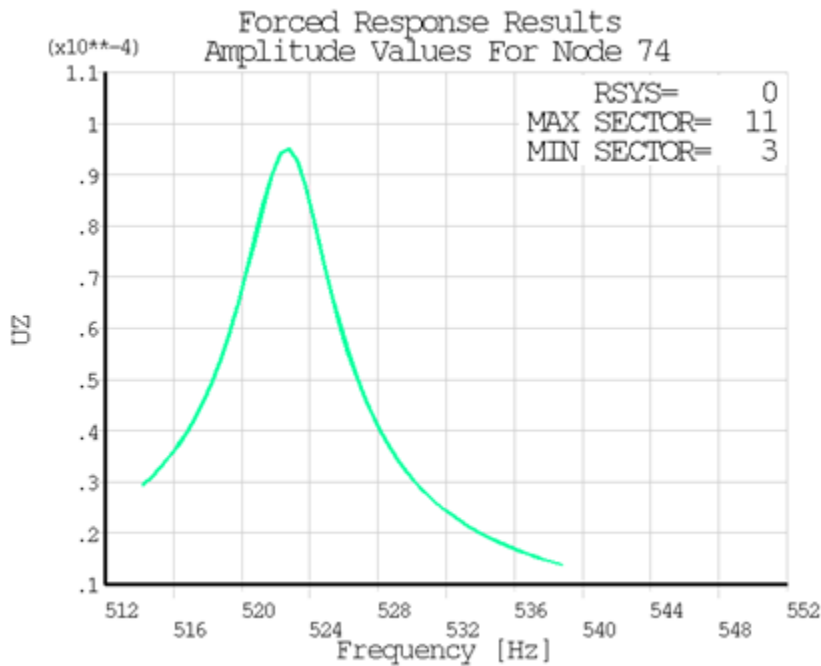
The plots indicate the occurrence of a resonance condition at 522.70 Hz. The displacement amplitude of nodes at symmetric angular positions on sectors 1 through 10 is plotted. The plots show strong agreement between the cyclic and full-model results.

You can also retrieve a maximum result value which occurs among all sectors of the model and all frequency points using **CYCSPEC** and **CYCCALC**. With these commands, you can extract tables of displacement, stress, and/or strain data for all computed harmonic solutions and for all sectors. The extracted data can be plotted using **PLCFREQ** and **PLCHIST**.



For the tuned response analysis, the maximum directional deformation at the blade tip along the Z-direction is plotted using **PLCFREQ**, as shown in the following figure:

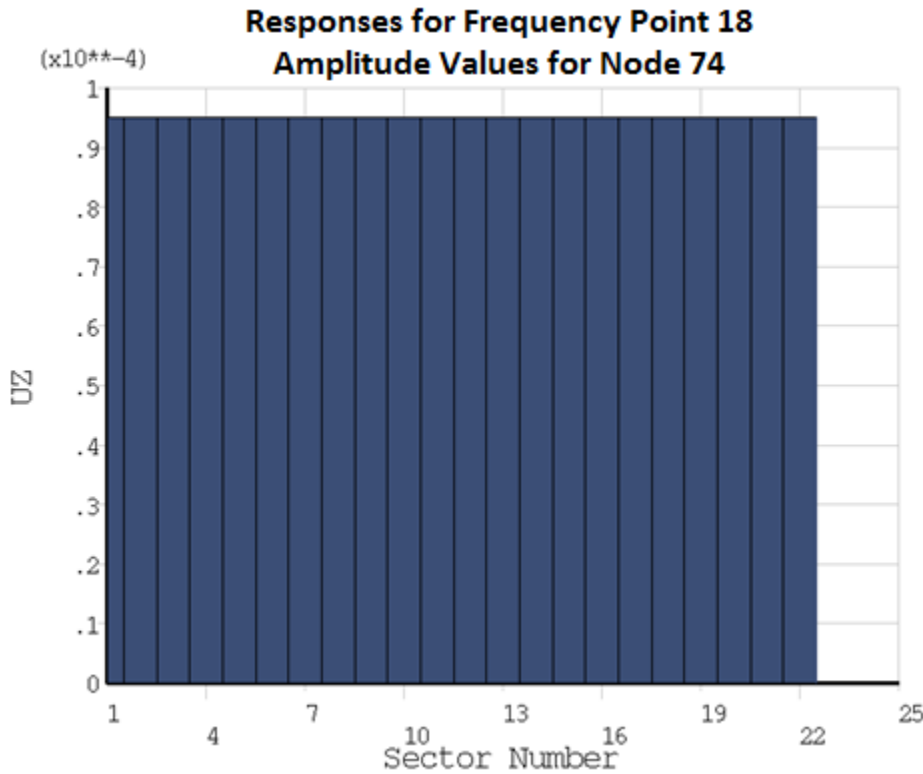
**Figure 45.19: Directional Deformation at the Blade Tip Along the Z-Direction**



The plot clearly indicates the sector numbers which contain the maximum and minimum values for the directional deformation along the Z-direction.

**PLCHIST** plots a histogram of the directional deformation along the Z-direction at the requested frequency of 522.76 Hz; one bar corresponds to one sector:

**Figure 45.20: CYCSPEC Histogram Response Plot at Frequency 522.76**



For the nonlinear prestressed mistuned response analysis, the following figures compare the postprocessing (**POST1**) results of the cyclic-sector model to the results of the full 360° model:

**Figure 45.21: Total Deformation Pattern (Real Only) at Frequency of 534.76 Hz**

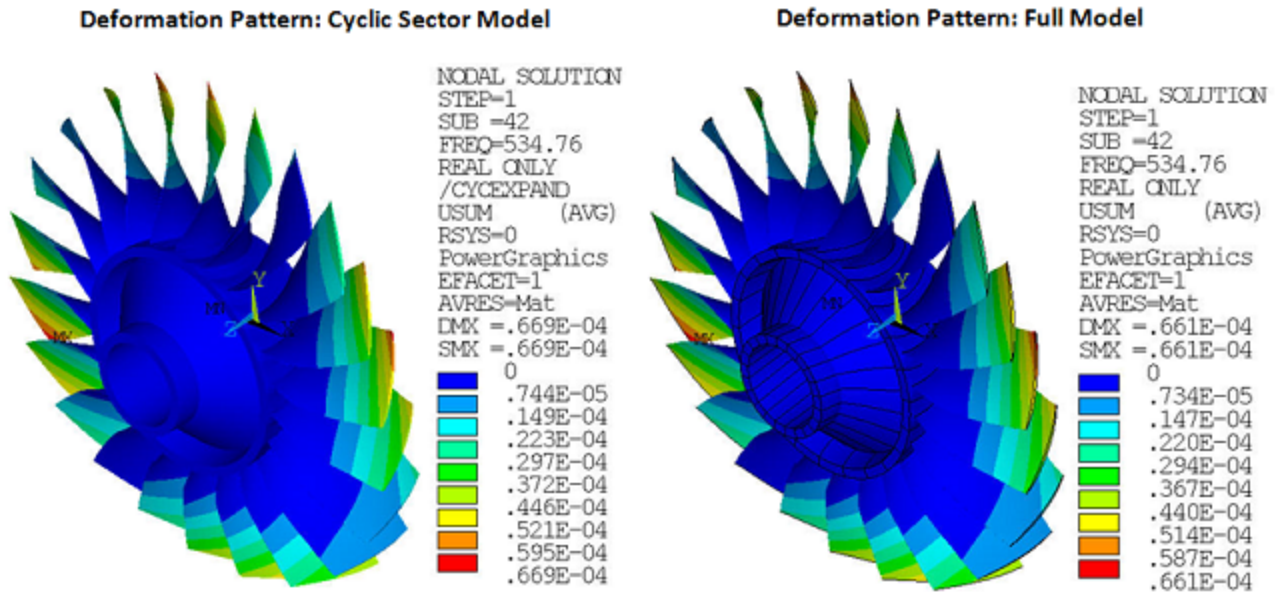


Figure 45.22: Equivalent Stress Pattern (Real Only) at Frequency of 534.76 Hz

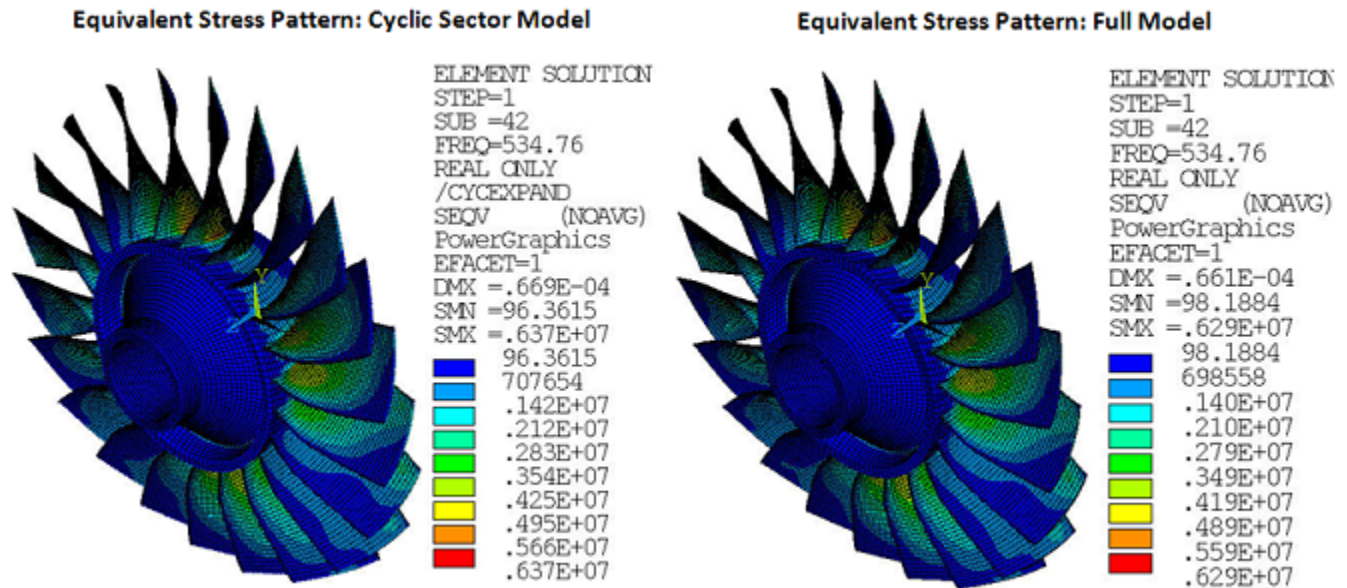
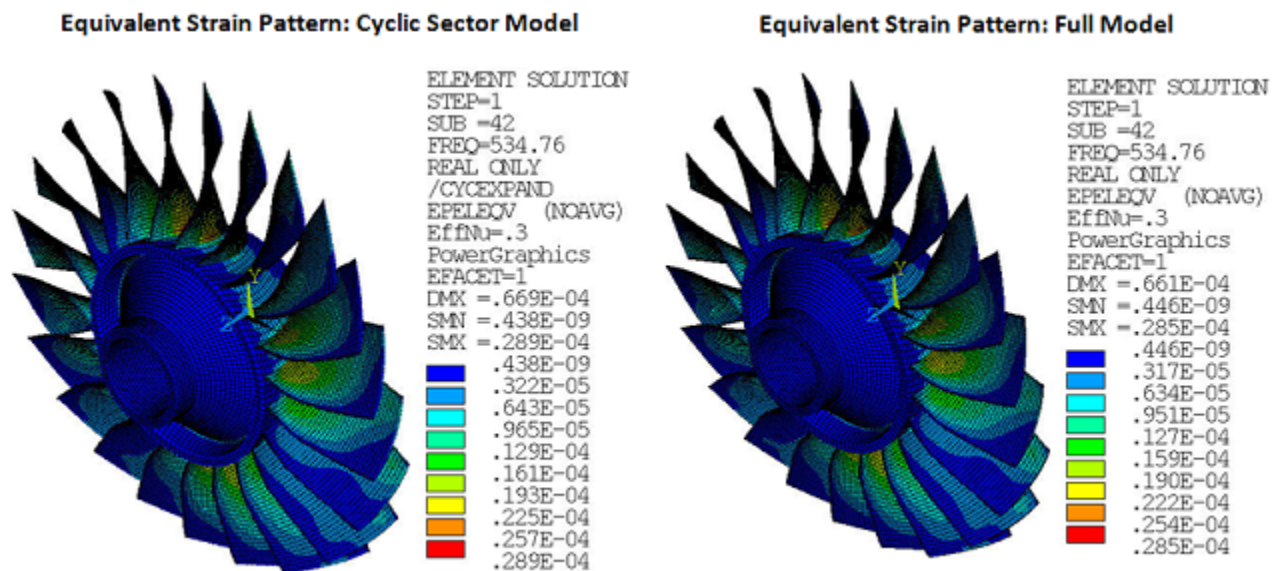


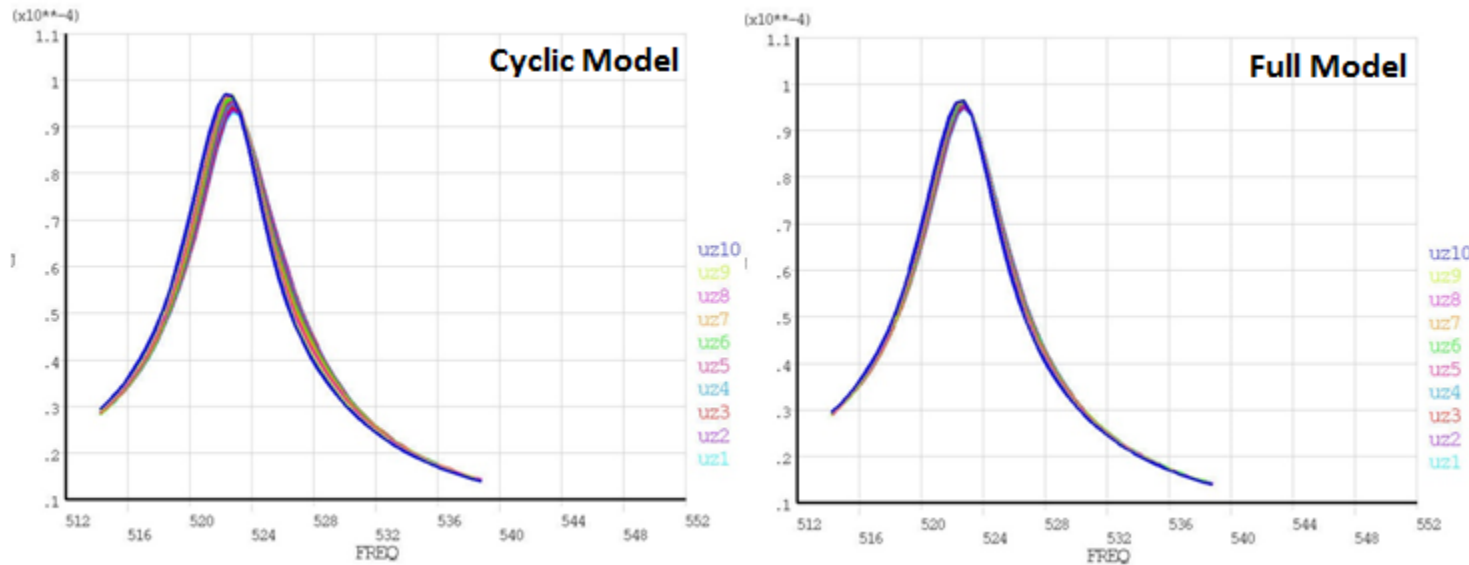
Figure 45.23: Equivalent Strain Pattern (Real Only) at Frequency of 534.76 Hz



The results show strong agreement between the cyclic-sector model and the full 360° model.

The nodal solution plots (**NSOL**) show the amplitude of a nodal degree-of-freedom (DOF) value with respect to the frequency of excitation:

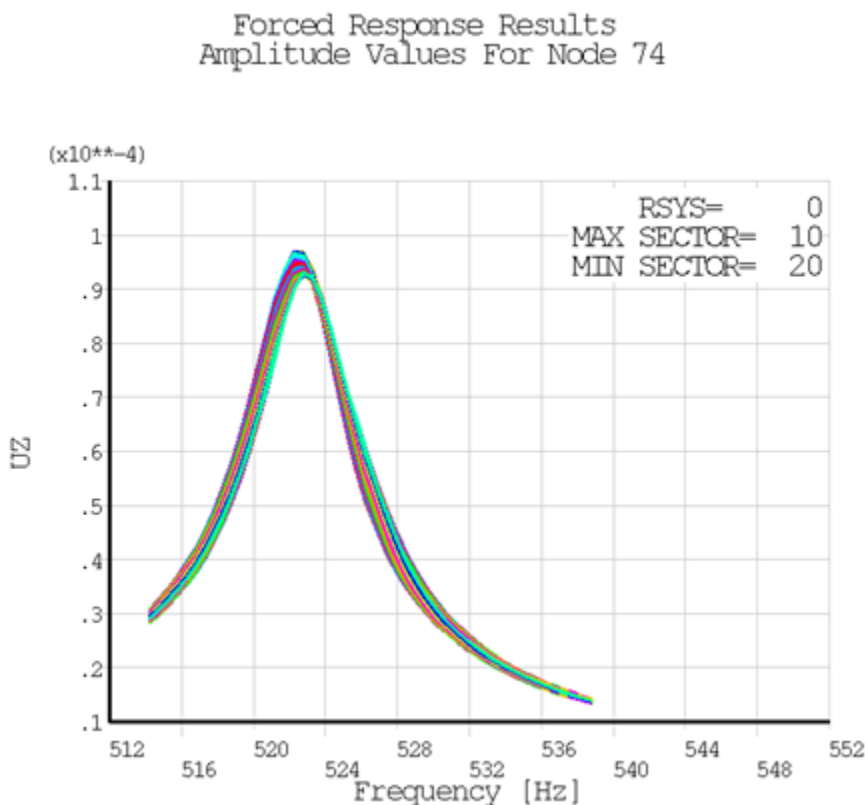
**Figure 45.24: Nodal Solution Plots with Respect to the Frequency of Excitation**



The plots indicate the occurrence of a resonance condition at 522.70 Hz. The displacement amplitude of nodes at symmetric angular positions in sectors 1 through 10 is plotted. The plots show strong agreement between the cyclic-sector and full 360° model results.

For the mistuned response analysis, the maximum directional deformation at the blade tip along the Z-direction is plotted using **PLCFREQ**, as shown in the following figure:

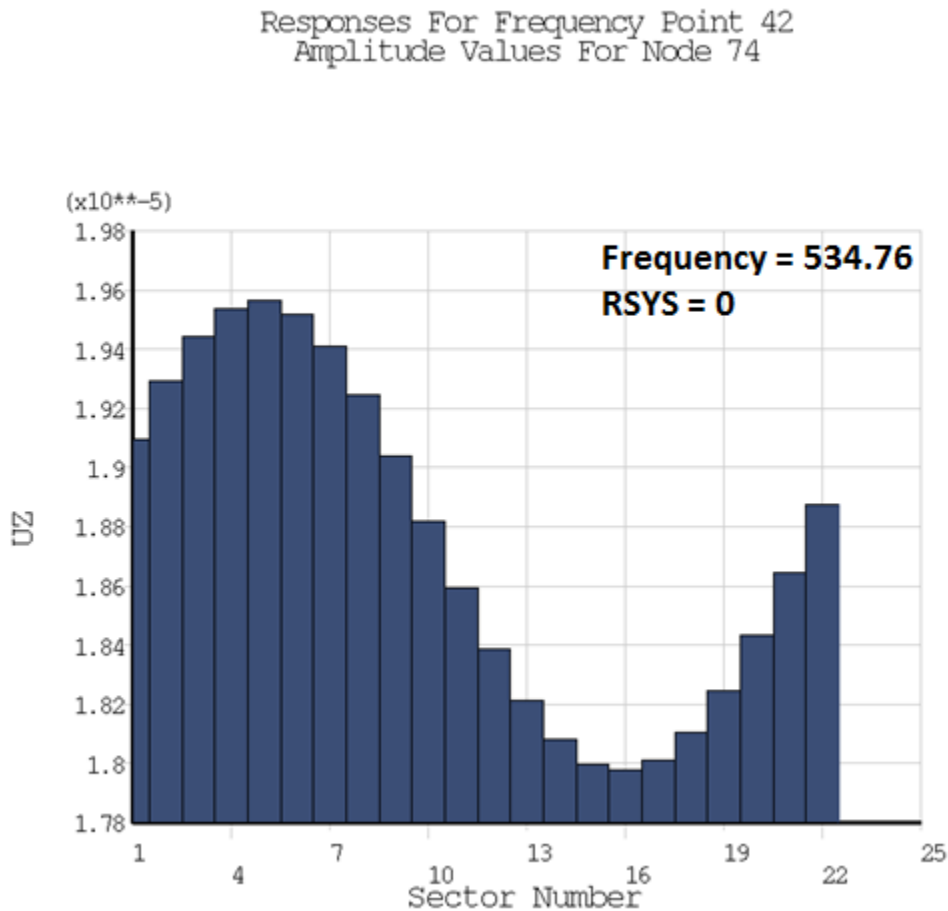
**Figure 45.25: Directional Deformation at the Blade Tip Along the Z-Direction**



The plot clearly indicates the sector numbers which contain the maximum and minimum values for the directional deformation along the Z-direction.

**PLCHIST** plots a histogram of the directional deformation along the Z-direction at the requested frequency of 534.76 Hz; one bar corresponds to one sector:

**Figure 45.26: CYCSPEC Histogram Response Plot at Frequency 534.76 Hz**



## 45.9. Recommendations

To perform a similar type of analysis, consider the following recommendations:

- The bladed disk must be meshed such that the blade elements and the node interface separating the blade from the disk and/or the platform are readily accessible.
- For good interpolation of the pressure data while mapping between the fluid-structural domains, it is recommended that you define the mesh density of the structural blade closely to the mesh density of the CFD model.
- Be sure to extract all modes that may contribute to the harmonic response. As a general guideline, modes contributing to the harmonic response fall in the range  $\frac{1}{2}\Omega$  to  $2\Omega$ , where  $\Omega$  is the harmonic frequency (**HARFRQ**) used in the subsequent harmonic solution. If mistuned, a range of  $\frac{1}{2}\Omega$  to  $5\Omega$  is recommended.
- The mistuning in a bladed disk should always be considered as small.

- For the case of a mistuned response analysis, all harmonic indices must be included.

## 45.10. References

The following references are used in this example problem:

1. Lim, S.H., et al. "Compact, Generalized Component Mode Mistuning Representation for Modeling Bladed Disk Vibration." *AIAA Journal*. 45.9 (2007): 2285-2298.
2. Singh, M.P., et al. "SAFE Diagram: A Design and Reliability Tool for Turbine Blading." *17th Turbomachinery Symposium*. Dallas, TX (1988).
3. Castanier, M.P., C. Pierre. "Modeling and Analysis of Mistuned Bladed Disk Vibration: Status and Emerging Directions." *Journal of Propulsion and Power*. 22.2 (2006).  
  
Rzadkowski, R., et al. "Forced Response of the Mistuned First Stage Compressor Bladed Disc of an Aircraft Engine - Experimental and Numerical Results." *13th World Congress in Mechanism and Machine Space*: Guanajuato, Mexico (2011).
4. Elder, R., S. Patil, W. Homes. "Investigation of Efficient CFD Methods for the Prediction of Blade Damping." *Proceedings of ASME Turbo Expo 2013*: San Antonio, TX, (2013).
5. Zhang, C., Z. Ye, F. Liu. "Numerical Researches on Aeroelastic Problem of a Rotor Due to IGV/Fan Interaction," *AIAA Aerospace Sciences Meeting Including the New Horizons Forum and Aerospace Exposition*: Orlando, FL (2009).

## 45.11. Input Files

The following files are used in this problem:

### CFX Pressure Data:

- `CFX_ExportResults_FT_10P_EO2.csv` – The common unsteady flow pressure data in .CSV format, exported from CFX.

### Cyclic-Sector Model:

- `sector_FE_model.dat` – The common input file for the cyclic-sector model of the rotor fan blade.
- `cyc_modal_analysis.dat` – Input file for the cyclic symmetry modal analysis of the rotor fan blade.
- `cyc_pre_modal_analysis.dat` – Input file for the cyclic symmetry nonlinear prestressed perturbed modal analysis of the rotor fan blade.
- `cyc_pre_tun_resp_analysis.dat` – Input file for the cyclic symmetry nonlinear prestressed perturbed mode-superposition harmonic (tuned response) analysis of the rotor fan blade.
- `cyc_pre_mis_resp_analysis.dat` – Input file for the cyclic symmetry nonlinear prestressed perturbed mode-superposition harmonic (mistuned response) analysis of the rotor fan blade.

### Full 360° Model:

- `full_360_FE_model.dat` – The common input file for the full model analysis of the rotor fan blade.

- `full_360_FE_model_mist.dat` – The common input file for the full model analysis of the mistuned rotor fan blade.
- `full_modal_analysis.dat` – Input file for the modal analysis of the full model rotor fan blade.
- `full_pre_modal_analysis.dat` – Input file for the nonlinear prestressed perturbed modal analysis of the full model rotor fan blade.
- `full_pre_tun_resp_analysis.dat` – Input file for the nonlinear prestressed perturbed mode-superposition harmonic (tuned response) analysis of the full model rotor fan blade.
- `full_pre_mis_resp_analysis.dat` – Input file for the nonlinear prestressed perturbed mode-superposition harmonic (mistuned response) analysis of the full model rotor fan blade.

The files are available in the `td-45` folder. See [Obtaining the Input Files \(p. xxxv\)](#) for more information.





---

# Index

## Symbols

3-D surface flaws, 235  
304L stainless steel plates , 421

## A

acoustic analysis, 501  
    boundary layer impedance (BLI) model, 631  
    examples, 461  
    low reduced frequency model, 631  
    noise mitigation, 631  
    normal surface velocity, 631  
    surface port, 631  
acoustic waves: absorbing, 461, 501  
adiabatic surfaces, 91  
aeroacoustics  
    viscothermal resonator, 631  
aircraft fuselage construction, 79  
aluminum liner, 127  
anisotropic hyperelasticity with viscoelasticity, 489  
anterior cruciate ligament (ACL) simulation, 489  
augmented Lagrangian formulation, 1, 15, 61, 175, 249  
automatic time stepping, 103  
axiharmonic meshing, 203  
axisymmetric and nonaxisymmetric parts: using both, 103  
axisymmetric models: performance benefits, 203

## B

B-bar method, 61  
back pain, 139  
beam element technology, 351  
bilinear isotropic hardening material, 401  
biomechanics, 139, 267, 377, 489  
biphasic model, 139  
Block Lanczos eigensolver, 175, 513  
Block Lanczos solver, 115, 203, 299, 311, 351  
BM3 piping system, 159  
bolt preload, 603  
bonded contact, 1, 79, 103, 175, 203, 299  
bonding, 421  
brake squeal, 1  
buckling analysis, 311

## C

C\*-integral calculation, 665  
calibrating a hyperelastic constitutive model, 225  
Campbell diagram analysis, 203  
camshaft, 103  
cardiovascular stent simulation, 377

centrifugal impeller blade, 175  
ceramic materials, 267  
Chaboche nonlinear kinematic hardening material, 115  
Class IV flextensional underwater acoustic transducer, 501  
co-rotational frame, 591  
coherency functions, 513  
cohesive zone model, 79  
complex eigensolvers, 1  
complex geometry: representing with beams, 351  
complex material orthotropy, 127  
component mode synthesis (CMS), 281  
composite laminated T-joint, 553  
composite material, 79, 351  
composite overwrapped pressure vessel (COPV), 127  
computational fluid dynamics (CFD), 91  
constitutive model parameters: selecting, 225  
contact, 1, 15, 43, 61, 79, 103, 115, 175, 203, 225, 249, 267, 299, 377, 389, 401  
contact friction, 421  
containing vessel, 363  
contour integral, 235  
convection loading, 91  
convergence difficulties: overcoming, 15, 61  
cooled turbine blade, 91  
copper bar, 249  
coupled pore-pressure element technology, 139  
coupled-field analysis, 421  
crack-growth simulation example, 553  
creep, 535  
creep response, 139  
critical speeds: identifying, 203  
cubic interpolation, 351  
curve fitting, 43, 225  
curved-shell structures, 147, 445  
cyclic symmetry analysis, 175  
    and linear perturbation, 175  
    example, 175  
cyclical thermal loading, 535

## D

damping, 1, 203  
debonding, 79  
deformed mesh: repairing, 61  
delamination, 79  
denture, 267  
Der Kiureghian CQC method, 159  
digger-arm assembly, 281  
displacement, 281  
displacement extrapolation method, 235

**E**

effective plastic strain, 61  
elastic material behavior, 249  
elastomeric compressive sealing, 15, 43  
elastoplastic material behavior, 249  
elastoplasticity, 535  
elbow element technology, 115, 159  
element birth and death, 377  
external pressure loading, 311

**F**

failure criteria (FC) analysis, 127  
far-field postprocessing, 461, 501  
fiber reinforcing, 127  
fictive temperature, 267  
filament winding, 127  
finite-deformation effects, 281  
fixed partial denture (FPD), 267  
flange sealing, 15, 43  
flexible and rigid parts, 281  
flextensional transducer analysis, 501  
fluid and solid interaction, 139  
fluid mass and compressibility, 363  
fluid-pressure penetration loading, 43  
fluid-structure interaction (FSI), 461, 501  
forced response analysis, 685  
Fourier nodes, 103, 203  
Fourier terms: specifying, 115  
fracture analysis, 235  
fracture mechanics  
    C\*-integral, 665  
    crack-growth simulation, 553  
friction stir welding (FSW), 421  
frictional contact, 1, 43  
full harmonic cyclic symmetry analysis, 175  
full linear non-prestressed modal analysis, 1  
full transient analysis, 159

**G**

gas material model, 363  
general axisymmetric elements, 103  
GPU Accelerator, 461  
ground motion  
    coherency and incoherency, 513  
    response spectrum, 513  
Gupta method, 159  
gyroscopic effects, 203

**H**

harmonic analysis, 461, 501  
harmonic response analysis, 603  
HHT time-integration method, 249

hot-rolling structural steel, 401  
hydrostatic fluid, 363  
hyperelastic constitutive model, 225  
hyperelastic seal, 15

**I**

impact, 249  
impact constraints, 363  
impeller blade assembly, 175  
incompressible hyperelastic material, 389  
inflated tire model, 363  
input files for these problems, xxxv  
interaction integral method, 235  
intervertebral disc (IVD), 139  
introduction, xxxv  
irregular and complex geometry modeling, 489

**J**

J-integrals, 235  
joints, 103, 281

**K**

knee ligament simulation, 489

**L**

large strain effects, 389  
large-deflection effects, 61, 103, 115, 127, 389  
large-rotation effects, 281  
layered-composite structure, 79  
lead-free solder bumps, 535  
Lindley-Yow method, 159  
line-to-surface contact, 377  
linear (eigenvalue) buckling analysis, 311  
linear elastic fracture mechanics, 235  
linear elastic isotropic material, 1  
linear perturbation  
    example, 1, 175  
linear perturbation method, 603  
linear static analysis, 235  
lumbar motion segment, 139

**M**

mesh distortion: repairing, 15, 61, 401  
mesh refinement, 15, 61, 401  
mesh: axiharmonic, 203  
metal bar on rigid wall impact, 249  
metal forming, 61  
missing mass response, 159  
mistuning, 685  
mixed u-P formulation, 61, 377, 401  
mixed-mode stress-intensity factors, 235  
modal analysis, 115, 203, 299, 461, 513

---

modal harmonic cyclic symmetry analysis, 175  
mode-superposition, 299  
Mooney-Rivlin hyperelastic models, 225, 377  
multibody system, 281  
multiframe restart, 15, 61  
multilinear kinematic hardening material, 115  
multipoint constraint (MPC), 1, 103, 175, 203, 281

## N

Nelson-Vaugh rotor, 203  
Neo-Hookean material model, 389, 591  
nesting, 15  
Newmark time-integration method, 249  
nonaveraged results file format, 351  
nonaxisymmetric and axisymmetric parts: using both, 103  
nonlinear buckling analysis, 311  
nonlinear large-deformation analysis, 61  
nonlinear perturbed modal analysis, 1  
nonlinear sparse solver, 15  
nonlinear stabilization, 43, 79, 311, 377  
nonlinear static analysis, 115, 127  
nonlinear structural analysis, 267  
nonlinear transient analysis, 103  
nonlinear transient dynamic analysis, 249  
nozzle extension  
    fabrication, 147  
    operation, 445  
nuclear island, 513  
nuclear piping system, 115, 159  
nuclear power plant, 513

## O

o-ring seal, 43  
offsets, 127, 147, 311, 445  
Ogden hyperelasticity, 15, 43  
orbit plot, 203  
orthotropic thermal expansion, 147, 445  
output controls, 235  
overconstraint, 281  
overview, xxxv  
overwrapped pressure vessel, 127

## P

Parker seal, 15  
partial nonlinear perturbed modal analysis, 1  
perfectly matched layers (PML), 461  
phase transformation, 617  
piezoelectric materials, 501  
plastic heat generation, 421  
plastic strain, 61  
post-buckling analysis, 311

postprocessing  
    sound pressure level (SPL), 461  
    velocity, 461  
power spectral density (PSD) analysis, 299, 513  
pressure loading, 311  
prestress effects, 175  
prestressed modal analysis, 115, 603  
prestressed modal cyclic symmetry analysis, 175  
primitives, 401  
printed circuit board (PCB), 299  
pseudoelasticity, 617

## Q

QRDAMP eigensolver, 1

## R

reduced-order CFD model, 91  
reinforcing, 127, 363  
reinforcing element technology, 127  
remeshing, 15, 61  
residual stresses, 267  
residual vectors, 299  
response power spectral density (RPSD), 299  
response-spectrum analysis (RSA), 159  
results discrepancies, xxxv  
rezoning  
    example, 15, 61, 401  
rigid and flexible parts, 281  
rigid material behavior, 249  
rigid responses, 159  
rigid-flexible contact, 389  
ring-gear forging, 61  
Robin boundary condition, 501  
rocket nozzle extension  
    fabrication, 147  
    operation, 445  
rotating-shaft sealing, 15, 43  
rotational velocity, 175  
rotordynamic analysis, 203  
rubber boot seal, 389

## S

secondary creep deformation, 665  
section offsets, 127, 147, 311, 445  
seismic event response, 513  
seismic loading, 115  
self contact, 389  
shaft assembly, 203  
shape memory alloy, 617  
shape memory effect, 617  
sheet aluminum alloy, 311  
shift function, 267

sintering, 267  
sliding frictional contact, 1  
SMA (see shape memory alloy)  
soft tissue, 139  
solid and fluid interaction, 139  
solid-shell element technology, 79  
speaker system: acoustic analysis of, 461  
spectrum analysis, 159  
spinal problems, 139  
square root of the sum of the squares (SRSS) method , 159  
static pressure, 175  
static structural analysis, 267  
stent-artery interaction, 377  
stiffened composite panel, 79  
stress linearization, 127  
stress-intensity factors (SIFs), 235  
structural-acoustic coupling, 461  
structural-shell element technology, 147, 445  
structural-thermal analysis, 421  
summary of technology demonstration problems, xxxv  
superelements, 281  
surface flaws, 235  
surface-projection-based contact, 389, 421  
symmetric expansion, 401, 461  
symmetric FSI, 461

## T

T-joint, 553  
T-stress, 235  
tapered beam section, 351  
technology demonstration tutorials, xxxv  
temperature distribution, 267  
thermal analysis, 267  
thermal loading, 147, 445  
thermal loading: cyclical, 535  
thermal-stress analysis, 91  
thermo-mechanical analysis, 535  
time integration, 249  
time stepping: automatic, 103  
time-incrementation controls (element-level), 249  
tire model, 363  
Tool-Narayanaswamy shift function, 267  
transducer, 501  
transient dynamic analysis, 249, 281  
transient effects , 103  
transient thermal analysis, 267  
transition zones: defining, 115  
turbine blade, 91

## U

unbalance response analysis, 203

unstable modes: predicting, 1  
unstable structures, 311  
UNSYM eigensolver, 1  
user-defined material model, 591  
UserMat subroutine, 591

## V

validating a hyperelastic constitutive model, 225  
VCCT, 553  
veneer, 267  
vertebral body, 139  
vibration: extreme, 203  
viscoelasticity, 267  
viscothermal resonator, 631  
von Mises stress, 91, 115, 139, 267  
vulcanized natural rubber material, 225

## W

welding: friction stir, 421  
whirl, 203  
wind turbine blade, 351  
wire bonding ultrasonic transducer, 603

## Z

zero period acceleration (ZPA), 159  
ZPA frequency, 159